M.J.N. PRIESTLEY
G.M. CALVI
M.J. KOWALSKY

Displacement-Based Seismic Design of Structures

ABSTRACT

Displacement-Based Seismic Design of Structures is a book primarily directed towards practicing structural designers who are interested in applying performance-based concepts to seismic design. Since much of the material presented in the book has not been published elsewhere, it will also be of considerable interest to researchers, and to graduate and upper-level undergraduate students of earthquake engineering who wish to develop a deeper understanding of how design can be used to control seismic response.

The design philosophy is based on determination of the optimum structural strength to achieve a given performance limit state, related to a defined level of damage, under a specified level of seismic intensity. Emphasis is also placed on how this strength is distributed through the structure. This takes two forms: methods of structural analysis and capacity design. It is shown that equilibrium considerations frequently lead to a more advantageous distribution of strength than that resulting from stiffness considerations. Capacity design considerations have been re-examined, and new and more realistic design approaches are presented to insure against undesirable modes of inelastic deformation.

The book considers a wide range of structural types, including separate chapters on frame buildings, wall buildings, dual wall/frame buildings, masonry buildings, timber structures, bridges, structures with isolation or added damping devices, and wharves. These are preceded by introductory chapters discussing conceptual problems with current force-based design, seismic input for displacement-based design, fundamentals of direct displacement-based design, and analytical tools appropriate for displacement-based design. The final two chapters adapt the principles of displacement-based seismic design to assessment of existing structures, and present the previously developed design information in the form of a draft building code.

The text is illustrated by copious worked design examples (39 in all), and analysis aids are provided in the form of a CD containing three computer programs covering moment-curvature analysis (*Cumbia*), linear-element-based inelastic time-history analysis (*Ruaumoko*), and a general fibre-element dynamic analysis program (*SeismoStruct*).

The design procedure developed in this book is based on a secant-stiffness (rather than initial stiffness) representation of structural response, using a level of damping equivalent to the combined effects of elastic and hysteretic damping. The approach has been fully verified by extensive inelastic time history analyses, which are extensively reported in the text. The design method is extremely simple to apply, and very successful in providing dependable and predictable seismic response.

DISPLACEMENT-BASED SEISMIC DESIGN OF STRUCTURES

M.J.N. PRIESTLEY
Centre of Research and Graduate Studies
in Earthquake Engineering and Engineering Seismology (ROSE School),
Istituto Universitario di Studi Superiori (IUSS),
Pavia, Italy

G.M. CALVI
Department of Structural Mechanics,
Università degli Studi di Pavia,
Pavia, Italy

M.J. KOWALSKY
Department of Civil, Construction, and Environmental Engineering,
North Carolina State University,
Raleigh, USA

"Every truth passes through three stages (before it is recognized)
In the first, it is ridiculed
In the second, it is violently opposed
In the third, it is regarded as self evident"

Arthur Schopenhauer (1788-1860)

"Analysis should be as simple as possible, but no simpler"

Albert Einstein (1879-1955)

"Strength is essential, but otherwise unimportant"

Hardy Cross[1] (1885-1959)

---

[1] Hardy Cross was the developer of the moment distribution method for structural calculation of statically indeterminate frames, generally used from the late thirties to the sixties, when it was superseded by structural analysis computer programs. It seems somehow prophetic that a brilliant engineer, who based the solution of structural problems on relative stiffness, wrote this aphorism that must have sounded enigmatic in the context of elastic analysis and design.

CONTENTS

PREFACE

Performance-based seismic design is a term widely used by, and extremely popular with, the seismic research community, but which is currently rather irrelevant in the practice of design and construction. In its purest form, it involves a large number of probabilistic considerations, relating to variability of seismic input, of material properties, of dimensions, of gravity loads, and of financial consequences associated with damage, collapse or loss of usage following seismic attack, amongst other things. As such, it is a difficult tool to use in the assessment of existing structures, and almost impossible to use, with any expectation of realism, in the design of new structures, where geometry becomes another variable, and an almost limitless number of possible design solutions exists.

Currently, probability theory is used, to some extent, in determination of the seismic input, which is typically based on uniform-hazard spectra. However, structural engineers take this information and design structures to code specified force levels which have been determined without any real consideration of risk of damage or collapse. Structural displacements, which can be directly related to damage potential through material strains (structural damage) and drifts (non-structural damage), are checked using coarse and unreliable methods at the end of the design process. At best, this provides designs that satisfy damage-control criteria, but with widely variable risk levels. At worst, it produces designs of unknown safety.

This text attempts to bridge the gap between current structural design, and a full (and possibly unattainable) probabilistic design approach, by using deterministic approaches, based on the best available information on analysis and material properties to produce structures that should **achieve**, rather than be bounded by, a structural or non-structural limit state under a specified level of seismic input. Structures designed to these criteria might be termed "uniform-risk" structures. The approach used is very simple — equivalent in complexity to the most simple design approach permitted in seismic design codes (the "equivalent lateral force procedure"), but will be unfamiliar to most designers, as the design displacement is the starting point. The design procedure determines the base-shear force, and the distribution of strength in the structure, to achieve this displacement. The process (displacements lead to strength) is thus the opposite of current design, where strength leads to an estimate of displacement. Although this requires a change in thinking on the part of the designer, it rapidly becomes automatic, and we believe, intellectually satisfying.

This book is primarily directed towards practising structural designers, and follows from two earlier books with which the principal author has been involved ("Seismic Design of Reinforced Concrete and Masonry Structures" (with T. Paulay), John Wiley, 1992, and "Seismic Design and Retrofit of Bridges" (with F. Seible and G.M. Calvi), John Wiley, 1996). These books primarily address issues of section design and detailing, and to a limited extent force-distribution in the class of structures addressed. Although great emphasis is given in these books to seismic design philosophy in terms of capacity design considerations, comparatively little attention is directed towards an examination of the optimum level of strength required of the building or bridge. This text addresses this aspect specifically, but also considers the way in which we distribute the required system strength (the base-shear force) through the structure. This takes two forms: methods of structural analysis, and capacity design. It is shown that current analysis methods have a degree of complexity incompatible with the coarseness of assumptions of member stiffness. Frequently, equilibrium considerations rather than stiffness considerations can lead to a simpler and more realistic distribution of strength. Recent concepts of inelastic torsional response have been extended and adapted to displacement-based design. Combination of gravity and seismic effects, and P-Δ effects are given special consideration.

Capacity design considerations have been re-examined on the basis of a large number of recent research studies. Completely new and more realistic information is provided for a wide range of structures. Section analysis and detailing are considered only where new information, beyond that presented in the previous two texts mentioned above, has become available.

The information provided in this book will be of value, not just to designers using displacement-based principles, but also to those using more conventional force-based design, who wish to understand the seismic response of structures in more detail, and to apply this understanding to design.

Although the primary focus of this book is, as noted above, the design profession, it is also expected to be of interest to the research community, as it provides, to our knowledge, the first attempt at a complete design approach based on performance criteria. A large amount of new information not previously published is presented in the book. We hope it will stimulate discussion and further research in the area. The book should also be of interest to graduate and upper-level undergraduate students of earthquake engineering who wish to develop a deeper understanding of how design can be used to control seismic response.

The book starts with a consideration in Chapter 1 as to why it is necessary to move from force-based to displacement-based seismic design. This is largely related to the guesses of initial stiffness necessary in force-based design, and the inadvisability of using these initial stiffness values to distribute seismic lateral force through the structure. Chapter 2 provides a state-of-the-science of seismic input for displacement-based design, particularly related to characteristics of elastic and inelastic displacement spectra. The fundamental concepts behind "direct displacement-based seismic design" – so-called because no iteration is required in the design process – are developed in Chapter 3.

... tools specially relevant to displacement-based design are discussed in Chapter ... The principles of displacement-based design are then applied to different structural ... frames, walls, dual wall/frames, masonry and timber buildings, bridges, ... with seismic isolation and added damping, wharves) in the following chapters, ... are subsequently adapted to seismic assessment in Chapter 13. Finally, the principles ... presented in Chapter 14 in a code format to provide a possible basis for future ... The text is illustrated by design examples throughout.

... design procedure outlined in this book has been under development since first ... in the early 1990's, and is now in a rather complete form, suitable for design ... Much of the calibration and analytical justification for the approach has ... in a considerable number of research projects over the past five or so years, and ... consequently wish to particularly acknowledge the work of Juan Camillo ... Alejandro Amaris, Katrin Beyer, Carlos Blandon, Chiara Casarotti, Hazim ... Damian Grant, Pio Miranda, Juan Camillo Ortiz, Didier Pettinga, Dario Pietra, ... Suarez, and Tim Sullivan, amongst others.

... design verification examples described in the book have been prepared with the ... of Rui Pinho, Dario Pietra, Laura Quaglini, Luis Montejo and Vinicio Suarez. ... structural analysis software employed in such design verifications has been kindly ... by Prof. Athol Carr, Dr. Stelios Antoniou, Dr. Rui Pinho and Mr. Luis Montejo, ... agreed to make these programs available in the Structural Analysis CD.

... people who need special acknowledgement are Prof. Tom Paulay and Dr. Rui ... who each read sections of the manuscript in draft form, noted errors and made ... for improvements. Their comments have significantly improved the final ... and remaining errors are the responsibility of the authors alone. Advice from ... John Bommer, Prof. Ezio Faccioli, and Dr. Paul Somerville on aspects of ... and of Prof. Guido Magenes on masonry structures is also gratefully ... edged.

... Priestley, *Christchurch*
... Calvi, *Pavia*
... Kowalsky, *Raleigh*

... 2007

1

INTRODUCTION: THE NEED FOR DISPLACEMENT-BASED SEISMIC DESIGN

1.1 HISTORICAL CONSIDERATIONS

Earthquakes induce forces and displacements in structures. For elastic systems these are directly related by the system stiffness, but for structures responding inelastically, the relationship is complex, being dependent on both the current displacement, and the history of displacement during the seismic response. Traditionally, seismic structural design has been based primarily on forces. The reasons for this are largely historical, and related to how we design for other actions, such as dead and live load. For such cases we know that force considerations are critical: if the strength of the designed structure does not exceed the applied loads, then failure will occur.

It has been recognized for some considerable time that strength has a lesser importance when considering seismic actions. We regularly design structures for less than anticipated elastic force levels, because we understand that well-designed structures possess ductility, and can deform inelastically to the required deformations imposed by the earthquake without loss of strength. This implies damage, but not collapse. Since design-level earthquakes are by definition rare events, with a typical annual probability of occurrence (or exceedence) of about 0.002, we accept the possibility of damage under the design earthquake as economically acceptable, and benefit economically from the reduced construction costs associated with the reduced design force levels.

The above premise is illustrated in Fig. 1.1, which is based on the well known "equal-displacement" approximation. It has been found, from inelastic time-history analyses, that for many structures whose fundamental period is in the range of (say) 0.6 – 2.0 seconds, maximum seismic displacements of elastic and inelastic systems with the same initial stiffness and mass (and hence the same elastic periods) are very similar. Later, in Section 4.9.2 g. the assumptions behind these analyses will be questioned. Figure 1.1 represents idealized elasto-plastic seismic force-displacement envelopes of three simple bridge structures of equal mass and elastic stiffness, but of different strength. As is discussed in relation to Fig.1.4, the assumption of equal stiffness, but different strength is not compatible with properties of sections with equal dimensions, and is adopted here purely to facilitate discussion. According to the equal displacement approximation, each structure will be subjected to the same maximum displacement Δ_{max}.

Figure 1.1 allows us to introduce the concepts of "force-reduction factors" and "ductility", which are fundamental tools in current seismic design. For a structure with

1
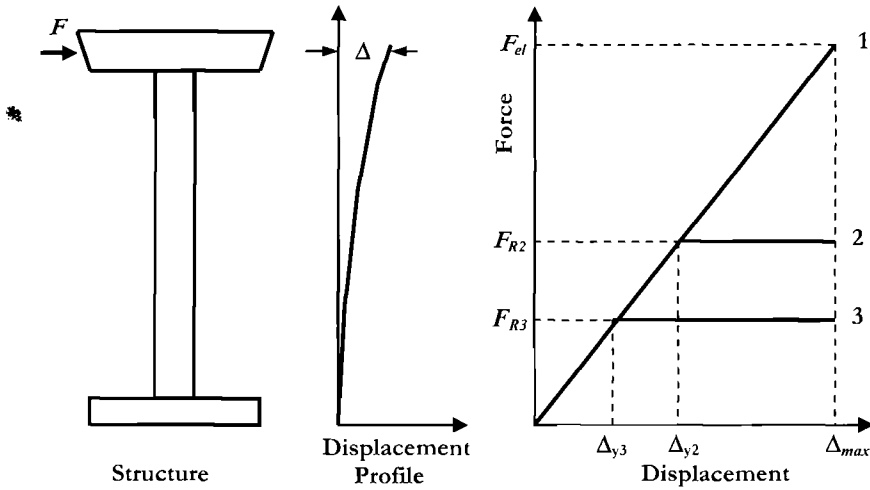
Fig. 1.1 **Seismic Force-Displacement Response of Elastic and Inelastic Systems:
The "Equal Displacement" Approximation**

linear elastic response to the design earthquake, the maximum force developed at peak displacement is F_{el}. We label this as Structure 1. Structures 2 and 3 are designed for reduced ultimate strength levels of F_{R2} and F_{R3} where the strengths are related to the elastic response level by the force-reduction factors

$$F_{R2} = F_{el} / R_2 \qquad\qquad F_{R3} = F_{el} / R_3 \qquad\qquad (1.1)$$

"Ductility" can relate to any measure of deformation (e.g. displacement, curvature, strain) and is the ratio of maximum to effective yield deformation. In this context, "maximum deformation" could mean maximum expected deformation, in which case we talk of ductility demand, or it could mean deformation capacity, in which case we use the term ductility capacity. In the case of Fig.1.1, lateral displacement is the measure of deformation, and the displacement ductility factors for the two inelastic systems are thus

$$\mu_2 = \Delta_{max} / \Delta_{y2} = F_{el} / F_{R2} = R_2 \; ; \quad \mu_3 = \Delta_{max} / \Delta_{y3} = F_{el} / F_{R3} = R_3 \qquad (1.2)$$

Thus, for the equal displacement approximation, the displacement ductility factor is equal to the force-reduction factor.

An important conclusion can be made from Fig.1.1. That is, for inelastic systems, the strength is less important than the displacement. This is obvious, since the strengths F_{R2} and F_{R3} have little influence on the final displacement Δ_{max}. It would thus seem more logical to use displacement as a basis for design. For elastic systems, it is exactly equivalent to use either displacement or force as the fundamental design quantity. This is

illustrated in Fig.1.2, where the design earthquake, for a typical firm ground site is represented by both acceleration (Fig.1.2a) and displacement (Fig.1.2b) spectra.

(a) Acceleration Spectrum for 5% damping   (b Displacement Spectrum for 5% damping
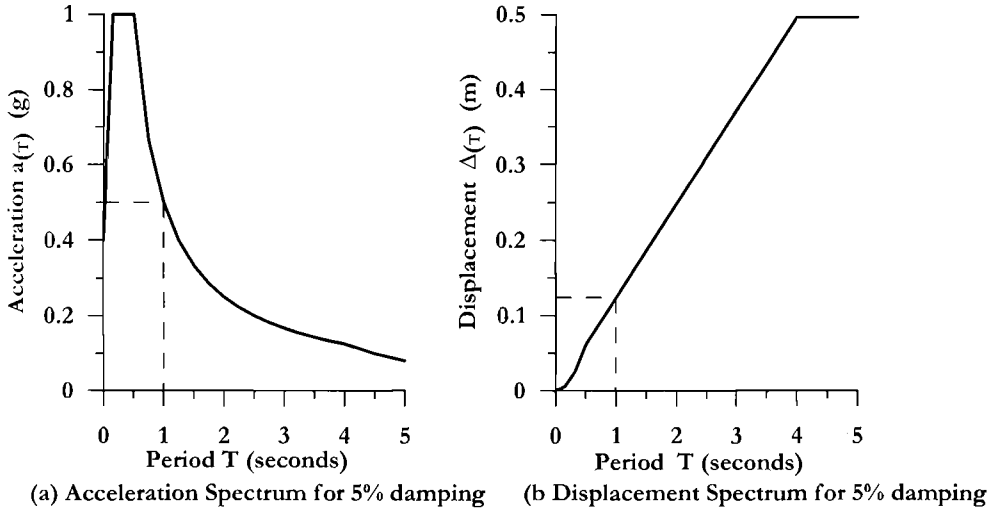
Fig. 1.2 Acceleration and Displacement Response Spectra for Firm Ground (0.4g)

Traditional seismic design has been based on the elastic acceleration spectrum. For an elastically responding single-degree-of-freedom (SDOF) structure, the response acceleration, $a_{(T)}$, corresponding to the fundamental period T, is found and the corresponding force, F and displacement Δ are given by

$$F = m \cdot a_{(T)} \cdot g ; \qquad \Delta = F / K \qquad (1.3)$$

where K is the system stiffness, m is the system mass and g is the acceleration due to gravity.

Alternatively the displacement spectrum of Fig.1.2(b) could be used directly. In this case the response displacement $\Delta_{(T)}$ corresponding to the elastic period is directly read, and the corresponding force calculated as

$$F = K \cdot \Delta_{(T)} \qquad (1.4)$$

In both cases the elastic period must first be calculated, but it is seen that working from the displacement spectrum requires one less step of calculation than working from the acceleration spectrum, since the mass is not needed once the period has been calculated. Although both approaches are directly equivalent, it would seem that using

response displacement rather than response acceleration would be a more logical basis for design of elastic systems, as well as inelastic systems.

An approximate relationship between peak acceleration and displacement response based on steady-state sinusoidal response is given by:

$$\Delta_{(T)} = \frac{T^2}{4\pi^2} . a_{(T)} g \tag{1.5}$$

where $a_{(T)}$ is expressed as multiples of the acceleration of gravity (as in Fig.1.2(a)). Although this relationship has been widely used in the past, it is approximate only, with the errors increasing with period.

The reason that seismic design is currently based on force (and hence acceleration) rather than displacement, is, as stated above, based largely on historical considerations. Prior to the 1930's, few structures were specifically designed for seismic actions. In the 1920's and early 1930's several major earthquakes occurred (Japan: 1925 Kanto earthquake, USA: 1933 Long Beach earthquake, New Zealand: 1932 Napier earthquake). It was noted that structures that had been designed for lateral wind forces performed better in these earthquakes than those without specified lateral force design. As a consequence, design codes started to specify that structures in seismic regions be designed for lateral inertia forces. Typically, a value of about 10% of the building weight, regardless of building period, applied as a vertically distributed lateral force vector, proportional to the mass vector, was specified.

During the 1940's and 1950's, the significance of structural dynamic characteristics became better understood, leading, by the 1960's, to period-dependent design lateral force levels in most seismic design codes. Also in the 1960's with increased understanding of seismic response, and the development of inelastic time-history analysis, came awareness that many structures had survived earthquakes that calculations showed should have induced inertia forces many times larger than those corresponding to the structural strength. This lead to development of the concept of ductility, briefly discussed earlier in this chapter, to reconcile the apparent anomaly of survival with inadequate strength. Relationships between ductility and force-reduction factor, such as those of Eq.(1.2), and others such as the "equal energy" approximation, which appeared more appropriate for short-period structures, were developed as a basis for determining the appropriate design lateral force levels.

During the 1970's and 1980's much research effort was directed to determining the available ductility capacity of different structural systems. Ductility considerations became a fundamental part of design, and key text books written in the 1960's and 1970's [e.g. C13,N4,P31] have remained as the philosophical basis for seismic design, essentially till the present time. In order to quantify the available ductility capacity, extensive experimental and analytical studies were performed to determine the safe maximum displacement of different structural systems under cyclically applied displacements. This may be seen as the first departure from force as the basis for design. Required strength

was determined from a force-reduction factor that reflected the perceived ductility capacity of the structural system and material chosen for the design. Nevertheless, the design process was still carried out in terms of required strength, and displacement capacity, if directly checked at all, was the final stage of the design. Also during this era the concept of "capacity design" was introduced[P31], where locations of preferred flexural plastic hinging were identified, and alternative undesirable locations of plastic hinges, and undesirable modes of inelastic deformation, such as shear failure, were inhibited by setting their strength higher than the force levels corresponding to that of the desired inelastic mechanism. Ductility was perceived as more important than displacement capacity, though the two were clearly related.

In the 1990's, textbooks [e.g. P1, P4] with further emphasis on displacement considerations and capacity design became widely used for seismic design of concrete and masonry structures, and the concept of "performance-based seismic design", based largely on displacement considerations, and discussed in further detail at the end of this chapter, became the subject of intense research attention. It may be seen from this brief description of the history of seismic design, that initially design was purely based on strength, or force, considerations using assumed rather than valid estimates of elastic stiffness. As the importance of displacement has come to be better appreciated in recent years, the approach has been to attempt to modify the existing force-based approach to include consideration of displacement, rather than to rework the procedure to be based on a more rational displacement basis.

1.2 FORCE-BASED SEISMIC DESIGN

Although current force-based design is considerably improved compared with procedures used in earlier years, there are many fundamental problems with the procedure, particularly when applied to reinforced concrete or reinforced masonry structures. In order to examine these problems, it is first necessary to briefly review the force-based design procedure, as currently applied in modern seismic design codes.

The sequence of operations required in force-based seismic design is summarized in Fig. 1.3.

1. The structural geometry, including member sizes is estimated. In many cases the geometry may be dictated by non-seismic load considerations.

2. Member elastic stiffnesses are estimated, based on preliminary estimates of member size. Different assumptions are made in different seismic design codes about the appropriate stiffnesses for reinforced concrete and masonry members. In some cases (e.g. uncracked section) stiffness is used, while in some codes reduced section stiffness is taken, to reflect the softening caused by expected cracking when approaching yield-level response.

3. Based on the assumed member stiffnesses, the fundamental period (equivalent lateral force approach) or periods (multi-mode dynamic analysis) are calculated. For a MDOF representation of the structure, the fundamental period is given by:
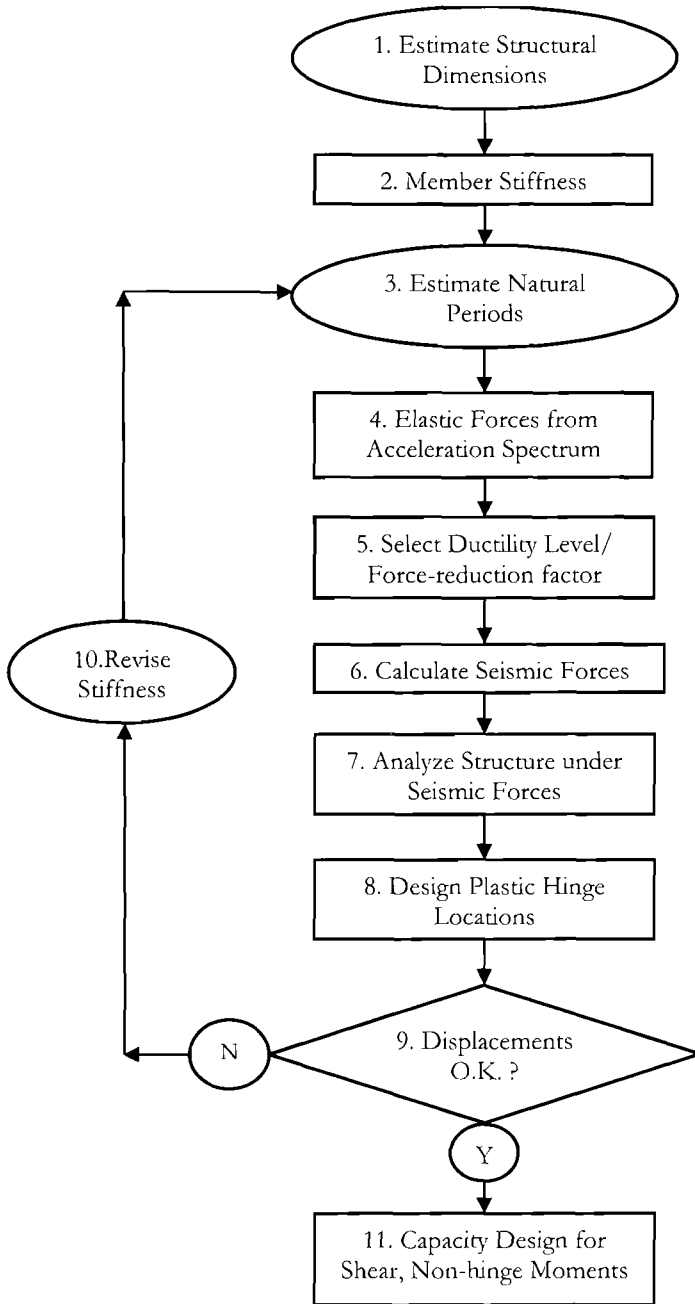
Fig. 1.3   Sequence of Operations for Force-Based Design

$$T = 2\pi\sqrt{\frac{m_e}{K}} \qquad (1.6)$$

where m_e is the effective seismic mass (normally taken as the total mass).

In some building codes a height-dependent fundamental period is specified, independent of member stiffness, mass distribution, or structural geometry. The typical form[X9] of this is given in Eq.(1.7):

$$T = C_1 (H_n)^{0.75} \qquad (1.7)$$

where C_1 depends on the structural system, and H_n is the building height. Recently USA codes[X4] have expressed the exponent of Eq.(1.7) as a variable dependent on structural material and system, with the value varying between 0.75 and 0.9.

Lateral force levels calculated from stiffness-based periods (single mode or multi-mode) are not permitted to deviate from the forces based on the height-dependent period equation by more than some specified percentage.

4. The design base shear $V_{Base,E}$ for the structure corresponding to elastic response with no allowance for ductility is given by an equation of the form

$$V_{Base,E} = C_T \cdot I \cdot (gm_e) \qquad (1.8)$$

where C_T is the basic seismic coefficient dependent on seismic intensity, soil conditions and period T (e.g. Fig. 1.2(a)), I is an importance factor reflecting different levels of acceptable risk for different structures, and g is the acceleration of gravity.

5. The appropriate force-reduction factor R_μ corresponding to the assessed ductility capacity of the structural system and material is selected. Generally R_μ is specified by the design code and is not a design choice, though the designer may elect to use a lesser value than the code specified one.

6. The design base shear force is then found from

$$V_{Base} = \frac{V_{Base,E}}{R_\mu} \qquad (1.9)$$

The base shear force is then distributed to different parts of the structure to provide the vector of applied seismic forces. For building structures, the distribution is typically proportional to the product of the height and mass at different levels, which is compatible with the displaced shape of the preferred inelastic mechanism (beam-end plastic hinges plus column-base plastic hinges for frames; wall-base plastic hinges for wall structures). The total seismic force is distributed between different lateral force-resisting elements, such as frames and structural walls, in proportion to their elastic stiffness.

7. The structure is then analyzed under the vector of lateral seismic design forces, and the required moment capacities at potential locations of inelastic action (plastic hinges) is determined. The final design values will depend on the member stiffness.

8. Structural design of the member sections at plastic hinge locations is carried out, and the displacements under the seismic action are estimated.

9. The displacements are compared with code-specified displacement limits.

10. If the calculated displacements exceed the code limits, redesign is required. This is normally effected by increasing member sizes, to increase member stiffness.

11. If the displacements are satisfactory, the final step of the design is to determine the required strength of actions and members that are not subject to plastic hinging. The process known as capacity design [P1, P31] ensures that the dependable strength in shear, and the moment capacity of sections where plastic hinging must not occur, exceed the maximum possible input corresponding to maximum feasible strength of the potential plastic hinges. Most codes include a prescriptive simplified capacity design approach.

The above description is a simplified representation of current force-based design. In many cases the force levels are determined by multi-modal analysis (sometimes called dynamic analysis). The way in which the modal contributions are combined will be discussed in some detail in sections relating to different structural systems. Some design codes, such as the New Zealand Loadings Code [X1] define inelastic acceleration design spectra that directly include the influence of ductility rather than using an elastic spectrum and a force-reduction factor (see Fig. 1.20(a), e.g.).

1.3 PROBLEMS WITH FORCE-BASED SEISMIC DESIGN

1.3.1 Interdependency of Strength and Stiffness

A fundamental problem with force-based design, particularly when applied to reinforced concrete and reinforced masonry structures is the selection of appropriate member stiffness. Assumptions must be made about member sizes before the design seismic forces are determined. These forces are then distributed between members in proportion to their assumed stiffness. Clearly if member sizes are modified from the initial assumption, then the calculated design forces will no longer be valid, and recalculation, though rarely carried out, is theoretically required.

With reinforced concrete and reinforced masonry, a more important consideration is the way in which individual member stiffness is calculated. The stiffness of a component or element is sometimes based on the gross-section stiffness, and sometimes on a reduced stiffness to represent the influence of cracking. A common assumption is 50% of the gross section stiffness [X2, X3], though some codes specify stiffnesses that depend on member type and axial force. In the New Zealand concrete design code [X6] values as low as 35% of gross section stiffness are specified for beams. Clearly the value of stiffness assumed will significantly affect the design seismic forces. With the acceleration spectrum of Fig. 1.2(a), the response acceleration between $T = 0.5$ sec and $T = 4.0$ sec is inversely proportional to the period. In this period range the stiffness-based period

Eq.(1.6) implies a reduction in seismic design force of 40% for a section stiffness of 35% gross versus 100% gross stiffness.

Regardless of what assumption is made, the member stiffness is traditionally assumed to be independent of strength, for a given member section. To examine this assumption, consider the flexural rigidity which can be adequately estimated from the moment-curvature relationship in accordance with the beam equation:

$$EI = M_N / \phi_y \qquad (1.10)$$

where M_N is the nominal moment capacity, and ϕ_y is the yield curvature based on the equivalent bi-linear representation of the moment-curvature curve. The assumption of constant member stiffness implies that the yield curvature is directly proportional to flexural strength, as shown in Fig. 1.4(a). Detailed analyses, and experimental evidence show that this assumption is invalid, in that stiffness is essentially proportional to strength, and the yield curvature is essentially independent of strength, for a given section, as shown in Fig.1.4(b). Verification of this statement is provided in Section 4.4

(a) Design Assumption
(constant stiffness)

(b) Realistic Conditions
(constant yield curvature)
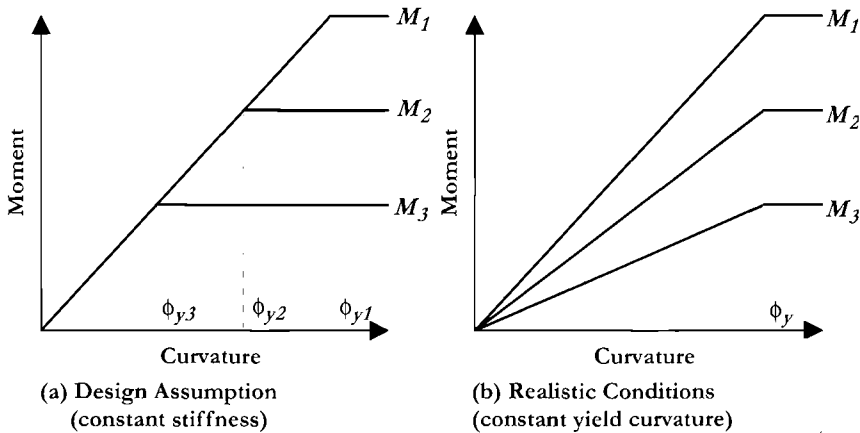
Fig. 1.4 Influence of Strength on Moment-Curvature Relationship

As a consequence of these findings it is not possible to perform an accurate analysis of either the elastic structural periods, nor of the elastic distribution of required strength throughout the structure, until the member strengths have been determined. Since the required member strengths are the end product of force-based design, the implication is that successive iteration must be carried out before an adequate elastic characterization of the structure is obtained. Although this iteration is simple, it is rarely performed by designers, and does not solve additional problems associated with initial stiffness representation, outlined later in this chapter.

It should be noted that the problem of estimating stiffness is not unique to concrete and masonry structures. In design of a steel frame structure, the general dimensions of

storey height, bay width, and even approximate beam depth may be established before the seismic design is started. The approximate beam depth will normally be defined by selecting an ASCE W-group [e.g. W18] or equivalent. Within each W-group, the variation in weight (and in corresponding strength) is achieved by varying the distance between the rollers defining the total section depth. Within each W-group, the strength can vary by several hundred percent, as the flange thickness changes. It has been shown[S3] that despite the variation in strength, the yield curvature is essentially constant over the W-group, and hence the strength and stiffness are proportional, as for concrete beams. The constant of proportionality, however, varies between different W-groups. This is discussed in more detail in Section 5.3.6

The assumption that the elastic characteristics of the structure are the best indicator of inelastic performance, as implied by force-based design is in itself clearly of doubtful validity. With reinforced concrete and masonry structures the initial elastic stiffness will never be valid after yield occurs, since stiffness degrades due to crushing of concrete, Bauschinger softening of reinforcing steel, and damage on crack surfaces. This is illustrated in the idealized force-displacement hysteresis for a reinforced concrete structure shown in Fig. 1.5. A first cycle of inelastic response is represented by the lines **1, 2, 3, 4, 5,** and **6.** A second cycle to the same displacement limits is represented by the lines **7, 8, 9**. After yield and moderate inelastic response, the initial stiffness **1** becomes irrelevant, even to subsequent elastic response. Reloading stiffnesses **4, 7,** and **9** are substantially lower than the initial value, as are the unloading stiffnesses **3, 6,** and **8**. It would seem obvious that structural characteristics that represented performance at maximum response might be better predictors of performance at maximum response than the initial values of stiffness and damping.
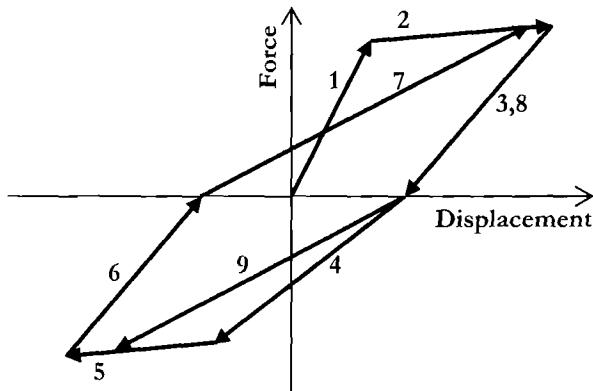
Fig. 1.5 Idealized Reinforced Concrete Force-Displacement Response

1.3.2 Period Calculation

As discussed in the previous section, considerable variation in calculated periods can result as a consequence of different assumptions for member stiffness. When the height-

dependent equations common in several codes are considered, the potential variations are exacerbated. As part of a recent study[P2], fundamental periods of a number of structural wall buildings were calculated based on different design assumptions and compared. The results are shown in Table 1.1

Values based on the code equation refer to Eq. (1.7) with C_I =0.075, and H_n in metres, in accordance with EC8, the European seismic code[X9]. The centre column of Table 1.1 presents results of modal analysis based on 50% of the gross section stiffness. Values in the column labelled Moment-Curvature also are based on modal analysis, but the wall stiffnesses are found from moment-curvature analyses of the designed walls. It is clear that the height-dependent equation results in very low estimates of fundamental period, and that the use of $0.5I_{gross}$, though less conservative, is still unrealistically low.

It is often stated that it is conservative, and hence safe, to use artificially low periods in seismic design. However, as has been already discussed, strength is less of an issue in seismic design than is displacement capacity. Calculated displacement demand based on an artificially low period will also be low, and therefore non-conservative. Methods for estimating displacement demand for structures designed by force considerations are discussed in Section 1.3.7.

Table 1.1 Fundamental Periods of Wall Buildings from Different Approaches[P2]

WALL STOREYS	EQUATION (1.7)	$I = 0.5I_{gross}$	Moment-Curvature	EQUATION (1.12)
2	0.29	0.34	0.60	0.56
4	0.48	0.80	1.20	1.12
8	0.81	1.88	2.26	2.24
12	1.10	2.72	3.21	3.36
16	1.37	3.39	4.09	4.48
20	1.62	3.65	4.77	5.60

It should be noted that for a number of years NEHRP[X8] has shown figures comparing measured building periods with equations similar to Eq.(1.7), with reasonable agreement. However the measurements have been taken at extremely low levels of excitation (normally resulting from ambient wind vibration), where non-structural participation is high, and sections (in the case of concrete and masonry buildings) are uncracked. The periods obtained in this fashion have no relevance to response at or approaching nominal strength of the building, which, as is discussed in Section 1.3.3 is appropriate for elastic structural characterization.

It is worth noting that an alternative to the height-dependent Eq.(1.7), that in the past has been incorporated in some building codes for frame structures is:

$$T = 0.1n \tag{1.11}$$

where **n** is the number of storeys. Recent research[C5] has suggested the use of an alternative simple expression:

$$T = 0.1H_n \ (\textbf{\textit{H}}_n \text{ in m}) \qquad = 0.033H_n \ (\textbf{\textit{H}}_n \text{ in ft}) \qquad (1.12)$$

where $\textbf{\textit{H}}_n$ is the building height. With a 3m storey height, Eq.(1.12) predicts effective periods three times that from Eq.(1,11). As noted, Eqs.(1.11) and (1.12) refer to frame buildings. However it is of interest to compare the results predicted from Eq.(1.12) with the wall periods of Table 1.1. These structures had storey heights of 2.8m. The predictions of Eq.(1.12) are included in the final column of Table 1.1, and are seen to be in very close agreement with the results from modal analysis based on moment-curvature derived stiffnesses for walls up to 12 storeys, and are still acceptable up to 20 storeys. This may indicate that fundamental elastic periods of frame and wall buildings designed to similar drift limits (as in this case) will be rather similar.

1.3.3 Ductility Capacity and Force-Reduction Factors

The concept of ductility demand, and its relation to force-reduction factor was introduced in relation to Fig.1.1. Although the definitions of Eq.(1.2) appear straightforward in the context of the idealizations made in Fig. 1.1, there are problems when realistic modelling is required. It has long been realized that the equal-displacement approximation is inappropriate for both very short-period and very long-period structures, and is also of doubtful validity for medium period structures when the hysteretic character of the inelastic system deviates significantly from elasto-plastic.

Further, there has been difficulty in reaching consensus within the research community as to the appropriate definition of yield and ultimate displacements. With reference to Fig. 1.6(b), the yield displacement has variously been defined as the intersection of the line through the origin with initial stiffness, and the nominal strength (point **1**), the displacement at first yield (point **2**), and the intersection of the line through the origin with secant stiffness through first yield, and the nominal strength (point **3**), amongst other possibilities. Typically, displacements at point **3** will be 1.8 to 4 times the displacements at point **1**. Displacement capacity, or ultimate displacement, also has had a number of definitions, including displacement at peak strength (point **4**), displacement corresponding to 20% or 50% (or some other percentage) degradation from peak (or nominal) strength, (point **5**) and displacement at initial fracture of transverse reinforcement (point **6**), implying imminent failure.

Clearly, with such a wide choice of limit displacements, there has been considerable variation in the assessed experimental displacement ductility capacity of structures. This variation in assessed ductility capacity has, not surprisingly, been expressed in the codified force-reduction factors of different countries. In the United States of America, force-reduction factors as high as 8.0 are permitted for reinforced concrete frames [X4]. In other countries, notably Japan and Central America, maximum force-reduction factors of about 3.0 apply for frames. Common maximum values for force-reduction factors for

different structural types and materials specified in different seismic regions are provided in Table 1.2. With such a wide diversity of opinion as to the appropriate level of force-reduction factor, the conclusion is inescapable that the absolute value of the strength is of relatively minor importance. This opinion has already been stated in this text.

(a) Equal Displacement Approximation

(b) Definition of Yield and Ultimate Displacement
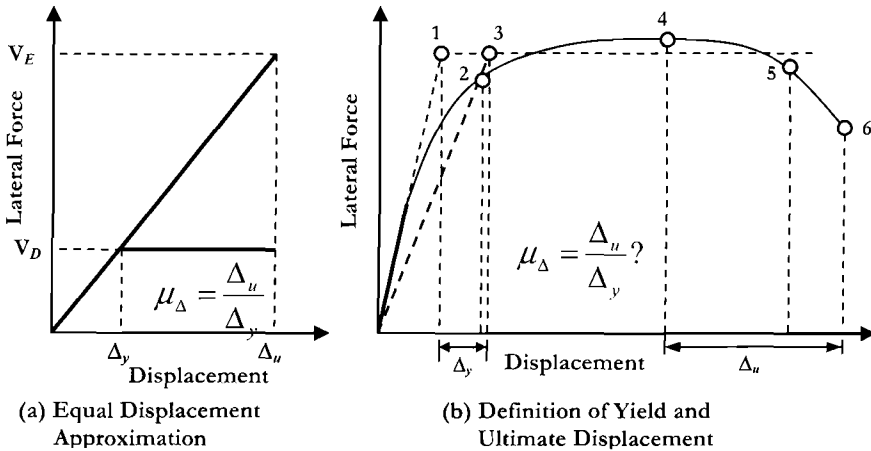
Fig.1.6   Defining Ductility Capacity

Table 1.2   Examples of Maximum Force-Reduction Factors for the Damage-Control Limit State in Different Countries

Structural Type and Material	US West Coast	Japan	New** Zealand	Europe
Concrete Frame	8	1.8-3.3	9	5.85
Conc. Struct. Wall	5	1.8-3.3	7.5	4.4
Steel Frame	8	2.0-4.0	9	6.3
Steel EBF*	8	2.0-4.0	9	6.0
Masonry Walls	3.5	-	6	3.0
Timber (struct. Wall)	-	2.0-4.0	6	5.0
Prestressed Wall	1.5		-	-
Dual Wall/Frame	8	1.8-3.3	6	5.85
Bridges	3-4	3.0	6	3.5

Eccentrically Braced Frame   **S_P factor of 0.67 incorporated.

1.3.4   Ductility of Structural Systems

A key tenet of force-based design, as currently practiced, is that unique ductility capacities, and hence unique force-reduction factors can be assigned to different structural systems. Thus force-reduction factors of 6 and 4 might be assigned to reinforced concrete frame and wall structures respectively, and concrete bridges might be assigned a value of 3. Note, however, that we have already established that different

codes will provide different force-reduction factors for identical systems and materials. In this section we investigate the validity of this tenet in some detail, and show it to be inappropriate.

Before embarking on this journey, it is necessary to state our definition of ductility capacity. With reference to Fig. 1.6, the yield displacement is taken to be defined by point **3**, and the ultimate displacement by the lesser of displacement at point **6** or point **5**, where point **5** is defined by a strength drop of 20% from the peak strength obtained. This assumes a bi-linear approximation to force-displacement (and to moment-curvature) response and enables direct relationships to be established between the displacement ductility and force-reduction factors. The choice of a yield displacement based on secant stiffness through the first-yield point is also based on rational considerations. A reinforced concrete structure loaded to first yield, unloaded and then reloaded, will exhibit essentially linear unloading and reloading, along the line defined by point **3**. Thus once cracking occurs, the line from the origin to point **3** provided the best estimate of elastic stiffness at levels close to yield. For steel structures, points **1** and **3** will essentially be identical, and the argument is thus also valid.

The calculation of nominal strength, initial stiffness, and yield and ultimate displacement are covered in some detail in Chapter 4. It is noted that for design purposes, a maximum displacement for the damage-control limit state should be reduced from the expected ultimate, or collapse displacement by a displacement-reduction factor of approximately $\phi_\Delta = 0.67$.

(a) Bridge Columns of Different Heights: An example of the influence of structural geometry on displacement capacity is provided in Fig. 1.7, which compares the ductility capacity of two bridge columns with identical cross-sections, axial loads and reinforcement details, but with different heights. The two columns have the same yield curvatures ϕ_y and ultimate curvatures ϕ_u and hence the same curvature ductility factor $\mu_\phi = \phi_u / \phi_y$. Yield displacements, however, may be approximated by

$$\Delta_y = \phi_y H^2 / 3 \tag{1.13}$$

where H is the effective height, and the plastic displacement $\Delta_p = \Delta_u - \Delta_y$ by

$$\Delta_p = \phi_p L_p H \tag{1.14}$$

where $\phi_p = \phi_u - \phi_y$ is the plastic curvature capacity, and L_P is the plastic hinge length. The displacement ductility capacity is thus given by

$$\mu_\Delta = \frac{\Delta_y + \Delta_p}{\Delta_y} = 1 + 3\frac{\phi_p L_P}{\phi_y H} \tag{1.15}$$

(a) Squat Column, $\mu_\Delta = 9.4$ (b) Slender Column, $\mu_\Delta = 5.1$
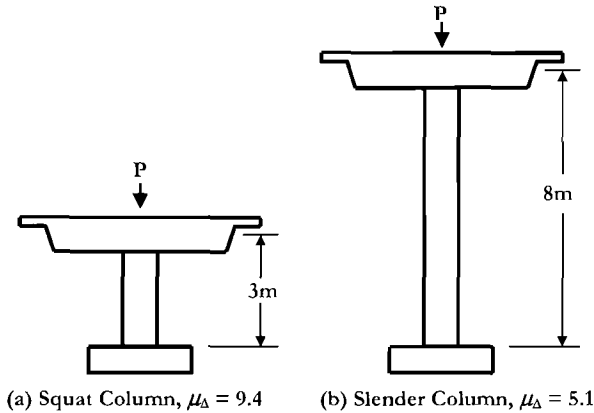
Fig.1.7 Influence of Height on Displacement Ductility Capacity of Circular Columns (P = 0.1f'$_c$A$_g$; 2% longitudinal, 0.6% transverse reinforcement)

As is discussed in Section 4.2.8, the plastic hinge length depends on the effective height, extent of inclined shear cracking, and the strain penetration of longitudinal reinforcement into the footing. As a consequence, L_P is rather weakly related to, and is frequently assumed to be independent of, H. Referring to Eq.(1.15) it is thus seen that the displacement ductility capacity reduces as the height increases. Using the approach of Section 4.2.8 where the height-dependency of L_P is considered, it is found that the squat column of Fig. 1.7(a) has a displacement ductility capacity of $\mu_\Delta = 9.4$, while for the more slender column of Fig. 1.7(b), $\mu_\Delta = 5.1$. Clearly the concept of uniform displacement ductility capacity, and hence of a constant force-reduction factor is inappropriate for this very simple class of structure.

(b) Portal Frames with Flexible Beams: Current seismic design philosophy requires the selection of members in which plastic hinges may form, and the identification of members which are to be protected from inelastic action (capacity design: see Section 4.5). It will be shown that the elastic flexibility of the capacity-protected members influences the displacement ductility capacity of the structure, and hence might be expected to influence the choice of force-reduction factor in force-based design.

Consider the simple portal frame illustrated in Fig.1.8. For simplicity of argument, we assume that the column bases are connected to the footings by pinned connections, and thus no moments can develop at the base. If the portal in Fig.1.8 was representative of a section of a building frame, the design philosophy would require that plastic hinges should form only in the beam, and that the column remain elastic. If the portal was representative of a bridge bent supporting a superstructure, hinging would develop at the top of the columns, and the cap beam would be required to remain elastic. In the argument below, we assume the latter (bridge), alternative to apply, though identical conclusions are arrived at if hinging is assumed to develop in the beam.
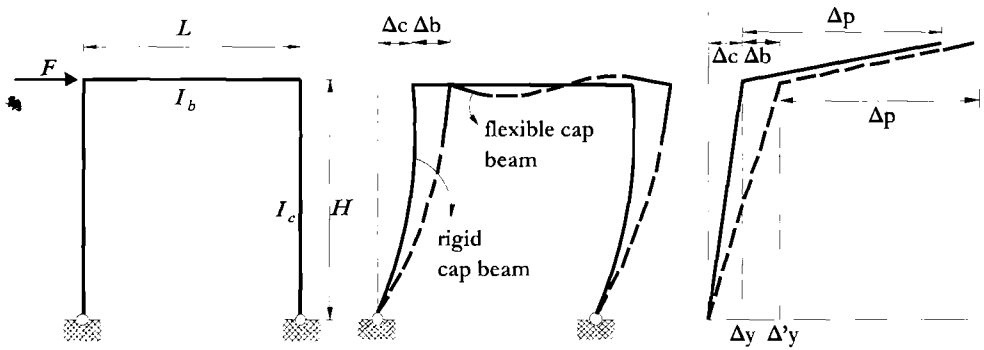
Fig. 1.8   Influence of Member Flexibility on Displacement of a Portal Frame

Consider first the case where the cap beam is assumed to be rigid. The yield displacement under lateral forces F is thus $\Delta_y = \Delta_c$, resulting solely from column flexibility. All plastic displacement originates in the column plastic hinge regions, since the design philosophy requires the cap beam to remain elastic. With a plastic displacement of Δ_p corresponding to the rotational capacity of the column hinges, the structure displacement ductility is

$$\mu_{\Delta r} = 1 + \frac{\Delta_p}{\Delta_c} \tag{1.16}$$

where the subscript r refers to the case with rigid cap beam.

Cap beam flexibility will increase the yield displacement to $\Delta_y = \Delta_c + \Delta_b$, where Δ_b is the additional lateral displacement due to cap beam flexibility (see Fig. 1.8(b)), but will not result in additional plastic displacement, since this is still provided solely by column hinge rotation. For bent dimensions $H \times L$, as shown in Fig. 1.8(a), and cracked-section moments of inertia for beam and columns of I_b and I_c, respectively, the yield displacement is now

$$\Delta_y = \Delta_c + \Delta_b = \Delta_c\left(1 + \frac{0.5I_c L}{I_b H}\right) \tag{1.17}$$

and the structural displacement ductility capacity is reduced to

$$\mu_{\Delta f} = 1 + \frac{\Delta_p}{\Delta_c + \Delta_b} = 1 + \frac{\Delta_p}{\Delta_c\left(1 + 0.5I_c L / I_b H\right)}$$

where the subscript f refers to the case with flexible cap beam. Thus:

$$\mu_{\Delta f} = 1 + \frac{\mu_{\Delta r} - 1}{1 + 0.5 I_c L / I_b H} \tag{1.18}$$

As an example, take $L = 2H$, $I_b = I_c$, and $\mu_{\Delta r} = 5$. From Eq.(1.18) it is found that the displacement ductility capacity is reduced to $\mu_{\Delta f} = 3$. Again it would seem to be inappropriate to use the same force reduction for the two cases. Although consideration of this effect has been recommended elsewhere[P4], it is not included in any design codes, and is rarely adopted in force-based design practice.

It is obvious that similar conclusions will apply to frame buildings, where the elastic flexibility of the columns will reduce the building displacement ductility capacity compared to that based on beam ductility capacity alone.

(c) Cantilever Walls with Flexible Foundations: Similar conclusions to those of the previous section are obtained when the influences of foundation flexibility are considered, or ignored, in seismic design. Consider the structural wall shown in Fig.1.9. The displacements at first yield (Fig.1.9(b) at the effective height H_e (centre of lateral force) are increased by rotation of the wall on the flexible foundation, while the plastic displacement, Δ_p is a function of the rotational capacity of the wall-base plastic hinge detail alone, since the foundation is expected to remain elastic. In fact, in the example shown, a small increase in displacements due to foundation flexibility will occur as the wall deforms inelastically, since the base shear, as shown in Fig. 1.9(c) continues to

(a) Structure	(b) Profiles at Yield	(c) Base Shear/Displacement Response
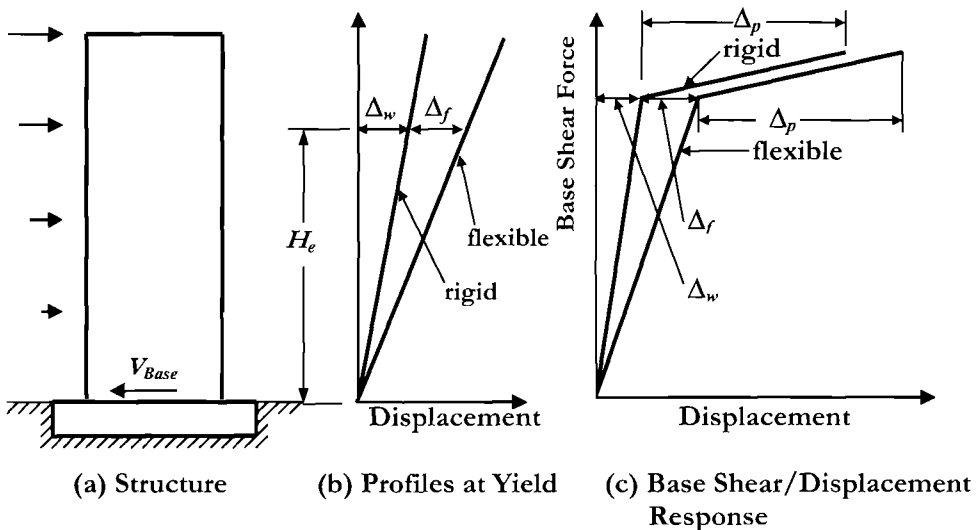
Fig.1.9 Influence of Foundation Flexibility on Displacement Ductility Capacity

increase, due to strain hardening of longitudinal reinforcement. This minor effect is ignored, in the interests of simplicity, in the following.

The similarity to the case of the previous example of the portal frame is obvious. By analogy to the equations of that section, the displacement ductility of the wall, including foundation flexibility effects can be related to the rigid-base case by

$$\mu_{\Delta f} = 1 + \frac{\Delta_p}{\Delta_w + \Delta_f} = 1 + \frac{\mu_{\Delta r} - 1}{\left(1 + \Delta_f / \Delta_w\right)} \tag{1.19}$$

where Δ_w and Δ_f are the wall displacements at yield due to structural deformation of the wall, and foundation rotation respectively, and $\mu_{\Delta r} = 1 + \Delta_p / \Delta_w$.

The reduction in displacement ductility capacity implied by Eq.(1.19) is more critical for squat walls than for slender walls, since the flexural component of the structural yield displacement, which normally dominates, is proportional to the square of the wall height, whereas the displacement due to foundation flexibility is directly proportional to wall height. It is not unusual, with squat walls on spread footings, to find the displacement ductility capacity reduced by a factor of two or more, as a consequence of foundation rotation effects. Similar effects have been noted for bridge columns on flexible foundations[P4]. To some extent, however, the effects of additional elastic displacements resulting from this cause may be mitigated by additional elastic damping provided by soil deformation and radiation damping[C17]. For simplicity, shear deformation of the wall has not been considered in this example.

In the past it has been common for designers to ignore the increase in fundamental period resulting from the foundation flexibility discussed above. It may be felt that this to some extent compensates for the reduction in displacement ductility capacity, since the structure is designed for higher forces than those corresponding to its "true" fundamental period. However, the consequence may be that story drifts exceed codified limits without the designer being aware of the fact.

(d) Structures with Unequal Column Heights: Marginal wharves (wharves running parallel to the shore line) typically have a transverse section characterized by a simple reinforced or prestressed concrete deck supported by concrete or steel shell pile/columns whose free height between deck and dyke increases with distance from the shore. An example is shown in Fig.1.10(a).

Conventional force-based design would sum the elastic stiffnesses of the different piles to establish a global structural stiffness, calculate the corresponding fundamental period, and hence determine the elastic lateral design force, in accordance with the sequence of operations defined in Fig.1.3. A force-reduction factor, reflecting the assumed ductility capacity would then be applied to determine the seismic design lateral force, which would then be distributed between the piles in proportion to their stiffness. Implicit in this approach is the assumption of equal displacement ductility demand for all pile/columns.

The illogical nature of this assumption is apparent when the individual pile/column force-displacement demands, shown in Fig.1.10(b), are investigated. Design is likely to be such that only one, or at most two pile designs will be used, varying the amount of prestressing or reinforcing steel, but keeping the pile diameter constant. In this case the pile/columns will all have the same yield curvatures, and yield displacements will be proportional to the square of the effective height from the deck to the point of effective fixity for displacements, at a depth of about five pile diameters below the dyke surface. This effective height is shown for piles **F** and **C** in Fig. 1.10(a) as H_F or H_C.
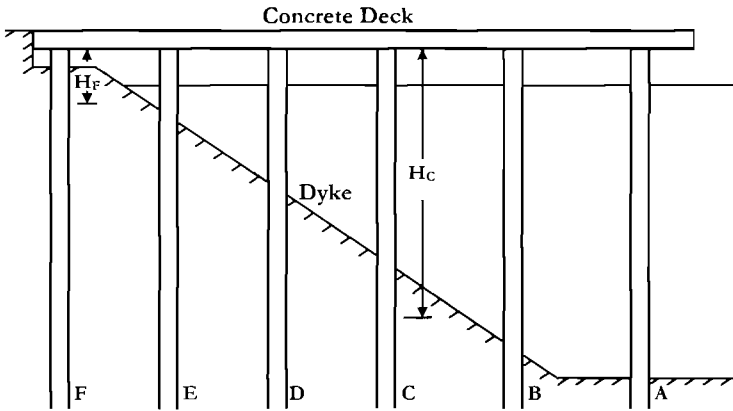
(a) Transverse Section through Wharf
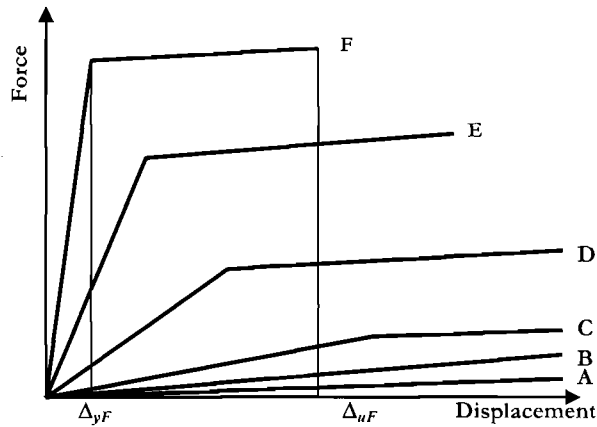
(b) Force-Displacement Response of Individual Piles

Fig.1.10 Transverse Seismic Response of a Marginal Wharf

The structure lateral force displacement response can be obtained by summing the individual pile/column force-displacement curves, shown in Fig.1.10(b). Force-based

design, allocating strength in proportion to the elastic stiffnesses would imply design strengths for the different pile/columns equal to the forces intersected by the line drawn in Fig.1.10(b) at Δ_{yF}, the yield displacement of pile/column **F**. Since the yield displacements of the longer piles are much greater, the full strength of these piles will thus be under-utilized in the design. It is also clearly a gross error to assume that all piles will have the same ductility demand in the design-level earthquake. Fig. 1.10(b) includes the full force-displacement curves, up to ultimate displacement, for pile/columns **F** and **E**. The ultimate displacements for the longer pile/columns are beyond the edge of the graph. Clearly at the ultimate ductility capacity of the shortest pile column, **F**, the ductility demands on the longer columns are greatly reduced. Pile/columns **A**, and **B** will still be in the elastic range when the ultimate displacement of pile **F** is reached. The concept of a force-reduction factor based on equal ductility demand for all pile/columns is thus totally inapplicable for this structure. Wharf seismic design is discussed in depth in Chapter 12.

Similar conclusions (as well as a means for rationally incorporating the above within the framework of force-based design) have been reached by Paulay[P26] referring to response of a rigid building on flexible piles of different lengths. The procedure suggested by Paulay requires that the concept of a specified structural force-reduction factor, which currently is a basic tenet of codified force-based design, be abandoned, and replaced by rational analysis.

A second example, that of a bridge crossing a valley, and hence having piers of different heights, is shown in Fig.1.11. Under longitudinal seismic response, the deflections at the top of the piers will be equal. Assuming a pinned connection between the pier tops and the superstructure (or alternatively, fixed connections, and a rigid superstructure), force-based design will allocate the seismic design force between the columns in proportion to their elastic stiffnesses. If the columns have the same cross-section dimensions, as is likely to be the case for architectural reasons, the design shear forces in the columns, V_A, V_B, and V_C, will be in inverse proportion to $H_A{}^3$, $H_B{}^3$, and $H_C{}^3$ respectively, since the stiffness of column i is given by

$$K_i = C_1 EI_{i,e} / H_i^3$$ (1.20a)

where $I_{i,e}$ is the effective cracked-section stiffness of column i, typically taken as $0.5I_{gross}$, for all columns. The consequence of this design approach is that the design moment at the bases of the piers will be

$$M_{Bi} = C_2 V_i H_i = C_1 C_2 EI_{i,e} / H_i^2 ,$$ (1.20b)

that is, in inverse proportion to the square of the column heights (in Eqs.(1.20), C_1 and C_2 are constants dependent on the degree of fixity at the pier top). Consequently the shortest piers will be allocated much higher flexural reinforcement contents than the longer piers. This has three undesirable effects. First, allocating more flexural strength to the short piers will increase their elastic flexural stiffness, $EI_{i,e}$, even further, with respect to the more lightly reinforced longer piers, as has been discussed in relation to Fig.1.4.
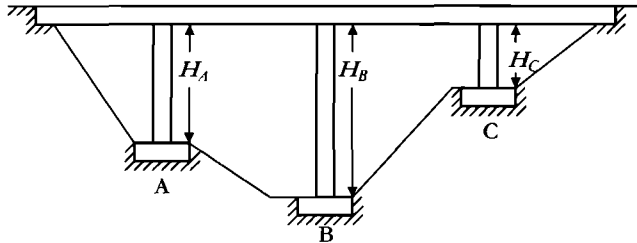
Fig.1.11 Bridge with Unequal Column Heights

A redesign should strictly be carried out with revised pier stiffnesses, which, in accordance with Eq. (1.20) would result in still higher shear and moment demands on the shorter piers. Second, allocating a large proportion of the total seismic design force to the short piers increases their vulnerability to shear failure. Third, the displacement capacity of the short piers will clearly be less than that of the longer piers. As is shown in Section 1.3.5, the displacement capacity of heavily reinforced columns is reduced as the longitudinal reinforcement ratio increases, and hence the force-based design approach will tend to reduce the displacement capacity.

As with the marginal wharf discussed in the previous example, the ductility demands on the piers will clearly be different (inversely proportional to height squared), and the use of a force-reduction factor which does not reflect the different ductility demands will clearly result in structures of different safety.

Design of bridges with unequal column heights is considered further in Chapter 10.

1.3.5 Relationship between Strength and Ductility Demand.

A common assumption in force-based design is that increasing the strength of a structure (by reducing the force-reduction factor) improves its safety. The argument is presented by reference to Fig.1.1, of which the force-deformation graph is duplicated here as Fig.1.12(a). Using the common force-based assumption that stiffness is independent of strength, for a given section, it is seen that increasing the strength from S1 to S2 reduces the ductility demand, since the final displacement remains essentially constant (the "equal displacement" approximation is assumed), while the yield displacement increases. It has already been noted, in relation to Fig.1.4 that this assumption is not valid. However, we continue, as it is essential to the argument that increasing strength reduces damage.

The reduction in ductility demand results in the potential for damage also being decreased, since structures are perceived to have a definable ductility demand, and the lower the ratio of ductility demand to ductility capacity, the higher is the safety.

We have already identified three flaws in this reasoning: 1) stiffness is not independent of strength; 2) the "equal displacement" approximation is not valid; and 3) it is not possible to define a unique ductility capacity for a structural type.
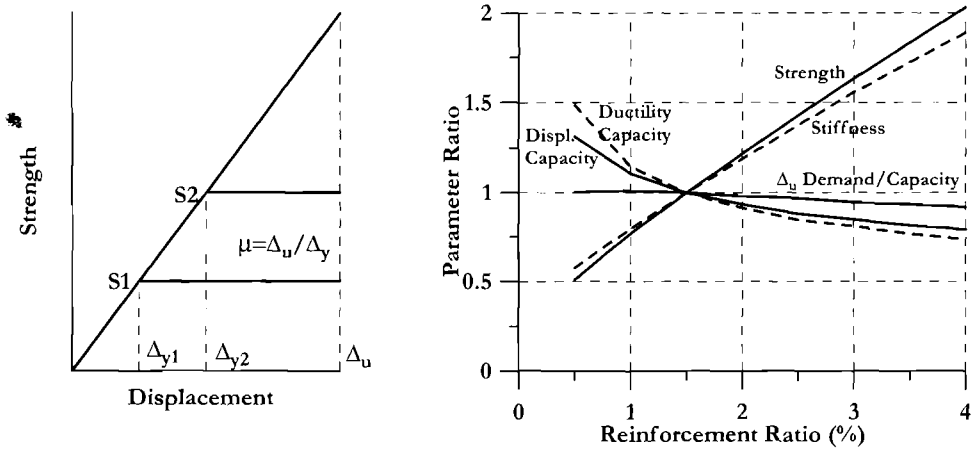
(a) Strength vs Ductility	(b) Influence of Rebar % on Parameters

Fig.1.12   Influence of Strength on Seismic Performance

It is of interest, however, to examine the argument by numeric example. The simple bridge pier of Fig.1.1 is assumed to have the following properties: Height = 8 m (26.2 ft), diameter = 1.8 m (70.9 in), flexural reinforcement dia. = 40 mm (1.58 in), concrete strength f'_c = 39 MPa (5.66 ksi), flexural reinforcement: yield strength f_y = 462 MPa (67 ksi), f_u = 1.5f_y; transverse reinforcement: 20 mm (0.79 in) diameter at a pitch of 140 mm (5.5 in), f_{yh} = 420 MPa (60.9 ksi); cover to main reinforcement = 50 mm (1.97 in), axial load P= 4960 kN (1115 kips) which is an axial load ratio of $P/f'_c A_g$ = 0.05.

A reference design with 1.5% flexural reinforcement is chosen, and analyses carried out, using the techniques described in Chapter 4 to determine the influence of changes to the flexural strength resulting from varying the flexural reinforcement ratio between the limits of 0.5% and 4%. Results are presented for different relevant parameters in Fig.1.12(b) as ratios to the corresponding parameter for the reference design.

As expected, the strength increases, almost linearly with reinforcement ratio, with ratios between 0.5 times and 2.0 times the reference strength. We can thus use these data to investigate whether safety has increased as strength has increased. First we note that the effective stiffness has not remained constant (as assumed in Fig.1.12(a)) but has increased at very nearly the same rate as the strength. More importantly, we note that the displacement capacity displays the opposite trend from that expected by the force-based argument: that is, the displacement capacity decreases as the strength increases. At a reinforcement ratio of 0.5% it is 31% higher than the reference value, while at 4% reinforcement ratio the displacement capacity is 21% **lower** than the reference value. Thus, if the "equal displacement" approach was valid, as illustrated in Fig.1.12(a), we have **decreased** the safety by increasing the strength, and we would be better off by reducing the strength.

Of course, the discussion above is incomplete, since we know that the yield displacements are not proportional to strength, since the stiffness and strength are closely

related as suggested in Fig. 1.4(b), and demonstrated in Fig.1.12(b). We use this to determine the influence on displacement **ductility** capacity, and find that it decreases slightly faster than the displacement capacity (see Fig.1.12(b)). However, since the elastic stiffness increases with strength, the elastic period reduces, and the displacement demand is thus also reduced. If we assume that the structural periods for all the different strength levels lie on the constant-velocity slope of the acceleration spectrum (i.e. the linear portion of the displacement response spectrum: see Fig.1.2(b)), then since the period is proportional to the inverse of the square root of the stiffness (Eq.1.6), the displacement **demand** will also be related to $1/K^{0.5}$. We can then relate the ratio of displacement demand to displacement capacity, and compare with the reference value.

This ratio is also plotted in Fig.1.12(b). It will be seen that taking realistic assessment of stiffness into account, the displacement demand/capacity ratio is insensitive to the strength, with the ratio only reducing from 1.25 to 0.92 as the strength ratio increases by 400% (corresponding to the full range of reinforcement content). Clearly the reasoning behind the strength/safety argument is invalid.

1.3.6 Structural Wall Buildings with Unequal Wall Lengths

A similar problem with force-based design to that discussed in the previous section occurs when buildings are provided with cantilever walls of different lengths providing seismic resistance in a given direction. Force-based design to requirements of existing codes will require the assumption that the design lateral forces be allocated to the walls in proportion to their elastic stiffness, with the underlying assumption that the walls will be subjected to the same displacement ductility demand. Hence the force-reduction factor is assumed to be independent of the structural configuration.

It was discussed in relation to Fig.1.4(b), that the yield curvature for a given section is essentially constant, regardless of strength. It will be shown in Section 4.4.3 that the form of the equation governing section yield curvature is

$$\phi_y = C \cdot \varepsilon_y / h \tag{1.21}$$

where h is the section depth, and ε_y is the yield strain of the longitudinal reinforcement. Since the yield displacement can be related to the yield curvature by Eq.(1.13) for cantilever walls, as well as for columns, it follows that the yield displacements of walls of different lengths must be in inverse proportion to the wall lengths, regardless of the wall strengths. Hence displacement ductility demands on the walls must differ, since the maximum response displacements will be the same for each wall.

Figure 1.13 represents a building braced by two short walls (**A** and **C**) and one long wall (**B**) in the direction considered. The form of the force-displacement curves for the walls are also shown in Fig.1.13. Force-based design mistakenly assumes that the shorter walls can be made to yield at the same displacement as the longer wall **B**, and allocates strength between the walls in proportion to $l_w{}^3$, since the elastic stiffnesses of the wall differ only in the value of the wall effective moments of inertia, I_e, which are proportional
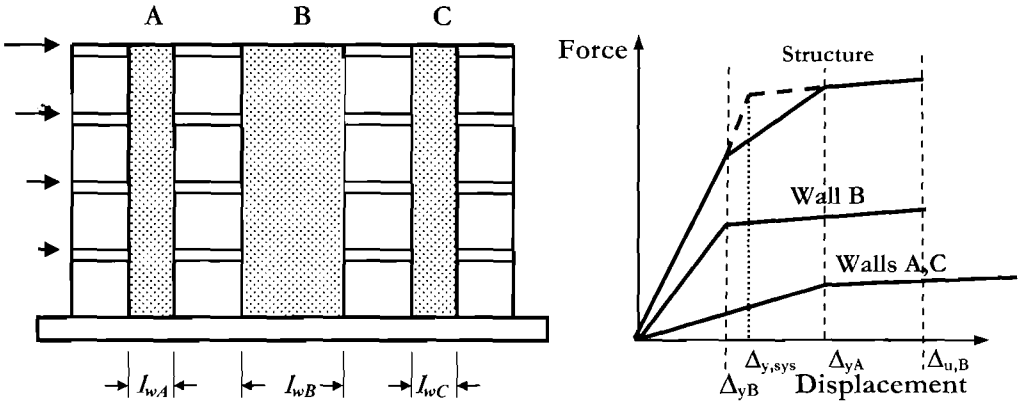
Fig.1.13 Building with Unequal Length Cantilever Walls

to the cube of wall length. Again strength is unnecessarily, and unwisely concentrated in the stiffest elements, underutilizing the more flexible members. A more rational decision would be to design the walls for equal flexural reinforcement ratios, which would result in strengths proportional to the square of wall length.

As with the previous two examples, the code force-reduction factor for the structure will not take cognizance of the fact that the different walls must have different displacement ductility demands in the design earthquake.

1.3.7 Structures with Dual (Elastic and Inelastic) Load Paths.

A more serious deficiency of force-based design is apparent in structures which possess more than one seismic load path, one of which remains elastic while the others respond inelastically at the design earthquake level. A common example is the bridge of Fig.1.14(a), when subjected to transverse seismic excitation, as suggested by the double-headed arrows. Primary seismic resistance is provided by bending of the piers, which are designed for inelastic response. However, if the abutments are restrained from lateral displacement transversely, superstructure bending also develops. Current seismic design philosophy requires the super-structure to respond elastically[P4]. The consequence is that a portion of the seismic inertia forces developed in the deck is transmitted to the pier footings by column bending (path **1** in Fig.1.14(b)), and the remainder is transmitted as abutment reactions by superstructure bending (path **2**). Based on an elastic analysis the relative elastic stiffnesses of the two load paths are indicated by the two broken lines in Fig.1.14(b), implying that column flexure (path **1**) carries most of the seismic force. A force-reduction factor is then applied, and design forces determined.

The inelastic response of the combined resistance of the columns is now shown by the solid line (path **3**, in Fig.1.14(b)), and on the basis of the equal displacement approximation it is imagined that the maximum displacement is Δ_{max}, the value predicted by the elastic analysis. If the superstructure is designed for the force developed in path **2**
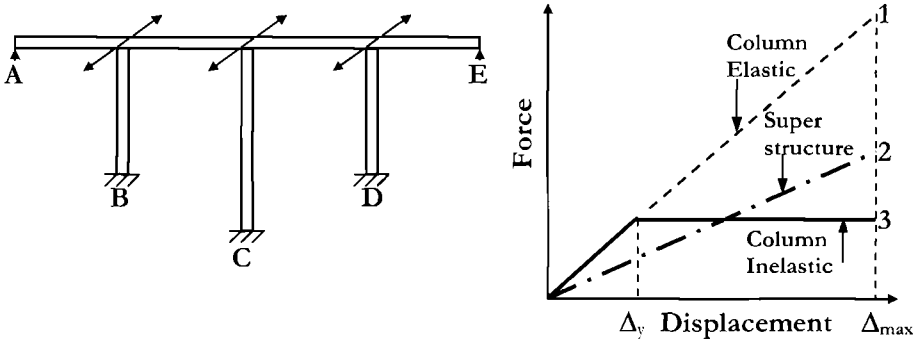
(a) Structure   (b) Load-path Characteristics

Fig.1.14   Bridge with Dual Load Paths under Transverse Excitation

at the column yield displacement, it will be seriously under-designed, since the forces in this path, which are required to be within the elastic range, continue to rise with increasing displacement. Thus the bending moment in the superstructure, and the abutment reactions at **A** and **E** are not reduced by column hinging, and a force-reduction factor should not be used in their design.

It is also probable that the maximum response displacement will differ significantly from the initial elastic estimate, since at maximum displacement, the effective damping of the system will be less than expected, as hysteretic damping is only associated with load path **3**, which carries less than 50% of the seismic force at peak displacement response in this example. This may cause an increase in displacements. On the other hand, the higher strength associated with the increased post-yield stiffness of load path **2** may result in reduced displacement demand. Elastic analysis and the force-reduction factor approach give no guidance to these considerations.

A slightly different, but related problem occurs with dual wall/frame buildings (see Fig.
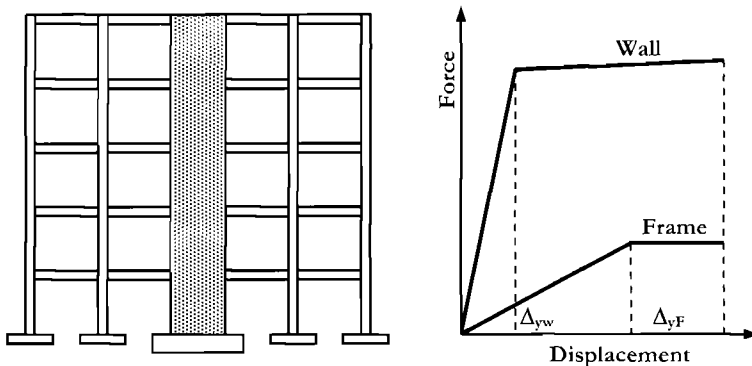
(a) Structure   (b) Force-displacement Response

Fig.1.15   Dual Wall/Frame Building

1.15). If the seismic force is distributed between the frame and the wall in proportion to their elastic stiffness, the load-carrying capacity of the frame will be unnecessarily discounted. The yield displacement of the frame will inevitably be several times larger than that of the wall, so the proportion of seismic force carried by the frame at maximum response will be larger than at first yield of the wall (Fig. 1.14(b)). In this example both systems eventually respond inelastically, but the frame system remains elastic to larger displacements.

Note that the interaction between the frame and wall due to resolving the incompatibilities between their natural vertical displacement profiles will also be modified by inelastic action, and bear little resemblance to the elastic predictions. This is discussed further in Chapter 7.

1.3.8 Relationship between Elastic and Inelastic Displacement Demand

Force-based design requires assumptions to be made when determining the maximum displacement response. The most common assumption is the equal-displacement approximation, which states that the displacement of the inelastic system is the same as that of the equivalent system with the same elastic stiffness, and unlimited strength (refer to Fig.1.1). Thus, with reference to Fig.1.2, the design displacement is estimated as

$$\Delta_{\max,ductile} = \Delta_{\max,elastic} = \frac{T^2}{4\pi^2} \cdot a_{(T)}g \qquad (1.22)$$

and hence $\mu = R$. Equation (1.22) is based on the approximation that peak displacements may be related to peak accelerations assuming sinusoidal response equations, which is reasonable for medium period structures.

The equal displacement approximation is known to be non-conservative for short-period structures. As a consequence, some design codes, notably in Central and South American, and some Asian countries, apply the equal-energy approximation when determining peak displacements. The equal energy approach equates the energy absorbed by the inelastic system, on a monotonic displacement to peak response, to the energy absorbed by the equivalent elastic system with same initial stiffness. Thus the peak displacement of the inelastic system is

$$\Delta_{\max,duct} = \Delta_{\max,elastic} \cdot \left(\frac{R^2+1}{2R}\right) = \frac{T^2}{4\pi^2} \cdot a_{(T)}g \cdot \left(\frac{R^2+1}{2R}\right) \qquad (1.23)$$

where R is the design force-reduction factor. Since $\Delta_{\max,elastic} = R\Delta_y$, and the actual displacement ductility demand is $\mu = \Delta_{\max,duct}/\Delta_y$, the ductility demand implied by Eq.(1.23) is

$$\mu = \frac{R^2 + 1}{2} \tag{1.24}$$

Where codes employ inelastic design spectra [e.g. X1], design is based on specified ductility, rather than force-reduction factor, and the design spectral accelerations for short-period structures are adjusted to correct for displacement amplification.

In the United States, where until recently the dominant building code for seismic regions has been the UBC [X5], design displacements were estimated as

$$\Delta_{max,duct} = \Delta_y \cdot \frac{3R}{8} \tag{1.25}$$

where Δ_y is the yield displacement corresponding to the reduced design forces, found from structural analysis. Since the structure is designed for a force-reduction factor of R, this would appear to imply that the displacement ductility is

$$\mu = \frac{3R}{8} \tag{1.26}$$

and the displacement of the ductile system is 3/8 of the equivalent elastic system. However, the apparent reason behind this seemingly unconservative result is that the **actual** force-reduction factor was substantially lower than the **design** force-reduction factor, as a consequence of the design period being pegged to an unrealistic height-dependent equation of the form of Eq.(1.7). The consequences of this are explained with reference to Fig.1.16.
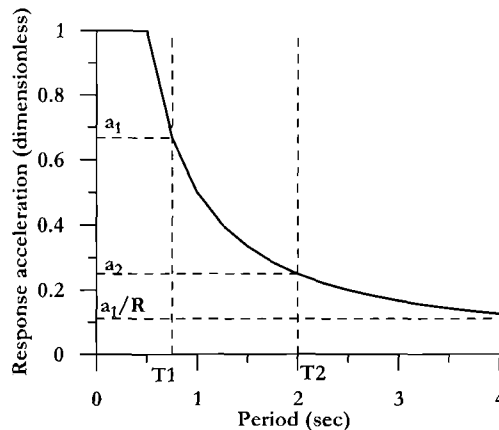
Fig.1.16　Influence of Under-predicted Period on Actual Force-Reduction Factor

In Fig.1.16, **T1** and **T2** are the fundamental periods corresponding to the code height-dependent equation, and rational structural analysis respectively. The elastic response accelerations corresponding to these periods are a_1 and a_2 respectively. If the design

force-reduction factor corresponding to **T1** is R, then the real force-reduction factor, corresponding to **T2** is $R' = Ra_2/a_1$. If the equal displacement approximation were valid at **T2**, and assuming a constant velocity range for the response spectrum, then Eq.(1.26) would be correct if **T2 = 2.67 T1**. Examination of Table 1.1 indicates that this is close to the ratio of periods calculated by rational analysis and by the period dependant code equation.

Clearly there are compensatory errors involved in this approach, which should be removed by using more realistic periods, and force-reduction factors that have a close relationship to the ductility capacity, as is incorporated in other codes. Recently, USA practice, incorporated in the IBC code[X4], has changed, with the $3R/8$ factor of Eq.(1.25) being replaced by a coefficient dependent on structural form and material. The approach is, however, still illogical, with effective ratios varying between $0.5R$ and $1.2R$.

A comparison of the different predictions provided by Eqs (1.22), (1.24) and (1.26) is presented in Fig. 1.17, for a design force-reduction factor of $R=4$. The range of different possible answers is disturbingly large.
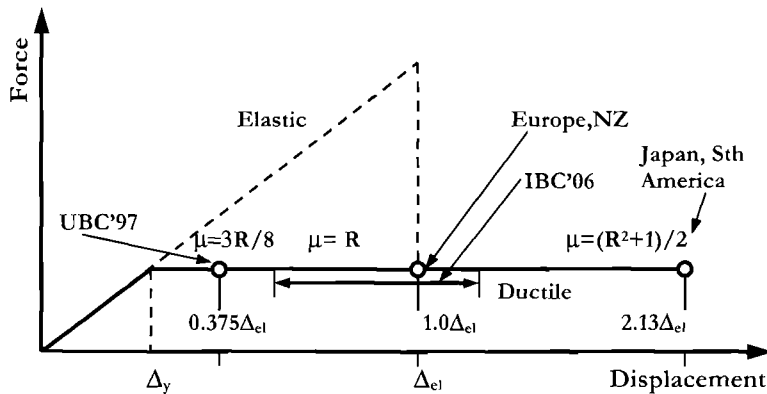
Fig.1.17 Estimates of Design Displacement from Different Force-Based Codes for R = 4

Force-based seismic design does not normally take account of the different hysteretic characteristics of different materials and structural systems. Thus the fact that seismic isolation systems absorb much more hysteretic energy than reinforced concrete structures, which in turn absorb more than prestressed concrete structures is not directly considered, though different force-reduction factors may be assigned to different materials. Figure 1.18 examines the validity of the equal displacement approximation for a range of different periods, and for three different hysteresis rules: elastic, bilinear elasto-plastic (representative of isolation systems), Takeda[O1], (representative of reinforced concrete structures, and flag-shaped with β=0.35 (representative of hybrid unbonded prestressed structures - see Fig 4.33).

Analyses were first carried out for a range of periods between 0.25sec and 2.5 seconds using elastic time-history analyses and a suite of seven accelerograms compatible with the

EC8 design spectrum for firm ground [X3]. The design yield strength for the three ductile systems was found by dividing the average maximum elastic response moment by a factor of R=4. All three ductile systems adopted the same force-displacement envelope, with a post-yield stiffness of 5% of the initial stiffness, and thus only differed in terms of unloading and reloading rules. Elastic damping was taken as 5% of critical, related to the tangent stiffness (see Section 4.9.2(g) for a discussion on modelling elastic damping).

In Fig.1.18, results are expressed as the ratio ductile peak displacement for ductile response to displacement of the elastic system of equal initial period. For the equal displacement approximation to hold, all values should be 1.0. It is seen that significant differences occur, depending on the period and hysteresis rule. Differences are particularly marked in the period range T <0.75 seconds, as expected, but are also significant at other periods.

(a) Absolute Peak Displacement   **(b) Average of Positive and Negative Peaks**
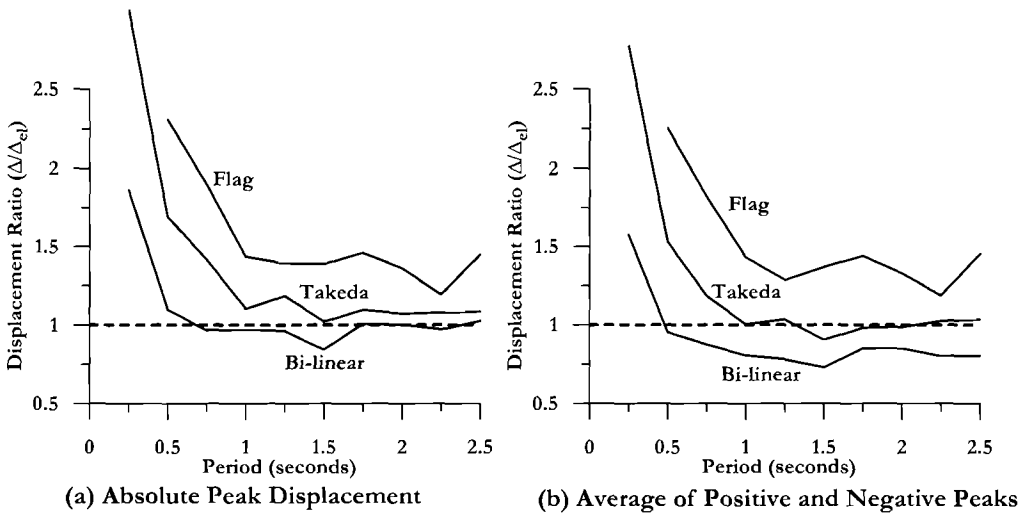
Fig.1.18   Ratio of Ductile to Elastic Peak Displacement for different Hysteresis Rules based on EC8 Design Spectrum for Firm Ground

The differences between the hysteretic rules, and also from the elastic results are particularly apparent when the average of the positive and negative peaks (Fig. 1.18(b)), rather than the absolute maximum (Fig. 1.17(a)), are considered, as suggested in Section 4.9.2(h), reflecting the larger residual displacements in the Bilinear elasto-plastic results, which affects the absolute peak displacement more than the average of positive and negative peaks.

The results of this brief section indicate that force-based design is not ideally suited to estimating the maximum displacements expected of structures in seismic response. Considering that it is now accepted that peak displacements are critical in determining the level of damage that can be expected, this is a serious criticism of the method.

1.3.9 Summary

In this section, we have identified some of the problems associated with force-based design. These can be summarized as follows:

- Force-based design relies on estimates of initial stiffness to determine the period and the distribution of design forces between different structural elements. Since the stiffness is dependent on the strength of the elements, this cannot be known until the design process is complete.

- Allocating seismic force between elements based on initial stiffness (even if accurately known) is illogical for many structures, because it incorrectly assumes that the different elements can be forced to yield simultaneously.

- Force-based design is based on the assumption that unique force-reduction factors (based on ductility capacity) are appropriate for a given structural type and material. This is demonstrably invalid.

Despite these criticisms it should be emphasized that current force-based seismic design, when combined with capacity design principles and careful detailing, generally produces safe and satisfactory designs. However, the degree of protection provided against damage under a given seismic intensity is very non-uniform from structure to structure. Thus, the concept of "uniform risk" which is implicit in the formulation of current seismic design intensity, has not been continued into the structural design. We believe that it should be.

1.4 DEVELOPMENT OF DISPLACEMENT-BASED DESIGN METHODS

1.4.1 Force-Based/Displacement Checked

Deficiencies inherent in the force-based system of seismic design, some of which have been outlined in the preceding sections, have been recognized for some time, as the importance of deformation, rather than strength, in assessing seismic performance has come to be better appreciated. Consequently a number of new design methods, or improvements to existing methods, have been recently developed. Initially the approaches were designed to fit within, and improve, existing force-based design. These can be characterized as *force-based/displacement checked*, where enhanced emphasis is placed on realistic determination of displacement demand for structures designed to force-based procedures.

Such methods include the adoption of more realistic member stiffnesses for deformation (if not for required strength) determination, and possibly use of inelastic time-history analysis, or pushover analysis, to determine peak deformation and drift demand. In the event that displacements exceed the code specified limits, redesign is required, as suggested in Fig.1.3. Many modern codes [e.g. X1, X2, X3, X4]require some version of this approach. Several recent design approaches have used this approach [e.g. F1, F2, X8]. In general, no attempt is made to achieve uniform risk of damage, or of collapse for structures designed to this approach.

Paulay[1] has suggested that the deficiencies noted in previous sections can be eliminated within a force-based design approach. As explained in detail in section 4.4, yield displacement Δ_y can be determined from section and structure geometry without a prior knowledge of strength. Displacement demand, Δ_d, at least for frame buildings will normally be governed by code drift limits and the building geometry. The yield strength V is assumed, and hence the initial stiffness $K = V/\Delta_y$ is calculated. The elastic period is calculated from Eq.(1.6), and the elastic displacement demand from Eq. (1.22). This is compared with the code drift limit, and the strength adjusted incrementally until the elastic displacement equals the drift limit. Strength is then distributed between the different lateral-force resisting elements based on experience, rather than on elastic stiffness. This has been termed a *displacement focused force-based approach*.

There are, however, problems associated with this approach. Although the yield displacements of the lateral-force resisting elements may be known at the start of the procedure, the equivalent system yield displacement will not be known until the distribution of strength between elements is decided. The approach relies on assumptions about the equivalence between elastic and ductile displacements (e.g. the equal displacement approximation), which as discussed in relation to Fig.1.18 may be invalid, and considerable experience is required of the designer. The procedure is suitable for those well versed in seismic design, but ill-suited for codification. As will be shown in subsequent chapters of this text, a design approach based directly on displacements is simpler, better suited to codification (see Chapter 14), and does not require assumptions to be made about elastic/inelastic displacement equivalence.

1.4.2 Deformation-Calculation Based Design

A more refined version of the *force-based/displacement-checked* approach relates the detailing of critical sections (in particular details of transverse reinforcement for reinforced concrete members) to the local deformation demand, and may hence be termed *deformation-calculation based design*. Strength is related to a force-based design procedure, with specified force-reduction factors. Local deformation demands, typically in the form of member end rotations or curvatures are determined by state-of-the-art analytical tools, such as inelastic pushover analyses or inelastic time-history analyses. Transverse reinforcement details are then determined from state-or-the-art relationships between transverse reinforcement details and local deformation demand, such as those presented in Chapter 4.

Initial work on this procedure was related to bridge structures[P6], and followed by work on reinforced concrete buildings[M1]. Many additional variants of the approach have recently been developed [e.g. B1, K1, P7]. In the variant suggested by Panagiatokos and Fardis[P7] the structure is initially designed for strength to requirements of direct combination of gravity load plus a serviceability level of seismic force, using elastic

---

[1] *Pers. comm. T.Paulay*

analysis methods. The designed structure is then analysed using advanced techniques such as inelastic time-history analysis or inelastic pushover analysis to determine the required transverse reinforcement details. It is not clear that this is an efficient design approach when response to the full design-level earthquake is considered, since inelastic time-history analyses of frame buildings by Pinto et al [P15] have indicated that member inelastic rotations are rather insensitive to whether gravity loads are incorporated in the analysis, or ignored. An alternative procedure for combination of gravity and seismic loads is suggested in Section 3.7. The approaches described in this section have the potential of producing structures with uniform risk of collapse, but not with uniform risk of damage.

1.4.3   Deformation-Specification Based Design

Recently a number of design approaches have been developed where the aim is to design structures so that they achieve a specified deformation state under the design-level earthquake, rather than achieve a displacement that is less than a specified displacement limit. These approaches appear more philosophically satisfying than those of the preceding two sections. This is because damage can be directly related to deformation. Hence designing structures to achieve a specified displacement limit implies designing for a specified risk of damage, which is compatible with the concept of uniform risk applied to determining the design level of seismic excitation. It thus means that different structures designed to this approach will (ideally) have the same risk of damage, rather than the variable risk associated with current design approaches, as discussed in Section 1.3. Using state-of-the-art detailing/deformation relationships, structures with uniform risk of collapse, as well as of damage can theoretically be achieved.

Different procedures have been developed to achieve this aim. The most basic division between them is on the basis of stiffness characterization for design. Some methods [e.g. A1, C2, S1], adopt the initial pre-yield elastic stiffness, as in conventional force-based design. Generally some iteration is required, modifying initial stiffness and strength, to achieve the desired displacement, as discussed in relation to the approach suggested by Paulay in Section 1.4.1. These approaches also rely on existing relationships between elastic and inelastic displacement, such as the equal-displacement, or equal-energy approximations. It is shown in Section 4.9.2(g) that these approximations have been based on invalid elastic damping assumptions.

The second approach utilizes the secant stiffness to maximum displacement, based on the *Substitute Structure* characterization[G1,S2], and an equivalent elastic representation of hysteretic damping at maximum response [e.g. P8, K2, P9]. Generally these methods require little or no iteration to design a structure to achieve the specified displacement, and are hence known as *Direct Displacement-Based Design* (**DDBD**) methods. The different stiffness assumptions of the two approaches are illustrated for a typical maximum hysteretic force-displacement response in Fig.1.19, where K_i and K_s are the initial and secant stiffness to maximum response respectively. It will be recalled that one of the principal problems with force-based seismic design is that reliance on initial stiffness

results in illogical force distribution between different structural elements. It will be shown in Chapter 3 that this problem disappears when the secant stiffness is used.
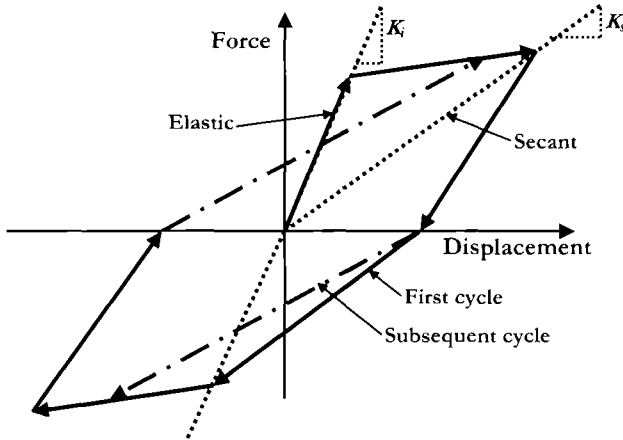
Fig.1.19   Initial and Secant Stiffness Characterization of Hysteretic Response

The way in which hysteretic energy dissipation is handled also varies between the methods. Two main classes of procedure can be identified − those that use inelastic spectra, and those that use equivalent viscous damping. Inelastic spectra are generally related to acceleration, though there is no inherent reason why inelastic displacement spectra cannot be generated (see Section 3.4.3(e)). They are generated by single-degree-of-freedom analyses of structures of different initial elastic periods, using a specified hysteresis rule, and a specified maximum ductility. Since the ductility demand cannot generally be predicted prior to the analyses, the analyses are carried out using a range of specified force-reduction factors, and the spectrum for a given ductility factor is found by interpolation within the results of the analyses. Alternatively, simplified relationships between force-reduction factor and ductility that vary between equal-displacement at long periods, and equal energy at short periods are directly generated. An example based on this approach, using the basic EC8[X3] acceleration spectrum for firm ground and peak ground acceleration of 0.4g is shown in Fig.1.20(a).

As will be apparent from the discussion related to Fig.1.18, different inelastic spectra would need to be generated for different structural systems and materials that exhibited different hysteretic characteristics. Methods for generation of inelastic spectra are discussed in Section 3.4.3(e).

The second alternative is to represent ductility and energy dissipation capacity as equivalent viscous damping, using relationships based on inelastic time-history analyses. This procedure is only appropriate when the secant stiffness to maximum response is used in the design process. The procedure for design using displacement spectra requires little or no iteration and hence is termed *Direct Displacement-based Seismic Design* (**DDBD**).

The method is discussed in detail in Chapter 3.

An example of a spectral displacement set for different damping levels is shown for the displacement spectrum of EC8, firm ground, 0.4g PGA, in Fig.1.20(b). It will be evident that a single spectral set, covering the expected range of equivalent viscous damping, will apply for all hysteretic characteristics, provided the relationships between equivalent viscous damping, ductility, and hysteretic rule have been pre-calibrated by inelastic time-history analyses. It is also possible, as discussed above, to express the displacement spectra in terms of ductility, rather than equivalent viscous damping, in a form analogous to that used for the acceleration spectra of Fig.1.20(a). It will be shown in Chapter 3 that inelastic displacement spectra can be generated using precisely the same data and analyses used to generate the rules relating ductility to damping for a given hysteresis rule, and that the approaches are then directly equivalent. The disadvantage of this approach is that inelastic spectra must be generated for each hysteresis rule, and the determination of equivalent system ductility requires careful consideration.

(a) Inelastic Acceleration Spectra   (b) Damped Displacement Spectra
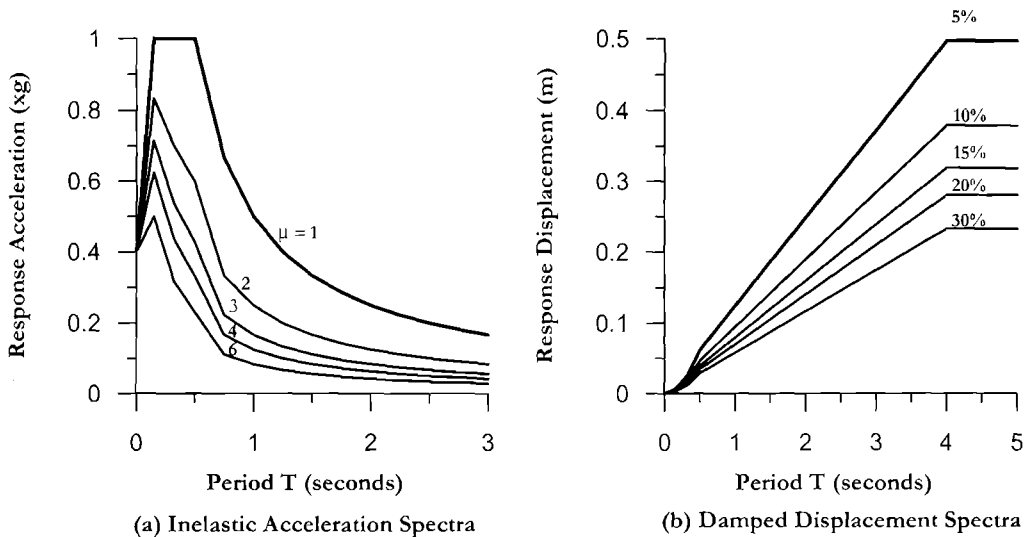
Fig.1.20   Alternative Spectral Representations of Ductility for EC8 Firm Ground, PGA=0.4g.

1.4.4   Choice of Design Approach

Comprehensive presentation and comparison of different displacement-based designs methods is available in two recent documents[P4, C16]. Apparent in these and other recent documents is a plethora of different nomenclature to describe the new design processes. This includes the use of *"Displacement-Based Design"*, *"Limit-states Design"*, *Performance Based Design"* and *"Consequence Based Design"* amongst others. In our view, all attempt generally the same goal: that of providing satisfactory displacement solutions to seismic design problems, and so the term *"Displacement-Based Design"* will be used exclusively in this book.

It is also our view that the *Direct Displacement-Based Design* approach is the most intellectually satisfying, and best equipped to address the deficiencies of conventional force-based design, which were presented in some detail in Section 1.3. This approach has also been developed in rather more complete form than other methods, and has been applied to a wider category of structures. Finally, we claim that the method is simpler to apply, and better suited to incorporation in design codes. Because of the simplicity of generation, and wider applicability, representation of hysteretic energy absorption by equivalent viscous damping will be preferred to the use of inelastic spectra.

As a consequence of these considerations, the theoretical basis of the **DDBD** approach is developed in detail in Chapter 3. This is preceded in Chapter 2 by a short discussion of relevant aspects relating to seismicity and intensity characterisation, while Chapter 4 covers analytical tools appropriate, or necessary, for Direct Displacement-Based Design. Chapters 5 to 12 describe application of the method to different types of structural systems, while Chapter 13 discusses application of the **DDBD** procedures to assessment of existing structures. Finally, Chapter 14 presents the design method for buildings in a typical *"Code plus Commentary"* format, to be used as a possible format for future codification.

2

SEISMIC INPUT FOR DISPLACEMENT-BASED DESIGN

2.1 INTRODUCTION: CHARACTERISTICS OF ACCELEROGRAMS

Our understanding of the response of structures to earthquakes, and our design methodologies, either force-based or displacement-based, are critically dependent on recordings of strong ground motion by accelerographs. Accelerograms are recordings of ground acceleration made by accelerographs during earthquakes, and the earliest records date back to the 1930's. Early accelerograms were recorded in analogue form on photographic film, and required digitization to put them in a form where their characteristics could be examined. Accuracy was limited, and the dynamic characteristics of the accelerographs themselves meant that useful data for preparing response spectra could be extracted only up to periods of about two to three seconds. In the past twenty years, digital accelerographs, with much higher resolution and longer range of period integrity have become increasingly common, and the quality of data from recorded earthquakes is steadily improving as more digital records become available.

This text will not attempt to present seismological information about source mechanisms, physical and temporal distributions of earthquakes, attenuation relationships and modern developments in source modelling. The interested reader is encouraged to read any of the many specialized seismological texts [e.g. S7, K8]. The treatment here will be limited to information of specific relevance for displacement-based seismic design. Nevertheless, a brief treatment of some of the common terms and a similarly brief discussion of the characteristics of accelerograms is warranted.

The vast majority of earthquakes are initiated on or adjacent to tectonic plate boundaries by the slow relative movement of the plates. These are termed interplate earthquakes. Intraplate earthquakes, occurring far away from plate boundaries are less common, but nevertheless can be significant for specific sites (for example the New Madrid region of the central USA, Charleston, South Carolina, USA and various parts of Australia).

The two basic terms used to provide a measure of the importance of a particular earthquake are the magnitude and intensity. The magnitude, normally related to the Richter scale[P1] is a measure of the energy release at the fault zone, while the intensity is a measure of the local significance of ground motion at a given site, as described by locally

recorded accelerograms, or by subjective scales, such as the Modified Mercalli scale. The magnitude depends on the length and transverse dimension of fault that fractures during the earthquake, and on the average stress-drop in the rock immediately adjacent to the fault, resulting from rupture. A magnitude 5.0 -5.5 earthquake may result from faulting over a length of a few km, while a magnitude 8 earthquake may involve fault slip over a length as much as 400 km. The energy release is related to magnitude in proportion to $10^{1.5M}$, implying that the energy released increases by a factor of 32 for each unit increase of magnitude. Earthquakes with low magnitude occur frequently, and those of large magnitude occur less frequently. Averaged globally the relationship between magnitude and annual probability of occurrence agrees well with a Gumbel extreme type 1 distribution[P1]. However, this relationship becomes less reliable as the area sampled reduces in size. The concept of a stationary value for the annual probability of occurrence of small to moderate earthquakes near a given site is generally reasonable, but for larger earthquakes, particularly where a site is affected predominantly by earthquakes on a single fault, this assumption may be less valid. Immediately after a major earthquake and its related aftershocks have ended, the probability of major fault movement of the same section of fault is significantly reduced, potentially reducing the major contribution to local seismic hazard. An example is the stretch of plate boundary along the coast of Chile, where major earthquakes tend to occur on specific segments of the fault at rather regular time intervals, and with comparatively uniform magnitudes. This of course will not be the case with smaller earthquakes, and even for large earthquakes where fracture of one segment of a fault may create additional stress on the adjacent section, increasing the probability of fracture of this section in the near future. An example is the Anatolian fault in Turkey, and the subduction boundary between the Nazca and South American tectonic plates where fault rupture tends to occur on successive adjacent segments of the fault in a comparatively regular sequence. Nevertheless, it is common in seismic hazard analysis to assume that the local risk is time-invariant.

Intensity is dependent on magnitude of the causative earthquake, distance from the fault zone, mechanism and direction of rupture propagation, and ground conditions at the site at which intensity is observed, and between the fault zone and the site. There is no exact means of measuring intensity, since it is generally assessed through the effect that the earthquake has at a given site on the built environment. This has typically been defined in the past through descriptive scales such as the modified Mercalli scale[P1]. Attempts to relate such scales that are dependent on observations of damage to different structural types and materials, to such measurable quantities as peak ground acceleration or velocity have not been particularly successful, as different ground motion quantities have different significance to different structural types. Thus peak ground acceleration may be important to structures that have brittle failure modes, but may be of little importance to a flexible well-confined structure. Duration of shaking may be a key parameter for a flexible structure without adequate confinement.

No two accelerograms are identical, even when the earthquakes originate in the same part of a fault, with similar magnitudes, and the site where the accelerograms are recorded is the same. Some of the differences and similarities between accelerograms are illustrated

by the three examples of Fig.2.1. The first of these is from the moderate Whittier earthquake of 1987 ($\mathbf{M_W}$ = 6.0), recorded in analogue form at a distance of 15km from the rupture. The second is from the $\mathbf{M_W}$ = 6.7 Northridge earthquake of 1994, recorded at the Sylmar site, at a distance of 6km from the fault rupture, and the final record is from the $\mathbf{M_W}$ = 6.9 1995 Kobe earthquake, recorded immediately adjacent to the fault. None of the records shows the complete duration of recorded motion, but all include the section of greatest interest, including before, during and immediately after the strong ground motion. All three records are plotted to the same time and acceleration scales.

The record from the smaller Whittier earthquake has a comparatively short period of strong ground motion compared with the other two records, the peak ground acceleration ($\mathbf{PGA}$) is lower, and it appears that high frequency components are more dominant. On the other hand, all records show an initial period of comparatively high frequency/low amplitude acceleration before the onset of the strong-motion period of response, corresponding to the time period between arrival of the $\mathbf{P}$ and $\mathbf{S}$ waves. Both the Sylmar and Kobe records show high amplitude/low frequency pulses in the initial stages of the strong ground motion, corresponding to a focusing effect related to the mechanism of energy release and the local geology, known as a velocity pulse. In the case of the Kobe record, this is primarily a result of forward directivity where the fault fractures over a short period of time from one end to another, focusing the energy in the downstream direction. In the Sylmar record, the reasons are apparently more complex, involving basin edge effects[S5].

It is also of some interest to examine the time sequence of ground displacement, found by double integration of the acceleration records. These are shown for the same three records in Fig.2.2, and are plotted to the same time scales, but with a factor of 30 difference between the displacement scales of the Whittier and the other two records. It should be noted that integration of the acceleration records to obtain displacement records is inevitably subject to some error. Small systematic errors in the acceleration record can lead to large errors in the displacement record, causing the apparent displacement to drift in one direction. Base-line corrections are typically carried out to remove this drift, but the accuracy of such corrections is uncertain.

It will be apparent from comparison of Figs.2.1 and 2.2 that the differences between the displacement records are more pronounced than between the acceleration records. Although the $\mathbf{PGA}$s for the three records only vary by a factor of about 2.5, the peak ground displacements ($\mathbf{PGD}$) vary by a factor of about 25. All three records exhibit much less high frequency content in displacement terms than in acceleration terms, but the Whittier record is significantly richer in high frequency components than the other two records. The two more intense records appear to show dominant long-period ground displacement response. In the case of the Sylmar record, this appears to correspond to a period of about 3 to 4 seconds.

Intensity, for a given earthquake, decreases with distance from the fault. Attenuation relationships are used to describe this reduction in intensity. However, there is a large spatial variation in recorded ground motions between different sites at equal distances from the epicentre of an earthquake. Attenuation relationships are averages found from
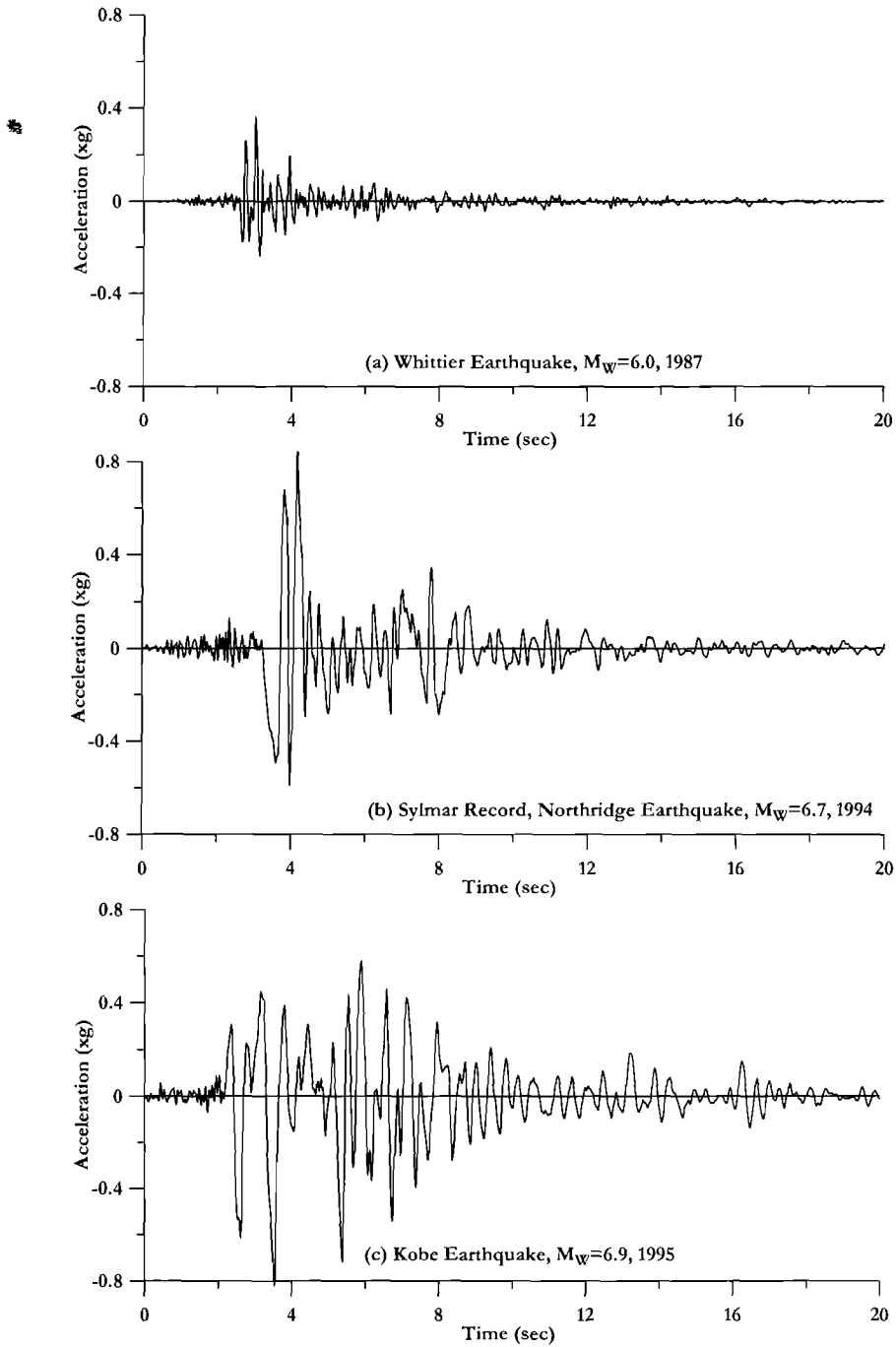
Fig.2.1   Selected Time-Windows of Different Accelerograms
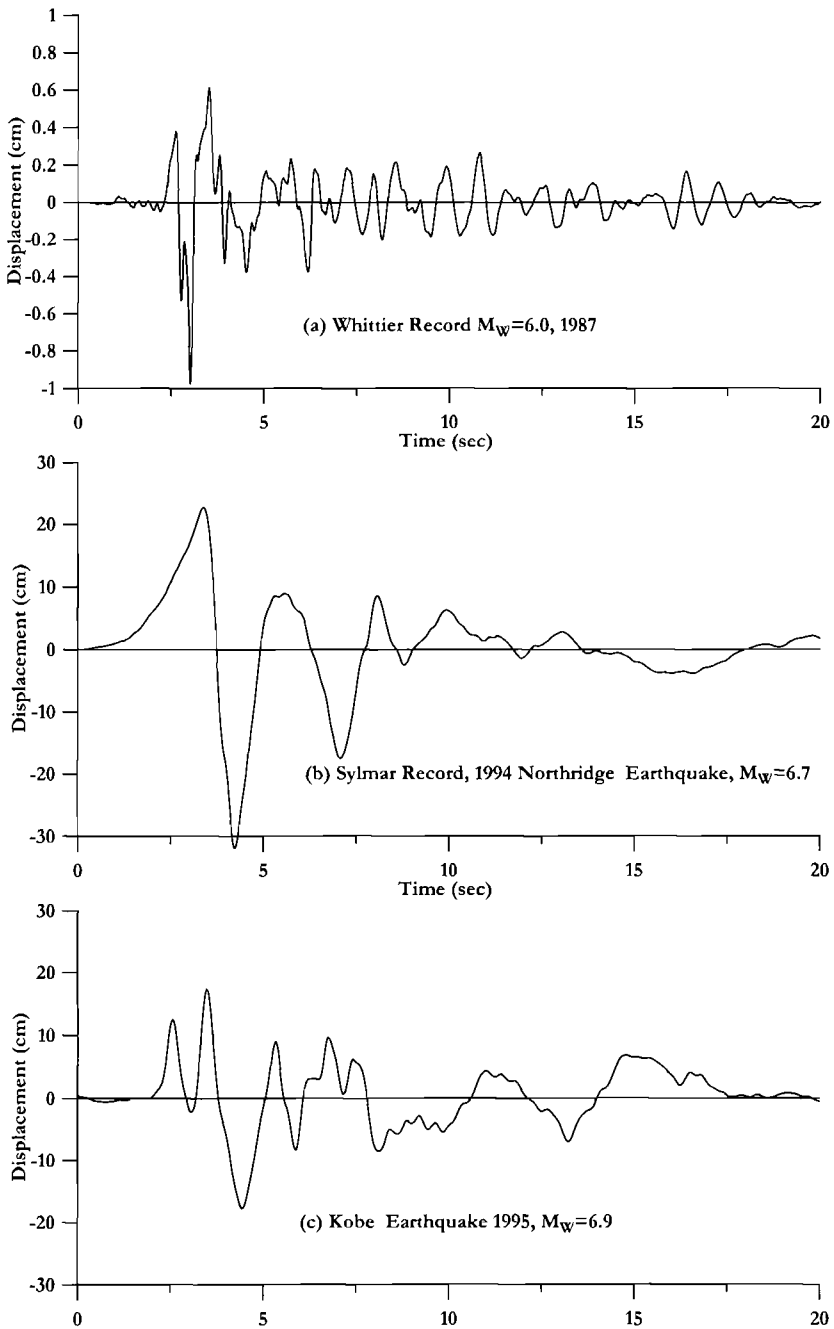
Fig.2.2 Selected Time-Windows of Ground Displacement from the
Accelerograms of Fig.2.1

recorded accelerograms, and typically do not account for many of the factors known to influence intensity. Somerville et al[S5] have noted that the variations in ground motion, which are particularly apparent at periods greater than one second (and hence are of particular importance to structural design – whether force-based or displacement-based) "can usually be attributed to features of the earthquake source such as the orientation of the fault plane, the style of faulting (strike-slip or dip-slip), and the evolution and distribution of slip on the fault plane"[S5]. Thus it is reasonable to assume that the current uncertainty associated with site intensity predicted by probabilistic seismic hazard analyses (**PSHA**) will be reduced as site and source modelling improves.

A number of the factors affecting spatial variation of ground motion from a given earthquake are discussed in [S5] in relation to the Los Angeles Basin. The following notes provide a summary of the discussion in [S5]:

Near fault rupture directivity pulse: Near fault recordings from recent earthquakes indicate that ground motion is dominated by a large long-period narrow-band pulse in the fault-normal motion, whose period increases with magnitude[S6]. This pulse may have a dominant period of about 1 sec. for earthquakes of magnitude $M_w = 6.7 - 7.0$, and as high as 4 sec. for earthquakes of magnitude $M_w = 7.2 - 7.6$.

Reverse faulting earthquakes: Ground motions from reverse faulting earthquakes are systematically stronger than ground motions from strike-slip earthquakes. The influence may be as much as 20-40%.

Buried faulting earthquakes: Ground motions from shallow earthquakes that do not break the ground surface are systematically stronger than from earthquakes that result in surface faulting. Again the influence may be in the order of 20 40%. The 1989 Loma Prieta, and the 1994 Northridge earthquakes are examples of shallow earthquakes without surface faulting.

Ground motion from large surface faulting earthquakes: Ground motions from earthquakes that produce large surface faulting (e.g. the Chi-Chi earthquake in Taiwan) tend to be significantly lower than predicted by current ground motion models, and substantially lower than ground motions from buried faulting earthquakes.

Basin effects: Current codes modify design ground motions on the basis of the shear-wave velocity in the upper 30m of soil. This is only appropriate for rather short-period motion, as at periods greater than one second, seismic wave lengths are much longer than 30m, and response is likely to be influenced by soil properties at depths of hundreds, and perhaps thousands of metres. Basin edge effects can also be significant, with constructive interference between waves entering from the edge and from the basin below, particularly when the basin has steep fault-controlled margins.

Recently developed hybrid simulation procedures[G4] are capable of incorporating all of the above features in calculating broadband ground motion time-histories for prescribed earthquake scenarios. **PSHA**s based on these techniques are already more reliable than those based on attenuation relationships, and it can confidently be expected that improved characterization of seismicity of specific sites will continue. It is likely that future developments will be less towards improved accuracy of code spectra, than

towards improved mapping of local characteristics defining seismicity, with spectral shape as well as spectral ordinates being a mapped variable.

2.2 RESPONSE SPECTRA

2.2.1 Response Spectra from Accelerograms

The fundamental information extracted from accelerograms or **PSHA**'s for use in design is typically expressed in the form of response spectra, which represent the peak response of single-degree-of-freedom oscillators of different periods of vibration to the accelerogram. The quantities most commonly represented in response spectra are absolute acceleration (with respect to "at rest" conditions), and relative displacement (with respect to instantaneous ground displacement), though relative velocity response spectra are also sometimes computed. The procedure is represented in Fig.2.3 where five different **SDOF** oscillators are depicted in Fig.2.3(a) subjected to the earthquake ground motion $\ddot{a}_g$. The peak absolute acceleration and relative displacements recorded during response to the accelerograms are plotted against the period of the structure in Fig.2.3(b).

Normally response spectra provide information on the peak elastic response for a specified elastic damping ratio (typically 5%), and are plotted against the elastic period. It is, however, also possible to plot inelastic spectra related to specified displacement ductility levels. In this case the period may represent the initial elastic period, or the effective period at peak displacement demand, related to the effective stiffness.

(a) SDOF Oscillators   (b) Elastic Response Spectra
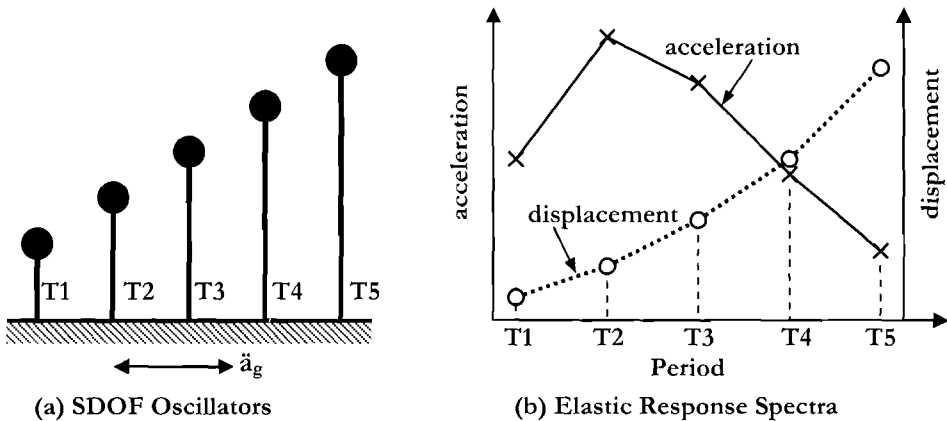
Fig.2.3 Formation of Response Spectra

Examples of elastic acceleration and displacement spectra for the three accelerograms represented in Figs.2.1 and 2.2 are shown in Fig.2.4. The spectra are shown for four levels of elastic damping, expressed as ratios to the critical damping. Some interesting conclusions can be drawn from examination of these figures. The Whittier accelerogram has a **PGA** of about 0.4g (see Fig.2.1(a)), and a peak response acceleration of more than
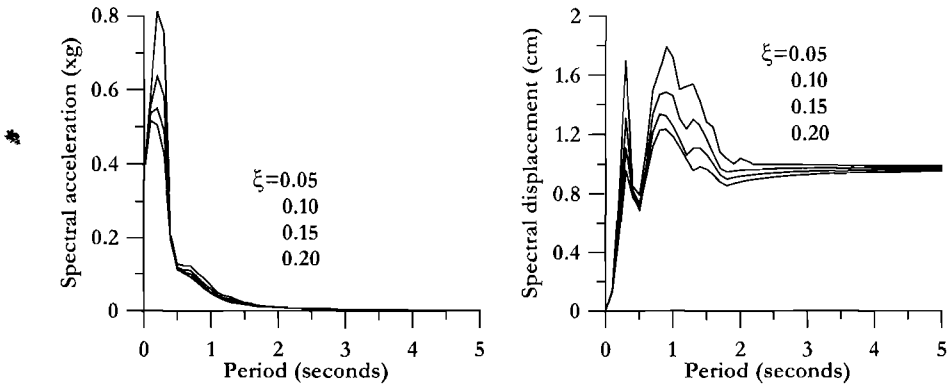
(a) Whittier (M_W=6.0)
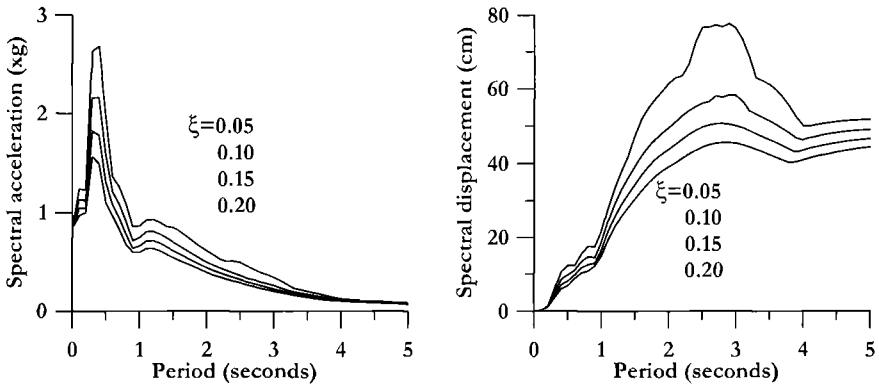
(b) Sylmar (Northridge,1994; M_W=6.7)
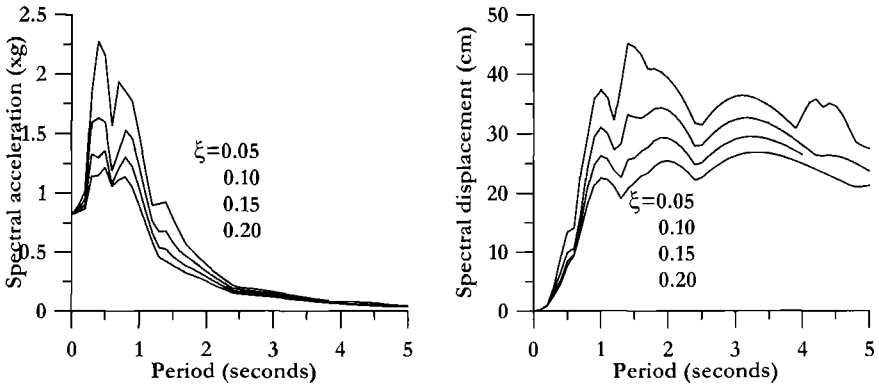
(c) Kobe (M_W=6.9)

Fig.2.4   Acceleration and Displacement Elastic Response Spectra for
Accelerograms of Figs.2.1 and 2.2

0.8g at a period of about 0.25 sec. This might be considered to represent reasonably strong ground motion, since design **PGA**'s and peak response accelerations for high-seismicity regions are often in the range 0.4g and 1.0g respectively. However, when we examine the displacement spectra from the same accelerogram, we find that the peak response displacement is less than 20mm (0.79in), for a damping level of 5% of critical damping. Thus, if a given structure is capable of sustaining this very minor peak response displacement within the elastic range of response, no damage would be expected, despite the high peak response acceleration. To put this in perspective, information provided in Section 4.4.6 indicates that for reinforced concrete frame buildings of typical proportions, effective yield displacements for two- and four-storey buildings might be approximately 45mm (1.8 in) and 90mm (3.6in) respectively – significantly larger than the peak displacement response for this accelerogram. It is apparent that only very stiff and brittle structures would be expected to be at risk from an accelerograms similar to the Whittier record. This is in agreement with the recorded damage in the Whittier earthquake.

Another point of interest is apparent from Fig. 2.4(a). Information from the acceleration response spectra cannot be extracted for periods of T > 1.5 sec since the response accelerations are so low. The displacement spectra provide much more readily accessible information for the medium to long period range, but indicate surprisingly regular displacements at periods greater than about 2 seconds. In fact this is false data, since the accelerogram was recorded by an analogue, rather than digital accelerograph, and a filter at 3 seconds was used to determine the displacement response. Bommer et al[A8] have shown that the roll-off associated with filtering makes the response spectra unreliable for periods greater than about 2/3rds of the filter period. Thus the data in the displacement spectra of Fig.2.4(a) are meaningless for periods greater than about 2 sec.

The Northridge Sylmar acceleration spectra of Fig.2.4(b) show peak acceleration response for 5% damping of about 2.7g – about three times the response for the Whittier earthquake. The displacement spectra, which result from a digital accelerograph, and are reliable up to significantly longer periods, indicate peak displacement response of about 800mm (31.5in) – more than 40 times that of the Whittier record. Clearly this record would be expected to have much greater potential for damage than the Whittier record. Note that after reaching a peak response at about 3 sec., displacement response decreases at higher periods.

The Kobe record of Fig.2.4(c) also has high peak displacement response, and somewhat similar characteristics to the Sylmar record, though the peak displacement response appears to occur at a reduced period.

2.2.2 Design Elastic Spectra

(a) Elastic Acceleration Spectra: Until recently, design spectra for seismic design of structures were typically specified in design codes as a spectral shape related to soil conditions, modified by a design **PGA**, reflecting the assessed seismicity of the region where the structure was to be built. Typically only acceleration spectra were provided, and

mapping of the variation of **PGA** with location was coarse. This is still the case with many seismic design codes.

Recently, more detailed information has been provided in different design codes, such as the IBC[X4] of the USA, and the new Italian seismic design code[X14], where spectral acceleration ordinates at two or three key periods are provided for a given site for different return periods. Typically this is provided through a computerized data base, enabling design data to be extracted based on site longitude and latitude. However, this is typically provided only for acceleration response spectra; peak displacement response is not yet available in many design codes.

The typical form of elastic acceleration response spectra is illustrated in Fig.2.5(a). The shape is smoothed, reflecting the average of many accelerograms, and is based on probabilistic estimates of the contribution to seismic risk of a larger number of smaller earthquakes, and a reduced number of larger earthquakes. The result is a spectrum where the acceleration ordinates have uniform probability of occurrence for a given return period (see Section 2.2.2(c) below).

The spectrum rises from the **PGA** at **T** = 0 to a maximum value at a period T_A (typically about 0.15 seconds). For soft soils, codes typically amplify the **PGA** above the value applicable for firm ground, or rock. The plateau typically has a response acceleration of about 2.5 to 2.75 times the **PGA**. The acceleration plateau continues to a period of T_B, the value of which depends on the ground conditions in the near-surface layers, with larger values applying to soft soils, as indicated in Fig.2.5(a). The value of T_B also typically depends on the magnitude of the earthquake, as is apparent from Fig.2.4, with smaller values being appropriate for earthquakes of lower magnitude. For periods greater than T_B the response acceleration reduces, typically in proportion to T, implying a constant-velocity response. In many codes this constant-velocity part of the spectrum continues indefinitely. More advanced codes specify an upper limit of $T = T_C$ for the constant-velocity range, above which the acceleration decreases in proportion to T^2. A completely opposite trend is apparent in some less advanced codes, where a constant plateau corresponding to a minimum specified response acceleration is sometimes defined. This is shown by the dash-dot line in Fig.2.5(a). The intent of such a provision is to ensure that the lateral strength of a structure is not less than a code-specified minimum value. However, this is better controlled by limits on **P-Δ** moments (see Section 3.8). As discussed below, when the logic of the minimum acceleration plateau of the acceleration spectrum is translated to equivalent displacements, impossible trends result.

The general form of the elastic acceleration spectrum can be defined by the following equations:

$$0 < T < T_A: \quad S_{A(T)} = PGA \cdot \left(1 + \left(C_A - 1\right)\frac{T}{T_A}\right) \tag{2.1a}$$

$$T_A < T < T_B: \quad S_{A(T)} = C_A \cdot PGA \tag{2.1b}$$

$$T_B < T < T_C: \quad S_{A(T)} = C_A \cdot PGA \cdot \frac{T_B}{T} \qquad\qquad (2.1c)$$

$$T > T_C: \qquad S_{A(T)} = C_A \cdot PGA \cdot \frac{T_B \cdot T_C}{T^2} \qquad\qquad (2.1d)$$

In Eqs.(2.1) S_A is the spectral acceleration, and C_A is the multiplier (e.g. 2.5) applied to the **PGA** to obtain the peak response acceleration. Figure 2.5(a) has been developed from these equations with the following parameters:

    firm soil: **PGA** $= 0.4$g, $T_A = 0.15$ sec, $T_B = 0.5$ sec, $T_C = 4.0$ sec, $C_A = 2.5$.
    soft soil: **PGA** $= 0.48$g, $T_A = 0.15$ sec, $T_B = 0.8$ sec, $T_C = 4.0$ sec, $C_A = 2.5$

(b) Elastic Displacement Spectra: Although many codes still do not define design displacement spectra, they are becoming more common [see, e.g. X2, X3, X4, X8]. Ideally these should be developed separately, though using the same data, from acceleration spectra. However, most code-based design displacement spectra are generated from the acceleration spectra assuming that the peak response is governed by the equations of steady-state sinusoidal response. Thus the relationship between displacement and acceleration can be expressed as

$$\Delta_{(T)} = \frac{T^2}{4\pi^2} S_{A(T)} g \qquad\qquad (2.2)$$

where g is the acceleration due to gravity, and $S_{A(T)}$ is expressed as a multiply of g as in Fig.2.5(a). Equation (2.2) has been used to generate the elastic displacement spectra of
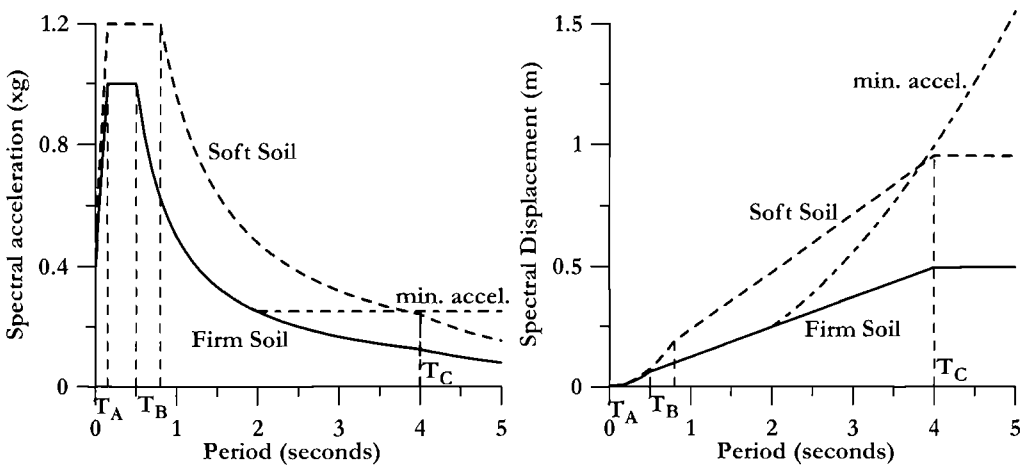
(a) Acceleration Spectra   (b) Displacement Spectra

Fig.2.5 Design Elastic Acceleration and Displacement Spectra

Fig.2.5(b) from the acceleration spectra of Fig.2.5(a). Some characteristics are immediately obvious:

- The displacement spectra are essentially linear with period up to the period T_C. For obvious reasons this is termed the *corner period*. The non-linearity at low periods, corresponding to $T < T_B$, will be found to have little relevance to most displacement-based designs, as will become apparent in later chapters of this text.

- The general shape agrees reasonably well with the response spectra generated from specific accelerograms in Fig.2.4. The peak displacements are also compatible with the more intense accelerograms of Fig.2.4(b) and (c) considering differences in *PGA*.

- The displacement spectrum corresponding to a minimum design acceleration as shown in Fig.2.5(a) has completely unrealistic displacement demands for long period structures. This curve, again shown by the dash-dot line in Fig.2.5(b) has only been shown up to a period of 5 seconds. At 10 seconds the response displacement would be 6.2 m (20ft). This illustrates the illogical nature of some design codes that specify minimum design acceleration levels, and require displacement demand to be determined from Eq.(2.2).

A more general form of the elastic displacement response spectrum is defined by Eurocode EC8[X9] and is shown in Fig.2.6. This shows the linear displacement increase up to the corner period T_C, with a subsequent plateau of displacement up to a period T_D, followed by a decrease in displacement up to a period T_E, at which stage the response displacement has decreased to the peak-ground displacement (*PGD*). Information on the period at which the response displacement starts to decrease is less reliable than data on other key periods in Figs 2.5 and 2.6, and is of little interest to the designer of other than extremely long-period structures such as suspension bridges and large-diameter fluid storage tanks, where convective modes of vibration may be very long. It will be
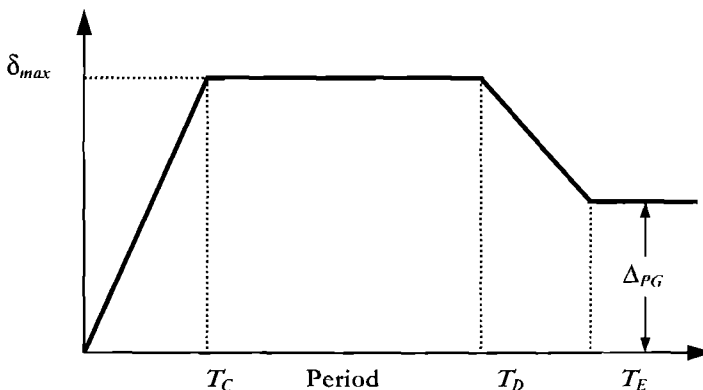
Fig.2.6   General Characteristics of Elastic Displacement Response Spectra[X9]

conservative to assume that the plateau displacement remains constant with period above T_C. However, it is worth noting that all three of the displacement spectra shown in Fig.2.4 conform to the general shape defined by Fig.2.6.

Recent work by Faccioli et al[F6] analyzing a large number of recent high-quality digital records, has provided new information on the factors influencing the shape of displacement spectra. The records investigated included the very large data set from the large 1999 Chi-chi (Taiwan) earthquake, (magnitude $M_w = 7.6$), and a number of moderate European and Japanese earthquakes in the magnitude range $5.4 < M_w < 6.9$.

Their findings include the following points:

- The 5% damped displacement spectra tend to increase essentially linearly with period up to a "corner period". Beyond this, the response displacement either stays essentially constant (for large earthquakes), or tends to decrease (for moderate earthquakes). It is thus conservative to assume a constant spectral displacement for periods higher than the corner period.

- The 10-second spectral displacement for 5% damping can be considered to be a measure of the peak ground displacement.

- Soil amplification of displacement occurs throughout the period range, up to 10 seconds. There is a slight tendency for the corner period to increase for soft soils with large earthquakes, but this is less obvious for moderate earthquakes.

- Soft soil amplification is more pronounced at longer distances (30-50 km) for both moderate and large earthquakes.

- The corner period appears to increase almost linearly with magnitude. For earthquakes with moment magnitude greater than $M_w = 5.7$, the following relationship seems conservative:

$$T_c = 1.0 + 2.5(M_w - 5.7) \text{ seconds} \tag{2.3}$$

- Peak response displacement, δ_{max}, depends on the magnitude, the epicentral distance r km (or nearest distance to the fault plane for a large earthquake), and the stress drop during rupture (generally in the range 1 -10 MPa). Based on analytical considerations, Faccioli et al derive the following relationship for peak response displacement, δ_{max}, in cm, for firm ground conditions:

$$\log_{10} \delta_{max} = -4.46 + 0.33 \log_{10} \Delta\sigma + M_w - \log_{10} r \quad \text{(cm)} \tag{2.4}$$

where $\Delta\sigma$ is the stress drop, in MPa, M_w is the moment magnitude, and r is the epicentral (or fault plane) distance in km. Substituting an average value of $\Delta\sigma = 6$ MPa, and reformatting as a power expression, with δ_{max} in mm:

$$\delta_{max} = C_S \cdot \frac{10^{(M_W - 3.2)}}{r} \quad \text{(mm)} \qquad \rightarrow \text{for 5\% damping} \tag{2.5}$$

where C_S =1.0 for firm ground. The response displacements resulting from Eq.(2.5) should be modified for other than firm ground. Tentative suggestions are as follows:

    Rock: $C_S = 0.7$
    Firm Ground: $C_S = 1.0$
    Intermediate Soil: $C_S = 1.4$
    Very soft Soil: $C_S = 1.8$

These tentative coefficients for C_S have been interpreted from typical acceleration modifiers for *PGA* and period T_B (see Fig.2.5(a)). More refined estimates can be expected as further analyses of digital records become available.

Equation (2.5), with $C_S = 1.0$ is plotted in Fig.2.7 together with Eq.(2.3) for moment magnitudes of 6.0, 6.5, 7.0 and 7.5. The very strong influence of magnitude and epicentral distance on spectral shape and maximum displacement is clearly evident in Fig.2.7. It should be noted, however, that it is probable that the peak displacements for high seismic intensity and low ($r = 10$ km) epicentral distance are overestimated by Eq.(2.5). Within 10 km of the fault rupture, spectral parameters tend to saturate, and the values for 10 km can be assumed to apply for distances less than 10 km. Note also that the peak displacements predicted for earthquakes on the low end of the moderate range (i.e. 5.5 $<M_w$ <6.0) are rather small, even at epicentral distances of 10km. In these cases, most frame buildings of three or more storeys in height, in either reinforced concrete or steel construction, would have effective yield displacements exceeding the 5% damped peak displacement δ_{max} and hence these buildings would be expected to respond elastically to the design-level earthquake. At this early stage in the development of spectral displacement characteristics, the above recommendations should be viewed as preliminary. The consequences in terms of the shape of uniform-risk spectral displacement spectra are also less obvious than for specific earthquake intensities.

The current Eurocode EC8[X9] regulations specify that the corner period T_C (Fig.2.6) is taken as 1.2 sec. for causative earthquakes with M_W < 5.5, and 2.0 sec. for $M_W \geq$ 5.5. This would imply elastic response for most buildings with more than about 8 storeys. It has been suggested by Boore and Bommer[B7] that this low corner period is a result of interpretation of data from analogue records which have been processed with low-order filters set at periods that make the interpretation unreliable at periods above 2 seconds.

NEHRP recommendations[X8], based primarily on seismology theory include the following relationship between corner period and moment magnitude:

$$\log_{10} T_C = -1.25 + 0.3 M_W \tag{2.6}$$

As a consequence of the current interest in displacement-based design, new data are continually being developed by seismologists, related to displacement spectra. A current study of Italian seismicity with the aim of developing design information for displacement
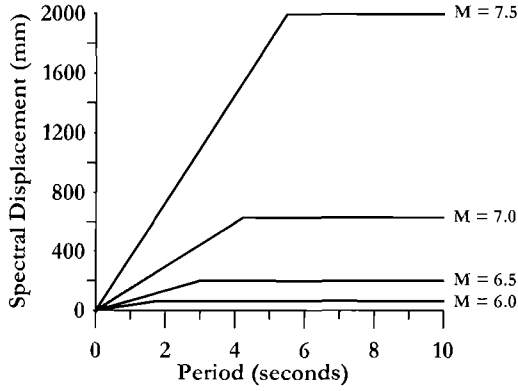
(a) r = 10 km
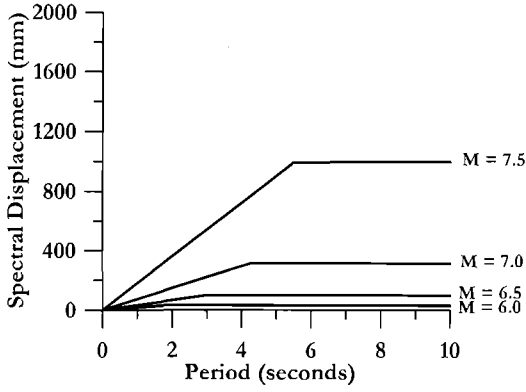
(b) r = 20 km
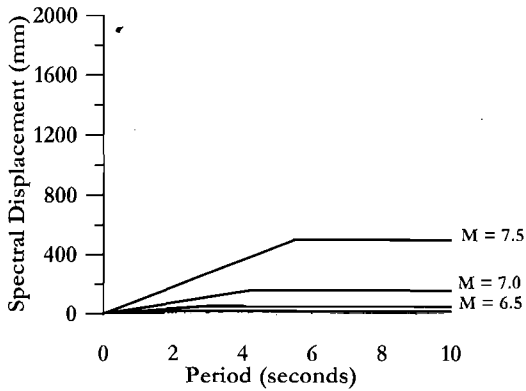
(c) r = 40 km

Fig.2.7   Influence of Magnitude and Distance on 5% Damped Displacement
Spectra for Firm Ground Using Eqs.(2.3) and (2.5) [after F6]

based design in a form similar to the maps of spectral accelerations at key defined periods seems likely to end up with mapped corner periods and peak response displacements in a data base related to GPS coordinates. Preliminary results from this study indicate that both the corner period and the peak elastic response period given by Eqs.(2.3) and (2.5) respectively may be revised upwards by approximately 20%.

Figure 2.8 compares the different equations for corner period as a function of magnitude. It is clear that the current EC8 equation is severely non-conservative, and there are significant differences between the **NEHRP** equation, and the equation determined from the work by Faccioli et al[F6]. It appears that the work in progress in Italy, using a world-wide data-base of some 1700 digital records, and shown tentatively in Fig.2.8 by three dots interpreted from data supplied by Faccioli[2] may lie somewhere between Eq.(2.3) and (2.6).

Figure 2.9 shows average displacement spectra interpreted by Faccioli et al from the world-wide data base of 1700 digital records for earthquakes of magnitude $6.4 < M_W < 6.6$ at different distances from the fault plane. The records have been grouped in distance bands (10-30 km; 30-50km etc), so the averages can be interpreted as appropriate for the average distance (20km, 40km etc). Also shown are bi-linear displacement spectra fitted to the average spectra to obtain the best fit in the plateau range, while still satisfying normal acceleration/displacement relationships in the shorter period range. It will be noted that the corner period shows only slight increase with distance, and that the plateau displacements decrease with distance at a rate that is very close to, but slightly more rapid than that predicted by Eq.(2.5).
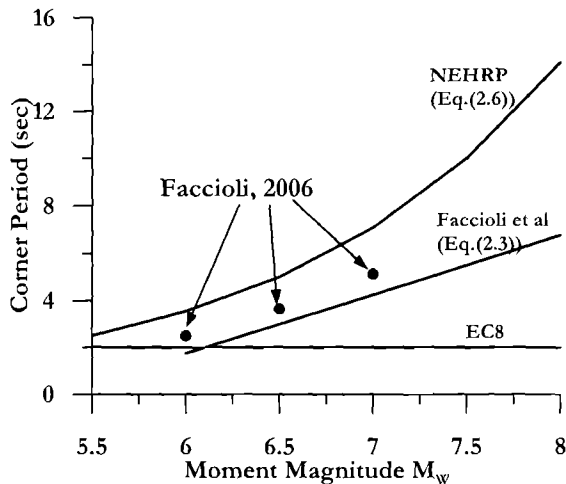
Fig.2.8   Relationship between Corner Period, T_C of Displacement Spectrum and Moment Magnitude M_W

---

[2] Pers. Comm. Prof. E. Faccioli
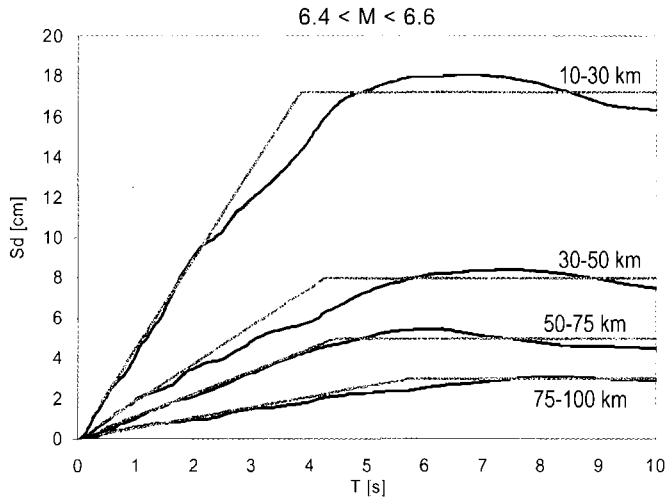
Fig.2.9   Comparison of Average Displacement Spectra from World-Wide Data Base of Digital Accelerograms with Bi-linear Approximations[3]

The consequences of the differences in corner period estimation are potentially serious for long-period structures. Consider a frame building 60m tall (i.e. about 20 storeys). The structure is founded on firm soil, and the design **PGA** is 0.4g, with the majority of seismic risk resulting from an $M_W = 7$ earthquake on a nearby fault. As noted in Section 1.3.2 (Eq.(1.12)) a reasonable approximation of the structural period is 0.1×60 = 6.0 sec. Combining Eqs.(2.1c) and (2.2), the displacement at the corner period (and hence the peak elastic response displacement) can be expressed as

$$\Delta_C = C_A \cdot PGA \cdot T_B \cdot T_C \cdot g / (4\pi^2) \qquad (2.7)$$

Taking $T_B = 0.5$ sec, and $g = 9.805 \text{m/s}^2$, Eq(2.7) results in corner-period displacement estimates of 250mm (9.8in), 530mm (20.9in) and 880mm (34.6in) from the current EC8 value of $T_C = 2$ sec, the value from Eq.(2.3) ($T_C = 4.25$ sec), and the NEHRP value from Eq.(2.6) ($T_C = 7.1$ sec) respectively. For both the EC8 and the Faccioli approach the structural period would exceed the corner period, and hence the response displacement equals the peak response displacement (assuming validity for the "equal-displacement" approximation). Since the NEHRP equation for corner period (Eq.(2.6)) exceeds the estimated elastic period, the response displacement is estimated from Eq.(2.7) using the elastic period of 6 seconds, instead of T_C, resulting in a displacement of 740mm (29.1in). The Italian work in progress would appear to suggest a value of about 640mm (25 in) corresponding to a period of $T_C = 5.1$ sec. It is felt that the correct answer may lie somewhere between Eqs.(2.3) and (2.6). The yield displacement of the frame building can

---

[3] Pers.Comm. Prof. E. Faccioli

be estimated at approximately 400mm (15.7in) using procedures developed in Section 4.4. Thus the EC8 approach would predict that the response would be elastic, with a maximum displacement of about 60% of yield, while the other two approaches would predict inelastic response with displacement ductility demands of about 1.3 and 1.8 respectively.

In this text we shall in some cases use code-specified displacement spectra, and in others, generate displacement spectra based on Eqs.(2.3) and (2.5) to illustrate the general procedure, while recognizing that the corner period may well be revised upwards in the future. We will discount the current EC8 value of 2 seconds for the corner period as being unrealistically low and unsafe.

It should be noted that the difference between current procedures affects the design and response only of long-period structures, and also does not affect the validity of the displacement-based seismic design approach developed in the subsequent chapters of this text. It should also be noted that criticism of displacement-based design approaches on the basis that they use the lengthened effective period corresponding to peak displacement response, where greater uncertainty on spectral ordinates exists as noted above, rather than the initial period, where spectral ordinates may be better defined, is invalid. Force-based seismic design relies on displacement-equivalence rules relating the elastic displacement to the displacement of the effective ductile structure (see Section 1.3.8). Since the effective degraded period of the ductile structure is greater than the elastic period, the displacement-equivalence rules are subject to exactly the same uncertainty as is present in designs based on the effective stiffness.

(c) Design Return Periods: It is customary to assign different return periods, or more correctly annual probabilities of exceedence, for design to different limit states. For example, Eurocode EC8[X3] defines three levels of design earthquake corresponding to different limit states:

(i) Level 1 Seismicity - Serviceability limit state: The level 1 design-level seismicity has a probability of exceedence of 50% in 50years, approximately corresponding to an average return period of 72 years. Under an earthquake with this probability of exceedence, there should be no damage requiring repair, and normal operations of the structure should not be significantly affected.

(ii) Level 2 Seismicity - Damage control limit state: The level 2 design-level seismicity has a probability of exceedence of 10% in 50 years, approximately corresponding to an average return period of 475 years. Repairable damage is permitted under an earthquake with this probability of exceedence, and normal operations may be suspended while repairs are carried out.

(iii)Level 3 Seismicity - Life-safety Limit State: The level 3 design-level seismicity has a probability of exceedence of 2% in 50 years, approximately corresponding to an average return period of 2500 years. The structure should not collapse under ground shaking with this probability of occurrence, but it may not be possible to economically repair the structure following the earthquake.

It is common for only the first two limit states to be considered for structures of other

than special importance. In Europe the life-safety limit state is not used for new designs, but is considered in assessment of existing structures.

There are some problems with a probabilistic approach such as that defined in EC8 and other similar definitions of seismicity, particularly when only the first two limit states are used for design. In regions of high seismicity, such an approach tends to produce rational increments of seismic intensity for the different limit states. However in regions of lower seismicity the seismic intensity corresponding to the first two limit states may be very low, as the seismicity is defined by very rare, but very intense ground shaking. Thus the intensity corresponding to the life-safety earthquake may be much greater than that corresponding to the damage control earthquake.

Consider a rather artificial case where seismic hazard is dominated by a fault which fractures every 1000 years, on average inducing *PGA*'s at the site being considered of 0.8g. The remainder of seismic risk is attributed to background seismicity capable of inducing *PGA*'s of only 0.2g. A probabilistic analysis might then determine the 475 year risk as being characterized by a *PGA* of 0.4g, since the probability of occurrence of the design earthquake occurring within the 475 year period is approximately 50%. However, the earthquake either occurs during that period, or it doesn't. If the structure is designed for 0.4g and the earthquake occurs, the structure fails, since the intensity is much greater than the design strength. If the earthquake doesn't occur, the structure is over-designed.

In the USA a slightly different approach has been used in recent times[X4, X8]. A "maximum considered earthquake" (**MCE**) is defined with a return period of 2500 years – essentially the same as the Level 3 seismicity defined above. The structure is then designed for an intensity of 0.67×**MCE** to the performance criteria applicable to the damage-control limit state. For regions of high seismicity there is little difference from the 10% in 50 years seismicity defined above for the Level 2 seismicity, but for other regions, particularly those with infrequent large earthquakes, the difference is large. The justification for the 2/3rds factor is that structures are expected to have a 50% excess displacement capacity above that corresponding to design to the damage-control limit state performance criteria.

In many existing codes the design acceleration spectra for Level 1 or Level 3 seismicity are found by multiplying the spectrum for the Level 2 seismicity by specified multipliers. These can differ quite markedly between different codes. For example, in Europe and New Zealand the multipliers for the serviceability-level seismicity are 0.4 and 0.167 respectively. This approach does not seem reasonable, as high annual probabilities of exceedence (Level 1 seismicity) are dominated by earthquakes of smaller magnitude, while low annual probabilities of exceedence (Level 3 seismicity) are generally dominated by larger earthquakes with significantly different spectra shapes. The consequences of this difference are examined in Example 2.1 below.

(d) Example 2.1 Design Spectra for a Site Adjacent to an Active Fault: We consider a rather idealized situation where the seismicity of a site is governed by proximity to an active fault. The three design levels defined in the previous section are to be considered. A probabilistic seismic hazard analysis indicates that for a probability of exceedence of

50% in 50 years (serviceability level design), seismic hazard is dominated by an earthquake of magnitude 6.15 at a distance of 10 km. For Level 2 seismicity (10% probability in 50 years), seismic hazard is dominated by a M7.0 earthquake at 10 km, and for the life-safety considerations (Level 3 seismicity; 2% probability in 50 years), the seismic hazard is dominated by an M7.5 earthquake which is the maximum considered feasible for the fault segment adjacent to the site, at a distance of 10km. The ratio of the magnitudes for the earthquakes with probability of 10% in 50 years and 50% in 50 years corresponds roughly to the average applicable to the entire circum-pacific belt. Although very large variations from this ratio could occur at different sites we consider the average to be appropriate for this site, for the purpose of example.

With the information above, the design displacement spectra can be generated for the three limit states, using Eqs.(2.3 and 2.5). The results for corner period and peak response displacement are summarized in Table 2.1, and the spectra are plotted in Fig.2.10(a), based on firm ground conditions.

Table 2.1 Design Parameters for Elastic Spectra for Example 2.1

	Level 1 EQ	Level 2 EQ	Level 3 EQ
Prob. of exceedence	50% in 50 yrs	10% in 50 yrs	2% in 50 yrs
Magnitude, M_W	6.15	7.0	7.5
Corner Period, T_C (sec)	2.13	4.25	5.5
Corner Disp. δ_{max}, (mm)	89	631	1995
Period T_B (Fig.2.5) (sec)	0.3	0.5	0.7
Peak Ground Acc. (xg)	0.22	0.47	0.83
Peak Spectral Acc. (xg)	0.55	1.18	2.08

Acceleration spectra can be generated from the displacement spectra inverting Eqs. (2.2) and (2.7), provided an assumption is made about the period T_B at the end of the response acceleration plateau (see Fig.2.5(a)). Values assumed for T_B increase with earthquake magnitude, and are listed in Table 2.1. A further necessary assumption is that the response acceleration plateau commences at a period of $T_A = 0.15$ sec., and that the ratio of peak spectral acceleration to PGA is $C_A = 2.5$. On the basis of these assumptions the peak ground accelerations are found to be 0.22g, 0.47g, and 0.83g respectively, with peak response accelerations 2.5 times these values, as listed in Table 2.1. The resulting acceleration spectra are plotted in Fig.2.10(b). Values for the PGA and peak response acceleration do not seem unreasonable. Note that the ratio between PGA for the serviceability and damage-control limit states (0.47) is higher than would apply to Eurocode EC8[X3] or the NZ loadings code[X1].

The very significant differences in the displacement spectra for the three limit states are immediately apparent, and appear more significant than the differences in the acceleration spectra. This is a consequence of the influence of variations in the corner

(a) Displacement Spectra

(b) Acceleration Spectra
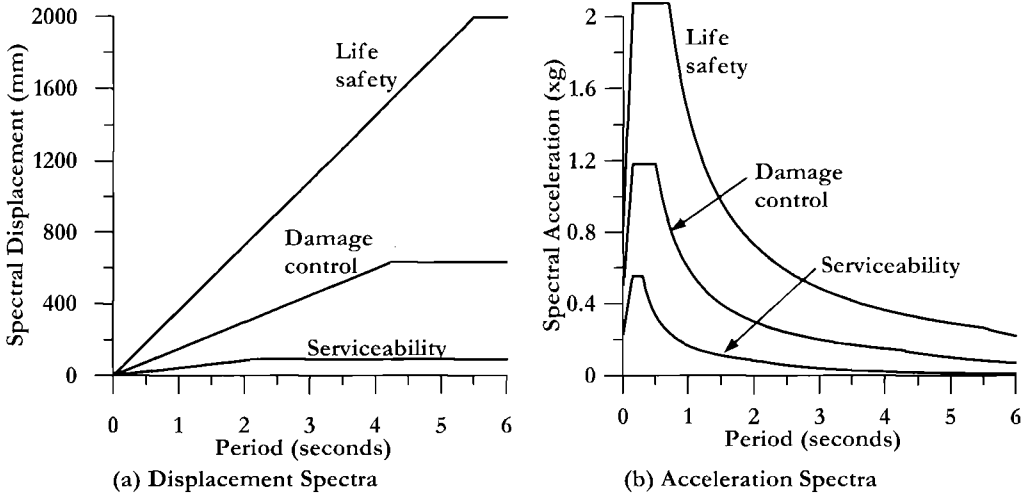
Fig.2.10   Design Spectra for Example 2.1

period. With a peak elastic response displacement of only 89mm (3.5in) most frame buildings of four or more storeys would respond elastically, regardless of elastic period, as discussed in more detail in Chapter 5.

The spectra developed by the approach outlined in this example are rather different from spectra resulting from simple scaling of a standard spectral shape.

2.2.3   Influence of Damping and Ductility on Spectral Displacement Response

Displacement-based seismic design using a secant stiffness representation of structural response requires a modification to the elastic displacement response spectrum to account for ductile response. The influence of ductility can be represented either by equivalent viscous damping or directly by inelastic displacement spectra for different ductility levels. Figure 2.11 shows both options for a firm-soil site, with **PGA** = 0.4g, and corner period of T_C = 4 sec. The use of spectra modified by different levels of damping requires relationships between ductility and damping to be developed for different structural hysteretic characteristics as discussed in detail in Section 3.4.3, but enables a single design spectrum to be used for all structures (e.g. Fig.2.11(a)). The use of spectra modified by different levels of ductility (e.g. Fig.2.11(b)) is perhaps more direct, but requires the ductility modifiers to be determined for each hysteretic rule considered.

If a relationship between initial-period elastic displacement and inelastic displacement such as the equal-displacement approximation is assumed, the inelastic spectra of Fig.2.11(b) can be directly computed. The procedure is considered in detail in Section 3.4.3(e). Using this procedure, and assuming validity of the equal displacement approximation the data in Fig.2.11(b) have been calculated for an elasto-plastic response. Different relationships apply for different post-yield stiffnesses, but not to   different hysteretic energy absorption within the loop, provided that the equal-displacement

(a) Modified by Equivalent Viscous Damping   (b) Modified by Displacement Ductility
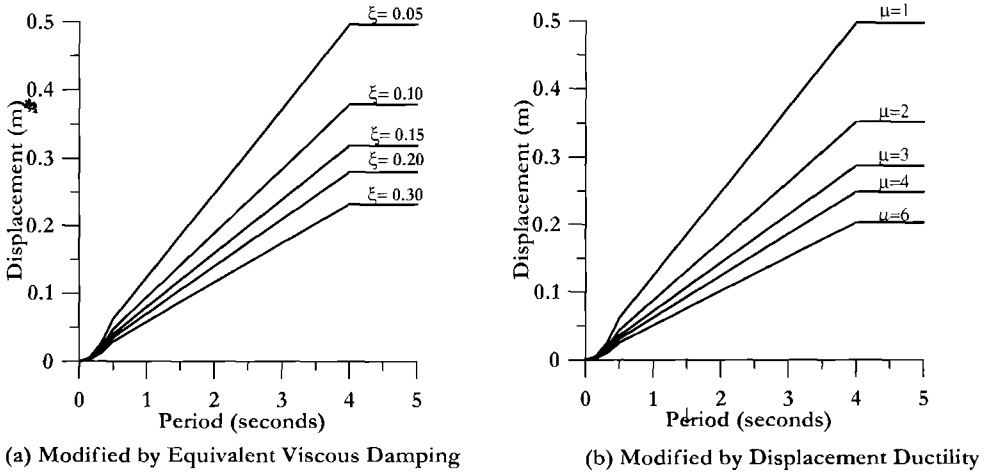
Fig. 2.11   Representation of Inelastic Response by Displacement Response Spectra

approximation is assumed to be valid. However, recent research presented in Section 4.9.2(g) indicates that the equal-displacement approximation is in fact non-conservative. The consequence is that inelastic spectra based on displacement ductility (e.g. Fig.2.11(b)) must be calibrated for each different hysteretic rule.

Because of these reasons, the equivalent viscous damping approach, presented in Fig.2.11(a) is preferred, since codified specification is simpler. However, there appears to be still some uncertainty amongst seismologists as to the appropriate form of the damping modifier R_ξ to be applied to the elastic displacement spectrum for different levels of damping ξ. A commonly used expression was presented in the 1998 edition of Eurocode EC8[X3], and is shown below in Eq.(2.8):

$$R_\xi = \left(\frac{0.07}{0.02 + \xi}\right)^\alpha \tag{2.8}$$

where α = 0.5. In the 2003 revision to EC8, Eq.(2.8) was replaced by

$$R_\xi = \left(\frac{0.10}{0.05 + \xi}\right)^{0.5} \tag{2.9}$$

In both Eq.(2.8) and (2.9), ξ is expressed as a damping ratio related to the critical damping. An alternative expression proposed by Newmark and Hall[N2] in 1987 is defined by Eq.(2.10):

$$R_\xi = \left(1.31 - 0.19\ln(100\xi)\right) \tag{2.10}$$

The three expressions are compared in Fig.2.12 for different levels of damping. It will be seen that the expression given by Eq.(2.10) appears very conservative compared with the other two expressions. Our analyses using both spectral compatible earthquake records and actual accelerograms supports the 1998 EC8 expression for accelerograms without near-field forward directivity velocity pulse characteristics. A comparison is shown in Fig.2.13 for the average response of a suite of seven spectrum-compatible records used for design in the Port of Los Angeles[E1], California. The design elastic displacement spectrum was determined from a site-specific probabilistic seismic hazard analysis, and seven two-component accelerograms from earthquake records appropriate to the site, distance from fault and expected magnitude were manipulated to match the spectrum for a damping ratio of $\xi = 0.05$. The fourteen individual modified accelerograms were then subjected to spectral analysis to determine the effect of different levels of damping. The averages for the records are shown in Fig.2.11 by the solid lines. The dashed lines represent the spectra resulting from modifying the design spectrum for the damping ratio of $\xi = 0.05$ in accordance with Eq.(2.8), with $\alpha = 0.5$. It will be seen that the agreement with the curves from spectral analysis is very good, on average. Similar agreement has been obtained from analyses of real records[K8].

It would also be desirable to have an equivalent expression for sites where forward directivity velocity pulse characteristics might be expected. It has been suggested[P3] based on limited data, that a modification to the 1998 EC8 expression given by

$$R_\xi = \left(\frac{0.07}{0.02 + \xi}\right)^{0.25} \tag{2.11}$$
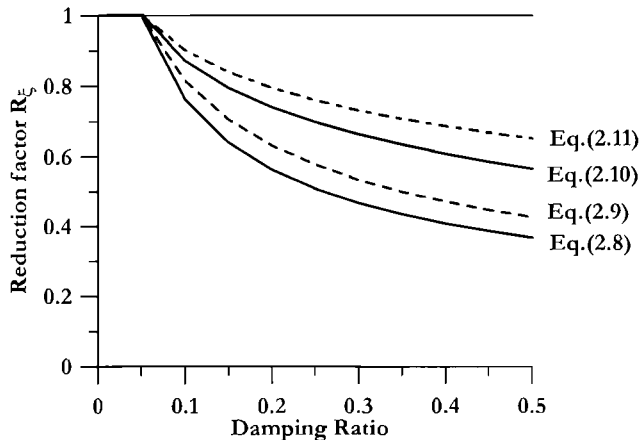
Fig.2.12 Damping Modifiers to Elastic Spectral Displacements
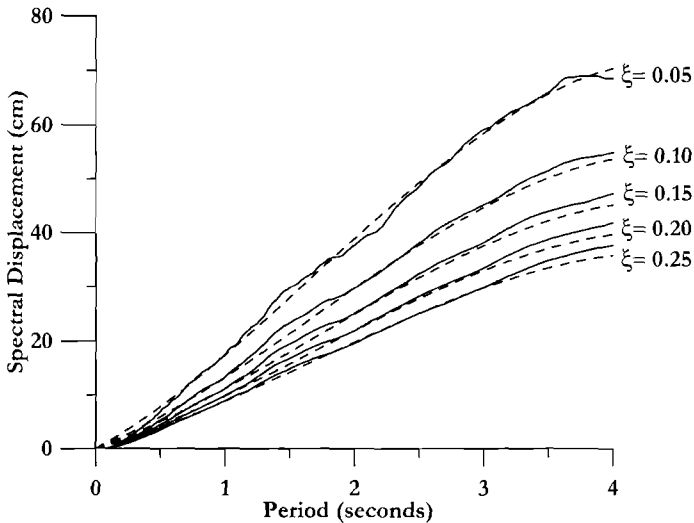
Fig. 2.13   Comparison of Spectral Analysis Results and Eq.(2.8) for a Suite of 14 Spectrum-Compatible Accelerograms

might be appropriate. It will be seen that Eq.(2.11) is the same as Eq.(2.8) but with $\alpha = 0.25$ instead of 0.50. The effect of this modification is to increase the value of R_ξ compared with the value applying for "normal" accelerograms. The reduction factor resulting from Eq.(2.11) is included in Fig.2.12 for comparison with the other expressions, and Fig.2.14 compares the dimensionless displacement modifiers for the 1998 EC8 expression (Eq.2.8) and the expression suggested for near-field forward directivity conditions (Eq.(2.11)). The data in Fig.2.14 are based on the shape of the displacement spectrum for firm ground plotted in Fig. 2.5(a). Some qualified support for Eq.(2.11) is available in work by Bommer and Mendis[B8] who provide additional discussion of this topic. Their work indicates that the scaling factors may be period-dependent, which is not currently considered in design.

It will be shown in Section 3.4.6 that use of displacement spectra for near-field forward-directivity effects results in a requirement for higher base-shear strength when compared to requirements for "normal" conditions. This requirement has been recognized for a number of years, in particular since the 1994 Northridge earthquake, and is incorporated empirically in recent force based codes [e.g. X4, X8]. This is an example of conditions where it has been recognized that existing displacement-equivalence rules are inadequate in force-based design. With displacement-based design, the influence of near-field effects are directly incorporated in the design, provided the reduced influence of damping (and ductility) in modifying displacement response is recognized by graphs such as Fig.2.14(b).
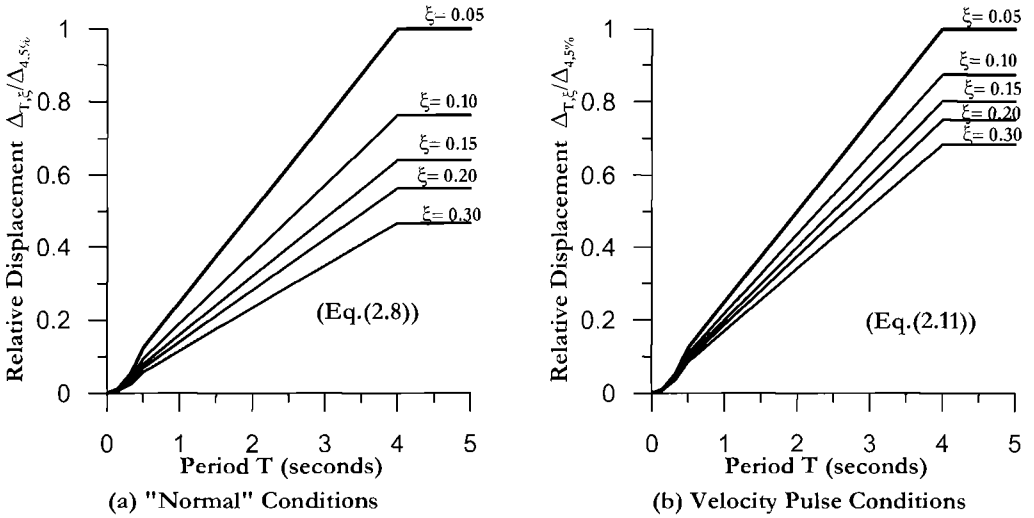
Fig.2.14 EC8 (1998) Damping Reduction Factor, and Tentative Factor for Forward Directivity Effects

As discussed earlier in this chapter, displacement spectra for design are in a developmental stage, with rather rapid progress being made by seismologists. The same statement can be applied to developments in definition of acceleration spectra. It is probable that displacement spectra, and modifiers for damping, period and ductility will change from the tentative values suggested in this Chapter. However, this should not be taken to reduce the utility of the work presented in subsequent chapters. The approaches developed are independent of the displacement spectra, and several different shapes will be used in different examples, to illustrate the flexibility of the direct displacement-based design method.

It should also be noted that the material presented in this chapter is at least as valid as acceleration spectra currently used for force-based design (see p53). Taken together with the extensive research described in Chapters 3 and 4 on relationships between ductility and damping, the procedures developed are significantly less susceptible to errors than resulting from current force-based design, and much better adapted to achieving specified limit states.

2.3 CHOICE OF ACCELEROGRAMS FOR TIME-HISTORY ANALYSIS

The most reliable method at present for determining, or verifying the response of a designed structure to the design level of intensity is by use of non-linear time-history analysis. The selection and characteristics of accelerograms to be used for this requires careful consideration. The reader is referred to Section 4.9.2(h) where this is discussed in some detail.

3

DIRECT DISPLACEMENT-BASED DESIGN: FUNDAMENTAL CONSIDERATIONS

3.1 INTRODUCTION

The design procedure known as *Direct Displacement-Based Design* (**DDBD**) has been developed over the past ten years[P8,P9,P10,P11] with the aim of mitigating the deficiencies in current force-based design, discussed in some detail in Chapter 1. The fundamental difference from force-based design is that **DDBD** characterizes the structure to be designed by a single-degree-of-freedom (**SDOF**) representation of performance at peak displacement response, rather than by its initial elastic characteristics. This is based on the *Substitute Structure* approach pioneered by others[G1,S2].

The fundamental philosophy behind the design approach is to design a structure which would achieve, rather than be bounded by, a given performance limit state under a given seismic intensity. This would result in essentially uniform-risk structures, which is philosophically compatible with the uniform-risk seismic spectra incorporated in design codes. The design procedure determines the strength required at designated plastic hinge locations to achieve the design aims in terms of defined displacement objectives. It must then be combined with capacity design procedures to ensure that plastic hinges occur only where intended, and that non-ductile modes of inelastic deformation do not develop[P1]. These capacity design procedures must be calibrated to the displacement-based design approach. This is discussed further in general terms in Sections 3.9 and 4.5, and in specific structure-related terms in the appropriate structural chapters. It will be shown that capacity design requirements are generally less onerous than those for force-based designs, resulting in more economical structures.

This chapter deals with fundamental aspects of the approach that are common to all materials and structural systems. Subsequent chapters deal with detailed application to different structural systems, including verification by design/analysis examples.

3.2 BASIC FORMULATION OF THE METHOD

The design method is illustrated with reference to Fig.3.1, which considers a **SDOF** representation of a frame building (Fig.3.1(a)), though the basic fundamentals apply to all structural types. The bi-linear envelope of the lateral force-displacement response of the **SDOF** representation is shown in Fig.3.1(b). An initial elastic stiffness K_i is followed by a

post yield stiffness of rK_i.

While force-based seismic design characterizes a structure in terms of elastic, pre-yield, properties (initial stiffness K_i, elastic damping), **DDBD** characterizes the structure by secant stiffness K_e at maximum displacement Δ_d (Fig.3.1(b)), and a level of equivalent viscous damping ξ, representative of the combined elastic damping and the hysteretic energy absorbed during inelastic response. Thus, as shown in Fig. 3.1(c), for a given level of ductility demand, a structural steel frame building with compact members will be assigned a higher level of equivalent viscous damping than a reinforced concrete bridge designed for the same level of ductility demand, as a consequence of "fatter" hysteresis loops (see Fig.3.2).

(a) SDOF Simulation

(b) Effective Stiffness K_e

(c) Equivalent damping vs. ductility

(d) Design Displacement Spectra

Fig. 3.1 Fundamentals of Direct Displacement-Based Design

(a) Idealized Steel   (b) Reinforced Concrete   (c) Friction Slider
    Frame Response   Frame Response   Response

(d) Bridge Column with   (e) Non-linear Elastic   (f) Unsymmetrical
    High Axial Load   with P-Δ Strength
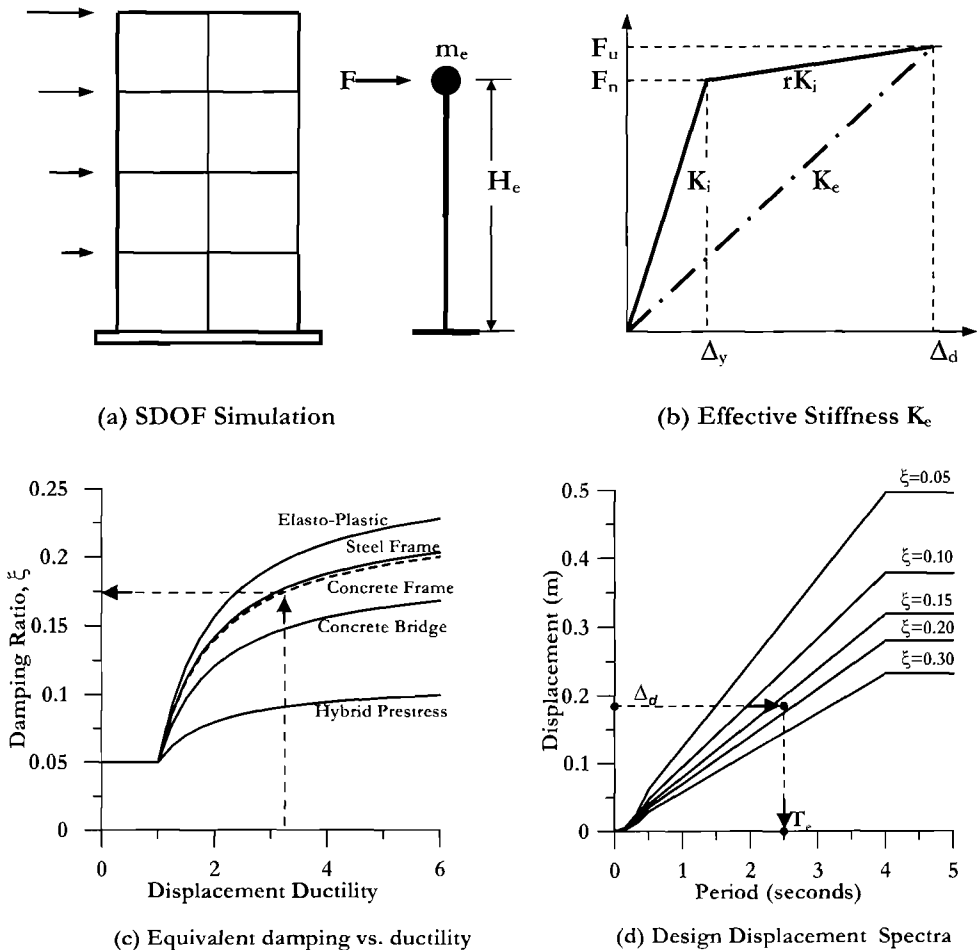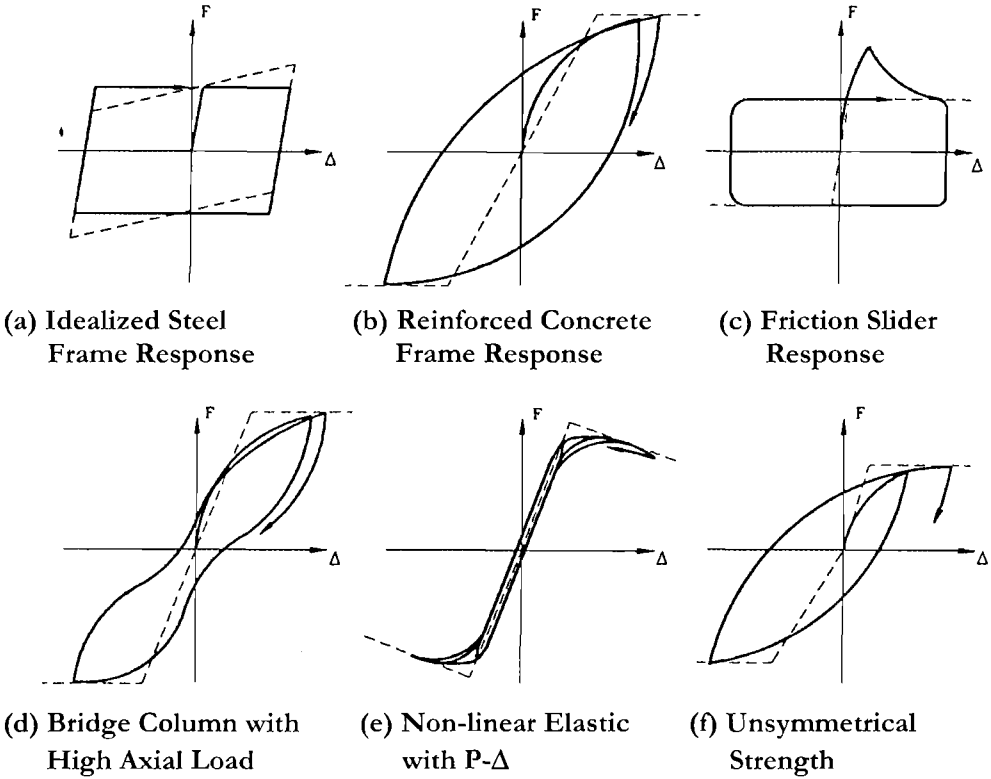
Fig.3.2   Common Structural Force-Displacement Hysteresis Response Shapes

With the design displacement at maximum response determined, as discussed in Section 3.4.1, and the corresponding damping estimated from the expected ductility demand (Section 3.4.3), the effective period T_e at maximum displacement response, measured at the effective height H_e (Fig.3.1(a)) can be read from a set of displacement spectra for different levels of damping, as shown in the example of Fig.3.1(d). The effective stiffness K_e of the equivalent **SDOF** system at maximum displacement can be found by inverting the normal equation for the period of a **SDOF** oscillator, given by Eq. (1.6), to provide

$$K_e = 4\pi^2 m_e / T_e^2 \tag{3.1}$$

where m_e is the effective mass of the structure participating in the fundamental mode of vibration (see Section 3.5.3). From Fig.3.1(b), the design lateral force, which is also the design base shear force is thus

$$F = V_{Base} = K_e \Delta_d \tag{3.2}$$

The design concept is thus very simple. Such complexity that exists relates to determination of the "substitute structure" characteristics, the determination of the design displacement, and development of design displacement spectra. Careful consideration is however also necessary for the distribution of the design base shear force V_{Base} to the different discretized mass locations, and for the analysis of the structure under the distributed seismic force. These will be discussed later.

The formulation of **DDBD** described above with reference to Figs 3.1(c) and (d) has the merit of characterizing the effects of ductility on seismic demand in a way that is independent of the hysteretic characteristics, since the damping/ductility relationships are separately generated for different hysteretic rules. It is comparatively straightforward to generate the influence of different levels of damping on the displacement response spectra, (see Section 2.2.3) and hence figures similar to Fig. 3.1(d) can be generated for new seismic intensities, or new site-specific seismicity using standard techniques[G6].

It is also possible, however, to combine the damping/ductility relationship for a specific hysteresis rule with the seismic displacement spectral demand in a single inelastic displacement spectra set, where the different curves directly relate to displacement ductility demand, as illustrated in the example of Fig.3.3.
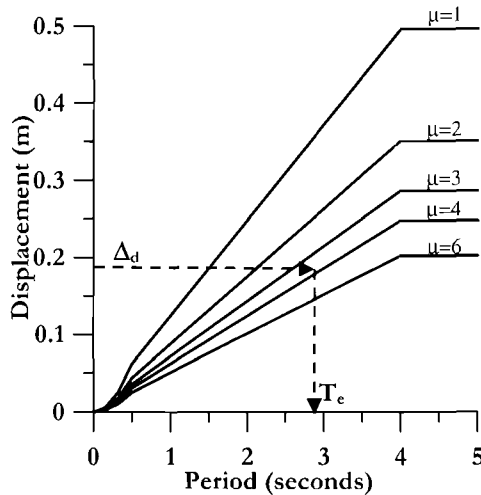
Fig.3.3   Example of an Inelastic Displacement Spectra Set Related to Effective Period for a Specific Hysteresis Rule

With the seismic demand characterized in this fashion, the design procedure is slightly simplified, as one step in the process is removed. The inelastic displacement spectra set is entered with the design displacement (to be discussed subsequently) and the design effective period is read off for the level of the design displacement ductility. Although this is a slightly simplified procedure, it requires that inelastic displacement spectra be generated for different hysteresis rules for each new seismic intensity considered. Since this is a rather lengthy process, we will use the formulation of Fig.3.1 in the examples of

this text. However, we show in Section 3.4.3(e) how the inelastic displacement spectra can be generated from the damping/ductility relationship, the displacement reduction factor for levels of damping above the basic 5% level, and the elastic displacement spectrum.

3.2.1 Example 3.1 Basic DDBD

A five-story reinforced concrete frame building is to be designed to achieve a design displacement of 0.185 m (7.28 in), corresponding to a displacement ductility demand of μ = 3.25. (Procedures to determine design displacement and ductility are discussed in Section 3.4.1). The seismic weight contributing to first mode response (also discussed subsequently, in Section 3.5.3) is 4500 kN (1012 kips). Using the design information of Fig.3.1(c) and (d) determine the required base shear strength.

Equivalent Viscous Damping: Entering Fig.3.1(c) at a ductility of 3.25, and moving up to the curve for concrete frames (follow the dashed lines and arrows), the damping ratio is found to be $\xi = 0.175$ (17.5%).

Effective Period: Entering Fig.3.1(d) with a design displacement of $\Delta = 0.185m$ and moving horizontally to the line corresponding to a damping ratio of $\xi = 0.175$, the effective period is found to be $T = 2.5$ sec.

Effective Stiffness: The effective mass is $m_e = 4500/g$ where g=9.805m/s². Hence from Eq.(3.1) the effective stiffness is

$$K_e = 4\pi^2 m_e / T_e^2 = 4\pi^2 \times 4500/(9.805 \times 2.5^2) = 2900kN/m$$

Base Shear Force: Hence from Eq.(3.2), the required base shear force is

$$V_{Base} = K_e \Delta_d = 2900 \times 0.185 = 536kN \quad (120.5 \text{ kips})$$

3.3 DESIGN LIMIT STATES AND PERFORMANCE LEVELS

In recent years there has been increased interest in defining seismic performance objectives for structures. This has been defined as the "coupling of expected performance levels with expected levels of seismic ground motions" in the "Vision 2000" document[O2], which has had a significant influence in recent seismic design philosophy. In the Vision 2000 document, four performance levels, and four levels of seismic excitation are considered. The performance levels are designated as:

- **Level 1: Fully operational.** Facility continues in operation with negligible damage.
- **Level 2: Operational.** Facility continues in operation with minor damage and minor disruption in non-essential services.

- **Level 3: Life safe.** Life safety is essentially protected, damage is moderate to extensive
- **Level 4: Near collapse.** Life safety is at risk, damage is severe, structural collapse is prevented.

The relationship between the four levels of seismic excitation, and the annual probabilities of exceedence of each level will differ according to local seismicity and structural importance, as discussed in Section 2.2.2(c). In California, the following levels are defined[S1]:

- **EQ-I:** 87% probability in 50 years: 33% of EQ III
- **EQ-II:** 50% probability in 50years: 50% of EQ-III
- **EQ-III:** approximately 10% probability in 50 years.
- **EQ-IV:** approximately 2% probability in 50 years: 150% of EQ-III.

The relationship between these performance levels and earthquake design levels is summarized in Fig.3.4. In Fig.3.4 the line "Basic Objective" identifies a series of performance levels for normal structures. The lines "Essential Objective" and "Safety Critical Objective" relate performance level to seismic intensity for two structural classes of increased importance, such as lifeline structures, and hospitals. As is seen in Fig.3.4, with "Safety Critical Objective", operation performance must be maintained even under the EQ-IV level of seismicity.

Although the Vision 2000 approach is useful conceptually, it can be argued that it requires some modification, and that it provides an incomplete description of performance. The performance levels do not include a "damage control" performance level, which is clearly of economic importance. For example, it has been noted that although the performance in the 1995 Kobe earthquake of reinforced concrete frame
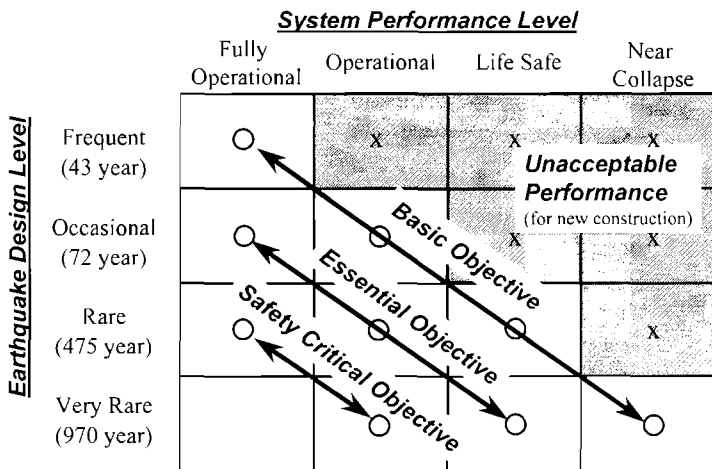
Fig. 3.4   Relationship between Earthquake Design Level and Performance Level (after Vision 2000 [O2])

buildings designed in accordance with the weak-beam/strong-column philosophy satisfied the "Life safe" performance level, the cost of repairing the many locations of inelastic action, and hence of localized damage, was often excessive, and uneconomic[O3]. The performance level implicit in most current seismic design codes is, in fact, a damage-control performance level. Further, it has been argued that residual drift, which is not considered in the Vision 2000 classification, should be considered an important measure of performance[P14].

In order to better understand the relationship between structural response levels and performance levels, it is instructive to consider the relationship between member and structure limit states[P4].

3.3.1 Section Limit States

(a) Cracking limit state: For concrete and masonry members the onset of cracking generally marks the point for a significant change in stiffness, as shown in the typical moment-curvature relationship of Fig.3.5(a). For critical members expected to respond in the inelastic range to the design-level earthquake, this limit state has little significance, as it is likely to be exceeded in minor seismic excitation, even lower than that corresponding to the EQ-I level of Vision 2000. The limit state may, however, be important for members that are expected to respond essentially elastically to the design-level earthquake. For example, the appropriate stiffness to be used for a prestressed bridge superstructure will depend on whether or not the cracking limit state is exceeded.

(b) First-yield limit state: A second significant change in stiffness of concrete and masonry members occurs at the onset of yield in the extreme tension reinforcement. This is also the case in structural steel members. This limit state is useful for defining the appropriate elastic stiffness to be used in analyses of ductile systems using simplified hysteresis rules, such as bi-linear response, shown in Fig.3.5(a) by the dashed line.

(c) Spalling limit state: With concrete or masonry sections, the onset of spalling of the cover concrete or masonry may be a significant limit state, particularly for unconfined sections, or sections subjected to high levels of axial compression, where spalling is typically associated with onset of negative incremental stiffness and possibly sudden strength loss. Exceedence of this limit state represents a local condition that can be expected to require remedial action. For well-confined sections, this is likely to be the only significance of onset of spalling, since the member can be expected to support much larger deformations without excessive distress. Strength may in fact continue to increase beyond this limit state. Conservatively, a compression strain of $\varepsilon_c = 0.004$ may be assumed for concrete structures, and a rather lower value for masonry structures.

(d) Buckling limit state: With reinforced concrete or masonry members, initiation of buckling of longitudinal reinforcement is a significant limit state. Beyond this limit state, remedial action will often require removal and replacement of the member. With

structural steel members, particularly flanged beams and columns, onset of buckling also represents a significant limit state for the same reasons as for concrete members.

(a) Section Limit States   (b) Structure Limit State
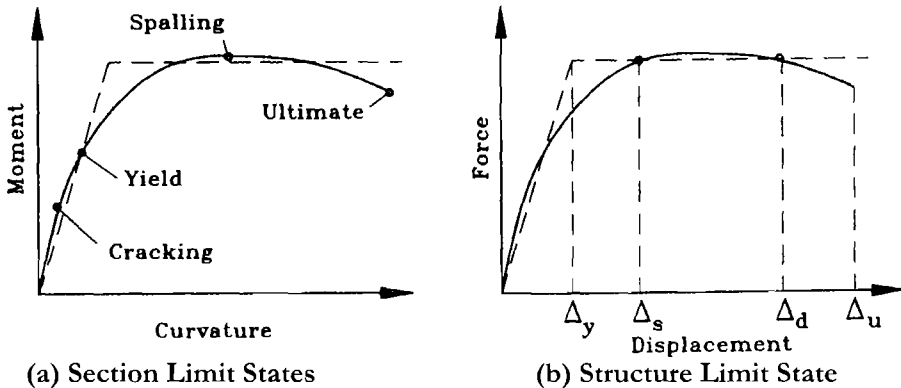
Fig.3.5   Member and Structure Design Limit States

(e) Ultimate limit state: Definition of the ultimate limit state for members is somewhat subjective. It is sometimes taken to correspond to a critical physical event, such as fracture of confinement reinforcement in a potential plastic hinge zone of a concrete member, or weld fracture of a structural steel connection. Another common definition relates to a specified strength drop (20% is often used) from the maximum attained (or sometimes from the design) strength. Neither definition truly corresponds to an ultimate limit state, since at least some residual strength is maintained for further increase of displacement. A true ultimate limit state would refer to inability to carry imposed loads, such as gravity loads on a beam, or axial forces in a column. However, the occurrence of negative incremental stiffness of the moment-curvature characteristic, which is associated with strength drop, is cause for concern under dynamic response, since it implies redistribution of strain energy from elastically responding portions of the structure into the member with negative stiffness. This has potentially explosive consequences.

3.3.2 Structure Limit States.

(a) Serviceability Limit State: This corresponds to the "fully functional" seismic performance level of Vision 2000. No significant remedial action should be needed for a structure that responds at this limit state. With concrete and masonry structures, no spalling of cover concrete should occur, and though yield of reinforcement should be acceptable at this limit state, residual crack widths should be sufficiently small so that injection grouting is not needed. As suggested by Fig.3.5(b), structural displacements at the serviceability limit state will generally exceed the nominal yield displacement.

For masonry and concrete structures this limit state can be directly related to strain limits in the extreme compression fibres of the concrete or masonry, and in the extreme

tension reinforcement. With structural steel buildings, the limit state is more likely to be related to non-structural elements, as discussed in the following.

Potential for non-structural damage must also be considered when determining whether or not the serviceability limit state has been exceeded. Ideally, non-structural elements, such as partition walls, and glazing, should be designed so that no damage will occur to them before the structure achieves the strain limits corresponding to the serviceability limit state. Even with brittle partitions this can be achieved, by suitable detailing of the contact between them and the structure, normally involving the use of flexible jointing compounds. However, when the typical construction involves brittle lightweight masonry partitions built hard-up against the structure, significant damage to the partitions is likely at much lower displacement levels than would apply to the structure. For example, reinforced concrete or structural steel building frames are likely to be able to sustain drifts (lateral displacements divided by height) of more than 0.012 before sustaining damage requiring repair. In such cases, the serviceability limit state is unlikely to govern design. A very different conclusion will result if low-strength lightweight masonry infill is placed in the frames, without flexible connection. The infill is likely to reach its limit state at drift levels less than 0.005, and design to avoid non-structural damage in the infill may well govern the structural design. This is considered in more detail in Chapter 5.

(b) Damage-Control Limit State: As noted above, this is not directly addressed in the Vision 2000 document, but is the basis for most current seismic design strategies. At this limit state, a certain amount of repairable damage is acceptable, but the cost should be significantly less than the cost of replacement. Damage to concrete buildings and bridges may include spalling of cover concrete requiring cover replacement, and the formation of wide residual flexural cracks requiring injection grouting to avoid later corrosion. Fracture of transverse or longitudinal reinforcement, or buckling of longitudinal reinforcement should not occur, and the core concrete in plastic hinge regions should not need replacement. With structural steel buildings, flange or shear panel buckling should not occur, and residual drifts, which tend to be larger for structural steel than concrete buildings should not be excessive. With well designed structures, this limit state normally corresponds to displacement ductility factors in the range $3 \leq \mu_\Delta \leq 6$.

Again, non-structural limits must be considered to keep damage to an acceptable level. This is particularly important for buildings, where the contents and services are typically worth three to five times the cost of the structure. It is difficult to avoid excessive damage when the drift levels exceed about 0.025, and hence it is common for building design codes to specify drift limits of 0.02 to 0.025. At these levels, most buildings - particularly frame buildings - will not have reached the structural damage-control limit state. It will be noted that this limitation will not normally apply to non-building structures such as bridges and wharves, and consequently structural limits will govern design to the damage-control limit state for these structures. Effective drift limits for these structures are often in the range 0.03 to 0.045. This limit state is represented in Fig.3.5(b) by the displacement Δ_d.

(c) Survival Limit State: It is important that a reserve of capacity exists above that corresponding to the damage-control limit state, to ensure that during the strongest ground shaking considered feasible for the site, collapse of the structure should not take place. Protection against loss of life is the prime concern here, and must be accorded high priority in the overall seismic design philosophy. Extensive damage may have to be accepted, to the extent that it may not be economically or technically feasible to repair the structure after the earthquake. In Fig.3.5(b) this limit state is represented by the ultimate displacement, Δ_u.

Although the survival limit state is of critical importance, its determination has received comparatively little attention. Clearly this limit state is exceeded when the structure is no longer able to support its gravity loads, and collapses. This occurs when the gravity-load capacity is reduced below the level of existing gravity loads as a result of (say) total shear failure of a critical column, resulting in progressive collapse. Alternatively, collapse results from a stability failure, when the **P-Δ** moments exceed the residual capacity of the structure, as illustrated in Fig.3.6 for a bridge column. If the ultimate displacement capacity assessed from the intersection of the resistance and **P-Δ** curves exceeds the maximum expected in the survival-level earthquake, collapse should not occur.
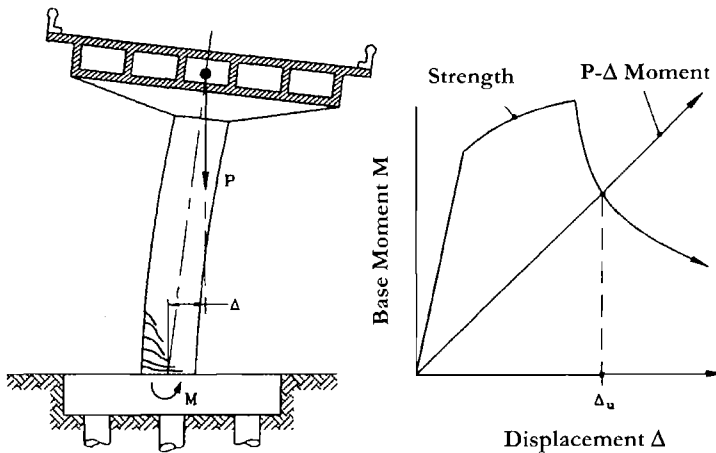
Fig.3.6 P-Δ Collapse of a Bridge under Transverse Response[P4]

3.3.3 Selection of Design Limit State

The discussion in the previous sections indicates that a number of different limit states or performance levels could be considered in design. Generally only one – the damage-control limit state, or at most two (with the serviceability limit state as the second) will be considered, except for exceptional circumstances. Where more than one limit state is considered, the required strength to satisfy each limit will be determined, and the highest chosen for the final design. More information on strain and drift limits corresponding to

different performance levels are included in Section 4.2.5, and in the relevant chapters on different structural systems.

3.4 SINGLE-DEGREE-OF-FREEDOM STRUCTURES

3.4.1 Design Displacement for a SDOF structure

The design displacement will depend on the limit state being considered, and whether structural or non-structural considerations are more critical. For any given limit state (see previous section) structural performance will be governed by limiting material strains, since damage is strain-related for structural elements. Damage to non-structural elements can be generally considered drift-related.

It is comparatively straightforward to compute the design displacement from strain limits. Consider the vertical cantilever structure of Fig.3.7(a). The most realistic structure conforming to the assumptions of a SDOF approximation is a regular bridge under transverse excitation. Two possible reinforced concrete sections, one circular and one rectangular are shown in Fig.3.7(b). The strain profile at maximum displacement response is shown together with the sections. Maximum concrete compression strain ε_c and reinforcement tensile strain ε_s are developed. The limit-state strains are $\varepsilon_{c,ls}$ and $\varepsilon_{s,ls}$ for concrete compression and steel tension respectively. These will not generally occur simultaneously in the same section, since the neutral axis depth c is fixed by the reinforcement ratio, and the axial load on the section. Consequently there are two possible limit state curvatures, based on the concrete compression and the reinforcement tension respectively:

$$\phi_{ls,c} = \varepsilon_{c,ls} / c \qquad \text{(concrete compression)} \qquad (3.3a)$$

$$\phi_{ls,s} = \varepsilon_{s,ls} /(d - c) \qquad \text{(reinforcement tension)} \qquad (3.3b)$$

The lesser of $\phi_{ls,c}$ and $\phi_{ls,s}$ will govern the structural design. The design displacement can now be estimated from the approach in Section 1.3.4(a) as

$$\Delta_{d,ls} = \Delta_y + \Delta_p = \phi_y \left(H + L_{SP}\right)^2 /3 + (\phi_{ls} - \phi_y)L_p H \qquad (3.4)$$

where ϕ_{ls} is the lesser of $\phi_{ls,c}$ and $\phi_{ls,s}$, Δ_y is the yield displacement (see Section 3.4.2), H is the column height (see Fig.3.7), L_{SP} is the effective additional height representing strain penetration effects (see Section 4.2.7) and L_p is the plastic hinge length.

If the limit state has a code-specified non-structural drift limit θ_c the displacement given by Eq.(3.4) must be checked against

$$\Delta_{d\theta} = \theta_c H \qquad (3.5)$$
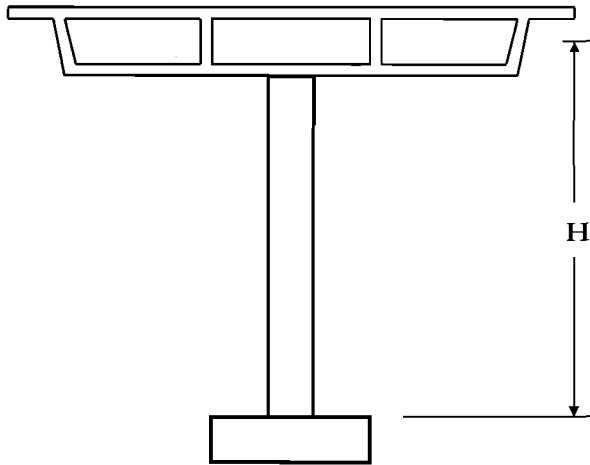
(a) Cantilever Bridge Column
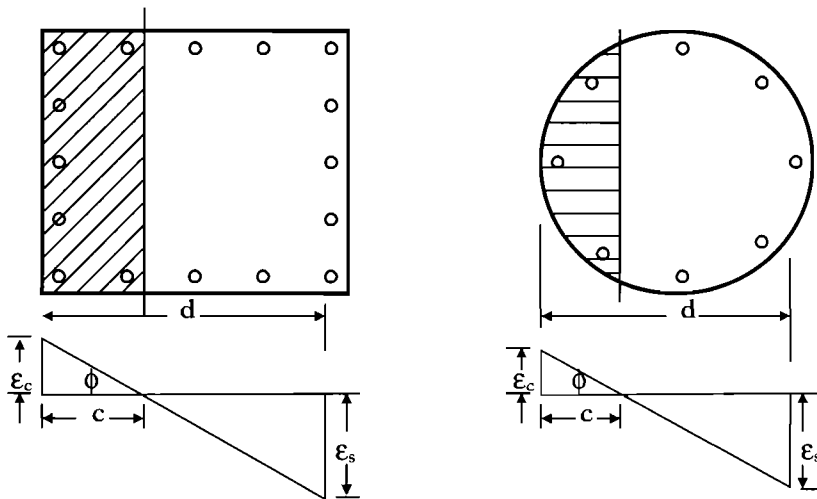
(b) Column Sections and Limit State Strains

Fig.3.7 Curvatures Corresponding to Limit Strains for a Bridge Pier

The lesser of the displacements given by Eqs. (3.4) and (3.5) is the design displacement.

Note that in many cases the design approach will be to design the structure for a specified drift, and then determine the details to ensure the strain limits are achieved.

For example, as is shown in Section 4.2.4(a), the limiting concrete strain for the damage-control limit state is determined from the transverse reinforcement details. Thus the concrete strain corresponding to the drift limit can be determined by inverting Eqs.(3.4) and (3.3a), and the required amount of transverse reinforcement calculated. This simplifies the design process.

3.4.2 Yield Displacement

For a **SDOF** vertical cantilever, the yield displacement is required for two reasons. First, if structural considerations define the limit displacement (Eq.3.4), the yield displacement and yield curvature must be known. Second, in order to calculate the equivalent viscous damping, the displacement ductility $\mu_\Delta = \Delta_d / \Delta_y$, which depends on the yield displacement, must be known.

Analytical results presented in Section 4.4 indicate that for reinforced concrete (and masonry) members, the yield curvature is essentially independent of reinforcement content and axial load level, and is a function of yield strain and section depth alone. This was discussed in relation to Fig.1.4. The form of the equation governing yield curvature was given in Eq.(1.21). Based on the more extensive results presented in Section 4.4, the following equations for yield curvature of some different section shapes provide adequate approximations:

$$\text{Circular concrete column:} \qquad \phi_y = 2.25\varepsilon_y / D \qquad (3.6a)$$

$$\text{Rectangular concrete column:} \qquad \phi_y = 2.10\varepsilon_y / h_c \qquad (3.6b)$$

$$\text{Rectangular concrete wall:} \qquad \phi_y = 2.00\varepsilon_y / l_w \qquad (3.6c)$$

$$\text{Symmetrical steel section:} \qquad \phi_y = 2.10\varepsilon_y / h_s \qquad (3.6d)$$

$$\text{Flanged concrete beam:} \qquad \phi_y = 1.70\varepsilon_y / h_b \qquad (3.6e)$$

where ε_y is the yield strain of the flexural reinforcement ($=f_y/E_s$), and D, h_c, l_w, h_s and h_b are the section depths of the circular column, rectangular column, rectangular wall, steel section and flanged concrete beam sections respectively. Note that Eq.(3.6) gives the curvature at the yield of the equivalent bi-linear approximation to the moment-curvature curve, corresponding to point **3** on the force-displacement response in Fig.1.6. As such it is a useful reference value when using bi-linear force-displacement modelling.

For a **SDOF** vertical cantilever, such as a bridge pier, or a low rise cantilever wall, the yield displacement can be satisfactorily approximated for design purposes by

$$\Delta_y = \phi_y \left(H + L_{SP} \right)^2 / 3 \qquad (3.7)$$

For reinforced concrete and structural steel frames, as established in Section 4.4.6, the yield drift can be developed from the yield curvature expressions of Eqs.(3.6) as

$$\text{Reinforced concrete frame:} \qquad \theta_y = 0.5\varepsilon_y L_b / h_b \qquad (3.8a)$$

$$\text{Structural steel frame:} \qquad \theta_y = 0.65\varepsilon_y L_b / h_b \qquad (3.8b)$$

where L_b is the beam span, and h_b is the concrete or steel beam depth. It will be noted that the yield drifts, and hence the yield displacements of reinforced concrete and

structural steel frames with similar geometries differ only by 30%, and that concrete frames are typically stiffer.

3.4.3 Equivalent Viscous Damping

The design procedure requires relationships between displacement ductility and equivalent viscous damping, as shown in Fig. 3.1(c). The damping is the sum of elastic and hysteretic damping:

$$\xi_{eq} = \xi_{el} + \xi_{hyst} \tag{3.9}$$

where the hysteretic damping ξ_{hyst} depends on the hysteresis rule appropriate for the structure being designed. Normally, for concrete structures, the elastic damping ratio is taken as 0.05, related to critical damping. A lower value (typically 0.02) is often used for steel structures.

Some discussion of both components of Eq.(3.9) is required.

(a) Hysteretic Damping: Initial work on substitute-structure analysis (i.e. analyses using secant, rather than initial stiffness, and equivalent viscous damping to represent hysteretic damping) by Jacobsen[J1], was based on equating the energy absorbed by hysteretic steady-state cyclic response to a given displacement level to the equivalent viscous damping of the substitute structure. This resulted in the following expression for the equivalent viscous damping coefficient, ξ_{hyst}:

$$\xi_{hyst} = \frac{A_h}{2\pi F_m \Delta_m} \tag{3.10}$$

In Eq. (3.10), A_h is the area within one complete cycle of stabilized force-displacement response, and F_m and Δ_m are the maximum force and displacement achieved in the stabilized loops. Note that the damping given by Eqs.(3.9) and (3.10) is expressed as the fraction of critical damping, and is related to the secant stiffness K_e to maximum response (see Fig.3.8). It is thus compatible with the assumptions of structural characterization by stiffness and damping at peak response.

Although this level of damping produced displacement predictions under seismic excitation that were found to be in good agreement[P11] with time-history results for systems with comparatively low energy absorption in the hysteretic response, such as the modified Takeda rule, it was found to seriously overestimate the effective equivalent viscous damping for systems with high energy absorption, such as elasto-plastic, or bilinear rules[C2]. A reason for this can be found when considering the response of two different systems with the same initial backbone curve (e.g. lines **1** and **2** in Fig.3.8) to an earthquake record with a single strong velocity pulse, which might be considered an extreme example of near-fault ground motion. Assume that one system has a bilinear
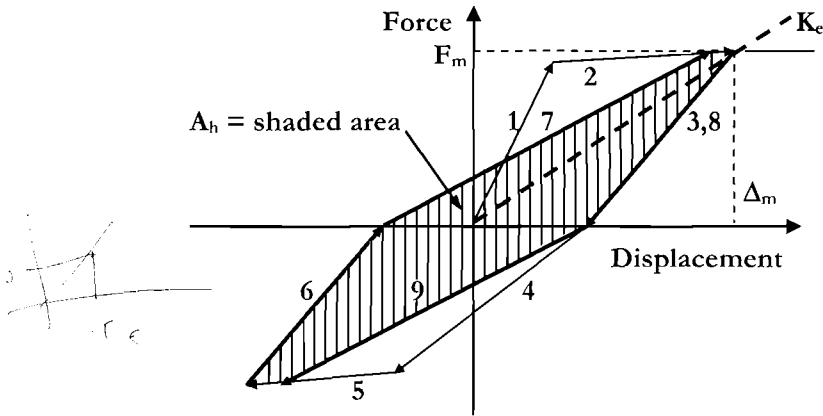
Fig. 3.8   Hysteretic Area for Damping Calculation

elasto-plastic hysteresis response, while the other, with the same initial and post-yield stiffness, is bi-linear elastic. That is, it loads up and unloads down the same backbone curve, without dissipating any hysteretic energy. If the inelastic response results from a single pulse, or fling, the peak response of the two systems should be identical, since no hysteretic energy will be dissipated on the run up lines 1 and 2 to the peak response. After the peak response, the behaviour of the two systems will differ. The bi-linear elastic system will continue to respond on lines 1 and 2, while the bilinear elasto-plastic system will unload down a different curve, and will dissipate hysteretic energy. Although real accelerograms do not consist of a pure velocity pulse, the behaviour described above is likely to form a component of the response, to a greater or lesser degree, depending on the accelerogram characteristics.

Later attempts[J1, J2] to determine the appropriate level of equivalent viscous damping were based on equating the total energy absorbed by the hysteretic and substitute-structure during response to specific accelerograms, rather than equating steady-state response to sinusoidal excitation. It is not obvious, however, that such an approach has relevance to the prediction of peak displacement response, which is the essential measure of success, or otherwise, of the substitute structure method. See [D1] for a full discussion of the development of methods relating equivalent viscous damping to ductility.

The approach adopted in this book is to use values of equivalent viscous damping that have been calibrated for different hysteresis rules to give the same peak displacements as the hysteretic response, using inelastic time-history analysis. Two independent studies, based on different methodologies were used to derive the levels of equivalent viscous damping. The first involved the use of a large number of real earthquake accelerograms[D1], where the equivalent viscous damping was calculated for each record, ductility level, effective period and hysteresis rule separately, and then averaged over the records to provide a relationship for a given rule, ductility, and period. The second study[G2], using a wider range of hysteresis rules was based on a smaller number of spectrum-compatible artificial accelerograms where the results of the elastic and inelastic

analyses were separately averaged, and compared. In each case the equivalent viscous damping was varied until the elastic results of the equivalent substitute structure matched that of the real hysteretic model.

(a) Elasto-plastic (EPP)   (b) Bi-linear, $r = 0.2$ (BI)

(c) Takeda "Thin" (TT)   (d) Takeda "Fat" (TF)

(e) Ramberg-Osgood (RO)   (f) Flag Shaped (FS)
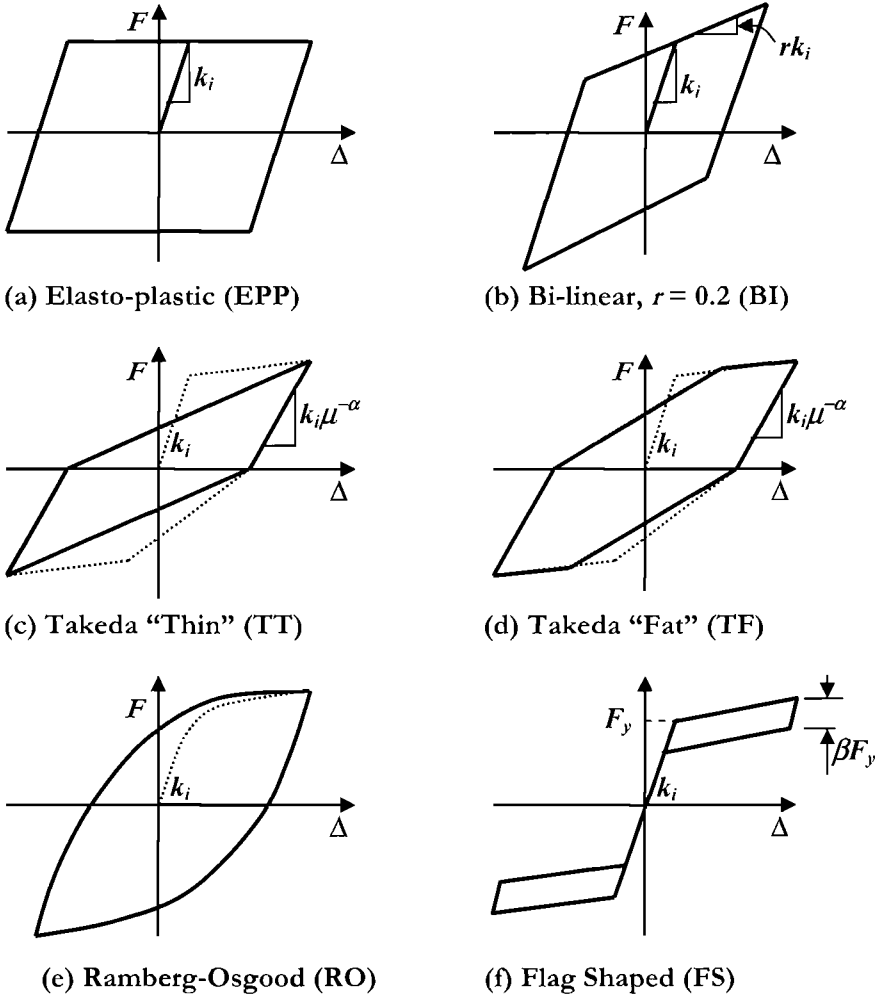
Fig.3.9 Hysteresis Rules Considered in Inelastic Time History Analysis[G2]

The hysteresis rules considered in the second study are described in Fig.3.9. The elastic-perfectly plastic rule (Fig 3.9(a)) is characteristic of some isolation systems, incorporating friction sliders. The bi-linear elasto-plastic rule of Fig.3.9(b) had a second slope stiffness ratio of $r = 0.2$, and is also appropriate for structures incorporating various types of isolation systems, though the value of r can vary considerably. The two Takeda

rules: Takeda Thin (Fig 3.9(c)) and Takeda fat (Fig. 3.9(d)), represent the response of ductile reinforced concrete wall or column structures, and ductile reinforced concrete frame structures respectively. Figure 3.9(e) shows a bounded Ramberg Osgood rule calibrated to represent ductile steel structures, and the flag-shaped rule of Fig.3.9(f) represents unbonded post-tensioned structures with a small amount of additional damping. Further information on these rules is provided in Section 4.9.2(g).

The two studies identified above [D1,G2] initially were carried out without additional elastic damping, for reasons that will become apparent in the following section. Figure 3.10 compares the resulting average relationships for an effective period of T_e = 2.0 seconds for the four hysteresis rules common to both studies. It was found that the approaches resulted in remarkably similar relationships for equivalent viscous damping for all hysteresis rules except elastic-perfectly plastic (**EPP**), where the discrepancy was about 20%. It is felt that the difference for the **EPP** rule is a consequence of the use of real records, with comparatively short durations of strong ground motion in [D1], and artificial records, with longer strong ground motion durations in [G2]. It is known that the **EPP** rule is sensitive to record duration, as the displacements tend to "crawl" in one direction, particularly when **P-Δ** effects are included[P8]. Both studies showed the scatter between results from different accelerograms to be greater for the **EPP** rule than for other rules investigated. It is likely that the results from the [G2] study will be somewhat conservative for shorter duration (i.e. lower magnitude earthquakes), but more realistic for longer duration (higher magnitude) earthquakes. In the following discussion, the average of the two studies has been used.

The Dwairi and Kowalsky[D1] study represented the hysteretic component of response in the form:

$$\xi_{hyst} = C \cdot \left(\frac{\mu - 1}{\mu \pi} \right)$$ (3.11)

where the coefficient C depended on the hysteresis rule. This has an obvious relationship to the theoretical area-based approach of Eq.(3.10) for the **EPP** rule, for which C = 2. Some period-dependency was found for effective periods T_e < 1.0 seconds.

The study by Grant et al[G2], which considered a wider range of hysteretic rules, used a more complex formulation of the relationship between ductility and equivalent viscous damping, the hysteretic component of which is given by:

$$\xi_{hyst} = a \left(1 - \frac{1}{\mu^b} \right) \left(1 + \frac{1}{(T_e + c)^d} \right)$$ (3.12)

Equation (3.12) includes the period-dependency of the response, in the coefficients c and d. Table 3.1 lists the coefficients for the various hysteresis rules investigated.

(a) Elasto-Plastic

(b) Thin Takeda

(c) Fat Takeda

(d) Flag, β=0.35
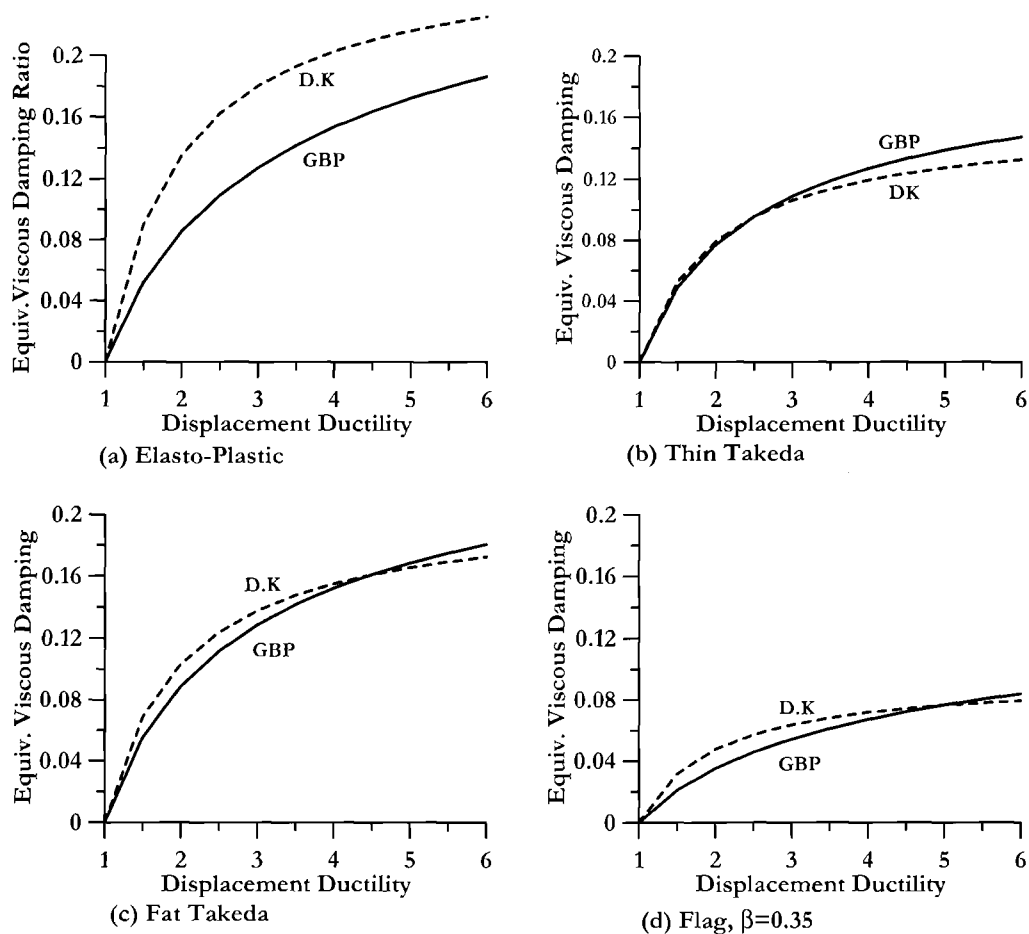
Fig 3.10 Hysteretic Component of Equivalent Viscous Damping from Two Independent Studies (D.K=Dwairi and Kowalsky[D1], GBP=Grant et al[G2])

Table 3.1 Equivalent Viscous Damping Coefficients for Hysteretic Damping Component using Eq.(3.12)[G2]

Model	a	b	c	d
EPP	0.224	0.336	-0.002	0.250
Bilinear, r=0.2 (BI)	0.262	0.655	0.813	4.890
Takeda Thin (TT)	0.215	0.642	0.824	6.444
Takeda Fat (TF)	0.305	0.492	0.790	4.463
Flag, β=0.35 (FS)	0.251	0.148	3.015	0.511
Ramberg-Osgood (RO)	0.289	0.622	0.856	6.460

The period-dependency part of Eq.(3.12) is plotted for the various hysteretic rules of Fig.3.9 in Fig.3.11, where the hysteretic damping is related to the stable value found for long periods, estimated at T= 4 sec. As with the other study[D1] the period dependency was generally insignificant for periods greater than 1.0 seconds, with the **EPP** rule again being the only exception. Since it is conservative to use low estimates of damping, and since it will be unusual for regular structures such as frame and wall buildings, and bridges to have effective periods less than 1.0 seconds, it will generally be adequate, and conservative to ignore the period-dependency in design.
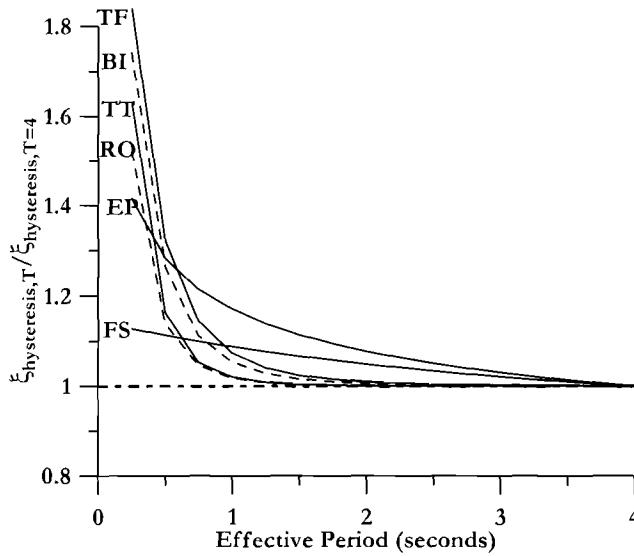
Fig.3.11 Period Dependency of Hysteretic Component of Equivalent Viscous Damping[G2]

(b) Elastic Damping: Equation (3.9) includes an elastic component of equivalent viscous damping. Elastic damping is used in inelastic time-history analysis (see Section 4.9.2(g)) to represent damping not captured by the hysteretic model adopted for the analysis. This may be from the combination of a number of factors, of which the most important is the typical simplifying assumption in the hysteretic model of perfectly linear response in the elastic range (which therefore does not model damping associated with the actual elastic non-linearity and hysteresis). Additional damping also results from foundation compliance, foundation non-linearity and radiation damping, and additional damping from interaction between structural and non-structural elements.

For single-degree-of-freedom (**SDOF**) systems, elastic damping is used in the dynamic equation of equilibrium:

$$m\ddot{x} + c\dot{x} + kx = -m\ddot{x}_g \tag{3.13}$$

where x is the response relative displacement, $\ddot{x}_g$ is the ground acceleration, m and k are the mass and stiffness, and the damping coefficient, c is given by

$$c = 2m\omega_i\xi = 2\xi\sqrt{mk} \tag{3.14}$$

where $\omega_i = \sqrt{k/m}$ is the circular frequency, and ξ is the fraction of critical damping.

The damping coefficient, and hence the damping force depends on what value of stiffness is adopted in Eq.(3.14). In most inelastic analyses, this has been taken as the initial stiffness. This, however, results in large and spurious damping forces when the response is inelastic, which, it is argued in Section 4.9.2(g) is inappropriate, and that tangent stiffness should be used as the basis for elastic damping calculations. With tangent stiffness, the damping coefficient is proportionately changed every time the stiffness changes, associated with yield, unloading or reloading, etc. This results in a reduction in damping force as the structural stiffness softens following yield, and a reduction in the energy absorbed by the elastic damping. Since the hysteretic rules are invariably calibrated to model the full structural energy dissipation subsequent to onset of yielding, this approach to characterization of the elastic damping is clearly more appropriate than is initial-stiffness elastic damping. The significance to structural response of using tangent-stiffness rather than initial-stiffness damping is discussed in detail in Section 4.9.2(g).

However, in **DDBD**, the initial elastic damping adopted in Eq.(3.14) is related to the secant stiffness to maximum displacement, whereas it is normal in inelastic time-history analysis to relate the elastic damping to the initial (elastic) stiffness, or more correctly, as noted above, to a stiffness that varies as the structural stiffness degrades with inelastic action (tangent stiffness). Since the response velocities of the "real" and "substitute" structures are expected to be similar under seismic response, the damping forces of the "real" and "substitute" structures, which are proportional to the product of the stiffness and the velocity (Eq.(3.13)), will differ significantly, since the effective stiffness k_{eff} of the substitute structure is approximately equal to $k_{eff} = k_i /\mu$ (for low post-yield stiffness). Grant et al[G2] has determined the adjustment that would be needed to the value of the elastic damping assumed in **DDBD** (based on either initial-stiffness or tangent-stiffness proportional damping) to ensure compatibility between the "real" and "substitute" structures. Without such an adjustment, the verification of **DDBD** by inelastic time-history analysis would be based on incompatible assumptions of elastic damping.

The adjustments depend on whether initial-stiffness damping (conventional practice), or tangent-stiffness damping (correct procedure, we believe) is adopted for time-history analysis. If initial-stiffness damping is chosen, the elastic damping coefficient used in DDBD must be larger than the specified initial-stiffness damping coefficient; if tangent-stiffness is chosen, it must be less than the specified tangent-stiffness coefficient.

This is explained further in Fig.3.12, which examines the stabilized response (i.e., ignoring the initial transient response) of a bilinear hysteretic model to steady-state

harmonic excitation. The c = constant line in Fig.3.12(b) represents the initial-stiffness damping assumption, and the dashed line the damping associated with the substitute structure, if both are assigned the same numeric value for damping. The energy dissipated by elastic damping in the substitute structure is less than in the "real" structure (if we accept initial-stiffness damping as correct), because $k_{eff} < k_i$. Consequently, to model the initial-stiffness damping in displacement-based design, the value of ξ_{el} in Eq.(3.9) should exceed the initial-stiffness damping coefficient.

(a) Bi-linear Hysteresis   (b) Damping force vs Displacement
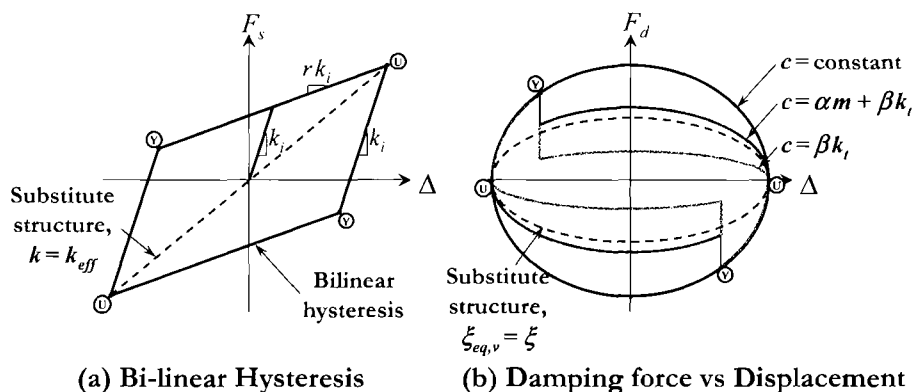
Fig.3.12   Steady-State Harmonic Response of Different Elastic Damping Models[G2]

Figure 3.12(b) also includes the damping force/displacement characteristic for the assumption of tangent-stiffness proportional damping. At points marked **Y**, the damping force reduces because of the change in slope of the hysteretic envelope. It is seen that the total energy dissipated in an stabilized cycle by the tangent stiffness assumption is now less than the substitute structure damping (dashed line) for the same numeric value of damping in Eq.(3.10). Thus, to model the tangent-stiffness damping in displacement-based design, the value of ξ_{el} in Eq.(3.9) should be less than the tangent-stiffness damping coefficient.

A further line with $c = \alpha m + \beta k_t$ represents tangent-stiffness Rayleigh damping, where the elastic damping is a combination of mass-proportional and stiffness proportional terms. This is often used in multi-degree of freedom time-history analyses. It is shown in Section 4.9.2(g) that even if tangent-stiffness elastic damping is specified within a Rayleigh damping environment, the damping force in the first, and critical mode is largely the same as initial-stiffness damping. This is not relevant to the current discussion.

It is possible to generate analytical relationships between the substitute-structure and "real" structure elastic damping coefficients that are correct for steady-state harmonic response[G2]. However, as with the hysteretic component, these are not appropriate for transient response to earthquake accelerograms, though the trends from time-history response follow the form of the theoretical predictions. Hence, to obtain the appropriate

correction factors, it is again necessary to rely on the results of inelastic time-history analyses. Grant et al[G2] compared results of elastic substitute-structure analyses with inelastic time history results to determine the correction factor to be applied to the elastic damping coefficient for the assumptions of either initial-stiffness or tangent-stiffness elastic damping. The form of Eq.(3.9) is thus slightly changed to:

$$\xi_{eq} = \kappa\xi_{el} + \xi_{hyst} \qquad (3.15)$$

where, based on the time-history analyses, κ takes the form:

$$\kappa = \mu^{\lambda} \qquad (3.16)$$

where μ is the displacement ductility factory, and λ depends on the hysteresis rule, and elastic damping assumption. Values for λ from [G2] are listed in Table 3.2, and the correction factor μ^{λ} is plotted for the different hysteresis rules and damping model assumptions in Fig.3.13.

(a) Tangent Stiffness Damping   (b) Initial Stiffness Damping
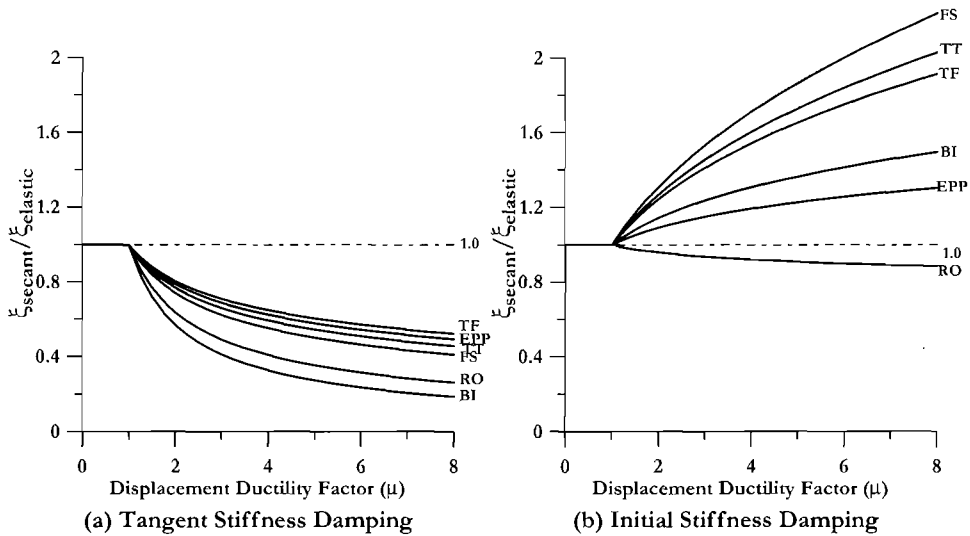
Fig.3.13   Secant Stiffness Equivalent Elastic Viscous Damping Related to Initial Elastic Stiffness and Elastic Damping Model (μ^{λ})

As noted above, although data are provided for both tangent-stiffness and initial-stiffness damping models, we strongly believe that tangent-stiffness damping is the more correct, though this has not been the basis for most inelastic time-history analyses in the past. Recent shaking-table tests[R4,P43] of structures support this view.

Table 3.2 Secant Stiffness Correction Factors λ (Eq.(3.16)) For Elastic Damping

Model*	Initial Stiffness	Tangent Stiffness
EPP	0.127	-0.341
Bilinear (BI)	0.193	-0.808
Takeda Thin (TT)	0.340	0.378
Takeda Fat (TF)	0.312	-0.313
Flag,β =0.35 (FS)	0.387	-0.430
Ramberg-Osgood (RO)	-0.060	0.617

*see Fig.3.9

(c) Design Recommendations: The data provided in the previous section are sufficient to provide a basis for the equivalent viscous damping (Eq.(3.9)) for most designs to the **DDBD** procedure. Thus, for example, if a reinforced concrete wall was to be designed for a displacement ductility of $\mu = 5$, an effective period of $T_e = 2.0$ sec., and an elastic damping ratio of 0.05 (5%), related to tangent-stiffness elastic damping, the appropriate equivalent viscous damping would be found as follows:

From Table 3.1, for **TT**, $a = 0.215$. $b = 0.642$, $c = 0.824$, $d = 6.444$. Hence, from Eq.(3.12):

$$\xi_{hyst} = 0.215 \cdot \left(1 - \frac{1}{5^{0.642}}\right) \cdot \left(1 + \frac{1}{(2.0 + 0.824)^{6.444}}\right) = 0.139$$

From EQ.(3.16), with $\lambda = -0.378$ from Table 3.2:

$$\kappa = \mu^{\lambda} = 5^{-0.378} = 0.544$$

Hence, from Eq.(3.15):

$$\xi_{eq} = 0.544 \times 0.05 + 0.139 = 0.166$$

For most designs, it is, however, possible to simplify the process, by noting that (a) the period-dependency is insignificant for most rules for $T > 1$ sec (which will encompass most designs, see Fig.3.11), and (b) an elastic damping ratio of 0.05 may be assumed. The consequent ductility/damping relationships for the hysteretic rules considered are plotted in Fig.3.14, for both tangent-stiffness and initial-stiffness elastic damping.

If we also acknowledge that the simplified Eq.(3.11) provides almost identical results to the more complete expression of Eq.(3.12), if the period-dependency of Eq.(3.12) is ignored, it is possible to include the ductility dependency of the elastic damping inside the basic form of the equivalent viscous damping equations. The coefficients C in Eq.(3.11) are adjusted so that final value is correct with ξ_{el} taken as 0.05.

(a) Tangent Stiffness Elastic Damping   (b) Initial Stiffness Elastic Damping
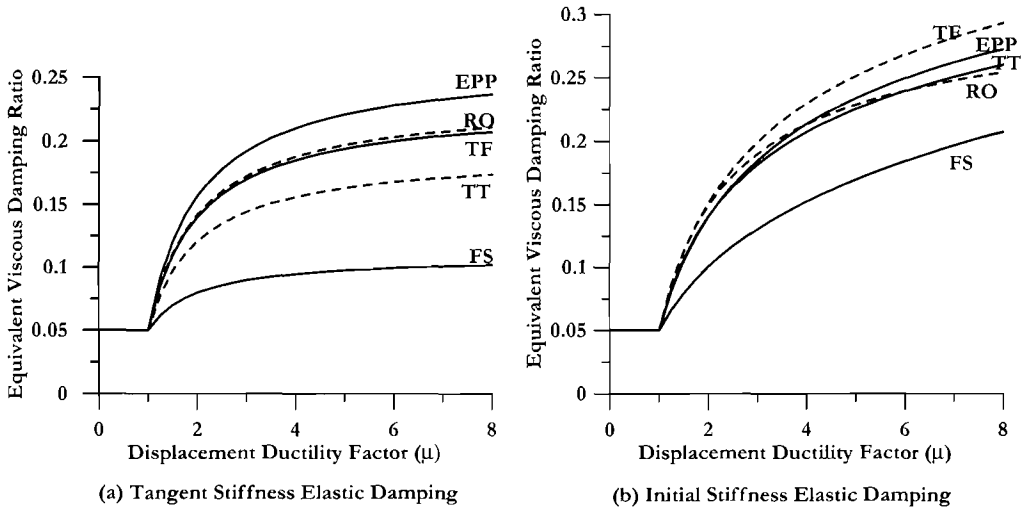
Fig.3.14 Design Equivalent Viscous Damping Ratios for 5% Elastic Damping

We list these equations below for tangent-stiffness elastic damping only, since this is felt to be the correct structural simulation. Further, these equations cannot be altered to apply for different levels of elastic damping by replacing the coefficient 0.05 by (say) 0.02, since the coefficient C is valid only for $\xi_{el} = 0.05$. If different levels of ξ_{el} are to be used, the more complete formulation of Eq.(3.12) and Table 3.1 should be adopted. Where appropriate, the corresponding structural type and material is identified in the following equations:

Concrete Wall Building, Bridges (TT): $\xi_{eq} = 0.05 + 0.444\left(\dfrac{\mu - 1}{\mu\pi}\right)$ (3.17a)

Concrete Frame Building (TF): $\xi_{eq} = 0.05 + 0.565\left(\dfrac{\mu - 1}{\mu\pi}\right)$ (3.17b)

Steel Frame Building (RO): $\xi_{eq} = 0.05 + 0.577\left(\dfrac{\mu - 1}{\mu\pi}\right)$ (3.17c)

Hybrid Prestressed Frame (FS, β =0.35): $\xi_{eq} = 0.05 + 0.186\left(\dfrac{\mu - 1}{\mu\pi}\right)$ (3.17d)

Friction Slider (EPP): $\xi_{eq} = 0.05 + 0.670\left(\dfrac{\mu - 1}{\mu\pi}\right)$ (3.17e)

Bilinear Isolation System (BI, r =0.2): $\xi_{eq} = 0.05 + 0.519\left(\dfrac{\mu - 1}{\mu\pi}\right)$ (3.17f)

Note that the equations for the hybrid prestressed frame, and the bilinear isolation system apply only for the parameters β =0.35 and r =0.2 respectively used in the analyses, and will differ for other systems. Equations (3.17d) and (3.17f) should not be used

without checking that the values of β or r are appropriate. This is addressed in more detail in the relevant structural systems chapters.

Ideally, when hysteretic rules whose characteristics differ from those considered in the above sections are used, an appropriate ductility/damping equation should be developed based on inelastic time-history analyses (**ITHA**), in similar fashion to that described above. It is recognized, however, that this will seldom be practical in a design environment, though new equations are expected to be developed with on-going research. Some reasonable estimates of the relationship can, however, be obtained by comparing the relationships between the area-based viscous damping, given by Eq.(3.10) which can readily be computed for any new system, provided the hysteretic response is known, with the hysteretic component of the calculated viscous damping (Fig. 3.9, or Table 3.1) for specific levels of the displacement ductility. This relationship is plotted in Fig. 3.15 for the six hysteresis rules considered above.
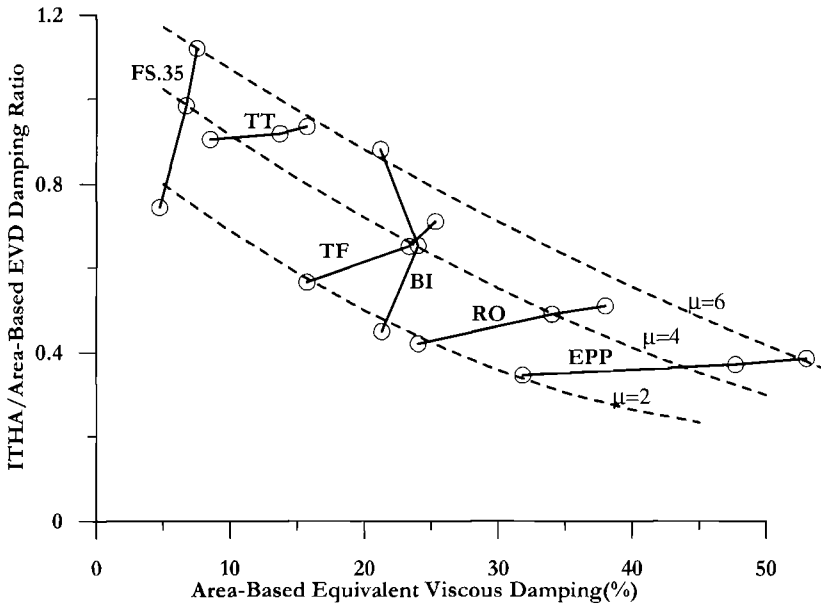
Fig.3.15: Correction Factors to be Applied to Area-Based Equivalent Viscous Damping Ratio (Eq.(3.10))

The vertical axis in Fig.3.15 is the ratio of the hysteretic component of the equivalent viscous damping (**EVD**) found from time-history analysis, as reported above, to the area-based **EVD** from Eq.(3.10). This can thus be considered as a correction factor to be applied to the area-based **EVD**. The three data points for each hysteresis rule correspond to displacement ductilities of 2, 4, and 6. It will be noted that the trends are well represented by the dashed lines for the three ductility levels, with no more scatter than might be expected from the inherent scatter of the time-history results. Fig.3.15 can thus

be used to "correct" the **EVD** calculated from the area-based Eq.(3.10), for a known displacement ductility level. Note that the elastic damping, in accordance with Fig.3.13 or Table 3.2 then needs to be added to the hysteretic damping. This approach is suggested as a suitable alternative to extensive time-history analyses for hysteretic rules that are not represented by one of the equations (3.17).

(d) Example 3.2:
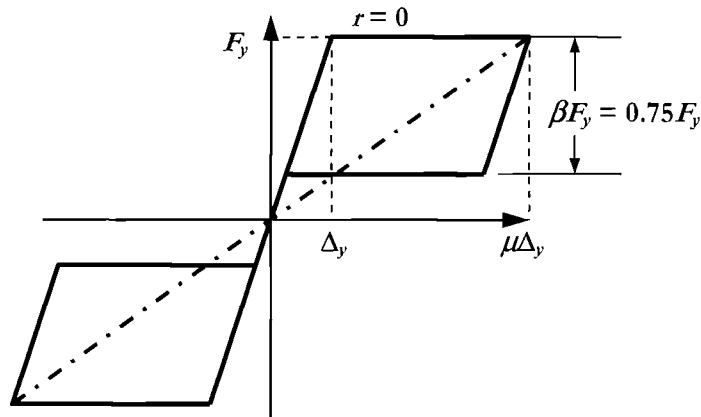
Fig.3.16 Steady-State Harmonic Response of Hybrid Prestressed Structure with
r=0, and *β*=0.75 (Example 3.2)

As an example of this approach, consider the flag-shaped hysteresis loop of Fig.3.16, for which $r = 0$, and $\beta=0.75$. The area A_h of a complete cycle can be written as

$$A_h = 2\times0.75F_y(\mu-1)\Delta_y,$$

and hence, from Eq.3.10, the area-based **EVD** is

$$\xi_{area} = \frac{2\times0.75F_y(\mu-1)\Delta_y}{2\pi F_y.\mu\Delta_y} = \frac{0.75(\mu-1)}{\pi\mu} \tag{3.18}$$

For displacement ductilities of $\mu = 2, 4$ and 6, Eq.(3.18) yields $\xi_{area} = 0.119, 0.179$ and 0.199 respectively. From Fig.3.15, the corresponding correction factors are 0.65, 0.76 and 0.88 respectively. Hence the hysteretic components of the EVD to be used in design are (0.65×0.119=0.0774), (0.76×0.179=0.136), and (0.88×0.199=0.175) respectively. The appropriate elastic damping from Fig.3.13 or Table 3.2 must then be added to these values to obtain the total **EVD** to be used in design.

(e) Generation of Inelastic Displacement Spectra

In Section 3.2 it was mentioned that inelastic displacement spectra sets could be developed for different levels of displacement ductility as shown in the example of Fig.3.3. If a relationship between initial-period elastic displacement and inelastic displacement such as the equal-displacement approximation is assumed, the inelastic spectra can be directly computed. Assuming that the skeleton force-displacement response can be represented by a bi-linear approximation with a ratio of post-yield to elastic stiffness equal to r, the secant period T_e to maximum displacement response is related to the elastic period T_i by the relationship

$$T_e = T_i \left(\frac{\mu}{1 + r(\mu - 1)} \right)^{0.5} \tag{3.19}$$

Since the inelastic displacement at T_e must equal the elastic displacement at T_i for the equal displacement approximation to hold, and noting that elastic displacement response is directly proportional to period, the modification factor R_μ to be applied to the elastic spectrum is

$$R_\mu = \left(\frac{1 + r(\mu - 1)}{\mu} \right)^{0.5} \tag{3.20}$$

Different relationships thus apply for different post-yield stiffnesses, but not to different hysteretic energy absorption within the loop, provided that the equal-displacement approximation is assumed to be valid. However, as is established in Section 4.9.2(g), the equal displacement approximation relies on the assumption that elastic damping can be characterized by initial-stiffness proportional damping, which we have demonstrated to be invalid.

It is, however, possible to generate inelastic spectra sets directly from the data used to generate the damping-ductility relationships of Eqs.(3.17). Substituting the reduction factor for elastic damping values greater than 0.05 from Eq.(2.8) into the damping ductility equations (Eqs.(3.17), spectral displacement reduction factors in the form

$$R_\mu = \left(\frac{0.07}{0.07 + C\left(\frac{\mu - 1}{\mu\pi} \right)} \right)^{\alpha} \tag{3.21}$$

can be derived. Note that different relationships apply for different values of α (the coefficient dependent on whether "normal" or "velocity-pulse" conditions apply), for different values of C and also, for different values of the elastic damping displacement reduction relationship. As we have discussed in Section 2.2.3 there is still some

uncertainty about the optimum form of this relationship. Consequently we believe it is better to use, at this time, the more fundamental elastic displacement spectra set with calibrated equations representing the damping/ductility relationship, than to combine these in the form of Eq.(3.21).

For comparison, Fig.3.17 plots the inelastic displacement spectra resulting from Eqs.(3.20) and (3.21) for the elastic-perfectly plastic (**EPP**) hysteretic rule (i.e. $r = 0$ in Eq.(3.20); $C = 0.6^7$ in Eq.(3.21). The differences between the two approaches are quite considerable. It will be noted that for displacement ductilities of $\mu \geq 3$ it would be reasonable to use a constant reduction factor, simplifying design. We arrive at similar conclusions for inelastic displacement spectra derived for other hysteretic rules.
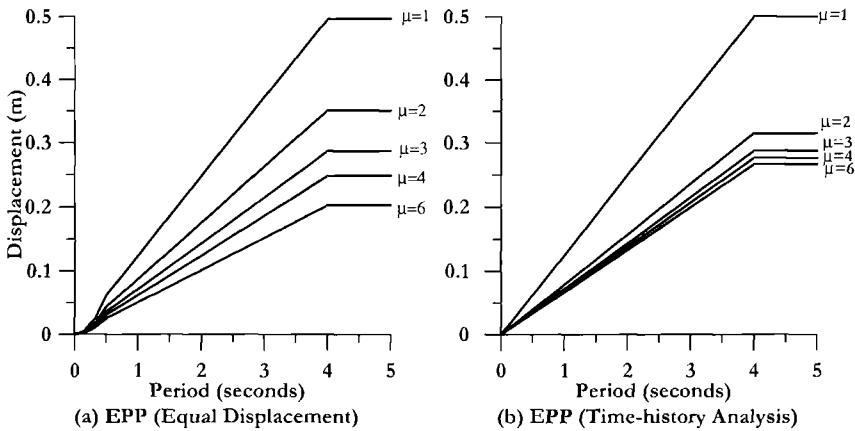
Fig.3.17   **Inelastic Displacement Spectra for Elastic-Perfectly Plastic Hysteresis**

3.4.4 Design Base Shear Equation

It will be clear that the approach described above can be simplified to a single design equation, once the design displacement and damping have been determined. As noted earlier, the displacement spectra are in many cases linear with effective period. The small non-linearity at low periods is unlikely to be significant for displacement-based designs, since it is the effective period at peak displacement response, approximately $\mu^{0.5}$ times the elastic period, that is of relevance. In Figs 3.1(d) and 2.5(b) the displacements are capped at a period of 4 seconds, which in accordance with Eq.(2.3) might be considered appropriate for an $M_w = 6.9$ earthquake. Let $\Delta_{c,5}$ be the displacement at the corner period T_c (e.g. $T_c = 4$ seconds in Fig. 3.1(d)) for the displacement spectrum corresponding to 5% damping. For a design displacement of Δ_d and design damping ξ, the effective period is, from Fig. 3.1(d) and Eq.(2.8):

$$T_e = T_c \cdot \frac{\Delta_d}{\Delta_{c,5}} \cdot \left(\frac{0.02 + \xi}{0.07} \right)^\alpha \tag{3.22}$$

where α = 0.5 and 0.25 for normal and velocity pulse conditions respectively. From Eq. (3.1) the effective stiffness at peak response is thus

$$K_e = \frac{4\pi^2 m_e}{T_c^2} \cdot \frac{\Delta_{c,5}^2}{\Delta_d^2} \cdot \left(\frac{0.07}{0.02+\xi}\right)^{2\alpha}$$ (3.23)

Finally from Eqs (3.2) and (3.23)

$$V_{Base} = K_e \Delta_d = \frac{4\pi^2 m_e}{T_c^2} \cdot \frac{\Delta_{c,5}^2}{\Delta_d} \cdot \left(\frac{0.07}{0.02+\xi}\right)^{2\alpha}$$ (3.24)

3.4.5   Design Example 3.3: Design of a Simple Bridge Pier.

The simple bridge column of Fig.3.7(a) is to be designed for a region of high seismicity (**PGA** = 0.7g) using **DDBD** principles. The bridge is founded on firm ground and the spectral shape for the 5% damping displacement spectrum can be scaled from Fig.3.1(d). On the basis of preliminary design, a circular column of 2.0m (78.74in) has been selected, and the reinforcement yield strength is f_y = 470 MPa (68.3 ksi). Two conditions are considered: normal ground motion, and ground motion with velocity fling effects. The design limit state is represented by the more critical of a displacement ductility of μ =4, or a drift of θ_d = 0.035. The effective column height is 10m (32.8ft) to the centre of superstructure mass, and the tributary weight contributing to seismic inertia of the column is 5000 kN (1124 kips). In this example, for simplicity, we ignore strain penetration into the foundation (see Section 4.2.7). E_s = 200GPa.

Design Displacement: From Eq.(3.6a) the yield curvature is

> ϕ_y =2.25×(470/200,000)/2.0 = 0.00264/m where E_s = 200 GPa.

Thus from Eq. 3.7 the yield displacement is

> Δ_y = 0.00264×10^2/3 =0.0881m (3.47 in.)

Based on the design ductility limit of μ = 4, and the drift limit of θ_d = 0.035, the design displacement is the lesser of

> Δ_d = 4×0.0881 = 0.353m and Δ_d = 0.035×10 = 0.350m (13.8 in.)

In this case the two limits produce almost identical results. Since the drift limit governs, the ductility at design displacement is

> μ = 0.35/0.0881 = 3.97

Equivalent viscous damping: From Eq.(3.17a), the equivalent viscous damping at peak response is:

$$\xi_e = 0.05+0.444(3.97-1)/3.97\pi = 0.155 \quad (15.5\%)$$

Maximum spectral displacement for 5% damping: The corner period for peak displacement response is $T_c = 4.0$sec. Scaling to a **PGA** of 0.7 sec. from Fig. 3.1(d), which applies for a **PGA** of 0.4g, the corresponding displacement is

$$\Delta_{C,5} = 0.5 \times 0.7/0.4 = 0.875m \; (34.4 \text{ in.})$$

Design Strength for Normal Ground Motion: Equation (3.24) could be used directly. However, for clarity, the steps leading to Eq. (3.24) are taken sequentially. Applying the damping correction factor of Eq.(2.8) the corner-period response displacement for 15.5% damping is

$$\Delta_{C,15.5} = 0.875 \times \left(\frac{0.07}{0.02+0.155}\right)^{0.5} = 0.553m$$

Thus, by proportion, the effective response period of the bridge is

$$T_e = 4 \times 0.35/0.553 = 2.53\text{sec}.$$

Note that Eq.(3.22) could have been used directly for the previous two steps.
From Eq.(3.1), with the mass of (5000/g) tonnes, effective stiffness at peak response is

$$K_e = 4\pi^2 m_e /T_e^2 = 4\pi^2 5000/(9.805 \times 2.53^2) \; = 3145 \text{ kN/m}$$

Finally, from Eq. 3.2, the design base shear force is

$$V_{Base} = K_e\Delta_d = 3145 \times 0.35 = 1100 \text{ kN} \; (247 \text{ kips})$$

Design Strength for Velocity Pulse Ground Motion: For this case, Eq. (3.24) is used directly, with $\alpha = 0.25$:

$$V_{Base} = \frac{4\pi^2 5000}{9.805 \times 4^2} \cdot \frac{0.875^2}{0.35} \cdot \left(\frac{0.07}{0.02+0.155}\right)^{2 \times 0.25} = 1741 \text{ kN} \; (391 \text{ kips})$$

This is 58% higher than for the normal ground condition case.

3.4.6 Design When the Displacement Capacity Exceeds the Spectral Demand

There will be occasions, with very tall or flexible structures, when the design displacement capacity, calculated from Eqs.(3.4) or (3.5) exceeds the maximum possible spectral displacement demand for the damping level calculated from Eq.(3.17). For example, with reference to the response spectra set of Fig.3.1(d), it will be seen that if the design displacement Δ_d is calculated to be 0.35m, and the corresponding damping is 20%, there is no possible intersection between the design displacement and the 20% damping curve. At the corner period of 4 sec. the peak displacement in Fig.3.1(d) for 20% damping is 0.282m. In such cases there are two possible conditions to be considered:

(a) Yield Displacement Exceeds 5% Damping Value at the Corner Period: With extremely flexible structures, or when the design seismic intensity is low, it is possible that the yield displacement exceeds the 5% damping elastic response displacement ($\Delta_{c,5}$) at the corner period T_c (in Fig.3.1(d) this is $\Delta_{c,5} = 0.5$ m). In this case the calculated elastic response period will be larger than T_c, the response displacement will be equal to $\Delta_{c,5}$, and the design base shear force is given by

$$V_{Base} = K_{el}\Delta_{c,5} \tag{3.25}$$

where K_{el} is the elastic stiffness. Note, however, that a unique design solution cannot be found, since the stiffness, K_{el} depends on the elastic period, which depends, in turn, on the strength. This is clarified in Example 3.4 below.

(b) Yield Displacement is Less than the 5% Damping Value at the Corner Period: This case will be more common. Inelastic response will occur, but not at the level of ductility corresponding to the displacement or drift capacity of the structure. Note that if the yield displacement is less than $\Delta_{c,5}$, this means that the elastic period is less than T_c. As the structure softens, a final effective period of $T \geq T_c$ will be achieved, with a displacement response level that is compatible with the damping implied by that displacement. The following trial and error solution method is recommended:

1. Calculate the displacement capacity Δ_{dc}, and the corresponding damping, ξ_c. Confirm that the two are incompatible with the displacement spectra set, as above.
2. Estimate the final displacement response Δ_{df}. This will be somewhere between Δ_{c,ξ_c} and Δ_{dc}.
3. Calculate the displacement ductility demand corresponding to Δ_{df} ($\mu = \Delta_{df}/\Delta_y$).
4. Calculate the damping ξ corresponding to the ductility demand μ.
5. Calculate the displacement response Δ at T_c corresponding to ξ.
6. Use this value Δ as the new estimate for the final displacement Δ_{df}.
7. Cycle steps 3 to 6 until a stable solution is found. Typically this requires only one or two iterations.

Again there is no unique solution, as the effective stiffness could correspond to any period $T \geq T_c$. Any value of design base shear **less** than $V_{Base} = 4\pi^2 m_e \Delta_{df}/T_c^2$ will satisfy the design assumptions. A higher value will imply a response at an effective period **less** than T_c, and hence the response displacement will be incompatible with the effective damping. In both cases discussed above the provided strength will not affect the displacement response. Minimum strength requirements for **P-Δ** effects (Section 3.6) or gravity loads will govern the required strength.

3.4.7 Example 3.4: Base Shear for a Flexible Bridge Pier

Example 3.3 is redesigned for somewhat different conditions. First, (case (a)), the 10m (32.8ft) high bridge pier is designed for normal ground motion with a reduced peak

ground acceleration of 0.35g, and a spectral displacement spectra set proportional to Fig.3.1(d). Second, (case (b)), the physical dimensions of the column cross section are maintained, but the effective height is increased to 25m (82ft).

Case (a): Design Displacement: Limit state conditions have not changed from Example 3.3, so the design displacement capacity is still 0.35m (13.8 in.), and the corresponding displacement ductility capacity is μ =3.97. The corresponding equivalent viscous damping at the design displacement capacity is again 15.5%.

Maximum spectral displacement for 5% damping: With a corner period of 4.0 sec., and 0.35g PGA, the corner-period elastic displacement is scaled from Fig.3.1(d) which applies for a PGA of 0.4g to give $\Delta_{c,5}$ = 0.5×0.35/0.4 = 0.438 m (17.2 in.).   This exceeds the yield displacement of 0.0881m, so the pier will respond inelastically.

Maximum spectral displacement for 15.5% damping: By proportion from Example 3.3, the corner displacement for 15.5% damping is:

$$\Delta_{4,15.5} = 0.533 \times 0.35 / 0.7 = 0.277m$$

This is less than the displacement capacity of 0.35m, and hence the response displacement will be less than the displacement capacity. We use the iterative approach outlined in Section 3.4.7(b):

2. The final displacement will be somewhere between the corner displacement, 0.277 m and the displacement capacity, 0.35 m. We make an initial estimate of Δ_d = 0.30 m.

3. With the yield displacement at Δ_y = 0.0881 m (see Example 3.3) the displacement ductility is μ = 0.30/0.0881 = 3.41.

4. From Eq.(3.17a) the corresponding equivalent viscous damping ratio is

$$\xi = 0.05 + 0.444 \frac{(3.41 - 1)}{3.41\pi} = 0.150 \ (15\%)$$

5. The corresponding displacement at the corner period T_c is again found from Eq.(2.8):

$$\Delta_{4,\xi} = 0.438 \cdot \left(\frac{0.07}{0.02 + 0.15} \right)^{0.5} = 0.281m$$

Use this as the new estimate of Δ_d.

6. Cycling once more through the sequence yields: μ = 3.19, ξ = 0.147, and $\Delta_{4,\xi}$ = 0.284 m (11.2 in.).   The result has stabilized.

The reference effective stiffness is thus found, using $T = T_c$ = 4.0 sec. in Eq.(3.1) as:

$$K_e = 4\pi^2 \cdot (5000 / 9.805) / 4^2 = 1258 \text{ kN/m} ,$$

and the **maximum** design base shear force, from Eq.(3.2) as

$$V_{Base} = 1258 \times 0.284 = 357.3 \text{kN. (80.3 kips)}$$

Gravity load or **P-Δ** requirements will govern the choice of the actual design strength.

Case (b): Design Displacement: The yield curvature is unchanged, and the yield displacement is calculated, from Eq.(3.7), as

$$\Delta_y = \phi_y H^2 / 3 = 0.00264 \times 25^2 / 3 = 0.55 \text{ m (21.7 in.)}.$$

Note that this is independent of the final strength. This displacement exceeds the elastic displacement at the corner period, $\Delta_{4,5} = 0.438$ m. Hence there is no point in further calculating the displacement capacity, as the pier will respond elastically to the design level of intensity, with a response displacement of 0.438 m.

Now, since the structure responds elastically, with a known displacement, the allocated strength is in fact arbitrary, as noted above. For example, if we allocated a yield strength of 500 kN, the stiffness would be $K_{el} = 500/0.55 = 909$ kN/m. The calculated elastic period would be:

$$T_{el} = 2\pi \sqrt{(5000/(9.805 \times 909))} = 4.71 \text{ seconds}.$$

The response displacement would be 0.438 m, and the maximum response force would be

$$V_{Base} = 909 \times 0.438 = 398 \text{ kN (89.5 kips)}.$$

However, if we arbitrarily allocated a yield strength of 350kN, the stiffness would be $K_{el} = 350/0.55 = 636$ kN/m, and the elastic period would be 5.63 seconds. The response displacement, (see Fig.3.1(d)), would still be 0.438 m, and the maximum response force would be 278 kN (62.5 kips). **P-Δ** moments for this case would be 36% of the base moment from the horizontal inertia force, and, in accordance with Section 3.6, would need to be carefully considered.

Note that if the strength was arbitrarily set higher than 692 kN, (say 800 kN), then the elastic period would be found to be less than 4 sec. (in this case, $K_{el} = 1455$ kN/m, and $T_{el} = 3.72$ sec, and the structure would respond with a displacement less than 0.438 m, (in this case 0.407 m (16.0 in)), in accordance with the elastic 5% displacement spectrum for the calculated period.

In fact, the example is probably artificial. The base moment would be very high, in either case, and redesign with a larger column diameter (and hence smaller yield displacement) would be advisable. The pier would also be excessively flexible for gravity loads.

3.5 MULTI-DEGREE-OF-FREEDOM STRUCTURES

For multi-degree-of-freedom (**MDOF**) structures the initial part of the design process requires the determination of the characteristics of the equivalent **SDOF** *substitute structure*[S2]. The required characteristics are the equivalent mass, the design displacement, and the effective damping. When these have been determined, the design base shear for the substitute structure can be determined. The base shear is then distributed between the mass elements of the real structure as inertia forces, and the structure analyzed under these forces to determine the design moments at locations of potential plastic hinges.

3.5.1 Design Displacement

The characteristic design displacement of the substitute structure depends on the limit state displacement or drift of the most critical member of the real structure, and an assumed displacement shape for the structure. This displacement shape is that which corresponds to the inelastic first-mode at the design level of seismic excitation. Thus the changes to the elastic first-mode shape resulting from local changes to member stiffness caused by inelastic action in plastic hinges are taken into account at the beginning of the design. Representing the displacement by the inelastic rather than the elastic first-mode shape is consistent with characterizing the structure by its secant stiffness to maximum response. In fact, the inelastic and elastic first-mode shapes are often very similar.

The design displacement (generalized displacement coordinate) is thus given by

$$\Delta_d = \sum_{i=1}^{n} \left(m_i \Delta_i^2\right) / \sum_{i=1}^{n} \left(m_i \Delta_i\right) \tag{3.26}$$

where m_i and Δ_i are the masses and displacements of the n significant mass locations respectively. For multi-storey buildings, these will normally be at the n floors of the building. For bridges, the mass locations will normally be at the centre of the mass of the superstructure above each column, but the superstructure mass may be discretized to more than one mass per span to improve validity of simulation (see Section 4.9.2(e)(iii)). With tall columns, such as may occur in deep valley crossings, the column may also be discretized into multiple elements and masses.

Where strain limits govern, the design displacement of the critical member can be determined using the approach outlined in Section 3.4.1. Similar conclusions apply when code drift limits apply. For example, the design displacement for frame buildings will normally be governed by drift limits in the lower storeys of the building. For a bridge, the design displacement will normally be governed by the plastic rotation capacity of the shortest column. With a knowledge of the displacement of the critical element and the design displacement shape (discussed further in the following section), the displacements of the individual masses are given by

$$\Delta_i = \delta_i \cdot \left(\frac{\Delta_c}{\delta_c}\right) \tag{3.27}$$

where δ_i is the inelastic mode shape, and Δ_c is the design displacement at the critical mass, c, and δ_c is the value of the mode shape at mass c.

Note that the influence of higher modes on the displacement and drift envelopes is generally small, and is not considered at this stage in the design. However, for buildings higher than (say) ten storeys, dynamic amplification of drift may be important, and the

design drift limit may need to be reduced to account for this. This factor is considered in detail in the relevant structural design chapters.

3.5.2 Displacement Shapes

(a) Frame Buildings: For regular frame buildings, the following equations, though approximate, have been shown[P17] to be adequate for design purposes:

Building frames: for **n** ≤ 4: $\delta_i = H_i / H_n$ (3.28a)

for **n** > 4: $\delta_i = \dfrac{4}{3} \cdot \left(\dfrac{H_i}{H_n}\right) \cdot \left(1 - \dfrac{H_i}{4H_n}\right)$ (3.28b)

In Eq.(3.28) H_i and H_n are the heights of level *i*, and the roof (level *n*) respectively. Displacement shapes resulting from Eq.(3.28b) provide improved agreement between predicted displacements and those resulting from inelastic time-history analysis for taller buildings, compared with the linear profile appropriate for shorter buildings

(b) Cantilever Wall Buildings: For cantilever wall buildings the maximum drift will occur in the top storey. The value of this drift may be limited by the code maximum drift limit, or by the plastic rotation capacity of the base plastic hinge. Assuming a simple triangular distribution of first-mode curvature with height at yield, as shown in Fig. 3.18, to compensate for tension-shift and shear deformation, (see Section 6.2.1 for justification of this) the yield drift θ_{yn} at the top of the wall will be

$$\theta_{yn} = \phi_y H_n / 2$$

where $\phi_y = 2\varepsilon_y/l_w$ from Eq.(3.6c), and l_w is the wall length . Hence,

$$\theta_{yn} = \varepsilon_y H_n / l_w \tag{3.29}$$

As a reasonable approximation (see Section 6.2.1(b)), the plastic rotation may be concentrated at the wall base. The critical drift at the top of the wall will thus be

$$\theta_{dn} = \theta_{yn} + \theta_{pn} = 1.0\varepsilon_y H_n/l_w + \left(\phi_m - 2.0\varepsilon_y/l_w\right)L_p \leq \theta_c \tag{3.30}$$

where θ_{pn} is the plastic rotation at the top of the wall corresponding to the design limit state, ϕ_m is the corresponding base curvature, and L_p is the plastic hinge length (see Section 4.2.7). The yield displacement at height H_i is given by:

$$\Delta_{yi} = \frac{\varepsilon_y}{l_w} H_i^2 \left(1 - \frac{H_i}{3H_n}\right) \tag{3.31}$$
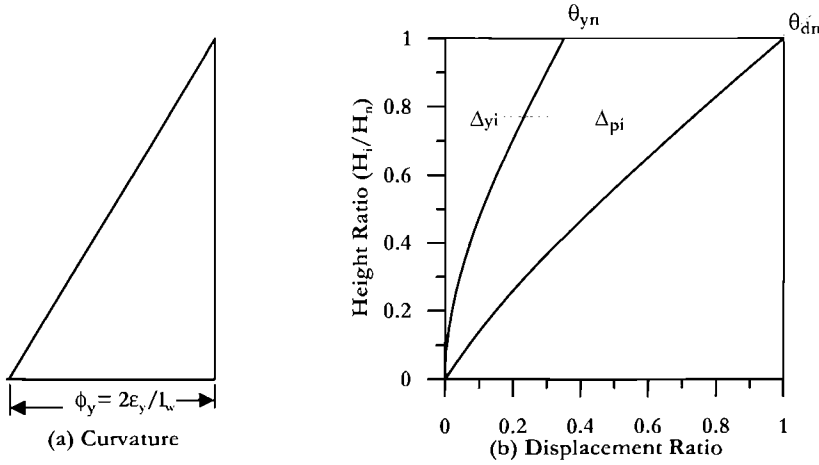
Fig.3.18 Yield and Design Displacements for Cantilever Walls

If the roof drift from Eq (3.30) is less than the code drift limit θ_c, then the design displacement profile is given by

$$\Delta_i = \Delta_{yi} + \Delta_{pi} = \frac{\varepsilon_y}{l_w} H_i^2 \left(1 - \frac{H_i}{3H_n}\right) + \left(\phi_m - \frac{2\varepsilon_y}{l_w}\right) L_p H_i \qquad (3.32a)$$

If the code drift limit governs the roof drift, the design displacement profile is given by

$$\Delta_i = \Delta_{yi} + \left(\theta_c - \theta_{yn}\right) H_i = \frac{\varepsilon_y}{l_w} H_i^2 \left(1 - \frac{H_i}{3H_n}\right) + \left(\theta_c - \frac{\varepsilon_y H_n}{l_w}\right) H_i \qquad (3.32b)$$

Although Eq. (3.32) can be manipulated to provide a generalized displacement shape δ_i to be compatible with Eq. (3.27), there is little value in so doing, since the full displacement profile must first be found. Further information on displacement profiles for cantilever walls is provided in Chapter 6.

(c) Multi-Span Bridges: With bridges it is less easy to initially determine a design displacement profile, particularly for transverse seismic response. Figure 3.19 illustrates two possible bridge configurations out of a limitless potential range. The example of Fig. 3.19(a) has piers of uniform height, while those in Fig. 3.19(b) vary in height. The transverse displacement profiles will depend strongly on the relative column stiffnesses, and more significantly, on the degree of lateral displacement restraint provided at the abutment, and the superstructure lateral stiffness. For each bridge type, three possible transverse displacement profiles are shown, corresponding to an abutment fully restrained against transverse displacement, a completely unrestrained abutment, and one where the abutment is restrained, but has significant transverse flexibility.
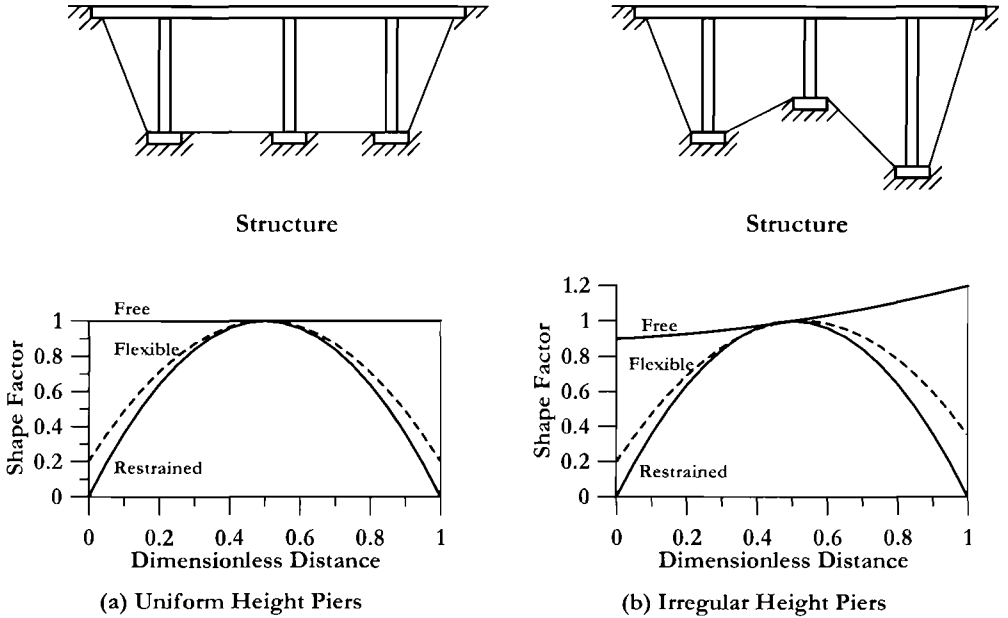
Fig.3.19 Design Transverse Displacement Profiles for Bridges

For the case of Fig. 3.19(a), the critical pier will be the central one, and with the appropriate displacement profile chosen, Eq. (3.27 and 3.26) can be applied directly. For the irregular bridge of Fig. 3.19(b) the critical pier may not be immediately apparent, and some iteration may be required. Iteration may also be required for the case of finite translational flexibility of the abutments for both the regular and irregular bridges to determine the relative displacements of abutment and the critical pier. Generally a parabolic displacement shape between abutments and piers can be assumed for initial design. Further information on displacement profiles for bridges is given in Chapter 10.

3.5.3 Effective Mass

From consideration of the mass participating in the first inelastic mode of vibration, the effective system mass for the substitute structure is

$$m_e = \sum_{i=1}^{n} (m_i \Delta_i) / \Delta_d \tag{3.33}$$

where Δ_d is the design displacement given by Eq.(3.26). Typically, the effective mass will range from about 70% of the total mass for multi-storey cantilever walls to more than 85% for frame buildings of more than 20 storeys. For simple multi-span bridges the effective mass will often exceed 95% of the total mass. The remainder of the mass participates in the higher modes of vibration. Although modal combination rules, such as

the *square-root-sum-of-squares* (**SRSS**) or *complete quadratic combination* (**CQC**)rules[C.3] may indicate a significant increase in the elastic base shear force over that from the first inelastic mode, there is much less influence on the design base overturning moment. The effects of higher modes are inadequately represented by elastic analyses, as will be shown in the chapters devoted to specific structural forms, and are better accommodated in the capacity design phase, rather than the preliminary phase of design.

3.5.4 Equivalent Viscous Damping

(a) System Damping: The effective damping depends on the structural system and displacement ductility demand, as illustrated in Fig.3.1(c) and Eqs.3.17. This requires determination of the displacement ductility demand of the *substitute structure*. This poses few problems, since the design displacement Δ_d has already been determined, from Eq.(3.26). The effective yield displacement Δ_y needs to be interpolated from the profile of displacements at yield (e.g. Eq.(3.31) for cantilever walls, or Eq.(3.8) for frames). For frames it is adequate to assume that the yield drift is constant with height (i.e. the yield displacement profile is linear with height), and hence the yield displacement is

$$\Delta_y = \theta_y . H_e \tag{3.34}$$

where θ_y is given by Eq.(3.8). For walls, the yield displacement is found from Eq.(3.31) with $H_i = H_e$. In both cases this requires knowledge of the effective height of the *substitute structure*, which may be taken as:

$$H_e = \sum_{i=1}^{n}\left(m_i \Delta_i H_i\right) / \sum_{i=1}^{n}\left(m_i \Delta_i\right) \tag{3.35}$$

The design ductility factor, for use in Eq.(3.17) is then

$$\mu = \Delta_d / \Delta_y \tag{3.36}$$

in the usual fashion.

Note that provided reasonable ductility is implied by the design displacement Δ_d, Fig.3.1(c) and Eq.(3.17) indicate that the damping is not strongly dependent on the ductility, and average values may be adopted. This is also implied in Fig.3.17(b). Note also, that concrete and masonry structures are much more flexible than normally assumed by designers, and hence code drift limits, rather than displacement ductility capacity tends to govern design (see Section 5.3.1, e.g.). As a consequence, the design ductility, and the effective damping are known at the start of the design process, and no iteration is needed in determining the design base shear force.

When the lateral resistance of a building in a given direction is provided by a number of walls of different length, the ductility demand of each wall will differ, since the yield displacements of the walls will be inversely proportional to the wall lengths (see Eq.(3.6c)), while the maximum displacements at design-level response will be essentially

equal, subject only to small variations resulting from torsional response and floor diaphragm flexibility. This was discussed in Section 1.3.6, with reference to Fig.1.13. Hence the system damping will need to consider the different effective damping in each wall.

In the general case, where different structural elements with different strengths and damping factors contribute to the seismic resistance, the global damping may be found by the weighted average based on the energy dissipated by the different structural elements. That is,

$$\xi_e = \sum_{j=1}^{m} \left(V_j \Delta_j \xi_j \right) / \sum_{j=1}^{m} V_j \Delta_j \qquad (3.37)$$

where V_j, Δ_j and ξ_j are the design strength at the design displacement, displacement at height of centre of seismic force, and damping, respectively, of the jth structural element. Alternatively, the energy dissipated may be related to the moment and rotation of different plastic hinges ($V_j\Delta_j =M_j\theta_j$). This form may be more appropriate for frame structures.

With multiple in-plane walls, the displacements of the different walls will all be the same, and hence Eq.(3.37) can be simplified to

$$\xi_e = \sum_{j=1}^{m} \left(V_j \xi_j \right) / \sum_{j=1}^{m} V_j \qquad (3.38)$$

where V_j and ξ_j are the base shear force and damping of the m walls in a given direction. Some modification of Eq.(3.38) may be required when torsional response of a building containing more than one plane of walls in a given direction is considered. In this case, Eq.(3.37) applies. However, the error involved in using Eq.(3.38) is small, even when torsional response is expected.

A rational decision will be to apportion the total base shear force requirement between the walls in proportion to the square of the length. This will result in essentially constant reinforcement ratios between the walls. With wall strength proportional to length squared, Eq.(3.38) may be rewritten as:

$$\xi_e = \sum_{j=1}^{m} \left(l_{wj}^2 \xi_j \right) / \sum_{j=1}^{m} l_{wj}^2 \qquad (3.39)$$

(b) Influence of Foundation Flexibility on Effective Damping: Although the influence of foundation flexibility on seismic design can be incorporated into force-based design, albeit with some difficulty, it is rarely considered. Foundation flexibility will increase the initial elastic period, and reduce the ductility capacity corresponding to the strain or drift limit states[P4]. It is comparatively straightforward, however, to incorporate the influence of elastic foundation compliance into Direct Displacement-Based Design. If the limit state being considered is strain-limited, then the design displacement will be increased by the elastic displacement corresponding to foundation compliance (this

requires a knowledge of the design base moment and shear force, and hence some iteration may be required). If, however, the limit state is defined by code drift limits, there will be no change in the design displacement, thus implying reduced permissible structural deformation.

(a) Foundation   (b) Structure   (c) Foundation + Structure
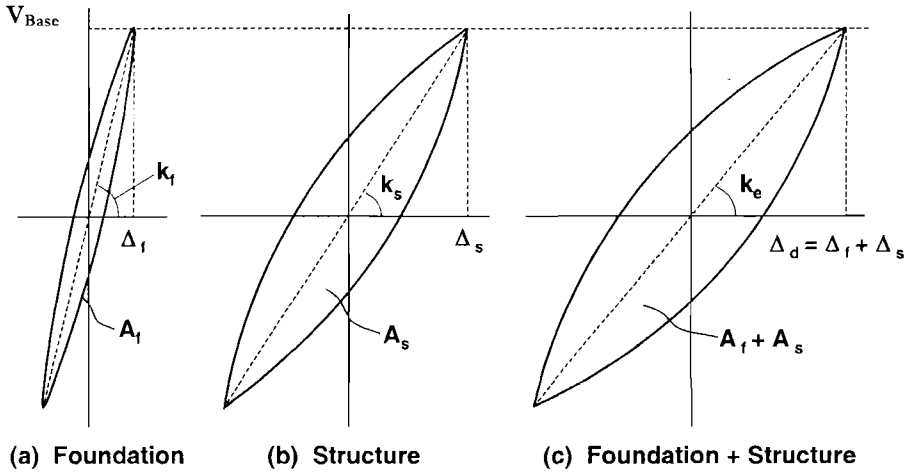
Fig.3.20   Damping Contributions of Foundation and Structure

The second influence relates to the effective damping. Both foundation and structure will contribute to the damping. Consider the force-displacement hysteresis loops of Fig.3.20, where foundation (Δ_f) and structure (Δ_s) components of the peak response displacement $\Delta_d = \Delta_s + \Delta_f$ have been separated for a cantilever wall building. Assuming sinusoidal displacement response, the area-based equivalent viscous damping for the foundation and for the structure can be separately expressed as

Foundation: $$\xi_{f,area} = \frac{A_f}{2\pi V_{Base}\Delta_f} \qquad (3.40a)$$

Structure: $$\xi_{s,area} = \frac{A_s}{2\pi V_{Base}\Delta_s} \qquad (3.40b)$$

where A_f and A_s are hysteretic areas within the loops (i.e. energy absorbed per cycle) for foundation and structure respectively. As shown in Fig.3.20, the hysteretic area of the combined structure/foundation system will be the sum of the two components, and hence the system equivalent viscous damping will be

System: $$\xi_e = \frac{A_f + A_s}{2\pi V_{Base}\left(\Delta_f + \Delta_s\right)} = \frac{\xi_f \Delta_f + \xi_s \Delta_s}{\Delta_f + \Delta_s} \qquad (3.40c)$$

Equation (3.40) is based on the assumption that the ratios of the effective damping of the structure and foundation is equal to the ratios of the hysteretic areas. However, it will be seen that the identical final result would be obtained from the more general form of Eq.(3.37).

3.5.5 Example 3.5: Effective Damping for a Cantilever Wall Building
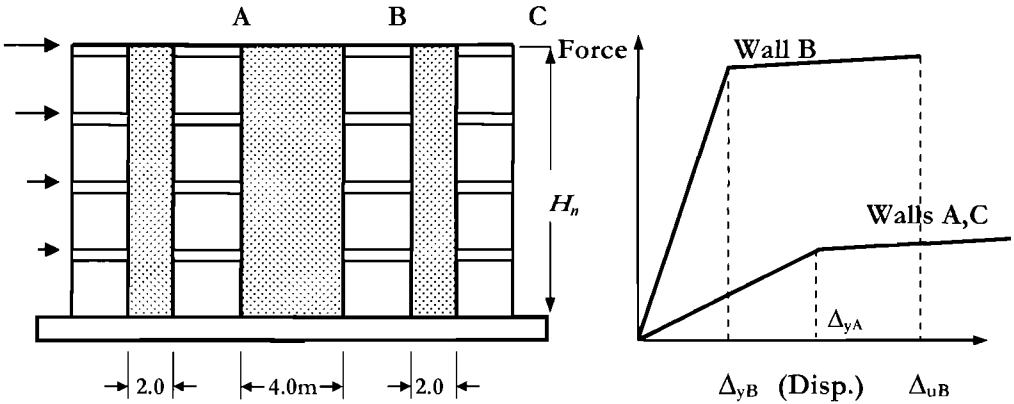
Fig.3.21 Structural Wall Building for Examples 3.5, 3.6, and 3.7

The four-storey building of Fig.3.21 is used as an example. Storey heights are uniform at 3.2m (10.5 ft), and floor masses are constant at 100 tonnes (220.5 kips) per floor. Lateral resistance in the direction considered consists of three walls, one long and two short as shown in Fig.3.21, on each opposite side of the building. Wall lengths are l_{wB} = 4m (13.1 ft) and $l_{wA} = l_{wC}$ =2m (6.56 ft). A code drift limit of θ_c =0.02 governs the design displacements. Rebar for the walls has a yield strength of 400 MPa (58 ksi). It is assumed that distances between the walls are such that slab-coupling of the walls is negligible (see Section 6.8). Hence the walls may be considered as cantilevers linked by flexible struts with zero moment capacity. Strain penetration effects are neglected in this and the following two related examples (but see Section 4.2.7)

Design displacements: Since the code drift limit governs, floor-level displacements are given by Eq.(3.32b). Because of its higher stiffness and strength, the longer 4m wall will dominate the displaced shape. Substituting in Eq.(3.32b), with H_n =4×3.2 = 12.8m, and ε_y = 400/200,000 =0.002:

$$\Delta_i = \frac{0.002}{4} H_i^2 \left(1 - \frac{H_i}{3 \times 12.8} \right) + \left(0.02 - \frac{0.002 \times 12.8}{4} \right) H_i$$

Displacements resulting from the above expression, and other parameters needed in the assessment of the equivalent viscous damping, are listed in Table 3.3.

Table 3.3   Calculations for Example 3.5

Height H_i (m)	Δ_i	Δ_i^2	$H_i\Delta_i$
3.2	0.0482	0.00232	0.1542
6.4	0.1041	0.01084	0.6662
9.6	0.1651	0.02726	1.5850
12.8	0.2287	0.05230	2.9270
Sum =	0.5461	0.09272	5.332

From Eq.(3.26), noting that the masses are all equal, the design displacement of the SDOF substitute structure is

$$\Delta_d = \sum_{i=1}^{n}\left(m_i\Delta_i^2\right)/\sum_{i=1}^{n}\left(m_i\Delta_i\right) = 0.09272/0.5461 = 0.1698\text{m (6.68 in.)}$$

Yield displacements: The effective height of the SDOF substitute structure is given by Eq.(3.35):

$$H_e = \sum_{i=1}^{n}\left(m_i\Delta_i H_i\right)/\sum_{i=1}^{n}\left(m_i\Delta_i\right) = 5.332/0.5461 = 9.765\text{m } (=0.763H_n)$$

Yield displacements of the 4 m and 2 m walls are given by Eq.(3.31). For the 4 m wall:

$$\Delta_{yi} = \frac{\varepsilon_y}{l_w}H_e^2\left(1 - \frac{H_e}{3H_n}\right) = \frac{0.002}{4}\times 9.765^2\left(1 - \frac{9.765}{3\times 12.8}\right) = 0.0355\text{m (1.40 in.)}$$

The yield displacement of the 2m wall will be twice this, i.e. 0.0710m (2.80in).

Wall displacement ductility factors: From Eq.(3.36), the displacement ductility factors for the walls are:

      4 m wall: $\mu = 0.1698/0.0355 = 4.78$

      2 m wall: $\mu = 0.1698/0.0710 = 2.39$

Wall damping factors: From Eq.(3.17a), the individual wall damping factors are:

      4 m wall: $\xi_4 = 0.05 + 0.444(4.78 - 1)/(4.78\pi) = 0.162$

      2 m wall: $\xi_2 = 0.05 + 0.444(2.39 - 1)/(2.39\pi) = 0.132$

Structure equivalent viscous damping: Finally, assuming a distribution of base shear force in proportion to (wall length)^2, as discussed in section 3.5.4, then, from Eq.(3.39), the effective damping, to be used in design is:

      $\xi_e = ((2\times 2^2)\times 0.132 + 4^2\times 0.162)/(2\times 2^2 + 4^2) = 0.152$ (15.2%)

3.5.6   Distribution of Design Base Shear Force

The principles outlined in the previous sections enable the design base shear to be established for a **MDOF** system. This base shear force must be distributed as design

forces to the various discretized masses of the structure, in order that the design moments for potential plastic hinges can be established. Assuming essentially sinusoidal response at peak response, the base shear should be distributed in proportion to mass and displacement at the discretized mass locations. Thus the design force at mass i is:

$$F_i = V_{Base}(m_i \Delta_i) / \sum_{i=1}^{n} (m_i \Delta_i)$$ (3.41)

Similarity with force-based design for multi-storey buildings will immediately be apparent. The difference is that the design inelastic displacement profile, rather than a height-proportional displacement is used, and the form of Eq.(3.41) is generalized to all structures (including, e.g. bridges and wharves), not just buildings. It will be shown in Chapter 5 that minor modification of Eq.(3.41) is advisable for taller frame buildings to avoid excessive drift in upper storeys.

The distribution of the design base shear force between different parallel lateral force-resisting elements (walls, and frames) is, to some extent, a design choice, as will be discussed in more detail in individual chapters relating to different structural systems.

3.5.7 Analysis of Structure under Design Forces

Analysis of the structure under the lateral force vector represented by Eq.(3.41) to determine the design moments at potential plastic hinge locations is analytically straightforward, but nevertheless needs some conceptual consideration. In order to be compatible with the *substitute structure* concept that forms the basis of **DDBD**, member stiffness should be representative of effective secant stiffnesses at design displacement response.

For cantilever wall buildings, this can be simplified to a distribution of the vertical force vector between walls in proportion to l_w^2, as suggested above, with the walls then analysed separately. The designer should not, however, feel unduly constrained by this suggested strength distribution, as there will be cases where the adoption of other distributions is more rational. This is discussed further in Chapter 6.

For reinforced concrete frame and dual (wall/frame) system buildings, more care is needed. With weak-beam/strong-column frame designs, beam members will be subjected to inelastic actions, and the appropriate beam stiffness will be:

$$(EI)_{beam} = E_c I_{cr} / \mu_b$$ (3.42)

where $E_c I_{cr}$ is the cracked-section stiffness, found in accordance with the methods developed in Chapter 4, and μ_b is the expected beam displacement ductility demand. Analyses have shown that the member forces are not particularly sensitive to the level of stiffness assumed, and thus it is acceptable to assume that $\mu_b = \mu_s$, the frame design ductility.

Since the columns will be protected against inelastic action by capacity design procedures, their stiffness should be taken as $E_c I_{cr}$ with no reduction for ductility. Note

that in the initial stages of the design, the beam and column flexural strengths will not be known, and the arguments presented in Chapter 4 indicate that it will thus not be possible to accurately define the cracked section stiffnesses of the beams or columns. However, as noted above the member forces are not strongly dependent on the stiffness, and it is the relative effective stiffness of beams and columns that is of importance, rather than the absolute values. Thus average values of cracked-section stiffness may be taken from the material presented in Chapter 4, with adequate accuracy. Displacements predicted from the analyses may have significant errors, but since the displacement is in fact the design input, and has already been fully considered in the design process, this is of little consequence.

Analysis of frames and dual wall/frame systems under the design forces is considered in detail in the relevant chapters, where it is shown that simplified hand methods of analysis may often be used instead of computer analyses, even for multi-storey buildings, without loss of accuracy.

3.5.8 Design Example 3.6: Design moments for a Cantilever Wall Building

We continue with the cantilever wall building started in design example 3.5. Design is based on a site-specific seismic survey which establishes that essentially all of the risk is associated with a fault 10 km from the site, capable of a earthquake of magnitude $\mathbf{M_w} =$ 6.8. Because of the proximity to the fault, velocity pulse conditions are considered a real possibility. This information is used to generate the design displacement spectrum, using the approach suggested in Section 2.2.2.

Design displacement spectrum: From Eq.(2.3), the corner period of the displacement spectrum is:

$$T_c = 1.0 + 2.5(6.8 - 5.7) = 3.75 \text{ sec.}$$

The corresponding displacement for 5% damping is given by Eq.(2.5), at a distance of $r = 10$ km:

$$\delta_{max} = 10^{(6.8 - 3.2)}/10 = 398 \text{ mm (15.7 in)}$$

This is the value $\Delta_{c,5}$ used in Eq.(3.22). With velocity pulse conditions, and the effective damping of 0.152 calculated in Example 3.5, the displacement for 15.2% damping at the corner period is given by Eq.(2.11) as

$$\Delta_{c,15.2} = 398 \cdot \left(\frac{0.07}{0.02 + 0.152} \right)^{0.25} = 318 \text{ mm (12.5 in)}$$

For completeness, the full displacement response spectra, for damping ratios between 0.05 and 0.30, and for periods up to 5 seconds, are plotted in Fig.3.22.

By proportion, the effective period, for the design displacement of $\Delta_d = 169.8$ mm found in Example 3.5 is

$$T_e = 3.75 \times 169.8/318 = 2.0 \text{ sec. (see Fig.3.12)}$$

The effective mass is found from Eq.(3.33) and Table 3.3 as:

$$m_e = 100 \frac{\sum \Delta_i}{\Delta_d} = 100 \frac{0.5461}{0.1698} = 321.6 \text{ tonnes.}$$

From Eq.(3.1) the effective stiffness is $K_e = 4\pi^2 m_e / T_e^2 - 4\pi^2 \times (321.6/2.0^2) = 3174\text{kN/m}$

The total base shear design force is thus, from Eq.(3.2):

$$V_{Base} = 3174 \times 0.1698 = 539 \text{ kN} \quad (121.2 \text{ kips}) \quad (13.7\% \text{ of the building weight}).$$

We now distribute this base shear force between the walls in proportion to length squared. Recalling that there are two 4 m walls and four 2 m walls:

$V_{Base,4}$ (4 m wall) $= 539 \times 4^2/(2 \times 4^2 + 4 \times 2^2) = 180$ kN (40.4 kips)
$V_{Base,2}$ (2 m wall) $= 0.25 \times 180 \qquad\qquad = 45$ kN (10.1 kips)

The base shear forces for the individual walls are now distributed up the height of the building in accordance with Eq.(3.41), enabling the distributing of shear force and bending moment up the wall to be calculated. Considering only a 4 m wall, and noting that the floor masses are all equal:

$$F_i = V_{Base}(m_i \Delta_i) / \sum_{i=1}^{n} (m_i \Delta_i) = 180\Delta_i/0.5461 = 329.6\Delta_i.$$

where $\sum \Delta_i = 0.5461$ m from Table 3.3. The calculations are listed in Table 3.4.
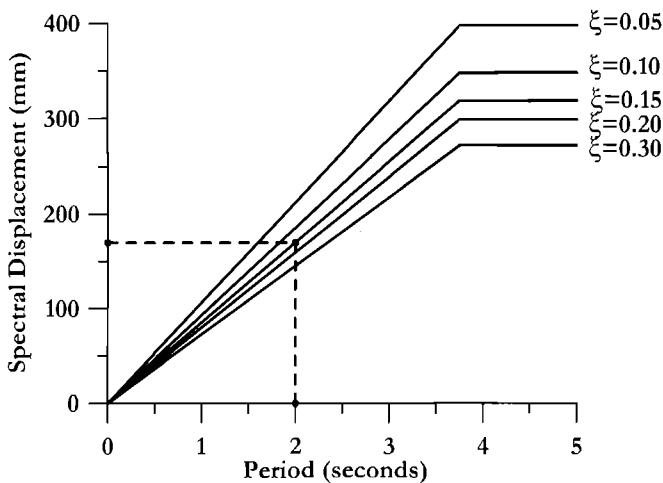
Fig.3.22 Displacement Response Spectra for Example 3.6

Table 3.4   Design Forces for 4m Wall of Example 3.6

Height H_i (m)	Displacement Δ_i (mm)	Floor Force F_i (kN)	Shear Force V_i (kN)	Moment (kNm)
12.8	0.2287	75.4	0/75.4	0
9.6	0.1651	54.4	75.4/129.8	241.3
6.4	0.1041	34.3	129.8/164.1	656.6
3.2	0.0482	15.9	164.1/180.0	1182
0.0	0.0	0.0	180.0	1758

Thus the critical design moment for the plastic hinge at the wall base is 1758 kNm (395 kips). The design moment for the base of the 2 m wall will be 25% of this.

3.5.9 Design Example 3.7: Serviceability Design for a Cantilever Wall Building

We now check the performance of the cantilever wall building designed in Design Examples 3.6 and 3.7 at the serviceability limit state. This could be done as an assessment exercise, using the procedures developed in Chapter 13, where we determine the seismic intensity corresponding to the serviceability limit state, and compare it with the serviceability seismic intensity. In effect this would be a classic capacity/demand comparison, based on seismic intensity. The alternative, which we follow in this example, is to redesign the structure and determine the required base-shear strength to satisfy the serviceability limit state criteria.

In Design Example 3.6 the seismic risk for the damage-control return period was dominated by an earthquake of M_W =6.8 within 10km of the site. For the serviceability limit state, the risk is dominated by a M_W = 6.2 earthquake, also within 10km. This rather high seismic intensity indicates the site to be located in a region of intense seismic activity. However, forward directivity effects are not expected, and α = 0.5 applies.

We first consider limit state criteria appropriate to a construction environment where internal partitions are light and flexible, and capable of withstanding drifts of 0.01 without significant damage. Serviceability limit-state strains must also be considered. In a second case we relocate the building in a location where unreinforced masonry partitions are used. For these, a drift limit of 0.005, as specified in several European design codes, is defined.

Design Displacement Spectrum: Applying the same equations as in Example 3.6 to an M_W = 6.2 earthquake at 10km, we calculate a corner period of 2.25 sec., and a corresponding displacement of 100mm (3.94 in).

Case 1: Flexible Partitions: The lesser of displacements corresponding to the limit state curvature or the limit-state drift of 0.01 at roof level will define the serviceability limit-state displacement. We investigate the strain limits first.

Serviceability Limit State: In Section 6.2.1(c) it is established that the serviceability limit-state curvature for cantilever walls can be expressed as $\phi_S = 0.0175/l_w$. The stiffer 4m wall will govern: $\phi_S = 0.0175/l_w = 0.0175/4 = 0.004375/m$.

4m Wall: Plastic hinge length: Based on Eq.(6.7) the plastic hinge length for the 4m wall is found to be 1.089m. The yield curvature is found from Eq.(3.6c) as $\phi_y = 0.001/m$. The plastic curvature is thus $\phi_p = \phi_S - \phi_y = 0.003375/m$. We check the roof drift corresponding to these curvatures from Eq.(3.30), which simplifies to:

$$\theta_{dn} = \varepsilon_y H_n / l_w + \phi_p L_p = 0.002 \times 12.8/4 + 0.003375 \times 1.089 = 0.010$$

This is also the drift limit, so both strain and drift limits apply simultaneously. The displacement profile can now be found. Equation(3.32a) applies, and simplifies to:

$$\Delta_i = 0.5\phi_y H_i^2 \left(1 - \frac{H_i}{3H_n}\right) + \phi_p L_p H_i .$$

The displacements corresponding to this equation are listed in Table 3.5, together with the necessary data to calculate the design displacement and the effective height, in columns (1) to (3). From these data (follow steps in Example 3.5) the design displacement and effective height are found to be

$$\Delta_d = 0.075 \text{ m (2.95 in), and } H_e = 9.99 \text{ m (32.8 ft)}.$$

Note the effective height has increased from the value applying at the damage-control limit state.

Table 3.5 Calculations for Example 3.7

Height H_i (m)	(1) Case 1 Δ_i (m)	(2) Case 1 Δ_i^2	(3) Case 1 $H_i\Delta_i$	(4) Case 2 Δ_i (m)	(5) Case 2 Δ_i^2	(6) Case 2 $H_i\Delta_i$
12.8	0.1017	0.01033	1.301	0.04265	0.001819	0.5460
9.6	0.0698	0.00488	0.670	0.02699	0.000729	0.2591
6.4	0.0406	0.00165	0.260	0.01333	0.000178	0.0853
3.2	0.0165	0.00027	0.053	0.00367	0.000013	0.0117
Sum =	0.2285	0.01713	2.284	0.08664	0.002739	0.9021

Yield displacement: From Eq.(3.31):
$$\Delta_y = (0.002/4) \times 9.99^2 (1-9.99/(3 \times 12.8)) = 0.0369/m$$

Displacement ductility: $\mu = 0.075/0.0369 = 2.03$

Equivalent viscous damping: From Eq.(3.17a): $\xi_d = 0.121$

2m Walls: The design displacement is still 0.075m, but the yield displacement increases to Δ_{y2} = 2×0.0369 = 0.0738. The displacement ductility is 1.015, and the damping is thus assumed to be ξ_2 = 0.05.

System Damping: From Eq.(3.39) ξ_e = (16×0.121+8×0.05)/24 = 0.097

Effective mass: It would be conservative to assume the same effective mass as for Example 3.6, but we re-calculate, for completeness. From Eq.(3.33) and Table 3.5:

m_e = 100×0.2286/0.075 = 304.8 tonnes (672kips/g)

Damping Reduction Factor: From Eq.(2.8): R_ξ = $(0.07/(0.02+0.097))^{0.5}$ = 0.774
The corner-period displacement corresponding to T_c =2.25 sec and 9.7% damping is thus $\Delta_{C,0.097}$ = 100×0.774 = 77.4 mm. (3.05 in)

Effective Period: By proportion: T_e = 2.25(0.075/0.0774) = 2.18 sec.
Effective Stiffness: From Eq.(3.1) K_e = $4\pi^2 \times 304.8/2.18^2$ = 2533kN/m
Base Shear: From Eq.(3.2): V_{Base} = 2533×0.075 = 190kN (42.7 kips).
This is substantially lower than the base shear needed for the damage-control limit state of 539 kN from design example 3.6. The damage-control limit state thus governs.

Case 2: Masonry partitions: The drift limit for this case is 0.005. Since a drift limit of 0.01 corresponded to a displacement ductility of 2.03 on the 4m walls, it is clear that the response for a maximum drift of 0.005 will be at close to the yield displacement for the 4m walls, and less than yield for the 2m walls. We check the yield drift at roof level, from Eq.(3.29): θ_y = 0.002×12.8/4 = 0.0064. This exceeds the design drift limit of 0.005 and hence all walls respond elastically. The displacement profile is found by reducing the yield displacement profile in the proportion 0.005/0.0064 = 0.781. From Eq.(3.31) the displacement profile is thus:

$$\Delta_i = 0.781 \frac{\varepsilon_y}{l_w} H_i^2 \left(1 - \frac{H_i}{3H_n}\right) = 0.781 \times \frac{0.002}{4} H_i^2 \left(1 - \frac{H_i}{38.4}\right) \quad \text{typo}$$

The displacements and other data needed to calculate the design displacement and effective height are listed in columns (4) – (6) of Table 3.5. From these, using the same procedures as for Case 1, we calculate the design displacement to be Δ_d = 0.0316m, and the effective height to be H_e = 10.4m. The effective damping is ξ_e= 0.05 since both walls remain elastic. The remaining steps are summarized below:

Effective Mass: m_e = 274.2 tonnes
Damping Reduction Factor: R_ξ = 1.00 (damping = 0.05)
Effective Period: T_e = 0.711 sec
Effective Stiffness: K_e = 21,400 kN/m
Base Shear: V_{Base} = 677 kN (152.2 kips)

Note that this is 36% higher than required for the damage-control limit state of Design Example 3.6, and 256% higher than required for Case 1, when the drift limit was effectively 0.01. This illustrates the very non-linear nature of the strength/displacement requirement noted subsequently in Section 3.10.1. Since the 2m walls will only develop about 50% of their nominal flexural strength at the serviceability design drift limit, the total nominal base shear **capacity** will need to be larger than 677kN (in fact, about 810kN). It should also be noted, however, that the low drift limit of 0.005 has been imposed because of the requirement to limit damage to masonry infill panels. In the initial stages of response, the infill will provide substantial additional lateral resistance to the building, which should be considered when determining the required strength of the cantilever walls. Since the infill walls are expected to be severely damaged at the damage control limit state, their contribution to lateral resistance at this level of response would be discounted. It is thus quite possible that the structure would also satisfy the required strength for this rather stringent serviceability limit state if designed to the damage-control limit state. Design considering masonry infill is discussed in Section 5.12.

3.6 P-Δ EFFECTS

3.6.1 Current Design Approaches

As structures displace laterally, as suggested, for example, in the single-degree-of-freedom approximation of Fig.3.23(a), gravity loads induce overturning moments in addition to those resulting from lateral inertia forces. Using the nomenclature of Fig.3.23, the base moment M is

$$M = FH + P\Delta \tag{3.43}$$

(a) Structure   (b) Moments   (c) Force-Displacement Response
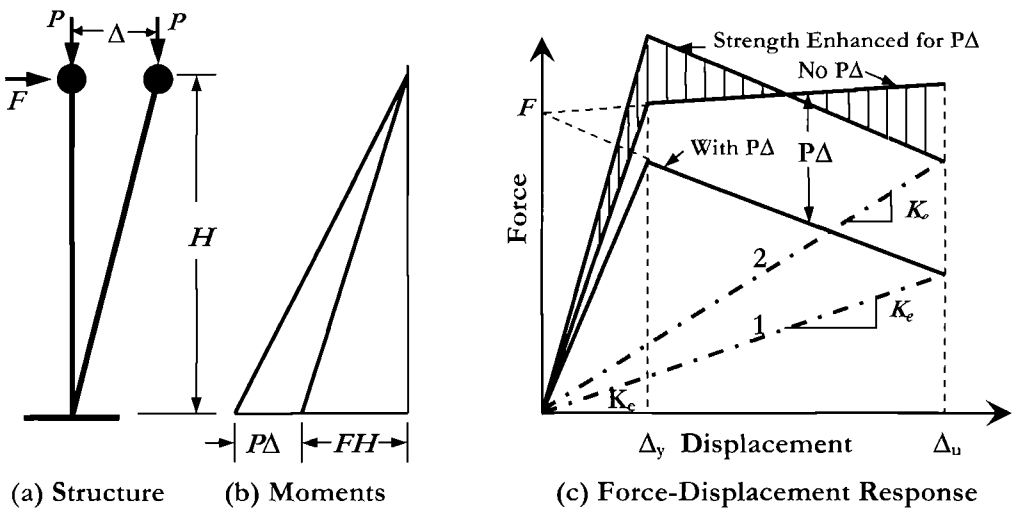
Fig.3.23 P-Δ Effects on Design Moments and Response

If the base moment capacity M_D is developed in inelastic response, then the lateral inertia force that can be resisted reduces as the displacement increases, according to the relationship

$$F = \frac{M_D - P\Delta}{H} \tag{3.44}$$

This effect is illustrated in Fig.3.23(c), where it is apparent that the **P-Δ** effect not only reduces the lateral force, but also modifies the entire lateral force-displacement characteristic. The effective initial stiffness is reduced, and the post-yield stiffness may become negative.

The significance of **P-Δ** effects is recognized in most seismic design codes, and is typically quantified by some form of "stability index", θ_Δ which compares the magnitude of the **P-Δ** effect at either nominal yield, or at expected maximum displacement, to the design base moment capacity of the structure. Since the **P-Δ** effect is of maximum significance at the design level of seismic response, we relate the stability index to conditions at maximum response, as recommended in [P1]:

$$\theta_\Delta = \frac{P\Delta_{max}}{M_D} \tag{3.45}$$

In conventional force-based design, one of two different approaches is typically adopted to account for P-Δ effects. One approach is to increase the expected design displacement to Δ^*_{max} :

$$\Delta^*_{max} = \frac{\Delta_{max}}{1 - \theta_\Delta} = \frac{\mu_\Delta \Delta_y}{1 - \theta_\Delta} \tag{3.46}$$

The alternate approach is to increase the strength in an attempt to avoid an increase in the expected design displacement. Paulay and Priestley[P1], discussing the design of reinforced concrete frame buildings, recommend that when the stability index is less than θ_Δ=0.085, **P-Δ** effects may be ignored. For higher values of the stability index, an equal-energy approach is adopted to determine the required strength increase, as suggested in Fig. 3.23(c). This implies that the required nominal strength increase, ignoring **P-Δ** effects is somewhat greater than 50% of the calculated **P-Δ** effect.

3.6.2 Theoretical Considerations

Inelastic time-history analyses[B2,M2,M3] indicate that the significance of **P-Δ** effects depends on the shape of the hysteretic response. With the adoption of an elasto-plastic characteristic it can be shown[M3] that if the earthquake record is long enough, instability

i.e. an increase in displacements until $P\Delta=M_D$) will eventually occur, when **P-Δ** effects are included in the dynamic analysis. This can be explained with reference to Fig. 3.24(a). After an initial inelastic pulse resulting in a maximum displacement corresponding to point **A**, the structure unloads down a line of stiffness equal to the initial elastic stiffness to point **B**. In further response cycles it is more probable that the strength envelope will be reached at point **A** rather than point **C** on the opposite yield boundary, since a higher level of elastic response is needed to attain point **C**. Consequently, once the first inelastic pulse occurs, it creates a tendency for continued displacement in the same sense, and response continues incrementally to **D** and **E**, and if the earthquake record is long enough, failure eventually occurs.

Although elasto-plastic hysteretic characteristics may be a reasonable approximation to steel structure response, concrete structures are better represented by the modified Takeda hysteretic rule[O1], illustrated in Fig. 3.24(b), which has a positive post-yield stiffness, an unloading stiffness that is significantly less than the initial loading stiffness, and subsequent re-loading stiffness greatly reduced from the initial stiffness. The positive post-yield stiffness compensates, to some extent for the strength loss associated with **P-Δ** moments. Furthermore, unloading from the same displacement (point **A**) as for the elasto-plastic case results in much lower residual displacement at point **B**, because of the reduced unloading stiffness. Subsequent elastic cycles result in gradual reduction of the residual displacement (shake-down, lines **B-F-G** in Fig. 3.24(b)) due to the reduced stiffness in the reverse direction, and no preferential direction for cumulative displacement develops.

(a) Elasto-plastic Hysteresis   (b) Takeda Degrading Stiffness Hysteresis
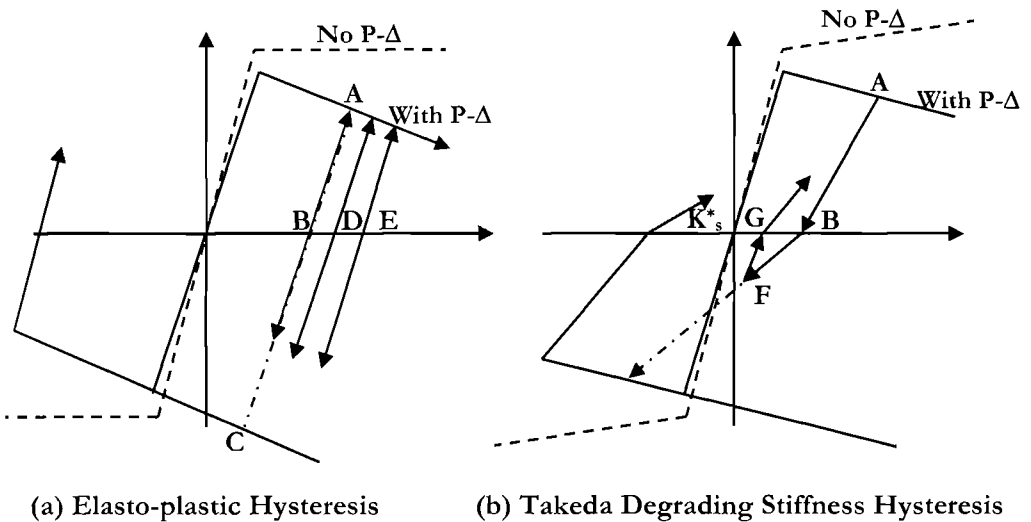
Fig 3.24 Influence of Hysteresis Rule on P-Δ Response

Analyses have shown[M3] that provided the second slope stiffness K^*_s of the stabilized loop shape, including **P-Δ** effects is positive, as in Fig. 3.24(b), structural response is stable, with only minor increase in displacement compared with response where P-Δ effects are ignored. It has been shown[M3,P4] that for Takeda response, a positive stabilized second slope stiffness of at least 5% of the initial elastic stiffness is assured provided the stability index satisfies:

$$\theta_\Delta \leq 0.3 \tag{3.47}$$

where the stability index is defined by Eq.(3.45).

3.6.3 Design Recommendations for Direct Displacement-Based Design

It will be recognized that there are significant difficulties in rationally considering **P-Δ** effects in force based design. As was noted in Section 1.3.7, estimation of maximum expected displacement from different codified force-based designs is subject to wide variability. Hence large errors in calculated **P-Δ** moments can be expected, depending on which design code is used. Further, most force-based codes seriously underestimate the elastic and inelastic displacements, and hence underestimate the severity of **P-Δ** effects.

The treatment of **P-Δ** effects in **DDBD** is comparatively straightforward, and is illustrated in Fig. 3.23(c). Unlike conditions for force-based design, the design displacement is known at the start of the design process, and hence the **P-Δ** moment is also known before the required strength is determined. **DDBD** is based on the effective stiffness at maximum design displacement. When **P-Δ** moments are significant, it is the stiffness corresponding to the degraded strength and the design displacement (see K_e in Fig.3.23(c)) that must match the required stiffness.   Hence, Eq.(3.2) defines the required residual strength. The initial strength, corresponding to zero displacement, is thus given by

$$F = K_e \Delta_d + C \cdot \frac{P\Delta_d}{H} \tag{3.48}$$

and hence the required base-moment capacity is

$$M_B = K_e \Delta_d H + C \cdot P\Delta_d \tag{3.49}$$

Note that it is more consistent to define the **P-Δ** effect in terms of the base moment, than the equivalent lateral force. In Eq.(3.49), for consistency with the design philosophy of **DDBD**, we should take $C=1$. However, examination of the hysteretic loops indicates that more energy will be absorbed, for a given final design displacement and degraded strength, than for a design when **P-Δ** design is not required, particularly for concrete-like response. It is also apparent from time-history analyses that for small values of the stability index, displacements are only slightly increased when **P-Δ** moments are ignored,

as noted above. It is also clear that steel structures are likely to be more critically affected than will concrete structures. Consideration of these points leads to the following design recommendations, which have recently been confirmed by time-history analyses[P44].

(a) Steel structures: When the structural stability index defined by Eq. 3.45 exceeds 0.05, the design base moment capacity should be amplified for **P-Δ** considerations as indicated in Eq.(3.49), taking C=1. This is represented by line **1** in Fig 3.25. Note that this implies greater strength enhancement than indicated by the upper line in Fig.3.23(c). For lesser values of the stability index, **P-Δ** effects may be ignored.

(b) Concrete structures: When the structural stability index defined by Eq.(3.45) exceeds 0.10, the design base moment capacity should be amplified for **P-Δ** effects as indicated in Eq.(3.49), taking C=0.5. This is represented by line **2** in Fig.3.25. This corresponds to the upper line, marked "strength enhancement for **P-Δ**" in Fig.3.23(c). For lesser values of the stability index, **P-Δ** effects may be ignored.

For both steel and concrete structures, it is recommended that the Stability Index, given by Eq.(3.45) should not exceed 0.33[P4].
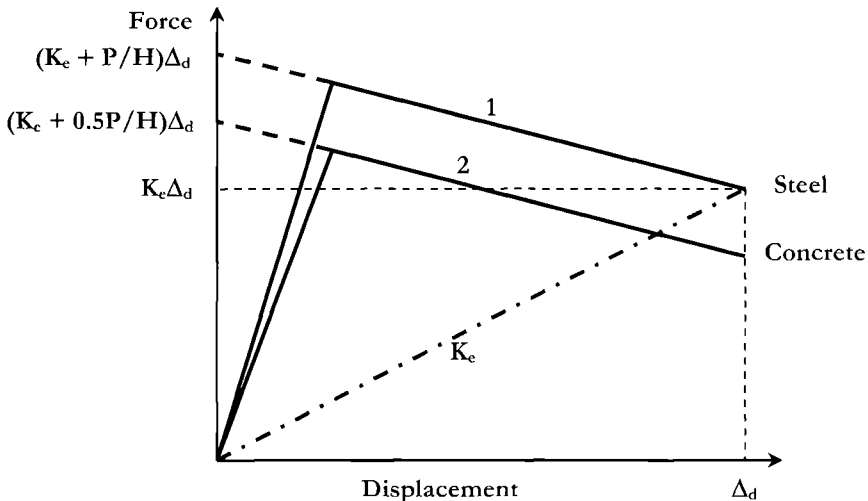
Fig. 3.25 Required P-Δ Strength enhancement in Displacement-Based Design

3.7 COMBINATION OF SEISMIC AND GRAVITY ACTIONS

3.7.1 A Discussion of Current Force-Based Design Approaches

Force-based seismic design codes normally require that actions (moments and shears) resulting from seismic design forces (reduced from the elastic level by specified force-

reduction factors) be directly added to gravity moments and shears to determine the required design strength. Since this can result in very unbalanced moment demands at different critical locations of a structure, limited moment redistribution is advocated in some design texts (e.g.[P1]), and permitted in some design codes to improve structural efficiency. There are a number of illogical aspects related to the current philosophy for combination of gravity and seismic actions, and these will be examined before making design recommendations.

Consider the bridge bent subjected to gravity loads (G) from two bridge girders, and seismic lateral forces (E), illustrated in Fig. 3.26. The columns are circular, and under seismic response, the normal design philosophy is adopted, that plastic hinges should form only in the columns and not in the cap beam. Gravity load moments will often be determined from an analysis assuming gross (un-cracked) section stiffness. The results from such an analysis are shown by the solid line in Fig. 3.26(b), with key relative magnitudes included in parentheses.

Seismic moments may well be calculated using different stiffness assumptions – typically the column stiffnesses will be reduced to take some allowance for the effects of cracking, at moments corresponding to the yield moment (see Section 4.4). It should be noted, however, that combining results from different analyses using different stiffness values violates compatibility requirements. The results of such an analysis, shown in Fig. 3.26(c), corresponding to the elastic moments (M_E) from a response-spectrum analysis, reduced by the design force-reduction factor, R, (i.e., $M_{E,reduced} = M_E/R$) are significantly larger than the gravity moments, as would be expected from a region of moderate seismicity. Relative moment magnitudes are again shown in parentheses in Fig.3.26(c).

In the following discussion, it is assumed that the "equal displacements" approximation is reasonably valid (but see Section 4.9.2(g) for a discussion of this assumption), and hence the displacement ductility factor $\mu_\Delta = R$.

The gravity and reduced seismic moments are combined in Fig. 3.26(d). It is seen that very different moment demands are created in the two columns, and that the critical locations are the top (**A**) and bottom (**B**) of the right column, with moments of 15 and 13 units respectively.

In the following, the influence of seismic axial load, which will affect the moment capacity of the two columns by different amounts will be ignored. The first consideration to be made is that designing for these combined magnitudes will result in an inefficient structure. Under reversal of the direction of the seismic force E, the left hand column will become critical, and hence both columns will have to be designed for the same flexural strength. We assume that the columns are circular, and that the moment capacities of the potential plastic hinges are equal in both directions of loading. Under seismic response, the pattern of moments shown in Fig. 3.26(d) by the solid line may be a reasonable approximation at first yield of the bent, but as the structure continues to deform to maximum displacement response, the left hand column will quickly develop plastic hinges at top and bottom, at the design strength of 15 units, assuming the reinforcement is the same at top and bottom of the columns. The pattern of moments throughout the

(a) Structure

(b) Gravity Moments

(c) Seismic Moments

(d) Gravity + Seismic Moments

(e) Moment-Curvature Response
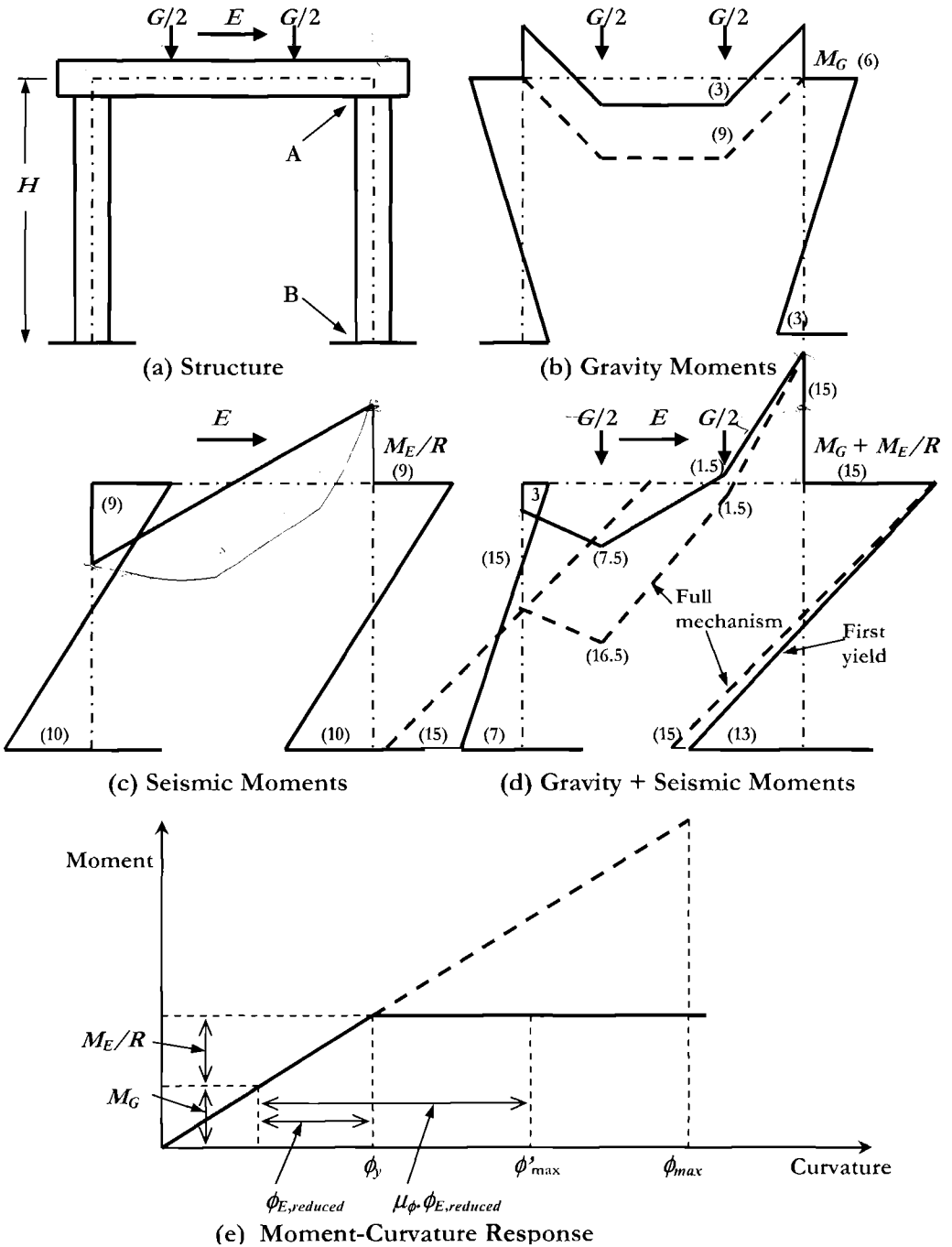
Fig. 3.26   Addition of Seismic and Gravity Moments for a Bridge Bent

structure when a full plastic hinge mechanism has formed is shown in Fig. 3.26(d) by the dashed line.

At first yield, for the direction of seismic force indicated in Fig.3.26(d), the right-hand column carries a shear force of $(15+13)/H$, where H is the column height, while the left-hand column carries a shear of only $(3+7)/H$. The total seismic force is thus $38/H$. Note that this is also the value obtained directly from the design seismic moments of Fig.3.26(c), without consideration of the gravity loads. However, when the full mechanism forms, each column carries $(15+15)/H$, for a total of $60/H$. The actual lateral strength developed will thus be $60/38 = 1.58$ times the design lateral force used to determine the design seismic moments. If section strength reduction factors are adopted and conservative estimates are made of material strengths, then the probable lateral strength may well exceed two times the design lateral force. Strain hardening will increase the overstrength even further.

Moments induced in the cap-beam are also greatly influenced by the difference between the moment patterns at first yield and full mechanism (solid and dashed lines in Fig.3.25(d)), with the peak design moment increasing from 7.5 units to 16.5 units. Since the cap-beam is designed to remain elastic, it is essential that this moment increase be accounted for in design.

The second consideration relates to the column stiffness assumed for the gravity load analysis, which as noted above will probably be the gross-section stiffness. During design-level seismic response, the effective stiffness of the columns will reduce to about 30-50% of the gross stiffness (see Section 4.4) when the column reaches first yield, and to perhaps 10% or less of the gross-section stiffness at maximum displacement response. As a consequence of the reduced column stiffness, the gravity load moments in the columns will almost entirely dissipate during the seismic response, as suggested by the dashed line in Fig. 3.26(b). The question should be asked as to whether the values of gravity moments are more relevant at the start of the seismic response than at the maximum response displacement. Certainly the increase in positive gravity load bending moment in the cap beam from 3 to 9, which can be expected to remain after seismic response must be considered in design.

The enhanced lateral strength of the structure indicates that the overall displacement ductility demand will be proportionately less than intended. Although it may be argued that this is necessary to avoid excessive curvature ductility demand, at the critical section **A** at the top of the column, it is in fact easy to show that this is a fallacy. As noted above, we assume that the "equal displacement" approximation holds, and hence the expected displacement ductility is $\mu_\Delta = R$. The curvature ductility demand at **A** corresponding to μ_Δ is μ_ϕ. The combination of moments and of curvatures is shown in Fig.3.26(e), which relates to the moment-curvature response of section **A**, with a maximum design curvature of $\phi_{max} = \mu_\phi \cdot \phi_y$. The moment corresponding to the reduced seismic force is less than the nominal moment capacity (60% of capacity, in the above example), and hence, assuming a bi-linear moment-curvature response, as shown in Fig.3.26(e), the seismic curvature is less than the yield curvature by an equal amount. This is indicated in Fig.3.26(e) as $\phi_{E,reduced}$. The curvature demand will thus not be ϕ_{max}, since only the seismic component

of the yield curvature will be increased by the expected curvature ductility factor to give $\mu_\phi \cdot \phi_{E.reduced}$, not $\mu_\phi \cdot \phi_y$, as shown in Fig.3.26(e). The curvature corresponding to the gravity moment will be added to this, giving the final curvature as ϕ'_{max}, as shown in Fig.3.26(e). Thus the full expected design curvature at **A** has not been used.

It is best to illustrate this numerically. We assume that the design force reduction factor and displacement ductility are $R = \mu_\Delta = 5$, and the corresponding design curvature ductility demand is $\mu_\phi = 10$. Using the numerical values for gravity and seismic moment in Fig. 3.26, the seismic curvature corresponding to the reduced seismic force is $\phi_{E,reduced} = 0.6\phi_y$. The plastic seismic curvature will be $(\mu_\phi - 1)\phi_{E,reduced} = 9 \times 0.6\phi_y = 5.4\phi_y$.

The total curvature will thus be $\phi_y + 5.4\phi_y = 6.4\phi_y$, and the curvature ductility demand, at 6.4, is 64% of the design value. Thus even the most critical of the sections is subjected to a much lower ductility demand than intended in the design.

On the basis of the above arguments, it is clear that direct addition of gravity and reduced seismic moments is illogical, and unnecessarily conservative. A logical improvement for force-based design would be to recognize that it is the sum of the gravity and **unreduced** seismic curvatures which should equate to the design curvature limit. It follows from this that the gravity and seismic moments should be combined according to:

$$(M_G + M_E)/R \le M_N \tag{3.50}$$

where M_N is the nominal moment capacity of the section. The gravity moments should be calculated using stiffness values that are compatible with those used for the seismic analyses. This approach greatly reduces the influence of gravity moments in seismic design, and in many cases gravity moments will become insignificant.

3.7.2 Combination of Gravity and Seismic Moments in Displacement-Based Design

The arguments developed above become more critical when related to direct displacement-based design. Because of the great differences in effective stiffness used to determine gravity moments (gross section stiffness) and seismic moments (cracked-section stiffness reduced by ductility factor – see Section 4.4) resulting moment combinations would be meaningless. The appropriate combination must be consistent with the design philosophy that we are concerned with conditions at maximum displacement response, not in the elastic state. Therefore, the gravity moments should be determined using the same effective stiffness as appropriate for the seismic design. In the example above, this would mean using greatly reduced elastic stiffness for the columns, with the end results that gravity moments would become almost insignificant.

It should be noted, however, that the reason that the above approach is valid, is that the gravity moments in the columns are based on compatibility, rather than equilibrium requirements. Care is needed to ensure that structures, or parts of structures where gravity moments are based on equilibrium considerations, do not have their moments

reduced. Provided the suggested approach of analyzing the structure using reduced stiffness in ductile members is adhered to, equilibrium will automatically be satisfied. In the bridge bent example discussed above, the automatic result will be greatly reduced gravity moments in the columns, and increased mid-span gravity moments in the cap-beam.

In many structures, the result of such an analysis will be that the effects of gravity moments are very small in comparison with the seismic moments. This leads to an alternate, and simpler approach: The critical (ductile) elements are designed for the higher of factored gravity moments (to ensure satisfactory serviceability), and seismic moments ignoring gravity moments. Non-ductile members are designed for capacity design forces corresponding to plastic hinge formation at material overstrength, together with gravity moments and shears. Inelastic time-history analyses of frame structures designed without consideration of gravity moments by Pinto et al[P15] have shown that the response is virtually identical whether the gravity moments were considered or ignored in the time-history analysis. Combination of seismic and gravity moments is discussed in more detail for frames in Section 5.6.1, and general equilibrium requirements are discussed in some detail in Section 4.6.

3.8 CONSIDERATION OF TORSIONAL RESPONSE IN DIRECT DISPLACEMENT-BASED DESIGN

3.8.1 Introduction

Structures with asymmetry in plan are subjected to torsional rotations as well as direct translation under seismic response. Examples of asymmetric plan layouts are shown in Fig.3.27. In each case three important locations are identified: centre of mass (C_M), centre of stiffness, or rigidity (C_R) and centre of shear strength (C_V). In traditional elastic analysis of torsional effects in buildings only the first two are considered, and a structure is considered to have plan eccentricity when C_M and C_R do not coincide, but it has recently become apparent that for structures responding inelastically to seismic excitation, the centre of strength is at least as important as the centre of rigidity[P26].

The structure in Fig.3.27(a) has walls of different length on opposite sides resulting in stiffness eccentricity, and probably, though not necessarily, also in strength eccentricity. As shown, centres of strength and stiffness in general will not coincide. It is assumed that the floor plan is supported by internal columns which do not contribute to seismic resistance. Eccentricity in plan is also apparent in the frame building of Fig. 3.27(b), as a result of an architectural requirement for a large open space in a small building plan. The third example is the common example of an eccentric service core constructed from walls enclosing stairs, elevators etc., in a regular frame plan layout. The first two structures are eccentric in both **X** and **Z** directions, while the third is eccentric only in the **X** direction.

The eccentricity of the centre of stiffness from the centre of mass is found from:

$$e_{RX} = \sum_{1}^{n} k_{Zi} x_i \Big/ \sum_{1}^{n} k_{Zi} \ ; \qquad e_{RZ} = \sum_{1}^{m} k_{Xj} z_j \Big/ \sum_{1}^{m} k_{Xj} \qquad (3.51)$$

where k_{Zi} and k_{Xj} are element (i.e. walls or frames) stiffness in the Z and X directions respectively, and x_i and z_j are measured from the centre of mass.
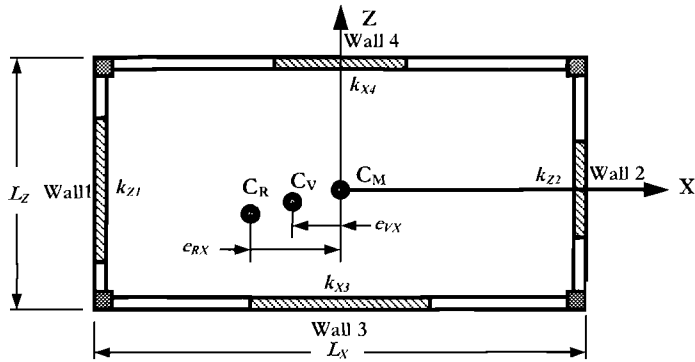
(a) Structural Wall Building
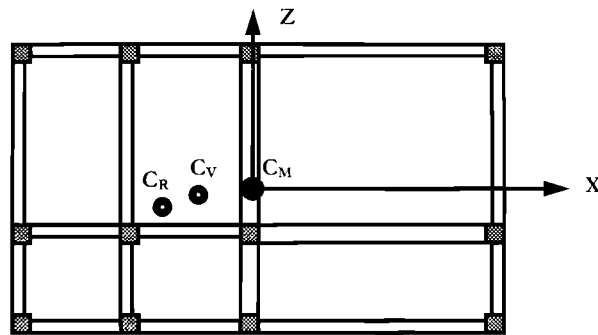
(b) Eccentric Frame Building
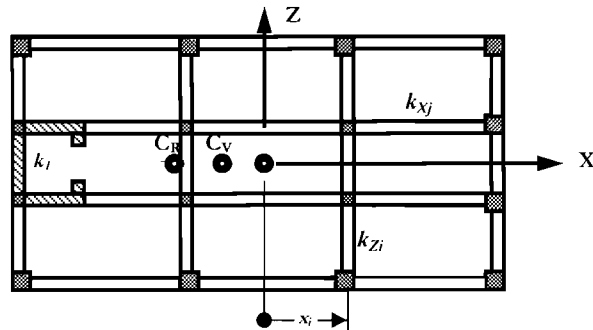
(c) Frame with Eccentric Service Core

Fig.3.27 Examples of Structures Asymmetric in Plan

The eccentricity of the centre of strength, C_V, is defined by

$$e_{VX} = \sum_1^n V_{Zi} x_i / \sum_1^n V_{Zi} \; ; \qquad e_{VZ} = \sum_1^m V_{Xj} z_j / \sum_1^m V_{Xj} \qquad (3.52)$$

where V_{Zi} and V_{Xj} are the design base shear strengths for elements in the Z and X directions respectively. Note that relative, rather than absolute values may be used to establish the locations of centres of stiffness and strength in the initial stages of design.

Most design codes require consideration of accidental eccentricity between centre of mass and centre of stiffness, in addition to the calculated eccentricity. Accidental eccentricity is intended to provide consideration of uncertainty in calculations of mass and stiffness distributions. Typically this is effected in force-based design by considering two alternate positions of the centre of mass, separated by $\pm 0.05 L_X$ from the calculated location of C_M, where L_X is the building plan dimension perpendicular to the direction of seismic force considered. However, as has been pointed out by Paulay[P26] this appears to be inconsistent with other aspects of seismic design, where larger uncertainties may exist. In particular, calculation of the location of the centre of mass is likely to be one of the most reliable of the calculated parameters in seismic design. Also, design for accidental eccentricity is likely to be ineffectual, since it involves increasing the strength of all elements which will not reduce the apparent torsional strength eccentricity, e_V. In fact, it can be argued that it will exacerbate the problem, since the overall base shear capacity will be increased in proportion to the strength increase of the individual elements, without reducing the strength eccentricity. Hence torsional moments are likely to increase. As a consequence of these considerations we do not recommend consideration of accidental eccentricity, which will not be discussed further in this text.

3.8.2 Torsional Response of Inelastic Eccentric Structures

Torsional response of asymmetric structures responding to seismic excitation is complex, involving both strength and stiffness eccentricity, as well as the torsional mass inertia. Peak response displacements at opposite sides of an asymmetric building do not occur simultaneously, nor do they correspond to peak torsional response. As such it is not possible to provide exact analytical methods appropriate for simple preliminary design. However, analytical studies in recent years, particularly by Castillo et al[C6] and Beyer[B4] have enabled the following guidelines to be established:

Maximum response displacements of structures with stiffness eccentricities, with or without strength eccentricity can be calculated as the sum of direct ($\Delta_{Z,CM}$) and torsional components of displacement. For response in the Z direction (Fig.3.28):

$$\Delta_{Zi} = \Delta_{Z,CM} + \theta(x_i - e_{VX}) \qquad (3.53)$$

taking care with signs. Thus for walls 1 and 2 in Fig.3.28:

$$\Delta_1 = \Delta_{CM} - \theta(0.5 L_X - |e_{VX}|) \; ; \quad \Delta_2 = \Delta_{CM} + \theta(0.5 L_X + |e_{VX}|) \qquad (3.54)$$
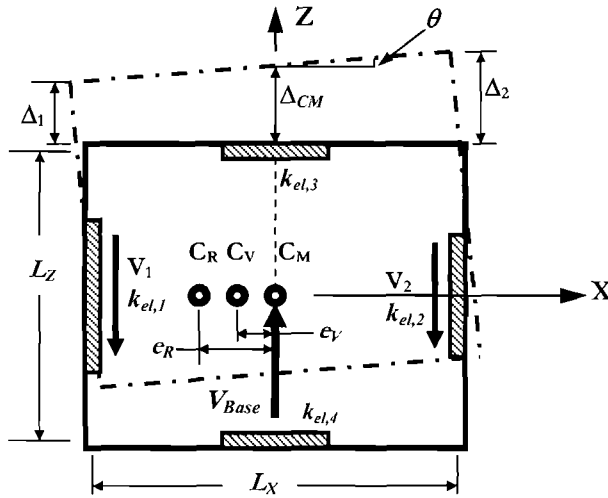
Fig.3.28 Torsional Response of an Asymmetric Wall Building (Plan View)

Note that the **strength** eccentricity is used in Eq.(3.53). The twist angle θ to be considered in Eq.(3.53) is found from the total building strength in the direction considered, V_{BZ}, and the effective rotational stiffness $J_{R,eff}$ as

$$\theta = V_{BZ} \cdot e_{RX} / J_{R,eff} \qquad (3.55)$$

where

$$J_{R,eff} = \frac{1}{\mu_{sys}} \cdot \sum_{1}^{n} k_{el,Zi} \left(x_i - e_{RX} \right)^2 + \sum_{1}^{m} k_{el,Xj} \left(z_j - e_{RZ} \right)^2 \qquad (3.56)$$

Note that the **stiffness** eccentricity is used in Eq.(3.56), and the elastic stiffness of elements responding in the Z direction is reduced by the design system ductility, μ_{sys}. Since the transverse (X direction) elements are expected to remain elastic, or nearly elastic, their elastic stiffness is not reduced. Thus, with reference again to Fig.3.28 under Z direction excitation:

$$J_{R,eff} = \left[k_{el,1} \left(0.5L_X - |e_R| \right)^2 + k_{el,2} \left(0.5L_X + |e_R| \right)^2 \right] / \mu_{sys} + 2k_{el,3} \left(0.5L_Z \right)^2 \qquad (3.57)$$

Note that the stiffness eccentricity e_{RX} in Eq.(3.55) can be based on ether elastic or effective stiffness. Since the latter are each taken as k_{el}/μ_{sys}, identical values are obtained. In Eq.(3.57), it is assumed that the elastic stiffness of walls 3 and 4 is the same.

Since torsional eccentricity is most common in wall buildings the justification for the above approach, and further discussion of torsional effects, is presented in Chapter 6.

3.8.3 Design to Include Torsional Effects

(a) Design to Avoid Strength Eccentricity: The first objective in consideration of torsion will be to investigate the possibility of eliminating the problem. With a building whose plan layout is symmetrical in location and in dimensions of lateral force-resisting elements this is of course no problem. Even when the plan layout of lateral force resisting elements is unsymmetrical, it may be possible to eliminate strength eccentricity. With respect to Fig.3.28, it may be possible to assign equal strengths to the two end walls (**1** and **2**) despite their different lengths by increasing the flexural reinforcement content of wall **2** in comparison with that of wall **1**. This would occur during allocation of the total base shear between the different elements (Section 3.5.6). Note that the approach outlined in the previous section indicates that there will still be a torsional component of response despite the zero strength eccentricity, which needs to be considered in the design process outlined in (c) below. Torsional response of systems with stiffness eccentricity, but no strength eccentricity is confirmed by inelastic time-history results[B4].

(b) Design to Minimize Strength Eccentricity: When the plan layout of lateral force-resisting elements is such that strength eccentricity is unavoidable, the design objective will generally be to minimize the strength eccentricity, so that the inelastic twist will be minimized. This will be the case when the drift of the most flexible element governs displacement-based design, but may not be the optimum solution when ductility capacity of the stiffest element governs (see Section 6.4.5).

(c) Modification of Design Displacement to Account for Torsion: The most common design situation, particularly for frame buildings, but also for many wall buildings of more than four storeys, will be that design displacements are governed by code drift limits. In these cases, the code drift will apply to the element with greatest displacement, including torsional effects, meaning that the design displacement at the building centre of mass, used in the **SDOF** design, will need to be reduced in proportion to the torsional displacements. The design displacement for the centre of mass will thus be found, reorganizing Eq.(3.53) to give:

$$\Delta_{ZM} = \Delta_{i,cr} - \theta(x_{i,cr} - e_{VX})\qquad\qquad(3.58)$$

where $\Delta_{i,cr}$ is the drift-controlled displacement of the critical element. With reference again to Fig.3.28, and assuming that drift limits apply to wall 2, the design displacement for the **SDOF** substitute structure will be

$$\Delta_{CM} = \Delta_2 - \theta(0.5L_X + |e_{VX}|)\qquad\qquad(3.59)$$

It is also possible, particularly for low-rise wall buildings, or buildings containing walls with low height/length aspect ratios, that the displacement capacity of the stiffest wall corresponding to material strain limits may govern design. In this case the design displacement at the centre of mass will be larger than the displacement of the critical element. Equation (3.56) still applies, with due consideration of signs, and with reference to Fig.3.28, the design displacement for the substitute structure will be

$$\Delta_{CM} = \Delta_1 + \theta\left(0.5L_X - |e_{VX}|\right) \tag{3.60}$$

In general it will be necessary to adopt an iterative approach to determine the design displacement when torsional effects are significant, since θ depends on J_R, e_R and e_V which in turn depend on the relative strengths assigned to the lateral force-resisting elements in both orthogonal directions, and the system ductility. However, adequate simplifying assumptions can often be made to avoid the necessity for iteration. Since this is mainly relevant to the behaviour of wall structures, it is discussed in further detail in Chapter 6.

3.9 CAPACITY DESIGN FOR DIRECT DISPLACEMENT-BASED DESIGN

Direct displacement-based design is a procedure for determining the required strength of different structural systems to ensure that a given performance state, defined by flexural strain or drift limits, is achieved under a specified level of seismic intensity. From this design strength, the required moment capacity at intended locations of plastic hinges (or shear capacity of seismic isolation devices, with seismic isolated structures) can be determined. As with force-based design, it is essential to ensure that inelastic action occurs only in these intended locations, and only in the desired inelastic mode. For example, a cantilever wall building will have intended plastic hinges at the bases of the various walls, where inelastic action will be required to occur by inelastic flexural rotation. Special measures are required to ensure that unintended plastic hinges do not occur at other locations up the wall height, where adequate detailing for ductility has not been provided, and to ensure that inelastic shear displacements, which are accompanied by rapid strength degradation, do not occur.

Moments and shears throughout the structure resulting from the distribution of the base shear in accordance with Sections 3.5.6 and 3.5.7 include only the effects of the first inelastic mode of vibration. This is adequate for determining the required strength at plastic hinge locations. However, actual response of the structure will include effects of higher modes. These will not affect the moments at the plastic hinge locations, as these are defined by, and limited to, the first inelastic mode values, but will influence moments and shears at other locations.

A further factor to be considered is that conservative estimates of material strengths will normally be adopted when determining the size of members, and (for reinforced concrete design) the amount of reinforcing steel. If the material strengths exceed the design values, as will normally be the case, then the moments developed at the plastic

hinge locations will exceed the design values. Since response is inelastic, it is the **actual** strength, not the theoretical design strength that will be developed under the design level of seismic intensity. All moments throughout the structure corresponding to the first inelastic mode will then increase in proportion.

Required strengths at these locations, or for actions other than flexure, are found from capacity design considerations[P1]. Basic strengths S_E for these locations and actions corresponding to the first-mode force distribution are thus amplified by an overstrength factor ϕ^o to account for maximum feasible flexural overcapacity at the plastic hinge locations, and by a dynamic amplification factor ω to represent the potential increase in design actions due to higher mode effects. The relationship between design strength S_D and basic strength S_E is thus

$$\phi_S S_D = S_R = \phi^o \omega S_E \qquad (3.61)$$

where S_R is the required dependable strength of the design action S, and ϕ_S is the corresponding strength reduction factor. As is discussed in Chapter 4, a value of $\phi_S = 1$ should be adopted for flexural design of plastic hinges, but values of $\phi_S < 1$ are appropriate for other actions and locations.

The conventional approach currently adopted in force-based design is explained with reference to design of a cantilever wall building. For the required moment capacity of cantilever walls, the base moment is amplified to account for material overstrength, and a linear distribution of moments is generally adopted up the wall height to account for higher mode effects. As is apparent from Fig.3.29(a), this implies higher amplification of moments at mid-height than at the base or top of the wall. Reinforcement cut-off is determined by consideration of tension shift effects. This is achieved by vertical offset of the moment profile.

Shear forces corresponding to the design force distribution are amplified by the flexural overstrength factor, and the dynamic amplification factor ω_v directly in accordance with Eq.(3.61), as shown in Fig.3.29(b). The factor adopted in this figure has been obtained from previous research, related to force-based design and is presented elsewhere[P1] in the following form:

$$\omega_v = 0.9 + n/10 \qquad for \quad n \le 6$$
$$\omega_v = 1.3 + n/30 \qquad for \quad 6 < n < 15 \qquad (3.62)$$

where n is the number of storeys in the wall, and need not be taken greater than 15. It is shown in Section 6.6 that this equation is generally non-conservative, and alternative recommendations are made for displacement-based design.

For frame structures, beam shear forces, and moments at locations other than potential plastic hinges are amplified by the flexural overstrength factor. Since higher modes are not normally considered for beam design, the dynamic amplification factor is not normally included. However, it should be noted that vertical response is essentially a

higher mode, and may amplify the gravity moments considerably. A strict formulation of capacity design would take this into account.

Column end moments and shear forces are amplified for both beam plastic hinge overstrength and dynamic amplification. For one-way frames, upper limits for dynamic amplification of column moments of 1.80 have been recommended, with 1.3 for column shear forces. Further amplification for beam flexural overstrength is required[P1].

In this section we have discussed conventional capacity design, as currently applied to force-based design of structures. We show in Section 4.5 and the design chapters related to specific structural types that modifications to the capacity factors for both flexural overstrength, and dynamic amplification are appropriate for direct displacement-based design.

(a) Moment Profiles   (b) Shear Force Profiles
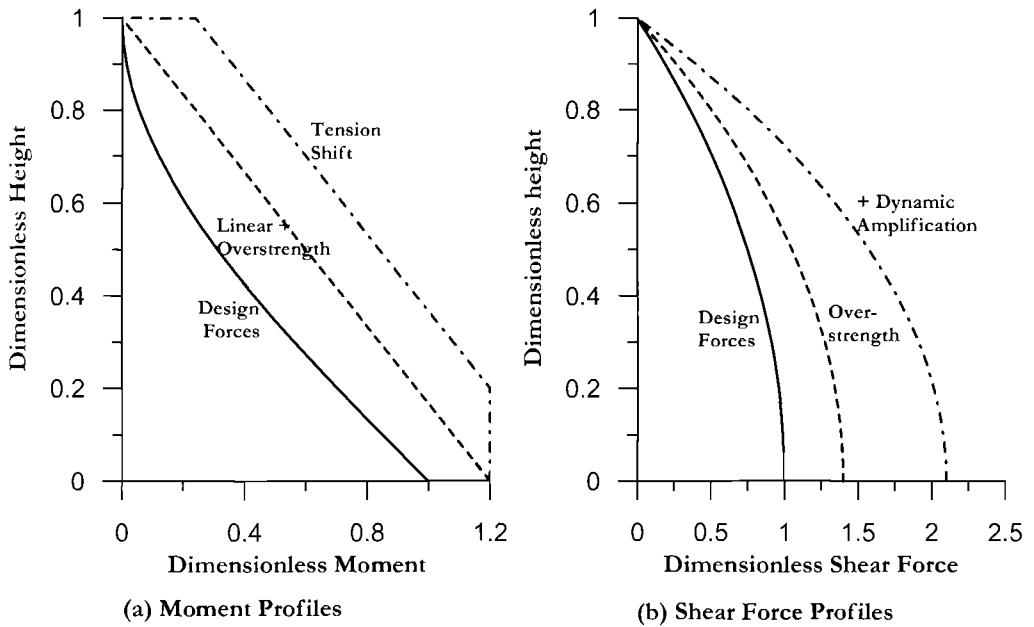
Fig. 3.29   Recent Recommendations for Dynamic Amplification of Design Forces for Equivalent Lateral Force Design of Cantilever Walls[P1]

3.10   SOME IMPLICATIONS OF DDBD

3.10.1   Influence of Seismic Intensity on Design Base Shear Strength

Direct displacement-based seismic design implies significantly different structural sensitivity to seismic intensity than found from current codified force-based design procedures. This can be illustrated with reference to Fig.3.30, where acceleration spectra (Fig.3.30(a)), and displacement spectra (Fig.3.30(b)) are shown for two seismic zones.   It

is assumed that the spectral shapes for the two zones are identical, and each are found by multiplying a base-level spectrum by the zone factors Z_1 or Z_2.

Consider the design of two reinforced concrete buildings, one designed for each of the seismic zones, where the structural geometry, including member sizes (but not reinforcement contents) are identical for the two buildings. We assume that structures are designed to exactly satisfy the strength requirements for the two zones. If the buildings are designed by conventional force-based procedures, the fundamental periods of the two buildings will be assumed to be the same, since the same allowance for reduction of gross-section stiffness will be made. Assuming the same force-reduction factor is used for each design it is thus clear (see Fig.3.30(a)) that the required base-shear design forces V_{b1} and V_{b2} for the two buildings are related by:

$$V_{b2} = V_{b1} \frac{Z_2}{Z_1} \qquad (3.63)$$

(a) **Acceleration Spectra**   (b) **Displacement Spectra**
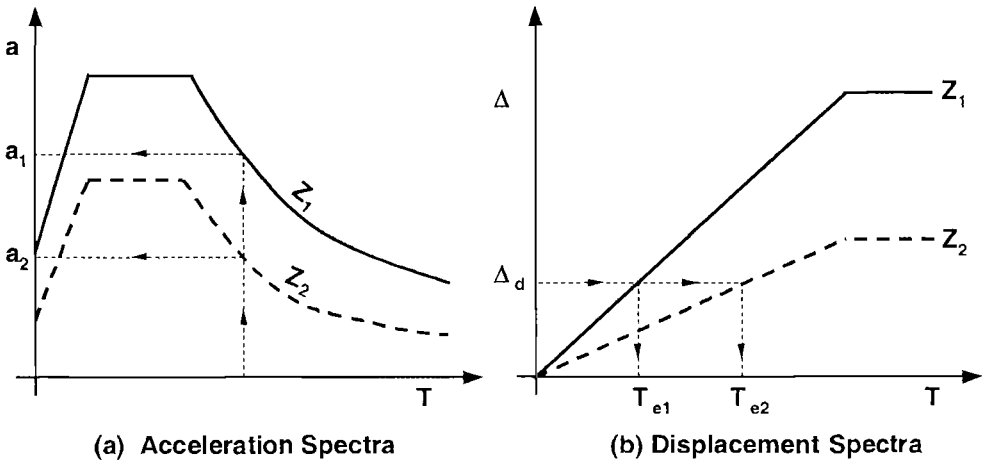
Fig.3.30 Influence of Seismic Intensity on Design Base Shear Force

Under direct displacement-based design, the assumption of equal geometry ensures that the yield displacements, and the limit-state design displacements, based on drift limits, for the two buildings are the same. Hence the ductility, and also the effective damping will also be the same for the two buildings. As may be seen from Fig.3.30(b), with equal design displacements and damping, the effective periods at design displacement response will be related to the zone intensity by:

$$T_{e2} = T_{e1} \frac{Z_1}{Z_2} \qquad (3.64)$$

From Eq.(3.1) the required effective stiffness is inversely proportional to the period squared, hence:

$$K_{e2} = K_{e1} \left(\frac{Z_2}{Z_1} \right)^2 \tag{3.65}$$

Further, since the design displacements are equal, Eq.(3.2) yields the ratio of base shear forces as:

$$V_{Base2} = V_{Base1} \left(\frac{Z_2}{Z_1} \right)^2 \tag{3.66}$$

Thus the required base shear strength is proportional to the **square** of the seismic intensity. This is a fundamentally important difference between the two approaches, particularly for regions of low (or very high) seismicity. It should be noted however, that the difference between the conclusions resulting from force-based or displacement-based considerations is largely a consequence of the assumption in the force-based approach that stiffness may be assumed to be equal to a constant fraction of the gross-section stiffness. As has been pointed out in relation to Fig.1.4, and is discussed in some detail in Section 4.4, stiffness of a member is directly proportional to strength. Thus the elastic stiffness of the members of the structure in the lower seismic zone will be less than for the structure in the higher seismic zone. An iterative force-based solution, correcting the stiffness of the structural members based on the strength found from the previous iteration would eventually come to a similar conclusion to that resulting from **DDBD**.

3.10.2 Influence of Building Height on Required Frame Base Shear Strength

A further finding of some interest can be obtained by examining the sensitivity of required base shear strength of buildings with identical plan geometry and storey mass, but with different numbers of storeys. We assume for simplicity that the section dimensions of structural members are not affected by building height, and that the design deflected shape is also independent of building height. Clearly this latter assumption will become increasingly crude when large variations in building height are considered, but is reasonable for frame buildings up to about 10 storeys, and for dual wall/frame buildings up to 20 storeys. Figure 3.31 compares two frames of different heights. Let n = number of storeys, with constant mass m per storey. In the following, C_1 to C_6 are constants.

Effective mass: $\qquad\qquad\qquad\qquad m_e = C_1 nm \qquad\qquad\qquad\qquad (3.67a)$

Design Displacement: $\qquad\qquad\quad \Delta_d = C_2 n \qquad\qquad\qquad\qquad\quad (3.67b)$

(a) Building 1   (b) Building 2   (c) Design Displacements
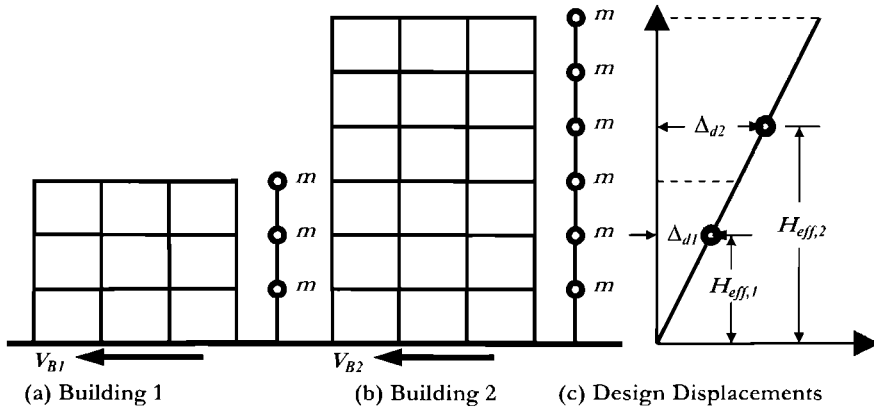
Fig.3.31 Design Displacement Profiles of Buildings Differing only in Height

With the above assumptions, both the yield displacement, and the design displacement will be proportional to height. Hence the design displacement ductility and thus the effective damping will be independent of height, and the design displacement response of the buildings will lie on the same damping curve (see Fig.3.1(d)). Provided that the design displacement given by Eq.(3.67b) is less than the displacement at peak period (e.g. T_e =4 sec. in Fig.3.1(d)), and that the design displacement spectrum is linear with period, the effective period can thus be expressed as:

$$T_e = C_3\Delta_d = C_3C_2n \tag{3.67c}$$

From Eq.(3.1), the effective stiffness will be:

$$k_e = \frac{4\pi^2 m_e}{T_e^2} = \frac{C_4C_1nm}{(C_3C_2)^2 n^2} = C_5\frac{m}{n} \tag{3.67d}$$

From Eqs.(3.2), (3.67b) and (3.67d) the design base shear will be

$$V_{Base} = k_e\Delta_d = C_5\frac{m}{n}C_2n = C_6m \tag{3.67e}$$

Recalling that m is the mass of one storey, it is seen that the design base shear strength is independent of the number of storeys. This might seem to point the way towards further possible design simplifications.

3.10.3 Bridge with Piers of Different Height

We return to the example of a bridge crossing a valley, with piers of different heights, first discussed in Section 1.3.4, and subjected to longitudinal seismic excitation. Figure 1.11 from Section 1.3.4 is reproduced below as Fig.3.32(a).

(a) Structure   (b) Force-Displacement Response
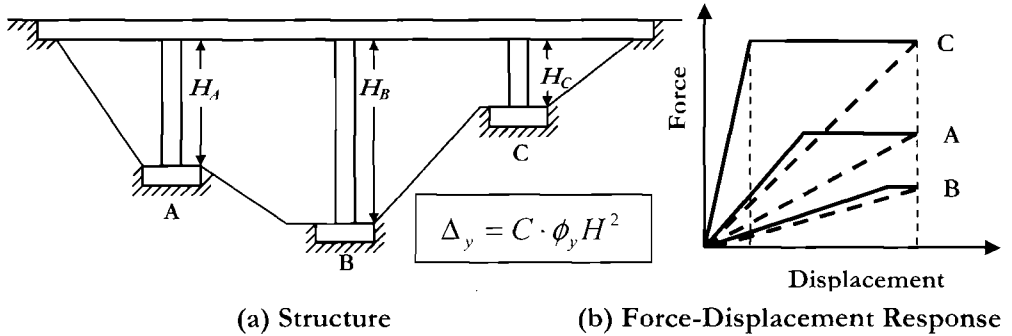
Fig.3.32 Bridge with Unequal Pier Heights under Longitudinal Excitation

As was discussed in Section 1.3.4, designing in strict accordance with force-based design would require allocating shear between the piers in proportion to the elastic stiffnesses of the piers. This is based on the assumption that yield displacements, and ductility demands for the piers can be equalized by distributing strength in proportion to stiffness. We have shown this to be invalid, since the yield curvature, and hence the yield displacement is essentially independent of strength. The consequences, as noted in Table 3.6 are that flexural reinforcement ratios for the piers should be approximately in proportion to the inverse of pier height squared. The sequence of design operations follows the arrow in the second column of Table 3.6

With **DDBD**, the initial stiffness is largely irrelevant, and the relationship between flexural reinforcement ratios in the piers is the designer's choice. Normally equal reinforcement ratios will be chosen, and the moment capacities of the flexural plastic hinges will be essentially equal. This implies distributing the total seismic force between the piers in inverse proportion to height, as indicated in Table 3.6, Column 3, which also shows that the sequence of design operations, indicated by the arrow, is the exact reverse of that for force-based design. Of course it would be possible to use a rational reinforcement distribution for force-based design, but only if the concept of the importance of initial stiffness is abandoned.

Table 3.6 Difference between Force-based and Displacement-Based Design Parameters for Bridge under Longitudinal Excitation

ITEM	Force-Based Design	DDBD
Yield Displacement	Equal	$\alpha\ H^2$
Ductility Demand	Equal	$\alpha\ 1/H^2$
Stiffness	$\alpha\ 1/H^3$	$\alpha\ 1/H$
Design Shear Force	$\alpha\ 1/H^3$	$\alpha\ 1/H$
Design Moment	$\alpha\ 1/H^2$	Equal
Reinforcement Ratio	$\alpha\ 1/H^2$	Equal

3.10.4 Building with Unequal Wall Lengths

The structural wall building shown in Fig.3.33, also considered in Chapter 1, and in Design Examples 3.5 to 3.7 is now considered. Force-based design, relying on initial stiffness distributes the design base shear force between the different length walls in proportion to wall length cubed on the invalid assumption that the walls can be made to yield at the same displacement. Since the yield curvature is inversely proportional to wall length, so will the yield displacements be. Table 3.7 compares the proportions of the design parameters based on initial-stiffness force-based design, and direct displacement-based design.
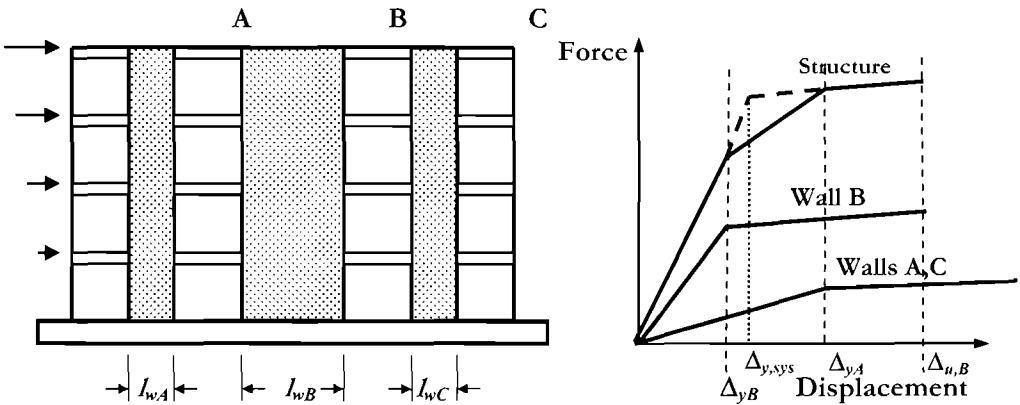
Fig.3.33 Building with Unequal Length Cantilever Walls

Table 3.7 Comparison of Design Parameters for Force-Based and DDBD Designs of a Cantilever Wall Building

ITEM	Force-Based Design	DDBD
Yield Displacement	Equal	$\alpha\, 1/l_w$
Ductility Demand	Equal	$\alpha\, l_w$
Stiffness	$\alpha\, l_w^{3}$	$\alpha\, l_w^{2}$
Design Shear Force	$\alpha\, l_w^{3}$	$\alpha\, l_w^{2}$
Design Moment	$\alpha\, l_w^{3}$	$\alpha\, l_w^{2}$
Reinforcement Ratio	$\alpha\, l_w$	Equal

4

ANALYSIS TOOLS FOR DIRECT DISPLACEMENT-BASED DESIGN

4.1 INTRODUCTION

It is beyond the scope of this book to include a detailed treatment of material properties, methods of analysis for determining section strengths, and general global structural analysis methods. There are, however, a number of aspects of these topics which are of special relevance for direct displacement based design (**DDBD**), particularly related to the strength and deformation characteristics of reinforced concrete and masonry sections. Hence this chapter provides a detailed examination of selected topics. More general treatments are available in other sources [P1,P4] to which the interested reader is referred.

4.2 FORCE-DISPLACEMENT RESPONSE OF REINFORCED CONCRETE MEMBERS

(a) Structure   (b) Deflection   (c) Moment-Curvature   (d) Force-Displacement
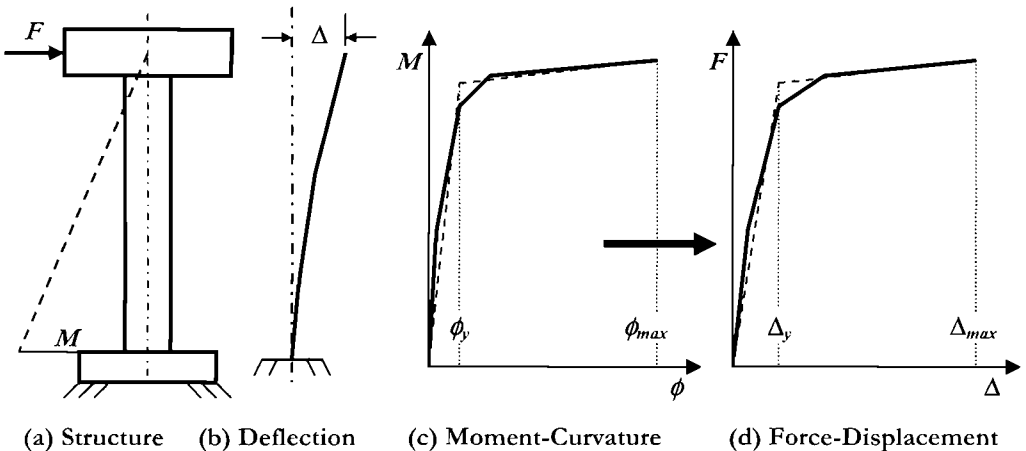
Fig.4.1 Lateral Deformation of a Bridge Column

One of the most basic tools for **DDBD** is the moment-curvature analysis of reinforced concrete and masonry sections. This is used to define section strengths, limit state curvatures, and also the elastic stiffness. From these data, member and structure force-

displacement characteristics can be directly generated, as discussed in Section 4.2.8, and suggested in Fig.4.1 for a simple bridge pier. The treatment in the following relates specifically to reinforced concrete sections, though the principles are identical for reinforced masonry. In general, moment-curvature analysis of steel sections is un-necessary, since the elastic stiffness is directly known. Generation of force-displacement response of steel sections is briefly covered in Section 4.3.

4.2.1   Moment-Curvature Analysis

(a) Symmetrical section   **(b) Strains**   **(c) Stresses**
n layers of rebar
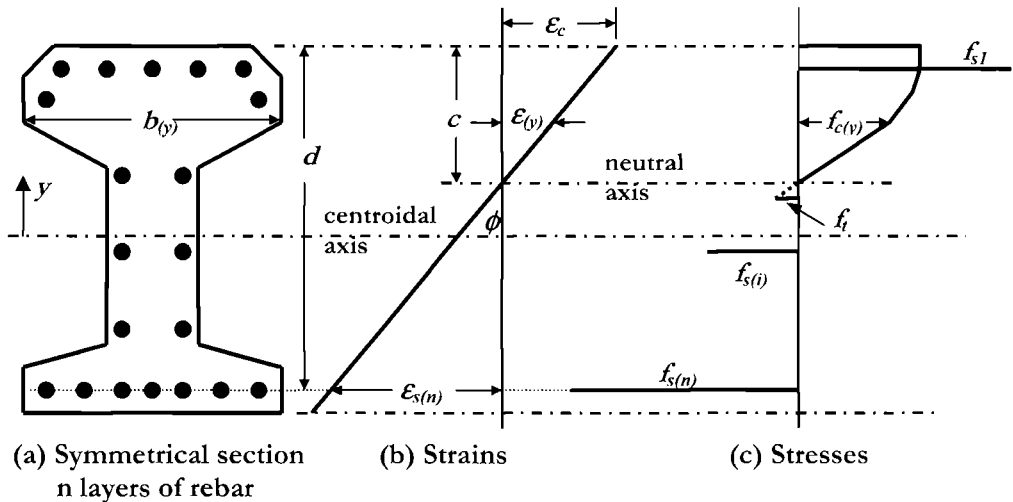
Fig.4.2   Strains and Stresses in an Arbitrary Symmetrical R.C. Section

Figure 4.2 shows an arbitrary symmetrical reinforced concrete section subjected to bending, with the top of the section in compression. The normal assumptions for flexural analysis are made:

- The strain profile is linear at all stages of loading up to ultimate (i.e. the Navier-Bernoulli "plane-sections" hypothesis holds).
- Steel strain and concrete strain at a given distance from the neutral axis (see Fig. 4.2) are identical (i.e. perfect bond between steel and concrete exists).
- Concrete and reinforcement non-linear stress-strain relationships are known:

$$f_{c(y)} = \Phi_c(\varepsilon_{c(y)}) = \Phi_c(\varepsilon_{(y)}) \qquad (4.1(a))$$

$$f_{s(y)} = \Phi_s(\varepsilon_{s(y)}) = \Phi_s(\varepsilon_{(y)}) \qquad (4.1(b))$$

- Concrete tension strength is ignored in the analysis.
- Axial force (if any) is applied at the section centroid.

As discussed subsequently, different concrete stress-strain relationships will apply to core and cover concrete. Note that the reason that concrete tension strength is ignored in the analysis is that the section will be subjected to reversed loading under seismic attack. Since the neutral axis will generally be on the compression side of the section centroid, cracks under reversed loading will extend through the entire section. That is, the compression zone will occur in a location previously cracked under moment of the opposite sign, and no tension capacity will exist after application of service loads, or preliminary low-level seismic response. Further, the contribution of concrete tension strength to flexural strength is normally negligible.

Let the axial force on the section be denoted by N. Then for axial force equilibrium at any level of response, using the nomenclature of Fig.4.2:

$$N = \int f_{c(y)} b_{(y)} dy + \sum_1^n f_{si} A_{si} = \int \Phi_c(\varepsilon_{(y)}) b_{(y)} dy + \sum_1^n \Phi_s(\varepsilon_{(y)i}) A_{si} \qquad (4.2)$$

where A_{si} is the total area of all reinforcing bars at layer i, distance y_i from the centroidal axis. Analytically, the position of the neutral axis is adjusted by trial and error until Eq.(4.2) is satisfied.

Taking moments of the stress resultants about the section centroid:

$$M = \int \Phi_c(\varepsilon_{(y)}) b_{(y)} y.dy + \sum_1^n \Phi_s(\varepsilon_{(y)i}) y_i A_{si} \qquad (4.3)$$

The corresponding curvature is given by:

$$\phi = \frac{\varepsilon_c}{c} = \frac{\varepsilon_{sn}}{(d-c)} \qquad (4.4)$$

where ε_c and ε_{sn} respectively are the extreme-fibre compression strain, and strain at the level of the reinforcing bars at maximum distance from the neutral axis (see Fig.4.2).

Moment-curvature analysis is normally organized in accordance with the following steps:
1. Divide the section into a number of slices perpendicular to the loading axis. Determine the area of unconfined cover concrete, confined core concrete, and reinforcing steel in each layer.
2. Select an extreme fibre compression strain, starting with the lowest value.
3. Assume a neutral axis location.
4. Calculate concrete and steel stresses at the centre of each layer, and hence the concrete and steel forces in each layer
5. Check axial force equilibrium in accordance with Eq.(4.2).
6. Modify the neutral axis position to improve agreement in Eq.(4.2).

7. Cycle steps 3 to 6 until satisfactory agreement is obtained between external and internal forces.
8. Calculate the moment (Eq.(4.3)) and curvature (Eq.(4.4)).
9. Increment the extreme fibre compression strain, and repeat steps 3 to 8.
10. Continue incrementing the extreme fibre compression strain until the ultimate compression strain (discussed subsequently) is reached.

4.2.2 Concrete Properties for Moment-Curvature Analysis
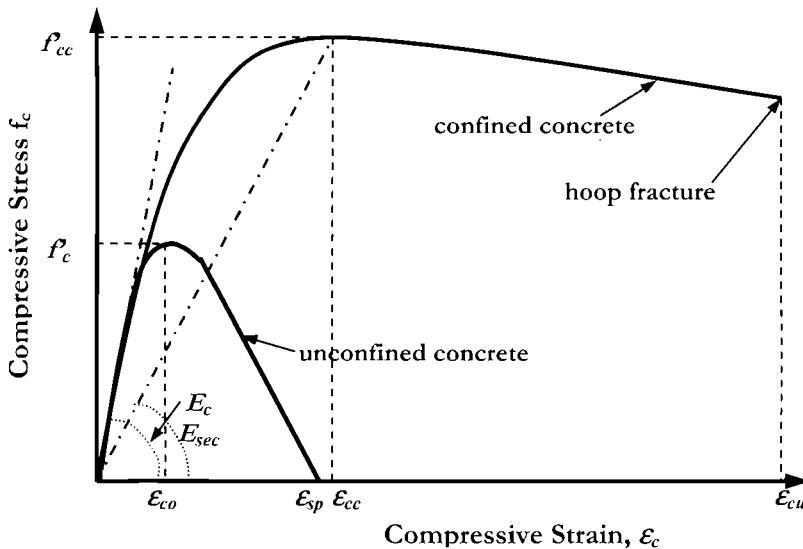
Fig.4.3   Stress-Strain Model for Concrete in Compression [M4]

As noted above, separate stress-strain relationships should be used for the compression response of unconfined cover concrete and confined core concrete. As shown in Fig. 4.3, confined concrete has increased compression strength, and more importantly, increased compression strain capacity. The enhancement of compression stress- strain characteristics of the core concrete is a result of the action of well-detailed transverse reinforcement in the form of hoops or spirals. In conjunction with longitudinal reinforcement, close-spaced transverse reinforcement acts to restrain the lateral expansion of the concrete that accompanies the onset of crushing, maintaining the integrity of the core concrete.

Figure 4.4 shows four column sections confined by different configurations of transverse reinforcement. In Fig.4.4(a), the confinement is provided by circular spirals or hoops. As the concrete attempts to expand, it bears uniformly against the hoop or spiral, placing it in tension, resulting in a uniform radial compression on the concrete.

(a) Circular hoops   (b) Rectangular hoops   (c) Rectangular octagonal
    or spirals   with cross-ties   hoops

(d) Overlapping rectangular (e) Confinement by   (f) Confinement by
    hoops   transverse rebar   longitudinal rebar
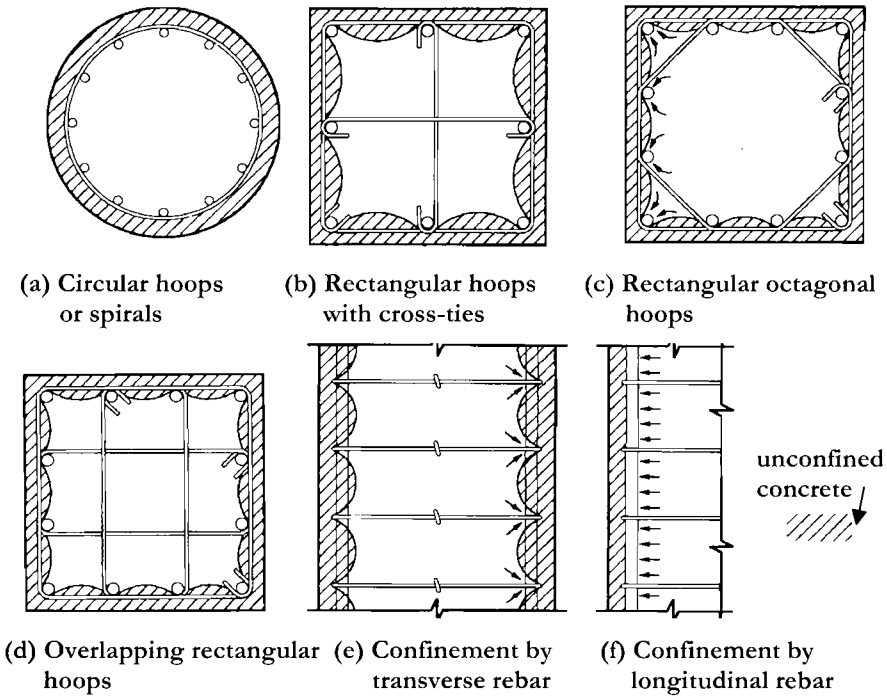
Fig.4.4   Confinement of Column Sections by Transverse Hoops and Spirals[P4]

In Fig.4.4 the unconfined cover concrete is shown shaded.   It is normally assumed that the maximum effective radial confining pressure, f_l that can be exerted on the core concrete occurs when the spirals or hoops are stressed to their yield stress f_{yh}.   Taking a free body across the column diameter, and noting that this exposes two bar forces $f_{yh}A_h$ where A_h is the spiral or hoop cross-sectional area, the confining stress in the core is:

$$f_l = \frac{2f_{yh}A_h}{D's} = 0.5\rho_v f_{yh} \tag{4.5}$$

where s is the spacing of the hoop or spiral along the column longitudinal axis, D' is the diameter of the confined core, measured to the centreline of the hoop or spiral, and $\rho_v = 4A_h/D's$ is the volumetric ratio of transverse hoops or spirals.

Note that the longitudinal spacing s of the hoops or spiral also affects confinement efficiency, as shown in Fig. 4.4(e), since the confining effect is concentrated as a line load at the level of the spiral.   However, this load is partially distributed to the longitudinal reinforcement which tends to make the confining effect more uniform (see Fig.4.4(f)), illustrating the importance of the longitudinal reinforcement to confinement of concrete.

The hoops or spirals also act to restrain the longitudinal reinforcement from buckling when in compression. Buckling may occur after longitudinal reinforcement is first subjected to inelastic tension strain under one direction of seismic loading. When the loading direction is reversed, the bars initially transfer all the compression force on the section, and must yield in compression before previously formed cracks close. It is during this stage of response that the bars are susceptible to buckling. Once the cracks close, the compression stiffness of the concrete can be expected to restrain the tendency for bar buckling. It will thus be seen that bar buckling is more dependent on the inelastic tensile strain developed in a previous yield excursion, than on pure compression characteristics. To ensure inelastic buckling does not occur, the maximum spacing of transverse hoops or spirals must be related to the bar diameter, as discussed further in Section 4.2.5(c).

With rectangular sections, it is possible to develop different levels of lateral confining stress in orthogonal directions. If A_{shx} is the total amount of lateral reinforcement in a hoop layer crossing a section perpendicular to A_{shx}, then the maximum confining stress that can be developed in that direction is

$$f_{lx} = \frac{C_e A_{shx} f_{yh}}{h_{cy} s} = C_e \rho_{ax} f_{yh} \tag{4.6}$$

where ρ_{ax} is the area ratio of transverse reinforcement in the x direction, s is again the spacing of hoop sets along the member axis, and C_e is a confinement effectiveness coefficient, relating the minimum area of the effectively confined core (see Fig.4.4) to the nominal core area bounded by the centreline of the peripheral hoop, and h_{cy} is the core width perpendicular to the direction considered, measured to the centreline of the peripheral hoop.

Clearly a similar expression can be developed in the orthogonal direction. Ideally, rectangular sections should be designed to have equal area ratios of confining reinforcement in the orthogonal directions, in which case the volumetric confinement ratio is:

$$\rho_v = \rho_{ax} + \rho_{ay} = 2\rho_a \tag{4.7}$$

and the lateral confining stress is given by

$$f_l = 0.5 C_e \rho_v f_{yh} \tag{4.8}$$

The similarity to Eq.4.5 is obvious. Note that a confining effectiveness coefficient C_e is sometimes also assigned to circular sections, but since it will normally be higher than 0.95 for typical designs, it is generally taken as 1.0. For rectangular sections, values of between 0.75 and 0.85 are appropriate, depending on the ratio s/h_c, and the number of longitudinal bars in the section. For walls, $C_e = 0.5$ is generally appropriate.

The stress-strain relationships illustrated in Fig. 4.3 can be described by the Mander model[M4]:

$$f_c = \frac{f'_{cc} x \cdot r}{r - 1 + x^r}$$

(4.9)

where f'_{cc} is the compression strength of the confined concrete which is related to the unconfined compression strength and the lateral confining pressure by:

$$f'_{cc} = f'_c \left(2.254 \sqrt{1 + \frac{7.94 f_l}{f'_c}} - 2 \frac{f_l}{f'_c} - 1.254 \right)$$

(4.10)

and

$$x = \varepsilon_c / \varepsilon_{cc} ,$$

(4.11)

$$\varepsilon_{cc} = 0.002 \left[1 + 5 \left(\frac{f'_{cc}}{f'_c} - 1 \right) \right] ,$$

(4.12)

$$r = \frac{E_c}{E_c - E_{sec}} ,$$

(4.13)

$$E_c = 5000 \sqrt{f'_c} \, (MPa) = 60,000 \sqrt{f'_c} \, (psi) ,$$

(4.14)

$$E_{sec} = \frac{f'_{cc}}{\varepsilon_{cc}}$$

(4.15)

4.2.3 Masonry Properties for Moment-Curvature Analyses

Stress-strain curves for masonry are similar to those for concrete[P1]. For unconfined masonry, the peak compression strength is typically reached at a slightly lower strain than for unconfined concrete, but the confinement provided at critical sections, such as at the base of cantilever walls, by stiff supporting members (e.g. foundation beams) enhances the critical strain parameters such that use of equations for unconfined concrete are normally adequately conservative.

It is rather unusual to confine masonry by use of transverse reinforcement to improve the compression stress-strain characteristics. Clearly confinement is difficult in hollow-cell masonry as a result of constraints provided by limited grout spaces. However, tests on masonry walls where confining bars or plates were inserted in the mortar beds indicate a significant improvement in ductility capacity, and also a deferred onset of damage to the masonry in the form of the typical vertical splitting of zones with high compression stress[P1].

4.2.4   Reinforcing Steel Properties for Moment-Curvature Analyses
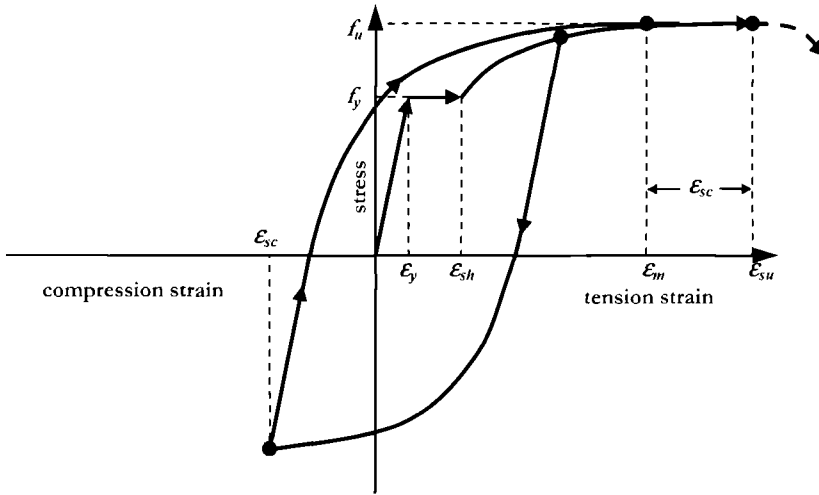
Fig. 4.5   Reinforcing Steel Stress-Strain Characteristics

In conventional seismic design the reinforcing steel design strength is often taken as the yield strength. That is, the increase in stress due to strain-hardening is generally ignored. When carrying out moment-curvature analyses however, it is important that the most realistic representation of the full stress-strain characteristic be utilized, including the strain-hardening portion. This is particularly important for **DDBD**, because the design attempts to match the strength at the expected design displacement to the required strength, rather than to use an artificially low nominal "yield" strength.

Figure 4.5 illustrates the characteristics of typical monotonic and cyclic stress-strain response of reinforcing steel. The monotonic response can be represented by three phases:

Elastic: $0 \leq \varepsilon_s \leq \varepsilon_y$: $f_s = E_s \varepsilon_s \leq f_y$ (4.16)

Yield plateau: $\varepsilon_y \leq \varepsilon_s \leq \varepsilon_{sh}$: $f_s = f_y$ (4.17)

Strain-hardening: $\varepsilon_{sh} \leq \varepsilon_s \leq \varepsilon_{su}$: $f_s = f_u \left[1 - \left(f_u - f_y \right) \left(\dfrac{\varepsilon_{su} - \varepsilon_s}{\varepsilon_{su} - \varepsilon_{sh}} \right)^2 \right]$ (4.18)

In Eq.(4.16) to (4.18), ε_s and f_s and the reinforcing steel strain and stress, E_s is the elastic modulus, and the other symbols are defined in Fig.4.4. Note that the curve only continues up to ε_{su}, the strain at ultimate stress, as behaviour past this point is

characterized by local necking of the reinforcement, with reduction of stress elsewhere, and cannot be relied on in design.

Typical values for the characteristic stresses and strains depend on the type, and grade of reinforcement used. In seismic applications in the American continent, ASTM 706[X9] grade 60 reinforcement (f_y minimum = 414MPa) is normally used. Strain-hardening usually starts at about ε_{sh} = 0.008, the ultimate strain is about ε_{su} = 0.10 to 0.12, and the ratio of ultimate to yield stress is typically f_u/f_y = 1.35 to 1.50. In Europe tempcore reinforcement is almost always used, with a higher yield stress (typically f_y = 500MPa (72.5ksi)), an ultimate strain of about 0.09, a ratio of ultimate to yield stress of about f_u/f_y = 1.2, and essentially no pronounced yield plateau.

As is illustrated in Fig. 4.5, the cyclic characteristics of the reinforcing steel differ from the monotonic curve. On unloading and reloading, the stress-strain curve softens early, due to the Bauschinger effect, and no pronounced yield plateau is apparent. However, it is found that force-displacement response predicted from moment-curvature characteristic based on the monotonic stress-strain curves for both concrete and reinforcement provide a good envelope to measured cyclic response. Where full cyclic moment-curvature response is required (this is more normally the case for research applications rather than for design), more complete equations are appropriate, and the reader is referred elsewhere[M4].

4.2.5 Strain Limits for Moment-Curvature Analysis

(a) Damage-Control Compression Strain: The useful limit to confined concrete compression strain is usually taken to occur when fracture of the transverse reinforcement confining the core occurs. This may be estimated by equating the increase in strain-energy absorbed by the concrete, above the value appropriate for unconfined concrete to the strain-energy capacity of the confining steel. Considering a unit volume of core concrete under uniform axial compression, the increase in strain-energy absorbed can be expressed as:

$$SE_{conc} = C_1 f'_{cc} \varepsilon_{cu} \tag{4.19}$$

where C_1 is a coefficient dependent on the shape of the unconfined and confined stress strain curves. Similarly, the strain-energy capacity of the transverse reinforcement, related to the same unit volume of core concrete can be expressed as

$$SE_{rebar} = C_2 \rho_v f_{yh} \varepsilon_{su} \tag{4.20}$$

where C_2 depends on the shape of the reinforcing steel stress-strain curve. Thus equating (4.19) and (4.20), and assuming that the unconfined ultimate strain of the concrete is 0.004, the following expression for the ultimate compression strain for confined concrete can be derived:

$$\varepsilon_{c,dc} = 0.004 + \frac{C_2 \rho_v f_{yh} \varepsilon_{su}}{C_1 f'_{cc}} = 0.004 + 1.4 \frac{\rho_v f_{yh} \varepsilon_{su}}{f'_{cc}} \qquad (4.21)$$

In Eq.(4.21) an average value of C_2/C_1=1.4 is adopted, based on typical steel and concrete stress-strain shapes. Equation (4.21) is approximate for a number of reasons:

- It is based on pure axial compression of the core concrete. Under combined axial compression and flexure, the equation will predict conservatively low estimates for ε_{cu}.

- It does not take into account the additional confinement of the critical section by the adjacent member. If the member is a column supported on a foundation, then the foundation will act to restrain lateral expansion of the critical lower part of the column plastic hinge, thus adding to the confining effect. Similarly, the end portion of the plastic hinge of a beam framing into a column will be confined to some extent by the column, provided the column remains elastic.

- Although experiments[M7] have shown the equation to provide good estimates of ultimate compression strain, the logic (energy balance) does not appear to apply at reduced levels of extreme fibre compression strain. At these levels, inverting Eq.(4.21) to provide estimates of transverse reinforcement strain (ε_s rather than ε_{su}) over-predicts the measured strains.

The combined effects of these approximations results in effective ultimate compression strains under combined axial force and flexure that exceed the predicted values by a factor of about 1.3 to 1.6. The influence on ultimate displacement is similar. Our view is that this degree of conservatism is appropriate for structures designed to a "damage control" limit state (see Section 3.3.2).

(b) Serviceability Limit Compression Strain: The limit compression strain for concrete corresponding to the serviceability limit state should be a conservative estimate of the strain at which spalling initiates. Below this strain-limit repair should not be needed which is compatible with performance criteria for the serviceability limit state. In seismic response, maximum compression strains almost always occur adjacent to a supporting member (e.g. a foundation beam, for a concrete column or wall), which provide an additional restraint against initiation of spalling. Experiments[P4] have indicated that a compression strain of $\varepsilon_{c,s} = 0.004$ is a conservative lower limit to initiation of spalling, and this value will be used for concrete structures in this text. For masonry structures a somewhat more conservative estimate is appropriate, and we recommend $\varepsilon_{c,s} = 0.003$.

(c) Damage-Control Tension Strain Limit: It is inappropriate to use ε_{su} , the strain at maximum stress of the reinforcing steel found from monotonic testing, as the maximum permissible tension strain for moment-curvature analysis for several reasons. First, under cyclic loading, the effective ultimate tensile strain is reduced by the peak compressive strain, ε_{sc}, achieved under a previous reversal of loading direction, as

suggested in Fig. 4.4[D5]. Second, once high tensile strains have been developed, the longitudinal reinforcement becomes susceptible to buckling when subjected to reversed loading that puts the reinforcement in compression. This buckling typically occurs before the previously developed flexural cracks are closed, and while the bars are still subject to tensile strain (but compressive stress). This engenders low-cycle fatigue of the reinforcing bar at levels of tensile strain significantly below ε_{su}. The level of strain will depend on the volumetric ratio and longitudinal spacing of the transverse reinforcement. Finally, slip between reinforcing steel and concrete at the critical section, and tension-shift effects result in reinforcement strain levels being lower than predicted by a "plane-sections" hypothesis. Based on these considerations, the ultimate curvature of the section analysed should be based on a steel tension strain limit of $\varepsilon_s = 0.6\varepsilon_{su}$, if this occurs before the concrete ultimate compression strain ε_{cu} is developed. To ensure this level of strain is attainable without the reinforcement buckling, the spacing of transverse reinforcement hoops or layers should not exceed $s = (3 + 6(f_u/f_y - 1))d_{bl}$ (d_{bl} = longitudinal bar diameter).

(d) Serviceability Limit Tension Strain: It has been common in the past to require "elastic" or "near-elastic" response at the serviceability limit state. This is generally taken to mean that the displacement ductility demand should be $\mu \leq 1$, implying reinforcement tension strains that are at, or only slightly above yield strain. This is, in our view excessively conservative, as strains of several times the yield strain can be sustained without creating damage requiring repair. The critical aspect is likely to be the crack widths developed by the seismic response. Moreover, it is not the instantaneous maximum value occurring during seismic response, but the residual crack width that will be of concern, since potential corrosion is the issue here. Analyses reported elsewhere[P4] indicate that for structural elements with compression gravity loading (walls, columns), a maximum tension strain of 0.015 during seismic response will correspond to residual crack widths of about 1.0 mm (0.04in), and for members without axial compression (e.g. beams) a peak strain of about 0.010 is appropriate. A residual crack width of 1.0mm should not need remedial action in normal environments. In aggressively corrosive environments, lower residual crack widths may be appropriate, with correspondingly reduced serviceability tensile strain limits.

4.2.6 Material Design Strengths for Direct Displacement-Based Design

In gravity-load design of structures, it is common practice to assume minimum, or characteristic lower bound values for material strengths when determining the nominal strength of sections. This is typically combined with a strength reduction factor (or with partial material factors) to ensure a conservative estimate of the section strength. Thus, the design flexural strength requirement may be expressed as:

$$\phi_f M_N \geq M_R \tag{4.22}$$

where ϕ_f is the flexural strength reduction factor (typically $\phi_f \le 0.9$), and M_N and M_R are the nominal (designed) and required moment capacities.

This conservative approach has obvious relevance for gravity-load design, where the consequences of the dependable strength ($\phi_f M_N$) being less than the moment demand could be catastrophic failure. However, in seismic design, it is expected that under design seismic attack, the moment capacity will be considerably less than the demand resulting from fully elastic response. Consequently, incorporation of extreme conservatism in estimates of material strengths, and use of strength reduction factors will not result in "protecting" the section against inelastic action. All that will happen is that the section strength will be higher than needed, but will still be developed, with considerable ductility demand, under design seismic attack. A small reduction in displacement demand might result, but this is best directly incorporated into the specified design displacement.

Consequently it is recommended that flexural strength reduction factors not be used when designing locations of intended plastic hinging. Based on recommendations for seismic design of bridges[P4] it is also recommended that the following design material strengths be adopted:

$$\textbf{\textit{Concrete:}} f'_{ce} = 1.3f'_c \qquad (4.23a)$$
$$\textbf{\textit{Steel:}} \quad f_{ye} = 1.1f_y \qquad (4.23b)$$

In Eq.(4.23) f'_{ce} and f_{ye} are low estimates of expected strength. The value for f_{ye} is felt to be appropriate for both reinforcing and structural steel. The concrete strength acknowledges the influence of conservative batching practice (average 28-day compression strength is typically 20% above the specified value), and the increase in strength after 28 days before the structure is subjected to the design loading, which will certainly occur later than 28 days.

As is discussed in Section 4.5, it will also be necessary to obtain estimates of maximum feasible strength in plastic hinges, for capacity design calculations, using upper-bound material strengths. The following values are recommended:

$$\textbf{\textit{Concrete:}} f'_{co} = 1.7f'_c \qquad (4.24a)$$
$$\textbf{\textit{Steel:}} \quad f_{yo} = 1.3f_y \qquad (4.24b)$$

4.2.7 Bilinear Idealization of Concrete Moment-Curvature Curves

For design purposes, it is generally of sufficient accuracy to use a bilinear approximation to the moment-curvature response, consisting of an initial "elastic" branch, and a post-yield "plastic" branch. For reinforced concrete and masonry sections, it is important that the elastic branch not be based on the initial uncracked section stiffness, as this value is only appropriate for very low levels of seismic response. The normal procedure is to use the secant stiffness from the origin through first yield as the effective elastic stiffness. First yield is defined as the point on the moment-curvature

response when the extreme tension reinforcement (i.e. the rebar furthest from the neutral axis) first attains yield strain, or when the extreme concrete compression fibre (again, at maximum distance from the neutral axis) attains a strain of 0.002, which ever occurs first. The moment and curvature at first yield are denoted M_y and ϕ'_y respectively. This line defining the elastic stiffness is extrapolated up to the nominal moment capacity, which is defined by an extreme fibre compression strain of 0.004 or an extreme tension reinforcing bar strain of 0.015, which ever occurs first. The corresponding curvature is termed the nominal yield curvature ϕ_y.

The plastic branch is defined by connecting the nominal yield point (M_N, ϕ_y) to the ultimate condition: M_u, ϕ_u.

This procedure is illustrated for a rectangular column section in Fig. 4.6, where the full moment-curvature relationship is shown in Fig.4.6(a), and the initial portion is shown in Fig.4.6(b) to expand the elastic branch. From Fig. 4.6(b) it is seen that the nominal yield curvature is defined as:

$$\phi_y = \frac{M_N}{M_y}\phi'_y \qquad (4.25)$$

The elastic stiffness is the slope of the initial branch. That is:

$$EI_{el} = \frac{M_y}{\phi'_y} = \frac{M_N}{\phi_y} \qquad (4.26)$$

and the stiffness of the plastic branch is given by:

$$EI_{pl} = \frac{M_u - M_N}{\phi_u - \phi_y} \qquad (4.27)$$

The column represented in Fig. 4.6 had a square section, 800×800mm (31.5×31.5 in), had a longitudinal reinforcement ratio of 1.88%, and a transverse reinforcement area ratio of 0.436% (equivalent to a volumetric ratio of 0.872%). Material properties were f'_c = 30MPa (4350 psi), $f_y = f_{yh}$ = 425 MPa (61,600 psi), and axial load = 2MN (450 kips).

In Fig. 4.6(b), the cracking moment M_{cr} and curvature ϕ_{cr} have also been identified. For reasons elaborated above in section 4.2.1 these have been based on the assumption of zero tension strength for the concrete. Note that the elastic stiffness defined by Eq.(4.26) is only about 40% of the initial stiffness of the un-cracked section.
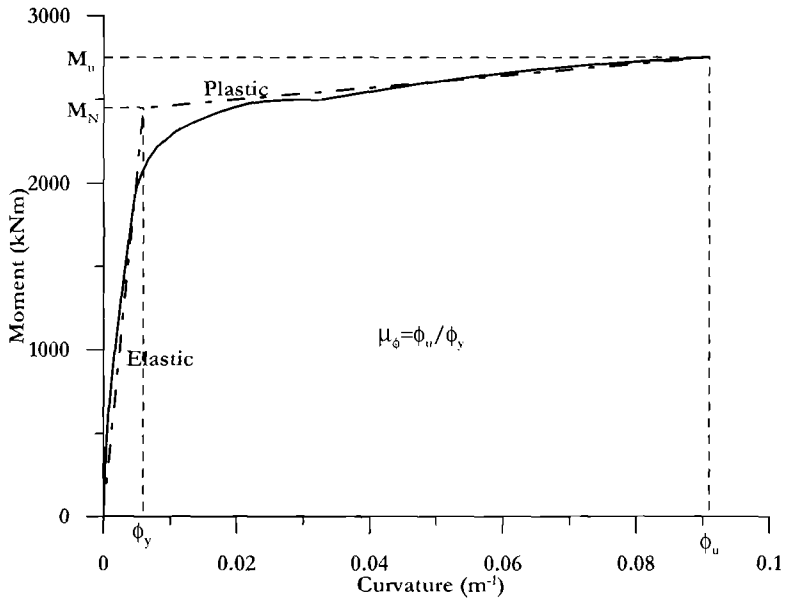
(a) Full Moment-curvature response
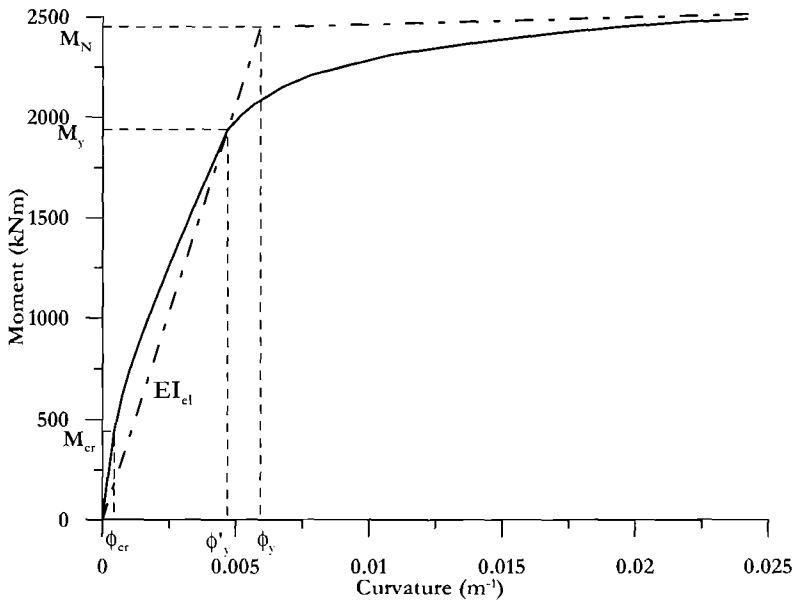
(b) Initial section Of Moment-Curvature Response

Fig.4.6   Example Moment-Curvature Curve for an 800×800 mm (31.5×31.5 in) Column Section

4.2.8 Force-Displacement Response from Moment-Curvature

(a) Structure   (b) Moments   (c) Curvature   (d) Displacement
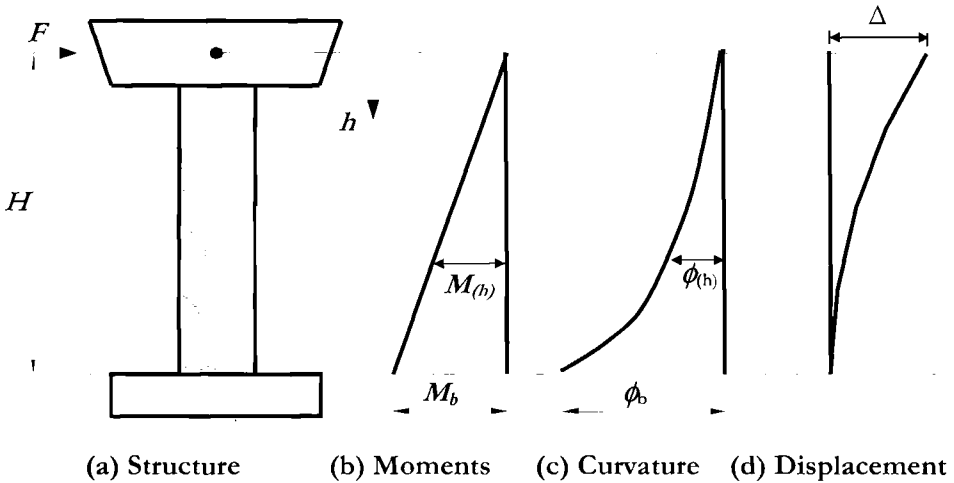
Fig.4.7 Obtaining Displacements from Curvature Distributions

Figure 4.7 illustrates what might appear to be the obvious method for obtaining the displacement at the top of a simple bridge pier subjected to a specified lateral force F, from the moment-curvature relationship, and to hence build the force-displacement response. The procedure, though related to a bridge pier for simplicity, is general for columns and walls, and can be easily adapted to develop force-rotation response, which may be more general for (say) beam members. Using the nomenclature of Fig.4.7, and measuring the distance h down from the line of application of the inertia force, the moment at h, and at the base ($h = H$) will be given by:

$$M_{(h)} = F \cdot h; \quad \text{and} \quad M_b = F \cdot H \tag{4.28}$$

The curvatures at all heights h could then be read from the moment-curvature relationship to produce the curvature distribution $\phi_{(h)}$ shown in Fig. 4.7(c), which could be integrated to provide the top displacement, Δ, as:

$$\Delta = \int_0^H \phi_{(h)} h.dh \tag{4.29}$$

Repeating this process for values of $0 \leq F \leq M_u/H$ would then be expected to provide the full force-displacement response.

Unfortunately this process does not produce force-displacement predictions that agree well with experimental results. There are a number of reasons for this:

- Tension shift is ignored. As shown in Fig.4.7(a), the influence of shear force is likely to incline the flexural cracks from the horizontal orientation appropriate for pure flexure. The result is that the "plane-sections" hypothesis is incorrect, and reinforcement tension strains at a given level will be higher than predicted from the moment at that section[P1]. Thus a simple integration of the theoretical curvature distribution is an approximation.

- The approach ignores shear deformation, though this can be separately added to the displacement response (see Section 4.8, e.g.).

- Anchorage deformation (strain-penetration) is ignored. Equation (4.29) implies that the curvature drops to zero immediately below the column base (or, for a beam, at the column face). In fact, strains of the tension reinforcement will only drop to zero at a depth equal to the true development length of the reinforcement. This implies a partial pullout of the bar at the column base section, which can be estimated by integrating the reinforcement strain profile below the base. On the other side of the column, the concrete compression strains will also not immediately drop to zero at the base, but will gradually dissipate with depth. The reinforcement tension strain effect is more important, and it is useful to define a "strain penetration" length L_{SP}, over which the curvature may be considered constant and equal to the column base curvature.

- In some cases the moment-curvature response will exhibit negative stiffness; that is, the moment will decrease as the curvature increases. This will generally be the result of reduced effective section size caused by spalling of cover concrete. Attempting to integrate the curvature distribution in accordance with Eq.(4.29) will result in only one section (the base) of infinitesimal length, being subjected to increased curvature as the moment drops. All other sections will not have reached the peak moment, and hence will presumably have a reduction of curvature. Strict application of Eq.(4.29) would then result in the ultimate displacement being obtained as soon as the critical section reached the peak moment. This does not accord with observations that the displacement continues to increase as the moment decreases.

The solution to these problems is to use a simplified approach based on the concept of a "plastic hinge", of length L_P, over which strain and curvature are considered to be equal to the maximum value at the column base. The plastic hinge length incorporates the strain penetration length L_{SP} as shown in Fig.4.8. Further, the curvature distribution higher up the column is assumed to be linear, in accordance with the bilinear approximation to the moment-curvature response. This tends to compensate for the increase in displacement resulting from tension shift, and, at least partially, for shear deformation.

The strain penetration length, L_{SP} may be taken as:

$$L_{SP} = 0.022 f_{ye} d_{bl} \ (f_{ye} \text{ in MPa}); \quad L_{SP} = 0.15 f_{ye} d_{bl} \ (f_{ye} \text{ in ksi}) \qquad (4.30)$$
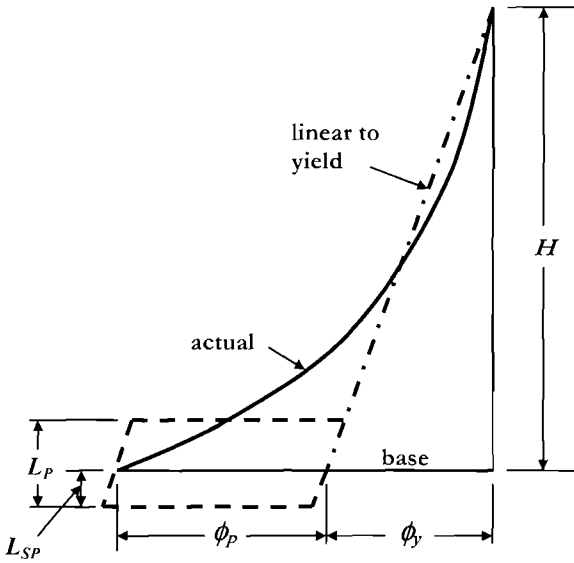
Fig.4.8   Idealization of Curvature Distribution

where f_{ye} and d_{bl} are the yield strength and diameter of the longitudinal reinforcement, and the plastic hinge length, L_P, for beams and columns, is given by:

$$L_P = kL_C + L_{SP} \geq 2L_{SP} \qquad (4.31a)$$

where

$$k = 0.2\left(\frac{f_u}{f_y} - 1\right) \leq 0.08 \qquad (4.31b)$$

and where L_C is the length from the critical section to the point of contraflexure in the member. Equation (4.31b) emphasises the importance of the ratio of ultimate tensile strength to yield strength of the flexural reinforcement. If this value is high, plastic deformations spread away from the critical section as the reinforcement at the critical section strain-hardens, increasing the plastic hinge length. If the reinforcing steel has a low ratio of ultimate to yield strength, plasticity concentrates close to the critical section, resulting in a short plastic hinge length. A modification of Eq.(4.31) for walls is suggested in Section 6.2.1(b).

In Figs. 4.7 and 4.8, $L_C = H$. The lower limit of $L_P = 2L_{SP}$ implies strain penetration both down into the foundation, and also up into the column, and applies when L_C is short. The force displacement response, for the cantilever column of Fig.4.7 can then be assembled from the moment-curvature response using the following equations:

$$F = M / H \tag{4.32}$$

$$\Delta_y = \phi_y \left(H + L_{SP} \right)^2 / 3 \tag{4.33}$$

$$\Delta_u = \Delta_y + \Delta_p = \Delta_y + \phi_p L_p H = \Delta_y + \left(\phi_u - \phi_y \right) L_P H \tag{4.34}$$

Equation (4.34) implies that the centre of plastic rotation occurs at the member end. This will be exact when $L_P = 2L_{SP}$, and is an acceptable approximation in all cases. However, when $0.08L_C \ge L_{SP}$, an improved estimate of the plastic displacement can be obtained by replacing H in Eq.(4.34) by the distance from the centre of the plastic hinge to the point of contraflexure for members in single bending, and by the centre to centre distance of plastic hinges at member ends for members in double bending.
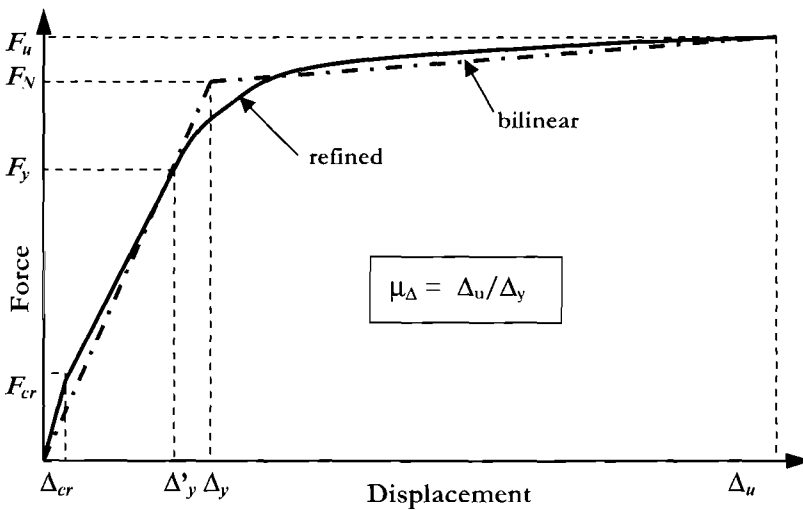
Fig.4.9   Force-Displacement Response

The resulting bilinear force-displacement response is shown as the dash-dot line in Fig.4.9. This is normally adequate for design purposes. However, a more accurate representation is possible, as shown by the solid line in Fig.4.9. In this "refined" approach, suitable for prediction of experimental response, the elastic portion is represented by a bilinear characteristic, with the cracking force and displacement at the corner, joined to the force and displacement at first yield. Above first yield, the displacement is based on the effective plastic curvature related to the first-yield curvature, and taking into account the increased strength. Thus:

Cracking: $\Delta_{cr} = \phi_{cr} H^2 / 3$, $F_{cr} = M_{cr} / H$ $\qquad$ (4.35)

First Yield: $\Delta'_y = \phi'_y \left(H + L_{SP} \right)^2 / 3$; $F_y = M_y / H$ $\qquad$ (4.36)

After Yield: $\Delta = \Delta'_y \dfrac{M}{M_y} + \left(\phi - \phi'_y \dfrac{M}{M_y} \right) L_P H$; $F = M / H$ $\qquad$ (4.37)

Again the accuracy can be improved by replacing H in Eq.(4.37) by the distance from the centre of the plastic hinge length to the point of contraflexure.

In both bilinear and refined representations, the displacement ductility capacity is related to the nominal yield displacement (Eq.(4.33):

$$\mu_\Delta = \Delta_u / \Delta_y \qquad (4.38)$$

4.2.9   Computer Program for Moment-Curvature and Force-Displacement

The CD provided with this book includes a computer program, CUMBIA[M14], for moment-curvature and force-displacement analysis of reinforced concrete members of circular or square section, based on the principles and equations outlined in the previous sections. A manual for operating the program is also provided.

4.3   FORCE-DISPLACEMENT RESPONSE OF STEEL MEMBERS

As noted earlier, it will rarely be necessary to carry out moment-curvature analyses of steel sections, since the elastic stiffness is unaffected by cracking, and the yield moment and plastic moment can be readily calculated. However, it should be emphasised that in calculating the plastic moment capacity, strain-hardening should be considered, and the level of maximum useable compression strain should be restricted to about 0.02 to avoid local buckling of flanges etc. The principles developed above for moment-curvature and force-displacement analysis of concrete sections can of course be equally applied to steel sections. This may be advisable when unsymmetrical sections are considered.

4.4   ELASTIC STIFFNESS OF CRACKED CONCRETE SECTIONS

It was mentioned in Chapter 1 that, contrary to common assumptions made in force-based seismic design, the elastic stiffness of cracked concrete sections is essentially proportional to strength, and the concept of a constant yield curvature independent of strength is both valid, and important in terms of direct displacement-base design. A summary of the research leading to these statements, and to Fig.1.4 is included below. A more complete presentation is available in [P3]. The research is based on moment-curvature analysis of different concrete sections, and the bilinear representation described in Section 4.2.7. It has been verified in numerous experiments[P4].

4.4.1 Circular Concrete Columns

Circular reinforced concrete columns are the most common lateral force-resisting elements for bridges in seismic regions[P4]. In order to investigate the effective stiffness of circular columns, a parameter analysis was carried out varying the axial load ratio and flexural reinforcement ratio for a typical bridge column. The following basic data were assumed:

- Column diameter D = 2m (78.7 in)
- Cover to flexural reinforcement   = 50 mm (2 in)
- Concrete compression strength f'_{ce} = 35 MPa   (5.08 ksi)
- Flexural reinforcement diameter d_{bl} = 40 mm   (1.575 in)
- Transverse reinforcement: spirals   = 20mm (0.79in) at 100mm (4in) spacing
- Steel yield strength f_{ye} = 450 MPa (65.3 ksi)
- Axial load ratio $N_u/f'_{ce}A_g$ = 0 to 0.4   (9 levels)
- Flexural reinforcement Ratio ρ_l/A_g = 0.005 to 0.04 (5 levels)

A selection of the moment-curvature curves resulting from analysis with the program CUMBIA provided on the attached CD is shown in Fig.4.10 for two levels of flexural reinforcement ratio, and a range of axial load ratios. Only the initial part of the moment-curvature curves has been included, to enable the region up to, and immediately after yield to be clearly differentiated. Also shown in Fig. 4.10 are the calculated bilinear approximations for each of the curves. Note that the apparent over-estimation by the bilinear representations of the actual curves is a function of the restricted range of curvature plotted, and is resolved when the full curve is plotted. It will be seen that the moment capacity is strongly influence by the axial load ratio, and also by the amount of reinforcement. However, the yield curvature of the equivalent bilinear representation of the moment-curvature curves does not appear to vary much between the curves.

Data from the full set of analyses for nominal moment capacity, and equivalent bilinear yield curvature are plotted in dimensionless form in Fig.4.11. The dimensionless nominal moment capacity and dimensionless yield curvature are respectively defined as

$$M_{DN} = \frac{M_N}{f'_{ce} D^3} \tag{4.39}$$

and

$$\phi_{Dy} = \phi_y D / \varepsilon_y \tag{4.40}$$

where $\varepsilon_y = f_{ye}/E_s$ is the flexural reinforcing steel yield strain.

The influence of both axial load ratio and reinforcement ratio on the nominal moment capacity is, as expected, substantial in Fig. 4.11(a), with an eight-fold range between maximum and minimum values. On the other hand, it is seen that the dimensionless yield curvature is comparatively insensitive to variations in axial load or reinforcement ratio.
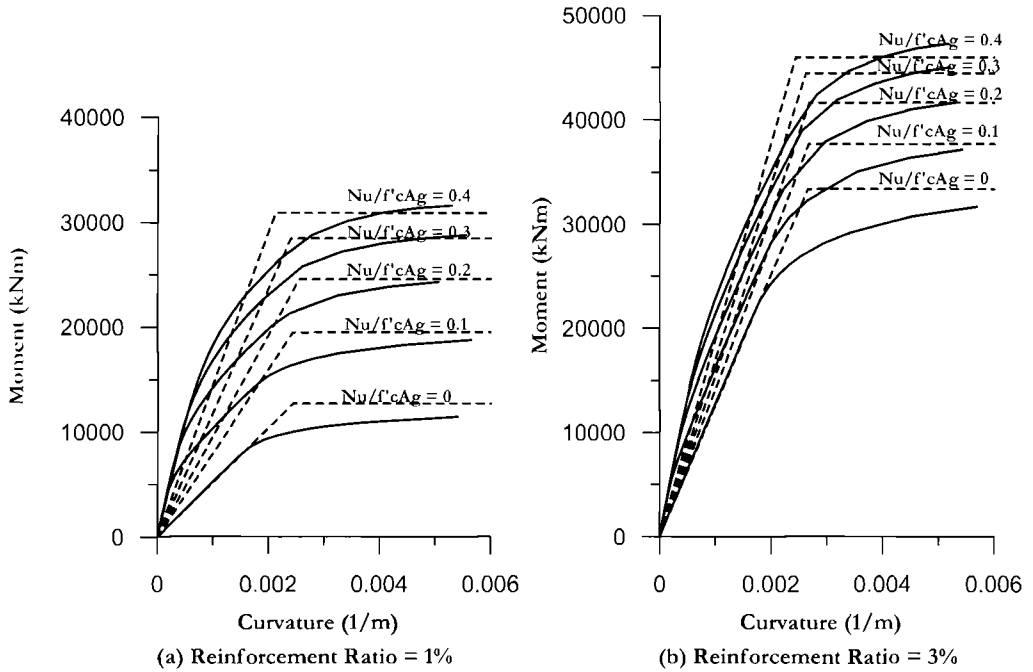
Fig.4.10 Selected Moment-Curvature Curves for Circular Bridge Columns
$(D = 2m; f'_{ce} = 35 \text{ MPa}; f_{ye} = 450 \text{ MPa})$[P3]
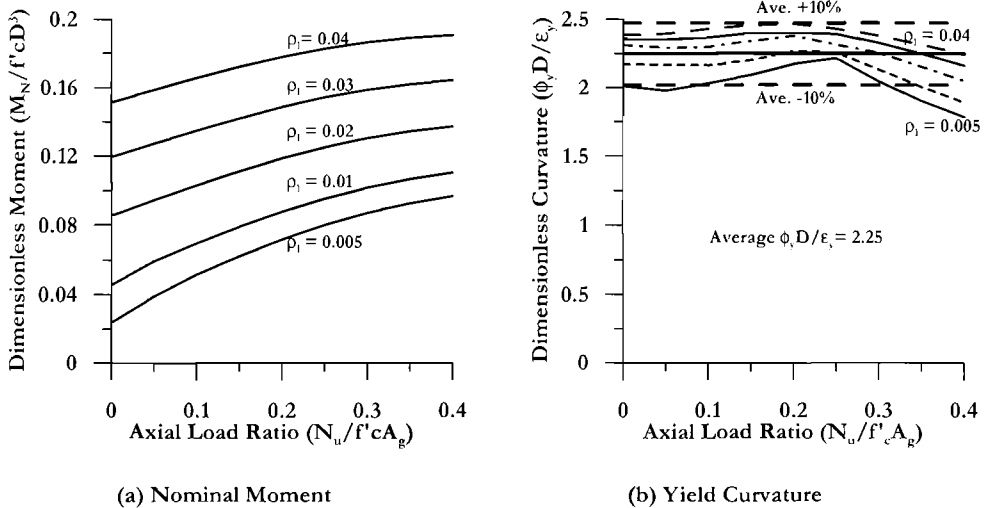
Fig.4.11 Dimensionless Nominal Moment and Yield Curvature for
Circular Bridge Columns[P3]

Thus the yield curvature is insensitive to the moment capacity. The average value of dimensionless curvature of ϕ_{Dy} = 2.25 is plotted on Fig 4.11(b), together with lines at 10% above and 10% below the average. It is seen that all data except those for low reinforcement ratio coupled with very high axial load ratio fall within the ±10% limits.

It should be noted that though the data were generated from a specific column size and material strengths, the dimensionless results can be expected to apply, with only insignificant errors, to other column sizes and material strengths within the normal range expected for standard design. The results would not, however apply to very high material strengths (say f'_c>50MPa (7.25ksi), or f_y>600MPa (87ksi)) due to variations in stress-strain characteristics.

The data in Figs. 4.10 and 4.11 can be used to determine the effective stiffness of the columns as a function of axial load ratio and reinforcement ratio, using Eq. (4.26). The ratio of effective stiffness to initial uncracked section stiffness is thus given by

$$\frac{EI_{eff}}{EI_{gross}} = \frac{M_N}{\phi_y EI_{gross}} \tag{4.41}$$

Results are shown in Fig. 4.12 for the ranges of axial load and reinforcement ratio considered. It will be seen that the effective elastic stiffness ratio varies between 0.13 and 0.91. For the most common values of the variables, however, the ratio will be between 0.3 and 0.7.
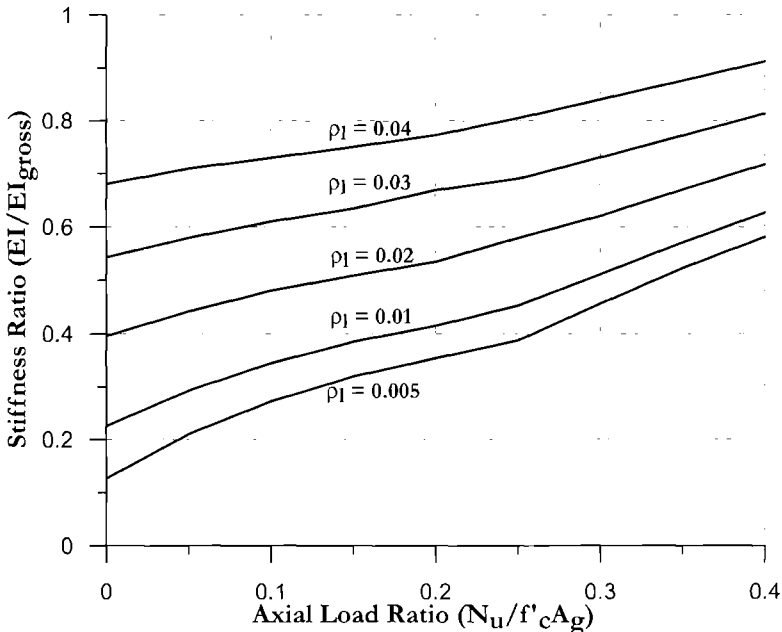
Fig.4.12 Effective Stiffness Ratio for Circular Bridge Columns[P3]

It should be noted that for convenience in computing the stiffness ratios of Fig 4.12, the gross stiffness of the uncracked section has been calculated without including the stiffening effect of the flexural reinforcing steel. That is

$$I_{gross} = \frac{\pi D^4}{64}$$ (4.42)

Since the reinforcement increases the uncracked section moment of inertia by as much as 60% for the maximum steel ratio of 4%, the stiffness ratios related to true un-cracked sections would be lower, particularly for the higher reinforcement ratios. The value of the concrete modulus of elasticity used in computing Fig. 4.12 was

$$E = 5000\sqrt{f'_c} \quad \text{(MPa)}; \qquad E = 60000\sqrt{f'_c} \quad \text{(psi)}$$ (4.43)

4.4.2 Rectangular Concrete Columns

Ductile rectangular columns can occur in bridge design, and at the base level of multi-storey frame buildings. For the purposes of this study the special case of a square column with flexural reinforcement evenly distributed around the perimeter was investigated. The following basic data were assumed:

- Column dimensions $b = h = 1.6$ m   (63.5 in)
- Cover to flexural reinforcement   = 50mm (2 in)
- Concrete compression strength $f'_{ce} = 35$ MPa (5.08 ksi)
- Flexural reinforcement diameter   = 32 mm (1.26 in)
- Transverse reinforcement: hoops   = 20mm dia. (0.79in) /5 legs per layer
- Steel yield strength $f_{ye} = 450$ MPa (65.3 ksi)
- Axial load ratio $N_u/f'_{ce}A_g = 0$ to 0.4 (9 levels)
- Flexural reinforcement ratio $\rho_l/A_g = 0.005$ to 0.04 (5 levels)

Moment-curvature trends predicted by CUMBIA for the rectangular sections followed the same trends apparent for circular columns[P3].

Data from the full set of analyses for nominal moment capacity, and equivalent bilinear yield curvature are plotted in dimensionless form in Fig.4.13. The dimensionless nominal moment capacity, and dimensionless yield curvature are respectively defined as:

$$M_{DN} = \frac{M_N}{f'_c bh^2}$$ (4.44)

and

$$\phi_{Dy} = \phi_y h / \varepsilon_y$$ (4.45)

(a) Nominal Moment   (b) Yield Curvature
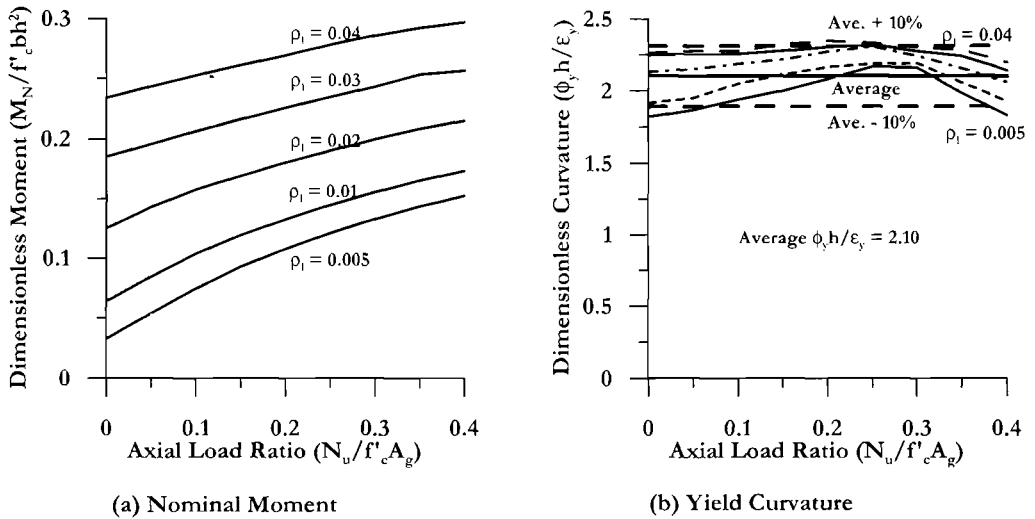
Fig. 4.13   Dimensionless Nominal Moment and Yield Curvature for Large Rectangular Columns[P3]

where b and h are the column width and depth respectively.

Trends for the rectangular columns, apparent in Fig.4.13, are similar to those displayed in Fig.4.11 for circular columns. Nominal moment capacity is strongly dependent on both axial load ratio and reinforcement ratio, with approximately an eight-fold increase in moment capacity from minimum axial load and reinforcement ratio to maximum axial load and reinforcement ratio. Dimensionless yield curvature is only weakly dependent on axial load ratio and reinforcement ratio, thus implying that the yield curvature is insensitive to the nominal moment capacity. The average value of dimensionless curvature of ϕ_{Dy} =2.10 is plotted on Fig.4.13(b), together with lines at 10% above and 10% below the average.   It is seen that all data except those for ρ_l =0.005 at both low and high axial load ratio fall within the +/- 10% limits of the average value.

As with the circular columns, the dimensionless results of Fig.4.13 can be expected to apply to other column sizes and material strengths within the normal range of material strengths.   Small errors can be expected for small column dimensions, where the ratio of cover to core dimensions will be significantly larger than for the data presented here. As with the circular column data, results should not be applied to rectangular columns with very high strength concrete or reinforcing steel.

The data of Figs.4.13 have been used to develop curves for the effective section stiffness ratio, based on Eq.(4.41). Results are presented in Fig.4.14. For ease of application of the results, the stiffness of the gross uncracked section was computed ignoring the stiffening effect of flexural reinforcement as, $I_{gross} = bh^3/12$, with the modulus of elasticity given by Eq.(4.43).
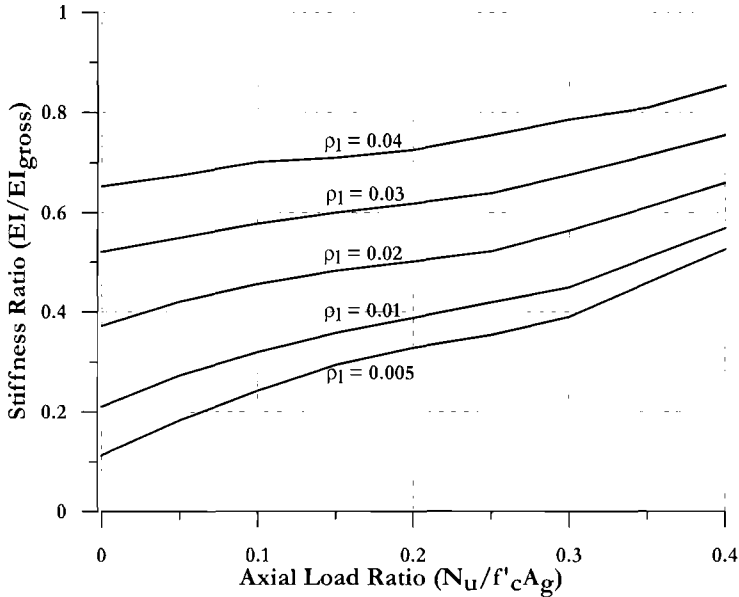
Fig.4.14   Effective Stiffness Ratio for Large Rectangular Columns[P3]

The range of effective stiffness calculated in accordance with Eq.(4.41) is from 0.12 to 0.86 times the gross section stiffness, indicating the strong dependence of effective stiffness on axial load ratio and reinforcement ratio. Clearly the common assumption of a constant section stiffness independent of flexural strength is entirely inappropriate.

Results from Fig.4.14 can be applied to other column sizes than those used to generate the graph by appropriate substitution of section dimensions into Eq.(4.41).

4.4.3   Walls

(a)   Rectangular Concrete Walls: Similar calculations to those reported in the previous two sections can also be carried out for rectangular structural walls, and have been fully presented elsewhere for both concrete and masonry walls[P21,A7]. Analyses for concrete walls considered two separate cases – one where the flexural reinforcement was distributed uniformly along the wall length, and the second, more common case where most of the flexural reinforcement was concentrated at the wall ends, with a comparatively light amount of reinforcement distributed along the wall length. It is emphasized that though the latter is the more common case, this is largely because of the misconception that concentrating the flexural reinforcement at the wall ends increases the flexural capacity when compared with the same total amount of reinforcement distributed uniformly along the wall length. In fact, the flexural strength associated with the two distributions will be very similar, as simple trial calculations will show.

Results are presented in Fig.4.15 for the dimensionless yield curvature for walls with different axial load ratios and reinforcement ratios, in similar fashion to the above analyses for columns. However, lower ranges of axial load ratio (with a maximum of $N_u/f'_{ce}A_g$= 0.125), and reinforcement ratio (with a maximum of ρ_l = 0.02) were adopted since these were considered to be practical upper limits for structural walls. Two different conditions were considered. In the first, a reinforcement ratio of 0.005 was considered to be uniformly distributed along the wall length, with the remainder concentrated near the wall ends. In the second case the full amount of reinforcement was uniformly distributed. In Fig.4.15 the yield curvature has been made dimensionless by multiplying by the wall length l_w, and dividing by the yield strain ε_y of the flexural reinforcement, in similar fashion to columns.

Average values of dimensionless curvature of ϕ_{Dy} =1.85 and 2.15 for concentrated and distributed rebar are plotted in Figs.4.15 (a) and (b) respectively. An average value of

$$\phi_{Dy} = \phi_y l_w / \varepsilon_y = 2.0 \quad \pm 15\% \tag{4.46}$$

essentially covers all data from the concentrated and distributed analyses. We recommend that this is sufficiently accurate to be used for design of all rectangular walls.
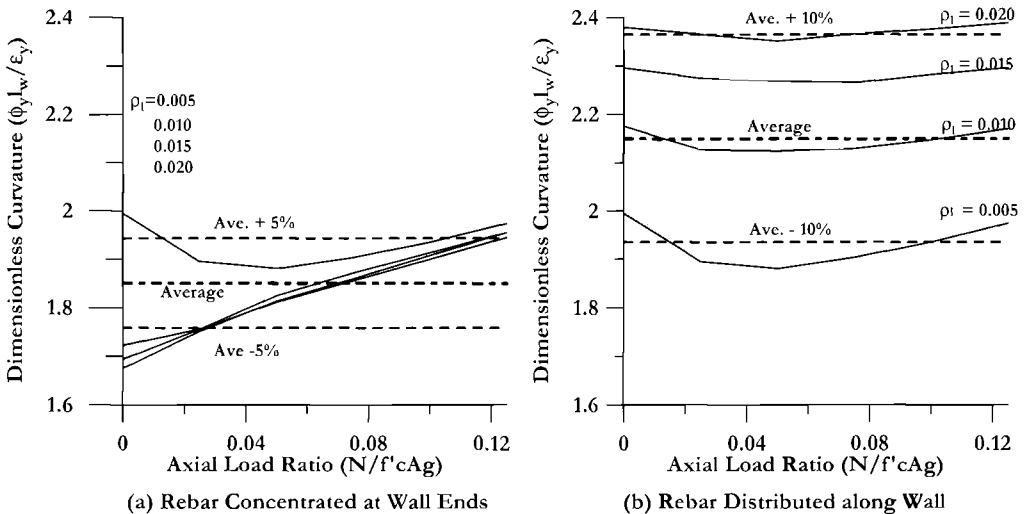
Fig.4.15 Dimensionless Yield Curvature for Rectangular Walls

Analyses where all the flexural reinforcement was distributed uniformly along the wall length resulted in an average dimensionless curvature approximately 10% higher than given by Eq.(4.46), with about twice the scatter of Fig.4.15[P21]. The effective stiffness for rectangular walls can thus be calculated, as a fraction of gross wall stiffness as

$$EI / EI_{gross} = \frac{M_N}{\left(\phi_{Dy}\varepsilon_y / l_w\right)} \cdot \frac{1}{E\left(tl_w^3 / 12\right)} \tag{4.47}$$

where t is the wall width, and M_N is the calculated nominal flexural strength. Typical values are about 0.2 to 0.3. In Eq. (4.47), ϕ_{Dy} may be taken from Eq. (4.46) for all walls or the more accurate averages from the analyses of the walls with concentrated or distributed reinforcement may be adopted.

(b) Rectangular Masonry Walls: Similar analyses to those described above have been carried out for masonry walls[A7]. The coefficient for the dimensionless curvature defined by Eq.(4.46) was found to vary between 2.06 for unconfined concrete masonry with uniformly distributed flexural reinforcement to 2.17 for confined clay or concrete masonry, also with distributed flexural reinforcement. It is recommended that an average value of 2.10 be used in all cases.

(c) Flanged Walls: Paulay[P27] has investigated the dimensionless yield curvature for different sections, including flanged concrete structural walls. For I-section and T-section walls with the flange in compression, he recommends dimensionless curvature coefficients (Eq.(4.46)) of 1.4. Paulay's values for rectangular walls are on average about 10% below the values established above. The main reason for this difference appears to be some simplifying assumptions made by Paulay, including ignoring the effects of strain-hardening of the flexural reinforcement, which is included in our analyses. Spot comparisons for flanged walls indicate a similar influence of strain-hardening, and we therefore recommend a coefficient of 1.5 for flanged walls where the flange is in compression. Note that for T-section walls with the flange in tension, or I-section walls loaded perpendicular to the web, the higher values defined in Section 4.4.3(a) above are recommended.

4.4.4 Flanged Reinforced Concrete Beams

Similar studies have been carried out to investigate the influence of flexural reinforcement ratio on the stiffness of flanged beams. These were based on the section shown in Fig. 4.16, and have been fully reported elsewhere[P3,P22]. The appropriate value for the stiffness of a beam in a building frame under seismic action will be the average of the values applicable for positive and negative bending, as a result of the moment reversal along the beam length. As with columns and walls, it was found that the flexural strength and stiffness increased essentially proportionately as the reinforcement content increased, and that effective stiffness ratios (related to the gross section stiffness) varied between 0.17 and 0.44.

If strain-hardening is ignored, and based on the average of positive and negative bending, it was found that the dimensionless curvature could be written as
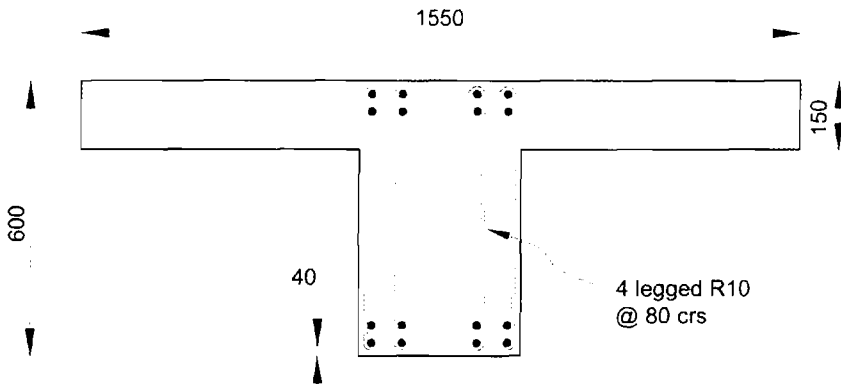
Fig.4.16 Reinforced Concrete Beam Section Analysed for Yield Curvature[P22]

$$\phi_{Dy} = \phi_y h_b / \varepsilon_y = 1.7 \pm 10\% \qquad\qquad (4.48a)$$

Including the effects of strain-hardening increased the dimensionless yield curvature to

$$\phi_{Dy} = \phi_y h_b / \varepsilon_y = 1.9 \pm 10\% \qquad\qquad (4.48b)$$

For rectangular-section beams rather than flanged beams, average values for dimensionless curvature were about 10% higher than given by Eq (4.48), and with somewhat increased scatter. It is thus clear that the concept of a constant dimensionless yield curvature for concrete beam sections is an adequate approximation.

4.4.5 Steel Beam and Column Sections

There is less need for studies on steel sections, of the type reported in the previous sections for concrete and masonry members, since the elastic section stiffness can be directly computed from the known section dimensions. However, at the start of the design process, the overall depth of the section may be approximately known, but the flange thickness, and hence the strength and stiffness of the section will be chosen after strength requirements have been computed. In force-based design, a trial and error approximation should be carried out to ensure assumed stiffness and final flexural strength are compatible. For direct displacement-based design, however, the initial yield curvature is of greater interest, as it defines the yield displacement, and hence the ductility demand, enabling the effective damping to be computed.

It will be readily appreciated that for a symmetrical structural steel section, of overall depth *h* the first-yield curvature will be given by:

$$\phi'_y = \frac{\varepsilon_y}{h/2} = 2\frac{\varepsilon_y}{h} \tag{4.49}$$

This curvature applies at the first-yield moment. For typical steel beam and column sections the nominal flexural strength will be only slightly higher than the yield moment (say $M_N \approx 1.1\ M_y$), and hence the effective yield curvature can be written as:

$$\phi_y = 2.2\frac{\varepsilon_y}{h} \tag{4.50}$$

It is of interest to note that this value is almost identical to concrete column sections reinforced with steel of the same yield strength.

4.4.6 Storey Yield Drift of Frames

The comparative invariance of dimensionless yield curvature of beams and columns indicates that storey yield drift of frames might similarly be essentially independent of reinforcement ratio and strength. Fig.4.17(a) shows a typical concrete beam/column subassemblage extending half a bay width either side of the joint, and half a storey height above and below the joint. This can be considered a characteristic element of a frame building. Since bay width will normally exceed storey height, and column curvatures will typically be less than beam curvatures as a consequence of capacity design procedures (see Section 5.8), beam flexibility is likely to be the major contributor to the deformation.

The deflected shape is shown in Fig.4.17(b). The yield drift θ_y can be expressed as

$$\theta_y = \theta_{by} + \theta_{jy} + 2\Delta_c / L_c + 2\Delta_s / L_c \tag{4.51}$$

where θ_{by} and θ_{jy} are the rotations of the joint centre due to beam flexure and joint shear deformation respectively, Δ_c is the flexural deformation of the column top relative to the tangent rotation at the joint centre, and Δ_s is the additional deformation of the column top due to shear deformation of beams and columns. To allow for strain penetration of longitudinal reinforcement into the joint region, it is assumed that the yield curvature in the beam develops at the joint centroid, and reduces linearly to zero at the beam midspan, as shown in Fig.4.17(c).

The yield drift due to beam flexure is thus:

$$\theta_{by} = \frac{\phi_y(0.5L_b)}{3} = \frac{\phi_y L_b}{6} \tag{4.52}$$

For a concrete frame, ignoring strain-hardening, and thus substituting from Eq.(4.48(a)):

$$\theta_{by} = 0.283\varepsilon_y \left[\frac{L_b}{h_b}\right] \tag{4.53}$$

Typical calculations based on a storey height/bay length ratio of 0.533 (storey height = 3.2m, bay length =6m) and a maximum column curvature of $0.75\phi_y$ indicate column displacement Δ_c will add about 40% to the yield drift in Eq. (4.51). It is further assumed, based on experience, that the joint deformation and member shear deformation add 25% and 10% respectively to the yield drift. As a consequence, the yield drift for a reinforced concrete frame may be estimated as

$$\theta_y = (1.0 + 0.4 + 0.25 + 0.1) \times 0.283\varepsilon_y \left[\frac{L_b}{h_b}\right]$$

$$= 0.5\varepsilon_y \left[\frac{L_b}{h_b}\right] \tag{4.54}$$

Equation (4.54) is compared in Fig.4.18 with the results from 46 beam/column test assemblages which included a wide range of possibly relevant parameters[P22], including

- Column height/beam length aspect ratio (H_c/L_b)   : $0.4 - 0.86$
- Concrete compression strength (f'_{ce})   : $22.5 - 88$MPa ($3.3 - 12.8$ksi)
- Beam reinforcing steel yield strength (f_{ye})   : $276 - 611$MPa ($40 - 89$ ksi)
- Maximum beam reinforcement ratio ($A'_s/b_w d$)   : $0.53\% - 3.9\%$
- Column axial load ratio ($N_u/f'_{ce}A_g$)   : $0 - 0.483$
- Beam aspect ratio (L_b/h_b)   : $4.4 - 12.6$

Test units with equal, and with unequal top and bottom reinforcement ratios were considered, as were units with and without slabs and/or transverse beams framing into the joint. Note that Eq.(4.54) only includes two of these parameters (beam reinforcement yield strength (which dictates the yield strain $\varepsilon_y = f_y/E_s$), and beam aspect ratio), on the assumption that the other parameters are not significant variables. As is apparent from Fig.4.18, the agreement between experimental drifts and predictions of Eq.(4.54) is reasonable over the full, and rather wide range of yield drifts. The average ratio of experiment to theory is 1.03 with a standard deviation of 0.16. Considering the wide range of parameters considered, the comparatively narrow scatter is rather satisfactory. Note that the two test units with experimental drifts of about 1.5% are thought to have suffered beam slip through the column joint region, resulting in excessive yield drift, but have been included in the averaging. The significance of different experimental parameters included in the list of variables noted above, to the theoretical/experimental drift ratio has been examined elsewhere[P3, P22]. In no case was the significance of any of the parameters not included in Eq.(4.54) found to be high enough to warrant inclusion in the design equation.
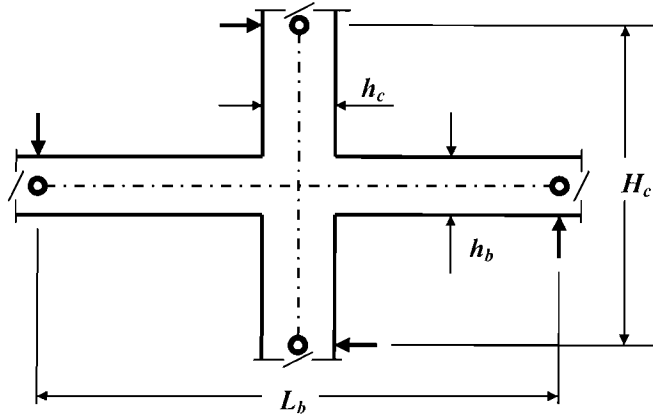
(a) Subassemblage Dimensions and Loading
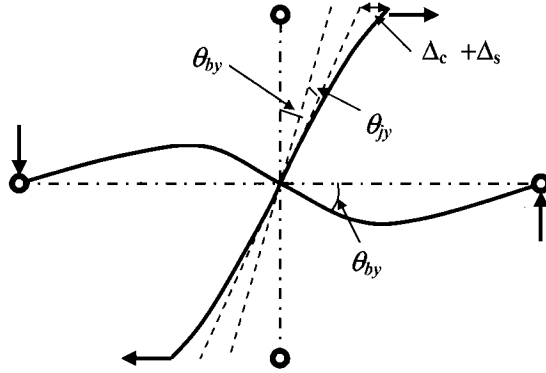
(b) Drift Components
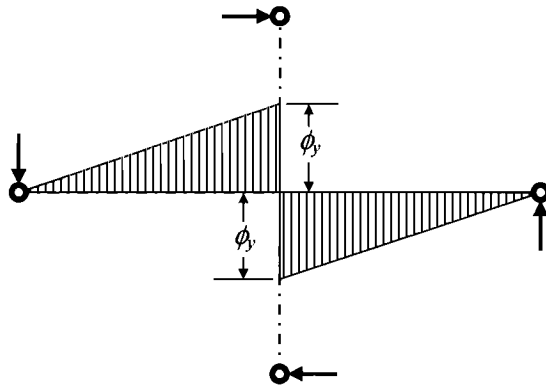
(c) Assumed Beam Curvature Distribution

Fig. 4.17 Elastic Deformation Components to Drift of a
Beam Column Subassemblage[P22]
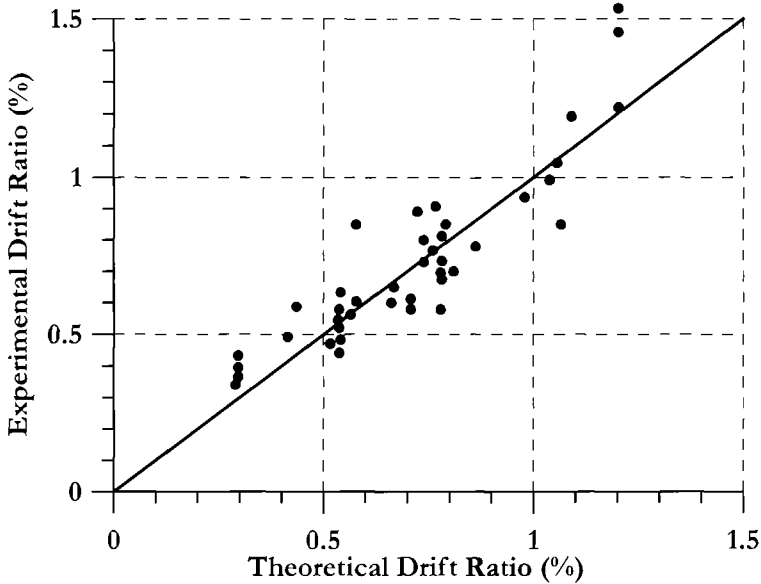
Fig. 4.18   Experimental Yield Drifts of Reinforced Concrete Beam/Column Test Units Compared with Predictions of Eq.(4.54)[P22]

It is evident that the procedure adopted above to estimate the yield drift of reinforced concrete frames can also be adapted to predict the yield drift of structural steel frames. Substituting from Eq.(4.50) into Eq.(4.52), the drift due to beam flexure will be:

$$\theta_{by} = 0.367\varepsilon_y \left[\frac{L_b}{h_b} \right]$$ (4.55)

and making the same assumptions about the percentage increase of yield drift from joint rotation, column flexure, and shear deformation, the following drift predictor results

$$\theta_y = 0.65\varepsilon_y \left[\frac{L_b}{h_b} \right]$$ (4.56)

That is, the yield drift for a structural steel frame is expected to about 30% higher than for a reinforced concrete frame with the same gross dimensions, and the same steel yield stress.   This equation has not, however, been checked against experimental results.

4.4.7   Summary of Yield Deformations.

From the moment-curvature analyses reported in the previous sections, it was found that stiffness and strength are effectively proportional, for a given structural member type and size, or structure type. The independent parameter, for stiffness calculations, is thus

the yield curvature, or yield displacement. The following yield curvatures are applicable for the "corner" of the equivalent bilinear approximation of force/deformation response:

- Circular column: $\qquad \phi_y = 2.25\varepsilon_y / D$ (4.57a)

- Rectangular column: $\qquad \phi_y = 2.10\varepsilon_y / h_c$ (4.57b)

- Rectangular concrete walls: $\qquad \phi_y = 2.00\varepsilon_y / l_w$ (4.57c)

- T-Section Beams: $\qquad \phi_y = 1.70\varepsilon_y / h_b$ (4.57d)

- Flanged concrete walls: $\qquad \phi_y = 1.50\varepsilon_y / l_w$ (4.57e)

- Rectangular masonry walls: $\qquad \phi_y = 2.10\varepsilon_y / l_w$ (4.57f)

The equation for flanged walls applies for I-section walls and for T-section walls when the flange is in compression. For reinforced concrete and structural steel frames, the yield drift can be expressed, with adequate accuracy as

Concrete frames: $\qquad \theta_y = 0.5\varepsilon_y \dfrac{L_b}{h_b}$ (4.58a)

Structural steel frames: $\qquad \theta_Y = 0.65\varepsilon_y \left[\dfrac{L_b}{h_b} \right]$ (4.58b)

4.5 ANALYSES RELATED TO CAPACITY DESIGN REQUIREMENTS

In Section 3.9, capacity design was introduced. The basic philosophy is that **DDBD** is used as a means to determine the required strength of locations where inelastic rotations (plastic hinges) are intended. To ensure that plastic hinges do not occur at other parts of the structure, and to ensure that undesirable modes of inelastic deformation, such as shear failure do not develop, the dependable strength of these locations and actions is set to be higher than the force levels at these locations, corresponding to the maximum feasible strength being developed at the plastic hinges. This is in recognition that in ductile design, it is the actual strength, rather than the conservative design strength, that will be developed in the design-level earthquake.

This premise is illustrated in Fig. 4.19, which examines the force-displacement response of a simple bridge pier under lateral seismic response. If the pier had very high strength, it could respond elastically to the inertia forces, and have the maximum displacement and force corresponding to point **A** in Fig.4.19(c). The design strength is however much lower, and if the actual strength exactly equalled the required strength, the expected maximum response is defined by point **B**. If the actual strength exceeds the design strength, then it will be this strength that is developed, unless the actual strength

exceeds that corresponding to point **A**. The response corresponding to actual strength is defined by point **C**. Note that the different strengths of **A** and **B** imply different stiffness.

(a) Structure   (b) Deflection   (c) Force-Displacement
                        Profile   Response
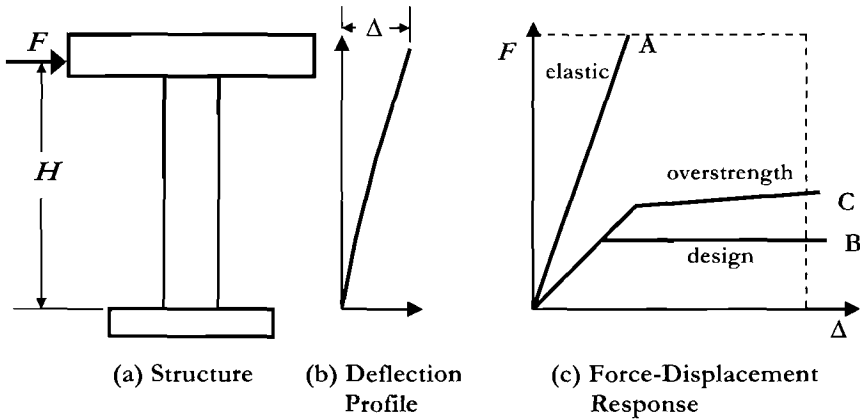
Fig.4.19   Strength Developed in Design Earthquake by a Simple SDOF Pier

There are a number of reasons why the actual flexural strength may exceed the design strength:

- Material strengths (e.g. concrete compression strength, steel yield strength) may exceed the nominal or characteristic values used in design.
- Dependable flexural strength may incorporate a strength reduction factor (or partial material factors).
- Strain-hardening of reinforcement or structural steel may not have been considered in determining the flexural capacity of the section.
- The section size or reinforcement content may exceed the exact values required to equal the required strength.

A section or action being capacity-protected would need to take these possible increases of the plastic hinge flexural strength into account, and be designed for the appropriate action in equilibrium with the enhanced strength of the plastic hinge. In addition to this, the basic design for the plastic hinges may be based on a **SDOF** estimate of response, as is the case with **DDBD**. Amplification of the action requiring capacity protection due to higher mode effects must also be taken into account.

The general requirement for capacity protection is defined by Eq.(3.61), which is reproduced here as Eq.(4.59) for convenience:

$$\phi_S S_D \geq S_R = \phi^o \omega S_E \tag{4.59}$$

where S_E is the value of the design action being capacity protected, corresponding to the design lateral force distribution found from the **DDBD** process, ϕ^o is the ratio of overstrength moment capacity to required capacity of the plastic hinges, ω is the

amplification of the action being considered, due to higher-mode effects, S_D is the design strength of the capacity protected action, and ϕ_S is a strength-reduction factor relating the dependable and design strengths of the action. Further background is given in Section 3.9.

With conventional design, the value of the overstrength factor ϕ^0 can be large, because of the reasons elaborated in the four bullets above. Since **DDBD** is based on the required strength at maximum displacement demand, with less conservative assumptions about material strengths and strength-reduction factors (see Section 4.2.6), lower overstrength factors are appropriate, reducing the cost of implementing capacity design. This is illustrated in the following example.

4.5.1 Design Example 4.1: Design and Overstrength of a Bridge Pier Based on Moment-Curvature Analysis

The simple circular bridge pier of Fig.4.19 has been designed by **DDBD** for a drift of 4%. The required lateral force at this drift is F = 2690kN (605kips). It is required to determine the longitudinal and transverse reinforcement requirements, and the expected maximum feasible overstrength in the plastic hinge. The following data are applicable:

Height H= 10m (32.8ft); column dia.= 1.8m (6ft); cover to long. rebar = 50mm (2in)
Long. rebar: d_{bl}=40mm (1.575in); f_y – 420MPa (60.9ksi); f_u = 630MPa (91.4ksi)
Trans.rebar: d_{bt} = 20mm (0.787in); f_y = 420MPa; f_u = 630MPa; ε_{su} =0.12
Concrete: f'_c = 30 MPa (4.35ksi).
Axial Load: N_u = 3.82MN (858kips) (= $0.05f'_cA_g$)

In accordance with the recommendations of Section 4.2.6 the following are the design strengths applied to seismic design:

Concrete: f'_{ce} = $1.3f'_c$ = 39 MPa (5.66ksi)
Long Rebar: f_{ye} = $1.1f_y$ = 462 MPa (67.0ksi) (ε_y = 462/200,000 =0.00231)
                      f_{ue} = $1.1f_u$ = 693 MPa (100.5ksi)
Trans Rebar: f_{yh} = $1.0f_y$ = 420 MPa (60.9ksi)

The following steps summarize the analysis process for section design.

Design Displacement: Δ_D = 0.04×10,000 = **400 mm (15.75in)**
Strain Penetration: From Eq.(4.30), L_{SP} =0.022$f_{ye}d_{bl}$=0.022×462×40=**406.5mm**
Yield Displacement: From Eq.(4.57a), the yield curvature is
      ϕ_y = $2.25\varepsilon_y/D$=2.25×0.00231/1.8=**0.00289/m** (73.4E-6/in)
Thus the yield displacement is Δ_y =$\phi_y(H+L_{SP})^2/3$=0.00289(10+0.407)^2/3=0.1043m
      i.e. Δ_y =**104.3mm (4.11 in)**

Plastic Hinge Length: From Eq.(4.31), k = 0.08 and hence L_P=$0.08H+L_{SP} \geq 2L_{SP}$
i.e. L_P = 0.08×10000+406.5 = **1206.5mm (47.5in)**
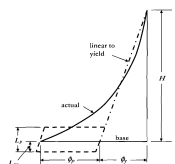
Fig.4.8 Idealization of Curvature Distribution

Plastic Curvature: Plastic displacement $\Delta_P = \Delta_D - \Delta_y$ = 400-104.3 =**295.7mm(11.6in)**
Hence, inverting Eq.(4.34): $\phi_P = \Delta_P/(L_P H)$ = 0.2957/(1.206×10) = **0.0245/m(622E-6/in)**

Design Curvature: $\phi_D = \phi_y + \phi_P$ = 0.00289+0.0245 = **0.0274/m (0.000696/in)**
Design Moment: M_D = 2690×10 = **26,900kNm (238,100 kip.in.)**

An initial section analysis is carried out using CUMBIA (see provided CD) with a typical volumetric ratio of transverse reinforcement of ρ_v = 0.006. Since $\rho_v = 4A_h/D$'s, this would result in a spacing of the hoops of
    s = 4×314/(1800-2×50+20)×0.006 = 122mm (4.80in).
This analysis results in a required flexural reinforcement area of **63,600mm² (98.6in²)** to provide the design moment at the design curvature. The analysis also indicates that the neutral axis depth, c, at the design curvature will be about **460mm (18.1in)**.

The required flexural reinforcement area corresponds to a longitudinal reinforcement ratio of: ρ_l = 63600/(0.785×1800²) = 0.025, which is within the practical range of 0.008 $\leq$ $\rho_l \leq$ 0.04, and requires 50.6 D40 bars. It is decided to use 52 bars to provide a whole number of bars in each quadrant.

Ultimate Compression strain: From the required design curvature and the neutral axis depth, the required ultimate compression strain is given by Eq.(4.4) as
    $\varepsilon_{cu} = \phi_D \cdot c$ = 0.0274×0.46 = 0.0126.

Transverse Reinforcement Ratio: Inverting Eq.(4.21):

$$\rho_v = \left(\varepsilon_{cu} - 0.004\right)\frac{f'_{cc}}{1.4 f_{yh}\varepsilon_{su}} \tag{4.60}$$

Solving Eq.(4.60) requires a knowledge of the confined compression strength of the concrete (f'_{cc}), which depends on the lateral confining pressure (Eq.(4.10)), which in turn depends on the transverse reinforcement ratio (Eq.(4.5)). Using the initial guess of ρ_v = 0.006, and substituting into Eq.(4.5): f_l = 0.5×0.006×420 = 1.26MPa. Substituting this value in Eq.(4.10):

$$f'_{cc} = 39\left(2.254\sqrt{1+\frac{7.94\times1.26}{39}} - 2\frac{1.26}{39} - 1.254\right) = 47.1 MPa(6.83ksi)$$

(Note that design aids for determining confined concrete compression strength are provided in Fig.10.9). With the calculated value, substituting into Eq.(4.60):

$$\rho_v = (0.0126 - 0.004)\cdot\frac{47.1}{1.4\times420\times0.12} = 0.00574$$

This is very close to the initial assumption of 0.006, and no further modification is required. The spacing of transverse reinforcement is thus set at **120mm (4.75in).**

Design Verification and Capacity Design Factors: A moment-curvature analysis is now run with the design longitudinal reinforcement of 52D40 bars (65,300mm²), and the transverse hoops of D20@120 crs. using the expected material strengths. The results are shown in Fig.4.20 by the line identified as "Design". At the design curvature of 0.0274/m the moment capacity is M_D = **27,200kNm (241,000 kip.in)**. This is 1.2% above the required design value.

Also shown in Fig.4.20 are two moment-curvature curves designated "Overstrength" **A** and **B**. Curve **A** corresponds to maximum feasible overstrength. For this case, f'_{co} =1.7f'_c = 51MPa (7.4ksi); f_{yo} = 1.3f = 546MPa (79.1ksi); and f_{yho} = 1.3f_{yh} = 546MPa (79.1ksi), in accordance with the recommendations of Section 4.2.4. At the design curvature of 0.0274, the moment capacity is **31,900kNm (283,000 kip.in)**, which is 18.7% higher than the design requirement. Thus the appropriate value of ϕ^0 to use in Eq. (4.59) is ϕ^0 = 1.187. This would be appropriate if it were used to determine required strength in other members of the bridge (say the superstructure). It would, however, be inconsistent to use this value of overstrength for determining the required shear strength of the column, since it is based on maximum feasible strengths of concrete and transverse reinforcement, whereas the shear capacity will use lower values. It is clear that the same values should be used for concrete strength and transverse reinforcement yield strength for both overstrength demand, and shear capacity since they apply to the same region of the structure.
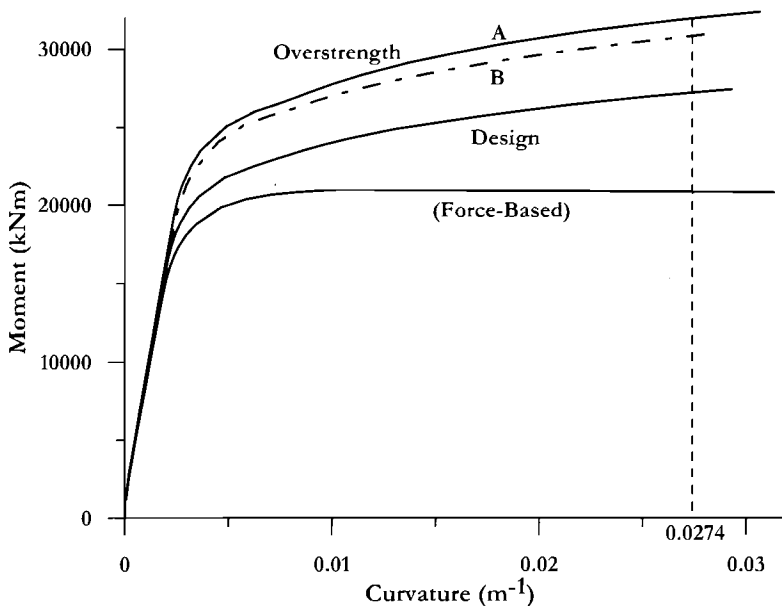
Fig.4.20 **Moment-Curvature Response for Example 4.1**

Accordingly, Fig. 4.20 shows a second overstrength curve (**B**), which is based on f'_{co} : f'_{ce} = 39MPa, and f_{yho} = f_{yh} =420 MPa, since these values should be used in estimating the shear capacity (see Section 4.7). It will be seen that this results in a rather small reduction in the overstrength moment capacity, and little inefficiency would result from using curve **A**. At the design curvature, the moment capacity of curve **B** is **30,840kNm (272,900 kip.in)**, which implies ϕ^0 = 1.146.

An additional curve, labelled "(Force-Based)" is included in Fig. 4.20. This is based on conventional force-based design assumptions that the minimum specified material strengths (f'_c, f_y, f_{yh}) should be used in design, and that strain-hardening of the flexural reinforcement should be ignored. The nominal capacity would be estimated at an extreme fibre compression strain of 0.003. For the material properties and reinforcement details used in the final design above, this would result in a nominal flexural strength of M_N = **20,400kNm (180,500 kip.in),** which is well below the required design strength. Using the same assumptions about material strengths, it would be necessary to increase the longitudinal reinforcement to 93,650 mm² (a 48% increase) to match the required strength. The resulting overstrength demand can be estimated by the ratio of the capacity of curve **A** to the nominal strength of the (Force-Based) curve, resulting in

$$\phi^0 = 31,943/20,800 = 1.536.$$

If a flexural strength reduction factor of ϕ_f = 0.9 were incorporated in the design, as is common practice in many codes, the overstrength factor would increase to ϕ^0 = 1.706. The extreme and unnecessary conservatism of current force-based design procedures is thus apparent in this example.

4.5.2 Default Overstrength Factors

For some simple structures the design effort involved in determining the required flexural overstrength factors for capacity design may be excessive. In these cases it would be permissible to use conservative default values for the overstrength factor ϕ^0. Provided the design is based on a strain-hardening model for the flexural reinforcement, it is recommended that the default value should be ϕ^0 = 1.25. If strain-hardening is ignored in determining required section properties, it is recommended that ϕ^0 = 1.6 be assumed.

4.5.3 Dynamic Amplification (Higher Mode Effects)

Dynamic Amplification due to higher mode response is dependent on the type of structure being designed. As such, it is separately dealt with in each of the special chapters devoted to different structural types. Note that in Ex. 4.1 there were no higher modes.

4.6 EQUILIBRIUM CONSIDERATIONS IN CAPACITY DESIGN

Equilibrium must be satisfied at all stages of design, whether design level or overstrength is considered. This is illustrated in Fig.4.21 for a simple portal frame

subjected to both gravity and seismic loading, at design and overstrength levels. It is assumed that the columns are ductile, and reach their capacity in both design and overstrength response, as discussed in Section 4.5. For simplicity the moment capacities at top and bottom of the columns are assumed to be identical.

(a) Design Moments and Forces   (b) Overstrength Moments and Forces
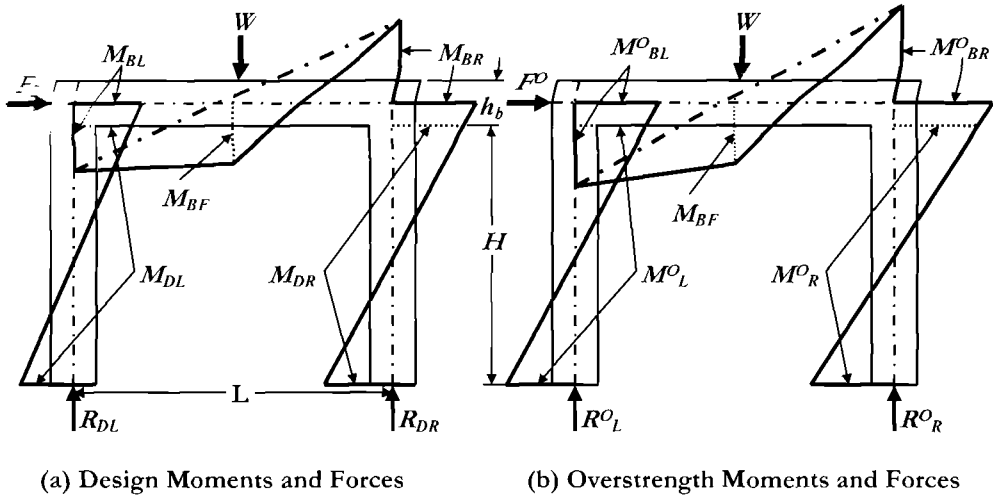
Fig.4.21 Equilibrium of Moments and Forces in a Portal Frame (moments drawn relative to member centrelines on tension side of member)

(a) Design-Level Response: The design lateral force F_D is in equilibrium with the sum of the shears in the two columns. The design moments in the columns form at the column base and at the soffit of the beam. Since the shear in the columns is the slope of the bending moment, the following equilibrium equation applies:

$$F_D = \frac{2M_{DL} + 2M_{DR}}{H} \tag{4.61}$$

where H is the clear height to the soffit of the beam, and M_{DL} and M_{DR} are the design moment capacities in the left and right columns respectively. Note that $M_{DL} \neq \mathbf{M_{DR}}$, since the axial forces in the two columns are different. Note also that gravity moments have no influence on the validity of Eq.(4.61), since the column **capacity** is developed regardless of the ratio of seismic and gravity moments in the columns.

To determine the moment capacities of the two columns, it is thus necessary to determine the axial forces in the columns.

Vertical force equilibrium requires that the axial forces in the columns must equal the beam shears at the beam/column joint centroids. To find the beam shears we first note that the beam and column moments must also be in equilibrium at the joint centroids,

and that the column moments at the joint centroids exceed the moments at the beam soffit:

$$M_{BL} = M_{DL} \frac{(0.5H + 0.5h_b)}{0.5H} = M_{DL}(H + h_b)/H \qquad (4.62a)$$

$$M_{BR} = M_{DR}(H + h_b)/H \qquad (4.62b)$$

Note that the gravity load moments resulting from the load **W** again have no influence on the moments at the joint, which are totally defined by the column moment capacities. The shear in the beam can be separated into the gravity load and seismic force components:

Gravity: $V_B = W/2$ \qquad (4.63a)

Seismic: $V_B = \dfrac{(M_{BL} + M_{BR})}{L}$ \qquad (4.63b)

The sign of the gravity-load shear changes at the two ends of the beam, while the seismic shear is constant. The reactions at the base of the columns (ignoring the column weights) are thus:

$$R_{DL} = \frac{W}{2} - \frac{(M_{BL} + M_{BR})}{L}; \quad R_{DR} = \frac{W}{2} + \frac{(M_{BL} + M_{BR})}{L} \qquad (4.64)$$

The moment capacities of the column hinges must be calculated with the appropriate value of the axial force, given by Eq.(4.64). This may involve iteration, though normally one or two cycles are sufficient. In the initial design phase, when the design force F_D is known, and the column design moments are required, it is useful to recall that the moment-axial force relationship is likely to be nearly linear over the range of axial force expected, and hence the required flexural reinforcement content (for a reinforced concrete design), can be found from the approximate combination:

$$M_D \cong F_D \cdot H/4; \quad N_u = R_{ave} = W/2 \qquad (4.65)$$

This should then be checked with a detailed analysis, using the relationships of Eq.(4.62) and (4.64).

(b)   Overstrength Response: The principles utilised in the previous section indicate that when the overstrength moment capacity is estimated at plastic hinge locations, the axial force should be adjusted to reflect the increased beam seismic shear resulting from the increased plastic hinge moment capacity of the columns. With respect to Fig. 4.21(b), the following relationships apply for seismic response force and seismic beam shear respectively:

$$F^O = \frac{2\left(M_L^O + M_R^O\right)}{H} \tag{4.66}$$

$$V_B^O = \frac{\left(M_L^O + M_R^O\right)\cdot\left(1 + h_b/H\right)}{L} \tag{4.67}$$

The seismic overstrength moment capacities, and the overstrength column shear demands for capacity design thus need to be determined in conjunction with the revised column axial forces:

$$R_L^O = W/2 - V_B^O; \qquad R_R^O = W/2 + V_B^O \tag{4.68}$$

Required shear strength for the columns is given directly from the overstrength moment distribution as:

$$V_L^O = 2M_L^O/H; \qquad V_R^O = 2M_R^O/H \tag{4.69}$$

and the beam maximum required shear strength, at the right end of the beam is

$$V_{BR}^O = V_B^O + W/2 \tag{4.70}$$

The principles applied in this section are simple fundamental requirements of equilibrium, and should be self-evident to all designers. Unfortunately we find that equilibrium is not afforded the same emphasis as (say) matrix analysis methods in engineering curricula, and have hence provided this rather basic treatment of the subject.

4.7 DEPENDABLE STRENGTH OF CAPACITY PROTECTED ACTIONS

The discussion on capacity protection has thus far concentrated on demand. Equation (4.59) requires that the dependable capacity of the capacity protected action, $\phi_S S_D$ is at least equal to the demand. Note that in this case the use of a strength reduction factor, ϕ_S is justified, since the consequence of the strength of the required action being less than that of the demand may be catastrophic. An example is the shear strength of a building or bridge column. Insufficient shear strength to cope with shears associated with flexural overstrength in plastic hinges could result in shear failure followed by reduction in capacity to support gravity loads to the extent that failure occurs.

4.7.1 Flexural Strength

Members where plastic hinges are not prescribed must have adequate flexural strength to ensure that unexpected plastic hinges do **not** occur. This is to ensure that undesirable

deformation modes such as soft-storey mechanisms in building frames do not develop. Aspects related to this are fully covered in [P1] and Section 5.2.3.

Determination of nominal flexural strength M_N is straightforward, and basic to all aspects of structural design, and again will not be further elaborated. However, we recommend that advanced section analyses, based on moment-curvature analyses, and including the effects of reinforcement strain-hardening be included in the design. Capacity should be based on nominal, or characteristic material strengths, rather than the enhanced values used for determining strength of plastic hinges, defined in Section 4.2.5. For concrete sections, nominal capacity should be determined at an extreme fibre compression strain of 0.004, or a reinforcement strain of 0.015, whichever occurs first. A flexural strength reduction factor of $\phi_f = 0.9$ should be adequate to cope with possible material understrength, though the value will depend on local code requirements for material strengths, and expected construction quality.

4.7.2 Beam/Column Joint Shear Strength

Integrity of beam/column joints is essential to the successful performance of building, bridge, wharf and industrial frames, and requires careful consideration of the force transfer through the joint region. This has been extensively covered for buildings in [P1] and for bridges in [P4]. Since an adequate coverage of this important topic requires considerable length, it is not repeated here, and the interested reader is referred to the above texts.

4.7.3 Shear Strength of Concrete Members: Modified UCSD Model

There is also a great body of information relating to the shear strength of concrete members in the research literature [e.g. P4, K4, A9 etc], with a significant divergence between design approaches and design equations required by different national codes. Many of these do not recognise that flexural ductility affects the shear strength in plastic hinge regions, and the influence of axial force resulting from gravity and from prestress is often treated quite differently. In [P4] a new approach for determining the shear strength of concrete columns was outlined that considers most of the critical parameters, and since this has subsequently been upgraded to improve agreement with experimental results[K4], the modified approach, generally referred to as the **modified UCSD model** is outlined here. Independent studies have indicated that this approach provides a better agreement with experimental results than other methods[E3].

In the modified UCSD model, the shear strength of concrete sections is found from the additive equation:

$$V_{des} = \phi_s V_{cap} = \phi_s \left(V_C + V_S + V_P \right) \tag{4.71}$$

where V_C, V_S, and V_P are shear strengths provided by concrete mechanisms, transverse reinforcement truss mechanisms, and axial force mechanisms respectively. These are described separately in the following sections.

(a) Concrete Shear-Resisting Mechanisms, (V_C): The key component of the strength of concrete shear-resisting mechanisms in flexurally cracked members is provided by aggregate interlock on the rough flexure/shear cracks. In plastic hinge regions, the strength of aggregate interlock reduces as the flexure/shear crack widens under ductility. The strength is also dependent on the aspect ratio of the member, defined as the distance from the critical section to the point of contraflexure, divided by the section depth, (i.e. $M/(VD)$, where M and V are the moment and shear at the critical section and D is the total section depth) and on the volumetric ratio of longitudinal reinforcement, $\rho_l = A_{st}/A_g$. The strength is thus given by:

$$V_C = k\sqrt{f'_{ce}}.A_e = \alpha\beta\gamma\sqrt{f'_{ce}} \cdot \left(0.8 A_g\right) \tag{4.72}$$

$$\text{where} \quad 1.0 \leq \alpha = 3 - \frac{M}{VD} \leq 1.5 \tag{4.72a}$$

$$\beta = 0.5 + 20\rho_l \leq 1.0 \tag{4.72b}$$

and γ is given by Fig. 4.22, for concrete columns. Note that in Fig.4.22, the prime variable is the curvature ductility demand, which is directly related to the width of flexure/shear cracks in the plastic hinge region. A secondary variable is the mode of ductility. It has been found[A3,P1] that the strength of concrete shear-resisting mechanisms of members subjected to ductility demands in two orthogonal directions (biaxial ductility) degrades more rapidly than sections subjected to uniaxial ductility. This is reflected in Fig.4.22.

(a) Design of New Members   (b) Assessment of Existing Members
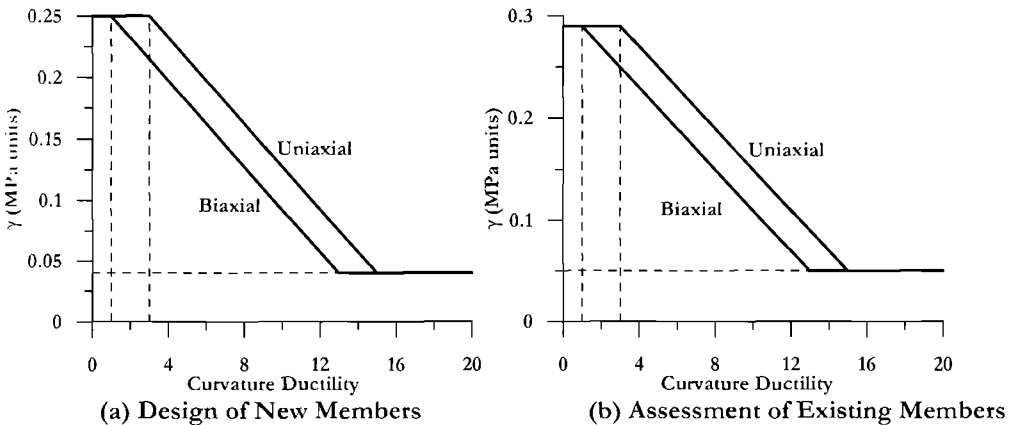
Fig.4.22 Ductility Component of Concrete Shear-Resisting Mechanism for Columns (Modified UCSD Model)

Figure 4.22 also distinguishes between design of new members, and assessment of existing members. A less conservative approach is appropriate for the latter, since the consequences of excessive conservatism is assessment may be unnecessary strengthening.

For concrete beam sections, it is suggested that the strength given by Eq.(4.72) be reduced by 20% to compensate for the conditions of concrete confinement which are less satisfactory than for columns, and that the tension, rather the total reinforcement area be used to determine β.

Note that the reduction in shear strength with ductility only applies to the plastic hinge regions of members designed for ductility. In parts of members between plastic hinges, and in members protected against plastic hinging by a capacity design approach, the value of γ used in Eq.(4.72) will be the value at a curvature ductility of 1.0.

(b) Axial Load Component, V_P: In many design equations for concrete shear strength the axial load on the section is combined in a composite equation with the concrete shear-resisting mechanisms. This would imply that the well-known enhancement of shear strength with increased axial compression would reduce with flexural ductility. This is not supported by experiments. In the UCSD model, the shear strength enhancement resulting from axial compression is considered as an independent component (see Eq.(4.71)), resulting from a diagonal compression strut, as illustrated in Fig. 4.23 for columns, and in Fig.4.24 for the beam of a portal frame (the extension to other beams with seismic moment-reversal along the length is obvious). It will be noted that the axial force in beams will often be low, and it is traditional to ignore its influence on shear strength. Nevertheless, in some structures, particularly bridge bents, the influence can be substantial. This will particularly be the case if the beam is prestressed.

(a) Double Bending   (b) Single Bending
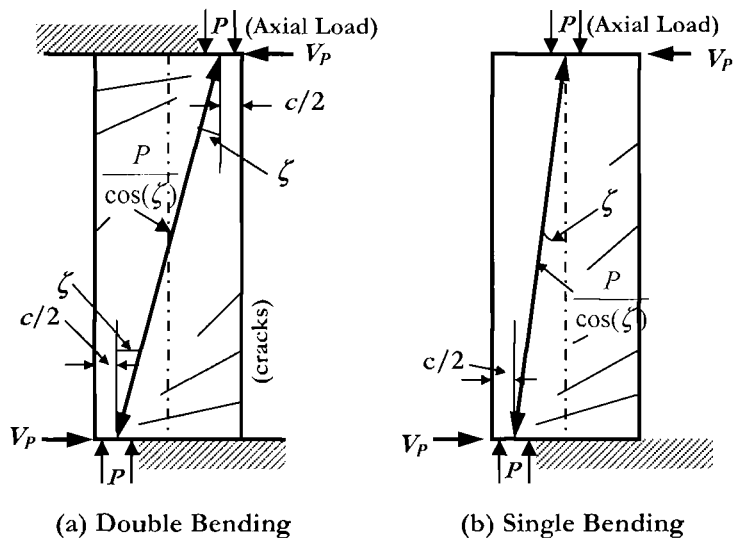
Fig. 4.23   Contribution of Axial Force to Column Shear Strength
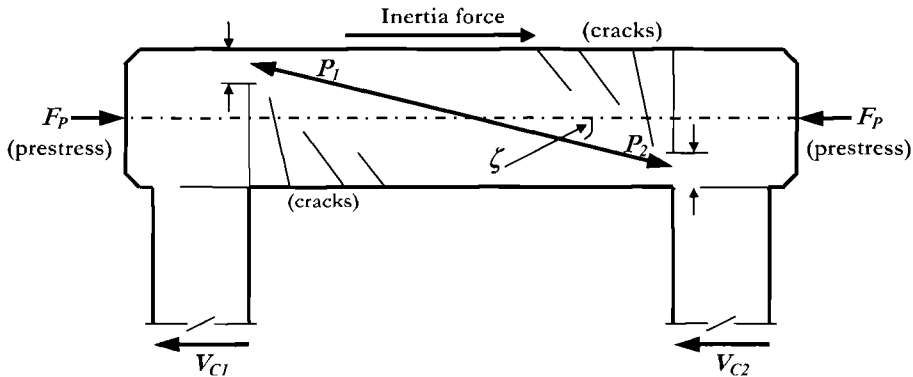
Fig. 4.24 Contribution of Axial Force to Shear strength of a Portal Frame[P4]

In Figs.4.23 and 4.24, the average inclination of the strut involving the axial force is shown at an angle ζ to the member axis. For the column of Fig. 4.23(a) which is restrained from rotation at top and bottom, the axial force is effectively applied to the column through the centre of the flexural compression zone at the beam top, and exits through the centre of flexural compression at the bottom. The horizontal component of this strut acts to resist the applied shear force, thus enhancing the column shear strength. For the cantilever column of Fig.4.23(b), the axial load is applied at the centre of the column at the top, but again exits through the centre of flexural compression at the bottom. The angle of the strut to the column axis is less than in Fig. 4.23(a), and hence the resistance to lateral shear is less. In Fig.4.24, due to the uniformly distributed inertia force, the axial force varies along the length of the beam, which will be subjected to axial tension at one end, and axial compression at the other, unless prestressed, as suggested in Fig.4.24. The vertical component of the inclined strut either adds to, or resists the applied shear force, depending on whether the axial force is tensile or compressive.

In assessment of existing structures the full axial force component should be relied on. For new structures a more conservative approach, where the axial force component is reduced by 15% has been proposed[P4]. The following equations thus apply for V_P:

Design: $V_p = 0.85P.\tan\zeta$ (4.73a)

Assessment: $V_p = P.\tan\zeta$ (4.73b)

where ζ is the angle between the strut and the member axis.

(c) Transverse Reinforcement Truss Shear-Resisting Mechanism: The strength of transverse reinforcement truss mechanisms is illustrated in Fig.4.25 for rectangular and circular columns. The rectangular column illustration (Fig.4.25(a)) is also relevant for rectangular or T-section beams. The critical flexure-shear crack crosses the section at an

(a) Rectangular column   (b) Circular column
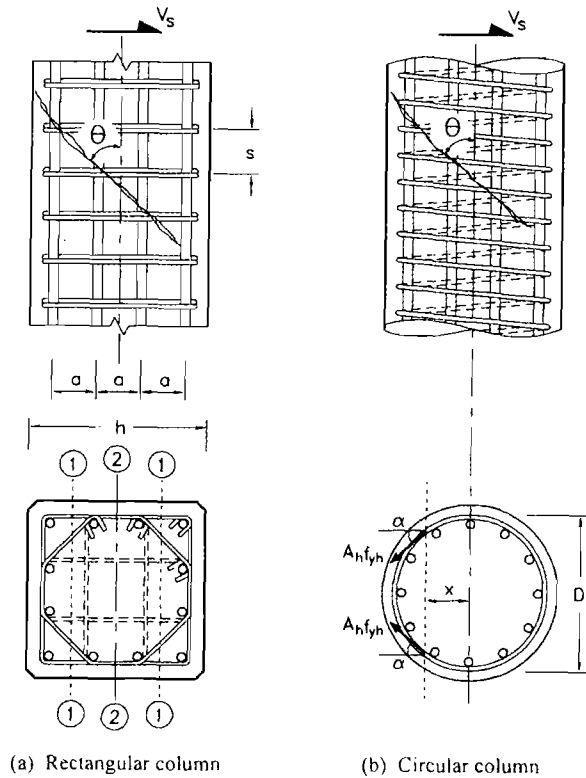
Fig.4.25   Effectiveness of Transverse Reinforcement for Shear Resistance of Columns[P4]

average angle of θ to the vertical axis. The layers of transverse reinforcement crossed by the crack act to transfer some of the shear force across the crack. The maximum force that can be transferred by a layer of area A_v depends on the yield strength of the transverse reinforcement, and the orientation of the bars of the layer with respect to the axis along which the shear is applied. For example, at the vertical sections denoted **1** in Fig.4.25(a), the octagonal hoop, which forms part of the layer will provide resistance at 45° to the direction of applied shear, and the effective area of this hoop at this section will be $A_h/\sqrt{2}$, where A_h is the area of the hoop bar, whereas the outer peripheral rectangular hoop will be fully effective at both sections **1** and **2**.   It can be shown[P4] that for the case of one peripheral and one octagonal hoop, the average effective area is $A_v = 3.61A_h$. If however, the transverse reinforcement consists of a peripheral hoop and two overlapping internal hoops (shown by dashed lines in Fig. 4.25(a)), the average effective area is $A_v = 4.67A_h$.

   With a circular column (Fig.4.25(b)), the orientation of the hoop forces restraining a flexure shear crack depends on the position of the individual hoop where the crack

intersects it. At the column centreline, the hoop force $A_h f_{yh}$ is parallel to the applied shear force, but as the distance from the column centreline increases, the inclination α to the direction of applied force also increases, and the effective force restraining the crack, i.e. $A_h f_{yh} \tan \alpha$ decreases. Given that there are two forces restraining the crack (Fig.4.25(b)), the average restraining force, taking all possible locations of the hoop or spiral with respect to the intersecting crack, can be shown to be

$$F = \frac{\pi}{2} A_h f_{yh} \tag{4.74}$$

If the angle of the flexure-shear crack to the member axis is θ, for either the rectangular or circular column, the depth from the extreme compression fibre to the neutral axis is c, and the cover to the centre of the peripheral hoop is c_o, then the number of layers of hoop crossed by the inclined crack is

$$n = \frac{(D - c - c_o)}{s} \cdot \cot(\theta) \tag{4.75}$$

where s is the spacing of hoops or spirals along the member axis.

The total shear resistance provided by the transverse reinforcement for the rectangular column can thus be estimated as:

Rectangular column: $$V_S = \frac{A_v f_{yh} (D - c - c_o) \cdot \cot(\theta)}{s} \tag{4.76a}$$

where A_v is the effective area of hoops in a single layer, as discussed above, and for a circular column with circular hoops or spirals:

Circular column: $$V_S = \frac{\pi}{2} \cdot \frac{A_h f_{yh} (D - c - c_o) \cdot \cot(\theta)}{s} \tag{4.76b}$$

Equation (4.76a) may be considered "exact", but Eq.(4.76b) is approximate since the average effective force given by Eq.(4.74) is exact only if the crack penetrates the full width of the column. However, it has been shown that the error is small, and conservative[K4]. Although standard practice in the United States adopts an angle of $\theta = 45°$, this has been found to be unnecessarily conservative, provided longitudinal reinforcement is not prematurely terminated. European practice is based on plasticity theory and a variable angle θ. It has been found that sufficiently conservative designs can be obtained taking $\theta = 35°$. For assessment of existing structures the less conservative value of $\theta = 30°$ is appropriate[P4]. The principles and equations outlined in this section can also be applied to concrete beam sections.

(d) Strength Reduction Factor for Shear Capacity: For design it is appropriate to include a strength reduction factor in addition to the conservatism applied in the equations for the individual shear-resisting components described above. It is recommended that this be taken as $\phi_S = 0.85$ (see Eq.(4.71)). For assessment of existing structures, where the required shear strength has been determined in accordance with the capacity-protection measures of Section 4.5, no shear strength reduction factor need be applied, since a "best estimate" of performance will be required.

(e) Comparison of Assessment Equations with Circular Column Test Data: Figure 4.26 compares shear strength predictions of Eq.(4.71) using the assessment values of the component strengths, and a strength reduction factor $\phi_S = 1.0$, with experimental data for a wide range of circular columns. Brittle and ductile shear failures are those for which the initial shear strength (curvature ductility $=1$) was less than or more than, respectively, the shear corresponding to flexural strength. Measured, rather than nominal, material properties were used in the predictions which are very satisfactory, regardless of what variable is used to organize the test results. Note that the columns failing in flexure have strengths below the predicted shear strength. This does not indicate unsatisfactory behaviour, since the strength was dictated by the flexural capacity which was less than the shear strength. Design shear strength, including the $\phi_S = 0.85$ factor, is shown by the dashed line, and is a lower bound to all shear failures.

(f) Prediction of Ductility Capacity for Flexure-Shear Failure of Existing Columns: With new designs, the design procedure should ensure that shear failure does not occur. With existing columns, however, it may be found that shear failure is predicted. When this occurs at less than the flexural strength of the column, brittle failure is expected, though the displacements will be larger than assessed from a simple bilinear approximation based on flexure alone[M6]. This is explained in relation to Fig.4.27.

Figure 4.27 shows the force-displacement response of bridge columns roughly based on Example 4.1. The bilinear flexural response is indicated by the solid line, and the "refined" response, including onset of cracking and non-linearity of the post-first yield behaviour in shown by the dashed line labelled "**A**". The second dashed line, labelled "**B**" includes shear deformation calculated in accordance with recommendations made in Section 4.8. Three possible shear strength envelopes are shown, each corresponding to a different spacing of the transverse reinforcement. Strength envelope **1** corresponds to close spacing of the transverse reinforcement, and shear failure is not expected before the full displacement capacity is reached, whether shear deformation is included or not.

Shear strength envelope **2** degrades to intersect the predicted force-displacement response. The failure displacement (and force) depends on whether shear displacement is included or ignored. The values are 284mm and 297mm (11.2in and 11.7in) respectively. In terms of displacement-based design the differences are not significant, particularly when the slight reduction in strength resulting from the increased displacement associated with the response including shear deformation is considered. The bilinear and refined displacement curves are identical in this region.
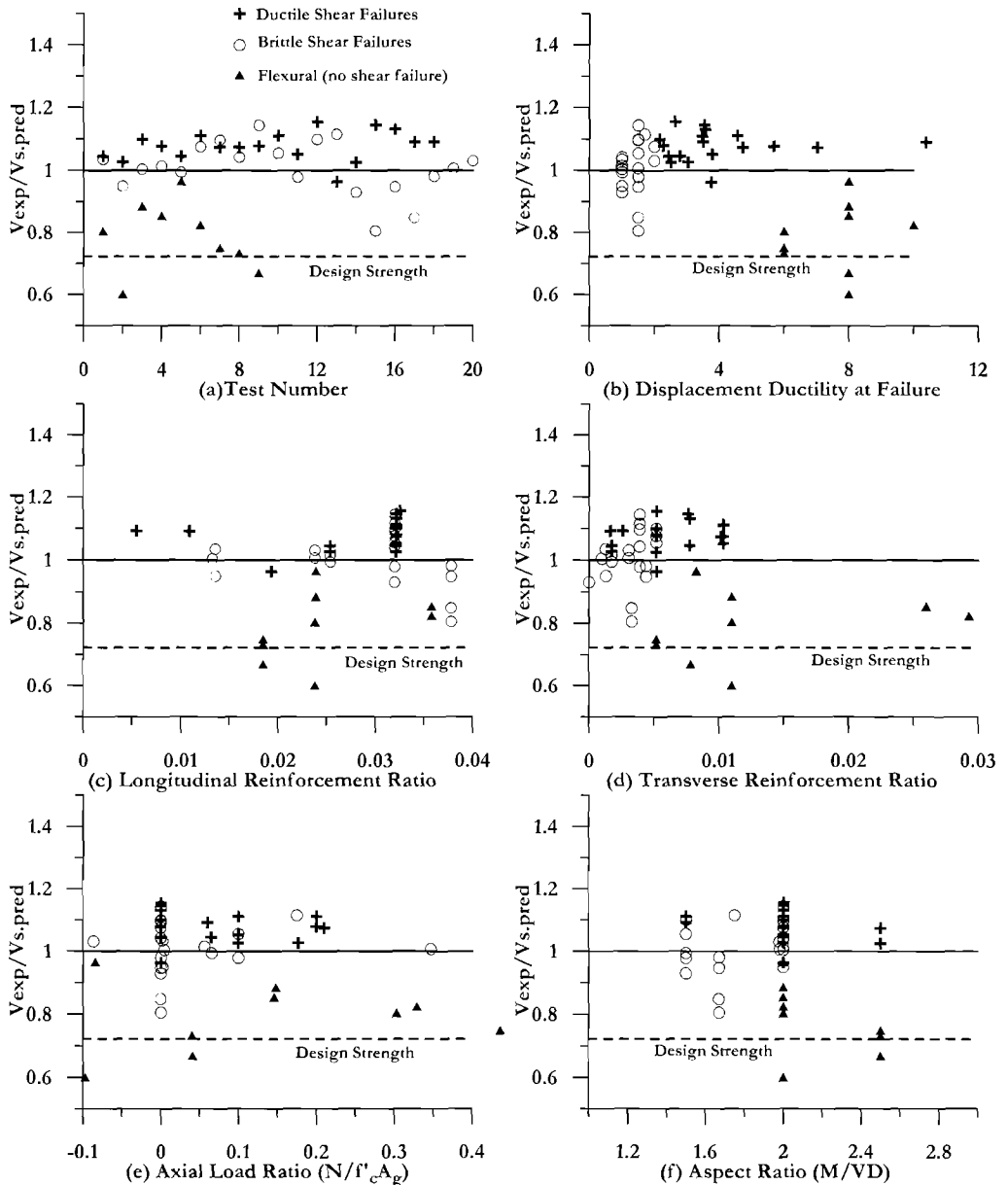
Fig.4.26 Shear Strength Comparison: Circular Column Data vs Assessment Prediction Organized by Significant Variables (Design Strength Shown Dashed)

With shear strength envelope **3**, corresponding to wide-spaced transverse reinforcement, there is a significant difference in the predicted failure displacements depending on which force-displacement curve is used, with the values being 100mm, 135mm and 149mm (3.9in, 4.3in, and 4.9in) for the bilinear, refined, and refined+shear

deformation respectively. In displacement-based assessment of an existing structure the higher displacements would translate into a significant increase in seismic intensity able to be accommodated by the structure, particularly when the enhanced damping associated with the implied ductility is included in the analysis. Note that shear deformation has conservatively not been applied to the strength envelopes in the above discussion.
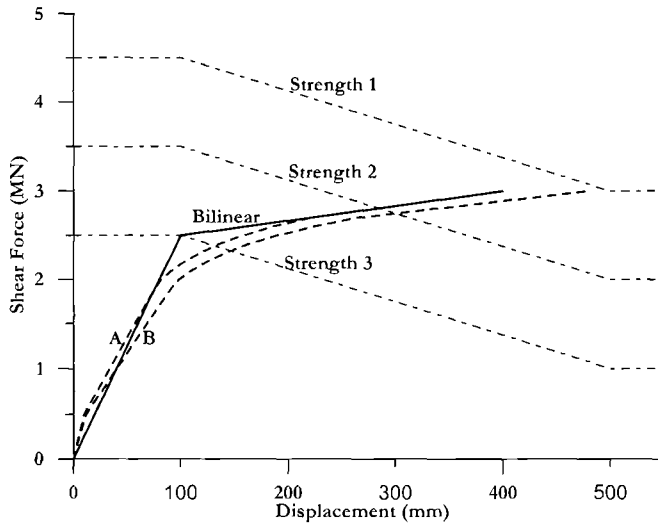
Fig.4.27 Force-Displacement Response of Columns with Different Shear Strengths

4.7.4   Design Example 4.2: Shear Strength of a Circular Bridge Column

The bridge column of Design Example 4.1, presented in Section 4.5.1, is analysed to see if it has adequate shear strength to satisfy the design requirements of Sec. 4.7.3. Additional information required is that the column is expected to have similar ductility demands in orthogonal directions, and hence the biaxial data of Fig.4.22 apply for determining the strength of the concrete shear-resisting mechanisms.

Design shear force: Curve **B** of Fig.4.20, which is based on overstrength flexural reinforcement properties, but expected concrete strength, applies. Thus, as noted in Section 4.4.1, the overstrength moment capacity is 30.8 MNm (273,000 kip.in). With a column height of 10m (32.8ft), the overstrength shear force is thus:

V^o = **3.08MN (693kips).**

A shear strength reduction factor of ϕ_f = 0.85 is specified. There is no dynamic amplification to be applied, and hence the capacity-design Eq.(4.71) can be expressed as:

$$V_N = V_C + V_S + V_P \geq \frac{V^o}{\phi_f} = \frac{3.08}{0.85} = 3.63 MN (815 kips)$$

Concrete shear-resisting mechanisms: From Ex.4.1, the curvature ductility is: $\phi_D/\phi_y = 0.0274/0.00289 = 9.48$. Interpolating from the biaxial line of Fig. 4.22, the concrete strength coefficient is $\gamma = 0.101$. Since the column aspect ratio exceeds 2, and the longitudinal reinforcement ratio is 0.025, both α and $\beta = 1.0$. The strength of the concrete shear-resisting mechanisms, with $f'_{ce} = 39$ MPa, is thus, from Eq.(4.72):

$$V_C = \alpha.\beta.\gamma\sqrt{f'_{ce}}(0.8A_g) = 0.101\sqrt{39}(0.8\times2.543) = 1.283 MN(289 kips)$$

Axial Load component: The axial load is 3.82MN, and the depth of the compression zone, c, is 460mm. The angle of the axial load strut is thus given by $\tan\zeta = (0.9-0.23)/10 = 0.067$. From Eq.(4.73a), the shear strength resulting from the axial load component is:

$$V_P = 0.85P.\tan\zeta = 0.85\times3.82\times0.067 = 0.218 MN(49 kips)$$

Transverse reinforcement component: Equation (4.76b) applies, with $\theta = 35°$. The pitch of the hoops is $s = 120$mm, and hence the available strength is

$$V_S = \frac{\pi}{2}\cdot\frac{A_h f_{yh}(D-c-c_o)\cot(\theta)}{s} = \frac{\pi}{2}\cdot\frac{314\times420(1800-460-40)\cot35}{120} = 3.214 MN(723 kips)$$

The total shear strength is thus:

$$V_N = V_C + V_S + V_P = 1.283 + 0.218 + 3.214 = 4.715 MN > 3.628 MN \qquad (OK).$$

In fact, a spacing of 180mm (7.1in) would be adequate for required shear strength, but the more critical confinement requirement of 120mm governs, and is thus specified. Note that the shear requirement is not added to the confinement requirement – the same reinforcement can simultaneously provide confinement and shear strength. If the reinforcement is stressed by shear strength requirements, it will bear against the core concrete, providing effective confinement to the concrete. On the other hand, if the transverse reinforcement is in tension due to confinement, this stress can be used to transfer shear force across open cracks. If it is further considered that the peak shear and confinement demands occur in orthogonal directions, it is clear that the column need only be designed for the more critical of shear and confinement.

4.7.5 Shear Strength of Reinforced Concrete and Masonry Walls

(a) Shear Demand: The design shear force for reinforced concrete or masonry walls is strongly influence by capacity design influences – particularly higher mode effects. This is discussed in some detail in Section 6.6, and is only briefly considered here. Figure 4.28 shows two profiles of moment up the height of a cantilever wall, with Fig.4.28(a) corresponding to the design distribution of lateral forces, resulting from the **DDBD** procedure, and Fig.4.28(b) including a possible distribution resulting in maximum feasible base shear. In Fig.4.28(b) the base moment M^o exceeds the design moment M_D, as a result of material strengths exceeding expected values (see Sections 4.2.4 and 4.5).
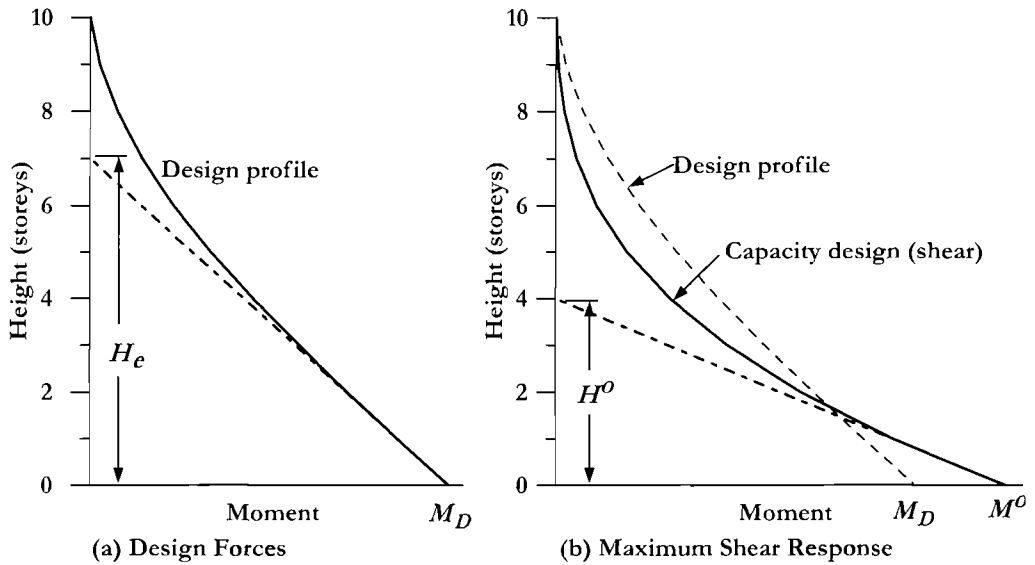
(a) Design Forces   (b) Maximum Shear Response
Fig.4.28   Moment Profiles for a Cantilever Structural Wall

Critical higher mode effects result in a much more rapid decrease in moments with height than for the design profile, and hence the overstrength base shear force, given by the slope of the moment profile at the wall base ($V^o=M^o/H^o$) is significantly larger than the design base shear force ($V_D =M_D/H_e$). In the example shown in Fig.4.28, with $M^o = 1.25M_D$, the overstrength shear is $V^o = 2.2V_D$.

(b) Concrete Shear-Resisting Mechanisms: The strength of the concrete shear-resisting mechanisms can be determined from Section 4.7.3(a) as for columns. However, it could be noted that at maximum shear response, the ductility demand is unlikely to be as high as the design level, since the design level for displacement and ductility demand is dominated by first mode response, while peak shear demand will be strongly influenced by second, and perhaps third-mode response, which are unlikely to occur simultaneously with peak first mode response. The aspect ratio for the wall to be used when determining the factor α in Eq.(4.72a) should be based on the overstrength effective height; that is,

$$M/VD = H^o/l_w.$$

With flanged walls, it is recommended that the effective shear area be based on the web dimensions (in the direction considered) and that the area of any flanges be conservatively ignored.

(c) Axial Force Component: The concepts outlined in Section 4.7.3(b) for the contribution of axial force in shear resistance were related to a single axial force component. In multi-storey walls, axial force, and its influence on shear strength will be composed of a number of components; one for each floor level. Thus Eq.(4.73) should

be replaced by a summation of the effects from each floor considered separately. The load at each floor should be considered to be applied through the geometric centroid of the wall, and the resulting angle of the compression strut calculated separately for each floor.

(d) Transverse Reinforcement Mechanisms: Again the recommendations of Section 4.7.3(c) can be directly used. When the wall flexural reinforcement is uniformly distributed along the wall length, as we recommend, it will help to control the diagonal flexural-shear cracking, and hence enhance the concrete shear-resisting mechanisms. Also, with longer walls, the critical 35° angle of diagonal cracking is likely to intersect a floor slab, potentially mobilizing additional shear resistance. With typical storey heights of 3m (10ft) this can be expected for walls longer than about 2.5m (8.2ft). Although this may not be relied upon in design, it provides additional security against shear failure.

4.7.6   Response to Seismic Intensity Levels Exceeding the Design Level

When structures are designed to the damage-control limit state under a level **2** earthquake, there remains the possibility that they may be subjected to higher intensity levels, perhaps corresponding to level **3** (see Section 2.2.2.(c)). It is clearly important that to satisfy the life-safety performance criterion required for a Level **3** earthquake, shear failure must not occur. The influence of increased seismic excitation on shear strength is expressed in the proposed design approach by an increase in curvature ductility, which results in a decrease in the strength of the concrete shear-resisting mechanisms (see Fig.4.22). Generally the inherent conservatism of the proposed shear design approach will be sufficient to ensure safe performance under a Level **3** earthquake. However, if the concrete shear-resisting mechanisms provide a large portion of the total shear strength, added conservatism in the shear design would be appropriate. This could be effected, for example, by using the minimum levels for the parameter λ in Fig.4.22(a).

4.8   SHEAR FLEXIBILITY OF CONCRETE MEMBERS

4.8.1   Computation of Shear Deformations

For slender members, with aspect ratios $M/VD > 3$, shear deformation will be small, and can be ignored. It will be recalled that in Section 4.2.7 the use of a linear elastic curvature distribution in predicting force-displacement response was partly to compensate for shear deformation. It should also be noted that ignoring shear deformation is not necessarily unconservative in a displacement-based design environment, since shear deformation will increase the displacement capacity corresponding to strain-based flexural limit states.

For members of low aspect ratio, and particularly when assessing the force-displacement characteristics of existing structures, it may be advisable to consider shear deformation. In this context it should be pointed out that only approximate methods for

predicting shear deformations of concrete members are available, though compression-field theory[C8] provides a means for predicting total deformation, including shear components, for monotonic response of members with positive stiffness. The following simplified approach is modified from an approach developed by Miranda et al[M6], and assumes a bilinear flexural force-displacement approximation is utilized. Adaptation to the "refined" approach of Fig.4.9 is obvious.

Calculation of shear deformation is divided into three phases of the force-displacement response:

(a) Elastic, Prior to Shear Cracking: With the bilinear approximation to response, it is assumed that the elastic phase is represented by constant flexural section stiffness of

$$EI_{eff} = M_N / \phi_y \tag{4.77}$$

In the elastic range, prior to the formation of diagonal shear cracks, flexural cracking reduces the shear stiffness approximately in proportion to the reduction in flexural stiffness. Thus, the shear stiffness in this phase may be approximated by:

$$k_{s.eff} = k_{s.gross} \cdot \frac{EI_{eff}}{EI_{gross}} \tag{4.78}$$

where the shear stiffness for an uncracked cantilever column of shear area A_s, shear modulus G and length H is given by:

$$k_{s.gross} = \frac{GA_s}{H} \tag{4.79}$$

For solid sections, the shear area may be taken as $A_s = 0.87A_{gross}$, with adequate accuracy, and the shear modulus as $G = 0.43 E$, for concrete and masonry structures.

Shear cracking may conservatively be assumed to occur when $V=V_C$, given by Eq.(4.72), with $\gamma = 0.29$ (MPa units; $\gamma = 3.5$, psi units). Note that this corresponds to the initial strength for the assessment model, which is used here in preference to the design model, since a best estimate of deformation is required. The displacement at onset of diagonal cracking is thus:

$$\Delta_{s1} = V_C / k_{s.eff} \tag{4.80}$$

(b) Elastic, After Shear Cracking: The shear stiffness for incremental displacements after onset of diagonal shear cracking is based[M6] on a model developed originally by Paulay[P31]. This considers the shear flexibility of an equivalent strut-and-tie model, incorporating both the compression of the diagonal strut, and the extension of the tie representing the transverse reinforcement. The unitary shear stiffness (i.e. shear stiffness of a unit length of member) for members with transverse reinforcement perpendicular to the axis is given by

$$k_{s.cr} = \frac{\rho_a \sin^4 \theta . \cot^2 \theta}{\sin^4 \theta + n\rho_a} \cdot E_s b_w d \tag{4.81}$$

where θ is the angle the diagonal strut makes with the member axis, ρ_a is the area ratio of transverse reinforcement, $n = E_s/E_c$ is the steel/concrete modular ratio, b_w is the effective width of the section, and d is the effective depth of the section.

There are some problems associated with the use of Eq.(4.81), particularly in applying it to circular sections. One general problem, however, is that for typical values of n and ρ_a it implies that the shear stiffness *increases* as the angle θ reduces from 45° to 30°. This appears counter-intuitive, as members suffering shear distress typically exhibit a decreasing angle θ as shear force increases to maximize shear strength (see Eq.(4.76),e.g). That this should be accompanied by decreasing shear deformation is unlikely, and is not supported by experimental results, so far as we are aware. Nevertheless, Eq.(4.81) gives reasonable prediction of shear deformation of rectangular columns[M6] when $\theta = 45°$. With this approximation, Eq.(4.81) can be simplified to:

$$k_{s.cr} = \frac{0.25\rho_a}{0.25 + n\rho_a} \cdot E_s b_w d \tag{4.82}$$

A further problem with Eqs(4.81 and 4.82) is the evaluation of the modular ratio. This will increase as the flexural strength of the column is approached, resulting in a decrease in effective shear stiffness. This occurs as a result of softening of the diagonal compression strut. Consequently, the value for n should reflect this. An average value of $n = 10$ is recommended.

For circular columns, as mentioned earlier, additional problems are associated with definition of ρ_a, b_w and d. The following approximate values are suggested:

$$\rho_a = \frac{\pi}{2} \cdot \frac{A_h}{D's} = 0.39\rho_v \qquad \text{and} \qquad b_w = d = 0.8D \tag{4.83}$$

where ρ_v is the volumetric ratio of transverse reinforcement (see Sec.4.2.2).

The shear stiffness defined by Eq.(4.82) applies for shear forces between diagonal cracking, and nominal flexural strength. At nominal flexural strength the shear deformation is thus:

$$\Delta_{s,N} = \Delta_{s,1} + (V_N - V_C)/k_{s,cr} \tag{4.84}$$

where V_N is the shear force corresponding to flexural strength.

(c) Ductile phase: In the post-yield phase the concrete compression struts within the plastic hinge region will continue to soften, and thus shear deformation will continue to increase. Experiments on columns where shear failure does not occur have indicated that the shear deformation, as a fraction of total deformation remains essentially constant, or

reduces slightly, as the ductility increases. Since rational computation of the shear deformation in this phase of response is difficult, and the significance to total deformation is typically small, it is recommended that the shear deformation be increased in proportion to the flexural deformation after yield. That is:

$$\Delta_s = \Delta_f \cdot \frac{\Delta_{s,N}}{\Delta_{f,N}} \qquad (4.85)$$

If the "refined" force-displacement representation of Section 4.2.7 is adopted, Eq.(4.85) should be applied after the member has attained its nominal flexural strength.

4.8.2   Design Example 4.3: Shear Deformation, and Failure Displacement of a Circular Column

The column of Design Examples 4.1 (Section 4.5.1) and 4.2 (Section 4.7.4) is now re-analysed with the effective column height reduced from 10m (32.8ft) to 5m (16.4ft) to make it more shear-critical. Note that the column aspect ratio is now 5/1.8 = 2.8, indicating that shear deformation probably should be considered. Longitudinal and transverse reinforcement, and axial load remain as in the previous examples. First the force-displacement response needs to be reassessed.

Table 4.1 Force-Displacement Data for Example 4.3 (1MN=225kips, 1m=39.37in)

Row	Moment (MNm)	Curvature (m⁻¹)	Shear Force(MN)	Flexural Disp. (mm)	Shear Disp (mm)	Total Disp (mm)
1	0.0	0.0	0.0	0.0	0.00	0.00
2	18.87	0.00242	3.774	24.23	1.81	26.04
3	19.88	0.00260	3.976	24.75	2.95	28.70
4	21.31	0.00298	4.262	28.55	456	33.11
5	22.36	0.00339	4.472	31.22	4.75	36.98
6	24.08	0.00450	4.816	37.70	7.70	44.40
7	24.13	0.00571	4.826	44.24	8.88	53.12
8	24.73	0.00695	4.946	50.57	9.56	60.14
9	26.21	0.00814	5.242	56.59	10.10	66.70
10	26.72	0.00928	5.344	62.42	11.14	73.55
11	27.14	0.01038	5.428	68.00	12.13	80.10
12	27.85	0.01250	5.570	78.66	14.04	92.70
13	28.39	0.01453	5.678	88.78	14.84	104.62
14	28.89	0.01651	5.778	98.62	17.60	116.22
15	29.34	0.01849	5.868	108.44	19.35	127.79
16	29.72	0.02044	5.944	118.06	21.07	139.13
17	30.36	0.02421	6.072	136.60	24.38	160.98
18	30.84	0.02533	6.168	142.31	24.39	167.70

Table 4.1 includes data necessary to construct the force-displacement response. The moment and curvature are values found from moment-curvature analysis of the column, using the procedures outlined in Section 4.2, and the overstrength data corresponding to curve **B** in Fig.4.20. The data in Row 2 correspond to first-yield of the extreme longitudinal reinforcement. Because the axial compression stress is low, flexural cracking occurs at a very low moment, if the recommendation to take tension strength as zero is adopted. Consequently, the moment-curvature response is essentially linear up to first yield, and intermediate values have been omitted, for simplicity. The "refined" force-displacement approach of Section 4.2.7 can thus also be assumed to be linear before first yield. Shear force is simply found from $V=M/5$.

Flexural displacement: Since the yield strength for this assessment is taken as $1.3f_y = 546\text{MPa}$ (79.1ksi), the strain penetration length needs to be recalculated from the value used in Example 4.1: $L_{SP} = 0.022f_{ye}d_{bl} = 0.022\times546\times40 = $ **480.5mm (18.9in)**

Plastic hinge length: From Eq.(4.31), $L_P = 0.08\times5000+480.5 = 880.5 \geq 2\times480.5$ i.e. L_P =**961mm (37.8in)**

First yield displacement: From Table 4.1, Row 2, the first yield curvature is $\phi'_y = 0.00242$. Thus, $\Delta'_y = 0.00242\times(5+0.481)^2/3$ m = **24.23mm (0.95in).**

Subsequent flexural displacement: From Eq.(4.37), the flexural displacement for moments higher than first yield are given by:

$$\Delta = \Delta'_y \frac{M}{M_y} + \left(\phi - \phi'_x \frac{M}{M_y}\right)L_P H = 24.23\frac{M}{18.87} + \left(\phi - 0.00242\frac{M}{18.87}\right)0.961\times5000mm \quad (4.86)$$

The displacements resulting from Eq.(4.86) are listed in Table 4.1 in Column 5 (Flexural Disp. (mm)), and the force vs. flexural displacement is plotted in Fig.4.29 by the dashed line labelled Flex. Disp.

Shear displacements prior to shear cracking: Following the recommendations of Sec. 4.8.1, the shear stiffness in the elastic range of flexural response is given by Eq.(4.79). This requires the ratio of effective to gross flexural stiffness to be calculated. The effective stiffness can be calculated from the moment-curvature data at first yield as

$$EI_{eff} = M_y / \phi'_y = 18.87/0.00242 = 7798 MNm^2$$

Now:

$$I_{gross} = \pi D^4 / 64 = \pi(1.8)^4 / 64 = 0.515m^4, \text{ and from Eq.(4.43)}$$
$$E_C = 5000\sqrt{39} = 31.2GPa.$$
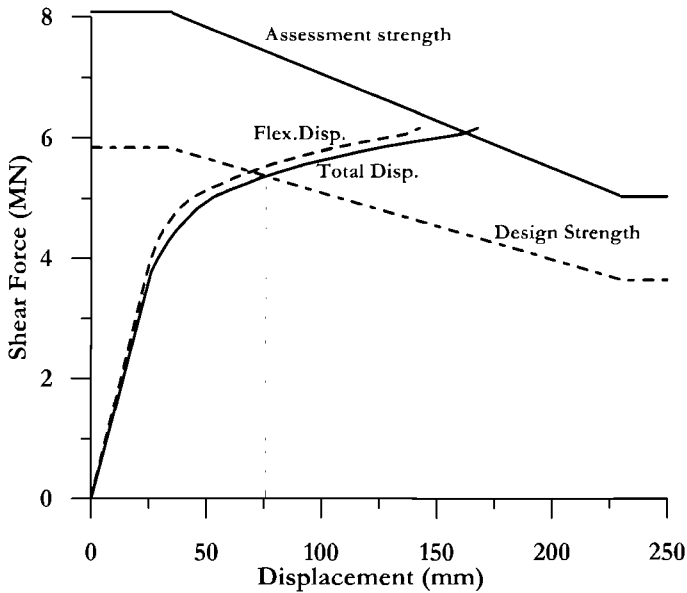
**Fig.4.29   Force-Displacement Response, and Shear Strength, for Example 4.3
(1MN = 224.8kips; 1mm = 0.0394in)**

Hence:

$$EI_{eff} / EI_{gross} = 7798 / (31,200 \times 0.515) = 0.485$$

The shear force at diagonal cracking is, from Eq.(4.72) with $\alpha = \beta = 1.0$:

$$V_C = 0.29\sqrt{39} \times 0.8 \times 2.543 = 3.68MN (827kips)$$

The elastic shear displacement at diagonal cracking is thus, with G=0.43×31.2 =13.42GPa and $A_s = 0.87 \times 2.543 = 2.212$m²:

$$\Delta_{s,el} = \frac{V_{cr}}{k_{s,eff}} = \frac{V_{cr}H}{GA_s} \cdot \frac{EI_{gross}}{EI_{eff}} = \frac{3.68 \times 5000}{13,420 \times 2.212 \times 0.485} = 1.28mm(0.05in)$$

Note that in this case diagonal shear cracking and flexural yield occur almost at the same shear force.

Shear displacement after diagonal cracking: Using the recommendations of Eq.(4.81) for circular columns, the effective area ratio of transverse reinforcement is taken as $\rho_a = 0.39\rho_v = 0.39 \times 0.006 = 0.00234$, and $b_w = d = 0.8 \times 1.8 = 1.44$m. Substituting into Eq.(4.82):

$$k_{s.cr} = \frac{0.25\rho_a}{0.25+n\rho_a} \cdot E_s b_w d = \frac{0.25 \times 0.00234}{0.25+10 \times 0.00234} \cdot 200,000 \times 1.44^2 = 885MN$$

This is the unitary stiffness (stiffness for a unit column height). The column shear stiffness is thus

$$k_{col.cr} = k_{s,cr} / H = 885/5 = 177MN/m$$

The incremental shear displacement for shear forces higher than the diagonal cracking shear force V_C is thus:

$$\Delta_s = \frac{(V-V_C)}{0.177}mm \cdot$$

Displacements resulting from this equation are added to the elastic shear displacement at diagonal cracking (see Eq.(4.84)), and listed in Column 6 of Table 4.1. These apply only up to the nominal flexural strength. In accordance with Eq.(4.85) the shear displacements have been increased pro-rata with the flexural displacements from Row 9 (which corresponds to nominal flexural capacity based on the enhanced yield strength) onwards. It will be seen that shear displacements are about 18% of the flexural displacements. Column 7 of Table 4.1 lists the total (flexural+shear) displacements, which are plotted by the solid line, marked "Total Disp." in Fig.4.29.

Shear strength: Again, it is assessed that the column could be subjected to ductile response in orthogonal directions, and thus the biaxial data of Fig. 4.22(b) apply.

Initial shear strength: At a displacement corresponding to $\mu_\phi = 1$, the assessed shear strength will be as follows:

$V_C = 0.29\sqrt{39} \times 0.8 \times 2.543$	= 3.68MN
$V_P = 3.82(0.9-0.23)/5$	= 0.512MN
$V_S = 3.887MN$ (from Ex. 4.2, but with $\theta=30°$)	= 3.887MN
Total	**= 8.083MN (1817kips)**

Shear strength at full ductility: At curvature ductilities of $\mu_\phi \geq 13$, the assessed strength of the concrete shear-resisting mechanisms decreases to:

$$V_C = 0.05\sqrt{39} \times 0.8 \times 2.543 = 0.635MN \text{ (143kips)},$$

and the total shear strength is thus **4.034MN (1132kips).** The displacements at which these to limits apply have been calculated from the biaxial approximation to the force-displacement response, conservatively ignoring shear displacement.

The assessment shear strength envelope is plotted in Fig.4.29 by the solid line. It will be seen that it intersects with the total displacement curve at 162mm (6.4in), which is very close to the assessed flexural displacement limit. Thus the assessment is that shear failure

is unlikely to occur before the displacement capacity is reached (since the force-displacement response is based on maximum feasible flexural reinforcement strength). Note that for a new design, however, a more conservative approach is required, using the design strength components of Sec.4.7.3 and a shear strength reduction factor of 0.85. The design strength envelope based on this approach is also shown in Fig.4.28 (by the dash-dot line), and indicates a safe design displacement of only 76mm (3.0in), about 50% of the displacement that would be permitted in an assessment situation. Note that satisfying the conservatism of the design approach would be easy to provide (the hoop spacing in the potential plastic hinge would be reduced to 75mm (2.95 in)) but the consequence of excessive conservatism in assessment of an existing column could mean expensive retrofit measures.

4.9 ANALYSIS TOOLS FOR DESIGN RESPONSE VERIFICATION

4.9.1 Introduction

Direct displacement-based design (**DDBD**) is a simple method for determining the required strength of plastic hinges to satisfy a specified performance limit state, defined by strain or drift limits. Combined with capacity-design requirements defined in the structure-related sections of this book, it provides a complete seismic design approach for comparatively simple and regular structures. It may also be used to provide preliminary estimates for member strengths for structures which do not fit the "simple and regular" criteria. In these latter cases, and in cases where the structure has special importance, due to function, or cost, design verification by additional analysis will be required.

It has already been established (see Section 1.3), that elastic modal analysis should be considered unsuitable as a design tool, for a number of reasons. Similarly, elastic modal analysis will generally be considered unsuitable for design verification, though the deficiencies cited related to determination of initial stiffness no longer apply, since it will be possible to use reasonable estimates of stiffness based on actual provided strength (see Section 4.4). However, the inability of elastic modal analysis methods to model the variation of flexural stiffness with axial force remains. This leaves two candidates for acceptable analysis methods: time history analysis, and static inelastic (pushover) analysis. Aspects relating to these methods are discussed in the following sections.

4.9.2 Inelastic Time-History Analysis for Response Verification

(a) Elastic or Inelastic Time History Analysis?. Although some design procedures accept elastic time-history analysis (**ETHA**) as an analysis approach, our view is that there is little value in its use for design verification. It suffers from most of the deficiencies apparent in elastic modal analysis, and cannot represent the differences resulting from structural systems with different hysteretic characteristics. With one-dimensional (line) element modelling, computational times are generally not large, even with inelastic time

history analysis (**ITHA**), and current lap-top computers are capable of analysing complex structures under three-dimensional response. As a consequence of these considerations, the following discussion is limited to **ITHA**.

Inelastic time-history analysis provides the most accurate method for verifying that inelastic deformations and rotations satisfy the design limits, and also for determining the higher mode effects, which are needed for defining the required design strengths of capacity-protected members.

Despite the above comments relating to the suitability of lap-top computers for analysis, and by inference, the viability of **ITHA** in the design office environment, it must be recognized that a large number of subjective modelling decisions will generally be needed, and it is essential that the importance of these choices be properly understood by the analyst, who should have appropriate experience in **ITHA**, and knowledge of material behaviour before using it for design verification. The following attempts to provide some guidance in these choices.

(b) **Degree of Sophistication in Element Modelling:** The degree of sophistication in modelling, and the computational time, will largely be dictated by the choice of elements used in member modelling: line, fibre or solid elements. The choice should be dictated by Einstein's maxim, that analysis should be as simple as possible, but no simpler. In general this will result in a decision to use line elements.

(i) Line elements: Beams and columns in structural frames, bridge piers, wharf piles and other members whose connection to adjacent members can be idealized as a point connection are normally represented by line members. With suitable moment-rotation hysteresis characteristics, the non-linear flexural response characteristics can be modelled with considerable accuracy, and simplified representations of axial and shear deformations can also be included. Non-linear axial force/moment interaction envelopes enable the strength characteristics of columns to be represented with adequate accuracy.

Normally, bilinear moment rotation properties will be used to represent the strength envelope, with a lumped-plasticity representation. For concrete and masonry members, elastic and post-yield stiffness characteristics should be based on moment-curvature analysis of the member (see Section 4.2.1), with the elastic stiffness represented by the secant stiffness to the "first yield" point of the response (Fig.4.6). Thus, using the formulation of Section 4.2.6, the effective moment of inertia will be:

$$I_{eff} = \frac{M_N}{E.\phi_y} = \frac{M_y}{E.\phi_y'}$$ (4.87)

The post-yield stiffness will also be found from the moment-curvature response of the member considered, and a hysteretic rule will be chosen characteristic of the member type and material used. Hysteretic rules are discussed in more detail in Section 4.9.2(f).

In Section 4.4 it was noted that the elastic stiffness of reinforced concrete and (by analogy) reinforced masonry columns and walls is a function of the axial force. Thus in a frame, where the column axial force varies as a result of seismic response (e.g. columns **A** and **C** in Fig.4.30(a)), the elastic stiffness should also vary. Although many inelastic analysis computer codes can model the axial force/moment strength interaction, few have the capability of modelling the axial force/stiffness interaction. An exception is the 2D/3D code "**Ruaumoko**"[C1]. A "student" version of Ruaumoko, with restricted capabilities is included on the CD provided with this book. Lack of ability to model the axial force/stiffness relationship can result in significant errors in column member forces, particularly in the elastic range of response, but is unlikely to result in significant errors in displacements and inelastic rotations, nor in significant errors in steel frame member forces.

With frame analysis, careful consideration of modelling the beam-column joint stiffness is needed. A common error is to model the joint as effectively rigid. However, due to strain penetration, and joint shear deformation, the joint region is far from rigid, and may contribute as much as 30% to total lateral deformation[P1]. As illustrated in Fig. 4.30(b), a minimum acceptable representation of the joint region will be to use lumped-plasticity line members to represent the beam between the column faces, with a linear elastic portion of elastic stiffness equal to the beam elastic stiffness, from the joint centroid to the column face. If the column is to be modelled by an inelastic element, a

(a) Column Seismic Axial Forces   (b) Joint Representation
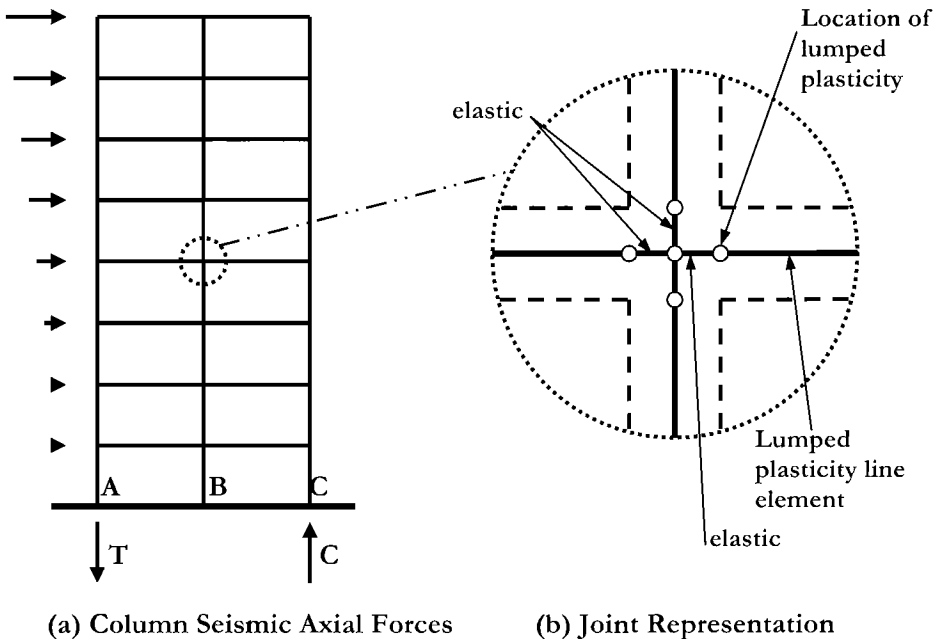
Fig. 4.30 Modelling a Regular Frame with Line Elements

similar treatment will be provided. However, if the design philosophy is to keep the column elastic, it may be adequate to use a simple column element from joint centroid to joint centroid, and eliminate the nodes at the top and bottom of the beam. Elastic members will not be appropriate for ground-floor columns, where column-base plastic hinges are expected to form. Some time-history analysis codes (e.g. Ruaumoko[C1]) enable special joint deformation elements to be located between the nodes at the joint boundaries. This will normally only be appropriate when it is desired to model joint failure.

The effects of strain penetration from critical sections into supporting members, briefly discussed above in relation to beam/column joints, must also be considered at the base of frame columns, and at top and bottom of bridge piers by additional elastic members. Numerical simulation of this is discussed in detail in Section 4.2.7. It is also important that the effects of foundation flexibility, including the foundation structure and the supporting soil be adequately modelled. There is little point in carrying out a sophisticated **ITHA** if a flexible foundation is unrealistically modelled as rigid. Vertical, translational and rotational stiffness may be modelled by elastic or inelastic springs. Specific advice is provided in chapters dealing with specific structural types.

(ii) Fibre elements: A number of **ITHA** codes (e.g. SeismoStruct[S11]) for concrete structures are based on representing the cross-section of linear members by a number of fibres, separately representing the concrete and reinforcing steel, as illustrated in Fig.4.31. The length of the member is divided into a number of segments, with each segment represented by fibre elements, and with the sections delimiting the segments following the Navier-Bernoulli approximation that plane sections remain plane. Each of the fibres represents an area of concrete, or a longitudinal reinforcing bar, and is given appropriate material properties to model reversed loading (i.e. arbitrary tension/compression histories). Typically, separate material rules are used for the unconfined cover concrete, and the confined core concrete, and in advanced formulations (e.g. SeismoStruct), the stress-strain properties of the confined concrete are automatically generated. Material stress is normally assumed constant between integration points along the fibre segment. The advantages of this more sophisticated representation of linear members are:

- No prior moment-curvature analysis of members is needed.
- The hysteretic response is defined by the material properties, and hence does not need to be defined.
- The influence of varying axial force on strength and stiffness is directly modelled.
- Simulation of biaxial loading, is as straightforward as uniaxial loading, with interaction between flexural strength in orthogonal directions being directly computed.
- Member post-peak strength reduction resulting from material strain-softening or failure can be directly modelled.

There are, however, also draw-backs to modelling using fibre-elements. With current formulations:
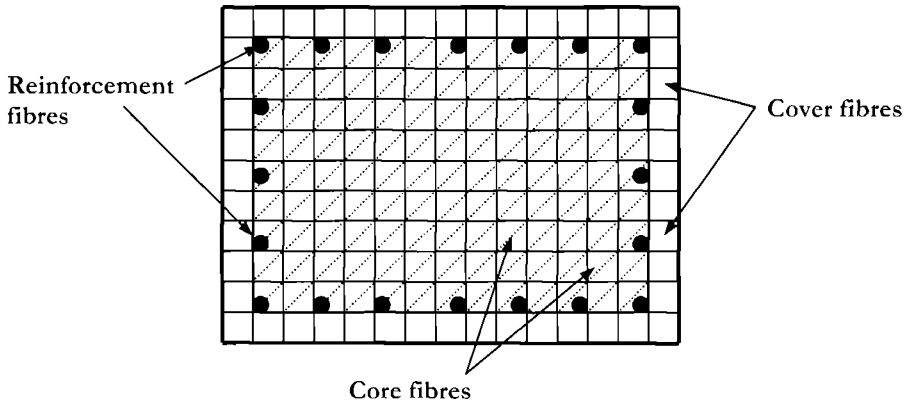
Fig.4.31   Section Modelling with Fibres

- Fibre elements model only flexural response. Shear strength and shear deformation are generally not modelled.
- The interaction between flexural ductility and shear strength (see Section 4.7.3) is not modelled.
- Shear deformation in joint regions must be modelled by special non-fibre elements.
- Integration of the segment curvatures to obtain rotations and displacements suffers from the same problems identified in Section 4.2.6 for direct integration of curvature from linear-member analysis. To some extent this can be obviated by adopting a critical segment length equal to the plastic hinge length computed in accordance with Eq.(4.30).
- If the moment in a segment is determined at the segment centroid, then the capacity of the structure may be over-estimated, since the moment at the critical section will exceed that at the segment centroid, which is the location where strength will be determined. Again this can be corrected in the analysis, by adjusting the location of critical segment boundaries (e.g. the beam-end at a beam-column interface) such that the integration gauss points coincide with the true boundary.
- Strain-penetration into foundations etc, requires special treatment.
- Properties for the confined core concrete may have to be manually defined. However, in some fibre analysis programs, as with some moment-curvature programs, the stress-strain characteristics of the core concrete are directly determined from the transverse reinforcement.
- Because of the large number of fibre elements needed to fully model a complex structure, computer time for **ITHA** can be very large with current computing power – as much as 24 hours for a single run. This makes design verification

impractical if (say) seven records are to be run. The problem may be particularly severe if 3-D response is needed.

It should be emphasised that in fibre analysis it is not essential, nor even desirable that all members (or even all segments of a member) be modelled by fibres. Joint rotations and foundation flexibility effects can be modelled by elastic or inelastic springs, with the appropriate degrees of freedom, and members expected to remain elastic with essentially constant stiffness may be modelled by elastic line elements. In fact, given the major current drawback of excessive computational time, this simplification should be adopted wherever possible. The fibre program "**SeismoStruct**" is provided on the attached CD.

(iii) Three-dimensional solid elements: Three-dimensional solid elements are used rather infrequently in ITHA, are of value only when modelling of complex intersections between members is required, and should only be attempted by highly specialized organizations. Computational effort is considerable, and in our view, existing formulations do not adequately represent bond-slip and anchorage of reinforcement, confinement effects, and the behaviour of unconfined or confined concrete under reversed flexure and shear loading where separate patterns of intersecting cracks may develop. The cost of ITHA using inelastic 3-D elements is typically high, and the accuracy of the results is difficult to assess. For these reasons, we believe design verification should be confined to line and fibre elements at the current state of the art.

*(c) **Two-dimensional or Three-dimensional Structural Representation?:*** All structures are three-dimensional. However, in many cases it will be reasonable to independently consider the seismic response in the principal directions, and hence to provide simpler two-dimensional representations of the structure. Examples are straight bridges, and symmetrical buildings where response in the orthogonal directions are likely to be essentially independent. Two-dimensional structural representation is generally significantly easier to develop and to interpret the results from than is the case with 3-D representation. Further, when columns are expected to respond inelastically in orthogonal directions (bridges, building column bases), 3-D analyses will require special hysteretic rules modelling the interaction of strength and ductility in orthogonal directions, unless fibre elements are used. Such rules are not readily available, and the current state-of-the-art is to model the ductility effects independently, though a biaxial strength envelope may be available, depending on the computer program used.

When significant torsional response is possible, as in wharves (see Chapter 12), and some buildings (Chapters 5, 6 and 7), then 3-D representation of the structural response is necessary. However, as, for example, discussed in Chapter 12 for wharves, it is sometimes possible to capture the salient features of the 3 D response with 2-D structural modelling.

*(d) **Strength Interaction Modelling:*** As discussed in Section 4.9.2(b) above, many **ITHA** programs provide means for modelling the axial-force/flexural-strength interaction, either directly, as in the case of fibre elements, or as specified input, as in the

case of line elements. However, as was discussed in Section 4.7.3 there is also an interaction between flexural ductility and shear strength with concrete structures. This is much more difficult to represent in **ITHA**, and we are not aware of any general-purpose **ITHA** program currently capable of modelling this interaction. For design verification this is not generally a problem, as the design philosophy will be to avoid shear failure, and the results from the **ITHA** in terms of member ductility and shear demand can be used in conjunction with the shear strength model of Section 4.7.3 to design the transverse reinforcement.

Where **ITHA** is used to assess the safety of an existing structure, the inability to model the shear-strength/flexural-ductility interaction envelope, and the subsequent rapid reduction in shear strength once the envelope has been reached is of more serious concern. Although it may be possible to identify the level of seismic intensity corresponding to just reaching the envelope, the increment of intensity required to cause collapse is currently beyond the capabilities of existing commercially available programs.

(e) Mass Discretization: Masses will normally be lumped at nodes, implying a degree of mass discretization. In some computer programs the discretization will be carried out automatically from values of element mass per unit length provided as input; in other programs the nodal masses will be directly input.

(i) Frame buildings: Referring again to Fig. 4.30(a), nodal masses in 2-D representations will normally be provided at the intersections of all beams and columns. This will enable realistic values for seismic axial forces in the beams to be determined. In some cases these axial forces can have a significant effect on beam moment capacities. However, in most cases it will be admissible to lump the entire floor mass at one representative node. In the case represented in Fig.4.30(a), this would clearly be the node defined by the central column. Note that tributary column mass is generally lumped at the floor levels above and below the column considered. Note also that increasing the number of nodal masses will increase the number of significant elastic modes, some of which will have very low periods. This can result in computational problems, and so excessive refinement of the mass distribution should be avoided.

When 3-D modelling and 2-D or 3-D seismic input is adopted, it is important that the mass torsional inertia is correctly represented. Referring to the plan simulation of a rectangular floor slab shown in Fig.4.32, a minimum of four nodes is required to fully represent the mass torsional inertia. Assuming that the mass is uniformly distributed, the distances of the mass node points are at the torsional radii of gyration respectively $(L/\sqrt{12})$ and $(B/\sqrt{12})$ from the floor centroid in the longitudinal and transverse directions.

(ii) Wall buildings: Similar considerations apply for wall buildings. Generally floor masses will be concentrated at the centreline of the wall or walls. Again, excessive refinement in the assumptions of the mass distribution should be avoided.
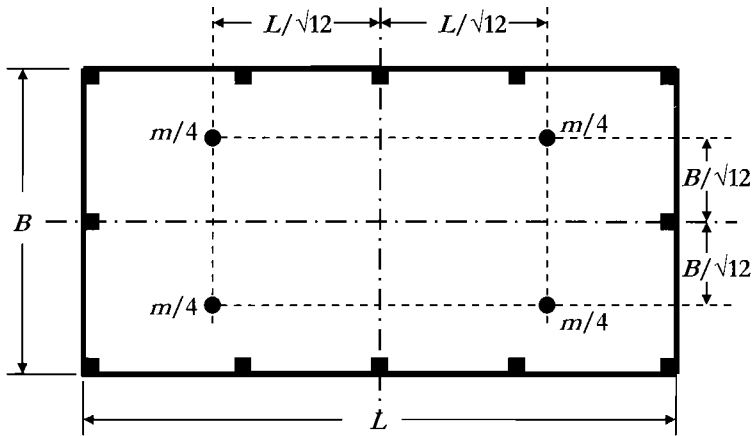
Fig.4.32   Plan Distribution of Mass for Torsional Inertia Modelling of a Building Floor Slab

(a) Multi-span Bridge

Deflection   Pier Geometry   Mass and Stiffness
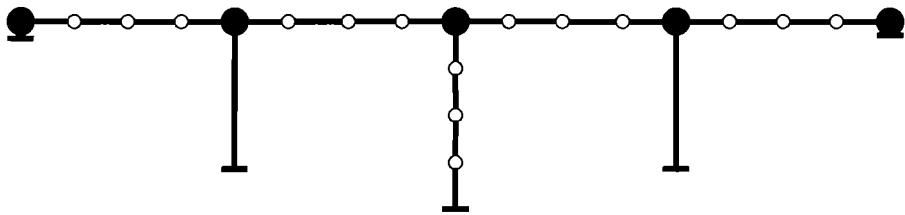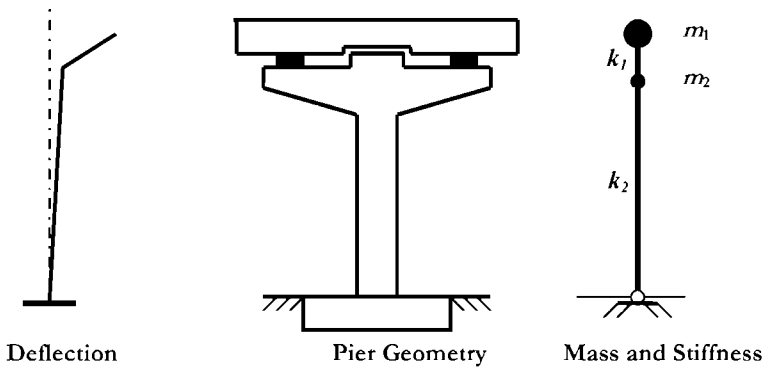
(b) Bearing-supported Superstructure

Fig.4.33   Mass Discretization for Bridge Inelastic Time-History Analysis

(iii)   Bridges: In most cases adequate accuracy can be obtained by lumping the superstructure mass above each pier, as indicated by the solid circles in Fig.4.33(a), which represent the tributary mass from a half-span on either side of the pier. A tributary mass is also shown at each abutment which should be included when abutment flexibility is modelled in the analysis. The lumped mass at the top of each pier should be located at the height of the centre of mass of the superstructure, and should include the pier-cap mass, and a proportion of the pier mass. If the pier is prismatic, and inelastic response is expected, then 1/3rd of the pier mass should be added to the superstructure mass[P4]. The simulation described will normally be adequate to obtain pier displacements and ductility demands.

Where superstructure moments and shears are of concern it may be necessary to represent the superstructure between piers by an increased number of elements, and to distribute the superstructure mass proportionately to the nodes, as suggested by the hollow circles in Fig. 4.33(a). Three internal nodes per span will generally be sufficient for this purpose. Similarly, for tall piers, where significant moments from the inertial response of the distributed pier mass can be expected, additional nodes up the pier height will be needed. Again, three internal nodes, as shown for the central column in Fig. 4.33~4.32(a) will generally be sufficient for this purpose.

When the superstructure is separated from the piers by flexible bearings (e.g. Fig.4.33(b)), and where pier mass is a significant proportion of the total mass, it will be necessary to separate the superstructure mass m_1 and the effective pier mass m_2 and locate each at the appropriate mass centres, because of the large difference in displacement between the top of the pier and the superstructure centre of mass. The discretization is shown to the right of Fig.4.33(b) where the different stiffness of the bearings (k_1) and pier (k_2) is identified, and a short strain-penetration length is indicated below the column base.

Further discussion on modelling bridges for **ITHA** is included in Chapter 10 and a more complete treatment of the subject is available in [P4].

(iv)   Wharves and piers: Mass modelling for concrete piers supported on moment-resisting piles follows the principles discussed in relation to Figs. 4.31 and 4.32, and is discussed in detail in Chapter 12.

(f)   *Hysteresis Rules:* The inelastic response of members in **ITHA** based on line members is defined by force-deformation equations describing the loading, unloading and reloading of the members. The collective equations describing the response for a given member are termed the hysteresis rule for the member. It is important that the hysteresis rule provides an accurate representation of the material and structural response of the member. It is demonstrated in Fig.4.37 that the equal-displacement approximation, which can be interpreted to indicate that the choice of hysteresis rule is of little importance, is based on invalid assumptions.

Figure 4.34 illustrates the basic shapes of a selection of hysteresis rules appropriate for structural analysis. In the sketches of Fig.4.34, response for stable cyclic response is

shown with the elastic and initial inelastic cycles shown by dotted lines, and subsequent cycles shown by solid lines. Where the initial and subsequent cycles coincide they are shown by solid lines. The elasto-plastic rule of Fig.4.34(a) has been widely used in **ITHA** in the past, but is of comparatively restricted applicability. It can be considered an approximation to the flexural response of steel beams and columns, provided the critical sections can be considered compact (no flange buckling) under inelastic response. However, the reduction of stiffness on unloading, (the Bauschinger effect) which causes rounding of the hysteretic response and a reduction of energy absorption of about 20% compared with elasto-plastic response, is not modelled. Elasto-plastic response is appropriate for seismic isolation systems using planar coulomb friction isolation sliders (e.g. **PTFE**/stainless steel flat bearings). For these elements the initial stiffness normally results from the structural elements, with the inelastic portion defined by essentially rigid/perfectly plastic behaviour of the slider.

The bilinear hysteretic response of Fig. 4.33(b) has a post-yield stiffness of 20% of the initial stiffness (i.e. $r = 0.2$), though the actual value of the post-yield stiffness will vary depending on the specific application. Compact steel sections are better represented by bilinear response with $0.02 < r < 0.05$ than by elasto-plastic response, which is a special case of bilinear response with $r = 0$. The high value of $r = 0.2$ in Fig 4.34(b) is representative of seismic isolation provided by elastomeric bearings or friction-pendulum systems, with the value of r depending on the initial structural stiffness, and the isolation system characteristics.

Figures 4.34(c) and 4.34(d) are based on the modified Takeda hysteresis rule[O1], and represent a range of hysteresis shapes appropriate for reinforced concrete and reinforced masonry structures. The modified Takeda rules are characterised by unloading and reloading stiffnesses that are significantly lower than the initial "elastic" stiffnesses. The "thin" hysteretic response of Fig. 4.34(c) is appropriate for inelastic members with significant axial load, such as building columns, bridge piers, walls and piles, and is a special case of the more general "fat" Takeda rule shown in Fig.4.34(d). For the thin Takeda rule the unloading stiffness is defined as:

$$k_u = k_i . \mu^{-0.5} \tag{4.88}$$

where μ is the displacement ductility at the initiation of unloading. On the initial cycle the rule reloads to the elastic yield point in the reversed direction, but on subsequent cycles it reloads to the previous maximum force-displacement point. This is a special case of the "fat" rule, with $\beta = 0$.

The "fat" Takeda rule of Fig.4.34(d) incorporates the "thin" rule as a special case, as noted above, and has an unloading stiffness defined by

$$k_u = k_i . \mu^{-\alpha} \tag{4.89}$$

(a) Elasto-Plastic (Steel)

(b) Bilinear, r=0.2 (Isolation Unit)

(c) "Thin" Modified Takeda (r.c.column)

(d) "Fat" Modified Takeda (r.c. beam)

(e) Flag (Hybrid prestressed concrete)

(f) Gapping (soil)
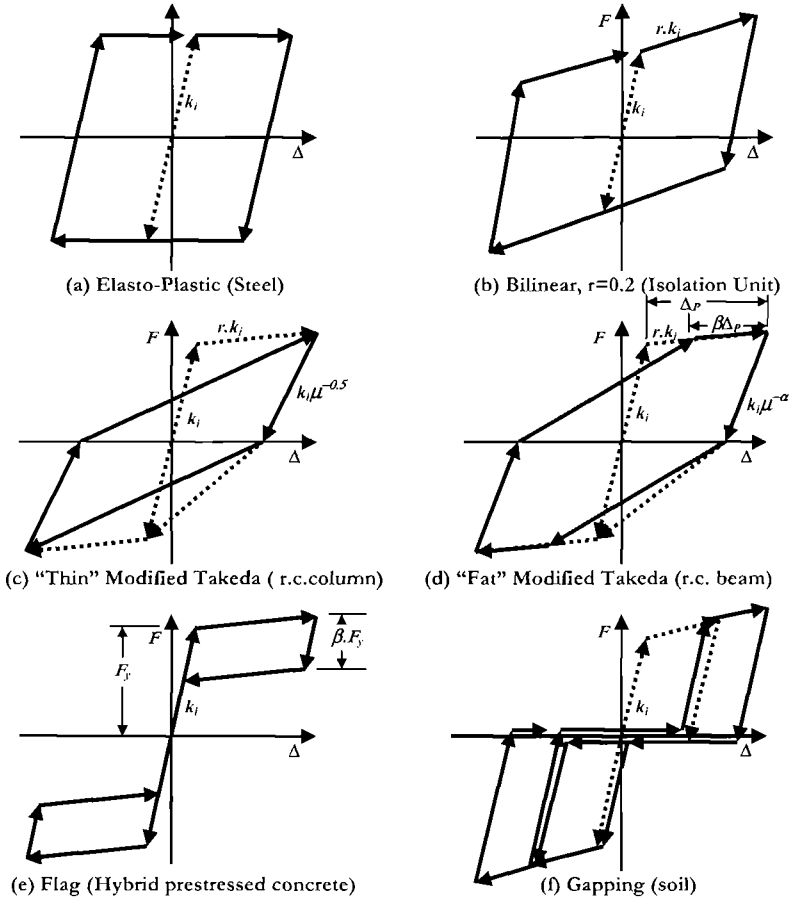
Fig. 4.34   A Selection of Hysteresis Rules Appropriate for Inelastic Time-History Analysis

where $0 < \alpha < 0.5$, and μ is again the displacement ductility. A value of $\alpha = 0$ implies unloading with the initial stiffness. The rule reloads to a point defined by $\beta \Delta_P$ (see Fig. 4.34(d)) from the previous peak displacement in the direction of loading considered, where Δ_P is the plastic displacement. For well-detailed reinforced concrete beams, values of $\alpha = 0.3$, and $\beta = 0.6$ are generally considered to be appropriate.

Note that with the Takeda rules, the initial stiffness should be the value applying at first yield, taking into account the reduction in effective stiffness resulting from flexural and shear cracking (Eq.(4.86)).

Figure 4.34(e) describes a flag-shaped hysteresis rule suitable for modelling the response of hybrid prestressed members. In hybrid members (see Section 5.11.2) the prestressing steel is unbonded, resulting in a non-linear elastic force-displacement

characteristic. The energy dissipation in hybrid systems, shown in Fig.4.33(e) results from yield of special mild-steel bars which contribute to both flexural strength and energy dissipation. Further details are given in Chapter 5.

Finally, Fig. 4.34(f) shows a hysteresis rule appropriate for a spring representing non-linear soil response, such as might occur in the soil near the top of a laterally loaded pile. After an initial cycle involving inelastic response of the soil spring, the soil separates from the pile, leaving a gap. On reloading in the same direction there will be no soil reaction until this gap is closed. Typically inelastic soil response has a comparatively high post-yield stiffness, as illustrated in Fig.4.34(f).

(g) Elastic Damping Modelling: It is common to specify a level of elastic damping in **ITHA** to represent damping in the initial stages of response, before hysteretic damping is activated. This is normally specified as a percentage, typically 5%, of critical damping. There are a number of ways this damping could be defined, as discussed subsequently, but the principal difference is whether the damping force is related to the initial or tangent stiffness. In the hysteresis rules of Fig.4.34, the initial stiffness is k_i in all cases, but the tangent stiffness, rk_i (see Fig 4.34) reduces to a lower value once the displacements exceed yield.

Typically research papers reporting results on single-degree-of-freedom (**SDOF**) **ITHA** state that 5% elastic damping was used, without clarifying whether this has been related to the initial or tangent stiffness. With multi-degree-of-freedom (**MDOF**) analyses, the situation is often further confused by the adoption of Rayleigh damping, which is a combination of mass-proportional and stiffness-proportional damping. It is our understanding that many analysts consider the choice of the initial elastic damping model to be rather insignificant for either **SDOF** or **MDOF** inelastic analyses, as the effects are expected to be masked by the much greater energy dissipation associated with hysteretic response. This is despite evidence by others (e.g. [O4]) that the choice of initial damping model between a constant damping matrix and tangent-stiffness proportional damping matrix could be significant, particularly for short-period structures.

The difference between initial-stiffness and tangent stiffness damping is discussed with reference to Fig. 4.34(d). For **SDOF** systems, the constant value of the damping coefficient is determined with respect to the initial vibration frequency, $\omega = \sqrt{k_i / m}$, the initial loading stiffness k_i and a specified fraction of critical damping, ξ:

$$c = 2m\omega_i \xi = 2\xi \sqrt{mk_i} \ . \tag{4.90}$$

The damping force at any instant is thus

$$F_D = c\dot{x} \tag{4.91}$$

where $\dot{x}$ is the instantaneous relative velocity.

With tangent-stiffness damping the damping coefficient is proportional to the instantaneous value of the stiffness and it is updated whenever the stiffness changes. Thus the damping coefficient given by Eq.(4.90) is multiplied by $\sqrt{k_t/k_i}$, where k_t is the instantaneous tangent stiffness. With reference to Fig.4.34(d), the damping coefficient will equal that associated with the initial-stiffness value only in the initial elastic response. After first yield, the damping coefficient will be referenced to the post-yield, the unloading or the reloading stiffness. With the case of elasto-plastic response, the damping force will be zero while the structure deforms along a yield plateau.

There are three main reasons for incorporating elastic damping in **ITHA**:

- The assumption of linear elastic response at force-levels less than yield: Many hysteretic rules, including all those shown in Fig.4.34 make this assumption, and therefore do not represent the nonlinearity, and hence hysteretic damping within the elastic range for concrete and masonry structures, unless additional elastic damping is provided.
- Foundation damping: Soil flexibility, nonlinearity and radiation damping are not normally incorporated in structural time-history analyses, and may provide additional damping to the structural response.
- Non-structural damping: Hysteretic response of non-structural elements, and relative movement between structural and non-structural elements in a building may result in an effective additional damping force.

Discussing these reasons in turn, it is noted that hysteretic rules are generally calibrated to experimental structural data in the inelastic phase of response. Therefore additional elastic damping should not be used in the post-yield state to represent structural response except when the structure is unloading and reloading elastically. If the hysteretic rule models the elastic range nonlinearly (as is the case for fibre-element modelling) then no additional damping should be used in ITHA for structural representation. It is thus clear that the elastic damping of hysteretic models which have a linear representation of the elastic range, and which hence do not dissipate energy by hysteretic action at low force levels would be best modelled with tangent-stiffness proportional damping, since the elastic damping force will greatly reduce when the stiffness drops to the post-yield level. It should, however, be noted that when the post-yield stiffness is significant, the elastic damping will still be overestimated. This is particularly important for hysteretic rules such as the modified Takeda degrading stiffness rule which has comparatively high stiffness in post-yield cycles.

If the structure deforms with perfect plasticity, then foundation forces will remain constant in the structural post-yield stage, and foundation damping will cease. It is thus clear that the effects of foundation damping in **SDOF** analysis are best represented by tangent stiffness related to the structural response, unless the foundation response is separately modelled by springs and dashpots.

It is conceivable, though unlikely, that the non-structural damping force is velocity-dependent rather than strength-limited, and hence a constant damping coefficient may bea reasonable approximation for the portion of "elastic" damping that is attributable to

non-structural forces. There are two possible contributions to non-structural damping that should be considered separately:
- Energy dissipation due to hysteretic response of the non-structural elements
- Energy dissipation due to sliding (relative movement) between non-structural and structural elements.

For a modern frame building, separation between structural and non-structural elements is required, and hence they should not contribute significantly to damping. Further, even if not separated, the lateral strength of all non-structural elements is likely to be less than 5% of the structural lateral strength (unless the non-structural elements are masonry infill). If we assume 10% viscous damping in these elements, an upper bound of about 0.5% equivalent viscous damping related to the structural response seems reasonable. Non-structural elements are unlikely to play a significant role in the response of bridges.

Sliding will normally involve a frictional force, with the value dependent on the friction coefficient, and the weight of the non-structural element. Unless the non-structural elements are masonry, the friction force is likely to be negligible. It should be noted that it is probable that so-called non-structural masonry infill initially contributes more significantly to strength, stiffness, and damping than is the case with (e.g.) lightweight partitions. However, it is known that the strength degrades rapidly for drift levels > 0.5% (which is generally less than structural yield drift). The damping force is also likely to degrade rapidly.

It is thus recommended that for modern buildings with separated or lightweight non-structural elements, elastic damping should be modelled by tangent stiffness proportional damping. The effects of non-structural masonry infill should be modelled by separate structural elements with severely degrading strength and stiffness - not by increased viscous damping.

It is instructive in determining the influence of alternative elastic damping models to consider the steady-state, harmonic response of an inelastic **SDOF** oscillator subjected to constant sinusoidal excitation. This enables direct comparison between hysteretic and elastic damping energy, and also between elastic damping energy using a constant damping coefficient and tangent-stiffness proportional damping models. To this end, Fig.4.35 shows response of a simple **SDOF** oscillator with initial period of 0.5 sec and a "thin" modified Takeda hysteresis rule (Fig.4.34(c)) subjected to 10 seconds of a 1.0 Hz forcing function. The steady-state response of the pier corresponded to a displacement ductility of about 7.7 — at the upper limit of reasonable ductile response.

Results for the stabilised loops, ignoring the transitory first three seconds of response are plotted in Fig. 4.35(a) (initial-stiffness proportional damping) and Fig. 4.35(b) (tangent-stiffness proportional damping). In each case the hysteretic response associated with nonlinear structural response is plotted on the left, and the elastic damping force-displacement response is plotted to the right. The areas inside the loops indicate the relative energy absorption. For the case with initial-stiffness proportional damping, the

energy absorbed by elastic damping is approximately 83% of the structural hysteretic energy dissipation, despite the high ductility level. This might be surprising when it is considered that the elastic damping corresponds to 5% of critical damping, while the hysteretic damping is equivalent to about 20% of critical damping.   This apparent anomaly is due to the different reference stiffness used.   The elastic damping is related to
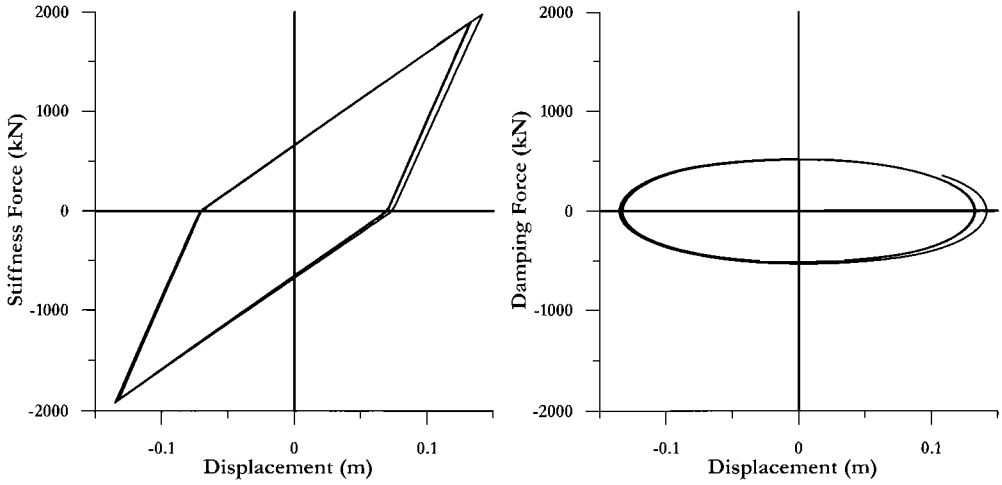
(a) Analysis with Initial Stiffness Damping
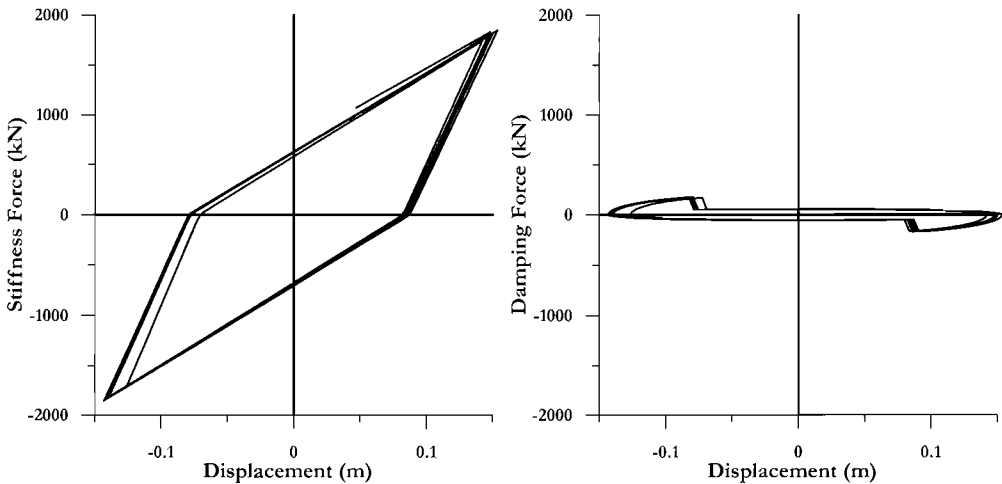
(b) Analysis with Tangent Stiffness Damping

Fig.4.35   Steady-state Inelastic response of an SDOF oscillator with "Thin" Modified Takeda hysteresis

the initial stiffness, whereas the hysteretic damping is related to the secant stiffness to maximum response.

When the elastic damping is tangent-stiffness proportional, as we believe to be most appropriate for structural response, the elastic damping energy is greatly reduced, as can be seen by comparing the upper and lower right-hand plots of Fig. 4.35. In the lower plot, the reduction in damping force corresponding to the stiffness change is clearly visible. In this case, the area of the elastic damping loop is only about 15% of the structural hysteretic energy dissipation.

Analyses of **SDOF** systems subjected to real earthquake records show that the significance of the elastic damping model is not just limited to steady-state response. Figure 4.36 shows a typical comparison of the displacement response for **SDOF** oscillators with initial stiffness and tangent stiffness elastic damping. In this example the El Centro 1940 NS record (amplitude scaled by 1.5) has been used, the initial period was 0.5 seconds, a Takeda hysteretic rule with second slope stiffness of 5% was adopted, and the force-reduction factor was approximately 4. The peak displacement for the tangent-stiffness elastic damping case is 44% larger than for the initial-stiffness damping case, indicating a very significant influence.

A selection of results from a series of analyses of oscillators with different initial periods between 0.25 sec and 2.0 sec, subjected to ATC32[X2] spectrum-compatible
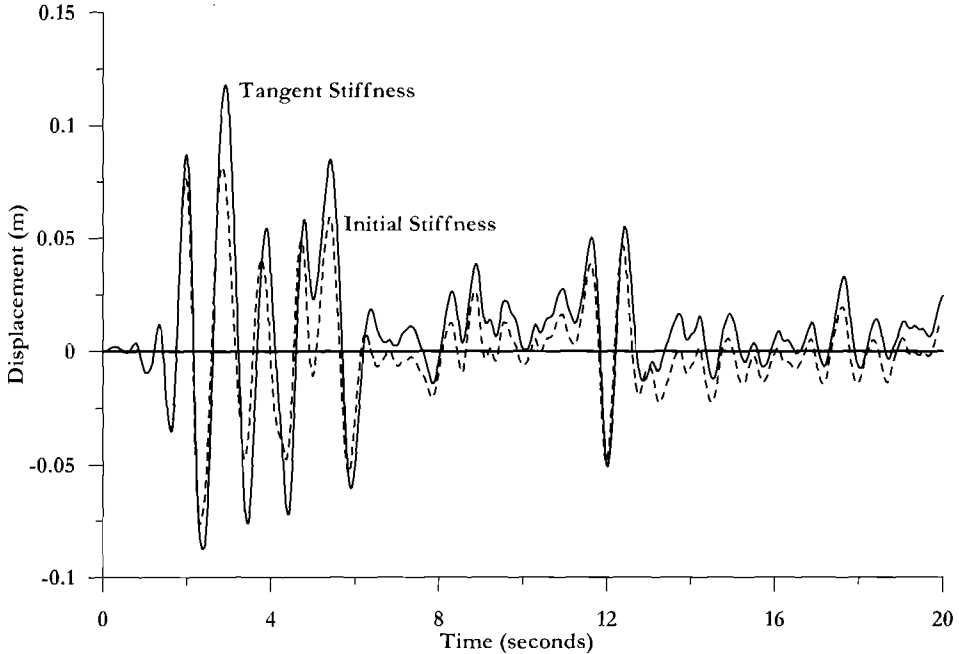
Fig 4.36   Response of an SDOF Oscillator to 1.5×El Centro 1940,NS (T=0.5 sec)

accelerograms is shown in Figure 4.37, which plots the ratio of peak inelastic displacement response to peak elastic displacement response. Elastic analyses, using 5% damping (note that the choice of damping model is irrelevant for elastic analysis) were first carried out, then inelastic analyses where either initial-stiffness or tangent-stiffness 5% damping were specified, with yield strengths based on force-reduction factors of R=2, 4 and 6 based on the average elastic response peak force. Modified Takeda (representing concrete response), Bilinear (approximating steel) and Flag (representing hybrid prestressed precast concrete) hysteresis rules were considered.

The second-slope stiffness ratio for the "Thin" Takeda (Fig.4.34(c)) and bilinear rules for these analyses was $r = 0.002$ (the minimum value considered), but similar results were obtained for $r = 0.05$ (the maximum considered). The flag hysteresis results in Fig.4.36 were based on the minimum additional damping considered in the hybrid precast modelling (β =0.35, see Fig.4.34(e)). Note that in some cases the displacement ratios at T = 0.25 sec. have not been plotted as they exceed the range included by the graph axes.

From examination of Figure 4.37 it will be noted that there is a significant difference between the response of the initial-stiffness and tangent-stiffness (identified as **IS** and **TS** respectively) models, that this difference is rather independent of initial period, for T>0.5 seconds, that the difference increases with force-reduction factor, and is dependent on the hysteretic rule assumed. It will also be noted that though the "equal displacement" approximation (represented by a displacement ratio of 1.0 in Figure 4.37) is reasonable for initial stiffness damping and initial periods greater than T = 1.0 seconds, it is significantly non-conservative for tangent-stiffness elastic damping.

It is thus recommended that for modern buildings with separated or lightweight non-structural elements, elastic damping should be modelled by tangent-stiffness proportional damping. Note, however, that the specification of tangent-stiffness Rayleigh proportional damping for **MDOF**, multi-storey buildings will not have the desired effect, since most of the elastic damping in the critical first mode will be mass-proportional, which is constant with inelastic action. Consider the basic form for the fraction of critical damping in the Rayleigh damping model:

$$\xi = \frac{1}{2}\left(\frac{\alpha}{\omega_n} + \beta\omega_n \right) \tag{4.92}$$

where α and β are the coefficients associated with mass proportional and stiffness proportional damping respectively, and ω_n is the circular frequency. If we specify the same value (say 5%) for ξ at two different frequencies, where the higher one is κ times the lower (fundamental) frequency, then:

$$\xi = \frac{1}{2}\left(\frac{\alpha}{\omega_1} + \beta\omega_1 \right) \tag{4.90}$$

and

(a) Takeda (concrete) hysteresis

(b) Bilinear hysteresis

(c)Flag Hysteresis
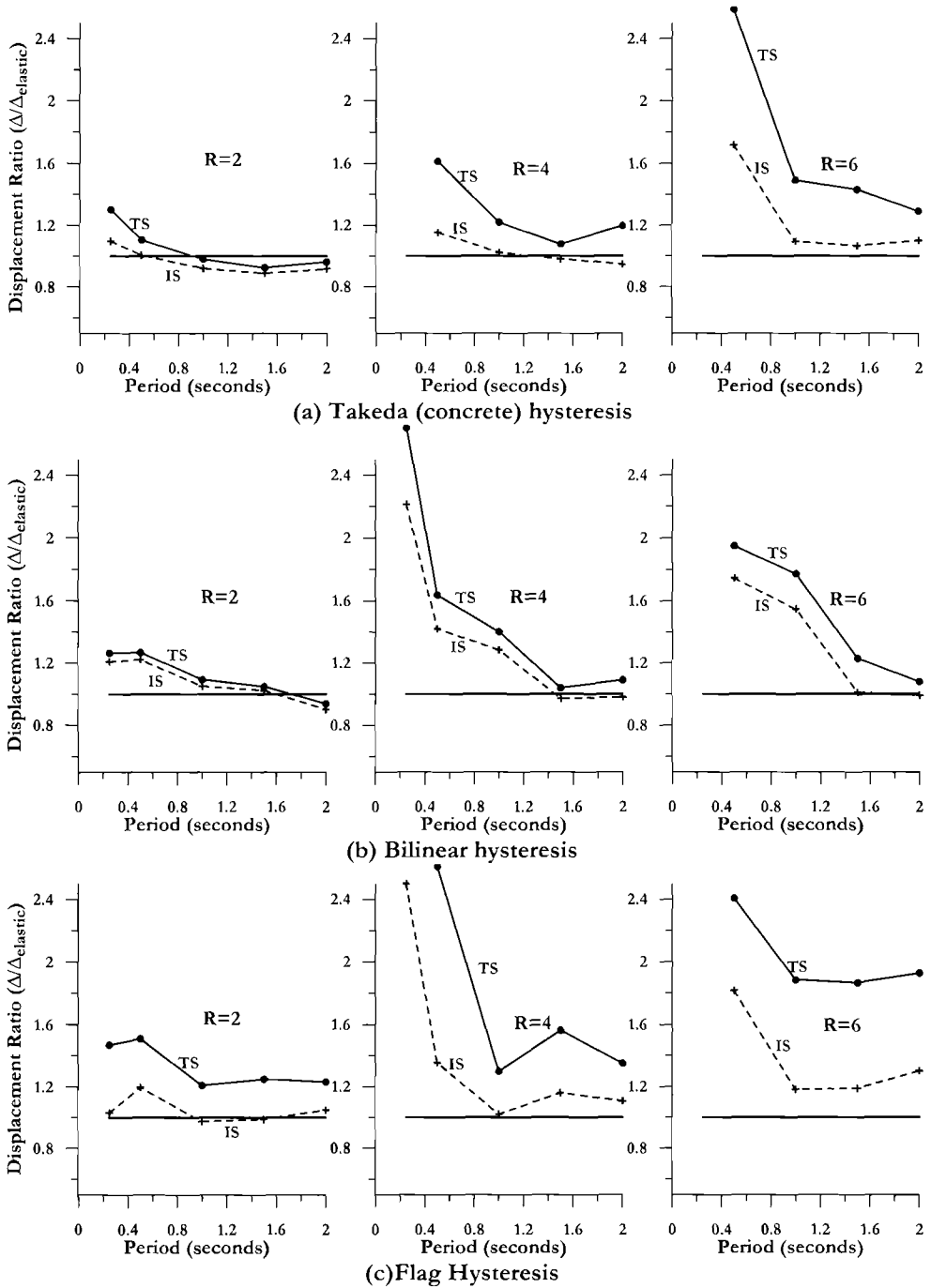
Figure 4.37   Response of SDOF Oscillators to ATC32 Spectrum-Compatible
Accelerograms

$$\xi = \frac{1}{2}\left(\frac{\alpha}{\kappa\omega_1} + \beta\kappa\omega_1 \right) \qquad (4.91)$$

Subtracting Eq. (4.91) from κ times Eq.(4.90):

$$\xi(\kappa-1) = \frac{\alpha}{2\omega_1}\left(\frac{\kappa^2 - 1}{\kappa} \right), \qquad (4.92)$$

and hence the damping $\alpha/2\omega_1$ associated with mass proportional damping in the first mode is $\xi\kappa/(\kappa+1)$, while the damping attributed to stiffness proportional damping in the first mode is $\xi/(\kappa+1)$.

Consider the case where we specify 5% damping at T_1 = 1.5 sec and T_2 = 0.3 sec. Hence $\kappa = 5$. Then, even if we specify tangent-stiffness proportional Rayleigh damping, only 0.83% is stiffness proportional in the critical first mode, while 4.17% is mass proportional, and hence acts in an identical manner to initial-stiffness damping when the structure responds inelastically.

It is clear from the above discussion that it will be difficult to obtain the correct simulation of tangent-stiffness elastic damping, when Rayleigh damping is specified. It will always be preferable to specify pure tangent-stiffness damping, at least for the fundamental mode. This option may not be available with commercially available **ITHA** codes, and an acceptable alternative is to specify an artificially low damping coefficient, ξ^* in the fundamental mode. Based on the discussion on significance of elastic damping to **DDBD**, presented in Section 3.4.3, this value should be approximately:

$$\xi^* = \frac{\xi(1 - 0.1(\mu - 1)(1 - r))}{\sqrt{\mu/(1 + r\mu - r)}} \qquad (4.93)$$

A more complete discussion of the issues related to elastic damping is available in [P16, and G2].

(h) Choice, Number, and Character of Accelerograms for Design Verification:

(i) Number of records: Two alternatives are generally defined by codes (e.g. X3,X4) for the number of accelerograms to be used in design verification. The first involves using three spectrum-compatible records, with the design response being taken as the maximum from the three records, for the given response parameter (displacement, shear force etc) investigated. The second uses a minimum of seven spectrum compatible records, with the average value being adopted for the response parameter considered. Because of the simplicity of **ITHA** with modern computing power, the latter approach is now almost always adopted, and there appears to be a tendency to increase the number of records above the minimum of seven, to ensure a more representative average.

(ii) Selection of records: There are three basic choices for the means of obtaining spectrum-compatible accelerograms:

- Amplitude scaling of acceleration records from real earthquakes to provide a "best fit" to the design spectrum over the period range of interest.
- Generating artificial spectrum-compatible records using special purpose programs.
- Manipulating existing "real" records to match the design spectrum over the full range of periods.

When the records are obtained by amplitude scaling of existing records, the scatter between records is likely to be large, and hence a larger number of records might be needed to obtain a reliable average. Care has to be exercised in selecting the period range over which the spectrum matching is obtained. In Fig. 4.38, which shows the matching referred to the 5% damping elastic displacement spectrum, the matching has been reasonably achieved over the period range encompassing the first three elastic periods, which might be considered adequate. However, it is seen that at periods longer than the fundamental period, displacements of the scaled spectrum are significantly lower than the design spectrum. It is important to match the spectrum for a period range that includes the period shift expected as the structure responds inelastically. This is shown in Fig.4.38 for a displacement ductility of $\mu = 3$. In this example, the scaled displacement spectrum becomes increasingly deficient in displacement demand, compared with the design spectrum, as the period increases above the elastic period, resulting in an unconservative estimate of the inelastic displacement from the time-history analysis. Of course, this argument applies to a single record. If a large number of records are used such that the average of the displacement spectra over the full range from elastic to inelastic period matches the design spectrum, valid average results can be expected. Unfortunately this is unlikely to be the case for longer period structures, since the large majority of records used in the analyses tend to have peak spectral displacements at periods from 1.0-2.0 seconds. In this case there is likely to be a consistent deficit in displacement demand at the degraded (inelastic) fundamental period, regardless of how many records are used. Thus conclusions about structural response for structures with expected displacement ductilities of (say) $\mu = 4$ and elastic periods of $T > 0.75$ seconds can be expected to be suspect, unless the earthquake records are very carefully chosen. Note that though the argument above has referred to code spectrum matching, it also applies to more general studies related to investigation of the relationship between elastic and inelastic displacement.

The second alternative involves artificially generated accelerograms, using programs such as SIMQKE[G6]. These can be matched to the design spectrum for the full period range with comparatively small error, and can be given the general character of an initial segment of increasing intensity, a duration of essentially constant intensity, and a final segment of reducing intensity. A lesser number of records are required to obtain a meaningful average using artificial records. An objection commonly voiced about artificial records is that they are too severe, in that real records are not spectrum-compatible over
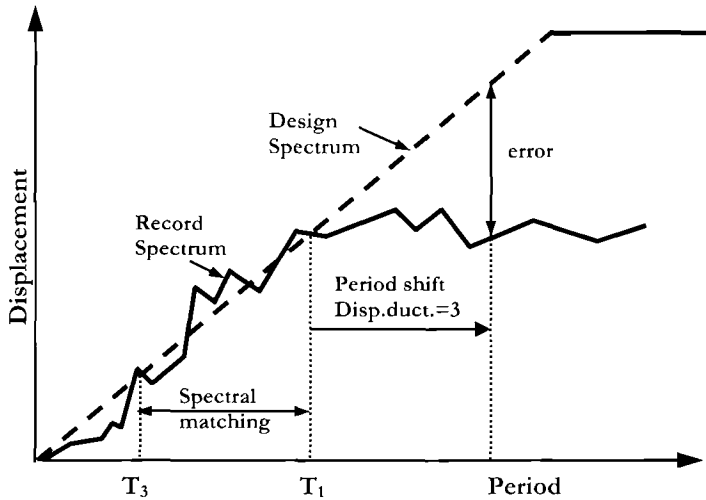
Fig.4.38   Displacement Spectrum Matching for Inelastic Time-History Analysis

the full period range, and that artificial records typically have a longer duration than real records. The first of these arguments cannot be accepted, since the larger number of real records needed to obtain a full spectrum matching should produce essential identical results, and the artificial records can be considered as a more efficient means of obtaining the same results. The second objection – excessive duration – is unlikely to be of concern when the analyses are being carried out for verification of a new design. When the analysis is carried out on an existing structure which is expected to degrade in strength under the design spectrum, then duration may be significant. However, it should be recognized that few **ITHA** programs based on line elements have the ability to accurately model strength degradation, though this is sometimes available with fibre elements.

Recently, the third option, where existing recorded accelerograms are manipulated to obtain full spectrum matching, has become more common. This method has the advantage over pure artificial records that the essential character of the original record is preserved. Thus, records that conform to the type of source characteristics expected (e.g. strike/slip, subduction, near-field forward directivity etc.) can be selected. This is important, since the spectrum matching will normally be done at 5% damping, and the characteristics at different levels of effective damping will depend on the source characteristics and distance from the fault plane. However, to obtain the required spectrum matching, the duration of the record typically has to be extended, opening the method to the same objection as directed against artificial records. Figure 4.39 shows typical spectral matching of acceleration and displacement spectra based on manipulating seven real accelerograms.

(iii) Multi-component Accelerograms: When structural response is likely to be influenced by 2-D or 3-D effects – that is, when the response in orthogonal directions cannot reasonably
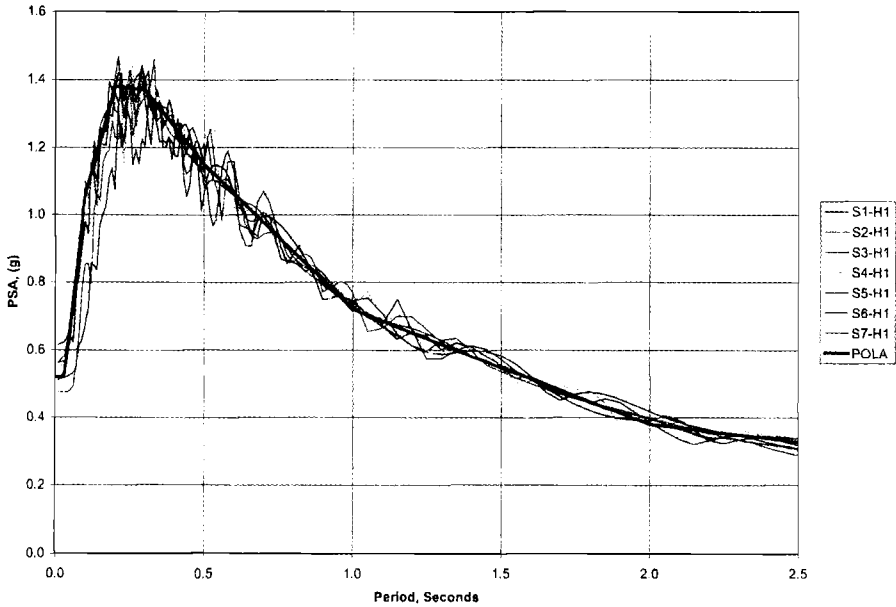
(a) Acceleration Spectra
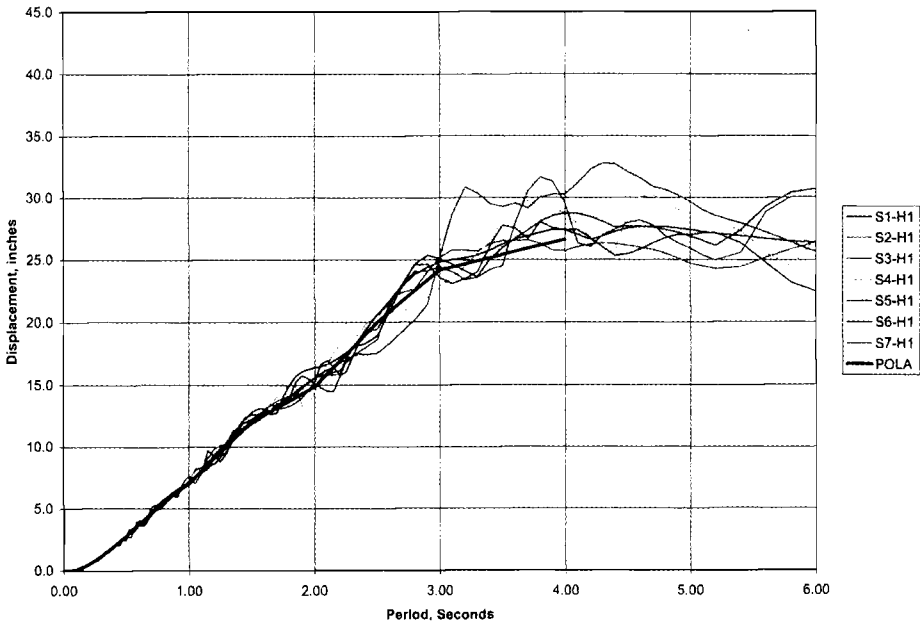
(c) Displacement Spectra
Fig. 4.39   5% Spectral Matching Using Manipulated Real Records[E1]

be de-coupled, the accelerograms will have to include two or three orthogonal components. The generation of the characteristics of the various components needs careful consideration. Examination of recorded three-component accelerograms reveals that the two horizontal components have different spectral shapes and intensities, but it does not seem that there is a consistent difference when decomposed to fault-normal and fault-parallel directions. Thus choice of a predominant, or principal direction of attack does not seem feasible at this stage of knowledge. Consequently site-specific design spectra are generally generated using the average of fault-normal and fault-parallel attenuation relationships. In the event that a code-specified spectrum is adopted, this will almost certainly be independent of orientation.

The vertical component typically has lower peak spectral acceleration intensity – a value of 0.67 times the peak horizontal spectral acceleration intensity is often quoted, though this appears to depend on distance from the fault, hypocentral depth, and ground material – and a systematic difference in spectral shape, with peak acceleration intensity typically occurring at a lower period than for the horizontal components, and with intensity reducing with period more rapidly than with the horizontal components[E1]. Recent near-field accelerograms of shallow earthquakes have indicated vertical accelerations that have in many cases exceeded the peak horizontal components.

The above discussion raises the question of how the orthogonal components of real records should be scaled. In the following it is assumed that no preferential direction for the design spectrum has been identified. There are a number of possibilities:

- Systematically rotate the axes of the two horizontal records, to determine the principal direction, and generate new major and minor principal-direction accelerograms. Scale the major principal record to the design spectrum, and use the same scaling factor for the minor horizontal and the vertical components.

- Scale the larger of the records to the design spectrum, without determining the principal direction, and use this scaling factor for the other two components.

- Scale both horizontal records independently to the design spectrum, and scale the vertical spectrum to the vertical design spectrum.

It might appear that the first, or possibly the second alternative is the most satisfactory. However, without a knowledge of the direction in which the major component should be applied with respect to the structure axes (which is the current state of the science), multiple analyses would be required, with the direction of the horizontal components rotated by (say) 15° between successive analyses to capture the maximum response. This approach also has the disadvantage of not recognizing how the design spectrum is obtained. As noted above, attenuation relationships used to generate site-specific design spectra normally are based on the average of fault-normal and fault-parallel response. Thus no specific principal direction is implied by the design spectrum. It thus appears that both records should be scaled to the design spectrum. Since the records will have low cross-correlation, it is expected that the elastic response displacement in any direction will be similar, when the two horizontal components are applied simultaneously in any two orthogonal directions. This is illustrated in Fig. 4.40, where the response displacements for different bearings are compared with the design

1-Second Period,
Ave.=7" vs. target=7.05"

1.5-Second Period,
Ave.=11.7" vs target=12.1"

2-Second Period,
Ave.=15.2" vs target=14.8"

3-Second Period
Ave.=23.6" vs target=24.2"

4-Second Period,
Ave.=27.2" vs target=26.6"

5-Second Period,
Ave.=25.5" vs target=27.8"
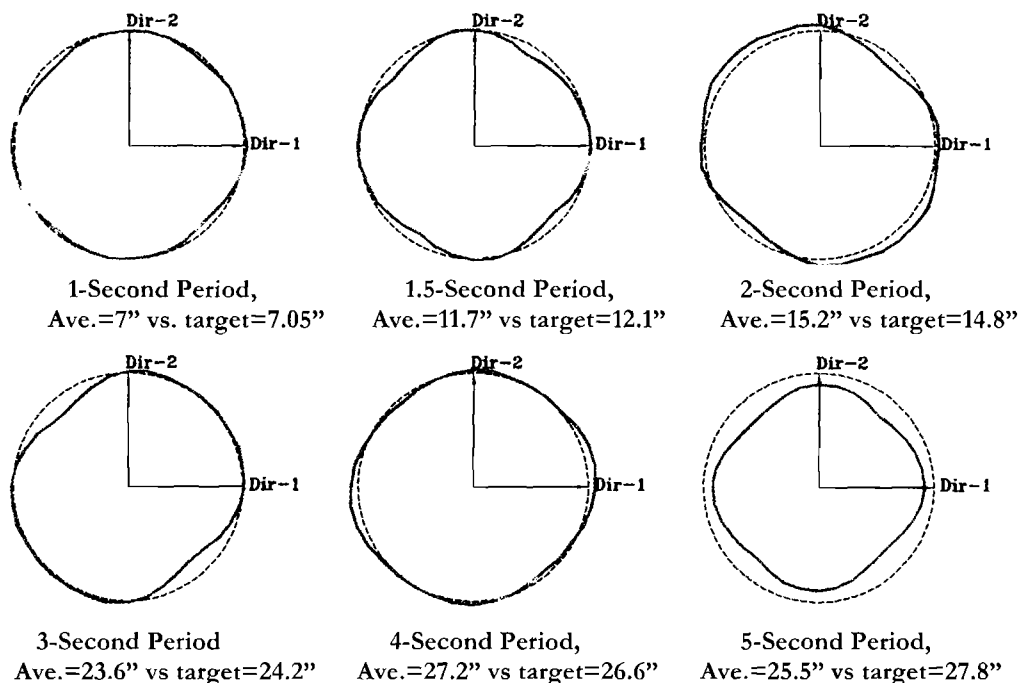
Fig.4.40   Response Displacements in Different Bearings for Two-component Spectrum-Compatible Records Applied in the NS and EW directions, Compared with the Spectrum Targets[E1]

values for different specified elastic periods, and with the two spectrum-compatible components applied in the NS and EW directions. The data, and records, relate to a study for the Port of Los Angeles[E1] and are the average of seven spectrum-compatible accelerogram pairs. It will be seen that good agreement with the circular design response is obtained for all except T=5sec, which was beyond the period range of interest.

This approach appears more compatible with the way in which the design spectra are generated, and has the great advantage that a single analysis related to any chosen set of axes is sufficient, rather than the multiple analyses required by the first two alternatives. It should, however, be applied with some caution. When excitation in one direction produces significant displacement response in the orthogonal direction, it would appear that use of two spectrum-compatible records will produce higher estimates of peak displacement than use of scaled major and minor principal-direction accelerograms rotated to a series of possible orientations, as discussed above.

(i) Averaging Results from Multiple Analyses: It might be considered that averaging the results from a set of (say) seven spectrum-compatible records or record pairs is
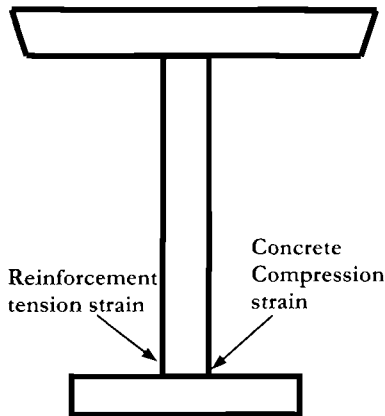
Maxima Displacements

Record	Δ Positive	Δ Negative
1	6.341	**-6.347**
2	4.891	**-7.945**
3	**8.948**	-3.179
4	4.486	**-6.543**
5	**6.148**	-4.569
6	**6.198**	-4.710
7	4.667	**-7.032**
Average	**5.954**	**-5.761**

Fig.4.41 Bridge Pier Response Displacements from Seven Spectrum-Compatible Accelerograms

straightforward. In fact some careful consideration of rather simple probabilistic aspects is required. Consider the response displacements of the simple bridge pier shown in Fig. 4.41, subjected to uniaxial seismic excitation. The table indicates the positive and negative displacement maxima obtained from each of seven spectrum-compatible accelerograms, and the averages for the positive and negative directions. The maximum of the positive and negative displacement for each record is highlighted with bold text. What is the correct average response displacement? If the absolute value of the response displacement is of interest, then the average of the highlighted values should be used, giving a value of 7.023, which is 18% and 22% higher than the averages in the positive and negative directions respectively. However the absolute maximum displacement, regardless of sign, is unlikely to be a significant design parameter. If longitudinal response is considered, the displacement may be required to determine whether a movement joint closes up, causing impact, or opens up sufficiently to cause unseating. In this case, since the critical displacements will be different in the different directions, the sign of the displacement is important.

Under transverse (or longitudinal) response, the displacements may be critical to determine whether steel and concrete strain limits are exceeded in the plastic hinge region. The critical locations of the pier for positive displacement are indicated in Fig. 4.41. For these two locations and design parameters (concrete compression strain, and reinforcement tension strain) it would clearly be inappropriate to include the negative displacements in the averaging, since these provide strains of the incorrect signs in the critical region.

The argument supporting the inclusion of the larger negative displacements is to note that the polarity of the excitation for a given record is arbitrary, and hence the displacement signs are arbitrary, indicating that averaging the larger of the positive and

negative displacements is correct. This argument is, however, invalid, as it implies considering the response for both negative and positive polarities, (which essentially implies consideration of 14 rather than 7 accelerograms), selecting the response of the seven largest, and discarding the response of the seven smallest. From a probabilistic viewpoint it would be equally valid to select the seven smallest and discard the seven largest. In fact it is obvious that no selection can be justified, and if both positive and negative polarities are considered, the results of all 14 records should be averaged. Using the data of Fig. 4.41, this would result in a design displacement of 5.858, 17% lower than the value from averaging the peak displacement magnitudes.

Averaging the positive and negative displacements would only be valid if the structure has symmetric strength and stiffness characteristics in the opposite directions. For non-symmetric structures, the positive and negative displacements should be separately averaged. Alternatively, additional analyses could be run, reversing the polarity of the records to provide 14 valid values for averaging.

The illogicality of selecting the maximum of the positive and negative displacements becomes even more apparent when 2-D or 3-D excitation is considered. If the critical polarity of each component is to be adopted, then four possible combinations of the 2 D components (+ve/+ve; -ve/-ve; +ve/-ve; -ve/+ve) and eight possible combinations of the 3-D components would need to be considered.

There are, however, additional problems with determining the correct average for response under multi-axial excitation. Consider the case of the simple wharf segment shown in plan view in Fig. 4.42 which has considerable eccentricity between the centre of mass and the centre of strength (effective stiffness), as a result of short piers on the landward edge and long piers on the seaward edge, as illustrated in Fig. 12.1(a). Because of the significant torsional response under longitudinal (X direction) excitation the transverse and longitudinal response cannot be decoupled, and simultaneous excitation in the orthogonal (X and Y) directions must be modelled.
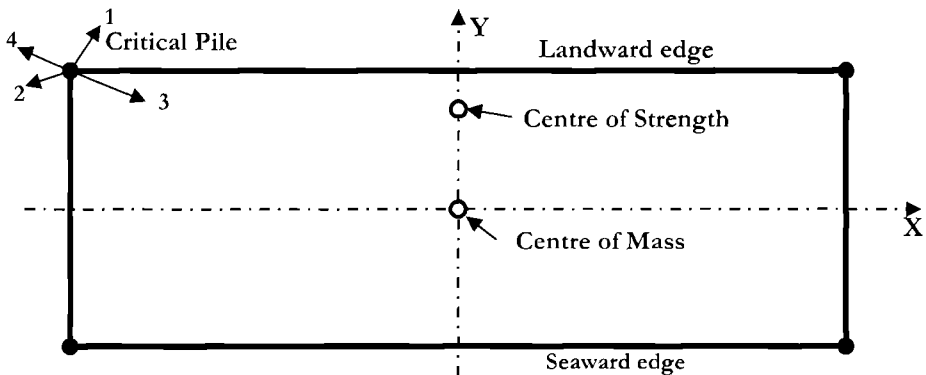
Fig 4.42 Peak Corner Displacements for Critical Corner Pile of a Wharf (Plan View)

The critical design parameter will be the average displacement from the seven (or more) pairs of accelerograms (record pairs) of a corner pile. As with the previous example of the bridge pier, the average displacement is of interest because it can be directly correlated to the pile limit strains.

Output from the **ITHA** will be in the form of X and Y displacements (as well as member forces etc). Normally the peak values $\Delta_{max,X}$ and $\Delta_{max,Y}$ from the analysis will also be listed in a summary table. However, it is not possible to combine these vectorially to obtain the peak response displacement for the record under consideration, since $\Delta_{max,X}$ and $\Delta_{max,Y}$ are unlikely to occur at the same time. Instead, at each time interval i, the vectorial displacement Δ_i must be calculated according to:

$$\Delta_i = \sqrt{(\Delta_{i,X}^2 + \Delta_{i,Y}^2)} \tag{4.93}$$

and the peak displacement for the record determined from the full range of Δ_i thus obtained. This peak displacement will occur in a specific direction. In Fig. 4.42, the critical displacements and directions for the first four of the record pairs are indicated by vectors. It will be clear that these cannot be averaged as scalars to obtain the design response displacement, as they occur in different directions. The correct method of averaging becomes apparent when one considers the condition that defines the limit strains. Let us first consider the peak response in a specified direction (say 15° from the X axis). The average displacement response **in this direction** will define whether the limit strains on the diagonal defined by the direction are satisfactory. To obtain this average, the displacement **in this direction** must be obtained for each record pair, and for each time step. The full time-history of response displacements in this direction is searched for each record pair to obtain the maximum value, and the average of the maxima **in this direction** from the seven (or more) record pairs is found.

This procedure must be carried out for a series of directions around the full 360°. Normally directions at 15° intervals provide sufficient accuracy. The average response displacements in the different directions are then searched to find the critical direction, and thus the critical displacement.

It is noted that this procedure represents a departure from what has been customary practice in the past, but we believe it represents the only logical interpretation of the averaging process for response under a number of accelerograms.

4.9.3   Non-Linear Static (Pushover) Analysis

Pushover analysis involves an inelastic analysis of the structure considered, under a gradually increasing vector of forces or displacements, representing the expected pattern of inertia forces or response displacements in the structure. It has the ability to track the formation, and plastic rotation of plastic hinges in the structure, and hence can be of value in design verification. There are, however, limitations to the utility of the method.

First, it can not be directly used to determine the overall displacement demand on the structure under the design seismic intensity. This must be obtained from some other means, such as modal analysis, since what is obtained is essentially a generalised force-displacement response of the structure. Given knowledge of the displacement demand, the pushover analysis can be carried out until the displacement at some characteristic location reaches the assessed demand, and hence the local inelastic strains and structural drifts can be determined. Thus assumptions made in the direct displacement-based design approach about the deflected shape can be tested, but not the absolute value of the displacements.

A further limitation of the pushover method is that at the current stage of development pushover analysis in commercially available analysis codes is generally restricted to modelling response of a single mode, generally the fundamental mode. Dynamic amplification of drifts, moments and shear forces due to higher mode effects cannot be accurately modelled with single-mode pushover analysis. Considerable research effort has been expended in recent years towards developing multi-mode pushover analysis[G3,P24]. In our view these have not yet reached maturity, and require excessive computational effort. This severely restricts the applicability of the method to design verification.

A final limitation is that with a uni-directional push, the hysteretic characteristics of the structure cannot be included for straight design verification. Thus, a structure with non-linear elastic hysteretic characteristics will have the same pushover response of a bilinear elasto-plastic system with the same backbone response. In some computer pushover approaches[C1], however, cyclic pushover analyses can be carried out. These can be used to determine the energy dissipation characteristics of sub-assemblages of the structure, enabling them to be modelled with a reduced number of degrees of freedom in **ITHA**, or in the design process. This is of considerable value in soil-structure interaction problems. An application to the response of wharves is presented in Chapter 12.

In carrying out a pushover analysis, a decision must be made as to whether to control the response by an imposed force-vector or by an imposed displacement-vector. Both approaches have limitations. The force approach tends to become unstable as maximum resistance is approached, and cannot follow response when strength degrades. It also results in a force vector that is generally incompatible with the generated displacements, since in a single-mode pushover, the force vector should be proportional to the product of mass and displacement at each level. In some approaches[X10], more than one shape of force vector is specified (typically corresponding to a linear or constant displacement with height), and the results from the worst case is taken. This implies considerable doubt as to the accuracy of the results.

The displacement approach is very suitable for **SDOF** systems, since it can follow response in the post-peak strength region. However, spurious local forces can develop when applied to **MDOF** structures, and the specification of a displacement vector can inhibit soft-storey failure mechanisms. In both force-controlled and displacement-controlled cases, care must be taken in applying an appropriate force or displacement vector that represents the expected modal response. Recently developed pushover

algorithms, termed "adaptive pushovers" modify the applied force or displacement vector incrementally to model the changing deflection shape resulting from the structural analysis[P25], and should be used where possible.

It is pointed out that data preparation and interpretation for a pushover analysis is very similar to that required for **ITHA**, and with current computing capacity, the increased time to execute an **ITHA** compared with a pushover analysis is of little consequence, unless fibre elements are used. Considering the limitations of pushover analysis, outlined above, we see limited applications for the approach, at this stage of development of the method, in design verification studies, beyond the specific examples noted above. It should be noted however, that the increased complexity of fibre elements which creates problems in excessive time of analysis for **ITHA**, can enhance the accuracy of pushover analyses without involving excessive analysis time.

5

FRAME BUILDINGS

5.1 INTRODUCTION

This chapter builds on the basic material provided in Chapter 3 relating to the fundamentals of direct displacement-based seismic design (**DDBD**), to provide a rather complete procedure for the seismic design of buildings whose primary lateral force-resisting systems is comprised of frames. The relevant equations from Chapter 3 are first summarized, and extended, where appropriate. Information on elastically responding frame buildings is provided, since in many regions of low to moderate seismicity frame buildings can be expected to respond elastically to the design-level seismic intensity.

Simplified methods of analysis under the design seismic force-vector are presented, since it is shown that traditional elastic analyses are invalid for frames that respond inelastically. Details on the necessary strength margins of columns to satisfy capacity design requirements are considered in some detail. Design examples are used throughout to illustrate the complete design process, for both steel and concrete frame buildings.

5.2 REVIEW OF BASIC DDBD PROCESS FOR FRAME BUILDINGS

5.2.1 SDOF Representation of MDOF Frame

Chapter 3 introduced the fundamentals of **DDBD** with respect to Fig.3.1, which is reproduced here for convenience as Fig.5.1. The first stage of the design process is the representation of the multi-degree-of-freedom (**MDOF**) structure by an equivalent single-degree-of-freedom (**SDOF**) structure modelling the first inelastic mode of response (Fig.5.1(a)). The following equations were developed:

(a) Design Storey Displacements: The design floor displacements of the frame are related to a normalised inelastic mode shape δ_i, where $i = 1$ to n are the storeys, and to the displacement Δ_c of the critical storey by the relationship

$$\Delta_i = \delta_i \left(\frac{\Delta_c}{\delta_c} \right) \tag{5.1}$$

(a) SDOF Simulation   (b) Effective Stiffness K_e

(c) Equivalent damping vs. ductility   (d) Design Displacement Spectra
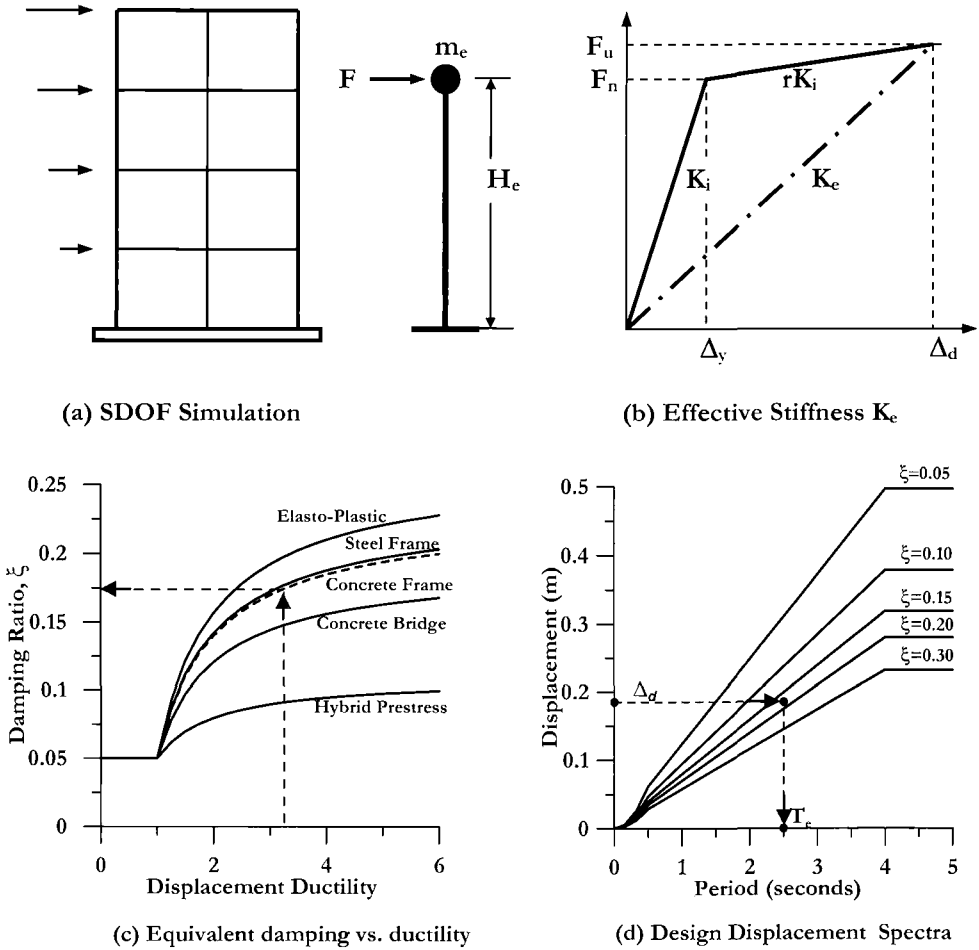
Fig.5.1   Fundamentals of Direct Displacement-Based Design

where the normalized inelastic mode shape depends on the height, H_i, and roof height H_n according to the following relationships:

$$\text{for n} \leq 4: \qquad \delta_i = \frac{H_i}{H_n} \tag{5.2a}$$

$$\text{for n} > 4: \qquad \delta_i = \frac{4}{3} \cdot \left(\frac{H_i}{H_n} \right) \cdot \left(1 - \frac{H_i}{4H_n} \right) \tag{5.2b}$$

(b) Equivalent SDOF Design Displacement: The equivalent design displacement is related to the storey displacements by the relationship:

$$\Delta_d = \sum_{i=1}^{n}\left(m_i\Delta_i^2\right)/\sum_{i=1}^{n}\left(m_i\Delta_i\right) \tag{5.3}$$

where m_i is the mass at height H_i associated with displacement Δ_i.

(c) Equivalent Mass: The equivalent **SDOF** mass m_e is given by:

$$m_e = \sum_{i=1}^{n}\left(m_i\Delta_i\right)/\Delta_d \tag{5.4}$$

(d) Effective Height: The effective height H_e of the **SDOF** structure (see Fig.5.1(a)) is given by:

$$H_e = \sum_{i=1}^{n}\left(m_i\Delta_i H_i\right)/\sum_{i=1}^{n}\left(m_i\Delta_i\right) \tag{5.5}$$

(e) Design Displacement Ductility: The **SDOF** design displacement ductility factor is related to the equivalent yield displacement Δ_y by:

$$\mu = \frac{\Delta_d}{\Delta_y} \tag{5.6}$$

It was shown in Section 4.4.6 that the yield drift of a storey in a frame depended on geometry, and was independent of strength. The following expressions were developed:

for reinforced concrete frames: $\quad \theta_y = 0.5\varepsilon_y \cdot \dfrac{L_b}{h_b}$ $\qquad$ (5.7a)

for steel frames: $\qquad \theta_y = 0.65\varepsilon_y \cdot \dfrac{L_b}{h_b}$ $\qquad$ (5.7b)

where L_b and h_b are the beam span between column centrelines, and overall beam depth respectively, and ε_y is the yield strength of the flexural reinforcement or structural steel. It

is generally sufficiently accurate to assume a linear yield displacement profile for the purpose of estimating ductility demand, and hence the yield displacement is given by:

$$\Delta_y = \theta_y \cdot H_e \tag{5.8}$$

(f)   Equivalent Viscous Damping: From Section 3.4.3, the equivalent viscous damping of the substitute structure for frames can be conservatively related to the design displacement ductility demand (see Fig.5.1(c)) as follows:

Reinforced Concrete Frames: $\xi_{eq} = 0.05 + 0.565 \cdot \left(\dfrac{\mu - 1}{\mu \pi} \right)$ \hfill (5.9a)

Steel Frames: $\xi_{eq} = 0.05 + 0.577 \cdot \left(\dfrac{\mu - 1}{\mu \pi} \right)$ \hfill (5.9b)

Alternatively, the distributed ductility approach of Eq.(3.37) can be used.

(g)   Effective Period of Substitute Structure: The effective period at peak displacement response is found from the displacement spectra set (Fig.5.1(d)), entering with the design displacement and determining the period, T_e, corresponding to the calculated equivalent viscous damping.

(h)   Effective Stiffness of Substitute Structure: With reference to Fig.5.1(b) and Section 3.2, the effective stiffness at maximum displacement response of the substitute structure, F/Δ_d is given by:

$$K_e = 4\pi^2 m_e / T_e^2 \tag{5.10}$$

(i) Design Base Shear Force: Again with reference to Fig.5.1(b) and Section 3.2, the design base shear force for the **MDOF** structure is found from the substitute structure:

$$F = V_{Base} = K_e \Delta_d \tag{5.11}$$

5.2.2   Design Actions for MDOF Structure from SDOF Base Shear Force

(a) Distribution of Base Shear Force to Floor Levels: The base shear force from Eq.(5.11) is distributed to the floor levels in proportion to the product of mass and displacement as:

$$F_i = V_{Base} (m_i \Delta_i) / \sum_{i=1}^{n} (m_i \Delta_i) \tag{5.12}$$

(b) ***Design Moments for Plastic Hinges:*** The building is then analysed under the force vector represented by Eq.(5.12) to determine the required flexural strength at the plastic hinge locations. As discussed in Section 3.7 it is unnecessarily conservative to add the full gravity-load moments to these seismic moments. So doing, as well as increasing the cost of the structure would reduce the seismic response displacements to below the intended design level. The recommendation in Section 3.7 is to detail the beam plastic hinges for the lower of (i) the seismic moments, and (ii) the factored gravity-load moments. This is discussed further in Section 5.6.1.

Analysis of the building under the lateral force vector requires the adoption of member stiffness appropriate for the expected member ductility level, as discussed in Section 3.5.7. However, an alternative and simpler approach to determining the member forces is presented in Section 5.5.2.

5.2.3 Design Inelastic Displacement Mechanism for Frames

The desired mechanism of inelastic deformation for frames involves the formation of flexural plastic hinges at the ends of the beams, except, possibly, at roof level, combined with column-base plastic hinges, and column-top hinges if the roof-level beams do not hinge. This mechanism, shown in Fig.5.2(a) where beam hinges, rather than column hinges form at the roof level provides the greatest possible number of locations to dissipate seismic energy, and also results in plastic hinge rotations that are very nearly equal to the inelastic storey drift.

(a) Beam-Sway   (b) Column-Sway
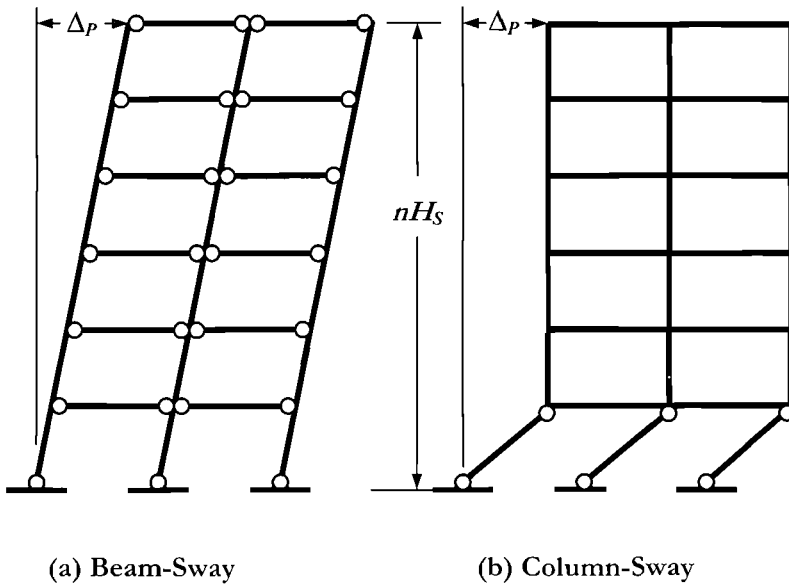
Fig.5.2 Mechanisms for Frame Inelastic Response

Capacity design measures, outlined in Sections 3.10 and 4.7 are required to ensure that this, and only this, inelastic mechanism can develop. Column flexural strengths at locations other than the base or top must be set sufficiently high to ensure that column hinges rather than beam hinges do not form, since this could result in a column sway mechanism with high plastic rotation demand on the column hinges[P1], as illustrated in Fig.5.2(b). The two alternative mechanisms in Fig.5-2 have the same plastic drift Δ_P at the roof level, but it will be immediately seen that the plastic rotation of the hinges in the column sway mechanism is approximately n times that of the beam-sway mechanism, where n is the number of storeys. It will also be appreciated that a single column failure could result in total building collapse, whereas failure of a single beam is unlikely to be critical. Column-sway (also known as soft-storey) mechanisms have been one of the most common forms of failure of frame buildings in earthquakes[P1].

Similarly, since shear failure is brittle, resulting in strength loss and potential catastrophic failure, the shear strength of both beams and columns must be set sufficiently high to ensure that shear failure cannot occur. Capacity design measures for frames are discussed further in Section 5.8.

5.3.   YIELD DISPLACEMENTS OF FRAMES

5.3.1 Influence on Design Ductility Demand

Frames are inherently flexible structures. Consider Eq.(5.7a) which gives the yield drift of a reinforced concrete frame. If we take typical values for beam span and depth of L_b = 6 m (19.7 ft), and h_b =600 mm (23.6 in), and a reinforcement yield strength of f_{ye} = 400 MPa, (58 ksi), implying a yield strain of ε_y = 0.002, then Eq.(5.7a) results in a yield drift of

$$\theta_y = 0.5 \times 0.002 \times \frac{6.0}{0.6} = 0.01 \qquad (5.13)$$

Note that in many countries higher yield stresses are common, and hence yield drifts would be proportionately larger.

Most seismic design codes set drift limits corresponding to a damage-control limit state (see Section 3.3.2) in the range 0.02 to 0.025, to limit non-structural damage. Design ductility or behaviour factors for frames are often set as high as 5 to 8 (see Table 1.2). It is apparent, however, that if the yield drift is of the order of 0.01, then the maximum structural displacement ductility demand at the non-structural drift limit will be in the order of μ = 2 to 2.5, and hence the structural ductility limits will almost never govern. This will be apparent in examples later in this chapter.

5.3.2 Elastically Responding Frames

A second consequence of the high yield drift of frames is that tall frames can be

expected to respond elastically if the design seismic intensity is low or moderate, since the yield displacement is likely to exceed the maximum displacement demand corresponding to elastic (e.g. 5%) damping at the start of the constant-displacement plateau of the displacement spectrum (see Fig.5.1(d), e.g.). Aspects which will influence this are:

- Yield drift (i.e. frame dimensions and reinforcement yield strength)
- Magnitude of earthquake
- Distance from fault rupture
- Number of storeys.

The tentative information given in Section 2.2.2.(b) relating to prediction of displacement spectra can be used to gain some insight into the probability that a given building will respond elastically to an earthquake of specified magnitude occurring on a known fault. Since it is more common to express design seismicity in terms of peak ground acceleration (**PGA**), we reformulate the information of Chapter 2 in terms of **PGA** as follows:

We assume a typical elastic spectral acceleration shape for firm ground, with a constant velocity slope starting at $T_B = 0.5$ seconds. Note that the assumption of a constant velocity slope, which is implicit in most seismic codes, is compatible with the linear displacement spectra of Fig.5.1. We also make the common assumption that the plateau acceleration is 2.5 times the effective peak ground acceleration **PGA**. With this information, and the relationship between corner period and magnitude given by Eq.(2.3) it is possible to directly relate the elastic acceleration spectrum and the displacement spectrum (see Fig.5.3), and calculate the maximum elastic response displacement. The ordinates of the acceleration spectrum for $0.5 < T < T_C$ sec are:

$$a_{(T)} = 2.5 PGA \cdot T_B / T = 1.25 \cdot PGA / T \tag{5.14}$$

In accordance with Eq.(2.3) the corner period T_C is taken as:

$$T_C = 1 + 2.5(M_W - 5.7) \quad \text{seconds} \tag{5.15}$$

Making the usual assumption of sinusoidal relationship between peak relative displacement and peak pseudo-acceleration, the corner elastic displacement is related to the **PGA** by:

$$\Delta_{TC} = \frac{T_C^2}{4\pi^2} \cdot a_{TC} = \frac{T_C^2}{4\pi^2} \cdot \frac{1.25 \cdot PGA}{T_C} \tag{5.16}$$

Substituting for T_C from Eq.(5.15) and simplifying:

$$\Delta_{TC} = 0.031 \times PGA(1 + 2.5(M_W - 5.7)) \tag{5.17}$$

(a) 5% Acceleration Spectrum   (b) 5% Displacement Spectrum
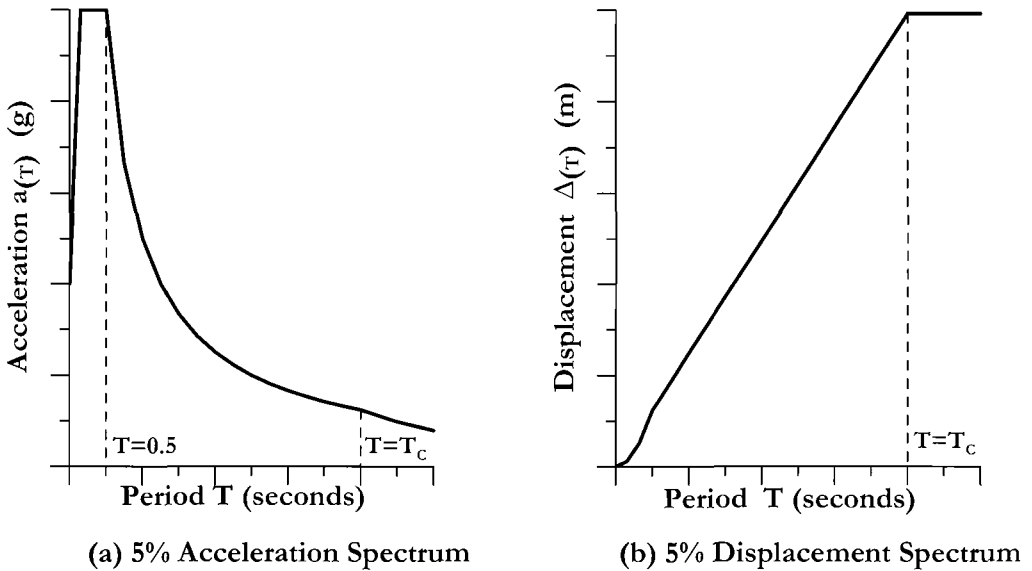
Fig.5.3   Design Elastic Acceleration and Displacement Response Spectra (no scale)

Note that the data used to generate the elastic displacement spectra in Section 2.2.2 imply that **PGA** is inversely proportional to distance from the fault plane for distances greater than 10 km. As a consequence, high **PGA**'s are possible for moderate seismic magnitudes M_W, provided the distance is small enough.

Equation (5.17) can be plotted as a function of **PGA** and M_W to provide the maximum displacement that can be expected at the effective height of the substitute structure (Eq.(5.5)). This can be compared with the yield displacement given by Eqs (5.7) and (5.8) to determine for a given structure, **PGA** and M_W, whether response is likely to be elastic or ductile. A typical comparison is displayed in Fig.5.4 for a reinforced concrete frame building, based on the following structural assumptions:

- flexural reinforcement yield strength f_{ye} = 400 MPa (58ksi)
- Storey height constant at 3.5 m (11.5 ft)
- Beam aspect ratio L_b/h_b = 10 (see Eq.(5.7))
- Effective height = $0.7H_n$ (H_n = total building height $=3.5n$ m (11.5n ft))
- Yield displacement profile is linear.

These assumptions are the same as used to derive Eq.(5.13) and hence the yield drift is θ_y = 0.01. The yield displacement at the effective height is thus:

$$\Delta_y = \theta_y.(0.7 \times 3.5n) = 0.01 \times 0.7 \times 3.5n = 0.0245n \qquad \text{(m)} \qquad (5.18)$$

where n is the number of storeys.
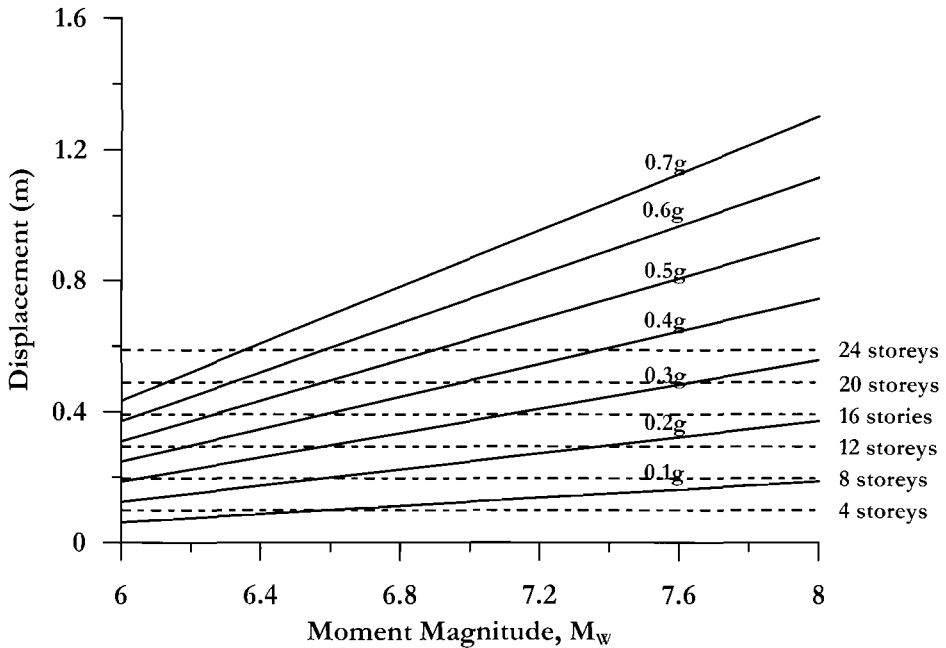
Fig.5.4 Comparison of Peak Elastic Spectral Displacement for 5% Damping as a function of PGA and Moment Magnitude, with R.C. Frame Yield Displacements

In Fig.5.4, the relationship between peak spectral displacement, peak ground acceleration and moment magnitude given by Eq.(5.17) is plotted as a series of sloping lines identified by **PGA**. The structural yield displacements for frames between 4 and 24 storeys based on Eq.(5.18) are plotted as dashed lines. If the yield displacement exceeds the peak elastic spectral displacement, then the response is expected to be elastic.

The results indicate that if the design **PGA** is 0.2g, and the causative earthquake is M_W < 6.6, then all frames of 8 storeys or higher, with similar to, or more flexible than, the characteristics of those on which Eq.(5.18) is based, will respond elastically. Twenty-four story frames in a zone with **PGA** = 0.3g will respond elastically for all M_W < 8, and in a zone with PGA = 0.5g will still respond elastically unless M_W > 6.9.

These results should be taken as indicative only, since they depend on the structural assumptions, and also the assumptions used to derive the displacement spectra. For the taller structures it is also possible that inelastic response could be developed in higher modes than the fundamental mode of vibration, thus requiring the consideration of capacity-design effects. With these provisos, however, it will be seen that elastic response of taller structures is probable, particularly in regions, such as Europe, where design earthquake magnitudes tend to be moderate (i.e. M_W ≤ 6.5). For such structures, simplified seismic design criteria would be appropriate.

5.3.3 Yield Displacement of Irregular Frames

It has long been recognized that good seismic performance is more likely to be achieved when the structure is "regular". Regular, in the context of frame buildings normally means that bay widths are equal, there are no vertical offsets, and the structure has no designed torsional eccentricity. Often the criteria of regularity will not be met, and in **DDBD** two issues will need consideration: the estimation of the yield displacement (so that the design ductility, and hence the equivalent viscous damping can be determined), and the distribution of the design base shear to different elements of an irregular structure. In this section we consider the former of these two considerations.

(a) Irregular Frame   (b) Overturning Moment
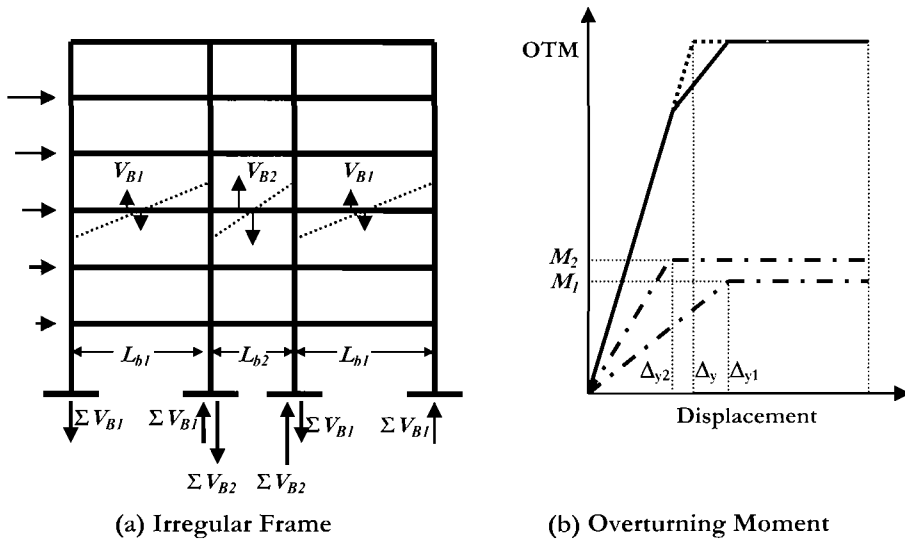
Fig.5.5 Seismic Response of an Irregular Frame

The frame in Fig.5.5 is irregular in that it has a short central bay with longer outer bays. It is recalled that when the yield drift of frames was discussed in Section 4.4.6, it was noted that Eq.(5.7) was found to apply for exterior, interior, and two-way beam-column subassemblages. It thus follows that the yield drift of the different bays of Fig. 5.5 can be calculated, with sufficient accuracy, independently of each other. From Eq.(5.7) it is clear that the beams in the outer bays will have yield drifts that are greater than the yield drift of the central bay. This is illustrated in Fig.5.5(b), where the bay contribution to overturning moment is plotted against displacement at the effective height of the substitute structure. From Eq.(5.7(a)) the yield drifts are:

$$\theta_{y1} = 0.5\varepsilon_y \frac{L_{b1}}{h_{b1}} \qquad \theta_{y2} = 0.5\varepsilon_y \frac{L_{b2}}{h_{b2}} \tag{5.19}$$

Thus if the beams in the different bays have the same depths, the yield drifts will be proportional to the span lengths. As is shown in Fig.5.5(b), the system yield displacement is found by combining the moment/displacement response of the individual bays to form an equivalent bilinear response. In this example, if M_1 and M_2 are the contributions to the overturning moment from an outer and inner bay respectively, then the total overturning moment and system yield displacement are:

$$M_{OTM,sys} = 2M_1 + M_2 \tag{5.20a}$$

$$\Delta_y = \frac{2M_1\theta_{y1} + M_2\theta_{y2}}{2M_1 + M_2} \cdot H_e \tag{5.20b}$$

Equation (5.20b) requires that the ratio of moment contribution to the overturning moment of the various bays, M_1/M_2 needs to be known before the yield displacement, and hence the ductility and equivalent viscous damping can be determined. Note that the absolute values of M_1 and M_2 are not needed. As will be seen shortly, a rational decision will be to design both the short and long beams at a given level for the same moment capacity. For generality we assume different positive and negative moment capacities of M_{+ve} and M_{-ve} respectively. The seismic moments at full mechanism development are indicated in Fig.5.5(a) at the third floor. Beam seismic shears in the short and long spans will thus be in inverse proportion to the span lengths:

$$V_{B1} = \frac{M_{+ve} + M_{-ve}}{L_{b1}} \quad ; \quad V_{B2} = \frac{M_{+ve} + M_{-ve}}{L_{b2}} \tag{5.21}$$

For the development of a full seismic mechanism, the seismic axial forces induced in each of the columns by the beams of the outer and inner bays are ΣV_{B1} and ΣV_{B2} respectively. Ignoring the column-base moments as a relatively small proportion of the total overturning capacity, the contributions of the outer and inner frames to the system overturning capacity are thus:

$$M_1 \approx \sum_{i=1}^{n} V_{B1,i} \cdot L_{b1} = \sum_{i=1}^{n} (M_{+ve,i} + M_{-ve,i}) \tag{5.21a}$$

$$M_2 \approx \sum_{i=1}^{n} V_{B2,i} \cdot L_{b2} = \sum_{i=1}^{n} (M_{+ve,i} + M_{-ve,i}) \tag{5.21b}$$

That is, the bays contribute equally to the overturning capacity, regardless of the beam length. This simplifies calculation of the effective yield displacement.

Note that the decision to make the beam moment capacities of the inner and outer bays equal, though rational, is not essential: any ratio may be assumed, and the effective yield displacement calculated. It will be noted, however, that elastically calculated seismic moments will be higher in the short spans than the longer spans, while gravity load moments will be largest in the long spans, reinforcing the rationality of the above approach. It should also be noted that if elastically calculated seismic moments are much larger than gravity moments, as would be the case for tube frames in regions of high seismicity, then conventional design would require the moment capacity of the short beams to be increased above that for the long span (refer to the relative stiffness in Fig.5.5(b)). This is another example of the irrationality of design based on initial stiffness since increasing the strength of the inner beams, either by increasing reinforcement content or beam depth (or both) would further increase the relative stiffness of these beams, initially attracting higher seismic moments.

Two examples of frame buildings with vertical irregularity provided by setbacks are shown in Fig.5.6. The symmetrical layout of Fig.5.6(a) requires no special consideration in design, unless the storey heights vary significantly, since the ratio of storey mass to stiffness will remain essentially the same up the height of the building as for a building without setbacks. The unsymmetrical layout of Fig.5.6(b) also has no influence on the design process in the direction displayed, unless there is also a setback in the direction perpendicular to the frame displayed. In the perpendicular direction, the eccentricity of the upper portion of the frame will result in a torsional response in the lower storeys of the building, which will need consideration using the techniques developed in Section 3.7.

(a) Symmetrical layout   (b) Unsymmetrical Layout
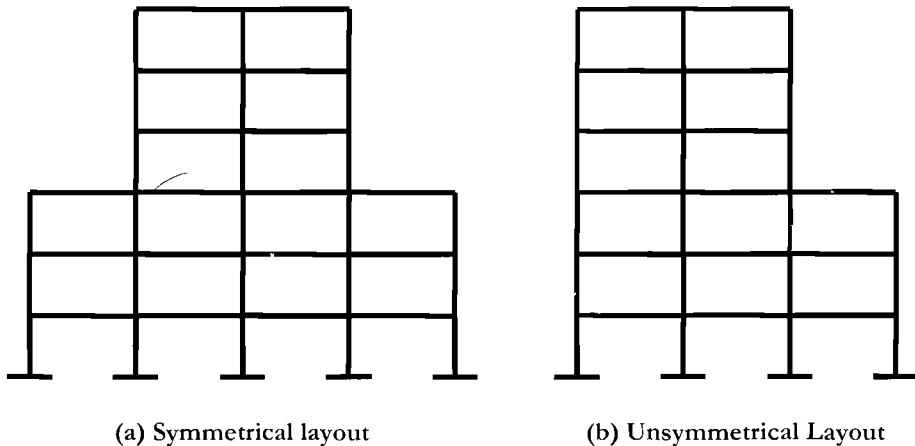
Fig.5.6 Frame Buildings with Vertical Irregularity

Frames with irregular storey heights also require little special consideration in the **DDBD** approach to determine required base shear strength, and distribution of lateral forces to the different storey levels. However, the assumed displacement profile defined

by Eq.(5.2) will be increasingly inaccurate as the variation in storey heights increases, and should be checked by analyses after a preliminary design is completed, using the techniques outlined in Section 4.9.

5.3.4 Design Example 5.1: Yield Displacement and Damping of an Irregular Frame
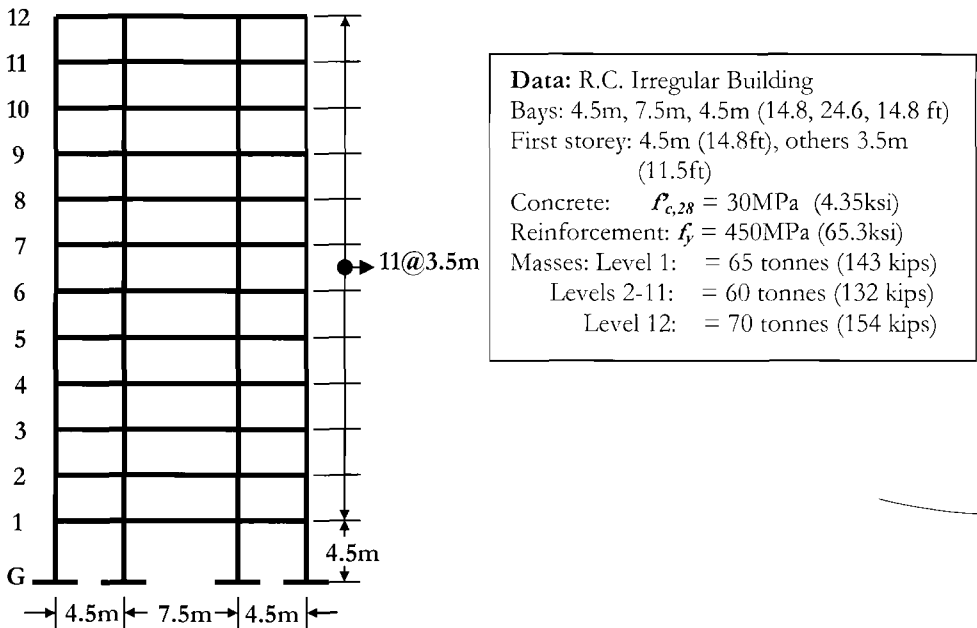
Fig.5.7   Reinforced Concrete Frame for Design Example 5.1

The twelve-storey reinforced concrete frame illustrated in Fig.5.7 is irregular in the bay lengths. It also has vertical irregularity, in that the first storey is significantly higher than the upper storeys, as is often the case. The building consists of four identical frames, and the masses contributing to inertial response of each frame are indicated in Fig.5.7. Roof mass exceeds that at lower floors due to equipment and water storage located at roof level. It is required to determine the design ductility level, and equivalent viscous damping, for a **DDBD** of the frame, based on a design drift limit of 0.025.

Solution: To determine the system ductility, and hence equivalent viscous damping, it is first necessary to determine the substitute structure displacement (Eq.(5.3)) and effective height (Eq.(5.5)). The necessary calculations are summarized in Table 5.1.

Table 5.1 Calculations for Design Displacement, and Effective Height, Design Example 5.1

Storey, i (1)	Height H_i (m) (2)	Mass, m_i (tonnes) (3)	δ_i (4)	Δ_i (m) (5)	$m_i\Delta_i$ (6)	$m_i\Delta_i^2$ (7)	$m_i\Delta_iH_i$ (8)
12	43.0	70	1.000	0.828	57.95	47.97	2491.7
11	39.5	60	0.943	0.781	46.86	36.60	1851.1
10	36.0	60	0.882	0.731	43.84	32.03	1578.2
9	32.5	60	0.817	0.677	40.59	27.47	1319.3
8	29.0	60	0.747	0.619	37.13	22.98	1076.8
7	25.5	60	0.673	0.557	33.45	18.65	853.0
6	22.0	60	0.595	0.492	29.55	14.55	650.1
5	18.5	60	0.512	0.424	25.43	10.78	470.4
4	15.0	60	0.424	0.351	21.09	7.41	316.3
3	11.5	60	0.333	0.275	16.53	4.55	190.1
2	8.0	60	0.236	0.196	11.75	2.30	94.0
1	4.5	65	0.136	0.112	7.31	0.82	32.9
Sum					371.47	226.11	10923.8

Displacement Profile: Column (4) in Table 5.1 lists the inelastic mode shape defined by Eq.(5.2b). This shape implies that the maximum drift occurs between the ground and first floor. The design displacement at the first floor is thus $\Delta_1 = 0.025\times4.5 = 0.1125$m. The design displacement profile, listed in column (5) is thus found from Eq.(5.1) as

$$\Delta_i = \delta_i \frac{\Delta_1}{\delta_1} = \delta_i \frac{0.1125}{0.136} = 0.828\delta_i$$

Substitute Structure Design Displacement: Substituting from the sums of columns (7) and (6) into Eq.(5.3):

$$\Delta_d = \sum_{i=1}^{n}\left(m_i\Delta_i^2\right)/\sum_{i=1}^{n}\left(m_i\Delta_i\right) = \frac{226.11}{371.47} = 0.609m \text{ (24 in)}$$

Substitute Structure Effective Height: Substituting from the sums of columns (8) and (6) into Eq.(5.5):

$$H_e = \sum_{i=1}^{n}\left(m_i\Delta_iH_i\right)/\sum_{i=1}^{n}\left(m_i\Delta_i\right) = \frac{10923.8}{371.47} = 29.4m \text{ (96.4ft, 68.4\% of building height)}$$

Yield Displacement: The specified reinforcement yield strength is $f_y = 450\text{MPa}$ (65.2ksi). In accordance with the recommendations of Section 4.2.5 the design yield strength is taken as $f_{ye} = 1.1f_y = 495$ MPa (71.8ksi). The yield strain is thus $\varepsilon_y = f_y/E_s = 495/200,000 = 0.002475$.

Three different design options are considered. In the first, the beam depth in all bays is kept constant at 600mm (23.6in), and moment capacities of the outer and inner frames are made equal, as suggested in Section 5.3.3. Thus $M_1 = M_2$. In the second option, influenced by elastic considerations of seismic force distribution, the outer and inner beam depths are taken as $h_1 = 750$mm (29.5in), $h_2 = 600$mm respectively, and $M_1 = 1.67M_2$. In the final option, influenced by gravity moment distribution, outer and inner beam depths are taken as $h_1 = 500$mm (19.7in), $h_2 = 600$mm respectively, and $M_1 = 0.6M_2$.

Option 1: $h_1 = h_2 = 600$ mm; $M_1 = M_2$: From Eq.(5.19):

$$\theta_{y1} = 0.5 \times 0.002475 \frac{4.5}{0.6} = 0.00928 \qquad \theta_{y2} = 0.5 \times 0.002475 \frac{7.5}{0.6} = 0.0155$$

Hence, from Eq.(5.20b), the equivalent system yield displacement is:

$$\Delta_y = \frac{2M_1\theta_{y1} + M_2\theta_{y2}}{2M_1 + M_2} H_e = \frac{2 \times 0.00928 + 0.0155}{3} \times 29.4 = 0.334m \quad (13.2\text{in})$$

The system displacement ductility is thus $\mu = 0.609/0.334 = 1.82$ and from Eq.(5.9a) the equivalent viscous damping for **DDBD** is:

$$\xi_{hyst} = 0.05 + 0.565 \cdot \left(\frac{1.82-1}{1.82\pi}\right) = 0.131 \quad (13.1\%)$$

Option 2: $h_1 = 750$ mm; $h_2 = 600$ mm; $M_1 = 1.67M_2$. From Eq.(5.19):

$$\theta_{y1} = 0.5 \times 0.002475 \frac{4.5}{0.75} = 0.007425 \qquad \theta_{y2} = 0.5 \times 0.002475 \frac{7.5}{0.6} = 0.0155$$

From Eq.(5.20b), the system yield displacement is:

$$\Delta_y = \frac{2M_1\theta_{y1} + M_2\theta_{y2}}{2M_1 + M_2} \cdot H_e = \frac{2 \times 1.67 \times 0.007425 + 0.0155}{2 \times 1.67 + 1} \times 29.4 = 0.273m \quad (10.7\text{in})$$

The system ductility is thus increased to $\mu = 0.609/0.273 = 2.23$, and from Eq.(5.9a), the equivalent viscous damping is:

$$\xi_{hyst} = 0.05 + 0.565 \cdot \left(\frac{2.23 - 1}{2.23\pi} \right) = 0.149 \quad (14.9\%)$$

Option 3: h_1 = 500 mm; **h_2** = 600 mm; **M_1** = 0.6M_2. From Eq.(5.19):

$$\theta_{y1} = 0.5 \times 0.002475 \cdot \frac{4.5}{0.5} = 0.01114 \qquad \theta_{y2} = 0.5 \times 0.002475 \frac{7.5}{0.6} = 0.0155$$

From Eq.(5.20b), the system yield displacement is:

$$\Delta_y = \frac{2M_1\theta_{y1} + M_2\theta_{y2}}{2M_1 + M_2} . H_e = \frac{2 \times 0.6 \times 0.01114 + 0.0155}{2 \times 0.6 + 1} \cdot 29.4 = 0.386m \quad (15.2in)$$

The system ductility is thus decreased to $\mu = 0.609 / 0.386 = 1.58$, and from Eq.(5.9a), the equivalent viscous damping is:

$$\xi_{hyst} = 0.05 + 0.565 \cdot \left(\frac{1.58 - 1}{1.58\pi} \right) = 0.116 \quad (11.6\%)$$

It is thus seen that changing the relative strengths of the beams in the outer and inner bays also changes their ductility and hence the effective viscous damping. From Eq.(3.21) it is thus seen that the system base shear will also be changed. If we adopt the EC8 recommendation for relationship between damping and displacement reduction given by Eq.(2.8), then the required base shear strengths, from Eq.(3.24), for the three cases will be in proportion to

$$\left(\frac{0.07}{0.02 + \xi} \right)^{1.0}$$

assuming "normal" rather than near-field conditions. Using Option 1 as a base, this implies that the required strength for Options 2 and 3 will be 10.6% lower, and 10.9% higher respectively than Option 1. Note that an independent design, using the distributed ductility/damping approach of Section 3.5.4(a) gave almost identical results, confirming that the simplified approach described in this section may be used with some confidence.

The resulting relative strengths required of the outer and inner bays for the three cases are compared in Fig.5.8, referenced to the total overturning moment requirement for Option 1. It is seen that the required contribution to overturning moment from the outer bays is not greatly influenced by the changes in beam depth and relative strength of the outer and inner bays, but the required beam strength for the longer inner bay has a strength range of approximately ±50% of the Option 1 value.

Option 2 is the most economical in terms of total required strength, but this is

achieved at the expense of a lower yield displacement. Damage will occur to the beams of the outer bays at a lower level of seismic intensity than for the other two options. It would appear that this would be the optimum choice for a site where the seismicity is characterized by infrequent large earthquakes, since serviceability requirements under moderate earthquakes are not likely to be critical. On the other hand, Option 3 would appear to be attractive for a location where moderate earthquakes are frequent, and hence where serviceability might govern design, since the onset of damage to the shorter outer bay beams would occur at a larger proportion of the design displacement. However, this would be achieved at the expense of a higher design base shear, and hence higher overall cost.
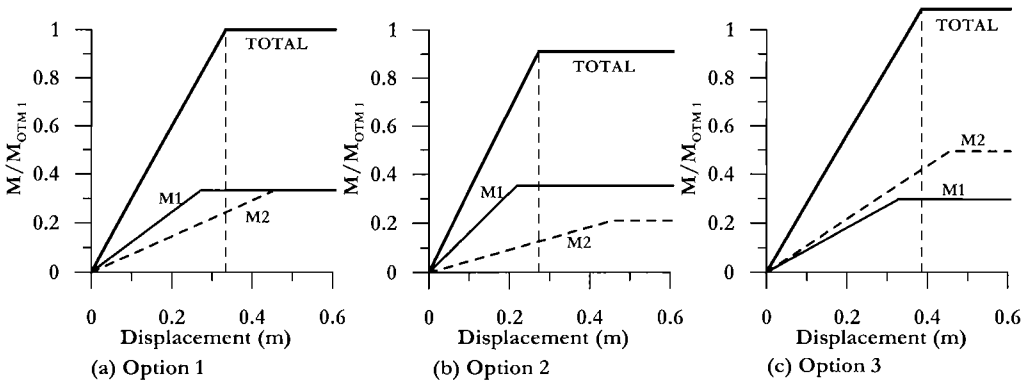
Fig.5.8 Comparative Overturning Moment Demands for Example 5.1

5.3.5 Yield Displacement and Damping when Beam Depth is Reduced with Height

A further complication may exist when the beam depth is reduced with height, to reflect the reduction in seismic moments in the upper level beams. Unless the beam depth reduction is unusually large, however, it will have little effect on the yield displacement at the effective height of the substitute structure, which is effectively controlled by the response of the lower level beams. Consequently it will generally be acceptable to base the yield displacement and equivalent viscous damping on the assumption that beam depth is constant up the height of the building, or to make an arbitrary small reduction to the equivalent viscous damping based on judgement. In cases where the beam-depth variation is too large to be ignored with comfort, the equivalent viscous damping can be calculated with greater accuracy from Eq.(5.22), where there are m locations of plastic hinges at each beam level, and θ_i is the design drift at level i subsequently defined by Eq.(5.26). The damping ξ_i at level i is based on the drift ductility at that level: $\mu = \theta_i/\theta_{yi}$, where the yield drift at level i is found from Eq.(5.7). Thus:

$$\xi_e = \frac{\sum_{i=1}^{n}\left(\sum_{k=1}^{m}m_k\right)\cdot\theta_i\xi_i}{\sum_{i=1}^{n}\left(\sum_{k=1}^{m}m_k\right)\cdot\theta_i} \tag{5.22}$$

Finally it is noted that when irregularity becomes extreme, it will be advisable to check the design using inelastic time-history analysis, as discussed in Section 4.9.

5.3.6 Yield Displacement of Steel Frames

Equation (5.7b) defines the yield drift of steel frames in terms of a known section depth, h_b. Steel beams utilized in building construction typically conform to the W-series ASCE classification[A2]. However, the beam depth is unlikely to be known at the start of the design process, even if the W-group of steel section has been decided. This is because each W-group consists of a range of beams with different strengths and weights, where the variation in strength and weight is achieved by varying the distance between the rollers defining the total section depth. Thus the internal profile between the insides of the flanges is kept constant, while the flange thickness is increased, resulting in an increase in the section depth.

It would thus appear necessary to carry out an iterative process on the design, using successive estimates of the beam depth. An alternative process has been suggested by Sullivan et al[S3], based on the following argument. It is noted that the nominal bilinear yield curvature of a section (see Section 4.2.6) can be expressed as

$$\phi_y = \frac{M_N}{M_y}\cdot\frac{M_y}{EI} = \frac{M_N}{EI} \tag{5.23}$$

where M_y and M_N are first yield moment and nominal flexural strength respectively. Now since the flexural strength can be expressed as $M_N = Z_P f_y$ where Z_P is the plastic section modulus, Eq.(5.23) can be rewritten as

$$\phi_y = \frac{Z_P f_y}{EI} = \frac{Z_P}{I}\cdot\varepsilon_y \tag{5.24}$$

Sullivan et al[S3] found that the ratio Z_P / I is essentially constant for a given W-group of steel beams, with the values as listed in Table 5.2. The similarity between Eqs.(4.50) and (5.24) is obvious. Equating, we can obtain an "effective" depth for use in the drift equation (Eq.(5.7b)):

$$\phi_y = 2.2\cdot\frac{\varepsilon_y}{h_b} = \frac{Z_P}{I}\cdot\varepsilon_y \quad \text{hence} \quad h_b = 0.45\cdot\frac{I}{Z_P} \tag{5.25}$$

Table 5.2 Z_P/I Values for ASCE Beam Section Groups[S3]

W-Shape Group	Z_P/I (in^{-1})	Z_P/I (m^{-1})
W14	0.140	5.52
W16	0.136	5.36
W18	0.119	4.67
W21	0.103	4.04
W24	0.087	3.44
W27	0.077	3.04
W30	0.066	2.58
W33	0.072	2.82

5.4 CONTROLLING HIGHER MODE DRIFT AMPLIFICATION

The design displacement profiles defined by Eq.(5.2) imply that the design storey drifts will be equal to, or less than the maximum value in the lowest storey of the building at all higher levels. Differentiating Eq.(5.2) with respect to H_i/H_n and normalizing to a value of 1.00 at the base of the frame, the vertical distribution of design drift can be expressed as

$$\theta_i / \theta_0 = 1.00 - 0.5 \frac{H_i}{H_n} \qquad (5.26)$$

Thus the design drift at the top of the frame is expected to be 50% of the drift at the base. It should, however, be recognized that this is primarily the drift associated with first inelastic mode response. Drifts at higher levels of the building will be influenced by higher mode effects, and can be expected to exceed values predicted by Eq.(5.26).

Analyses[P17] have indicated that control of higher mode drifts is critically affected by two parameters: the design displacement profile (and hence the design drift associated with the inelastic first mode), and the vertical distribution of the design base shear force resulting from the **DDBD** process. Since these are inter-related, they are considered together in the following discussion.

Figure 5.9 compares displacement and drift envelopes found from inelastic time-history analyses for two different **DDBDs** of 16 storey frames. In the first case (Fig.5.9(a)), the design displacement profile was defined by Eq.(5.2b), and the resulting design base shear was distributed to the floor masses in proportion to Eq.(5.12). In the second case, the same design profile was adopted, but a modified form of Eq.(5.12) was used, where 10% of the base shear force was allocated to the roof level, and the remaining 90% was distributed in accordance with Eq.(5.12). The revised equation is thus:

$$F_i = F_t + 0.9 V_B \cdot (m_i \Delta_i) / \sum_{i=1}^{n} m_i \Delta_i \qquad (5.27)$$

where $F_t = 0.1V_B$ at roof level, and $F_t = 0$ at all other levels. This is similar to the approach adopted in several seismic design codes (e.g. [X1]).

The peak design drift was nominally the same for the two cases, at 0.02, though due to use of an early version of the damping/ductility relationships in the first case (Fig.5.9(a)), the base shear was about 15% too high, reducing displacements below the design level. In both cases the designed structures were subjected to inelastic time-history analyses using five spectrum-compatible accelerograms. Full details of the analyses are available in Pettinga and Priestley[P17].
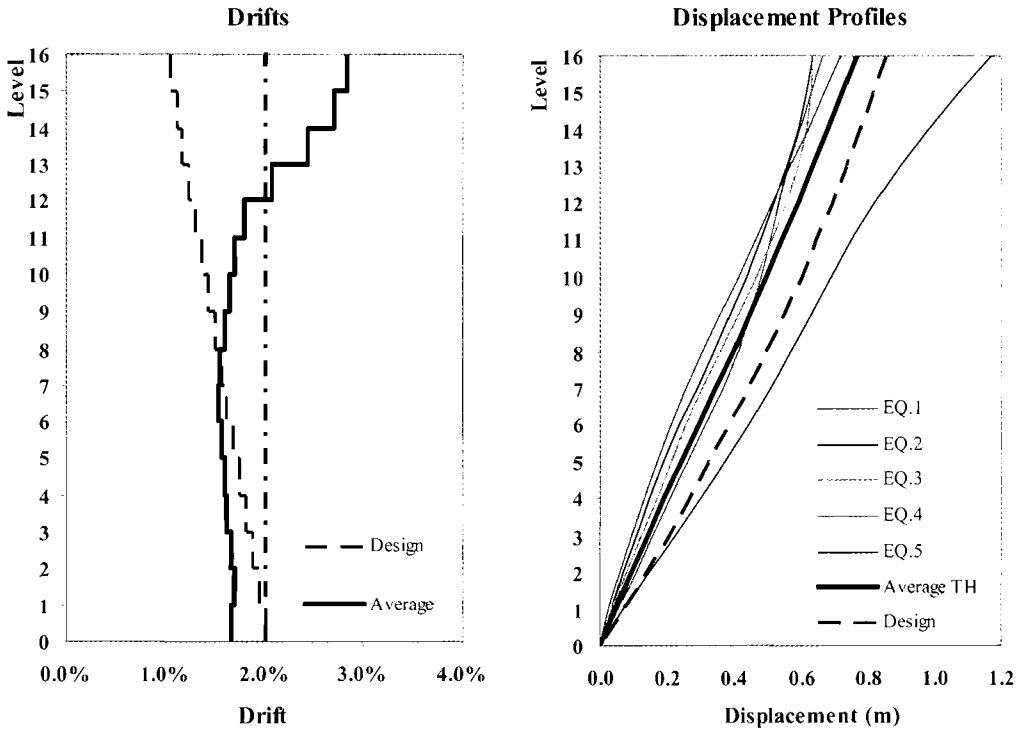
Fig.5.9(a) Maximum Storey Drifts and Displacement Profiles for a 16 Storey Frame, using Design Displacement Profile of Eq.(5.2b)

In the case without additional force at roof level (Fig.5.9(a)), it will be seen that higher mode effects increase the drifts in the upper storeys of the frame, not only above the design levels corresponding to the presumed first mode shape, but also significantly above the 2% design drift limit. The average displacement profile from the results of the five accelerograms agrees well with the shape of the design profile, but is low by about 10%, for the reasons discussed above. For the case with redistributed base shear, resulting in additional lateral force at roof level (Fig.5.9(b)), and hence stronger beams in the upper levels, recorded drifts again exceed the design first mode values, particularly in

the upper levels, but the excess over the 2% drift limit is only about 12%. Again the agreement between the design and recorded displacement profiles is good.

It should be noted that the designs for the structures represented in Figs.5.9 used a version of the damping/ductility relationships defined in Eq.5.9 that pre-dated the verification analyses described in Section 3.4.3, and did not include the drift reduction factor ω_θ described below.
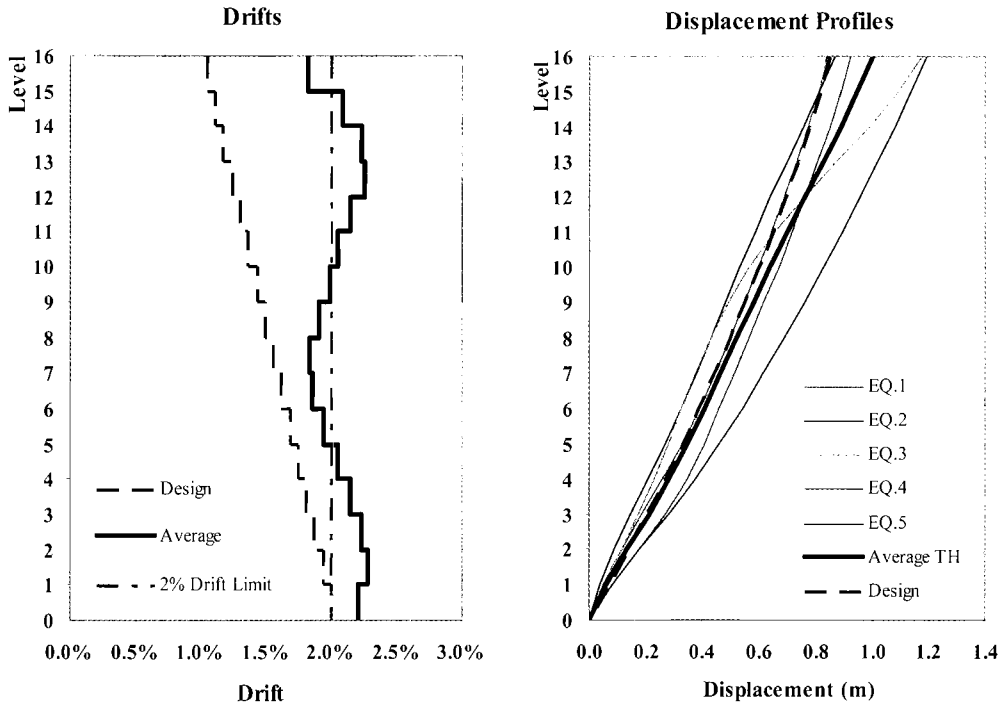
Fig.5.9(b) Maximum Storey Drifts and Displacement Profiles for a 16 Storey Frame, using Design Displacement Profile of Eq.(5.2b) and Eq.(5.27)

Figure 5.9 indicates that higher-mode effects can also increase the drift at the base of the frame. Analyses of building frames between 4 and 20 storeys indicated that the significance of the higher modes on first-storey drift increased as the number of storeys increased. For shorter buildings the peak drifts resulting from time-history analyses tended to be up to 10% less than the design limit, while for the tallest frames peak drifts exceeded the design limit by up to 15%. The analyses also indicated that allocating 10% of the base shear to the roof controlled upper level drifts to within the design limit in all cases, though it was a little conservative for buildings below 10 storeys in height.

On the basis of these results it is recommended that a drift reduction factor be incorporated in design for taller buildings. It is apparent that this reduction could be expressed in terms of number of storeys, height, or effective period. However, the effective period will not be known at the start of the design process, and building height

is more fundamentally connected to higher mode effects than is number of storeys. On the basis of the analyses reported in [P17], it is thus recommended that buildings be designed to peak displacements of:

$$\Delta_{i,\omega} = \omega_\theta \cdot \Delta_i \qquad \qquad (5.28a)$$

where:

$$\omega_\theta = 1.15 - 0.0034 H_n \leq 1.0 \ (\textbf{\textit{H}}_n \text{ in m}); \ = 1.15 - 0.001 H_n \leq 1.0 \ (\textbf{\textit{H}}_n \text{ in ft}) \ (5.28b)$$

In Eq.(5.28a), the floor displacements Δ_i are those found from application of Eqs.(5.1) and (5.2).

In summary, to allow for drift amplification resulting from higher mode response, it is recommended that frame buildings be designed for the reduced displacements defined by Eq.(5.28), and that the vertical distribution of base shear force conform with Eq.(5.27).

5.5 STRUCTURAL ANALYSIS UNDER LATERAL FORCE VECTOR

There are two possible methods for determining the required moment capacities at potential hinge locations for frames designed by **DDBD**. The first requires a conventional frame analysis, considering relative stiffnesses of members, while the second is based solely on equilibrium considerations. Each is considered in turn.

5.5.1 Analysis Based on Relative Stiffness of Members

This approach was briefly discussed in Section 3.5.7, and is examined in more detail here, with respect to the four-storey regular frame of Fig.5.10. To be consistent with the principles of **DDBD** the frame structure analysed should represent the relative stiffness of members at the peak displacement. Thus beams, which are expected to sustain ductility demands should have their stiffnesses reduced from the elastic cracked-section stiffness in proportion to the expected member displacement ductility demand. For frame members of normal proportions, it will be adequate to reduce the elastic stiffness of all beam members by the system displacement ductility level μ_Δ. However, as will be obvious from Eq.(5.26), which indicates that the first-mode design drifts, and hence member ductilities reduce with height, this will overestimate the relative stiffnesses of beams at lower levels and underestimate relative stiffnesses at higher levels. An improved solution will result if the member ductilities at different levels are proportional to the drift demands (assuming that the beams at different levels have constant depth). Thus the member ductility at the first floor beams will be taken as $1.33\mu_\Delta$, and at the roof level, as $0.667\mu_\Delta$.

The design philosophy of weak beams/strong columns will require that the columns between the first floor and the roof remain essentially elastic. Hence, the stiffness of these columns should be modelled by the cracked-section stiffness, without any reduction for ductility.

Base Overturning Moment

$$OTM = \sum F_i \cdot H_i$$

$$OTM = T \cdot L_b + \sum M_{Cj}$$

$$OTM = \sum V_{Bi} \cdot L_{base} + \sum M_{Cj}$$
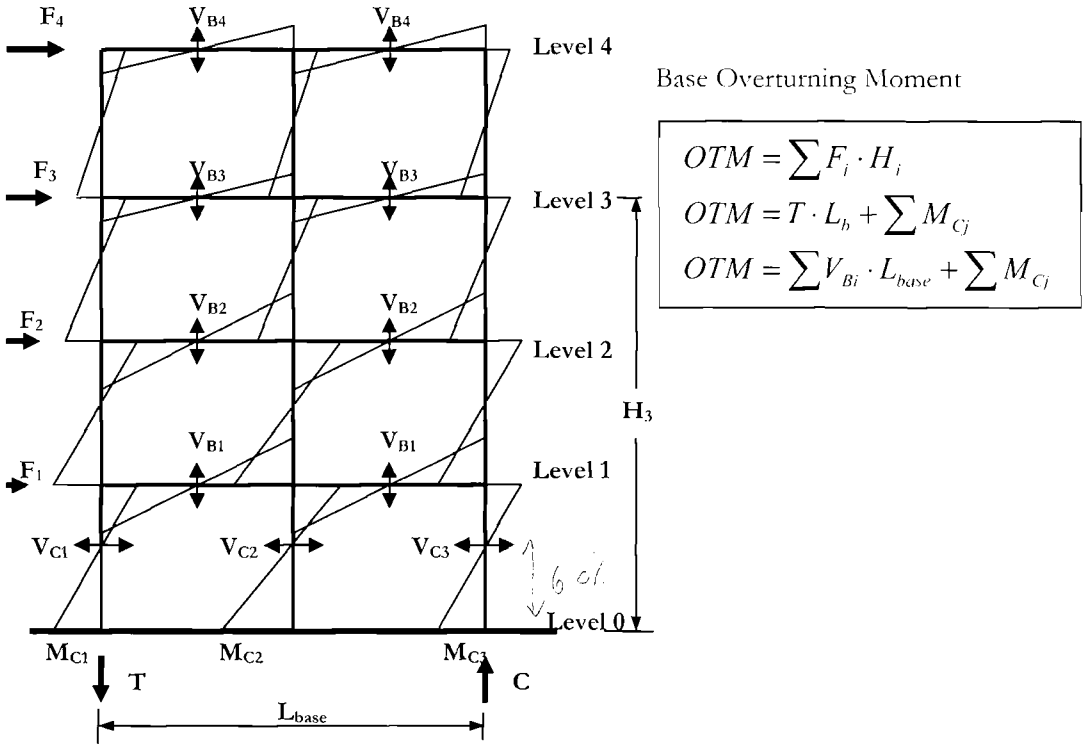
Fig.5.10   Seismic Moments from DDBD Lateral Forces

A problem occurs with the structural characterization of the columns between the ground and first floors. The design philosophy requires that plastic hinges be permitted to form at the ground floor level to complete the desired beam-sway mechanism (see Fig.5.2(a)), but that the first-storey columns remain elastic at the first floor level, to ensure that a soft-storey (column sway) mechanism of inelastic displacement cannot develop. It is thus not clear how the stiffness of the ground floor columns should be represented in the structural analysis.

The solution to this problem relies on the recognition that any structural analysis is approximate (compare the relative structural approximations involved in an initial-stiffness and a secant-stiffness representation, both of which are valid at different levels of seismic response), and that the fundamental requirement is that equilibrium is maintained between internal and external forces. With this in mind, we realise that it is possible for the designer to select the moment capacities of the column-base hinges, provided that the resulting moments throughout the structure are in equilibrium with the applied forces. Since our design criterion is that column hinges do not form at the underside of the level 1 beams, it would appear logical to design in such a way that the point of contraflexure in the columns occurs approximately at 60% of the storey height.

The design moment at the column base will thus be $0.6V_CH_I$ where V_C is the column shear and H_I is the storey height to the centre of the first floor beam. As will be clear from the representation of a typical interior column in Fig.5.11, where it is assumed that the beam depth at the first floor is approximately $0.15H_I$, this implies that the maximum column moment at the base of the first floor beam under first-mode response is about $0.325V_CH_I$, or about 54% of the column-base moment capacity. Assuming that column flexural strength is kept constant up the height of the first floor columns, this strength margin provides adequate protection against a soft-storey mechanism forming under higher mode response. Note, however, that beam elongation under ductile response may increase the moment at the top of the first-storey column at one end of a frame above this value[F3, X1], and fully ductile detailing is necessary here.
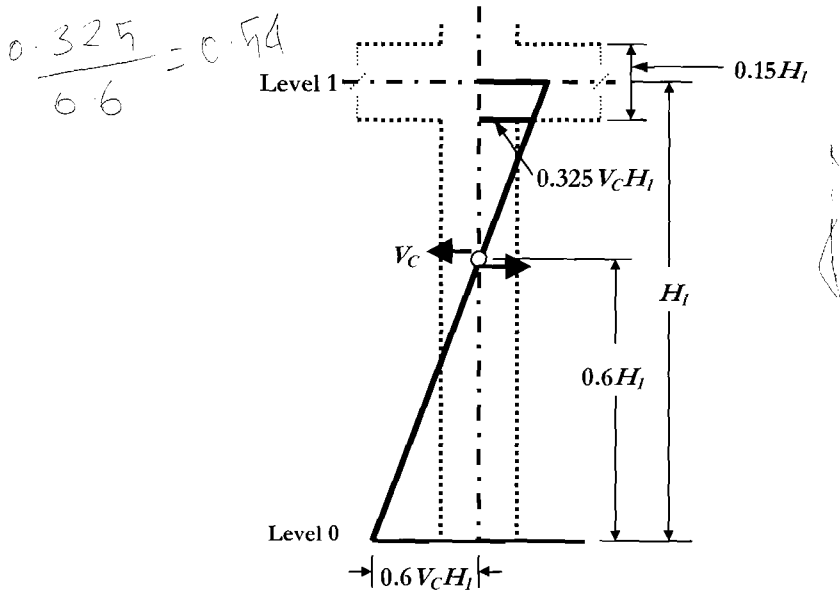
Fig. 5.11   Moments in Ground Floor Columns Based on Contraflexure at $0.6H_1$

We note that the column shear can be directly determined from the lateral forces, provided logical decisions are made about the distribution of storey shears between columns. Thus, with reference to the four-storey frame of Fig.5.10, the total base shear of

$$V_{Base} = F_1 + F_2 + F_3 + F_4 = V_{C1} + V_{C2} + V_{C3} \qquad (5.29)$$

should be distributed between the columns in proportion to the beam moment input. If we design for equal positive and negative moment capacity of the beams at a given level, then the moment input from the beams to the central column will be twice that for the

exterior columns. The corresponding distribution of the base shear between the columns will thus be

$$V_{C2} = 2V_{C1} = 2V_{C3} = 0.5V_{Base}$$
(5.30)

The desired column-base moment capacities can then be defined before the structural analysis for required flexural strength of beam plastic hinges.

The structural analysis then proceeds with the first-storey columns modelled as having cracked-section stiffness, and pinned-base conditions. The base moments (e.g. $M_1 = 0.6V_{C1}H_1$) are then applied as forces to the column-base hinges, in addition to the applied lateral forces F_1 to F_4. The results of the analysis will then define the required beam moments to satisfy the lateral force distribution, and the preferred column-base moments.

Typically, a commercially available frame analysis computer program will be used for the analysis. However, as mentioned in Section 3.5.7, a major problem with the relative stiffness approach is that the member stiffnesses depend on the flexural strengths (see Section 4.4), which will not be known until after the structural analysis is completed. This implies that an iterative process will be needed to determine the required beam moment capacities, modifying the stiffnesses to reflect the required strengths from an earlier iteration of the analysis.

Note that the decision to constrain the position of contraflexure in the columns may appear arbitrary, but is in fact much less so than the possible designer's choice between a fixed base and a pinned base design for the columns. The latter choice is not uncommon for steel building columns.

5.5.2 Analysis Based on Equilibrium Considerations

The final results from a frame analysis based on relative member stiffness will generally be modified somewhat in the design process to rationalize the design. For example, average negative beam moments at a given level may be adopted rather than the exact moment demands so that the same flexural reinforcement layout may be used at a number of sections. Considering the inevitable approximate nature of the structural analysis process, discussed in the previous sections, it is clear that alternative, simplified analysis procedures may be attractive. The following is based on simple equilibrium.

(a) Beam Moments: We again refer to the regular frame of Fig.5.10, and consider equilibrium at the foundation level. The lateral seismic forces induce column-base moments, and axial forces in the columns. The total overturning moment (*OTM*) induced by the lateral forces at the base of the building is

$$OTM = \sum_{i=1}^{n} F_i H_i$$
(5.31)

where n is the number of storeys. For a regular building, as shown in the example of Fig.5.10, seismic axial forces will be induced in the exterior columns by the seismic beam shears (V_{Bi}). If the beam negative moment capacities at all critical sections at a given level are equal, and similarly, all beam positive moment capacities at that level are equal (but not necessarily equal to the negative moment capacities), for the interior column, the axial force component from the beam shears at opposite sides of the column will cancel, and no seismic axial force will be induced. The OTM induced by the external forces must be equilibrated by the internal forces. Thus

$$OTM = \sum_{j=1}^{m} M_{Cj} + T \cdot L_{base} \tag{5.32}$$

where M_{Cj} are the column base moments (m columns) $T=C$ are the seismic axial forces in the exterior columns, and L_{base} is the distance between T and C. The tension force T (and the compression force C) is the sum of the beam shear forces, V_{Bi} up the building:

$$T = \sum_{i=1}^{n} V_{Bi} \tag{5.33}$$

Equations (5.31) to (5.33) can be combined to find the required sum of the beam shears in a bay:

$$\sum_{i=1}^{n} V_{Bi} = T = \left(\sum_{i=1}^{n} F_i H_i - \sum_{j=1}^{m} M_{Cj} \right) / L_{base} \tag{5.34}$$

Any distribution of total beam shear force up the building that satisfies Eq.(5.32) will result in a statically admissible equilibrium solution for the **DDBD**. Thus as with the choice of column-base moment capacity, it is also to some extent a designer's choice how the total beam shear force is distributed. Once the individual beam shears have been decided in such a way that Eq.(5.34) is satisfied, the lateral force-induced beam design moments at the column centrelines are given by

$$M_{Bi,l} + M_{Bi,r} = V_{Bi} \cdot L_{Bi} \tag{5.35}$$

where L_{Bi} is the beam span between column centrelines, and $M_{Bi,l}$ and $M_{Bi,r}$ are the beam moments at the column centrelines at the left and right end of the beam, respectively. These will normally not be equal, even if equal top and bottom beam flexural reinforcement is provided, due to the influence of slab reinforcement increasing the beam negative moment capacity. The seismic design moments at the column faces will be reduced from this value dependent on the column width h_c:

$$M_{Bi,des} = M_{Bi} - V_{Bi} h_c / 2 \tag{5.36}$$

A possible choice in the distribution of the total seismic beam shear would be to give all beams up the height of the building equal moment capacity, and hence identical reinforcement details. Although this would satisfy equilibrium at the base of the building, it would violate it, severely, at higher levels, implying a single lateral inertia force at roof level. The consequence would be excessive variation in beam ductility demand up the height of the building, which would be reflected in local drifts exceeding the design limit. This is illustrated in Fig.5.12, where the 16 storey frame, results of which are shown in Fig.5.9(a) was redesigned for a linear displacement profile and uniform beam strengths up the height of the building.
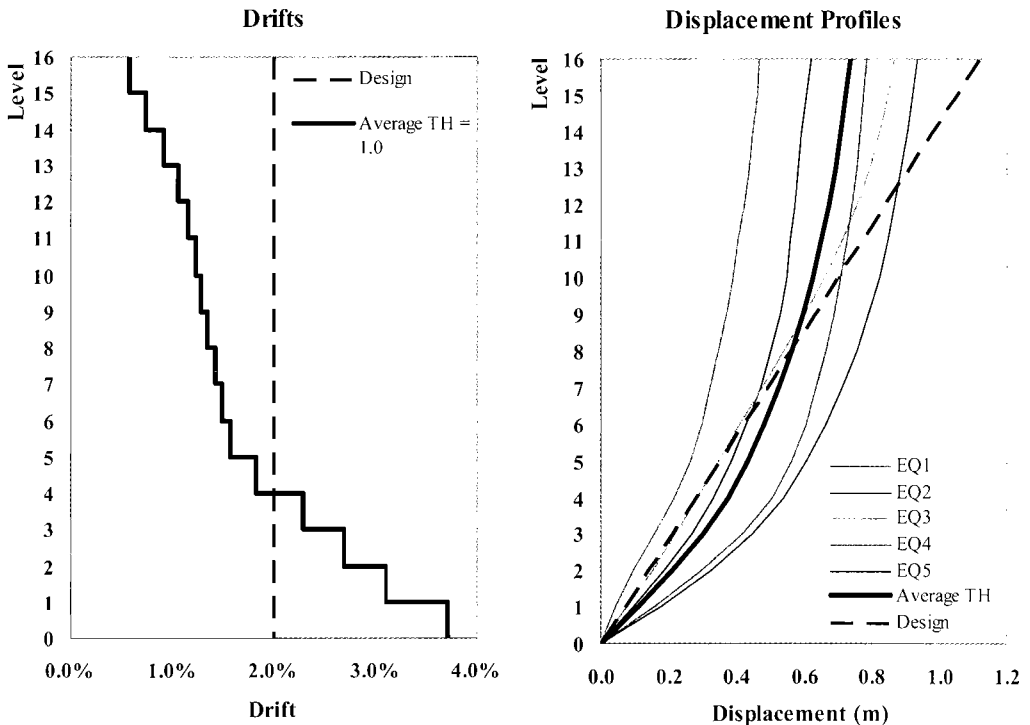
Fig.5.12 Average Time-History Response of a 16 Storey Frame Designed with Uniform Beam Strength up Building Height[P17]

The average displacement profile from time-history (TH) analysis is seen to differ markedly from the design profile, and drift at the lowest floor is almost twice the design level, while drift in the upper storeys is very low. Thus to ensure that drifts do not exceed the design limits it is important that the vertical distribution of beam shears follows the seismic demand. This can best be achieved by allocating the total beam shear from Eq.(5.34) to the beams in proportion to the storey shears in the level below the beam under consideration. This can be expressed as

$$V_{Bi} = T \cdot \frac{V_{S,i}}{\sum\limits_{i=1}^{n} V_{S,i}} \tag{5.37}$$

where

$$V_{S,i} = \sum_{k=i}^{n} F_k \tag{5.38}$$

are the storey shear forces and T is given by Eq.(5.34). The complete analysis procedure for regular frames is as follows:

- Determine the design base shear and floor inertia forces from **DDBD** principles (Eqs.(5.1) to (5.12)).
- Determine the **OTM** from the **DDBD** forces (Eq.(5.31)).
- Design (chose) the column-base moment capacities.
- Determine the column-base tension force T from Eq.(5.34).
- Determine the storey shear forces from Eq.(5.38).
- Determine the vertical distribution of beam shears from Eq.(5.37).
- Calculate the column-face beam seismic moments from Eqs.(5.35) and (5.36).

As noted above, it will be common to design the beam flexural strengths with the negative capacity exceeding the positive capacity to reflect the gravity load demand, and also the typical enhancement of beam negative moment capacity caused by slab flexural reinforcement.

Extension of this analysis procedure to the irregular frames discussed in Section 5.3.3 is straightforward. Each bay is considered separately, with the total base shear force being allocated to the different bays in proportion to the chosen contribution to the *OTM*. Thus, with reference to the frame of Fig.5.5, the base shear forces V_{CB1} and V_{CB2} allocated to each of the exterior bays, and the interior bay respectively will be

$$V_{CB1} = V_B \cdot \frac{M_1}{2M_1 + M_2} \; ; \quad V_{CB2} = V_B \cdot \frac{M_2}{2M_1 + M_2} \tag{5.39}$$

The procedure for each bay then follows the last five bullets in the list above. Distribution of the total base shear between the columns will normally be in the ratio of 1:2 for external/internal columns. The required beam shears V_{B1i} for the outer bay will thus be given by

$$\sum_{i=1}^{n} V_{B1i} = T = \frac{M_1}{2M_1 + M_2} \cdot \left(\sum_{i=1}^{n} F_i H_i - \sum_{j=1}^{m} M_{Cj} \right) / L_1 \tag{5.40}$$

where L_1 is the span length of the exterior bay. Similarly the sum of the beam shears V_{B2i} for the interior bay will be given by

$$\sum_{i=1}^{n} V_{B2i} = T = \frac{M_2}{2M_1 + M_2} \cdot \left(\sum_{i=1}^{n} F_i H_i - \sum_{j=1}^{m} M_{Cj} \right) / L_2 \tag{5.41}$$

Inelastic time-history analyses of frames designed in accordance with the above approach have indicated satisfactory performance in terms of drift magnitude and distribution (see Fig.5.9(b) e.g.).

(b) Column Moments: The analysis carried out for beam moments in accordance with the above equilibrium considerations also implies that column moments can be directly calculated. The total storey shear force given by Eq.(5.38) is divided between the columns, normally in the ratio of 1:2 for external/internal columns, as noted above. Then, since the moment input from the beams at each level is known from the above analysis, the column moments can be found, working up from the level 1 joints. This is illustrated with respect to Fig.5.13, which represents an internal column between level 0 (ground floor) and level 2, and is an extension of Fig.5.11.

The point of contraflexure in the column between levels 0 and 1 has been chosen at $0.6H_1$, and the beam moments at levels 1 and 2 have been found as described in the previous section. The moment at the top (beam centreline) of column 01 will be

$$M_{C01,t} = 0.4 V_{C01} \cdot H_1 \tag{5.42}$$

Beam moments at the Level 1 joint centroid are $M_{B1,l}$ and $M_{B1,r}$ for the beams to the left and right of the joint centroid respectively. Hence, for equilibrium of moments at the joint centroid, the moment at the bottom of column 12 will be

$$M_{C12,b} = M_{B1,l} + M_{B1,r} - M_{C01,t} \tag{5.43}$$

Since the shear force, V_{C12} in column 12 is known, as discussed above, the moment at the top of column 12 can also be directly calculated:

$$M_{C12,t} = V_{C12} \cdot H_2 - M_{C12,b} \tag{5.44}$$

Note that in the above discussion, all moments have been considered positive values, in the sense indicated in Fig.5.13.

The procedure continues with consideration of equilibrium at the level 2 joint, working its way up the building until the top level is reached. It should be noted, however, that this procedure will result in column contraflexure points that are close to

column mid-heights, and that the actual design values will be modified from the values calculated above to allow for beam flexural overstrength, higher mode effects, and biaxial actions (see Section 5.6.2 below). As such, a simpler design approach of assuming central points of contraflexure in each column is acceptable, thus resulting in equal column moments at top and bottom of each column equal to $M_{Ci} = 0.5V_{Ci}H_i$ is acceptable. It should be noted that it is the sum of moment capacities at top and bottom of a column rather than individual values at top or bottom that is important in guarding against formation of a column-sway mechanism.
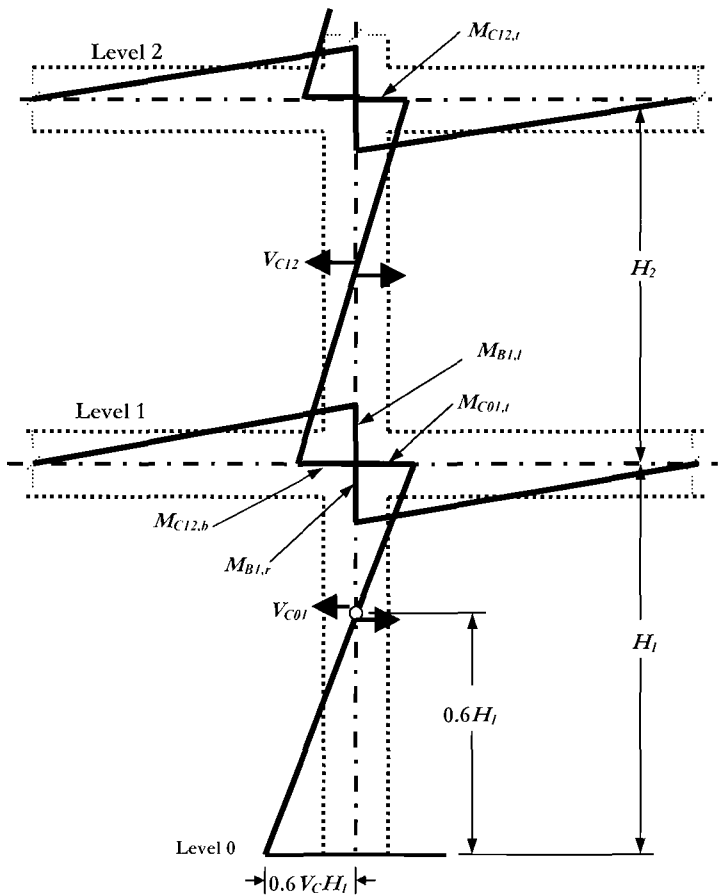
Fig.5.13   Determination of Column Moments from Consideration of Joint Equilibrium

5.6   SECTION FLEXURAL DESIGN CONSIDERATIONS

5.6.1   Beam Flexural Design

Reference should be made to Sections 3.7.2, and 4.2.5. The former discusses the combination of seismic and gravity moments for beams, while the latter defines material strengths to be used in flexural design of plastic hinges. It is recommended that beams be designed for the larger of the factored gravity moments and seismic moments ignoring gravity moments. The rationale for not combining the gravity and seismic moments is that this combination increases the required section strength and reduces the response drift levels below the target values. Comparative time-history analyses of frames where the gravity moments are included or ignored in the analysis have indicated that the influence on drift is negligible[P15]. This is because the gravity moments increase the total moment at one end of the beam, and reduce it at the other end. Paulay and Priestley[P1] discussing force-based design of frames recommend allowing redistribution of moments under combined gravity and seismic actions by up to 30% of the peak moment demand in the beams at a given level of the frame. This has a similar effect to the (simpler) suggestion made in Section 3.7.2, as can be seen from the following example.

We consider a typical interior beam of a frame of an office building. For simplicity of argument we assume that the beam is part of a one-way frame, and that beam span and tributary slab width are both 6m (19.7ft). The beam size is 600×400mm (23.6×15.7in), and the slab thickness, including topping is 150mm (5.9in). Thus the dead load supported by the beam is :

$$w_D = 23.5(6\times0.15+0.45\times0.4) = 25.4 \text{ kN/m}$$

Basic live load for an office building is taken as 2.5 kPa (45lb/sq.ft). A live load reduction factor based on tributary area of 36m² (388ft²) is found to be 0.85 for gravity load calculations, with a further reduction factor of 0.4 for seismic load combinations. Thus the following live loads apply:

> Gravity: w_L = 6×0.85×2.5 = 12.75 kN/m (0.87kips/ft)
> Seismic: w_{LE}= 0.4×12.75 = 5.1 kN/m   (0.35kips/ft)

Assuming full fixity of the beam ends, the gravity load moments at the column centrelines are thus:

> Dead load: M_D = 25.4×6²/12 = 76.2 kNm (674 kip.in)
> Live load (gravity): M_L = 12.75×6²/12 = 38.3 kNm (339 kip.in)
> Live load (seismic): M_{LE}= 5.1×6²/12   = 15.3 kNm (135 kip.in)

For "conventional" design incorporating moment-redistribution for the seismic load combination, assuming a flexural strength reduction factor of ϕ = 0.9 for gravity loads

only, the following strength requirements apply (Note load factors from the Appendix to ACI[X7] for gravity load are used for this comparison):

$$M_{des1} \geq (1.4M_D + 1.7M_L)/\phi \qquad \qquad \text{(5.45a)}$$

$$M_{des2} \geq (1.0M_D + 1.0M_{LE} + M_E) \times 0.7 \qquad \qquad \text{(5.45b)}$$

where M_E is the seismic moment. Note that Eq.(5.45b) incorporates the 30% reduction for redistribution which would require a corresponding increase (in value, not percentage) at other locations.

The recommendations provided in this text are that, in addition to the conventional gravity load design (we again assume that Eq.(5.45a) applies, including the strength reduction factor), the seismic design case is given by Eq.(5.45c):

$$M_{des3} \geq M_E \qquad \qquad \text{(5.45c)}$$

Substituting the calculated values for dead and live load we obtain:

$$M_{des1} \geq 190.9 \text{ kNm} \quad (1689 \text{ kip.in})$$
$$M_{des2} \geq (76.2+15.2) \times 0.7 + 0.7M_E = 64.1 + 0.7M_E \text{ kNm} \quad (567+0.7M_E \text{ kip.in})$$
$$M_{des3} \geq M_E \text{ kNm}$$

For conventional design permitting moment redistribution, the larger of the first two values will apply. Thus for low values of seismic moment, the gravity load combination will govern. For the approach suggested herein, the larger of the first and the third values will apply.

Figure 5.14 plots design moment against seismic moment for the two approaches. For low levels of seismic moment, M_{des1} governs for both approaches. It is seen that the seismic moment starts to govern at a very similar level of seismic input with both approaches, and that except for a very small range of seismic input, the approach suggested herein is more conservative than the approach allowing moment redistribution. This adds support to the simple recommendation that gravity loads be ignored in the seismic load combination, and that design strength be based on the larger of gravity and seismic moments.

Section 4.2.5 discusses material properties for intended plastic hinge locations, and it is recommended that design values for seismic design exceed the specified, or characteristic material strengths is accordance with $f'_{ce} = 1.3f'_c$; $f_{ye} = 1.1f_y$.

As explained in Section 4.2.5, these values are recommended in recognition that material strengths will normally exceed specified strengths at the building age when seismic attack occurs, and that use of artificially low material strengths does not reduce the probability that inelastic response will occur at the design level of seismic input, nor does it improve safety. The main consequence of design to artificially low material strengths is an increase in cost, particularly for capacity-protected actions. In accordance
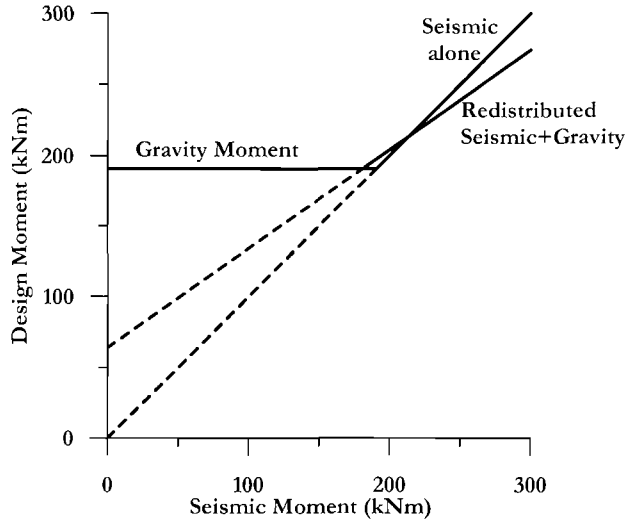
Fig.5.14   Beam Design Moment Incorporating Seismic Loading Based on Recommendations in this Text Compared with Conventional Design Permitting Moment Redistribution of 30%.

with the recommendations of Section 4.2.5, strength enhancement of flexural reinforcement may be considered when determining required flexural reinforcement quantities, and the use of a flexural strength reduction factor for seismic actions of intended plastic hinges is viewed to be inappropriate.

Methods for flexural design of beams are covered in all standard texts on reinforced concrete design, and need no further elaboration here, though guidance relating to material properties and use of moment-curvature analysis is given in the recommendations of Section 4.2.6. Particular reference is made to [P1] for details on contribution of slab reinforcement to flexural strength, and other matters specifically related to seismic design of frames. It is noted, however, that the conventional distribution of flexural reinforcement in beams, where negative-moment reinforcement is concentrated near the top of the section, and positive-moment reinforcement is concentrated near the bottom of the section, as illustrated in Fig.5.15(a), can cause problems with congestion and concrete placement, particularly in two-way frames, where intersecting layers of reinforcement occur at the top of the joint region. If the same quantity of flexural reinforcement is distributed down the sides of the section, as shown in Fig.5.15(b), the flexural strength of the beam will be essentially the same as for the conventional distribution, as trial calculations will show, since a larger proportion of the total reinforcement will act in tension for a given sense of moment, compensating for the reduced lever arm from the centre of tension to the centre of compression in the section. Distributing the flexural reinforcement down the sides clearly reduces congestion

problems, and also improves bond conditions for beam reinforcement through the joint, reduces joint shear stresses, and improves beam shear performance[W1].

(a) Conventional   (b) Vertically Distributed
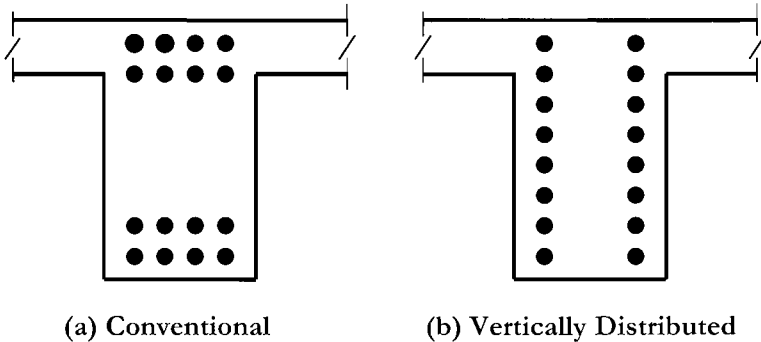
Fig.5.15   Alternative Distributions of Beam Flexural Reinforcement for Reinforced Concrete Frames[W1]

5.6.2 Column Flexural Design

As with beam design, design of columns is well covered in standard texts and needs little discussion here. However, a more conservative design approach than that for beams is appropriate since the columns should be required to remain essentially elastic, except at the column base, and possibly immediately below the roof beams. It should be noted that column moments need to be amplified above values corresponding to the design lateral seismic force to allow for:

- Potential overstrength capacity at beam plastic hinges resulting from material strengths exceeding the values specified for design.
- Dynamic amplification of column moments resulting from higher mode effects, which are not considered in the structural analysis carried out in accordance with Sections 5.5.1 or 5.5.2
- Biaxial effects for columns that form part of two-way frames.

It should also be noted that practice in the USA, requiring that the sum of column moment capacity in a given direction framing into a joint should exceed 1.2 times the sum of beam moment capacity in that direction, framing into the joint does not provide adequate protection against columns forming accidental plastic hinges, with potentially serious consequences.

(a) Beam Overstrength Capacity: The consequence of overstrength flexural capacity being developed at intended plastic hinge locations was discussed in Section 4.5. The maximum feasible flexural strength of beam hinges can be assessed by moment-curvature analysis, adopting high estimates of probable material strengths, and incorporating strain-hardening of flexural reinforcement and confinement of core concrete, as outlined in

Section 4.5, or conservative default factors may be adopted for simplicity, as discussed in Section 4.5.2. Since the column is required to remain elastic, column dependable flexural strength should be required to satisfy Eq.(4.59).

(b) Higher Mode Effects: These are discussed in some detail in Section 5.8.4.

(c) Biaxial Attack: When columns form part of a two-way seismic frame, biaxial input must be considered. There will normally be equal probability that the maximum seismic excitation will occur in any orientation (including diagonal) with respect to the principal axes, and this will be accompanied by simultaneous excitation, normally at a lesser intensity, in the orthogonal direction. Although the strength of a frame building in the diagonal direction will be larger than in the direction parallel to one of the principal axes, (see Section 5.7) it is probable that simultaneous development of beam plastic hinge mechanisms will occur in both principal frame directions, unless the design displacement ductility in the principal directions is very low. Consequently, since it is required that the columns remain essentially elastic when beam-hinge mechanisms form, the columns must be able to resist moments corresponding to simultaneous beam hinging in orthogonal directions.
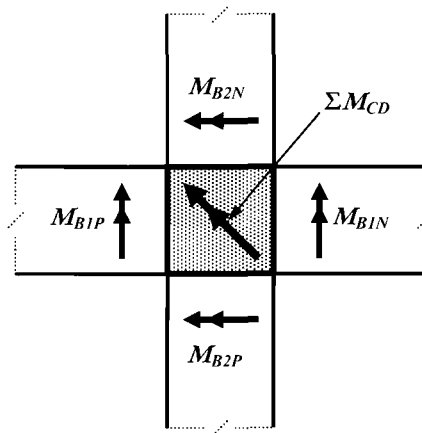
Fig.5.16   Plan View of Moment Input to Interior Column of a Two-way Frame

This is illustrated for the interior column of a two-way frame in Fig.5.16, where the beam moment vector inputs are represented with double-headed arrows, using the right-hand rule. All moments are the values applicable at the joint centroid, and the suffixes *P* and *N* indicate positive and negative beam moments respectively. The required sum of column diagonal moment capacities of columns in the storey above and below the level considered, measured at the joint centroid is given by:

$$\sum M_{CD} \geq \sqrt{\left(M_{B1P} + M_{B1N}\right)^2 + \left(M_{B2P} + M_{B2N}\right)^2}$$ (5.46a)

The most usual case for two-way frames will have the moment capacity of the beams in the orthogonal directions being equal, and the columns having square cross-sections. Experiments and analyses indicate that the moment capacity of symmetrically reinforced square columns in the diagonal direction is very similar to the capacity in the principal directions. Hence the required sum of column moment capacities in the **principal** directions, above and below the joint centroid can be determined as

$$\sum M_C \approx \sum M_{CD} = \sqrt{2} \cdot \left(M_{B1P} + M_{B1N}\right)$$ (5.46b)

For an interior column, as depicted in Fig.5.16, the seismic axial force will be close to zero, and hence the required column reinforcement can be determined based on the assumption of probable gravity loads. For an exterior column, however, seismic beam shears will generate significant axial forces, either tensile or compressive (see Fig.5.10, e.g.) which should be considered when determining the required column flexural reinforcement. It could be argued that permitting column hinging in the tension exterior column is justified, since this in itself will not imply development of a soft-storey mechanism, which would require all columns in a given frame to hinge. Although this might appear technically and economically justified, it should be noted that exterior columns are more susceptible to joint shear failure than are interior (either one-way or two-way) columns, and vertical joint shear resistance in these columns is normally provided by under-utilized capacity of the flexural reinforcement in the columns, assured by the capacity design procedure[P1]. If the columns are permitted to hinge, then this excess capacity will not be available for joint shear resistance, and special vertical joint reinforcement will be needed.

Note that for diagonal attack the procedure for determining the required column capacities, outlined in Section 5.5.2(b) needs some modification. In Eqs.(5.42) and (5.44) the column shears V_{C01} and V_{C12} must be replaced with the corresponding column shears V_{CD01} and V_{CD12} developed under diagonal attack. For a structure with equal beam strength and bay length in the orthogonal directions, $V_{CD01} = \sqrt{2}V_{C01}$ etc. The beam moment input to the joint, given in Eq.(5.43) as $M_{B1,l} + M_{B1,r}$, must be replaced by the vectorial summation of the beam input moments, given by the expression on the right hand side of the inequality of Eq.(5.46(a)). It is also suggested that the base moment capacity of the columns be increased to $0.7V_{C01}H_1$, where V_{C01} is the principal-direction column shear.

It should be noted that the common force-based design approach of determining the required column biaxial moment capacity from consideration of simultaneous seismic input of 100% and 30% design intensity in orthogonal directions, using elastic modal analysis, with the elastic moment demands then reduced by the code-specified force-reduction factor (or behaviour factor, or ductility factor, as it is often known) will provide

inadequate protection against formation of a soft-storey sway mechanism in the ground floor columns, since the procedure implies input beam moments of only 30% of capacity in one of the orthogonal directions. In fact, it is the displacement demand in the orthogonal direction that should be reduced to 30%, not the moment. If the design ductility demand exceeds 3.3, then the full moment capacity should be expected to be simultaneously developed in the (minor) principal direction, as well as the (major) principal direction. For diagonal attack, 100%/30% is non-conservative for $\mu > 2$.

Corner columns require special attention, since these can be subjected to high seismic axial tensions or compressions from the response of both orthogonal frames incident in the corner columns. There is comparatively little experimental information on the shear performance of corner columns when subjected to biaxial beam input and high variations in seismic axial force from tension to compression. However, it should be noted that the collapse of the newly-constructed Royal Palm Hotel in the 1993 Guam earthquake has been attributed to failure of the (admittedly poorly reinforced) joints of the corner columns, as shown in Fig. 5.17. A design option that should be considered for two-way frames is to provide separate exterior columns for the orthogonal frames, rather than a common corner column, as suggested in Fig. 5.18(b). Flexibility of the floor slab between the orthogonal exterior columns provides continuity without excessive shear transfer. This has the merit of reducing the design moments, axial force variation, and joint shear force on these corner columns. In some cases of low to moderate seismicity, the architectural appearance of full two-way structural continuity into the corner column can be achieved with an alternate design where the seismic frame consists of less bays than the full number along the side of the building. The seismic frame is connected to the non-seismic columns, including the corner columns, by gravity beams without moment connection to the columns. In New Zealand, frames have been constructed with reduced beam depth adjacent to corner columns, and hence reduced moment input to the critical columns, to produce a similar reduction in corner column actions.

(d) Column-Base Flexural Design: Although it has been recommended above that the seismic axial force be considered when determining the required column reinforcement for capacity-protected exterior and corner columns, the same is not required when designing the intended column-base plastic hinge. If the simplified analysis procedure of Section 5.5.1 is adopted, then equal column-base design moments M_C would result for the exterior tension and compression columns. If the axial force from the tension column was used to determine the required amount of column flexural reinforcement, then the moment capacity of the compression column would exceed the design moment significantly. This is illustrated by the dashed line for the column axial-force/moment interaction diagram shown in Fig.5.19. With this option, it is seen that the flexural capacity of the tension column (with reduced axial force $G-E$) is matched to the required capacity M_C. The capacity of the compression column, with axial force $G+E$ is M_3. The total resisting capacity of the structure, in terms of base overturning moment thus will exceed the demand corresponding to the design distribution of lateral forces.
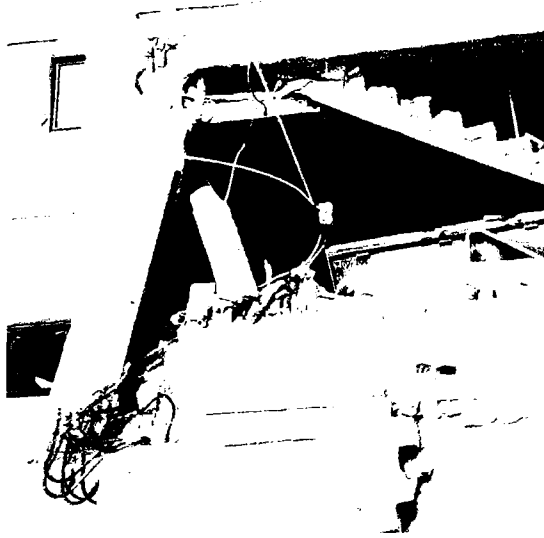
**Fig.5.17 Failure of Royal Palm Hotel Corner Joints in the 1993 Guam Earthquake
(photo courtesy Gary Hart)**

(a) Conventional Layout   (b) Alternative Layout
   with Corner Column   No Corner column
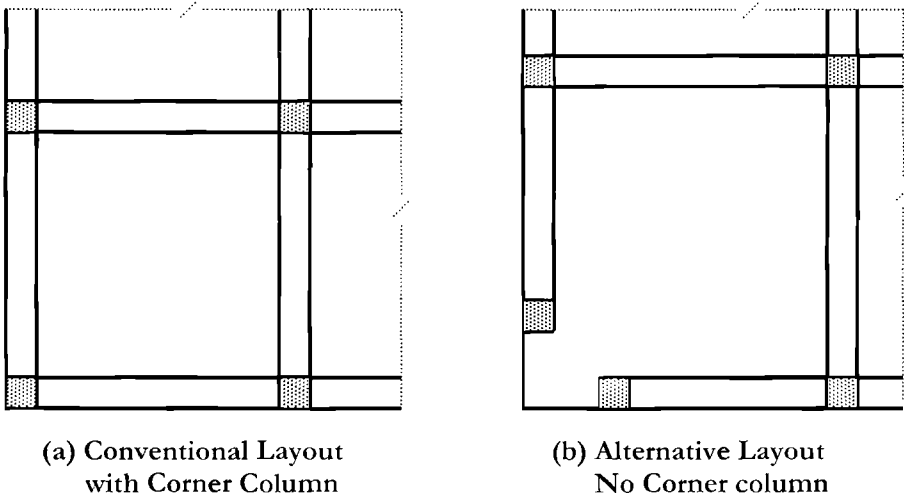
Fig.5.18   Plan View of Two-Way Frame Layout Options

An alternative approach would be to determine the required column flexural reinforcement based on the design moment and the axial gravity load **G** alone. This option is represented by the solid line in the interaction diagram of Fig.5.19. The reinforcement content ρ_{l2} will be less than for the former alternative, and the moment

capacities of the tension and compression columns will then be M_1 and M_2 respectively. Examination of Fig.5.19 indicates that the average moment capacity will be very close to the required value of M_C. Thus a more efficient design has been achieved.
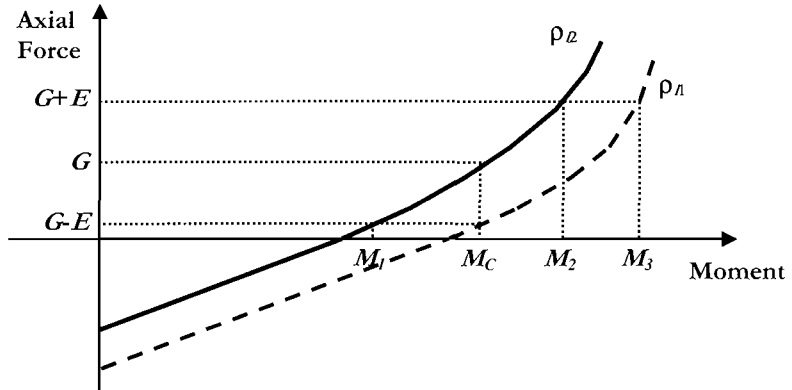
Fig.5.19 Axial Force/Moment Interaction Diagram for Exterior Columns

Note that this could have been recognized at the start of the design process, where the total base shear force was allocated between the columns, and the base moment capacities were chosen (see Section 5.5.2(b)). A lower shear force and base moment could have been allocated to the tension column, with a corresponding increase in the values for the compression column. It will be noted that this is analytically a logical approach in that it recognizes that the tension column has lower elastic stiffness than the compression column (see Section 4.4.2), and hence attracts less seismic shear and moment. It is recommended that a moment of $0.3 Th_c$, where T is the seismic tension force in the outer column, and h_c is the column depth, be subtracted from the tension column and added to the compression column.

5.7 DIRECT DISPLACEMENT-BASED DESIGN OF FRAMES FOR DIAGONAL EXCITATION

In the previous section the importance of designing columns of two-way frames for diagonal excitation was discussed. A related aspect that requires consideration is the control of drift when the excitation is in the diagonal direction. Implicit in the discussion thus far has been the assumption that design for specified drift or ductility limits in the principal directions will provide a design that also satisfies drift or ductility limits in the diagonal direction. We now show that to indeed be the case by considering a two-way frame building with equal strength and stiffness in the orthogonal directions.

Consider the building response illustrated in Fig.5.20. Figure 5.20(a) shows the yield and design displacements in the principal (X and Y) and diagonal (D) directions in plan view. Yield displacements are Δ_{yX} and Δ_{yY} in X and Y directions respectively. For

simplicity we assume a square building with equal strengths and stiffnesses in the two principal directions, so $\Delta_{yX} = \Delta_{yY} = \Delta_{yP}$. If the building is displaced in the diagonal direction, yield will not occur until the displacements in the two principal directions are equal to their yield values, and hence the diagonal yield displacement is

$$\Delta_{yD} = \sqrt{2}\Delta_{yP} \tag{5.47}$$

(a) Design Displacements, Principal and Diagonal

(b) Force-Displacement Response

(c) Displacement Spectra
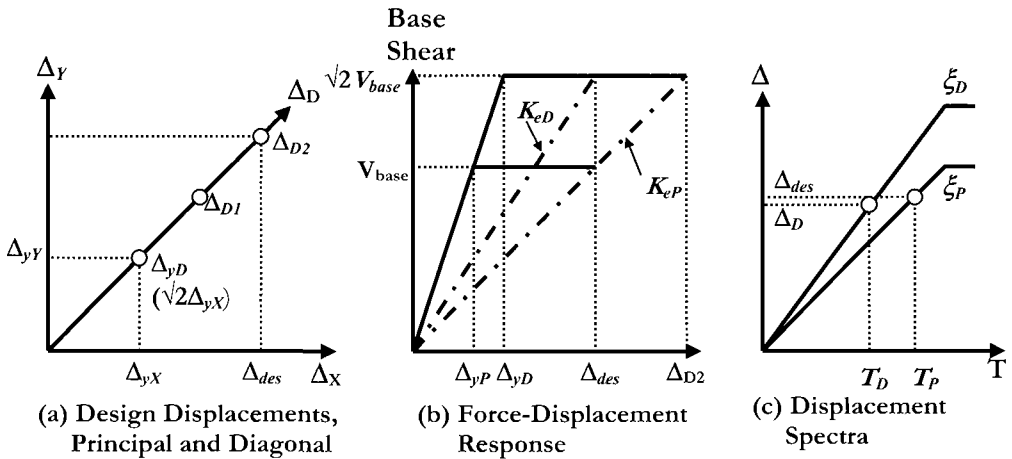
Fig.5.20 Comparison of Displacement Response in Principal and Diagonal Directions

The relationship between design displacements in the principal and diagonal directions will depend to some extent on whether strain or non-structural drift defines the design limit. In the first case, the diagonal limit displacement corresponds to achieving the limit strains in the principal directions, and hence the diagonal limit dis-
placement is $\Delta_{D2} = \sqrt{2}\Delta_{des}$. If the design displacement is limited by non-structural drift, then it could be argued that the maximum displacement in the diagonal direction under diagonal attack should not exceed the displacement limit applying in the principal directions. This displacement is represented in Fig.5.20(a) by Δ_{D1} where $\Delta_{D1} = \Delta_{des}$. Clearly this is the more critical of the two cases, though it can be argued that a larger design displacement is appropriate in the diagonal direction, even if non-structural drift limits the design, since non-structural elements will normally be oriented parallel to one of the principal directions, and achieving the design drift in the diagonal direction will not correspond to critical non-structural displacement.

If the design response in the diagonal direction exceeds the diagonal yield displacement given by Eq.(5.47), then the strength of the frames will be developed in the principal directions. Resolving the strength of all frames in the **X** and **Y** directions into the diagonal direction, it is obvious that the diagonal base shear strength is $\sqrt{2}V_{base}$ where

V_{base} is the design strength in each of the principal directions.

The force-displacement response of the structure in principal (**P**) and diagonal (**D**) directions is represented in Fig.5.20(b), where it is assumed that the diagonal displacement response is either Δ_{D1} or Δ_{D2}. As explained above, we consider only the more critical case of $\Delta_{D1} = \Delta_{des}$. We first assume that the structure is designed in the principal directions, and then checked to determine whether or not response in the diagonal direction satisfies the displacement limit. It is seen that if the structure achieves the design displacement in the diagonal direction, the stiffness K_{eD} is greater than the stiffness K_{eP} in the principal directions. This would appear to imply that the displacement demand in the diagonal direction will be less than in the principal direction, since the effective period will be higher (Eq.5.10). However, the ductility demand in the diagonal direction will also be less than in the principal direction, since the yield displacement is larger (Eq.5.47) and hence the effective damping will be less, and displacement will increase. The two conditions – principal and diagonal – are represented in the displacement spectra of Fig. 5.20(c). Since the effects of reduced period and reduced damping are counteractive, it is not immediately clear whether displacement response will be larger or smaller in the diagonal direction.

For a given level of ductility, μ in the principal direction, this can be resolved by an iterative analysis as follows, making the initial assumption that the diagonal response displacement is equal to the principal response displacement. Diagonal and principal stiffnesses will thus be related by

$$K_{eD} = \sqrt{2} \cdot K_{eP} \tag{5.48}$$

Since the effective period is given by $T_e = 2\pi\sqrt{m_e / K_e}$, and the mass is the same whether principal or diagonal attack is considered, the diagonal and principal effective periods will be related by

$$T_{eD} = T_{eP} / \sqrt[4]{2} = 0.841 T_{eP} \tag{5.49}$$

Diagonal and principal direction ductilites are related by

$$\mu_D = \mu_P / \sqrt{2} \tag{5.50}$$

Assuming a reinforced concrete building, the ratio of effective damping in diagonal and principal directions can be found from Eq.(5.9a) as

$$\xi_D = \frac{0.05 + 0.565(\mu_D - 1)/\mu_D\pi}{0.05 + 0.565(\mu_P - 1)/\mu_P\pi} \cdot \xi_P \tag{5.52}$$

$$R_i = \left(\frac{0.07}{0.02 + \xi} \right)^x$$

Based on Eq.(2.8), the displacement spectra applicable to diagonal and principal attack will thus be related, for a given period T, by

$$\Delta_{DT} = \frac{\left(0.07/\left(0.02 + \xi_D\right)\right)^{0.5}}{\left(0.07/\left(0.02 + \xi_P\right)\right)^{0.5}} \cdot \Delta_{PT} \tag{5.53}$$

Combining the effects of Eqs.(5.49) and (5.53), the response displacement in the diagonal direction is related to the principal direction design displacement as

$$\Delta_D = \frac{T_{eD}}{T_{eP}} \cdot \frac{\Delta_{DT}}{\Delta_{PT}} \cdot \Delta_{des} \tag{5.54}$$

If, as will normally be the case, the value of Δ_D from Eq.(5.54) is not equal to Δ_{des} then the period and ductility given by Eqs.(5.49) and (5.50) respectively must be factored by the ratio $R = \sqrt{(\Delta_D/\Delta_{des})}$, and Eqs.(5.51) to (5.53) cycled until successive approximations for Δ_D are sufficiently close.

This procedure has been carried out for principal-direction ductilities between 1 and 6, and the resulting ratios of diagonal to principal-direction response displacements are plotted in Fig.5.21. As expected the diagonal-direction displacements are equal to principal-direction displacements for elastic, and near-elastic response (since stiffness and damping are identical), but at higher displacement ductilities, the diagonal displacement response is increasingly lower than the principal direction response.
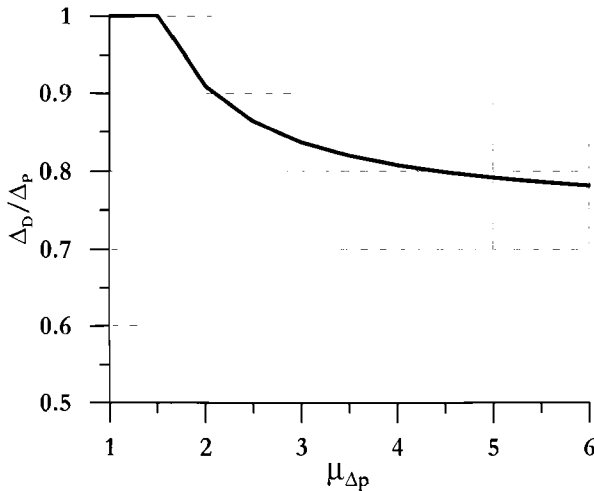
Fig.5.21 Maximum-Displacement Ratio for Diagonal and Principal Direction
Excitation for a Square Frame Building

Note that the calculations summarized in Fig.5.21 are based on "normal" response spectra (see Section 2.2.3). For near-field response spectra showing significant forward directivity effects, the influence of damping will be less significant than shown here, as will be seen by substituting 0.25 for 0.5 in the power factors of Eq.(5.53), while the period influence will be unaffected. In this case the ratio of diagonal to principal direction displacements will be less than shown in Fig.5.21.

5.8 CAPACITY DESIGN FOR FRAMES

5.8.1 General Requirements

General requirements for capacity design are considered in Sections 3.9 and 4.5. The basic required strength is governed by the inequality defined in Eq.(3.57), reproduced here as Eq.(5.55) for convenience:

$$\phi_S S_D \geq S_R = \phi^o \omega S_E \qquad (5.55)$$

where S_E is the value of the design action being capacity protected, corresponding to the design lateral force distribution found from the **DDBD** process, ϕ^o is the ratio of overstrength moment capacity to required capacity of the plastic hinges, ω is the amplification of the action being considered, due to higher mode effects, S_D is the design strength of the capacity protected action, and ϕ_S is a strength-reduction factor relating the dependable and design strengths of the action. In frames, capacity design considerations will relate to beam flexural and shear strength, column flexural and shear strength, and possibly column axial load capacity. These are considered in turn.

5.8.2 Beam Flexure

It is normal, in seismic design of frames, to consider that there is no dynamic amplification of beam shears or moments, and thus only moment overstrength, represented in Eq.(5.55) by the ϕ^o factor needs to be considered. Although this is correct for the beam moments induced as a result of seismic inertial response of the structure as a whole, there may be dynamic amplification of the gravity load moments as a result of amplification of vertical accelerations. There have been reports in earthquakes of objects on floors of multi-storey buildings being bodily thrown off the floor, implying vertical response accelerations exceeding 1g. This is a phenomenon that has apparently received little research attention.

Figure 5.22 shows components of moments and shears for a typical beam of a seismic frame, where the units for both moment and shear are arbitrary. In Fig. 5.22(a), two gravity-load moment profiles are shown. $F.G$ corresponds to moments of factored gravity loads, and G_E is the moment profile for reduced gravity loads to be considered in the seismic load combinations. Seismic moments corresponding to the design lateral

(a) Beam Moments
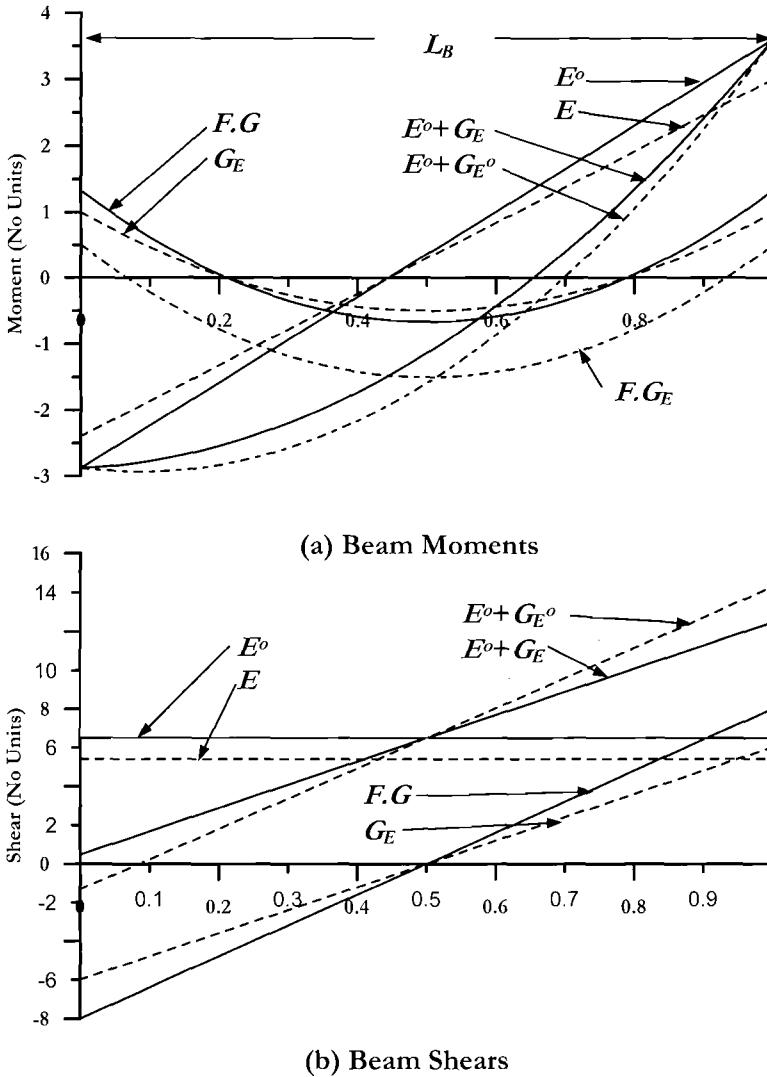
(b) Beam Shears

Fig.5.22   Design Moments and Shears for Beams

forces, and corresponding overstrength seismic moments are E and E^o respectively. In accordance with the recommendations of Section 5.6.1, flexural design of the beam plastic hinges is based on the larger of $F.G$ and E, and it is seen that the seismic case governs. For the regions between the beam plastic hinges, design moments are found from the combination of reduced gravity loads applicable for the seismic design combination, and overstrength moment capacity at the beam hinges. Since the beam moments cannot exceed the overstrength values at the plastic hinge locations, the design moments within the beam span L_B are found by adding the gravity moments

corresponding to simple support to the seismic moments in the span. Thus, at a distance x from the left support, the total moment is given by _reduced_

$$M_x = M^o_{E,l} + \left(M^o_{E,r} - M^o_{E,l}\right) \cdot \frac{x}{L_B} + \frac{w_G L_B}{2} \cdot x - \frac{w_G x^2}{2} \tag{5.56}$$

where moments $M^o_{E,l}$ and $M^o_{E,r}$ are the moments at the left and right column centrelines, taking due account of signs, and distances x and L_B are measured from the left column centreline. In Eq.(5.56) the gravity load w_G is assumed constant along the span.

The midspan design moment from this combination will generally significantly exceed the gravity moments. This is apparent in the combination $E^o + G_E$ in Fig.5.22(a), where the beam midspan moment exceeds the factored gravity moment by a substantial margin. This again raises the question of vertical response of the beam. Figure 5.22(a) also includes the combination $E^o + G_E^o$, where the seismic gravity moments are amplified by 30% to account for elastic vertical response of the beam to vertical ground accelerations, which may be accentuated by wave propagation up the columns, particularly in the upper storeys of multi-storey buildings.

Finally, it should be recognized that subsequent to building response to an earthquake, softening of the beam plastic hinges may result in a redistribution of gravity moments, with a reduction at the beam ends, and a corresponding increase at the beam midspan. This case is represented in Fig.5.22(a) by the line $F.G_E$, where the beam-end negative moments are reduced to 37.5% of the fixed-end values. For the example considered, the beam factored gravity midspan moment has increased to a value equal to the critical seismic combination, including effects of vertical excitation. This effect is not generally considered in design. Although the safety will not be affected, since the negative moment capacity should still be available at the beam ends, it may affect the serviceability following an earthquake.

As with force-based design, the beam plastic hinges will be designed for the moments at the column faces, not at the column centrelines. Aspects of beam flexural design are considered in Sections 5.6.1 and 4.2.5.

5.8.3 Beam Shear

Gravity and seismic beam shears, and their design combinations are illustrated in Fig.5.22(b), using the same nomenclature as for the beam moments. Seismic shears corresponding to beam plastic hinging are constant along the beam. When combined with reduced gravity shears applicable for seismic load combinations ($E^o + G_E$), beam shears will frequently have the same sign along the beam length, as shown in Fig.5.22(b). As with beam flexural design, it will be prudent to consider the effects of beam vertical response on design shear force (see line $E^o + G_E^o$). This is more important for shear design than for flexural design. Using the same nomenclature as with Eq.(5.56), and again taking care with signs, the design shear force along the beam is given by

reduced

$$V_x = \frac{\left(M_{E,r}^o - M_{E,l}^o\right)}{L_B} + \frac{w_G^o L_B}{2} - w_G^o \cdot x \qquad (5.57)$$

Aspects of beam shear design are considered in Section 4.7.3.

5.8.4 Column Flexure

(a) Existing Methods Accounting for Dynamic Amplification: Most seismic design codes include specific requirements for required flexural strength of columns. The seismic design requirements of the American Concrete Institute[X7] specify that the sum of the column design moment capacities (i.e. the dependable flexural strength based on nominal material properties and incorporating a flexural strength reduction factor) measured at the joint centroid shall be related to the sum of the beam design moment capacities at the joint centroid by the relationship

$$\sum M_C \ge \frac{6}{5} \cdot \sum M_B \qquad (5.58)$$

In U.S. design, the flexural strength reduction factor for columns is lower than for beams (typically $\phi_f = 0.7$ for columns and 0.9 for beams), and hence the actual margin of strength between beam and column nominal capacities is in fact greater than the 20% implied by Eq.(5.58). In comparison with Eq.(5.55), it would appear that the US approach is probably adequate to account for flexural overstrength of the beam plastic hinges, but does not include consideration of dynamic amplification effects. The apparent basis for this approach is that required column flexural strengths will normally be based on multi-modal analysis, and hence higher mode effects, which are responsible for dynamic amplification effects are already considered, or if the simpler equivalent lateral force procedure is used, required column moment capacities will be higher than resulting from the multi-modal approach. This, however, ignores the fact that beam design moments will similarly be higher, and the protection against column hinging has therefore not been increased by the higher required strength.

In New Zealand, higher mode effects are directly included in the concrete design code[X6], based on recommendations in [P1]. Column shear is amplified from the values corresponding to the design lateral forces in direct accordance with Eq.(5.55), though the strength reduction factor relating to the flexural strength is taken as unity, on the basis that adequate conservatism is present in the values for overstrength and dynamic amplification factors. The dynamic moment amplification factor ω_f is thus applied in the modified form:

$$M_N \ge \phi^o \omega_f M_E \qquad (5.59)$$

where ω_f is separately defined for one-way and two-way frames, as illustrated in Fig.5.23.

Note that for two-way frames, ω_f is applied to the column moment M_E resulting from design forces corresponding to one-way action. Note also that ω_f is height dependent, and equal to 1.0 or 1.1 at base and top of the column for one-way and two-way frames respectively, since column base hinging is expected at the base, and permitted at the top. It will be noted that with the minimum value of $\phi^o = 1.47$ appropriate for the New Zealand code, the minimum required column moment capacity will be 2.48 or 2.64 times the moment corresponding to lateral design forces, for one-way and two-way designs respectively. It should also be noted that the moment amplification is independent of the level of design ductility demand.
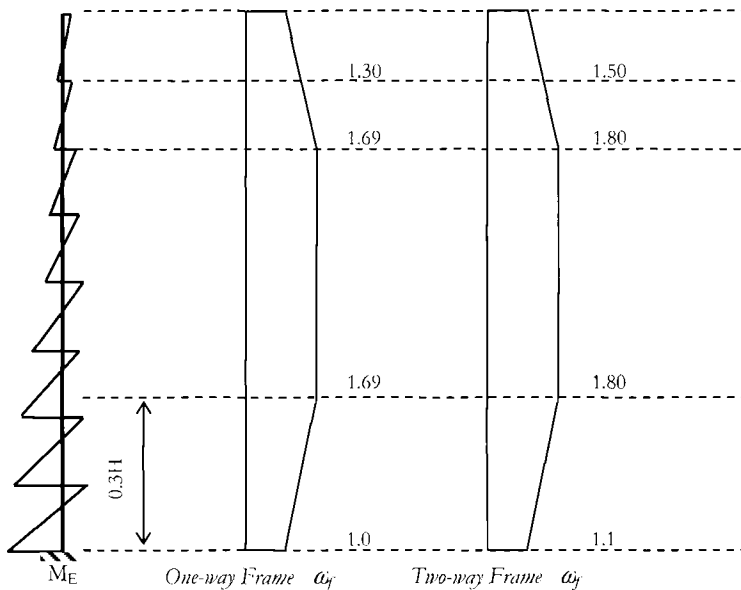
Fig.5.23   Column Dynamic Moment Amplification Factor for Flexure in N.Z. Design[P1].

In Eurocode EC8[X3] higher mode effects for column moments are directly considered by combination of the modal moments by either **SRSS** or **CQC** combination rules.

(b) Results of Inelastic Time-History Analyses: Pettinga and Priestley[P17] report results of dynamic amplification of column moments in one-way frames of 2-storeys to 20-storeys in height, designed by **DDBD** principles for displacement ductilities of about 2.7. These results indicated that the EC8 elastic modal superposition approach was generally non-conservative, while the New Zealand approach was generally significantly over-conservative. The analyses were carried out for different levels of seismic intensity, corresponding to 50%, 100% and 200% of the design intensity. It was found that although the base-shear strength of the buildings remained the same as the intensity was changed, the dynamic amplification of the column moments increased with intensity,

except at the column base, where moment was controlled by the moment capacity. Results for four-storey to sixteen-storey frames are shown in Fig.5.24.

In Fig.5.24, the column moments are the sum of all column moments in the different columns at a given level, and the absolute maximum values, without sign, have been plotted. Lines **TH I** = 0.5, 1.0 and 2.0 represent the average results from five spectrum-compatible accelerograms at intensities of 50%, 100% and 200% of the design intensity. Note that the **DDBD** design moments for the columns, shown by dashed lines in Fig.5.24, were calculated in accordance with the suggestion of Section 5.5.2(b) that the input moment-sum from beam plastic hinging be equally divided between the columns above and below the joint. The analyses do not include material overstrength, except for the component resulting from strain-hardening, which is a small component of the total. Strain-hardening of column-base reinforcement is responsible for the small amount of moment increase with intensity, at the column base. Note that in the lower third of the building height, column moments at the top of each storey are significantly higher than at the bottom of the same storey, and that the difference increases as the seismic intensity increases. This is partly a result of anchoring the column-base moment in the bottom storey at the plastic hinge capacity. It is clear from these results that dynamic amplification of column moments is dependent on the ductility demand, since this (for a given design) increases approximately proportionately with the intensity of excitation. It is also apparent from examination of the plots that the amplification factor of 1.6 suggested in [P1] for the central part of the column height is excessive at the design intensity, but quite reasonable at 200% of the design intensity.

(c) Design Recommendations: The data in Fig.5.24 lead to the following revised approach for determining the required column flexural strength:

$$\phi_f M_N \geq \phi^o \omega_f M_E \tag{5.60}$$

- In Eq.(5.60) the overstrength factor ϕ^o is calculated in accordance with the recommendations of Section 4.5
- The dynamic amplification factor ω_f is height and ductility dependent as shown in Fig.5.25, where from the first storey to the ¾ point of structure height

$$\omega_{f,c} = 1.15 + 0.13(\mu^o - 1) \tag{5.61a}$$

and at the top of the structure, where hinging at the column top is acceptable,

$$\omega_{f,t} = 1.00 \tag{5.61b}$$
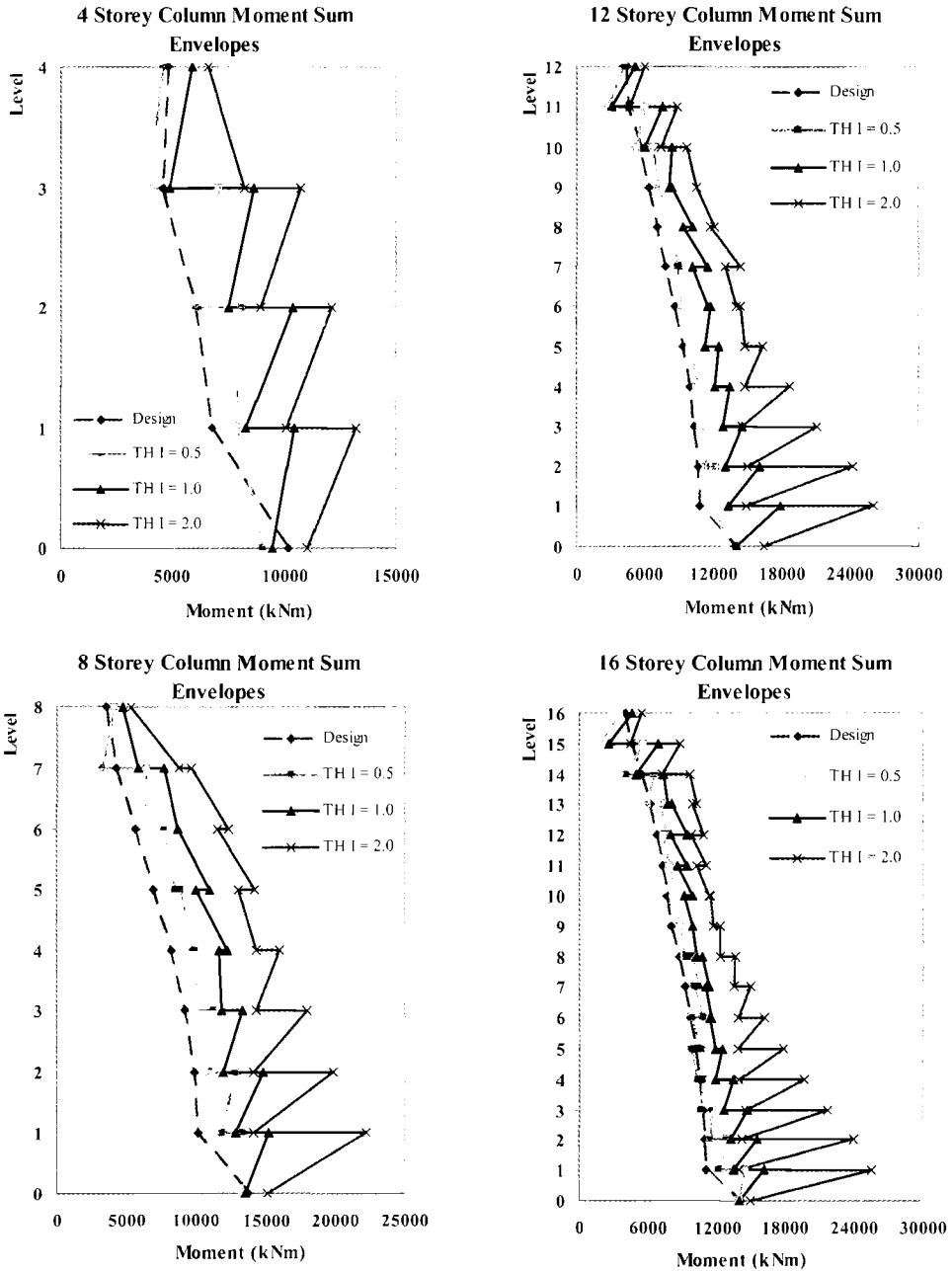
Fig.5.24   Column Moment Envelopes from Time-History Analyses at Different
Seismic Intensities, Compared with Design Envelopes[P17]

In Eq.(5.61) the ductility is the reduced ductility corresponding to the average overstrength capacity of the beam hinges:

$$\mu^o = \frac{\mu}{\phi^o} \geq 1 \tag{5.62a}$$

where μ is the design ductility level at expected strength.

- The dependable column flexural strength is based on nominal material strengths and a strength reduction factor of $\phi_f = 0.9$.
- For two-way frames, the moment M_E corresponding to design lateral force levels includes biaxial effects, as discussed in Section 5.6.2(c), and the amplification factor is found from Eq.(5.61), with the overstrength diagonal ductility demand given by

$$\mu_D^o = \frac{\mu}{\sqrt{2} \cdot \phi^o} \geq 1 \tag{5.62b}$$
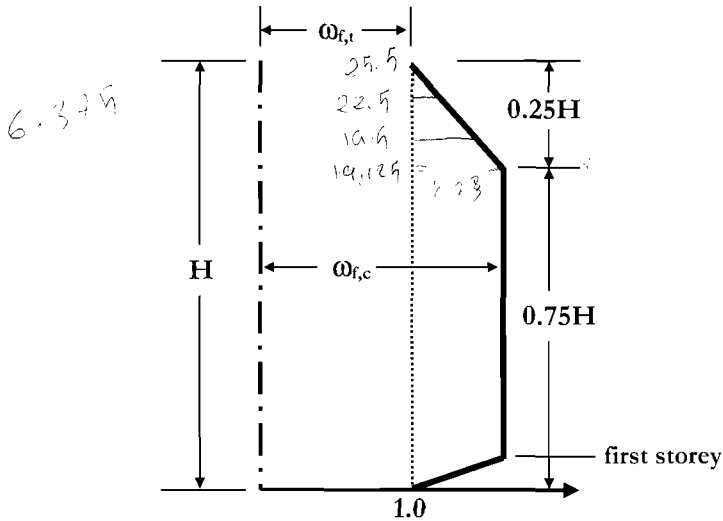
Fig.5.25 Dynamic Amplification of Frame Column Moments, to Eq.(5.61)

Equation (5.61) gives a good average estimation of the average dynamic amplification factor at a given level for four-storey to twelve-storey frames, but is a little conservative for taller frames, as will be seen in Section 5.9. It should be noted that it does not totally envelope the moment demands, since time-history analyses have found it unnecessarily

conservative to ensure that no incipient plastic hinging can develop in columns. It will be recognized, however, that the suggested approach is more conservative than all except existing New Zealand provisions for column design.

5.8.5 Column Shear

(a) Existing Methods Accounting for Dynamic Amplification: Seismic design codes generally include more restrictive provisions for the capacity-design shear forces in columns, in recognition of the potentially catastrophic consequences of column shear failure. The U.S. IBC code[X4] is perhaps the least conservative, as its provisions are related only to flexural overstrength issues. Dynamic amplification of column shears is not directly addressed. The basic requirement is that the design shear force shall be at least as high as the lower of the shear corresponding to overstrength beam moment input (based on a yield strength of $1.25f_y$, and no flexural strength reduction factor), and the shear corresponding to development of probable moment capacity (at $1.25f_y$) at the top and bottom of the column.

New Zealand practice again follows recommendations in [P1], which were based on earlier time-history analyses. Apart from in the first-storey columns, the maximum column shear is amplified for overstrength and higher-mode effects in accordance with Eq.(5.55), where

$$\text{For one-way frames,} \qquad \omega_S = 1.3 \qquad\qquad (5.63a)$$

$$\text{For two-way frames,} \qquad \omega_S = 1.6 \qquad\qquad (5.63b)$$

For first storey columns, hinging is expected at the base, and may also occur below the first-floor beams as a result of beam extension[F3], even when protected by the design approach suggested in Section 5.5.2(b). Consequently the column shear in the critical first floor column is calculated assuming overstrength hinging at both locations:

$$V_{col,1} = \frac{M_{1,b}^o + M_{1,t}^o}{H_c} \qquad\qquad (5.64)$$

where H_c is the clear column height to the soffit of the Level 1 beam.

Eurocode EC8[X3] specifies that column shear force shall be determined by modal superposition. Problems with modal superposition for shear forces are discussed in some detail in Chapters 6 and 7. It is sufficient to note here that elastic modal superposition is non-conservative for ductile structures because it incorrectly assumes that the higher mode shears can be reduced by the ductility, or behaviour factor applicable to the first mode response.

(b) Results of Inelastic Time-History Analyses: The analyses reported in [P17] and described above, also provide information on dynamic amplification of column shear.

Results of the analyses at levels of seismic intensity between 50% and 200% of design intensity are shown in Fig.5.26 for four-storey to sixteen-storey buildings. Results for two-storey and twenty-storey followed similar trends and are reported in [P17]. As with the column moments, the design shear envelope corresponding to the **DDBD** lateral forces is included as a dashed line, and values plotted correspond to the sum of all columns in the frame at a given level. Material overstrength was not modelled in the analyses, except for the fraction resulting from strain-hardening of reinforcement.

Results follow similar trends to, and are compatible with those noted for column moments, in that column shear force increases with increasing seismic intensity. As discussed above, this can be interpreted to imply that dynamic shear amplification increases with ductility, since ductility increases with intensity for a given structure. This influence is not included in existing design methods. It will also be seen that the shape of the time-history envelopes is generally similar to the design-force envelope, though a constant offset of shear demand above design-force envelope with height would seem more appropriate, particularly for the lower structures, than a constant multiplier as recommended in [P1].

(c) Design Recommendations: Based on the above observations, the following form of the dynamic amplification factor for column shear is proposed:

$$\phi_S V_N \geq \phi^o V_E + 0.1 \mu V_{E,base} \leq \frac{M_t^o + M_b^o}{H_c} \tag{5.65}$$

The following comments relate to Eq.(5.65):
- The overstrength factor ϕ^o is calculated in accordance with the recommendations of Section 4.2.5.
- The shear demands V_E correspond to the design lateral force distribution found from the **DDBD** process. $V_{E,base}$ is the value of V_E at the base of the column.
- The system ductility μ is not reduced by ϕ^o since this factor cancels with the same amplification of V_E.
- The upper limit of column shear corresponds to development of plastic hinging, at overstrength capacity at the top and bottom of the column, separated by the clear column height, H_c.
- The approach suggested provides a good estimate of the shear demand up the height of two-storey to eight-storey frames. For taller frames, the shear force at roof level predicted by Eq.(5.65) becomes increasingly conservative, but is likely to be controlled by the upper limit. Generally, prescriptive confinement requirements will govern transverse reinforcement design in the upper levels.

As discussed in Section 5.6.2(c), and 5.8.5(a), maximum feasible column shears will be increased in two-way frames under biaxial attack. The shear force may be found from the vectorial addition of the principal direction shears. The following considerations apply:
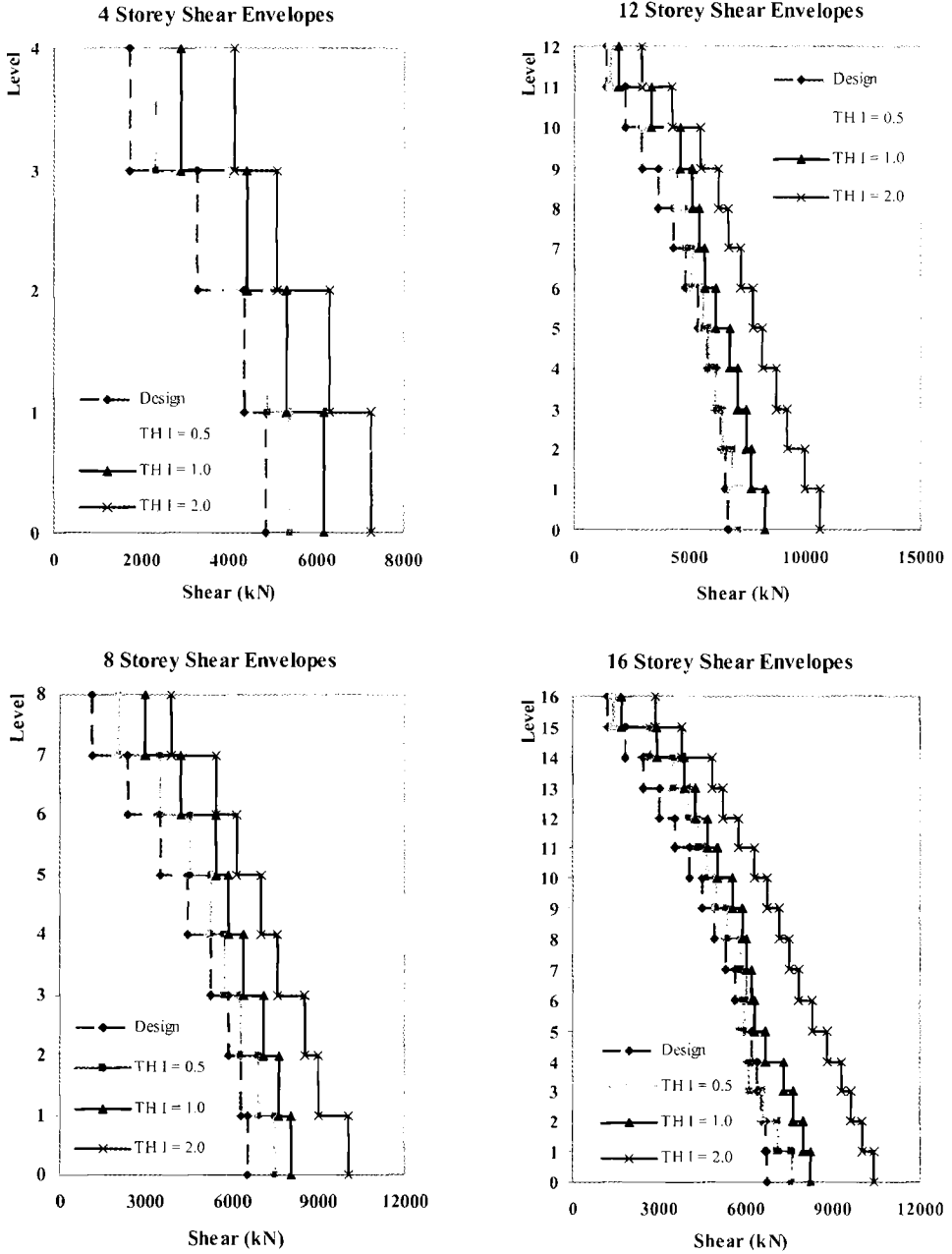
Fig.5.26 Column Shear Envelopes from Time-History Analyses for Different Seismic Intensities Compared With DDBD Envelope[P17]

- Shear strength of square columns is essentially the same in principal and diagonal directions.
- Maximum diagonal ductility demand is less than the principal direction demand by a factor of $\sqrt{2}$ (see Section 5.7)

Thus, for square columns of two-way frames, the required nominal shear strength in a principal direction, is given by

$$\phi_S V_{N,2} \geq \sqrt{2}(\phi^o V_{E,1} + 0.1\frac{\mu}{\sqrt{2}} V_{E,base,1}) \leq \frac{M_t^o + M_b^o}{H_c} \tag{5.66}$$

where the suffices $_1$ and $_2$ relate to actions for one-way and two-way response respectively.

5.9 DESIGN VERIFICATION

Much of the design recommendations in the previous section have resulted from an extensive analytical study described in detail elsewhere[P17], though the dynamic amplification factors for shear and moment are new. In this section we briefly compare design predictions with the average results from time-history analyses reported in [P17].

5.9.1 Displacement Response

The full analytical study investigated 2, 4, 8, 12, 16 and 20 storey regular frames. We limit comparison to 4, 8, 12 and 16 storeys, in the interests of brevity. Results for the 2-storey were similar to the 4-storey, and results for the 20-storey were similar to the 16-storey frame.

Figure 5.27 compares the average time-history response for an intensity ratio of I=1.0 with the design profile in terms of displacement envelopes. Also shown is the average time-history response for intensity ratios of I=0.5 and 2.0, for comparative purposes. In all cases the drift envelopes (see [P17]) had peak values within 10% of the design limit of 0.02. For the shorter frames the maximum drift was not greatly affected by higher mode effects, and peak drifts occurred at the first storey. For the 16 and 20-storey frames, higher mode drift amplification was substantial, and maximum drifts occurred at about 80% of the frame heights.

Comparison of the design displacement profile and the I=1.0 time history results indicates excellent agreement in all cases.

5.9.2 Column Moments

Figure 5.28 compares the sum of column moments at a level with the predictions based on dynamic amplification in accordance with Eq.(5.61) and Fig.5.25. Note that the time-history analyses were carried out using the design expected values for the material

4 Storey Displacement Envelopes

12 Storey Displacement Envelopes

8 Storey Displacement Envelopes

16 Storey Displacement Envelopes
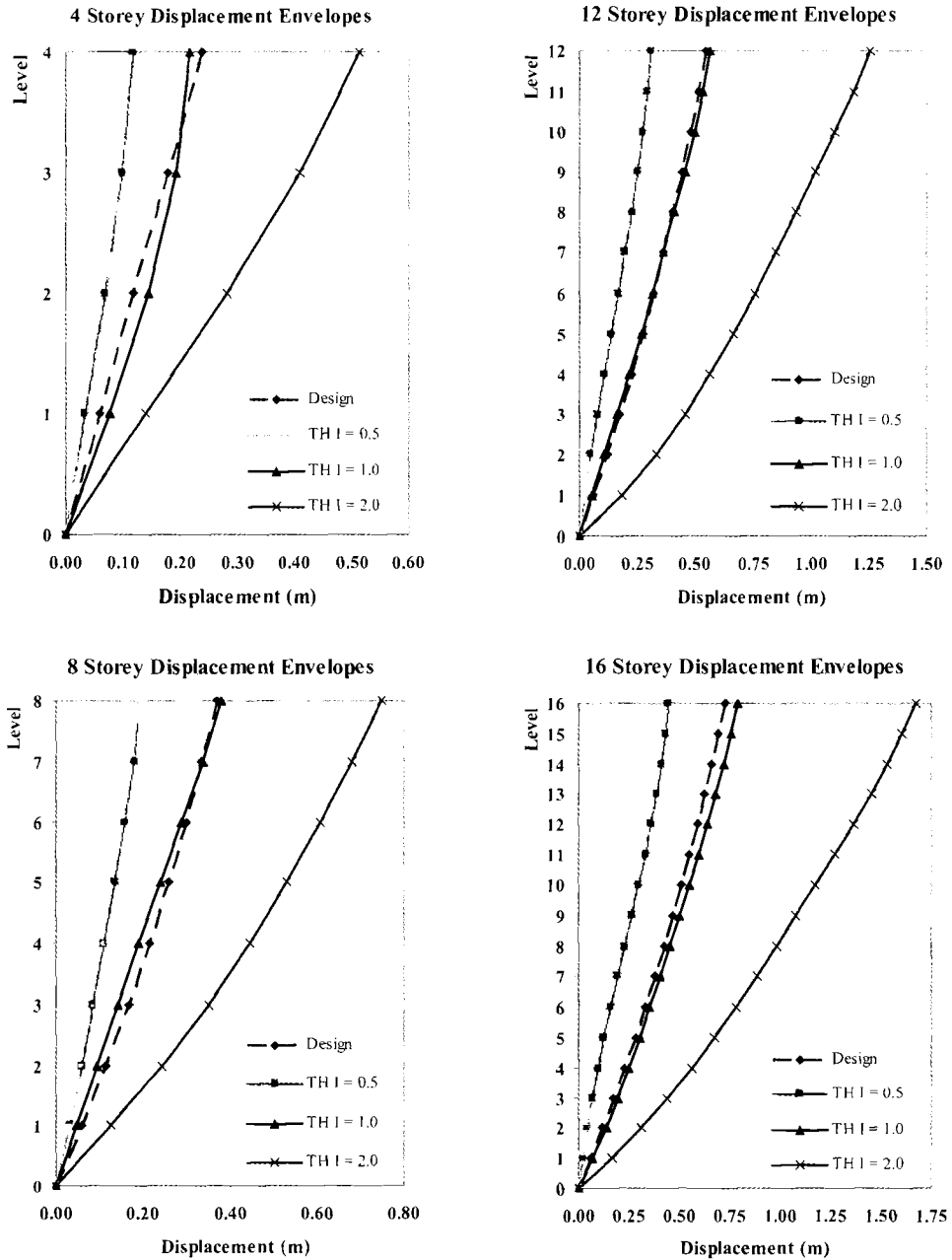
Fig.5.27   Design Displacement Profiles Compared with Average Time-History
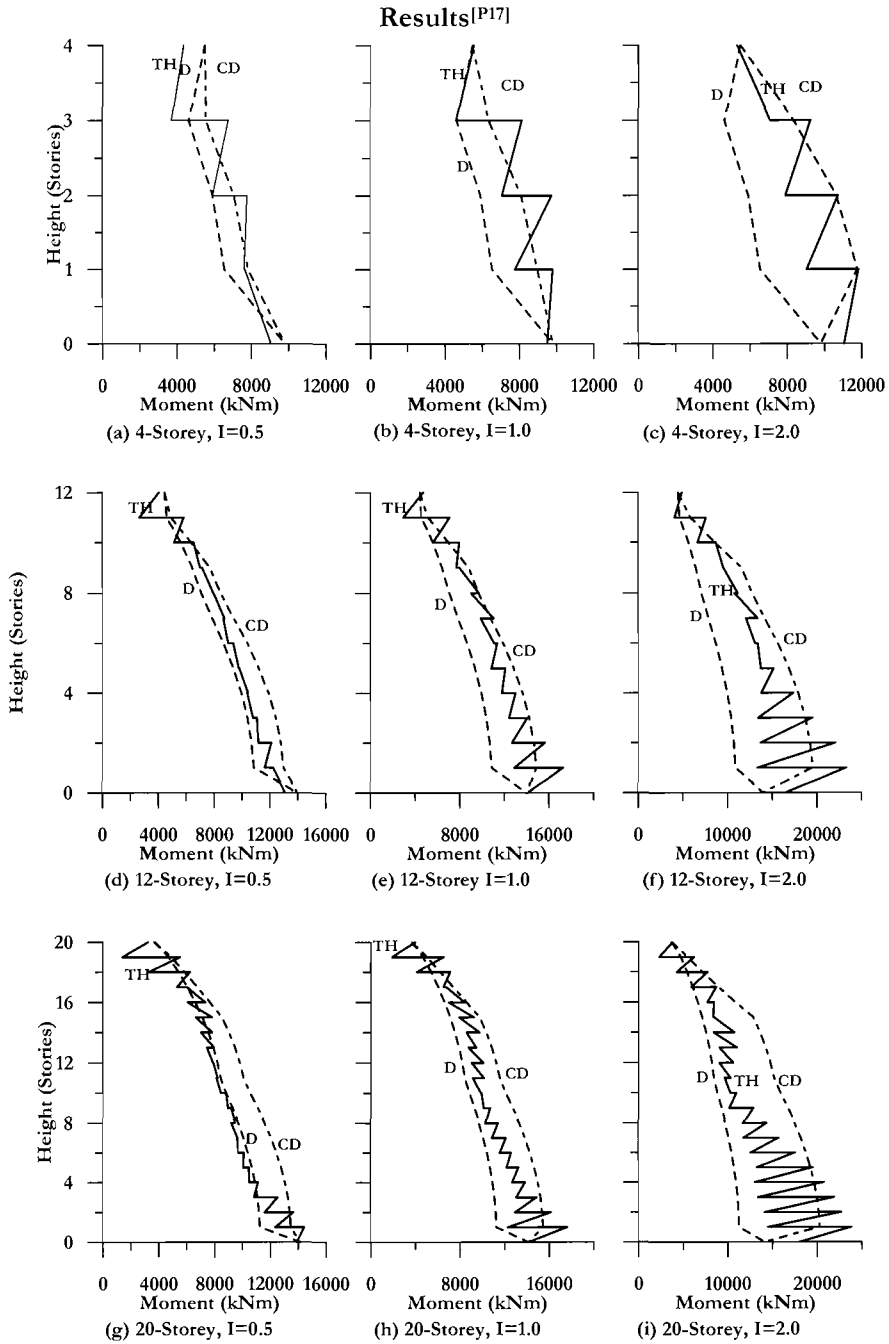
Fig.5.28 Capacity Storey-Moment Envelopes Compared with Time-History
Results (D = DDBD; TH= time history results; CD = Eq.(5.61))

strengths, and hence the material overstrength factor was taken as $\phi^o = 1.0$. In fact some strain hardening beyond that accounted for in design occurred for intensity ratio I=2, and a slightly higher amplification of the design moments would be appropriate.

Note that the moments plotted in Fig.5.28 are the sum of the moments in all columns at a given level, and are plotted without sign. The design moment envelope is identified by "D". Generally peak moments at one end of a column do not occur at the same time instant as peak moments at the other end of the column. It is seen that the simple modifier suggested in Eq.(5.61) provides a good envelope for all the three frames depicted, at all three levels of intensity (and hence of ductility). It will be noted that in a few cases maximum column moments from the time-history analyses exceed the capacity design envelope (identified by CD in the figures) by a small amount. This should not be of concern, since the resulting ductility demand on the columns will be very low. It is felt that providing an absolute envelope to the time-history results is not economically justified, given the substantial ductility capacity of modern well-confined columns.

5.9.3 Column Shears

Column storey-shears (i.e. the sum of shears in all columns in a given storey) from time-history analyses at different seismic intensities are compared in Fig.5.29 with the shear envelopes defined by Eq.(5.65). Note that the upper limit provided in Eq.(5.65) by the shear associated with column hinge formation at top and bottom of a column has not been considered in the time-history analysis, nor in the capacity design envelope.

As with the column storey-moments, the capacity design shears envelope the time-history results except in a very few cases. The degree of conservatism is not high, though it could perhaps be considered excessive for the I = 2, 20-storey case in the upper half of the frame. At the design intensity level (I = 1.0) the agreement between the time history and capacity design envelopes given by the simple design approach is very satisfactory.

An alternative formulation of capacity design effects for column moments and shears which involves specific consideration of higher mode contributions has been proposed in [P17]. This approach is more cumbersome to use, and does not give significantly improved agreement. If more accurate estimation of capacity design column moments and shears is required, it is recommended that inelastic time-history analysis of the structure be carried, based on the principles outlined in Section 4.9.

5.9.4 Column Axial Forces

In determining the reinforcement requirements for flexure and shear in the columns, the axial forces also need to be known. These can be found from the gravity loads, plus the axial forces contributed by the beam seismic shear forces. Note that for corner columns, the beam shears from both orthogonal directions must be considered, potentially doubling the seismic contribution to column axial force. If the resulting axial forces, particularly the uplift force on the corner tension column are too high, redesign may be appropriate, as suggested in Section 5.6.2(c), to reduce the column axial force
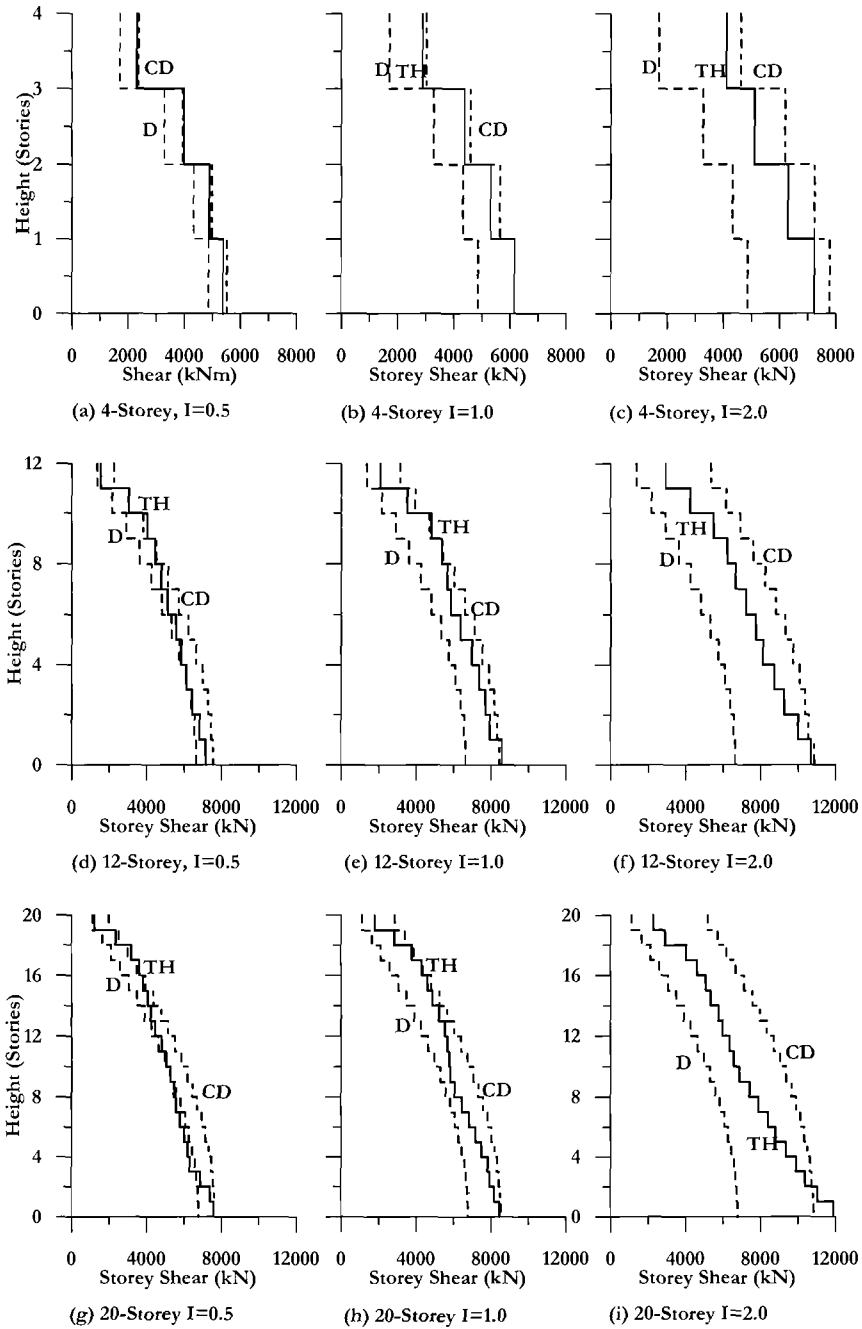
Fig.5.29   Capacity Storey-Shear Envelopes Compared with Time-History Results
(D = DDBD; TH = time history results; CD = Eq.(5.65))

levels. In most cases for buildings of less than 12 storeys the column axial forces need not be explicitly calculated, provided reinforcement contents for the tension and compression outer columns are averaged, using the gravity loads on the columns as the appropriate axial forces, as recommended in Section 5.6.2(d), for all levels of the building, not just the column bases.

5.10 DESIGN EXAMPLE 5.2: Member Design Forces for an Irregular Two-Way Reinforced Concrete Frame

We continue with Design Example 5.1 (Section 5.3.4) to determine required base shear strength, and beam and column design moments and shear forces. The following additional data are required. The building has a square plan, and the layout of frames in the two principal directions is identical. Hence the lateral resistance is provided by two-way frame action. The building is in a high seismicity region, with peak ground acceleration of 0.7g, and a maximum causative earthquake of $M7.5$ at a distance of about 14km. The design elastic 5% damping displacement spectrum is shown by the solid line in Fig.5.30, with a corner period of 5.5sec, and a corresponding response displacement of 1400mm (refer to Section 2.2.2(b)). It is required to determine the design moments and shears for the frame members, for Option 1 (see Design Example 5.1) which assumed equal moment capacities of beams in the short and long bays.
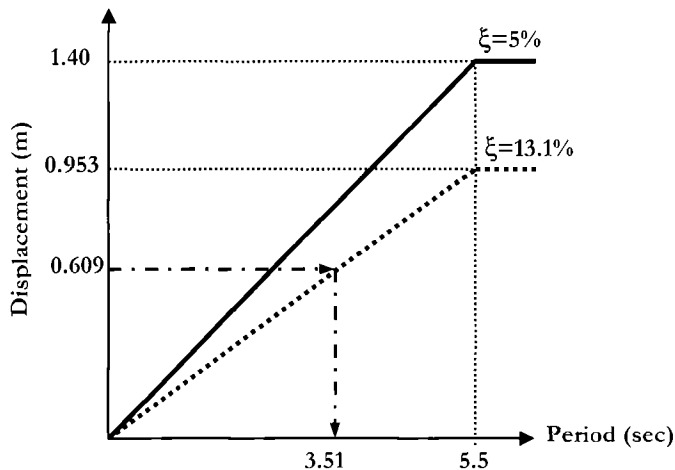
Fig.5.30 Displacement Spectra for Design Example 5.2

Solution: From Example 5.1 we recall that for Option 1, the design displacement, ductility and damping were $\Delta_d = 0.609$m (24.0 in), $\mu = 1.82$ and $\xi = 13.1\%$ respectively. A check for drift amplification in accordance with Eq.(5.28b) indicates a value of $\omega_\theta = 1.004$, which is ignored as being sufficiently close to unity.

Design Base Shear Force: The steps to determine the frame design base shear force are listed below. Relevant data from Table 5.1 are included in the first three columns of Table 5.3.

From Eq.(5.4) the substitute structure equivalent mass is (refer Table 5.3,Col.(3))

$$m_e = \sum_{i=1}^{n}\left(m_i\Delta_i\right)/\Delta_d = 371.5/0.609 \quad = 610 \text{ tonnes (1345 kips)}$$

The reduction factor to be applied to the 5% damping displacement spectrum for 13.1% damping is given by Eq.(2.8) as

$$R_\xi = \left(\frac{0.07}{0.02+0.131}\right)^{0.5} = 0.680$$

Thus the corner displacement at T = 5.5 sec for ξ = 13.1% damping is 0.680×1.4 =0.953m. The corresponding displacement spectrum is shown in Fig.5.30 as a dotted line. By proportion, the effective period of the substitute structure is

$$T_e = 5.5 \cdot \frac{0.609}{0.953} = 3.51\sec$$

Table 5.3 Calculations for Example 5.2 (1kN = 0.225 kips, 1 m =39.4 in)

Level, i (1)	Height H_i (m) (2)	$m_i\Delta_i$ (4)	F_i (kN) (9)	$V_{s,i}$ (kN) (10)	OTM (kNm) (11)	V.beam1 (kN) (12)	M.beam1* (kNm) (13)
12	43.0	57.95	286.1	286.1	0.0	69.4	138.8
11	39.5	46.86	135.1	421.3	1001.4	102.1	204.3
10	36.0	43.84	126.4	547.6	2475.7	132.8	265.6
9	32.5	40.59	117.1	664.6	4392.3	161.1	322.3
8	29.0	37.13	107.1	771.7	6718.6	187.1	374.2
7	25.5	33.45	96.5	868.2	9419.6	210.5	421.0
6	22.0	29.55	85.2	953.4	12458.2	231.2	462.3
5	18.5	25.43	73.3	1026.7	15794.9	248.9	497.9
4	15.0	21.09	60.8	1087.5	19388.2	263.7	527.3
3	11.5	16.53	47.7	1135.1	23194.4	275.3	550.4
2	8.0	11.75	33.9	1169.0	27167.2	283.4	566.8
1	4.5	7.31	21.1	1190.1	31258.6	288.5	577.1
0	0	0	0.0	1190.1	36613.9	0.0	0.0
Sum		371.47	1415.0	10121.1		2454.0	

* At column face

The substitute structure stiffness is found from Eq.(5.10):

$$K_e = 4\pi^2 m_e / T_e^2 = 4\pi^2 \times 610 / 3.51^2 = 1955 kN / m$$

Hence, from Eq.(5.11), the design base shear force is

$$F = V_{Base} = K_e \Delta_d = 1955 \times 0.609 = 1190 kN \quad (16.5\% \text{ of weight}).$$

Distribution of Base shear to Floor Levels: The modified form of Eq.(5.12) allowing for an additional force at roof level, given in Eq.(5.27) is used to determine the floor forces:

$$F_i = (F_t) + 0.9 V_{Base} \cdot (m_i \Delta_i) / \sum_{i=1}^{n} m_i \Delta_i \text{ where } F_t = 0.1 V_{Base} \text{ at the roof, and}$$

zero elsewhere. Hence

$$F_i = (119) + 1071 \times (m_i \Delta_i) / 371.5$$

Values for F_i are tabulated in Col.(9) of Table 5.3.

Storey Shear Force and Overturning Moments: Storey shear forces are found by summing the floor forces above the storey considered. These are listed in Col.(10) of Table 5.3. Storey overturning moments at the floor levels are also found from the lateral forces as

$$OTM_i = \sum_{j=i}^{12} F_j \left(H_j - H_i \right)$$

The overturning moments at each level are tabulated as Col.(11) in Table 5.3. The base overturning moment for the frame is $OTM_{Base} = 36,614$ kNm.

Column Base Moments: In Section 5.5.1 it was recommended that the point of contraflexure in the ground floor columns be set at $0.6H_1$ for one-way frames. For two-way frames, Section 5.6.2(c) suggested this be modified to $0.7H_1$. In this design we adopt a compromise, at $0.65H_1$. Note that we use this value for determining one-way response. The actual point of contraflexure for biaxial response will be lower.

The total resisting moment provided at the column base will thus be

$$\sum M_{cj} = V_{Base} \times 0.65 H_1 = 1190 \times 0.65 \times 4.5 = 3481 kNm$$

This is less than 10% of the total base **OTM.**

Beam Seismic Shears in an End Bay Corresponding to Design Lateral Forces: We adopt the analysis procedure based on equilibrium considerations, outlined in Section 5.5.2. For irregular frames, the sum of the beam shear forces in the end and inner bays is given by Eqs.(5.40) and (5.41) respectively. With the assumption of equal beam strengths in the outer and inner bays, the moments M_1 and M_2 in these equations are equal (see Section 5.3.3). Hence, for the outer bays:

$$\sum_{i=1}^{n} V_{B1i} = T = \frac{M_1}{2M_1 + M_2} \cdot \left(\sum_{i=1}^{n} F_i H_i - \sum_{j=1}^{m} M_{Cj} \right) / L_1 = \frac{1}{3}(36614 - 3481)/4.5 = 2454kN$$

As recommended in Section 5.5.2(a) this tension force is distributed to the beams of the end bay in proportion to the storey shears immediately below the beam considered (Eq.(5.37)):

$$V_{Bi} = T \cdot \frac{V_{S,i}}{\displaystyle\sum_{i=1}^{n} V_{S,i}} = 2454 \times V_{S,i} / 10121$$
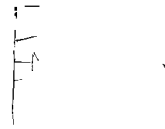
The resulting beam seismic shears are tabulated in Col.(12) of Table 5.3.

Beam Seismic Moments in an End Bay: Design seismic moments for the end bay corresponding to the design lateral forces are calculated at the column faces. Assuming the columns are 500×500 mm (20×20in) the clear span between columns in the end bay is 4.0 m (13.1ft), and the average of positive and negative seismic moments will be

$$M_{b,i} = V_{b,i}(L_1 - h_c)/2 = 2V_{b,i}$$

These moments are tabulated in Col.(13) of Table 5.3. As noted, these are the average of positive and negative moments. The designer can chose to increase the negative moment capacity at the expense of the positive moment to reflect gravity moment demand, and also to utilize slab reinforcement. For detailed consideration of beam design, the reader is directed to [P1].

At this stage, the beam seismic moments would be compared with the factored gravity moments (see Sections 3.7.2 and 5.6.1), and the larger adopted for design. In this case we assume that the seismic demands govern. A quick check is carried out to determine whether the beam depth of 600 mm (24 in) is suitable. At the roof, and first floor levels, the beam moments are 139 kNm and 577 kNm respectively. The lever arm of internal stress resultants will be approximately 500mm, and the required reinforcement tension forces will thus be

Roof: $A_s f_y = 139 / 0.5 = 277.5kN$

First floor. $A_s f_y = 577 / 0.5 = 1154kN$

The expected reinforcement yield stress is 1.1×450 = 495MPa (71.8 ksi) (see Example 5.1), and hence the required steel areas are

Roof. $A_s = 0.2775/495m^2 = 561mm^2$ (0.87 in²)

First floor. $A_s = 1.154/495m^2 = 2332mm^2$ (3.62 in²)

Assuming beam widths of 250mm (9.8in) at the roof level and 300mm (11.8in) at first floor, with an effective depth of 550mm, these correspond to reinforcement ratios of 0.0041 and 0.0141 respectively, which are acceptable. The roof level value is a little below the normal code minimum of about 0.5%, but would probably be increased to satisfy gravity load design.

The procedure outlined above should also be carried out for the inner bay, particularly if it had been decided to use different moment capacities. Even with the same nominal beam moment capacities at the column centrelines, it is found that the moments at the column faces are 5% larger for the longer span, and hence govern design. The designer may opt to just design both bays for the larger moment in the inner bay, or redistribute some of the inner bay moment to the outer bay, and design both bays for the average demand. The additional calculations are repetitive, and are hence not listed.

overstrength is considered for shear

Beam Design Shear Forces: ✓ Beam design shear forces are assessed at flexural overstrength of beam plastic hinges, as discussed in Section 5.8.3. The overstrength may result from material strengths (particularly reinforcement yield strength) exceeding the design values, strain-hardening, and the provision of more reinforcing steel area than is needed to satisfy the moment demands of Table 5.3, Col.(13). This should ideally be assessed for each beam, but in the interests of brevity, here we assume a constant overstrength factor of $\phi^o = 1.35$. Gravity loads on the beams appropriate to the seismic load case, including an allowance of 30% for vertical dynamic amplification are, in this example, $w_G^o = 43.8kN/m$ (3.0 kips/ft). Beam moments in Table 5.3, Col.(13) apply at the column faces, and the moment demands at opposite ends of the beam are equal and opposite. Hence Eq.(5.57) is modified to read

$$V_x = \frac{2\phi^o M_B}{L_c} + \frac{w_G^o \cdot L_c}{2} - w_G^o x = \frac{2 \times 1.35 M_B}{4} + \frac{43.8 \times 4}{2} - 43.8x = 0.675 M_B + 87.5 - 43.8x$$

where M_B is the moment given in Table 5.2,Col.(13), L_c is the clear beam span between column faces, and x is now measured from the beam face. The maximum value of V_x occurs at the column face ($x = 0$) and is listed in Table 5.4, Col.(14).

Column Design Moments: Analysis for column flexure follows the suggestions at the end of Section 5.5.2(b), where beam moment input to a joint is shared equally between the columns above and below the joint. Since the structure is comprised of two-way frames, concurrent yielding of beams must be anticipated, as discussed in Section

5.6.2(c). Column moments for a corner column corresponding to design-level seismic forces (i.e., Col.(9), Table 5.3) are thus given by

$$\sum M_C \approx \sum M_{CD} = \sqrt{2}\left(M_{Bj}\right)$$

where the beam moments, M_{Bj} are the beam moments at the joint centroid, which are 12.5% higher than the column-face moments listed in Col.(13) in Table 5.3. With an equal division of input moment above and below the joint, the column moment, at the joint centroid is thus $M_C = M_{CD} = M_{Bj}/\sqrt{2}$. For a fully interior column, the moments will be twice this. Note that at the roof level, there is no column above the joint, and hence the column capacity below the joint must balance the entire beam input.

Table 5.4 Capacity Design Calculations for Outer Bay for Example 5.2

Level, i (1)	V^o_B (kN) (14)	$M_{C1,f}$ (kNm) (15)	ω_f (16)	$M_{C1,des}$ (kNm) (17)	$M_{C2,des}$ (kNm) (18)	$V_{C1,des}$ (19)	$V_{C2,des}$ (20)
12	181.2	220.8	1.00	298.0	596.0	259.3	518.6
11	225.3	162.5	1.05	240.6	481.2	302.3	604.6
10	266.7	211.2	1.10	365.9	731.8	342.5	685.0
9	305.0	256.3	1.15	398.0	796.0	379.7	759.4
8	340.1	297.6	1.15	462.1	924.2	413.8	827.5
7	371.6	334.8	1.15	519.8	1039.6	444.5	888.9
6	399.5	367.7	1.15	570.9	1141.7	471.5	943.2
5	423.5	395.9	1.15	614.8	1229.5	494.9	989.8
4	443.4	419.4	1.15	651.2	1302.3	514.3	1028.5
3	459.0	437.8	1.15	679.7	1359.4	529.4	1058.8
2	470.1	450.9	1.15	669.5	1339.0	540.2	1080.3
1	477.0	459.0	1.15	650.6	1301.3	546.9	1093.8
0			1.00	580.3	1160.6		

Corner column moments for diagonal response, based on these assumptions, and corresponding to the design-level forces, are listed in Table 5.4, Col.(15). These must now be amplified to account for material overstrength and dynamic amplification effects. As noted above, a beam overstrength factor of $\phi^o = 1.35$ is assumed. In accordance with Section 5.8.4(c), the diagonal ductility demand to be used in Eq.(5.61) is given by Eq.(5.62(b)), as

$$\mu^o = \frac{\mu}{\sqrt{2}\cdot\phi^o} = \frac{1.8}{1.414\times1.35} = 0.943 < 1.0$$

Hence a value of 1.0 is adopted. From Eq.(5.61) the dynamic amplification factors over the central half, and at the top of the building are 1.15, and 1.00 respectively. The distribution with height follows Fig.5.25, and is tabulated in Table 5.4, Col.(16). Design corner column moments are thus given by

$$M_{C1,des} = 1.35 \times \omega_f \times M_{C1,f}$$

where $M_{C1,f}$ are listed in Table 5.4 Col.(15). The resulting moments are tabulated in Table 5.4, Col.(17). Note that these are the required dependable moment capacities at the joint centreline, and will be reduced at the critical sections at top and bottom of the beam.

Interior column moments are simply twice these values, and are listed in Col.(18) of Table 5.4. Note that side columns (as distinct from corner columns) on an exterior frame will have input moment from three beams, and the moment-demand will hence be intermediate between the corner and interior columns. Analyses for this are straightforward, but are not included in this example.

Column Design Shear Forces: Column design shear forces are determined in accordance with Section 5.8.5(c). Equation (5.65) applies. Since the ductility demand in the diagonal direction, at flexural overstrength is taken as 1.0, Eq.(5.65) simplifies to

$$\phi_s V_{N,2} \geq \sqrt{2}(1.35 V_{E,1} + 0.1 V_{E,base,1}) \leq \frac{M_t^o + M_b^o}{l_c}$$

In this example, storey shears are divided between the exterior and interior columns in the proportion 1:2. Hence, under one-way action, the exterior and interior columns carry 1/6th and 1/3rd of the frame shear respectively. Values for required dependable shear strength for corner and interior columns are thus found from the above equation, with $V_{E,1}$ given by the appropriate fraction of the storey shear (Col.(10), Table 5.3). These are tabulated in Cols.(19 and 20) in Table 5.4. The shears have not been checked against the upper limit, set by the overstrength column moment capacities, as these depend on the individual details of the column flexural designs, which have not been assessed here. However, rough calculations indicate that the shears thus determined will be very similar to the values tabulated.

5.11   PRECAST PRESTRESSED FRAMES

5.11.1   Seismic Behaviour of Prestressed Frames with Bonded Tendons

Precast frames can conveniently be separated into two categories: those which emulate cast *in situ* reinforced concrete frames, and hence need no special consideration beyond that already presented, and those which utilize ductile connections between the precast members, and have different hysteretic characteristics than *in situ* construction. Recent

research in precast frame construction has concentrated on prestressed beams utilizing unbonded tendons[P18,P19]. Although prestressed concrete has not generally been favoured for seismic resistance, tests on both *in situ*[B3] and precast[C4] beam-column sub-assemblages with fully grouted tendons have developed ductility comparable to monolithic reinforced concrete. However, after moderate ductility levels had been achieved, these subassemblages suffered excessive stiffness degradation at low displacements. This reduction was caused by a reduction in effective prestress clamping force through the column, resulting from inelastic strain of the prestressing tendon at the critical section. This behaviour is shown in idealized form in Fig. 5.31(a) which refers to a typical prestressing steel stress-strain curve.
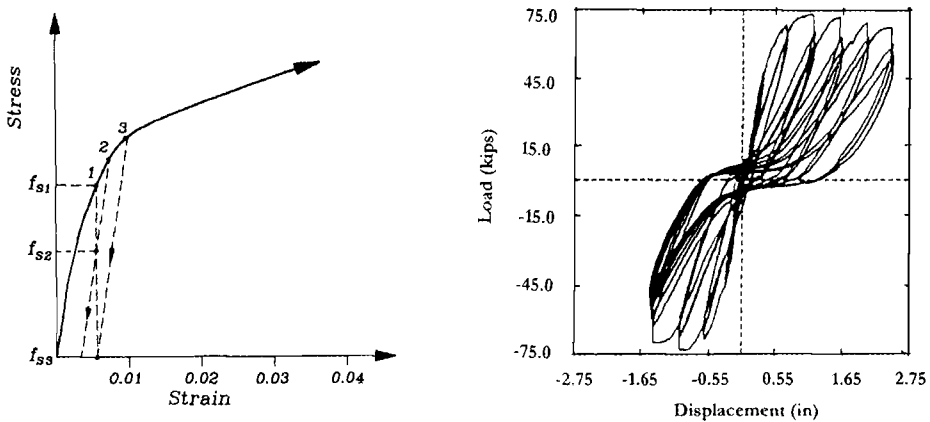
(a) Prestress loss due to inelastic response   (b) Force-displacement hysteretic response

Fig.5.31   Seismic Response of a Beam-to-Column Unit Prestressed with Bonded Tendons[C4]

In Fig.5.31(a), f_{si} is the initial steel stress after prestress losses. During low-level seismic response, fluctuations of the steel stress will be within the elastic range, and no loss of prestress will result. At a ductility level of (say) μ =2, represented by point **2** in Fig.5.31(a), the maximum prestressing steel response is expected to be on the inelastic portion of the stress-strain curve. On unloading, the steel follows a linear descending branch essentially parallel to the initial elastic portion. Hence, when the structure returns to zero deformation, the effective steel stress is reduced to f_{s2}.

On unloading from higher ductility levels, involving larger inelastic strains as indicated by point **3** in Fig.5.31(a), the entire prestress may be lost. This is clearly undesirable, particularly for precast connections where the surfaces between the beam and column are planar, rather than a rough naturally forming crack as may be the case for monolithic reinforced concrete construction. Prestress shear-friction, which would be relied on to transmit gravity shear forces from the beam to the column would then be ineffective.

The result of this behaviour is excessive pinching of the force-deflection hysteresis loops, as indicated in the typical response of a prestressed subassemblage, shown in Fig.5.31(b)[C4]. Response at low ductility levels is satisfactory, and peak lateral strength is maintained at high displacement ductilities. After displacing to these high levels, however, lateral stiffness is almost completely lost at low displacement levels. The test results shown in Fig.5.31(b) refer to a test unit without additional gravity load on the beams. If the gravity loads been modelled in this test, the performance would have been even less desirable.

5.11.2 Prestressed Frames with Unbonded Tendons

(a) Performance Advantages: The use of unbonded, or partially unbonded tendons, where the tendon is unbonded through the joint and for some distance on either side, as indicated in Fig.5.32(a) has been suggested as a means for improving performance[P20]. The following advantages were proposed:

- If the length of debonding is sufficient, the required ultimate displacement could be achieved without exceeding the limit of proportionality of the prestressing steel. Consequently there would be no loss of prestress on unloading from the design level of displacement. Shear friction on the beam-to-column interfaces would be maintained at all response levels, and support of gravity loads would not be jeopardized.

- Design of the beam-to-column joint region would be simplified, since the joint shear forces would largely be transferred by a diagonal strut, as shown in Fig.5.32(b). This is a consequence of the prestress forces on either side of the joint being equal for each tendon, because the tendons are debonded through the joint. Thus, reduced levels of special joint reinforcement would be needed.

- The response would be essentially elastic, though nonlinear, as indicated in Fig. 5.32(c). Although it is recognized that this would have possibly undesirable consequences for energy absorption, it has the merit that, following response to the design level earthquake, the structure would return to its original position without residual displacement, and the initial stiffness would be restored.

(b) Lateral Force-Displacement Characteristics: Force-displacement characteristics of a typical debonded precast beam-to-column prestressed concrete subassemblage are indicated in Fig.5.33(b), based on the forces and relative displacements measured at the top of the beam-to-column subassemblage, as shown in Fig.5.33(a).

Assuming no tension capacity across the beam-to-column interface, nonlinearity of response will initiate at point **1** (Fig.5.33(b)) when pre-compression at the extreme fibre is lost, and a crack starts to propagate. Assuming further that the prestress centroid is at mid-height, the corresponding moment is

$$M_{cr} = T_i h_b / 6 \qquad\qquad (5.67)$$

(a) Beam/column connection

(b) Joint shear transfer

(c) Idealized force-deformation characteristic
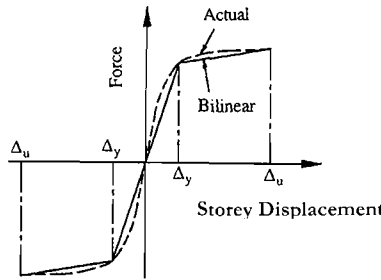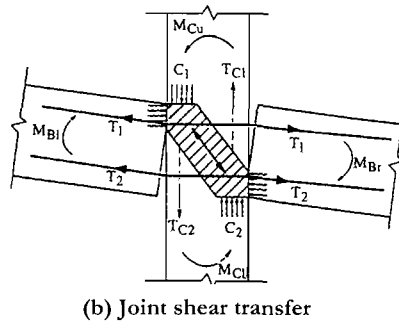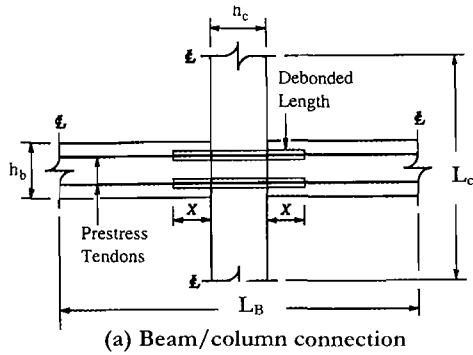
Fig.5.32   Beam-to-Column Connection with Debonded Tendons

for a rectangular section, where T_i is the initial total prestress force, and h_b is the beam depth. For the dimensions shown in Fig.5.32(a), the corresponding lateral force F will be:

$$F = \frac{2M_{cr}L_B}{(L_B - h_c)L_C} \tag{5.68}$$

where h_c is the column depth and L_c is the column height between contraflexure points.

   The corresponding displacement can be found from simple linear elastic analysis based on uncracked section properties.

(a) Subassemblage Configuration   (b) Non-linear Elastic Response
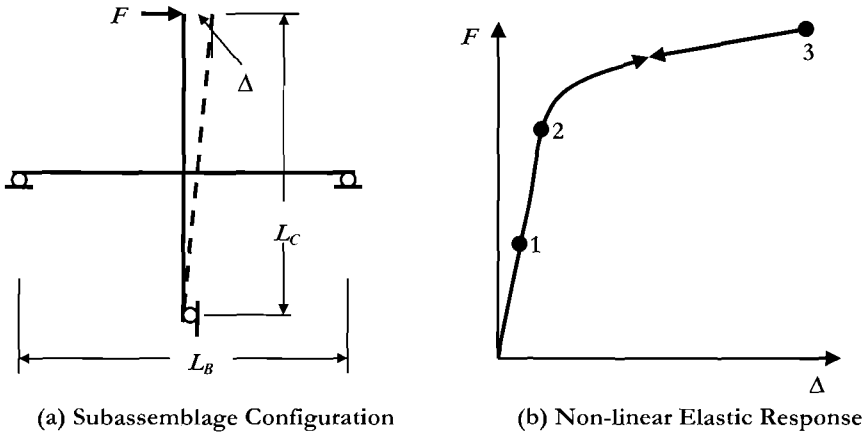
**Fig.5.33 Force-Displacement Response for a Debonded Prestressed
Beam-to-Column Subassemblage**

When the crack has propagated to the centroidal axis, corresponding to point **2** in Fig.5.33(b), the moment will be:

$$M_2 \approx T_i h_b / 3 \tag{5.69}$$

Deviation from the initial elastic stiffness between points **1** and **2** will be minimal, unless the average prestress level is fairly high ($f_{pc} > 0.25 f'_c$).

Beyond point **2** the precise force-displacement relationship is less simple to determine, since steel and concrete strains are not linearly related. However, since the aim will be to develop a bilinear approximation to the force-displacement response (see Fig. 5.32(c)), it is sufficient to compute the conditions at maximum displacement. In terms of design requirements, this may be taken as corresponding to the limit of proportionality of the prestressing steel. At this point, the tendon force, and also the tendon elastic extension above the initial condition are known. Assuming confined conditions for the concrete in the plastic hinge region the corresponding moment capacity M_3 can thus be found from standard section analysis. Further, assuming that the opening of the crack at the beam-column interface is directly related to the tendon extension by simple geometry, the displacement at point **3** can be shown[P20] to be:

$$\Delta_3 = \Delta_2 \frac{M_3}{M_2} + \frac{L_C}{E_s} \left(f_{slp} - f_{si} \right) \frac{\left(0.5h_c + x\right)}{\left(0.5h_b - c\right)} \tag{5.70}$$

where f_{slp} is the steel stress at the limit of proportionality, x is the unbonded length of tendon on one side of the joint (see Fig. 5.32(a)), and c is the depth from the extreme compression fibre to the neutral axis in the beam plastic hinge region (found from the

known confined concrete stress-strain parameters). Note that in all designs and experiments to date using unbonded tendons, the unbonded length x has been taken as half the beam span length. That is, the tendon has been fully debonded along its length, except at the anchorage. More complete details are provided in [P20].

Large-scale testing of interior and exterior beam-to-column subassemblages[P18] has shown the expected benefits of low residual displacement, high retained elastic stiffness, and reduced need for transverse reinforcement. They have also shown that damage levels are very much less than are obtained with equivalent reinforced concrete structures. Figure 5.34 shows condition of an interior joint at the design drift of 2%, and an exterior joint at 4%, twice the design drift. In both cases only superficial damage had occurred. Cracks in the joint region fully closed when lateral force was removed.

(a) Interior Joint at 2% drift   (b) Exterior Joint at 4% drift

Fig.5.34   Damage to Beam-to-Column Precast Units with Unbonded
Tendons[P18]

5.11.3   Hybrid Precast Beams

(a)   Conceptual Issues: A disadvantage with beams using unbonded tendons is that there is little additional damping provided by the inelastic response, and the response is,

as noted above essentially non-linear elastic. The implication is that displacements will be larger than with equivalent reinforced concrete structures, or, conversely, that the **DDBD** process will result in a higher required design force for a specified drift limit. Behaviour can, however, be improved by adopting a hybrid design, as illustrated in Fig.5.35.
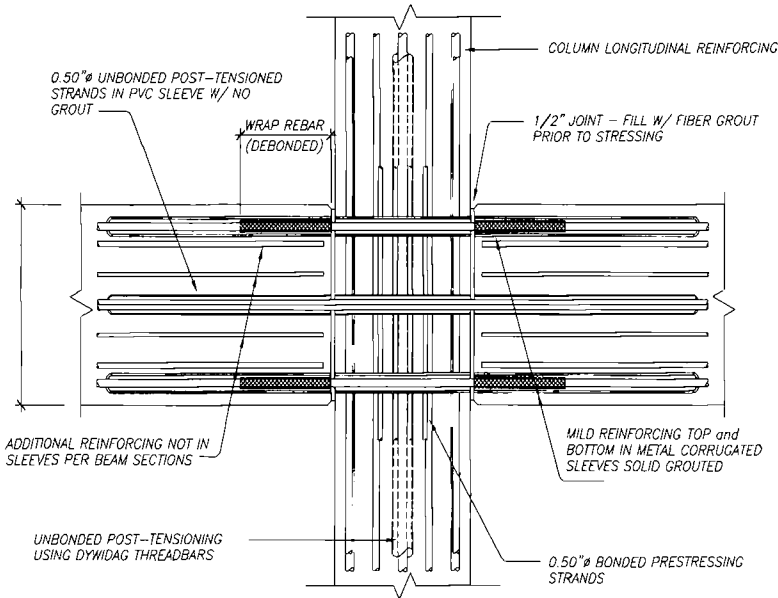
Fig.5.35   Hybrid Beam-to-Column Connection used in the UCSD 5-Storey Precast Building Test[N1]

This detail, which was one of several connection details tested in the 5-storey precast building test[N1,P19] carried out at the University of California, San Diego in 1999 uses a combination of central unbonded post-tensioning and conventional mild-steel reinforcement grouted into corrugated ducts in the beams and column at the connection. The mild-steel reinforcement yields sequentially in tension and compression under cyclic loading, dissipating energy, and adding to the flexural strength of the connection, but the clamping force of the unbonded tendon is sufficient to yield the reinforcement in compression when the lateral load is removed, hence removing any residual displacement. The resulting hysteresis loop is flag-shaped (see Section 4.9.2(f) and Fig.5.36).

Figure 5.36 illustrates the moment-rotation characteristics for a typical hybrid design, with a central prestressing tendon of area A_P, and mild steel reinforcement areas of A_S at top and bottom of the section, separated by a distance d' (see Fig.5.36(a)).

The response of the section based purely on the prestressing force is depicted in Fig.5.36(b) by the solid line. The moment capacity M_P is found as described above, based on conventional section analysis. Since the elastic portion of the moment-rotation response is governed by the uncracked stiffness of the beam section, the addition of mild

steel reinforcement has negligible effect on the initial elastic branch of the response, but the moment capacity is increased by the reinforcement couple $M_S = A_S f_y d'$, as a consequence of the reinforcement yielding in tension at the top, and compression at the bottom of the section (or vice versa, depending on the sign of the moment). The total moment-rotation response is depicted by the upper dashed line in Fig.5.36. When the loading direction is reversed, the yielded reinforcement must yield in the opposite sense (i.e. tension to compression, and compression to tension) before open cracks can close. The response on unloading is thus given by the lower dashed line on the right side of Fig. 5.36(b). To ensure that the advantages of low residual displacement are obtained, it is necessary that $M_S < M_P$.

(a) Beam Reinforcement   (b) Moment-Rotation Relationship
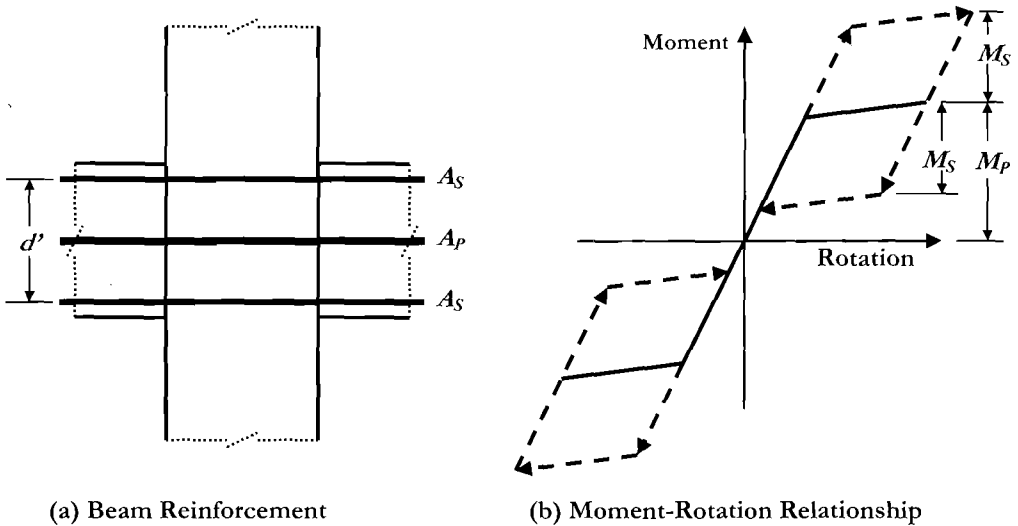
Fig. 5.36 Moment-Rotation Response of a Hybrid Beam-Column Connection

(b) Yield Displacement of Hybrid Frames: The increased stiffness of the prestressed beams, compared with equivalent conventionally reinforced sections reduces the yield drift, and hence increases the displacement ductility capacity of hybrid frames, for a given design drift. Beam flexural and shear displacements, and joint shear deformation will all be significantly less, but column flexural and shear deformations will be unaffected. Based on these considerations, yield drifts are estimated to be about 40-50% of those for a conventional concrete frame reinforced with mild steel of yield strength 400 MPa. Conservatively using the upper limit, the yield drift can thus be written as

$$\theta_y = 0.0005 \frac{L_B}{h_b} \tag{5.71}$$

Since hybrid designs will normally be incorporated in building designs as perimeter frames, with interior frames designed for gravity support only, beam span-to-depth ratios

will tend to be less than for two-way reinforced concrete frames, and yield drifts will be further reduced. In conventional force-based design this would imply increased design forces as a result of the reduced natural period. In **DDBD**, the reduced yield displacement results in increased ductility demand, and hence increased damping. As a consequence, the design force level is reduced.

(c) Equivalent Viscous Damping of Hybrid Frames: Example 3.2 (Section 3.4.3(d)) presents a method for determining the equivalent viscous damping for a flag-shaped hysteresis rule where the height of the flag is $\beta = 0.75 \times F_y$, (F_y is the yield force) and the post-yield stiffness is $r = 0$. This can be generalized for other values of β and r, giving the hysteretic component of the area-based viscous damping as

$$\xi_{hyst} = \frac{A_h}{2\pi F_m \Delta_m} = \frac{\beta(\mu - 1)}{\mu\pi(1 + r(\mu - 1))} \tag{5.72}$$

Note that in relation to the formulation given in the previous section (Fig.5.36) the flag height may be expressed as

$$\beta = \frac{2M_S}{M_S + M_P} \tag{5.73}$$

The damping calculated from Eq.(5.72) is multiplied by the correction factor from Fig.3.15, and added to the elastic damping component from Table 3.2 or Fig.3.13.

5.11.4 Design Example 5.3: DDBD of a Hybrid Prestressed Frame Building including P-Δ Effects.

Figure 5.37 shows details of a six-storey frame building of 25 × 25m (82 × 82ft) plan. The seismic bracing system consists of peripheral frames of precast hybrid beams and columns with internal non-seismic frames designed to carry gravity loads, and with sufficient displacement capacity to tolerate the seismic design drifts. As suggested in Fig.5.18(b), problems with corner columns, which are exacerbated in frames containing prestressed beams because of the need for intersecting anchorages, are avoided by terminating the beams before the corners, and linking to the orthogonal peripheral frame with either slabs, or non-seismic beams. Dimensions, material properties and floor weights are included in Fig.5.37.

The building is to be designed for a maximum drift of 0.025 when subjected to the design intensity represented by the displacement spectrum of Fig.5.38, and **P-Δ** effects are to be considered in the design.
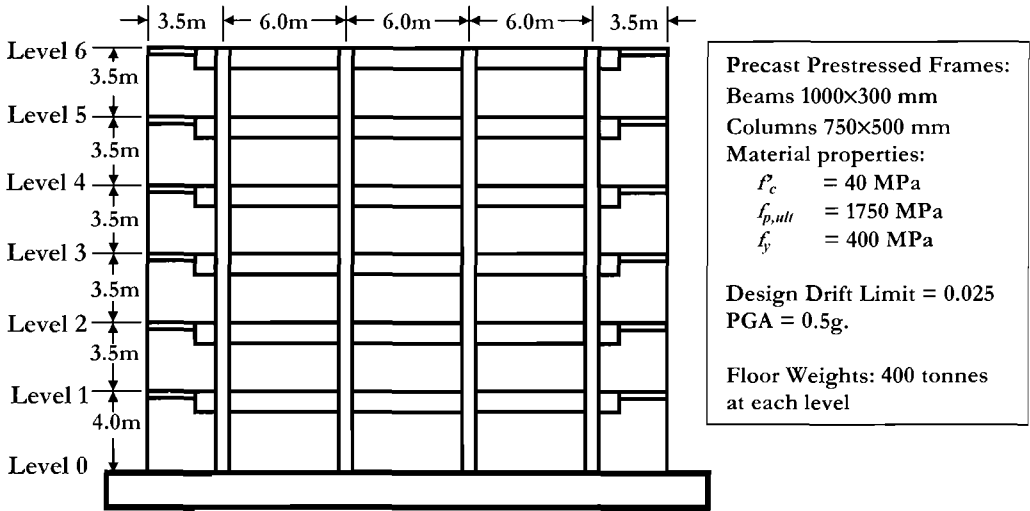
Fig.5.37   Structure for Example 5.3 (1m = 3.28ft; 1MPa =145psi; 1t = 2.205kips)
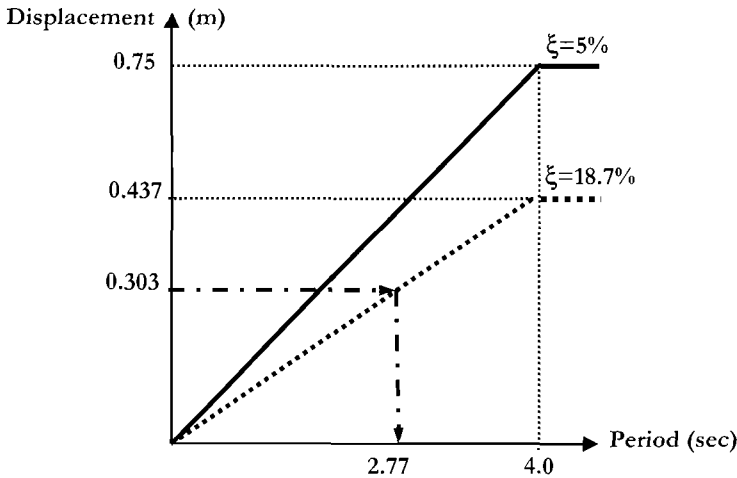
Fig.5.38 Design Displacement Spectra for Example 5.3 (1m = 3.28ft,
1MPa=145psi)

Solution: The initial data for calculating the substitute structure properties are listed in Table 5.5. Note that the storey height at level 1 is taken to the mid-height of the beam, and hence is 3.5m, not 4.0m. The design displacements at the various levels are found from Eq.(5.1) as

$$\Delta_i = \delta_i \left(\frac{0.025 \times 3.5}{0.213} \right) = 0.411 \delta_i$$

where the inelastic mode shape δ_i is found from Eq.(5.2) with $H_n = 21.0m$ (68.9ft).

Table 5.5 Substitute Structure data for Example 5.3 (1m=3.28ft, 1t=2.205kips)

Level, i (1)	Height H_i (m) (2)	Mass m_i (tonnes) (3)	δ_i (4)	Δ_i (m) (5)	$m_i\Delta_I$ (6)	$m_i\Delta_i^2$ (7)	$m_i\Delta_iH_i$ (8)
6	21.0	320.00	1.000	0.411	131.5	54.05	2762
5	17.5	400.00	0.880	0.362	144.6	52.28	2531
4	14.0	400.00	0.741	0.304	121.8	37.07	1705
3	10.5	400.00	0.583	0.240	95.9	22.99	1007
2	7.0	400.00	0.407	0.167	67.0	11.21	469
1	3.5	400.00	0.213	0.088	35.0	3.06	123
Sum					595.8	180.67	8596

Design Displacement: From Eq.(5.3), and Table 5.5, Cols (6) and (7):

$$\Delta_d = \sum_{i=1}^{n}\left(m_i\Delta_i^2\right)/\sum_{i=1}^{n}\left(m_i\Delta_i\right) = 180.7/595.8 = 0.303m \quad (11.9\text{in})$$

Effective Height: From Eq.(5.5) and Table 5.5, Cols (6) and (8):

$$H_e = \sum_{i=1}^{n}\left(m_i\Delta_iH_i\right)/\sum_{i=1}^{n}\left(m_i\Delta_i\right) = 8595.6/595.8 = 14.4m \quad (69\% \text{ of building height}).$$

Yield Displacement: From Eq.(5.71), the yield drift for a hybrid frame is estimated as

$$\theta_y = 0.0005\frac{L_b}{h_b} = 0.0005 \times 6.00/1.00 = 0.003$$

We assume a linear yield displacement profile with height, and hence the yield displacement at the effective height is

$$\Delta_y = 0.003 \times 14.4 = 0.0432m \quad (1.70\text{in})$$

System Ductility: From Eq.(5.6) the system ductility is thus

$$\mu = \frac{\Delta_d}{\Delta_y} = \frac{0.303}{0.0432} = 7.0$$

Note that this design ductility is much higher than has been used in earlier design examples with conventionally reinforced concrete beams, as a consequence of the low yield displacement and the low aspect ratios of the peripheral beams.

Equivalent Viscous Damping: We chose to design the hybrid beams such that the mild steel reinforcement provides 40% of the total beam moment capacity, and hence we have $M_P = 0.6\ M_T$ and $M_S = 0.4\ M_T$. Consequently, $\beta = 0.8$ (see Eq.(5.73)). We assume a reasonable post-yield stiffness ratio of $r = 0.04$. From Eq.(5.72), the area-based equivalent viscous damping is

$$\xi_{hyst} = \frac{\beta(\mu-1)}{\mu\pi(1+r(\mu-1))} = \frac{0.8(7.0-1.0)}{7.0\pi(1+0.04(7.0-1.0))} = 0.176$$

From Section 3.4.3(c), this damping value needs correction in accordance with Fig. 3.15. We conservatively take the value for $\mu = 6.0$ to be appropriate, resulting in a reduction factor of $R = 0.937$. We assume 5% tangent stiffness elastic damping, which needs to be converted to secant stiffness in accordance with Table 3.2, which, for a flag-shaped loop results in $\phi = -0.43$. The effective equivalent viscous damping is thus given by Eq.3.15, as

$$\xi_{eq} = \mu^{\phi}\xi_{el} + R.\xi_{hyst} = 7^{-0.43} \times 0.05 + 0.937 \times 0.176 = 0.187$$

The reduction factor for the corner displacement corresponding to a damping factor of 18.7% is given by Eq.(2.8) as

$$R_{\xi} = \left(\frac{0.07}{0.02+\xi_{eq}}\right)^{0.5} = \left(\frac{0.07}{0.02+0.187}\right)^{0.5} = 0.582$$

The corner displacement corresponding to 18.7% damping, and T=4 sec is thus 0.582×0.75=0.437m. This is shown by the dashed line in Fig. 5.38.

Equivalent Mass: From Eq.(5.4) and Table 5.5, the substitute structure equivalent mass is

$$m_e = \sum_{i=1}^{n}(m_i\Delta_i)/\Delta_d = 595.8/0.303 = 1966 \text{ tonnes (82\% of total mass)}$$

Effective Period: The effective period at design displacement response is found from the dashed line of Fig.5.38, by proportion as

$$T_e = 4.0 \times (0.303/0.437) = 2.77 \text{ sec}.$$

Effective Stiffness: From Eq.(5.10), the effective stiffness of the substitute structure is

$$K_e = 4\pi^2 m_e / T_e^2 = 4\pi^2 \times 1966 / 2.77^2 = 10121 kN/m$$

Design Base Shear: From Eq.(5.11), the design base shear is

$$V_{Base} = K_e \Delta_d = 10121 \times 0.303 = 3067 kN \quad (690 \text{ kips})$$

   This is the total base shear, and is carried by the two peripheral frames on opposite sides of the building. The base shear per frame is thus 1534kN. (345 kips)

Vertical Distribution of Base Shear: Since the building has only 6 storeys and is rather stiff, it is unlikely that higher mode effects will influence the ductility demands significantly in the upper floors. As a consequence the base shear is distributed to the floor levels in accordance with Eq.(5.12). That is, the 10% of base shear additionally allocated to the roof level recommended in Eq.(5.27) is not applied:

$$F_i = V_{Base}(m_i \Delta_i) / \sum_{i=1}^{n}(m_i \Delta_i) = 1534(m_i \Delta_i) / 595.8$$

   These floor forces are listed as Column (9) in Table 5.6.

Table 5.6 Design Forces (per frame) for Example 5.3 (1kN =0.225kips; 1m =39.4in)

Level, i (1)	Height H_i (m) (2)	F_i (kN) (9)	$V_{S,i}$ (kN) (10)	OTM (kNm) (11)	$F_{i,(P-\Delta)}$ (kN) (12)	$OTM_{P\Delta}$ (kNm) (13)	V_{beam} (kN) (14)	M_{beam}* (kNm) (15)
6	21.0	338.6	338.6	0.0	365.0	0.0	60.6	163.7
5	17.5	372.3	710.9	1185.2	401.3	1277.6	127.3	343.8
4	14.0	313.5	1024.5	3673.3	338.0	3959.8	183.5	495.4
3	10.5	246.9	1271.3	7258.9	266.1	7825.1	227.7	614.8
2	7.0	172.5	1443.8	11708.6	185.9	12621.9	258.6	698.2
1	3.5	90.1	1533.9	16761.8	97.1	18069.2	274.7	741.8
Sum		1533.9	6323.0	22130.6	1653.6	23856.8		

* At column face

Story Shear Force and Overturning Moments: Storey shear forces are found by summing the floor forces above the storey considered. These are listed in Col.(10) of Table 5.6. Storey overturning moments at the floor levels are also found from the lateral forces as

$$OTM_i = \sum_{j=i}^{12} F_i(H_j - H_i)$$

   The overturning moments at each storey are tabulated as Col.(11) in Table 5.6. The

base overturning moment for the frame is OTM_{Base} = 22131 kNm (196000 kip.in).

Check of P-Δ Effects: It is appropriate to check the P-Δ moments at this stage, and adjust the design forces, if necessary. The recommendations of Section 3.6.3 are that **P-Δ** effects be included when the stability index defined by Eq.(3.41) exceeds 0.1. Substituting in Eq.(3.41) with $M_N = OTM_B$, $\Delta_{max} = \Delta_d$ =0.303, and

P = (5×400+320)×9.8 = 22700 kN:

$$\theta_\Delta = \frac{P\Delta_{max}}{M_N} = \frac{22,700\times0.303}{2\times22130} = 0.155 > 0.1$$

Note that in the above equation the 2 in the denominator is because there are two frames resisting the seismic lateral forces, and the total OTM is thus 44260 kNm. The stability index is 55% above the 0.1 limit, and it could be argued that for hybrid frames, with their low residual displacements, **P-Δ** effects could be ignored. However, for completeness they are included in the following. According to Eq.(3.48), taking C = 0.5 for reinforced concrete:

$$F = V_{Base} = K_e\Delta_d + C\frac{P\Delta_d}{H_e} = 10,121\times0.303 + 0.5\frac{22,700\times0.303}{14.4} = 3305kN$$

Again, this is divided between the two parallel peripheral frames, and the required base shear strength per frame is thus increased to 1653 kN. This is a 7.8% increase. The revised lateral design forces and overturning moments are listed in Table 5.6 as Columns (12) and (13)

Column-Base Moments: Since the lateral force system is comprised of one-way frames, the point of contraflexure in the ground-floor columns is taken as 60% of the storey height. The total column-base moment, shared between the four columns of a frame is thus ΣM_{Cj} = 0.6×3.5×1653 = 3471kNm. We divide this between the outer and inner columns in the ratio 1:2, giving $M_{C,1} = M_{C,4}$ = 579kNm, $M_{C,2} = M_{C,3}$ = 1157kNm.

Beam Shears Corresponding to Design Lateral Forces:
From Eq.(5.34) the sum of the beam seismic shear forces up the height of the frame is

$$\sum_{i=1}^{n}V_{Bi} = T = \left(\sum_{i=1}^{n}F_iH_i - \sum_{j=1}^{m}M_{Cj}\right)/L_B = (23857 - 3471)/18 = 1133kN$$

Note that L_B = 18m is the distance between the two outer columns of the seismic frame.
   Hence, distributing this total to the beams as recommended in Eq.(5.37):

$$V_{Bi} = T \cdot \frac{V_{S,i}}{\sum\limits_{i=1}^{n} V_{S,i}} = 1133 V_{S,i} / 6323$$

These seismic beam shears are listed in Table 5.6 as Col.(14). Note that these will subsequently be amplified for flexural overstrength, and to include gravity shears. Note that the column storey shears of Table 5.6, Col.(10) should also be increased by 7.8%, to account for **P-Δ** effects, but since it is the ratio of these to the sum of the storey shears, which is of course unaffected by the increase, the corrected column storey shears are not listed. It will, however, be necessary to implement the increase when column capacity-design shears are computed.

Beam Seismic Moments: Since the seismic frames are peripheral, and precast, gravity loads will be small in comparison with seismic moments, and slab reinforcement will not directly add to the flexural strength (though this will depend on the connection details between the slabs and beams. If precast prestressed floor systems with cast *in situ* connections to dowel reinforcement in the precast beams are provided, the moment enhancement can be very significant[F8]). It is elected to have equal negative and positive moment capacity at the column faces. Assuming that the columns are 600×600 mm (23.6×23.6 in), the beam seismic moments at the column faces are given by Eq.(5.36) as

$$M_{Bi,des} = V_{Bi}(L_B - h_C)/2 = V_{B,i}(6.0 - 0.6)/2 = 2.7 V_{B,i}$$

The resulting beam design moments are listed in Table 5.6 as Column (15). As noted above, 60% of the required moment capacity will be provided by central prestressing, and 40% by mild steel reinforcement. Details of the design process are elementary, and are not included here.

Beam Design Shear Forces: Beam flexural design using post-tensioning is likely to result in lower overstrength factors than with conventionally reinforced sections, since the range of ultimate tensile strength of the prestressing steel is typically low. We design the sections using advanced models for steel and concrete stress-strain curves (see Section 4.2), and assess possible overstrength for the fraction of moment capacity provided by the prestressing as 10%, and for the fraction provided by the mild steel couple as 20%. Assuming a perfect match between required and provided steel areas, the overstrength factor can thus be assessed as $\phi^o = 0.6 \times 1.1 + 0.4 \times 1.2 = 1.14$. We adopt a value of 1.15.

Gravity loads on beams for the seismic load case, including a 20% vertical dynamic amplification factor are 8kPa (0.167kips/sq.ft). With a 3m tributary width, the distributed load on the peripheral beams is thus 24 kN/m. (1.64kips/ft). Modifying Eq.(5.57) by using the clear span, L_c between column faces:

$$V_x = \frac{2\phi^o M_B}{L_c} + \frac{w_G^o \times L_c}{2} - w_G^o x = \frac{2 \times 1.15 M_B}{5.4} + \frac{24 \times 5.4}{2} - 24x = 0.426 M_B + 64.8 - 24x$$

The maximum value of V_x occurs at the column face, and is listed in Table 5.7. Col.(16)

Table 5.7 Capacity Design Calculations for Example 5.3

Level, i	V^o_B (kN)	ω_f	$M_{C,ext}$ (kNm)	$M_{C,int}$ (kNm)	$V_{C,ext}$ (kN)	$V_{C,int}$ (kN)
(1)	(16)	(17)	(18)	(19)	(20)	(21)
6	134.5	1.000	209.2	418.4	258.8	517.6
5	211.3	1.406	308.8	617.6	331.2	662.4
4	275.8	1.812	572.9	1145.9	392.2	784.4
3	326.7	1.812	711.0	1422.1	440.2	880.5
2	362.2	1.812	807.5	1614.9	473.7	947.6
1	380.8	1.812	857.9	1715.8	491.3	982.6
0		1	694.3	1388.6	491.3	982.6

Column Design Moments: Analysis for column flexure follows the suggestions at the end of Section 5.5.2(b), where beam moment input to a joint is shared equally between the columns above and below the joint. With the overstrength factor of $\phi^o = 1.15$, as calculated above, the overstrength ductility demand, from Eq.(5.62a) is

$$\mu^o = \frac{\mu}{\phi^o} = \frac{7.0}{1.15} = 6.09$$

The dynamic amplifications factors for the region from the first floor to the ¾ point of height, and at roof level, are found from substitution into Eqs.(5.61a) and (5.61b) respectively as

$$\omega_{f,c} = 1.15 + 0.13(\mu^o - 1) = 1.15 + 0.13 \times 5.09 = 1.812 \quad \text{and}$$

$$\omega_{f,t} = 1.0$$

The full list of dynamic amplification factors for column moment, following the distribution of Fig.5.25, are provided in Table 5.7 as Col.(17). Column design moments at the joint centreline are thus found from Eq.(5.60):

$$\phi_f M_N \geq \phi^o \omega_f M_E = 1.15 \omega_f M_E$$

where M_E are the column moments corresponding to the design lateral forces. In accordance with the recommendations of Section 5.5.2(c) the beam moments at the joint centroid are equally distributed to the columns above and below the joint. Note again that the beam moments listed in Table 5.6 Col.(15) apply at the column faces, and have to be increased by 11.1% to obtain the joint centre beam moments. The above equation for required dependable column moment capacity at the joint centre can thus be rewritten as

$$\phi_f M_N \geq \phi^o \omega_f M_E = 1.15 \omega_f M_E = 1.15 \omega_f \left(1.11 \sum M_{beam} / 2\right)$$

where the input beam moment is the sum of moments from beams on opposite sides of the joint, and the denominator, 2, represents the equal subdivision of moment input to the columns above and below the joint. As with Example 5.2, the exception occurs at the roof, where all the moment is taken by the top of the upper level column. Resulting design moments at the joint centroid for the exterior and interior columns are listed in Table 5.7 as Col.(18) and (19) respectively. Note that, as is commonly the case with high ductility levels, the column reinforcement at level **1** may need to be significantly higher than at the column base, though it must be remembered that the design moments occur at the level of the top or bottom of the beam, and will be thus be lower than the values listed for levels 1 to 6 by an amount equal to $0.5 V^o h_b$, where V^o is the overstrength shear, calculated in accordance with the next section..

Column Design Shear Forces: Column design shear forces are determined in accordance with Section 5.8.5(c). Equation (5.65) applies. We divide the total storey column shear between the interior and exterior columns in the proportion 1:2, and hence the exterior column shears are given by

$$\phi_S V_{N,ext} \geq (\phi^o V_E + 0.1 \mu V_{E,base}) / 6 = (1.15 V_E + 0.1 \times 7 V_{E,base}) / 6 \leq \frac{M_t^o + M_b^o}{\left(l_c\right)}$$

The resulting shear forces for exterior and interior columns, based only on amplification of the design shears, are listed in Table 5.7 as Cols.(20) and (21). These values would need to be checked against the shear corresponding to development of overstrength moment capacity at top and bottom of the column, as indicated at the right of the above equation.

5.12   MASONRY INFILLED FRAMES

5.12.1   Structural Options

Masonry infill in frames is common in Europe, Asia, and Central and South America. Although it is less common in North American, New Zealand and Japanese design, it is still sometimes used in these countries to provide fire resistance between buildings on boundary frames. However, if the interaction between the frame and the infill is not

properly considered in design and construction, the consequences can be disastrous when subjected to high intensity seismic action. Examples of structural failures of infilled frames in earthquakes are common.

There are two different approaches to construction with masonry infill. One approach is to place flexible material between the frame and the infill so that the two elements (frame and infill) can deform independently under the design seismic intensity, without contact, except at the base of the infill. This requires special reinforcement in the infill, and some means of providing out-of-plane support[P1]. The alternative approach is to build the infill hard up against the frame, and to account for the structural interaction in the design. Generally when infill is built hard up against the frame, the infill is unreinforced, and susceptible to damage and failure at comparatively low drift angles. The philosophy adopted in countries where such construction is permitted is that failure of the infill is non-structural, and can be repaired after the earthquake.

5.12.2 Structural Action of Infill

(a) Full-height infill   (b) Partial height infill
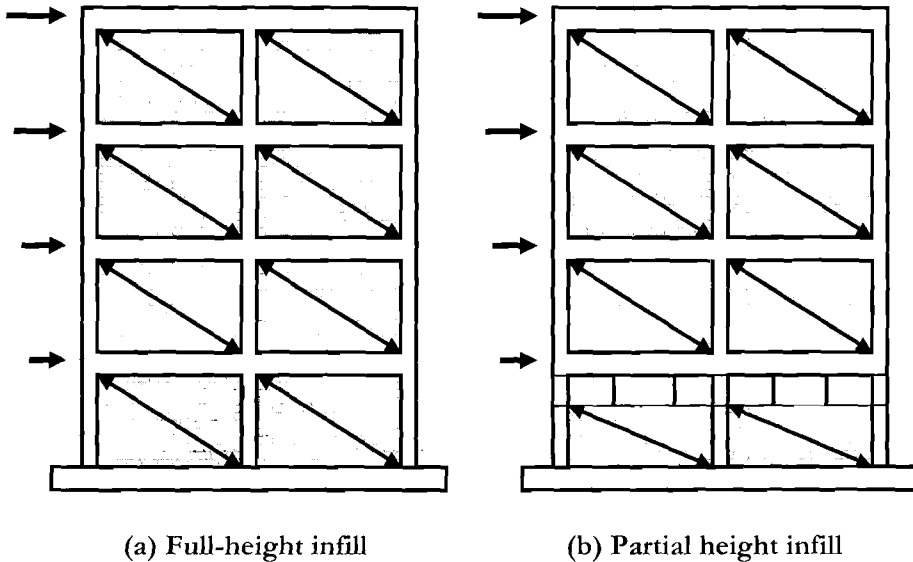
Fig.5.39   Masonry Infill in Structural Frames

The description of structural action in this section is based on the assumption of typically weak infill, using hollow tile bricks, as is common in European and South American countries. In the initial stages of seismic response, infill which is constructed in contact with the frame on all boundaries, as suggested in Fig.5.39(a), acts as a diagonal brace to resist frame action. High compression stresses develop in the infill at the ends of the brace, indicated in Fig.5.39(a) by the diagonal arrows, and separation between infill and frame occurs at the other two corners. Because of the high in-plane stiffness of the infill, forces induced in the frame members are modified to be primarily axial rather than

flexural. Stiffness of the frame members (assuming reinforced concrete) is close to the uncracked value, though the axial stiffness of the column placed in tension by the truss action of response (the left column in Fig.5.39(a)) may be significantly reduced by cracking. Overall stiffness of the building is very much higher than that corresponding to pure frame action, and initial periods of response are low.

At comparatively low drift angles – typically 0.003 to 0.005 - initial failure of the infill occurs, generally by crushing of the infill at the contact corners and severe diagonal cracking parallel to the strut. Sliding shear failures may also initiate along horizontal bed joints. Subsequent to this, the structural action modifies from a truss or braced-frame action to that of a pure frame action, with the infill playing no further structural part in the response. This transition is normally complete by a drift of about 0.01.

Where the infill is part height, as indicated in the ground floor of Fig.5.39(b), the upper end of the infill brace bears against the column. In the region of column above the infill, shown shaded in Fig. 5.39(b), the structural shear will be resisted by column flexure over a short length, with a potential for soft-storey shear failure developing, particularly if the infill has significant strength.

Perhaps the most dangerous condition occurs when the infill is not distributed evenly round the structural plan. It has been estimated that in the 1985 Mexico city earthquake, more than 40% of the building failures occurred to buildings on corner sites, where fire-resistant infill was placed only on the two boundaries next to the adjacent buildings, creating severe torsional eccentricity[P1]. This situation must be avoided at all costs.

5.12.3 DDBD of Infilled Frames

A two-stage design process will be necessary when structural infill is used in construction. The design philosophy will require that under a serviceability level earthquake, infill failure does not occur, while under the damage-control earthquake, frame response is acceptable. Normally this will mean restricting drifts under the serviceability earthquake to 0.005, and under the full design earthquake to 0.02 or 0.025, dependent on the code drift limit.

The logical procedure will be to design for the damage-control limit state using DDBD, on the assumption that the infill has no structural significance. The frame is then detailed to provide the required strength. An elastic analysis is then carried out with the infill modelled in place, using realistic estimates of the infill stiffness. The frame member stiffness should be assumed to be larger than that appropriate for yield. The following steps are taken in the check:

- Determine elastic period T_{el} and elastic fundamental mode shape δ_{el} by structural analysis.
- From the elastic displacement response spectrum (5%) for the serviceability-level earthquake, determine the fundamental mode response displacement Δ_{el}.
- From the elastic mode shape and the mass distribution, determine the effective height from Eq.(5.5), substituting the mode shape $\delta_{el,i}$ for the displacements Δ_i:

$$H_e = \sum_{i=1}^{n} \left(m_i \delta_{el,i} H_i \right) / \sum_{i=1}^{n} \left(m_i \delta_{el,i} \right) \tag{5.73}$$

- From the mode shape and the response displacement, Δ_{el} determine the displacements at the storey heights:

$$\Delta_i = \delta_{el,i} \frac{\Delta_{el}}{\delta_{He}} \tag{5.74}$$

where δ_{He} is the value of the mode shape at the effective height H_e.

- Determine the storey drifts from the displacement profile, and compare with the specified drift limit.

Information on the modelling of frame-infill interaction is available in a number of publications (e.g. [P1, C12])

5.13 STEEL FRAMES

5.13.1 Structural Options

Steel frames for buildings are generally divided into three basic categories: Moment resisting frames, Concentric Braced Frames, where there is no eccentricity of connection, and the elastic response may be described by truss action, and Eccentric braced frames, where eccentricity of connection is deliberately induced to provide a displacement mechanism which involves a mix of truss and flexural action. Examples of each are shown in Fig.5.40. Normally bracing will not be provided in all bays of a multi-bay frame.

The key elements of displacement-based design of steel moment frames have been addressed earlier in this chapter, and there is no conceptual difficulty in designing such structures. However, in the case of both concentric braced frames (**CBF**s) and eccentric braced frames (**EBF**s), issues related to target displacement profile, yield drift, and equivalent damping must be addressed. These three items will be the focus of the remainder of the brief discussion in this section. It is also important to note that both **CBF**s and **EBF**s require special attention to detailing with regard to selection of bracing and link members to ensure ductile response. The reader is referred elsewhere [B9] for a thorough discussion on detailing of such systems as that discussion is outside the scope of this text.

Although ductility capacity may be high, design displacements will generally be significantly lower than with moment-resisting frames. As a consequence, design base-shear levels will in general be significantly higher than with moment-resisting frames, which will generally be designed for code drift limits.
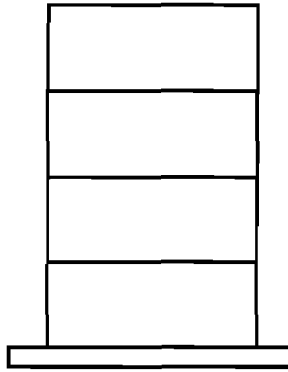
(a) Moment Resisting Frame
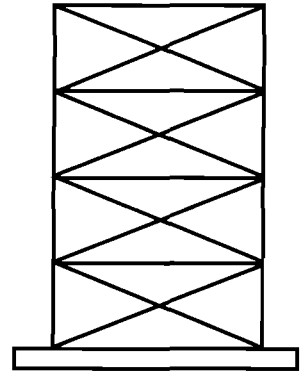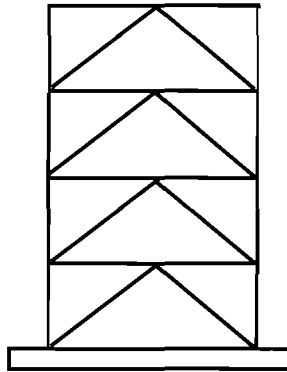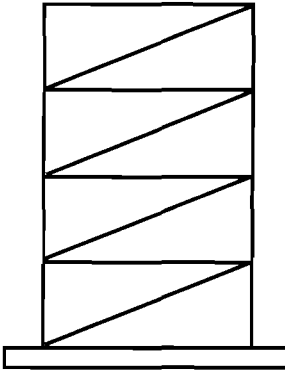
(b) Concentric braced frame Options
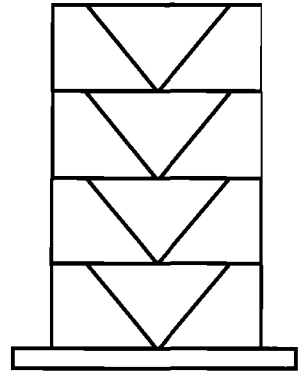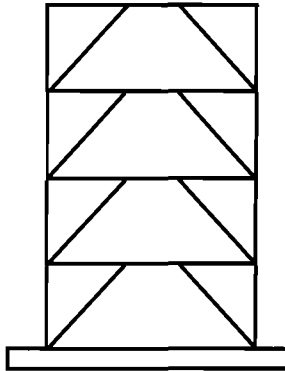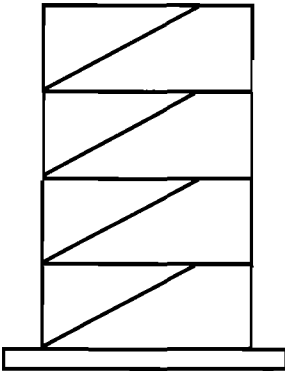
(c) Eccentric braced frame Options

Fig. 5.40   Steel Frames for Seismic Resistance

5.13.2   Concentric Braced Frames

(a) Conceptual Issues: **CBF**s, examples of which are shown in Fig. 5.40b, contain diagonal bracing elements subjected to tension and compression. The braces are subjected to large axial forces and minimal bending actions, and may consist of a variety of cross section types [B9]. Historically, **CBF**s were first utilized for lateral force resistance under wind loading, where the structural system is required to remain elastic. In such cases, the high elastic stiffness (compared to moment frames) could be used advantageously in design. When adapting **CBF**s for seismic resistance, inelastic considerations dominate. It is possible to design tall **CBF**s for elastic response in regions of low seismicity. However, when inelastic response is required this will normally be effected by permitting yield of the diagonal members, while ensuring the beams and columns remain elastic. Successful implementation of this concept requires careful detailing of bracing members and bracing connections, including checks of member slenderness and flange width to web thickness ratios. The most common type of **CBF** used in seismic design is the so-called X-Braced frame, illustrated in the right-hand example in Fig.5.40(b). Other variants of the **CBF**s shown in Fig. 5.40b have been proposed, such as the zipper frame[K7] which results in distribution of non-linear action over several braces in the frame.

Considering the X-braced frame concept, it will be immediately apparent that lateral response will induce axial tension in one of the braces in each storey and axial compression in the other. Although the tension brace will be ductile, it will be difficult to avoid inelastic buckling in the compression brace. Note that once the brace has yielded in tension, its elastic buckling force will also reduce due to the Bauschinger effect, which reduces the apparent elastic modulus of elasticity. The result is that response of the structure tends to be characterized by cyclic tensile yield and compression bucking of each brace. After a complete cycle of inelastic response both braces are likely to have residual lateral buckling displacements, with a severe reduction in the hysteretic energy of response.

It will also be apparent that soft-storey mechanisms can develop. If the brace or braces in one storey yield or buckle before those in the other storeys, the potential for a soft-storey response is real.

The cautionary comments made above for X-braced frames apply even more strongly to the options with single braces in each storey.

Note that **CBF**s with single braces in each storey can perform in a satisfactory manner when the brace includes a ductile damper designed to yield at a force level lower than the dependable elastic strength (tension or compression) of the brace. Designs of this type are separately considered in Section 11.3.3(c).

(b) Yield Displacement: The yield displacement of a **CBF** is governed by the conditions to cause yielding of the bracing elements. From geometry, and assuming that strains in the beams and columns are negligible with respect to strains in the brace, the

yield drift ratio is given by Eq. (5.75)[M10] where L_{bay} is the length of the frame bay, and H_s is the storey height.

$$\theta_y = \varepsilon_y \cdot \frac{L_{bay}}{H_s} \tag{5.75}$$

(c) Target Displacement Pattern: While there have been extensive studies on the dynamic response of **CBFs**, there does not appear to be a focused study on inelastic displacements patterns and the parameters that effect them. Nonetheless, several researchers[M15, M16, T1] have conducted studies that have involved varying levels of dynamic analysis of **CBFs** where displacement patterns have been reported. Buildings from 5 to 15 storeys have been considered in these studies on X-braced **CBFs**. From the results, there seems to be a clear trend that supports the use of Eq. (5.2a) which assumes a linear displacement pattern. For **CBFs**, Eq. (5.2a) should be used regardless of the number of storeys in the frame.

The system displacement ductility capacity adopted for **CBFs** should recognize the comments made in the previous section. Where possible, this should be based on calculations and experimental evidence of the performance of the braces under cyclic tensile yield and buckling. In any case we recommend a maximum design drift significantly lower than code drift limits, say 0.015.

(d) Equivalent Viscous Damping: The force-displacement hysteretic responses of **CBFs** will be highly dependent on the type of **CBF**. For the purposes of new design, it is assumed that the **CBF** will be detailed such that it will dissipate energy in a reliable manner, without reduction by buckling response. As noted above, this implies that ductility is kept to moderate levels. As such, Eq.(3.17c) may be adopted. It is important to note that in the case of assessment of existing **CBFs** which may be non-ductile, it is recommended that revised damping expressions using Fig. 3.15 be developed.

5.13.3 Eccentric Braced Frames

(a) Conceptual Issues: The **EBF**, examples of which are shown in Fig. 5.40c, utilizes the advantages provided by both the **CBF** and moment frames while addressing the shortcomings of each configuration. The unique component of the **EBF** is that each brace in the frame is connected to a beam segment which is termed a 'link' [B9]. Ductility of the frame is provided through either flexural or shear yielding of the link (depending on the link moment to shear ratio), while protecting all other members of the frame against inelastic action through the use of capacity design principles. The resulting system has high initial elastic stiffness as well as stable hysteretic response with significant energy dissipation and high ductility capacity. The configuration shown in the central option of Fig.5.40(c) is the most commonly adopted for architectural reasons: it is the easiest to provide a centrally located access door.

The displacement capacity will be largely dependent on the length of the link; longer links providing larger plastic drift capacity (but with lesser influence on the yield drift, as established below). Longer links will, however, require a deeper member size to provide the necessary flexural strength to resist the seismic shear forces induced in the links.

Since all plastic action will take place in the links, a soft-storey mechanism is not feasible. For this reason, **EBF**s are to be preferred to **CBF**s.

(b) Yield Displacement: Equation (5.76) represents a geometric relationship between frame bay length, L_{bay}, link length, L_l, link rotation, γ, and storey drift ratio, θ derived by Popov and Engelhardt[P37].

$$\theta = \frac{\gamma L_l}{L_{bay}} \qquad (5.76)$$

This is based on the assumption of infinitely rigid frame and brace members, and hence should be interpreted as an additional elastic drift to be added to the drift corresponding to elongation of the brace given by Eq.(5.75)

Evaluation of the **EBF** storey yield drift ratio will depend on whether the link behaviour is dominated by flexure or shear. Bruneau et al.[B12] provide Eqs. 5.77 and 5.78 to determine whether a link may be considered to be dominated by flexure or shear.

$$L_l \geq \frac{2.5 M_p}{V_p} \quad \text{(for flexural links)} \qquad (5.77)$$

$$L_l \leq \frac{1.6 M_p}{V_p} \quad \text{(for shear links)} \qquad (5.78)$$

where

$$M_p = Z_p f_y \qquad (5.79)$$

$$V_p = 0.55 h_l t_w f_y \qquad (5.80)$$

and h_l = link depth, t_w is link web width and Z_p is the section plastic modulus.

For flexural links (Eq.(5.77)), the yield curvature of a link may be approximated from Eq. 5.24 as:

$$\phi_y = \frac{Z_p}{I} \cdot \varepsilon_y \qquad (5.81)$$

where *I is* the section moment of inertia of the link. As the link is in double bending, the link yield rotation may be calculated using Eq. 4.52 to give Eq. 5.82.

$$\gamma = C_l \frac{\phi_y L_l}{6} \qquad (5.82)$$

where

$$C_l \approx 1 + 2\frac{h_l}{L_l}$$

is a flexibility coefficient to account for elastic rotation at the ends of the link.

Substituting Eq.(5.81) into Eq.(5.82) and the resulting expression into Eq.(5.76), and accounting for the drift due to brace elongation results in Eq.(5.83) which represents the storey yield drift ratio for an **EBF** with flexural links:

$$\theta_{y,f} = \varepsilon_y \frac{L_{bay}}{H_s} + C_1 \frac{Z_p \varepsilon_y L_l^2}{6I \cdot L_{bay}} \tag{5.83}$$

For links dominated by shear behaviour (Eq. 5.78), the link yield rotation may be obtained from Eq.(5.84) where δ_s is the link shear yield displacement given by Eq.(5.85). In Eq.(5.85), V_p is obtained from Eq.(5.80) and K_s, the link shear stiffness, is given by Eq.(5.86).

$$\gamma = \frac{\delta_s}{L_l} \tag{5.84}$$

$$\delta_s = \frac{V_p}{K_s} \tag{5.85}$$

$$K_s = \frac{12EI}{L_l^2} \tag{5.86}$$

Substituting Eqs.(5.86) and (5.80) into Eq.(5.85), the result into Eq.(5.84) and then into Eq.(5.76) produces Eq.(5.87) which represents the storey yield drift ratio for an **EBF** with shear dominated links.

$$\theta_{y,s} = \varepsilon_y \frac{L_{bay}}{H_s} + \frac{0.55h_l t_w \varepsilon_y L_l^3}{12I \cdot L_{bay}} \tag{5.87}$$

In the case where the link deformation consists of flexure and shear, it is recommended that both Eq.(5.83) and (5.87) be included in relative proportion to Eqs.(5.77) and (5.78). For example, if the link length is equal to $2.05M_p/V_p$ (exactly in the middle between Eqs. 5.77 and 5.78), the yield drift ratio should be obtained as $0.5\theta_{y,f} + 0.5\theta_{y,s}$.

(b) Target Displacement Pattern: Until further studies are available, it is recommended that the displacement profiles given by Eq.(5.2) be adopted. As the behaviour of **EBF**s is somewhere between that of **CBF**s and moment frames, and given the absence of additional data on displacement patterns, precision greater than that implied by Eq.(5.2) is not warranted. The critical plastic drift may be found from the rotation capacity of the link, in shear or flexure, as appropriate, using Eq.(5.76). Note that since frame drifts are significantly lower than link drifts (a ratio of 1:6 is typical), it may be difficult to obtain high dependable frame plastic drift ratios with **EBF**s.

(d) Equivalent Viscous Damping: Examination of typical force-displacement hysteretic responses of **EBF**s [P31] indicates that the level of energy dissipation is similar to that of a moment frame. As a result, it is recommended that the Eq.(3.17c) be applied, using the ductility implied by the calculated drift ductility demand for design of **EBF**s.

5.14   DESIGN EXAMPLE 5.4: Design Verification of Design Example 5.1/5.2

The design of the twelve-storey reinforced concrete frame of Design Example 5.1/5.2 is now subjected to design verification with inelastic time-history analysis (**ITHA**) using the program "**SeismoStruct**" provided in the CD with this book. The structure was modelled as a 2-D structure, using inelastic fibre elements with appropriate stress-strain relationships for the concrete and reinforcing steel (see Section 4.2) to model the beams and the columns of the structure. Since in fibre analysis it is necessary to explicitly model element reinforcement, the latter was computed using the results provided in Section 5.10 (beam reinforcement in storeys 2 to 11 was computed considering the design moments indicated in Table 5.3). Given that fibre element formulations account for the actual non-linear response characteristics of reinforced concrete members, even in the so-called "elastic" phase of response, a reduced value of 2.5% tangent-stiffness proportional elastic damping was introduced.

Seven **ITHA** were carried out, each of which using a different spectrum-compatible artificial record generated with SIMQKE[G6]. Results, in terms of storey response displacements and overturning moments are compared with the design profiles in Fig.5.41. The design profile is indicated through a solid line, whilst the average of the seven dynamic analyses is shown as a dashed line. It will be noted that the agreement between the design and analyses profiles is very good.

Input and output data files for the analyses carried out in this example are included on the CD provided with this book, together with an overview of modelling configuration and assumptions, and a summary of the most relevant results
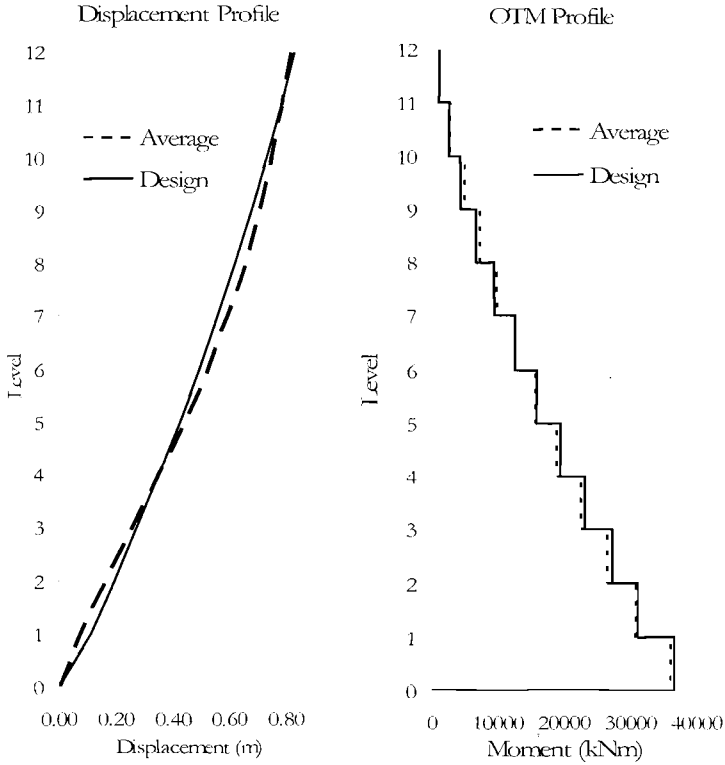
Fig.5.41 Mean Peak Storey Displacements Response/Overturning Moments vs. Design Values for Design Example 5.4

6

STRUCTURAL WALL BUILDINGS

6.1 INTRODUCTION: SOME CHARACTERISTICS OF WALL BUILDINGS

Buildings where the primary or only lateral-force resisting mechanism consists of walls are frequently called "shear wall" buildings. As has been pointed out elsewhere[P1], this has unfortunate connotations, as it implies that response is shear-dominated, whereas the desired response is ductile flexural action, with shear controlled by capacity design measures. Consequently we follow the lead of [P1] and use the terminology of this chapter's title.

The performance of structural wall buildings in recent earthquakes has generally been good, and complete collapse under even extreme seismic excitation is rare. Exceptions have occurred primarily as a result of foundation inadequacies. A detailed and complete discussion of the advantages and seismic performance of structural wall buildings is available in [P1], and only a brief summary will be provided herein.

6.1.1 Section Shapes

(a)   (b)   (c)   (d)   (e)
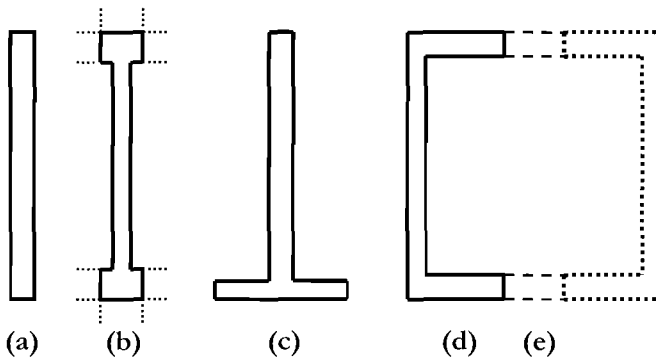
Fig.6.1 Common Section Shapes for Structural Walls

The choice of possible section shapes for structural walls is limitless, though simple and symmetrical shapes are to be preferred. Some of the more common shapes are illustrated in Fig. 6.1. For the rectangular section of Fig.6.1(a), flexural reinforcement may

313

be uniformly distributed along the length, or concentrated in end regions, with only nominal reinforcement distributed in the central region. Uniformly distributed reinforcement has the advantage of imparting improved shear resistance, particularly against sliding shear on the wall base, but results in a lower first-yield moment than will occur when much of the flexural reinforcement is concentrated at the ends. The flexural strength, however, will be little affected by the distribution of reinforcement, provided the total area is constant. A similar conclusion was noted for distribution of beam reinforcement, in Section 5.6.1.

The section of Fig.6.1(b) has boundary elements of increased width at each end of a rectangular wall section. This shape is often used when beams frame into the ends of the wall section, as suggested by the dotted lines. When the wall extends over the full length of one end of a building, there may also be intermediate boundary elements to accommodate beams of internal frames extending perpendicular to the wall, on one side. It should be noted that the structural system implied by this, of end walls providing seismic resistance in one direction, and frames in the perpendicular, and longer direction can result in undesirable seismic response. Under diagonal attack, the boundary element, which is essentially a column, at one end of the wall may be subjected to compression stresses close to the concrete compression strength from the cantilever action of the wall, while being deformed laterally by frame action in the orthogonal direction. The high compression stress in the boundary element reduces its moment capacity in the frame direction, and flexural yielding of the boundary element may result. Local **P-Δ** effects can become critical. The combined wall and frame action on this boundary element at levels 1 and 2 can result in instability and collapse of the end region of the wall, as was observed with several apartment buildings after the 1995 Kobe earthquake.

Fig.6.1(c) shows a T-section wall, which is common in buildings with internal central corridors, such as hotels and apartment buildings. In these cases the flanges form part of the corridor wall between doorways, and the web divides different hotel rooms or apartments. The behaviour of T-section walls in the direction parallel to the web is characterized by different strength and stiffness in the two possible loading directions, with the wall generally being stiffer and stronger when the flange is in tension than when it is in compression. The yield curvatures in the opposite directions, may also differ (see Section 4.4.3(c)). Frequently buildings will contain identical, but anti-symmetrical T-section walls when rooms are symmetrically placed on either side of a central corridor. This simplifies the structural characterization, since the average values for strength and stiffness for flange in tension and flange in compression can be adopted, and total system strength and stiffness will be the same in both directions.

Finally the C-section wall of Fig.6.1(d) is common when walls enclose a service core of lifts, stairs and possibly toilets, and is often combined with a symmetrically opposed C-section, as suggested by the section shown in dotted outline. These sections will often be connected by coupling beams, shown in Fig.6.1(e) as dashed lines, resulting in coupled-wall behaviour, discussed later in this chapter, in Section 6.8. As with the T-section walls of Fig.6.1(c) strengths and stiffness of a C-section wall differ depending on the direction

of response, and when loaded parallel to the web, torsional response must be expected unless a balancing symmetrically opposed element is present, as suggested in Fig.6.1(e).

6.1.2 Wall Elevations

(a) Cantilever Wall   (b) Wall with Openings   (c) Coupled Wall
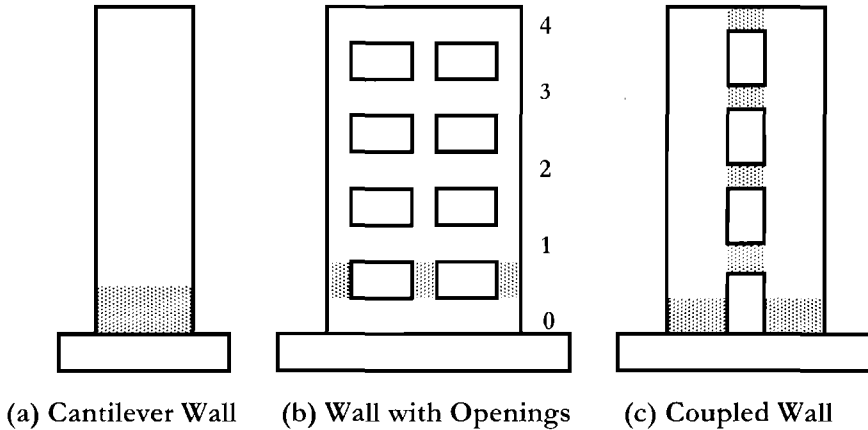
Fig.6.2   Categories of Structural Walls

The three main categories of structural walls are illustrated in Fig.6.2. Only two are suitable for seismic resistance. The cantilever wall of Fig.6.2(a) is the simplest, and the most straightforward in terms of predicting seismic performance. Provided proper attention is paid to dynamic amplification of moment and shear, inelastic action occurs in a flexural plastic hinge forming above the base of the wall, and extending some distance up the wall, as indicated by the shaded area. Above this region, the wall remains elastic.

The second category, shown in Fig.6.2(b) is a wall with openings, where the openings are insufficient to provide frame-like action. In the example shown, the piers between openings are smaller than the beams above and below the openings. With the proportions shown it is very difficult to avoid inelastic action occurring by flexural yielding or shear failure in the piers, generally below the first floor, as indicated by the shaded areas. This form of construction is unsuitable for seismic resistance unless response can be assured to be elastic, or near-elastic (displacement ductility demand less than 1.5).

Coupled walls, shown in Fig.6.2(c), are designed to form flexural plastic hinges at the wall bases and in the coupling beams. These provide an efficient mechanism for resisting seismic forces, with reduced displacements. These are separately considered in Section 6.8.

6.1.3 Foundations for Structural Walls

Foundations for structural walls are generally rather massive to enable the overturning moment to be resisted by gravity effects. This is illustrated in Fig.6.3, where the

overstrength shear V^o acts at an effective height of H_e above the wall base. The overturning moment at the base of the wall is approximated by

$$M_W^o = V^o H_e \approx (A_{st} f_y^o + W_W) \cdot l_w / 2 \qquad (6.1)$$

where W_W is the weight, including self weight, supported by the wall at the base. A_{st} is the total area of flexural reinforcement in the wall, with overstrength yield stress of f_y^o. The criterion for stability of the wall on its foundation under ductile overstrength response is given by

$$M_R = (W_W + W_F) \cdot (L_F - a)/2 \geq M_F^o = V^o (H_e + h_F) \qquad (6.2)$$

where any passive resistance of soil on the face of the footing is neglected, and L_F is the footing length, W_F is the footing weight, and a is the length of the footing in compression at ultimate soil bearing strength, $p_{b,u}$ given by

$$a = \frac{W_W + W_F}{p_{b,u} \cdot B_F} \qquad (6.3)$$

and where B_F is the footing width.
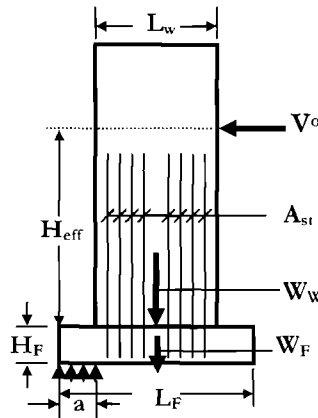
Fig. 6.3   Overturning Resistance of a Cantilever Wall

Equation (6.2) applies for a spread footing. The size of the footing can be reduced by supporting the footing on piles with tension capacity. The modification to Eq.(6.2) for the case where some overturning resistance is provided by tension piles follows the same

principles as outlined above, and is not developed further herein. Overturning resistance, M_R for walls is discussed further in Section 6.5.

6.1.4 Inertia Force Transfer into Walls

Since there will generally be much fewer walls in a structural wall building than columns in a frame building, floor inertia forces to be transferred into the walls can be large. To ensure satisfactory force transfer, special consideration must be given to internal force transfer within the floor diaphragm, and particularly to force transfer between the floor diaphragm and the wall. This is normally effected by shear-friction action. It should be noted that floor diaphragm inertia forces are strongly influenced by higher mode action[R2], and may be many times higher than the level predicted by the design distribution of storey force corresponding to the inelastic first-mode response, as used in the **DDBD** procedure. Higher-mode effects are discussed in detail in Section 6.6.

6.2 REVIEW OF BASIC DDBD PROCESS FOR CANTILEVER WALL BUILDINGS

The fundamentals of **DDBD** were introduced in Chapter 3, with reference to Fig.3.1 and were summarized in Section 5.2.1 for frames. Most of the equations are identical for wall buildings, and hence are not repeated here. Equivalent **SDOF** design displacement is given by Eq.(5.3), for equivalent mass by Eq.(5.4), for effective height by Eq.(5.5), for design ductility by Eq.(5.6), for effective stiffness of the **SDOF** structure by Eq.(5.10) and for design base shear by Eq.(5.11). The base shear is distributed to the floor levels in accordance with Eq.(5.12). Differences primarily relate to the deflection profiles and damping values to be adopted for design. These are discussed further here related to cantilever walls. Coupled walls are separately considered in Section 6.8.

6.2.1 Design Storey Displacements

(a) Yield Displacement: In Fig.3.18, the curvature profile up the wall was represented by a straight line from the yield value at the base to zero at the top of the wall. This may appear incompatible with the moment distribution corresponding to distributed lateral seismic forces, which results in a curved moment pattern, and since curvature is essentially proportional to moment, the curvature distribution should similarly be curved. Further, in the upper regions of the wall, the moments may be less than the cracking moment, and gross-section curvatures will be much less than cracked-section curvatures. This is illustrated in Fig.6.4, where the "design forces" curvature profile at yield corresponds to an inverted triangle distribution of lateral forces, and may be compared with the suggested linear distribution. In both cases, curvatures have been put in dimensionless form, dividing by the yield curvature at the wall base. Also shown in Fig.6.4 is the curvature distribution where the wall is considered to be uncracked for the

upper 50% of wall height, and where the uncracked-section curvature is 25% of the cracked-section curvature for the same moment.

Approximating the design-level displaced shape as linear with height, and assuming uniform mass with height, the effective height, given by Eq.(3.35) is approximately 70 75% of the wall height H_n. We assume a value of 70%, shown in Fig.6.4 by the solid horizontal line. The yield displacement is thus given by

$$\Delta_y = \int_0^{0.7H_n} \phi_h (0.7H_n - h) \cdot dh \tag{6.4}$$
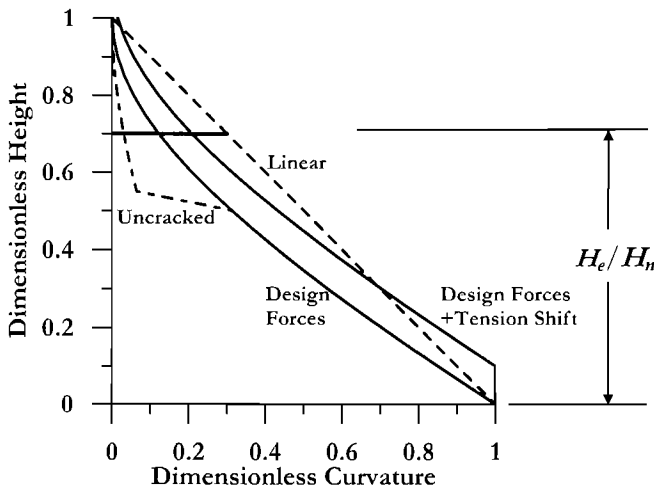
Fig.6.4   Cantilever Wall Curvatures at Yield

Carrying out the integration for the three curvature profiles described thus far, the displacement at the effective height corresponding to the linear profile is only 14.9% and 16.8% larger than the displacement corresponding to the curvatures derived from the design moments, with and without cracking in the upper portion respectively.

Although this difference is small, the real difference will be smaller, in most cases. This is because diagonal tension results in inclined flexure-shear cracking in the wall. The influence of this is to cause reinforcement tension strains, and hence curvatures, to be higher at a given level than that corresponding to the moment. This effect is known as tension shift[P1]. With typical transverse reinforcement details, the curvature profile is displaced vertically by a distance equal to $l_w/2$, from the value calculated for the applied moment. Taking a reasonably slender wall, with a height-to-length ratio $(H_n/l_w) = 5$, this implies shifting the curvature profile up by 10% of the wall height. This profile is also plotted in Fig.6.4. Integrating this curvature profile results in a displacement at the effective height of $0.7H_n$ that is 2.7% larger than that resulting from the suggested linear curvature profile. If the upper 50% of the wall is assumed to be uncracked, the agreement

is almost exact. It is thus seen that for typical conditions the linear curvature profile provides a reasonable prediction of the yield displacement at the effective height.

Recalling that the yield curvature for a reinforced concrete wall of rectangular section, given by Eq.(4.57c) is approximately $\phi_y = 2\varepsilon_y/l_w$, the height-dependent yield displacement profile can thus be determined from Eq.(6.4), with a linear curvature profile. This has already been reported as Eq.(3.31), repeated here for convenience as Eq.(6.5):

$$\Delta_{yi} = \frac{\varepsilon_y}{l_w} H_i^2 \left(1 - \frac{H_i}{3H_n}\right) \tag{6.5}$$

(b) Plastic Displacement: In Sections 3.5.2(b), and 4.2.8 it was noted that it is a reasonable approximation that the plastic rotation be considered to be concentrated at the end of the member. Equation (4.31) defines the equivalent plastic hinge length over which the plastic curvature ϕ_P is considered constant as $L_P = kL_C + L_{SP}$, where L_C is the distance from the critical section to the point of contraflexure, and L_{SP} is the length of strain penetration into the foundation, given by Eq.(4.30). In fact the centre of plastic rotation should strictly be concentrated at the centre of the plastic hinge. With reference to the cantilever wall of Fig.6.5, it will be seen that the centre of plastic rotation is located at a height of $(0.5L_P - L_{SP})$ above the base.

(a) Wall   (b) Curvature   (c) Plastic Displacement
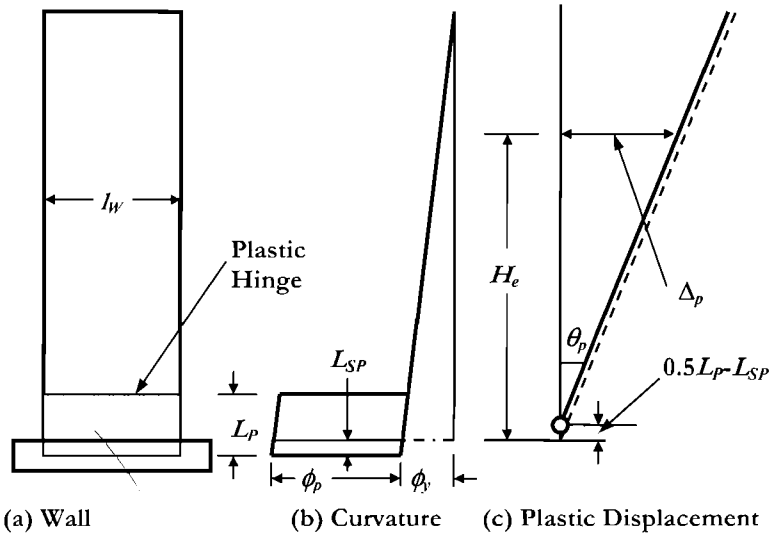
Fig.6.5 Plastic Deformation of a Cantilever Wall

The plastic displacement, measured at the effective height H_e should thus be

$$\Delta_P = \phi_P L_P \left(H_e - (0.5L_P - L_{SP})\right) = \theta_P \left(H_e - (0.5L_P - L_{SP})\right) \tag{6.6a}$$

In fact the error of using the simpler expression:

$$\Delta_P = \phi_P L_P H_e = \theta_P H_e \tag{6.6b}$$

will in most practical cases be negligible and within the accuracy of calculating L_P.

For wall structures, the plastic hinge length is more likely to be influenced by tension shift effects than is the case with beams or columns. Hence there should be an additional term in the plastic hinge equation relating to the wall length l_W. An additional component of $0.2l_W$ has been suggested[P1]. As definitive data are not available, we conservatively recommend $0.1l_W$. It should also be noted that in calculating the plastic hinge length H_e should be substituted for L_C, since it is the slope of the moment gradient at the critical section that dictates the spread of plasticity up the wall. The recommended form of the equation for plastic hinge length for walls is thus

$$L_P = k \cdot H_e + 0.1 l_W + L_{SP} \tag{6.7}$$

where, in accordance with Eq.(4.31), $k = 0.2(f_u/f_y - 1) \leq 0.08$.

In Eq.(6.6) the plastic curvature is found from

$$\phi_P = \phi_m - \phi_y = \phi_m - 2\varepsilon_y / l_W \tag{6.8}$$

where ϕ_m is the maximum design curvature, at the wall base, corresponding to the limit state considered. As noted in Section 3.5.2(b) this may correspond to limit concrete compression strain or reinforcement tension strain, or may be constrained by code drift limits. For cantilever walls the maximum drift will occur at roof level (see Fig.3.18). If the drift limit for the limit state considered is θ_C , then the maximum permissible rotation at the wall-base plastic hinge will be the lesser of

$$\theta_P = \theta_C - \theta_{yn} = \theta_C - \varepsilon_y H_n / l_w \text{ (a)} \quad \text{and} \quad \theta_P = \phi_P L_P \text{ (b)} \tag{6.9}$$

where $\theta_{yn} = \varepsilon_y H_n / l_w$ is the yield drift at the top of the wall.

(c) Limit State Curvatures and Moment Capacities: Figure 6.7 shows the variation of serviceability limit state and damage-control limit state curvatures and moments for cantilever walls with rectangular section shape, and flexural reinforcement uniformly distributed along the wall length in two layers, one adjacent to each side. The end detail of the wall on which the analyses were based is shown in Fig.6.6. Serviceability limit curvatures have been based on the lower of the curvatures corresponding to $\varepsilon_c = 0.004$ and $\varepsilon_s = 0.015$, as recommended in Section 4.2.5. Damage-control curvatures are based on the lower of the curvatures corresponding to $\varepsilon_c = 0.018$ and $\varepsilon_s = 0.06$. The concrete

limit strain was based on recommendations of Section 4.2.5 using the following information: Wall width 250mm (9.8in), transverse reinforcement 10mm (0.393 in) at 100mm (3.94in) centres across the wall in the end region, with 10mm bars along each side. Transverse reinforcement at s = 100mm (3.94in) vertically (see Fig.6.6).
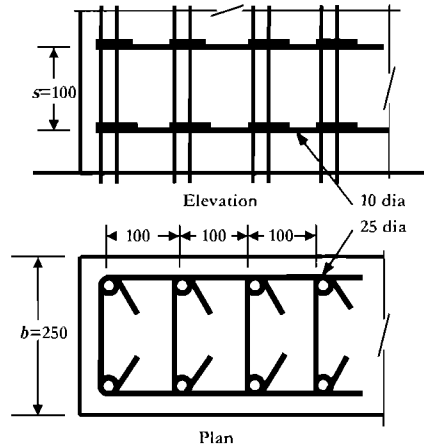
Fig.6.6   Wall-End Detail for Serviceability and Damage-Control Analyses

Area ratios of confinement in both directions are equal at

$$\rho_{ax} = \rho_{ay} = \frac{A_b}{sh} = \frac{78.5}{100 \times 100} = 0.00785$$

Adopting a confinement effectiveness coefficient of C_e = 0.5 for walls, as recommended in Section 4.2.2, the effective volumetric confinement ratio is thus, from Eq.(4.7)

$$\rho_v = \rho_{ax} + \rho_{ay} = 2(0.5 \times 0.00785) = 0.00785$$

From Eq.(4.21), taking the confined compression strength as $1.4f'_c$, and the strain capacity of the transverse reinforcement as 0.12, the ultimate compression strain is

$$\varepsilon_{cu} = 0.004 + 1.4 \frac{\rho_v f_{yh} \varepsilon_{su}}{f'_{cc}} = 0.004 + 1.4 \frac{0.00785 \times 450 \times 0.12}{1.4 \times 30} = 0.018$$

The strain limit for the longitudinal reinforcement is based on $0.6\varepsilon_{su}$ as recommended in Section 4.2.4(c), where the steel strain at maximum stress is 0.10. The results in Fig.6.7 were calculated based on expected concrete cylinder compression strength of f'_{ce} = 30 MPa (4.35ksi), and reinforcement yield strength of f_{ye} = 450 MPa (65ksi), with an ultimate/yield strength ratio of f_u/f_y = 1.3. However, as the data are expressed in dimensionless form, the results will be applicable to other concrete and reinforcement strengths within reasonable variation (say 20MPa $\leq f'_{ce} \leq$ 45MPa; 300MPa $\leq f_{ye} \leq$ 550MPa),

provided the ultimate steel strain is 0.10. Modifications for other ultimate strains are discussed below.

(a) Serviceability Curvature

(b) Serviceability Moment Capacity

(c) Damage Control Curvature

(d)Damage Control Moment Capacity
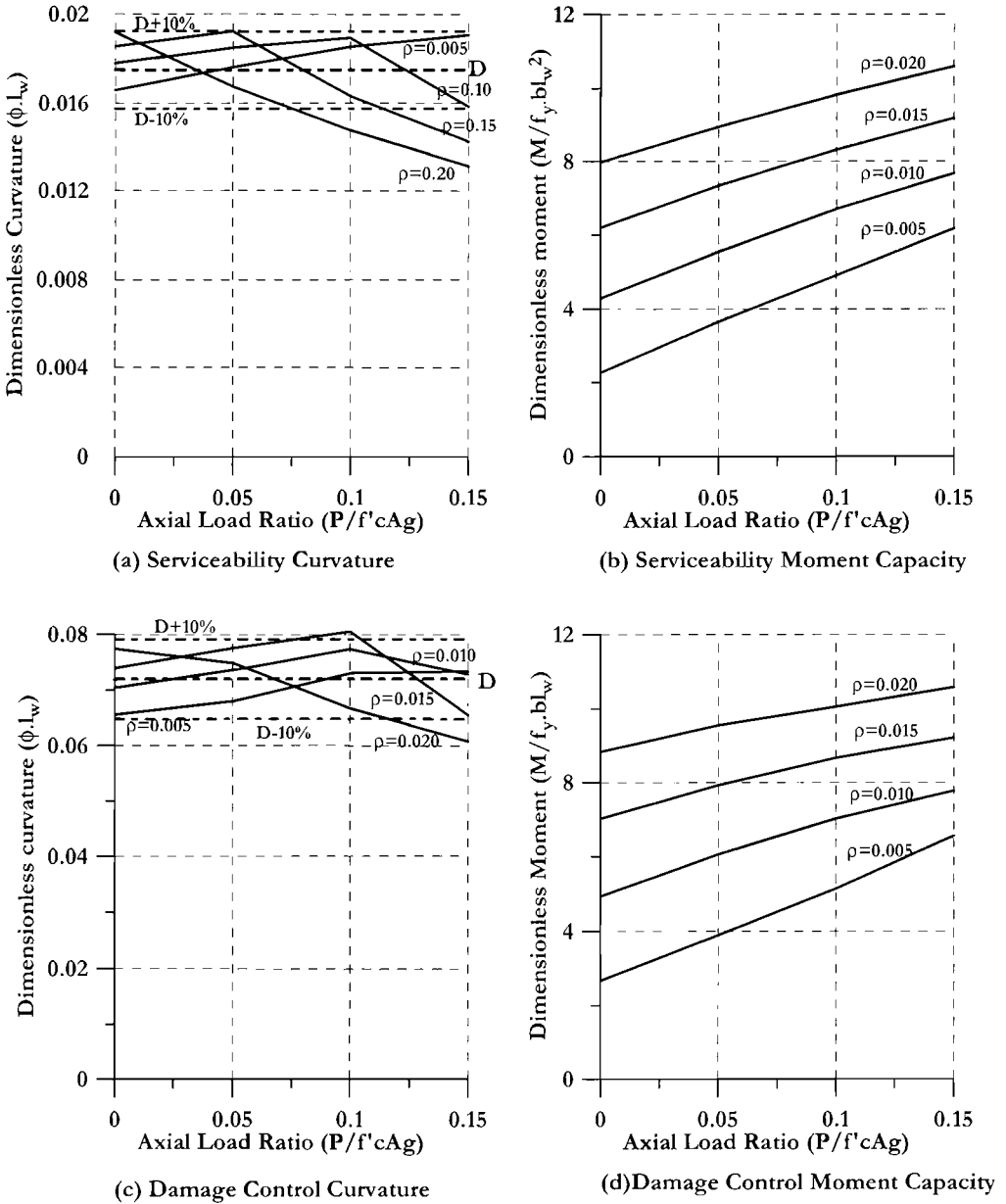
Fig.6.7   Curvatures and Moment Capacity for Rectangular Walls with Uniformly Distributed Reinforcement

Analyses were carried out for axial load ratios in the range $0 \le P/f_c'A_g \le 0.15$, and flexural reinforcement ratios in the range $0.005 \le \rho_l \le 0.02$. These ranges cover the common ratios of axial load and reinforcement found in practice with cantilever walls.

Serviceability and damage-control limit curvatures are shown in Figs.6.7(a) and (c) respectively, and have been made dimensionless by multiplying the analysis results by the wall length. They thus apply for walls of any length if the values from Figs.6.7(a) and (c) are divided by the actual wall length. The plots for serviceability and damage-control curvature display similar characteristics, though the values are quite different. In both cases the curvatures for low reinforcement ratios tend to be governed by the steel tension strain limit, and increase with axial load ratio. For high reinforcement ratios the compression strain limit governs, and limit curvatures decrease with axial load ratio. For intermediate reinforcement ratios the curvatures initially increase (governed by steel tension strain), then decrease, as the concrete compression strain limit is reached.

It will be observed that despite the above behaviour, the variation in limit curvatures is small, and average values provide an adequate estimate, within ±10% of the data for all except high axial load combined with high reinforcement ratio. Constant average values, denoted $\mathbf{D}$ in Figs.6.7(a) and (c), and lines corresponding to $\mathbf{D}$ ±10% are also plotted for comparison. The average values are:

serviceability curvature: $\qquad \phi_s \cdot l_w = 0.0175$ $\qquad\qquad$ (6.10a)

damage-control curvature: $\phi_{dc} \cdot l_w = 0.072$ $\qquad\qquad$ (6.10b)

In both cases the limit curvatures are dominated by the steel strain tensile limit. It will be noted that the serviceability and limit state average curvatures are almost in exact proportion to the limit steel strains. Hence the limit curvatures can be re-written as

limit curvature: $\qquad \phi_{ls} \cdot l_w = 1.2\varepsilon_{s,ls}$ $\qquad\qquad$ (6.10c)

where $\varepsilon_{s,ls}$ is the steel limit state strain. Equation (6.10c) can be used with adequate accuracy for both serviceability and damage-control limit states for values of limit state tension strains in the range $0.01 \le \varepsilon_{s,ls} \le 0.08$. However, for high values of the steel limit strain, extra confinement reinforcement should be provided to ensure compression strain limits do not govern.

Figures 6.7(b) and (d) plot variation in limit state design moment for serviceability and damage-control limit states respectively, in dimensionless form, dividing the analysis results by $f_y.b.l_w^2$. Traditionally dimensionless moment capacity has been related to concrete compression strength, rather than steel yield strength as has been used here, but the moments, for the axial load ratios relevant to walls are almost independent of concrete strength, and almost directly proportional to steel yield strength. The values in Figs.6.7(b) and (d) can thus be used for the normal range of steel yield strength and concrete compression strength.

Since the limit curvatures of Eq.(6.10) are directly related to maximum permissible tension strains, they will also apply, with reasonable accuracy, to flanged wall sections,

such as $\mathbb{T}$ and $\mathbb{C}$ sections, provided the flange is in compression. With the flange in tension behaviour will be similar to rectangular walls with high reinforcement ratios and limit curvatures may be reduced below the values given by Eq.(6.10).

It should be noted that extreme fibre compression strains can be reduced by concentrating the flexural reinforcement at the wall ends, rather than distributing it uniformly along the wall length as suggested in this section. This has been advocated elsewhere[P1], and is required by some codes (e.g. X6) when the flexural reinforcement ratio exceeds 0.005. This will, however, result in a reduction in the serviceability and damage-control curvatures, since these are governed by steel strain, rather than concrete strain limits, and the neutral axis depth will decrease when reinforcement is concentrated at the wall ends. Since distributed flexural reinforcement provides better control of sliding shear deformation, and reduces the potential for damage at wall ends resulting from buckling of reinforcement coupled with wall sliding, it is our view that distributed flexural steel is to be preferred.

(d) Design Displacement Profiles: The design displacement profile is thus given from the combination of the yield displacement profile from Eq.(6.5) and the plastic displacements corresponding to Eq.(6.6):

$$\Delta_i = \Delta_{yi} + \Delta_{pi} = \frac{\varepsilon_y H_i^2}{l_w}\left(1 - \frac{H_i}{3H_n}\right) + \theta_p H_i \tag{6.11}$$

The displacement profile corresponding to the limit-state curvatures is found substituting $\theta_p = \left(\phi_{ls} - \phi_y\right)L_P$ where ϕ_{ls} is given by Eq.(6.10), $\phi_y = 2\varepsilon_y / l_w$ (Eq.(4.57c)) and L_P is found from Eq.(6.7).

When the drift angle at roof level (Eq.(3.30)) exceeds the code drift limit θ_c, the plastic rotation used in Eq.(6.11) is $\theta_p = (\theta_c - \varepsilon_y H_n / l_w)$.

Having determined the design displacement profile, the **SDOF** design displacement at the effective height is found from Eq.(3.26) in the usual fashion. When the structural system includes walls of different lengths and strengths acting in the same direction, the design displacement profiles for the different walls may differ slightly up the wall for equal displacements at the effective height. Since the longer and stronger walls will dominate the response, it will normally be their displacement profile that is adopted for design, particularly if limit-state curvatures control the design. Although a more accurate approach would be to adopt an average of the displacement profiles chosen to have equal displacements at the effective height, and weighted by wall flexural strength, the additional computational effort will rarely be warranted.

Note that the different displacement profiles of walls of different lengths can imply diaphragm forces of significant magnitude, and significant modification of wall shear forces if the diaphragms are considered infinitely stiff in-plane. However, when flexibility of diaphragms, of connections between diaphragms and walls, and shear flexibility of

walls with diagonal cracking are considered, these compatibility-induced forces are greatly reduced, and may normally be ignored in design[B11].

6.3 WALL YIELD DISPLACEMENTS: SIGNIFICANCE TO DESIGN

6.3.1 Influence on Design Ductility Limits

In section 5.3 it was pointed out that elastic displacements of frames found from realistic modelling of flexural stiffness were such that design displacement ductility factors implied by codes were frequently unrealistically high. It is of interest to examine the ductility available with structural walls at typical code drift limits. From Eq.(3.29), assuming the linear curvature profile of Fig.6.4 for the reasons discussed in Section 6.2.1, the roof-level drift corresponding to the yield curvature is

$$\theta_{yn} = \varepsilon_y H_n / l_w = \varepsilon_y A_r \tag{6.12}$$

where A_r is the wall aspect ratio, measured at roof level. Thus if the wall aspect ratio exceeds

$$A_r = \theta_c / \varepsilon_y , \tag{6.13}$$

the drift limit will require that the wall responds elastically. Taking a yield strength of the flexural reinforcement as 450 MPa (65.3 ksi), implying $\varepsilon_y = 0.00225$, and assuming a code drift limit of 0.02, it will be seen that slender walls with aspect ratios greater than about 9 must be designed to respond elastically. There will some conservatism in these numbers, since curvatures in the upper part of the wall may be significantly lower than the linear profile of Fig.6.4. Although this does not affect the calculated displacements significantly, it may have a larger effect on roof drift. Paulay[1] recommends a factor of 0.7 be applied to the drift of Eq.(6.12). Note, however, that drifts in the upper levels may be significantly increased by higher mode effects, which will tend to compensate for conservatism in calculated first-mode roof-level drift.

The maximum available design ductility of walls with aspect ratios lower than that defined by Eq.(6.13) can be found as follows: Equation (6.5) defining the yield profile can be manipulated into the following form:

$$\Delta_i = \varepsilon_y A_r H_n \left(\frac{H_i}{H_n} \right)^2 \cdot \left(1 - \frac{H_i}{3H_n} \right) \tag{6.14}$$

Assuming equal floor mass at all heights, the effective **SDOF** yield displacement can be found from Eq.(6.14) and Eq.(3.26) as

---

[1] T.Paulay: pers. comm..

$$\Delta_{ye} \approx 0.45\varepsilon_y A_r H_n \qquad\qquad (6.15)$$

The corresponding effective height at yield, from Eq.(3.35) is $H_e \approx 0.77H_n$. The plastic displacement at this effective height, corresponding to a roof-level drift of θ_c is found from a plastic rotation of $(\theta_c - \theta_{yn})$, where θ_{yn} is given by Eq.(6.12), as

$$\Delta_{pe} = 0.77H_n(\theta_c - A_r\varepsilon_y) \qquad\qquad (6.16)$$

The available displacement ductility corresponding to the code drift limit is thus, from Eqs.(6.15) and (6.16):

$$\mu_{sys} = 1 + \frac{\Delta_{Pe}}{\Delta_{ye}} \approx 1 + 1.71\frac{(\theta_c - A_r\varepsilon_y)}{\varepsilon_y A_r} \qquad\qquad (6.17)$$

It will be noted that Eq.(6.17) is independent of the wall height, and depends only on wall aspect ratio and flexural reinforcement yield strain. The displacement ductilities implied by Eq.(6.17) are plotted against wall aspect ratio for code drift limits of 0.02 and 0.025 in Fig.6.8(a), based on a yield strength of 450 MPa (65.3 ksi), corresponding to ε_y =0.00225. If Eq.(6.17) is modified for Paulay's suggestion that $\theta_n = 0.7\varepsilon_y A_r$ the curves of Fig.6.8(b) results. The conclusions are not materially different.

(a) Yield Drift = $\varepsilon_y A_r$ (b) Yield Drift = $0.7\varepsilon_r A_r$
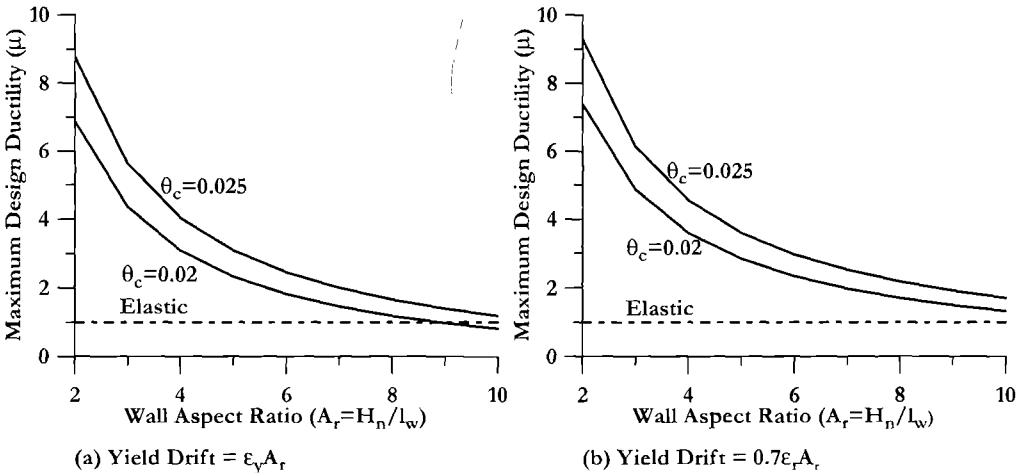
Fig.6.8   Maximum Design Ductilities for Cantilever Walls (ε_y=0.00225) Based on Specified Drift Limits

Typical codified displacement ductilities for walls are in the range $4 \le \mu \le 6$. Examination of Fig.6.8 indicates that design ductilities of this order will only be feasible for walls with aspect ratios less than 4. It should also be noted that the advantages often

claimed for the use of high strength flexural reinforcement would appear to be illusory. Higher yield strengths are claimed to reduce the area of flexural reinforcement required. However, examination of Eq.(6.17) indicates that with higher yield strength, and hence higher yield strain, the maximum design ductility demand corresponding to the code drift limit will reduce compared with the value available for lower yield strength. The steel area required will thus be almost independent of yield strength, when code drift limits apply. The same conclusion applies to other structural forms.

6.3.2 Elastically Responding Walls

In the previous section it was shown that cantilever walls of high aspect ratio would be required to respond elastically to satisfy code drift limits. It is also clear that tall slender walls may have system yield displacements that exceed the maximum elastic response displacement corresponding to the plateau following the corner period (see Section 2.2.2). In Section 5.3.2 it was shown that the plateau displacement could be related to moment magnitude of the earthquake, and local intensity expressed by the peak ground acceleration, following recommendations for spectral shape included in Section 2.2.2. The same seismological data used to generate Fig.5.4 are now used to examine elastic response of cantilever walls.

(a) SDOF Yield Displacement   (b) Plateau Displacements
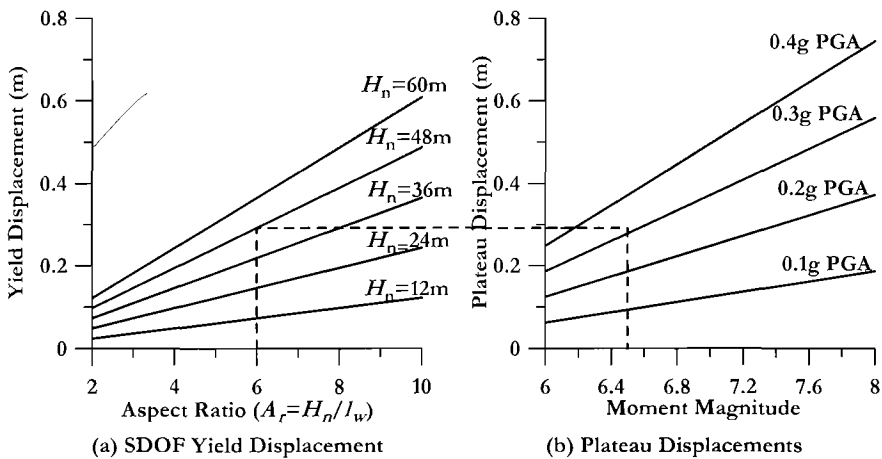
Fig.6.9 Wall Yield Displacements for $\varepsilon_y = 0.00225$ Compared with Plateau Displacements

Fig.6.9(a) plots system yield displacement for walls of different aspect ratio and height, based on Eq.(6.15) for a yield stress of 450MPa (65.3 ksi). These can be compared with the plateau displacements presented in Fig.6.9(b). An example of the use of this figure is shown by the dashed line in both figures. For a 16 storey wall with uniform storey heights of 3 m, (9.84 ft) and a wall length of 8 m (26.2 ft), the total height is 48 m (157.4 ft) and the aspect ratio is 6. Figure 6.9(a) is entered at $A_r = 6$, and the system yield displacement of 0.292 m (11.5 in) is transferred across to the seismological data of Fig.6.9(b). From this

it is seen that for a causative earthquake of $M_W = 6.5$, the wall will be expected to respond elastically if the design **PGA** is less than 0.3g.

6.3.3 Multiple In-Plane Walls

Aspects related to displacements and damping when several walls of different length are in the same plane or in parallel planes have been discussed in Section 3.5.4, and illustrated in the design example of Section 3.5.5. Aspects to be considered are the different ductility demands, and hence different equivalent viscous damping values for each wall, the distribution of strength between walls, and the global (system) damping. It was pointed out that the distribution of strength between walls is purely a designer's choice, uninfluenced by considerations of initial elastic stiffness, and that a common, logical choice will be to use equal flexural reinforcement ratios in all walls, leading to the base shear force being distributed to walls in inverse proportion to the square of the wall length. See also comments in Section 6.2.1(d).

6.4 TORSIONAL RESPONSE OF CANTILEVER WALL BUILDINGS

6.4.1 Elastic Torsional Response

A brief summary of consideration of torsional effects in **DDBD** was presented in Section 3.8. However, since the topic has special relevance to structural wall buildings, as a result of the potential for torsional eccentricity with building plans containing walls of different lengths, the topic is treated in greater detail in this chapter.

We start with consideration of elastic torsional response, which though not directly relevant to inelastic structural response, will be referenced and modified to develop an appropriate design approach. Until recently, torsion has been treated as an elastic pheno-menon. In the elastic approach shears resulting from distribution of the elastic base shear force between different lateral-force resisting elements are modified to include shear forces induced by twist of the building resulting from eccentricity between the centre of mass and the centre of elastic stiffness of the building. Typically this eccentricity is augmented to include "accidental" eccentricity resulting from uncertainties in distribution of mass, and in material properties, which hence result in uncertainty in the positions of the centre of mass and the centre of stiffness.

The approach is illustrated by reference to the plan representation of the wall building shown in Fig. 6.10, which has plan dimensions L_X and L_Z (**Y** is the building vertical axis). Walls **1** and **2**, of different lengths, resist seismic actions parallel to the **Z** axis, and walls **3** and **4**, also of different lengths, resist seismic actions parallel to the **X** axis. The centre of mass, C_M is assumed to be at the centre of the floor plan. The origin of the axes, taken at C_M is thus also in this case at the centre of the floor plan.

The centre of rigidity, or stiffness C_R is displaced from the centre of mass by distances e_{RX} and e_{RZ} in the **X** and **Z** directions respectively. Note that since stiffness of structural elements depends on strength, as established in Section 4.4, the actual stiffness

eccentricities will not be known until section strengths have been allocated. For clarity, only e_{RX} is shown in Fig.6.10.
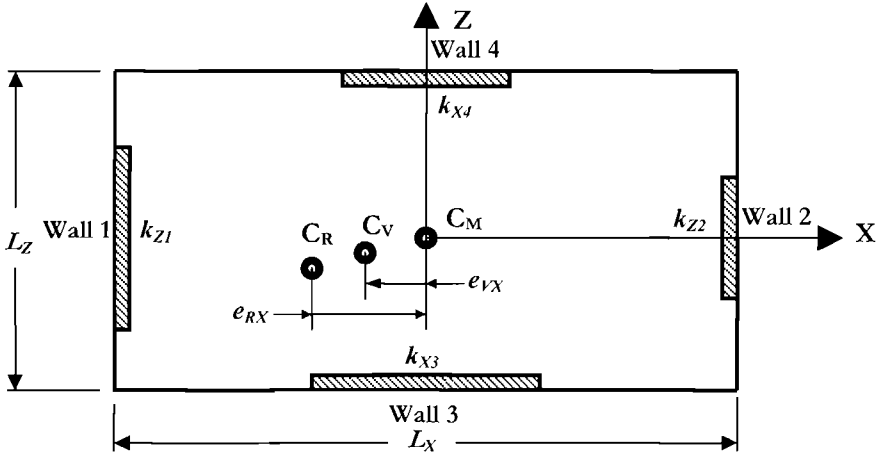
Fig.6.10 Definition of Terms for Elastic Torsional Analysis

Defining the stiffness (force/displacement at the height considered) of walls 1 and 2 in the **Z** direction as k_{Z1} and k_{Z2} respectively, and generalizing to the case of n walls parallel to the **Z** axis, the coordinates of the centre of rigidity are

$$e_{RX} = \sum_{1}^{n} k_{Zi} x_i / \sum_{1}^{n} k_{Zi} \; ; \quad e_{RZ} = \sum_{1}^{n} k_{Xi} z_i / \sum_{1}^{n} k_{Xi} \tag{6.18}$$

where x_i and z_i are the coordinates of wall i. It is assumed that the walls have negligible out-of-plane stiffness. The rotational stiffness J_R is found by determining the moment required to cause unit rotation about the centre of stiffness:

$$J_R = \sum_{1}^{n} k_{Zi} (x_i - e_{RX})^2 + \sum_{1}^{n} k_{Xi} (z_i - e_{RZ})^2 \tag{6.19}$$

The base shear $V_{Base,Z}$ acting in the **Z** direction is traditionally distributed between the walls based on translational and rotational considerations. The shear in wall i due to direct translation is:

$$V_{ZTi} = V_{Base,Z} \cdot \frac{k_{Zi}}{\sum_{1}^{n} k_{Zi}} \tag{6.20a}$$

while the shear due to rotation, resulting from the elastic torsional moment $M_T = V_{Base,Z} e_{RX}$ is

$$V_{ZZ\theta i} = V_{Base,Z} e_{RX} \cdot \frac{k_{Zi}(x_i - e_{RX})}{J_R}$$ (6.20b)

If a base shear $V_{Base,X}$ acts concurrently in the **X** direction, then additional shear is induced in wall i by the additional torque $V_{Base,X} \cdot e_{RZ}$:

$$V_{ZX\theta i} = V_{Base,X} \cdot e_{RZ} \cdot \frac{k_{Zi}(x_i - e_{RX})}{J_R}$$ (6.20c)

The total shear carried by the elastic wall is thus

$$V_{Zi} = V_{ZTi} + V_{ZZ\theta i} + V_{ZX\theta i}$$ (6.20d)

There are a number of criticisms that can be levelled at this classical approach to torsional response of structures. First, as with all aspects of force-based design, it relies on initial estimates of element stiffness, to determine both the centre of stiffness, and the torsional stiffness. As has been repeatedly pointed out, element stiffness is proportional to strength, and hence significant errors can be expected unless an iterative design approach is used to modify element stiffness after initial estimates of strength have been obtained. Typically, this is not done, and also, typically, member stiffnesses are significantly in error in conventional force-based design.

More importantly, the stiffness approach does not account for changes in performance once one or more of the walls yield, after which stiffness considerations become largely irrelevant, nor does it take into account the very significant role of torsional mass inertia in modifying the torsional rotation implied by Eqs.(6.20b) and (6.20c). As a consequence, the elastic representation of torsional effects cannot be used to predict the torsional response of ductile systems. This has been recognised for some time, and early considerations of ductile response of systems including torsional effects[P1,P12,P13] distinguished between so-called torsionally restrained and torsionally unrestrained systems. The distinction between these categories is clarified in Fig.6.11.

For seismic action parallel to the **Z** axis, the two transverse walls in Fig.6.11(a), which are in line with the centre of mass C_M can play no part in resisting any torsional moment. Thus if one or both of the walls (**1** and **2**) parallel to the **Z** axis yield, the torsional stiffness will drop to a very low value, dependent primarily on the post-yield stiffness of the yielding walls. Consequently, in early studies based only on static torsional mechanisms, it was expected that if one wall yielded before the other, the centre of stiffness would shift to coincide with the remaining elastic wall, and essentially unrestrained rotation would result. The system is thus classified as torsionally unrestrained, and earlier texts (e.g.[P1]) advised against such systems.

(a) Torsionally unrestrained   (b) Torsionally restrained
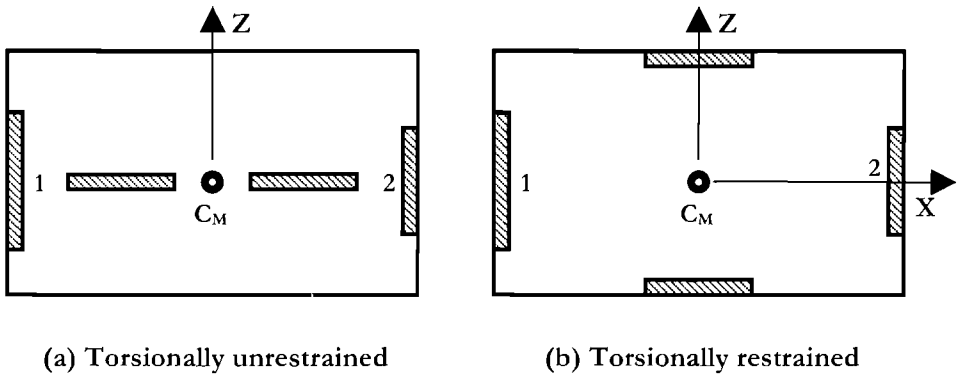
Fig.6.11   Different Wall Layout for Building Plan

The structure of Fig.6.11(b) has boundary elements on all four sides, and thus if walls 1 and/or 2 yield under seismic force parallel to the Z axis, the structure retains torsional stiffness, albeit reduced from the initial elastic value, as a result of the lever arm between the two transverse walls. The system is thus termed torsionally restrained, and was initially felt to be structurally more desirable than unrestrained systems.

Recent research by Castillo and Paulay[C6], followed and extended by Beyer[B4], have shown that torsional inertia plays an important role in modifying structural response of both unrestrained and restrained systems, but is difficult to quantify accurately, since peak translational and torsional response do not occur simultaneously. Both studies carried out extensive inelastic time-history analyses to investigate ductile response including torsional effects. The initial studies by Castillo and Paulay investigated 2D plan simulations of wall buildings. Beyer extended these studies, and also carried out a number of full 3D analyses. The following two sections present a brief summary of their findings.

6.4.2   Torsionally Unrestrained Systems

The studies of torsionally unrestrained (TU) systems by Castillo and Paulay[C6] showed that the modification to response resulting from torsional mass inertia was considerable. Considerations of static equilibrium would indicate that if we assume that the centre of mass C_M is at the centre of the building plan, and further assume that wall 2 in the TU system of Fig.6.12 is weaker, as well as less stiff than wall 1, then it will yield prior to wall 1, since the ratio of forces developed in the two walls is defined by geometry. Thus, again assuming that C_M is at the centre of the building plan, the forces in the two walls must be equal. For example, assume that the nominal strengths of the walls are related by $V_{N1}=1.4V_{N2}$; then when wall 2 yields, wall 1 will have an equal force, corresponding to $0.714V_{N1}$. Since the force in wall 2 will increase only slightly (due to post-yield stiffness of the force-displacement response) as the structure responds in the inelastic range, the force in wall 1 would never be expected to reach yield, and all system ductility would result from inelastic response of the weaker wall 2. This would imply an

expected ductility demand on wall 2 close to twice the system ductility demand, measured at the centre of mass. The corresponding displacement profile is shown in Fig.6.12 by the dashed line **A**.
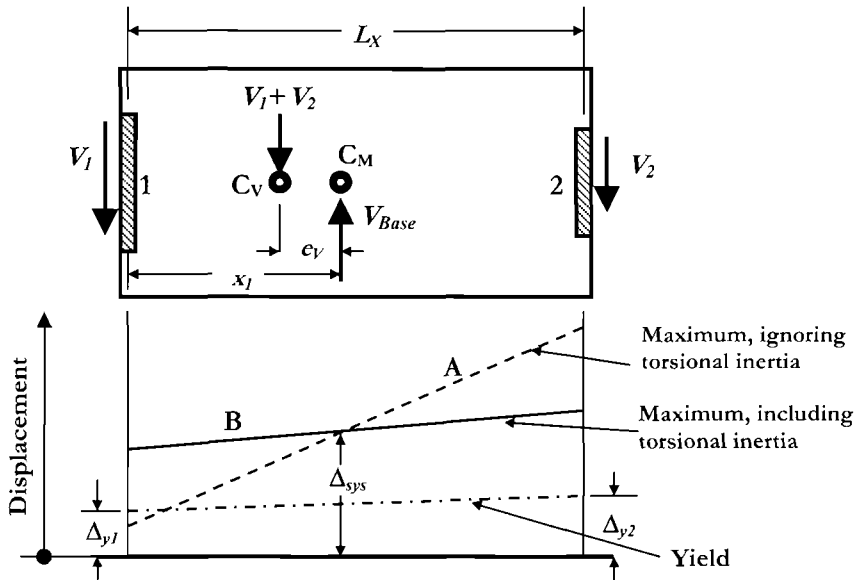
Fig.6.12   Displacement Response of a TU System

The inelastic time-history analyses of Castillo et al showed that this behaviour did indeed occur, but only if the torsional mass inertia was set to zero. When realistic values for torsional inertia were included in the analyses, it was found that the stronger wall would always yield, provided system ductility demand was significant, and would be subjected to considerable ductility demands. In fact the stronger wall would normally yield before the weaker wall, provided that the stronger wall was also stiffer than the weaker wall, as will usually be the case. The corresponding displacement profile is shown in Fig.6.12 by the solid line **B**. However, this line is a little misleading, as the peak displacements for walls **1** and **2** do not necessarily occur at the same time, nor does the peak rotational response occur simultaneously with either peak displacement.

Castillo et al recommended that **minimum** required strengths for elements of **TU** (and also of **TR**) systems should be based on considerations of static equilibrium. Thus, with reference to Fig. 6.12 the minimum nominal strength of walls 1 and 2 would be related to the total design base shear V_{Base} by:

$$V_{N1} \geq V_{Base} \cdot \frac{\left(L_X - x_1\right)}{L_X}; \qquad V_{N2} \geq V_{Base} \cdot \frac{x_1}{L_X} \qquad (6.21)$$

Excess strength, above that required by Eq.(6.21), for either wall would result in strength eccentricity e_V, (see Figs. 6.10 and 6.12) where

$$e_V = \frac{V_2}{V_1 + V_2} \cdot L_x - x_1 \qquad (6.22)$$

Normally excess strength would result from the longer wall needing less than the specified minimum reinforcement ratio to provide the required flexural strength corresponding to V_1, and hence actual strength would exceed required strength. Note that in accordance with capacity design principles the flexural strength will be matched to the moment corresponding to the required shear strength (see section 4.6). Castillo et al[C6] found that excess flexural strength in either wall did not adversely affect the performance of **TU** systems. For the normal case where the longer wall (wall 1) had excess strength, the displacement demand on both the centre of mass and the longer wall was, as expected, found to be reduced by the strength eccentricity resulting from excess strength. The displacement demand on the shorter, more flexible wall (wall 2) was found to be almost independent of the excess strength (and hence of the strength eccentricity) when the excess strength occurred in wall 1 only. Excess strength in wall 1 could thus be used to reduce the displacement demand on wall 1, without adversely affecting wall 2. Note however, that strength eccentricity is expected to increase torsional displacements as will be demonstrated shortly.

It will be noted that it may not be immediately clear which of the walls will govern the design. Normally, with different wall lengths as suggested in Fig.6.12, the ductility demand on the longer wall will be higher than on the shorter wall, which is contrary to expectations based on static equilibrium. Hence if material strains govern design, the longer wall will be critical. On the other hand, the shorter wall will be subjected to larger displacement demands, and hence if drift governs design, the shorter wall will be the critical element.

The conclusions of Castillo et al[C6] for **TU** walls can be summarized as follows:

- Nominal strength of any element should be not less than that required by static equilibrium considering zero strength eccentricity, for the chosen base shear force, regardless of the stiffness eccentricity.
- Strength eccentricity does not adversely affect the performance of **TU** systems, provided it only results from excess strength of one or more elements.
- If these guidelines are met, the displacements will not be greater than those estimated for zero strength eccentricity.
- The results are rather insensitive to the magnitude of torsional inertia, provided it is within reasonable bounds. (Castillo et al investigated variations of ±20% from a uniform mass distribution. Higher values, which are more probable than lower values, reduced twist).

6.4.3   Torsionally Restrained Systems
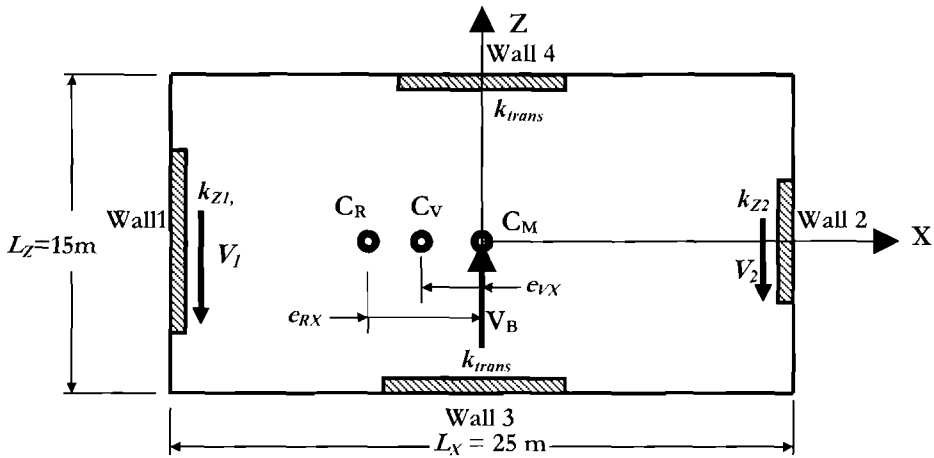
Fig.6.13   Torsionally Restrained Building with Strength and Stiffness Eccentricity for Z direction response (after Beyer[B4])

Castillo et al[C6] and Beyer[B4] both studied torsionally restrained (**TR**) systems, and, with a few exceptions, obtained generally similar results. The following comments are based on the more extensive studies by Beyer. These included 2D plan simulations of eight-storey buildings, and 3D studies of 2, 4, and 8 storey buildings with strength and stiffness eccentricities. Analyses were carried out with a suite of five artificial accelerograms spectrum-matched to a displacement spectrum linear with period to a period of 5 seconds. It was found that the spectral reduction values for levels of damping higher than 5% agreed closely with the "old" EC8 equation given by Eq.(2.8). Beyer's 2D analyses were based on a floor plan of 25m × 15m as shown in Fig.6.13, with the lengths of walls **1** and **2** being 8m and 4m respectively. The two transverse walls (3 and 4) each had lengths of 5m, and similar total system strengths were provided in both **X** and **Z** directions. A base-level design was chosen to provide an average drift of 0.02, with zero strength eccentricity, using displacement-based design procedures. Thus the strength provided to each wall in the **Z** direction was the same for the base-level design, despite the different wall lengths. Since the yield displacement for the walls would be in inverse proportion to wall length (see Section 4.4.3), this resulted in wall **1** having twice the elastic stiffness of wall **2**. Thus, though the strength eccentricity for the base-level structure was $e_V = 0$, the stiffness eccentricity was $e_R = 0.167L_X$. A series of analyses was carried out increasing the strength of the long wall relative to that of the short wall by ratios of $1.0 \le \lambda \le 1.8$ where $\lambda = V_1/V_2$, increasing both the strength and stiffness eccentricity. This was effected in two ways. In the first, the strength of wall **1** was increased while keeping the strength of wall **2** constant. The total system strength thus increased by a maximum

of 40%. In the second case, the strength of wall **2** (the short wall) was reduced as wall **1** strength was increased such that the total system strength remained constant. In both cases, the stiffness and strength eccentricities, with $k_{ZI}=2\lambda k_{Z2}$, are found from Eqs.(6.18) and (6.22) as:

$$e_{RX} = \frac{0.5(1-2\lambda)}{1+2\lambda} \cdot L_X \quad \text{(a)} \qquad \text{and} \quad e_{VX} = \frac{0.5(1-\lambda)}{(1+\lambda)} \cdot L_X \quad \text{(b)} \qquad (6.23)$$

Results of the analyses, averaged over the 5 accelerograms, are summarized in Fig.6.14. It will be noted that despite the zero strength eccentricity at λ=1.0, some torsional response is evident, as a result of the stiffness eccentricity, with displacements of the short and long walls being about 10% larger and smaller respectively than the centre-of-mass displacement. As the strength of the long wall increases, resulting in total system overstrength (Fig.6.14(a)), displacements of the centre-of-mass decrease, but the displacement of the short wall remains almost constant.

(a) Total Strength Increases   **(b) Constant Total Strength**
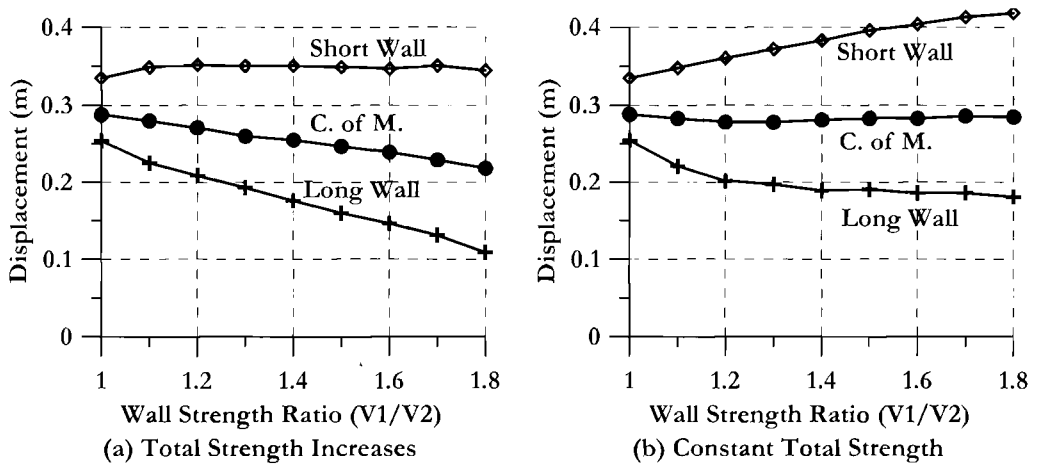
Fig.6.14 Displacements of TR Wall Building with Strength and Stiffness Eccentricity (after Beyer[B4])

When the total system strength is kept constant by reducing the strength of the short wall as the long wall strength increases, the centre-of-mass displacement remains essentially constant, while short and long wall displacements increase and decrease respectively. Apart from local variations which can be attributed to inevitable scatter resulting from the time-history analyses, the displacements appear to vary linearly with the wall **1** overstrength factor. Note that at $\lambda = 1.8$, corresponding to stiffness and strength eccentricities of $0.28L_X$ and $0.143L_X$ respectively, the displacements of the walls differ by about ±40% from the centre of mass displacement.

From the analyses of Beyer[B4] and Castillo et al[C6] the following conclusions can be drawn:

- Displacements of the centre-of-mass can be reliably estimated from a **SDOF** model based on the **DDBD** principles elaborated in this text. That is, the torsional response does not affect the centre-of-mass displacement.

- As with **TU** systems, increasing the strength of an element above that required to satisfy displacement demands in the structure will not result in increased displacements in other structural elements, provided the strength of those elements are not reduced.

- The results are largely insensitive to the value of rotational inertia, within typical expected variations from the value corresponding to uniform distribution of mass

- Varying the strength and stiffness of the transverse walls (Walls **3** and **4**, Fig.6.13), multiplying by factors of 0.5 and 2.0 had only minor effect on the rotational displacements, with displacements increasing only slightly for softer transverse walls.

- Allowing the transverse walls to yield under the rotational displacements also had only minor influence on the displacements of the long and short walls.

- Increasing the seismic intensity while keeping the system strength constant (i.e. increasing the system ductility demand) had little influence on the magnitude of twist associated with peak displacement demands when the strength eccentricity was zero. When appreciable strength eccentricity existed, the displacements of the walls increased almost in proportion to the displacement increase at the centre-of-mass. That is, the torsional component of peak displacements increased with ductility.

- Eccentricity of mass from the geometric centre of a building plan did not significantly affect response, provided stiffness and strength eccentricities were measured from the actual centre of mass.

- For buildings with eccentricity about only one axis (as, for example, in Fig.6.13), seismic excitation directed at a skew angle to a principle axis resulted in reduced peak displacements in the directions of the principal axes, and hence was not critical.

- For buildings with strength eccentricity about both principal axes (e.g. Fig.6.10), slight increases in displacements in the direction of the principal axes were possible under skew attack compared with values resulting from excitation in the direction of the principal axis. This increase was generally small (less than 10%).

- When the effective secant-stiffness period of the structure (at maximum displacement response) was larger than the corner period of the displacement spectrum (see Section 2.2.2) response was complicated by the fact that centre-of-mass displacement did not decrease if excess strength was provided to the stiffer wall. Hence displacements of the flexible wall increased.

6.4.4 Predicting Torsional Response

As noted above, **DDBD** provides an excellent estimate of the displacement response of the centre of mass of a torsionally eccentric building. It remains, however, to determine the displacements at the edge of the building, as effected by torsional rotations. No exact simplified method of analysis seems possible, as the time-history analyses have clearly shown that both strength and stiffness eccentricities affect response, and that peak displacements of centre of mass and the walls at opposite ends of the building do not occur at the same instant of dynamic response. The following approach, however, which is consistent with the principles of **DDBD** has been found to provide displacements of the building edges in close agreement with results of time-history analyses for both **TU** and **TR** systems.

The maximum displacements of a building plan can be approximated by a translation of the centre of mass, determined by **DDBD** principles plus a nominal rotation θ_N, where

$$\theta_N = V_{Base} \cdot e_R / J_{R,\mu} \tag{6.24}$$

where V_{Base} is the design base shear force, e_R is the **elastic** stiffness eccentricity, given by Eq.(6.18), and the ductile rotational stiffness, $J_{R,\mu}$ is modified from the elastic rotational stiffness J_R of Eq.(6.19), dividing the wall stiffness in the direction considered by the system ductility μ_{sys}:

$$J_{R,\mu} = \sum_{1}^{n} \frac{k_{Zi}}{\mu_{sys}} (x_i - e_{RX})^2 + \sum_{1}^{n} k_{Xi} (z_i - e_{RZ})^2 \tag{6.25}$$

Note that the elastic stiffness is used for wall elements perpendicular to the direction considered. Thus the effective stiffness of wall elements in both **X** and **Z** directions is used, since only the **Z** direction walls are expected to be subjected to significant ductility demand under **Z** direction excitation.

The displacements of the end walls (Fig.6.12 for **TU** systems or Fig.6.13 for **TR** systems) are then found from

$$\Delta_i = \Delta_{CM} + \theta_N \cdot (x_i - e_V) \tag{6.26}$$

Note that in Eq.(6.26) the **strength** eccentricity, rather than the effective stiffness eccentricity has been used. Similarity to the procedure outlined above for elastic torsional response will be recognized; the difference being that torsional stiffness is based on effective stiffness of the elements, and torsional displacement increments are based of distances from the centre of strength, C_V.

The approach outlined above has been checked against analytical results from Castillo et al[C6] and Beyer[B4], and found to give generally good agreement for both **TU** and **TR** systems. For **TR** systems with stiffness eccentricity but no strength eccentricity it was

found to accurately predict the incremental displacements resulting from torsion for levels of ductility between 1.3 and 7. Comparisons with average time-history results of the predictions for short wall and long wall displacements for **TU** and **TR** systems are shown in Figs 6.15(a) and (b) respectively. The **TU** systems of Fig.6.15(a) refer to the data of Castillo et al[C6], and were designed for an initial ductility of μ_{sys} =5.35 at zero strength eccentricity (i.e. $V_1 = V_2$). The ratio of wall lengths was $l_{W1} = 1.4 l_{W2}$. The strength of wall **1** was then increased up to a maximum of $1.86 V_2$ without changing the wall lengths, or modifying the strength of wall **2**. The increased system strength thus resulted in a reduction of the centre-of-mass displacement, as is apparent in Fig.6.15(a).

The **TR** systems of Fig. 6.15(b) refer to Beyer's data[B4], and were designed for centre-of-mass system displacement ductilities of approximately $\mu_{sys} = 3.0$. Wall **1** was twice as long as wall **2**, and strength ratios up to $V_1 = 1.8 V_2$ were considered, while keeping the total system strength constant. In each case the average results from the inelastic time-history analyses are plotted with data points and solid lines, and the predictions using the approach outlined above are shown as dashed lines. In both cases the centre-of-mass displacements have been used as the datum, with variations from this for the short and long walls calculated using Eqs. (6.24) to (6.26). It will be noted that the agreement is satisfactory over the full range of data, with the predictions tending to be slightly conservative (i.e. high) for both short and long walls.

(a)TU system, system strength increases
(Castillo's data)[C6]

(b) TR system, constant strength
(Beyer's data)[B4]
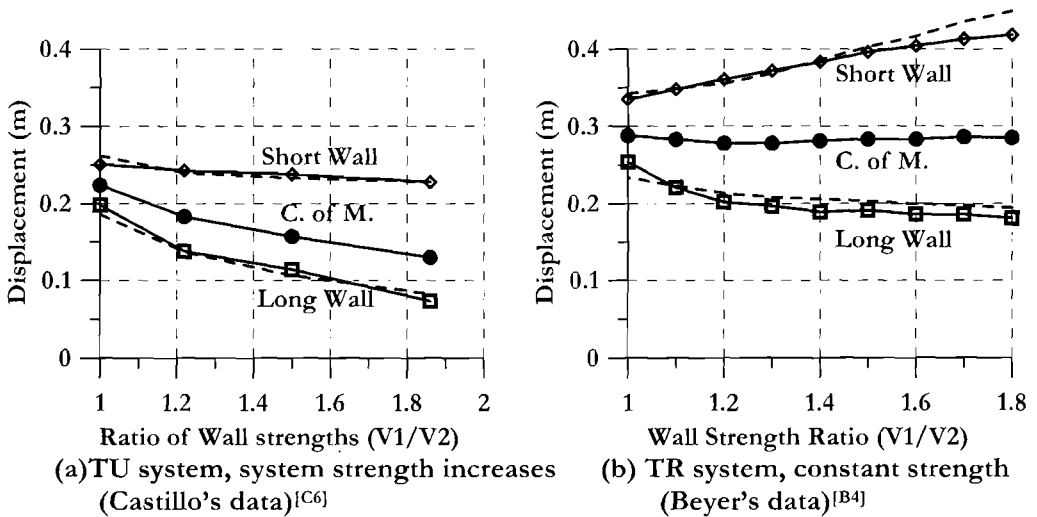
Fig.6.15 Comparison between Predicted Displacements (dashed lines) and Average Time-History Results (solid lines+data points) for TU and TR systems

Note that the **TU** and **TR** structures of Figs.6.15(a) and 6.15(b) are unrelated, with different masses, strengths and design ductilities, and no conclusions can be arrived at by comparison between the two figures.

6.4.5 Recommendations for DDBD

Again it is emphasised that the best design solution will be to eliminate strength eccentricity. As discussed subsequently, in such cases, the displacements due to twist are likely to be less than 10% of the system translational displacement, and thus in most practical cases could be ignored as well within the expected uncertainty of response. However, this approach may not always be feasible, and the following design approach is intended to provide a systematic approach, completely consistent with the **DDBD** philosophy of achieving a specified displacement limit state. A simplified approach, with additional conservatism is briefly discussed in Section 6.4.7.

(a) *Design* *when* T_e<T_C: In Section 3.8.3 it was noted that the preferred design approach to accommodate torsional effects was to design for zero strength eccentricity, regardless of stiffness eccentricity. If this is not possible, then the strength eccentricity should be minimized. However, it will be noted from the material presented in the previous sections that even when strength eccentricity is eliminated, stiffness eccentricity will result in torsional response. A procedure, outlined in Section 3.8.3(c) has been developed to allow consideration of simultaneous strength and stiffness eccentricity (and hence also the special case of stiffness eccentricity without strength eccentricity), but this approach, which requires knowledge of the effective torsional stiffness, as well as both stiffness and strength eccentricities, is more suited to analysis of designed structures rather than design of new structures. It is, however, suitable for an iterative design approach. For convenience, it is again summarized here.

For wall buildings of more than six storeys the most common design situation will be that design displacements are governed by code drift limits. In these cases, the code drift will apply to the wall with greatest displacement, including torsional effects, meaning that the design displacement at the building centre of mass, used in the **SDOF** design, will need to be reduced in proportion to the torsional displacements. The design displacement for the centre of mass will thus be found, reorganizing Eq.(6.26) to give

$$\Delta_{CM} = \Delta_{i,cr} - \theta_N (x_{i,cr} - e_{VX})$$ (6.27)

where $\Delta_{i,cr}$ is the drift-controlled displacement of the critical wall. With reference to Fig.6.13, and assuming that drift limits apply to wall **2**, the design displacement for the **SDOF** substitute structure will be

$$\Delta_{CM} = \Delta_2 - \theta_N (0.5L_X + |e_{VX}|)$$ (6.28)

It is also possible, particularly for low-rise wall buildings, or buildings containing walls with low height/length aspect ratios, that the displacement capacity of the stiffest wall corresponding to material strain limits may govern design. In this case the design displacement at the centre of mass will be larger than the displacement of the critical

element. Equation (6.27) still applies, with due consideration of signs, and with reference to Fig.6.13, the design displacement for the substitute structure will be

$$\Delta_{CM} = \Delta_1 + \theta_V \left(0.5 L_X - |e_{VX}| \right) \tag{6.29}$$

In general it will be necessary to adopt an iterative approach to determine the design displacement when torsional effects are significant, since the nominal torsional displacements depend on J_R, e_R and e_V which in turn will depend on the relative strengths assigned to the lateral force-resisting elements in both orthogonal directions, and the system ductility factor.

It is possible, however, to develop some recommendations to facilitate the design process, based on the material presented in the previous sections. In doing so, it is convenient to distinguish between cases where the design is governed by drift of a more flexible wall and cases where design is governed by material strains of a stiffer wall.

Step 1: Determine whether the stiffer or more flexible walls govern design. This may be done, with adequate accuracy, by estimating the roof-level displacements of the walls corresponding to the limit state considered, assuming zero strength eccentricity:

Stiffer wall: $\quad \Delta_{n,stiff} = \phi_{y,s} H_n^2 / 3 + \phi_{ls} L_P H_n \tag{6.30}$

where $\phi_{y,s}$ is the yield curvature of the stiffer wall, given by Eq.(4.57c), ϕ_{ls} is given by Eq.(6.10c) and L_P is given by Eq.(6.7).

More flexible wall: $\Delta_{n,flex} = \phi_{y,f} H_n^2 / 3 + \left(\theta_C - 0.5 \phi_{y,f} H_n \right) \cdot H_n \tag{6.31}$

We note that with zero strength eccentricity, and average ductility demand, and even large differences in wall length, the displacement at the centre of mass is typically 10% higher than that of the stiffer wall, and 10% lower than that of the more flexible wall. Thus

$$\Delta_{CM,n} \le 1.1 \Delta_{n,stiff} \quad \text{and} \quad \Delta_{CM,n} \le 0.9 \Delta_{n,flex} \tag{6.32}$$

Equation (6.32) will determine which of the walls is critical, and what the roof-level system displacement should be for zero strength eccentricity. The design displacement at the effective height can now be related to the roof-level centre-of-mass displacement based on the displacement profile of the stiffer wall, using Eqs.(6.11) and (3.26).

It should be noted that Eqs.(6.30) and (6.31) are based on the assumption that the stiffer wall is governed by material strains, and that the more flexible wall is governed by roof drift limitations. It is, of course, possible that both walls are governed by material strain limits, or that both walls are limited by drift. All possibilities must be considered.

Step 2: Flexible wall governs: If $0.9\Delta_{n,flex} < 1.1\Delta_{n,stiff}$ then the calculated value for Δ_{CM} is the largest value that can be adopted while satisfying the drift (or material strain)

limit for the flexible wall, and the value computed for the system base shear by **DDBD** will be the lowest possible base shear, as discussed subsequently.

Step 2a: Determine relative wall strengths for zero strength eccentricity: The analyses by Castillo et al[C.6] and Beyer[B4] confirm that the minimum required strength of the flexible wall is found from statics (refer to Fig.6.13) as

$$V_2 = V_{Base} \cdot \frac{(L_x - x_2)}{L_x} = V_{Base} \cdot \frac{|x_1|}{L_x} \tag{6.33a}$$

The minimum strength for the stiffer wall, also defined by statics will be

$$V_1 = V_{Base} \cdot \frac{(L_x - |x_1|)}{L_x} = V_{Base} \cdot \frac{x_2}{L_x} \tag{6.33b}$$

The situation envisaged by this is represented by Fig.6.16(a). If the strength of either wall is reduced below the values required by Eq.(6.33), then displacements of the flexible wall must be expected to exceed the drift limit. However, the strength of either wall may be increased above that required by Eq.(6.33) without increasing the drift of the flexible wall. As noted earlier, increased strength would most probably be allocated to the stiffer wall, as a consequence of flexural strength associated with the code-specified minimum flexural reinforcement ratio exceeding the required strength.

When the structural system comprises more than two walls in the direction considered, V_1 and x_1 in Eq.(6.33a) will refer to the total strength, and centre of strength, of all walls to the left of the centre of mass, and similarly for Eq.(6.33b) for all walls to the right of the centre of mass.

Step 2b: Determine system C_M design displacement: As noted above this is related to the critical C_M roof-level displacement by the displacement profile of the stiff wall, and Eq.(3.26).

Step 2c: Determine System ductility: This requires that the system yield displacement be determined. For the two-wall system of Figs.6.12, 6.13, and 6.16, this is found by weighting the wall displacements by the fraction of total base shear carried, as

$$\Delta_{y,sys} = \frac{V_1}{V_{Base}} \cdot \Delta_{y1} + \frac{V_2}{V_{Base}} \cdot \Delta_{y2} = 2\varepsilon_y \cdot \left(\frac{V_1}{V_{Base}} \cdot \frac{1}{l_{W1}} + \frac{V_2}{V_{Base}} \cdot \frac{1}{l_{W2}} \right) \tag{6.34a}$$

which can be generalized to

$$\Delta_{y,sys} = 2\varepsilon_y \sum_1^m \frac{V_i}{V_{Base}} \cdot \frac{1}{l_{Wi}} \tag{6.34b}$$

(a) Flexible Wall Drift Governs (b) Stiff Wall Strain Governs
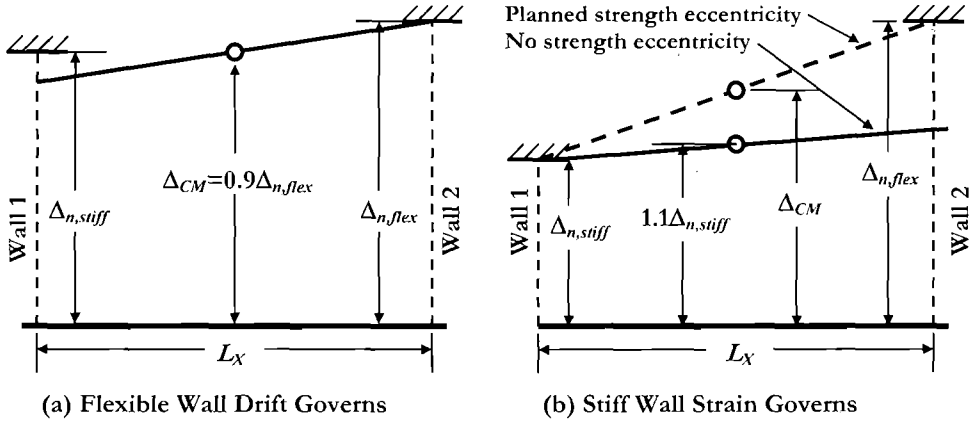
Fig.6.16 Roof-Level Displacements for Zero Strength Eccentricity (Plan View)

Although the individual wall strengths and the total base shear are not known at this stage of the design, the strength **ratios** of Eq.(6.34) are known from the assumption of zero strength eccentricity at the start of the design process, from Eqs.(6.33), and the yield displacements are known from the yield curvatures (Eq.4.57(c)), regardless of strength.

Step 2d: Determine required base shear strength, and hence minimum wall strengths: With the system displacement ductility known, the effective damping is known (Eq.3.17a), and the base shear strength can be directly calculated in the usual manner.

Step 3: Stiff wall governs: The situation is somewhat different from the case when the flexible wall governs, in that the required base shear strength associated with zero strength eccentricity is not necessarily a minimum design condition for the structure as a whole, as may be seen from Fig.6.16(b). In this case the roof-level centre-of-mass displacement corresponding to $1.1\Delta_{n,stiff}$ is significantly lower than that corresponding to $0.9\Delta_{n,flex}$. We could reduce the total design base-shear force by designing for planned strength eccentricity, shown by the dashed line in Fig.6.16(b). Since the centre-of-mass displacement and also the system ductility demand will be higher, the required base shear force will be lower. An optimum solution is found when both stiff and flexible walls achieve their limit displacement, though this should not occur at the expense of excessive strength eccentricity. In this respect it is suggested that $e_V = 0.15L_X$ should be considered an upper limit, unless special design verification, involving inelastic time-history analysis is carried out.

Step 3a: Determine design displacement and drift at roof level: Note that if we design for the optimum condition suggested by the dashed line in Fig.6.16(b), the design displacement and twist angle are directly known at roof level. The twist angle is given by

$$\theta_{nom,n} = \frac{\left(\Delta_{n,flex} - \Delta_{n,stiff}\right)}{L_X} \tag{6.35}$$

To determine the roof-level design displacement from Eq.(6.29) e_{VX} must be calculated using Eq.(6.23). We need to know the strength eccentricity, which is not, at this stage, known. Make an initial assumption of $\lambda = V_1 / V_2 = 1.4$.

Step 3b: Determine design displacement at effective height: Design values at the effective height, H_e are found using the stiff wall displacement profile as the basis for determining the system **SDOF** displacement, $\Delta_{D,sys}$:

$$\Delta_{D,sys} = \Delta_{n,sys} \cdot \frac{\Delta_{He,stiff}}{\Delta_{n,stiff}} \tag{6.36}$$

Step 3c: Determine system yield displacement: In this case the ratio of design forces between the walls is not known at the start of the design process. Again we initially assume a strength eccentricity factor of $\lambda = 1.4$. We note that the recommendation made above that the maximum eccentricity should be limited to $e_V/L_X = 0.15$ implies that the ratio of strengths between walls **1** and **2** must be within the range implied by $1 < \lambda = V_1/V_2 < 1.8$. Taking the rather extreme example where $l_{w1} = 2l_{w2}$, it is found, from substitution into Eq.(6.34), that the system yield displacement only varies by 10% as λ increases from 1.0 to 1.8. Since the effective damping ratio given by Eq.(3.17a) is rather insensitive to the displacement ductility factor μ (and hence to the yield displacement), the assumption of $\lambda = 1.4$ is likely to be adequate.

Step 3d: Determine system ductility: With the system limit-state and yield displacements known, the ductility, and hence the damping can be found in the usual manner.

Step 3e: Determine the SDOF base shear force: The procedure is standard.

Step 3f: Determine the rotational stiffness: Carry out a preliminary allocation of strength between the walls. It is again suggested that $\lambda = 1.4$ be initially assumed. Hence, noting that $k_{Z1} = V_1/\Delta_{y1}$ etc., determine the rotational stiffness from Eq.(6.25). It is assumed that the strengths (and hence stiffness) of the transverse walls in the **X** direction (if any) is known at this stage. If not, assume the total strengths in the orthogonal directions are equal, which is a reasonable assumption, when designed by **DDBD**.

Step 3g: Determine the stiffness eccentricity: Rearranging Eq.(6.24) the stiffness eccentricity is found from the known rotation θ_{nom} (Eq.6.35) as

$$e_R = \frac{\theta_{nom} \cdot J_{R,\mu}}{V_B} \tag{6.37}$$

Care is required with signs here. With the structural layout and axes of Fig.6.13, the twist angle has a negative sign, and the eccentricity is negative. For a known ratio of wall lengths ($l_{W1} = \alpha l_{W2}$), the strength ratio between the walls can then be found from Eq.(6.18). For the special, though common case of walls equally spaced from the centre of mass, Eq.(6.23a) can be generalized to give

$$e_R = \frac{0.5(1-\alpha\lambda)}{1+\alpha\lambda} \cdot L_X \quad \text{(a)} \quad \text{and hence} \quad \lambda = \frac{(0.5 - e_R/L_X)}{\alpha(0.5 + e_R/L_X)} \quad \text{(b)} \qquad (6.38)$$

If the value of λ found from this process implies a strength eccentricity greater than $e_V/L_X = 0.15$, it may be advisable to redesign for a smaller centre-of-mass displacement, with $\lambda = 1.8$

Step 3h: Iterate steps 3a to 3g to achieve stability: Only small changes in the design base shear force will occur between iterations, and two or three cycles will be adequate.

(b) Recommendations when $T_e > T_C$: It was noted in the summary of Section 6.4.3 that torsional response appears to be more severe when the effective period exceeds the corner period of the displacement spectrum. In such cases, the procedure outlined above could be non-conservative, resulting in displacements of the flexible wall that exceed the limit state values. Research is on-going into this behaviour. Until definitive recommendations are available, it is conservatively suggested that the corner period be ignored, and the displacement spectrum be continued linearly up to the effective period. This will mean designing for a higher base shear than would result from designing to the plateau displacement applying for $T_e > T_C$. Since there is uncertainty associated with the correct value for T_C as noted in Chapter 2, such an approach is doubly prudent.

(c) Consideration of Accidental Eccentricity: As noted in Section 3.8.1, design for accidental eccentricity is likely to be ineffective, since it involves increasing the strength of all structural elements, which simply results in an increase in the torsional moment. Although the overall consequence will be a reduction in displacements, the effect will be minor. Hence we do not recommend consideration of accidental eccentricity in **DDBD**.

(d) Design for Bi-directional Eccentricity: Thus far, the discussion of torsional response has assumed that the direction of seismic attack is parallel with one of the two principal axes of the structure. In fact, there will normally be excitation components in both principal directions simultaneously, with the resultant inertia force acting at an angle to the structure principal axes, as suggested in Fig.6.10 and 6.17. The example of Fig.6.17 shows a plan view of a building braced with four boundary walls of different sizes, resulting in strength eccentricity in both principal directions. The inertia force V_I acts through the centre of mass, C_M, with the centre of strength, C_V, eccentric by a distance e_v measured perpendicular to the line of action of the inertia force.

It is clear that there is a torsional moment acting on the building, given by $V_I e_V$. It is also clear that if the seismic intensity is sufficiently high, all four walls will develop their flexural strength. In this case the inertia and resisting forces are given by:

$$V_I = V_R = \sqrt{(V_1 + V_2)^2 + (V_3 + V_4)^2} \qquad (6.39)$$
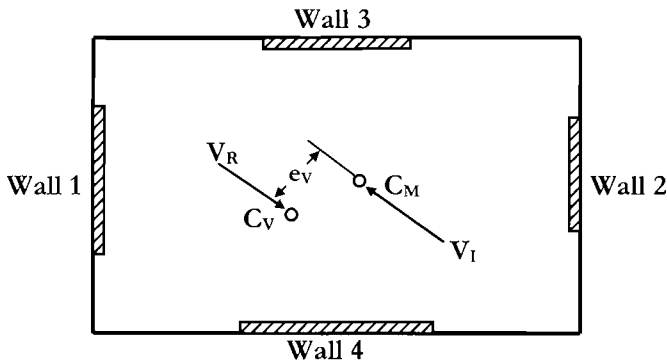
Fig.6.17 Diagonal Seismic Attack, Plan View

where V_1, V_2, V_3, and V_4 are the base shears corresponding to flexural strength of walls **1** to **4** respectively. Note that if all walls yield, the directions of the inertia and resisting forces are fixed, and are not necessarily parallel to the resultant ground excitation direction.

Given that all four walls have yielded, there is no further torsional resistance available to limit rotation under the torsional moment. However, torsional mass inertia, resulting from the distributed nature of the mass across the floor plan will limit the rotation, as with the torsionally unrestrained case discussed in Section 6.4.2. It would seem that an estimate of maximum feasible rotation should be available by determining the displacement response in the diagonal direction, and hence the ductility in the two orthogonal directions. The effective rotational stiffness can then be determined from a modified form of Eq.(6.25):

$$J_{R,\mu} = \sum_{1}^{n} \frac{k_{zi}}{\mu_Z}\left(x_i - e_{RX}\right)^2 + \sum_{1}^{n} \frac{k_{xi}}{\mu_X}\left(z_i - e_{RZ}\right)^2 \tag{6.40}$$

where μ_X and μ_Z are the average (system) displacement ductility demands in the **X** and **Z** directions respectively. The procedure for determining expected displacement response for a designed structure by **DDBD** principles is covered in Chapter 13.

In fact, it will rarely be necessary to carry out these calculations for new buildings. Since the strength in the diagonal direction will be greater than in a principal direction (typically by about 40%), displacements in the diagonal direction of the centre of mass will be less than the displacements in the principal directions under orthogonal excitation parallel to the principal direction considered. The component of the diagonal displacement in the principal directions will be even smaller, resulting in a large reserve in displacement capacity to allow for torsional rotation. Consequently, torsional rotation under diagonal excitation will not normally be considered in the design process.

6.4.6 Design Example 6.1: Torsionally Eccentric Building

(a) Floor Plan   (b) Design Displacement Spectra
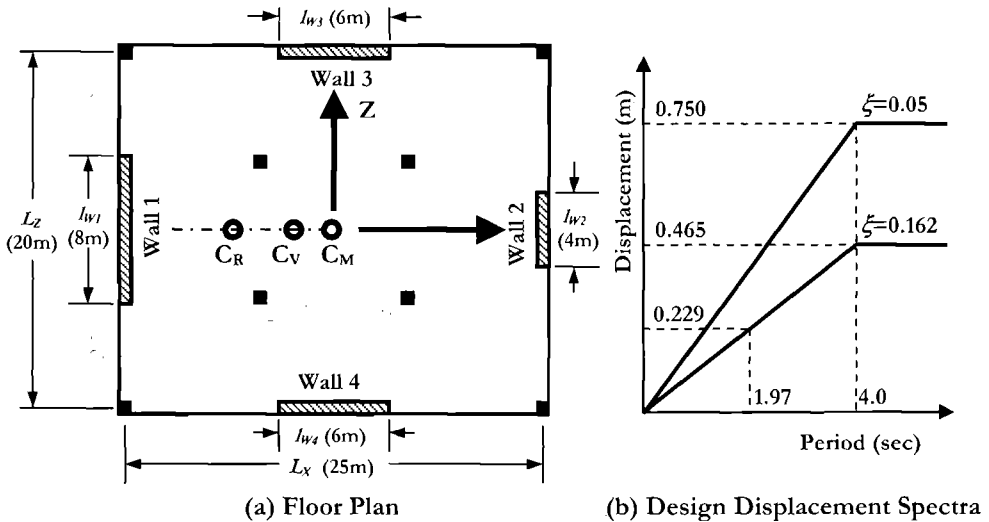
Fig. 6.18   Data for Example 6.1

The building shown in plan in Fig.6.18(a) has six storeys, with a uniform storey height of 2.8 m (9.2 ft), and equal floor weights of 3000kN at each level, including the roof. The structural system consists of boundary walls, as indicated in Fig.6.18(a), with internal prop-columns and flat-slab floors which do not contribute significantly to the lateral resistance in either of the principal directions. The building dimensions are L_X = 25 m (82 ft) and L_Z = 20 m (65.6 ft). The two walls in the Z direction have lengths l_{W1} = 8 m (26.2 ft) and l_{W2} = 4 m (13.1 ft). Wall widths of 250mm (9.8 in) are selected. The difference in wall length results from wall 1 being on a boundary adjacent to other buildings, while wall 2 is on a road frontage, where minimum disruption to access is desired. In the X direction the structure is symmetrical, with two walls of 6 m (19.7 ft) length. The building is to be designed to a damage-control limit state, for which the code drift limit is θ_C = 0.025. Specified material strengths are f'_c = 30 MPa (4.35 ksi) and f_y = 420 MPa (60.9 ksi). The flexural reinforcing steel will be 20mm (0.79 in) diameter tempcore steel with a ratio of ultimate to yield strength of f_u/f_y = 1.25, and a strain at ultimate strength of 0.10.

The structure is to be constructed in a region of high seismicity, corresponding to a **PGA** of 0.6g, with the displacement-spectrum for 5% damping given in Fig.6.18(b). Displacement reduction for damping conforms to Eq.(2.8).

Solution: The design process follows the procedure outlined in Section 6.4.5(a).

Step 1: Determine critical wall: Determine critical roof displacements for 8m and 4m walls respectively. The following information is common to both walls: Expected yield strength: from Eq.(4.23(b)), $f_{ye} = 1.1f_y = 462$ MPa (67 ksi), hence $\varepsilon_y = 0.00231$.

Strain penetration length: from Eq.(4.30) $L_{SP} = 0.022 f_{ye} d_{bl} = 0.022 \times 462 \times 0.02 = 0.203$ m (8 in).

Factor for plastic hinge length: from Eq.(4.31): $k = 0.2(f_u/f_y - 1) = 0.2 \times 0.25 = 0.05$ (<0.08, OK)

Effective height: unknown, but an average value for walls of $H_e = 0.75 H_n$ may be assumed, leading to $H_e = 0.75 \times 6 \times 2.8 = 12.6$ m (41.3 ft).

8 m wall:

    plastic hinge length: from Eq.(6.7):

$$L_P = k \cdot H_{eff} + 0.1 l_w + L_{SP} = 0.05 \times 12.8 + 0.1 \times 8 + 0.203 = 1.633 m \quad (64.3 in)$$

    yield curvature: from Eq.(4.57c):

$$\phi_y = 2\varepsilon_y / l_w = 2 \times 0.00231 / 8 = 0.000578 / m$$

    roof yield displacement: from Eq.(4.33):

$$\Delta_{yn} = \phi_y (H_n + L_{SP})^2 / 3 = 0.000578 \times (16.8 + 0.203)^2 / 3 = 0.0557 m \quad (2.20 \text{ in})$$

    roof yield drift: from Eq.(3.26):

$$\theta_{yn} = \varepsilon_y (H_n + L_{SP}) / l_w = 0.00231 \times 17.03 / 8 = 0.00492 \text{ rad.}$$

    strain-based plastic rotation: Eq.(6.10b) applies directly, since $\varepsilon_{su} = 0.10$:

$$\theta_p = \left(0.072 / l_w - \phi_y\right) \cdot L_P = \left(0.072 / 8 - 0.000578\right) \times 1.633 = 0.0138$$

    strain-based roof drift: at roof level, the sum of yield and plastic rotations is

$$\theta_n = \theta_{yn} + \theta_p = 0.00492 + 0.0138 = 0.0187$$

This is less than the specified drift limit of 0.025, hence material strains limit the response for the 8 m wall.

    Roof-level limit displacement: The roof displacement is the sum of yield and plastic displacements:

$$\Delta_n = \Delta_{yn} + \Delta_{pn} = \Delta_{yn} + \theta_p H_n = 0.0557 + 0.0138 \times 16.8 = 0.288 m \quad (11.3 in)$$

4 m wall: The same equations apply as above. The results are listed below

    plastic hinge length: $L_P = 0.05 \times 12.6 + 0.1 \times 4 + 0.203 = 1.233 \quad (48.5 in)$

    yield curvature: $\phi_y = 2 \times 0.00231 / 4 = 0.001156$

    roof yield displacement: $\Delta_{yn} = 0.001156 \cdot (16.8 + 0.203)^2 / 3 = 0.1113 m \quad (4.4 in)$

    roof yield drift: $\theta_{yn} = 0.00231 \times 17.03 / 4 = 0.00984$

    strain-based plastic rotation: $\theta_p = \left(0.072 / 4 - 0.001156\right) \times 1.233 = 0.0208$

    Strain-based roof drift: $\theta_n = 0.00984 + 0.0208 = 0.0364$

a_w 0.316δ

b_w 0.33

348   Priestley, Calvi and Kowalsky. Displacement-Based Seismic Design of Structures

This exceeds the drift limit of 0.025, and hence drift limits the performance of the 4 m wall. The maximum permissible plastic drift is thus $\theta_p = 0.025 - 0.00984 = 0.0152$

Roof-level limit displacement: $\Delta_n = 0.1113 + 0.0152 \times 16.8 = 0.367m$ (14.4in)

Substituting the roof-level displacements for the stiff wall and flexible wall into Eq.(6.32) it is found that the stiff wall will govern the design. As a consequence we move to step 3 of the procedure in Section 6.4.5(a), choosing planned strength eccentricity to simultaneously achieve the design limits for the stiff and flexible walls.

Step 3a: Calculations necessary to determine the displacement profiles, and hence the effective heights and design displacements for walls **1** and **2** are summarized in Tables 6.1 and 6.2 respectively.

Table 6.1 Calculations for Wall 1 (Stiff) for Example 6.1

Col.(1)	Col.(2)	Col.(3)	Col.(4)	Col.(5)	Col.(6)	Col.(7)
Floor (i)	H_i (m)	Δ_{yi} (m)	Δ_{Pi} (m)	Δ_{Di} (m)	Δ^2_{Di} (m)	$\Delta_{Di}H_i$
6	16.8	0.0557	0.2318	0.2875	0.0827	4.830
5	14	0.0421	0.1932	0.2353	0.0554	3.294
4	11.2	0.0292	0.1546	0.1838	0.0338	2.058
3	8.4	0.0178	0.1159	0.1337	0.0179	1.123
2	5.6	0.0086	0.0773	0.0859	0.0074	0.481
1	2.8	0.0025	0.0386	0.0411	0.0017	0.115
0	0	0	0	0	0	0
Sum				0.9673	0.1987	11.901

Table 6.2 Calculations for Wall 2 (Flexible) for Example 6.1

Col.(1)	Col.(2)	Col.(3)	Col.(4)	Col.(5)	Col.(6)	Col.(7)
Floor (i)	H_i (m)	Δ_{yi} (m)	Δ_{Pi} (m)	Δ_{Di} (m)	Δ^2_{Di} (m)	$\Delta_{Di}H_i$
6	16.8	0.1113	0.2570	0.3683	0.1357	6.188
5	14	0.0841	0.2142	0.2983	0.0890	4.177
4	11.2	0.0584	0.1714	0.2298	0.0528	2.573
3	8.4	0.0356	0.1285	0.1641	0.0269	1.379
2	5.6	0.0173	0.0857	0.1030	0.0106	0.577
1	2.8	0.0049	0.0428	0.0478	0.0023	0.134
0	0	0.0000	0.0000	0.0000	0.0000	0.000
Sum				1.2113	0.3173	15.027

In Tables 6.1 and 6.2 the storey heights are given in Col.(2); the yield displacement profile, according to Eq.(6.5), with H_n =16.8 m and l_w = 8 m and 4 m respectively for walls **1** and **2** are listed in Col.(3); the plastic displacements, based on the critical plastic

rotations calculated above, are listed in Col.(4), and the total design displacements are listed in Col.(5). Column (6) lists the square of the design displacements, and Col.(7), the product of height and design displacement profile.

roof twist angle: From Eq.(6.35) :
$$\theta_{nom,n} = (\Delta_{n,flex} - \Delta_{n,stiff}) / L_X = (0.3666 - 0.2875) / 25 = 0.003167$$

strength eccentricity: Initially assume $\lambda = 1.4$, hence:
$$e_V = (1.0/2.4) \cdot 25 - 12.5 = -2.08 \ (-6.82\text{ft})$$

design C. of M. displacement at roof level: From Eq.(6.29):
$$\Delta_{CM} = \Delta_1 + \theta(0.5L_X - |e_{VX}|) = 0.2875 + 0.003167(12.5 - 2.08) = 0.321 \text{ m} \quad (12.6\text{in})$$

Step 3b: Effective height: The effective heights for the two walls can be found from the data in Tables 6.1 and 6.2, and Eq.(3.35), noting the masses are equal at all floors:
$$H_e = \sum_{i=1}^{n} (m_i \Delta_i H_i) / \sum_{i=1}^{n} (m_i \Delta_i) = 11.90/0.967 = 12.3 \text{ m} \quad (\text{wall } \mathbf{1}) \quad (40.3\text{ft})$$
$$= 15.03/1.211 = 12.4 \text{ m} \quad (\text{wall } \mathbf{2}) \quad (40.7\text{ft})$$

design displacement at effective height, stiff wall: From Eq.(3.26):
$$\Delta_d = \sum_{i=1}^{n} (m_i \Delta_i^2) / \sum_{i=1}^{n} (m_i \Delta_i) = 0.1987/0.9673 = 0.2055 \text{ m}$$

design C. of M. displacement at effective height: From Eq.(6.36):
$$\Delta_{D.sys} = \Delta_{n,sys} \cdot \Delta_{He,stiff} / \Delta_{n,stiff} = 0.321 \times 0.2055 / 0.2875 = 0.229 \text{ m} \ (9.0 \text{ in})$$

nominal twist at effective height: By proportion:
$$\theta_{nom,sys} = \theta_{nom,n} \cdot \Delta_{He,stiff} / \Delta_{n,stiff} = 0.003167 \times 0.2055 / 0.2875 = 0.00226$$

Step 3c: System yield displacement: Substituting $H_i = H_e = 12.3$ m in Eq.(6.5) we find the yield displacements for the two walls, at the effective height are $\Delta_{y1} = 0.0331$ m and $\Delta_{y2} = 0.0661$ m. Since we have assumed $\lambda = 1.4$, the system yield displacement at the effective height is, from Eq.(6.34):
$$\Delta_{y,sys} = (V_1 / V_B)\Delta_{y1} + (V_2 / V_B)\Delta_{y2} = (1.4/2.4) \times 0.0331 + (1/2.4) \times 0.0661 = 0.0468m$$

Step 3d: The system displacement ductility demand is thus:
$$\mu_{sys} = \Delta_{D,sys} / \Delta_{y,sys} = 0.229 / 0.0468 = 4.9$$

Step 3e: Base shear force: The effective damping is found from Eq.(3.17a) as:
$$\xi_{eq} = 0.05 + 0.444 \left(\frac{\mu - 1}{\mu\pi} \right) = 0.05 + 0.444 \left(\frac{4.9 - 1}{4.9 \times \pi} \right) = 0.162$$

The displacement reduction coefficient, from Eq.(2.8) is
$$R_\xi = (0.07/(0.02 + \xi))^{0.5} = 0.620$$

and the corner displacement, at T=4.0 sec, corresponding to $\xi = 0.162$ is thus $0.75 \times 0.620 = 0.465$ m. (18.3 in). The damped spectrum is included in Fig.6.18(b). By proportion, the effective period of the **SDOF** system is:

$$T_e = 4.0 \times 0.229 / 0.465 = 1.97 \sec$$

From Eq.(3.33) the effective mass of the SDOF system is:

$$m_e = \sum_{i=1}^{n} (m_i \Delta_i) / \Delta_d = 3000 \times 0.9673 / (g \times 0.2055) = 14120 kN / g \quad (3173 \text{ kips/g})$$

From Eq.(3.1), the effective stiffness at design response level is

$$K_e = 4\pi^2 m_e / T_e^2 = 4\pi^2 \times (14120 / 9.805) / 1.97^2 = 14657 kN / m$$

and finally, the base shear, from Eq.(3.2) is:

$$F = V_{Base} = K_e \Delta_d = 14657 \times 0.229 = 3356 kN \quad (754 \text{ kips})$$

Step 3f: To determine the torsional stiffness, we first need to estimate the stiffnesses of walls **1** to **4**. Continuing with the initial assumption of $\lambda = 1.4$, the design strengths of walls **1** and **2** are

$$V_1 = 3356 \times (1.4 / 2.4) = 1958 kN; \quad \text{and} \quad V_2 = 3356 \times (1 / 2.4) = 1399 kN$$

From the yield displacements calculated above, the elastic stiffnesses are thus:

$$k_1 = V_1 / \Delta_{y1} = 1958 / 0.0331 = 59154 kN / m$$

$$k_2 = V_2 / \Delta_{y2} = 1399 / 0.0661 = 21165 kN / m$$

The stiffness of walls **3** and **4** in the transverse (**X**) direction, are based on the assumption of equal base shear strength in the orthogonal directions, and a yield displacement, based on a wall length of 6m, of 0.0441, resulting in:

$$k_3 = k_4 = 0.5 \times 3356 / 0.0441 = 38050 kN / m$$

Since the walls are symmetrically placed with reference to C_M, and noting that the wall length ratio is $\alpha = 2$, the stiffness eccentricity is given by Eq.(6.38a) as

$$e_{RX} = \frac{0.5(1 - \alpha\lambda)}{1 + \alpha\lambda} \cdot L_X = \frac{0.5(1 - 2 \times 1.4)}{1 + 2 \times 1.4} \cdot 25 = -5.92m \quad (19.4 \text{in})$$

The first estimate of the rotational stiffness can now be made. From Eq.(6.25):

$$J_{R,\mu} = \sum_{1}^{n} \frac{k_{zi}}{\mu_{sys}} (x_i - e_{RX})^2 + \sum_{1}^{n} k_{Xi} (z_i - e_{RZ})^2$$

$$= \left(59.2(-12.5 + 5.92)^2 + 21.1(12.5 + 5.92)^2\right) / 4.9 + 2 \times 38.1 \times 10^2 = 9577 MNm^2$$

Step 3g: New estimate of stiffness and strength eccentricities: From Eq.(6.37) the revised estimate of the stiffness eccentricity is:

$$e_R = \frac{\theta_{nom} \cdot J_{R,\mu}}{V_B} = \frac{-0.00226 \times 9577 \times 10^3}{3356} = -6.45m \quad (21.1 \text{ ft})$$

The revised estimate for the wall strength ratio is given by Eq.(6.38b) as:

$$\lambda = \frac{(0.5 - e_R / L_x)}{\alpha(0.5 + e_R / L_X)} = \frac{(0.5 + 6.45/25)}{2(0.5 - 6.45/25)} = 1.57$$

Second cycle: With the new estimate of λ, the following revisions result:

Design displacement: $\Delta_{D,sys} = 0.2275$ m (8.96 in)
Yield displacement: $\Delta_{y,sys} = 0.0454$ m (1.79 in)
Design ductility: $\mu = 5.01$
Effective damping: $\xi = 0.163$
Reduction factor: $R_\xi = 0.618$
Corner displacement: $\Delta_{C,\xi} = 0.464$ m (18.3 in)
Effective period: $T_e = 1.97$ sec (unchanged)
Base Shear: $V_{Base} = 3356$ kN. (754 kips) (unchanged)
Design Strengths: $V_1 = 2050$ kN (461 kips)
$V_2 = 1306$ kN (293 kips)
Wall stiffnesses: $k_1 = 61900$ kN/m
$k_2 = 19800$ kN/m
Torsional stiffness: $J_{R,\mu} = 9491$ MNm²
Stiffness eccentricity: $e_{RX} = -6.39$ m (21.0ft)
Wall strength ratio: $\lambda = 1.55$

It is clear that the solution has essentially stabilized, and the final values for the wall strengths are

$V_1 = 2040$ kN (458 kips)
$V_2 = 1316$ kN (296 kips)

Wall Design Moments and Shears: The wall base shears are now distributed to the floor levels in accordance with Eq.(3.41), and the shears and moments for the walls, corresponding to the design forces are calculated. The results are summarized in Table 6.3. Note that, except for the wall base moments, the moments and shears will need to be amplified for potential excess flexural strength of the base hinges, and for higher mode effects (see Sections 3.9 and 4.5). Capacity design for walls is discussed further in Section 6.6.

Flexural design at wall bases: From Table 6.3 it is seen that the design base moments for walls **1** and **2** are 25100 kNm and 16300 kNm (222,300 kip in and 144,400 kip in) respectively. The axial loads at the wall bases, including self weight are estimated to be 2200 kN and 1700 kN (495 kip and 383 kip) respectively. The design moments apply at the design displacement, and hence the provided flexural strength should match these values at the curvatures developed in the two walls at the design displacements.

Table 6.3   Design Forces and Moments, Design Example 6.1

Floor	Height (m)	Wall 1 Δ_i (m)	Wall 1 F_i (kN)	Wall 1 V_i (kN)	Wall 1 M_i (kNm)	Wall 2 Δ_i (m)	Wall 2 F_i (kN)	Wall 2 V_i (kN)	Wall 2 M_i (kNm)
6	16.8	0.288	606	606	0	0.367	400	400	0
5	14	0.235	496	1103	1698	0.297	324	724	1121
4	11.2	0.184	388	1490	4785	0.229	250	974	3150
3	8.4	0.134	282	1772	8957	0.163	178	1152	5877
2	5.6	0.086	181	1953	13920	0.102	112	1264	9100
1	2.8	0.041	87	2040	19390	0.048	52	1316	12640
0	0	0	0.0	2040	25100	0	0.0	1316	16330
Sum		0.967	2040			1.205	1316		

Wall **1** is governed by the material strain limits, and hence the design curvature is

$$\phi_{D,8} = 0.072 / l_w = 0.009 / m$$

Wall **2** is governed by the roof drift limit. A maximum plastic rotation was calculated as $\theta_P = 0.0152$. The design curvature for wall 2 is thus:

$$\phi_{D,4} = \phi_y + \phi_P = 0.001156 + 0.0152 /(L_P = 1.233) = 0.0135 / m$$

It is decided to use uniform distribution of flexural reinforcement along the lengths of both walls. As was noted in Section 5.6.1 in relation to flexural design of beams, distributing the flexural reinforcement uniformly along a section, rather than concentrating the same amount at the section ends has little effect on the flexural capacity of the section. Distributed reinforcement results in better control of shear deformations, a reduced tendency for bar buckling, and better **P-Δ** control as a consequence of higher post-yield stiffness.

Moment-curvature analyses including the effects of reinforcement strain-hardening and concrete confinement result in flexural reinforcement areas of 8600 mm² (13.3 in²) corresponding to a reinforcement ratio of 0.43% for wall 1, and 18500 mm² (28.7 in²), corresponding to a reinforcement ratio of 1.92% for wall 2. Although these are within typically accepted limits for walls (0.3% to 2.0%), the ratio for the 4 m wall is rather high. It is decided to increase the width of the wall from 250 mm to 300 mm. Redesign results in a reduced reinforcement area of 17000 mm² (26.4 in²), with a corresponding reinforcement ratio of 1.42%.

6.4.7 Simplification of the Torsional Design Process

The approach developed in the previous sections has been presented in the interests of completeness, and because of the philosophical basis of **DDBD**, which aims to achieve the limit-state displacement in the design seismic event. However, the procedure is somewhat lengthy, and for minor structures, the economy associated with designing for

a minimum base shear force may not justify the additional design effort. In such cases a conservative design approach may be adopted.

When the flexible wall governs the design (see Section 6.4.5(a) Step 2), the process is straightforward, and no simplification seems warranted. However, when the stiffer wall governs the design, then a reasonable simplification will be to design for a centre-of-mass displacement equal to $1.1\Delta_{stiff}$, determined at the effective height, based on the stiff wall displacement profile. The design steps are then identical to the case when the more flexible wall governs design.

6.5 FOUNDATION FLEXIBILITY EFFECTS ON CANTILEVER WALLS

6.5.1 Influence on Damping

The influence of foundation flexibility effects in **DDBD** was briefly introduced with specific reference to cantilever walls in Section 3.5.4(b), where it was noted that foundation flexibility increases the elastic displacements, but has a lesser, or zero influence on the design displacement, depending on whether the design displacement is strain-limited or drift-limited. In both cases the design system ductility demand is reduced by foundation flexibility, and as a consequence, the effective damping may also be reduced. The topic was also introduced in Section 1.3.4(c) with reference to problems considering foundation flexibility within a force-based design environment.

In Fig.6.19, the elastic displacement at the effective height resulting from foundation flexibility is Δ_F, increasing the yield displacement from Δ_y to Δ'_y. If the design displacement Δ_D is strain-limited, then the design displacement also increases by essentially the same amount to Δ'_D. A small additional increase may result from the increased base shear resulting from the post-yield stiffness of the structural response causing additional rotation on the flexible base. In this case the displacement ductility demand is found to be

$$\mu = \frac{\Delta_D + \Delta_F}{\Delta_y + \Delta_F} \tag{6.41a}$$

If the design displacement is limited by a code specified maximum drift, then foundation flexibility will increase the yield displacement, but not the design displacement, and the design displacement ductility demand will be

$$\mu = \frac{\Delta_D}{\Delta_y + \Delta_F} \tag{6.41b}$$

In both cases, the design ductility demand will be less than for the equivalent rigid-base case, and hence the equivalent viscous damping will also generally be reduced.

(a) Structure   (b) Force-Displacement
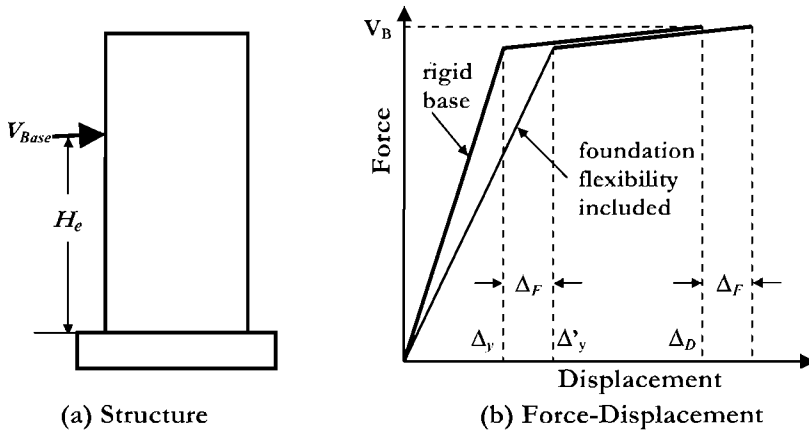
Fig.6.19 Influence of Foundation Flexibility on Design Displacement

However, as noted in Section 3.5.4(b) foundation deformation will generally also be accompanied by additional damping, ξ_F resulting from hysteretic soil response, and radiation damping. As shown in Section 3.5.4(b), this can be included in the **DDBD** procedure by using a system equivalent viscous damping of

$$\xi_e = \frac{\xi_F \Delta_F + \xi_S \Delta_S}{\Delta_F + \Delta_S} \qquad (6.42)$$

where ξ_S is the structural damping associated with the structural displacement ductility demand $\Delta_S/\Delta_y = (\Delta_D - \Delta_F)/\Delta_y$. Limited experimental evidence[2] supports foundation damping ratios in the range 0.05, for foundations responding without uplift, to 0.15 for foundations uplifting and reaching maximum overturning moment capacity.

6.5.2 Foundation Rotational Stiffness

Unless very massive foundation structures or support on piles with tension uplift capacity are provided, some uplift on the tension edge on the foundation/soil interface must be expected. This has a significant influence on the effective rotational stiffness of the foundation, which must be included when estimates are made of the foundation-induced displacement at the effective height.   Consider the wall foundation shown in Fig.6.20. The foundation has been sized to provide a static factor of safety against gravity loads of 6, and the soil is represented by elasto-plastic response with a soil deformation at yield of 25 mm (1 in). Under gravity loads the settlement is thus approximately 4 mm (0.16 in).

---

[2] pers. comm. R. Paolucci
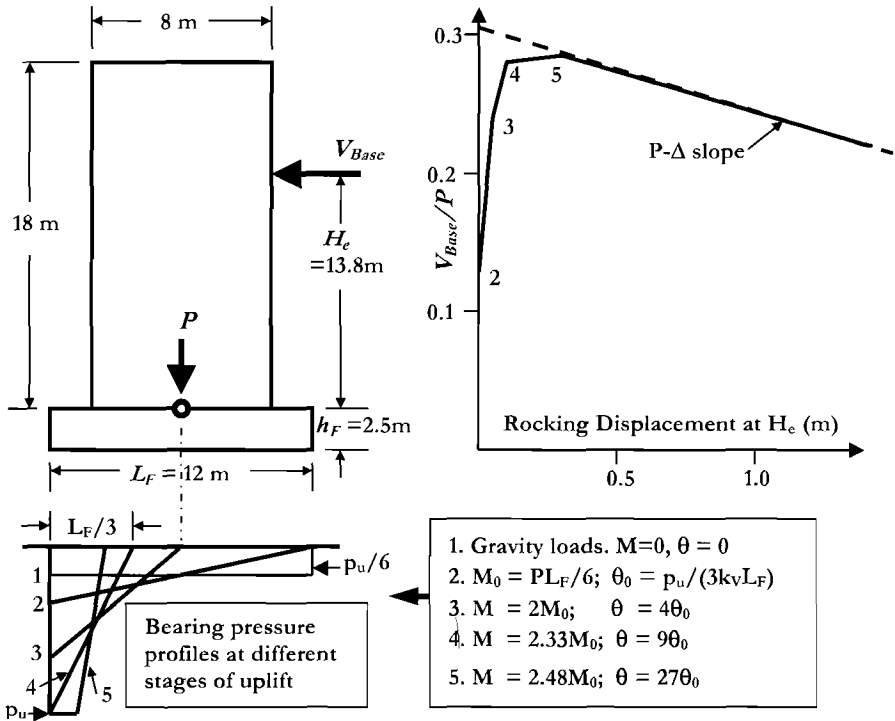
Fig.6.20 Foundation Compliance Effects for an Uplifting Spread Footing

The initial elastic rotational stiffness K_θ can be determined by imposing a unit rotation on the footing/soil interface resulting in

$$K_\theta = k_V \cdot \frac{B_F L_F^3}{12} = k_V I_\theta \qquad (6.43)$$

where k_V is the vertical subgrade modulus for the soil/foundation (kN/m³, or kips/in³), and B_F and L_F are the width and length of the footing/soil interface.

The foundation rotation due to a design base-shear force V_{Base} for an elastic foundation will thus be

$$\theta_F = V_{Base}(H_e + h_F) / K_\theta \qquad (6.44)$$

and the rotation-induced displacement at the effective height will be

$$\Delta_F = \theta_F \left(H_e + h_F\right) = V_B \left(H_e + h_F\right)^2 / K_\theta \qquad (6.45)$$

However, the above formulation applies for conditions where the footing remains in contact with the soil along the full length of the footing. This is unlikely to be the case in many spread footing designs, as it would require uneconomically large spread footings.

In fact, foundation rocking may be beneficial to structural response as additional damping is provided, and the displacements resulting from foundation rocking may reduce the structural displacement demand, and hence the damage potential.

Figure 6.20 includes bearing pressure profiles at different stages of uplift, numbered **2** to **5**. At profile **2** the footing has zero stress at the tension edge, corresponding to the limit for which Eqs.(6.43) to (6.45) apply. The peak bearing stress is twice the gravity load bearing stress. At profile **3** the footing has uplifted over 50% of the length, and the maximum bearing stress is twice that for profile **2** (i.e. four times gravity load bearing stress). The moment required to develop this profile is twice that for profile **2,** but the foundation rotation has increased by a factor of 4. The effective stiffness is thus only 50% of that given by Eq.(6.43).

At profile **4,** only $1/3^{rd}$ of the footing remains in contact with the soil, and the maximum compression stress is 6 times the gravity load value – equivalent to the ultimate bearing stress in this example. The moment is now 2.33 times that for profile 2, and the rotation is 9 times larger, indicating an effective (secant) stiffness that is only 26% of the fully elastic value. The footing can continue to rotate with small increase in moment capacity, by plastic deformation of the soil (profile **5**), with continual degradation of the effective stiffness. For the conditions represented in this example, the shear force/rocking displacement relationship has been included in the plot of Fig.6.20, which includes the bounding envelope resulting from **P-Δ** effects (see Section 3.6). Although the peak lateral force (at approximately 0.29P) seems large, it should be recalled that structural walls generally have substantially larger tributary areas for inertia force than for gravity load.

The recommendations for stability of cantilever walls (Section 6.1.3) suggested matching the ultimate overturning moment capacity of the foundation to the input corresponding to overstrength conditions at the base hinge. Assuming an overstrength factor of $\phi^o = 1.25$, this would imply that conditions at the design lateral forces would correspond almost exactly to profile **3** (uplift of 50% of the foundation length). This limit condition for design of spread footings is included in many design codes. It is apparent, then, that the appropriate stiffness to use for estimating foundation compliance effects is $0.5K_\theta$ where K_θ is given by Eq.(6.43).

It is of interest to investigate the significance of foundation flexibility for the typical example shown in Fig.6.20. Using standard **DDBD** procedures the effective height is found to be 13.8 m (45.3ft). Flexural reinforcement expected yield strength is $f_{ye} = 462$ MPa (67 ksi).

Structural yield: From Eq.(6.5): $\Delta_{yi} = \dfrac{0.00231}{8} \cdot 13.8^2 \left(1 - \dfrac{13.8}{3 \times 18}\right) = 40.9mm$ (1.61 in)

Foundation displacement: We assume that at design strength, the foundation uplift corresponds to profile **3**, as noted above. In this case we do not need information about

the soil stiffness or the base shear force. The maximum bearing stress is $0.67p_u$ and hence the maximum settlement is $0.67 \times 25mm = 16.75$ mm. The foundation rotation is hence $\theta_F = 0.01675/6 = 0.00279$ radians, and the displacement at the effective height is

$$\Delta_F = \theta_F \left(H_e + h_F \right) = 0.00279(13.8 + 2.5) = 45.5mm \quad (1.79 \text{ in})$$

Thus the displacement at the effective height, resulting from foundation compliance, is 10% larger than the structural component of yield displacement. The influence on design will be considerable.

6.6 CAPACITY DESIGN FOR CANTILEVER WALLS

The need for protection of locations and actions against unintended inelastic response has been emphasised already in different parts of this text (e.g. Sections 3.9, 4.5 and 5.8). In particular, the treatment of Section 3.9 used as an example a current, widely accepted approach for determining the required distribution of flexural and shear strength up cantilever walls to account for flexural overstrength at the wall-base plastic hinges, and for dynamic amplification resulting from higher-mode contributions to response.

It was noted in Section 5.8, in relation to capacity design of frames, that existing methods for capacity protection did not adequately account for the influence of ductility demand. Inelastic time-history analyses (ITHA) showed that when the intensity of excitation (and hence the system ductility demand) was increased, the influence of higher-mode effects in amplifying the envelopes of column flexure and shear also increased. Simple design equations were presented to represent this effect.

Investigations into the response of cantilever wall structures[P2] using ITHA has indicated similar, though more pronounced trends. In this study, six walls, from 2 storeys to 20 storeys were designed to a linear displacement spectrum with a corner period at 4.0 sec, and corner displacement of 0.594 m (23.4 in) for 5% damping. This corresponds to a PGA of 0.4g, and medium soil conditions.

The walls (see Fig.6.21) all had the same tributary floor mass of 60 tonnes, and gravity load of 200 kN at each level, and were designed in accordance with DDBD design principles to achieve maximum drifts of about 0.02 at roof level. Wall lengths (l_w), widths (b), reinforcement contents (ρ_l) and bar sizes (d_b) varied from wall to wall in order to satisfy the design displacement criteria. Details are listed in Table 6.4, which also includes the calculated plastic hinge length (L_P), the expected displacement and curvature ductility demands (μ_Δ, μ_ϕ), the effective period at maximum displacement $(T_e,$ approximately equal to $T_{el} \cdot \sqrt{\mu_\Delta}$), and design base shear force and bending moment $(V_{Base},$ and $M_{Base})$.

Note that limiting the drift to 0.02 results in displacement ductility demands that are less than typical code limits of $\mu_\Delta = 5$ in all but the two-storey wall. The six designs were subjected to time-history analysis using a suite of five spectrum-compatible earthquake records. These records were intensity-scaled to 50%, 100%, 150% and 200% of the

design intensity to investigate the sensitivity of the results to intensity, and hence to displacement ductility demand.
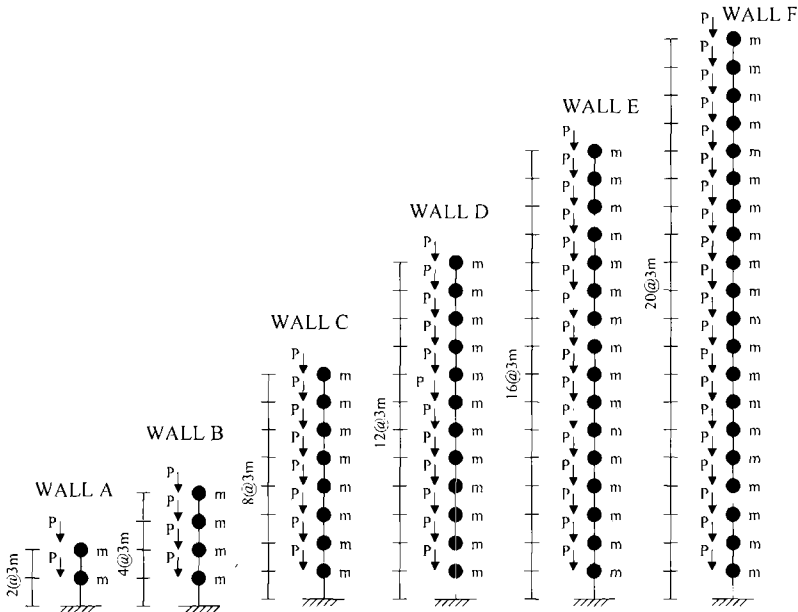
Fig.6.21 Idealization of Cantilever walls in Capacity Design Study[P2]

Table 6.4 Wall Details for Capacity Design Study

Wall	b (m)	l_w (m)	ρ_l	d_b (mm)	l_p (m)	μ_Δ	μ_ϕ	T_e (sec)	V_b (kN)	M_b (kNm)
A	0.20	2.0	0.0046	14	0.58	6.4	20.6	1.2	242	1232
B	0.20	2.5	0.0080	14	0.86	3.4	12.6	1.8	312	2917
C	0.20	3.3	0.0162	20	1.49	1.9	6.0	2.6	446	8114
D	0.25	4.0	0.0172	28	2.22	1.3	2.7	3.1	590	16222
E	0.25	5.0	0.0161	24	2.83	1.2	2.2	3.7	664	24372
F	0.30	5.6	0.0177	28	3.52	1.0	1.0	3.9	830	38739

Averaged results from the **ITHA** are presented in Figs. 6.22 and 6.23 for moment and shear envelopes respectively, and compared with values based on two different current design approaches. The first design approach is the procedure represented in Fig.3.28, and adopted in several design codes[X1,X3], and the second is a modal superposition approach, also commonly specified in design codes, where the design envelopes for shear and moment are determined from an elastic modal superposition using the elastic acceleration spectrum, with the results then divided by the design displacement ductility demand. In Figs.6.22 and 6.23, these alternative approaches are identified as **Cap.Des** and **SSRS/μ** respectively. Note that the **SSRS** method of modal

combination was used in the latter case, but identical results would have been found from the more rigorous **CQC** method since the modes were well-separated. In these figures "**IR**" indicates the intensity factor applied to the standard spectrum-compatible records. Thus "**IR** = 1.5" indicates 150% of the design intensity, and so on. The results, for both **ITHA** and design methods include only the dynamic amplification, since material overstrength was not included in the analyses, except for the proportion of overstrength resulting from reinforcement strain-hardening.

Referring first to Fig.6.22, we see that the time-history analysis results indicate only small increases in wall base bending moment with increasing intensity, as expected, since the increase, once the nominal moment capacity has been reached is only the result of the post-yield stiffness of the moment-curvature characteristic at the wall base. However, at levels above the base, and particularly at wall mid-height, moments increase very significantly with increasing intensity, especially for the eight- to twenty-storey walls. It is apparent that both existing design procedures are non-conservative at the design intensity, (**IR** = 1.0) and increasingly so at higher intensities. For the two- to eight-storey walls, where the design displacement ductility exceeds 2 (see Table 6.4), the multi-modal moment envelope is non-conservative even at 50% of the design intensity.

In Fig.6.23 it is again seen that the time-history shear force envelopes are strongly influenced by seismic intensity, (and hence by ductility level), and that both the capacity design and multi-modal design envelope are significantly non-conservative. For the two-, four-, and eight-storey walls, the time-history base shear force at **IR**=1 is almost twice the multi-modal value, with a slightly smaller discrepancy for the capacity design envelope, and for these three walls, the shear profiles at **IR**=0.5 exceed the design profile at all heights. At intensity ratios of **IR**=2, base shear force is between 2.5 and 3.7 times the multi-modal design envelope. For the taller walls the **SSRS/μ** envelope exceeds the capacity design envelope, and thus the discrepancy from the capacity design value is even higher.

The discrepancies between the capacity design and time-history shear forces are more problematic than the corresponding moment discrepancies of Fig.6.22. Although un-intentional plastic hinging (which could be the consequence of designing to either the **Cap.Des** or **SSRS/μ** capacity moment envelopes of Fig.6.22) at levels above the base is undesirable, some limited ductility demand should be sustainable without failure. However, the consequences of the imposed shear demand exceeding the shear capacity, by such large margins, could be catastrophic shear failure.

6.6.1 Modified Modal Superposition (MMS) for Design Forces in Cantilever Walls

Examination of Fig.6.23 indicates that at an intensity ratio of **IR**=0.5, where ductility demand is low, or non-existent for all walls, the shape of the shear force envelope is well predicted by the modal analysis procedure. This suggests that it might be possible to predict the shear force and moment envelopes by simple modification of the modal response spectrum (**SSRS/μ**) approach.
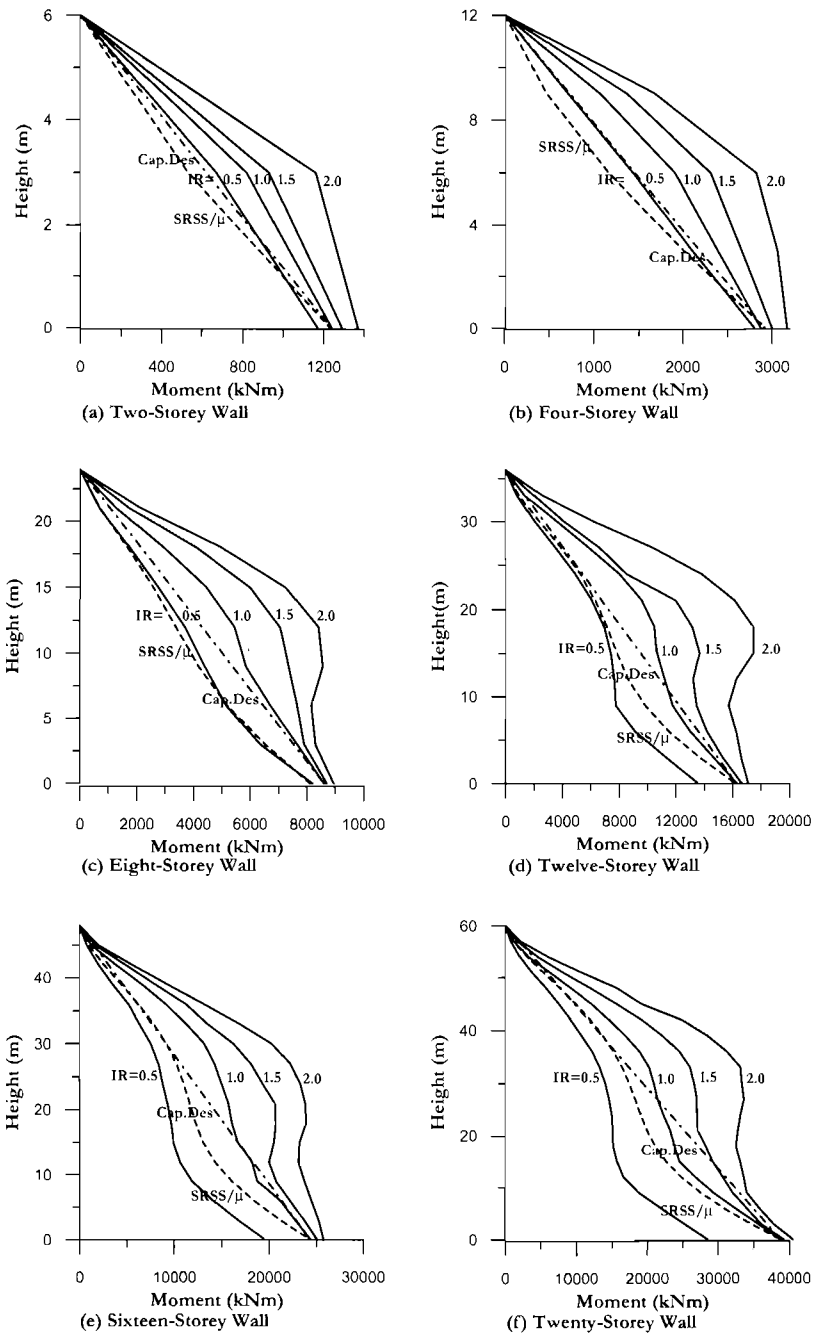
Fig.6.22   Comparison of Capacity Design Moment Envelopes with Results of
Time-History Analyses for Different Seismic Intensity Ratios[P2]
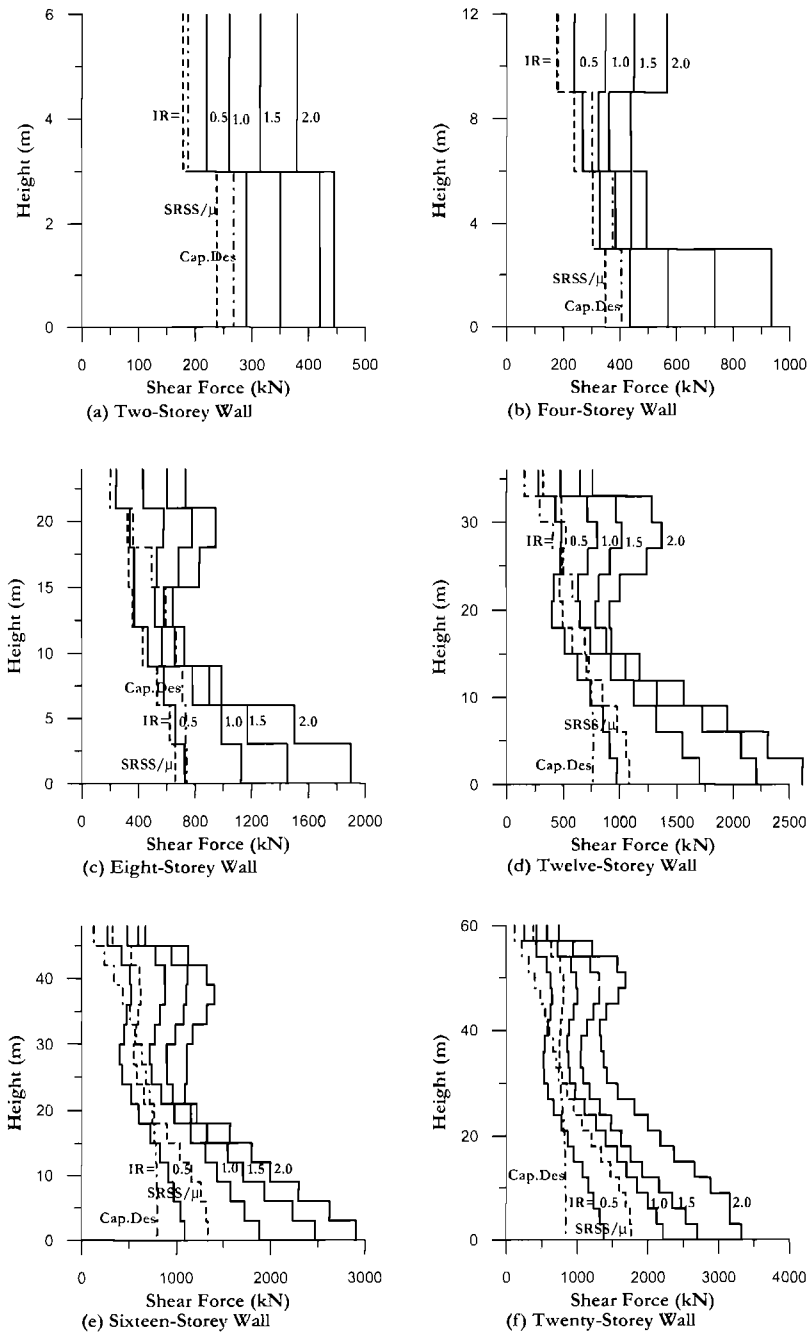
Fig.6.23 Comparison of Capacity Design Shear Force Envelopes with Results of Time-History Analyses for Different Seismic Intensity Ratios[P2]

A basic and simple modification to the modal superposition method is available by recognizing that ductility primarily acts to limit first-mode response, but has comparatively little effect in modifying the response in higher modes. If this were to in fact be the case, then first-mode response would be independent of intensity, provided that the intensity was sufficient to develop the base moment capacity, while higher modes would be directly proportional to intensity. This approach is very similar to that proposed by Eibl and Keintzel[F2] as a means for predicting shear demand at the base of cantilever walls.

This modified modal superposition approach is clearly an approximation to response. Although the first-mode inelastic shape is very similar to the elastic shape, and hence the approximation should be reasonably valid for the first mode, it is clear that the higher modes will be modified to some extent by the first-mode ductility, since a basic feature of the modified higher modes will be that, when acting together with ductility in the first mode, they cannot increase the base moment demand, which will be anchored by the moment capacity of the base plastic hinge. The approach suggested below extends the basic method of Eibl and Kreintzel for shear forces to the full height of the wall, and also provides a method for determining the appropriate capacity-design moment envelope. Modifications to this approach are discussed in relation to dual wall/frame structures in Chapter 7, and to bridges in Chapter 10. A brief discussion of possible further improvements in included in Section 6.6.1.(c).

(a) Shear Force Profiles: To investigate the appropriateness of a simple approach based on the above arguments, shear force profiles were calculated based on the following assumptions.

- First-mode shear force was equal to the shear profile corresponding to development of the base moment capacity, using the displacement-based design force vector. However, for low seismic intensity, where plastic hinging was not anticipated in the wall, simple elastic first mode response, in accordance with the elastic response spectrum was assumed.
- Higher-mode response was based on elastic response to the acceleration spectrum appropriate to the level of seismic intensity assumed, using the elastic higher-mode periods. Force-reduction factors were not applied.
- The basic equation to determine the shear profile was thus:

$$V_{MMS,i} = \left(V_{1D,i}^2 + V_{2E,i}^2 + V_{3E,i}^2 + ...\right)^{0.5}$$

(6.46)

where $V_{MMS,i}$ is the shear at level i, $V_{1D,i}$ is the lesser of elastic first mode, or ductile (**DDBD** value) first-mode response at level i, and V_{2Ei}, and V_{3Ei} etc are the elastic modal shears at level i for modes 2, 3 etc. Predictions for shear force profiles based on this equation are included in Fig.6.25.

(b) Moment profiles: A simple modal combination, similar to that of Eq.(6.46), but multiplied by a factor of 1.1, over the top half of the wall, with a linear profile from mid-

height to the moment capacity at the base of the wall was found to provide best results for moment profiles (see Fig.6.24). The combination equation over the top half of the wall is thus:

$$M_{MMS,i} = 1.1(M_{1D,i}^2 + M_{2E,i}^2 + M_{3E,i}^2 + ...)^{0.5}$$ (6.47)

where $M_{MMS,i}$ is the moment at level i, $M_{1D,i}$ is the lesser of the elastic first mode moment and the ductile design moment, and $M_{2E,i}$ and $M_{3E,i}$ etc are the elastic modal moments at level i for modes 2, 3 etc.

It is seen that the **MMS** approach provides a good representation of the time-history moment profiles in Fig.6.24 at the design intensity (IR=1.0), for all walls. There is a tendency for the **MMS** predictions to be slightly unconservative for the shorter walls, and slightly conservative for the taller walls, though the discrepancies are generally small. The change in shape of the moment profiles with increasing intensity is also well represented by the **MMS** predictions. As discussed above, slight unconservatism in the moment profiles is acceptable, as it implies only limited ductility demand, and there is a case for deleting the 1.1 factor in Eq.6.47.

Similar behaviour is apparent for the shear force comparisons of Fig.6.25. At the design intensity the agreement between the **MMS** and **THA** profiles is extremely close for the four- to twenty-storey walls, and is adequate, though a little unconservative for the two-storey wall. Similar conclusions apply at different intensity levels, though the **MMS** approach becomes increasingly conservative for the taller walls at high intensity ratios.

(c) Effective Modal Superposition: As noted in Chapter 10 with relation to capacity design of bridges, a simple and philosophically attractive (from a **DDBD** viewpoint) further modification to the **MMS** approach is to carry out the modal analyses using **effective** stiffness of members at maximum displacement response, as is used in the design process. Thus, for a cantilever wall, the stiffness of the first storey would be reduced in proportion to the displacement ductility demand when defining the structure for modal analysis. With this modification, the approach is identical to that presented in the previous section.

6.6.2 Simplified Capacity Design for Cantilever Walls.

In many cases the additional analytical effort required to carry out modal analysis of the designed wall structure to determine the capacity design distribution of moments and shears will be unwarranted, and a simpler, conservative approach may be preferred. The following approach, based on the data presented herein, is suggested.

The results for both moment and shear-force envelopes indicate that dynamic amplification increases as the intensity ratio increases. This would indicate that displacement ductility demand should be included in the design equation. Also, it would appear obvious that the number of storeys, which has been used in the past as a key
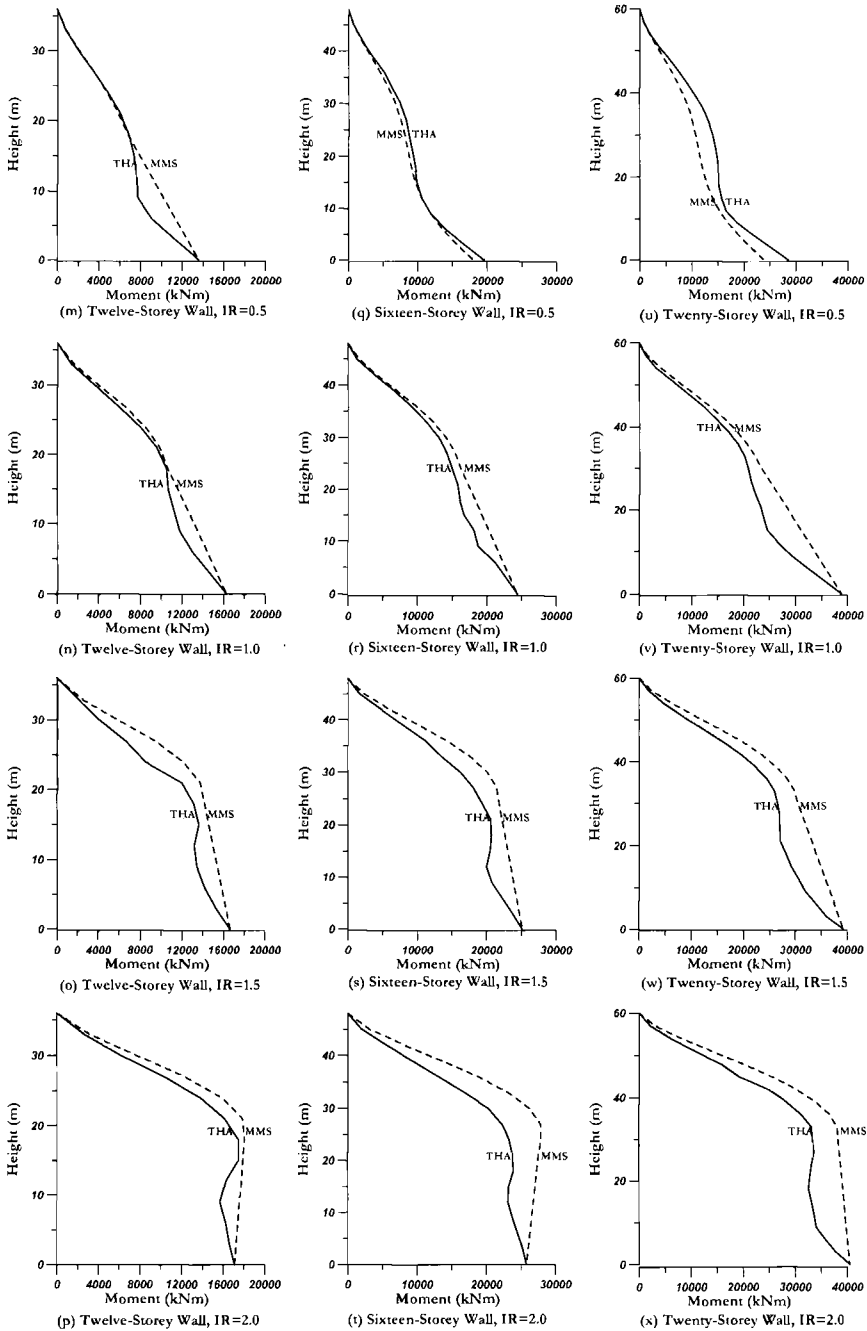
Fig.6.24   Comparison of Modified Modal Superposition (MMS) Moment Envelopes with ITHA results, for Different Seismic Intensities
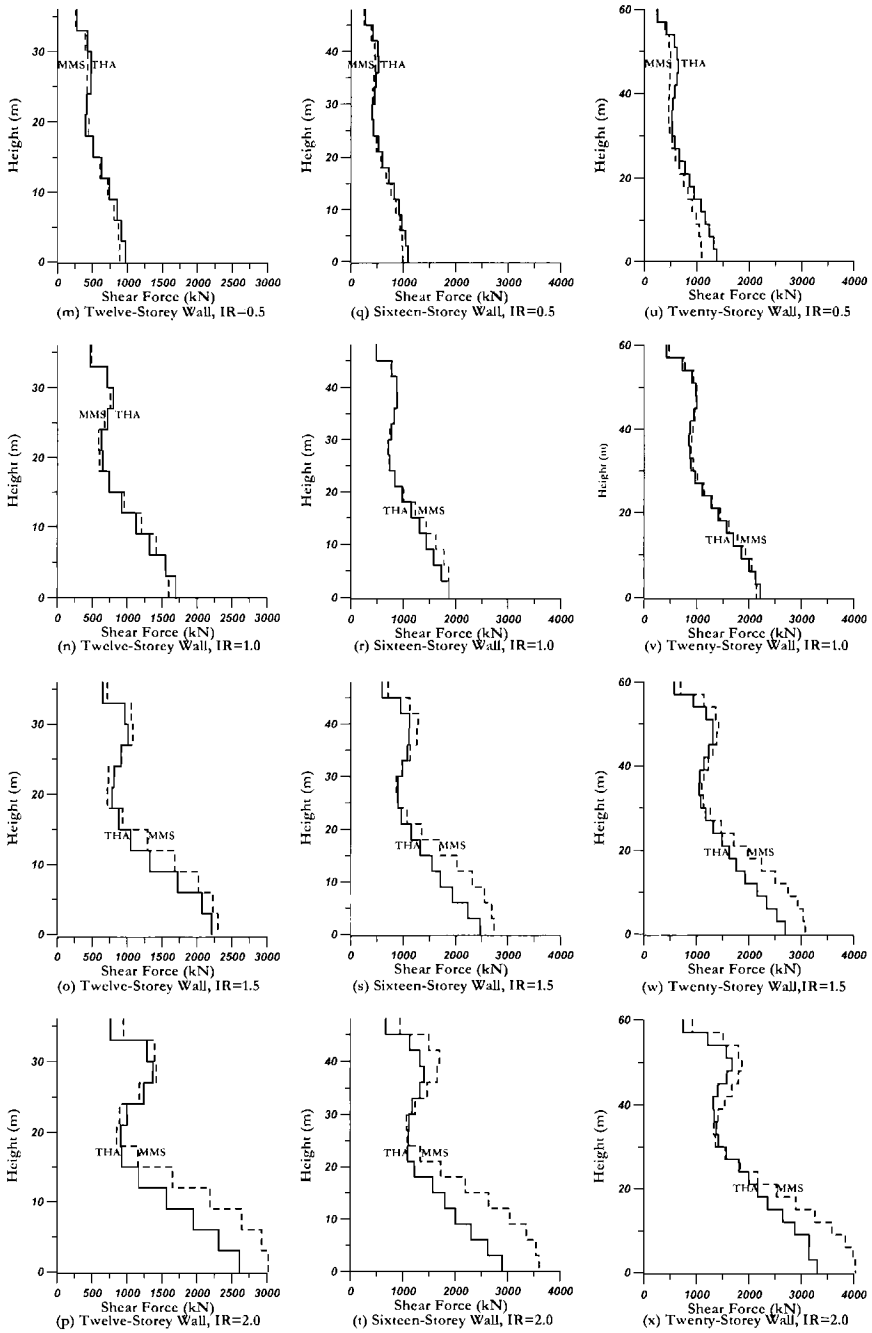
Fig.6.25 Comparison of Modified Modal Superposition (MMS) Shear Force Envelopes with ITHA Results, for Different Seismic Intensities

parameter for capacity design (see Eq.(3.62), e.g.) should be less significant than the fundamental elastic period T_i of the wall. This leads to the following recommendations:

(a) Moment Capacity-Design Envelope: A bilinear envelope is defined by the overstrength base moment capacity $\phi^o M_B$, the mid-height overstrength moment $M^o{}_{0.5H}$, and zero moment at the wall top, as illustrated in Fig.6.26(a) for a four-storey wall. The overstrength base moment is determined from section and reinforcement properties, as suggested in Section 4.5. The mid-height moment is related to the overstrength base moment by the equation:

$$M^o_{0.5Hn} = C_{1,T} \cdot \phi^o M_B, \quad \text{where} \quad C_{1,T} = 0.4 + 0.075 T_i \left(\frac{\mu}{\phi^o} - 1 \right) \geq 0.4 \quad (6.48)$$

(a) Moment Capacity Envelope   (b) Shear Force Capacity Envelope
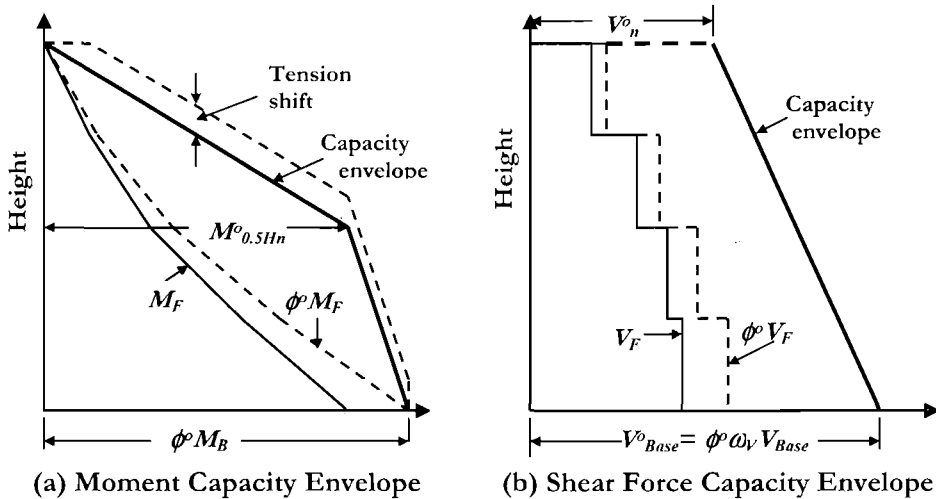
Fig. 6.26 Simplified Capacity Design Envelopes for Cantilever Walls

Note that μ/ϕ^o is the effective displacement ductility factor at overstrength, and that tension shift effects should be considered when terminating flexural reinforcement. Tension shift, resulting from inclined flexure/shear (diagonal tension) cracking results in flexural reinforcement stress at a given level being related to the moment at a level closer to the wall base. In effect, this "shifts" the design moment profile upwards, as suggested by the upper dashed line in Fig.6.26(a). The tension shift depends on wall length and the amount of transverse reinforcement provided, but it is reasonably conservative to assume a tension shift equal to $l_W/2$, where l_W is the wall length. A complete discussion of tension shift is available in [P1].

(b) Shear Force Capacity-Design Envelope: The shear force capacity envelope is defined by a straight line between the base and top of the wall, as indicated in Fig.6.26(b).

The capacity-design base shear force is related to the **DDBD** base shear force by:

$$V_{Base}^o = \phi^o \omega_V V_{Base}.$$ (6.49)

where $\omega_V = 1 + \dfrac{\mu}{\phi^o} C_{2,T}$ and $C_{2,T} = 0.067 + 0.4(T_i - 0.5) \leq 1.15$ (6.50)

The design shear force at the top of the wall, V_n^o is related to the shear at the bottom of the wall by:

$$V_n^o = C_3 V_{Base}^o \quad \text{where} \quad C_3 = 0.9 - 0.3T_i \geq 0.3$$ (6.51)

In Eqs.(6.48), (6.50) and (6.51), T_i is the elastic fundamental period.

Predictions for the ratio of wall moment at mid-height to base moment, and dynamic amplification factor for base shear force are compared with values obtained in the **ITHA** for different elastic periods and ductility levels in Fig.6.27.
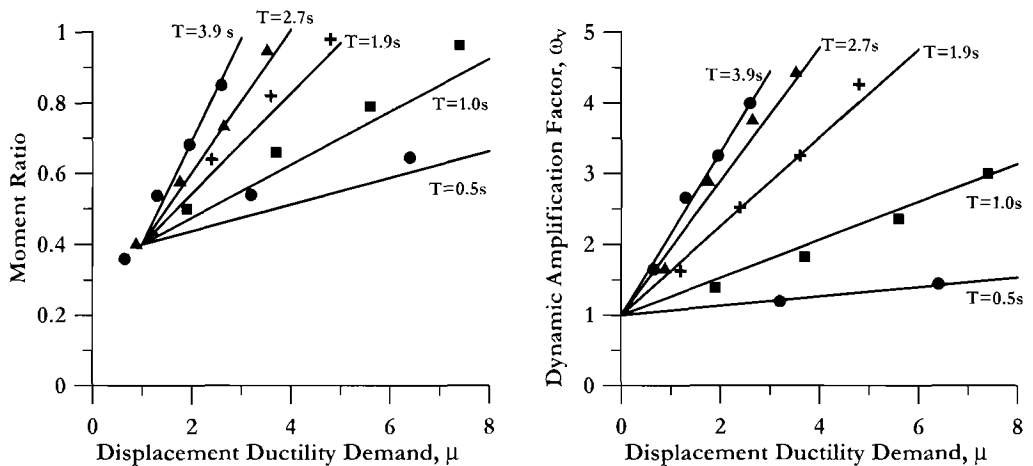
(a) **Ratio of Midheight to Base Moment**   (b) **Base Shear Dynamic Amplification**

Fig.6.27   Comparison of Capacity Design Equations (6.48) and (6.50) with Time History Results for Different Elastic Periods and Ductility Levels

In Fig.6.27, the results from the **ITHA** are shown by solid data points, with the same symbol used for all different ductility levels (i.e. different seismic intensities) for a given wall. Predictions by the equations are shown as continuous lines. Agreement is good for both mid-height moment ratio and base shear force. The slightly unconservative nature of the wall mid-height moment ratio prediction has been deliberately imposed since minor inelastic response at levels above the base is acceptable. However, it should be

noted that since nominal flexural strength will be matched to the capacity envelope, and since inelastic response occurs at moments lower than the nominal moment of the bilinear moment-curvature approximation (see Fig.4.6(a), e.g.), the inelastic response may in some cases be significant.

(c) Strength Reduction Factors for Capacity Design: When determining the required amount of transverse reinforcement for shear strength, a strength reduction factor of ϕ_V = 0.85 should be used, together with conservative estimates of material strength, as discussed in Section 4.5. However, with flexural strength this may not be practicable, nor necessary. Since moment demand may reduce only slowly up the wall, designing for conservative material strengths together with a flexural strength reduction factor can mean that flexural reinforcement content is required to **increase** at levels above the base, particularly when it is remembered that axial load, which contributes to flexural strength of walls will decrease with height. Recognizing, again, that the consequences of minor inelastic flexural action at levels above the base are acceptable, we recommend that flexural reinforcement areas at levels above the base be determined using the same expected material strengths used to design the wall base, without inclusion of a flexural strength reduction factor. This is of course reasonable, as the flexural reinforcement at the base is likely to extend, with uniform strength for a considerable height above the base (note that use of short starter bars with lapping of flexural reinforcement at the wall base is undesirable, as the strength of lap-splices tends to degrade under repeated load reversals, and the plastic hinge length is condensed below levels implied by Eq.(6.7)).

(d) Overstrength factors for Capacity Design: A consequence of the argument presented in the previous section is that the flexural overstrength factor adopted in Eq.(6.48) should only include the component resulting from strain-hardening, and not from excess yield strength. Since strain-hardening will normally be included in the **DDBD** process for determining required flexural reinforcement at the wall base, this implies that ϕ^o = 1.0 for flexural design. If strain-hardening is ignored in determining required base flexural reinforcement content, a value of ϕ^o = 1.2 should be adopted, as implied by Section 4.5.2

For shear design, the value of ϕ^o should include allowance for material overstrength, strain-hardening, and excess flexural reinforcement over that required to provide the design strength, if provided, and should normally be determined by moment-curvature analysis. If not, the values recommended in Section 4.5.2 should be adopted.

(e) Design Example 6.2: Capacity Design of a Wall Building: The capacity design moments and shear forces for the walls of Design Example 6.1 (Section 6.4.6) are to be determined using the simplified approach of Section 6.6.2. Note that moments and shears for the walls corresponding to the distributed base shear force are already included in Table 6.3.

Capacity Moments: Using the recommendations in Section 6.6.2(d) the over-strength factor to be used in Eq.(6.48) is taken as $\phi^o = 1.0$. From Section 6.4.7 the design system ductility was found to be $\mu_{sys} = 5.0$. Equation (6.48) requires the initial (elastic) period T_i to be calculated. This can be estimated from the effective period T_e using the relationship:

$$\frac{T_i}{T_e} = \sqrt{\frac{1 + r(\mu_{sys} - 1)}{\mu_{sys}}} \tag{6.52}$$

where r is the ratio of post-yield to elastic stiffness (refer Fig.3.1, e.g.). Taking a typical value of $r = 0.05$, and the effective period of $T_e = 1.97$ sec, the initial period is found to be $T_i = 0.975$ sec.

The mid-height moments are found from Eq.(6.48) as follows:

Coefficient C_1: $C_{1,T} = 0.4 + 0.075 T_i (\mu / 1 - 1) = 0.4 + 0.075 \times 0.975 \times 4 = 0.693$

8 m Wall: $M^o_{0.5H} = C_{1,T} \phi^o M_B = 0.693 \times 1 \times 25100 = 17400 kNm$ (153,000 kip in)

4 m Wall: $M^o_{0.5H} = 0.693 \times 16300 = 11300 kNm$ (100,000 kip.in)

The corresponding design overstrength moments are listed as M^o in Table 6.5, together with the moments M_i corresponding to the distributed base shear force from Table 6.3. Note that when designing the reinforcement content for each wall, tension shift should be applied to the moments of Table 6.5 in accordance with the recommendations of Section 6.6.2(a).

Capacity Shear Forces: Moment-curvature analyses using the maximum feasible yield strength of the reinforcement of $f_y^o = 1.3 f_y = 546 MPa$ (79.2 ksi) show that at the design curvatures (see Example 6.1) the overstrength factors for both walls are $\phi^o = 1.09$.

Wall Base: From Eq.(6.50): $C_{2,T} = 0.067 + 0.4(T_i - 0.5) = 0.067 + 0.4 \times 0.475 = 0.257$

and $\omega_V = 1 + (\mu / \phi^o) C_{2,T} = 1 + (5/1.09)0.257 = 2.18$

Hence from Eq.(6.49):

8 m Wall: $V^o_{Base} = \phi^o \omega_V V_{Base,F} = 1.09 \times 2.18 \times 2040 = 4847 kN$ (1089 kips)

4 m Wall: $V^o_{Base} = \phi^o \omega_V V_{Base,F} = 1.09 \times 2.18 \times 1316 = 3127 kN$ (703 kips)

Wall Top: The wall top shear force is related to the wall base shear force by Eq.(6.51), where $C_3 = 0.9 - 0.3 T_i \geq 0.3 = 0.9 - 0.3 \times 0.975 = 0.608$. Thus:

8 m Wall: $V^o_n = C_3 V^o_{Base} = 0.608 \times 4847 = 2944 kN$ (662 kips)

4 m Wall: $V^o_n = C_3 V^o_{Base} = 0.608 \times 3127 = 1901 kN$ (427 kips)

The corresponding design shear forces are listed as V^o in Table 6.5, together with the shears, V_i, from distribution of the design base shear force from Table 6.3.

Table 6.5   Capacity Moment Shears and Moments for Walls of Examples 6.1 and 6.2.

Floor	Height (m)	Wall 1 V_i (kN)	Wall 1 V^o (kN)	Wall 1 M_i (kNm)	Wall 1 M^o (kNm)	Wall 2 V_i (kN)	Wall 2 V^o (kN)	Wall 2 M_i (kNm)	Wall 2 M^o (kNm)
6	16.8	606	2940	0	0	400	1900	0	0
5	14	1100	3260	1700	5700	724	2105	1121	3770
4	11.2	1490	3580	4780	11300	974	2310	3150	7540
3	8.4	1770	3900	8960	17400	1152	2510	5880	11300
2	5.6	1950	4210	13920	19900	1264	2720	9100	12900
1	2.8	2040	4530	19390	22500	1316	2920	12640	14600
0	0	2040	4850	25100	25100	1316	3130	16330	16300

6.7 PRECAST PRESTRESSED WALLS

In Section 5.11.3 the concept was introduced of providing flexural strength and energy dissipation to precast concrete frames by prestressing beams through the columns with unbonded post-tensioned tendons, supplemented by bonded mild-steel reinforcement grouted into ducts passing through the column and into the beams on either side (so-called "hybrid" design). It is obvious that the concept of unbonded prestressing can also be applied to precast wall buildings. Fig. 6.28 shows two possible applications. In the first (Fig.6.28(a)), wall elements are stacked vertically and post-tensioned to a foundation. This essentially creates a structural system that behaves in the same way as a prestressed beam-to-column connection. A single crack can be expected to form at the critical section at the wall base, and will have non-linear elastic force-deformation characteristics. Note, however, that the footing must be of sufficient size and weight to ensure that rocking does not develop at the soil/footing interface. Note also that the gravity weight contributes to the flexural resistance of the wall base in exactly the same way as does the prestressing.

Figure 6.28(a) also shows additional mild steel bars running through the wall/footing interface. The normal way this would be achieved would be with bars cast into, and protruding below the lowest precast wall element, grouted into preformed holes in the foundation. These mild-steel bars are expected to yield in tension and compression as the base crack forms, in much the same fashion as conventional reinforcement. Since the gap opening at the wall base can be large, it is normal to de-bond the mild steel bars for some length into the precast panel, to ensure strains at maximum displacement response are kept to acceptable limits – normally less than 3%.

Provided that the combined axial force at the wall base resulting from gravity weight and prestressing exceeds the compression yield force of all the mild steel bars crossing the base interface, the residual displacements at zero lateral force will always be zero. In this case the mild steel bars provide additional strength and damping to the bilinear elastic response, resulting in the "flag-shaped" hysteresis loops of Figs.4.33 and 5.36. Wall designs using this concept have been tested[H7] with excellent results.

(a) Single Wall   (b) Linked Walls
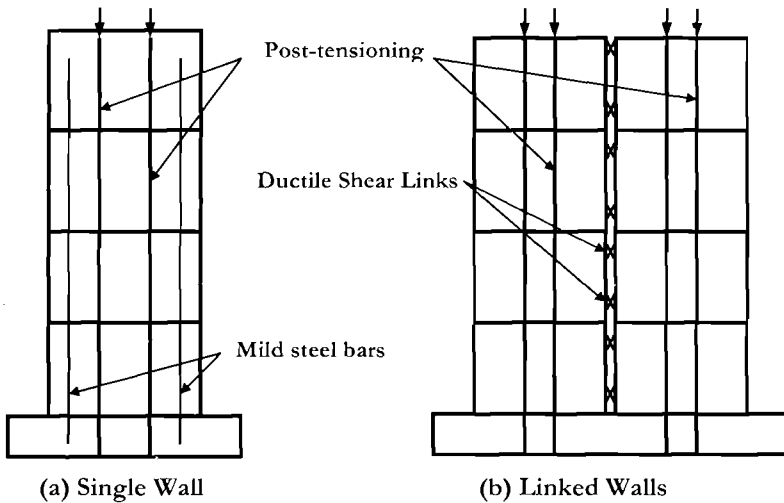
Fig.6.28 Precast Post-Tensioned Walls

An alternative configuration, also providing additional damping, is illustrated in Fig.6.28(b). Two parallel in-line precast walls are separately prestressed to the same foundation structure, and are linked by ductile shear links. Under lateral force, each wall rocks about its compression toe, resulting in relative vertical deformation across the shear links which act as miniature coupling beams (see Section 6.8). If these are designed to have low yield displacements, considerable energy can be dissipated, and at the same time the overturning capacity of the complete system of two walls is enhanced above the sum of the capacities of the individual walls.

This system was adopted for the PRESSS five-story test building described in Section 5.11[P8,P19]. A photo showing the linked walls during construction of the test building is shown in Fig.6.29. Performance under simulated seismic loading was extremely satisfactory, with only superficial damage, characteristic of the serviceability limit state being observed under a level of seismic intensity equivalent to 150% of the Level 2 (damage-control) earthquake.

Design of precast post-tensioned walls closely follows the methodology introduced in Section 5.11. However, since the design deformation is dominated by the single crack at the base of the wall, the design displacement profile at the damage-control limit state may reasonably be assumed to be linear. Designs will always be governed by the code drift limits. Yield displacements can be based on the stiffness of the un-cracked wall sections up the full height, and effective damping levels for walls without supplemental damping can be assumed to be 5%, related to the effective stiffness. For systems with a portion of the flexural strength provided by added mild-steel reinforcement, or by shear links, the effective damping can be determined from the equation for flag-shaped hysteresis, in Section 5.11.3(c) (Eq.(5.72)).
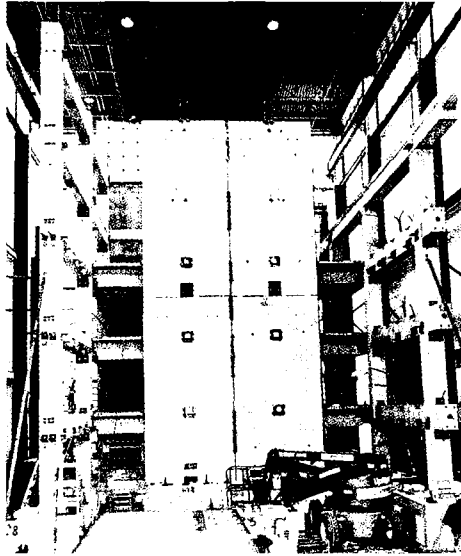
Fig.6.29   Precast Post-tensioned Wall Panels During Construction of the PRESSS Five-Storey Precast Building Test[P19].

6.8   COUPLED STRUCTURAL WALLS

6.8.1   General Characteristics

As already noted in Section 6.1.2, coupled structural walls form an efficient structural mechanism for resisting seismic actions. Since plastic hinges are intended to form not only at the bases of the walls but also at both ends of the coupling beams, energy dissipation is distributed over a more extensive region of the structure with the result being higher equivalent viscous damping than is the case with linked cantilever walls.

The general characteristics of coupled walls are described by reference to Figs.6.30 and 6.31. Coupled walls typically occur in the configuration suggested in Fig.30(a) where two symmetrically opposed channel-shaped walls enclosing service facilities such as elevators, stairs and toilets are linked at floor levels by beams. Typically these beams have low aspect ratios L_{CB}/h_{CB}, (see Fig.6.30(c)) and hence are susceptible to shear effects which must be carefully considered in the design, as discussed subsequently. In Fig.6.30 the service core is shown centrally located in the floor plan, but it is not uncommon for service cores to be constructed hard against a boundary to maximize free floor space. In this case torsional effects become critical and must be considered using the techniques described in Section 6.4. The structural system, excluding the coupled walls, may consist of structural beam/column frames connected to the service core by beams, in which case the seismic response is more complex since the lateral seismic forces are carried partly by the frames and partly by the coupled walls. The behaviour of dual wall/frame buildings is

(a) Floor Plan

(b) Walls Detail   (c) Coupling Beams
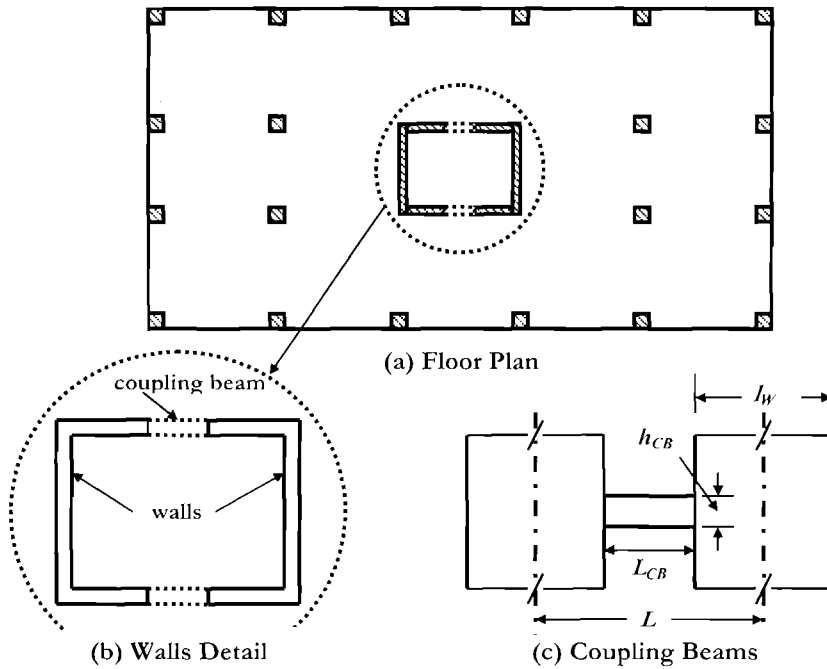
Fig.6.30 Structural Layout of a Coupled-Wall Building

considered in Chapter 7. More commonly the additional structural system will consist of flat-slab floors supported on prop columns, with little effect on the seismic response.

A typical elevation of a coupled-wall building is shown in Fig.6.31(a), where the additional structural system for gravity-load support consists of columns and slab. Lateral forces are resisted by two mechanisms: **1)** Bending moments are developed in the coupling beams which induce axial forces in the walls in exactly the same fashion as described for frames in Section 5.5.2. This results in a couple of seismic forces at the wall axes resisting a part of the overturning moment *(M_OTM)*, and **2)** The individual walls resist a portion of the base **OTM** by flexural action. The equations developed in Section 5.5.2 apply directly to this case, and are combined together in Eq.(6.53):

$$M_{OTM} = \sum_{i=1}^{n} F_i H_i = M_{W1} + M_{W2} + TL = M_{W1} + M_{W2} + \sum_{i=1}^{n} V_{CBi} L \qquad (6.53)$$

where V_{CBi} are the seismic shear forces in the coupling beams, L is the distance between wall centrelines and M_{W1} and M_{W2} are the base moments in walls 1 and 2 respectively, including the effects of the seismic axial forces T.
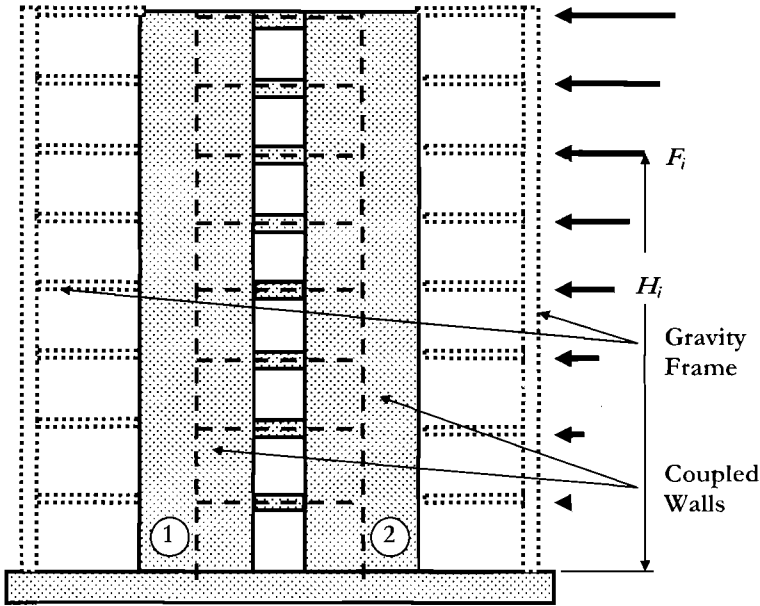
(a) Structure and Lateral Forces

(b) Overturning Moment (c)Coupling-Beam Moment (d)Wall Moments (Sum)
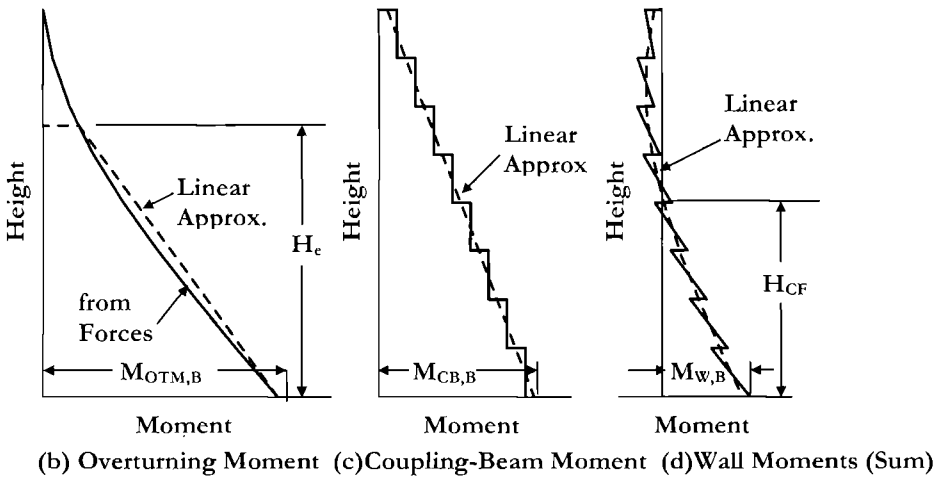
Fig.6.31 Elevation and Moment Profiles for Coupled Walls

The coupling beams modify the structural response not only by increasing the overturning capacity, and hence the base shear strength, but also by reducing the displacements of the structural system at nominal yield. The degree of coupling, and its influence on response is normally quantified by the ratio of the base moment $M_{CB,B}$

provided by the coupling beams to the total **OTM**. Hence

$$\beta_{CB} = M_{CB,B} / M_{OTM} = (\sum_{i=1}^{n} V_{CBi})L / M_{OTM} \tag{6.54}$$

The moment components for seismic response are illustrated in Fig.6.31(b) to (d). The total cantilever overturning moment $\Sigma F_i H_i$ is shown in Fig.6.31(b). The profile of moment resistance provided by the coupling beams is shown in Fig.6.31(c) and the sum of the moments provided by the two walls, found by subtracting Fig.6.31(c) from 6.31(b) is shown in Fig.6.31(d).

In the past, using initial stiffness force-based design, the value for β_{CB} has been based on elastic analysis. Paulay[P27] has shown, however, that elastic analysis is not a logical process for determining the distribution of forces in coupled walls, since most, if not all, of the coupling beams will yield at a fraction of the lateral base shear at which the walls yield. Paulay has suggested that the distribution of strength between the two mechanisms resisting lateral force, as described above, should be a designer's choice, and should not be dictated by the largely irrelevant initial stiffness of the coupling beams and walls. It will be noted that this approach agrees well with the **DDBD** principles developed in previous chapters. The actual value of β_{CB} adopted for design will normally be in the range 0.25 to 0.75, and will be chosen such that wall reinforcement ratios are within acceptable bounds. A further consideration is that the value of β_{CB} should not be so large that the shear forces in the coupling beams induce a tension force at the wall base that exceeds the gravity load. Note that even when coupling between walls is only by slabs, the influence on response can still be considerable, particularly for small buildings, and should be considered in the design process. With slab coupling, the value of β_{CB} will not normally be a design choice, but a consequence of slab reinforcement provided for gravity loads.

Paulay also suggested that the vertical distribution of coupling beam strength should also be a designer's choice, and that the rational choice will normally be to make the strength of all coupling beams equal. Thus, for a building of n storeys, the shear to be carried by each coupling beam will be

$$V_{CB,i} = \frac{\beta_{CB} M_{OTM}}{nL} \tag{6.55}$$

Assuming equal moment capacities at each end of the coupling beams, the required flexural strength is

$$M_{CB,i} = 0.5 V_{CB,i} L_{CB} \tag{6.56}$$

It will be shown shortly that the ductility demands on coupling beams will often be very large, and difficult to accommodate with conventional flexural reinforcement. The use of diagonal reinforcement for coupling beams, also pioneered by Paulay[P28], is more appropriate.

The design approach suggested by Paulay[P27] for coupled structural walls is well suited to **DDBD**, and is presented in the following, with some modifications and extensions.

6.8.2 Wall Yield Displacement

It is found from trial analyses that the displacement profile of the walls at design response is typically linear with height. The effective height to determine the yield and design displacements is given by Eq.(3.35). Given the discrete nature of the lateral floor forces, the ratio of effective height to total wall height varies with the number of storeys, *n*. Assuming that floor masses and storey heights are equal, the ratio of effective height to total height can be expressed, from Eq.(3.35) as

$$H_e / H_n = \left(\sum_{i=1}^{n} (m_i \Delta_i H_i) / \sum_{i=1}^{n} m_i \Delta_i \right) / H_n = \left(\sum_{i=1}^{n} i^2 / \sum_{i=1}^{n} i \right) / n \tag{6.57}$$

Equation (6.57) is plotted against **n** in Fig.6.32(a). For $8 \leq n \leq 20$, a value of $H_e/H_n = 0.7$ is a reasonable approximation. For buildings with numbers of storeys outside this range, or where floor mass or storey height vary significantly with height, the effective height should be found directly from Eq.(3.35). To illustrate trends, however, the effective height ratio of 0.7 will be used in the following discussion.

In Fig.6.31(b) the total overturning moment profile has been approximated by a straight line from the base to the effective height. As discussed in Section 6.2.1 this is a reasonable approximation. With $H_e/H_n = 0.7$, the **OTM** at the effective height is found to be $M_{OTM,He} = 0.147 M_{OTM,B}$ independent of the number of storeys, as can easily be verified. The profile of overturning moment resistance provided by the coupling beams (Fig.6.31(c)) may also be approximated by a straight line. The linearization, shown also in Fig.6.31(c), based on equal coupling-beam moment capacities up the height, has base-level and roof-level moments of

$$M'_{CB,B} = (n + 0.5) V_{CB,i} L \quad \text{(a)} \quad \text{and} \quad M_{CB,n} = 0.5 V_{CB,i} L \quad \text{(b)} \tag{6.58}$$

In Eqs.(6.58) $V_{CB,i}$ is the shear force corresponding to flexural strength of a characteristic coupling beam. The coupling-beam resisting moment at an effective height of $0.7 H_n$ is thus

$$M'_{CB,He} = (0.3n + 0.5) V_{CB,i} L \tag{6.59}$$

The yield displacement at the effective height can now be found by subtracting the displacement associated with the coupling-beam moment profile, Δ_{y2} from the displacement associated with the total overturning moment profile, Δ_{y1}, noting that the average yield curvature at the wall base is $\phi_{y,w}$ (see Section 4.4.3(c)) and by proportion, the

wall-base curvatures corresponding to the total overturning moment, ϕ_{y1} , and the coupling-beam moment, ϕ_{y2} are

$$\phi_{y1} = \phi_{yW}/(1-\beta_{CB}) \quad \text{(a)} \quad \text{and} \quad \phi_{y2} = \phi_{yW} \cdot \beta_{CB}/(1-\beta_{CB}) \quad \text{(b)} \tag{6.60}$$

Using simple moment-area analysis, the yield displacement at the effective height of $0.7H_e$ is thus found to be

$$\Delta_y = \Delta_{y1} - \Delta_{y2} = \left(\frac{0.175}{1-\beta_{CB}} - \left(\frac{\beta_{CB}}{1-\beta_{CB}} \right) \cdot \left(\frac{0.1225 + 0.188n}{n} \right) \right) \phi_{yW} H_n^2 = C_4 \cdot \phi_{yW} H_n^2 \tag{6.61}$$
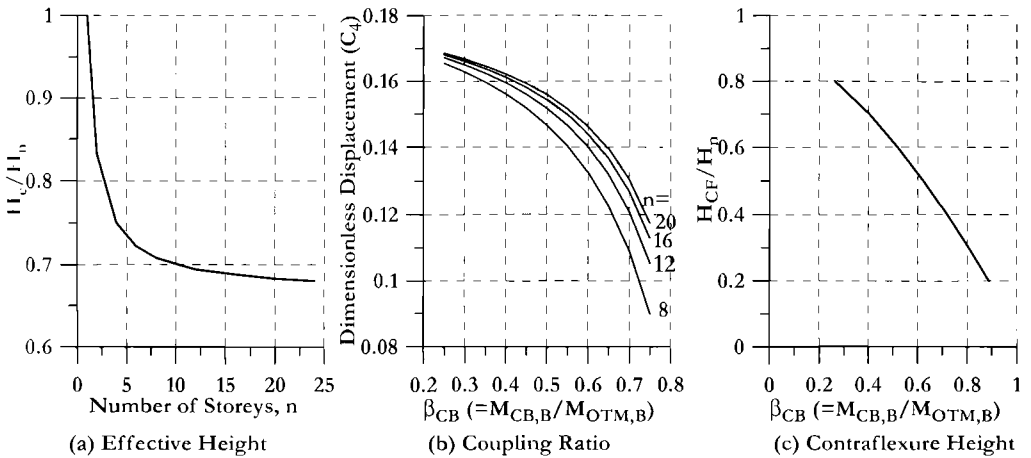
Fig.6.32 Design Parameters for Regular Coupled Walls

Note that Eq.(6.61) has been expressed in terms of the full wall height H_n rather than the effective height. The dimensionless coefficient C_4 in Eq.(6.61) has been plotted for the practical range of $0.25 \leq \beta_{CB} \leq 0.75$ in Fig.6.32(b) for walls of 8, 12, 16 and 20 storeys i.e. the range of storeys for which the approximation that $H_e = 0.7H_n$ is reasonable).

Figure 6.32(c) includes additional information that will be required in the design process; that is, the ratio of the height of the point of contraflexure in the wall moment profile (see Fig.6.31(d)) to the total wall height H_n. This defines the height at which the drift will be a maximum, since the moment reversal occurring above this point reduces the drift in the upper storeys. This height can be calculated by comparing the moments at height H_{CF} from the moment profiles of Figs.6.31(b) and (c). The results, which are based on the actual profile of overturning moment rather than the linearization in Fig.6.31(a) are plotted as a function of β_{CB} in Fig.6.32(c). It was found that the results for H_{CF} were very weakly dependent on number of storeys, and hence Fig.6.32(c) can be used for n ≥4, within the range of β_{CB} plotted.

6.8.3 Coupling Beam Yield Drift

It was asserted earlier that the coupling beams would generally yield at a much lower level of response than would the walls. It is of interest to examine this statement in some depth, requiring information on the yield drift of the coupling beams to be determined. This information will also be needed to determine the ductility demands on the coupling beams. Consider the generic relationship between wall drift and coupling beam drift at a given level, as illustrated in Fig.6.33. Although the wall drifts θ_W are related to the wall centrelines, they should more correctly be related to the neutral axes of the two walls. However, as Paulay[P27] has pointed out, this makes little difference to the relationship between wall and coupling beam drifts since the vertical displacement of the coupling beam is increased at the end adjacent to the wall with seismic compression, and reduced by an almost equal amount adjacent to the wall with seismic axial tension, compared with the approximation shown in Fig.6.33(a).

(a) Drift Geometry   (b) Coupling Beam Reinforcement
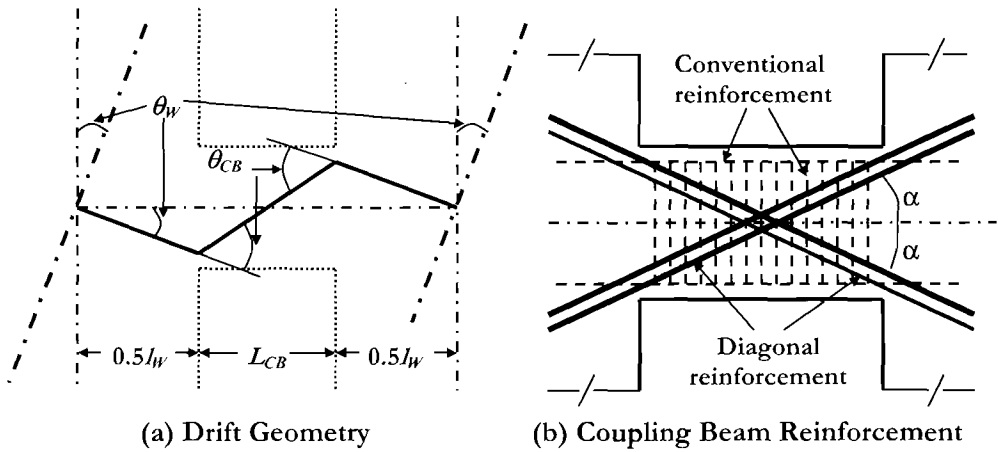
Fig.6.33 Deformation and Detailing of Coupling Beams

The rotation at the ends of the coupling beam is thus related to the wall rotation at the same level by

$$\theta_{CB} = \theta_W \left(1 + l_W / L_{CB}\right) \tag{6.62}$$

where l_W and L_{CB} are the wall and coupling beam lengths (see Fig.6.33(a)). As noted, the maximum wall drift will occur at the contraflexure height H_{CF}. Thus when the walls reach their (average) yield curvatures $\phi_{y,W}$, the corresponding drift in the coupling beams at the contraflexure height will be

$$\theta_{CB,W_y} = 0.5\phi_{yW}H_{CF}\left(1 + l_W / L_{CB}\right) \tag{6.63}$$

The yield drift of a conventionally reinforced coupling beam (see Fig.6.33(b)) may be related to its yield curvature $\phi_{y,CB}$ in similar fashion:

$$\theta_{CB,y} = 0.5\phi_{yCB}(0.5L_{CB} + L_{SP})(1 + F_V) \tag{6.64}$$

where L_{SP} is the strain penetration (Eq.4.30), and F_V is a flexibility coefficient to make approximate allowance for additional shear deformation, and which has been related to the coupling beam aspect ratio[P1] by $F_v = 3(h_{CB} / L_{CB})^2$. To gain some insight into the relative magnitudes of coupling beam drift given by Eqs.(6.63) and (6.64), we take the typical example of a 12-storey building with H_n=42 m (137.8 ft), l_W=5.6 m (18.4 ft), L_{CB}=1.8 m (70.9 in), h_{CB} =750mm (29.5 in). The shear-flexibility coefficient is found to be F_V = 0.52; We assume β_{CB} = 0.5, and hence, from Fig.6.32(c), $H_{CF} \approx 0.6H_n$.

From Eq.(6.63), with an average yield curvature from Section 4.4.3(c) of $1.75\varepsilon_y/l_W$

$$\theta_{CB,W_y} = 0.5 \times 1.75\varepsilon_y\left(0.6 \times 42 / 5.6\right)\left(1 + 5.6/1.8\right) = 16.2\varepsilon_y$$

From Eq.(6.64), with a yield curvature of $1.7\varepsilon_y/h_{CB}$ and L_{SP} =0.2 m (typical value)

$$\theta_{CB,y} = 0.5 \times 1.7\varepsilon_y(0.5 \times 1.8 + 0.2) \times 1.52 / 0.75 = 1.90\varepsilon_y$$

Thus the rotation of the coupling beam at the contraflexure height, imposed at wall yield, is about 8.5 times the yield drift of the coupling beam, assuming reinforcement with equal yield strength in the walls and coupling beam. Although the imposed rotations at levels above and below the critical level will be lower than the value found above, it is clear that all coupling beams will yield before the walls reach yield curvature.

If the coupling beams are reinforced with diagonal reinforcement, as indicated in Fig.6.33(b), the yield drift will be somewhat larger than indicated by Eq.(6.64), since reinforcement stress will be close to constant along the bars [P1]. However, the diagonal bars will ensure that shear deformation is negligible. Allowing for some tension stiffening and the influence of additional conventional "basketting" reinforcement, it is recommended that the value given by Eq.(6.64), with F_V = 0, be increased by 50%.

6.8.4 Wall Design Displacement

The wall design displacement may be governed by wall-base material strains, or by wall drift (at H_{CF}) in the usual manner. It may also be limited by the material strains in the coupling beams. All three options will need to be examined.

(a) Wall-base Material Strains: The limit-state curvatures of Section 6.2.1(c) may be used directly with reasonable accuracy. Hence the design displacement, corresponding to

material strain limits is

$$\Delta_{D\varepsilon} = \Delta_y + \left(\phi_{ls} - \phi_y\right)L_P H_e \tag{6.65a}$$

where the yield displacement Δ_y is given by Eq.(6.61) (or by Fig.6.32(b), or more generally from first principles, since the inflexion height is known), and the plastic hinge length is given by Eq.(6.7).

(b) Wall Drift Limit: As noted above, the critical drift occurs at the contraflexure height, H_{CF} (Fig.6.32(c)). In this case, the design displacement will be

$$\Delta_{D\theta} = \Delta_y + \left(\theta_C - 0.5\phi_{yW}H_{CF}\right)H_e \tag{6.65b}$$

where θ_C is the code drift limit.

(c) Coupling Beam Material Strain Limit: Coupling beam material strains may limit the design displacement capacity of coupled walls, particularly when conventional reinforcement, rather than diagonal reinforcement is used. We consider the two options in turn:

(i) Conventional reinforcement: The standard equations for plastic rotation advanced in Section 4.2 may be modified and used to predict the coupling beam rotation limit. Equation (4.31) defines the plastic hinge length. For coupling beams, the low length/depth aspect ratio invariably results in the strain penetration limit governing. That is, $L_P = 2L_{SP}$. Assuming the concrete is well-confined by transverse reinforcement, which will also be necessary to restrain the compression bars from buckling, the tensile strain limit will govern the plastic rotation capacity. Again making an assumption that the distance from the centroid of tensile reinforcement to neutral axis is $0.75h_{CB}$, the limit-state rotation capacity of the coupling beam for damage control will be

$$\theta_{CB,ls} \approx \frac{0.6\varepsilon_{su} \times 2L_{SP}}{0.75h_{CB}} \quad (damage\text{-}control)$$

and the corresponding critical wall rotation, at H_{CF} will be

$$\theta_{W,CB} = \frac{\theta_{CB,ls}}{1 + l_W / L_{CB}} \tag{6.65c}$$

The design displacement can now be found substituting $\theta_{W,CB}$ for θ_C in Eq.(6.65b). This will frequently be found to be more critical than the code drift limit. Taking the example discussed in Section 6.4.3, and assuming a limit-state strain of $\varepsilon_{su} = 0.10$, we find

$$\theta_{CB,ls} = \frac{0.6 \times 0.1 \times 2 \times 0.2}{0.75 \times 0.75} = 0.0427 \quad \text{and hence} \quad \theta_{W,CB} = \frac{0.0427}{1 + 5.6/1.8} = 0.0104$$

This is approximately half of the typical code drift limit of 0.02-0.025 and thus governs.

(ii) Diagonal reinforcement: With diagonal reinforcement, in the configuration shown in Fig.6.33(b), the reinforcing steel behaves like a steel truss. The stress (and therefore the strain) in a diagonal bar is essentially constant for the full length of the diagonal bar, in either tension or compression, depending on the direction of seismic response. As a consequence, the wall rotation at the end of the coupling beam is significantly larger than in the case of conventional reinforcement. The damage-control limit state rotation capacity of the coupling beam can again be related to a limit-state strain of $0.6\varepsilon_{su}$, constant over half the beam length plus the strain penetration:

$$\theta_{CB,dia} \approx \frac{0.6\varepsilon_{su}\left(0.5L_{CB} + L_{SP}\right)}{0.75h_{CB}} \tag{6.65d}$$
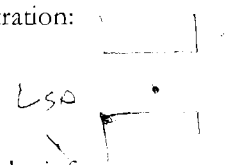
Using the same numeric values adopted for conventional reinforcement, we find that

$$\theta_{CB,dia} = \frac{0.6 \times 0.1(0.9 + 0.2)}{0.75 \times 0.75} = 0.117 \quad \text{and hence:} \quad \theta_{W,CB} = \frac{0.117}{1 + 5.6/1.8} = 0.0285$$

In this case, the coupling beam is unlikely to limit the design displacement response.

6.8.5 Equivalent Viscous Damping

It would be overly conservative to estimate the equivalent viscous damping on the basis of the wall structural ductility demand $\mu = \Delta_D/\Delta_y$, since the coupling beams, which may well contribute the major portion of seismic resistance (i.e., if $\beta_{CB} \geq 0.5$) will have much higher ductility demands, with a hysteretic shape associated with higher damping potential. It is thus clear that a weighted average should be used, similar to the formulation presented in Section 3.5.4. Since the lateral forces carried by wall and coupling-beam action are in proportion to the base moments carried by the two actions, and the associated displacements are identical, Eq.(3.37) can be modified to provide the following appropriate formulation:

$$\xi_{sys} = \left(1 - \beta_{CB}\right)\xi_W + \beta_{CB}\xi_{CB} \tag{6.66a}$$

where ξ_W and ξ_{CB} are the damping associated with wall and coupling-beam action. The former is calculated directly from the wall ductility demand, using Eq.(3.17a). The latter should be based on the average ductility demand of all the coupling beams. This is approximately 0.67 times the peak ductility demand, which occurs at H_{CF}. The corresponding value for equivalent viscous damping (ξ_{CB}) should be based on Eq.(3.17b).

If the coupling beam strength is not uniform over the building height, the more

complete form of the damping equation given by Eq.(6.66b) should be used:

$$\xi_{sys} = (1 - \beta_{CB})\xi_W + \beta_{CB}\frac{\sum \xi_{CBi}V_{CBi}}{\sum V_{CBi}} \qquad (6.66b)$$

6.8.6 Summary of Design Process

The design process proceeds in the following steps:

Step 1: Chose structural geometry.

Step 2: Chose proportion of *OTM* carried by coupling beams: β_{CB}. Avoid values that will induce resultant tension force in either of the walls, and ensure that reasonable steel ratios are obtained for the walls. This may require some iteration.

Step 3: Determine the height of contraflexure, by calculation, or for regular buildings from Fig.6.32(c)

Step 4: Determine the effective height from Eq.(3.35) or for regular buildings from Fig.6.32(a)

Step 5: Calculate wall yield displacement from Eq.(6.61) (or from first principles, if preferred), or for regular buildings from Fig.6.32(b).

Step 6: Calculate yield drift of coupling beams at the contraflexure height H_{CF} from Eq.(6.64), increasing this by 50% if diagonally reinforced coupling beams are used.

Step 7: Calculate the system design displacement from the alternatives of Eq.(6.65)

Step 8: Calculate the drift at the contraflexure height at the design system displacement

Step 9: Calculate the wall and coupling beam average displacement ductility demands. If the coupled walls are symmetrically opposed, use the average curvature here (Refer to Section 4.4.3).

Step 10: Calculate the system equivalent viscous damping from Eq.(6.66)

Step 11: Determine the required base shear force and overturning moment by **DDBD** principles in the usual manner. Distribute this overturning moment between walls and coupling beams in proportion to the chosen value for β_{CB}.

Step 12: Calculate the seismic shear to be carried by each coupling beam from Eq.(6.55).

Step 13: Calculate the required strength for each coupling beam from Eq.(6.56), and design the coupling beams.

Step 14: Design the wall-base flexural reinforcement.

Step 15: Use capacity design procedures to design the wall for flexure above the base, and for shear. Note that if coupling beams are designed with diagonal reinforcement, the bars act to resist both flexure and shear. Hence there is no need to adopt a capacity design approach for coupling beams with diagonal reinforcement.

6.8.7 Design Example 6.3: Design of a Coupled–Wall Building.

A 12-storey structural wall building with a floor plan similar to that of Fig.6.30 is to be constructed in a region where the seismicity is characterised by a linear displacement

response spectrum for 5% damping with a corner period of 5 sec and a corresponding displacement of 1.00 m (39.4 in) for the damage-control limit state. A code drift limit of 0.02 may govern design. The floor weights at each level, including an allowance for seismic live-load, are 5 MN (1120 kips). A coupled-wall solution is selected, and the following geometry chosen as step 1 of the design process:

   Channel walls: flange length l_W = 5 m (16.4 ft), web length 8 m (26.2 ft); wall thickness 250mm (9.84 in); storey height = 3.2 m (10.5 ft).

   Coupling beams: Length L_{CB} = 1.8 m (70.9 in); depth h_{CB} = 800 mm (31.5 in)

   Material properties: f'_c = 25 MPa, (3.63 ksi) f_y = 450 MPa (65.3 ksi) f_u/f_y = 1.2

   Reinforcing bar diameters of 28 mm and 20 mm (1.1 in. and 0.787 in.) diameter are envisaged for flexural reinforcement of coupling beams and walls respectively.

   We consider only the design for the direction parallel to the coupling beams, and follow the steps outlined in the previous section.

Step 1: The geometry has already been defined.

Step 2: Initial calculations indicate that to avoid net tension in either wall, no more than 60% of the OTM should be carried by the coupling action. Hence we chose β_{CB} = 0.6

Step 3: The building is regular, and from Fig.6.32(c) the contraflexure height is $0.52H_n$.

   Since the building height is H_n = 12×3.2=38.4 m, H_{CF} = 0.52×38.4=20.0m (65.5 ft)

Step 4: From Fig.6.32(a) the approximation that the effective height is $H_e=0.7H_n$ is satisfactory; hence H_e=0.7×38.4=26.9m   (88.2 ft)

Step 5: Yield displacement: From Fig.6.32(b), the yield displacement coefficient is C_4 = 0.14. Adopting an average yield curvature coefficient of 1.75:

$$\phi_{y,W} = 1.75\varepsilon_y / l_W = 1.75 \times 0.002475 / 5 = 0.000866 / m$$

   Note that the yield strain is based on an expected yield stress of f_{ye}=1.1f_y. The yield displacement is thus

$$\Delta_y = C_4\phi_{y,W}H_n^2 = 0.14 \times 0.000866 \times 38.4^2 = 0.179m \quad (7.05 \text{ in})$$

Step 6: It is decided to use diagonally reinforced coupling beams to take full advantage of code displacement limits (see step 7). We require the strain penetration length, L_{SP}, and the beam yield curvature $\phi_{y,CB}$:

   For D28 bars, from Eq.(4.30): $L_{SP} = 0.022 f_{ye}d_{bl} = 0.022 \times 495 \times 28 = 305mm$

   From Section 6.8.3, with diagonal bars, $F_V = 0$

   From Eq.(4.57(d)): $\phi_{y,CB} = 1.7\varepsilon_y / h_{CB} = 1.7 \times 0.002475 / 0.8 = 0.00526$

   Hence, modifying Eq.(6.64) as suggested for diagonally reinforced coupling beam, with $F_V = 0$,

$$\theta_{CB,y} = 0.5\phi_{y,CB}(0.5L_{CB} + L_{SP})(1 + F_V)(\times 1.5) = 0.5 \times 0.00526 \times 1.205 \times 1.0 \times 1.5 = 0.00475$$

Step 7: Design Displacement: The three alternatives are separately considered:

(a) Wall strain limits: We assume ε_{su} = 0.10. Hence Eq.6.10(b) applies directly for the damage-control limit state:

$\phi_{dc} = 0.072/l_W = 0.072/5 = 0.0144/m$

The strain penetration length for D20 reinforcement is 218 mm, hence from Eq.(6.7), with H_e replaced by H_{CF}, the plastic hinge length is

$L_P = 0.2(f_u/f_y - 1)H_{CF} + 0.1l_W + L_{SP} = 0.04 \times 20 + 0.1 \times 5 + 0.218 = 1.52m$

Hence from Eq.(6.65a):

$\Delta_{D\varepsilon} = \Delta_y + (\phi_{ls} - \phi_y)L_P H_e = 0.179 + (0.0144 - 0.00087) \times 1.52 \times 26.9 = 0.723\,m$

(b) Wall drift limit at H_{CF}: From Eq.(6.65b):

$\Delta_{D\theta} = \Delta_y + (\theta_C - 0.5\phi_{yW}H_{CF})H_e = 0.179 + (0.02 - 0.5 \times 0.00087 \times 20)26.9 = 0.482\,m$

(c) Coupling Beam drift limit (from Material strains): From Eq.(6.65d):

$\theta_{CB,dia} = \dfrac{0.6\varepsilon_{su}(0.5L_{CB} + L_{SP})}{0.75h_{CB}} = \dfrac{0.6 \times 0.1(0.9 + 0.305)}{0.75 \times 0.8} = 0.1205rad$

The corresponding wall drift, from Eq.(6.65c) is

$\theta_{W,CB} = \dfrac{\theta_{CB,ls}}{1 + L_W/L_{CB}} = \dfrac{0.1205}{1 + 5/1.8} = 0.0319$

This exceeds the wall drift limit of 0.02, and hence the coupling beams do not limit the design. Note, however, if conventional reinforcement was used in the coupling beams it would be found that the maximum wall drift would be 0.0161, limited by the coupling beam drift capacity.

Case (b) governs, and hence the design displacement is $\Delta_D = 0.482$ m (19.0 in).

Steps 8 and 9: Since the code drift limit governs the design, the maximum coupling beam drift is found from Eq.(6.62) as

$\theta_{CB} = 0.02(1 + 2.78) = 0.0756$

The displacement ductility demands are thus:

Wall: $\mu_W = 0.482/0.179 = 2.7$
Coupling Beams: $\mu_{CB} = 0.0756/0.00475 = 15.9$

This is the peak ductility demand, applying at the contraflexure height. The average ductility demand is taken as $0.67\mu_{CB} = 10.7$.

Step 10: System ductility demand: The damping ratios for the wall and coupling beams are found from Eqs.(3.17a and b):

$\xi_W = 0.05 + 0.444(\mu_W - 1)/\pi\mu_W = 0.05 + 0.444 \times 1.8/(\pi \times 2.8) = 0.139$

$\xi_{CB} = 0.05 + 0.565(\mu_{CB} - 1)/\pi\mu_{CB} = 0.05 + 0.565 \times 9.7/(\pi \times 10.7) = 0.213$

Substituting into Eq.(6.66):

$$\xi_{sys} = (1 - \beta_{CB})\xi_W + \beta_{CB}\xi_{CB} = 0.4 \times 0.139 + 0.6 \times 0.213 = 0.183$$

Step 12: DDBD to determine total base shear: The procedure is straightforward and has been elaborated in many previous examples. A summary of results is provided here:

Displacement spectrum reduction factor for $\xi = 0.183$: R_ξ $= 0.586$
Corner period displacement for $\xi = 0.183$: $\Delta_{5,0.184} = 0.586$ m
Effective period: $T_e = 4.11$ sec
Effective mass: $m_e = 46.4\text{MN/g}$
Effective stiffness: $K_e = 11.1\text{MN/m}$
Design base shear: $V_{Base} = 5.33$ MN
Design Base **OTM** $M_{OTM} = 143.4$ MNm

Step 13: Coupling Beam Shear: With $\beta_{CB}=0.6$, the shear force to be carried by each beam is given by Eq.(6.55), noting there are two coupling beams at each level, as

$$V_{CB,i} = \frac{\beta_{CB}M_{OTM}}{2nL} = \frac{0.6 \times 143.4}{24(5+1.8)} = 0.527 MN \quad (118.5 \text{ kips})$$

With reference to Fig.6.33(b), allowing two layers of reinforcement in each diagonal, with a distance of 100 mm between the coupling beam corners and the centres of the layers of diagonal bars, the angle α of the diagonal bars is $\alpha = \tan^{-1}(0.6/1.8) = 16.7^0$. Each diagonal contributes a shear resistance of $A_{sd}f_{ye}\sin\alpha$, as a tension or compression force, and hence, with $f_{ye} = 495$ MPa, the steel area required in each diagonal is

$A_{sd} = 0.527/(495 \times 2\sin\alpha)$ m² $= 1852$ mm² (2.87 in²). This can be provided by 4D24 bars (2.3% short-fall in capacity, which is not significant). Note that development length of these bars into the wall should be conservatively designed as a consequence of the high force to be anchored, and the less than ideal conditions for anchorage in the slender wall flanges[P1].

Step 14: Calculations for the reinforcement requirements for the walls are not included here as they are straightforward. It should be noted that the distribution of the total wall moment of $0.4 \times 143.4 = 57.3$MNm between the two walls is a designers choice. The seismic axial force in the walls must be considered when determining the reinforcement requirements. Since the wall with axial compression from the coupling beam shears will have a naturally higher flexural strength than the wall with axial tension, more moment capacity will normally be allocated to it. Final reinforcement details for the walls will also need to consider requirements for seismic resistance in the orthogonal direction (not considered in this example). Note that the total uplift force on the tension wall from coupling beam shears is 24×0.527MN $= 12.6$MN. This is less than the assessed gravity load of 13.0MN, and hence the design suggestion of no net tension force in the wall is met.

Step 15: The walls must be designed for dynamic amplification of moment and shear. The procedures developed in Section 6.6 can conservatively be adopted unless design

rules specifically applicable to coupled walls are available. Note that coupling beam flexural strength may be enhanced by the contribution of slab reinforcement in an adjacent monolithically connected floor slab. This will increase the system shear capacity, which must be considered when checking the shear capacity of the walls.

7

DUAL WALL-FRAME BUILDINGS

7.1 INTRODUCTION

Chapters 5 and 6 have respectively considered the DDBD of frame buildings and wall buildings. In many cases buildings will have both frames and walls contributing to seismic resistance, as illustrated in Fig.7.1.
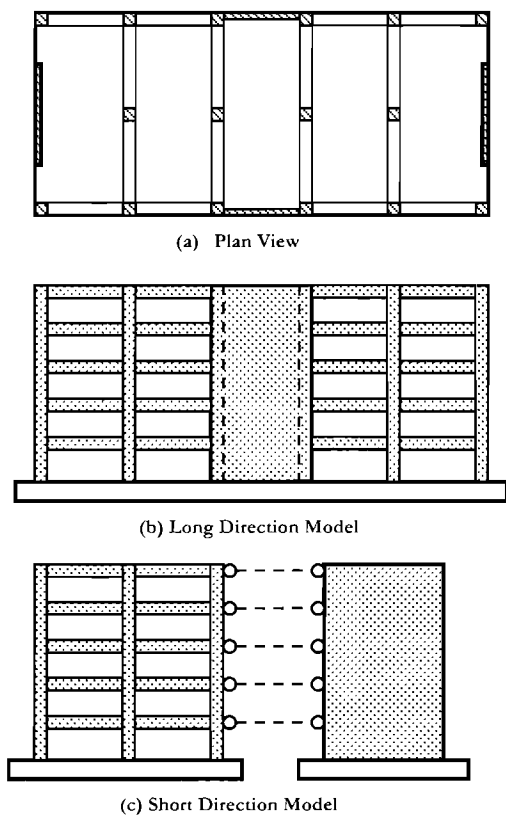

(a) Plan View

(b) Long Direction Model

(c) Short Direction Model

Fig.7.1 Different Wall-Frame Configurations

In the long direction of the floor plan, the structural system consists of boundary frames integrally linked to central structural walls by moment-resisting beams. Some columns of the frames act as boundary elements to the walls. In the short direction, the structural system consists of end walls and parallel one-way frames. The lateral deformations of the frames and walls are constrained to be equal by the in-plane stiffness of the floor diaphragm, as suggested by the dashed links in Fig.7.1(c) but there is no moment transfer between the frames and the beams. In the analysis model described by Fig.7.1(c) the strength and stiffness properties of four frames and two walls will be represented by the frame and wall shown.

The behaviour, and design, of dual wall-frame systems has similarities to that of coupled walls, which were considered in Section 6.8. The typically large stiffness variation between the frames and the walls will mean that the walls yield at significantly lower lateral displacements than do the frames, and hence distributions of lateral force between walls and frames based on initial elastic stiffnesses have little relevance to ductile response of the structure. Consequently, as suggested by Paulay [P29], similar freedom is available to the designer in choosing the share of lateral resistance provided by walls and frames as has been suggested for coupled walls. The designer may chose the proportion of base shear force carried by the frames based on experience and judgement rather than on elastic analysis based on generally invalid estimates of wall and frame stiffness. Typically the proportion of base shear carried by the frames will be between 15% and 50% of the total base shear - rather less than for frame action with coupled walls- but the value will depend on the size of the walls, and the relative numbers of frames and walls in the structural configuration.

7.2 DDBD PROCEDURE

The design and response of dual wall-frame structures has been investigated from a **DDBD** procedure in detail by Sullivan et al[S3]. The following description relies heavily on that work, and on earlier design suggestions by Paulay[P29].

7.2.1 Preliminary Design Choices

As briefly discussed above, two subjective design choices are made before any design calculations are initiated:

(a) Frame Shear Ratio: The proportion β_F of total base shear V_{Base} carried by the frame is selected. Hence:

$$V_F = \beta_F V_{Base}; \quad \text{(a)} \qquad \text{and} \qquad V_W = (1 - \beta_F)V_{Base} \quad \text{(b)} \tag{7.1}$$

where V_F and V_W are the base shear force carried by the frames and walls respectively. Note that β_F is similar to the coupling ratio β_{CB} describing the coupling of walls, but is related to base shear rather than overturning moment.

(b) Vertical Distribution of Beam Strength: The second choice available to the designer is how the frame strength is distributed vertically. Since displacement response will be effectively controlled by the stiffness of the walls, there is little danger of a soft-storey mechanism of frame displacement developing, and there is much more freedom of choice available to the designer. Paulay[29] has suggested a distribution of beam strength that results in constant frame shear at all levels. This implies that the frames are loaded laterally by a single point load at roof level, equal to V_F as shown in Fig.7.2(b), which is effected by designing beams at all levels for equal strength except at roof level, where the beam strength should be 50% of the strength at other levels. The lateral forces carried by the walls are then found by subtracting the frame lateral force from the total lateral forces. As suggested in Fig.7.2(c) this implies lateral forces equal to the total forces at all levels except the roof, where the lateral force will often be in the reversed direction.

The shear forces resulting from this distribution of lateral forces are shown in Figs.7.2(d) to 7.2(f).

7.2.2 Moment Profiles for Frames and Walls

Total overturning moments resulting from the lateral forces are shown in Fig.7.2(g), together with the vertical distribution of overturning moment for the frames. Although these are schematic, they have been based on an eight-storey structure with uniform storey heights, and a chosen frame shear ratio of $\beta_F = 0.35$. The vertical distribution of wall moments, shown in Fig.7.2(i) is found by subtracting the linear distribution of frame moments from the total. For this case (and most cases) this implies a wall contraflexure point at a height H_{CF}, as indicated in Fig.7.2(i). This contraflexure height is an important parameter in determining the wall design displacements.

It is useful at this stage to consider the distribution of moments induced in the frame by V_F, as illustrated in Fig.7.3. Here we assume that all frames in a given direction are identical, and the calculations relate to the combined strength of all frames. We also assume a point of contraflexure at mid-column heights at each storey. Initially we assume that all storey heights are equal at H_S. In each storey the sum of the column shears is

$$\sum V_C = V_1 + V_2 + V_3 = V_F \tag{7.2}$$

Consideration of moment equilibrium at the beam/column joint centres requires for constant storey height H_S that the sum of all beam-end moments at all levels except roof level, measured at the column centrelines must be

$$\sum M_{bi} = M_{i,1} + M_{i,2} + M_{i,3} + M_{i,4} = \sum V_C H_S \tag{7.3}$$

(a) Total Forces   (b) Frame Forces   (c) Wall Forces

(d) Total Shears   (e) Frame Shears   (f) Wall Shears

(g) Total Moments   (h) Frame Moments   (i) Wall Moments
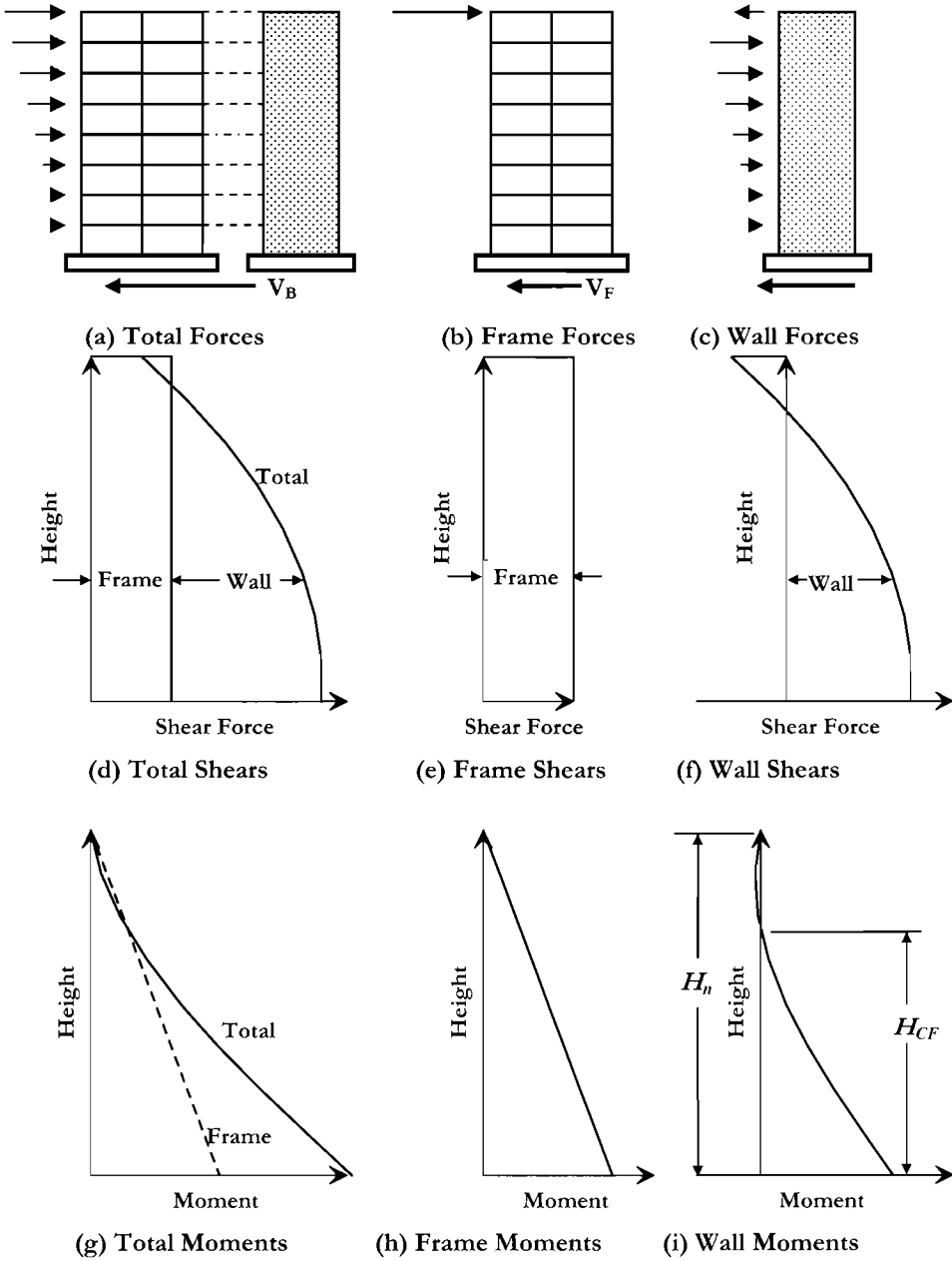
Fig.7.2   Suggested Distribution of Lateral Forces and Overturning Moments in a
Dual Wall-Frame Building without Link Beams
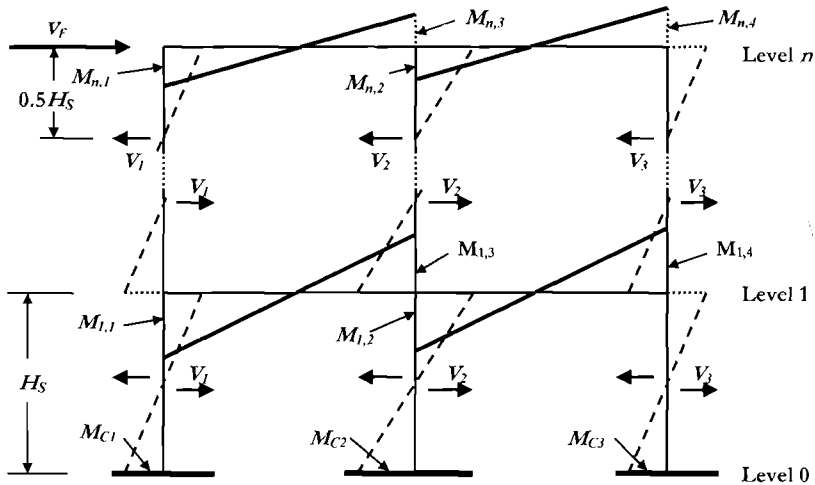
Fig.7.3 Frame Moments and Shears for Constant Frame Shear, V_F

At roof level, the sum of beam moments should ideally be half that given by Eq.(7.3) since the moment input from the columns at the joint centres is 50% of that at other levels. If this suggestion is not adopted, the shear carried by the column in the top storey will be greater than in other storeys, unless the column flexural strength is reduced to provide a column hinge at the appropriate moment capacity. However, some excess strength of the roof level beams, especially in buildings taller than (say) 10 storeys, is unlikely to adversely affect performance.

Column base moments are governed by

$$\sum M_C = \sum V_C H_S / 2 = 0.5 V_F H_S \quad \text{and} \quad M_{Ci} = 0.5 V_i H_S \tag{7.4}.$$

The strength defined by Eq.(7.4) is less than that recommended for column bases in Section 5.5.1. This is necessary to maintain the required uniformity of frame shear with height. The reason for selecting a higher base moment capacity for pure frame structures was to provide protection against a soft-storey mechanism developing in the ground floor columns. With a dual wall-frame building, the stiffness of the wall above the base plastic hinge provides adequate protection against such a soft-storey mechanism, and hence the lower moment, defined by Eq.(7.4) is acceptable.

Note that the designer may select the way in which the total shear force V_F is distributed between the different columns in recognition of the different axial forces in the columns, and to optimise beam flexural design. If the storey heights vary up the height of the building, the modifications to beam design moments is obvious, substituting $0.5(H_i + H_{i+1})$ for H_S in Eq.(7.3) where H_i is the height of the storey below the beam

considered. Beam moments at roof level, and column base moments are found using the adjacent storey height in the appropriate equation.

7.2.3 Moment Profiles when Frames and Walls are Connected by Link Beams

The discussion above relates to the situation when the frames and walls are not linked by link beams. It thus applies to the design and response in the short direction of Fig.7.1, but must be modified for the long direction, where beams frame into the edges of walls. The two-bay frame of Fig.7.3 is now modified by connecting it to a wall by link beams in Fig.7.4. Note that this does **not** represent the long direction of Fig.7.1(b) where the wall is central, and linked on either side to two-bay frames. A typical beam together with the beam moment profile is shown in Fig.7.4(a). If the shear carried by the frames is still given by Eq.(7.1(a)), then examination of equilibrium at the joints shows that Eq.(7.3) needs modification by addition of the moment M_{br} at the right end of the link beam since this contributes to joint equilibrium of the left column. For equal positive and negative moment capacities in the beams, the required beam moment capacity, measured at the joint centres is

$$M_b = V_F H_S / n_{be} \qquad (7.5)$$

where n_{be} is the number of beam ends framing into beam-column joints (n_{be} = 5 in Fig.7.4(a), but 4 in Fig.7.3).

When the beam moment capacities at each end of the link beam are developed, the slope of the moment diagram in the beam results in a larger moment increment, $M_{b,wall}$ being developed at the wall centreline. From geometry,

$$M_{b,wall} = M_{bl} + (M_{bl} - M_{br})l_{W,CL} / L_b \qquad (7.6)$$

where M_{bl} is the link beam moment at the centreline of the column which is integral with the wall, L_b is the link beam span length between column centrelines, $l_{W,CL}$ is the distance from the integral column centreline to the wall axis, and it is noted that beam moments at opposite ends of the link beam have opposite signs.

The wall moment increments from link beam action reduce the moment demand on the wall in the lower regions of the wall, but increase it in the upper regions, as indicated in Fig.7.4(b). The point of contraflexure will also be lowered. Although Fig.7.4(b) is schematic, it has been plotted to scale from the example in Fig.7.2(i), where β_F =0.35 and the required total beam moment at each level is divided between five moment locations, as is appropriate for Fig.7.4(a). The wall length was assumed to be $l_W = L_b$. In this example, the link beams result in a decrease in the base moment demand for the wall of 37%. The reduction in the wall moment demand at level 0 is compensated by the restraining moment resulting from the axial force (T in Fig.7.4(a)) developed in the wall

by the beam seismic shear force, balanced by the equal and opposite force C developed in the external column. Although these forces would be the same as those developed in the outer columns of a two-bay frame without linking to the wall, and with equal beam moment capacities to the linked example of Fig.7.4(b), the lever arm between the line of action of the seismic axial forces is increased, hence increasing the overturning moment.
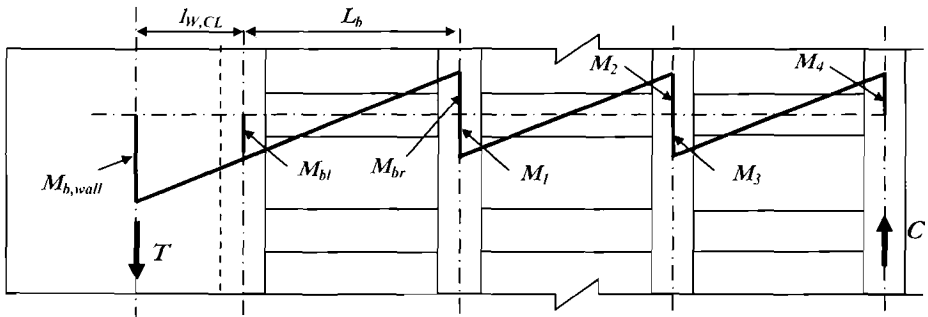
(a) Wall Moment Increment from Link Beam
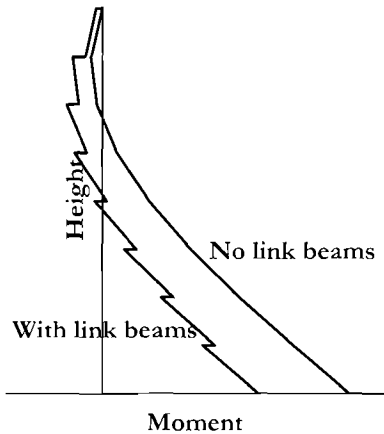
(b) Influence of Link Beams on Wall Moment Profiles

Fig.7.4   Moments in a Wall-Frame with Link Beams.

Note that if beams frame into both ends of the wall, as indicated for the long direction in Fig.7.1, the reduction in moment demand will occur from the link beams at each end, the axial force in the wall will not be influenced by seismic action, and the reduction in wall-base moment will be balanced by the couple of axial forces developed in the opposite end columns. Again, the distance between these forces is increased compared with the case of two frames without linking to the central wall.

The height of the contraflexure point in the walls, which is required for determining the yield displacement profile, as discussed in the next section, and also for determining the maximum drift, may be determined from the characteristic moment profiles shown in

Fig.7.4(b) using standard interpolation techniques. Note that although the actual values of wall moments will not be known at the start of the design process, the shape is completely defined by the chose of β_F, and the relative strengths of beams connecting to the walls, when link beams are used.

7.2.4   Displacement Profiles

(a) Yield Displacement Profile: In the normal situation, where walls carry at least 50% of the total building base shear force, the displacement pattern at yield is effectively dictated by the wall moment profile. As has been discussed in relation to coupled walls (Section 6.8.2), it is reasonable to represent the wall curvature profile as being linear from the yield curvature at the base to zero at the point of contraflexure. It is also reasonable, and conservative, to assume that the curvature above the contraflexure point is zero when determining storey yield displacements. On the basis of these assumptions, the yield displacement profile can be found from standard moment-area analysis as

for $H_i \le H_{CF}$: $\Delta_{yi} = \phi_{yW}\left(\dfrac{H_i^2}{2} - \dfrac{H_i^3}{6H_{CF}} \right)$ (7.7a)

for $H_i > H_{CF}$: $\Delta_{yi} = \phi_{yW}\left(\dfrac{H_{CF}H_i}{2} - \dfrac{H_{CF}^2}{6} \right)$ (7.7b)
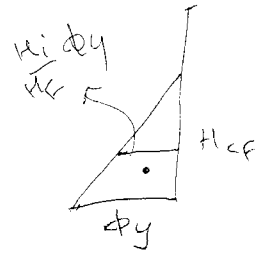
where ϕ_{yW} is the yield curvature at the wall base, from Section 4.4.3.

(b) Design Displacement Profile: It is reasonable to assume that frame strain limits will not be critical in determining the design displacement profile. Hence, design displacements will either be limited by material strains in the wall plastic hinges, or (more commonly) by drift limitations. As with coupled walls, drifts will be a maximum at the contraflexure height, H_{CF}.

(i) Wall base material strains govern: The limit state curvatures of Section 6.2.1(c) may be used directly. The design displacement profile is thus

$$\Delta_{Di} = \Delta_{yi} + \left(\phi_{ls} - \phi_{yW} \right) L_P H_i$$ (7.8)

where L_P is the plastic hinge length, given by Eq.(6.7), using H_{CF} instead of H_e unless $H_{CF} > H_e$. The corresponding drift at the contraflexure height is

$$\theta_{CF} = \phi_{yW} H_{CF} / 2 + \left(\phi_{ls} - \phi_{yW} \right) L_P$$ (7.9)
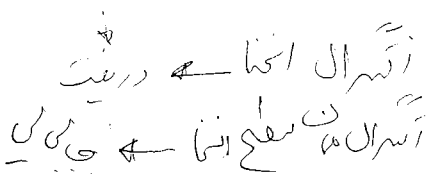
(ii) Code drift governs: If the drift at the contraflexure height given by Eq.(7.9) exceeds the code drift limit θ_C, then code drifts will govern the design, and the design displacement profile will be defined by:

$$\Delta_{Di} = \Delta_{yi} + \left(\theta_C - \phi_{yW} H_{CF} / 2\right) H_i \tag{7.10}$$

(iii) Correction for drift amplification: Work by Sullivan et al[S3] has shown that higher mode effects can amplify the drifts above the design targets implied by the first-mode design displacement profile for buildings with large numbers of storeys, and where β_F is high. For these cases, they recommend that the drift limit to be used in Eq.(7.10) be reduced by multiplying by a drift reduction factor ω_θ:

$$\theta_{CD} = \omega_\theta \theta_C = \left(1 - \left(\frac{n-5}{100}\right) \cdot \left(\frac{M_{OTM,F}}{M_{OTM}} + 0.25\right)\right) \theta_C \tag{7.11}$$

where $M_{OTM,F}$ is the total resisting moment provided by the frames at the base, M_{OTM} is the total overturning moment at the base, and n is the number of storeys. This correction factor will have negligible influence for $n \leq 10$.

(iv) Design substitute structure displacement: The design displacement of the **SDOF** substitute structure is then given by Eq.(3.26):

$$\Delta_D = \sum_{i=1}^{n} \left(m_i \Delta_{Di}^2\right) / \sum_{i=1}^{n} \left(m_i \Delta_i\right) \tag{3.26}$$

(c) Elastically Responding Walls and Design Ductility Limits: Section 6.3 investigated the maximum feasible ductility demand for cantilever walls based on code-specified drift limits being developed at roof level. These are too conservative for dual wall-frame buildings where the critical drift occurs at the contraflexure height, H_{CF}. For example, the aspect ratio developed in Eqs.(6.12) and (6.13), above which a wall must be designed for elastic response force-levels should be replaced by

$$H_{CF} / l_W = \theta_C / \varepsilon_y \tag{7.12}$$

That is, the aspect ratio is related to the contraflexure height rather than the full building height. It is not possible to uniquely define a relationship between wall aspect ratio and maximum design ductility demand for a given code drift limit, as is provided in Fig.6.8 for cantilever walls, since the relationship also depends on contraflexure height. However, the data in Fig.6.8 form a conservative lower bound for dual wall-frames. In similar fashion, the data of Fig.6.9, relating elastic response to seismic intensity is too

conservative for wall-frames. For a contraflexure height of $H_{CF}=0.5H_n$ yield displacements will be about $2/3^{rd}$ those plotted in Fig. 6.9.

7.2.5 Equivalent Viscous Damping

The equivalent viscous damping to be used in the **DDBD** will need to be a weighted average of the damping provided by the frames and by the walls, each of which have different displacement ductility demands. Sullivan et al[S3] have shown that for wall-frames the weighting should be related to the total base resisting moment provided by the different structural elements, shown in Fig.7.2(h) and (i). The equivalent elastic damping to be used in design is thus

$$\xi_{sys} = \frac{\xi_W M_{OTM,W} + \xi_F M_{OTM,F}}{M_{OTM}} \tag{7.13}$$

where ξ_W and ξ_F are the damping associated with ductile wall and frame response respectively. These require that the wall and frame ductility demands be separately evaluated. The wall ductility demand is directly given by

$$\mu_W = \Delta_D / \Delta_{yW} \tag{7.14}$$

where Δ_D is given by Eq.(3.26) and Δ_{yW} is found substituting the effective height H_e (from Eq.(3.35)) into Eq. (7.7). The wall damping is then found substituting μ_W into Eq.(3.17a).

The frame ductility demand may be estimated with adequate accuracy dividing the design displacement by the frame yield displacement at the effective height. Thus

$$\mu_F = \Delta_D / (\theta_{yF} H_e) \tag{7.15}$$

where the frame yield drift, θ_{yF}, is given by Eq.(3.8a) or (3.8b) for concrete and steel frames respectively. For irregular frames the method described in Section 5.3.3 should be used to estimate the effective yield drift. The frame damping is then found substituting μ_F into Eq.(3.17b) for concrete frames, or Eq.(3.17c) for steel frames.

Equation (7.13) may be used with adequate accuracy for both independent walls and frames, and for walls connected to frames with link beams. In the latter case, the frame resisting moment $M_{OTM,F}$ should be taken as $M_{OTM} - M_{OTM,W}$ where the wall moment has been reduced by the link-beam moment increments as shown in Fig. 7.4(b). This makes allowance for the additional energy dissipated by the link-beam plastic hinges. It should be noted, however, that a more accurate, and slightly less conservative approach has been suggested by Sullivan et al[S3].

7.2.6 Design Base Shear Force

The subsequent design procedure is standard, involving calculation of effective mass (Eq.(3.33)), effective period (Fig.3.1(d)), effective stiffness (Eq.(3.1)), and hence base shear force (Eq.(3.2)). The base shear is then distributed between the walls and frames in accordance with the initial choice of β_F, and the required plastic hinge locations (wall bases, beam ends and column bases are designed for flexural strength).

7.2.7 Design Results Compared with Time History Analyses

Sullivan et al[S3] carried out a large number of designs of wall-frame structures using the methodology described in the previous sections, and compared the design predictions with average **ITHA** results obtained from a suite of seven spectrum-compatible accelerograms. Buildings from four to twenty storeys, with and without (Fig.7.1(c)) link beams were considered, with different proportions of base shear carried by the frames. A selection of results presenting displacement and drift envelopes is shown in Fig.7.5 for eight-storey and sixteen-storey buildings with and without link beams.

These buildings were designed for a design displacement spectrum representing soft soil, with a peak ground acceleration of 0.35g. For the eight-storey buildings, the frames were allocated 30% and 40% of the total base shear for the cases without and with link beams respectively, and for both the sixteen storey buildings the frames carried 50% of the total base shear. All buildings were designed to satisfy wall material strain limits corresponding to Eq.(6.10b), and a drift limit of 2.5%. Material strain limits governed for the eight-storey buildings, though the corresponding drifts were close to the 2.5% limit. The sixteen-storey buildings were governed by the 2.5% drift limit. In order to allow for drift amplification, the drift reduction factor defined by Eq.(7.11) was applied to the designs of the sixteen-storey buildings.

Typical displacement ductility levels for the walls and frames were $\mu_W \approx 6$ and $\mu_F \approx 2$. Typical base shears were about 17% and 9% of building weight for the eight-storey and sixteen-storey buildings respectively, with the base shears for the cases with link beams being about 10% lower than for the cases without link beams. The comparatively high values for base shear were a consequence of the high design displacements defined by the soft soil spectrum. Note that the design base shears for the eight- and sixteen-storey buildings differed only by about 5% for reasons discussed in Section 3.10.2.

The plots of Fig.7.5 include the design displacement and drift profiles corresponding to first-mode response shown as solid lines, and the average envelopes of displacement and drift from the inelastic time-history analyses shown as dashed lines. Typical scatter from the average values was less than ±20% from the mean value. Also shown is the code drift limit of 2.5%. Good agreement between the design and time-history results for displacement profiles is apparent in all cases with the time-history results generally indicating smaller displacements than the design values. Drifts also agree well with first-mode values, except for the sixteen-storey "with link-beams" analyses (Fig.7.5(h)), where the use of the drift amplification factor has kept the drifts within the code limit.
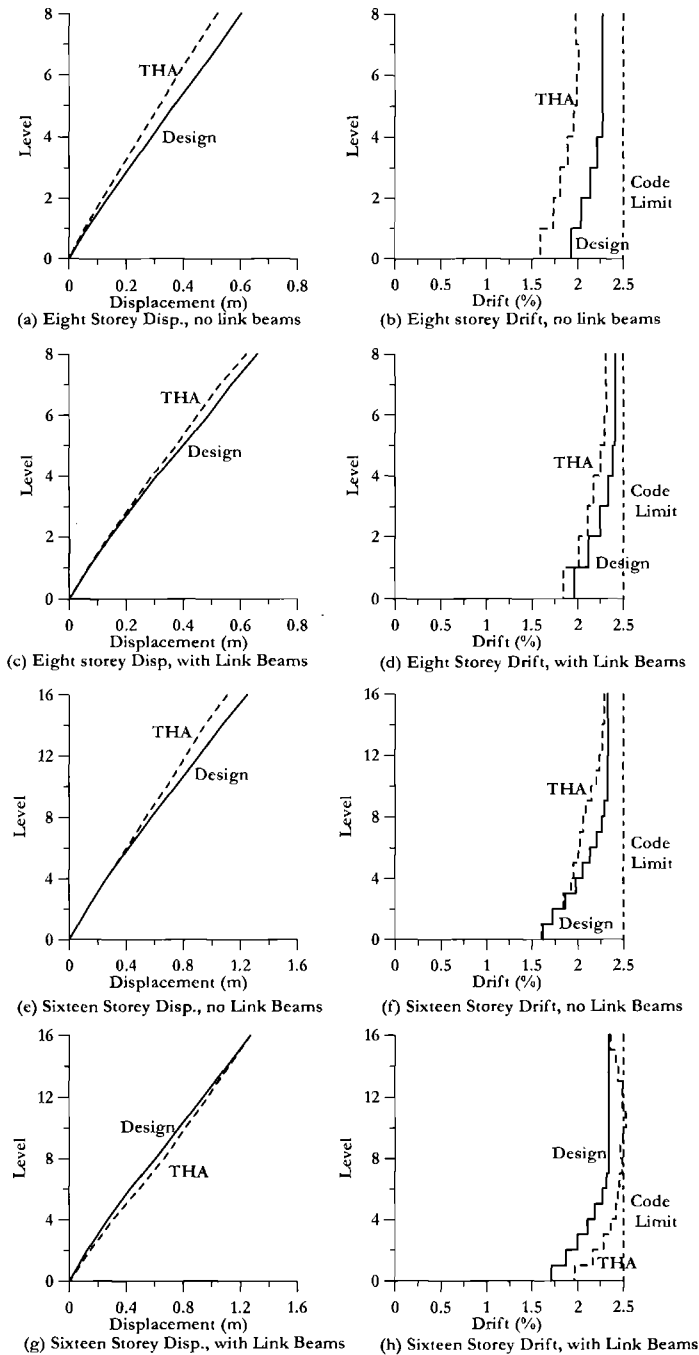
Fig.7.5   First-Mode Design Parameters Compared with Average Results from
Seven Spectrum-Compatible Time-History Analyses[S3]

7.3   CAPACITY DESIGN FOR WALL-FRAMES

The work by Sullivan et al[S3] included a detailed investigation of amplification of wall and frame shears and moments by higher mode effects. It was found that the modified modal superposition (**MMS**) approach advanced in Chapter 6 for dynamic amplification of moments and shears in walls provided a good agreement with inelastic time-history results (**THA**) for the walls of four-storey and eight-storey wall-frame buildings, but became increasingly conservative as the height of the building (and hence its natural periods) increased.

The reason for this increasing conservatism can be explained with reference to Fig.7.6, which investigates the influence of period shift, caused by ductility, on the second-mode period with respect to the elastic acceleration response spectrum. For low-rise buildings, the initial (elastic) second mode period is likely to be on the rising branch, or constant acceleration plateau of the acceleration response spectrum, as indicated by $T_{2,1}$ in Fig.7.6. Inelastic response in the fundamental mode will inevitably induce a lengthening of the higher-mode periods, as indicated by the period shift arrow. However, for low-rise buildings the response acceleration is unlikely to decrease since the period will remain on the plateau. In fact, for very stiff buildings, there may be an increase in the acceleration response associated with the period shift. In such cases the **MMS** approach has been found to be slightly non-conservative.
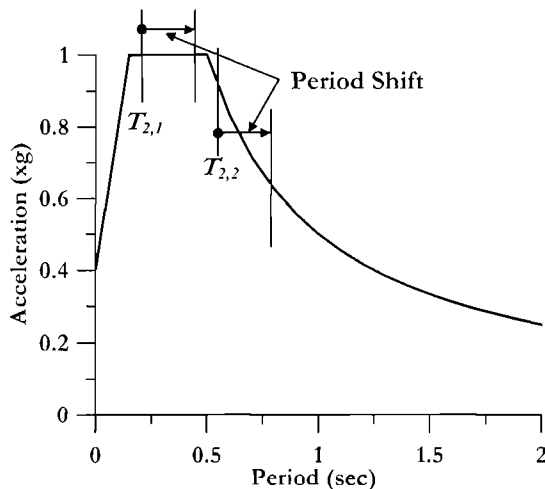
Fig.7.6   Influence of Second-Mode Period Shift on Response Acceleration

For higher-rise buildings, the period shift associated with inelastic first-mode response may result in a reduction in acceleration response associated with the second-mode (see $T_{2,2}$ in Fig.7.6), as the period moves down the constant velocity slope of the acceleration response spectrum. In such cases the **MMS** approach can be expected to be conservative.

7.3.1 Reduced Stiffness Model for Higher Mode Effects

Sullivan et al[S3,S4] report improved agreement with **THA** results when the modal superposition approach adopted in the **MMS** procedure is based on a modified elastic analysis, where the structure has the stiffness of potential plastic hinge regions reduced to values appropriate to the post-yield branch of a bilinear approximation to the moment-curvature characteristic (see Section 4.2.7). For a dual wall frame building the appropriate model for modal analysis can be simplified to the representations of Fig.7.7. In Fig.7.7(a) the stiffness of the wall-base and column-base have been reduced to the appropriate post-yield stiffness values, together with similar treatment for the beam-end plastic hinges. The simplified model of Fig.7.7(b) recognizes that the beam-end post-yield stiffness will often be low, and a reasonable approximation is to treat them as having zero stiffness. In this case a simple linear model may be used where the base plastic hinge has the sum of the post-yield stiffness of all walls and columns, and the vertical element has the summed elastic (cracked-section) stiffness of walls and columns.

(a) Structure with Reduced-stiffness plastic hinges   (b) Simplified Model
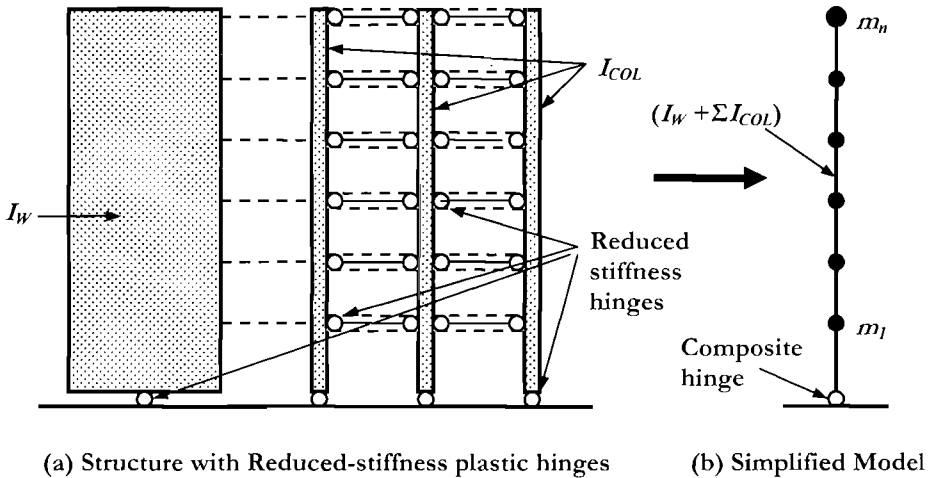
Fig.7.7 Models for Estimating Higher Mode Response Using Post-Yield Stiffness in Plastic Hinge Locations[S3]

The application of this method is very similar to that described in Section 6.6.1. The distribution of wall shear force with height conforms to Eq.(6.46), where the shears from modes 2 and higher are found using one of the models of Fig.7.7. Design moment envelopes are found using a directly analogous equation to (6.46) where the shears are replaced by the modal moments. Thus, the 1.1 factor of Eq.(6.47) is replaced by unity, and the equation taken to apply to the entire height of the wall, not just to the top half. In both cases the first-mode component is identical to that in Section 6.6.1, being defined by the actual strength of the structure in first-mode response. As noted above, this model

gave improved representation of higher mode effects, particularly for column forces, and wall shears, though it tended to be over-conservative for wall moments, and somewhat under-conservative for wall shears.

A further modification of the method, termed *Effective Modal Superposition* (**EMS**) uses the secant stiffness of all members at maximum (design) displacement. This method is described in Section 10.5.2(c) related to capacity-design effects in bridges, where it was found to produce better estimates of higher mode effects than the **MMS** method described in Chapter 6, or the reduced stiffness model described in this section. Although it has not yet been tested for wall or dual wall/frame structures, it is expected to produce superior predictions.

7.3.2 Simplified Estimation of Higher Mode Effects for Design

Examination of **ITHA** results for wall-frame buildings indicates that the interaction between the frames and walls generally reduces the influence of higher mode response to both the walls and the frames. It is possible to write conservative design rules for both elements, that can be used as an alternative to the modified modal analysis described above. Clearly the interaction of walls and frames requires that a significant proportion of the total base shear be carried by each of the structural types, and it is recommended that the following rules only be applied when the proportion of base shear allocated to the frames falls within the range $0.2 \leq \beta_F \approx \leq 0.6$. When $\beta_F < 0.2$ it is recommended that the capacity-design procedures for the walls follow the recommendations of Section 6.6.2, and when $\beta_F > 0.6$ capacity design procedures for the frames follow Section 5.8.4(c).

(a) Column moments: As recommended in Section 7.2.2, the frames may be designed so that the beam flexural strengths are equal at all levels except the roof, where beam flexural strength should be reduced by 50%. This is compatible with the assumption of constant frame shear force between levels 1 and the roof. It was also recommended that column-base flexural strength be chosen to satisfy Eq.(7.4) which ensures that the ground floor design shear force is the same as at upper levels. If these measures are adopted, then the required column flexural strength to satisfy capacity design requirements may be taken as

$$\phi_f M_C \geq M^o = 1.3\phi^o M_{CE} \qquad (7.16)$$

where M_{CE} is the corresponding column moment resulting from the design frame shear force, assuming column moments are equal above and below the joint, and ϕ^o is the overstrength factor associated with beam hinging. With beam ductility levels typically being low ($\mu_F < 2.5$), a value of $\phi^o = 1.1$ can generally be assumed, since consequences of column yielding are minor. As column moments were found to be only weakly dependent on ductility demand, ductility has not been included in Eq.(7.16).

Note that the above provisions may not provide absolute security against column hinging at levels above the base. This is, however, not critical, as the stiffness of walls, which will remain essentially elastic above the base hinge, will protect the building against formation of a soft-storey mechanism. Indeed, it might appear reasonable, on the basis of this argument to further relax the conservatism of Eq.(7.16).

*(b) **Column shears:*** Again, column shears are not greatly influenced by ductility demand, nor by variation in accelerogram characteristics[S3]. An average value of

$$\phi_V V_C \geq V^o = 1.3\phi^o V_{CE} \qquad (7.17a)$$

may be used for design, where V_{CE} is the shear corresponding to the design frame shear force. Note, however, that if the beams at roof level have not been designed for reduced flexural strength as recommended above, the shear in the upper floor columns should be taken as

$$\phi_V V_C \geq \phi^o (M_{Ct} + 1.3 M_{Cb}) / H_{(n,n-1)} \qquad (7.17b)$$

Similarly, if additional strength has been provided in the column base plastic hinge, then a similar modification should be used for the design shear force in the ground floor columns.

*(c)   **Wall Moment Capacity Envelope:*** A bilinear moment envelope of the form suggested by Fig.6.26(a) was found to be adequate, with the dependency on ductility demand being clearly apparent. Equation (6.48) can be directly applied, provided the ductility demand is taken as the system, rather than wall ductility demand. Although this is occasionally non-conservative, it provides a good average agreement with wall mid-height moment demand. As noted, the consequences of minor ductility demand at levels above the wall base are not serious.

*(d)   **Wall Shear Force Capacity Envelope:*** Application of the linear shear force envelope defined by Eqs.(6.49) to (6.51) for cantilever walls was found to be excessively conservative at the base, while being a little non-conservative at the top. However, the ITHA results indicated a strong dependence on ductility demand. Equation (6.49) can be directly applied, with Eqs.(6,50) and (6.51) modified as follows:

$$\omega_V = 1 + \frac{\mu_{sys}}{\phi^o} C_{2,T} \quad \text{where} \quad C_{2,T} = 0.4 + 0.2(T_i - 0.5) \leq 1.15 \qquad (7.18)$$

The design shear force at the top of the wall may be taken as 40% of the amplified wall-base shear. That is

$$V_n^o = 0.4 V_B^o \qquad (7.19)$$

7.4   DESIGN EXAMPLE 7.1: TWELVE-STOREY WALL-FRAME BUILDING

7.4.1   Design Data

The building shown in Fig.7.8(a) and (b) is twelve storeys high. The seismic structural system consists of two-way moment-resisting structural-steel frames with channel walls of reinforced concrete at each end of the building containing elevators, stairs and toilets. The plan is regular, based on an 8m × 8m (26.2ft × 26.2ft) bay module.
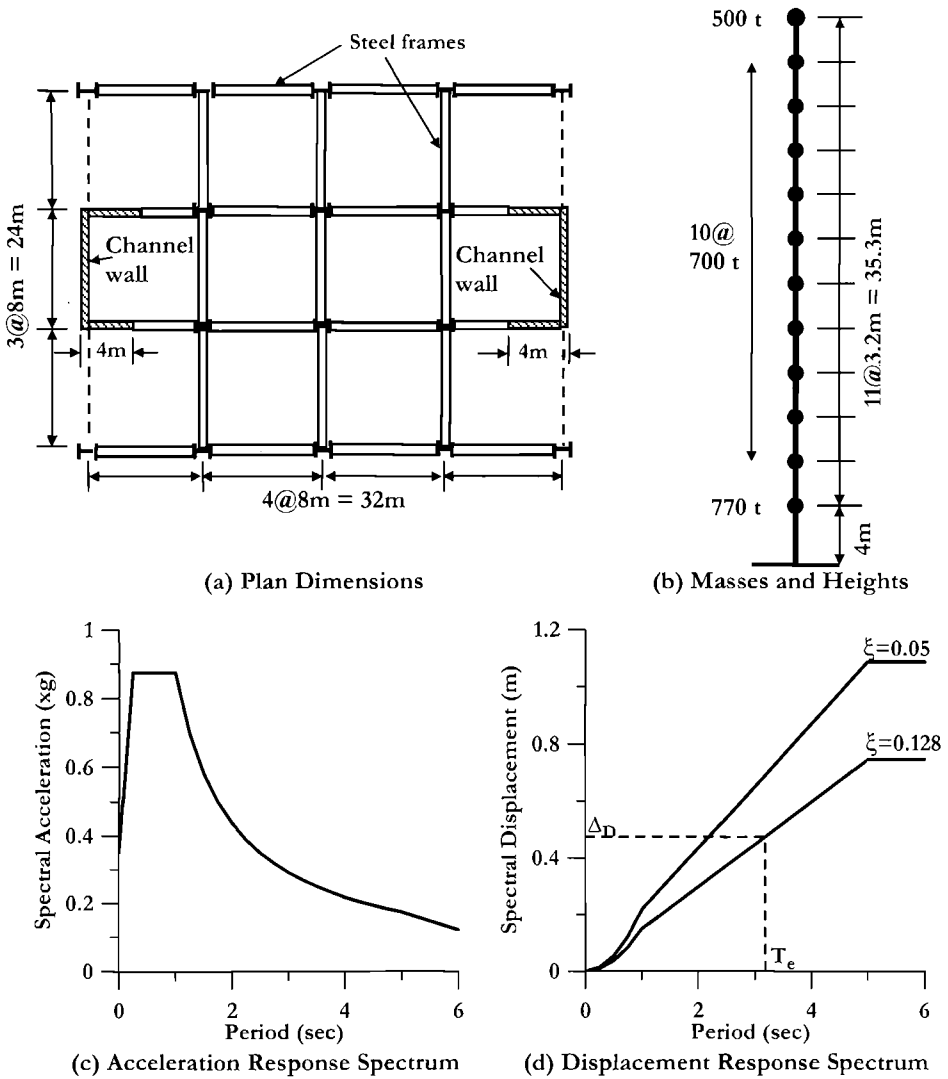

(a) Plan Dimensions   (b) Masses and Heights

(c) Acceleration Response Spectrum   (d) Displacement Response Spectrum

Fig.7.8   Data for Example 7.1

In the transverse (short) direction, there are three steel frames acting parallel to the end channel walls. Gravity steel beams simply supported at both ends connect the channels to the corner column, and thus do not induce seismic actions in the reinforced concrete walls.

In the longitudinal direction the internal steel frames are connected to the ends of the wall flanges with steel beams that are moment-resisting at the columns, but pinned to the wall ends. Although no moment will be transmitted to the wall at the beam end, the seismic shear in the beam will induce moments at the channel axis, reducing the base moment demand in the channel weak-axis direction.

Storey heights are 4m (13.1 ft) for the ground floor, and 3.2m (10.5 ft) at all other levels. Storey masses, including allowance for seismic live-load and wall weight are 770 tonnes (1698 kips) at level 1; 700 tonnes (1544 kips) at levels 2 to 11, and 500 tonnes (1103kips) at roof level. A basement foundation box provides effective rigidity at Level 0.

The building is to be constructed in a region of moderate seismicity, with a **PGA** of 0.35g. The site is classified as soft soil, and the elastic acceleration response spectrum has a plateau at 0.875g between 0.25 and 1.0 sec, with a subsequent constant velocity slope to 5.0sec, as shown in Fig.7.8(c). The design code does not include information on the displacement spectrum so it is generated from the acceleration spectrum in accordance with the recommendations of Section 2.2.2(b). The resulting displacement spectrum for 5% damping is shown in Fig.7.8(d). Note that the corner period is assumed to be 5 sec. It will be found that this does not influence the design in any way as the effective structural period is less than this value. The design drift limit is $\theta_C = 0.02$.

Initial sizing for the design indicates beam depths of 800mm (31.5 in) with the channel flange thickness at 400mm (15.7in) and web thickness at 300mm (11.8 in). Overall section dimensions of the channel walls are 8m × 4m (26.2ft × 13.1ft).

Specified material strengths are

      concrete: $f'_c = 30$ MPa (4.35 ksi)

      reinforcing steel: $f_y = 400$ MPa (58 ksi); $f_u = 1.35f_y$

      structural steel $f_y = 350$ MPa (50.8 ksi)

7.4.2 Transverse Direction Design

The transverse design is considered in detail. Subsequently, in Section 7.4.3, the initial stages of the longitudinal design will be carried out.

Step 1: Design Choices: Based on the number of frames and the channel sizes it is decided to allocate 40% of the base shear to the frames: $\beta_F = 0.4$. The same size steel beams will be used for all beams at all levels but the roof, where a reduced depth and smaller flange thickness will be adopted to ensure beam strength is approximately 50% of that at the lower levels. Hence the frame storey shear will be constant up the height of the building, and the internal columns will carry twice the moment and shear of the external columns.

Step 2: Wall Contraflexure Height: The initial stages of analysis, necessary to determine the wall contraflexure height are summarised in Table 7.1

We initially assume that the displacement vector is linear with height. This could be modified later, but is only used at this time to calculate the contraflexure height. Small errors in this calculation are not significant. With that assumption, the lateral forces will be proportional to m_iH_i. These products are listed in Col.4 of Table 7.1. The relative forces at the different levels are then proportional to $m_iH_i/\Sigma m_iH_i$, as listed in Col.5. Still using these relative forces, the total shear force (Col.6), total overturning moment (Col.7), and frame shear (Col.8) can be found. The wall shear (Col.9) is found subtracting Col.8 from Col.6, and the vertical profile of wall moments found from the relationship

$$M_i = M_{i+1} + V_{i+1}(H_{i+1} - H_i)$$

These are listed in Col.10. Note that the final values for moments and shears will be found by multiplying the relevant values in Table 7.1 by the base shear force V_{Base}.

Table 7.1 Design Example 7.1 - Preliminary Calculations to Determine H_{CF}

1	2	3	4	5	6	7	8	9	10
Level	Height H_i (m)	Mass m_i (t)	m_iH_i	F_i (rel.)	V_{Ti} (rel.)	$M_{OTM,i}$ (rel.)	$V_{F,i}$ frame	$V_{W,i}$ wall	$M_{W,i}$ wall
12	39.2	500	19600	0.1127	0.1127	0.00	0.4	-0.287	0.00
11	36	700	25200	0.1449	0.2576	0.36	0.4	-0.142	-0.92
10	32.8	700	22960	0.1320	0.3897	1.19	0.4	-0.010	-1.37
9	29.6	700	20720	0.1192	0.5088	2.43	0.4	0.109	-1.41
8	26.4	700	18480	0.1063	0.6151	4.06	0.4	0.215	-1.06
7	23.2	700	16240	0.0934	0.7085	6.03	0.4	0.309	-0.37
6	20	700	14000	0.0805	0.7890	8.30	0.4	0.389	0.62
5	16.8	700	11760	0.0676	0.8567	10.82	0.4	0.457	1.86
4	13.6	700	9520	0.0548	0.9114	13.56	0.4	0.511	3.32
3	10.4	700	7280	0.0419	0.9533	16.48	0.4	0.553	4.96
2	7.2	700	5040	0.0290	0.9823	19.53	0.4	0.582	6.73
1	4	770	3080	0.0177	1.0000	22.67	0.4	0.600	8.59
0	0	0	0	0.0000	1.0000	26.67	0.4	0.600	10.99
Sum		8270	173880	1					

From Col.10, the wall contraflexure point is between levels 6 and 7. Interpolating linearly,

$$H_{CF} = 20 + 3.2 \times 0.62/0.99 = 22.0m \quad (72.2 \text{ ft})$$

Step 3: Wall Yield Displacement: The expected yield strength of the reinforcing steel, from Eq.(4.23b) is $f_{ye}=1.1f_y = 440$ MPa. Hence $\varepsilon_y = 0.0022$. The yield curvature for the wall is estimated from Eq.(4.57) as

$$\phi_y = 1.5\varepsilon_y / l_W = 1.5 \times 0.0022 / 8 = 0.000413 / m$$

From Eq.(7.7a) for $H_i \le 22.0$m: $\Delta_{yi} = \phi_{yW}\left(\dfrac{H_i^2}{2} - \dfrac{H_i^3}{6H_{CF}}\right) = 0.000413\left(\dfrac{H_i^2}{2} - \dfrac{H_i^3}{6 \times 22}\right)$

From Eq.(7.7b) for $H_i > 22.0$m: $\Delta_{yi} = \phi_{yW}\left(\dfrac{H_{CF}H_i}{2} - \dfrac{H_{CF}^2}{6}\right) = 0.000413\left(\dfrac{22H_i}{2} - \dfrac{22^2}{6}\right)$

The vertical profile of yield displacements from the above equations is listed in Col.4 of Table 7.2.

Table 7.2   Design Displacement Information for Example 7.1

1	2	3	4	5	6	7	8
Level	Height H_i (m)	Mass m_i (t.)	Δ_{yi} (m)	Δ_{Di} (m)	$m_i\Delta^2_{Di}$	$m_i\Delta_{Di}$	$m_i\Delta_{Di}H_i$
12	39.2	500	0.145	0.705	248.2	352.3	13810
11	36	700	0.130	0.644	290.6	451.0	16240
10	32.8	700	0.116	0.584	238.8	408.9	13410
9	29.6	700	0.101	0.524	192.1	366.7	10850
8	26.4	700	0.087	0.464	150.5	324.5	8570
7	23.2	700	0.072	0.403	113.9	282.4	6550
6	20	700	0.058	0.343	82.4	240.2	4800
5	16.8	700	0.043	0.283	56.2	198.3	3330
4	13.6	700	0.030	0.225	35.3	157.2	2140
3	10.4	700	0.019	0.167	19.6	117.1	1220
2	7.2	700	0.010	0.112	8.8	78.6	570
1	4	770	0.003	0.060	2.8	46.4	190
0	0	0	0.000	0.000	0	0	0.0
Sum		8270			1439.2	3023.6	81670

Step 4: Design Displacement Profile: We first consider material strains, then check to see if drift governs:

(a) Wall Material Strains: With no information on the strain at maximum stress for the wall reinforcing steel, we conservatively assume $\varepsilon_{su} = 0.10$. The limit-state curvatures of Section 6.2.1(c) are likely to be slightly high for flanged walls, with the flange in compression, and we conservatively reduce the damage control curvature from Eq.(6.10b) by 10%:

$$\phi_{dc} = 0.9 \times 0.072 / l_W = 0.0648 / 8 = 0.0081 / m$$

Plastic hinge length: from Eq.(6.7) with $f_u/f_y = 1.35$: $k = 0.2(1.35\text{-}1) = 0.07$, and for $d_{bl} =$

25mm, L_{SP} = 242 mm:

$$L_P = kH_{CF} + 0.1l_W + L_{SP} = 0.07 \times 22 + 0.1 \times 8 + 0.242 = 2.58m \quad (8.46 \text{ ft})$$

Check if drift limit at H_{CF} is exceeded: From Eq.(7.9):

$$\theta_{CF} = \phi_{yW} H_{CF} / 2 + \left(\phi_{dc} - \phi_{yW} \right) L_P = 0.000413 \times 11 + (0.0081 - 0.00041)2.58 = 0.0244$$

This exceeds the drift limit of 0.02, hence code drift limits govern the wall design.

(b) Drift Limits: Since the building is tall, drift amplification should be considered. From Table 7.1 we note that the base overturning moment carried by the frames is the difference between the total *OTM* and the wall moment, i.e. 26.7 − 11.0 = 15.7 (related to unit base shear force). From Eq.(7.11):

$$\omega_\theta = \left(1 - \left(\frac{n-5}{100} \right) \cdot \left(\frac{M_{OTM,F}}{M_{OTM}} + 0.25 \right) \right) = \left(1 - 0.07 \left(\frac{15.7}{26.7} + 0.25 \right) \right) = 0.941$$

The design drift is thus reduced to 0.941×0.02=0.01882

The design profile is thus given by Eq.(7.10):

$$\Delta_{Di} = \Delta_{yi} + \left(\theta_C - \phi_{yW} H_{CF} / 2 \right) H_i = \Delta_{yi} + (0.01882 - 0.000413 \times 11) H_i = \Delta_{yi} + 0.0143 H_i$$

The corresponding design displacement profile is listed in Col.5 of Table 7.2. At this point it would be possible to refine the initial stages of design listed in Table 7.1 based on the displacement profile of Table 7.2, but the errors resulting from the initial assumption of a linear displacement profile will be found to be negligible.

Step 5: Design SDOF Displacement: The necessary calculations are listed in Cols. 6 and 7 of Table 7.2. From Section 7.2.3(b)(iv) the design displacement, given by Eq.(3.26) is

$$\Delta_D = \sum_{i=1}^{n} \left(m_i \Delta_{Di}^2 \right) / \sum_{i=1}^{n} \left(m_i \Delta_i \right) = 1439 / 3024 = 0.476m \quad (18.7 \text{ in})$$

Step 6: Effective Height: The additional necessary calculations are shown in Col.8 of Table 7.2. From Eq.(3.35):

$$H_e = \sum_{i=1}^{n} m_i \Delta_i H_i / \sum_{i=1}^{n} m_i \Delta_i = 81670 / 3024 = 27.0m \quad (88.6\text{ft})$$

Step 7: Equivalent Damping: The displacement ductility demands of walls and frames must first be evaluated:

(a) Walls: The yield displacement of the **SDOF** substitute structure is found substituting H_e into Eq.(7.7b), since $H_e > H_{CF}$:

$$\Delta_{iy} = \phi_{yW} \left(\frac{H_{CF} H_e}{2} - \frac{H_{CF}^2}{6} \right) = 0.000413 \left(\frac{22 \times 27}{2} - \frac{22^2}{6} \right) = 0.0893m$$

From Eq.(7.14): $\mu_W = \Delta_D / \Delta_{yW} = 0.476 / 0.0893 = 5.33$

From Eq.(3.17a): $\xi_W = 0.05 + 0.444\left(\dfrac{\mu-1}{\mu\pi}\right) = 0.05 + 0.444\left(\dfrac{4.33}{5.33\pi}\right) = 0.165$

(b) Frames: With a steel frame, with $f_{ye} = 1.1f_y = 385$ MPa (55.8ksi) the yield drift is given by Eq.(3.8b) as:

$$\theta_{yF} = 0.65\varepsilon_y L_b / h_b = 0.65 \times 0.00193 \times 8 / 0.8 = 0.0125$$

From Eq.(7.15): $\mu_F = \Delta_D / \left(\theta_{yF} H_e\right) = 0.476 / (0.0125 \times 27) = 1.41$

From Eq.(3.17c): $\xi_F = 0.05 + 0.577\left(\dfrac{\mu-1}{\mu\pi}\right) = 0.05 + 0.577\left(\dfrac{0.41}{1.41\pi}\right) = 0.103$

Finally, from Eq.(7.13), using **OTM** values for unit base shear from Table 7.1:

$$\xi_{sys} = \frac{\xi_W M_{OTM,W} + \xi_F M_{OTM,F}}{M_{OTM}} = \frac{0.165 \times 11.0 + 0.103 \times 15.7}{26.7} = 0.128$$

Step 8: Base Shear Force: From Eq.(2.8) the spectral displacement reduction factor for damping is

$$R_{0.128} = \left(\frac{0.07}{0.02 + 0.128}\right)^{0.5} = 0.688$$

(a) Effective period: At T=5.0 sec., the spectral displacement for 5% damping is 1.087m (42.8 in) (see Fig.7.8d). Thus at 5 sec, the corner displacement for 12.8% damping is 1.087×0.688= 0.748m. The effective period (see Fig.7.8(d)) is found by proportion as

$$T_e = 5 \times 0.476 / 0.748 = 3.18 \sec$$

(b) Effective mass: From Eq.(3.33) and Table 7.2,

$$m_e = \sum_{i=1}^{n} m_i \Delta_i / \Delta_D = 3024 / 0.476 = 6353 tonnes \qquad (0.77\Sigma m_i)$$

(c) Effective Stiffness: From Eq.(3.1):

$$K_e = 4\pi^2 m_e / T_e^2 = 4\pi^2 \times 6353 / 3.18^2 = 24.8 MN / m$$

(d) Base Shear: From Eq.(3.2):

$$V_{Base} = K_e \Delta_D = 24.8 \times 0.476 = 11.8 MN \quad (2653 \text{ kips};\ = 14.5\% \text{ of total weight})$$

Step 9: Wall Base Flexural Design: From Table 7.1, the total wall-base moment will be

$$M_{W,Base} = 11.0 V_{Base} = 11.0 \times 11.8 = 129.8 MNm \ (1149,000 \text{ kip.in})$$

This is shared between the two end walls, resulting in a design moment of 65MNm/wall. The axial load supported at the base of the walls is estimated as 5.0MN, including self weight. A detailed flexural design is inappropriate at this stage, as the wall also has to be

designed for flexure in the orthogonal direction, which will affect the distribution of reinforcement between the web and the flange. However, trial analyses indicate that reinforcement ratios of about 0.004 in the web and 0.005 in the flanges will provide the required design strength. Although on the low side, these are acceptable. It is probable that a smaller reinforcing bar size than the 25 mm initially assumed would be chosen to ensure spacing between the bars is not excessive.

Step 10: Frame Beam Flexural Design: The design was based on the assumption of equal beam strength up the building, and at each beam at each level, the exception being the top level. The total shear force to be carried by the frames is $0.4 \times 11.8 = 4.72$MN, and hence the shear force per frame is $4.72/3 = 1.57$MN. At each level, there are six potential plastic hinges per frame, and hence, from Eq.7.3, with all beam plastic hinges having equal strength:

$$M_{bi} = V_F H_S / 6 = 1.57 \times 3.2 / 6 MNm = 837 kNm \quad (7407 \text{ kip.in})$$

At roof level, the required moment capacity will be half this. Note that this moment demand applies at the joint centroid, and will be reduced to find the design moment at the column face in proportion to the ratio of column width to beam span. The beam design seems reasonable, requiring a flange area of about 5000mm² (7.8 in²) (say 300×16mm = 12×0.65 in)

Step 11: Column Base: The design shear force for the columns in the short direction will be $1.57/6 = 0.262$MN for the outer columns and $1.57/3 = 0.524$MN for the inner columns. In order to maintain the required storey shear in the taller ground storey, the moment capacity of the columns at the base will need to be $V_{col} H_{01} - 0.5 \Sigma M_{bi}$. Hence:

Outer column: $M_{CB} = 4.0 \times 0.262 - 0.837/2 = 0.63$MNm (630kNm = 5576 kip.in).

Inner column: $M_{CB} = 2 \times 0.63 = 1260$kNm (11,150 kip.in)

Since the columns are subjected to biaxial moment demands, these moments will be amplified in accordance with the suggestions of Section 5.6.2(c) once strength requirements in the long direction have been determined.

Step 12: Capacity Design for Walls: Strictly, this should not be carried out until the design requirements in the orthogonal direction are defined, since the overstrength factor may be influenced by the provision of excess reinforcement, above that required for the transverse direction. However, since detailed design calculations will not be provided for the orthogonal direction, we assume a perfect match for required and obtained base moment capacity at the design ductility level. The system displacement ductility can be found from the base shear forces weighted by ductility demand:

$$\mu_{sys} = \frac{\mu_W V_{W,Base} + \mu_F V_{F,Base}}{V_{Base}} = \frac{5.33 \times 0.6 + 1.41 \times 0.4}{1.0} = 3.76$$

(a) Mid-height moment: From Section 7.3.2(c), with an elastic period of $T_i \approx T_e/\sqrt{\mu}$ = =3.22/√3.76 = 1.66 sec, the required moment capacity at wall mid-height is given by Eq. (6.48), with ϕ^o =1.0 as recommended in Section 6.6.2(d):

$$C_{1,T} = 0.4 + 0.075 T_i \left(\mu_{sys} - 1\right) = 0.4 + 0.075 \times 1.66 \times 2.76 = 0.743$$

Hence, $M_{0.5Hn} = 0.743 M_{WB}$

(b) Wall shear force: As no specific analysis has been undertaken to assess the overstrength factor, we assume a value of $\phi^o = 1.2$, as suggested in Section 4.5.2. Equation (7.18) lead to:

$$C_{2,T} = 0.4 + 0.2(T_i - 0.5) = 0.4 + 0.2(1.66 - 0.5) = 0.632 < 1.15$$

Hence: $\omega_V = 1 + \dfrac{\mu_{sys}}{\phi^o} C_{2,T} = 1 + \dfrac{3.76}{1.2} \times 0.632 = 2.98$ and   from   Eq.(6.49)   the

overstrength shear demand on each of the two walls is:

$$V_{Base}^o = \phi^o \omega_V V_{W,Base} = 1.2 \times 2.98 \times 0.5(0.6 \times 11.8) = 12.7 MN \quad (2846 \text{ kips})$$

At the wall top, in accordance with Eq.(7.19)

$$V_n^o = 0.4 V_B^o = 0.4 \times 12.7 = 5.08 MN \quad (1142 \text{ kips})$$

A quick check on the wall shear stress levels is appropriate at this stage. At overstrength, the maximum shear stress is 12.7/(8×0.3)=5.29MPa (767psi). This is less than 13.5% of the expected compression strength of 39MPa, and though high, should be acceptable. Since the shear design is routine, it is not presented here (see Section 4.7.5).

Step 13: Capacity Design for Columns: Again this should wait till the column required design strengths have been determined also for the orthogonal direction. However, the overstrength requirements are based on the beam strengths, not the column strengths. From Section 7.3.2, Eqs.(7.16) and (7.17) require that the design moments and shears for the columns (except for the column base hinges) be designed for the moments and shears resulting from the design forces amplified by a factor of $1.3\phi^o = 1.3 \times 1.2 = 1.56$. Note that the column base has a moment demand that is already 51% higher than at other levels to provide the required shear force in the ground floor. This is close to the capacity design enhancement factor, implying that the same column size could be used up the height of the building. Note that steel column flexural strength is only marginally influenced by axial load level, and strength will increase slightly at higher levels.

7.4.3 Longitudinal Direction Design

As noted above, a detailed design will not be carried out for longitudinal response, as it is largely repetitive of the transverse design. However, we investigate the initial stages of design below.

Step 1: At each floor level there are 28 beam hinge locations in the longitudinal direction, compared with 18 hinges in the transverse direction. This, together with the expectation that wall moment capacity will be reduced in the longitudinal direction indicates that more of the base shear should be allocated to the frames. We chose $\beta_F = 0.5$. Again we will select a design where all beam moments are equal, allowing efficiency in design and construction since the same beam size can be selected at all levels except the roof.

Step 2: Contraflexure Height: Calculations similar to those summarised in Table 7.1 for unit base shear would indicate a base moment to be carried by the two walls of 7.07MNm. This does not, however, include the effects of having the beams between the wall flange-ends and the adjacent columns being moment-resisting at the columns. With 28 beam hinges, and $\beta_F=0.5$, the beam moment corresponding to unit base shear can be found from Eq.(7.3) as

$$M_{Bi} = V_F H_S / 28 = 0.5 \times 3.2 / 28 = 0.057$$

From Eq.(7.6), noting that $M_{bl} = 0$ because of the hinged connection between beam and wall, and that the geometric centre of the wall is 2.75m from the flange ends:

$$M_{b,wall} = M_{bl} + (M_{bl} - M_{br})l_{W,CL} / L_b = 0 - 0.057 \times 2.75 / 4 = -0.039$$

Twelve increments of this moment (corresponding to the twelve storeys) reduces the wall base moment to $6.62V_{Base}$. The contraflexure height is found to be $H_{CF} = 14.85$m (48.7 ft). The procedure follows that for the transverse direction. It will be found that the drift limit again governs the wall design, and that higher base shear strength is needed because of the greater elastic flexibility, which results in lower ductility and hence lower damping.

7.4.4 Comments on the Design

The design illustrates a number of important beneficial aspects of combining frames and walls in the same structural system. Briefly these are:

- The **SDOF** design displacement is increased compared with the design displacement for a pure frame, or a pure structural wall building, when code drift limits govern the design, which will normally be the case.
- Equivalent viscous damping is increased compared with a pure frame design.
- The combination of the two points above mean that the design base shear force is significantly reduced compared with a pure frame design.
- In the specific example considered above, the beam and column design moments are reduced to about 1/3rd of the values that would apply to a pure frame design. The resulting economies are obvious, and substantial, particularly when it is considered that the walls can be used as surrounds for essential services, and hence need not impinge on freedom of space utilization.

It is clear from these comments that dual wall/frame buildings are a particularly appropriate structural form to maximise the efficiency advantages resulting from DDBD.

8

MASONRY BUILDINGS

8.1 INTRODUCTION: CHARACTERISTICS OF MASONRY BUILDINGS

8.1.1 General Considerations

Conventions for masonry construction in seismic regions differ greatly between different countries. In some countries – particularly the United States, New Zealand and Japan, masonry constructed in seismic regions will normally be hollow-unit concrete masonry, where the units have provision for both vertical and horizontal reinforcement, resulting in construction that can be termed "reinforced concrete emulation". Although the compression strength tends to be lower than with reinforced concrete, the seismic response is sufficiently similar for there to be no significant conceptual difference from reinforced concrete. Material presented in Chapters 5, 6 and 7 thus applies directly. Detailed discussion of seismic design of this form of masonry construction is available in [P1], and will not be repeated here.

In Europe, central and south America, and Australia, unreinforced, or very lightly reinforced masonry is often constructed in seismic regions. It is this form of construction that is considered in this chapter.

Unreinforced masonry is often considered a construction material to be avoided in high seismicity areas, because of an assumed inherent high vulnerability that cannot be eliminated even by appropriate design approaches and construction rules. This opinion is motivated by poor performance often observed during and after earthquakes, but does not have a rational scientific base and can therefore be added to the long list of myths in seismic engineering. While it is true that many unreinforced masonry buildings have suffered significant damage or have collapsed due to earthquake action, it is also evident that many other masonry buildings survived over centuries, with little damage resulting from repeated seismic events[M13].

Considering the problem from a displacement "*capacity versus demand*" viewpoint, it is true that masonry elements and structures attain specified performance levels in terms of sustained damage at lower interstorey drifts when compared with other construction types. On the other hand it has to be noted that fundamental periods of masonry buildings are also naturally lower than those of other structural types, and consequently the displacement demand is also comparatively smaller.

Masonry buildings of the class considered in this chapter are characterized by a limited number of storeys (normally not exceeding four or five; possibly less in high seismicity regions) and by the presence of walls with a large total resisting section area with respect to the floor area. Typical ratios between total resisting section area and floor area may range between 3% and 7% for the case of masonry structures, against values commonly between 1% and 2% for concrete wall buildings.

Examples of plan structural layout of masonry buildings are shown in Fig.8.1. It should be noted that structural elements are used in conjunction with non-structural masonry partitions to a much higher extent than for other construction types. This implies that the estimate of acceptable drifts for different performance levels based on structural and non-structural constraints tends to coincide. As a consequence, drift limits derived from non-structural constraints are less likely to limit structural performance.
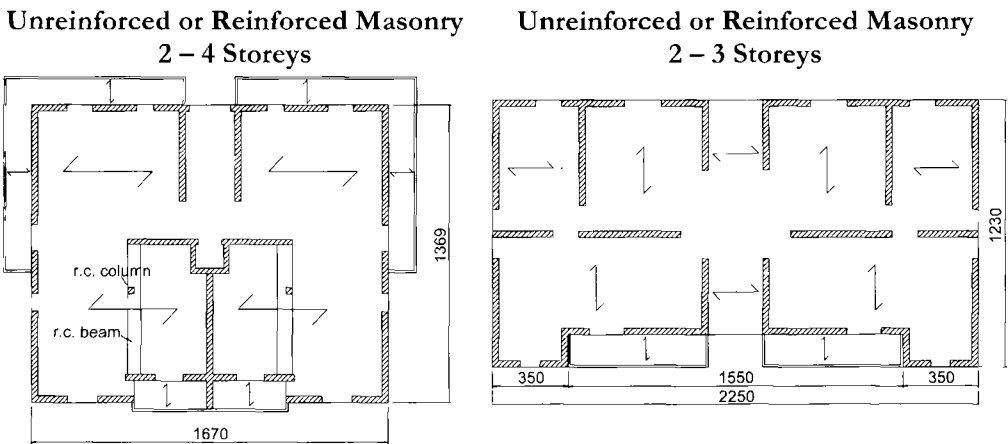
Unreinforced or Reinforced Masonry
2 – 4 Storeys

Unreinforced or Reinforced Masonry
2 – 3 Storeys

Fig.8.1   Typical Plan Layout for Masonry Buildings

In countries with seismic design traditions, it is also noticeable that masonry buildings often have regular plan shapes, with symmetric or almost symmetric wall distribution in both directions, and the external walls in most cases are part of the system resisting horizontal forces. This obviously implies a rather low sensitivity to torsional problems.

It is often prescribed in codes of practice that perpendicular walls should be well connected to each other at each intersection, and sometimes it is also prescribed to provide each shear wall with some flange at both ends. A proper connection between perpendicular walls may actually be important in existing buildings, where floor slabs may be inadequate to provide any diaphragm action to redistribute the horizontal forces to the wall system and to provide adequate out of plane restraints. However, in the case of new buildings constructed with strong and stiff floor slabs, normally using reinforced concrete, we do not see any reason for provisions of this kind. At the connection between web and flange, high shear forces may result from the deformation constraints, producing local damage and diagonal cracking. We would in general recommend the

choice of planar walls for new construction, or at least to neglect composite action in analysis.

Typical structural wall elevations for new buildings are shown in Fig.8.2. Simple structural walls rising from the foundation level, or from a reinforced concrete basement, are coupled by bending and shear action of floors and possibly by concrete beams or masonry lintels. Typically, masonry walls have adequate width such that the vertical distance between horizontal slabs is not larger than 15 times the wall thickness (this limit applies more appropriately to the distance between contraflexure points considering the out of plane response of walls). The geometric aspect ratio of each pier, as resulting from openings, is normally not larger than $H_w/l_w = 3$, where H_w is the height of the pier and l_w is its depth. Because of the generally low height and low periods of the class of masonry buildings considered in this chapter, higher-mode effects are often less significant than with conventional reinforced concrete buildings. This is particularly the case when forces in a pier are considered. As discussed subsequently, capacity protection can be provided by ensuring that piers have adequate slenderness to favour a flexural rocking mode of inelastic response.

Foundation flexibility normally does not significantly affect the response and design. In the standard case of multiple walls sitting on a continuous foundation, wall rocking is forced to occur on the top of the foundation structure, rather than on the supporting soil. For cantilever walls the indications given in Section 6.5 are directly applicable with minor obvious modifications.
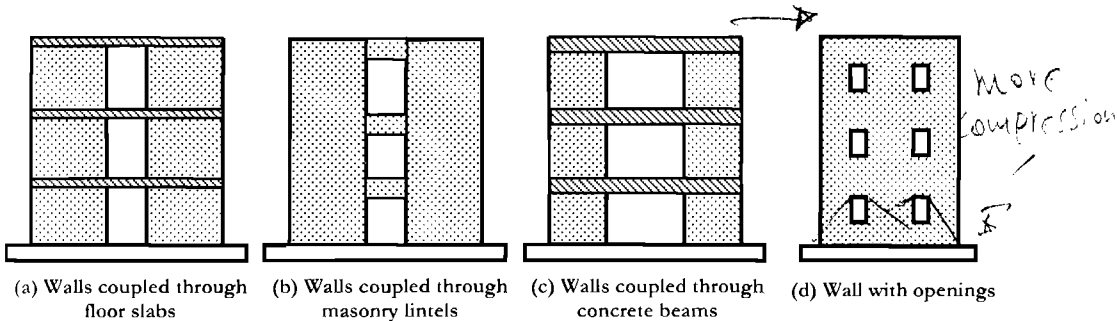

(a) Walls coupled through floor slabs   (b) Walls coupled through masonry lintels   (c) Walls coupled through concrete beams   (d) Wall with openings

Fig.8.2   Typical Wall Shapes

8.1.2   Material Types and Properties

The materials used for construction of masonry structures can be extremely heterogeneous and can be characterized by a wide range of strength, deformation and energy dissipation properties. The strength and stiffness properties result from a combination of the properties of bricks or blocks and those of the mortar. As an example consider the values reported in Table 8.1, where the recommendation given in the current Italian code for existing buildings are summarized[X17]. The average values given there are compression strength (f_{mc}), shear strength (v_{mv}) elastic modulus (E_m), shear modulus (G_m)

and weight per unit volume (w_m). The table refers to assessment of existing buildings rather than to design of new buildings, and the values given are considered to be appropriate for low quality mortar and poor masonry texture (multiplying factors in the range of 1.3 – 1.5 are recommended in case of good quality mortar or presence of regularizing block layers).

Although the data do not refer to new design, it is of interest to note that the strength and stiffness values can vary in a range of 5 – 10 times with even higher variation for the case of shear strength. It is also noticeable that the typical values of shear strength are in the range of 3 – 6 % of the compression strength.

Table 8.1 Average Values of Strength and Stiffness Properties of Masonry[X17]

Masonry type	f_{mc}		v_{mv}		E_m		G_m		w_m	
	min max		min max		min max		min max			
	MPa	ksi	kPa	psi	MPa	ksi	MPa	ksi	kN/m³	kip/ft³
Natural stone of various types and shapes	0.6	0.087	20	2.90	690	100.1	115	16.68	19	0.121
	0.9	0.131	32	4.64	1050	152.3	175	25.38		
Natural stone, with exterior walls and interior mixed filling	1.1	0.160	35	5.08	1020	147.9	170	24.66	20	0.127
	1.55	0.225	51	7.40	1440	208.8	240	34.81		
Natural stone, well connected irregular blocks	1.5	0.218	56	8.12	1500	217.5	250	36.26	21	0.134
	2	0.290	74	10.73	1980	287.2	330	47.86		
Natural stone: Low strength regular blocks (tuff, sandstone)	0.8	0.116	28	4.06	900	130.5	150	21.75	16	0.102
	1.2	0.174	42	6.09	1260	182.7	210	30.46		
Natural stone, well connected regular blocks	3	0.435	78	11.31	2340	339.4	390	56.56	22	0.140
	4	0.580	98	14.21	2820	409.0	470	68.17		
Solid clay bricks and lime mortar	1.8	0.261	60	8.70	1800	261.1	300	43.51	18	0.115
	2.8	0.406	92	13.34	2400	348.1	400	58.01		
Solid clay bricks and cement mortar	3.8	0.551	240	34.81	2800	406.1	560	81.22	15	0.096
	5	0.725	320	46.41	3600	522.1	720	104.4		
Clay blocks and cement mortar (holes area < 45%)	4.6	0.667	300	43.51	3400	493.1	680	98.62	12	0.076
	6	0.870	400	58.01	4400	638.1	880	127.6		
Clay blocks, unfilled vertical joints (holes area < 45%)	3	0.435	100	14.50	2580	374.2	430	62.36	11	0.070
	4	0.580	130	18.85	3300	478.6	550	79.77		
Concrete blocks (holes area between 45% and 65%)	1.5	0.218	95	13.78	2200	319.1	440	63.81	12	0.076
	2	0.290	125	18.13	2800	406.1	560	81.22		
Concrete blocks (holes area < 45%)	3	0.435	180	26.11	2700	391.6	540	78.32	14	0.089
	4.4	0.638	240	34.81	3500	507.6	700	101.5		

For new construction, the masonry compression strength to be used in design is often given in codes as a function of the properties of blocks and mortar. An example of recommended European characteristic (i.e. lower 5%) values for clay blocks and cement mortar is reported in Table 8.2. Different values will apply in different countries. The shear strength is normally in the range of $0.1 - 0.3$ MPa (in the absence of axial stress, as discussed in Section 8.2.1 (c)), the elastic modulus is around $E_m \approx 1000 f_{mc}$, and the shear modulus $G_m \approx 400 f_{mc}$. Due to the high variability of the properties and the influence of cracking, an evaluation based on experimental testing is generally recommended.

Table 8.2   Masonry Compression Strength Based on Blocks and Mortar Strength

Blocks strength [MPa, *ksi*]		Mortar strength [MPa, *ksi*]					
		15.0	*2.18*	**10.0**	*1.45*	**5.0**	*0.73*
5.0	*0.73*	3.5	*0.51*	3.4	*0.49*	3.3	*0.48*
10.0	*1.45*	6.2	*0.9*	5.3	*0.77*	4.7	*0.68*
15.0	*2.18*	8.2	*1.19*	6.7	*0.97*	6	*0.87*
20.0	*2.90*	9.7	*1.41*	8	*1.16*	7	*1.02*
30.0	*4.35*	12	*1.74*	10	*1.45*	8.6	*1.25*

In the case of reinforced masonry, the possible addition of horizontal reinforcement in the mortar beds and of vertical and horizontal reinforcement in cavities obtained from the appropriate combination of special blocks can further vary the global properties of the resulting construction material. In the case of horizontal reinforcement alone, an increase of shear strength can be obtained, resulting in a flexural failure mode in most cases. Vertical reinforcement can increase both flexural and shear strength. Both horizontal and vertical reinforcement can also reduce the probability of out of plane failure of a masonry panel. The geometric percentage of both vertical and horizontal reinforcement can be as low as 0.05% in European designs for the type of lightly-reinforced masonry discussed in this chapter. It is again emphasised that reinforced concrete emulation is not considered herein.

In this chapter, construction materials characterised by relatively low compression and shear strength will be considered, resulting from an average consideration of holes in blocks, with specific reference to design of new structures. Even with this limitation, the material properties can range from those of high strength stone and concrete mortar to those of aerated concrete and glued joints. Minimum required strength values, measured on gross sections, are often set around 5 MPa (0.725 ksi) for compression strength of blocks in the vertical direction, to 1.5 MPa (2.175 ksi) for compression strength of blocks in the horizontal direction and to 5 MPa for compression strength of mortar.

Detailed discussion of masonry properties can be found elsewhere[D7, H2, T1]; the focus here will be on general design aspects for standard materials.

8.2 TYPICAL DAMAGE AND FAILURE MODES

8.2.1 Walls

(a) General Aspects: The principal in-plane failure mechanisms of masonry piers with little or no vertical reinforcement subjected to gravity loads and seismic actions can be summarized as follows.

- Flexural (rocking) failure: As horizontal force and displacement demand increases, bed joints crack in tension and shear is carried by the compressed masonry; final failure is obtained by crushing of the compressed corner and possibly simultaneous overturning of the wall.
- Diagonal shear cracking: Peak resistance is governed by the formation and development of inclined diagonal cracks, which may follow the path of bed and header joints or may go through the bricks, depending on the relative strength of mortar joints, brick-mortar interface, and brick units.
- Shear sliding: due to the formation of tensile horizontal cracks in the bed joints, subjected to reversed seismic action, potential sliding planes can form along cracked bed joints; this failure mode is possible for squat walls, with low levels of vertical load and/or low friction coefficients and mortar properties.

(b) Flexural Rocking Response: The maximum horizontal shear which can be resisted by a rocking pier failing under static in-plane loading may be approximated introducing an appropriate stress distribution for the masonry in compression and neglecting the tensile strength of bed joints. With reference to Fig.8.3, equilibrium leads to the following standard expressions for the flexural strength, M_u, of the base section, and the associated shear force, V_{fl} :

$$M_u = P\left(\frac{l_w - a}{2}\right) = P\frac{l_w}{2}\left(1 - \frac{a}{l_w}\right) \qquad (8.1)$$

$$V_{fl} = \frac{M_u}{H_0} = P\frac{l_w}{2H_0}\left(1 - \frac{a}{l_w}\right) \qquad (8.2)$$

The depth of the compression zone a/l_w is equal to the ratio between average vertical stress (f_m), and masonry compression strength (f_{mc}) reduced by a coefficient (C) which takes into account the vertical stress distribution at the compressed toe (a common assumption is an equivalent rectangular stress block with $C = 0.85$). As a consequence the value of a/l_w does not vary much, being commonly between 0.10 and 0.30.

An approximate estimate of the shear force corresponding to the flexural strength of a masonry panel can be therefore obtained from Eq.(8.2) as:

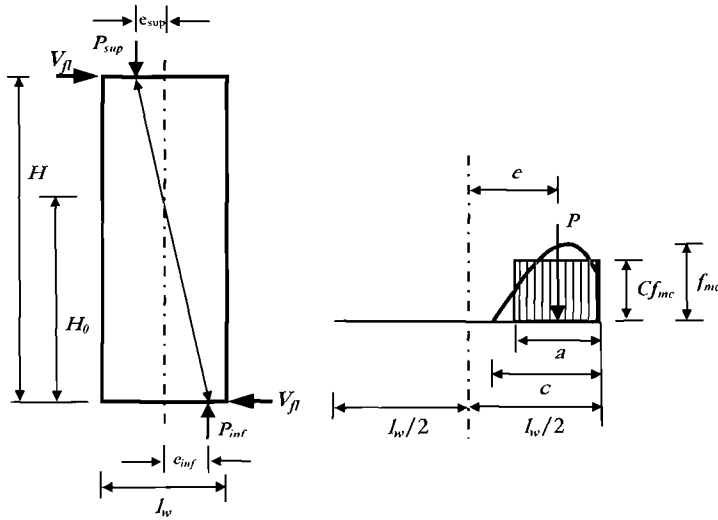$$V_{fl} \approx 0.4P\frac{l_w}{H_0} \qquad (8.3)$$

Fig.8.3   Equilibrium and Base Stress Conditions for Flexural Response of a Pier

The height to the point of contraflexure H_0 should be determined considering appropriate boundary conditions of the wall. It is theoretically equal to the height of the wall when fixity is assumed at the base and free rotation at the top, and to half of the height when the pier is assumed fixed at both ends (see Fig.8.3 for the second option). As pointed out, for common situations of relatively low mean vertical stress ($f_m/f_{mc} \leq 0.2$), a precise evaluation of compression strength and average vertical action is not critical, due to the low sensitivity of the results to the parameters C and f'_{mc}, while wall geometry and boundary constraints are strongly influencing the shear capacity.

Typical horizontal force–displacement loops for flexural response are shown in Fig.8.4. The rocking nature of the response is evident from the shape of the loops, which show relatively large displacement without significant strength loss but are characterized by relatively low energy dissipation and correspondingly low equivalent viscous damping, but low residual displacement.

The design drift for a damage-control performance can be theoretically obtained limiting the masonry strain at the compressed toe of the wall and assuming a reasonable curvature distribution in the lower part of the wall. This is shown in Fig.8.5, where the curvature is assumed to vary linearly from the maximum value at the base, limited by the assumed strain capacity of masonry (a reasonable value is $\varepsilon_{cm} = 0.004$), to zero at a height equal to the distance from the neutral axis to the tensile edge of the wall (i.e. a 45^0 spread is assumed). Assuming a maximum compression depth equal to 20% of the depth of the wall, i.e. $c = 0.2\, l_w$, the design drift is:

$$\theta_{d,fl} = \frac{\varepsilon_{cm}}{c} \cdot \frac{l_w - c}{2} = \frac{\varepsilon_{cm}}{2} \cdot \left(\frac{l_w}{c} - 1\right) = 0.002 \times 4 = 0.008 \tag{8.4}$$
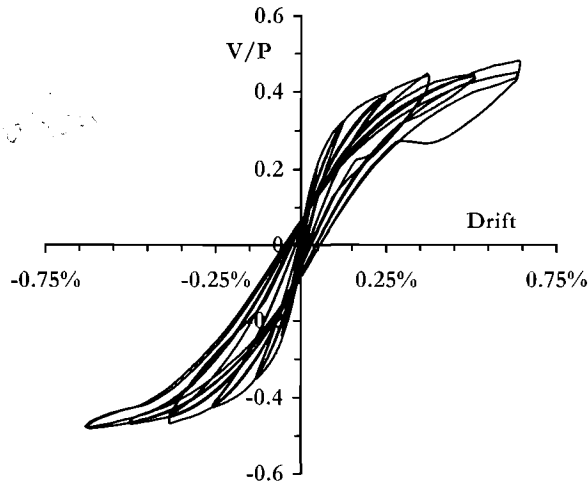
**Fig.8.4 Typical Horizontal Force–Displacement Loops for Rocking Response
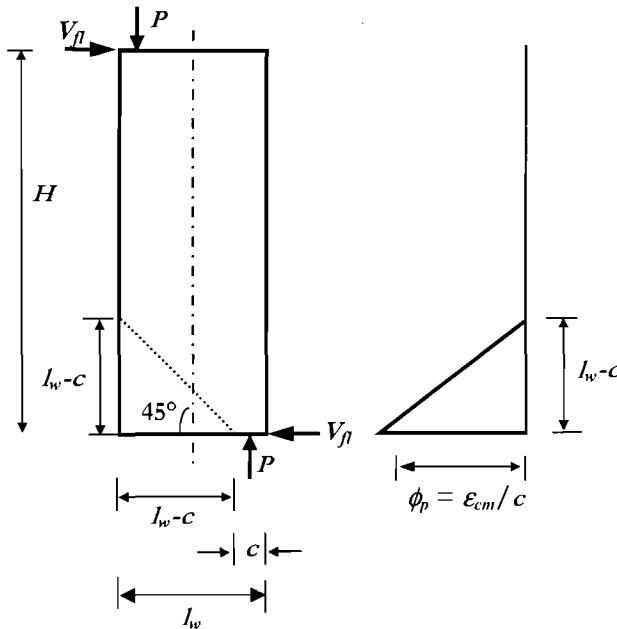(after [A6])**

Fig.8.5   Assumption for Curvature Distribution for Flexural Failure Mode

Although experimental results have shown that larger values may be obtained it is thus recommended that a limit of $\theta_{d,fl} = 0.8\%$ is assumed in design. This value is also consistent with practical considerations, related to the drift levels characterizing other failure modes and non-structural damage. It may be noted that this corresponds to an

equivalent plastic hinge length equal to $0.4l_w$, with the assumptions for ε_{cm} and c made above.

In principle, the total drift or displacement should be computed adding the elastic values to those obtained from Eq.(8.4). However, this is normally of little interest for design, since the elastic displacement should be calculated using gross section properties and will normally be in the range of one tenth of the plastic displacement capacity.

The area–based values of the equivalent viscous damping resulting from the typical flexural cycles have been estimated[M11] as $\xi_{e,fl} \approx 5\,\%$ related to the secant stiffness. Some sample experimental data are reported in Fig.(8.6). It may be argued that some additional dissipation may be obtained from radiation damping resulting from rocking response; this is generally small and will be neglected.

(c) Shear Failure Mode: The evaluation of the strength capacity of a masonry pier failing in shear is theoretically much more complex than in the case of flexural collapse. Diagonal shear cracking may originate in parts of the element where no flexural cracking is present (e.g. the central area of the panel); in this case the strength should be evaluated considering the whole horizontal section. It may also originate where the presence of flexural cracks would suggest consideration of a cracked section (such as at the base of the panel). In addition, cracks may propagate essentially through mortar layers (bed joints and head joints), in which case the most relevant parameters would be related to mortar (cohesion and friction coefficient), or may be initiated and propagated due to shear – tensile cracking of blocks.
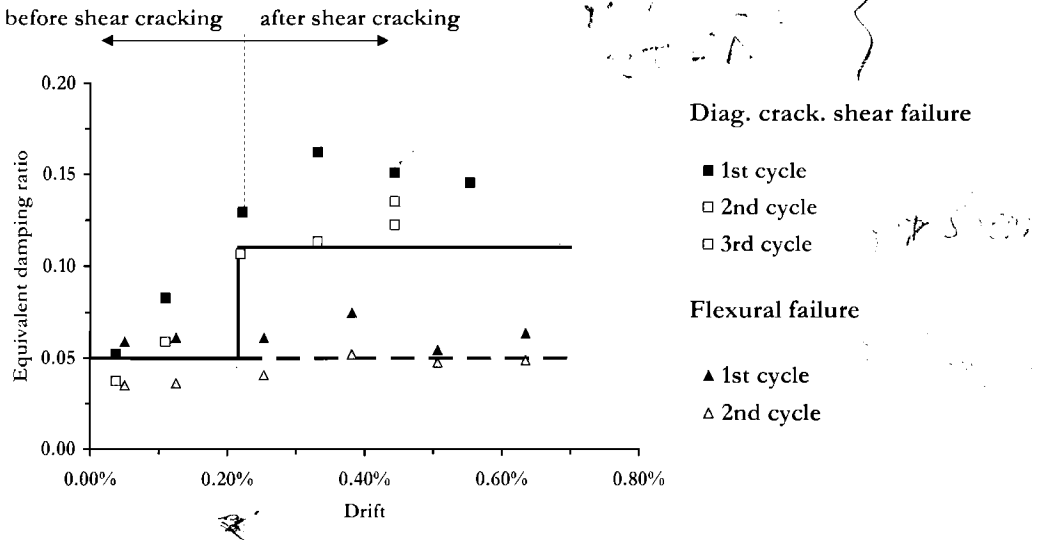

Fig.8.6   Equivalent Element Damping (area based)[M11]

Formulations to predict different kinds of collapse are available in the literature (e.g. [X9, X10, X16, X17]), but require a careful determination of the constitutive equation of blocks, mortar and block–mortar interface and are consequently of more interest for detailed analysis based on finite element modeling.

Code equations to predict the shear strength V_{sh} tend to condense the required parameters into some equivalent global friction value μ_{mf} and material shear strength v_{mv}, to be normally applied to the uncracked part of the critical section of the pier:

$$V_{sh} = \mu_{mf} \cdot P + v_{mv} \cdot a \cdot b_w$$ (8.5)

where b_w is the wall thickness, and the other symbols have already been defined.

Considering the expression for the compression depth a discussed in the previous section, and assuming that it will not vary significantly in case of shear failure, Eq.(8.5) can be rearranged as:

$$V_{sh} = P \cdot \left(\mu_{mf} + \frac{1}{C} \cdot \frac{v_{mv}}{f'_{mc}} \right)$$ (8.6)

If reasonable values are assumed, e.g. $\mu_{mf} = 0.4$, $C = 0.85$ and $v_{mv}/f'_{mc} \approx 0.05$, it is obvious that the shear strength is dominated by the value of the axial force, resulting approximately in:

$$V_{sh} \approx 0.46P$$ (8.7)

Note that comparing Eqs.(8.3) and (8.6), a flexural failure mode is predicted when the height of the point of contraflexure is higher than 0.87 times the length of the wall. It is reasonable to use a conservative estimate of 1.0 times the wall length.

Typical horizontal force–displacement loops for walls dominated by shear response are shown in Fig.8.7.

Compared to the case of flexural response (Fig.8.4), the cycles in Fig.8.7 are characterized by significantly larger energy dissipation loops, but they also show considerable strength and stiffness deterioration even for cycles repeated at the same displacement demand, and lower displacement capacity. Data in the available literature[A5, M9, M11, M12] consistently indicate design drifts for a damage-control performance of around $\theta_d \approx 0.4 - 0.5\%$, compared with 0.8% recommended above for flexural response.

Experimental data on area–based values of the equivalent viscous damping resulting from typical cycles indicate values consistently larger than $\xi_{e,sh} = 10\%$, for cycles that take place after the opening of diagonal shear cracks (see Fig.8.6, where data referring to flexural and shear response are compared[M11]). However, it should be kept in mind that these (and all other) available data refer to specific masonry materials; care should therefore be exercised in relation to the already discussed heterogeneity of the available materials.
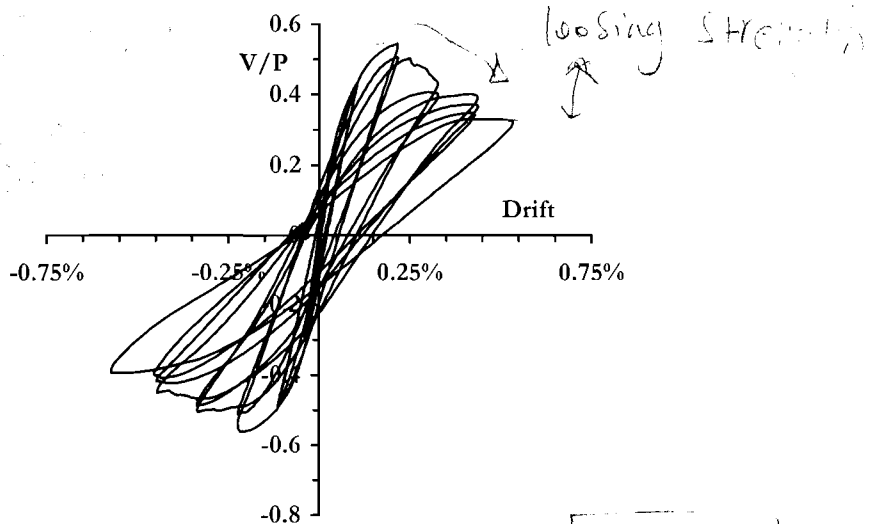
Handwritten annotations: "loosing strength"

Fig.8.7 Typical Horizontal Force–Displacement Loops for Shear Response (after [A6])

(d) Sliding Failure Mode: From a conceptual point of view, the case of sliding along bed joints differs from the previous case and is appropriately defined by the following equation, where no contribution of cohesion is considered, assuming that the joint is already cracked in tension due to flexure:

$$V_{sl} = \mu_{mf} \cdot P \tag{8.8}$$

The friction coefficient value to be used in this equation is different, in principle, from the value to be adopted in Eq.(8.5), since in this case we are dealing with a more proper frictional response, while in the previous case the value to be adopted must account for the complexity of the possible different phenomena involved.

In code approaches it is commonly accepted to neglect this failure mode, considering it to be included in the verification related to Section 8.2.1(c) above. Actually, from a displacement-based design point of view, a shear sliding damage mode should be regarded as more conservative (i.e. more desirable) than a shear mode, since the associated equivalent viscous damping would be larger, and the displacement capacity will be again limited only by practical considerations, non-structural limit states and combination with other failure modes. These may be considered good additional reasons to neglect this collapse mode in design.

Consider also that this failure mode is favoured by low quality mortar properties and solid bricks, it is therefore unlikely to take place in new construction.

(e) Reinforced Masonry: It is again emphasized that in the context of this chapter, reinforced masonry is not masonry designed for reinforced concrete emulation. The addition of relatively low amount of reinforcement (maximum levels of reinforcement percentage commonly specified in codes are of the order of 1.0% for the vertical reinforcement and 0.5% for the horizontal reinforcement) may significantly change the expected response of masonry walls, in terms of strength, deformation capacity and energy dissipation.

The evaluation of flexural strength can be carried out in analogy with reinforced concrete, assuming a compression depth equal to 0.8 times the neutral axis depth, a constant stress in the compression area equal to 0.85 f'_{mc}, and a limit strain at the compressed masonry toe of $\varepsilon_{mc} = 0.003$–0.004. The strain limit for steel can again be taken as in the case of concrete, but it is unlikely to govern the collapse mode.

The shear strength can be obtained by adding to the computed masonry strength (Eq.(8.7)) a term that takes into account the steel contribution:

$$V_{s,sh} = \frac{0.6l_w}{s} A_{sw} f_{yd} \tag{8.9}$$

It has to be noted that the steel contribution is reduced to 60 % of what would result considering 45° cracks and full yield of the horizontal reinforcement. This derives from experimental results and reflects the reduced anchoring capacity of masonry when reinforcement is laid in bed joints.

The possibility of diagonal strut compression failure due to low masonry strength in the horizontal direction should also be checked. Codes frequently indicate a limit of 30% of the compression capacity of the wall section, or lower.

In the case of reinforced masonry buildings, it will be recommended (see Section 8.3) to apply capacity design principles to avoid any possibility of shear failure in walls. While in the case of unreinforced masonry this may be difficult to obtain due to geometric constraints, appropriate use of bed-joint reinforcement may allow this objective to be satisfied. As a consequence, displacement capacity and equivalent viscous damping of reinforced masonry walls are primarily of interest related to flexural failure modes.

It may be argued that the displacement capacity could be calculated in analogy to what has been presented in relation to reinforced concrete walls, and consequently derive an expression similar to Eq.(6.7) to evaluate the length of a plastic hinge, and this can actually apply to the case of "reinforced concrete emulation". In this case, the *k* value to be obtained from Eq.(4.31b) should be increased to consider the reduced bond capacity of masonry and the consequent larger spreading of steel deformation into the wall. As well, and for the same reason, the strain penetration length into the wall will significantly increase. The following equation is therefore recommended, based on experimental evidence and engineering judgment:

$$L_{p,mw} = 0.04H_e + 0.1l_w + L_{sp} \geq 3L_{sp} \tag{8.10}$$

where L_{sp} is obtained from the standard expression (Eq.(4.30)). The equivalent yield drift can be derived from Eq.(6.15) as:

$$\theta_{y,mw} \approx 0.6\varepsilon_y \frac{H_n}{l_w} \approx 0.0014 \frac{H_n}{l_w} \qquad (8.11)$$

To calculate the total drift (or displacement) capacity, the plastic hinge length resulting from Eq.(8.10) should be multiplied by the plastic curvature (ϕ_p) resulting from the difference between the limit state curvature (ϕ_{ls}) controlled by masonry maximum compression strain (ε_{ls}) and the curvature corresponding to yield (ϕ_y). Assuming for example for a damage-control limit state with $\varepsilon_y = 0.0025$, $\varepsilon_{dc} = 0.004$ and $c/l_w = 0.2$ for both yielding and ultimate conditions, it is found that $\phi_{d-c} = 0.02/l_w$, $\phi_y = 0.0031/l_w$, and therefore:

$$\theta_{p,mw} \approx L_{p,mw} \frac{0.0169}{l_w} \qquad (8.12)$$

The equivalent viscous damping can be computed applying Eq.(3.17a). For typical values of aspect ratio and plastic hinge length, Eqs.(8.10), (8.11) and (8.12) will predict a displacement ductility of the order of 2 and the resulting equivalent viscous damping will be approximately 7%, to be added to the initial damping of 5%. Considering the value of the area–based equivalent viscous damping recommended for flexural response of unreinforced masonry buildings, a total minimum equivalent viscous damping equal to $\xi_e = \xi_v + \xi_{e,fl} = 0.05+0.05=0.10$ can be conservatively assumed for most preliminary designs. Note that because of the low ductility no adjustment to elastic damping is recommended.

8.2.2 Coupling of Masonry Walls by Slabs, Beams or Masonry Spandrels

(a) General Aspects: As discussed in Section 8.1.1, masonry walls are normally coupled by slabs and/or concrete beams but may also be coupled by masonry spandrels. As shown in Fig.8.8, different geometries and coupling conditions may lead to soft-storey failure modes or to global collapse modes that will first require a non-linear response of the coupling elements.

The bending and shear forces transmitted by coupling elements may increase the building lateral strength, may produce additional damping, increase the apparent stiffness of the walls and may modify the height of the point of contraflexure. However, the magnitude of the forces must be compatible with the capacity of the walls to assure equilibrium. These issues will be discussed in the following sections.

(b) Coupling Slabs: It is straightforward to calculate the bending moment that a coupling beam can transmit to the adjacent walls, based on its moment capacity. When coupling is by concrete slabs, consideration should be given as to what contributing width of slab should be adopted. Recommendations on this aspect are provided in several text books (e.g. [P1]).
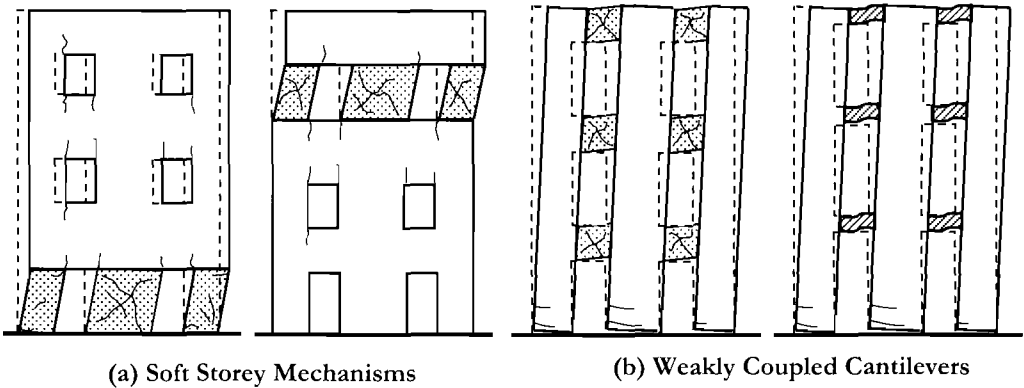
(a) Soft Storey Mechanisms   (b) Weakly Coupled Cantilevers

Fig.8.8   Possible Failure Mechanisms of Coupled Masonry Walls

It is however recommended to be cautious in adopting large width values, in consideration of the significant local deformability of masonry walls. A width corresponding to the thickness of the wall plus a similar width on each side of it is considered appropriate for determining design strength. Larger widths are appropriate for upper-bound estimates necessary for capacity-protection considerations. The maximum transmittable shear is then obtained by equilibrium of the coupling beam, as the sum of the moments divided by the span.

The capacity of an unreinforced masonry wall to equilibrate moments and shears depends essentially on the weight transmitted by the beam or slab and by the upper wall. With reference to Fig.8.9, the following equilibrium equation can be written:

$$M_1 + V_1 \frac{l_w}{2} + M_2 + V_2 \frac{l_w}{2} \leq W_w \frac{l_w}{2} + \left(W_w + W_s\right)\frac{l_w}{2} \tag{8.13}$$

which implies the following limitation:

$$\frac{M_1 + M_2}{l_w} + \frac{V_1 + V_2}{2} \leq W_w + \frac{W_s}{2} \tag{8.14}$$

where M and V are the moments and shears transmitted by the beam/slab, and W_w and W_s are the weight supported by the wall (including self weight) above the level considered, and the tributary weight of the beam/slab respectively.

Modifications to be considered for the case of an end wall or of a top storey floor are obvious, though in the latter case the coupling moment for an end wall will depend on the direction of lateral force. Note that when coupled by composite beam/slabs (rather than by slabs alone) coupling moments of opposite sign may be significantly different because of the presence of the slab, which may be in compression or in tension.
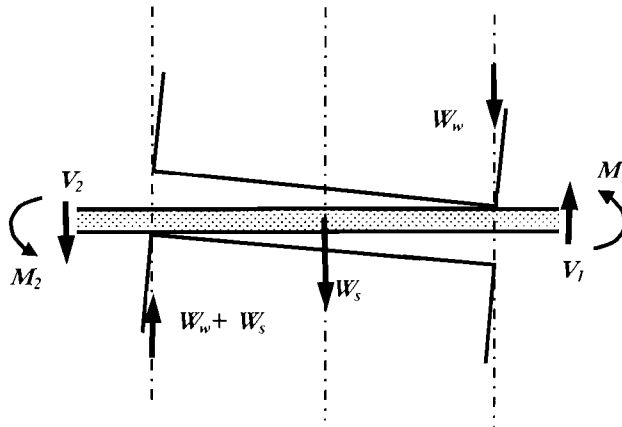
Fig.8.9 Equilibrium Conditions of a Coupling Beam Intersecting a Masonry Wall

In the case of reinforced masonry, the modifications are also rather obvious, but of less interest, since in this case it is unlikely that the equilibrium of the wall poses a limit to the maximum transmittable bending moment and shear.

(c) Masonry Spandrels: In principle, moment input from masonry coupling beams spandrels) can only be considered if a compression force is dependably assured in the horizontal direction, or when some horizontal elements, such as steel ties or floor slabs/beams or flexural resisting lintels can provide a tensile force capable to provide horizontal equilibrium. The alternatives are explained in Fig.8.10.

If a compression force is provided, the evaluation of the maximum transmittable bending moment and shear do not differ from that discussed in relation to masonry walls coupled with reinforced concrete beams and slabs. However, the compression strength of masonry in the horizontal direction should be considered, which can be significantly lower than that in the vertical direction. In addition, the aspect ratio (obviously to be considered with reference to the horizontal axis) is often such that a shear collapse will be predicted (considering the double-bending condition, this case has to be expected for a ratio between width of the opening l_s and height of the spandrel h_s lower than $l_s/h_s = 2$). In this case, the opening of diagonal shear cracks in both directions may imply a strong deterioration of the spandrel capacity with cyclic loading.

The same consideration may apply in the most common case of a restraining tensile force provided by a slab or lintel. As shown in Fig.8.10(a) a masonry spandrel located on top of a beam or slab will act as a compression strut, resulting in a bending moment close to zero at the compression wall and in a maximum bending moment, at the tensile wall, approximately equal to the tensile force developed in the beam multiplied by a lever arm equal to the depth of the spandrels minus one half of the compression depth.
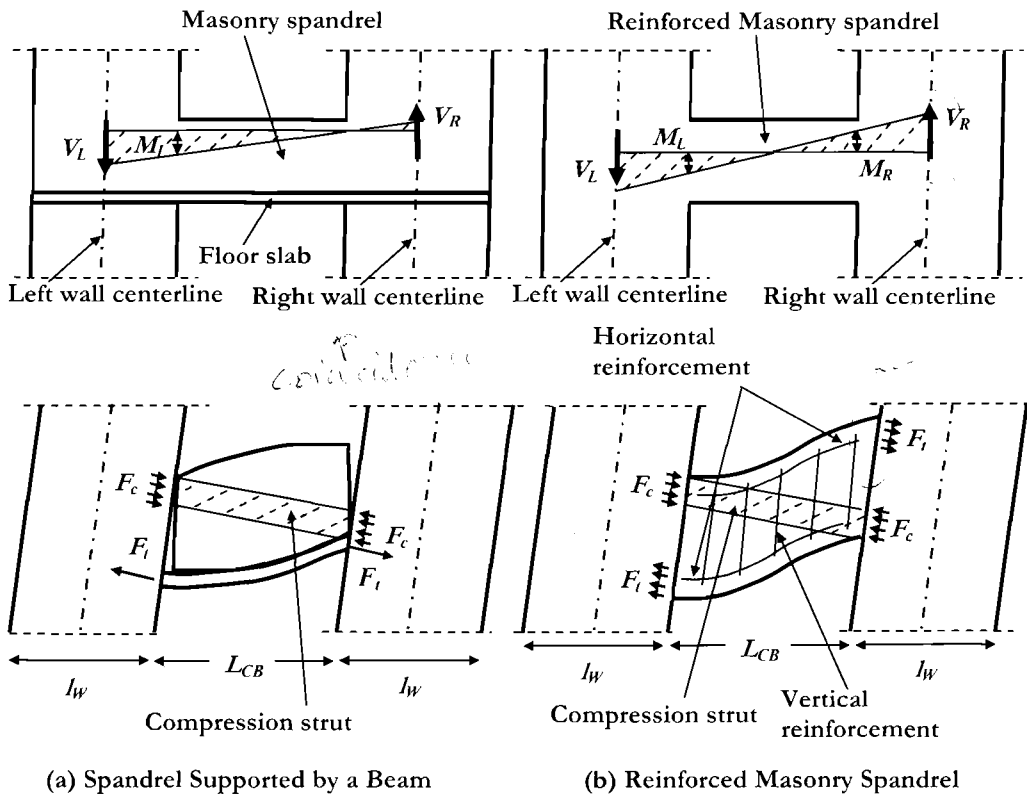
Fig.8.10   Equilibrium of Masonry Spandrels

The bending moment will also be limited by the compression capacity of masonry in the horizontal direction, by the maximum admissible masonry strain, and by the shear capacity of the spandrel. In addition, if the beam reinforcement is considered to provide the computed tensile force, it will not also contribute to the development of the beam bending moment, or vice versa.

For all the above reasons, it is not recommended to design considering the contribution of unreinforced masonry spandrels to increase the coupling between different walls, except in special cases where all the actual parameters are carefully considered.

In the case of reinforced masonry, the tensile force required to assure the horizontal equilibrium can be provided by the horizontal reinforcement, as shown in Fig.8.10(b). However, it may still be difficult to avoid a shear failure if the aspect ratio is relatively low, because of the possible difficulties in locating significant amounts of vertical reinforcement (see again Fig.8.10(b)). Even in the case of predicted shear damage, the presence of reinforcement will reduce the opening of diagonal cracks and the cyclic strength deterioration; therefore a contribution of the spandrels can be more reliably accounted for.

In all cases, however, the capacity of the spandrels to cope with the local imposed drift resulting from geometry and compatibility with the design drift assumed for the walls should be carefully considered. As discussed with reference to coupling beam drift (see Section 6.8.3) the rotation at the ends of a coupling beam is always larger than the wall rotation, as expressed by Eq.(6.62), reported here as Eq.(8.15) for convenience.

$$\theta_{CB} = \theta_w \left(1 + l_w / L_{CB}\right) \tag{8.15}$$

Since it will be difficult to provide a much larger rotation capacity to the coupling beam than to the wall, it is recommended to neglect the spandrels contribution unless the width of the opening (L_{CB}) is significantly larger than the width of the adjacent walls (l_w) and the spandrel rotation demand is therefore limited to, say, 1.5 times the wall rotation.

8.3 DESIGN PROCESS FOR MASONRY BUILDINGS

8.3.1 Masonry Coupled Walls Response

(a) Introduction: The design process for masonry buildings will not differ conceptually from that discussed in Chapter 3 from a general point of view and in Chapter 6 with specific reference to wall buildings.

In general, less emphasis should be placed on torsional response, because masonry buildings are always highly redundant restrained systems; this topic will be therefore initially neglected and only briefly addressed in Section 8.4.

Second order (*P-Δ*) effects are also unlikely to be relevant, due to the limitation imposed to the acceptable displacement. Therefore they will not be considered (though the principles discussed for wall buildings are directly applicable).

Masonry buildings are in general simple, small structures and it is therefore appropriate to consider simplified design approaches. This is particularly the case for unreinforced masonry buildings, for which even the application of capacity design principles is difficult and often unreliable, since it is not possible to modify the shear and flexural capacities independently without modifying element aspect ratios. For unreinforced masonry buildings an absolute maximum of three storeys is considered appropriate in high seismicity regions.

More complex approaches, including relevant capacity design rules, should be considered for reinforced masonry (of the type considered in this chapter) based on the recommendations of Chapter 6. In this case a limit of five storeys is recommended.

(b) Coupling Action: In general, masonry buildings will be designed in each direction with structural walls coupled by reinforced concrete beams and/or slabs. As a consequence, the procedure will be similar to that discussed in Section 6.8 for the case of coupled shear walls, and the relevant parameters will be the effective height (H_e), the coupling ratio (β_{CB}) and the height of contraflexure (H_{CF}).

It is interesting to observe that the limited number of storeys does not imply significant differences from the trends discussed with reference to Fig.6.32. Effective and contraflexure height are shown in Fig.8.11 as a function of total number of storeys (n), total height (H_n) and coupling ratio.

The effective height is essentially constant at around 0.8 times the height of the building; the contraflexure height is not significantly affected by the small number of storeys and its variation with β_{CB} is similar to that shown in Fig.6.32. Note, however, that the coupling degree will not be a design choice, but will depend essentially on the characteristics of the floor slabs and ring beams. The factor β_{CB} will normally assume relatively low values, say below 0.5, in which case the height of contraflexure will not differ significantly from the effective height.
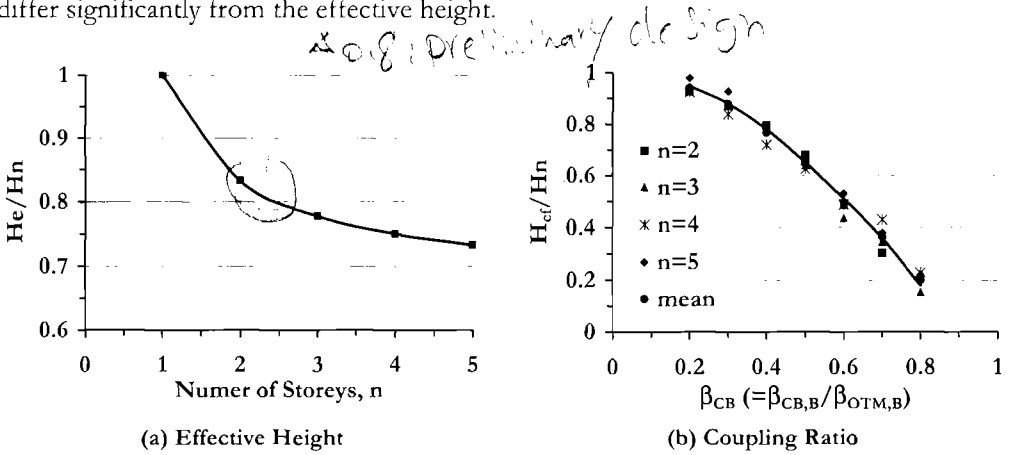

(a) Effective Height   (b) Coupling Ratio

Fig.8.11   Effective and Contraflexure Height as a Function of Number of Storeys and Coupling Action

A fundamental difference from the case of reinforced concrete coupled walls is that in this case the coupling ratio is a design datum rather than a variable. As discussed in Section 8.2.2, only the coupling provided by concrete beams and slabs will be accounted for. It will obviously be assumed that for each coupling beam i, the bending moment capacity M_{yi} and the corresponding yield rotation θ_{ybi} have been calculated. The yield rotation can be computed from the equations derived in Section 3.4.2, appropriately modified to this specific case.   Including some 10% contribution from the shear deformation, Eq.(8.16) is obtained:

$$\theta_{ybi} = 0.35\varepsilon_y \frac{l_{bi,eff}}{h_{bi}}$$

(8.16)

An extended effective length of the beam ($L_{bi,eff}$) is considered, to take into account some curvature penetration into the masonry wall, as a function of the beam section depth h_{bi}:

$$L_{bi,eff} = L_{bi} + 2h_{bi} \tag{8.17}$$

The rotation demand of each beam can be computed as discussed with reference to Fig.6.33 and Eq.(6.62), considering a rigid rotation at the wall bases. When several walls and openings are considered, as shown in Fig.8.12, the rotation demands for each beam are:

$$\theta_{b1} = \theta_w \left(1 + \frac{l_{w1} + l_{w2}}{2L_{b1,eff}} \right) \tag{8.18a}$$

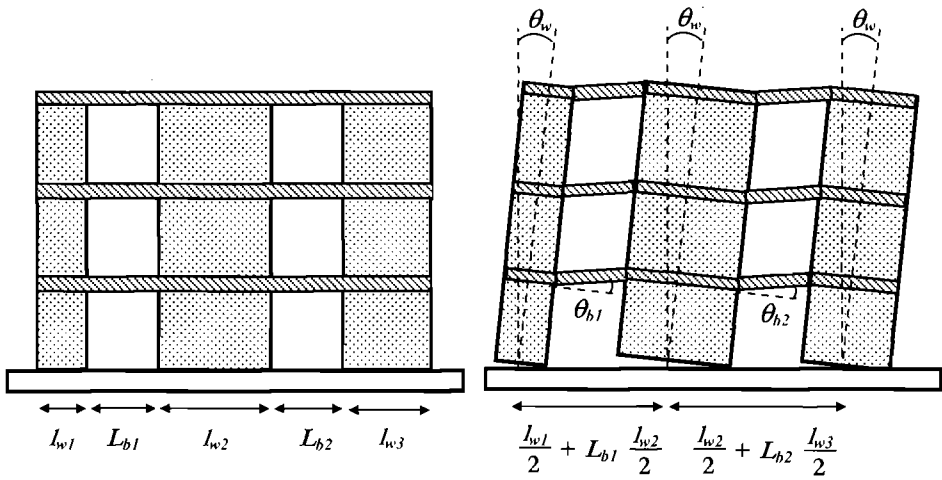$$\theta_{b2} = \theta_w \left(1 + \frac{l_{w2} + l_{w3}}{2L_{b2,eff}} \right) \tag{8.18b}$$

Fig.8.12 Walls and Coupling Beams Rotations

Note that θ_w is the wall design drift, which will be known at the start of the design process.

Since for each beam the rotation demand and the yield rotation are known, the bending moment (M_{bi}) transmitted by each beam to a wall will be computed as:

$$M_{bi} = M_{ybi} \qquad \text{if } \theta_{bi} \geq \theta_{ybi} \tag{8.19a}$$

$$M_{bi} = \frac{\theta_{bi}}{\theta_{ybi}} M_{ybi} \qquad \text{if } \theta_{bi} \leq \theta_{ybi} \tag{8.19b}$$

The shear forces corresponding to the bending moment will be immediately computed by equilibrium. In the case of unreinforced masonry walls, bending moments and shear forces have to be compatible with Eqs.(8.13) and (8.14).

8.3.2 Design of Unreinforced Masonry Buildings

(a) General Aspects: As already pointed out, unreinforced masonry buildings in high seismicity areas are normally simple buildings with a limited number of storeys (a maximum of three is here assumed). A desired structural layout is known at the start of the design process, resulting from architectural choices and constraints. Therefore the design is essentially an assessment of the expected performance, possibly followed by an adjustment of the layout of the structural walls. As a consequence, there is little possibility of applying any sort of capacity design principle, given that wall geometries and capacities are essentially defined and damage and collapse modes can hardly be modified.

As discussed, only planar (rectangular section) walls coupled by concrete beams will be considered part of the structural system. Different choices will not imply conceptual modification of the design approach, but will generally require careful consideration of all possible damage modes.

On the basis of these premises, a simple design approach will be presented and discussed, without considering any preliminary application of capacity design procedures and therefore accepting in principle the possibility of shear damage in the walls. Shear collapses will be likely to be predicted for one-storey buildings with relatively low wall aspect ratios or in cases with rather high coupling between walls, provided by slabs or spandrels (which will substantially reduce the contraflexure height). It is however considered appropriate to initially assume a flexural response for all walls, and to check that this is actually the case at the end of the design process. Modifications of the procedure to obtain more efficient structural layouts does not present any conceptual difficulty; however, careful verification of the actual response should be required.

(b) Design Displacement and Equivalent Viscous Damping: In general, the structural system will be composed by either walls where a flexural damage mode is expected, or walls where a shear damage mode will be predicted. However, since only coupling from floor slabs will be considered, it is assumed that in all cases a global pier mechanism (Fig.8.8(b)) will take place, rather than soft-storey mechanisms (Fig.8.8(a)).

As discussed in Section 8.2, in the case of flexural response a drift of $\theta_{d,fl} = 0.8\%$ and a total equivalent viscous damping ratio $\xi_{e,fl}=0.10$ may be assumed for initial design. This damping level will imply a reduction factor to be applied to the 5% damped displacement spectrum of $R_\xi=0.76$, from Eq.(2.8), for "normal" earthquake characteristics.

In the case of a shear damage mode, a drift of $\theta_{d,sh} = 0.4\%$ and a total equivalent viscous damping of $\xi_{e,sh} = 0.15$ have been recommended. This damping level will imply a reduction factor to be applied to the 5% damped displacement spectrum of $R_\xi = 0.64$.

Designing for a shear failure mode will thus require an effective period 41% shorter than for a flexural failure, and a lateral strength 184% higher than for a flexural mode (see Eqs.(3.1) and (3.2)).

(c) Equivalent Mass and Height: The equivalent mass can be assumed in all cases equal to 90% of the total mass, with adequate accuracy. As shown in Fig.8.11, the effective height can be assumed as $H_e = 0.8H_n$ (with the obvious exception of a single storey building where $H_e = H_n$). The design displacement on the 10% damped spectrum will thus approximately be:

$$\Delta_{d,10\%} = 0.0064 H_n \tag{8.20}$$

(d) Coupling Action and Contraflexure Height: Based on the design displacement (or drift), the drift demand and the corresponding moment and shear values can be computed for each one of the coupling beams, as discussed in Section 8.3.1(b) and expressed in Eqs.(8.18) and (8.19) (with the limitations defined by Eqs.(8.13) and (8.14)). For each wall it is thus possible to calculate the total moment resulting at the wall base due to the presence of the coupling beam ($M_{CB,B}$, equal to the sum of all beam moments and shear force contributions at the wall centreline).

For each wall it is also possible to calculate the moment capacity (M_{uw}), applying Eq.(8.1). Note that in this case the axial force P may include a component from the coupling beam shear forces (see below). The total overturning moment capacity will be $M_{OTM} = M_{uw} + M_{CB,B}$ and, as discussed in Section 6.8.1, the degree of coupling will be expressed as (Eq.(6.54)):

$$\beta_{CB} = M_{CB,B} / M_{OTM} \tag{8.21}$$

The height of contraflexure for each wall will be read from Fig.8.11(b) and it will be straightforward to check that a flexural collapse mode will actually control, verifying that the shear demand resulting from Eq.(8.2) (with the appropriate value of $H_0 = H_{CF}$) is lower than the capacity resulting from Eq.(8.6). If this should not be the case for any wall, either the geometry should be modified, or the displacement capacity and equivalent viscous damping typical of a shear damage mode should be adopted.

It has to be noted that yielding of coupling beams, if any, will contribute to increase the total dissipated energy, and may consequently affect the damping value, reducing the displacement demand. This effect can be relevant if significant ductility demand is predicted in the coupling beams and a significant coupling is resulting for several walls (relatively high values of β_{CB}). If this should be the case, the system damping can be recalculated applying Eq.(3.17b) to compute the beam equivalent viscous damping, Eq.(6.66a) to each wall–coupling beams system and then combining the wall damping values as discussed in Section 3.5.4 for structural elements working in parallel. The design displacement will thus be reduced and an iteration of the process will be required.

(e) Strength Demand and Capacity: The design process will proceed as usual; therefore the global strength demand will result from entering the displacement spectrum with the appropriate design displacement and equivalent viscous damping, reading the

corresponding period of vibration, T_e, calculating the equivalent stiffness (Eq.(3.1)) based on the equivalent mass and finally multiplying stiffness and displacement (Eq.(3.2)).

Note that the global strength capacity is simply the sum of the capacity of each wall and consequently if an insufficient global strength is assessed, it will be a design choice to decide which wall should be made stronger, provided that symmetry is conserved.

Note, as well, that the process outlined has not considered the axial force variation in the masonry piers due to coupling. With reference to Fig.8.2, the axial force variation will be small for any interior wall (such as wall **2** in Fig.8.2), since the shear forces on the two opposite sides will have opposite signs, while it can be significant for an end wall (such as walls **1** and **3** in Fig.8.2). In all cases, the axial force variation will compensate, increasing compression on one end wall and decreasing on the other one. The total shear strength will be only marginally affected. It is however straightforward to include the effect of axial force variation in the evaluation of strength, or to check that its global effect on the total strength is negligible, since the beam shear forces are known and the axial force variation at the wall base is simply the sum of the shear values in the beams.

(f) **Example 8.1:** To illustrate the procedure, consider the simple case of two-storey coupled shear walls separated by a continuous opening and coupled by floor beams (Fig.8.13).

The total length of walls plus opening is 7.5 m (24.6 ft); various configurations of walls will be considered. The appropriate floor weight (dead plus seismic live load) is assumed to be 8 kN/m² (0.17kip/ft²), with possible tributary widths of 5 m (16.4 ft) (i.e. floor load 40 kN/m) or 1 m (3.28 ft) (i.e. floor load 8 kN/m).

The masonry walls are assumed to be 250 mm (9.8in) thick, with compression strength f_{cm} = 6 MPa (870psi), shear strength f_{mv} = 0.4 MPa (58psi) and weight per unit volume w_m = 15 kN/m³ (96lb/ft³).

The floor beams are assumed 250 mm thick, with a moment capacity M_{bi} = 45 kNm (398 kip.in) in both directions, calculated considering an appropriate equivalent width. The reinforcement steel has a yield stress f_y = 500 MPa (72.5ksi).

The building is located in a moderate seismicity area, with the input ground motion represented by a displacement spectrum with a corner period at 2 s. and a corresponding corner displacement demand equal to 200 mm (7.9in).

(i) case one – wall 1 = 2 m (78.7 in), opening = 2.5 m (98.4 in), wall 2 = 3 m (118.1 in), tributary floor 5 m (196.9 in) wide:

Wall 1

Load at the base: W_1 = (2×3.25×40)+(6×2×0.25×15)   = 305 kN (68.6 kips)

Average stress: f_{m1}=305/(2×0.25)   = 0.61 MPa (88.5 psi)

Compression depth: a_1/l_{w1} = 0.61/(0.85×6) = 0.12

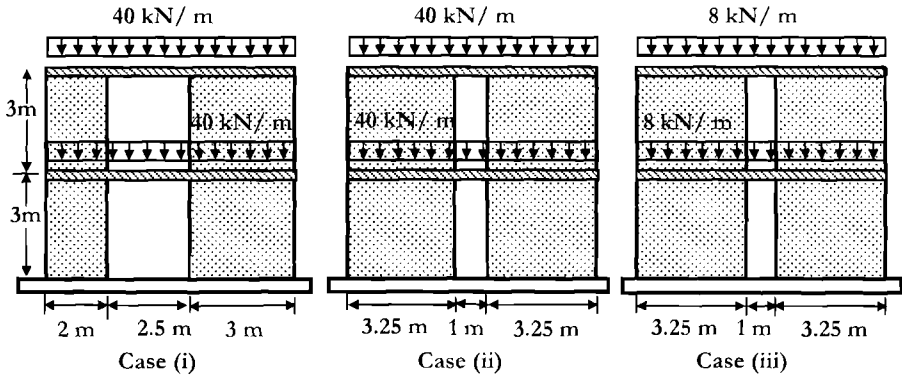Flexural capacity, from Eq.(8.1): M_{w1} = 305×(2/2)×(1-0.12) =268.5kNm (2375kip·in)

Fig.8.13 Coupled Walls of Example 8.1

Wall 2

Load at the base: $W_2 = (2 \times 4.25 \times 40) + (6 \times 3 \times 0.25 \times 15) = 407.5$ kN (91.6 kips)

Average stress: $f_{m2} = 407.5/(3 \times 0.25) = 0.54$ MPa (78.3 psi)

Compression depth: $a_2/l_{w2} = 0.54/(0.85 \times 6) = 0.11$

Flexural capacity: from Eq.(8.1): $M_{w2} = 407.5 \times (3/2) \times (1 - 0.11) = 546.1$ kNm (4830kip·in)

Design displacement and damping

Effective height: from Section 8.3.2(c): $H_e = 0.8\ H_n = 4.8$ m (15.7ft)

Design drift: from Section 8.2.1(b): $\theta_d = 0.8$ %

Design displacement: $\Delta_d = \theta_d H_e = 0.008 \times 4.8m= 38.4$ mm (1.51 in)

Equivalent viscous damping: from Section 8.2.1(b): $\xi_e = 0.10\%$

Spectrum reduction factor: (Section 8.3.2(b)): $R_\xi = 0.76$

Hence damped corner displacement: $\Delta_{C,0.1} = 0.76 \times 200 = 152$ mm (5.98 in)

Strength demand

Equivalent mass: From Section 8.3.2(b): $m_e = 0.9\Sigma m = 0.9 \times (305 + 407.5)/9.8$

i.e. $m_e = 65.4$ kNs^2/m (0.373 kip·s^2/in)

Equivalent period of vibration: $T_e = 2 \times (38.4/152) = 0.505$ s

Equivalent stiffness: $K_e = 4\pi^2 \times 65.4/0.51^2 = 9920$ kN/m

Base Shear demand: $V_{Base} = 9920 \times 0.0384 = 381$ kN (85.6 kips)

Total overturning moment demand: $M_{OTM} = 381 \times 4.8 = 1829$ kNm (16189kip·in)

Coupling action

Beam coupling moment capacity: (at wall face) $M_{bi,y} = 45$ kNm (398 kip·in)

Beam coupling shear capacity: $V_{bi,y} = 2 \times 45/2.5 = 36$ kN (8.1 kips)

Check wall capacity (top of wall **1**, Eq.(8.14), noting that $M_2 = 0$ and $V_2 = 0$):

$(45+0)/2+(36+0)/2 = 40.5 < 0 + 3.25 \times 40/2 = 65$ (OK- full coupling)

Beam effective length (Eq.(8.17)): $l_{bi,eff} = 2.5 + 2 \times 0.25 = 3$ m (9.84 ft)

Beam yield rotation (Eq.(8.16)): $\theta_{bi,y}\ 0.35 \times 0.0025 \times 3/0.25 = 0.0105$ (1.05%)

Beam rotation demand corresponding to 0.8% design drift (Eq.(8.18)):

$\theta_{bi,d} = 0.008(1 + (2+3)/(2 \times 3)) = 0.0147$ (1.5%)

Thus the beams yield, and therefore: $M_{bi} = M_{bi,y}$ and $V_{bi} = V_{bi,y}$

Note that the ductility demand in the coupling beams is small; therefore the additional equivalent viscous damping can be neglected.

Total coupling moment: M_{CB} =2×(45+1×36+45+1.5×36) = 360 kNm 3190kip·in)

Axial force variation on each wall: $\Delta P_w = 2 \times V_{bi,y}$ = 72 kN

Coupling degree related to strength demand: Eq.(8.21):

$$\beta_{CB} = M_{CB}/ M_{OTM} = 360/1829 = 0.31$$

From Fig.8.11(b) the contraflexure height is approximately H_{CB} = 0.85 H_n, therefore the aspect ratio of the 3m (118.1 in) long wall is 0.85×2×3/3=1.7>1.0. There is thus no danger of shear collapse (this can easily checked applying Eq.(8.6) to each wall: the shear strength is significantly larger than the flexural strength).

Strength capacity

The total overturning moment capacity is thus approximately equal to $M_{OT,C}$ = 268.8 + 546.1 + 360.0 = 1175 kNm (10400 kip·in), significantly lower than the flexural demand M_d = 1829 kNm (16189 kip·in) and consequently the design should be revised. If we take the variation of axial force into account, the total overturning moment depends on the direction of lateral force, as a consequence of the different wall lengths, resulting in 1175±30kNm (10400±266 kip·in), for a minimum capacity of 1145kNm (10135 kip·in), only 63% of the required capacity. It is thus decided to reduce the opening to 1.5 m (59.1 in), increasing the coupling action, and designing two identical walls of 3.25m (128 in) length.

(ii) case two – wall 1 = wall 2 = 3.25 m (128 in), opening = 1.0 m (39.4 in), tributary floor 5 m (196.9 in) wide: Since the calculations are repetitive of those for case (i), only the final results are included:

Wall 1 and 2
Load at the base: W_i = 300 + 73.1= 371 kN (83kips)
Average stress: f_{mi} = 0.46 MPa (67 psi)
Compression depth: a_i/l_{wi} = 0.090
Flexural capacity: M_{wi} = 549 kNm (4860 kip·in)
Design displacement and damping
identical to the previous case.
Strength demand
Equivalent mass: m_e = 68.1 kNs²/m (0.389kip·s²/in)
Equivalent period of vibration: T_e = 0.51 sec
Equivalent stiffness: K_e = 10340 kN/m
Base Shear demand: V_{Base} = 397kN (89 kips)
Total overturning moment demand: M_{OTM} = 1905 kNm (16,900 kip·in)
Coupling action
Beam coupling moment capacity: $M_{bi,y}$ = 45 kNm
Beam coupling shear capacity: $V_{bi,y}$ = 90 kN

Check wall capacity (top of walls):   58.8 < 75 (OK- full coupling))
Beam effective length (Eq.(8.17)): $l_{bi,eff}$ = 1.5 m
Beam yield rotation (Eq.(8.16)): $\theta_{bi,y}$ = 0.0053
Beam rotation demand (Eq.(8.18)): $\theta_{bi,d}$ = 0.0253

The ductility demand in the coupling beams is in this case μ_d = 4.77 and would correspond to an equivalent viscous damping of ξ_{eq} = 0.19 (from Eq.(3.17b)) and some reduction of the displacement demand may result, which would be more relevant for higher values of β_{CB}.

Total coupling moment: M_{CB} = 765 kNm

Axial force variation on each wall: ΔP_w = 180 kN

Coupling degree: (related to demand strength) β_{CB} = 0.41

Again, the contraflexure height (H_{CB} = 0.77 H_n, from Fig.8.11) does not imply any potential for shear collapse.

The system global equivalent viscous damping can be evaluated from Eq.(6.66a), as:

$$\xi_{sys} = (1-0.41)\times 0.10 + 0.41\times 0.18 = 0.13$$

Strength capacity

The total overturning moment capacity $M_{OT,C}$ = 2 × 548.6 + 765 = 1862 kNm (16481 kip·in), is still slightly (2.3%)lower than the flexural demand M_{OTM} = 1905 kNm (16862 kip·in), but it can immediately be verified that introducing the spectrum reduction factor corresponding to the corrected equivalent viscous damping (R_ξ = 0.68), the equivalent period would be T_e = 0.56 sec and consequently the bending moment demand would decrease to 1580 kNm (13985 kip·in). The design is satisfactory, and a solution with wall lengths of 3m, and a coupling slab of 1.5m (59.1 in) might be investigated.

iii) case three – wall 1 = wall 2 = 3.25 m (128 in), opening = 1.0 m (39.4 in), tributary floor 1 m (39.4 in) wide: it is of interest to discuss a case where the limited floor tributary area significantly reduces the vertical load on the wall. In general, the coupled walls examined in the previous examples will participate in the global reaction system, and only for the sake of simplicity it was assumed to have the same total weight participating in the dynamic response. In other words, internal cross-walls reduce the gravity load on the walls in Fig.8.13(iii). It is here assumed that the global properties of the system have been previously evaluated resulting in the same displacement demand and equivalent period of vibration of the previous example (i.e. Δ_d 38.4 mm (1.512 in), T_e = 0.51 sec). The contribution of the wall to the global strength is here assessed.

Wall 1 and 2

Load at the base: W_i = 60 + 73.1 = 133 kN (30 kips)
Average stress: f_{mi} = 0.16 MPa (23.2psi)
Compression depth: a_i/l_{wi} = 0.032
Flexural capacity: M_{wi} = 209.3 kNm (1850 kip·in)

Coupling action

The coupling beam bending contribution is now lower, because it cannot rely on the contribution of the same amount of slab steel. It is assumed at 50 % capacity with respect to the previous situation.

Beam coupling moment capacity: $M_{bi,y}$ =22.5 kNm (199 kip·in)
Beam coupling shear capacity: $V_{bi,y}$ = 45 kN (10.1 kips)
Check wall capacity (top of walls): (Eq.(8.14):   29.9 > 15 (inadequate)

Full coupling action cannot therefore be transmitted at the top level. We approximate the coupling action by proportion from the equilibrium capacity/demand inequality as

Second floor beam coupling moment: $M_{bi,y}$ = 22.5×15/29.9=11.3 kNm (100 kip·in)
Second floor beam coupling shear: $V_{bi,y}$ = 22.5 kN (5.1 kips)
Check wall capacity (first storey):   58.8 < 118.1 (OK- full coupling)

Beam effective length, yield rotation and rotation demand are the same as before, but only at the first storey will this imply yielding, with: μ_{d1} = 4.77

Total coupling moment: M_{CB}= 286.8 kNm (2539 k ip·in)
Axial force variation on each wall: ΔP_w = 67.5 kN (15.2 kips)
Coupling degree: β_{CB} = 0.52

This high level of coupling corresponds to a height of contraflexure $H_{CF} \approx 0.62~H_n$ = 3.72 m (146.5 in), the shear force corresponding to a wall flexural capacity is V_{fl} = 56.2 kN (12.6 kips), while the shear collapse capacity is V_{sh} = 63.7 kN (14.3 kips) (from Eq.(8.6)). A flexural damage mode is therefore still predicted.

Strength capacity

The total flexural capacity of the coupled walls is now $M_{OT,C}$ = 2 × 209.3 + 286.8= 705.4 kNm (6244 kip·in), i.e., less than 40 % of the previous case.

Note that considering the effects of axial load variations on the two walls will lead to the following results:

Wall 1

Load at the base: W_1 = 133.1 – 67.5 = 65.6 kN (14.8 kips)
Average stress: f_{m1} = 0.081 MPa (11.75 psi)
Compression depth: a_1/l_{w1} = 0.016
Flexural capacity: M_{w1} = 104.9 kNm (928.5 kip·in)

Wall 2

Load at the base: W_2 = 133.1 + 67.5 = 200.6 kN (45.1 kips)
Average stress: f_{m2} = 0.25 MPa
Compression depth: a_2/l_{w2} = 0.04
Flexural capacity: M_{w2} = 310.2 kNm

The total resulting flexural capacity of the two walls is less than 1 % different from that computed neglecting the axial force variation. Clearly, the height of contraflexure for the two walls will now be different, and shear and flexural collapses will be predicted to be very close for wall 1. In fact, the predicted height of contraflexure is 3.24 m (127.6 in), with shear and flexural capacity approximately equal $V_{fl} \approx V_{sh} \approx 32$ kN (7.19 kips).

$$\mathcal{S} \mathcal{L} \, \circ \cdot \mathcal{A}$$

$$\theta_d = C \cdot b', \quad m_\varepsilon = c \cdot q n l$$

8.3.3 Design of Reinforced Masonry Buildings

$$\mathcal{S}_\theta = 10\%, \quad H_e = o.8 H$$

(a) General Aspects: Design of reinforced masonry buildings is conceptually different from the case of unreinforced masonry for several main reasons:

- Vertical reinforcement increases flexural strength and provides increased energy dissipation therefore increasing equivalent viscous damping. Horizontal reinforcement increases shear strength.
- The flexural and shear strength of masonry piers can be independently varied, within limits, by appropriate selection of the vertical and horizontal reinforcement percentages. As a consequence, capacity-design principles can be applied to avoid shear damage and collapse, and the required flexural strength can generally be obtained, without significant variation of the building geometry.
- The design displacement cannot be defined a priori on the basis of an accepted drift, since the actual drift capacity of each wall may be different, depending on geometry and on reinforcement details. In general, the presence of reinforcement will not imply significantly larger displacement capacity with respect to unreinforced masonry; design drifts larger than 1% are rarely attainable.
- Similarly, the equivalent viscous damping will depend on the final design, as a function of each wall's ductility demand. Normal ductility levels are in the range of 2 - 2.5 and the resulting equivalent viscous damping will not be much larger than in the case of unreinforced masonry. Values normally obtained are up to around 15 %.
- For the above reasons, design may imply some iteration, unless conservative choices are accepted for design displacement and equivalent viscous damping at the start.

The recommended design procedure will be similar to that suggested for unreinforced masonry, considering only planar walls coupled by concrete beams or slabs.

(b) Design Displacement and Equivalent Viscous Damping: As anticipated, a flexural failure mode will be assumed for all walls composing the structural system and only global pier mechanisms will be considered possible, without formation of any soft storey mechanisms.

As discussed in Section 8.2, minimum (default) values to be assumed for design drift and equivalent viscous damping are those characterizing a flexural response in unreinforced masonry, i.e. a drift $\theta_d = 0.8$ % and a total equivalent viscous damping $\xi_e = 10$ %.

To have a better feeling about the possibility of increasing the design drift, the following procedure can be applied, to take into account building geometry and reinforcement details:

1. Decide the diameter to be used for vertical reinforcement steel, apply Eq.(4.30) and evaluate the length of strain penetration (for example, with $d_{bl} = 16$ mm (0.63 in) and $f_{ye} = 500$ MPa (72.5 ksi), it follows that $L_{SP} - 176$ mm (6.9in));
2. Consider the height and length of each wall and calculate the minimum plastic hinge length from Eq.(8.10). Since the height of contraflexure in not known, assume low

coupling (this is reasonable, since coupling forces should not change with respect to unreinforced masonry, while pier strengths generally increase) and use the effective height (for example, assuming that the controlling wall is 3 m (118.1 in) long and 10 m (393.7 in) tall, $L_{p,mw}$ = 0.04×0.8×10 + 0.1×3 + 0.176 = 0.796 m (31.3 in))). Use this if it exceeds the value from Eq.(8.10);

3. Calculate approximate yield, plastic and design drifts from Eq.(8.11) and (8.12) (considering again a wall 3 m (9.8 ft) long and 10 m (32.8 ft) tall and using the same values as in Section 8.2.1, i.e. ε_y = 0.0025, ε_{dc} = 0.004 and c/l_w = 0.2, we obtain: $\theta_{y,mw}$ = 0.47 %, $\theta_{p,mw}$ = 0.45 %, $\theta_{d,mw}$ = 0.92 %. As anticipated, the design drift is not significantly larger than 0.8 %).

For evaluation of the equivalent viscous damping, the approximate yield drift can be computed for all walls, using Eq.(8.11). For each wall the approximate displacement ductility demand can thus be computed (dividing the design drift by the yield drift) and the corresponding equivalent viscous damping found from Eq.(3.17a). For example, using the data of the wall considered above, μ_Δ = 2.18 and ξ_e = 0.127 are obtained.

A proper evaluation of the system damping should be based on Eq.(3.38), but the relative strengths of each wall are not available at the start of the design process. However, the shear strength distribution between walls is to some extent a design choice. It is therefore possible and appropriate to assign relative capacities to different walls. For example, a possible choice is to assume each wall strength proportional to the square of the wall, as for reinforced concrete walls (see Eq.(3.39) in Section 3.5.4). In this case the system damping can be obtained from the following equation; modifications for different choices are obvious.

$$\xi_{w,sys} = \sum l_{wi}^2 \xi_{wi} \Big/ \sum l_{wi}^2 \tag{8.22}$$

The system equivalent viscous damping will have to be corrected considering the coupling degree and the associated damping of coupling beams, if appropriate.

(c) Equivalent Mass and Height: There is no difference with respect to the case of unreinforced masonry. Therefore it can be assumed that m_e = 0.9Σm and H_e = 0.8H_n with adequate accuracy.

(d) Coupling Action and Contraflexure Height: In the case of reinforced masonry, the coupling degree can be considered a design choice, within certain limitations, since equilibrium can be assured by tensile reinforcement connecting slab and wall, without a need for satisfying Eq.(8.14). Reinforcement of walls and of ring beams can be decided at the end of the design process.

Values lower than β_{CB} = 0.4 are recommended, in which case the height of the point of contraflexure will not be lower than the effective height.

Since the design drift is known, it is possible to calculate yield drift, drift demand and ductility demand for each coupling beam, from Eqs.(8.16), (8.17) and (8.18). The ductility demand of the beams will essentially depend on the span of the openings, and for this reason it is a good design choice to try to keep the opening size as uniform as possible. With an estimate of the average equivalent viscous damping of the coupling beam systems (ξ_{CB}, as usual calculated on the basis of the ductility demand using Eq.(3.17a)), it is possible to estimate the global system equivalent viscous damping, combining $\xi_{w,sys}$ (Eq.(8.22)) and ξ_{CB} into Eq.(6.66a).

(e) Flexural Strength Demand and Capacity: The design process will proceed in the usual sequence. Therefore the global strength demand will be found by entering the displacement spectrum with the appropriate design displacement and equivalent viscous damping, reading the corresponding period of vibration, calculating the equivalent stiffness based on the equivalent mass (Eq.(3.1)) and finally multiplying stiffness by displacement Eq.(3.2)).

The distribution of the required strength capacity, which is equal to the resulting strength demand, to the different walls participating into the resisting system is a design choice. As discussed, a possible choice is to make the bending moment capacity of each wall proportional to the square of the wall length.

As usual with coupled walls, the response to horizontal actions will induce some axial force variation in the masonry piers at the extremities. Although the global strength is not normally significantly affected, for the same reasons discussed with reference to unreinforced masonry, it is recommended to check whether the axial force variation should cause a different damage mode for individual walls.

(f) Shear Strength and Capacity Design: The horizontal reinforcement should be designed to avoid any potential of shear collapse, according to the usual capacity design principles. For this purpose, the flexural capacity of each wall should be calculated considering both directions of loading. The corresponding shear strength should be computed considering the contraflexure height corresponding to each case. Normally, the higher shear force will be obtained for the case with a higher axial load, since the increased coupling degree corresponding to a lower axial force is not enough to compensate for the lower flexural strength. The shear strength should be calculated by applying an appropriate protection factor to the higher value obtained (see Chapter 6). In determining the propensity for shear failure, conservatively high estimates of the flexural contributions from coupling beams or slabs should be assumed, as discussed previously.

(g) Design Example 8.2: The reinforced masonry building shown in Fig.8.14 is to be designed for a site where the seismic action at the damage-control limit state has been assessed as being represented by a displacement spectrum characterized by a corner point period of 3.0 seconds with a corresponding displacement demand of 412 mm (16.2 in) for 5% damping. Note that it is unlikely that masonry structures in high seismicity areas

will be designed for equivalent periods of vibration larger than the corner period, therefore in most cases only the slope of the spectrum is relevant to design.

The building has four storeys with a total height of 12 m (39.4 ft); the floor weight is 8 kN/m² (0.167 kip/ft²), and all walls are 300 mm (11.8 in) thick. The masonry properties are the same as in Design Example 8.1 (compression strength f_{cm} = 6 MPa (0.87 ksi), shear strength v_{mv} = 0.4 MPa (58 psi), weight per unit volume w_m = 15 kN/m³ (96 lb/ft³). The reinforcing steel has an expected yield strength f_{ye} = 500 MPa (72.5ksi).

Only the walls in the direction to be considered are shown in Fig.8.14, but only 50% of the floor load is assumed to be carried by the walls. This could be the result, for example, of a cast-insitu two-way flooring system, or from changing the direction of a one-way floor system at alternate storeys, which has beneficial effects on design, by avoiding both too low and too high vertical forces on the walls.

As shown, the structure is composed by three lines of walls. Lines **1** and **2** each have three 3 m (9.8ft) long walls linked by slabs through 1 m (3.3ft) wide openings. Line **3** has two 4 m (13.1ft) long walls with a central 3 m (9.8ft) wide opening. The floor structure, including the coupling beams, has a thickness of 250 mm (9.8in). The effective height is taken as H_e = 0.8 H_n = 9.6 m (31.5ft).
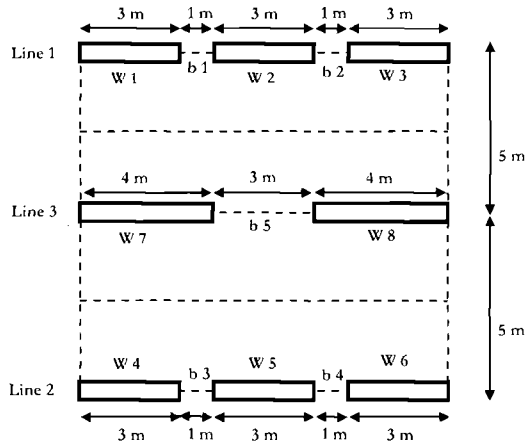

Fig.8.14   The Reinforced Masonry Building of Example 8.2: Floor Plan

It is assumed that 16 mm (0.63 in) diameter bars will be used for the vertical reinforcement steel; the strain penetration length is thus L_{SP} = 0.022 × 500 × 16 = 176 mm (6.9in) (from Eq.(4.30)). For each of the 3 m (9.8ft) wide (walls 1 to 6) and 4 m (13.1ft) wide (walls 7 and 8) walls, the following design parameters can be computed:

Plastic hinge length (Eq.(8.10)):

$$L_{p,w1-6} = 0.04 \times 9.6 + 0.1 \times 3 + 0.176 = 0.86m \ \ (33.9in)$$

$$L_{p,w7-8} = 0.04 \times 9.6 + 0.1 \times 4 + 0.176 = 0.96m \ \ (37.8in)$$

Yield drift (Eq.(8.11)):

$$\theta_{y,w1-6} = 0.60 \times 0.0025 \times 12/3 = 0.0060$$

$$\theta_{y,w7-8} = 0.60 \times 0.0025 \times 12/4 = 0.0045$$

Plastic drift (Eq.(8.12), approximate value, assuming a/l_w = 0.2):

$$\theta_{p,w1-6} = 0.86 \times 0.0169/3 = 0.0048$$

$$\theta_{y,w7-8} = 0.96 \times 0.0169/4 = 0.0041$$

Design drift (maximum value, $\geq$ 0.8%):

$$\theta_{d,w1-6} = 0.006 + 0.0048 = 0.0108$$

$$\theta_{d,w7-8} = 0.0045 + 0.0041 = 0.0086$$

Walls 7 and 8 thus govern, and it is decided to take advantage of the small increase over the default value of 0.008 and to design for θ_d = 0.86%. This implies the following ductility demand and equivalent viscous damping for each wall (Eq.(3.17a)):

$$\mu_{d,w1-6} = 0.86 / 0.6 = 1.43 \qquad \xi_{e,w1-6} = 0.092 \text{ from Eq.(2.8)}$$

$$\mu_{d,w7-8} = 0.86 / 0.45 = 1.91 \qquad \xi_{e,w7-8} = 0.117 \text{ from Eq.(2.8)}$$

It is now necessary to consider the coupling beams, all 250 mm (9.8 in) deep, 1 m long in Lines 1 and 2 (beams 1 to 4) and 3 m (9.8ft) long in Line 3 (beam 5). Their rotation and ductility demands are found as follows:

Effective beam lengths (Eq.(8.16)):

$$l_{eff,b1-4} = 1.0 + 2 \times 0.25 = 1.5m \quad (59.1in)$$

$$l_{eff,b5} = 3.0 + 2 \times 0.25 = 3.5m \quad (137.8in)$$

Beam yield drifts (Eq.(8.17)):

$$\theta_{y,b1-4} = 0.35 \times 0.0025 \times 1.5/0.25 = 0.0052$$

$$\theta_{y,b5} = 0.35 \times 0.0025 \times 3.5/0.25 = 0.0122$$

Beam rotation demand (Eq.(8.18)):

$$\theta_{d,b1-4} = 0.0086(1 + (3+3)/2 \times 1.5) = 0.0258$$

$$\theta_{d,b5} = 0.0086(1 + (4+4)/2 \times 3.5) = 0.0184$$

The ductility demand in beams 1 to 4 is therefore $\mu_{d,b1-4}$ = 2.58/0.52 = 4.96, while for beam 5 $\mu_{d,b5}$ = 1.84/1.22 =1.51. The equivalent viscous damping in the beams can be obtained from Eq.(3.17b) as $\xi_{e,b1-4}$ = 0.194 and $\xi_{e,b5}$ = 0.111.

It is now assumed that the required total shear strength will be distributed in equal part to the three lines of walls. This accounts for the higher vertical load and the larger

wall length of Line **3**, slightly increasing its load share with respect to a pure proportionality to the resisting section areas. It is also decided that 30 % of the required strength capacity for each alignment will be taken through coupling action and 70 % through walls flexural capacity (i.e. $\beta_{CB} = 0.3$). As discussed, these are design choices that could be revised at the end of the design process, adopting alternative solutions. Based on these choices, the equivalent viscous damping of each line and the system global equivalent viscous damping are obtained as follows:

Equivalent viscous damping of Lines **1** and **2** (Eq.(6.66a)):

$$\xi_{e,A1\text{-}2} = (1 - 0.3) \times 0.092 + 0.3 \times 0.194 = 0.123$$
$$\xi_{e,A3} = (1 - 0.3) \times 0.117 + 0.3 \times 0.111 = 0.115$$

System global equivalent viscous damping (Eq.(3.38)):

$$\xi_{sys} = 0.123 \times 2 / 3 + 0.115 / 3 = 0.120$$

The corresponding reduction factor to be applied to the 5% damped displacement spectrum is thus, from Eq.(2.8), $R_\xi = 0.707$. It is now possible to apply the usual procedure to obtain the total shear strength demand, as follows:

Total weight of floors: $W_{fl} = 8.0 \times 10.0 \times 11.0 \times 4 = 3520$ kN (791 kips)
Total weight of walls: $W_w = (3.0 \times 6 + 4.0 \times 2) \times 0.30 \times 12.0 \times 15.0 = 1404$ kN (316 kips)
Equivalent mass: $m_e = (3520 + 1404) \times 0.9 / 9.81 = 451.7$ tonnes (2.58 kip· s²/in)
Effective height: $H_e = 0.8 \times 12.0 = 9.6$ m (31.5 ft)
Design displacement: $\Delta_d = 0.0086 \times 9.6 = 0.0826$ m = 82.6 mm (3.25 in)
Effective period: $T_e = 3.0 \times 82.6 / (412 \times 0.707) = 0.851$ s
Effective stiffness: $K_e = 4 \times \pi^2 \times 451.7 / 0.851^2 = 24640$ kN/m (140.7 kip/in)
Design shear strength: $V_{Base} = 24640 \times 0.0826 = 2035$ kN (458 kips)
Design shear per line: $V_{d,A1\text{-}2} = 2035 / 3 = 678$ kN (152 kips)

Considering first Line **3** (Fig.8.15(a)), the same procedure discussed in Chapter 6 for coupled shear walls can be applied, calculating the axial forces acting at the base of each wall due to gravity with the assumption that 50% of the floor tributary weights is transmitted to walls oriented in the perpendicular direction.

Line 3

Overturning moment: $M_{OT,A3}$ = 678 × 9.6 = 6510 kNm (57,600 kip·in)
Coupling moment: $M_{CB,A3}$ = 6510 × 0.3 = 1950 kNm (17,250 kip·in)
Wall flexural strength: $M_{w7\text{-}8}$ = 6510 × 0.7 / 2 = 2280 kNm (20,200 kip·in)
Wall base gravity load: $P_{w7\text{-}8}$ = 4.0 × 0.3 × 12.0 × 15.0 + 5.0 × 5.5 × 8.00 × 4 / 2 =
= 216.0 + 400.0 = 616.0 kN (138 kips)
Wall base axial force variation: $\Delta P_{w7\text{-}8}$ = 1950 / (2.0 + 3.0 + 2.0) = 279 kN (63 kips)

The vertical reinforcement should be calculated applying the standard procedure used for reinforced concrete, as discussed. To have an idea of the approximate amount of

reinforcement required, it is possible to check what would be the flexural capacity of the wall without vertical reinforcement:

Average compression stress: $f_{m,w7-8}$ = 616000/(4000×300) = 0.51 MPa (74psi)
Compression depth: a_{w7-8}/l_{w7-8} = 0.51/(0.85×6.0) = 0.10
Flexural capacity: M_{wi} = 616.0×2.0×(1–0.10)= 1109 kNm (9815 kip·in)

The flexural capacity of each unreinforced wall should therefore be approximately doubled by adding an appropriate amount of reinforcement. It is easy to check that this could be obtained with a vertical reinforcement percentage on the order of 0.10 %, or approximately using 16 mm bars spaced at about 650 mm (25.6 in).

The shear strength to be provided to each wall will be based on capacity design principles, considering the situation with the minimum and maximum axial load, equal to P_{min} = 336.7 kN (75.7 kips) and P_{max} = 895.3 kN (201.3 kips). The second case is likely to govern.

The coupling beams should be designed for a total coupling moment $M_{CB,A3}$ = 1955.3 kNm (17307 kip·in). It is immediate to calculate the flexural strength to be provided to each beam and the corresponding shear. The shear strength of the beams, though, should be conservatively designed applying **CD** principles.

Beams flexural strength: $M_{CB,b5}$ = (1950/8)×1.5/3.5 = 104.5 kNm (925 kip·in)
Corresponding shear force: $V_{CB,b5}$ = 104.5×2/3.0 = 69.6 kN (15.7 kips)

The order of magnitude of flexural and shear actions in the beams are fully compatible with standard reinforced concrete design.

A similar procedure can be applied to Lines **1** and **2** (Fig.8.15(b)), considering appropriately the different geometry. Overturning and coupling moment demands will be the same as before.

Lines 1 and 2

Wall flexural strength: M_{w1-6} = 6510×0.7/3 = 1520 kNm (13,450 kip·in)
Wall base gravity load (approximate, considering equal share):
$$P_{w1-6} = 3.0×0.3×12.0×15.0 + 2.5×3.7×8.00×4/2 =$$
$$= 162.0 + 146.8 = 308.8 \text{ kN } 69 \text{ kips)}$$

Wall base axial force variation (between walls 1–3 and 4–6, essentially no change for walls 2 and 5):
$$\Delta P_{w1-3/4-6} = 1950/(1.5+1.0+3.0+1.0+1.5)$$
$$= 244 \text{ kN (54.9 kips)}$$

The flexural capacity of each wall from gravity loads is:
Average compression stress: $f_{m,w1-6}$ = 308.8/(3×0.3) = 0.34 MPa (49 psi)
Compression depth: a_{w1-6}/l_{w1-6} = 0.34/(0.85×6.0) = 0.07
Flexural capacity: M_{wi} = 308.8×1.5×(1–0.07)= 430.8 kNm (3813.1 kip·in)

A larger share of each wall flexural capacity should thus be provided through reinforcement, the approximate amount of required reinforcement percentage will be about $\rho_s \approx 0.2$ %.

The coupling beams should be designed for a flexural strength equal to $M_{CB,b1-4}$ = (1950/16)×0.5/2.0 = 30.6kNm (270.9 kip·in), corresponding to a shear force of $V_{CB,b1-4}$

= 30.6×2/1.0 = 61.1 kN (13.7 kips). The capacity-protected shear strength design should in this case consider a flexural ductility demand of about $\mu_{d,b1-4} = 3.2$.
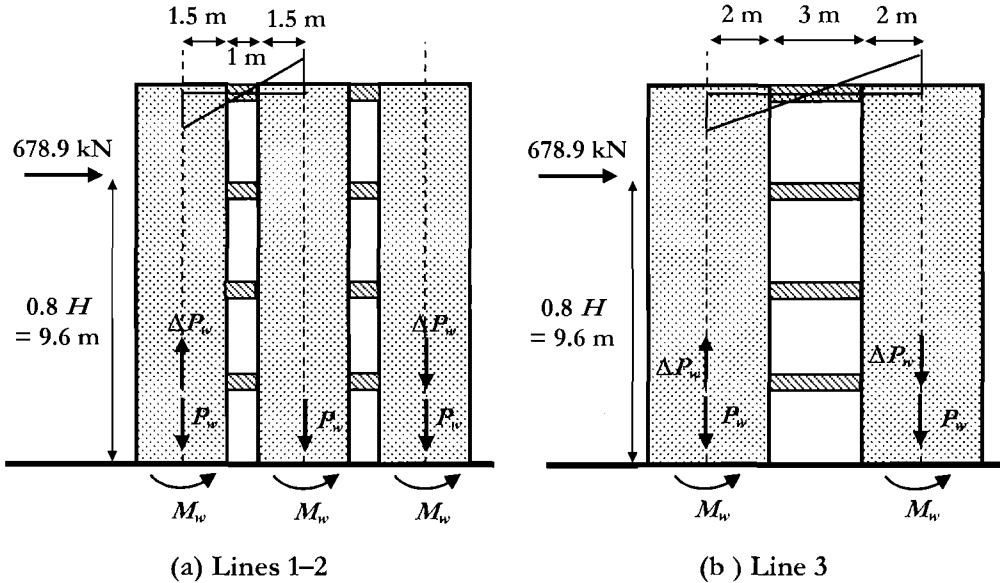

(a) Lines 1–2   (b) Line 3

Fig.8.15   Equilibrium of Lines 1–2 and Line 3 of Example 8.2

8.4 3-D RESPONSE OF MASONRY BUILDINGS

8.4.1 Torsional Response

(a) General Aspects: The treatment of torsional problems in displacement-based design has been addressed in general terms in Section 3.8 and discussed in more detail for wall buildings in Section 6.4. The approach illustrated there is fully applicable to masonry structures, with significant simplification related to the simpler design procedure illustrated in this chapter. This is particularly the case for unreinforced masonry buildings, for which it has been pointed out that all basic design parameters are known from the beginning and the whole procedure is more iterative assessment than a proper design.

In general, well designed masonry buildings are stiff and highly redundant. Therefore they are not particularly sensitive to torsional problems. In addition they are always restrained systems, with reference to the description and procedure of Sections 6.4.2 and 6.4.3.

Since masonry buildings are normally low-rise and relatively simple structures, it is even more advisable to eliminate strength eccentricity if at all possible. However, some indications on possible design procedures are presented in the following.

(b) *Unreinforced Masonry:* As already discussed in some detail, when designing an unreinforced masonry building, the geometry, loads and material properties are assumed to be generally known at the start of the design process with only minor adjustments to geometry possible. It has also been discussed how effective height, design drift and equivalent system damping can be assumed on the basis of an expected flexural collapse and verified at the end, once the height of contraflexure of each wall has been estimated.

In the case of unavoidable strength eccentricity, it is recommended to simply reduce the design displacement of the center of mass, to keep the drift demand of the wall where the additional displacement demand due to the nominal building plan rotation is a maximum within the drift limit capacity. An approximate, conservative evaluation of the drift reduction to be considered can be based on the following steps, derived from the procedure presented in detail in Section 6.4.5. Refer to Fig.6.10 for definition of symbols.

1. Since the strength capacity of each wall (V_i) is known, calculate the strength eccentricity in both directions:

$$e_{RX} = \sum_1^n V_{Zi} x_i \Big/ \sum_1^n V_{Zi} \quad ; \quad e_{RZ} = \sum_1^n V_{Xi} z_i \Big/ \sum_1^n V_{Xi} \tag{8.23}$$

2. Calculate a conservative estimate of the value for the rotational stiffness, assuming that the stiffness of each wall is proportional to its strength, i.e., assuming a constant drift for all walls (equal to 0.8 % of the effective height) and a secant stiffness to this drift value. This assumption is obviously approximate, since it is not considering the torsional response, but is acceptable if the plan rotation will be reasonably small. It also conservatively implies full inelastic response simultaneously in the orthogonal principal directions.

$$J_{R,V} = \frac{\sum V_{zi}(x_i - e_{RX})^2 + \sum V_{xi}(z_i - e_{RZ})^2}{0.008 H_e} \tag{8.24}$$

3. Estimate the plan rotation demand in each direction according to Eq.(6.24):

$$\theta_{N,x} = V_{D,x} \cdot e_{RZ} / J_{R,V} \quad ; \quad \theta_{N,z} = V_{D,z} \cdot e_{RX} / J_{R,V} \tag{8.25}$$

4. Reduce the design displacement of the center of mass in each direction by the amount equal to the displacement demand of the most external wall due to the plan rotation:

$$\Delta_{\theta,x} = \theta_{N,x} \cdot x_{i,max} \quad ; \quad \Delta_{\theta,y} = \theta_{N,y} \cdot y_{i,max} \tag{8.26}$$

(c) *Design Example 8.3: Torsional Response of an Unreinforced Masonry Building:* In order to show how relevant a strength eccentricity could be to design, consider the conceptual case in Fig.8.16, where a simple square building, 7 by 7 m (23 × 23 ft) in plan is considered, with a structural system braced against horizontal forces composed by two identical walls 3.5 m (11.5 ft) long in one direction and two walls 3 and 4 m (9.8 ft and 13.1 ft) long in the other direction. The building is 7 m (23 ft) high; each

storey weight is 400 kN (90 kips) and each wall is assumed to carry an equal share of the total weight. No coupling is considered here, for the sake of simplicity.

The effective height is $H_e = 0.8 \times 7 = 5.6$ m (18.4 ft). All material properties are assumed to be those used in Design Examples 8.1 and 8.2. The shear strengths of the walls have been assessed to be 74 kN (16.6 kips) (3 m wall), 87 kN (19.6 kips) (3.5 m walls) and 101 kN (22.7 kips) (4 m wall).

The following results are thus obtained, from Eqs. (8.23), (8.24), (8.25) and (8.26):

$$e_{RX} = (74 \times 3.5 - 101 \times 3.5)/(74 + 101) = -0.54m \ \ (-21.3\ in); \ e_{RZ} = 0$$
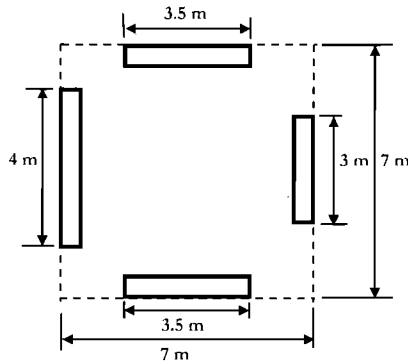
Fig.8.16 A Conceptual Unreinforced Masonry Building with Strength Eccentricity (Plan View)

$$J_R = 101(3.5 - 0.54)^2 + 74(3.5 + 0.54)^2 + 2 \times 87 \times 3.5/0.0448$$
$$= 59500 kNm^2 \ \ \left(144000 kip \cdot ft^2\right)$$
$$\theta_{N,z} = (74 + 101) \times 0.54/69529 = 0.0016$$
$$\Delta_{\theta,z} = 0.0016 \times 3.5 = 0.0056m \ \ \left(0.2205in\right) \approx 0.1\% H_e$$

The design drift in direction **Z** has therefore to be reduced to 0.7%.

(d) Reinforced Masonry: When designing reinforced masonry structures it is normally possible to avoid strength eccentricities, since the strength of each wall is a design parameter. If for some particular reasons it is decided to assign strength proportions to the walls that will result in a torsionally unbalanced structure, the conservative procedure described for unreinforced masonry is still applicable, with obvious modifications. Alternatively, the more accurate, and less conservative procedure of Section 6.4.5 can be directly applied.

A possible conceptual reason to design a building with strength eccentricities could be an attempt to optimize the demand/capacity ratio for each wall, increasing the drift demand on walls that have a larger drift capacity (see Section 6.4.5(a)). Since drifts related

to material strain normally govern design, stiffer walls tend to have smaller displacement capacities and if they are assigned a larger share of the strength the center of strength becomes closer to the wall, reducing their displacement demand.

Such a design philosophy is possible but makes design more complex and does not seem to produce significant benefits, since the differences in drift capacities are normally contained within a maximum of 20 %.

8.4.2 Out–of–Plane Response of Walls

(a) General Issues: The problem of out-of-plane stability of unreinforced masonry walls has traditionally been treated by comparing demand and capacity in terms of strength, but it is now fully recognized[M13] and confirmed by recent experimental and theoretical research[D6,G5] that only by considering displacement parameters is there a reasonable prospect of predicting the actual response.

As first pointed out by Priestley[P23], the problem is quite complex and requires the evaluation of the seismic demand considering the dynamic filtering effect of buildings (Fig.8.17) and the out-of-plane displacement capacity of walls.

Considering the problem within the framework of a simple approach to design (or more appropriately, to assessment), a procedure is suggested, with the aim of indicating possible areas of future research rather than providing specific values to be used; the reason simply being that the current research evidence is not yet adequate to allow the quantitative development of reliable approaches that can be widely applied. However, codified slenderness and minimum thickness and detailing requirements will generally prevent out-of-plane driven failures in new buildings.

(b) Response Assessment: It is assumed that all building walls have been designed considering in-plane action; the fundamental effective period of response of the structural system (T_e) and each storey design displacement relative to the ground (Δ_i) are therefore known in each direction. It is further assumed that the response of a wall excited by the storey motion in the direction perpendicular to its plane is essentially governed by the displacement demand obtained by the amplification of the absolute storey displacement as resulting from the interaction of two simple **SDOF** systems: one being the structure as a whole, and the second being the wall considered as an independent structure. The absolute storey displacement is calculated from a corrected displacement spectrum, as shown in Fig.8.18(a). The theoretical amplification due to the wall response can be obtained by the following equation, represented in Fig.8.18:

$$S_{OUT,\Delta} = 1 \Big/ \sqrt{\left(1 - \left(T_e/T_{out}\right)^2\right)^2 + 4\xi_{out}^2\left(T_e/T_{out}\right)^2} \tag{8.27}$$

where T_{out} and ξ_{out} are the response period and equivalent viscous damping of the wall in the out-of-plane direction.

Floor diaphragm response
amplifies accelerations and
transmits excitation to out-
of-plane walls

Shaking
motion

Parapet wall

In-plane shear walls
response filters the
ground motion and
transmits to floor
diaphragms

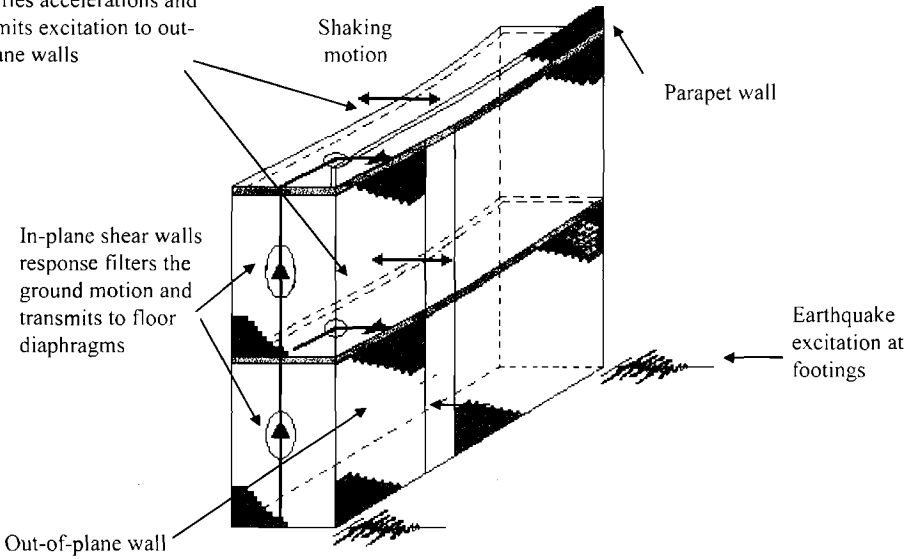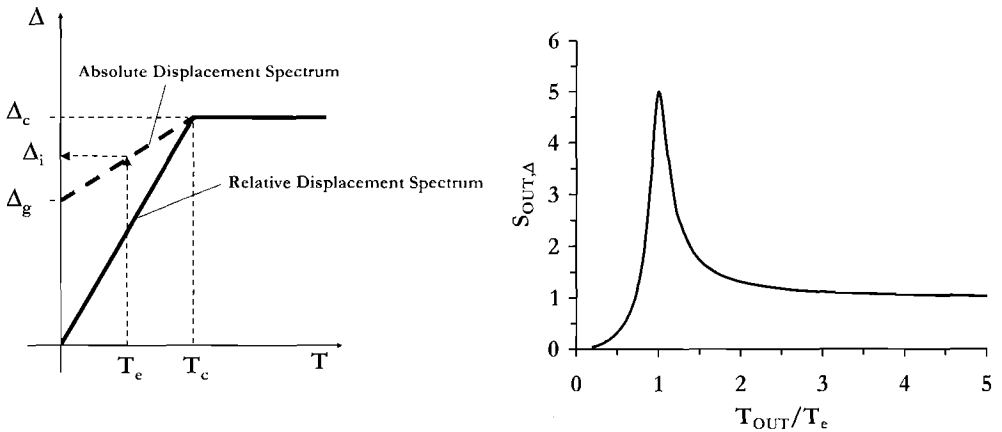Earthquake
excitation at
footings

Out-of-plane wall

Fig.8.17 Simplified Conceptual Representation of Out-of-Plane Seismic
Response[D6,P23]

(a) Absolute Displacement Spectrum   (b) Out-of-Plane Amplification Spectrum ($\xi_{out}=0.1$)

Fig.8.18 Out-of-Plane Response of a Masonry Wall to Building Period, Assuming
Steady-State Building Response

Clearly, the displacement demand is essentially a function of the equivalent viscous damping ratio of the wall responding out-of-plane (ξ_{out}), which can be assumed equal to 0.10 (this is possibly too high if referred to the actual equivalent viscous damping, but it compensates to some extent for the assumption of steady-state sinusoidal response of the building, inherently assumed in Fig.8.18), and of the ratio T_e/T_{out} between the period of vibration of the system and that of the wall. The maximum amplification, at theoretical resonance, is $S_{MAX} = 5$ for $\xi_{out} = 0.10$. The design amplification spectrum should be revised on the basis of extensive experimental and numerical studies as new information about the effective damping becomes available.

The displacement capacity can be estimated by considering the out-of-plane equilibrium of a wall in a displaced position (Fig.8.19). Though refined equations have been developed, a simplified set of equations is here suggested for design.
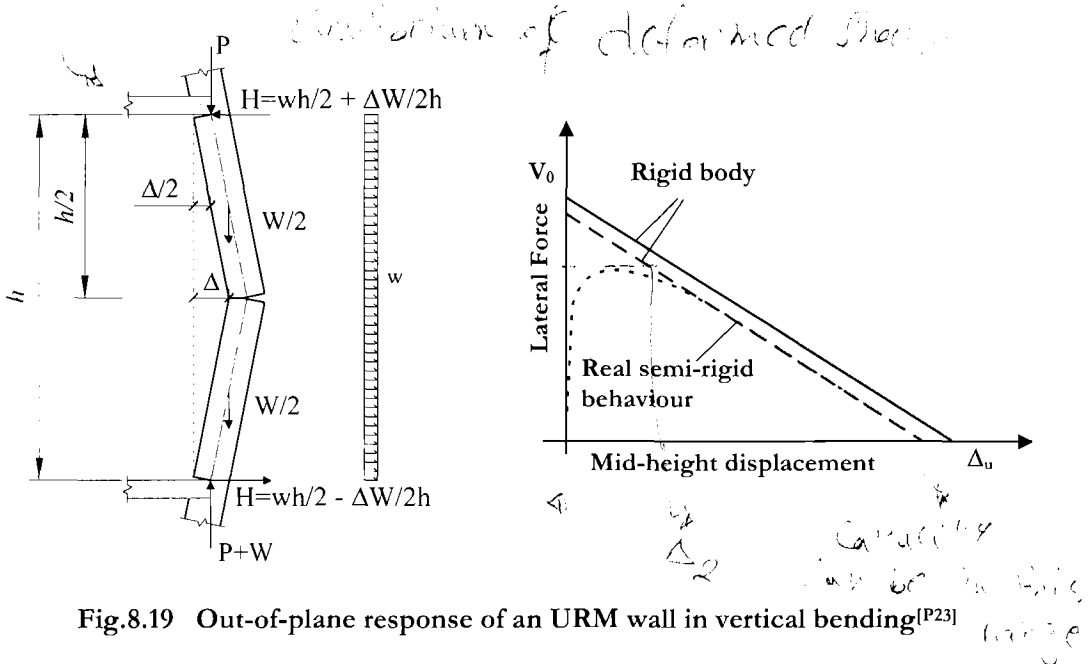

Fig.8.19   Out-of-plane response of an URM wall in vertical bending[P23]

With reference to Fig.8.19, the response is dominated by P-Δ effects. The ultimate wall displacement corresponding to zero lateral strength is evaluated considering a pure rigid body motion and an infinite material strength:

$$\Delta_{u,w} = \frac{b_w}{2} \cdot \frac{4P + 2W}{4P + W} \tag{8.28}$$

where W and P are the wall weight in the storey considered, and the supported load at the floor above respectively. Similarly, the maximum horizontal force at zero displacement is calculated as:

$$V_0 = \left(P + \frac{W}{2} \right) \cdot \frac{b_w}{h_w} \qquad\qquad (8.29)$$

(c) Design: The design (assessment) procedure will require some iteration to find what displacement demand of the wall will be compatible with the interaction with the building response. The following procedure is suggested:

1. Compute the force–displacement curve of the wall, based on Eqs.(8.28) and (8.29), and make an initial assumption of response displacement, e.g. : $\Delta_{r1} = 0.5\Delta_{u,w}$;
2. Compute the corresponding effective stiffness and corresponding period of vibration of the wall based on the assumed response displacement;
3. Enter the amplification spectrum and calculate the displacement demand, multiplying the average structure displacement at floors above and below the wall by the amplification factor, and iterate until the assumed response displacement and the obtained displacement demand are approximately equal.
4. Check that the predicted displacement is less than the displacement capacity by an acceptable factor (at least a factor of 2 is suggested).

(d) Design Example 8.4: Out-of-Plane Response of an Unreinforced Masonry Wall: As an example, consider a wall 250 mm (9.8 in) thick, 1 m (3.3 ft) wide and 3 m (9.8 ft) tall, located between the third and top floors of a building. Assume a load acting on the wall top of $P = 16$ kN (3.6 kips), a total wall weight $W = 11.25$ kN (2.5 kips). Assume also that the building effective period of vibration is $T_e = 0.4$ sec. and the average structural response absolute displacement of the third storey and roof is 60 mm (2.36 in). The wall effective mass is estimated as $m_{e,w} = 0.8m = 0.917$ tonnes (0.0052 kip·s²/ft). The procedure will give the following results.
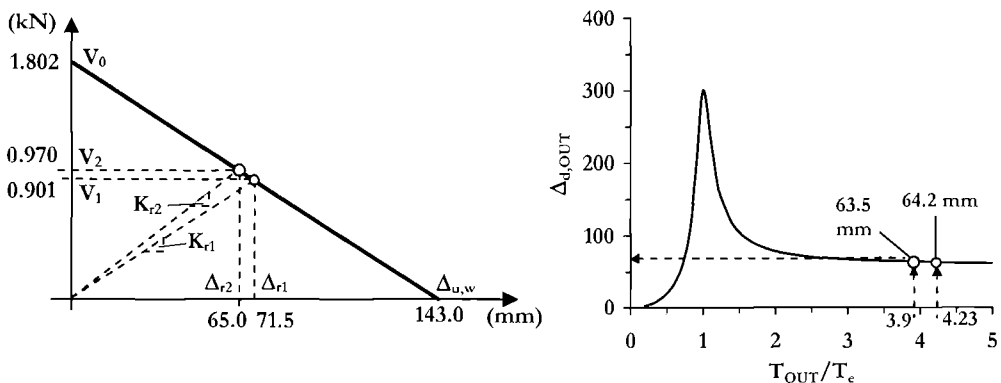

Fig.8.20 Iterative Procedure to Calculate the Displacement Demand in Example 8.4

Force – displacement limit curve (from Eqs.(8.28) and (8.29), see Fig.8.20):

$\Delta_{u,w} = 143$ mm (5.63 in), $V_0 = 1.802$ kN (405 lb)

First iteration:

$\Delta_{r1} = \Delta_{u,w}/2 = 71.5$ mm (2.81 in), $V_1 = V_0/2 = 0.901$ kN (202 lb)

$k_{r1} = V_1/\Delta_{r1} = 12.6$ kN/m, $T_{OUT1} = 2\pi(0.917/12.6)^{0.5} = 1.69$ s

The spectral displacement demand is obtained by entering Fig.8.18 (or applying Eq. (8.27)) with the ratio between the periods of vibration $T_{OUT1}/T_e = 4.23$.

A spectral amplification $S_{OUT1} = 1.06$ is obtained, to be applied to the storey displacement (60 mm). A displacement demand of $\Delta_{d1} = 63.5$ mm (2.5 in) is therefore obtained, lower than the assumed displacement of $\Delta_{r1} = 71.5$ mm (2.82 in).

For the second iteration we assume a response displacement close to the demand obtained in the first iteration:

$\Delta_{r2} = 65$ mm (2.6 in), $V_2 = V_0 (143 - 65)/143 = 0.970$ kN (214 lb)

$k_{r2} = V_2/\Delta_{r2} = 14.9$ kN/m (0.085 kip/in), $T_{OUT2} = 2\pi(0.917/14.9)^{0.5} = 1.56$ s

Proceeding as before, a spectral displacement demand amplification of $S_{OUT2} = 1.07$ is obtained, from a period ratio $T_{OUT2}/T_e = 3.9$. The corresponding displacement demand is $\Delta_{d2} = 64.2$ mm (2.53 in)

The displacement demand obtained from the second iteration is close to the assumed response displacement, it is therefore concluded that the approximate displacement demand on the wall will be 65 mm (2.56 in), compatible with its displacement capacity.

For comparison, assume now that the same wall is located at a lower level, where the average storey displacement is 20 mm (0.79 in) and the axial force from the upper storeys is 100 kN (22.5 kips). The following values will result, applying the same procedure as above.

Force – displacement limit curve: $\Delta_u = 128$ mm (5.04 in), $V_0 = 8.802$ kN (1.98 kips)

First iteration: $\Delta_{r1} = 64$ mm (2.5 in), $k_{r1} = 68.8$ kN/m (0.393 kip/in), $T_{OUT1} = 0.72$ s

Spectral displacement demand: $T_{OUT1}/T_{sys} = 1.81$, $S_{OUT1} = 1.42$, $\Delta_{d1} = 28.4$ mm (1.12 in)

Second iteration: $\Delta_{r2} = 46$ mm (1.8 in), $k_{r2} = 122.6$ kN/m (0.7 kip/in), $T_{OUT2} = 0.54$ s

Spectral displacement demand: $T_{OUT2}/T_e = 1.35$, $S_{OUT2} = 2.08$, $\Delta_{d2} = 41.6$ mm (1.64 in).

Third iteration: $\Delta_{r3} = 44$ mm (1.7 in), $k_{r3} = 131.3$ kN/m (0.75 kip/in), $T_{OUT3} = 0.53$ s

Spectral displacement demand: $T_{OUT3}/T_e = 1.31$, $S_{OUT3} = 2.24$, $\Delta_{d3} = 44.8$ mm (1.76 in).

In this case the displacement demand is assessed to be about 45 mm (1.8 in) again compatible with its displacement capacity.

In general, out of plane response will not be an issue for the case of reinforced masonry, but a similar procedure can be applied.

9

TIMBER STRUCTURES

9.1 INTRODUCTION: TIMBER PROPERTIES

As is illustrated in Fig.9.1, the stress-strain characteristics of timber are not suitable for ductile response. Timber is brittle in tension, failing with little warning, typically at knots and other imperfections, with a complete lack of ductility. In compression, the strain characteristics parallel to the grain are less undesirable, with some ductility apparent under monotonic loading. However, on unloading, the residual deformation is typically high, and strength degradation is apparent under cyclic loading. Flexural response will typically be dominated by the tensile strain limit, implying nearly elastic behaviour to failure. As a consequence seismic design of timber structures is generally required to be elastic where material strength governs the design.
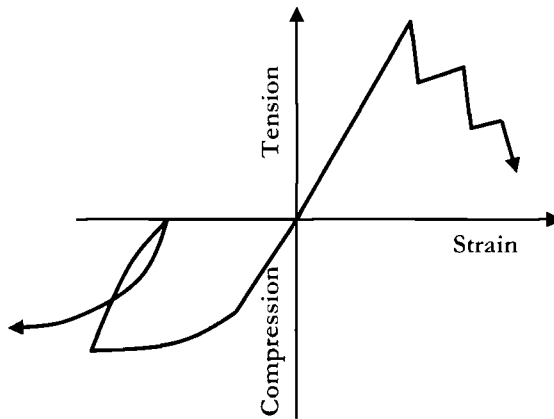

Fig.9.1   Timber Stress-Strain Characteristics

9.2 DUCTILE TIMBER STRUCTURES FOR SEISMIC RESPONSE

Although the brief description above indicates that timber, as a material must be considered non-ductile, this does not mean that ductile structures cannot be constructed from timber products. To obtain ductile response in timber structures, ductility must be

455

provided in the connections between structural members, and the timber members designed by capacity-design principles to ensure that their strength exceeds the maximum force that could be developed corresponding to overstrength capacity of the connections. The design philosophy is thus directly analogous to the *"ductile connection"* category of prestressed frames discussed in Section 5.11.1. A selection of possible categories of ductile-connection timber structures is shown in Fig.9.2.

(a) Ductile Moment-Resisting Frame   (b) Timber Shear Panel Bracing
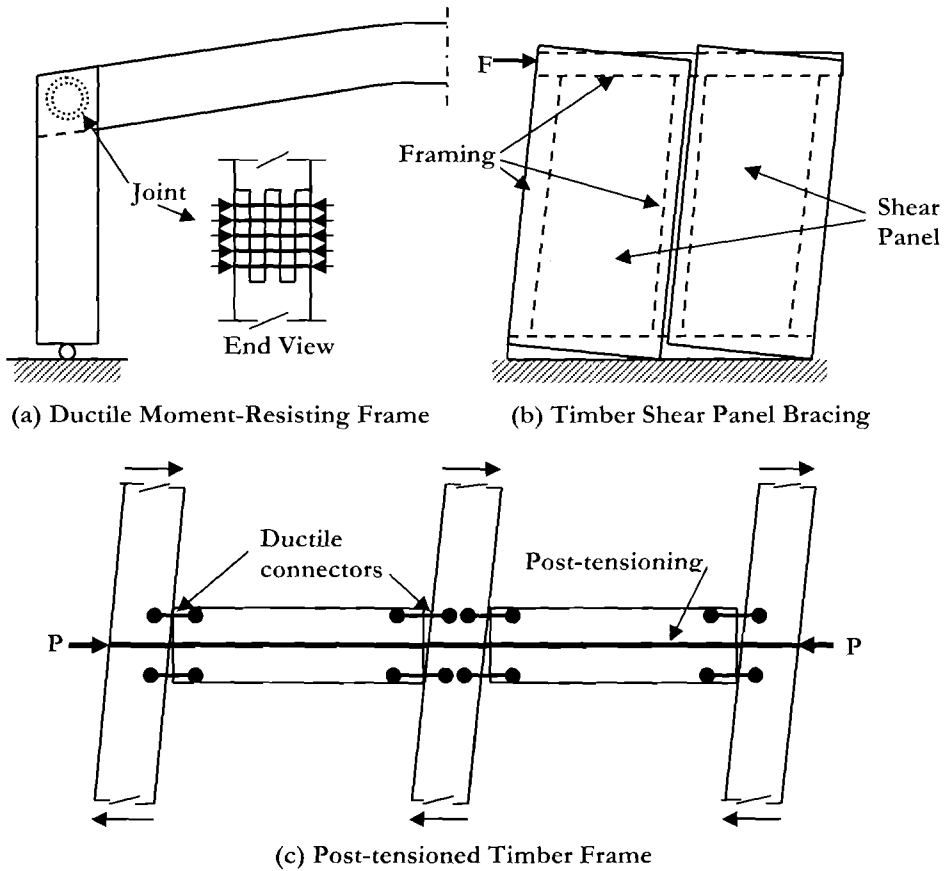

(c) Post-tensioned Timber Frame

Fig.9.2 Categories of Ductile Timber Structures

Figure 9.2(a) represents a glulam portal frame with moment-resisting connections at the knee joints provided by dowels (bolts) arranged in one or more concentric circular orientations. The rotational capacity of the connection is less than the dependable moment capacities of the column and the roof arch beam, and hence a ductile design approach is reasonable. Direct displacement-based design of this class of structure has been studied by Zonta et al[Z1]. It was pointed out in [Z1] that current force-based seismic

design to EC8[X3] is very coarse, with behaviour factors of q = 1.5 and 4 applying for dowels with diameter ≤ 12mm (0.47 in) and > 12 mm respectively, resulting in a large, and unrealistic apparent change in seismic resistance for a small increase in dowel diameter. Design using **DDBD** principles and experimental hysteretic characteristics of the connection would clearly improve the reliability of the designs.

Light structural buildings and houses are often braced laterally with plywood shear panels connected to timer or light steel framing, as suggested in Fig.9.2(b). Under seismic lateral force the nails connecting the shear panels to the framing slip, providing a measure of ductility to the connection. If the displacement capacity and hysteretic characteristics of the connections are known then the required strength to limit the drift of the shear panels to defined limit-state levels can immediately be found from application of **DDBD** principles, as has been shown by Filiatrault and Foltz[F9].

A third possible application is shown in Fig.9.2(c)[P34]. Glulam timber beams and columns are connected by prestressing and ductile connectors in exactly the same way as adopted for hybrid precast concrete frames described in Section 5.11.3.

The three categories of connection briefly outlined above are discussed in more detail in the following sections.

9.2.1 Ductile Moment-Resisting Connections in Frame Construction

The portal frame knee-joint connection using concentric rings of dowels shown in Fig.9.2(a) is popular in Europe[B9] and has been extensively researched by Cecotti[C9]. The straight smooth dowels are inserted in pre-drilled holes. Strength development is significantly lower than the capacity of the connected members, though some problems of splitting at service loads have been experienced [B9]. Hysteretic performance of the joint is characterized by the development of slackness in the connection as the timber surrounding the dowels crushes at moderate rotations. A characteristic moment-rotation plot is shown in Fig.9.3.
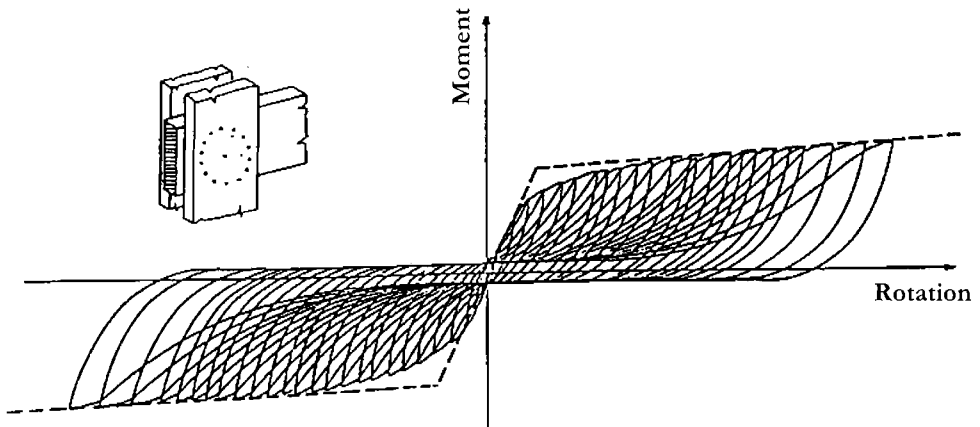

Fig.9.3 Hysteretic Response of a Dowelled Connection (after [C9])

Note that despite the very low stiffness at low rotations following high amplitude displacements, the strength is not significantly affected, and peak capacity is resumed for displacements only slightly higher than the previous maximum.

The hysteretic response indicated in Fig.9.3 implies that the effective viscous damping would actually decrease with increasing displacement ductility. Without specific information on hysteretic characteristics, a low value of equivalent viscous damping should be adopted in design. We suggest $\xi = 0.10$.

Many other connections suitable for timber frames have been developed. A summary is available in [B9], from which the categories sketched in Fig.9.4 have been taken. Figure 9.4(a) shows a portal frame knee-joint where the connection is made by steel nail plates. The plates have been necked to a reduced width at the line of the beam/column intersection to ensure that the flexural strength of the steel plate is the critical element. Fat hysteresis loops with high energy absorption result, with high equivalent viscous damping. The Ramberg-Osgood damping relationship of Eq.(3.17c) would be appropriate. Residual displacements after seismic response can, however, be high, and buckling of the plate is likely if steel strains are excessive. It can readily be shown that to ensure a plastic rotation capacity of $\theta_P = 0.02$ the height H of the reduced section must be at least $H = 0.33B$, where B is the depth of the "throat" of the reduced section (i.e. the dimension perpendicular to H) if steel strains are limited to $\varepsilon_s \leq 0.03$. Sufficient nails are driven through pre-formed holes in the steel plates to ensure that the bearing resistance of the nails in the timber exceeds the flexural capacity of the steel plate.
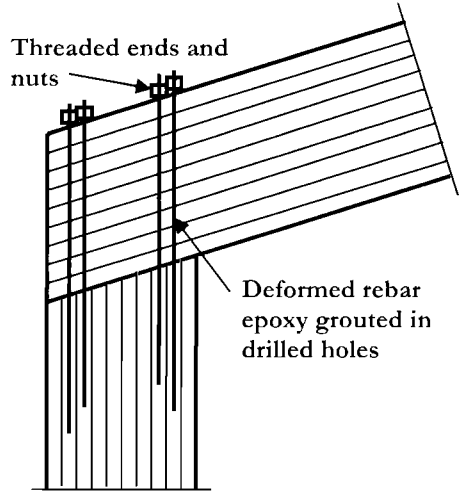
Fire resistance is a problem with this external steel plate connection detail. A modification which reduces the fire problem consists of inserting steel plates in slots in both the beam and column, and drilling holes *insitu* for connecting dowels. A further modification uses external plywood, instead of steel plates, though this results in the bearing capacity of the nails dominating performance, resulting in hysteretic characteristics similar to the dowelled connection of Fig.9.3.

Different connection details incorporating dowels epoxied into holes in the connected members are shown in the remaining sketches of Fig.9.4. In Fig.9.4(b) a portal frame knee-joint is connected by deformed reinforcing bars inserted and epoxied into holes drilled vertically through the beam and into the column. Provided the anchorage length is adequate, the dowels will yield alternately in tension and compression under cyclic flexural joint rotation. Improvement in performance can be obtained if the dowels have reduced diameter at the member interface and are debonded from the epoxy by wrapping the section of bar with reduced diameter with tape, to spread the yield over a length sufficient to keep peak strains to about 0.03 or less.

A similar technique is employed for the beam/column joint of Fig.9.4(c) where dowels are epoxy grouted in holes drilled into the beam ends, and through the column. Again more dependable performance would be expected if the dowels are debonded for a short length on either side of the beam/column interfaces. Tests on beam/column test units have shown[B9] that connections designed by capacity design principles to ensure that the connection is weaker than the members can sustain drift angles of more than 4% with displacement ductility capacities of about 6.
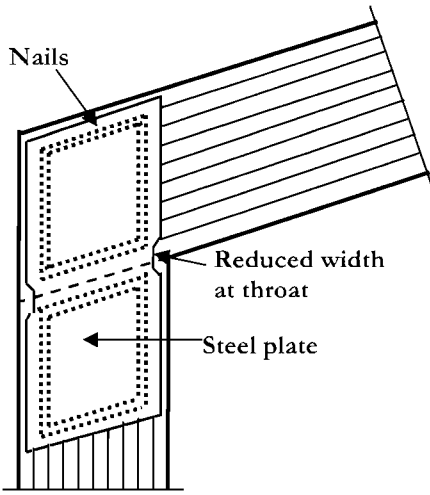
(a) Portal Frame, Ductile Steel Nail Plate (b) Portal Frame, Epoxied Dowels
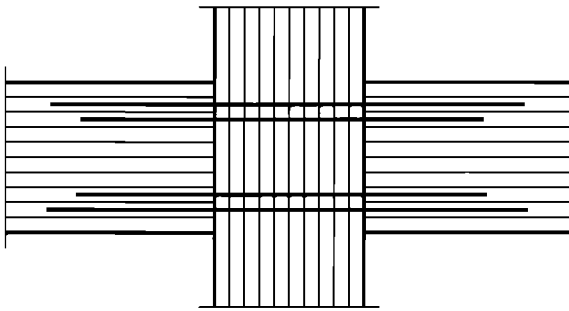
(c) Beam/Column Joint, Epoxied Dowels

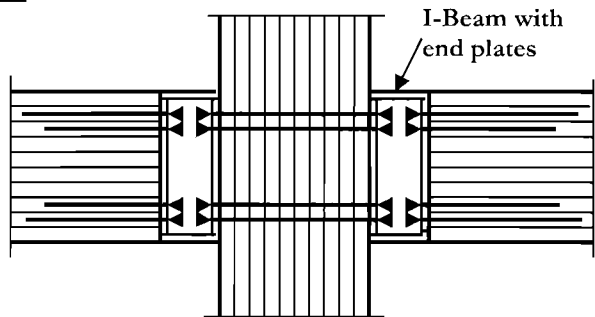(d) Beam/Column Joint with I-Beam and Epoxied Dowels

Fig.9.4 Ductile Connection Systems for Glulam Frames (after [B9])

Note that a concern with both of the connections of Fig.9.4(b) and (c) would be shear transfer across the member interface. Once cyclic yielding of the dowels has occurred, it is probable that a continuous gap will develop at the interface, and the dowels will be the

only available mechanism for transferring the shear force between members. Performance could be improved by placing ductile shear connectors across the interface.

The final alternative shown in Fig.9.4(d) also uses epoxied dowels, but in this case they are not intended to yield. Steel I-sections with welded end plates are placed between the beams and the column, and connected by threaded rods anchored by epoxy grouting in the members. Under cyclic flexural action, the flanges of the steel I section yield in tension and compression, providing the energy dissipation, and limiting the strength of the connection

9.2.2 Timber Framing with Plywood Shear Panels

This form of construction is very common for individual houses, and low-rise apartment buildings and offices in the USA and other countries. Recently, this form of construction has received considerable research attention, including full scale shake-table testing[F9,F10,F7,F5]. Initial information for plywood shear panels is available in [F9]. This study investigated the hysteretic response of 9.5mm (0.374 in) orientated strand board connected to timer framing with 50mm (2in) spiral nails, pneumatically driven. The shape of the force-displacement hysteresis loop of a single nail connection under racking load is idealized in Fig.9.5(a). A ductile envelope was obtained under monotonic response, with significant stiffness degradation, but little strength degradation under cyclic loading. A peak lateral strength exceeding 1kN (0.23kips) was obtained. The hysteretic response of an entire panel, shown in Fig.9.5(b) was similar to that of the individual nail.
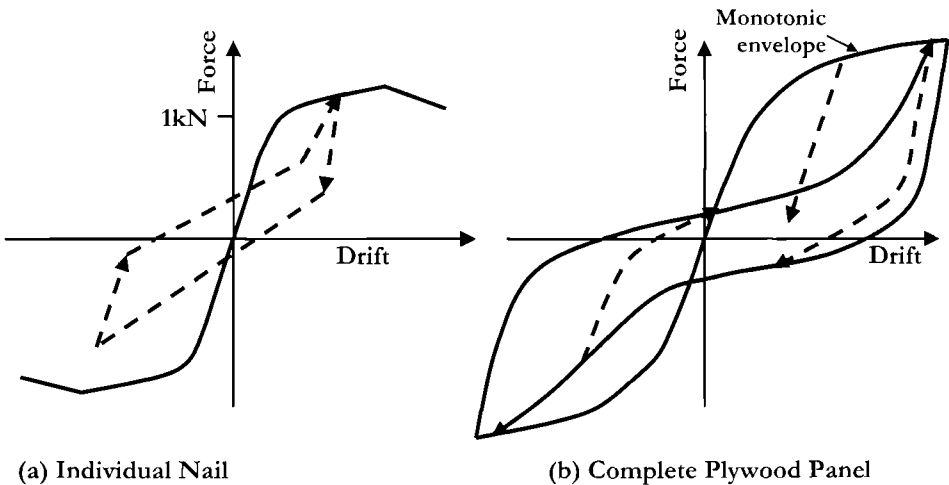

(a) Individual Nail   (b) Complete Plywood Panel

Fig.9.5 Idealized Hysteretic Response of a Nailed Plywood Panel

Modelling of the hysteretic response indicated that at 1% drift the equivalent viscous damping was approximately $\xi = 0.11$, while at 2% drift the damping increased to about $\xi = 0.15$. In both cases the damping included initial stiffness damping of $\xi_{el} = 0.02$. The analyses showed that these damping levels were essentially independent of the number of nails connecting the panel to the frame, and hence were independent of the strength. More recent information[F10] has suggested that these figures be revised upwards, with equivalent viscous damping ratios of $\xi = 50\theta$ for $\theta < 0.0035$, where θ is the drift angle, and $\xi = 0.18$ for $\theta > 0.0035$. Elastic damping should not be added to these values.

Drift limits of 1% and 2% were taken in [F9] to represent "*immediate occupancy*" and "*life-safety*" limit states, though it is our opinion that the 2% limit is rather low for life safety of timber frame structures, and might be more appropriate for a *damage control* limit state. More research is required to establish reasonable structural displacement limits for different performance levels for timber structures. Without such information, timber structures will probably be designed for drift limits corresponding to non-structural performance, noted above.

9.2.3 Hybrid Prestressed Timber Frames

At the time of finalizing this book an extensive experimental research program was in progress at the University of Canterbury, New Zealand, investigating application to laminated veneer lumber (**LVL**) structures of the principles of unbonded post-tensioning combined with special energy-dissipating elements developed for precast concrete structures under the PRESSS program[P19] and described in some detail in Section 5.11. A summary of the research program in available in [P34].

Tests have already been carried out on exterior beam/column joints (see Fig.9.2(c)) where the beam is connected to the column, which is continuous through the joint, with unbonded post-tensioning. Internal ducts for one or more post-tensioning tendons in both beam and column are formed during manufacture of the LVL members, which thus provide fire protection for the post-tensioning. To form a hybrid system, additional strength and energy dissipation is provided by special elements across the beam/column interface. Two different approaches have been investigated. The first consists of deformed rebar rods inserted and epoxied in drilled holes, in similar fashion to Fig.9.4(c). The rods are wrapped over a short length at the interface to reduce peak strain levels. Alternate tension and compression yield of the rods adds damping and strength to the connection. Since the rods are internal, fire proofing is achieved.

The second alternative uses external dissipaters consisting of rebar anchored at one end to the face of the beam and at the other end to the column, across the joint (see Fig.9.2(c)). The rebar rods pass through a loose steel sleeve whose purpose is to restrain the rod from inelastic buckling while in compression. A disadvantage of this external approach is that special fire proofing measures are needed. An advantage is that the devices can be checked, and replaced, if necessary, after high-level seismic response.

Excellent, stable hysteretic response has been obtained from test units with both internal and external dissipaters at drift levels exceeding 4%. An example, from a

beam/column test with external dissipaters is shown in Fig.9.6. Note the excellent stability of the hysteresis loops and the low residual displacement. Minor crushing of timber in the column at top and bottom of the beam interface has been noted at high drift angles in the tests, but without any apparent degradation of structural response. Note that timber crushing could be alleviated by "armouring" the beam/column connection using steel plates or angle sections bonded to the column face and to the beam ends, to distribute the flexural compression forces at the beam ends.
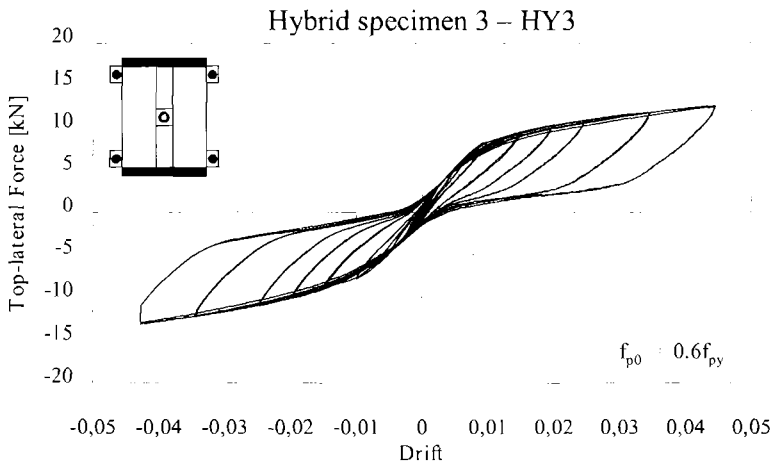

Fig.9.6   Hysteretic Response of a Hybrid LVL Beam/Column Connection using External Dissipaters[P34]

Hybrid technology has also been tested[P34] for the anchorage of LVL columns and walls to foundations, in similar fashion to that discussed for concrete walls in Section 6.7 with similarly excellent results.

9.3 DDBD PROCESS FOR TIMBER STRUCTURES

It is evident that there are no unique characteristics of timber structures that need special consideration in the **DDBD** process apart from the identification of appropriate displacement or drift limits, and hysteretic characteristics of connections. Material properties – particularly strength and stiffness – need to be defined on the basis of local information, as wide variations can exist between different locations as a consequence of timber type, growth rate, moisture content, and means of lamination for glulam or **LVL** construction.

Force-based seismic design is not well suited to timber design as a consequence of somewhat irregular hysteretic characteristics, and the lack of clearly definable ductility capacity. With the design details discussed above, code drift limitations, rather than material strains, are likely to define the performance limit states. Hence **DDBD** is ideally

suited to seismic design of timber structures, as has been noted by various researchers (e.g. F9, F10, Z1).

9.4   CAPACITY DESIGN OF TIMBER STRUCTURES

Often timber structures will essentially be **SDOF** systems, and the only implementation of capacity design principles will be to check that the timber strength is adequate to force ductile action into the elements intended to dissipate energy and provide strength limits. For multi-storey timber structures, the simplified design rules for capacity design proposed in the various structure related chapters of this text may be directly adopted. However, analytical research based on timber hysteretic characteristics is needed to determine rules specifically relevant to timber structures.

10

BRIDGES

10.1 INTRODUCTION: SPECIAL CHARACTERISTICS OF BRIDGES

Bridges are typically simple structures, in that the number of structural elements (piers, spans, abutments) is generally small. On the other hand they often are very irregular, with variable column heights, non-uniform span lengths, and sometimes with horizontal and/or vertical curvature of the superstructure. Since the structural form is less commonly dictated by architectural rather than structural considerations, the designer needs to be aware of the structural consequences of decisions made about structural form. The scope of this book allows only a brief review of these points. For more detailed consideration refer to [P4] and [K6].

10.1.1 Pier Section Shapes

(a) Rectangular

(b) Slab

(c) Chamfered Rectangular
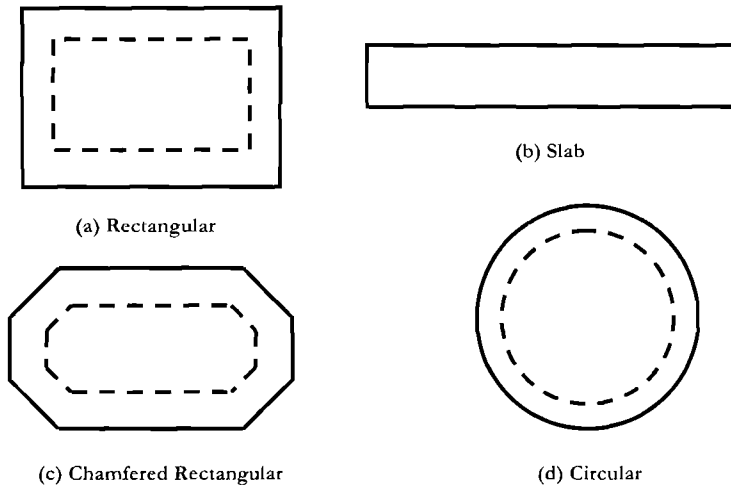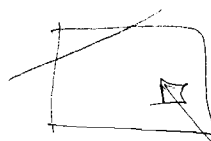
(d) Circular

Fig.10.1 Common Section Shapes for Bridge Piers

Figure 10.1 illustrates the principal choices of bridge column section shapes available to the designer. The principal choices will be between rectangular and circular sections,

465

$\phi = \dfrac{\varepsilon_{cu}}{C}$

increased neutral C

466   Priestley, Calvi and Kowalsky. Displacement-Based Seismic Design of Structures

and between single or multi-column piers, with a secondary choice between solid and hollow section shapes. Rectangular columns, (Fig.10.1(a)), though common in bridge design, are less desirable than circular columns because of the difficulty in providing adequate restraint by transverse hoops against buckling for the large number of longitudinal bars common in typically large column section dimensions. Circular columns (Fig.10.1(d)) are generally confined by spirals or circular hoops, are easy to construct, and have the advantage of omni-directional strength and stiffness characteristics. Construction can be further simplified, and performance improved by using a continuous spiral of unstressed prestressing strand as confinement and shear reinforcement[B5].

A further problem with rectangular columns is that under diagonal seismic response, cover spalling will initiate at lower seismic intensity than when responding in the principal directions, because the depth of the compression zone must be larger to provide the required compression force, resulting in lower curvatures corresponding to the extreme-fibre spalling strain.

With the chamfered rectangular section of Fig.10.1(c) the longitudinal reinforcement can be confined within a series of interlocking spirals, with the advantage of ease of construction noted above for circular sections.

When longitudinal response of a bridge with comparatively few spans is resisted principally by abutments an elongated rectangular pier section (Fig.10.1(b)) may be adopted. In the transverse direction the pier acts as a structural wall, but the flexibility in the longitudinal direction means that the pier contributes little to longitudinal response. Because of this flexibility, which aids in permitting thermal movements, it is generally not necessary to provide confinement reinforcement for longitudinal response[H3].

When large, long-span bridges have tall bents, hollow columns may be a viable option. These have the advantage of reducing concrete mass, thus reducing inertial response of the piers as vertical beams spanning between foundation and superstructure, and also reducing the tendency for thermally-induced cracking at an early age resulting from heat-of-hydration temperature variations. In Europe, hollow sections with large section dimension (up to 8m (26ft) maximum section depth or diameter) are common. Fig.10.1 includes alternatives based on hollow circular and hollow rectangular sections, suggested by the dashed lines representing the inner surface of the hollow section.

Hollow circular sections are less common than hollow rectangular sections despite theoretical considerations which would indicate improved seismic performance for the circular option, resulting from similar considerations to those noted above for solid sections. It has been shown that for hollow circular sections an inner layer of reinforcement provides little structural benefit, except as support for additional vertical reinforcement. Tests on hollow circular sections subjected to simulated seismic action[R1] have shown that hollow circular columns with all longitudinal and transverse reinforcement placed in a single layer close to the outer surface provide excellent stable hysteretic response provided extreme fibre compression strains are less than about 0.006. At higher extreme fibre strains, external cover concrete spalling can result in a sudden increase in the depth of the neutral axis, increasing the strain at the internal surface of the section to the stage where internal spalling, resulting in implosion, occurs.

10.1.2   The Choice between Single-column and Multi-column Piers

The choice between single-column and multi-column piers cannot be made independently of the choice of pier/superstructure connection type (see Section 10.1.3). With bearing-supported superstructures, the single-column design has the attraction that critical seismic response characteristics (strength and stiffness) can be made equal in orthogonal directions, since the pier will respond as a simple vertical cantilever in all directions. The location and performance of the potential plastic hinge will be known to a high degree of certainty.

Multi-column piers are more appropriate when monolithic pier/superstructure connection details are selected, and also when the superstructure width is large, resulting in a potential for high eccentric live-load moments in single-column piers. When the column has monolithic connections to the superstructure and foundation, it is again simple to make the seismic response characteristics omni-directional. Note, however, that if the superstructure is bearing-supported on a multi-column pier-cap, pier response will be as a vertical cantilever in the longitudinal direction, and by double-bending transversely, resulting in non-uniform strength and stiffness in orthogonal directions.

10.1.3   Bearing-Supported vs. Monolithic Pier/Superstructure Connection

(a) Bearing-supported Precast   (b) Monolithic Pier-superstructure.
    Beams with In-situ Deck   In-situ Construction
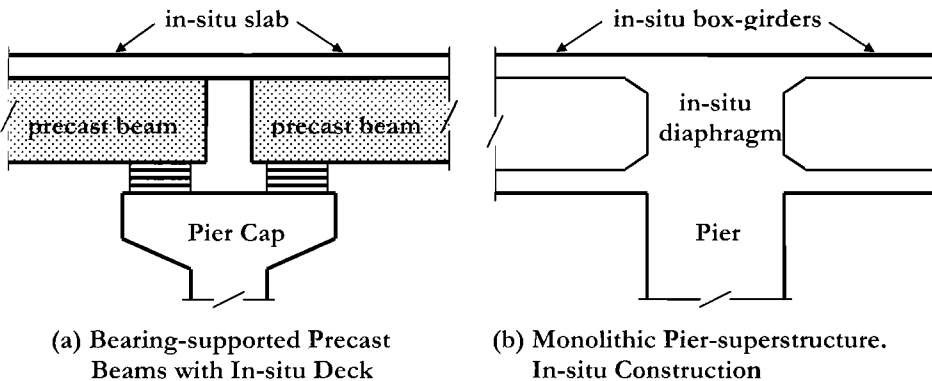
Fig.10.2   Different Pier/Superstructure Connection Options

Figure 10.2 presents the main options for pier/superstructure connection. With a moment-resisting connection, the potential for additional redundancy of energy dissipation exists, since plastic hinges can form at top and bottom of the columns, at least under longitudinal response. With multi-column piers this advantage also extends to transverse response. Lateral resistance will thus be increased for a given column flexural strength, and as a consequence, the column dimensions may be reduced. The fixed-top connection detail also allows the designer to consider the option of pinned connections between the column base and foundation, when multi-column piers are utilized. A major disadvantage of the monolithic connection detail is that seismic moments developed at the top of the pier are transmitted to the superstructure. This adds to the super-structure

gravity negative moments at the pier, and may also result in positive superstructure moments.   Resisting these may increase the cost of the superstructure. Clearly the monolithic detail is only appropriate when the superstructure is continuous over the pier, rather than simply supported. This might be felt to rule out designs where the construction uses precast concrete beams for the superstructure. However, connection details providing fully monolithic response of bridges with precast superstructures have been successfully tested under simulated seismic loading[H4].

Bearing-supported superstructures have the advantage of minimising the problems associated with moment transfer from the pier to the superstructure, and with joint-shear and anchorage issues. Different types of bearings may be considered, including pot-bearings, rockers, **PTFE**-stainless steel sliders and elastomeric bearings. These are discussed in some detail elsewhere[P4]. Bearing-supported connection details will almost always be chosen when a decision is made to provide seismic resistance by seismic isolation (see Chapter 10). Seismic displacements of bearing-supported superstructures will generally be larger than those of structures with monolithic connection, and the sensitivity to seismic intensity exceeding the design level will also be increased as noted above.

10.1.4   Soil-Structure Interaction

Bridges are often required to cross rivers and valleys where foundation conditions are less than ideal. As a consequence soil-structure interaction effects frequently require special consideration. Figure 10.3 illustrates three different foundation conditions where soil-structure interaction and foundation flexibility can be expected to affect the **DDBD** process. In Fig.10.3(a) the pier is supported on a spread footing. The situation is identical to that for structural cantilever walls on spread footings, which has been considered in some depth in Section 6.5. The influence on effective damping and ductility demand and capacity must be considered. As discussed in Section 6.5.2, the non-linearity of the foundation stiffness when partial uplift of the footing on the foundation material occurs must be considered when estimating elastic displacements resulting from foundation flexibility. A suitable design criterion is that at the design level of displacement response, at least 50% of the footing should still be in contact with the foundation material. This will ensure that the footing has sufficient overturning capacity to support the maximum feasible overturning moment found from capacity-design considerations.

Figure 10.3(b) represents a design where the column of a pier continues into a drilled hole in the foundation material to become the single supporting pile. In the example illustrated, the pile and column have identical dimensions and the same longitudinal and transverse reinforcement. Maximum moments will occur some distance (generally less than two pile diameters) below the ground surface. However, the elastic curvature in the pile below the location of the potential plastic hinge adds to the yield displacement, again affecting the damping, displacement, and ductility capacity.

The pile-supported footing of Fig.10.3(c) is similar in response to the spread footing of Fig.10.3(a).   However, since the soil strength and stiffness are likely to be lower with a

(a) Spread Footing

base rotation

yield

design

Displacement

Soil bearing pressure

(b) Column/Pile Shaft

pile elastic
rotation at hinge

yield

design

plastic hinge

Displacement

(c) Pile-Supported Footing

pile-cap
translation
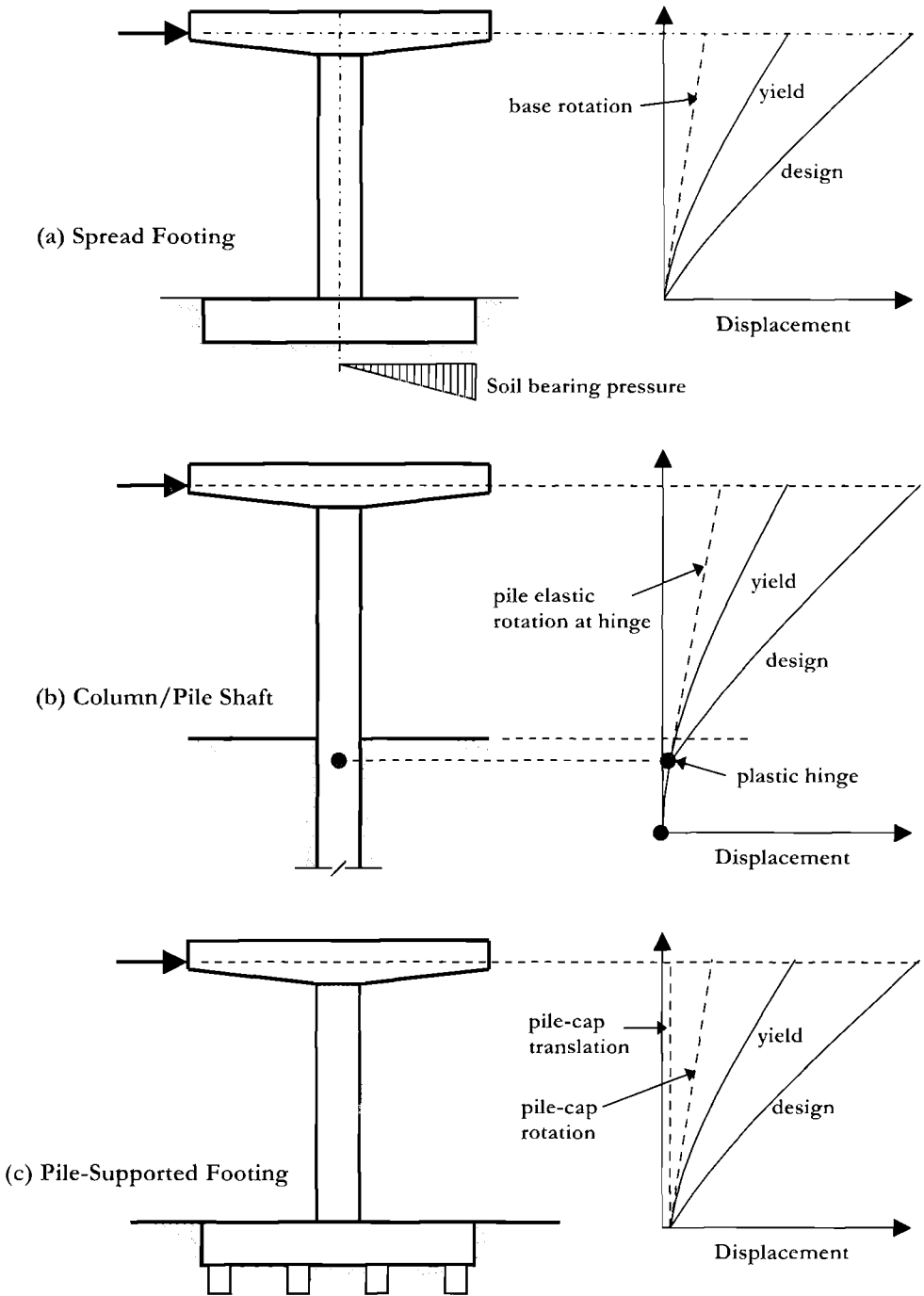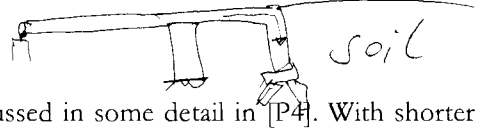
yield

pile-cap
rotation

design

Displacement

Fig.10.3 Soil-Structure Interaction for Different Support Conditions

pile-supported footing, horizontal translation of the pile cap can be more significant. On the other hand, if the piles are supported on a firm stratum, rotation effects may be lower.

10.1.5 Influence of Abutment Design

Different abutment design options are discussed in some detail in [P4]. With shorter bridges, of few spans, a monolithic connection between the superstructure and the abutment may be chosen. In such cases, effective periods are likely to be very short, and inertial response will be largely dictated by the peak ground acceleration. Design of the abutments will essentially be on a strength basis, and the concepts of ductile response are inappropriate. Damping, however, is likely to be significantly higher than the 5% elastic value often adopted for force-based elastic design. Special studies to determine the appropriate level of damping should be undertaken.

When the bridge is supported on bearings at abutments, a critical consideration will be whether the freedom of movement provided by the bearings occurs in just the longitudinal direction, or also in the transverse direction. In the former case, significant inertial reactions under transverse response will be transmitted back to the abutments by superstructure bending. The dual load path situation imposed by this action (see Section 1.3.7) requires special attention, and is considered later in this chapter (Section 10.4.2).

10.1.6 Influence of Movement Joints
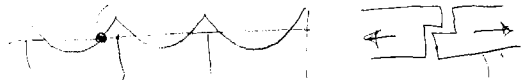
Superstructure movement joints are provided to accommodate thermal, creep and shrinkage displacements. Current practice is to use the minimum number possible of movement joints as they typically require continual maintenance. Movement joints also have an influence on the distribution of inertial forces, which primarily originate from superstructure inertial response, to supporting piers. Locations of movement joints should be considered from the seismic, as well as serviceability view point.

Modelling of movement joints is complex. Although longitudinal freedom is provided, impact may well occur across the joint under joint-closing displacements, particularly when combined with relative rotation of the superstructure segments on either side of the joint. Seismic force-transfer due to bearing stiffness or special seismic lock-up devices must be considered. Generally there will be additional damping associated with relative joint displacement. See Section 10.4.1 for comments relative to **DDBD**.

10.1.7 Multi-Span Long Bridges

Many bridges have considerable length – often several kilometres. It needs to be decided in the design phase if it is realistic to assume that the seismic input to all piers is coherent and in phase. There is, however, reasonable evidence based on analyses[P30] that the assumption of in-phase coherent input is conservative provided soil conditions are uniform along the bridge, and should be adopted unless special studies are carried out.

Normally bridges will be designed for transverse seismic response considering independent sub-structures, of perhaps five to eight spans (normally between movement joints) with simplified representation of the strength and stiffness of adjacent sections of the bridge. Where this is adopted, there should preferably be an overlap of spans in successive sub-structures designed.

10.1.8 P-Δ Effects for Bridges

P-Δ effects related to **DDBD** have been examined in Section 3.6. The effects are particularly important for bridges, as piers are often high, and drift limitations imposed by design codes for buildings will not normally be applied to bridges. Thus, although it is uncommon for buildings to be designed for drifts exceeding 0.025, bridges may be designed for response drifts of 0.04 or higher, generally governed by material strain limits.

10.1.9 Design Verification by Inelastic Time-History Analyses

As a result of the irregularity of many bridge structures, design verification by inelastic time history analyses (**ITHA**) should be considered, particularly for bridges with significant horizontal curvature. Typically the number of members to be modelled will be small, and hence the computational effort in data preparation and results interpretation will not be excessive. Refer to Section 4.9 for guidance in modelling and analysis.

10.2 REVIEW OF BASIC DDBD EQUATIONS FOR BRIDGES

Most of the basic design equations needed to determine the total design base shear force are identical to those for other structures and have been developed in Chapter 3, and summarized in Section 5.2.1 for frames. The equivalent **SDOF** design displacement is given by Eq.(5.3) (also Eq.(3.26)), and for effective mass by Eq.(5.4) (also Eq.(3.33)). The effective stiffness is defined by Eq.(5.10) (also Eq.(3.1)), and the total base shear by Eq.(5.11) (also Eq.3.2)). The total base shear is distributed to the masses by Eq.(5.12) (also Eq.(3.41)). In Section 4.9.2(e)(iii) it was noted that for **ITHA** of bridges it will normally be adequate to represent the distributed superstructure mass by lumped masses located above each pier. The same assumption will also normally be adequate for the **DDBD** process. However, the caveats noted in that section should also be reviewed, particularly when spans are long or columns are high.

However some aspects need special consideration. In particular the characteristic displacement shape (see Section 3.5.2) and the equivalent viscous damping are less obviously defined than for most building structures. We start by considering design for longitudinal response of straight bridges, and then developing to the more complex case of transverse design.

$$m_e = 0.9 \sim 0.95 \Sigma M$$

first mode is excited
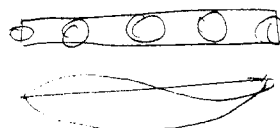
10.3 DESIGN PROCESS FOR LONGITUDINAL RESPONSE

The longitudinal response of straight bridges is simplified by the fact that except for very long bridges, the design displacements will be the same at all piers. For very long bridges it may be found that axial strains induced in the superstructure by inertia forces modify the design displacements to be different at different piers, but in such cases it is more appropriate to separately design segments of the bridge between movement joints, as noted above. The main issue for longitudinal design will thus be to determine the yield displacements and hence the equivalent viscous damping for the individual piers, and to combine these to form the system damping for **DDBD**.

10.3.1 Pier Yield Displacement

The pier yield displacement in the longitudinal direction depends on the degree of fixity provided at the pier top and bottom, the pier height, and the section yield curvature.

(a) Yield Curvatures: Yield curvatures for different solid sections have been summarized in Section 4.4.7 (Eq.(4.57)). It is worth noting, however, that these can also be used as reasonable estimates for hollow columns. As an example of this it is instructive to compare the moment-curvature response of two large-diameter circular columns with identical axial load and longitudinal reinforcement content. Both columns have a diameter of 4m (13.1ft), but one is solid, and the other is hollow with a wall thickness of 0.4m (15.7in), resulting in a net area 36% that of the solid column. Material properties are f'_{ce} = 40MPa (5.8ksi), f_{ye} = 450 MPa (65.3ksi). Transverse reinforcement is provided by 25mm (1in) diameter bars at 75mm spacing. Axial load is 25MN corresponding to axial load ratios of $P/f'_{ce}A_g$ =0.05 and 0.139 for the solid and hollow sections respectively, related to the net section area. Longitudinal reinforcement has a total area of 250,000 mm^2 in each case, corresponding to reinforcement ratios of 2% and 5.6% for solid and hollow sections respectively. The hollow section represents close to the limits of what would be considered appropriate for seismic conditions in terms of thinness of wall, and upper bound axial load and reinforcement ratios.

Moment-curvature plots for the two sections are compared in Fig.10.4. In the initial stages of response there is very little difference between the strength and stiffness of the two columns. The yield curvatures are found to be 0.001221m^{-1} and 0.001315m^{-1} for the solid and hollow sections, compared with the value predicted by Eq.(4.57a) of 0.00126. The discrepancy from the predicted value is less than 5% in each case. The biggest difference between the moment-curvature response of the solid and hollow sections results from the limitation of 0.006 on the extreme-fibre compression strain for the hollow column, in accordance with the recommendation made in Section 10.1.1. This limits the curvature ductility capacity to 4, compared with 16.4 for the solid section. However, as will shortly be shown, ductility demands on tall, large diameter columns are often rather small, and the limited ductility of the hollow columns will often be adequate.

Similar arguments apply to hollow rectangular columns, for which the yield curvature given by Eq.(4.47b) may be used with adequate accuracy.
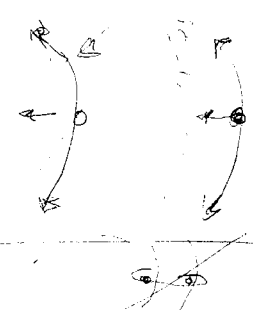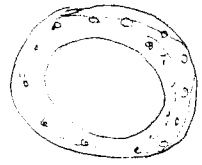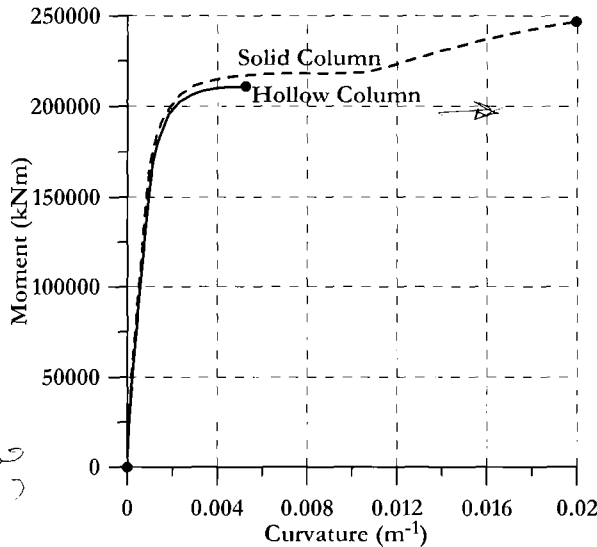
Fig.10.4 Comparison of Moment-Curvature Responses of Solid and Hollow Circular Columns (D=4m, D'=3.2m, P=25MN, A_{st}=2500cm²)
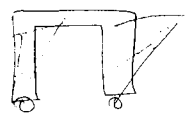
(b) Influence of End-Fixity Conditions: End-fixity conditions at both top and bottom of the pier will affect the yield displacement of the pier. A number of possible conditions are illustrated in Fig.10.5. In each case the yield displacement may be defined as

$$\Delta_y = C_1 \phi_y \left(H + L_{SP} \right)^2 \tag{10.1}$$

where L_{SP} is the total strain penetration and C_1 is a constant dependent on end fixity.

In Fig.10.5(a), the superstructure is bearing supported, and the footing is considered rigid against rotation and translation. The effective height H is measured to the centre of the bearing, the strain penetration length into the footing, from Eq.(4.30) is $0.022 f_{ye} d_{bl}$ (MPa) units, and the coefficient for Eq.(10.1) is $C_1 = 1/3$.

The footing in Fig.10.5(b) is also considered rigid, but the pier has a monolithic connection to the superstructure. The degree of fixity at the column top will depend on the relative stiffness of column and superstructure. Since strain penetration effects of pier reinforcement into both the footing and the superstructure will add apparent flexibility to the column, the value of L_{SP} to be used in Eq.(10.1) is $0.044 f_{ye} d_{bl}$. In most cases the superstructure stiffness will be much greater than the column stiffness, and rotation at the column top will be negligible. In such cases, the appropriate value of C_1 is $1/6$. Where the flexibility of the superstructure is considerable, the value of C_1 may be approximated as

$$C_1 = \frac{1}{6} \left(\frac{1}{1 - C_2} \right) \quad \text{where} \quad C_2 = \frac{4 EI_p \left(L_{S1} \cdot L_{S2} \right)}{6 I_{ss} \left(H + L_{SP} \right) \left(L_{S1} + L_{S2} \right)} \tag{10.2}$$

(a) Rigid Base, (b) Rigid Base, (c) Pinned Base, (d) Flexible (e) Pile/Column
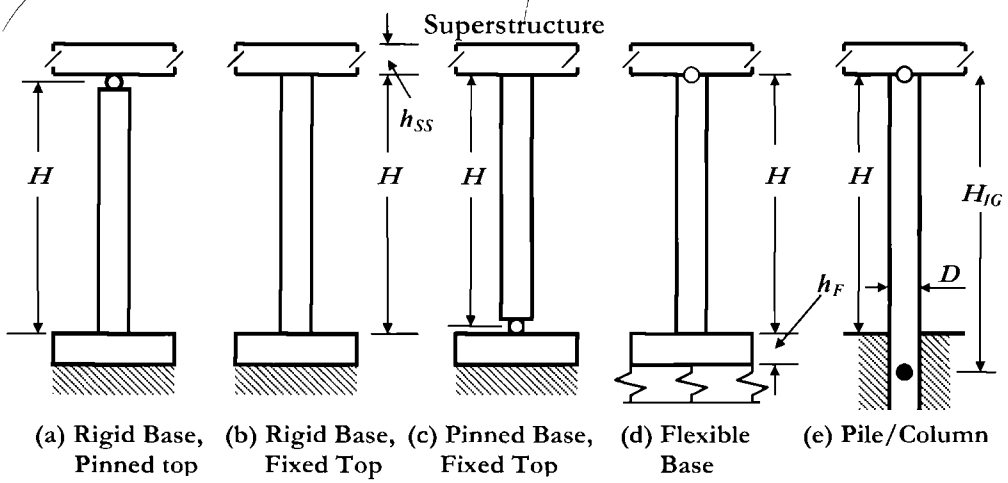   Pinned top   Fixed Top   Fixed Top   Base

Fig.10.5 Possible Fixity Conditions for Longitudinal Response

The equation for C_2 is found by displacing the pier longitudinally without joint rotation, then distributing the out of balance moment at the column top. In Eq.(10.2) EI_P is the pier stiffness, including effects of cracking and EI_{SS} is the superstructure stiffness (normally uncracked, particularly if prestressed). It is assumed that the superstructure has contraflexure points at the midpoint of the spans, length L_{SI} and L_{S2}, on either side of the pier. Modifications for end spans and spans with movement joints are obvious.

It is instructive to consider a typical example, with a stiff pier and a relatively flexible superstructure. The single-column pier has a diameter of 2 m (6.56 ft), and a clear height of 8 m (26.2 ft). The column stiffness is assumed to be $0.5EI_{gross} = 0.392E$ (metric units). The superstructure is 15 m (49.2 ft) wide, has a moment of inertia of 15 m⁴ and has span lengths on either side of the pier of 40 m (131.2 ft). From Eq.(10.2) the correction for pier-top flexibility, assuming a total strain penetration length of 0.6m is found to be $C_2 = 0.04$. This is less than the expected error in the yield curvature, and hence, even for this stiff-pier case, the superstructure may be considered effectively rigid.

The situation in Fig.10.5(c) is the inverse of that in Fig.10.5(a), with a hinge being located at the column base to reduce foundation moments, and a monolithic connection to the superstructure. This detail is only appropriate when the pier consists of more than one column, since a single-column design with this detail would be unstable transversely. Hinge details normally consist of terminating the column longitudinal reinforcement at the top of the footing, reducing the column diameter by placing a ring of flexible joint material between the column and footing, and placing special vertical hinge reinforcement at the centre of the column. Further details are available in [P4].

The example in Fig.10.5(d) has a flexibly supported footing (either a spread footing with soil of comparatively low subgrade modulus, or a pile-supported footing), and a pier/superstructure connection that could be either bearing supported or monolithic. The

situation is directly analogous to that of a cantilever wall supported on a footing, discussed in Section 6.5.2, where the additional displacement resulting from foundation flexibility can be rewritten as

$$\Delta_F = \left(M_B + V_B h_F\right)\left(H + h_F\right)/k_v I_\theta \tag{10.3}$$

where M_B and V_B are the design moment and shear at the base of the pier, h_F is the footing thickness, k_v is the soil vertical subgrade coefficient (kN/m³ or kips/in³), and I_θ is the moment of inertia of the footing soil interface, including possible effects of uplift.

It will be apparent that it is not possible to define a unique coefficient C_2 for this case, since the structural yield displacement is independent of the final pier strength while the additional displacement due to foundation flexibility is directly proportional to the final pier strength. Hence, when foundation flexibility effects are significant, an iterative approach may be necessary.

The final example, in Fig.10.5(e) consists of a pile/column design where the pile continues into the foundation material as a cast-in-drilled-hole (**CIDH**) pile. At the top of the column, the connection to the superstructure could be bearing-supported or monolithic. This situation has recently been studied by Suarez and Kowalsky[S4] who found that Eq.(10.1) could be used to predict the yield displacement, with the height H replaced by the distance H_{IG} from the in-ground hinge location to the pile top (see Fig.10.5(e)), and with values for C_1 determined from inelastic pushover analyses using an inelastic pile supported in the ground by realistic inelastic soil springs. Uniform sand and clay foundation materials were investigated. Internal friction values of the saturated sands varied from 30⁰ to 37⁰ corresponding to sand coefficients of lateral subgrade modulii between 5.5MN/m³ and 33.2MN/m³ (35 – 212 kips/ft³). Clay strengths varied between 20kPa and 40kPa (3-6 psi).

Results from the parameter study reported in [S4] are summarized in Fig.10.6, which provides information on the distance from the pile top to the in-ground hinge location, and the appropriate value of C_1 to be used in Eq.(10.1), for both pinned and fixed connections between the pile/column and the superstructure. Heights H_{IG} to the in-ground hinge (see Fig.10.5(e)) are expressed in dimensionless form, dividing by the column diameter, and are related to the above-ground height to the superstructure. It will be noted that the in-ground depth (H_{IG} - H) decreases as the dimensionless above-ground height H/D increases. The parameter study found that there was no significant difference in the value of H_{IG} between fixed-head and free-head conditions. As soil strength increased, depth to the in-ground plastic hinge decreased. As is clear from Fig.10.6(a) and (b), the relationships between H_{IG}/D and H/D are essentially linear and can be expressed by the following relationships:

$$\text{Sand, } \phi = 30^0: \quad (H_{IG}/D) = 4.39 + 0.82 \times (H/D) \tag{10.4a}$$

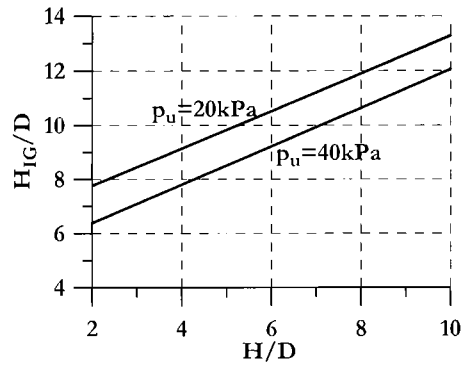$$\text{Sand, } \phi = 37^0: \quad (H_{IG}/D) = 3.40 + 0.84 \times (H/D) \tag{10.4b}$$

Clay, $p_u = 20$kPa: $(H_{IG}/D) = 6.38 + 0.69 \times (H/D)$ $\qquad$ (10.4c)

Clay, $p_u = 40$kPa: $(H_{IG}/D) = 4.96 + 0.71 \times (H/D)$ $\qquad$ (10.4d)

Coefficients C_I to be used in Eq.(10.1) are plotted in Figs.10.6(c) and (d) against column above-ground height. The differences between the relationships for different soil strength for pinned-head conditions are small, and for fixed-head conditions are negligible. The coefficients in these figures were determined using a bilinear approximation to the moment-curvature characteristics of the pile, following principles outlined in Section 4.2.6. For the pinned-head cases, the coefficient applies when the in-ground hinge develops the yield curvature given by Eq.(4.57a). For the fixed-head cases, (monolithic connection between pier and superstructure), the hinge at the top of the column develops at a lower displacement than the in-ground hinge. The coefficient in Figs.10.6(c) and (d) applies when the column-top hinge forms. At this stage the in-ground hinge may still be some way from forming.
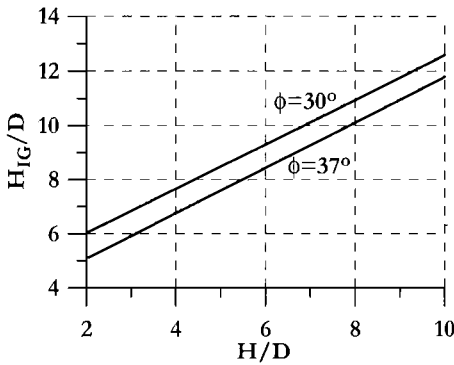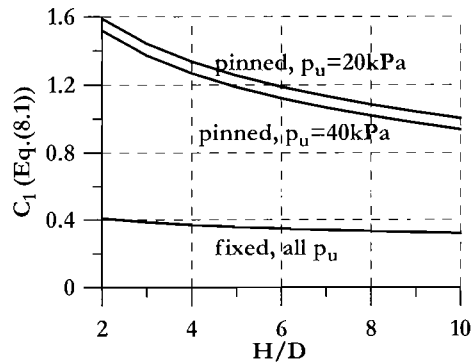

(a) Sand, Length to Fixity $\qquad$ (b) Clay, Length to Fixity
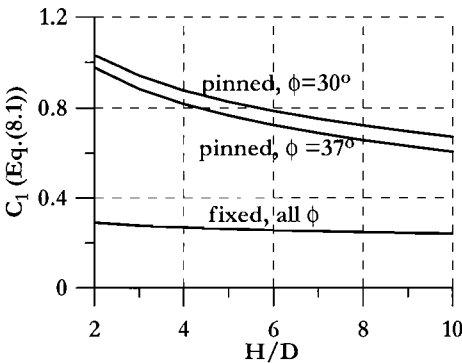
(c) Sand, Yield Displacement Parameter $\qquad$ (d) clay, Yield Displacement Parameter

Fig.10.6 Data for Yield Displacement Calculations for Pile/Columns (after [S4])

The coefficients in Figs.10.6(c) and (d) may be compared with the values of 0.333 and 0.167 applicable for columns fixed at the base, and fixed at base and top respectively. It will be seen that the yield displacements for pile/columns of equal above-ground heights to fixed-base columns are much larger. This is a consequence of the elastic rotation occurring at the position of potential in-ground hinge formation, resulting from soil-structure interaction. For short columns, the yield displacement may be as much as three times the value applicable to a fixed-base column with similar dimensions.

Suarez and Kowalsky[S4] found that the data in Fig.10.6 were applicable for columns with reinforcement ratios varying between 1% and 4%, within acceptable errors. The data in Figs 10.6(c) and (d) may be represented by the following equations:

$$\text{sand, pinned head, } \phi = 30^0: \quad C_1 = 1.187 - 0.223\ln(H/D) \tag{10.5a}$$

$$\text{sand, pinned head, } \phi = 37^0: \quad C_1 = 1.137 - 0.230\ln(H/D) \tag{10.5b}$$

$$\text{sand, fixed head, all } \phi: \quad C_1 = 0.310 - 0.030\ln(H/D) \tag{10.5c}$$

$$\text{clay, } p_u = 20 \text{ kPa:} \quad C_1 = 1.840 - 0.363\ln(H/D) \tag{10.5d}$$

$$\text{clay, } p_u = 40 \text{ kPa:} \quad C_1 = 1.767 - 0.360\ln(H/D) \tag{10.5e}$$

$$\text{clay, fixed head, all } p_u \quad C_1 = 0.447 - 0.055\ln(H/D) \tag{10.5f}$$

- **(c) Elastically Responding Piers:** In Chapters 5 and 6 it was pointed out that the yield displacements of tall buildings may exceed the peak elastic response displacement applying for periods larger than the corner period when design seismic intensities are moderate. Such structures would thus respond elastically to the design seismicity. Similar arguments, with similar conclusions apply to bridge piers. Since it will primarily be tall, large-diameter hollow columns with pinned connection to the superstructure that may be affected, the discussion is limited to this class of pier.

Based on the yield curvature of circular columns defined by Eq.(4.57a) and the yield displacement equation of Eq.(10.1), the yield displacement can be written as

$$\Delta_y = \phi_y\left(H + L_{SP}\right)^2/3 = 2.25\varepsilon_y\left(H + L_{SP}\right)^2/3D \tag{10.6}$$

Figure 10.7 plots the relationship defined by Eq.(10.6) for reinforcing steel with a yield strength of 500MPa (i.e., $\varepsilon_y = 0.0025$). Although Eq.(10.6) strictly applies to solid-section piers, it was pointed out in Section 10.3.1 that the error in applying it to hollow-section piers is negligible. Because of the similarity between the yield curvatures of circular and rectangular sections (see Eqs(4.57)), Fig.10.7 also applies to rectangular sections within a 10% error margin.

It is of interest to compare these displacements with the plateau displacements predicted by the approximate approach developed in Section 2.2.2, in a similar fashion to that used to develop Fig.6.9 for cantilever walls. The results are plotted in Fig.10.8 for piers with reinforcement yield strain of 0.0025. Yield displacements are shown for

cantilever piers with different aspect ratios in Fig.10.8(a) side-by-side with peak (plateau) displacements corresponding to different causative earthquake magnitudes with different site peak ground accelerations. As an example of the use of this figure, consider a cantilever column of effective height $(H+L_{SP})$ = 36m and diameter 4.5m. The aspect ratio is 8, and Eq.(10.6) and Fig.10.8(a) indicate that the yield displacement is 0.544m. This displacement is transferred to Fig.10.8(b) (follow the dashed line), which indicates that the yield displacement corresponds to a **PGA** of 0.4g with a causative moment magnitude of M_W = 7.2. Smaller magnitudes with the same **PGA**, or smaller **PGA**'s with the same magnitude will not be adequate to induce yield displacement.
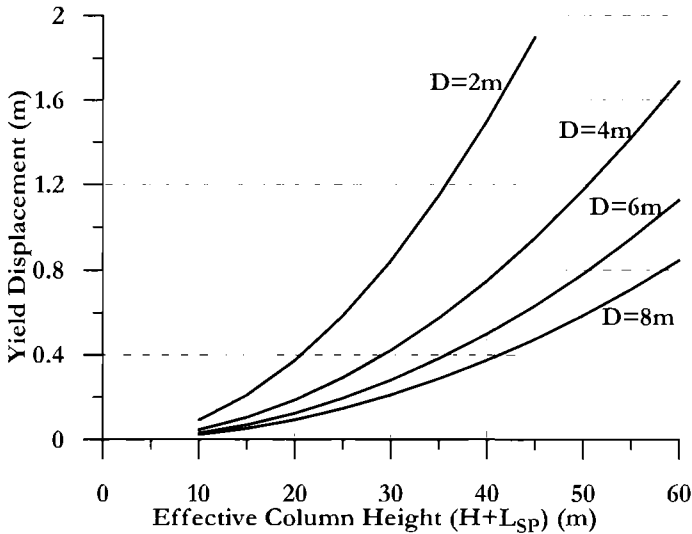

Fig.10.7 Yield Displacements of Cantilever Piers with Circular Sections
$(\varepsilon_y=0.0025)$

The modification to enable consideration of fixed-head columns is obvious, since the yield displacements will be one half those shown in Fig.10.8(a).

√10.3.2 Design Displacement for Footing-Supported Piers

As noted earlier the longitudinal design displacements for all piers will be normally be identical for a straight bridge. While in buildings it is normal for the design displacement to be set by drift limits, this is rarely the case for bridge piers. Occasionally there may be absolute design displacement limits, normally related to allowable relative displacements between superstructure and abutments, but more commonly material strain limits will govern the design displacements. **P-Δ** moments may also limit design displacements.

As has been noted in Section 3.4.1, when material strains govern the design, the design curvature will be found from the more critical (smaller) of the curvatures associated with the limit concrete strain and the limit tension strain. Thus:
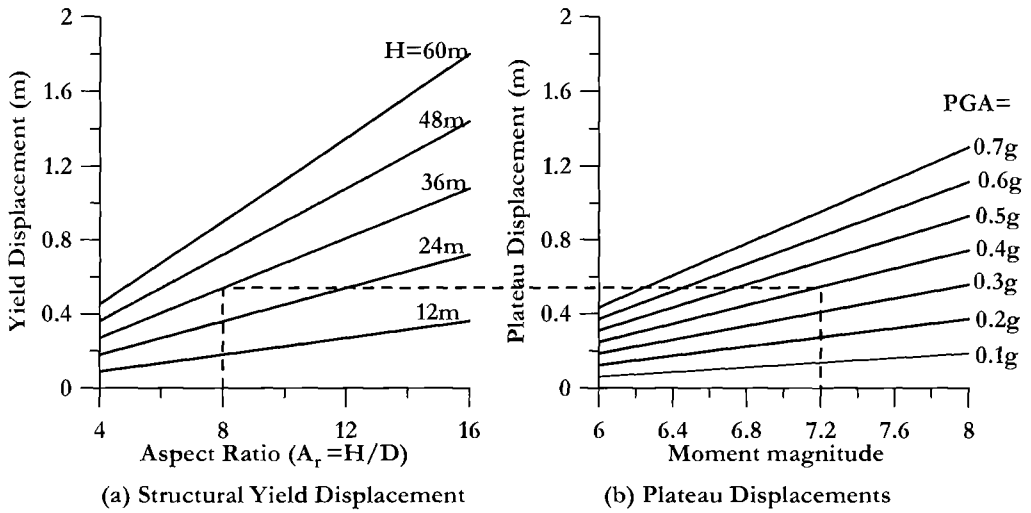
(a) Structural Yield Displacement   (b) Plateau Displacements

Fig.10.8   Cantilever Pier Yield Displacements for $\varepsilon_y = 0.0025$ Compared with Plateau Displacements

$$\phi_{ls,c} = \varepsilon_{c,ls} / c \quad \text{(a)} \quad \text{and} \quad \phi_{ls,s} = \varepsilon_{s,ls} / (d - c) \quad \text{(b)} \tag{10.7}$$

where c and d are the distances from the extreme compression fibre to the neutral axis and to the extreme tension reinforcing bar respectively.

The limit strains for **DDBD** are defined in Section 4.2.4. For the damage-control limit state, the maximum concrete compression strain is related to the volumetric ratio of transverse reinforcement, and is defined by Eq.(4.21), with the maximum reinforcement tension strain defined by $\varepsilon_{s,dc} = 0.6\varepsilon_{su}$. Since the curvature associated with the limit strains also depends on the neutral axis depth, c, (see Eq.(10.7)), it will not be possible to exactly define the limit curvature, and hence the design displacement, at the start of the design process, and some iteration is required. The alternative is to design for a specified drift, and determine the required amount of transverse reinforcement to provide the required damage control limit strain at the end of the design process. This will only work if the concrete strain governs design, which will generally be the case for circular columns.

Analyses indicate, however, that the neutral axis depth is rather insensitive to the axial force ratio and reinforcement content, particularly for circular columns, as is illustrated in Fig.10.9(a). Although the reinforcement ratio will not be known at the start of the **DDBD** process, the axial load ratio generally will be, except for transverse design of piers with multi-column bents. Sensitivity to reinforcement ratio is small, and taking an average value of 0.02, the neutral axis depth can be approximated as

$$c / D = 0.2 + 0.65 P / (f'_{ce} A_g) \tag{10.8}$$

where D is again the column diameter.

Design displacements using neutral axis depths based on Eq.(10.8) will have only small errors, which may be eliminated at the final stages of design by small adjustments to the final spacing of transverse reinforcement.

Figure 10.9 also includes additional design information in the ratio of confined concrete compression strength to expected unconfined compression strength, as a function of transverse reinforcement ratio and ratio of transverse reinforcement tension strength to expected unconfined compression strength. This is based on Eqs.(4.5) and (4.10) and simplifies the solution of Eq.(4.21) to determine the damage-control limit state compression strain. High values of f_{yh}/f'_{ce} have been included in Fig. 10.9(b) to enable values for high strength transverse reinforcement to be considered. Tests of columns with unstressed prestressing strand as transverse reinforcement[B5] have shown superior structural performance compared with mild steel reinforcement for both confinement and shear strength.

(a) Neutral Axis Depth   (b) Confined Concrete Strength
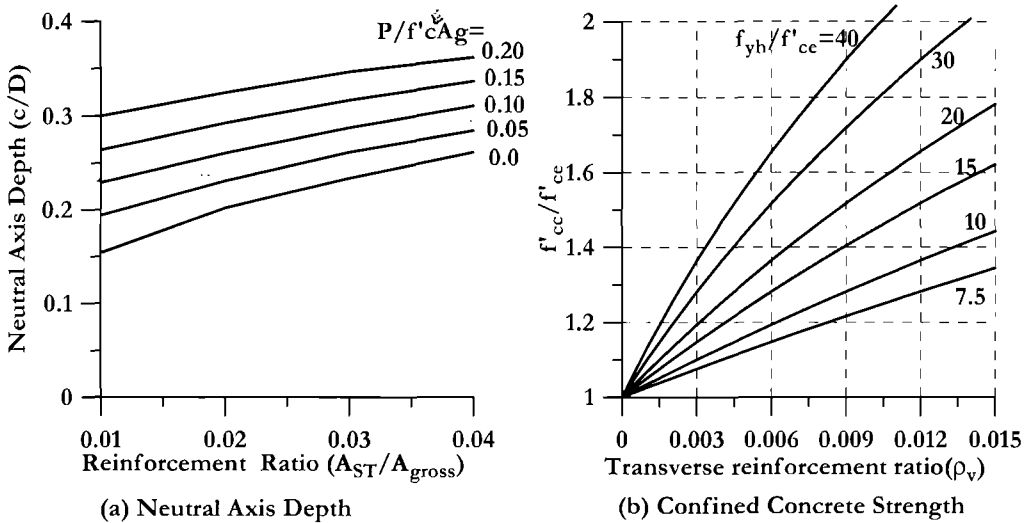
Fig.10.9   Design Aids for Design Displacement of Circular Columns

The design process to determine the damage-control design displacement for longitudinal response of circular columns can thus be expressed in the following steps. Modification for rectangular columns is obvious, using information provided in Section 4.2.2.

Step 1: For the critical column, chose the diameter and spacing, of transverse reinforcement, and hence the volumetric ratio from

$$\rho_v = \frac{4A_b}{D's} \tag{10.9}$$

where A_b is the bar area, and s the spacing of the transverse reinforcement, and D' is the core diameter, measured to the centres of the hoops.

Step 2: From Fig.10.9(b) or Eqs.(4.5) and (4.10) determine the confined compression strength of the core concrete.

Step 3: From Eq.(4.21), reproduced here as Eq.(10.10) determine the damage-control compression strain:

$$\varepsilon_{dc,c} = 0.004 + 1.4 \frac{\rho_v f_{yh} \varepsilon_{su}}{f'_{cc}} \tag{10.10}$$

Step 4: Determine the column axial force ratio.

Step 5: From Fig.10.9(a) or Eq.(10.8) estimate the neutral axis depth.

Step 6: From Eqs.(10.6) determine the critical limit-state curvature. 10.7

Step 7: Determine the plastic hinge length from Eq.(4.31), reproduced here as Eq.(10.11):

$$L_P = kL_C + L_{SP} \geq 2L_{SP} \tag{10.11}$$

where L_C is the distance from the critical section to the point of contraflexure, L_{SP} is the strain penetration length given by Eq.(4.30) and k depends on the flexural reinforcement ultimate/yield strength ratio, given by Eq.(4.31b).

Note, however, the modification below in Section 10.3.4 for pile/columns.

Step 8: Determine the design displacement from Eq.(10.12), where Δ_y is obtained in accordance with Section 10.3.1.

$$\Delta_D = \Delta_y + (\phi_{ls} - \phi_y)L_P H \tag{10.12}$$

10.3.3 Design Example 10.1: Design Displacement for a Footing-Supported Column

To illustrate the sequence of operations described in the previous section, we consider a footing-supported column monolithically connected to the superstructure, under longitudinal seismic response. The column diameter is 2.0 m (78.7 in), has a clear height of 12.0 m (39.4 ft), and supports an axial load, including self weight, of 10,000 kN (2250 kips). Specified material strengths are $f'_c = 30$ MPa (hence, from Section 4.2.5 $f'_{ce} = 1.3 \times 30 = 39$MPa (5.66 ksi)) and $f_y = f_{yh} = 420$MPa (hence from Section 4.2.5 $f_{ye} = 462$ MPa (67.0 ksi)). The ratio of ultimate to yield strength of the longitudinal reinforcement is 1.35. Longitudinal bar diameter is 40 mm (1.575 in), with 50 mm (1.97 in) cover, and the transverse reinforcement is initially selected as 20 mm (0.79 in) diameter at 100 mm (3.94 in) spacing along the column axis. Small adjustments to the spacing may be made after final design. Reinforcement strains at ultimate stress are 0.10 and 0.12 for longitudinal and transverse reinforcement respectively.

(a) Solution, Fixed Connection Case: We follow the steps in Section 10.3.2:

Step 1: The core diameter is $D' = 2000 - 2 \times 50 + 20 = 1920$ mm. Hence from Eq.(10.9):

$\rho_v = 4A_b / D's$ = 4×314/(1920×100)=0.00654

✓ **Step 2:** From Fig.10.9(b) with f_{yh}/f'_{ce}=420/39=10.8, we find f'_{cc}=1.23f'_{ce} = 48.0
MPa (6.96ksi).

✓ **Step 3:** The damage-control limit compression strain is found from Eq.(10.10) as

$$\varepsilon_{dc,c} = 0.004 + 1.4\frac{\rho_v f_{yh}\varepsilon_{su}}{f'_{cc}} =0.004+1.4(0.00654×420×0.12)/48.0=0.0136$$

✓ **Step 4:** Column axial force ratio: $P/f'_{ce} A_g$ =10/(39×3.14)=0.0816

✓ **Step 5:** We estimate the longitudinal reinforcement ratio as 1.8%. From Fig.10.9(a)

c/D = 0.240

✓ **Step 6:** The damage-control limit-state curvatures are thus, from Eqs.(10.7)

$\phi_{ls,c} = \varepsilon_{c,ls}/c$ =0.0136/0.48 =0.0283/m   ← governs

$\phi_{ls,s} = \varepsilon_{s,ls}/(d-c) = 0.06/(1.93-0.48) = 0.0414/m$

✓ **Step 7: Plastic Hinge Length**: From Eq.(4.31b)

$k = 0.2(f_u/f_{ye} -1)\le 0.08$ = 0.2×0.35=0.07

From Eq.(4.30), with d_{bl} = 40 mm the strain penetration length is

$$L_{SP} = 0.022f_{ye}d_{bl} =0.022×462×40 = 407 \text{ mm (16 in)}$$

Hence, with the column in double-bending, since it is fixed at the top, L_C= 6.0m, and

$L_P = kL_C + L_{SP} \ge 2L_{SP}$ =0.07×6+0.407 =0.827 m (32.6 in) from Eq.(10.11).

Step 8: Design Displacement: The yield curvature is found from Eq.(4.57a) as

$$\phi_y = 2.25\varepsilon_y / D =2.25(462/200,000)/2.0=0.0026/m$$

Since the column is in double bending, strain penetration applies at both top and
bottom, and the effective length for yield displacement is thus ($H+2L_{SP}$). We assume
both the footing and superstructure to be rigid. From Eq.(10.1) with C_1= 1/6:

$$\Delta_y = \phi_y(H + 2L_{SP})^2/6 = 0.0026×12.814^2/6=0.0712m$$

The design displacement is then, from Eq.(10.12):

$$\Delta_D = \Delta_y + (\phi_{ls} - \phi_y)L_pH =0.0712+(0.0283-0.0026)×0.827×12=0.326m \text{ (12.8in)}$$

The corresponding displacement ductility capacity is μ_Δ=0.326/0.0712=4.58.

✓ **(b) Solution, Pinned-Connection Case:** Note that if the column was pinned at the top,
the yield and damage-control curvatures would be unaffected. The plastic hinge length
would be increased to 0.07×12+L_{SP} = 1.247 m (49.1in), and the effective height for yield
calculation would be 12.407m (40.7ft). The yield displacement would increase to

$$\Delta_y = \phi_y\left(H + L_{SP}\right)^2 / 3 = 0.0026 \times 12.407^2/3 = 0.133\text{m, and the design}$$

displacement to

$$\Delta_D = \Delta_y + \left(\phi_{ls} - \phi_y\right)L_P H = 0.133 + (0.0283 - 0.0026) \times 1.247 \times 12 = 0.518\text{m (20.4 in)}$$

The corresponding displacement ductility is $\mu_\Delta = 0.518/0.133 = 3.90$. It should be noted that the displacements calculated for the pinned-head pile/column have been based on the assumption that relative displacement between superstructure and column top does not occur. If a translational bearing is supplied at the column top, superstructure displacement will be increased, and columns may not reach yield capacity if the bearing lateral strength is low compared with column strength.

These data will be used again in Design Examples 10.2 and 10.3.

10.3.4 Design Displacement for Pile/Columns

Most of the material presented in the previous section also applies to pile/columns (see Fig.10.5(e)). However, for pinned-head pile/columns, the plastic hinge forming in-ground is not affected by strain penetration, and may be approximated by the following equation, based on analyses by Chai[C7]:

$$L_P / D = 1 + 0.1\left(H - H_{CP}\right)/ D \le 1.6 \tag{10.13}$$

The nomenclature of Eq.(10.13) is clarified in Fig.10.10 for a fixed-head pile/column. When the pile column is pinned to the superstructure, $H_{CP} = 0$.
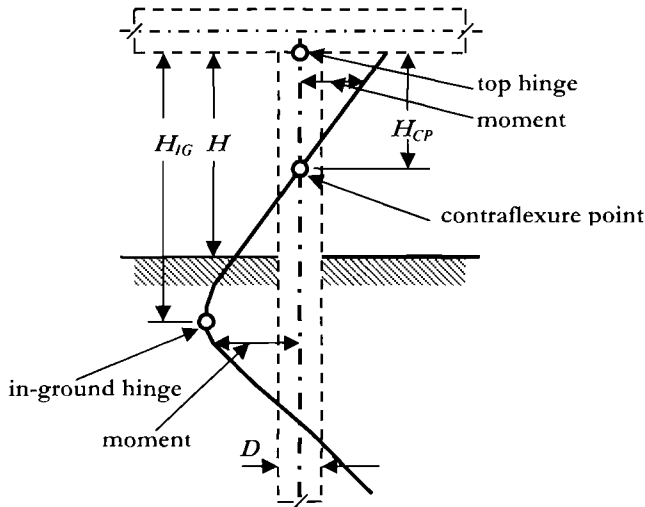

Fig.10.10 Moments in a Pile/Column with Monolithic Superstructure Connection

For fixed-head pile/columns the in-ground hinge will rarely govern design since the column-top hinge typically forms first, and has a shorter plastic hinge length, given by Eq.(10.11) with $L_C = H_{CP}$. Suarez and Kowalsky[S4] report average values of $H_{CP}/H_{IG} = 0.52$ and 0.57 for sand and clay respectively.

The sequence of steps for determining the design displacement of a pile/column are thus as follows:

Step A: Determine the height H_{IG} from the in-ground hinge to the superstructure using the appropriate plot from Fig.10.6, or from Eq.(10.4).

Step B: Follow steps 1 through 6 for a footing-supported pier, as outlined above.

Step C: Determine the plastic hinge length. For a pinned connection to the superstructure, rotation of the in-ground hinge is required, and Eq.(10.13) applies, with $H_{CP} = 0$. For a fixed connection to the superstructure, the in-ground hinge is not critical, and it is the rotation of the plastic hinge at the top of the column that governs. Equation (10.11) applies, with $L_C = H_{CP}$.

Step D: Determine the design displacement:

$$\text{Pinned-connection: } \Delta_D = \Delta_{y,IG} + \left(\phi_{ls} - \phi_y\right)L_{P,IG}H_{IG} \tag{10.14}$$

$$\text{Fixed connection: } \Delta_D = \Delta_{y,F} + C_3\left(\phi_{ls} - \phi_y\right)L_{P,T}H_{IG} \tag{10.15}$$

The coefficient C_3 results from the changing moment pattern down the pile/column as the inelastic rotation develops at the column top. Values of $C_3 = 1.68$ and 1.54 have been recommended for sand and clay respectively[S4]. Values for the yield displacement are found in accordance with the information provided in Section 10.3.1(b).

10.3.5   Design Example 10.2: Design Displacement for a Pile/Column

The data from Design Example 10.1 (Section 10.3.2) are now used to determine the design displacements and ductility capacities for two pile/column designs, one with a pinned connection and the other with a fixed connection to the superstructure. The height from the ground surface to the superstructure remains at 12m, as for the footing-supported example, and the soil is dense sand.

(a) Solution, Pinned-Connection Case: We follow the sequence of calculations outlined in the previous section:

Step A: With dense sand, the height from in-ground hinge to superstructure is given by Eq.(10.4b):

$$(H_{IG}/D) = 3.40 + 0.84 \times (H/D) = 3.4 + 0.84 \times 12/2 = 8.44. \text{ Hence } H_{IG} = 16.88\text{m}$$

Step B: The referenced steps to Section 10.3.2 result in the numerically identical values for yield and limit-state curvatures to those of Design Example 10.1

Step C: Plastic Hinge Length: From Eq.(10.13), with $H_{CP} = 0$:

$$L_P/D = 1 + 0.1H/D = 1 + 0.1 \times 12/2 = 1.6. \text{ Hence } L_P = 3.2\text{m}$$

~ **Step D:** Design Displacement. First we calculated the yield displacement. From Eq.(10.5b) the coefficient to be used in Eq.(10.1) is

$$C_1 = 1.137 - 0.230\ln(H/D) = 1.137 - 0.23\ln(6) = 0.725$$

Hence , from Eq.(10.1) with $L_{SP} = 0$

$$\Delta_{y,IG} = C_1\phi_y H_{IG}^2 = 0.725 \times 0.0026 \times 16.88^2 = 0.537 \text{m}$$

The design displacement, from Eq.(10.13) is

$$\Delta_D = \Delta_{y,IG} + (\phi_{ls} - \phi_y)L_{P,IG}H_{IG} = 0.537 + (0.0283 - 0.0026) \times 3.2 \times 16.88 = 1.925 \text{m}$$

This corresponds to a displacement ductility capacity of $\mu_\Delta = 1.925/0.537 = 3.6$. Note that both the yield and limit-state design displacements are very large, and it is unlikely that the column would be designed to respond at such large displacements. It is probable that **P-Δ** moments would be excessive.

(b) Solution, Fixed-Connection Case: Design in this case is governed by the column-top hinge.

✓**Step A:** The height from the in-ground hinge to the superstructure is unaffected by the column-top fixity, and $H_{IG} = 16.88$ m again.

Step B: The yield and limit-state curvatures are the same as in the pinned-connection case.

Step C: For sand, an average value of $H_{CP} = 0.52 H_{IG} = 0.52 \times 16.88 = 8.78$m applies. Hence from Eq.(10.11)

$$L_P = kL_C + L_{SP} \geq 2L_{SP} = 0.07 \times 8.78 + 0.407 = 1.022 \text{m}$$

Step D: From Eq.(10.5c) or Fig.10.6c) the displacement coefficient to be used in Eq.(10.1) is

$$C_1 = 0.310 - 0.030\ln(H/D) = 0.31 - 0.03\ln(6) = 0.256$$

The yield displacement is hence, from Eq.(10.1):

$$\Delta_{y,F} = C_1\phi_y(H_{IG} + L_{SP})^2 = 0.256 \times 0.0026(16.88 + 0.407)^2 = 0.199 \text{ m}$$

The design displacement is thus, from Eq.(10.15)

$$\Delta_D = \Delta_{y,F} + C_3(\phi_{ls} - \phi_y)L_{P,T}H_{IG} = 0.199 + 1.68(0.0283 - 0.0026) \times 1.022 \times 16.88$$
$$= 0.642 \text{ m}.$$

The displacement ductility capacity, related to yield of the top plastic hinge is $\mu_\Delta = 0.642/0.199 = 3.23$. Again the displacements are very much larger than for the footing-supported column of Design Example 10.1.

10.3.6 System Damping for Longitudinal Response

(a) Member Damping; Fixed-Head Piers Supported by Footings. When piers have a moment resisting connection to the superstructure, and are supported on rigid

foundations, computation of the individual pier damping is straightforward. If the potential plastic hinges at top and bottom of the columns have equal flexural strength, and rotations of footing and superstructure can be neglected (the usual case), then the displacement ductility is found directly, as in Design Example 10.1 above, and the corresponding pier damping from Eq.(3.17a). When flexibility exists in the footing and/or the superstructure, the plastic hinges may not form simultaneously, and the equivalent yield displacement, found from the intersection of the initial elastic, and post-yield stiffness response, as shown in Fig.10.11 should be used to determine the effective pier ductility.
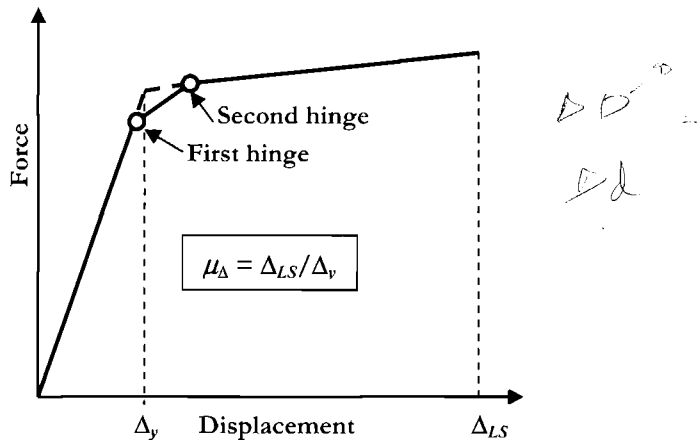

Fig.10.11   Yield Displacement of a Pier with Successive Hinge Formation

(b) Member Damping, Pinned connection Between Pier and Superstructure. If the pier is connected to the superstructure in such a way that relative longitudinal displacement between the pier top and the superstructure cannot occur, then the estimation of displacement ductility and hence damping is again straightforward, following the principles of the previous section. However, it is more likely in such cases that the superstructure will be bearing-supported on the pier cap, and the superstructure displacement will be significantly larger than that of the column top. Depending on the type of bearing, it is possible that the shear transmitted through the bearing will be insufficient to cause the pier to develop a flexural hinge at the base. This, of course, is the basic intention when the bearings are seismic isolating bearings, as discussed in some depth in Chapter 11. Hence only the case where the lateral strength of the bearing exceeds that of the pier, with the consequence that the pier responds inelastically to the design-level seismic excitation, will be discussed here.

The situation is described in Fig.10.12, where the superstructure is supported on the pier top by an elastomeric bearing (Fig.10.12(a)). At yield, the lateral flexibility of the bearing, which is designed to accommodate thermal and creep movements, results in bearing displacements Δ_B which in this case are similar in magnitude to the flexural

deformations Δ_{ys} of the pier. At the limit-state response, the lateral force is essentially the same as at yield, and hence the bearing deflection remains unchanged, while the pier deformation increases by Δ_P, the plastic deformation associated with the limit strains.

(a) Structure   (b) Displacement Profiles

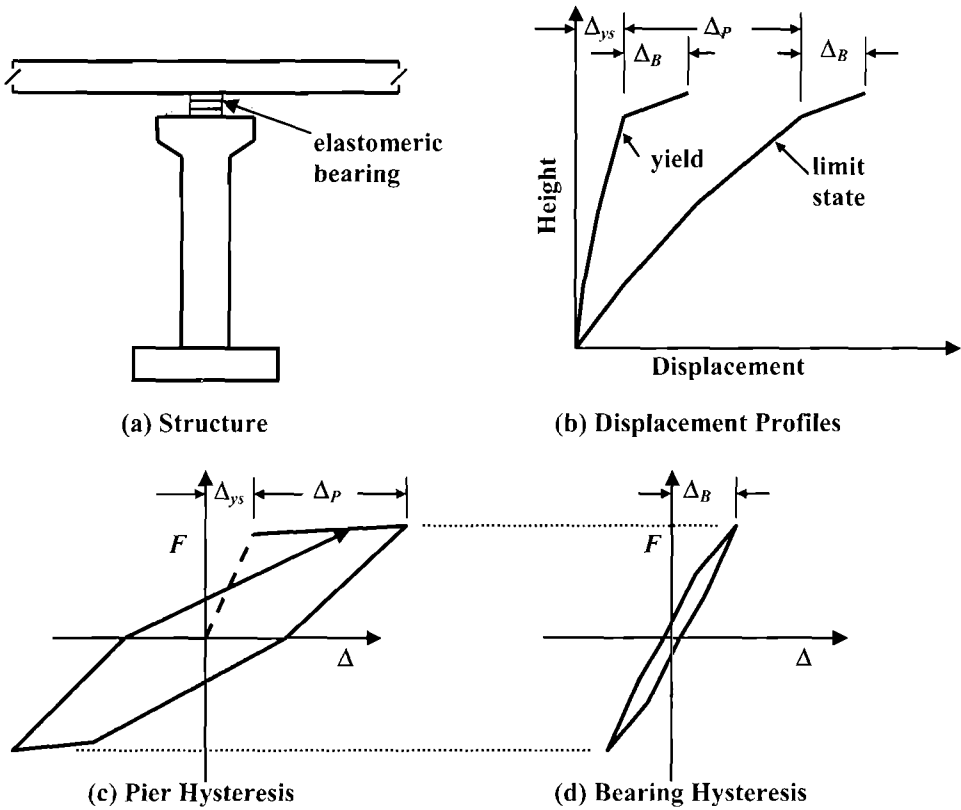(c) Pier Hysteresis   (d) Bearing Hysteresis

Fig.10.12   Damping for a cantilever pier with Elastomeric Bearing

The structural force-displacement hysteresis response is described in Fig.10.12(c). The damping ξ_P associated with this can be estimated from the structural displacement ductility demand $\mu_\Delta = 1+\Delta_P/\Delta_{ys}$, using Eq.(3.17a). There will also be damping ξ_B associated with the hysteretic response of the bearing itself. The value will depend on the characteristics of the elastomeric material, but is likely to be in the range 5%-12% unless high-damping rubber is used. The effective damping from the combined action of pier and bearing is directly analogous to the flexible foundation case discussed in Section 3.5.4(b), and can thus be found from Eq.(3.40c) as

$$\xi_e = \frac{\xi_P\left(\Delta_{ys} + \Delta_P\right) + \xi_B\Delta_B}{\Delta_{ys} + \Delta_P + \Delta_B} \tag{10.16}$$

(c) Member Damping, Pile/Column: With pile/column designs (Fig.10.5(e)) additional damping comes from inelastic response of the soil. Typically this initiates at response levels lower than structural yield, and can significantly enhance the total effective damping of a pier. Suarez and Kowalsky[S4] investigated this phenomenon by carrying out non-linear time-history analyses of free-had and fixed-head piers with clay and sand foundation material represented by appropriate hysteretic springs. The characteristics included the slackness associated with gapping (formation of a permanent hole around the pile) on unloading. Structural hysteresis was modelled by the "Fat" Takeda model (see Section 3.4.3) since the hysteretic response of the in-ground hinge would not be subjected to pinching from shear effects (shear is zero at the in-ground hinge). Results for the hysteretic component of equivalent viscous damping, including both the soil and structural hysteresis, but not any elastic damping are plotted in Fig.10.13. The effects of elastic damping, in accordance with Eq.(3.15) must be added to these plots for **DDBD**.

(a) Sand   (b) Clay
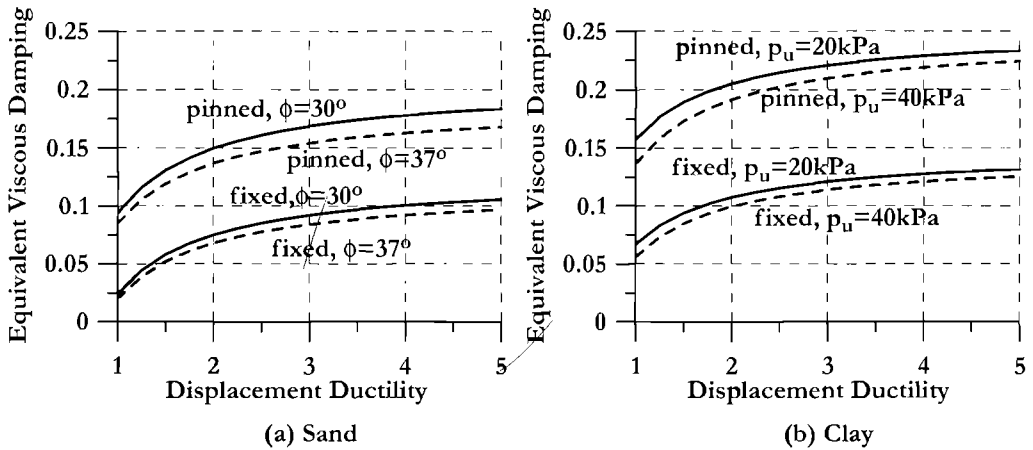
Fig.10.13   Hysteretic component of Equivalent Viscous Damping for Pile/Columns[S4]

Taking the recommendations of Table 3.2 for κ, the total effective damping for the eight cases represented in Fig.10.13 is as follows:

$$\text{sand, pinned head, } \phi = 30^0: \quad \xi_P = \xi_{el} \cdot \mu^{-0.313} + 0.094 + 0.112\left(\frac{\mu-1}{\mu}\right) \qquad (10.17a)$$

$$\text{sand, pinned head, } \phi = 37^0: \quad \xi_P = \xi_{el} \cdot \mu^{-0.313} + 0.085 + 0.104\left(\frac{\mu-1}{\mu}\right) \qquad (10.17b)$$

$$\text{sand, fixed head, } \phi = 30^0: \quad \xi_P = \xi_{el} \cdot \mu^{-0.313} + 0.024 + 0.102\left(\frac{\mu-1}{\mu}\right) \qquad (10.17c)$$

sand, fixed head, $\phi = 37°$: $\xi_P = \xi_{el} \cdot \mu^{-0.313} + 0.020 + 0.096\left(\dfrac{\mu-1}{\mu}\right)$ (10.17d)

clay, pinned head, 20kPa: $\xi_P = \xi_{el} \cdot \mu^{-0.313} + 0.158 + 0.094\left(\dfrac{\mu-1}{\mu}\right)$ (10.17e)

clay, pinned head, 40kPa: $\xi_P = \xi_{el} \cdot \mu^{-0.313} + 0.137 + 0.109\left(\dfrac{\mu-1}{\mu}\right)$ (10.17f)

clay, fixed head, 20kPa: $\xi_P = \xi_{el} \cdot \mu^{-0.313} + 0.067 + 0.081\left(\dfrac{\mu-1}{\mu}\right)$ (10.17g)

clay, fixed head, 40kPa: $\xi_P = \xi_{el} \cdot \mu^{-0.313} + 0.056 + 0.087\left(\dfrac{\mu-1}{\mu}\right)$ (10.17h)

The value of the elastic damping to be added in Eqs.(10.17) needs some careful consideration. Since foundation damping was directly modelled in the determination of the equivalent viscous damping values presented in Fig.10.13, and there is no interaction between structural and non-structural components (two of the three reasons for adding elastic damping to analyses (see Section 3.4.3(b)), only additional damping for the elastic range of structural response can be justified. Thus only a low value of elastic damping would be justified. We recommend 2-3%.

(d) System Damping: When all piers have the same characteristics in terms of height, strength and foundation conditions, and the abutments are free to move longitudinally with negligible friction, the system damping for longitudinal response will be the same as the member damping. However, when pier strength and or damping are not uniform along the bridge, and/or significant friction exists at the abutments, a weighted average of damping values will be needed. Since the displacements of all points during longitudinal response are essentially equal, the damping values are simply weighted by lateral shear force transmitted. That is:

$$\xi_{sys} = \frac{\displaystyle\sum_m V_i \xi_i}{\displaystyle\sum_m V_i}$$ (10.18)

where V_i and ξ_i are the shear force and equivalent viscous damping of the ith pier or abutment, and there are m supports (piers or abutments).

10.3.7 Design Example 10.3: Longitudinal Design of a Four Span Bridge

(a) Fixed-Head Design: The four-span bridge of Fig.10.14 has a superstructure depth of 2 m (6.56 ft) and monolithic connections between the piers and superstructure. Superstructure mass averages 190 kN/m (12.7 kip/ft) (including the weight of an internal
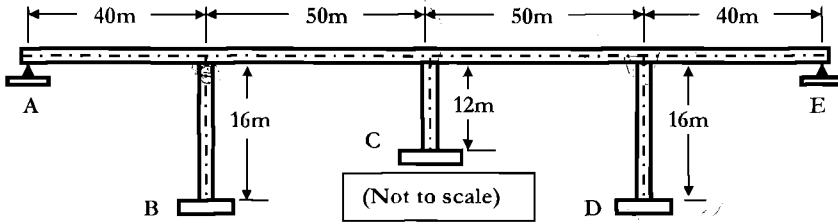
Fig.10.14 Bridge for Design Example 10.3

cap beam, but not the column weight). Initially we assume that the abutments are free to move longitudinally on frictionless bearings. The 2 m (6.56 ft) diameter single-column piers are based on the data for Design Example 10.1 (Section 10.3.3).

The design spectra, corresponding to a **PGA** of 0.6g are taken from ATC3[X2] for a medium ground condition, and are shown in Fig.10.15. Note that the displacement spectrum is not linear in this example, and there is no corner period.

(a) Acceleration Spectrum (5%)   (b) Displacement Spectra
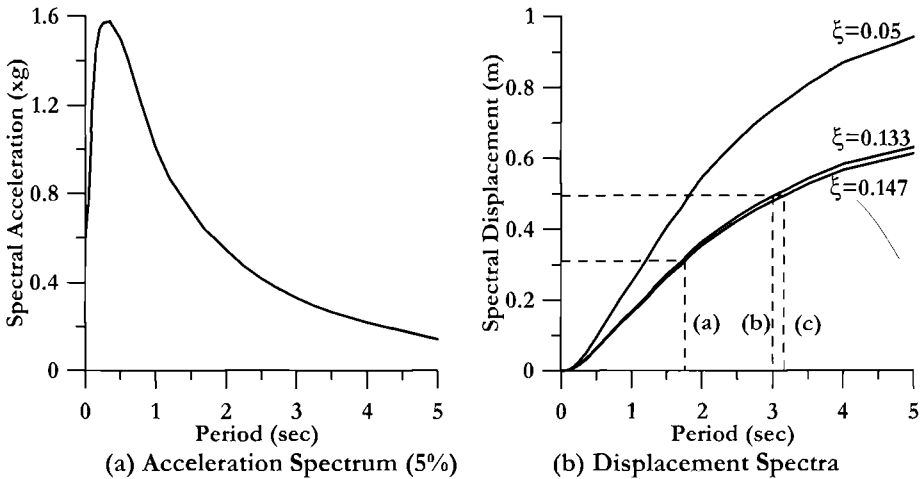
Fig 10.15   Design Spectra for Example 10.3

Solution: First we check that the column axial loads are compatible with the assumption of 10MN in Design Example 10.1.

Central Pier C: Using a tributary length of superstructure of 50m, and a self weight of $3.14m^2 \times 23.5kN/m^3 = 73.8kN/m$ the axial loads at top and bottom of the column are

        Column top: P =50×190 = 9,500kN   (2136kips)

        Column base: P =9500+12×73.8 = 10,400 kN   (2338kips)

Piers B and D: With a tributary superstructure length of 45m, the axial loads are

        Column top: P = 45×190 = 8550 kN   (1922kips)

Column base: P = 8550+16×73.8 =9700 kN   (2181kips)

These are all close enough to 10MN to justify the calculated value for depth of neutral axis of 0.48m (18.9in) used in Example 10.1

Design displacement: The displacement of the 12m central pier will govern. From Design Example 10.1 Δ_D = 0.326m (12.8in). The displacement capacity of piers B and D will exceed this, and hence do not need to be calculated.

Yield displacements: The yield displacement of pier C has already been calculated as 0.0712m. (2.8in)The yield displacement of piers B and D is

Piers B and D: $\Delta_y = \phi_y (H + 2L_{SP})^2 / 6$ =0.0026(16+2×0.407)²/6=0.123m (4.84in)

Pier C: Δ_y = 0.0712m (2.8in)

Displacement ductilities:

Piers B and D: μ_Δ = 0.326/0.123 = 2.65

Pier C: μ_Δ = 0.326/0.0712=4.58

Pier damping: From Eq.(3.17a):

Piers B and D: $\xi_{B,D} = 0.05 + 0.444\left(\dfrac{\mu-1}{\mu\pi}\right) = 0.05 + 0.444 \times \dfrac{1.65}{2.65\pi} = 0.138$

Pier C: $\xi_C = 0.05 + 0.444 \times \dfrac{3.58}{4.58\pi} = 0.160$

System damping: We chose to have the same flexural reinforcement ratio for all piers. As a consequence the flexural strength of all piers will be essentially the same, with small differences at top and bottom, as a consequence of differences in axial load, and also (smaller) differences between piers as a consequence of different levels of strain-hardening associated with different ductility demands. These can be resolved in the final design stage.

With equal moment capacities, the shears carried by the piers are in inverse proportion to their height. Hence V_C = 1.333V_A etc. From Eq.(10.18):

$$\xi_{sys} = \frac{\sum_m V_i \xi_i}{\sum_m V_i} = \frac{2 \times 1.0 \times 0.138 + 1 \times 1.333 \times 0.160}{2 + 1.333} = 0.147$$

Spectral reduction factor: From Eq.(2.8) the spectral reduction factor, to be applied to the 5% damped displacement spectrum is

$$R_\xi = \left(\frac{0.07}{0.02 + \xi_{sys}}\right)^{0.5} = \left(\frac{0.07}{0.02 + 0.147}\right)^{0.5} = 0.647$$

The displacement spectrum for the 14.7% damping is included in Fig.10.15(b).

Effective period: The effective period of response is found entering with a displacement of 0.326m, and intersecting the spectrum for ξ_{sys} =0.147, as shown by the dashed line, yielding T_e = 1.761 sec.

Effective mass: All of the superstructure mass will participate in the only longitudinal mode of significance. Reference [P4] recommends that 1/3 of the column mass be added to the mass lumped at the superstructure level. Hence the effective weight is

$$m_e.g = (190kN/m)\times180m + 0.333(12+2\times16)\times73.8kN/m = 35,300kN \quad (7936kips)$$

Effective stiffness: From Eq.(3.1):

$$K_e = \frac{4\pi^2 m_e}{T_e^2} = \frac{4\pi^2 \cdot 35.3}{9.805\times1.761^2} = 45.9 MN/m$$

Base shear force: From Eq.(3.2):

$$V_{Base} = K_e\Delta_D = 45.9\times0.326 = 14.95 MN \quad (3360kips)$$

This base shear is distributed to the columns in inverse proportion to their heights. Thus:

$$V_B = V_D = 14.95/3.33 = 4.49MN \rightarrow M_B = M_D = 4.49\times8 = 35.9MNm \;(318000kip.in)$$
$$V_C = 1.33\times14.95/3.33 = 5.97MN \rightarrow M_C = 5.97\times6 = 35.8MNm \;(317000kip.in)$$

P-Δ check: With bridge designs, the **P-Δ** moment should always be checked, in accordance with the recommendations of Section 3.6.3. From Eq.(3.45) the Stability Index is

$$\theta_\Delta = \frac{P\Delta_{max}}{M_D} = \frac{10\times0.326}{35.8} = 0.091$$

As this is less than 0.10, the recommendations of Section 3.6.3 indicate that P-Δeffects can be ignored.

Moment-curvature analysis indicates that with an axial load of 10MN, this moment can be provided, at a peak compression strain of 0.0136, by 91,200 mm^2 of flexural reinforcement (2.9%). The neutral axis depth, of 540mm is close to the assumed value of 480mm, though the hoop spacing may need to be reduced in the final design to provide the required design curvature. The required number of 40mm dia. bars is 72.6. This might be increased to 74 when the moment capacity of the longer columns is checked, because of their reduced axial load, and lower ductility demand.

(b) Pinned Connection to Superstructure: The design is repeated for a bridge where the piers and the superstructure are fixed against relative longitudinal displacement, but relative rotation is permitted. That is, the superstructure is supported on rotational pot-bearings. The information provided in Design Example 1(b) applies. Since the procedure is essentially identical to that of the fixed head design carried out above, only a summary of the results is provided.

Solution: Design displacement: From Design Example 10.1(b), Δ_D = 0.518m (20.4in)

Yield displacements: Piers B and D: Δ_y = 0.233m; Pier C: Δ_y = 0.133m
Displacement ductilities: Piers B and D: μ_Δ = 2.22; Pier C: μ_Δ = 3.89
Pier damping: Piers B and D: ξ_P = 0.133; Pier C: ξ_P = 0.155
System damping: ξ_{sys} = 0.133
Spectral reduction factor: R_ξ = 0.657
Effective period: The damped displacement spectrum for 13.3% damping is included in Fig.10.15(b). Entering with a design displacement of 0.518m, the effective period is found to be T_e = 3.0sec (follow dashed lines).

Effective stiffness: K_e = 15.8MN/m
Base shear force: V_{Base} = 8.18 MN. (1839 kips)
Column shears: Piers B and D: $V_{B,D}$ =2.46 MN; Pier C: V_C =3.27MN
Column base moments: M = 3.27×12=39.2MNm (347000kip.in)
Stability index: θ_Δ = 10×0.518/39.2 = 0.132

Since this exceeds 0.1, we add $0.5P\Delta$ = 0.5×10×0.518 = 2.6MNm to provide a total design moment of 41.8MNm. This is 17% higher than for the fixed connection case, requiring 114,000 mm² (177 in²) of flexural rebar, equivalent to a reinforcement ratio of 3.6%, which is at the upper limit of acceptable. This would require 92 bars 40mm dia. bars, which would need to be placed in two concentric rings to provide adequate spaces between bars. Again, reduced spacing of transverse reinforcement would be required to increase the ultimate compression strain, since the neutral axis depth will be larger than the 0.48m assumed, and hence the damage-control curvature will be less than assumed.

(c) Pinned Connection to Superstructure, Considering Abutment Friction: A third design is considered, where the ends of the bridge are supported at the abutments on **PTFE** sliding bearings. Although these have low friction under gradual movements such as creep and thermal movements, the friction factor under seismic velocities is much higher – typically about 8-12%, unless special lubrication is provided, and maintained. We assume 10% in this design. Hysteretic response of the sliders will be essentially elasto-plastic, with the elastic flexibility arising from displacements of the abutment. We assume that this is 25mm (1 in), though the actual value has little influence on the design.

The apparent ductility at the abutments will be μ_A = 0.518/0.025 = 20.7. From Eq.(3.17e):

$$\xi_{A,E} = 0.05 + 0.67\left(\frac{\mu-1}{\mu\pi}\right) = 0.05 + 0.67\frac{19.7}{20.7\pi} = 0.253$$

Axial load on bearings: The tributary length is 20m, hence P_A = P_E = 20×190 =3800 kN. The friction force is thus 0.1×3800 = 380 kN (85.4kips) at each abutment.

System damping: At this stage we do not know the exact relative lateral forces between the piers and abutment, but we conservatively assume that the total base shear remains constant at 8.18 MN, and hence the total shear carried by the three piers is 8.18 –

2×0.38 =7.42MN (1670kips). The approximate shears per pier are then $V_B = V_D = 2.23$MN, and $V_C = 2.97$MN. The system damping is thus:

$$\xi_{sys} = \frac{\sum_m V_i \xi_i}{\sum_m V_i} = \frac{2 \times 2.23 \times 0.133 + 2.97 \times 0.155 + 2 \times 0.38 \times 0.253}{8.18} = 0.152$$

This is essentially the same as for the fixed connection case.

Effective period: Again entering Fig.10.15(b) at a displacement of 0.518m, and reading the period from the intersection with the 0.147 damping curve (actually these are found by interpolation in a tabular form of Fig.10.15) the period is found to be $T_e = 3.16$sec.

Effective stiffness: We thus find: $K_e = 14.2$MN/m

Base shear force: $V_{Base} = 14.2 \times 0.518 = 7.36$MN (1655kips)

Pier shear forces: $V_{B,D} = (7.36 - 0.76)/3.33 = 1.98$MN (445kips)

$V_C = 2.63$MN (591kips)

Column base moment: $M = 31.6$MNm (280000kip.in)

A further iteration could be made to refine the damping, but is hardly warranted. Again the stability index for **P-Δ** effects exceeds 0.1, so we add 2.6MNm to provide a design moment of 34.2MNm (303,000kip.in). This is less than for the fixed connection detail, and can be provided by 85,000 mm² of reinforcement (2.7% reinforcement ratio).

It will be noted that the benefits in terms of structural efficiency in designing for a monolithic connection between pier and superstructure are comparatively minor (note that some reduction in the design moments for the fixed connection will be possible if abutment friction is considered, but the percentage reduction will be less than for the pinned case), and would need to be weighed against the possibly increased design moments for the superstructure resulting from resisting the pier-top moment, and increased complexity of the pier/superstructure joint detailing.

10.4 DESIGN PROCESS FOR TRANSVERSE RESPONSE

Transverse response of multi-span bridges is inherently more complex than longitudinal response. Consequently, the design process requires careful consideration. However, it will be shown in Section 10.4.6 that in many cases, transverse design requirements, though more complex, will be less critical than longitudinal design requirements for bridge piers.

The following special issues must be considered for transverse **DDBD**:

- Transverse design displacement profiles.
- Dual seismic load paths.
- Effective system damping.
- Degree of fixity to column top provided by superstructure rigidity.

Bridge transverse seismic design using **DDBD** procedures has been discussed in some detail in recent research papers (e.g. [A4, D3, P32]. The following sections draw on these earlier studies, extending and in some cases correcting the information provided.

10.4.1 Displacement Profiles

Displacement profiles for transverse response of bridges were briefly introduced in Section 3.5.2(c), where it was pointed out that the profile shape was strongly dependent on the degree of restraint provided at the abutments. This is further illustrated in Fig. 10.16, where six different situations are represented for continuous bridge superstructures (SS).

(a) Symm., Free at abuts.   (b) Asymm., Free at abuts.   (c) Symm., free at abuts.
   Rigid SS translation   Rigid SS translation+rotation   Flexible SS

(d) Symm,. Restrained at abuts. (e) Internal movement joint (f) Int. movement joint,
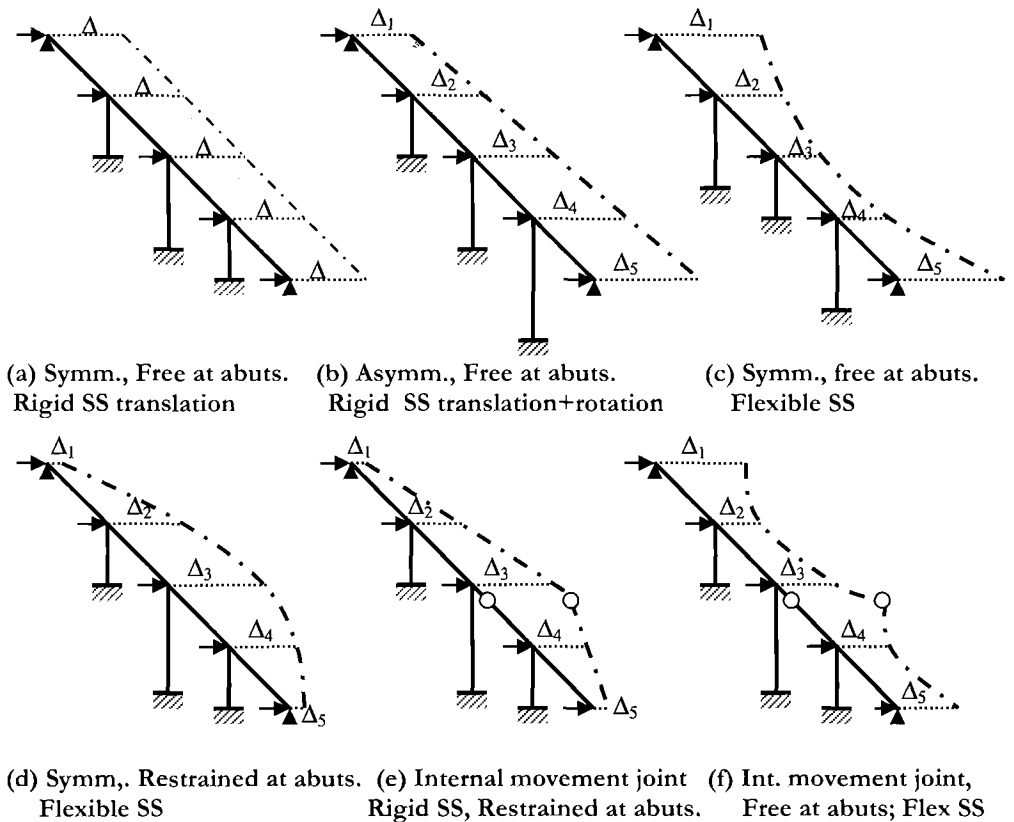   Flexible SS   Rigid SS, Restrained at abuts.   Free at abuts; Flex SS

Fig.10.16   Different Possible Transverse Displacement Profiles for Bridges

If the superstructure is constructed of simply-supported spans with rotational flexibility at the movement joints about the vertical axis, then it is reasonable to consider the design of each pier individually, based on the tributary superstructure mass and the pier

displacement capacity. Essentially the design becomes a series of individual **SDOF** designs, similar to that presented in Design Example 3.3 (Section 3.4.6).

With continuous superstructures, as illustrated in Fig.10.16, a major distinction will be whether or not the superstructure can be considered effectively rigid, when compared with the stiffness of the piers. If the superstructure is effectively rigid, then the displacement profiles are simplified, as illustrated in Figs.10.16(a), (b), and (e). The difference between these figures is that in Fig.10.16(a) the substructure is symmetric, and hence the displacement profile is characterized by rigid translation of Δ at all piers and abutments, while in Fig.10.16(b) the pier height are non-symmetric, and hence the superstructure displacement is a combination of rigid translation and rotation, with different displacements at each pier. In Fig.10.16(e) a superstructure movement joint close to the central pier means that the displacement profile is comprised of two rigid segments. Note that in Figs.10.16(a) and (b) the superstructure displacement at the abutments is considered to be unrestrained, and hence the design displacements will be governed by the displacement capacity of the piers. However, similar displacement profiles, though with smaller magnitude could also result if the abutments were partially restrained. In this case, it is likely that the displacement capacity of the abutment bearings or abutment structure would define the design displacement. The displacement profile of Fig.10.16(e) is based on the assumption of partially restrained abutments, but modification to consider free abutments is obvious.

Three cases with flexible superstructures are included in Fig.10.16. In Fig.10.16(c) the bridge is unrestrained at the abutments. Together with the short central pier this results in the displaced shape shown, with end displacements a maximum, and central displacement a minimum. The more common example of Fig.10.16(d) is laterally restrained at the abutments, and has a displacement shape that can be approximated by a sine or parabolic function. The end displacements at the abutments will depend on the support detail provided. If lateral shear keys are provided, the displacement will essentially correspond to that of the abutment structure, and in many cases can be assumed to be zero. The third example, in Fig.10.16(f) is unrestrained at the abutments, and has a flexible superstructure, and an internal movement joint close to the central pier. The displacement profile consists of two essentially parabolic segments meeting with an angle change at the internal movement joint. A further possibility, with flexible superstructure, internal movement joint and restraint at abutments is not shown, but will be intermediate between the profiles shown in Fig.10.16(d) and (e).

It will be apparent that it will not be possible to exactly define the displacement profile at the start of the design process, and hence some iteration will be required. This is discussed in some detail subsequently. If the shape of the profile (i.e. the inelastic first mode shape: see Section 3.5.1) can be reasonably approximated, then the magnitude of displacements at the piers and abutments can be identified by comparing the displacement capacities of the individual piers and abutments with the modal displacements, to determine which pier or abutment governs the design. The displacement profile is then given by Eq.(3.17), reproduced here for convenience as Eq.(10.19):

$$\Delta_i = \delta_i \cdot \left(\frac{\Delta_c}{\delta_c} \right) \tag{10.19}$$

where δ_i is the inelastic mode shape, and Δ_c and δ_c are the design displacement and modal value at the critical mass, c. The substitute **SDOF** structure design displacement is then given by Eq.(3.26), reproduced here as Eq.(10.20):

$$\Delta_d = \sum_{i=1}^{n} \left(m_i \Delta_i^2 \right) / \sum_{i=1}^{n} \left(m_i \Delta_i \right) \tag{10.20}$$

where m_i are the masses at the n mass locations, including the appropriate contribution of pier mass.

Some guidance as to when the superstructure may be considered to be rigid for purposes of determining the expected displacement profile is provided in [D3], where a **relative stiffness index, RS** relating the superstructure stiffness K_S to the sum of the pier stiffness ΣK_P is defined. The superstructure is assumed to be uncracked, while the pier stiffness is based on cracked-section stiffness. The superstructure stiffness is based on the assumption of pinned abutments and a uniformly distributed force calculated to give unit displacement at midspan, while the individual pier stiffness is calculated to produce unit displacement at the pier top. Thus, for a bridge with n piers, and assuming equal moduli of elasticity for superstructure and piers, the relative stiffness index is defined by

$$RS = \frac{K_S}{\sum_{i=1}^{n} K_P} = \frac{384 I_S}{5 L_S^3} \cdot \sum_{i=1}^{n} \frac{H_{Pi}^3}{C_{Pi} I_{Pi}} \tag{10.21}$$

where I_S and L_S are superstructure transverse moment of inertia and length respectively, and H_{Pi} and I_{Pi} are pier effective height and moment of inertia respectively. C_{Pi} is a coefficient dependent on the fixity provided at the pier top by the superstructure and is equal to 12 and 3 for fully fixed or free pier tops respectively. For a bridge with movement joints, the length L_S should be the distance between movement joints (also considering the abutments as movement joints).

It was found in [D3] that for bridges without restraint at abutments and with fixed pier tops, the superstructure could be considered effectively rigid if **RS>**0.6, though some variation was found depending on the distribution of pier heights along the bridge. For bridges with restraint at abutments it was difficult to define an effective stiffness index above which the displacement profile could be considered to be dominated by rigid body translation and rotation.

10.4.2   Dual Seismic Load Paths

The concept of dual seismic load paths was introduced in Section 1.3.7 where it was shown that for a bridge with lateral restraint at abutments some of the seismic inertia forces would be carried back by superstructure bending to the abutments, with the remainder being transmitted to the pier foundations by column bending. Since the superstructure would normally be required to respond elastically to all levels of seismic intensity, while the piers would normally be designed for ductile response, at least for Level 2 (damage control limit state) and Level 3 (collapse prevention) seismic intensities, the ratio of lateral force carried by the two load paths is expected to be a function of intensity, with the portion of lateral force carried by the superstructure increasing as intensity increases.

The superstructure lateral stiffness will normally be known at the start of the seismic design, but the pier effective stiffnesses will depend on the pier strengths and ductilities, and hence will not initially be known. This again implies that an iterative design approach will be needed, as outlined subsequently in Section 10.4.5. Note that the possibility of cracking of the superstructure under transverse seismic response will have to be carefully evaluated when determining the appropriate value for superstructure stiffness.

10.4.3   System Damping

Determination of the effective system damping to be used in the **SDOF** design model also requires special attention. Different piers may carry different shear forces, have different design displacement ductility demands (and hence different equivalent viscous damping levels) and be subjected to different displacements. The inertia force carried by the superstructure will normally have low associated damping, but any displacement of the abutment structure may have high associated damping. The generalized effective damping approach defined by Eq.(3.37), which involves weighting the individual damping components by the work done applies. This equation is reproduced here as Eq.(10.22) for convenience:

$$\xi_e = \sum_{i=1}^{n} \left(V_i \Delta_i \xi_i\right) / \sum_{i=1}^{n} \left(V_i \Delta_i\right) \tag{10.22}$$

where there are **n** different structural elements contributing to the seismic resistance.

This is illustrated with respect to Fig.10.17 where a typical four-span bridge with continuous superstructure responds transversely to seismic excitation. It is assumed that the displacement shape has been established, either as an initial estimate, or as the final profile following the iterative procedure described subsequently in Section 10.4.5. It is also assumed that the piers are comprised of single columns of circular section, with diameter D constant for the three piers.

Lateral inertia forces F_1 to F_5 are applied to lumped masses concentrated at the abutments and the pier tops, as discussed in Section 4.9.2(e)(iii). For initial stages of the
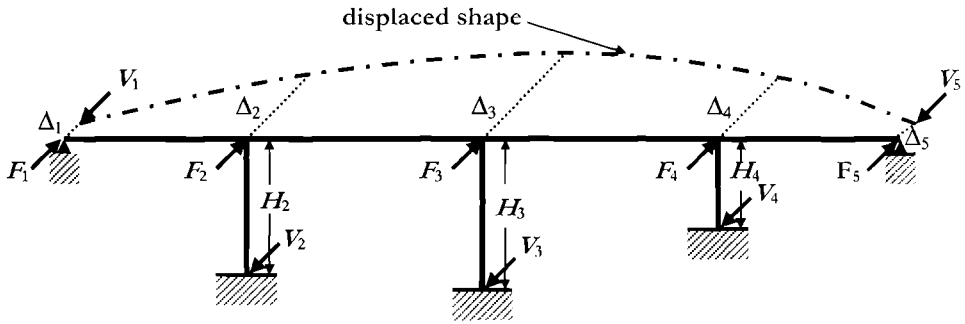
Fig.10.17 Components Contributing to Damping under Transverse Response

design it will be the relative proportions of the inertia forces, rather than the actual magnitudes that are assumed.

Reactions induced at reaction points (abutments, and pier bases) are V_1 to V_5, as shown in Fig.10.17. If we assume that the columns have the same vertical reinforcement ratios, and hence equal moment capacity, then provided all piers yield at the design seismic intensity, and pier mass is small enough such that self-weight inertia forces can be neglected, the pier shears V_2, V_3 and V_4 will be in inverse proportion to height H_i. We note that for equilibrium $\Sigma V_i = \Sigma F_i$. We finally assume that the fraction of total lateral inertia force carried back to the abutments by superstructure bending is x, that is:

$$V_1 + V_5 = x \cdot \sum_{i=1}^{5} F_i \tag{10.23}$$

and the pier shear forces are

$$V_i = (1-x) \cdot \sum_{i=1}^{5} F_i \cdot \left(\frac{1}{H_i} / \sum_{i=2}^{4} \frac{1}{H_i} \right) \tag{10.24}$$

The pier yield displacements are

$$\Delta_{yi} = C_1 \cdot \phi_y \cdot H_i^2 \tag{10.25}$$

where ϕ_y is the yield curvature, given by Eq.(4.57), H_i is the effective column height including strain penetration effects, and C_1 is the coefficient dependent on end fixity conditions ($C_1 = 1/3$ and $1/6$ for vertical cantilevers and columns fully fixed at base and top respectively; refer to Section 10.3.1(b) for other end conditions).

The displacement ductility demands for the three piers are given by

$$\mu_i = \Delta_i / \Delta_{yi} \tag{10.26}$$

and hence the pier damping values ξ_i can be found from Eq.(3.17).

If the superstructure lateral displacements at the abutments are small compared to the displacements at the piers, then it can reasonably be assumed that the superstructure damping is 5%, and the superstructure displacement is equal to the system displacement, Δ_d given by Eq.(10.20). The equivalent system damping is thus found substituting into Eq.(10.22) as

$$\xi_e = \frac{x\Delta_d \times 0.05 + (1-x)\left(\sum_{i=2}^{4}\frac{1}{H_i}\cdot\Delta_i\xi_i\right)/\sum_{i=2}^{4}\frac{1}{H_i}}{x\Delta_d + (1-x)\left(\sum_{i=2}^{4}\frac{1}{H_i}\cdot\Delta_i\right)/\sum_{i=2}^{4}\frac{1}{H_i}} \qquad (10.27a)$$

However, if the bridge displacements at the abutments are significant, due either to support on flexible bearings or to lateral displacements of the abutment structure itself, then the components of damping associated with the superstructure flexure and end displacements should be separately considered. A lower value of damping (say 2%) should be considered for the superstructure, and a higher value adopted for the end displacements. Thus:

$$\xi_e = \frac{x(\Delta_d - \Delta_a)\xi_{ss} + x\Delta_a\xi_a + (1-x)\left(\sum_{i=2}^{4}\frac{1}{H_i}\cdot\Delta_i\xi_i\right)/\sum_{i=2}^{4}\frac{1}{H_i}}{x(\Delta_d - \Delta_a) + x\Delta_a + (1-x)\left(\sum_{i=2}^{4}\frac{1}{H_i}\cdot\Delta_i\right)/\sum_{i=2}^{4}\frac{1}{H_i}} \qquad (10.27b)$$

where ξ_{ss} and ξ_a are the damping values assigned to the superstructure and abutments respectively, and Δ_a (=0.5(Δ_1+Δ_5) in Fig.10.17) is the average displacement of the bridge ends. Generalization of Eq.(10.27) to bridges with different numbers of spans is obvious.

10.4.4 Design Example 10.4: Damping for the Bridge of Fig.10.17

The procedure outlined above is illustrated by putting numeric values to the bridge of Fig.10.17. Span lengths are 40m, 50m, 50m, 40m (131ft, 174ft, 174 ft, 131ft), and the effective bridge weight, including contributions from bridge piers and end diaphragms is 200kN/m (13.7 kip/ft). Table 10.1 includes the effective weights, W_i, at the ends and pier tops. The cantilever columns at piers **2, 3** and **4** each have a diameter of 2.4m (7.87 ft) and have effective heights to the centre of the superstructure, including strain penetration at the column bases of 10m, 12m, and 8m respectively. The specified yield strength of the steel reinforcement is f_y = 400MPa (58 ksi) and hence, in accordance with the recommendations of Section 4.2.6, the design strength is 440MPa, and the yield strain is ε_y = 0.0022.

The design profile is initially estimated as indicated in Table 10.1 (Δ_i) based on a maximum drift of 0.035 at the central pier. Note that an end displacement of 50mm (2in)

is assessed as the maximum acceptable abutment displacements. The strength of the abutments will be based on the results of the design. Based on experience it is initially assumed that 40% of the inertia force will be carried back to the abutments by superstructure flexure. From Eq.(10.20) the design displacement is found as

$$\Delta_d = \sum_{i=1}^{n}\left(m_i\Delta_i^2\right)/\sum_{i=1}^{n}\left(m_i\Delta_i\right) = 3246/9690 = 0.335m \qquad (13.2\text{in})$$

Table 10.1 Calculations for Design Example 10.4 (1m=39.4in, 1kN=0.225kips)

Support	Height (m)	Weight (kN)	Δ_i (m)	$W_i\Delta_i$	$W_i\Delta_i^2$	Δ_{yi} (m)	μ_i	ξ_i
Abut 1		4000	0.05	200	10			
Pier 2	10	9000	0.30	2700	810	0.0687	4.37	0.159
Pier 3	12	10000	0.42	4200	176.4	0.0989	4.25	0.158
Pier 4	8	9000	0.27	2430	656.1	0.0439	6.14	0.168
Abut 5		4000	0.04	160	6.4			
			Sum =	9690	3246			

Note that seismic weights, rather than masses have been used in the above calculation.

Yield displacements, based on $\phi_y = 2.25\varepsilon_y/D = 2.25\times0.0022/2.4 = 0.00206/\text{m}$ (from Eq.4.57a) are calculated from Eq.(10.25) with $C = 1/3$, and are listed in Table 10.1 for the three piers. The displacement ductility demands, μ_i, from Eq.(10.26) and the pier damping values (from Eq.(3.17a)) are also listed in the table.

It is assessed that the displacements of the abutments are sufficiently small to allow the superstructure and abutment damping to be lumped together and estimated at 5%. Pier flexural reinforcement will be the same for the three piers, and hence the system damping can be estimated directly from Eq.(10.27a):

$$\xi_e = \frac{x\Delta_d \times 0.05 + (1-x)\left(\sum_{i=2}^{4}\dfrac{1}{H_i}\cdot\Delta_i\xi_i\right)/\sum_{i=2}^{4}\dfrac{1}{H_i}}{x\Delta_d + (1-x)\left(\sum_{i=2}^{4}\dfrac{1}{H_i}\cdot\Delta_i\right)/\sum_{i=2}^{4}\dfrac{1}{H_i}}$$

$$= \frac{0.4\times0.335\times0.05 + 0.6\left(\dfrac{0.3\times0.159}{10} + \dfrac{0.42\times0.158}{12} + \dfrac{0.27\times0.168}{8}\right)/\left(\dfrac{1}{10} + \dfrac{1}{12} + \dfrac{1}{8}\right)}{0.4\times0.335 + 0.6\left(\dfrac{0.3}{10} + \dfrac{0.42}{12} + \dfrac{0.27}{8}\right)/\left(\dfrac{1}{10} + \dfrac{1}{12} + \dfrac{1}{8}\right)}$$

$$= 0.116$$

10.4.5   Degree of Fixity at Column Top

Four different pier-top conditions are illustrated in Fig.10.18. If the pier consists of two or more columns (Fig.10.18(a)) it can be considered fully fixed at the top under transverse response, with equal moments at top and bottom of the columns, as shown to the right of the figure. Although the pier geometry of Fig.10.18(a) is based on an integral cap beam, the same conclusion applies for multi-column bents with separate cap beams supporting the superstructure via bearings.
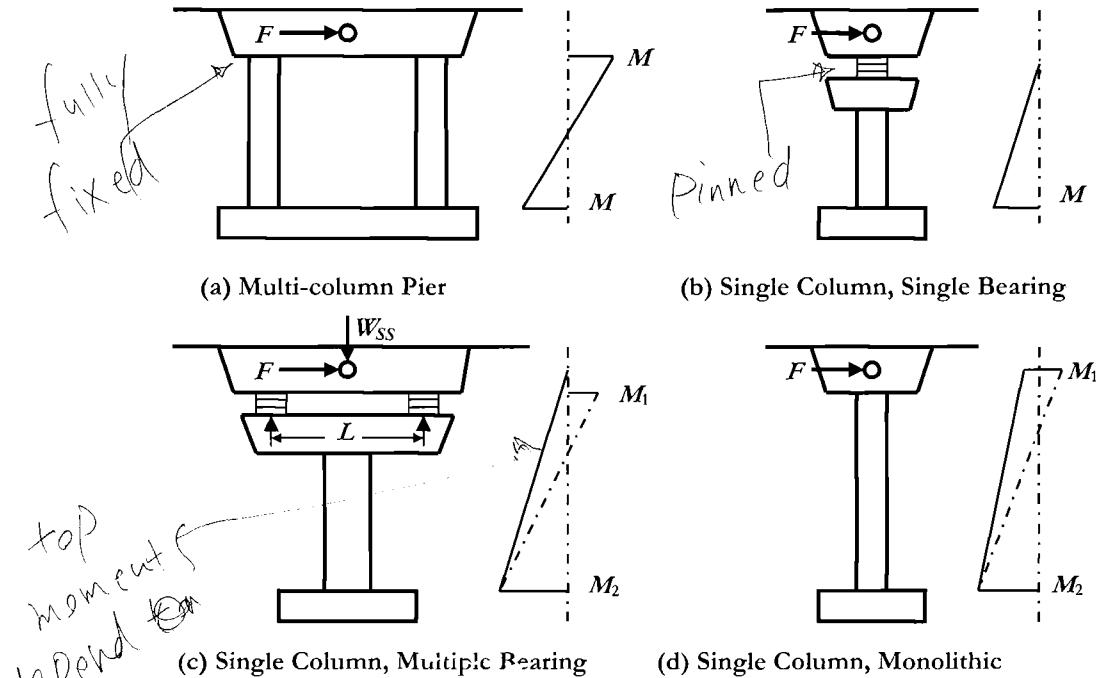

(a) Multi-column Pier   (b) Single Column, Single Bearing

(c) Single Column, Multiple Bearing   (d) Single Column, Monolithic

Fig.10.18   Transverse Response of Bridge Piers

The single-column bent of Fig.10.18(b) supports the superstructure on a single bearing with rotational freedom. Clearly for the bridge to be stable under transverse response the superstructure must be restrained against rotation about the bridge axis. This restraint would normally be provided at the abutments, and the superstructure torsional stiffness would have to be high – typically a closed box-girder section would be required. If these criteria are met the bridge acts as a true vertical cantilever under transverse response with the vertical distribution of bending moments as shown in Fig.10.18(b).

Although the pier illustrated in Fig.10.18(c) has a single column, the superstructure is supported on two or more bearings. Under transverse response the axial force transmitted through the bearings changes as a consequence of the inertia force being applied at a height above the bearings. This results in a moment M_1 being applied at the

height of the bearings, which could be of the same, or of opposite sign to the moment at the column base. If the superstructure is rotationally flexible, then the transverse response is that of a simple vertical cantilever, with the point of load application at the centre of lateral force, as shown by the solid line in the moment pattern to the right of the figure. If the superstructure is rotationally stiff about the longitudinal axis, then an incompatibility will develop between the rotation of the pier cap and the superstructure, which will tend to transfer the gravity load to the left bearing, for the direction of loading force shown in the figure. Assuming a lateral force F, and a distance L between the outer bearings, the maximum moment at the height of the centres of the bearings will be $M_1 = W_{SS}L/2$, where W_{SS} is the superstructure weight supported on the pier.

Finally, in Fig.10.18(d), a single-column bent with monolithic connection to the superstructure is shown. Although it would appear that behaviour would be that of a simple cantilever, moments of either positive or negative sign could be developed at the centre of mass. If the superstructure is torsionally stiff, and is restrained against uplift at the abutments, then moment reversal may develop over the height of the pier, as suggested by the dashed line in the moment pattern. On the other hand, if the super-structure is flexible, but has considerable width, as will often be the case, then torsional mass inertia will mean that moments of either sign could be developed at the height of the centre of mass, since the pier must be considered as a two-mode system. In the first case (torsionally stiff superstructure), the moment reversal should be directly considered in the **DDBD** process. With the second case, the moment may be considered to be zero at the pier top for the **DDBD** procedure, but the possible influence of the higher modes must be considered when determining the maximum feasible shear force in the column during capacity-design checks.

It is important to correctly model the expected moment pattern in the piers during the design process, as it will affect the yield displacement (and hence the displacement ductility demand), and the plastic hinge length (and hence the displacement capacity corresponding to a given limit state).

10.4.6 Design Procedure

As discussed earlier, an iterative design procedure will be necessary in many cases, incorporating two initial assumptions: the fraction of load carried by superstructure bending back to the abutments, and the displacement profile. The procedure follows the following steps, which for convenience are related to the example of Fig.10.17:

1. Estimate the fraction of lateral force, x, carried by the superstructure bending load path. Generally this will be based on experience. In the absence of guidance, assume $x = 0.5$ for restraint at abutments, and $x = 0$ for unrestrained bridge ends.
2. Estimate the initial displacement profile. This will involve choosing a displacement shape (inelastic mode shape) and determining the limit-state displacement capacities of the piers. The displacement profile is thus given by

Eq.(10.19). A parabolic or sine-based mode shape may be assumed for the initial iteration.

3. Determine the **SDOF** system displacement from Eq.(10.20).

4. Determine the effective mass from Eq.(3.33), including the appropriate contribution from pier mass (typically 1/3rd).

5. Determine the yield displacements of all piers (Eq.(10.1)), and hence their displacement ductility demands (Eq.(10.26)), and equivalent viscous damping. Note that it is possible that some piers will respond elastically, in which case the pier damping should be taken as $\xi = 0.05$.

6. Determine the ratios of shear force carried by the piers. If it is assumed that all piers have equal flexural reinforcement, and that all piers yield, the shears will be approximately in proportion to the inverse of the pier height. For the example of Fig.(10.17), Eq.(10.24) applies. If any of the piers are expected to remain elastic, at less than the yield capacity, then the proportion of force carried by that pier should be reduced from $1/H_i$ to μ_i/H_i where $\mu_i < 1$. The proportion carried by yielding piers remains unchanged.

7. Determine system damping, from Eq.(10.22), treating superstructure damping as recommended in Section 10.4.3.

8. Determine effective period, effective stiffness and total base shear V_{Base} from the design spectrum, Eq.(3.1) and Eq.(3.2) respectively, in the usual manner.

9. Distribute base shear as forces to inertia mass locations using Eq.(3.41), reproduced here for convenience as Eq.(10.28):

$$F_i = V_{Base}(m_i \Delta_i) / \sum (m_i \Delta_i)$$ (10.28)

10. Estimate the effective stiffness for each abutment and pier for the structural analysis model. This will require an estimate of the shears carried by piers and abutments based on the assumption for x. For the example of Fig.10.17, Eqs.(10.23) and (10.24) apply, where $\Sigma F_i = V_{Base}$. Since the displacement of each pier or abutment, Δ_i is known from Step 2, and the shear V_i is known from this step, the effective stiffness of each pier or abutment is known from $K_i = V_i/\Delta_i$. The superstructure translational and torsional stiffness will also be known, and remain constant throughout the analysis iterations.

11. Analyse the structure under the lateral forces F_i to estimate the displacement of the critical pier or abutment.

12. The displacement of the critical pier or abutment is compared with the limit state displacement. If the analysis indicates that the displacement of the critical pier exceeds the design limit, then the assumption for x, the fraction of total inertia force carried by superstructure bending is too high. More force needs to be allocated to the piers, which will increase their effective stiffness, and hence the total system effective stiffness. The displacements will thus be reduced. If the displacement is less than the design limit, then x is too low. Revise the estimate

for *x* upwards. This process will result in an increase or decrease in the shears carried by the individual piers (see Eq.(10.24)), and hence a change in the pier stiffnesses. Iterate, revising the value for *x* until the displacement of the critical pier or abutment from analysis equals the design value. If the abutment displacement differs from the design assumption, then the abutment stiffness can be adjusted to improve agreement. This will have little effect on pier displacements. However, the influence of higher modes on abutment forces, discussed in Section 10.5.2(b) needs to be considered.

13. The value of *x*, and the displacement profile resulting from Step 12 are now used as new estimates for Steps 1 and 2 above, and the procedure iterates through Steps 3 to 12, until convergence for *x*, and for the design profile is achieved.

The procedure described above generally converges rapidly. It can also be programmed with Matlab, Mathcad or Excel to proceed through the iterations automatically (see [A4 or D3] for example).

It should be noted that in some cases it will be found that even with *x* = 1.0 the displacement of the critical pier will be less than the design limit. This means that the stiffness of the superstructure is such that it dominates the response. Typically this occurs with short bridges of just a few spans. In such cases, the pier strength will be based on gravity load considerations. Ductile detailing may still be necessary, however, and an analysis using the known stiffnesses of superstructure and piers should be carried out to determine the expected displacements of the piers. A reduced level of transverse reinforcement may then be provided to ensure that the reduced displacement demand is provided, using a procedure similar to that adopted in Design Example 4.1 (Section 4.5.1).

10.4.7 Relative Importance of Transverse and Longitudinal Response.

It will be appreciated from the above discussion that determination of the correct design solution for transverse response is considerably more onerous than for longitudinal design. In many cases, however, it will not be necessary to carry out the transverse design, as it will be obvious that longitudinal design is more critical. This will particularly be the case when the bridge is free at the abutments to move longitudinally, but is restrained laterally, and when the fixity of column to superstructure is the same for both longitudinal and transverse response. That is, the connection can be considered either fully fixity or fully pinned for both longitudinal and transverse response. A further proviso for the longitudinal response to govern is that the pier has omni-directional strength and stiffness (i.e. either circular or square cross section).

To confirm the validity of the above statement, a series of four-span continuous bridges with three different pier height configurations, as shown in Fig.10.19(b), were designed for both longitudinal and transverse response. The piers had a circular section, and the heights of the piers were either equal, or varied in the ratio of 1:2, as shown. The critical pier (always the shorter one) was separately designed to achieve a displacement

ductility of $\mu = 4$ under both longitudinal and transverse response, and the resulting required design shear forces for this critical pier compared. Under longitudinal response it was assumed that end bearings had low friction and their contribution to seismic resistance could be ignored. The design displacement was dictated by the displacement capacity of the critical (short) pier or piers.
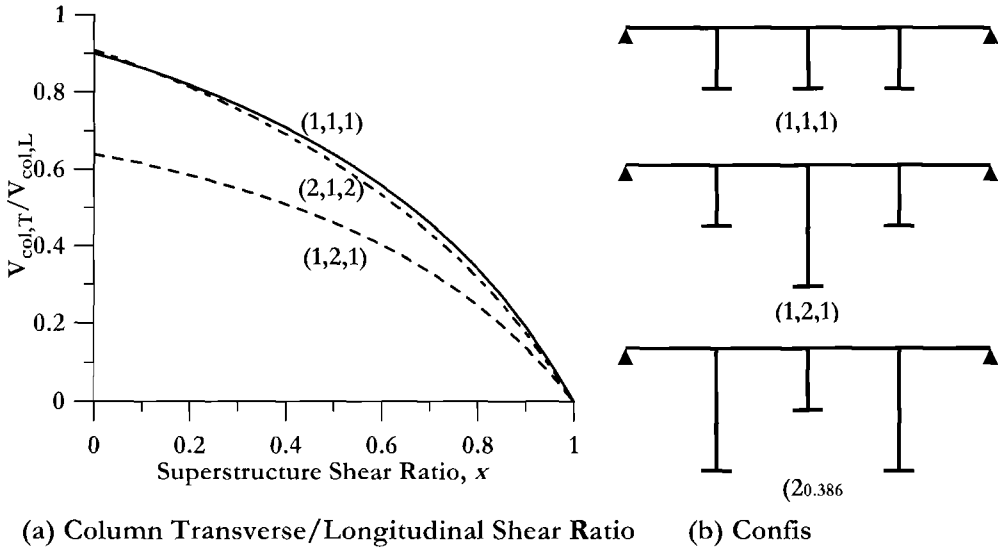

(a) Column Transverse/Longitudinal Shear Ratio   (b) Confis

Fig.10.19   Transverse/Longitudinal Design Shear Force Ratio for Critical Column of Four-Span Bridges

Under transverse design, the bridge ends were considered to be fully restrained (i.e. zero lateral displacement), with different fractions, x, of the total lateral inertia force carried by superstructure bending back to the abutments. For simplicity, a simple parabolic displacement shape was adopted for transverse response, anchored to the limit displacement corresponding to $\mu = 4$ for the critical pier. Thus for the 1,1,1 and the 2,1,2 configurations (see Fig.10.19(b)), the displacement of the central pier governed, while for the 1,2,1 configuration, the side piers governed. Note that the parabolic shape assumed will not be exact, but will have little influence on the results.

Results of the analyses are shown in Fig.10.19(a), which plots the transverse/longitudinal ratio of the required design shear force for the critical pier against x, the fraction of total inertia force carried by superstructure bending, for the three bridge configurations. In all cases the transverse/longitudinal design shear force ratio is less than 1.0, even when no shear is carried by the superstructure. In fact, this is a small error induced as a result of the assumed parabolic displacement shape. If no shear is carried by the superstructure, it will not influence the displaced shape, and hence the parabolic

shape will be inappropriate. The conclusion, that critical transverse design shear force will be less than the longitudinal shear force, is still, however, valid, since in this case the superstructure can be considered totally flexible in the transverse direction, and each pier will support its tributary weight of superstructure. It can readily be shown that this implies lower tributary mass for the critical pier than under longitudinal response.

It is of interest that the 1,2,1 configuration results in significantly lower transverse design force than the other two configurations. This is because the displacement profile for this case is governed by the side piers, with the result that the central displacement, and hence the design system **SDOF** displacement is larger than for the other two configurations. This translates into a lower design base shear force for the **SDOF** system (see Eq.(3.24), e.g.).

10.4.8   Design Example 10.5: Transverse Design of a Four-Span Bridge

The four-span bridge designed for longitudinal response in Design Example 10.3 and shown in Fig.10.14 is now designed for transverse response. As noted in Section 10.3.6 the bridge is supported on single-column piers, and we assume the support condition corresponds to that depicted in Fig.10.18(c). The superstructure is considered to be torsionally flexible, and hence the effective height is taken to the centre of the superstructure. This adds 1.0m (3.28ft) to the column heights, which are thus 17m (55.8ft) for Columns B and D, and 13m (42.6ft) for Column C for transverse design. Superstructure transverse moment of inertia is 40m⁴ (4630 ft⁴).

The bridge is restrained by shear keys at the ends, and the abutment structure is required to remain essentially elastic under the Level 2 earthquake defined by Fig.10.15. An abutment lateral displacement of 40mm (1.6in) is permitted. As this is small compared with the pier displacements, the superstructure and abutment damping levels are not separated, and a value of $\xi = 0.05$ is assumed for the component of lateral force carried by the superstructure.

The solution below follows the steps outlined in Section 10.4.5

Step 1 Estimate fraction of lateral force carried by superstructure bending: A value of $x = 0.5$ is selected as an initial guess for the fraction of lateral inertia force transmitted to the abutments.

Step 2 Estimate the initial displacement profile: The initial displacement profile is assumed to be parabolic with the displacement at piers B and D equal to 70% of the displacement of pier C. The magnitude of the displacement profile will be determined by the critical abutment or pier displacement. As described in the problem statement, the permitted displacement for abutments A and E is 40mm. The permitted displacements for piers B, C, and D will be a function of the strain-based damage criteria. From Example 10.1, the section yield curvature is given by:

$$\phi_y = 2.25\varepsilon_y / D = 2.25(462/200,000)/2.0 = 0.0026/m$$

while the limit state curvature, which is controlled by the concrete compression strain,

was given by:

$$\phi_{ls,c} = \varepsilon_{c,ls} / c = 0.0136/0.48 = 0.0283/\text{m}$$

With a strain penetration length given by:

$$L_{SP} = 0.022 f_{ye} d_{bl} = 0.022 \times 462 \times 40 = 407 \text{ mm (16.0 in)},$$

the yield displacement for piers B and D is given by:

$$\Delta_y = \phi_y \left(H + L_{SP}\right)^2 / 3 = 0.0026 \times 17.407^2/3 = 0.263\text{m (10.4 in)}$$

while for pier C, where the height is 13m, the yield displacement is 0.156m (6.1in). From Eq.(10.11), the plastic hinge length for piers B and D is:

$$L_P = kL_C + L_{SP} \geq 2L_{SP} = 0.07 \times 17 + 0.407 = 1.597\text{m (62.9 in)}$$

Similarly, for pier C, the plastic hinge length is 1.317m (51.9 in). The strain-based displacements for piers B, and D are then obtained from Eq. (10.12):

$$\Delta_D = \Delta_y + \left(\phi_{ls} - \phi_y\right)L_P H = 0.263 + (0.0283 - 0.0026) \times 1.597 \times 17 = 0.961 \text{ m (37.9 in)}$$

while for pier C, the strain-based limit displacement is 0.596m (23.5 in). For this example, it is clear that pier C will control the displacement profile as the initial estimate of displacements of piers B and D are 70% of 0.596m = 0.417m, which is less than the strain-based displacements for those piers. While for this example it was not necessary to determine the strain-based displacements for piers B and D as they clearly could not govern the magnitude of the displacement profile, it is likely that in some cases, it will not be immediately evident which pier will govern the profile. For example, if the central pier had been much taller than the two side piers, the side piers would likely govern the overall magnitude of the displacement profile. The initial displacement profile for this example is thus as follows: $\Delta_A = \Delta_E = 0.04\text{m}$; $\Delta_B = \Delta_D = 0.417\text{m}$; $\Delta_C = 0.596\text{m}$.

Step 3 Determine the SDOF system displacement: In order to determine the SDOF system displacement from Eq. (10.20), the inertia weight for each abutment and pier must first be defined. The inertia weights are assumed to include the tributary superstructure weight (190kN/m) and 1/3 of the weight of each pier. For abutments A and E, the inertia weight is $m_A = m_E = 20\text{m} \times 190\text{kN/m} = 3800\text{kN}$. For piers B and D, the inertia weight is $m_B = m_D = 45\text{m} \times 190\text{kN/m} + 16/3 \times 73.8\text{kN/m} = 8944\text{kN}$. For pier C, the inertia weight is $m_C = 50\text{m} \times 190\text{kN/m} + 12/3 \times 73.8\text{kN/m} = 9795\text{kN}$. The **SDOF** system displacement from Eq. (10.20) is then:

$$\Delta_d = \frac{2 \times 3800 \times 0.04^2 + 2 \times 8944 \times 0.417^2 + 9795 \times 0.596^2}{2 \times 3800 \times 0.04 + 2 \times 8944 \times 0.417 + 9795 \times 0.596} = 0.485\,\text{m (19.1 in)}$$

Step 4 Determine effective mass: From Eq. (3.33), the effective mass is:

$$m_e = \frac{2 \times 3800 \times 0.04 + 2 \times 8944 \times 0.417 + 9795 \times 0.596}{0.485 \times 9.81} = 2856 \text{ tonnes (3149kips)}$$

Step 5 Determine pier displacement ductility, and equivalent viscous damping: Pier yield and target displacements were calculated in Step 2. Therefore, displacement

ductilities for the three piers are

$$\mu_\Delta = \frac{0.417}{0.263} = 1.59 \text{ (Piers B and D)} \qquad \mu_\Delta = \frac{0.596}{0.156} = 3.82 \text{ (Pier C)}$$

The equivalent viscous damping for the Piers follows from Eq. (3.17a):

$$\xi = 0.05 + 0.444 \times \left[\frac{1.59 - 1}{1.59\pi}\right] = 0.102 \text{ for Piers B and D}$$

$$\xi = 0.05 + 0.444 \times \left[\frac{3.82 - 1}{3.82\pi}\right] = 0.154 \text{ for Pier C}$$

Step 6 Determine the ratios of shear force carried by the piers: From Eq.(10.24), the shear force the piers is given by:

$$V = (1 - 0.5) \times \frac{\dfrac{1}{17}}{2 \times \dfrac{1}{17} + \dfrac{1}{13}} \times \sum_{i=1}^{5} F_i = 0.151 \times \sum_{i=1}^{5} F_i \qquad \text{for Piers B and D}$$

$$V = 0.198 \times \sum_{i-1}^{5} F_i \qquad\qquad\qquad\qquad \text{for Pier C}$$

Step 7 Determine system damping: Since the superstructure and abutment damping are not treated separately, the system damping follows from Eq. (10.27a):

$$\xi_e = \frac{0.5 \times 0.486 \times 0.05 + 0.5\left(\dfrac{2 \times 0.417 \times 0.102}{17} + \dfrac{0.596 \times 0.154}{13}\right)\bigg/\left(\dfrac{2}{17} + \dfrac{1}{13}\right)}{0.5 \times 0.486 + 0.5\left(\dfrac{2 \times 0.417}{17} + \dfrac{0.596}{13}\right)\bigg/\left(\dfrac{2}{17} + \dfrac{1}{13}\right)} = 0.089$$

Step 8 Determine effective period, stiffness, and design base shear: From Fig. (10.15b), entering with the target system displacement of 0.485m and interpolating for a damping of 0.089, the effective period is estimated as $T_e = 2.31$ seconds. The effective stiffness, K_e, is obtained from Eq. (3.1) as shown below.

$$K_e = \frac{4\pi^2 \times 2856}{2.31^2} = 21183 \text{ kN/m}$$

The base shear, from Eq. (3.2) is then

$$V_{Base} = 21183 \times 0.485 = 10282 \text{ kN} \quad (2312 \text{ kips})$$

Step 9 Distribute base shear force to inertia mass locations: Utilizing Eq. (10.28), the base shear force to each of the five inertia mass locations is obtained. For abutments A and E, the applied lateral force is:

$$F = 10282 \times \frac{3800 \times 0.04}{2 \times 3800 \times 0.04 + 2 \times 8944 \times 0.417 + 9795 \times 0.596} = 115 \, \text{kN} \quad (25.9 \text{kips})$$

Similarly, the forces applied at the tops of Piers B and D are each 2820 kN (634 kips), while at the top of Pier C it is 4413 kN (992 kips).

Step 10 Estimate abutment and pier effective stiffness: In step 9, the forces applied to each inertia mass location were determined. In step 11, these forces will be applied to a structural analysis model. In this step, the properties for the analysis model will be obtained. In order to accomplish this, the shear forces carried by each abutment and pier must be estimated. From Eq. (10.23):

$$V_A + V_E = 0.5 \times 10282 = 5142 \, \text{kN} \, (1156 \text{kips})$$

Therefore, the shear force in each abutment may be estimated as 5142/2 = 2571 kN. From Eq. (10.24), the shear force in Piers B and D is given by

$$V = (1 - 0.5) \times 10282 \times \frac{\dfrac{1}{17}}{2 \times \dfrac{1}{17} + \dfrac{1}{13}} = 1554 \, \text{kN} \quad (349 \text{kips})$$

Similarly, for Pier C, the force is estimated as 2033 kN (457kips). The effective stiffness of each abutment and pier can then be obtained by dividing the shear force in each member by the displacement of each member from Step 2. For abutments A and E, the effective stiffness for the analytical model is 2571/0.04 = 64300 kN/m. For Piers B and D, the effective stiffness is 1554/0.417 = 3730 kN/m, while for Pier C, the effective stiffness is 2033/0.596 = 3410 kN/m.

Step 11 Analyze the structure under the applied lateral force vector: A structural analysis model incorporating the data from Step 10 for abutment and pier stiffness is developed. Applying the lateral force vector from Step 9 results in the following abutment and Pier displacements: Abutments A and E achieve a displacement of 0.0426m, Piers B and D achieve a displacement of 0.3826m, and Pier C achieves a displacement of 0.5724m.

Step 12 Revise the value of x, if needed: In Step 1, it was assumed that the abutments would carry 50% of the applied lateral force. Comparing the displacements from Step 11 with those from Step 2, which were: $\Delta_A = \Delta_E = 0.04\text{m}$; $\Delta_B = \Delta_D = 0.417\text{m}$; $\Delta_C = 0.596\text{m}$ indicates that the assumption of $x = 0.5$ is slightly low as the displacement of the central pier is somewhat less than the target. In order to increase the central pier displacement, the force resisted by the abutment will need to be increased, thus resulting in reduced pier strength and stiffness and hence an increase in the pier displacement. A value of $x = 0.54$ is selected. Past experience has indicated that to speed convergence, a value equal to twice that needed from scaling of the actual to desired displacements is appropriate. For this example, the calculation is shown below:

$$x_{new} = 0.5 + \frac{2 \times (596 - 572)}{572} \times 0.5 = 0.54$$

We then return to Step 10 to determine the revised estimate for abutment and pier stiffness. This results in abutment shear forces of 2776 kN, shear forces in Piers B and D of 1430 kN, and a shear force of 1870 kN in Pier C. For abutments A and E, the effective stiffness for the analytical model is then revised to 2776/0.04 = 69400 kN/m. For Piers B and D, the effective stiffness is 1430/0.417 = 3430 kN/m, while for Pier C, the effective stiffness is 1870/0.596 = 3140 kN/m. The structure is then re-analyzed with the same lateral force vector from Step 9 and the displacements compared with the target values. The results from this analysis result in the following displacements: $\Delta_A = \Delta_E = 0.041$m; $\Delta_B = \Delta_D = 0.396$m; $\Delta_C = 0.593$m. As the central pier displacement is now much closer the to target value of 0.596m from Step 2, the abutment forces due to superstructure bending have been correctly estimated resulting in a value of $x = 0.54$.

Step 13 Conduct additional iterations: The displacement profile is revised by scaling the profile from Step 12 to the target central pier displacement of 0.596m, while keeping the abutment displacements at 0.040m. The revised displacement profile is then $\Delta_A = \Delta_E = 0.04$m; $\Delta_B = \Delta_D = 0.398$m; $\Delta_C = 0.596$m. The value of $x = 0.54$ is also used in the second iteration. Steps 3 through 12 are then repeated until convergence is reached for the displacement profile and x. The calculations for Steps 3 through 12 are shown in Table 10.2 below. After the second iteration, convergence has been reached for both the value of x and the displaced shape, and the design is complete.

Table 10.2   Second Iteration for Example 10.5

Step 3	$\Delta_d = 0.477$m
Step 4	$m_e = 2834$ tonnes
Step 5	$\mu_\Delta = 1.52$ (Piers B and D); $\mu_\Delta = 3.83$ (Pier C)
	$\xi = 0.098$ (Piers B and D); $\xi = 0.154$ (Pier C)
Step 6	$V = 0.139 \times \sum_{i=1}^{5} F_i$ (Piers B and D); $V = 0.182 \times \sum_{i=1}^{5} F_i$ (Pier C)
Step 7	$\xi_e = 0.085$
Step 8	$T_e = 2.20$ sec; $K_e = 23191$ kN/m; $V_{Base} = 11061$ kN
Step 9	$F_A = F_E = 127$ kN; $F_B = F_D = 2969$ kN; $F_C = 4869$ kN
Step 10	$V_A = V_E = 2987$ kN; $V_B = V_D = 1538$ kN; $V_C = 2012$ kN
	$K_A = K_E = 74664$ kN/m; $K_B = K_D = 3865$ kN/m; $K_C = 3375$ kN/m
Step 11	$\Delta_A = \Delta_E = 0.039$m; $\Delta_B = \Delta_D = 0.406$m; $\Delta_C = 0.613$m
Step 12	$x = 0.51$
	$V_A = V_E = 2821$ kN; $V_B = V_D = 1639$ kN; $V_C = 2143$ kN
	$K_A = K_E = 70516$ kN/m; $K_B = K_D = 4117$ kN/m; $K_C = 3595$ kN/m
	$\Delta_A = \Delta_E = 0.040$m; $\Delta_B = \Delta_D = 0.395$m; $\Delta_C = 0.595$m

The solution developed in this example can be expected to provide good displacement control for the piers. However, as discussed in the following section, and illustrated in Design Example 10.6, the first-mode design solution, which is the basis of the **DDBD** approach will need to be modified for superstructure moments, and abutment reactions.

10.5 CAPACITY DESIGN ISSUES

Capacity design issues are discussed in general terms in Sections 3.9 and 4.5 to 4.7. The purpose of capacity design is to ensure that undesirable modes of inelastic deformation, such as plastic hinges at unintended locations, or shear failure, cannot occur, and that the influence of higher-mode effects is properly represented. This is effected by ensuring that the dependable strength of the action (shear; flexure etc) at a specific location exceeds the maximum feasible action under seismic response.

The general requirement for capacity protection is defined by Eq.(3.61), which is reproduced here as Eq.(10.29) for convenience of reference:

$$\phi_S S_D \geq S_R = \phi^o \omega S_E \tag{10.29}$$

where S_E is the value of the design action being capacity protected, corresponding to the design lateral force distribution found from the **DDBD** process, ϕ^o is the ratio of overstrength moment capacity to required capacity of the plastic hinges, ω is the amplification of the action being considered, due to higher mode effects, S_D is the design strength of the capacity protected action, and ϕ_S is a strength-reduction factor relating the dependable and design strengths of the action. Further background is given in Sections 3.9 and 4.5.

With bridge structures there are two separate areas to be considered – capacity design related to actions in the piers, and superstructure consideration.

10.5.1 Capacity Design for Piers

The primary concern is determining the maximum feasible shear force that can be developed in the piers. With reference to Eq.(10.29), it is primarily the overstrength factor ϕ^o that is involved, with dynamic amplification playing no, or at most a lesser part in amplifying the design shear force. The overstrength factor can be determined as suggested in Section 4.5. Dynamic amplification related to higher-mode effects can, however be significant in the following cases:
- When pier mass is a significant proportion of the total mass contributing to lateral inertia forces on a pier, then higher-mode response resulting from response of the pier as a distributed-mass vertical beam may increase column shears, and even curvature ductility factors, above the level corresponding to the **SDOF** distribution of design forces, and should be considered.
- It was mentioned in relation to Fig.10.18(d) that the torsional mass inertia of a

wide superstructure supported by a cantilever pier may induce a significant second mode response. This will be apparent in a potential variation in the height at which the column moment drops to zero. The position at which this occurs may be above, or below the centre of superstructure mass, and is best determined by nonlinear time-history analysis. If this is not carried out it is suggested that the maximum shear force be evaluated assuming that the point of zero moment (see Fig.10.18(d)) is dropped 15% below the centre of superstructure mass, thus corresponding to a 17.6% increase in the capacity design shear force.

- With flexible superstructures higher mode response may increase the response of piers at some distance from the bridge centre. For example, the four-span bridge of Fig.10.14 has a stiff central pier, and flexible outer piers. The displacement response of these piers may be increased by higher modes. Note, however, that if the bridge is symmetric about its centre, as is the case in Fig.10.14, the second mode, which is anti-symmetric will have a zero participation factor under transverse excitation, and displacements of the symmetric third mode, which would have the central pier displacing in the opposite direction from the two outer piers will induce small displacements. Since the main effect will be a small increase in the displacement ductility demand of the two outer piers, which will not be critical for design, this effect can generally be ignored.

All of these effects can be determined by the effective modal superposition approach described in Section 10.5.3 below.

10.5.2 Capacity Design for Superstructures and Abutments

Both overstrength at plastic hinges and higher mode effects may have a significant influence on the maximum transverse moments developed in the superstructure, and on the maximum abutment reactions. These are discussed separately in the following sections.

(a) Overstrength Capacity of Plastic Hinges: The situation with structures with dual seismic load paths is opposite from that occurring with single-load path structures. In the case of bridge structures with part of the inertia load being carried by ductile columns and part by an elastic superstructure, an increase in the strength of the ductile columns resulting from material overstrength will result in an increase in the effective secant stiffness of the columns at design level response. Since the superstructure stiffness remains unchanged at the elastic value, this means that the total stiffness of the structure has increased, and displacements, as a consequence will be decreased. The superstructure forces, and abutment reactions will thus reduce. It is thus clear that the ϕ^o value corresponding to flexural overstrength at plastic hinges should not be applied when estimating superstructure forces. As discussed below, it is in fact appropriate to use an estimate of plastic hinge capacity lower than the design level in determining the superstructure demands.

(b) Higher Mode Effects: It has been found[A4], that higher mode effects are generally less significant for bridges than with building structures. As already discussed in relation to Fig.10.18(d), the width of the superstructure may mean that with monolithic single-column/superstructure designs, the moment at the top of the column may be indeterminate, since the pier/superstructure is essentially a two-mode system. Analyses of typical designs indicate that pier moments at the height of the superstructure centre-of-mass will rarely exceed $M_1 = \pm 0.2M_2$ (see Fig.10.18(d)). This value could be used if detailed analyses are not carried out. The principal influence of this uncertainty will be a possible increase in the design shear force in the pier, as already discussed.

The second region where higher mode effects may be significant are in the superstructure transverse moments, and consequent abutment reactions, which are of course directly related to the superstructure moments in the end spans. Generally superstructure transverse seismic moments are not of great concern, as adequate capacity will normally be provided as a consequence of gravity load design. They should, however, be checked. Our analyses[A4] have indicated that the higher-mode amplification of superstructure transverse moments is normally not critical for bridges with four spans or less, when span lengths are 50m (164ft) or less.

Figure 10.20 shows results of displacement-based design and analysis of an irregular six-span bridge, where higher mode effects might be expected to be significant. The design displacement profile, following the procedure outlined in Section 10.4.5, is shown as the solid line in Fig.10.20(b). The short central pier is the critical design element. Average results from non-linear time-history analysis using a suite of seven spectrum-compatible accelerograms are shown as a dashed line in Fig.10.20(b). The agreement with the design profile is good, particularly at the critical central pier, but we note that displacements of piers P4 and P5 significantly exceed the design profile, presumably as a result of higher-mode effects. Note that this excess of displacement will not be critical, as all piers except the critical central one have displacements significantly less than the design limits.

The envelopes of superstructure transverse moments resulting from the single-mode **DDBD** procedure, and from the non-linear time-history analyses are shown in Fig.10.20(c). The single-mode design results, using the analysis procedure of Section 10.4.5 are again shown by the solid line. The results from time-history analysis are shown by the dashed line (the central of the three profiles shown). It is seen that the superstructure moments from midspan to the right abutment significantly exceed the values from the single-mode design approach, indicating that higher-mode effects are indeed important. Note, however, that the peak superstructure moment from time-history analysis is less than 10% higher than the peak **DDBD** value.

Of greater importance is the influence on abutment reactions, which are needed for determining the required strength of the abutment structure. These, of course, are directly provided from the time-history results, but can also be estimated from the slope of the moment profiles in the end spans. It will be seen at both the left, and particularly at the right abutment the slope of the transverse moment profile from the time-history results is

much higher than that from the **DDBD** process, and hence abutment forces, and displacements will have been underestimated by the first-mode design approach.
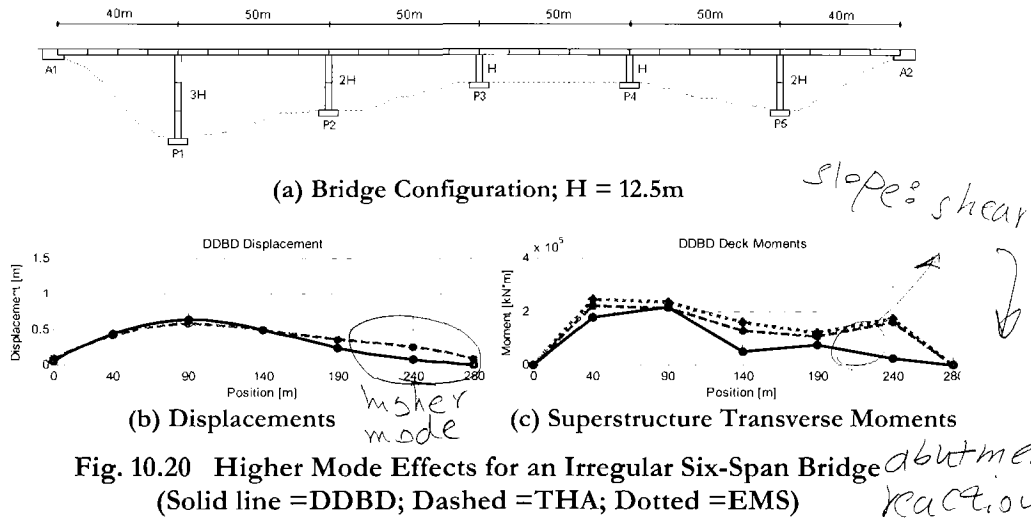

(a) Bridge Configuration; H = 12.5m

(b) Displacements   (c) Superstructure Transverse Moments

Fig. 10.20   Higher Mode Effects for an Irregular Six-Span Bridge
(Solid line =DDBD; Dashed =THA; Dotted =EMS)

(c) Estimation of Higher Mode Effects: Although bridges are often highly irregular, they are often comparatively simple in a structural sense, in that they are comprised of comparatively few structural elements. It is thus often feasible to carry out non-linear time history analyses to verify the design displacements, and to determine the influence of higher mode effects. The reader is referred to Section 4.9.2.

An alternative is to use simplified methods to account for higher mode effects, as have been provided in previous chapters dealing with building structures. In other chapters these have been in two forms: modified methods of modal superposition, and simple conservative design rules. Because of the potential for irregularity in bridge structural form, it appears, at this stage, difficult to develop simple conservative design rules that could be generally applied.   However, it has been found that a modal superposition approach that is similar to that proposed in Section 6.6.1 for cantilever walls, and in Section 7.3.1 for dual wall-frame structures gives satisfactory results. In both of these approaches, the inelastic first-mode design forces from the **DDBD** process were combined with the elastic forces from the higher modes, using appropriate combination rules (**SRSS** or **CQC**). The difference between the two approaches was in the structural modelling. For the cantilever walls, an elastic structural representation was used, based on effective cracked-section stiffness at yield. For dual wall-frame structures, the higher mode contributions were based on a structural model where very low stiffness was provided at potential plastic hinge locations.

For bridge structures an alternative approach, which is fully compatible with the **DDBD** philosophy has been investigated[A4]. For this, the structural representation was

such that stiffness of members with potential plastic hinges (e.g. piers) was taken as the secant stiffness to peak displacement response, while elastic elements (e.g. the superstructure) were modelled by initial-stiffness values. This conforms with the analysis model used to distribute the inertia forces described in Section 10.4.5, Steps 10 and 11. It was found that combining the higher-mode elastic forces from such analyses with the **DDBD** inelastic first-mode approach following the modified-modal superposition approach of Section 6.6.1 gave an excellent representation of force-envelopes. This procedure has been termed the *Effective Modal Superposition* approach (**EMS**) to distinguish it from the Modified modal superposition approach of Section 6.6.1. However, it is emphasised that the difference between the two approaches is solely in the values for stiffness of inelastic members used in the modal analyses.

Results using the **EMS** approach for the six-span bridge of Fig.10.20(a) are included in Fig.10.20(c) and shown by the dotted (top) line. It will be seen that this agrees closely with, and is slightly more conservative than, the average of the nonlinear time-history results (**THA**). The agreement noted in Fig.10.20(c) is typical of the results of the extensive range of bridges analysed in [A4].

It would appear that the **EMS** approach should also provide a better representation of higher-mode effects for building structures than does **MMS**. This has not, however, been verified at this stage, though we are rather confident of its success.

10.6 DESIGN EXAMPLE 10.6: Design Verification of Design Example 10.5

The design for transverse response of the four-span bridge of Design Example 10.5 is now subjected to design verification with inelastic time-history analysis using the program "**Ruaumoko**" provided in the CD with this book. The structure was represented as a 3-D structure, with the superstructure represented by an elastic member, while the piers used "Thin" Takeda hysteretic characteristics with a 5% second slope stiffness (see Section 4.9.2(f)). Elastic damping was represented by 5% tangent-stiffness damping. The abutments were represented by lateral springs with different properties in different analyses, as discussed subsequently. Each span was divided into five segments, with tributary mass distributed to the superstructure nodes.

Three spectrum compatible earthquake records were generated using wavelet theory[S10], using the three accelerograms (Kobe, Sylmar and Whittier) described in Chapter 2. These adjusted records are included on the CD provided with this book.

An initial set of analyses was carried out based on the design resulting from Design Example 10.5. Pier yield strength was reduced from the design strength at design displacement response based on the 5% post-yield stiffness, and the design displacement ductility. Since the design assumed elastic response of the abutments, the abutments were initially modelled as elastic elements. Results, in terms of response displacements and superstructure moment envelopes are compared with the design profiles in Fig.10.21(a). The design profiles are shown as solid bold lines, and the results from the individual records by light lines. The average of the three analyses is shown as a dashed bold line. It
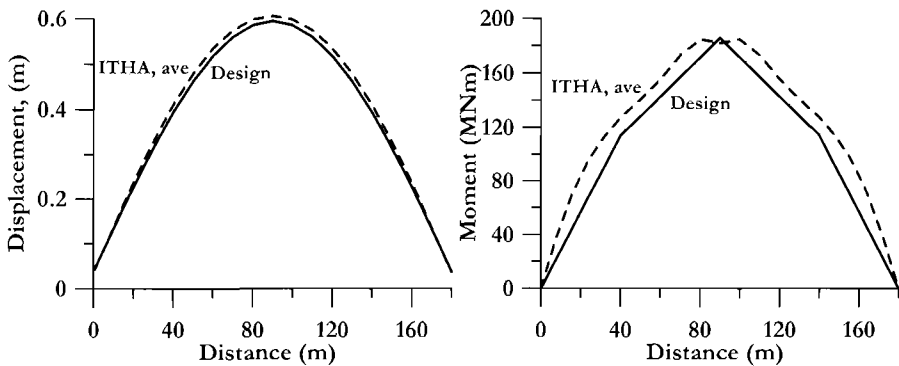
will be noted that the agreement between the design and analyses profiles is very good, and that the scatter between the results of the records is small.
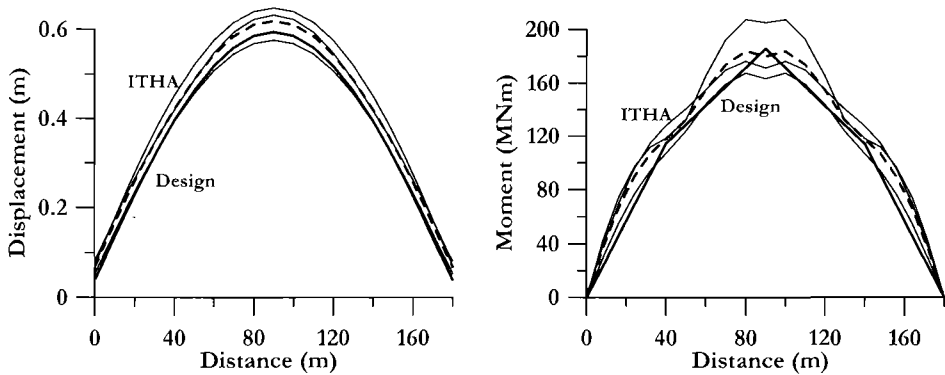
(a) Design, Elastic Abutments(Displacement envelopes; Moment envelopes)
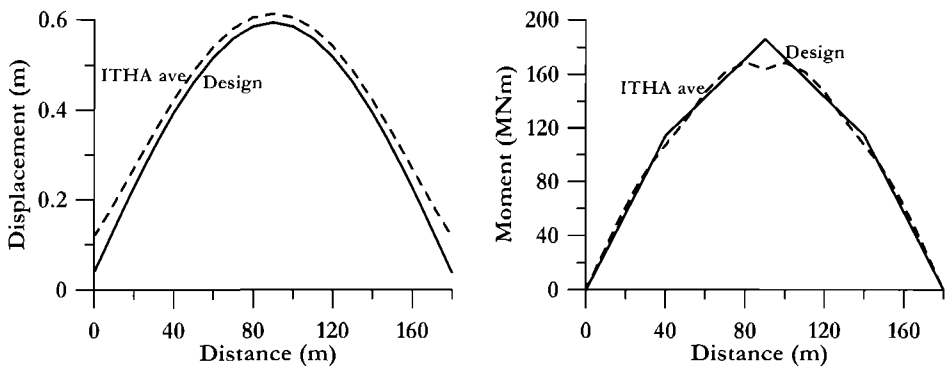
(b) Design, Elasto-plastic abutments (Displacement envelopes; Moment envelopes)

(c) Revised, Elasto-plastic abutments (Displacement envelopes; Moment envelopes)

Fig.10.21 Displacement and Moment Profiles from Design Example 10.6

The average central displacement is 4% larger than the design value of 0.595m, and peak superstructure moments are very close to the design values. However, though not very apparent in Fig.10.21(a), the displacements at the abutments, at an average of 68.5mm (2.7in) are 71% higher than the design value of 40mm (1.6in). It might be felt that this is an acceptable excess, as it only represents a small ductility demand. To provide further investigation of this, it is decided to rerun the analyses, with the abutments modelled as elasto-plastic springs, with the design strength from Example 10.5. Results from this set of analyses are shown in Fig.10.21(b), where for clarity only the average of the three analyses is compared with the design values. The peak displacement at the central pier is essentially unaffected (the excess is reduced to 3%), but the lateral displacements at the abutments are increased to 118mm (4.6in). This increase above the design value is due to higher-mode effects, as explained in the previous section. It might still be considered an acceptable result, but we decide to attempt to reduce the displacements to the design level. As discussed in the previous section, this could be based either on an **EMS** analysis or on time-history results. Since we have the results of the time-history analysis, we use them directly.

The initial elastic analyses indicated that the design forces in the abutments, including higher mode effects, were 71% higher than the design levels (note: this abutment insufficiency was also observed in an independent analysis run with the program "**SeismoStruct**", the results of which may be found in the Structural Analysis CD). This implies that the stiffness and strength of the abutments should be increased by a dynamic amplification factor of at least $w_a = 1.71$ if the displacements are to be constrained to the design level of 40mm. However, increasing the stiffness is likely to further increase the design forces, so, based on experience we chose to increase the abutment stiffness and strength by 100%.

A new set of analyses were run based on this assumption, (and with the abutments modelled as **E-P** elements) and the results are plotted in Fig.10.21(c). The displacement profile is now almost perfect, with a peak central displacement less than 2% above the design value, and the average abutment displacement is 37mm (1.5in), indicating elastic response. The higher-mode effects are clearly apparent in the slope of the moment profile at the abutment.

Data files for the analyses carried out in this example are included on the CD provided with this book.

11

STRUCTURES WITH ISOLATION AND ADDED DAMPING

11.1 FUNDAMENTAL CONCEPTS

11.1.1 Objectives and Motivations

The reasons for considering the possibility of isolating a structure are treated in detail in several books [C11, N3, S8] and will only be summarized here. Essentially, all the main issues may be condensed in a single objective: i.e. modification of global response to improve structural performance. This might be effected in a number of ways (see conceptual examples in Fig.11.1), resulting in the choice of:

- Protecting part of the structure, assuring its elastic response;
- Shifting the main period of vibration to a convenient value to modify both acceleration and displacement demand;
- Increasing the global energy dissipation capacity of the structure, thus reducing the displacement demand;
- Regularizing the response, modifying the relative effective stiffness and strength of different parts of the structure.

It is well known that the insertion of isolation and dissipation (I/D) devices generally results in an increase of both the period of vibration of the fundamental mode and the energy dissipation capacity of the system, but the two effects may have a significantly different relative importance.

For example, when an isolation system is inserted at the base of a building or of a stiff structure (Fig.11.1(a)), the main effect is the period shift, which generally results in lower elastic acceleration response and larger displacement demand. As discussed in Chapter 2, a reduction of the displacement demand may result from the added damping, due to the energy dissipated by the devices. However the local added damping rarely implies corresponding global equivalent viscous damping larger than 20% and consequently the increased displacement demand due to period shift is rarely compensated by the reduction due to the increased dissipation (see Fig.11.2). Clearly, this larger displacement demand will usually be concentrated at the isolation system level,
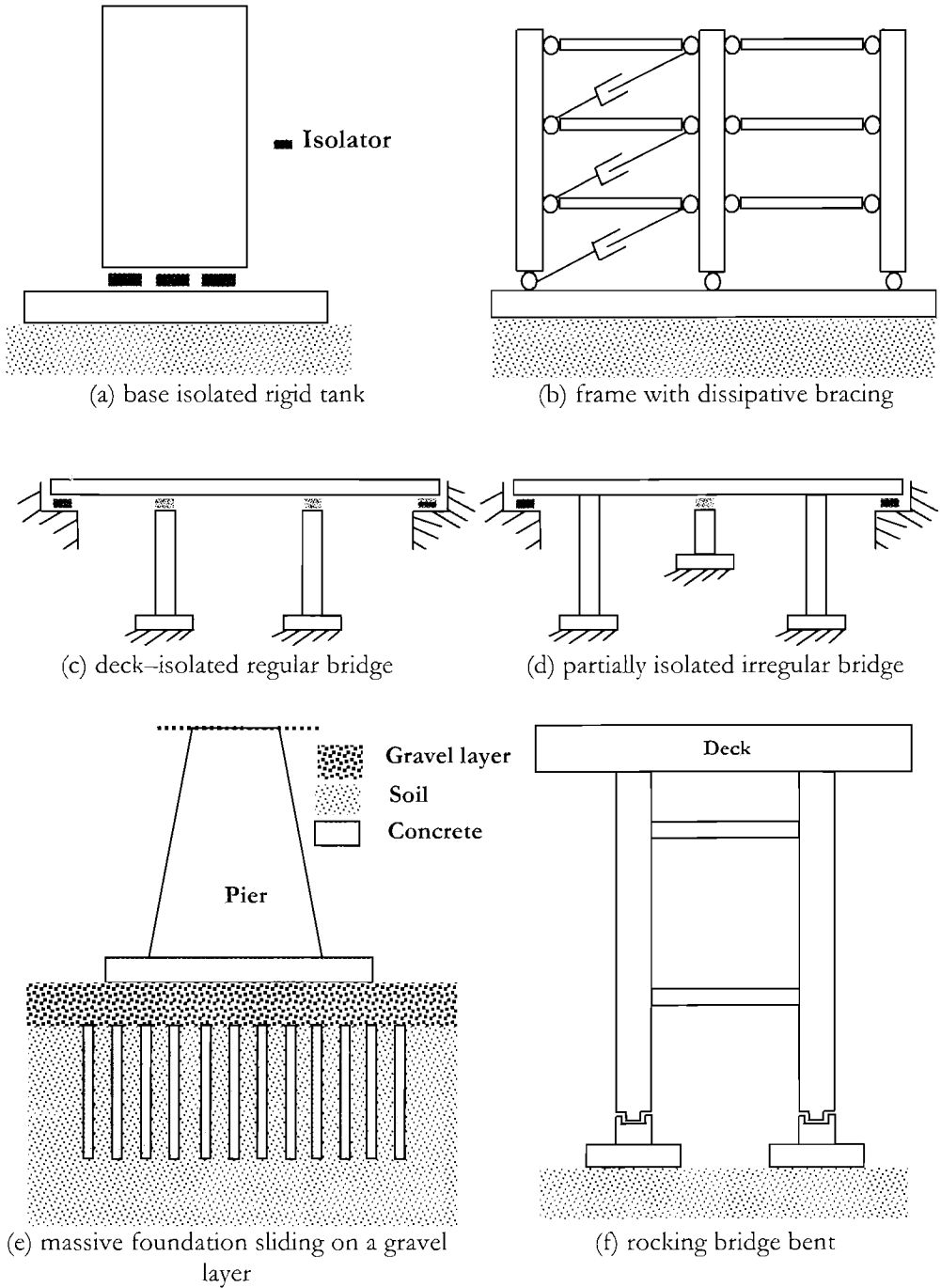
(a) base isolated rigid tank   (b) frame with dissipative bracing

(c) deck–isolated regular bridge   (d) partially isolated irregular bridge

(e) massive foundation sliding on a gravel   (f) rocking bridge bent
layer

Fig.11.1   Conceptual Examples of Location of Isolation/Dissipation Devices

(a) Acceleration Spectra   (b) Displacement Spectra
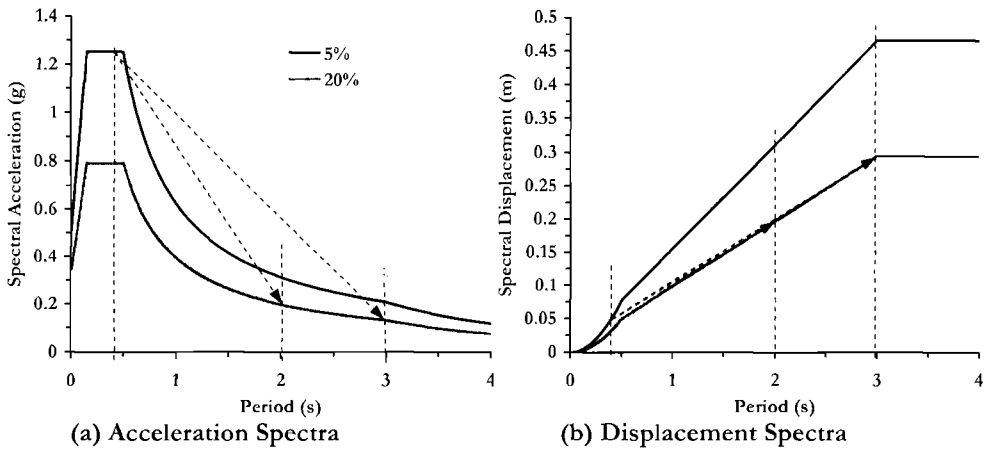
Fig.11.2   Examples of Acceleration and Displacement Demand Variations due to the Combination of Period Shift and Added Damping (Refer to Section 11.1.4)

while the internal deformation demand of the structure is limited within values not exceeding the yield drift.

On the other hand, the insertion of dissipative braces in a frame building (Fig.11.1(b)) or of dampers between pier and deck of a cable-stayed bridge normally results in minor modification of the main period of vibration and possibly significant local energy dissipation that may result in local equivalent viscous damping larger than 50% (e.g. for hydraulic dampers, see Section 11.2.4; note, however, that the additional structural deformation will imply a lower global equivalent viscous damping).

There are cases where only part of a structure is isolated (e.g. the deck of a bridge, as in Fig.11.1(c)) so that the shear force transmitted to the top of the pier is limited by the capacity of the device. In some cases it is conceivable to insert the devices only on shorter piers, if an elastic, or near-elastic response is expected for the taller ones (Fig.11.1(d)). In this case, one of the objectives may be a regularization of the expected response of the structure, with a more uniform distribution of the total shear.

A fundamental aspect that should be emphasized is the general objective of concentrating the whole inelastic demand within the **I/D** system, protecting the entire structure from inelastic demand, and from the consequent damage, by the application of concepts of capacity design that will be discussed later.

It is also noticeable that the general idea of isolation and added dissipation can be translated into a number of possible practical solution that may include not only specially designed devices, but use of foundation or internal rocking and sliding soil layers as shown in Figs.11.1(e) and (f), where solutions adopted for the Rion–Antirion Bridge[P35]) and for the South Rangitikei Bridge[C10] are conceptually visualized.

I/D devices allow for increased control of structural response and are largely sensitive to displacement, rather than force, demands, making them particularly suited for displacement-based design concepts.

11.1.2 Bearing Systems, Isolation and Dissipation Devices

As discussed in greater detail in Section 11.2, **I/D** devices can be characterized for design purposes in terms of their main properties, which are defined and briefly commented on below.

(a) Capacity for Carrying Gravity Loads. Normally dampers have no capacity of carrying vertical loads and may be used in combination with bearings. Vertical capacity of isolators may interact significantly with other parameters such as horizontal stiffness and therefore create important design constraints.

(b) Displacement Capacity. This is possibly the most fundamental parameter, particularly in a displacement-based design approach. Clearly, different displacement values should be considered in relation to different performance levels and structure displacements, but the basic design philosophy will always require that the maximum feasible displacement, under the largest earthquake considered, is within the displacement capacity of the device.

(c) Horizontal Force Capacity. This may be relevant to protection of other parts of the structure (low values generally desirable) or to increase the proportion of the energy dissipated by the system with respect to the structural damping (higher values preferred).

(d) Equivalent (Secant) Stiffness. Again, appropriate values will depend on the limit state considered. However it should be noted that in design the required horizontal strength will result from the accepted displacement level and resulting period and not vice-versa (see Section 3.1).

(e) Equivalent Viscous Damping. As shown in Section 3.4.3(c), equivalent viscous damping may be determined from the area of the hysteresis loops which is generally quite large for dampers and normally much smaller for isolators. Damping capacity may be reduced by re-centering requirements. In general, the global damping of the isolated structure will result from a combination of isolator and structure response and may be significantly lower than that of the device damping.

(f) Re-centering Capacity. Re-centering capacity may be considered a fundamental response parameter, particularly with regard to post-earthquake evaluations. It often depends on the post yield stiffness in essentially bilinear devices. To increase it may therefore imply a reduced energy dissipation capacity and correspondingly a lower equivalent viscous damping, since the equivalent viscous damping decreases as the post-yield stiffness increases.

(g) Post-elastic Response. In most cases, devices will respond non-linearly, allowing the definition of an equivalent yield-point in a bilinear approximation of response. The post yield stiffness may affect the re-centering capacity (higher slope favourable), the equivalent viscous damping (lower slope favourable), and the protection of other damage modes (lower slope favourable).

(h) Post-ultimate response: Softening, hardening, quasi-rigid impact and total disruption may have completely different consequences in terms of expected performances for larger than expected events and consequently imply different protection factors.

(i) Specific problems: may include high sensitivity to (1) axial force variation, (2) heat problems and (3) high sensitivity to environmental conditions or aging.

11.1.3 Design Philosophy/Performance Criteria

Although the general design philosophy will not differ from the approach generally presented in Chapters 1 and 3, it is appropriate to briefly discuss a few specific issues related to isolated structures.

(a) Design Displacement: As usual, the first step consists of defining the design displacement, which will result from a combination of the structural and the **I/D** device displacements. The design displacement of the structure is usually governed, essentially without reference to the limit state of interest, by the assumption of maintaining a quasi-elastic response, corresponding therefore to the yield displacement reduced to allow for possible overstrength of the devices. For a serviceability limit state, the structural displacement may correspond to a drift limit consistent with the desired limitation of non-structural damage, but it is often found that the two values (displacements corresponding to structure yielding and non-structural damage limitation) do not differ too much.

The isolation system displacement capacity is normally relevant for a damage-control or near-collapse limit state, and may be derived from considerations related to the device system capacity or from global displacement limit as produced by the combination of structure and device system displacement.

(b) Equivalent Viscous Damping: The evaluation of the equivalent viscous damping is the second step. This is normally obtained by calculating the device damping and combining it with the structural response. The procedure outlined in Section 3.5.4, with reference to the influence of foundation flexibility on effective damping, which led to Eq.(3.40) may apply for serial systems, such as those obtained from base or deck isolation, but may be inapplicable when it can not be assumed that the same force level characterizes the structural and the device systems. In these cases, where similar displacement demand between structure and device exists, more fundamental concepts derived from the evaluation of relative hysteretic energy dissipation should be applied. An example of such a case is presented in Section 6.8, with reference to coupled structural walls. Assuming that the wall displacement is limited to its yield value and inserting coupling dampers instead of concrete beams, from Eqs.(6.54) and (6.66), Eq. (11.1) can be derived to evaluate the approximate equivalent viscous damping of the entire system ξ_{sys}):

$$\xi_{sys} = \frac{\Sigma M_{Di} \xi_{Di}}{M_{OTM}} \qquad\qquad (11.1)$$

where ξ_{Di} and M_{Di} are the damping and overturning moment components associated with each damper and M_{OTM} is the total overturning moment (this subject will be more extensively discussed in Section 11.3.3). Once the appropriate damping level has been selected, **DDBD** follows in the usual manner.

While the application of capacity design principles to the relative strengths of **I/D** systems and structural components to assure that the structure will remain elastic is normally simple, in some case it may not be trivial to derive the properties of each single structural element from the global response parameters, including the appropriate dynamic amplification factors.

It should be noted, however, that the displacement-based design of conventional base isolated buildings is normally even simpler that designing a non–isolated building.

11.1.4 Problems with Force – Based Design of Isolated Structures

The advantages of displacement-based over force-based approaches for seismic design have been discussed in Chapters 1 and 3. It has to be noted, however, that in the case of isolated structures some more specific reasons to prefer displacements to forces as fundamental design variables apply.

The first basic point is related to the long period of vibration that is normally considered to be a fundamental feature of base isolated structures, in order to reduce the spectral acceleration ordinates. It has often been indicated that periods in the range of 2 – 3 seconds should be considered as reasonable target values for buildings, while similar or larger values are appropriate for bridges.

To make the point, we consider design of a stiff structure with an initial (non-isolated) period of 0.4 sec. in a relatively high seismicity region, which has a design peak ground acceleration equal to $a_g = 0.5$ g, including local soil amplification effects, with the plateau of the elastic acceleration spectrum terminating at a period value of 0.5 seconds. The isolation system has rigid/perfectly plastic characteristics (e.g. a coulomb slider), and thus does not affect the elastic period. The elastic acceleration response would thus be S_{ae} = 0.5×2.5=1.25g, since the response is on the plateau, and an amplification factor of 2.5 is appropriate (see Fig.11.2, and Section 2.2). The corresponding displacement response would be

$$\Delta_{ae} = \frac{S_{ae} T^2}{4\pi^2} = \frac{1.25 \times 9.805 \times 0.4^2}{4\pi^2} = 0.0496m \text{ (49.6mm, 1.95in)}$$

We investigate design of the isolated system to have a response period of either 2sec or 3sec. The period change is thus a factor of 5 or 7.5 respectively. With an elasto-plastic response, appropriate for a friction slider, the implied ductility demand is the square of

the period shift, corresponding to ductilities of 25 and 56 respectively – not a problem for a slider, which has no material strain limits. Using conventional force-based thinking, and the equal-displacement approximation, the implication is that the structure could be designed for lateral force levels of S_{ae}/μ = 0.05g and 0.022g for periods of 2 and 3 sec. respectively, while the displacement would remain at the elastic value of 49.6mm.

With displacement-based design, and target periods of 2 and 3 sec., we recognize that the equivalent viscous damping is unlikely to be significantly higher than 20%. From Eq.2.8, this represents a reduction factor of R_ξ = 0.564 to be applied to the elastic displacement spectrum, as shown in Fig.11.2. The elastic accelerations at 2 and 3 seconds are respectively

$$S_{ae,2} = 1.25g\frac{0.5}{2} = 0.313g \qquad \text{and} \quad S_{ae,3} = 1.25g\frac{0.5}{3} = 0.208g$$

while the corresponding elastic displacements are

$$\Delta_{ae,2} = \frac{0.313\times9.805\times2^2}{4\pi^2} = 311mm \quad \text{and} \quad \Delta_{ae,2} = \frac{0.208\times9.805\times3^2}{4\pi^2} = 429mm$$

Incorporating the reduction factor of 0.564, the design force levels are 0.177g and 0.117g respectively, with corresponding design displacements of 175mm (6.9in) and 242mm (9.5in). The corresponding design points are shown in Fig.11.2. Note that if the equivalent viscous damping were increased to 30%, which is effectively an upper bound, the design force and displacement levels would only be reduced by a further 17%.

It is therefore evident that designing from a conventional force-based approach would be entirely inappropriate, and unconservative. This is recognized is some design codes which require design for isolated systems based on effective, rather than initial, stiffness, and modified damping (e.g. [X4]).

Note that for base-isolated rigid structures (Fig.11.1(a)) the structural displacement corresponds to the device displacement and the global equivalent viscous damping corresponds to the isolation system damping. It is therefore possible, for this specific case, to attain equivalent viscous damping values as high as 20 – 25 %.

Finally, even more difficult problems may arise when concepts of isolation and added dissipation capacity are applied to complex structural systems, where, for example, the devices may be located internally to the structures and the structure flexibility can not be neglected (Fig.11.1(b)).

As a relatively simple example, consider the case of bridges with an isolation system between the piers and deck (Fig.11.1(c) and (d)). In this case, the objective may be to protect relatively low-mass piers and their foundations, reducing the shear force produced by the oscillation of the deck mass. Clearly, however, controlling the relative displacement demand between deck and piers is also an issue.

It is shown in Section 11.3.3(b) that considering as basic design parameters the deck, isolators and piers displacement capacities and demands will lead to a simple and effective

design approach which will only require the application of capacity design principles to protect piers and foundations. In contrast, a series of inconsistencies and ill-conditioned problems will arise from the application of standard force–based procedures, which will again imply an arbitrary selection of the assumed period of vibration.

11.1.5 Capacity Design Concepts Applied to Isolated Structures

It can be stated that capacity design (**CD**) principles may pursue one or more of four fundamental objectives:

- to avoid any possible brittle failure mode, protecting it by inducing some preceding weaker but more ductile force–limiting mechanism;
- to control the post–elastic deformed shape of the structure, increasing its global displacement capacity;
- to increase the energy dissipation capacity of the structural system, inducing a uniformly distributed inelastic demand in a large number of ductile elements;
- to assure an optimum proportionality between action intensity and induced damage, avoiding situations where a minor change in the action may induce catastrophic consequences.

In the case of isolated structures, the application of these objectives leads to a basic fundamental decision, that is: all essential non–linear phenomena should take place in the isolation or added-damping system, while the structure should respond quasi–elastically.

Taking the simplest case of a base-isolated rigid structure (Fig.11.1(a)), the required strength of the superstructure may be limited either by the equivalent response force of the isolation system or by the elastic spectral force corresponding to a low estimate of the equivalent period of vibration. Clearly, the same principles apply for the protection of the foundation system.

In the second case, i.e. when elastic response is assumed for the isolation system, the whole response is essentially linear and the residual displacement is close to zero.

In all cases, some care should be used to evaluate the possible coupling between the structure and the isolation system response, particularly for relatively flexible structural systems, in which case it will also be required to consider higher mode effects.

The case of a deck-isolated bridge (Fig.11.1(c) and (d)) is obviously more complex, since the isolation system can limit the force transmitted from the deck to the piers, but the pier inertial response still contributes, unmodified, to the shear and bending moment demand at the critical section at the base of the pier. For tall piers this inertial response may consequently govern the design of both pier and foundation system. For relatively tall and massive piers it is not uncommon to end up with shear force levels at the pier base for which as much as 70 % results from pier inertial response. Clearly in these cases a modification of the isolation system properties has only a modest effect on the design of the critical section at the base of the pier and of the foundation system. However, **CD** principles should still be applied to avoid shear collapse modes and foundation damage.

The case of a braced frame with added dissipative elements (Fig.11.1(b)) will imply a limiting force in the dissipative braces, that may be defined by imposing an elastic

response at the serviceability limit state action. When the demand exceeds this limiting value the dampers will start working, with the structural response becoming a controlled inelastic mechanism. As a consequence, the forces in all structural elements will not increase significantly and may be used to define the strength of capacity-protected elements.

In the above qualitative and preliminary discussion, it has been assumed that the device response is properly known and can therefore be dependably quantified. A detailed knowledge of the actual properties, including estimates of the coefficient of variation of the theoretical deterministic values or of dependable lower/upper limits under operational conditions is obviously important. With this information, appropriate capacity design factors to be applied to the nominal strength values and displacement demands of the isolated structure can be determined.

11.1.6 Alternative Forms of Artificial Isolation/Dissipation

It has to be noted that the broad class of structures employing isolation or added damping concepts to control the seismic response includes several non–conventional design solutions aimed at (1) limiting the forces to be transmitted between different parts of the structures (2) dissipating energy and (3) elongating the equivalent response period of vibration.

Since the 1950's it has been observed that foundation rocking could be regarded as a possible way to survive large earthquakes for structures with favourable characteristics, such as elevated water or storage tanks, characterized by large masses at some distance from the ground and comparatively narrow bases. For example after the Arvin Tehachapi earthquake (California, July 1952) it was found that a number of tall petroleum–cracking towers had escaped more serious damage by stretching their anchor bolts and rocking on their foundation pads [H5]. The first fundamental studies of the rocking response of a rigid block showed that the period of vibration of the rocking response increases with increasing amplitude of the motion and recognized that much of the advantage for a rocking structure depends on the efficiency of the mechanism in dissipating energy that may be obtained from impact on the ground, from friction between piles and soil, from yielding of pile reinforcement, from pull-out and/or yielding of connecting bolts, and from added devices specifically designed to modify response.

Simplified approaches to predict the response of rocking bridge piers are presented in [P4] where it is shown that equivalent viscous damping values deriving from soil impact are normally rather low and inversely proportional to the tendency of the structure to rock at relatively low values of excitation.

It is possible to conceive, design and construct structures that will rock in controlled ways at appropriate locations while providing dependable and adequate levels of energy dissipation. A very interesting case where these concepts have been successfully applied is the South Rangitikei bridge[C10] which has been designed to respond with a controlled rocking mechanism activated at the level of rocking pads that are inserted in the double legged piers close to their base along with shear keys and torsional–beam steel dampers

providing for a calibrated level of equivalent viscous damping. The concept is shown in Fig.11.1(f).

The concept of internal relative rocking between different parts of a structure can be extended to more complex response types, where rocking may occur over several interfaces. This concept can apply to segmental bridge piers [P36] designed with vertical post tensioning as well as precast concrete frames (as discussed in Section 5.11).

Examples of modern alternative forms of dissipation may include the combination of post tensioned and conventional reinforcement, such as used in the joints of precast frames, or the insertion of steel dampers at the vertical interface of shear walls discussed in Section 6.7 with reference to Fig.6.28 and 6.29.

An interesting recent example of the application of capacity design principles based on soil–structure interaction is offered by the design of the foundation of the Rion–Antirion bridge (see Fig.11.1(e), and Fig.11.3 [P35]), where a carefully calibrated gravel layer located between the pier base and the soil limits the value of the shear force that can be transmitted, consequently allowing relative sliding movements between soil and structure for larger demands.

(a) Section at Base of Pier   (b) Base shear vs Sliding Displacement
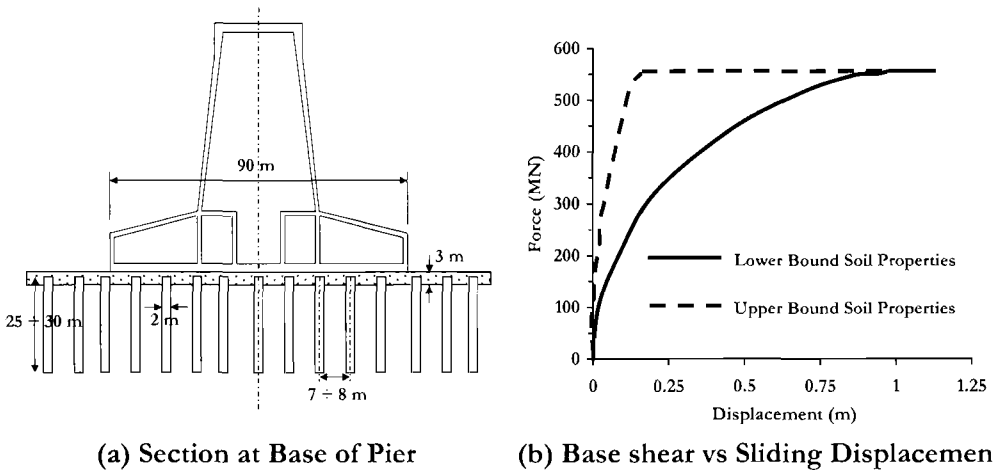
Fig.11.3 Rion–Antirion Bridge: A Calibrated Gravel Bed between Foundation and Soil Allows Relative Movement when the Force Reaches a Limit Value[P35]

11.1.7 Analysis and Safety Verification

The most relevant aspects of the response of an isolated structure in relation to the selection of appropriate models and analysis tools is the expected concentration of essentially all the non-linear response features in a few specially designed elements (isolators or dampers). In addition, these elements have well known properties including

their expected range of potential variability, not only for their equivalent yield force and displacement, but also for the entire force–displacement response.

Performing a full nonlinear analysis is therefore in general considerably easier than in the case of non-isolated structures, where one of the design objectives is often the widest and most uniform damage distribution, resulting in extensive distribution of the nonlinear response.

As a simple example consider the case of a base-isolated rigid structure, whose response is essentially reduced to that of a single degree of freedom spring (linear or non linear). It has to be noted, though, that in this case there is little need of a nonlinear analysis, because of the high reliability of the results obtainable using an equivalent linear design model, as discussed later.

However, if it is uncertain that the structure can really be considered as rigid, i.e. if the response of the structure can influence the response of the isolation system and vice–versa and the design of the isolation system has been conducted for simplicity assuming a rigid condition, a series of time-history analyses should be required in order to verify the design assumptions and the potential impact of higher-mode effects, which are difficult to estimate by simple methods. Note, however, that the Effective Modal Superposition (**EMS**) procedure described in Sections 6.6.1(c) and 10.5.2(c) can be applied for determining higher mode effects.

It has to be noted that for a well-designed structure the consequence of an appropriate application of capacity design principles will in general result in a single critical parameter, i.e. the displacement capacity of the isolation system, or of its components. The verification of the ratio between demand and capacity of these critical parameters may end up being the crucial objective of the whole nonlinear analysis and may assume a different meaning and require different protection factors depending on the expected consequences of the attainment of the considered limit state, as anticipated in Section 11.1.2.

11.2 BEARING SYSTEMS, ISOLATION AND DISSIPATION DEVICES

11.2.1 Basic Types of Devices

In this book, the wide variety of available devices will be divided into three fundamental classes, with reference to their essential features.

The first class will include simple bearings not necessarily designed for a reduced or controlled seismic response. Such bearings have been used for years for bridges or even for buildings when it has been necessary to allow relative movements with a relatively low transmission of forces. Normally, bearings may be based on the contact of two surfaces covered with low-friction material or on low-stiffness pads. In general, bearings transmit the vertical load and dissipate energy through friction or moderate viscous damping, however with little or no control of the horizontal relative displacement, of the dissipated energy and possibly without any re-centering capacity. In seismic design they are therefore usually coupled with additional devices.

The second class includes bearing devices capable of transmitting the vertical load, while being designed to control or reduce the horizontal seismic response. This category of devices may allow the definition of appropriate stiffness, dissipation capacity, equivalent yield force and displacement, post–yield stiffness, ultimate displacement or ductility level, and unloading stiffness.

The third class includes dissipation devices that are not intended to allow the transmission of vertical forces, being designed to control and reduce the response of structures, that may, or may not, be isolated using other kinds of bearings. The design variables are similar to those briefly addressed in the previous case.

In the following sections, a brief description of the main types of devices available will be presented, with emphasis on main features, common applications and potential problems. The focus will obviously be on the conceptual and design aspects related to displacement-based design rather than on technological issues. For this purpose, specific attention will be devoted to strength and geometric limitations and to the potential for displacement and energy dissipation capacity, discussing the relevant issues to define design displacements and equivalent viscous damping. The systems described should be regarded as useful examples to illustrate specific design problems and to allow extensions to other similar cases. More detailed treatment of this topic is available elsewhere [C11, N3, S8].

11.2.2 "Non-Seismic" Sliding Bearings

Typical sliding bearings not specifically designed for seismic response are based on a friction–type response where the equivalent yield level depends upon the coefficient of friction (μ_d) at the sliding interface and the normal force (N_{sd}) acting on that surface. Considering the standard case of flat sliding surfaces, the force transmitted through the device may therefore be expressed as:

$$V_d = \mu_d N_{sd} sign(\dot{d}) \tag{11.2}$$

Where d indicates here the relative displacement and its derivative is the relative velocity, which gives the sign to the force.

As discussed in Chapter 4, a low, but realistic value of the transmissible force should be used for design, while a maximum value should be used for capacity protection. The maximum value of the transmissible force should be evaluated considering an appropriate upper value of the friction coefficient and the expected maximum normal force, including the effects of the seismic response, which may induce significant normal-force variations, due to horizontal response and the vertical component of the seismic input. The shape of the hysteretic cycles is therefore rectangular, as shown in Fig.11.4 only if no variations of normal force and of the friction coefficient (which may depend on velocity) are assumed.

Typical bearings are manufactured using low friction material for the contact surfaces, such as **PTFE** on polished stainless steel, in which case the friction coefficient is normally in the range 0.02–0.03 (depending on possible lubrication) for very low slip

rates, such as in the case of temperature or creep movements. For non–lubricated devices this value may increase to values of the order of 0.10–0.15 at typical earthquake velocities. This high potential variability results in the need for recommending great care in using this kind of bearings for seismic isolation, particularly for what concerns a proper application of capacity design principles.
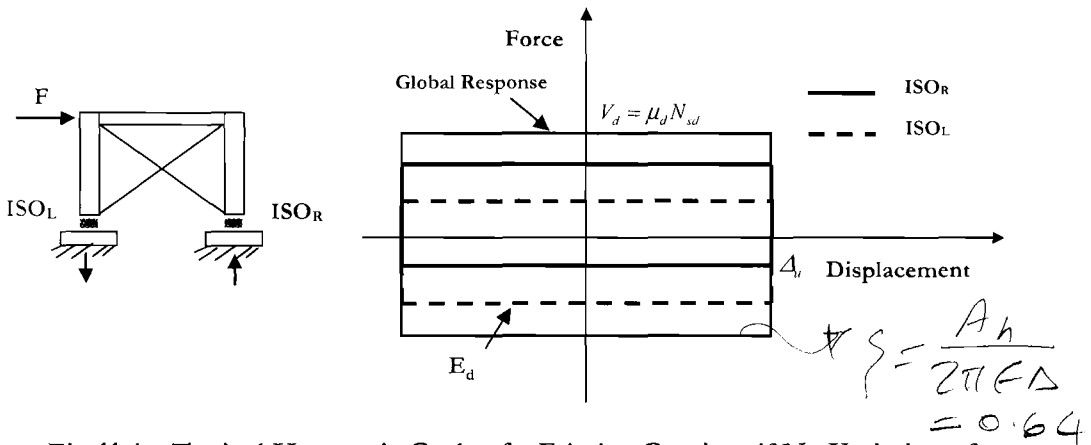

$$V_d = \mu_d N_{sd}$$

$$\xi = \frac{A_h}{2\pi F \Delta} = 0.64$$

Fig.11.4   Typical Hysteretic Cycle of a Friction Bearing, if No Variation of Friction Coefficient is Assumed

The displacement capacity is virtually unlimited and depends on geometry only, the local equivalent viscous damping tends to be extremely high (the energy–based damping is theoretically 64 %) and there is no re-centering capacity.

The main alternative to sliding bearings to carry the vertical load is offered by simple rubber bearings, which will not be discussed here, since they are implicitly described in the next section.

11.2.3   Isolating Bearing Devices

(a) Low and High Damping Laminated Rubber Bearings: In laminated rubber bearings, steel plates are inserted in a vulcanized piece of rubber to confine the rubber laterally, reducing its tendency to bulge and therefore increasing its vertical stiffness and improving its stability under horizontal forces. This type of bearing shows a substantially linear shear response, governed essentially by the rubber properties (see Fig.11.5).

The fundamental characteristic of this type of bearing is the interdependency of vertical load capacity, period of vibration and displacement capacity, essentially because the local horizontal shear strain in the rubber is governed by both the maximum vertical stress, which induces shear strain by bulging, and the shear deformation. The vertical load capacity is usually expressed by the following equation:

$$W \leq A'G_R S\gamma \tag{11.3}$$

where: W = allowable weight
           γ = allowable shear strain (of the order of 1)
           A' = mimimum permitted overlap of top and bottom area of the bearing at
           maximum displacement (usually approximately taken as one half of the
           horizontal section, i.e. $A/2$)
           G_R = shear modulus of rubber (of the order of 1 MPa (145 psi))
           S = shape factor (loaded area/force free area, e.g. for a circular disc of
           diameter D and thickness t, $S = D/4t$)
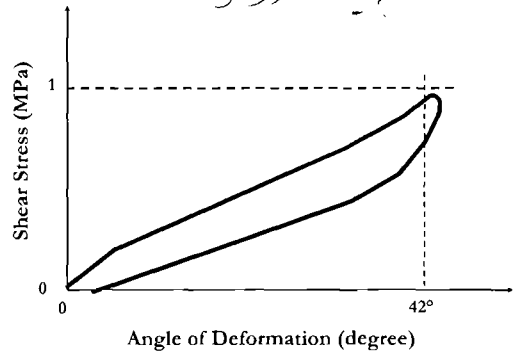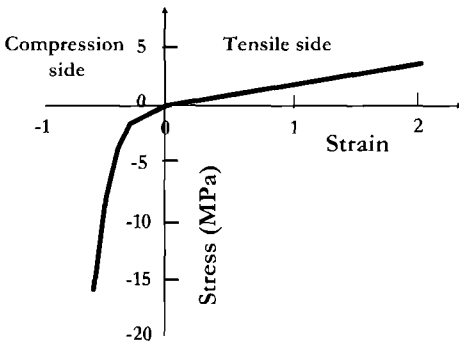
Fig.11.5 Typical Monotonic and Cyclic Response of Rubber

Considering for simplicity a bearing with a circular section, it can immediately be
verified that Eq.(11.3) implies that the maximum average vertical stress on the gross
section should be approximately equal to:

$$f_{ave,max} = \frac{G_R D}{8t} \tag{11.4}$$

where t is the distance between two steel plates. For normal geometries the maximum
stress is in the order of 10 MPa (1450 psi) (i.e. $t > D/80$).

The maximum displacement should be limited considering both the maximum shear
strain and the geometric limitation implied by the proportion of A' to A, as discussed
above. It may thus be controlled by the bearing diameter or by the bearing height, as
follows:

$$\Delta_{max} \leq \frac{D}{2} \tag{11.5}$$

$$\Delta_{max} \leq h \tag{11.6}$$

where h is the total height of the bearing.

Eq.(11.4) and (11.5) imply that, for bearings with an aspect ratio h/D larger than 0.5, the maximum displacement depends on vertical stress (f) and rubber layer thickness (t), according to the following relation:

$$\Delta_{max} \leq \frac{4tf}{G_R} \tag{11.7}$$

It is thus obvious that this type of bearing may have severe limitations regarding selection of vertical load and maximum displacement.

The response of the bearings to horizontal force is essentially linear, with a horizontal stiffness K_b typical of pure shear deformation:

$$K_b = \frac{G_R A}{h} \tag{11.8}$$

The period of vibration of the system can therefore be computed as:

$$T_b = 2\pi \sqrt{\frac{W}{gK_b}} \tag{11.9}$$

and thus:

$$T_b = 2\pi \sqrt{\frac{Wh}{gG_R A}} \tag{11.10}$$

where g is the acceleration of gravity.

For the case of relatively slender bearings, with $h/D \geq 0.5$, designed to support the maximum compatible load, Eq.(11.10) may be modified considering Eq.(11.3), and consequently the period will not depend on the plan dimensions, but only on the total height and the shape factor, according to the following equation:

$$T_b = 2\pi \sqrt{\frac{S\gamma h}{2g}} \tag{11.11}$$

Typical relationships between period and height for this specific case are depicted in Fig.11.6.

(i) *Displacement capacity:* As discussed above the maximum displacement capacity of this class of devices may be limited by either plan or height dimensions. Typical design capacities range on the order of 200 mm (7.9 in), with ultimate capacities up to 300 mm (11.8 in).
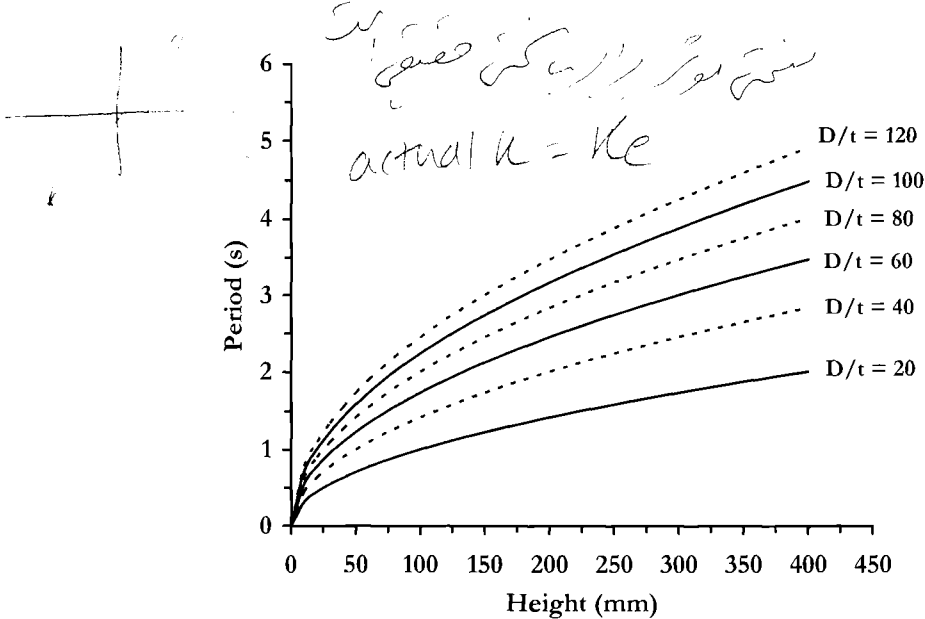
Fig.11.6   Typical Period of Vibration (T_b) vs. Total Height (h) for a Laminated Rubber Bearing Designed to Eq.(11.11)

(ii) Damping: For this class of devices the only available damping has a viscous nature and depends on the properties of the rubber. Standard bearings show a viscous damping of the order of 5% while special high damping rubber bearings (**HDRB**) can reach values on the order of 15 – 20%, related to secant stiffness.

(iii) Re-centering capacity: The obvious consequence of a quasi–elastic response is a complete re-centering capacity, with no residual displacement.

(iv) Maximum force: Again, since there is no equivalent yielding, the maximum transmissible force depends on stiffness and maximum displacement.

(v) Response at failure: At increasing displacement demand, two forms of instability might occur depending on the type of connection to the structure[N3]: Euler instability in the case of bolted bearings, which are able to sustain tensile stresses and are prevented from rotating at each end, and rollout instability with recessed (or doweled) devices (Fig.11.7). Although some tests have shown that rubber may be capable of sustaining quite high tensile stresses, the displacement capacity given by standard design equations implies the conservative assumption of adopting the rollout value as the displacement limit, even when bolted connections are used. This assumption implies a significant potential for sustaining larger displacement demands without dramatic consequences.
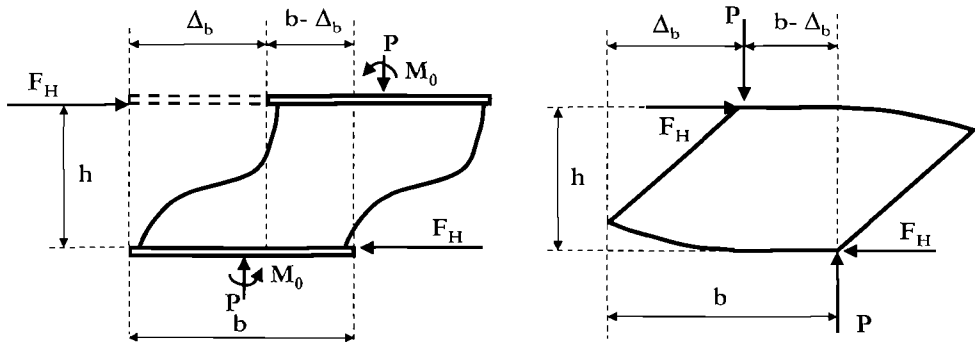
Fig.11.7 Euler (left) and Rollout Instability (right)

i) Problems with axial load: The complex relations between vertical and horizontal response of this class of devices may become a source of difficulty when the device is required to carry relatively low loads associated with a relatively large need for displacement capacity. In this case the bearing diameter is likely to be governed by the required displacement capacity, the average vertical stress is likely to be quite low, and a considerable height may be needed to obtain the desired period of vibration. As shown numerically in example (a) of Section 11.3.1, it is convenient, whenever possible, to design the devices with an average vertical stress reasonably close to their capacity, in order to limit the height of the device and reduce the cost of construction.

In addition, it has to be fully realized that for this class of devices the potential for significant vertical response amplification cannot always be neglected. The vertical stiffness (K_z) of a typical device is normally between 500 and 1,500 times the horizontal stiffness, showing a high variability as a function of the S factor. The vertical stiffness can be calculated according to the following equation, where the sum of the deflection due to the rubber shear strain and to the rubber volume change is considered:

$$K_z = \frac{6G_R S^2 A k}{(6G_R S^2 + k)h} \tag{11.12}$$

where all symbols have already been defined, with the exception of the bulk modulus of the rubber, $k \approx 2,000$ MPa (290 ksi).

The resulting value for the vertical period of vibration is on the order of 0.06 to 0.1 sec (i.e., $\approx 3\%$ of the horizontal one) and may imply some interaction between vertical and horizontal response, particularly for relatively low values of the shape factor.

(b) Lead–Rubber Bearings: Lead-rubber bearings are low-damping laminated rubber bearings with a lead plug inserted in the core of the device[R3]. The purpose of inserting the lead plug is to increase both the stiffness at relatively low horizontal force levels, and the energy dissipation capacity. The resulting horizontal force–displacement curve is a

very stiff

536   Priestley, Calvi and Kowalsky.   Displacement-Based Seismic Design of Structures

combination of the linear response of the rubber bearing, as discussed in the previous section, and the essentially elastic–perfectly plastic response of a confined lead plug.

The lead plug shows an initial shear modulus G_L approximately equal to 130 MPa (18.9 ksi) (i.e. $G_L \approx 130 \; G_R$) and a yield shear strain γ_{yL} of approximately 7.7 %. This implies that the insertion of a lead plug with section equal to $A_L = A_D/n$, where A_D is the original area of the rubber and n is possibly in the range $10 - 20$, produces an increased initial stiffness equal to:

$$K_{LR} = \frac{G_R(A_D - A_L) + G_L A_L}{h} = \frac{A_D G_R(129 + n)}{nh} \tag{11.13}$$

$$\Rightarrow \frac{K_{LR}}{K_R} = \frac{129 + n}{n - 1} \tag{11.14}$$

This is in the range of ten times larger than the initial stiffness of the original rubber bearing (K_R is the stiffness of a rubber bearing with area= $A_D–A_L$).

The yield displacement of the bearing will be governed by the height of the lead plug (i.e., by the height of the device):

$$\Delta_{yL} \approx 0.077h \tag{11.15}$$

The maximum displacement will be still governed by the allowable shear strain in the rubber or by the global stability of the device under vertical load, as expressed by Eqs.(11.5) to (11.7). Assuming that Eq.(11.6) governs, it results immediately that the maximum displacement will be approximately 13 times the yield displacement, with a corresponding value for the displacement ductility.

The post-yield stiffness will obviously correspond to the original stiffness of the rubber alone, reduced in proportion to the reduction of the section. The unloading branch of the force–displacement curve will be approximately parallel to the initial stiffness branch, up to yielding of the lead plug in the opposite direction.

With typical geometries and proportion between lead plug and rubber, the yield force will be in the range of one half of the ultimate force and the post-yield stiffness in the range of one tenth of the initial one.

Displacement capacity, response at failure, sensitivity to vertical input will be similar to those described for the case of rubber bearings.

(i) Equivalent stiffness and period of vibration: As briefly described and shown in Fig.11.8, the initial stiffness of a lead-rubber bearing will be approximately 10 times higher that that of a rubber bearing of similar size (and consequently the initial period of vibration will be reduced by a factor of about 3-4). After yielding, stiffness will be similar to that of the original device. As discussed in section 3.2 with reference to Fig.3.1(b), it is of interest to define an equivalent secant stiffness to the ultimate design displacement, that will be in the range of two times larger than that of the rubber bearing, with a corresponding

reduction of the equivalent period of vibration of the order of 1.4 times. It is also important to note that the secant stiffness to the ultimate displacement is approximately equal to 20% of the initial stiffness, with a corresponding period elongation of more than 100%.
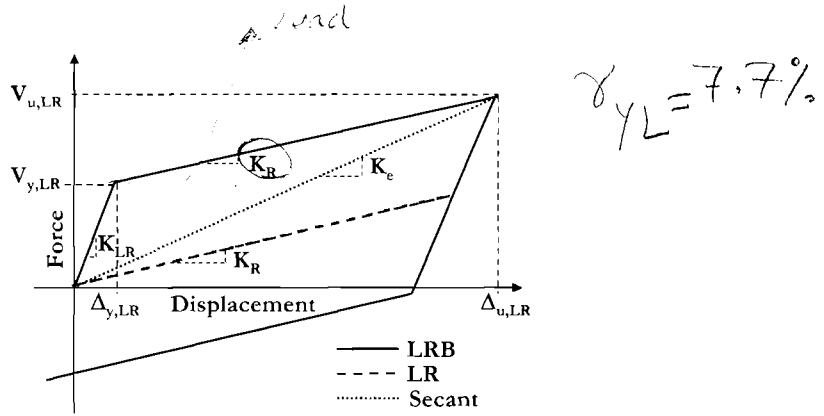

Fig.11.8   Typical Hysteresis Cycle of a Lead–Rubber Bearing

ii) Damping: It is evident from the discussion above that the global response of a device will imply significant energy dissipation due to hysteresis, as discussed in Section 3.4.3. For bilinear systems, the energy–based (or Jacobsen) damping coefficient equivalent to the dissipated energy can be calculated by applying Eq.(3.10), obtaining:

$$\xi_{hyst} = \frac{2}{\pi}\left(1 - \frac{1}{\mu}\right)\frac{V_y}{V_u} \tag{11.16}$$

where $\mu = \Delta_u/\Delta_y$. It has to be noted that this is not the equivalent viscous damping to be used for displacement-based design. The relationship between Jacobsen damping and equivalent viscous damping is discussed in Section 3.4.3 and graphically summarized in Fig.3.15. However, for the expected level of ductility of this kind of device, the reduction factor to be applied in order to obtain the proper value of the equivalent viscous damping is expected to be in the range $0.8 - 1.0$.

Equation (11.6) implies that an increase in strain hardening will result in a lower equivalent viscous damping coefficient, as a consequence of the reduced area of the hysteresis loops.

The curves resulting from Eq.(11.16) are shown in Fig.11.9, where it is evident that elastic-perfectly-plastic (**EPP**) systems have an asymptote at $\xi_h = 64\%$, that for displacement ductilities larger than 5 the curves tend to show only minor variations, and that for the typical values under consideration an equivalent viscous damping coefficient of the order of $20 - 30$ % might be expected.

Alternatively, an appropriate form of Eqs.(3.12) or (3.17f) could be used, having care of considering an appropriate *r* value (*r* gives the ratio of post yielding versus initial stiffness and for this kind of devices may range between 0.1 and 0.2).
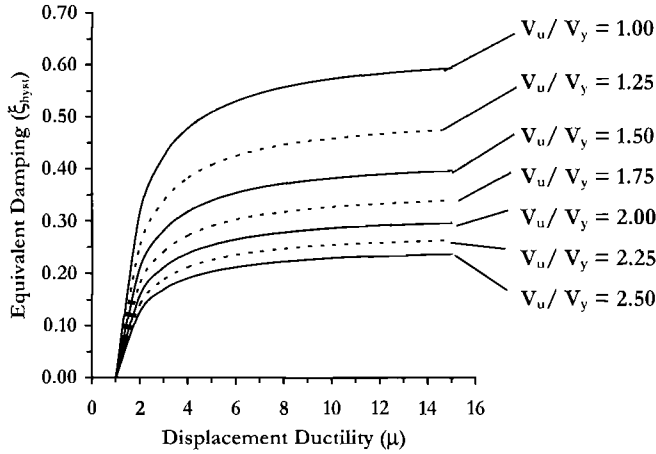

Fig.11.9   Energy–Based (Jacobsen) Equivalent Damping Coefficient for Bilinear Systems, as a function of Displacement Ductility and Force Ratio V_u/V_y

(iii) Re-centering capacity: The re-centering capacity of lead-rubber bearings depends on the ratio between post-yield and initial stiffness and on the ratio between ultimate and yielding strength. The residual displacement depends essentially on the loading history, with a natural tendency to re-center when some significant strain-hardening is shown[P3] due to the different distance to yielding when reloading starts from a displaced position (i.e. a lower force is needed to reach yielding when the force is directed towards the original position: it is essentially the opposite effect of that shown in Fig.3.24(a)).

However, a measure of the re-centering capacity of a device could be expressed as a function of the maximum possible residual displacement, as shown in Fig.11.10. For bi-linear systems as in the present case, the maximum residual displacement (Δ_{Rmax}) can be expressed as follows:

$$\Delta_{R\,max} = \Delta_y\left(\left(\frac{V_u}{V_y}-1\right)\frac{K_{LR}}{K_R}-1\right) \qquad\qquad for\,\frac{V_u}{V_y} \le 2 \qquad (11.17)$$

$$\Delta_{R\,max} = \Delta_y\left(\frac{K_{LR}}{K_R}-1\right) \qquad\qquad for\,\frac{V_u}{V_y} \ge 2 \qquad (11.18)$$

As expressed in Eq.(11.17) – (11.18) and shown in Fig.11.10, the maximum residual displacement is constant if $V_u/V_y \ge 2$. It can be shown that for the typical range of values

for the variable involved, $V_u/V_y \approx 2$ and $\Delta_{Rmax}/\Delta_u \approx 0.8$. Note that some slow recovery of part of the residual displacement has to be expected, because of creep of lead.
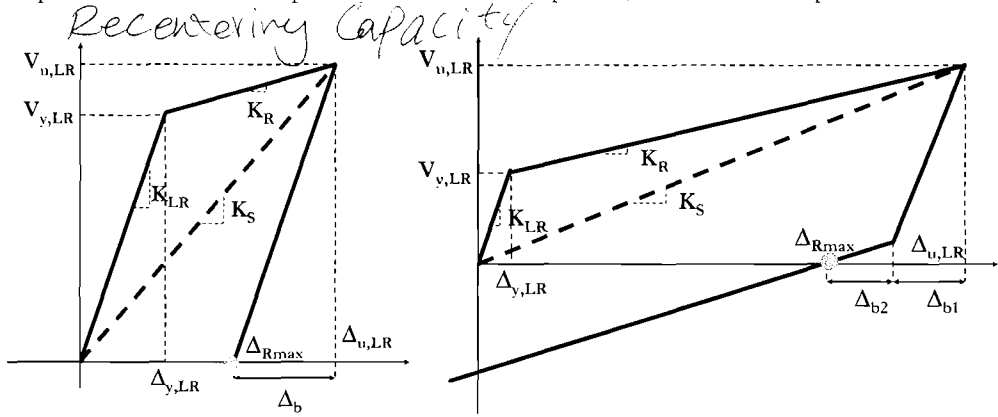

Fig.11.10   Maximum Residual Displacement for Bilinear devices

iv) Maximum force: Clearly the theoretical maximum transmissible force depends on the assumed displacement demand. However, it should be noted that the initial higher stiffness and the presence of some equivalent yielding reduces the potential variation with respect to the previous elastic case. Amplification factors for **CD** protection may thus be lower than in the case of rubber bearings.

(c) Friction Pendulum Devices: The friction pendulum systems of isolation (**FPS**) are based on the properties of a pendulum motion, as obviously implied by their name [Z.2]. The concept is simple, and can be illustrated with reference to Fig.11.11. The structure to be isolated is supported on an articulated teflon-coated load element sliding on the inside of a spherical surface. Any horizontal movement therefore implies a vertical uplift of the supported weight. If friction is neglected the equation of motion of the system is similar to that of a pendulum with equal mass and length equal to the radius of curvature of the spherical surface.

For a pendulum with weight W and radius of curvature R_c it is well known that the period of vibration (T_p) and the associated stiffness (K_p) are:

$$T_p = 2\pi\sqrt{\frac{R_c}{g}}$$

(11.19)

$$K_p = \frac{W}{R_c}$$

(11.20)

where g is the acceleration of gravity.

The expected force-displacement response of an **FPS** bearing is therefore rigid, for horizontal load lower than the resisting friction force at the contact between slider and surface of the bearing, and proportional to K_p for higher loads. If the horizontal force exceeds the friction force level the structure will oscillate with a period of approximately T_p for large displacements (the agreement is exact only if friction is zero).

The resisting friction force can obviously be expressed as a function of vertical load and friction coefficient (μ_f), as:

$$V_f = \mu_f W$$

(11.21)

The force–displacement curve is thus of the kind shown in Fig.11.12, where clearly both the corner point and the inclination of the second branch of the curve are linear functions of the vertical load, while the fundamental design variables are the radius of curvature and the material friction coefficient.

Clearly, there is relatively little control of the friction coefficient, which may normally vary between 2% and 5%. The radius of curvature is in principle a free variable, but its limits are actually a function of acceptable period of vibration, isolated stiffness or maximum residual displacement, often defined by codes of practice. Assuming for example that the pendulum period of vibration should not be longer than 6 sec (as prescribed in [X13]), Eq.(11.19) implies that the radius of curvature should not exceed 9 m (29.5 ft).

Note that there is no theoretical limit to the vertical capacity, since the contact surface between slider and spherical surface can be adjusted to the accepted level of stress, which should be relatively low to avoid unacceptable local deformations and to reduce the risk of high temperatures, as discussed later.
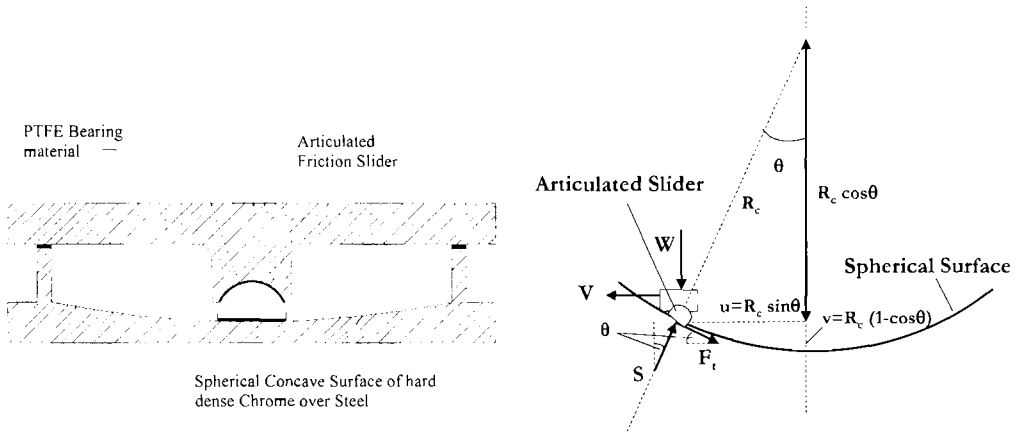

Fig.11.11   Typical Section of an FPS device and Description of Static Equilibrium in Displaced Configuration

(i) Displacement capacity: From the discussion above it is clear that there is no theoretical limit to the displacement capacity of an **FPS** system, provided that a device of the required dimensions can be manufactured. Devices with displacement capacity of the order of 1 m and radius of curvature of the order of 10 m (32.8 ft) have been successfully manufactured. An implicit limit to the horizontal displacement capacity is related to the acceptability of the corresponding vertical displacement, which is a function of the radius of curvature.
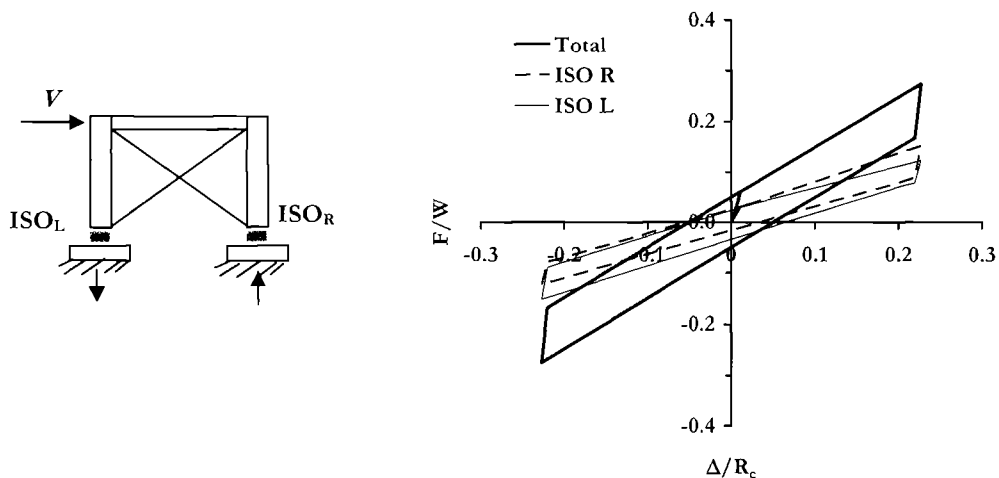
Fig.11.12 Typical Force – Displacement Cycle for an FPS Device, Neglecting any Axial Force Variation

(ii) Equivalent viscous damping: The area–based equivalent viscous damping can be evaluated as discussed in Section 3.4.3, calculating first the energy–based equivalent viscous damping and then applying the appropriate correction factors. The area of a full cycle is in this case equal to:

$$A_h = 4\mu_f W \Delta_m \tag{11.22}$$

The maximum force V_m is equal to:

$$V_m = W\left(\mu_f + \frac{\Delta_m}{R_c}\right) \tag{11.23}$$

and Eq.(3.10) thus becomes:

$$\xi_{hyst} = \frac{2\mu_f}{\pi\left(\mu_f + \dfrac{\Delta_m}{R_c}\right)} \tag{11.24}$$

Note that in the equations above μ_f is used to indicate the friction coefficient, not the ductility (the latter is not definable since the equivalent yielding displacement is equal to zero).

It has to be noted that the value of the friction coefficient (μ_f) has a limited variability, say between 2% and 5%, and that the ratio between Δ_m and R_c has to be limited to relatively small values to avoid excessive vertical displacements. Reasonable values may be between 7% and 15%. Considering these limits, possible values of the energy–based equivalent viscous damping are depicted in Fig.11.13, as resulting from the above discussion. It may be noted that reasonable values of the energy–based equivalent viscous damping obtainable from **FPS** systems are not larger than 20%. Also in this case, the correction factor discussed in Section 3.4.3 is expected to be close to unity and neglected.
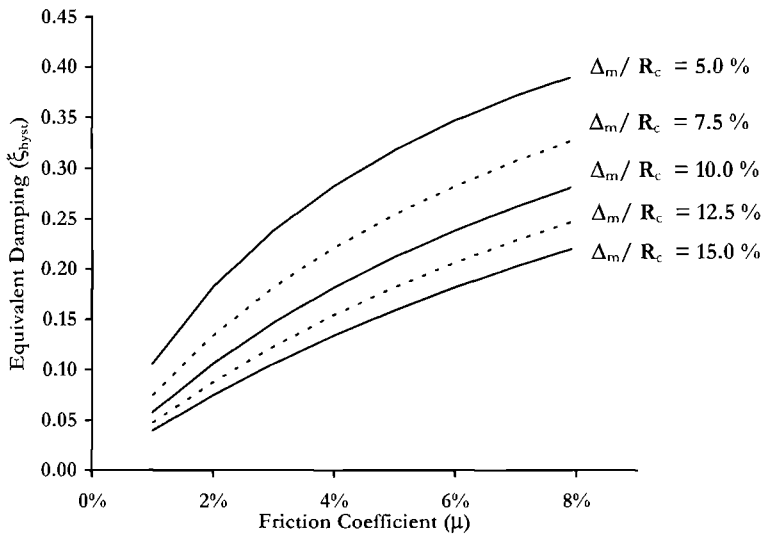
Fig.11.13   Equivalent Damping of an FPS Device, as a Function of Friction Coefficient and Ratio between Displacement Capacity and Radius of Curvature

(iii) Re-centering capacity: **FPS** systems exhibit favourable self-centering characteristics and calculation of the maximum possible residual displacement is straightforward. With reference to Fig.11.12, it is obvious that the maximum residual displacement does not depend on the maximum displacement demand, nor on the characteristics of the accelerogram, but only on the values of the equivalent yielding force and of the post–elastic stiffness, provided that the displacement demand is large enough to produce a force variation due to the pendulum stiffness larger than the equivalent yielding force. It is thus possible to express the maximum residual displacement, $\Delta_{R,max}$, according to the following equations:

$$\Delta_{R\,max} = \frac{V_y}{K_p} \tag{11.25}$$

and considering Eq.(11.20) and (11.21):

$$\Delta_{R\,max} = \mu_f R_c \tag{11.26}$$

As already discussed, maximum horizontal displacements should be less than $7 - 15$ % of the radius of curvature. This implies that the maximum residual displacement may be in the range of 20% to 50% of the displacement capacity. For standard cases, the maximum residual displacement will therefore be approximately 50% lower than for the case of lead-rubber bearings. Again, and for the same reasons, the actual residual displacement will generally be considerably smaller, and will depend on the actual input. Also in this case there is a natural tendency to re-center for subsequent cycles, due to the positive post–elastic stiffness. Some additional re-centering may also be expected during the final phases of motion, due to lower friction coefficient at lower velocities.

However, **FPS** system would not act as re-centering devices towards slow action such as thermal induced displacements, since the friction will keep the device in the deformed position.

(iv) Axial action effects: Considering Eq.(11.20) and (11.21), it is obvious that both equivalent yielding force and post–yielding stiffness directly depend on the supported weight, or, to state it more properly, on the axial force, which may vary significantly during the response.

A study on this subject[C14], dealing with bridge structures, has shown that a proper consideration of the effects of axial force variation is generally not relevant for determination of displacement demands, but may have significant effects on the shear force transmitted through the device, with variations that could exceed 60% to70% in curved bridge configurations, and/or when the vertical component of the ground motion is considered.

If not recognized in the design phase by appropriate capacity protection, such variations may result in undesired deformation modes, including shear and torsion failure.

For the case of bridges, these variations depend mainly upon the geometric configuration of the bridge and the magnitude of the vertical ground motion. In particular, large values are expected (i) as the bridge horizontal radius of curvature decreases, (ii) the pier/deck mass ratio decreases, and (iii) the vertical component of the record is considered.

(v) Heat problems: **FPS** systems may be particularly sensitive to problems related to increase of temperature due to high values of power per unit surface produced at the contact between roller and spherical surface. Some discussion of this issue is presented in Section 11.2.5.

(vi) Response at failure: **FPS** systems do not show any specific failure mode, since their response is unvaried up to the displacement capacity limit. Because of this reason, a limiting device in the form of a circular ring is normally provided. This implies that reaching the displacement capacity results in a sudden increase of the transmitted force. It is therefore appropriate to be conservative in defining the design displacement.

11.2.4 Dissipative Systems

(a) General: Typical passive energy dissipation devices considered in this text can be grouped in two main categories: (1) hysteretic or (2) viscoelastic devices. Devices of the first kind are normally based on metallic yielding, and consequently their dissipation capacity depends essentially on relative displacements. Devices of the second kind are based on deformation of viscoelastic polymers; their dissipation capacity is therefore a function of both relative displacements and velocities. Dampers based on different principles have been developed in the past, such as lead-extrusion dampers, and more recently, such as magneto–rheological and electro-inductive devices. They will not be explicitly addressed here, since no essential difference arises from a design point of view. Their properties and basic principle are extensively presented elsewhere [D4, X15]. Active dampers will not be examined in this book, since their potential for convenient application to seismic problems is still questionable. A comprehensive presentation of energy dissipation devices is given in [H6].

Dampers have the common property of modifying the structural response by increasing the energy dissipation, and consequently the equivalent viscous damping, with the insertion of a controlled system of internal forces. In general dampers are not capable of transmitting forces in directions other than the one of action and, therefore, cannot be used as isolating systems.

(b) Steel Dampers: Typical metallic dampers are characterized by a force–displacement law similar to the stress–strain relation of the material (normally steel) used to produce the device. Many types of dampers have been designed, with the common aim of maximizing the dissipation capacity, by having similar levels of strain throughout the damper. In the case of a flexural response this objective can not be achieved, since in each section the strain will vary linearly from the outer fiber to the neutral axis. It is however possible to reach the yield strain at both outer fibers of each section at the same time assuring that practically all material will plasticize. Consider the case of a cantilever element (Fig.11.14) where the goal is to determine the optimal shape to maximize the energy absorption, while requiring that full plasticization in each section occurs at the same value of applied load *F.*

If it is assumed that section depth varies only on the side perpendicular to the direction of the applied load (as in Fig.11.14(a)), the following equations apply (symbols refer to Fig.11.14):
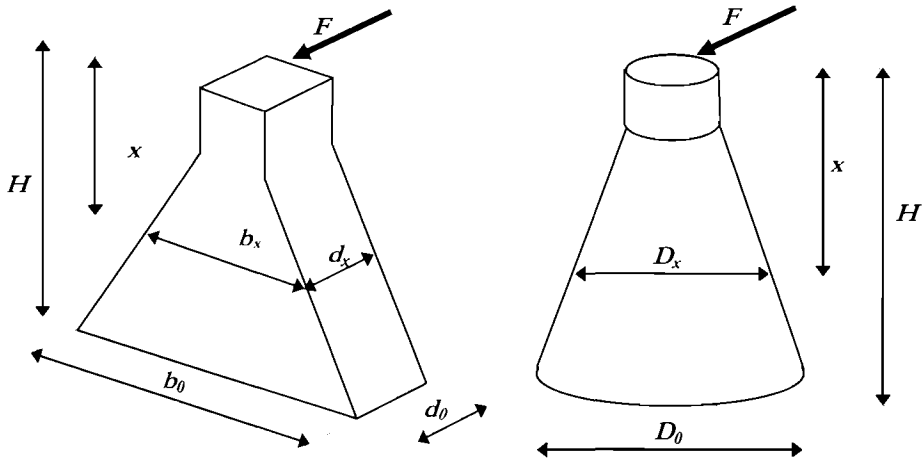
$$M_{P0} = \frac{b_0 d^2}{4} f_y \tag{11.27}$$

$$M_{Px} = \frac{b_x d^2}{4} f_y \tag{11.28}$$

$$M_{Px} = M_{P0} \frac{x}{H} = \frac{b_0 d^2}{4} f_y \cdot \frac{x}{H} \tag{11.29}$$

$$b_x = b_0 \frac{x}{H} \tag{11.30}$$

As a result, a linear variation of the side dimension is obtained.

(a)Rectangular; uni-directional   (b) Cylindrical, omni-directional

Fig.11.14 Optimal Shape for Cantilever Steel Dampers

If section depth varies only on the horizontal direction parallel to the direction of the applied load, equations similar to Eq.(11.27) – (11.29) will lead to:

$$d_x = d_0 \sqrt{\frac{x}{H}} \tag{11.31}$$

The resulting dimension of the section should vary with the square root of the height, a shape which is often defined as an "hour–glass".

If both sides are varied, at any level x the following hyperbolic relation between the sides would define the optimal shape:

$$d_x b_x^2 = d_0 b_0^2 \frac{x}{H} \rightarrow d_x b_x^2 = const(x) \tag{11.32}$$

where $const(x)$ indicates a linear function of x. Analogously, if a conical shape is adopted, as in Fig.11.14(b), the diameter should vary along the height of the device according to the following relation:

$$D_x = D_0 \left(\frac{x}{H} \right)^{1/3} \tag{11.33}$$

A linear variation of the diameter (as in Fig.11.14(b)), or of both sides of a square section, is generally considered an acceptable approximation of the optimal shape. A conical shape is clearly the only viable solution if the direction of the load is unknown.

This kind of reasoning has resulted in the production of a number of different dampers, based on flexural, shear or torsional response shaped in a variety of geometries.

In all cases, the allowable number of cycles is a function of the strain amplitude, as shown in Fig.11.15. Typical limit values for the material tension strain are in the range of a few percent, therefore allowing several tens of cycles at maximum amplitude.
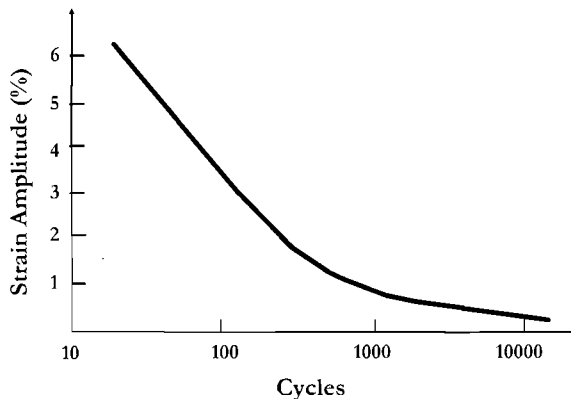
Fig.11.15 Fatigue Life for the Steel used for a Typical Damper

(i) Displacement capacity: As previously noted, the displacement capacity is essentially governed by the accepted material strain, but as a consequence of the possibility of defining any sort of geometry that suits the specific problem to be faced, there is no inherent limit.

As an example, consider again the case of the cantilever device shown in Fig.11.14(a). The top displacement can be computed as the section curvature (ϕ_x) multiplied by the

height (x), integrated along the height:

$$\Delta_x = \int_0^H \varphi_x \cdot xdx \tag{11.34}$$

with the curvature computed as two times the extreme fiber strain (ε_x) divided by the section depth d, constant over the height:

$$\Delta_x = \int_0^H \frac{2\varepsilon_x}{d} xdx = \frac{\varepsilon_x H^2}{d} \tag{11.35}$$

This equation will apply for both the yield displacement (with $\varepsilon_x \approx 0.2\%$) and the ultimate displacement (with ε_x possibly $\approx 3\%$, i.e. a ductility of the order of 15). Note that H and d will determine displacement capacity and stiffness, but they cannot be considered completely free parameters, since they have to be compatible with the required moment and shear capacity, which may be unknown at this point in the design phase.

(ii) Damping: The hysteresis loops of a steel damper are normally similar to those of the material itself. Since mild steel is normally used and the maximum strain is limited by fatigue problems, strain hardening is minor and apparent only when approaching the design displacement. As a consequence, very "fat" cycles are obtained, that may lead to the assumption that the hysteretic component of the equivalent viscous damping should be close to that of an elastic–perfectly–plastic system. Actually, for such cases, the discussion presented in Section 3.4.3 suggests that large correction factors should be applied, both to the viscous and to the area-based hysteretic component of the equivalent viscous damping. As a consequence, it is not easy to exceed values on the order of 30%.

As an example, consider that applying Eq.(3.12), and using the data given for a Ramberg–Osgood curve, with ductility equal to 15 and period equal to 2 second, the hysteretic component of the equivalent viscous damping equals to approximately 24 %. From Eq.(3.16) a correction factor for the elastic component of about 0.2 or 0.85 is computed, respectively for the tangent and initial stiffness case .

(iii) Re-centering capacity: The shape of the hysteresis cycle, discussed above, implies that steel dampers have poor re-centering capacity, unless coupled with spring-type elements, which will have the obvious consequence of modifying the combined loop shape. Clearly, this does not apply to low-level actions, such as small earthquakes and thermal effects: in such cases yielding is unlikely to take place and full re-centering capacity should be expected.

(iv) Response at failure: The limitation of the strain corresponding to the design displacement, already discussed, and the strain-hardening that should be expected at larger displacement values, imply that a good response should be expected for larger than expected demand. Failure will take place only for demands that should exceed

approximately two times the design displacement.

(c) ***Viscous Dampers:*** Viscous dampers are characterized by a constitutive law where the force (F) is a function of velocity (v):

$$F = Cv^\alpha \tag{11.36}$$

In the above equation, C is a constant expressed in units of a force divided by a velocity (kNs/m), and α is also a constant, normally in the range of $0.1 - 0.3$. The resulting curves are depicted in Fig.11.16, where it is evident that a lower value of α will result in a force that tends to be less dependent on the velocity.

Theoretically, for this class of devices the actual transmitted shear force cannot be calculated a priori, since it depends on the effective velocity of the system, but if the value of α is kept reasonably low (a value of $\alpha = 0.1$ is commonly used), the shear force tends to be similar to C

It may be noted that for large α values (greater than 2) the forces transmitted tend to be very low for low-velocity relative movements and to increase rapidly to very large values for increasing velocity. This is typically the case for lock–up devices, used for example in bridge movement joints, when slow movements due to temperature variations are permitted and relatively high-speed displacement demands (due for example to vehicle breaking forces) should be limited.
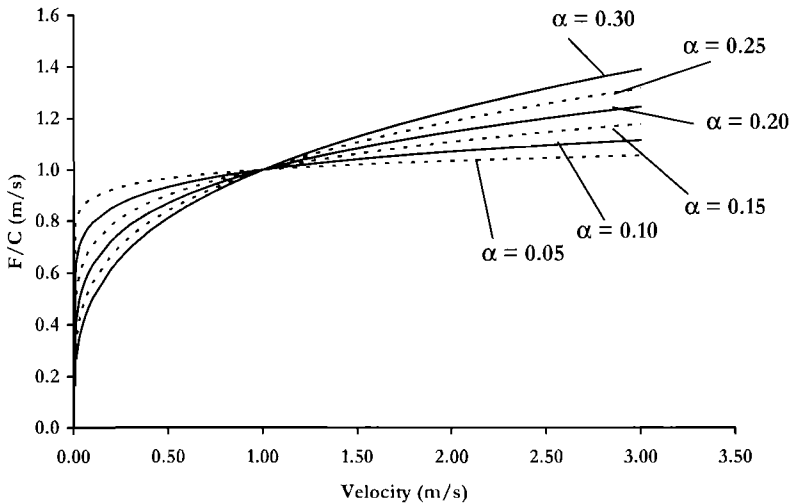
Fig.11.16   Axial Force in a Viscous Damper, as a Function of its Basic Parameters α and C (both axes are expressed in the same velocity units)

Viscous dampers are normally mounted in parallel with some other device or in structural locations where some elastic re-centering force is provided.

If $\alpha = 1$, the force–displacement loop corresponding to Eq.(11.36) is an ellipse (see Fig.11.18), described by the following equation:

$$\frac{F}{\Delta_D C \omega} = \pm \sqrt{1 - \left(\Delta / \Delta_D\right)^2} \tag{11.37}$$

where $\omega = 2\pi / T$ is the circular frequency, and Δ_D is the maximum displacement.

If $\alpha < 1$ is introduced, the ellipse tends to become closer to a rectangle.

The maximum force can be derived from Eq.(11.37), for $\Delta = 0$ as:

$$F_D = \Delta_D C \omega = \frac{2\pi C \Delta_D}{T} \tag{11.38}$$

(i) Displacement capacity: There is no inherent limit for the displacement capacity of hydraulic dampers. Specific limits will only depend on the length of the device. However, it has to be noted that the force to be transmitted may be limited by buckling potential. This is often not an issue, since in most cases this class of devices is used when there is a need for accommodating relatively large displacements combined with limited forces. In the case of the Rion–Antirion bridge[12] devices with a stroke of 1750 mm (68.9 in) and a force capacity of 3.5 MN have been manufactured and mounted to connect the cable-stayed deck to the piers (four for each pier), as shown in Fig.11.17. Note that five devices are present: the fifth one is a locker fuse, which does not allow any relative movement between deck and pier for relatively low shear forces. In the case of an earthquake, it breaks and the four dampers become operational. Similar devices, with a stroke of 2600 mm (102.4 in) were mounted at the transition piers at both ends of the bridge.

(ii) Viscous stiffness and damping: The typical steady–state force–displacement loop for a hydraulic damper is depicted in Fig.11.18. The large amount of energy dissipated per cycle is immediately evident, corresponding to the area included in the loop. The area of the loop can be calculated by integration, giving, for the purely theoretical case of $\alpha = 1$:

$$A_h = \pi F_D \Delta_D = \frac{2\pi^2 C \Delta_D^2}{T} \tag{11.39}$$

where T is the period of vibration, that may vary from cycle to cycle, depending on the excitation, and all other symbols have already been defined. For $\alpha \ll 1$, the area of the loop tends to become closer to $4F_D \Delta_D$.

In this case it is not appropriate to talk of hysteretic damping, since the dissipation mechanism is actually of a viscous type.
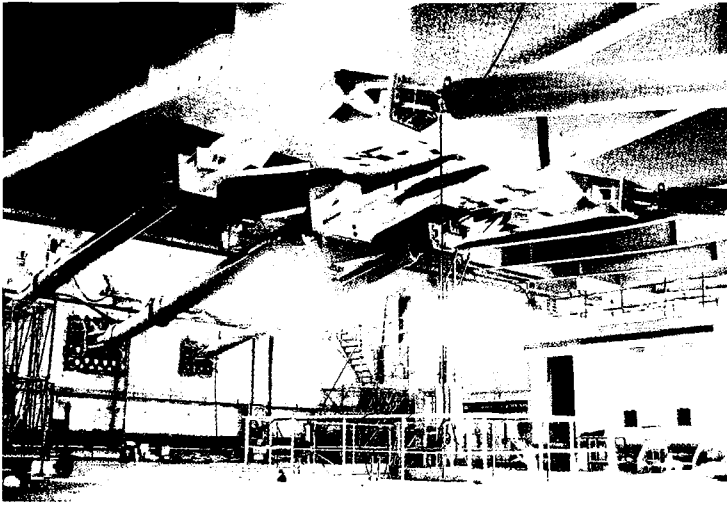
Fig.11.17   Viscous Dampers and Locker Fuse Connecting Deck and Pier of the Rion–Antirion Bridge (courtesy of FIP Industriale)
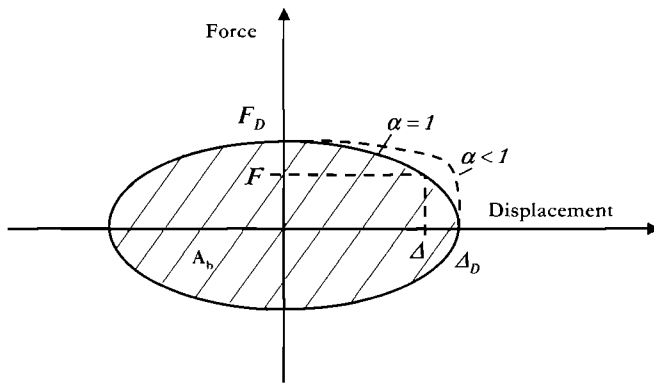

Fig.11.18   Variation of a Typical Force–Displacement Loop of a Viscous Damper as a Function of the α Value.

As already pointed out, however, some structural or artificial elements normally provide some elastic force in parallel with the viscous damper, as shown in Fig.11.19(a). The resulting global loop is depicted in Fig.11.19(c) and its actual shape depends essentially on the ratio between damper maximum force F_D (corresponding to zero displacement) and elastic maximum force F_S, corresponding to the maximum displacement, equal for the two systems (i.e. $\Delta_S = \Delta_D$).

Considering Eq.(11.39) in combination with Eq.(3.10), the area-based equivalent viscous damping for $\alpha = 1$ is:

$$\xi_h = \frac{A_h}{2\pi F_e \Delta_S} = \frac{\pi \Delta_D F_D}{2\pi F_S \Delta_S} = \frac{F_D}{2 F_S} \qquad (11.40a)$$

When α is small, say $\alpha < 0.2$, the damping hysteresis loop is closer to a rectangle than to an ellipse (see Fig.11.20). In this case it is more reasonable to base the effective stiffness on the sum of the elastic and damping forces: i.e. $K_e = (F_S + F_D)/\Delta_S$. Conservatively estimating the loop area to still be given by Eq.(11.39), the area-based equivalent viscous damping will then be

$$\xi_h = \frac{F_D}{2(F_S + F_D)} \qquad (11.40b)$$

(a) Elastic Force   (b) Viscous Damper   (c) Visco-Elastic Response
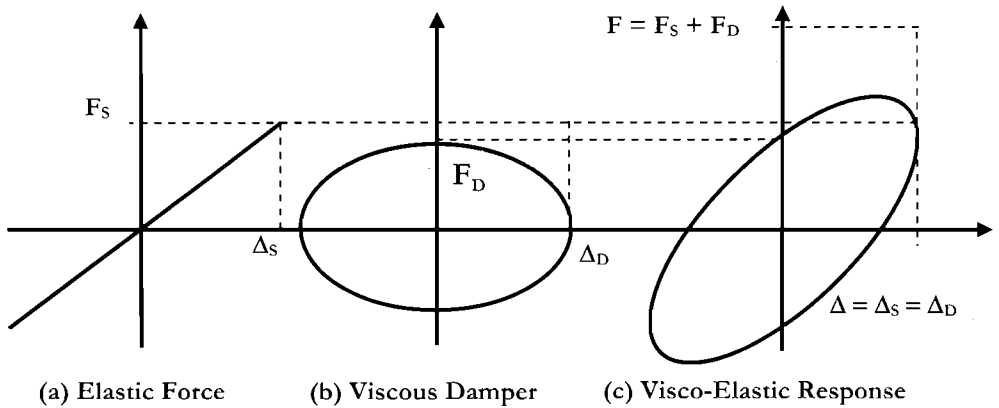
Fig.11.19 Typical Force – Displacement Loop Resulting from the Combination of a Spring Element and a Viscous Damper

It is therefore clear, once more, that the equivalent viscous damping diminishes with the increase of the re-centering force. A graphical explanation of Eq.(11.40) is depicted in Fig.11.20 for the common case of $\alpha \approx 0.1$, with the viscous damping approximated as a rectangle. A 25% equivalent viscous damping is obtained for $F_S = F_D$, in which case little re-centering should be expected at the end of the time history, while for $F_S = 2F_D$ the damping is reduced to 16.7%, while the residual displacement is halved.

Clearly, and as already discussed, these damping values are appropriate for the response of the isolator system, comprising damper plus spring element, alone; when combined in a structural system, there will be additional structural deformation and possibly additional (frictional) force. As a consequence, the structural damping coefficient may be lower.

It is noted that the force, and hence the acceleration, of the damper is higher at small displacements, being therefore out of phase with respect to the structure response force.
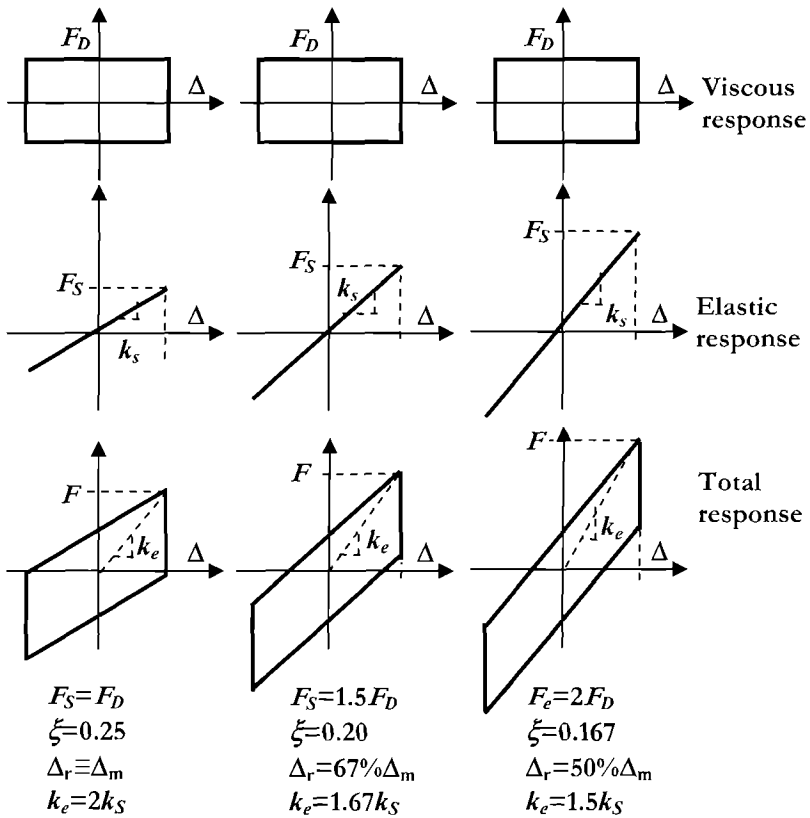
Fig.11.20   Combination of Viscous and Elastic Response for Various Values of
F_D / F_S

As already noted, for the normal case of dampers with low α the evaluation of the equivalent secant stiffness is:

$$K_e = \frac{F_e + F_D}{\Delta_e}$$
(11.41a)

While for $\alpha = 1$ it is:

$$K_e = \frac{F_e}{\Delta_e}$$
(11.41b)

(iii) Re-centering capacity: Devices of this kind are obviously unable to provide any re-centering, unless prestressed, or mounted in parallel with some spring–like element. As

noted, in this case there is a significant reduction of the damping and the re-centering capacity at the end of the ground motion can become significant with low expected residual displacements. Note, however, that when coupled with a spring element, the residual displacement will tend to diminish and become negligible for any value of the elastic force, since the spring force will tend to slowly reposition the damping device at the end of the ground motion.

(d) Electro-Inductive Devices: The response of these devices is based on a rotating system basically composed of two plates with permanent magnets and a conductive non-magnetic material and an endless screw to convert the linear earthquake motion into a rotation of the plates. The consequence is a generation of electrical power from vibration due to earthquake, which limits and damps the motion. The relative rotation velocity can be modified by a suitable selection of the ratio between linear and rotational motion. Their response is expressed by the same equation as hydraulic dampers (Eq.(11.37)).

Advantages of these devices are low maintenance, no ageing effects, no limitations on life cycles, low variability of the response and no temperature sensitivity. Though very promising for the future, no actual application is yet known.

(e) Electro and Magneto-rheological Dampers: Electro and magneto–rheological dampers typically consist of hydraulic cylinders containing micron-sized dielectric or magnetically polarizable particles suspended within a fluid. With a strong electric or magnetic field, the particles polarize and offer an increased resistance to flow. Varying the magnetic field strength has the effect of changing the apparent viscosity, allowing different non-linear, force–displacement loops to be obtained. These devices have to be used within a semi-active system and for this reason are simply mentioned here.

(f) Shape Memory Alloys Dampers: The development of devices based on shape-memory alloys has not yet reached sufficient maturity to allow them to be recommended for any practical application. However it is of some interest to briefly introduce the main features of devices that may be developed in the near future from shape-memory alloys.

They are based on binary or ternary metallic alloys that can be found in two different stable phases (austenite and martensite) at different thermo-mechanical states. The austenitic phase is stable before the application of stress; at a critical stress level the martensite becomes stable, yielding and showing a stress plateau; at larger strains the stiffness increases since they cause the martensite state to respond quasi–elastically.

The resulting typical force displacement loop is of the kind shown in Fig.11.21, with a strong tendency to recover the initial shape as soon as the external action is removed (a similar effect can be produced by an increasing temperature).

The resulting loop shape is of the flag–type, discussed in Section 3.4.3 (see Fig.3.9), with an optimal response in terms of re-centering capacity and an equivalent viscous damping of the order of 10%, as expressed by Eq.(3.17d).
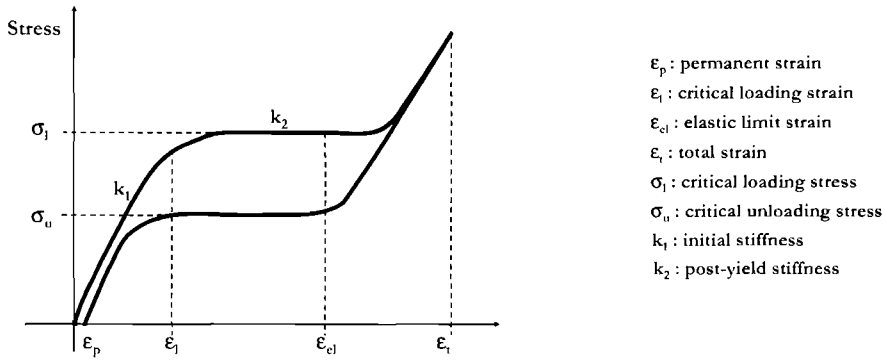
Fig.11.21 Typical Force–Displacement for Shape Memory Alloy Devices

11.2.5 Heat Problems

Any kind of device dissipating energy obviously produces heat, which will result in an increased temperature of the device itself before it is dispersed in the environment. A significant variation of the temperature may result in modified properties or may induce damage and possibly failure, as already mentioned for the case of friction pendulum systems. It is therefore of interest to briefly address the problem of evaluating the potential temperature increment for different device typologies.

To allow some comparison, we assume in all cases a period of vibration equal to 2 sec., a maximum displacement of ±250 mm (9.8 in) and we further assume 5 full reverse cycles at maximum amplitude.

(a) Steel Damper: Consider first the case of a steel damper working in pure flexure and in single bending, shaped like the conceptual device shown in Fig.11.14(a). The side of the rectangular section will therefore vary along the height, according to the expressions of Eq.(11.30) and the total height of the device will be equal to *H*. As discussed with reference to Fig.11.14, the strain at the extreme fiber of each section will be always equal. We assume a yield stress equal to $f_y = 350$ MPa (50.7 ksi), no strain–hardening and a design strain equal to $\varepsilon_d = 3\%$.

The energy dissipated per cycle (E_c) can be estimated according to the following equation:

$$E_c = 4 \int_0^H M_x \varphi_x dx \tag{11.42}$$

where M_x and ϕ_x are the plastic moment and the maximum curvature (corresponding to the design strain) of each section:

$$M_x = \frac{f_y b_x d_0^2}{4} \tag{11.43}$$

در رسم آلرجع (۱۱) وحوی ت سکست

$$\varphi_x = \frac{2\varepsilon_x H}{d_0 x} \tag{11.44}$$

The numerical result depends on the shape of the device (Eq.(11.30) to (11.33)). Assuming a linear variation of the sides and substituting we obtain:

$$E_c = 2 f_y \varepsilon_x b_0 d_0 H \qquad \Longleftarrow \qquad ربر \tag{11.45}$$

The temperature increase per cycle, assuming zero dissipation to the environment, can be evaluated as follows:

$$\Delta T = \frac{E_c}{C_t \rho V} = \frac{6 f_y \varepsilon_x}{C_t \rho} \tag{11.46}$$

where C_t is the thermal capacity of the steel (= 0.502 kJ/kg°C), ρ is the mass density, (7,850 kg/m³) and V is the volume of the device (V as well depends on the shape; for a linear variation: $V = b_0 d_0 H/3$). The resulting temperature increase is equal to $\Delta T = 5.25$ °C per cycle, or 26.3 °C total for five cycles, a value with no practical consequences.

(b) Lead-Rubber Bearing: Consider now the case of a **lead-rubber bearing**, assuming that the dissipation will take place in the lead plug only, with a yield shear strength of $\tau_y =$ 10 MPa (1450 psi) and a design shear strain $\tan\gamma = 1$.

The energy dissipated per cycle per unit volume is now:

$$E_c/V = 4 \tau_y \tan\gamma \tag{11.47}$$

and the temperature increase per cycle, as in the previous case, is:

$$\Delta T = \frac{E_c/V}{C_t \rho} \tag{11.48}$$

with C_t = 0.129 kJ/kg°C , and $\rho = 11,340$ kg/m³ in the case of lead. The resulting temperature increase is equal to $\Delta T = 27.3$ °C per cycle, or 136.5 °C total for five cycles, a value that raises some more concerns than in the previous case, since at this temperature level the mechanical properties of lead are significantly changed[R3].

(c) High-Damping Rubber: In the case of a high damping rubber bearing, we assume a viscous damping ratio equal to $\xi = 0.16$, a shear modulus of rubber equal to $G_R = 1.4$ MPa (203 psi) and a design shear strain $\tan\gamma = 2$.

The energy dissipated per cycle can be obtained deriving A_h from Eq.(3.10):

$$E_c = 2\pi \frac{GA}{h} \Delta_d^2 \xi \tag{11.49}$$

where A and h are the area and the height of the device (and therefore GA/h is the shear stiffness) and the design displacement Δ_d is equal to $2h$, considering the assumed shear strain.

The temperature increase per cycle can be calculated as in the previous cases, considering for the case of rubber $C_r = 0.8$ kJ/kg°C and $\rho = 1,100$ kg/m³. The temperature variation is thus equal to $\Delta T = 6.4$ °C per cycle, or 32 °C total for five cycles.

(d) FPS Bearing: Finally, take into consideration the case of a friction pendulum device (**FPS**). The total energy to be dissipated can immediately be calculated as the product of the average friction force (μW) and the total cumulative displacement between the two faces of the device. The potential for temperature increase, however, is essentially related to the produced power, whose average value is the energy divided by the total duration time, since the limited time would not allow any significant heat dispersion.

The crucial issue for an **FPS** is to keep the local pressure (or stress f_n) low enough to avoid too high values of produced power per unit of surface (p_u), that can be computed as follows:

$$p_u = \mu f_n v_m \tag{11.50}$$

where, μ is the friction coefficient and v_m is the average velocity during a full cycle.
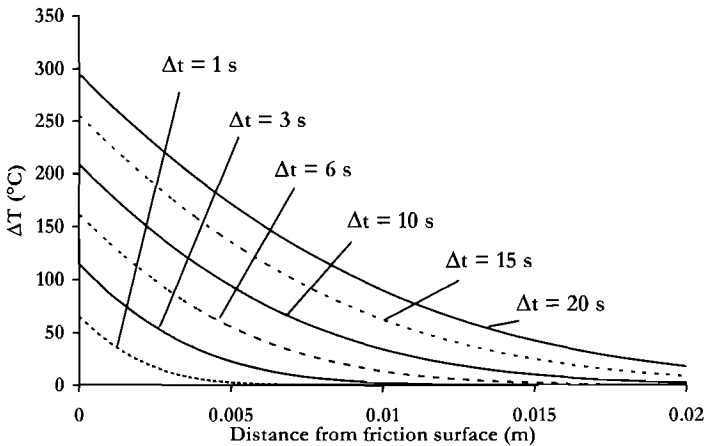

Fig.11.22   Temperature Increase with Distance from Contact Surface between Roller and Spherical Surface of an FPS device (data given in the text)

For example if it is assumed that $\mu = 0.05$, $f_n = 35$ MPa (5076 psi), $v_m = 0.5$ m/s (19.⁻ in/s), the resulting power per surface unit is equal to 0.87 MW/m².

The variation of the temperature in the device can be approximately calculated assuming that the heat produced at the contact between roller and spherical surface partially propagates into a cylindrical element supporting the roller, without any external dispersion. If it assumed that 50% of the produced power (thus in this case 0.435 MW/m²) is transformed into a thermal flux, and the following properties for stainless steel are used: thermal capacity C_t = 477 J/kg°C, conductivity λ = 14.9 W/m°C, mass per unit volume ρ = 7,850 kg/m³, the results obtained solving the Fourier equation are depicted in Fig.11.22. It is there evident that the local expected increase in temperature for a duration (Δt) of 10 seconds is larger than 200 °C. Since high temperatures may produce local damage to the coating of the spherical surface, it is generally recommendable to perform full scale dynamic testing, with appropriate input to verify performance.

11.2.6 Structural Rocking as a Form of Base Isolation

(a) Typical Response: If a controlled rocking at the base of a structure is permitted, the structural response can be regarded as a form of base-isolated response, since the base bending moment cannot increase beyond the values at which rocking starts. The effective stiffness and period of vibration depend essentially on the rocking motion characteristics, and effective damping may be produced by radiation into soil or by *ad hoc* devices.

Consider as an example the structural wall shown in Fig.11.23, where all symbols used in the following are also defined. Applying an external force F at a height H_e, and assuming that it is large enough to induce rocking, the equation of equilibrium in a displaced position can be written as:

$$F\left(H_e + \Delta_r \frac{l_w - a}{2H_e}\right) = R_t\left(l_w - c - \frac{a}{2}\right) + W\left(\frac{l_w - a}{2} - \Delta\right)$$
(11.51)

where R_t is a force restraining uplift, located at a distance c from the wall end. Assuming $a \approx 0.1\, l_w$, the previous equation can be simplified as:

$$F \approx \frac{W(0.45l_w - \Delta) + R_t(0.95l_w - c)}{H_e + 0.45l_w\Delta_r/H_e}$$
(11.52)

The second term of the denominator of Eq.(11.52) is normally less than 1% of H_e, and can therefore be neglected. Equation (11.52) can thus be rewritten as the equation of a line in a plane F–Δ, as shown in Fig.11.24:

$$F = \frac{0.45l_wW}{H_e} + \frac{0.95l_w - c}{H_e}R_t - \frac{W}{H_e}\Delta$$
(11.53)
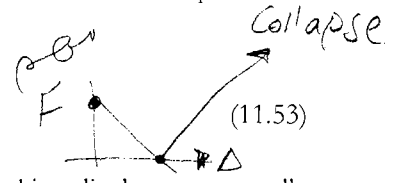
Note that the tensile force R_t can be proportional to the rocking displacement, totally or partially (e.g. when provided by unbonded restraining cables, with or without

prestressing). In this case the corresponding term will not be constant and will affect the slope of the line rather than its initial point.
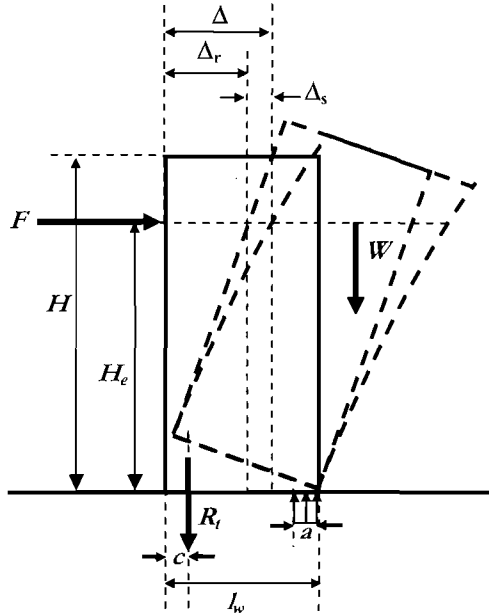

Fig.11.23   Equilibrium of a Rocking Wall in a Displaced Position

(b) Displacement Capacity: From Eq.(11.53) and from Fig.11.24, the displacement corresponding to zero force may be evaluated as:

$$\Delta_u = 0.45 l_w + (0.95 l_w - c)\frac{R_t}{W} \qquad when \quad \xi = 0 \tag{11.54}$$

An acceptable design displacement can therefore be defined as a fraction of Δ_u, say $0.3\Delta_u$, that also corresponds to the accepted strength decrease with respect to the force initiating the rocking motion. Note, however, that the design displacement resulting from non-structural damage limitation will govern in most cases; only for very slender walls ($H/l_w > 20$) can the maximum displacement be limited by the rocking motion.

(c) Damping: The equivalent viscous damping resulting from radiation damping[P4] is generally very small, and therefore negligible, except for squat walls, in which case it is unlikely that the earthquake will induce rocking. The damping can become significant if dissipating devices are introduced, for example as ductile tensile restraints. In this case the equivalent viscous damping will depend on the device characteristics.
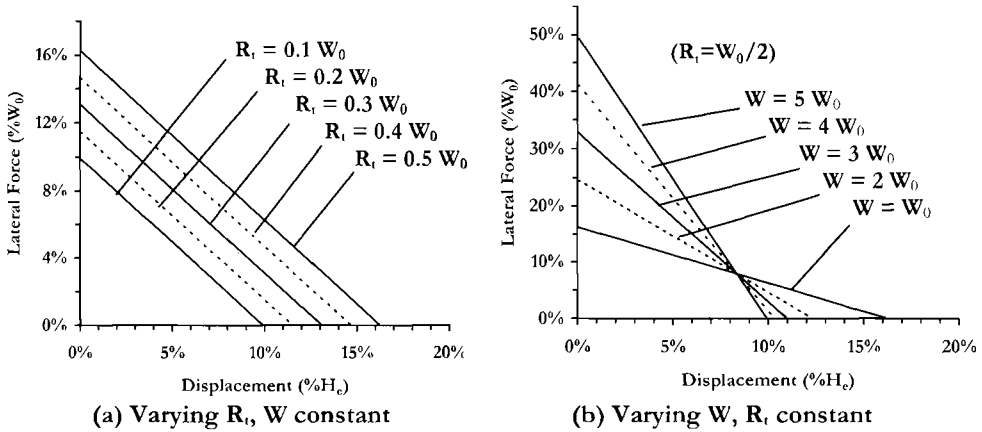
(a) Varying R_t, W constant

(b) Varying W, R_t constant

Fig.11.24 Force – displacement domain for a rocking wall, as a function of tensile force capacity (R_t) and total weight (W)

11.3 DISPLACEMENT-BASED DESIGN OF ISOLATED STRUCTURES

11.3.1 Base-Isolated Rigid Structures

The simplest design case is that of a structure whose fundamental isolated period is several times longer than the fundamental period of the structure alone, assuming a rigid base. This case may correspond to simple one or two-storey buildings, to concrete tanks (but in this case care should be used in evaluating the interaction between the response of the isolated structure and the sloshing modes of the contained liquid), to reactor buildings, etc. In such cases a rigid structure approximation, i.e. based on a **SDOF** system, with natural period and damping ratio corresponding to those of a model made by the isolation system and the mass of the building, gives accurate results in terms of prediction of displacement and force demands on the isolation system. In this context, "rigid structure" means that the period of vibration of the isolated model where the structure is simply considered as a rigid mass is several times (say at least 3) longer than the first natural period of vibration of the model of the structure alone, assuming a rigid base. This requirement can be more appropriately verified by comparing the expected displacement demand of the structure alone, considered to respond elastically (e.g. for a reinforced concrete frame applying Eq.(5.7a)) and the expected displacement demand of the isolation system.

In this case it is generally acceptable to separately design the structure and the isolation system, combining them together only for time-history analysis, if conducted. In general, however, care should be taken to check that higher-mode effects are considered, since they may be very significant in multistory isolated buildings.

The structure will normally have been subjected to a preliminary design for non–seismic load combinations, or for conventional horizontal base shear, possibly in the range of 5 to 10% of gravity. It can be assumed that the preliminary design will at least permit the total mass of the building to be accurately estimated. The potential need for some increased mass at the ground-floor level to allow the insertion of the isolation system between the foundation and the ground floor has to be considered. Note that this ground-floor mass, which has no significance for non-isolated designs can result in a significant increase in the effective mass of the isolated structure.

The structure itself will normally be required to remain in the elastic range when subjected to an excitation which is the design ground motion filtered by the isolation system. The base shear capacity of the structure will be assumed as a limit to be verified at the end of the design process, and which may need to be modified in case the shear force in the isolation system at the design displacement is larger. The inelastic displaced shape of the structure is shown in Fig.11.25, where a SDOF equivalent model and its effective height are also depicted.

The design of the isolation system will follow the simple basic steps described in Chapter 3 for a single degree of freedom structure. The design action will be represented in terms of appropriate displacement spectra, such as those of Fig.2.5, and the structural model will be described in terms of secant stiffness and equivalent viscous damping. It may be important to consider the effect of the local soil to define the actual design spectra, since this may imply larger displacement demand.

As discussed in the previous section, two basic choices will have to be considered: to use an elastic isolation system with a certain level of viscous damping (e.g. a high damping rubber bearing system) or to use a system characterized by an approximately bilinear response, with energy dissipation in the form of friction or hysteretic damping (e.g. friction or rubber bearing coupled with a dissipation device, or dissipating bearings such as lead–rubber or friction pendulum systems). In both cases, the design process will require the preliminary selection of a system displacement, as a function of design spectra and functional requirements (limitation of relative displacement between structure and foundation).
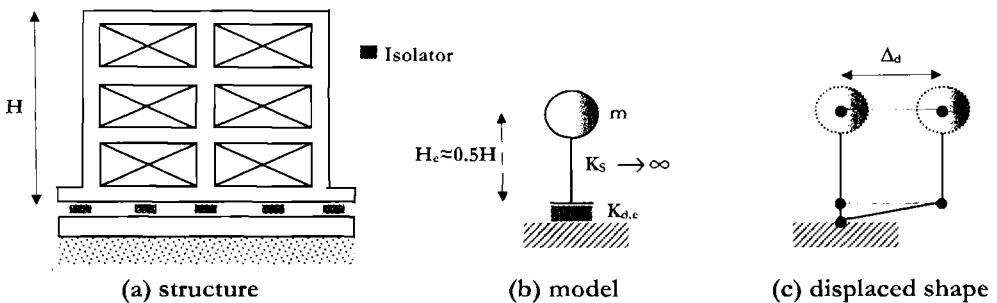

(a) structure   (b) model   (c) displaced shape

Fig.11.25   Idealization of a Base–Isolated Stiff Structure

Having determined or assumed the design displacement and equivalent viscous damping of the isolation system, which in this case is equal to the equivalent global damping, the period of vibration can be read from the appropriate displacement spectra, and equivalent stiffness and base shear forces can be computed according to Eq.(3.1) and (3.2). The base shear force has to be applied at the center of mass of the **SDOF** model (see Fig.11.25), therefore producing shear forces, bending moments and variation of axial forces in the structure. Subsequent amplification of these forces for higher mode effects will generally be necessary when designing the isolated structure.

(a) Design Displacement: The design displacement should be selected considering the actual displacement spectra, as a function of the local seismicity and the functional requirements. Note that a large dislocation displacement will normally occur between foundation and ground floor (i.e. at the level of the isolator), and the concepts of drift limits and material strain limits will normally be irrelevant. Displacement limits may, however, be imposed by the need to accommodate mechanical and electrical services which must pass through the isolation layer.

As discussed in Section 3.4.7, a crucial issue will be to decide whether it is acceptable to design for a displacement equal to that corresponding to the corner period ($T_{c,\xi}$) in the appropriately damped displacement spectrum. If this is not the case, i.e. the structure system will be designed for a displacement ($\Delta_{d,\xi}$) lower than that corresponding to the spectrum corner period, the standard design process discussed in Chapter 3 will be applied. As shown again for convenience in Fig.11.26 (case 1), T_d will be read form the spectrum and the following equations will apply:

$$K_{d,e} = \frac{4\pi^2 m_e}{T_d^2}$$ (11.55)

$$V_{Base} = K_{d,e}\Delta_d$$ (11.56)

If it is feasible to design for a displacement capacity larger than that corresponding to the spectrum corner period, the design displacement demand will be equal to $\Delta_{c,\xi}$ Fig.11.26, case 2) and the resulting design period of vibration will be undefined, the only requirement being that the equivalent period of vibration be greater than the corner period:

$$T_{d,e} \geq T_c$$ (11.57)

and consequently equivalent stiffness and required shear capacity will also be undefined, with the following limitations for equivalent stiffness and shear strength:
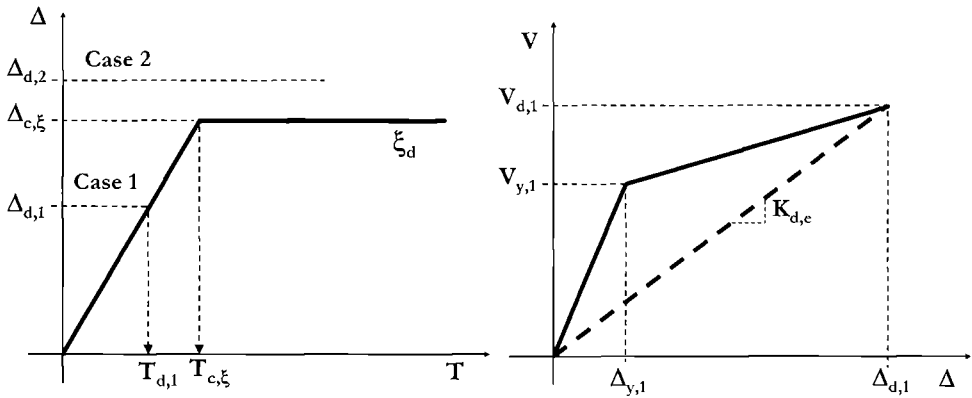
$$K_{d,e} \leq \frac{4\pi^2 m_e}{T_c^2}$$ (11.58)

Fig.11.26 Displacement Spectrum and Idealized Force–Displacement Response

$$V_{Base} \le \frac{4\pi^2 m_e}{T_c^2} \Delta_{c,\xi} \qquad (11.59)$$

It has to be noted, however, that the above limitations are needed only to predict that the corner period displacement will actually be reached under the design earthquake, and are irrelevant when assessing the safety of the structure. Higher equivalent stiffness and shear capacity will simply imply smaller displacement demand. It is therefore possible to conclude that when it is feasible to assume a displacement capacity larger than $\Delta_{c,\xi}$ the only additional requirement for the isolation system will be a shear strength lower than the yield shear capacity of the structure, to assure its elastic response.

(b) Equivalent Viscous Damping: The level of equivalent viscous damping obtainable from each type of isolation system has been discussed in Section 11.2 for each type of device and is summarized for convenience in Table 11.1. It is evident that reasonable values of the equivalent viscous damping coefficients range between 15 and 30%, depending on the type of device and the need to assure acceptable residual displacement values. Applying Eq.(2.11) and (2.12), it may be shown that these values imply reductions of the displacement demand corresponding to the 5% damped displacement spectrum to values between 50 and 60% for standard situations and between 70 and 80% in near-field situations. The selection of the isolation system may therefore depend on the relevance of reducing the displacement demand.

Note that only for the present case of a very stiff base–isolated structure the global damping is approximately equal to the isolation system damping.

(c) Design of the Isolation System: The isolation system will be designed considering the displacement capacity, equivalent viscous damping, strength and stiffness and the total weight of the structure. A regular distribution of the chosen device is normally

possible, to minimize torsional eccentricity, but care should be placed on the interaction between devices and the vertical elements of the ground floor of the structure, which may imply uneven distribution of the vertical load support.

If an irregular structure geometry is likely to induce torsional effects on the isolation system an inelastic time-history analysis (**ITHA**) should be conducted (See Section 4.9).

Table 11.1 Range of Equivalent Viscous Damping and Displacement Demand Reduction for Different Devices

Device	Range of ξ_{eq}	$\Delta_{d,\xi}/\Delta_{d,0.05}$ [%]	
		Standard input	Near field
LDRB	$0.05\text{-}0.07$	$90 - 100$	$95 - 100$
HDRB	$0.15\text{-}0.2$	$60 - 65$	$75 - 80$
LRB	$0.2\text{-}0.3$	$45 - 60$	$70 - 75$
FPS	$0.15\text{-}0.25$	$50 - 65$	$70 - 80$
Steel dampers[1]	$0.2\text{-}0.3$	$45 - 60$	$70 - 75$
Viscous dampers[1][2]	$0.4\text{-}0.5$	$35 - 40$	$60 - 65$

[1] Structure assumed to be supported on low friction pads

[2] High potential for large residual displacement

(d) Design of the Isolated Structure: It is assumed that a preliminary gravity load design of the system has been conducted and, as a result, the basic structural geometry is defined. This allows an estimation of the total mass, used in Eq.(11.55) to (11.59).

The structural design base shear force is then obtained from:

$$\phi_s V_{Base,s} = \phi^o V_{Base} \tag{11.60}$$

The overstrength factor ϕ^o is applied to the base shear calculated for the isolation system to capacity-protect the structure, as discussed in Sections 3.9 and 4.5. The value of ϕ^o depends on the uncertainty in the definition of the maximum shear transmissible through the isolation system; for example it should be higher for devices based on friction, due to the variability of the friction coefficient. In general, values between 1.1 and 1.25 are felt to be appropriate. The strength reduction factor ϕ_s is applied to the calculated structural strength to obtain dependable values. Values of ϕ_s between 0.9 and 1.0 are generally appropriate (see Section 3.9). The structure will thus respond elastically and will be designed accordingly with simplified detailing (see Sections 5.3.2 and 6.3.2).

The imposed elastic response of the structure will allow simplified design criteria, without any need for further application of capacity design principles or strength reduction factors, with the only exception being the higher-mode amplification factor ω. Even for stiff buildings higher mode effects can be relevant.

In general, the consideration of higher-mode effects may imply a distribution of the base shear to the floor levels that differs from the linear distribution (in proportion to

masses) implied by Eq.(5.12). **ITHA** or the Effective Modal Superposition (**EMS**) procedure outlined in Section 6.6.1(c) may be used to determine higher-mode effects.

Additional calculations may be required for irregular-plan buildings to distribute the floor actions between different resisting elements, as described in prior chapters (for example see Section 6.4).

Having defined the appropriate distribution of the base shear, an elastic analysis will give the design actions for each structural element. In general, a static analysis under the appropriate lateral force vector will be performed, using cracked–section stiffness, found in accordance with the methods developed in Chapter 4, without any further reduction.

(e) Design Example 11.1 – Alternative Isolation Systems for a Stiff Building:

(i) Design using high damping rubber bearings: Assume that a relatively small residential building has to be built in a high seismicity area. It is a two-storey building, with a square plan with a side of 12 m (39.4 ft) (Fig.11.27), preliminarily designed elastically for gravity loads and laterally for a base shear coefficient equal to 10% of gravity. All columns have sections of 400×400 mm (15.7×15.7 in) in plan; all beams are assumed to have a depth (h_b) of 600 mm (23.6 in).

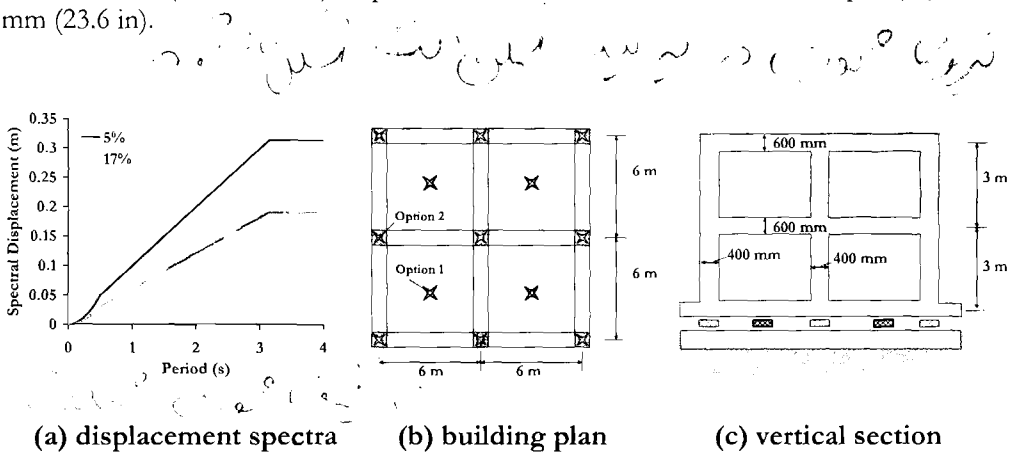(a) displacement spectra   (b) building plan   (c) vertical section

Fig.11.27   Design Example 11.1

The design earthquake is represented in terms of its elastic displacement spectrum, as shown in Fig.11.27(a), with a corner period at 3.15 seconds and a corresponding displacement demand equal to 315 mm (12.4 in). Standard, non near-fault, conditions can be assumed.

The total weight to be considered for seismic design has been computed as 4600 kN (1034.2 ksi), including the ground floor.

An isolation system made of high-damping rubber bearing devices, with a viscous damping coefficient of $\xi_d = 0.17$ is adopted. The design displacement spectrum, corresponding to this level of equivalent viscous damping, can thus be computed applying Eq.(2.8):

$$\Delta_{T,17} = \Delta_{T,5} \cdot \left(\frac{0.07}{0.02 + 0.17} \right)^{0.5} = 0.609 \Delta_{T,5}$$

The maximum displacement demand, corresponding to the corner period is therefore equal to 315×0.609 = 191 mm (7.5 in).

It is initially decided to design the isolation system for this level of displacement demand and it is to be verified that the building can be assumed to be rigid in comparison with the design displacement of the isolation system. The structure is assumed to respond elastically and therefore its yield drift demand can be estimated using Eq.(5.7a) (it is assumed that $\varepsilon_y = 0.2\%$)):

$$\theta_y = 0.5\varepsilon_y \frac{L_b}{h_b} = 0.5 \times 0.002 \frac{6}{0.6} = 0.01$$

Assuming an effective height equal to 4.2 m (13.8 ft), the yield displacement is 42 mm (1.65 in), in the range of one fifth of the corner displacement of the damped displacement spectrum. For a preliminary design this displacement could be ignored, as in this example, though it should be considered in the final design.

Designing the isolation system for a displacement of approximately 200 mm (7.9in) will imply the following limitations on the devices (Eq.(11.5) and (11.6)):

$$D \geq 2\Delta_{max} \approx 400mm \quad (15.7in)$$

and:

$$h \geq \Delta_{max} \approx 200mm \quad (7.9in)$$

Designing for the corner period implies also:

$$T_{d,e} = 3.15 \text{ sec}$$
$$K_{d,e} = 4\pi^2 m_e / T_{d,e}^2 = 4\pi^2 \times 4600/(9.81 \times 3.15^2) = 1866 \text{ kN/m (10.7 kips/in)}$$
$$V_{Base} = K_{d,e}\Delta_d = 1866 \times 0.2 = 373 \text{ kN (83.9 kips)}$$

Note that this value of shear corresponds to approximately 8% of the total design weight, which is less than the structural capacity of 10%, and therefore the structure will respond elastically, even considering $\phi^o = 1.1$ (refer to Eq.(11.60)). Higher-mode effects can probably be neglected for a two storey building.

Assuming a total of four identical devices, each one of them should have horizontal stiffness and strength equal to:

$$K_{d,i} = 1866 / 4 = 466 \text{ kN/m (2.7 kips/in)}$$
$$V_{d,i} = 373 / 4 = 93 \text{ kN (20.9 kips)}$$

Each device will carry one fourth of the vertical load, i.e.:

$$P_{d,i} = 4600 / 4 = 1150 \text{ kN (259 kips)}$$

For a diameter equal to 400 mm (15.7 in) (approximately the minimum required for a 200 mm (7.9 in) displacement demand, providing an overlap area ratio of close to 0.5), the resulting average vertical stress will be equal to:

$$f_{p,i} = 1150 /(200^2 \pi) = 9.15 \text{ MPa (1.33 ksi)},$$

i.e., an acceptable value. Note that the thickness of each rubber layer can be obtained from Eq.(11.4), or graphically from Fig.11.7. The appropriate thickness results to be $t = 5.4$ mm (0.213 in).

Assuming therefore a diameter equal to 400 mm (15.7 in), from Eq.(11.8), with $G_R = 1$ MPa (145 psi), the minimum required height can be computed as:

$$h_{min,i} = G_R A / K_{d,i} = \pi \cdot 200^2 / 466 = 270 \text{ mm (10.6 in)}$$

i.e. a value larger than 200 mm (7.9 in) and therefore acceptable.

It may be concluded that the isolation system may be made with four **HDRB** devices, with a diameter of 400 mm (15.7 in) and a height of 270 mm (10.6 in).

It is apparent, however, that this system will probably imply locating the devices at the centers of each one of the four slab areas between the columns, as indicated in Fig.11.27(b). This choice will consequently imply a heavy slab, or beam grid, to relocate the vertical forces from columns to isolators. It has also to be noted that the design base shear and the equivalent height imply a total overturning moment equal to:

$$M_{OTM} = 373 \times 4.2 = 1567 \text{ kNm (13900kip.in)}$$

and a consequent axial force variation on each device equal to:

$$\Delta P_{d,i} = 1567 /(6 \times 2) = 131 \text{ kN (29.5 kips)}$$

i.e. on the order of 10% of the gravity value.

Locating a device at the base of each column would require the use of nine devices. In this case, the same requirement of the previous case will apply to minimum diameter and minimum height to allow a displacement capacity equal to 200 mm (7.9 in), but a diameter equal to 400 mm (15.7 in) will result in significantly lower axial stresses and increased height to assure an appropriate stiffness. Assuming for simplicity the design of a system with nine identical devices, the results will be as follows:

$$K_{d,i} = 1866 / 9 = 207 \text{ kN/m (1.2 kips/in)}$$

$$V_{d,i} = 373 / 9 = 41 \text{ kN (9.2 kips)}$$

$$h_{min,i} = G_R A / K_{d,i} = \pi \cdot 200^2 / 207 = 607 \text{mm (23.9 in)}$$

Each device will carry a different share of the total weight, depending on the axial force on each column, approximately equal to 290 kN (65.2 kips) for the four corner columns, 575 kN (129.3 kips) for the four mid-side external columns and 1150 kN (258.5 kips) for the central one.

The same overturning moment of the previous case will be essentially equilibrated by the external devices, with axial force variation of the order of 43 kN (9.7 kips), still not implying tensile stresses and therefore acceptable.

However, the increased number of devices will therefore imply the need for a reduced stiffness, and since this cannot be accomplished with a reduction of the diameter, because of the influence on the displacement capacity, a significant increment of the height of the devices is necessary, with an obvious implication on cost and construction difficulties. Relatively low masses (and relatively low average axial stress) are not favourable for this class of devices, as pointed out in Section 11.2.3.

(ii) Alternative choice – use friction sliding bearings coupled with dampers: If friction sliding bearings are used to support the vertical load, it is not advisable to adopt viscous dampers, unless preloaded, to avoid possibly large residual displacement (though, part of it will be slowly recovered later).

However, if this should be the choice, an equivalent viscous damping as large as 45% could be assumed, for both frictional and the viscous response. Consequently, the corner period displacement will reduce to 121 mm (4.8 in), and following the same procedure discussed above, the following results would be obtained:

$T_{d,e}$ = 3.15 sec.
$K_{d,e}$ = 1866 kN/m (10.7 kips/in)
V_{Base} = 226 kN (50.8 kips)

This base shear value corresponds to approximately 5% of the total design weight, which is less than the assumed structural capacity of 10%, and therefore the structure will respond elastically.

Assuming a friction coefficient of the sliding bearings μ_f = 2.5 %, the design force for the viscous dampers will be:

$$F_{VD} = V_d - \mu W = (0.025 \times 4600) = 111 \text{ kN (25 kips)}$$

i.e. the dampers should take approximately 50% of the total base shear. As mentioned in Section 10.2.4(c), assuming α = 0.1, the viscous damper constant should be slightly higher than the design maximum force: we assume C = 125 kN(sec/m)$^{0.1}$ (19.5 kips(sec/in)$^{0.1}$).

It is possible to check that the actual force demand will be close to the design value calculating the velocity implied by the damped spectrum at the design period:

$$S_v = 2\pi \cdot \Delta_d / T_d = 2\pi \times 0.121 / 3.15 = 0.241 \text{ m/sec (9.5 in/sec)}$$
$$F_{VD} = C S_d^{0.1} = 125 \times 0.241^{0.1} = 108 \text{ kN (24.3 kips)}$$

If steel dampers are used, their equivalent viscous damping ratio will be about $\xi_{e,h}$ = 25%. Assuming that approximately 50% of the base shear will be taken by friction in the bearing, with an equivalent viscous damping $\xi_{e,f}$ = 45%, the global equivalent viscous damping will be ξ_e = 35%. Proceeding as above the following values are obtained:

$\Delta_{T,35}$ = 137 mm (5.4 in)

$T_{d,e}$ = 3.15 sec.

$K_{d,e}$ = 1866 kN/m (10.7 kips/in)

V_d = 256 kN   (57.8 kips)

F_{SD} = 141 kN (31.7 kips)

(iii) Alternative choice – use FPS bearings: The equivalent viscous damping coefficient will be approximately ξ_e = 20 % and consequently:

$\Delta_{T,35}$ = 177 mm   (7.0 in)

$T_{d,e}$ = 3.15 sec

$K_{d,e}$ = 1866 kN/m (10.7 kips/in)

V_{Base} = 330 kN   (74.2 kips)

This value of shear is still lower than the assumed structural capacity.

Assuming a design friction coefficient μ_{FPS} = 3.5%, the radius of curvature of the concave surface can be obtained by inverting Eq.(11.23):

$$R_c = W \frac{\Delta_d}{(V_d - \mu W)} = 4.73 \text{ m (15.5 ft)}$$

A radius R_c = 5 m (16.4 ft) may be adopted. As in case (a), four or nine devices can be used, and the vertical load acting on each of them will vary consequently. The size of the contact surface between slider and spherical surface will be adjusted to the accepted level of stress, considering the problem of heat generation (Sections 10.2.3 (c) and 11.2.5).

*(f) **Design for Rocking:*** If a stiff structure, e.g. a relatively squat wall, is designed to rock on its foundation, the elastic deformation of the structure itself can generally be neglected since it produces a displacement much smaller than that resulting from the rocking motion. The design displacement is thus calculated as described in Section 11.2.6 (b) and is normally dictated by non–structural limits. Note that if this is the case, even the geometry of the wall, i.e. its length, is not necessary at the start of the design.

As discussed in Section 11.2.6, the damping resulting from rocking is usually negligible and a value of ξ =0.05 should be initially assumed. Additional damping may be required for a more efficient design, but this will be provided, if needed, in a second iteration, by means of appropriate devices.

Entering the displacement spectrum, the period of vibration and corresponding stiffness will be readily obtained. The required strength is thus also obtained, multiplying stiffness and design displacement. Note that this is the strength required in the deformed position, and the force required to initiate rocking may be higher, as shown in Fig.11.28,

or lower, in the case of some restraint provided by displacement–proportional tensile forces or by other mechanisms. In the same figure it is also evident that the design point could correspond to different combinations of length l_w and tensile restraining force R_t. With a constant R_t all three pairs of parameters will result in the same line, while with R_t proportional to the wall displacement different geometries are compatible (refer to Fig.11.23 for definition of symbols). The actual combination of parameters should be obtained from Eq.(11.53) (appropriately modified if R_t is not constant), assuming one parameter and obtaining the other. A few iterations may be needed.

Two verifications are required to finally accept the design:

- the design displacement has to be a small fraction (in all cases lower than 30%) of the displacement corresponding to zero horizontal force (Eq.(11.54));
- the force required to initiate rocking should be low enough to assure that the rocking response will take place, i.e. lower than the design **PGA** multiplied by the effective mass.

Note that it is generally convenient to have a variable R_t, increasing with the displacement demand, with respect to both requirements. As an example consider the case of a tensile force provided by the elastic response of slightly post–tensioned unbonded cables, with elastic modulus E_s, section area A_s and total unbonded length H_{UNB} (note that this is a design choice).

l_w	R_t
H/10	$0.88\, W_0 \Delta_d$
H/6	$0.53\, W_0 \Delta_d$
H/4	$0.09\, W_0 \Delta_d$

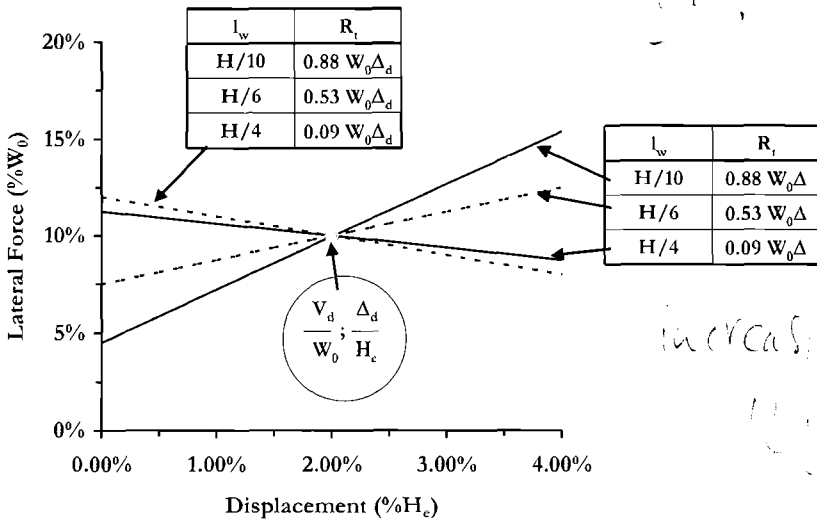| l_w	R_t
H/10	$0.88\, W_0 \Delta$
H/6	$0.53\, W_0 \Delta$
H/4	$0.09\, W_0 \Delta$

Fig.11.28 Force-Displacement Domain for a Rocking wall Considering R_t Variable, as a Function of l_w/H (design for $V_d=10\%\ W$ and $\Delta_d = 2\%H_e$)

The initial restraining force, which may be negligible, will then vary in proportion to the rocking displacement, according to the following equations, derived from geometric considerations:

$$\Delta_C = \frac{\Delta_r}{H_e}\left(l_w - c - a/2\right)$$

(11.61)

$$R_t = \frac{E_s A_s}{H_{UNB}} \frac{\Delta_r}{H_e}\left(l_w - c - a/2\right)$$

(11.62)

Finally, it has to be considered that it is possible to reduce the design displacement providing some form of artificial energy dissipation that will result in a higher equivalent viscous damping. For example, each side of the wall may be provided with steel or viscous dampers, which will produce a restraining tensile force corresponding to the yield or C value and an equivalent viscous damping equal to ξ_H or to ξ_V. An approximate evaluation of the global equivalent viscous damping can be obtained by considering the proportion of the total shear absorbed by the rocking response and by the tensile force component:

$$\xi_e = \frac{\left(0.05\left(\dfrac{0.45 l_w W}{H_e} - \dfrac{W}{H_e}\Delta_d\right) + \xi_H \dfrac{0.95 l_w - c}{H_e} R_t\right)}{\left(\dfrac{0.45 l_w W}{H_e} - \dfrac{W}{H_e}\Delta_d + \dfrac{0.95 l_w - c}{H_e} R_t\right)}$$

(11.63)

Again, some simple iteration may be needed to select an appropriate combination of wall length, restraining force and equivalent viscous damping.

Note that when dampers are used, it is generally appropriate to post-tension the wall internally with bonded cables, to avoid any possible cracking in the wall resulting from a tensile force exerted on the wall by the restraining force.

The qualitative force–displacement cycles resulting from the combination of rocking motion, variable restraining force and added dampers are depicted in Fig.11.29. Note that a variable restraining force has the effect of increasing the post-yield stiffness, which as a consequence may become positive. The combination of rocking and added energy dissipation produces typical flag-shape loops, which are quite appealing in terms of limiting the residual displacement and consequently the post–earthquake damage level, while providing a significant level of equivalent viscous damping.

Assuming that the fraction of the total overturning moment taken through the damper action is $M_D = \beta M_{OTM}$ (and therefore the same fraction applies to the base shear), and that the equivalent damper yield force is a fraction λ of the force corresponding to the design displacement, the approximate system area-based equivalent viscous damping can also be expressed as:

$$\xi_{sys} = \frac{1}{4\pi} \left(\frac{4 \cdot \lambda \cdot \beta \cdot V_{d,R} \Delta_{d,R}}{0.5 V_{d,R} \Delta_{d,R}} \right) = \frac{2\lambda\beta}{\pi} \tag{11.64}$$

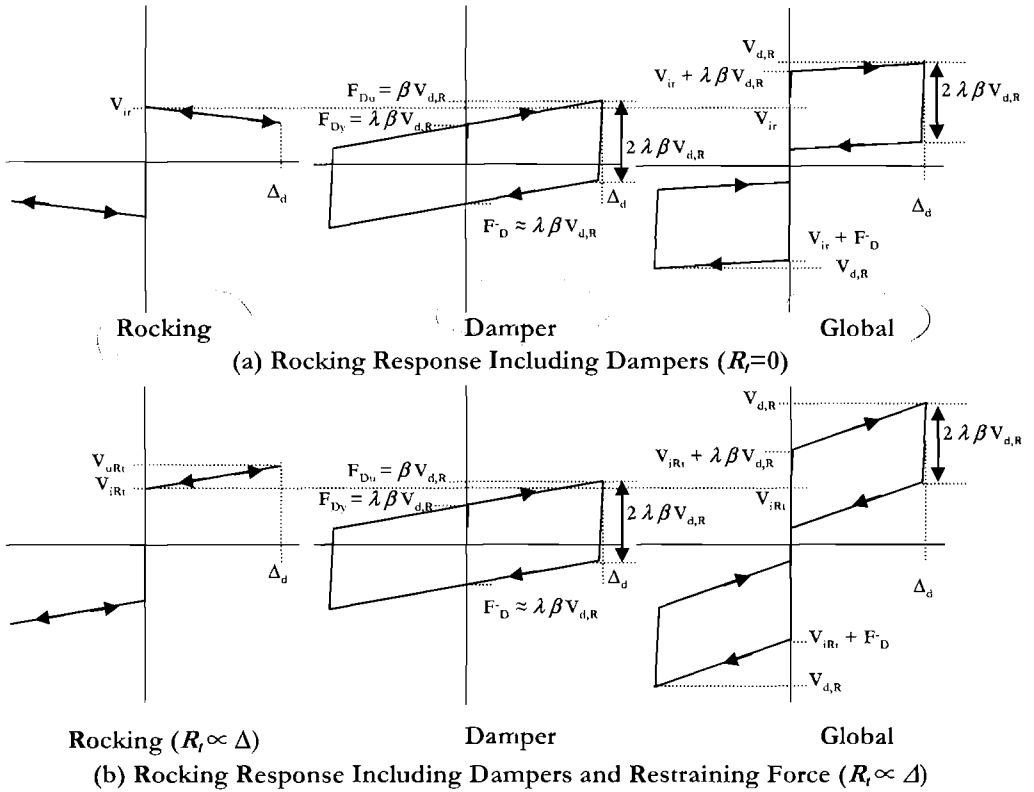This must be converted to equivalent viscous damping using Fig.3.15.

(a) Rocking Response Including Dampers (R_t=0)

(b) Rocking Response Including Dampers and Restraining Force ($R_t \propto \Delta$)

Fig.11.29 Hysteresis Loops of a Controlled Rocking System Including the Contribution of Restraining Force (R_t) and Hysteretic Dampers (F_D)

11.3.2 Base-Isolated Flexible Structures

When the structure to be isolated cannot be considered rigid with respect to the isolation system, i.e. when its fundamental period of vibration is preliminarily estimated as longer than 1/3rd of the period of the isolated structure, the conceptual design of the system should be based on a model that includes both isolation system and structure.

Note that also in this case it is simpler, more direct and consistent with a displacement-based approach to verify the "effective rigidity" criterion above in terms of

displacement demand, rather than of a period ratio. This is accomplished by comparing an estimate of the yield displacement of the structure alone with the displacement capacity that will be assigned to the isolation system, or, if this value has not yet been selected, with a displacement demand corresponding to the corner period in a damped (ξ_e ≈ 0.2 to 0.25) displacement spectrum or to a period of vibration of about 3 seconds (or whatever is expected to be the period of vibration of the isolated structure), whichever is less. Note that the period criterion above implies that the yield displacement of the structure alone should not be larger than about 10% of the isolation system displacement for the structure to be considered effectively rigid. Note also that the procedure outlined in the following is a generalization of what was discussed in Section 11.3.1 and is always applicable, even in the case of relatively stiff structures. The standard concept of **DDBD** can still be applied in a simple and rational form, defining a **SDOF** substitute structure as conceptually discussed in Sections 3.2 and 3.4.

(a) Design Displacement and Displacement Shape: The concept of base isolation, as discussed in Section 11.1, implies that the isolation system is the only critical element, that will have to behave non-linearly and to dissipate energy. As a consequence, the structure can be assumed to deform according to its yield displaced shape.

This assumption will allow estimation of the displacement values at each floor level, for all structural elements and consequently the yield displacement of the equivalent model.

The yield displaced shape of the structure alone can be found using the appropriate equations, as defined in the chapters related to frame and wall buildings (e.g. Eq.(5.7) for frames; Section 6.2.1 for walls). However, since the structural response will not be critical and is capacity protected, it is often adequate to assume a linear deformed shape (even for the case of cantilever wall structures).

In the case of a shorter frame building (less than 4 storeys) a linear displaced shape can be assumed and Eqs.(5.7) apply:

$$\theta_y = k\varepsilon_y \frac{L_b}{h_b} \tag{11.65}$$

where θ_y is the yield drift ε_y is the yield deformation of the reinforcement steel, L_b and h_b are length and depth of the beams and k is equal to 0.5 for concrete frames and 0.65 for steel frames. For taller frame buildings a refinement of the elastic displaced shape may be advisable.

For cantilever wall building the yield displacement at height H_j is expressed by Eq.(3.31):

$$\Delta_{yj} = \frac{\varepsilon_y}{l_w} H_j^2 \left(1 - \frac{H_j}{3H_n}\right) \tag{11.66}$$

where l_w is the wall length, H_j is the storey height and H_n is the roof height.

The effective height of the structure alone is expressed by Eq.(3.35):

$$H_e = \sum_{j=1}^{n} \left(m_j \Delta_j H_j\right) / \sum_{j=1}^{n} \left(m_j \Delta_j\right) \tag{11.67}$$

Note that the effective height of the substitute structure will be lower than for an unisolated structure, as a consequence of the concentrated displacement at the base of the structure due to the isolation system. As noted above, it will often be adequate to calculate the structure displacement at the effective height (Eq.(11.67)), and adopt a linear displacement profile up the wall. The design displacement of the structure alone ($\Delta_{d,es}$) should be assumed in the range of 80–90% of the calculated yield displacement. This accounts for the amplification factor will be applied to the shear strength resulting for the isolation system, to capacity protect the structure, as discussed in Section 11.3.1(c).

For irregular buildings reference should be made to the appropriate structural chapters.

The selection of the design displacement of the isolation system ($\Delta_{d,i}$), and consequently of the global structural system ($\Delta_{d,sys}=\Delta_{d,es}+\Delta_{d,i}$), is the starting point of the design process. $\Delta_{d,i}$ may depend on requirements imposed by the possible gap to be left around the slab resting on the isolation system, with the consequent requirements for mechanical and electrical services connected to the building. In general, larger displacements will correspond to longer periods of vibration, lower stiffness values and lower base shear strength requirements.

With reference to Fig.11.30, the global displacement shape will thus result from a combination of a displacement corresponding to the isolation system and a distributed deformed shape along the height of the building.
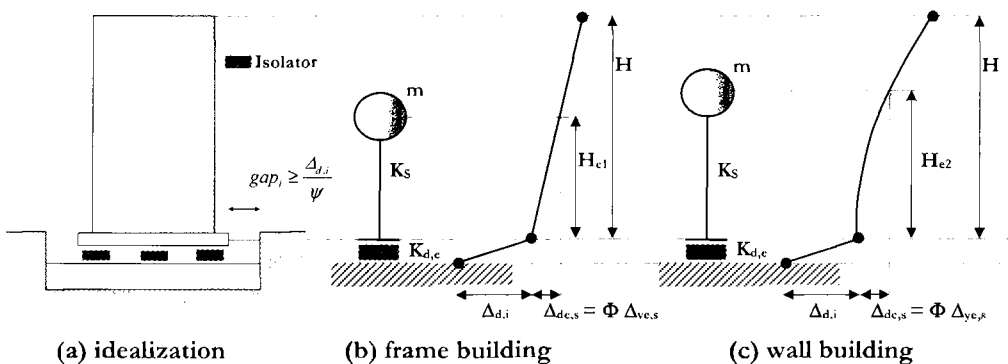

Fig.11.30 Displacement Shape of a Base–Isolated Building

(b) Equivalent Viscous Damping: Once the design displacement of the isolation system and of the structure alone have been preliminarily defined, the estimate of a global equivalent viscous damping of the system can proceed analogously to the procedure

presented in Section 3.5.4 for the case of a structure built on a flexible foundation. This implies an assumption on the equivalent viscous damping values to be assigned to the structure and to the isolation system.

For the structure, considering that an elastic response will be required and enforced, only a standard viscous damping should be accounted for, therefore normally the equivalent viscous damping will be assumed $\xi_{e,s}$ = 0.05. For the isolation system reference should be made to Table 11.1. Normal values will range between $\xi_{e,I}$ = 0.2 and $\xi_{e,I}$ = 0.3.

The system equivalent viscous damping ($\xi_{e,sys}$) will thus be computed from Eq.(3.36c), modifying the symbols:

$$\xi_{e,sys} = \frac{\xi_{e,s}\Delta_{d,es} + \xi_{e,i}\Delta_i}{\Delta_{d,es} + \Delta_i} \qquad (11.68)$$

where all symbols have been defined above.

Note that if the structure displacement is large with respect to the isolation system displacement, the effect of the energy dissipation of the isolation system on displacement control will be significantly reduced.

Based on the estimated global equivalent viscous damping, the appropriate reduction factor to be applied to the displacement response spectrum will be computed (e.g. using Eq.(2.8)).

(c) Effective Mass and Stiffness: Entering the appropriate displacement response spectrum with the design displacement, the period of vibration of the equivalent structure will be obtained and as usual the effective stiffness will be computed from Eq.(11.55). Note, however, that the equivalent mass to be used is likely to be greater than the equivalent mass of the building alone, due to the concentrated ground level displacement (the same comment applied to Eq.(11.67), where the effect was to have a lower equivalent height). The equivalent mass will be computed using Eq.(3.33):

$$m_e = \frac{\sum_j m_j \Delta_j}{\Delta_{d,sys}} \qquad (11.69)$$

where m_j and Δ_j are mass and total displacement of each floor, including the ground floor above the isolation system (see Fig.11.27), and $\Delta_{d,sys}$ is the displacement of the equivalent isolated structure.

(d) Design Base Shear and Design of the Isolation System: The design base shear is computed according to Eq.(11.56), i.e. multiplying equivalent stiffness and design displacement.

The isolation system will be designed considering the total weight of the structure and the requirements on shear capacity, stiffness, equivalent viscous damping, with no difference with respect to the case of a stiff structure. A verification time-history analysis is always recommended.

(e) Distribution of Design Base Shear Force and Design of the Structure: Again, no difference applies with respect to the case of stiff structures, with the exception of a proper consideration of higher-mode effects, that in this case may have higher relevance.

The application of an appropriate dynamic amplification factor ω to each action considered or the correction of the force vector according to what has been discussed in the previous chapters may be fundamental (e.g. refer to Eq.(4.59). In the event that time-history analysis is undertaken as design verification, the determination of higher-mode amplification will be automatic; if time-history analysis is not used, it is suggested that the Effective Modal Superposition approach described in Section 6.6.1(c) be used to determine higher mode effects. The approximate equations listed in Chapters 5 and 6 have not been verified for isolated structures, and are unlikely to apply.

(f) Design Example 11.2: Base Isolation of the Building of Example 6.1 (Section 6.4.7): It is assumed that the structural wall building of Example 6.1 is to be base isolated, to reduce the structural and non-structural damage under design level 2 (damage-control) seismicity. The structure geometry is shown in Fig.6.18, together with the displacement spectrum for 5% damping. The structure response is assumed to be elastic, and it is anticipated that an overstrength factor equal of $\phi^o = 1.25$ will be applied to the isolation system design base shear to capacity-protect the structure.

In Example 6.1 the yield displacement of the equivalent structure was calculated as $\Delta_{y,e} = 45.4$ mm (1.79 in). However, this applied at the effective height of the un-isolated structure. As noted previously, the effective height of the isolated structure will be significantly lower. We assume an effective height of 10m (32.8 ft) (a little above mid-height of the building), recognizing that some iteration may be needed. With this assumption, we calculate the system yield displacement at 10m as approximately 30mm (1.18 in). We reduce this by 20% to ensure that yield does not occur under the base shear amplified by the overstrength factor of 1.25. The displacement of the structure alone is therefore estimated as:

$$\Delta_{d,es} = 30 \times 0.8 = 24 \text{ mm (1.18 in)}$$

Based on non-structural design constraints, an isolation system design displacement is assumed equal to $\Delta_{d,i} = 200$ mm (7.9 in) (note that this will imply larger capacities). The system design displacement is therefore:

$$\Delta_{d,sys} = 24 + 200 = 224 \text{ mm (8.8 in)}$$

It is preliminarily assumed that lead-rubber bearings will be used, and a tentative equivalent viscous damping ratio of $\xi_i = 0.25$ is adopted for the isolation system. Consequently, the global equivalent viscous damping is:

$$\xi_{e,sys} = \frac{\xi_{e,s}\Delta_{d,es} + \xi_{e,i}\Delta_i}{\Delta_{d,es} + \Delta_i} = \frac{0.25 \times 200 + 0.05 \times 24}{200 + 24} = 0.229$$

The reduction factor to be applied to the displacement response spectrum is:

$$R_\xi = \left(\frac{0.07}{0.02 + 0.229}\right)^{0.5} = 0.53$$

The period of vibration resulting from the damped displacement spectrum is:

$$T_{e,sys} = \frac{224}{750 \times 0.53} \times 4 = 2.25 \, sec$$

The equivalent mass of the system is calculated from Eq.(11.69), assuming a linear deformed shape of the structure, or more accurately applying Eq.(11.66) to estimate the storey displacements. Note that the system must include the height of the isolation system (likely to be similar to the displacement capacity) and the thickness of the floor slab. In this example a total height of 400 mm (15.7 in) has been assumed. The additional mass corresponding to the isolated ground floor, assumed equal to the other storey masses (i.e. 306 t (674.9 kips)) must also be considered.

Table 11.2   Calculation of Equivalent Height and Mass for Example 11.2

Floor	Height [m]	Δ_i (linear) [mm]	Δ_i (wall) [mm]
6	17.2	255.82	263.59
5	14.4	246.73	248.20
4	11.6	237.65	233.63
3	8.8	228.56	220.71
2	6.0	219.47	210.26
1	3.2	210.39	203.10
0 is	0.4	200.0	200.0
0	0	0	0
Effective mass [t]		2060 (4544 kips)	2036 (4490 kips)
Equivalent height [m]		9.25 (30.4 ft)	9.34 (30.6 ft)
System Displ. (mm)		230 (9.1 in)	228 (9 in)

The displacements calculated for both assumptions are summarized in Table 11.2, where the resulting equivalent height, effective mass and system displacement are also shown. The differences are negligible, being of the order of 1%. The initial assumption of a system displacement of 224mm (8.8 in) is accurate enough for the estimation of system ductility, and hence no iteration is needed. As expected, the equivalent mass is larger than that calculated in Design Example 6.1, due to the added floor and to the comparative

uniformity of displacement with height, while for the same reasons the equivalent height is significantly lower.

The system equivalent stiffness is:

$$K_{d,e} = \frac{4\pi^2 m_e}{T_{e,sys}^2} = \frac{4\pi^2 \times 2036}{2.25^2} = 15890 \ \text{kN/m} \ (90.7 \ \text{kips/in})$$

The base shear force (at the isolation system level) is:

$$V_{Base} = K_{d,e} \Delta_{d,sys} = 15890 \times 0.228 = 3620 \quad \text{kN} \ (813.8 \ \text{kips})$$

The design shear of the isolation system should be properly factored to design the structure, to a value possibly around 4500 kN (1011.7 kips). The distribution to wall elements and different floors will be based on elastic analysis, as discussed in Chapter 6.

Considering the plan of the building, shown in Fig.6.18, it seems logical to check whether a system of 12 bearings would be feasible, in which case they will be located approximately at the base of each column and each wall, or to consider a system with 16 devices, placing two of them at the base of each wall. It should be noted, however, that providing a single bearing under each wall would imply that the ground floor structure would be subjected to very large local moments, probably requiring a significant increase in the size and weight of the ground floor, with a consequent influence on the design base shear force.

It is preliminarily assumed to design twelve identical devices and that the axial action due to gravity will be approximately the same for all of them, equal to $W_{dj} = 3000 \times 7/12 = 1750$ kN (393 kips). In this case, each device should have a displacement capacity significantly larger than $\Delta_{dj} = 200$ mm (7.9 in) (we suggest at least 1.5 × 200 mm), and a shear strength at this displacement equal to $V_{dj} = 3620/12 \approx 300$ kN (67.5 kips). It is further assumed to design for a ratio between the ultimate shear resisted by the device and the equivalent yield strength equal to $V_{uj}/V_{yj} = 2.25$, and the yield displacement is estimated as $\Delta_{yj} = 0.077 \times h \approx 0.0154$ m (0.606 in) (note, $h = \Delta_i$).

These assumptions would produce the idealized force–displacement curve shown in Fig.11.31, with the following stiffness values:

$K_R = (300 - 133)/(0.2 - 0.0154) = 905$ kN/m (5.2 kips/in)
$K_{LR} = 133/0.0154 = 8636$ kN/m (49.3 kips/in)
$K_e = 300/0.2 = 1500$ kN/m (8.6 kips/in)

The corresponding equivalent viscous damping is (Eq.(11.16)):

$$\xi_h = \frac{2}{\pi}\left(1 - \frac{1}{\mu}\right)\frac{V_y}{V_u} = \frac{2}{\pi}\left(1 - \frac{1}{13}\right) \times 2.25 = 0.26$$

The ratio between area of the device and area of the lead could be approximately obtained inverting Eq.(11.14):

$$n = \frac{A_D}{A_L} = \frac{129 K_R + K_{LR}}{K_{LR} - K_R} = \frac{129 \times 905 + 8636}{8636 - 905} = 16$$

To check whether a device with these characteristics can be produced, it is assumed to design for a height equal to h = 200 mm (7.9 in), which is the minimum compatible with the required displacement capacity. The required rubber area can be estimated from Eq.(11.8) as:

$$A_R = \frac{K_R \cdot h}{G_R} = \frac{905 \cdot 200}{1} = 181000 \text{ mm}^2 \ (280.6 \text{ in}^2)$$

Consequently the required area of the device is approximately 192000 mm² (298 in²) and the lead area is 11600 mm² (18 in²).
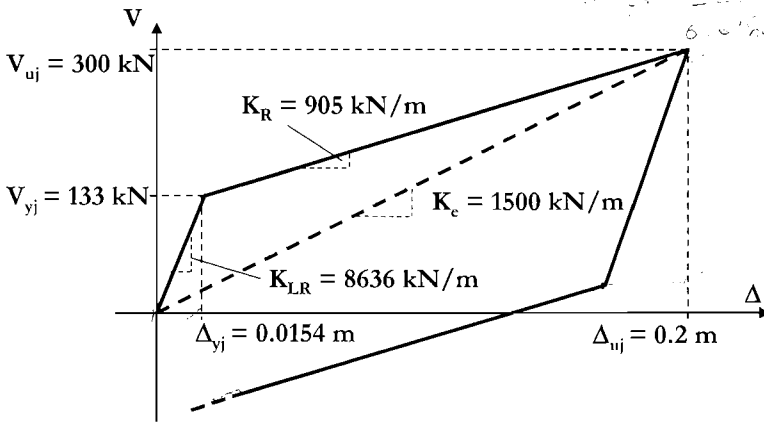
Fig.11.31 Ideal Force–Displacement Response of a Device for Example 11.1

According to these values, a device diameter equal to 500 mm (19.7 in) and a lead plug diameter equal to 130 mm (5.1 in) are selected. As a result:

A_D = 196349 mm² (304.3 in²)
A_L = 13273 mm² (20.6 in²)
A_R = 183076 mm² (283.8 in²)
K_R = 915 kN/m (5.2 kips/in)
K_L = 8627 kN/m (49.3 kips/in)
K_{LR} = 9542 kN/m (54.5 kips/in)
V_y = 147 kN (33.1 kips)
V_{200} = 316 kN (71 kips)
K_e = 1580 kN/m (9 kips/in)

The average compression stress on the rubber is equal to:

$$f_{ave} = \frac{1750000}{183076} = 9.56 \text{ MPa (1390 psi)}$$

The required thickness of the rubber layers between the steel plates can be evaluated from Eq.(11.3) (or from Eq.(11.4)):

$$S = \frac{W}{A'G\gamma} = \frac{1750000}{183076/2 \cdot 1 \cdot 1} = 19.12$$

$$t = D/4S = 6.54 \text{ mm (0.257 in)}$$

11.3.3 Controlled Response of Complex Structures

(a) General: As discussed with reference to Fig.11.1, the concepts of isolation and dissipation can be applied to a variety of complex systems, where isolating/dissipating devices could be inserted between different parts of the structural system with the purpose of dissipating energy, controlling relative displacements, and capacity–protecting structural elements against potentially brittle failure modes.

Common examples of application can be found in bridges, when the isolating system is located between pier top and deck, in frames braced with dissipative elements, in coupled shear walls and in different types of rocking structures.

In most cases the response of such structures is not easily captured with simple design approaches and it is therefore always recommended to perform some non-linear time-history analysis at the end of the design process. As previously discussed, an appropriate application of capacity-design principles may limit the non-linear response to the isolating/dissipating devices, simplifying the analysis.

(b) Isolation and Response Control of Bridges: A detailed discussion of appropriate bridge configurations, depending on geographical and architectural constraints, construction technology, material properties and performance objectives is presented elsewhere [P4]. Standard bridges, possibly with spans in the range of 40–80 m (130-260 ft), are normally designed with vertical piers and a horizontal deck. In many countries it is also common to design single-span or continuous decks resting on bearings located on the pier heads. In this case it is always convenient to verify whether the use of an isolation system would improve the bridge response, since the additional cost to substitute the bearings with isolation devices could be low.

It has to be noted that only the deck will be isolated, therefore if the piers are tall and massive, the shear and bending moment demand at the critical section at the base of the piers may depend to a large extent on the inertial response of the piers. For this reason, it may be difficult or sometimes impossible to fully capacity-protect the pier.

(i) Isolation of single-span or continuous deck: The principles and procedures for **DDBD** of bridges have been presented and discussed in Chapter 10, to which the reader is referred.

A distinction was made between longitudinal and transverse design. It will be shown that this distinction is less important in the case of deck-isolated bridges, since an appropriate design of the isolation system will allow an effectively rigid response of the deck.

It is generally assumed that a preliminary design of the bridge has been performed considering non–seismic loading conditions. The full geometry is therefore available and possibly a preliminary dimensioning of reinforcement.

The yield displacement of each pier can then be immediately calculated, applying Eq.(10.1), with $C_1 = 1/3$ if the soil–structure interaction is neglected, according to the configuration given in Fig.10.5(a), or considering the appropriate modifications to include the effects of soil deformation, as discussed in detail in Section 10.3.1 with reference to Fig.10.5(d) and (e).

Note that if the yield displacements of all piers exceed the peak response displacement corresponding to the corner period of the displacement response spectrum, there would be little sense in designing an isolation system, since the un-isolated bridge would respond elastically to the design seismicity. This may be the case of tall columns with pinned connection to the superstructure, to be built in areas where design seismic intensities are moderate, and the considerations presented in Section 10.3.1(c) would apply. Note that the graphical data presented in Fig.10.8 would allow a simple and immediate comparison of demand and elastic capacity.

If it is decided to provide each pier with an isolation device, the situation is described in Fig.11.32, which is similar to Fig.10.12, but shows a different response, since the non-linear behaviour is expected in the bearing rather than in the pier.

In the case of an isolation system with a non-linear response, therefore showing an equivalent yield point at a force demand corresponding to a fraction (depending on the post-elastic response of the isolation device this could vary between 40 and 90%) of pier yield, the lateral flexibility of the bearing will correspond to the equivalent yield displacement of the device, Δ_{yB}. At the limit-state response, the lateral force may be essentially the same as at yield or may be significantly larger, when the bearing shows significant post-elastic hardening. The pier deformation will essentially increase in proportion to the force increase (therefore possibly in the range of 2 times), while the bearing deflection will increase 10–15 times, depending on the accepted plastic deformation associated with the limit strains. This is indicated in Fig.11.32(b) by the difference between pier displacement profiles at yield and at limit-state response.

The structural and device hysteretic response are described in Fig.11.32(c) and (d). The damping associated with the pier response will remain essentially unchanged, while the isolation damping depends on the actual device, as discussed in Section 11.2.

The effective damping from the combined action of pier and bearing is directly analogous to the various cases of serial structural elements, already discussed, such as the flexible foundation case discussed in Section 3.5.4(b), and the bridge pier discussed in Section 10.3.5(b), and can thus be found from Eq.(3.40c) as:

$$\xi_e = \frac{\xi_P \Delta_{dP} + \xi_B \Delta_{dB}}{\Delta_{dP} + \Delta_{dB}}$$ (11.70)

Similar, though simpler, considerations will apply for the case of devices showing an essentially elastic response, as in the case of **HDRB**.

The design process will imply the definition of a uniform design displacement of the deck, which may correspond to different combinations of column and device displacement for each pier, and will therefore correspond to different equivalent viscous damping values for each pier–device system.

The global system damping will be computed as a weighted average of the piers damping values according to Eq.(10.18), since pier strength and damping are not uniform along the bridge. The discussion in Section 10.3.5(d) for the longitudinal response will now be applicable to the transversal direction as well, since each pier–device system will be designed to have similar strength and displacement capacities.

(a) Structure   (b) Displacement Profiles

(c) Pier Hysteresis   (d) Isolator Hysteresis
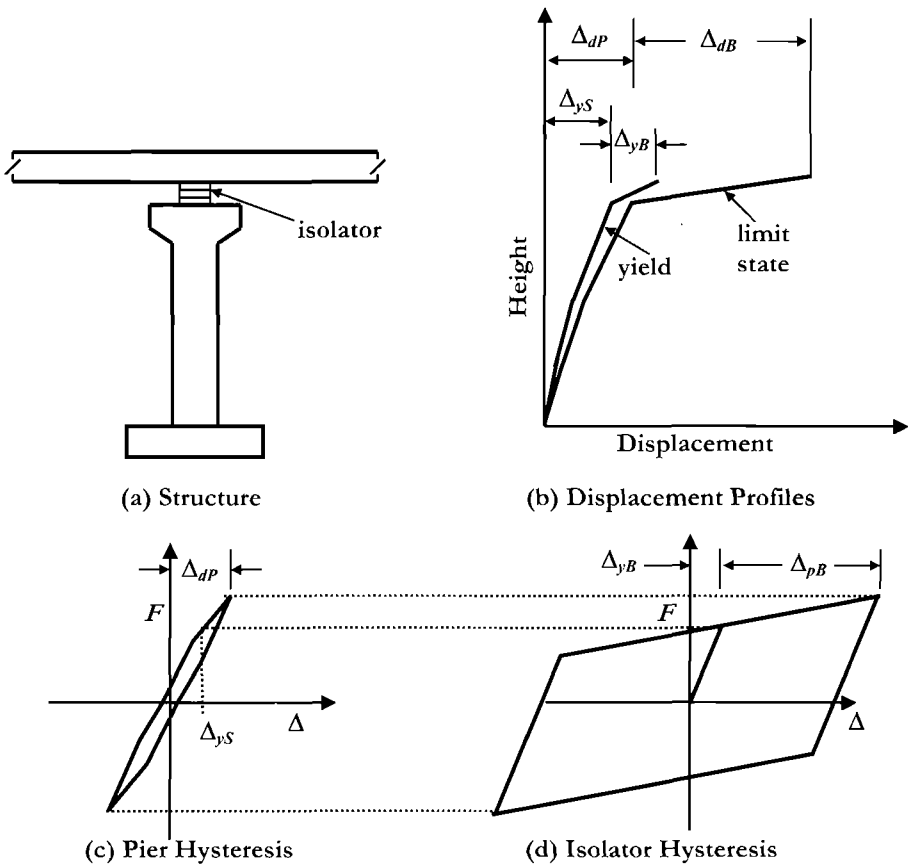
Fig.11.32 Damping for a Cantilever Pier with an Isolated Deck

The design process briefly outlined above conceptually allows isolation of only the piers where it is useful while adopting shear keys or fixed connections for taller piers whenever it is considered appropriate and convenient.

(ii) Design example 11.3: Design an isolation system for the bridge of example 10.3: the bridge of Example 10.3, is now reconsidered, assuming to isolate the deck. As discussed previously, the deck mass is considered to be equal to 190 kN/m (13.0 kips/ft), the columns are circular, with a diameter equal to 2 m (78.7 in) and the design ground motion is that described in Fig.10.15, with a **PGA** equal to 0.6 g. The deck is assumed to be continuous, supported by two devices at the top of each pier and at the abutments. It is also assumed to use friction pendulum devices. The bridge configuration is shown in Fig.11.33.
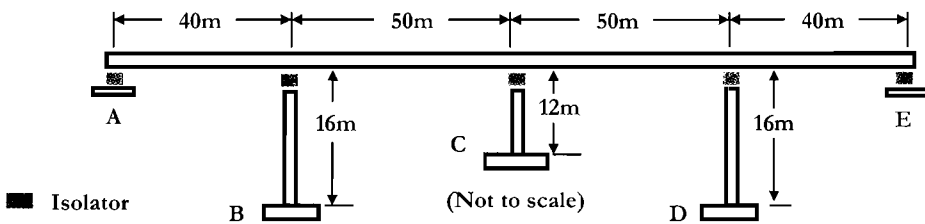
Fig.11.33   Bridge of Design Example 10.3, with an Isolated Deck

As discussed with reference to the case of pinned-pier top of Example 10.3, the following data can immediately be calculated:

- Strain penetration length: L_{sp} = 407 mm (16.0 in)
- Yield curvature: ϕ_y = 0.0026/m (66×10^{-6}/in)
- Yield displacement, pier B and D: Δ_{yB} = 0.233 m (9.2in)
- Yield displacement, pier C: Δ_{yC} = 0.133 mm (5.24 in)
- Weight on each abutment: P_A = 3,800 kN (854 kips)
- Weight on top of piers B ad D: P_B = 8,550 kN (1920 kips)
- Weight on top of pier C: P_C = 9,500 kN (2140 kips)

A design displacement equal to 0.5 m (19.7 in) is tentatively assumed.

It is also assumed that the equivalent viscous damping of the isolation system will be approximately equal to 20% and that the piers will be designed for a force level equal to 1.25 times the design strength of the corresponding isolator.

As shown in Fig.11.34, this implies the design displacements for the isolation devices (Δ_D) and the corresponding equivalent viscous damping for each pier–isolator system (ξ_P reported below:

Pier B and D:

$\Delta_{D,B}$ = 500 – 0.8 × 233 = 314 mm (12.4 in)

$$\xi_{P,B} = (0.20 \times 314 + 0.05 \times 186) / 500 = 0.144$$
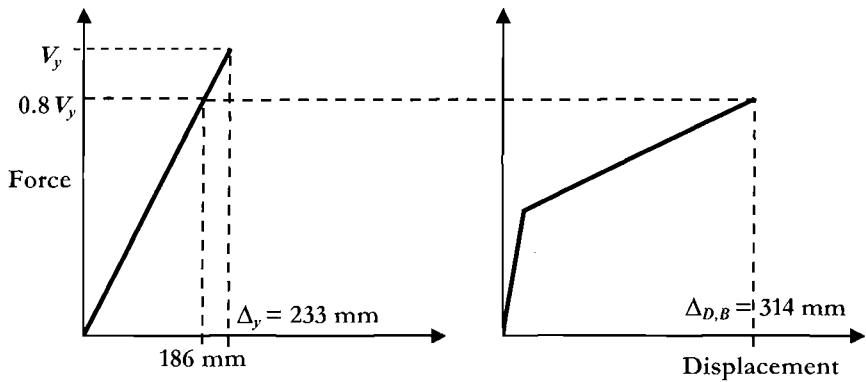
Pier C:

$$\Delta_{D,C} = 500 - 0.8 \times 133 = 394 \text{ mm (15.5 in)}$$
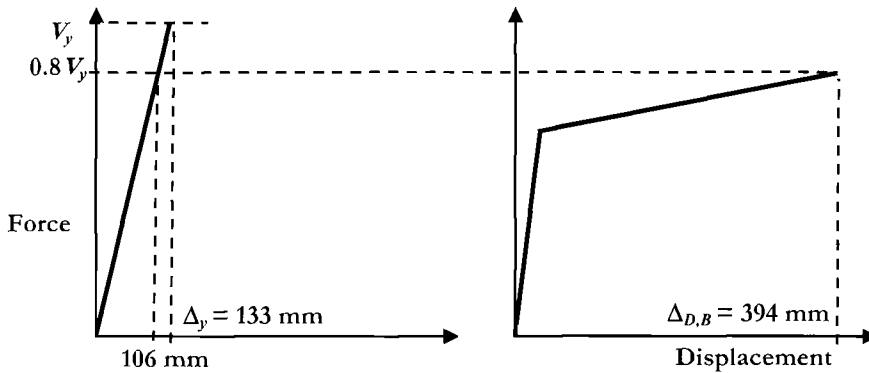$$\xi_{P,C} = (0.20 \times 394 + 0.05 \times 106) / 500 = 0.168$$

Abutments A and E (rigid abutment structure assumed):

$$\Delta_{D,A} = 500 \text{ mm (19.7 in)}$$

$$\xi_{P,A} = 0.2$$

(a) Force-Displacement: Pier B (left) and Isolator (right)

(b) Force-Displacement: Pier C (left) and Isolator (right)

Fig.11.34 Force – Displacement Diagrams for Piers B and C and the Corresponding Isolation System for Design Example 11.3

To calculate the global equivalent system damping, a decision is required about the distribution of shear between the piers. This could be in inverse proportion to height, as

in Example 10.3, which would result in equal bending moments for the piers, but different design forces for the isolators, or in proportion to supported weight, or dividing the total weight by the number of isolators, unifying the required strength of the isolators (but not the displacement demand). In this case it is assumed to distribute the total base shear in proportion to the weight supported by each abutment or pier, obtaining:

$$\xi_{sys} = \frac{0.20\times3800\times2 + 0.144\times8550\times2 + 0.168\times9500}{2(3800+8550)+9500} = 0.163$$

As a consequence, the spectral reduction factor to be applied to the 5% damped displacement spectrum is obtained from Eq.(2.8), as:

$$R_\xi = \left(\frac{0.07}{0.02+\xi_{sys}}\right)^{0.5} = \left(\frac{0.07}{0.02+0.163}\right)^{0.5} = 0.618$$

Entering the displacement spectrum of Fig.10.15 with a displacement equal to 500 mm (19.7 in) and incorporating the calculated reduction factor, a response period of approximately $T_e = 3.5$ sec is obtained.

To obtain the effective stiffness of the system it would be generally correct to calculate the appropriate values for the equivalent displacement, which would be less than the deck displacement because of the presence of the lumped-mass corresponding to the pier mass, and to calculate the equivalent mass, which will be larger than the deck mass, for the same reason. However, in Example 10.3 it was shown that the contribution of the pier masses is in the range of 3 % of the deck mass, and in the present case it would be less, possibly around 1%, being weighted by a smaller displacement.

The following equivalent stiffness is therefore obtained, simply considering a total effective weight corresponding to the deck weight, equal to 34,200 kN (7700 kips), as calculated for Example 10.3:

$$K_e = \frac{4\pi^2 m_e}{T_e^2} = \frac{4\pi^2 \cdot 34.2}{9.805\times3.5^2} = 11.2MN/m \ (64 \text{ kips/in})$$

The total base shear force due to the deck response is thus:

$$V_{Base} = K_e \Delta_D = 11.2\times0.5 = 5.6MN \ (1260 \text{ kips})$$

As assumed, this base shear is distributed to the columns in proportion to the supported weight:

$V_A = V_E = 5.6\times3.8/34.2 = 0.622$ MN (140 kips)

$V_B = V_D = 5.6\times8.55/34.2 = 1.40$ MN (314.8 kips) $\rightarrow M_B = M_D = 1.40\times16 =$ 22.4MNm (198000 kip·in) for longitudinal response. For transverse, the effective height is to the centre of mass of the pier, and a slightly higher moment results.

$V_C = 5.6\times9.5/34.2 = 1.56$ MN (350.7 kips) $\rightarrow M_C = 1.56\times12 = 18.7$MNm (166000 kip·in). Again the moment for transverse response will be a little higher.

To properly design the base section of the pier, these bending moment values have to

be multiplied by the isolator overstrength factor of $\phi^o = 1.25$, and additional bending moments corresponding to potential **P-Δ** and higher modes effects should be considered.

We first consider **P-Δ** effects. Since it is required to keep the piers elastic, the coefficient in Eq.(3.49) is taken as $C = 1$, as distinct from the value of 0.5 recommended for ductile response of concrete structures (see Section 3.6.3). The contribution of vertical load at maximum displacement is thus:

$M_{B,P\text{-}\Delta} = 8.55 \times 0.5 = 4.27$ MNm (37800 kip·in)

$M_{C,P\text{-}\Delta} = 9.50 \times 0.5 = 4.75$ MNm (42000 kip·in)

Regarding higher-modes effects, the contribution of the mass of each pier ($m = 7.52$ t/m (0.42 kips/in)) is obtained assuming a fixed–pinned configuration, a cracked stiffness (assuming a cracked moment of inertia equal to one third of the gross value, $I_{CR} = I_{gross}/3$) and a standard elastic approach, in which case the circular frequency of the first mode of vibration is equal to:

$$\omega_1 = 15.42\sqrt{EI_{eff} / mL^4}$$

The periods of vibration of each pier are thus obtained, and entering the acceleration spectrum of Fig.10.15 the corresponding accelerations (S_A) are read. The following column base bending moment are calculated:

Pier B and D:
$T_B = 0.102$ s
$S_{A,B} \approx 0.93$ g
$M_{base,B} = 2.19$ MNm (19400 kip·in)

Pier C:
$T_C = 0.57$ s
$S_{A,C} \approx 1.34$ g
$M_{base,B} = 1.78$ MNm (15800 kip·in)

The additional moments due to higher mode effects, and particularly **P-Δ** effects are quite relevant and cannot be neglected. The total bending moments for which the pier critical sections have to be designed are therefore:

$M_{B,base,total} = 22.4 \times 1.25 + 4.27 + 2.19 = 34.5$ MNm (305000 kip·in)

$M_{C,base,total} = 18.7 \times 1.25 + 4.75 + 1.78 = 30.0$ MNm (265000 kip·in)

Note that these values are of the same order as those found for the case of pinned connection between deck and piers, where abutment friction was considered. The main advantage for the isolated design will thus be that no damage should be expected in the pier at the design level of response.

The FPS isolators are designed assuming a friction coefficient $\mu_f = 5\%$, as follows.

Abutments:
Equivalent yield force $V_{yD,A} = 0.05 \times 3,800/2 = 95$ kN (91.4 kips)

Post-yield stiffness $K_{PD,A}$= (622/2 – 95)/0.5 = 432 kN/m (2.5 kips/in)
Radius of curvature (Eq.(11.20)) R_c = 1,900/432 = 4.4 m (173.2 in)
Equivalent viscous damping (Eq.(11.24)) $\xi_{h,A}$ = (2×0.05)/(π×(0.05 + 0.5/4.4)) =

$$= 0.195$$

Piers B and D:
$V_{yD,B}$ = 0.05×8,550/2 = 214 kN (48.1 kips)
$K_{PD,B}$ = (1,400/2 – 214)/0.314 = 1,548 kN/m (8.8 kips/in)
R_c = 4,750/1,548 = 2.8 m (110.2 in)
$\xi_{h,A}$ = 0.196

Pier C:
$V_{yD,C}$ = 0.05×9,500/2 = 237 kN (53.3 kips)
$K_{PD,C}$ = (1,556/2 – 237)/0.394 = 1,372 kN/m (7.8 kips/in)
R_c = 4,750/1,372 = 3.5 m (137.8 in)
$\xi_{h,C}$ = 0.194

The isolation devices have therefore different radii of curvature and different required displacement capacities (approximately 500 mm (19.7 in) for the abutments, 300 mm (11.8 in) for the external piers and 400 mm (15.8 in) for the central pier).

This has to be regarded as an idealized system that may be modified for economical or practical reason, for example assuming a common radius of curvature for all devices, e.g. equal to 3.5 m (11.5 ft), and this may result in an acceptable response of the bridge. In any case, a non-linear time-history analysis is recommended, because of the numerous simplifying assumptions adopted in comparison with the complexity of the structural response. The potential effects of axial force variation, which may become important if consideration of the vertical acceleration is made, may be accounted for. Also, the problem of heat dissipation should be taken into consideration, keeping the contact pressure between roller and spherical surface at a reasonably low value.

(c) Dissipative Braced Frames: An interesting class of complex systems with added damping for response control is given by different categories of braced frames endowed with added damping. We consider here the simple case of a pinned frame with diagonal bracings, as shown in Fig.11.35. The structural configuration implies a linear deformed shape, with the horizontal displacement controlled by the elongation of the diagonal braces. It is therefore possible to consider simply a one-bay one-storey substructure, with span equal to *L* and height equal to *H*, extending then the results to the entire frame.

It is assumed that the brace should not yield, being capacity-protected by the strength of the damper, which should thus be characterized by a yield or maximum force lower than the yield or buckling strength of the brace.

The yield displacement of the frame (Δ_y), will correspond to the yield deformation of the brace, as shown in Fig.11.35(b):

$$\varepsilon_y = \frac{L'_b - L_b}{L_b}$$ (11.71)

where L'_b and L_b are the deformed and the original length of the brace. Δ_y can be evaluated from the following equation, derived by simple geometrical consideration, assuming axial deformations of the beams, columns, and dissipators can be neglected:

$$\Delta_y = \sqrt{(L^2 + H^2)(1 + \varepsilon_y)^2 - H^2} - L$$ (11.72)

The corresponding interstorey drift (θ_y) is obtained dividing the yield displacement by the storey height:

$$\theta_y = \sqrt{((L/H)^2 + 1)(1 + \varepsilon_y)^2 - 1} - L/H$$

(a) At rest   (b) Yield   (c) Ductile Response
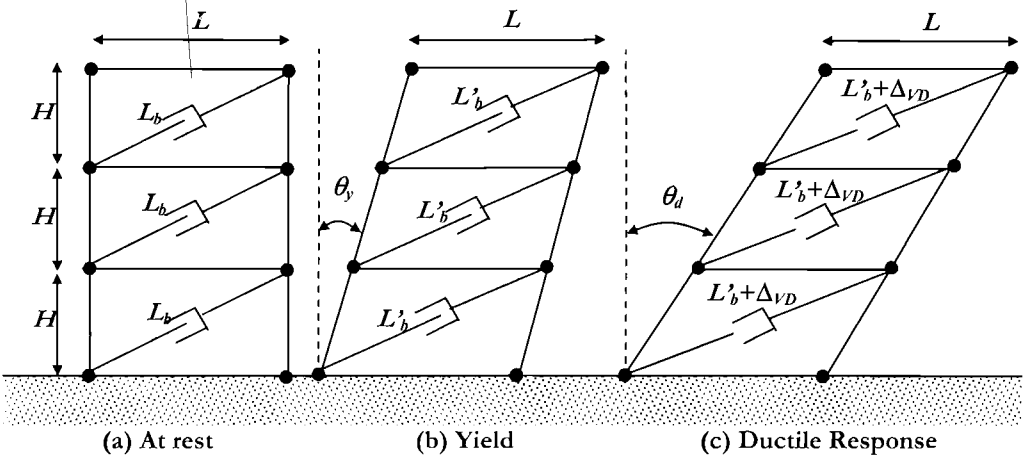
Fig.11.35 Deformation of a Braced Frame with Dissipators

It is evident that θ_y depends only on the ratio L/H and on the yield strain of the material used for the brace, as shown in Fig.11.36. For standard geometry and steel material properties a yield drift of the order of 0.4 - 0.5% results, a value similar to those commonly used to define non–structural limits at the serviceability limit state when masonry partitions are present.

Further displacement demands will not imply any additional elongation of the braces, but rather a deformation of the dampers (as shown in Fig.11.35(c)), assumed here to have rigid/perfectly-plastic deformation characteristics.
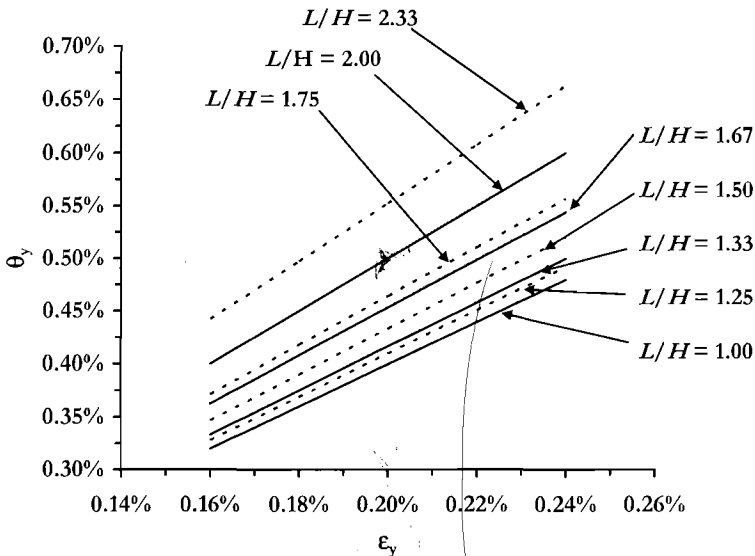
Fig.11.36 Yield Drift of a Braced Frame, as a Function of the Span over Height and of the Brace Yield Strain

The design process will proceed as usual:

- Assume a brace limit displacement factoring the yield displacement obtained from Eq.(11.71) and (11.72), say $\Delta_{yd} = 0.8\ \Delta_y$.
- Assume a design drift to limit the non-structural damage, say $\theta_d = 0.02$.
- Calculate equivalent ductility, $\mu = \Delta_d/\Delta_{yd}$, and corresponding equivalent viscous damping, applying the appropriate form of Eq.(3.17) (e.g., if a friction damper is used, apply Eq.(3.17e)).
- Enter the damped displacement spectrum with Δ_d and evaluate the period of vibration and the corresponding stiffness and shear force.
- By structural analysis determine the member forces: the forces in the frame, including the diagonal struts will be dimensioned for a force 1.25 times larger than those corresponding to the damper design force level.

(i) Design example 11.4: consider a building similar to that of Design Example 6.3 (Fig.6.30 and assume that the structural system resisting horizontal loading is now made by a number of dissipative braced frames, rather than structural walls. The number and location of the bracing system will be decided at the end of the design process. The seismicity is again characterized by a linear displacement spectrum for 5% damping with a corner period of 5 sec. and a corresponding displacement of 1.0m (39.4 in) for the damage–control earthquake. A code drift limit of 0.02 may govern the design. The building has 12 storeys and the floor weight at each level is 5 MN (1120 kips).

The storey height is 3.2 m (10.5 ft) and it is further assumed that the spans where the diagonal dissipative bracings will be located are 5 m (16.4 ft) long. The bracing system only will be designed here, without considering any torsional effect.

The braces are made from steel with ε_y = 0.0018 and provided with steel dampers. Modifications to be adopted for other kind of dampers will be obvious. Appropriate measures to avoid buckling of the braces are assumed to have been adopted.

The yield drift is calculated using Eq.(11.73):

$$\theta_y = \sqrt{((5/3.2)^2 +1)(1+0.0018)^2 -1} -5/3.2 =0.004$$

Note that this assumes that the damper yield displacement is negligible. If this is not the case, the additional drift corresponding to damper yield must be added. The total height of the building is 38.4 m (126 ft). Considering the linear deformed shape the effective height is H_e = 38.4×0.67 = 25.7 m (84.3 ft).

The yield and damage control design displacements are thus:

$$\Delta_{dy} = 0.004 \times 25.7 \times 0.8 = 0.082 \ \text{m (3.2 in)}$$
$$\Delta_d = 0.02 \times 25.7 = 0.51 \ \text{m} \ \ (20 \ \text{in})$$

and the corresponding displacement ductility is:

$$\mu_d = 0.51/0.082 = 6.3$$

Note that these horizontal displacement values correspond to brace elongations equal to $\Delta_{B,y}$ = 11 mm (0.433 in) and $\Delta_{B,d}$ = 54 mm (2.1in), as shown in Fig. 11.37.

It is now assumed to insert in each brace a steel damper, and the corresponding equivalent viscous damping is calculated applying Eq.(3.17c) as:

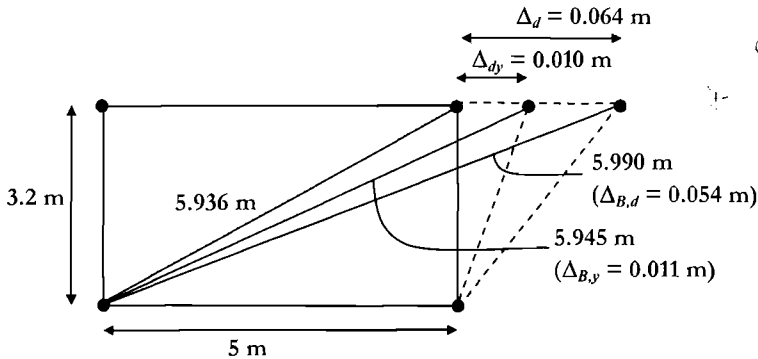$$\xi_{hyst} = 0.05 + \frac{0.577(6.3-1)}{6.3\pi} = 0.204$$

Fig.11.37   Deformed Shape of a Storey in Design Example 11.4

Note that the whole shear will be taken through the bracing system, therefore this is also the system damping ratio.

The procedure is now straightforward; a summary of results is provided here:

Displacement spectrum reduction factor for $\xi = 0.204$: $R_\xi = 0.559$

Corner period displacement for $\xi = 0.204$: $\Delta_{5,0.204} = 0.559$ m (22 in)

Effective period: $T_e = 4.56$ s

Effective mass: $m_e = 46.4$MN/g (10432kips/g)

Effective stiffness: $K_e = 8.98$MN/m (51.3kips/in)

Design base shear: $V_{Base} = 4.58$MN (1030kips)

The base shear, multiplied by 1.25, should now be transposed into member forces, to design each element. Note that the braces could be located on any number of bays, depending on the accepted action. Note also that the strength of the dampers should be tailored and will decrease from the bottom to the top of the building. The axial values resulting for the critical braces located at the ground storey can be immediately derived from the base shear, using the following equation, derived by pure geometrical considerations:

$$F_{Brace} = \frac{V_{Base}}{\cos(\tan^{-1}(H_i/l))} = 5.44\,MN \quad (1225kips)$$

The design axial forces resulting for the case of four braced bays will thus be: 1.36 MN (306 kips) per brace, while increasing the number of braced frames, the force will reduce proportionally. These forces will be used to design the damper strengths, while the braces will be designed for values 1.25 times larger. Columns and beams will also be capacity protected.

Note that in the procedure no allowance has been taken for higher mode effects. In this case, they may produce larger displacement demands rather than higher forces, since the forces will be controlled by the capacity of the dampers.

(d) Walls Coupled with Dissipative Elements: Coupled structural walls systems, discussed in Section 6.8, are convenient systems to be endowed with additional damping elements. The coupling beams could be substituted with various forms of dampers, to reach a high level of energy dissipation capacity. In combination, the bases of the walls can be designed elastically or for a desired level of local ductility, or, more efficiently, for a controlled rocking response.

The coupling links can be designed according to several configurations, as exemplified in Fig.11.38, but in general they can be treated similarly to the coupling beams presented in Section 6.8.1, where they were characterized by their aspect ratio L_{CB}/h_{CB}.

With reference to Section 6.8, there is no difference in calculating the wall yield displacement assuming yield is permitted, while the wall design displacement will be limited only by wall–base material strains (Eq.(6.65a)), or by wall drift limit, since the damping devices can be designed, in principle, for any design drift.

If the wall is prestressed and designed for a controlled rocking response, the displacement shape before rocking starts will be essentially elastic, based on gross section

properties, and could in many cases be neglected, assuming a rigid–plastic response. With slender walls, however, elastic displacements should be considered.
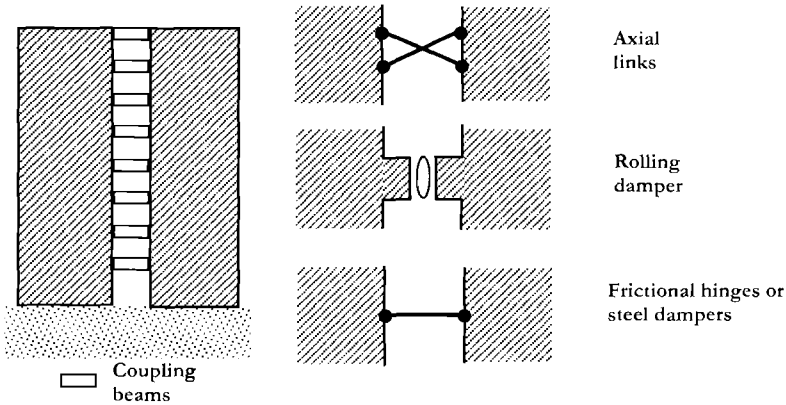

Fig.11.38   Shear Walls Coupled with Dissipative Links: Examples of Damping Devices

With reference to the discussion of rocking response (Section 11.2.4(f)), it should be noted that a tensile restraining force will always be present in this case, since the rocking motion will take place internally to the structure, between the wall and the foundation structure. This force will normally be provided by bars or cables which will be designed to respond elastically at the design displacement, providing a nominal post-tensioning force and an appropriate unbonded length, or an effective post-tensioning force with the addition of some dissipating device at the connection of wall and foundation. As a function of the design choices, the appropriate forms of Eq.(11.53) should be used.

In general, design will proceed as usual, and more specifically as presented in Section 6.8, assuming an appropriate share of the overturning moment to be taken by the walls and by the coupling system and consistently assuming a reasonable equivalent viscous damping value (applying Eq.(6.66)), to be checked at the end of the design process.

Though no interaction with floor slabs or with additional gravity resisting frames will generally be assumed in the design phase, these aspects may be relevant to the effective response, and should be checked in a design verification mode.

It is noticeable that the combination of wall controlled rocking and coupling damping device will be extremely effective in limiting the structural damage at the design displacement to essentially negligible levels. Also, the residual displacement will be small and due to the response of the damping system alone, because of the essential non-linear elastic behaviour of a rocking response. As already pointed out, in the case where viscous dampers are used, the residual elastic force due to gravity will slowly eliminate the residual displacement. In this case, however, the expected velocity levels should be examined, since low values may result as a consequence of long periods of vibration and small

relative displacements. An example of the performance of such a structure is provided by the PRESSS 5-storey precast building test, described in Section 6.7

The wide variety of the possible solutions is briefly addressed here with two numerical examples.

(i) Design example 11.5: Consider again the coupled–wall building of Design Example 6.3, presented in Section 6.8.7. All the data provided there remain unchanged, with the exception of the coupling beams which will now be replaced with damping devices. The structure is further modified by replacing each channel wall by two parallel walls, eliminating the flange.

Though not exact, the yield displacement is assumed to remain the same, to allow an easier comparison: $\Delta_y = 0.179$ m (7.05 in).

Since the damping system will be designed for the required drift capacity, the design displacement can now be controlled only by the wall strain limit or by the wall drift limit. The latter one will govern, as in the previous case. The design displacement will therefore remain unchanged: $\Delta_d = 0.482$ m (19.0 in), and consequently the wall ductility and equivalent viscous damping are again $\mu_W = 2.7$ and $\xi_W = 0.139$.

It is decided to design the links using appropriately shaped steel dampers. As an example dampers shaped like double triangles will be adopted, with the shear load parallel to the variable side (see Section 11.2.4). A ductility of about 15 can be obtained and an equivalent viscous damping of the order of 25 % can be assumed.

As in Example 6.3 it is decided to carry 60% of the total overturning moment (M_{OTM}) through coupling action ($\beta_{CB} = 0.6$). The system damping will thus be evaluated as:

$\xi_{sys} = 0.4 \times 0.139 + 0.6 \times 0.25 = 0.206$

Applying the usual procedure the following results are obtained:

Displacement spectrum reduction factor for $\xi = 0.206$: $R_\xi = 0.556$

Corner period displacement for $\xi = 0.206$:	$\Delta_{5,0.206} = 0.556$ m (21.9 in)
Effective period:	$T_e = 4.33$ s
Effective mass:	$m_e = 46.4$ MN/g (10432 kips/g)
Effective stiffness:	$K_e = 9.96$ MN/m (56.9 kips /in)
Design base shear:	$V_{Base} = 4.80$ MN (1079 kips)
Design overturning moment:	$M_{OTM} = 129$ MNm (1.145×10^6 kip·in)

The choice of the actual dampers will normally proceed considering the properties of commercially available devices, based on the actual capacity requirements in terms of shear, flexure and drift. The following considerations are conceptual in nature, to illustrate the logic of the design process.

The shear capacity required for each damper is immediately calculated as $V_{D,c} \geq 475$ kN (106.8 kips) (step 13 of Example 6.3), which will determine the minimum required shear area. Flexural capacity, drift demand and capacity will depend on the actual size of the dampers, which will not necessarily fill the entire distance between the walls. As

shown in Fig.11.39, where the meaning of the symbols is also defined, Eq.(6.62) will now take the following form:

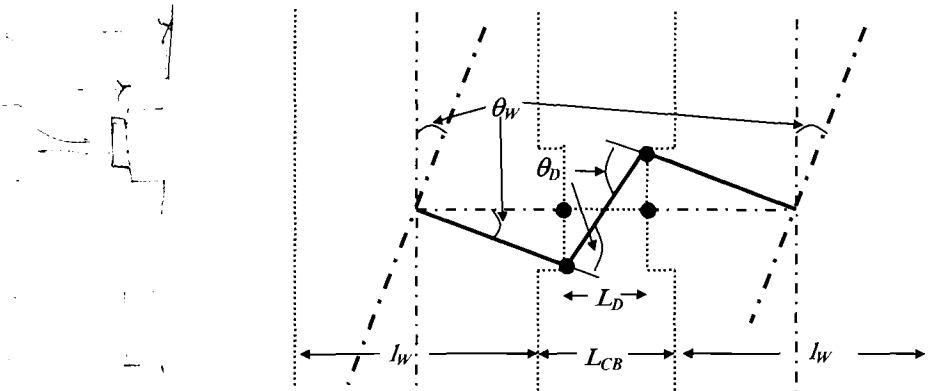$$\theta_D = \theta_W \left(\frac{l_W + L_{CB}}{L_D} \right) \tag{11.74}$$

Fig.11.39   Rotation Demand at the Damper, as a Function of Wall Rotation

Assuming constant curvature between the end of the device and the centre, with a reversal of curvature sign at the centre, the drift capacity of the device is found by dividing the relative displacement of the two ends by the length, as

$$\theta_D = 0.5\varepsilon_x \frac{L_D}{h_D} \tag{11.75}$$

where ε_x is the strain limit value and h_D is the height of the device (see Fig.11.40).

Combining the above two equations, assuming $\varepsilon_x = 0.03$ at the design displacement and inserting the values for $l_W = 5$ m (197 in), and $L_{CB} = 1.8$ m (70.9 in), the following relationship between the end depth and span of the device is obtained:

$$h_D = 0.11L_D^2 \ (m) \ \left(h_D = 0.0336L_D^2 \ (ft) \right) \tag{11.76}$$

The design procedure for the devices then proceeds in the following steps: 1) select the span length L_D, 2) calculate the end moment $M = 0.5 V_{D,c} L_D = 237.5 L_D$ kNm, 3) calculate the required device end depth from Eq,(11.76), 4) determine the required width from the relationship $M = f_y b h_D^2 / 4 = 237.5 L_D$ (kNm) (53.4L_D kip·in), 5) define the hour-glass shape, using the same equation, with the calculated value of b and the appropriate moment, 6) determine the minimum thickness to satisfy shear requirements. Assuming a yield strength of the steel $f_y = 360$ MPa (52.2 ksi), a possible solution is $L_D = 1.029$ m (40.5 in), $h_D = 116.5$ mm (4.59 in), $b = 200$ mm (7.9 in). The devices could be profile-cut from 100 mm (3.9 in) plate with two devices mounted side-by-side.

This possible solution is sketched in Fig.11.40. Clearly several other choices may well be possible, including completely different solutions, such as for example the shear link briefly described in Section 6.7.
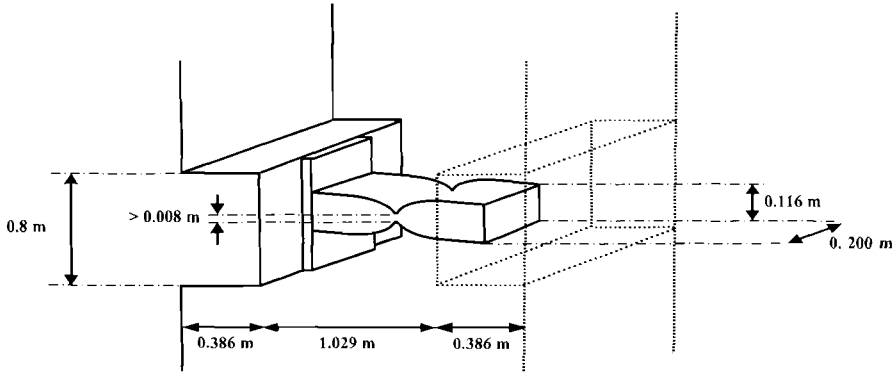

Fig.11.40   Geometry of a Damper for Example 11.5, and of its Connection to the Walls

With respect to the case presented in Section 6.8.7 (Example 6.3) it is worth noting that the global structural performance is similar, as expected, but the severe damage in the coupling beam will be avoided. If the dampers are removed and substituted after a major earthquake, part of the residual deformation should be recovered, as being related to the damage in the dampers.

(ii) Design example 11.6: The previous example was provided essentially for comparison, but did not take full advantage of the use of artificial damping in reducing damage, since significant ductility at the walls base was accepted.

Assume now we redesign the system using vertical post-tensioned cables throughout the height of the walls, unbonded for a certain length to allow a controlled rocking, and again provide dissipating devices between the walls.

As discussed, the elastic deformation of the walls may be neglected and the design displacement shape is assumed to correspond to that of a rigid body rotation. Although this is an approximation, it should be noted that since the walls are prestressed, we do not expect cracking, and the wall displacements at 80% of yield, should be about 25% of those in Example 6.3. This implies wall ductility of about 11, and the assumption of rigidity will certainly be adequate for an initial design. In consideration of this assumption, and of requirements for containing the non-structural damage, a constant drift along the height lower than 2% (e.g. 1.5%) could be reasonably assumed. For comparative reasons, however the 2% drift will still be adopted. Due to the linear displacement shape the equivalent height is still H_e = 0.7H ≈ 26.9m (88.3 ft) and the design displacement is Δ_d = 0.02×26.9=0.538 m (21.1 in).

Again to allow an easier comparison with the previous case, it is still assumed to carry 60% of the total overturning moment through coupling action: β_D = 0.6.

The equivalent viscous damping from the device is assumed to be equal to $\xi_{eD} = 30\%$; this is compatible with carefully designed steel dampers. The use of X-shaped viscous dampers is not advisable because of the low velocities that have to be expected. No additional dissipation is provided at the base of the walls, therefore the system total equivalent viscous damping is estimated using Eq.(11.63) (a similar value would be obtained from Eq.(11.64), with $\lambda \approx 0.5$):

$\xi_{sys} = 0.4 \times 0.05 + 0.6 \times 0.30 = 0.20$

Applying the usual procedure the following results can be obtained:

Displacement spectrum reduction factor for $\xi = 0.20$: $R_\xi = 0.564$

Corner period displacement for $\xi = 0.20$: $\Delta_{5,0.20} = 0.564$ m (22.2 in)

Effective period: $T_e = 4.77$ s

Effective mass: $m_e = 46.4$ MN/g (10432 kips/g)

Effective stiffness: $K_e = 8.21$MN/m (46.9 kips/in)

Design base shear: $V_{Base} = 4.42$ MN (993 kips)

Design overturning moment at base: $M_{OTM} = 118.9$ MNm (1.05×10^6 kip·in)

Wall Design: Since the flanges of the channel walls in Example 6.3 have been removed, we design four identical walls, The average bending moment for each wall is $M_w = 118.9 \times 0.40/4 = 11.9$ MNm (105,000 kip·in). Each wall will carry a total vertical load $W = 5.75$ MN (1349 kips) and will be restrained by a lightly prestressed high-strength cable located at 500 mm (19.7 in) from each end of each wall.

From Eq.(6.55) the force to be carried by each coupling beam and damper will be:

$$V_{CB,i} = \frac{0.6 \times 118.9}{24(5+1.8)} = 437 kN \quad (98 \text{ kips})$$

Hence the axial force from coupling action at the base of each wall will be $12 \times 0.437 = 5.25$ MN (1180 kips). This is less than the assessed gravity load of 5.75 MN (1290 kips) per wall, which is a little lower than for Design Example 6.3 because of reduced weight (no wall flange) and reduced tributary area of floor slab. The axial forces in each of the walls of a coupled pair of walls are thus $5.75-5.25 = 0.5$ MN (112.4 kips), and $5.75+5.25 = 11$ MN (2373 kips). The expected concrete compression strength is 32.5 MPa (4714 psi) (see Section 6.8.7), and hence, with a wall thickness of 250 mm (9.8 in), the depth of the compression blocks in the tension and compression walls are 0.073 m (2.9 in), and 1.59 m (62.6 in) respectively. The moment capacities corresponding to axial force in the walls are thus:

Tension wall: $M_T = 0.5(5/2-0.072/2) = 1.2$MNm (10900 kip·in)

Compression wall: $M_C = 11.0(5/2-1.59/2)$ $= 18.8$MNm (166,000 kip·in)

Total capacity: $M_T + M_C = 1.2+18.8$ $= 20$MNm (177,000 kip·in)

This is 3.8 MNm (33,635 kip·in) less than the required capacity of $2 \times 11.9 = 23.8$ MNm (2,000,000 kip·in), and hence additional capacity must be provided by an elastic restraining force, as envisioned in the design problem statement. With tendons 500 mm

(19.7 in) from the end of each wall, and conservatively assuming an increased average compression block length of 1.0m (39.4 in), the force required to be developed at the design drift of 2% is:

T_T =0.5 × 3.8/(5-0.5-1.0/2)=475 kN (107 kips)

We choose to limit the strain in the tendons at the design drift of 0.02 to ε_t = 0.004, corresponding to a stress of 800MPa (114.5 ksi). This makes provision for response at larger than the damage-control limit state, without exceeding the limit of proportionality of the tendon steel. Again assuming an average neutral axis depth of 1.0 m (39.4 in), the required extension of the tendon will be:

Δ_t = 0.02(5−0.5−1.0)=0.070 m (2.7 in).
The required debonding length is thus:
$L = \Delta_t/\varepsilon_t$ = 0.07/0.004≈17.5 m (689 in).
The required tendon area is
$A_t = T_t/f_t$ = 0.475/800 m² =594 mm² (0.92 in²)

Damper Design: The dampers have to be designed for a force of 437 kN (98 kips). The procedure follows that of Example 11.5 and is not repeated here.

11.4 DESIGN VERIFICATION OF ISOLATED STRUCTURES

In this Section the design verification of two previously described Design Examples (11.3 and 11.5) is carried out by means of inelastic time-history analysis (**ITHA**) using the program "**SeismoStruct**" provided in the CD with this book. Input and output data files for the analyses carried out are also included on the CD, together with an overview of modelling configuration and assumptions, and a summary of the most relevant results.

11.4.1 Design example 11.7: Design Verification of Design Example 11.3

The four-span bridge of Design Example 11.3 was modelled as a 3-D structure, with the superstructure represented by an elastic member, while the piers used inelastic fibre beam-column elements with appropriate stress-strain relationships for the concrete and reinforcing steel (see Section 4.2). Given that this is an isolated structure, and considering also the fact that fibre element formulations account for the actual non-linear response characteristics of reinforced concrete members, even in the so-called "elastic" phase of response, a reduced value of 1% tangent-stiffness proportional elastic damping was introduced. Strain penetration in footings at the base of the piers was considered by means of an increase of the length of the finite element, as discussed in Section 4.9.2(b).

Seven **ITHA** were carried out, each of which using a different spectrum-compatible artificial record generated with SIMQKE[G6]. The results, which are fully provided in the CD, showed mean peak response displacements that are very close to the values assumed during design (see Fig.11.41). The design objective of avoiding inelastic deformations in

the piers was also achieved, and the response of the isolators was as envisaged during design (see Fig.11.42).
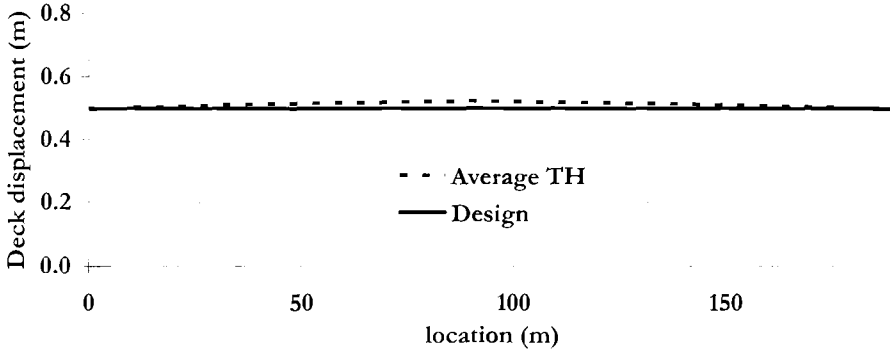

Fig. 11.41 Mean Peak Deck Displacements Response vs. Design Values for Design Example 11.7
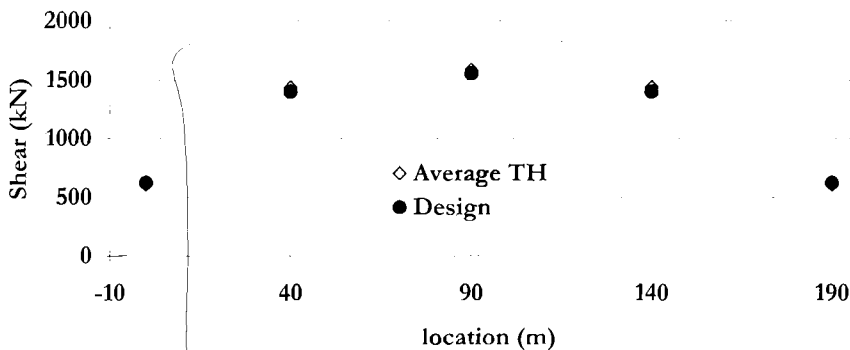

Fig. 11.42 Mean Peak Shear Demand in Isolators vs. Design Values for Design Example 11.7

A second set of analyses was also run, assuming equal radii of curvatures (R_c = 3.5 m) for all the devices, which effectively implies an increase of the isolators' post-yield stiffness at the abutments, and a decrease at the side piers. The results showed again very good agreement between design assumptions and the actual inelastic dynamic response.

11.4.2   Design example 11.8: Design Verification of Design Example 11.5

The wall building of Design Example 11.5, featuring double triangular-shaped steel damping devices as wall couplers (see Fig.11.40), was modelled as a 2-D structure using inelastic fibre elements with appropriate stress-strain relationships for the concrete and reinforcing steel (see Section 4.2) to represent the structural walls. The coupling system, on the other hand, was modelled by means of 1-metre long rigid line elements with end

bilinear moment-rotation hinges characterised by an initial stiffness of 20633 kNm/rad, a yield moment of 163 kNm and a post-yield hardening ratio of 0.032, following the design indications described in Section 11.3.3(d).

A new set of spectrum-compatible artificial records was again employed to run seven **ITHA**, leading to the average results that are shown in Fig.11.43, where it is observed that the design objective of avoiding interstorey drifts larger than 2% has been achieved in satisfactory manner; the maximum mean peak drift demand is around 1.8%.
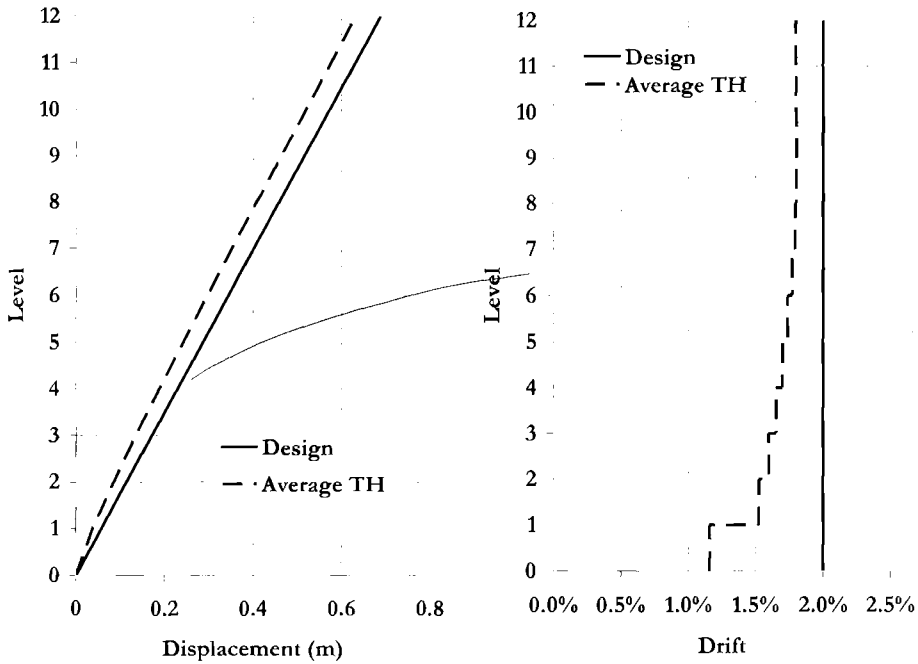
Fig. 11.43 Mean Peak Storey Displacements/Drifts Response vs. Design Values for Design Example 11.8

12

WHARVES AND PIERS

12.1 INTRODUCTION

In Chapter 1, Section 1.3.4(d), the design of marginal wharves was used as an example of a type of structure for which conventional force-based seismic design was particularly inappropriate. With reference to the example of Fig.1.10, reproduced here for convenience as Fig. 12.1, it was noted that conventional force-based design would sum the elastic stiffnesses of the different piles to establish a global structural stiffness, calculate the corresponding fundamental period, and hence determine the elastic design force from the elastic acceleration spectrum, with knowledge of the inertial mass. A force-reduction factor would be applied to determine the design seismic force, which would then be distributed between piles in proportion to their elastic stiffness. The implicit assumption of equal ductility demand, which is required if the force-reduction factor is applied to the total design force, is invalid, as is clear from Fig.12.1(b), where it is obvious that the ductility of the piles at the expected response displacement $\Delta_{\mu F}$ differs with the length of the pile. In fact the longest piles will be expected to remain elastic.

Forces in shear keys between adjacent segments of wharves cannot be determined directly from elastic analyses, whether these be single-mode or multi-mode analyses. This is because the force levels depend on both the response inertia forces in the adjacent wharf segments, and the displacement levels. Since the shear keys will be required to respond essentially elastically, it might be expected that the elastic forces from an elastic modal analysis might be reasonable. In fact these force levels are much higher than will result from inelastic response, whereas the force levels found by dividing the elastic shear-key force levels by the design force-reduction factor will seriously underestimate the true force levels.

Recently the Port of Los Angeles (POLA) in California has addressed these problems by developing an alternative seismic design approach based on performance criteria, and displacement-based design[P40]. Much of the material presented in the following sections of this chapter is based on this work, which has also been included in international seismic design guidelines for port structures[X12].

In this chapter, we discuss both marginal wharves and piers, with greater emphasis on the former. A marginal wharf is defined as a long wharf whose major axis is essentially

parallel to the shore. These structures are often very long, in the order of hundreds of metres, comprising several segments connected by shear keys to allow for thermal movements. Ships at marginal wharves are thus normally berthed parallel to the shore. Piers are structures whose major axis is essentially perpendicular to the shore, and ships will normally be berthed parallel to the pier long axis, and hence perpendicular to the shore. This is a rather simplistic characterization, as in many cases wharf structures will be more complex, either as a consequence of a non-linear shore line (marginal wharves), or piers with end segments parallel to the shore. The latter are sometimes termed terminals. Figure 12.2 describes some of the alternatives.
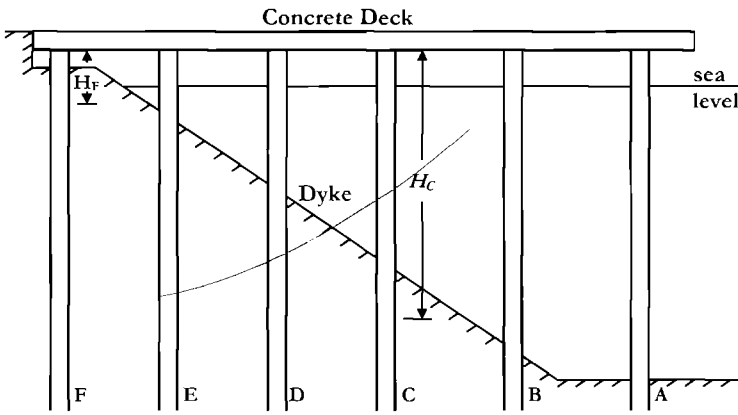
(a) Transverse Section through Wharf
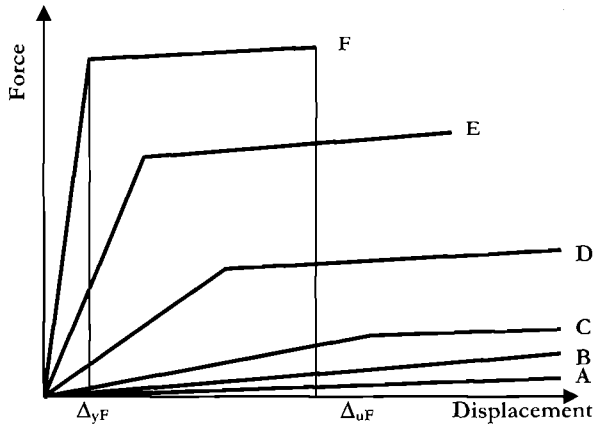
(b) Force-Displacement Response of Individual Piles

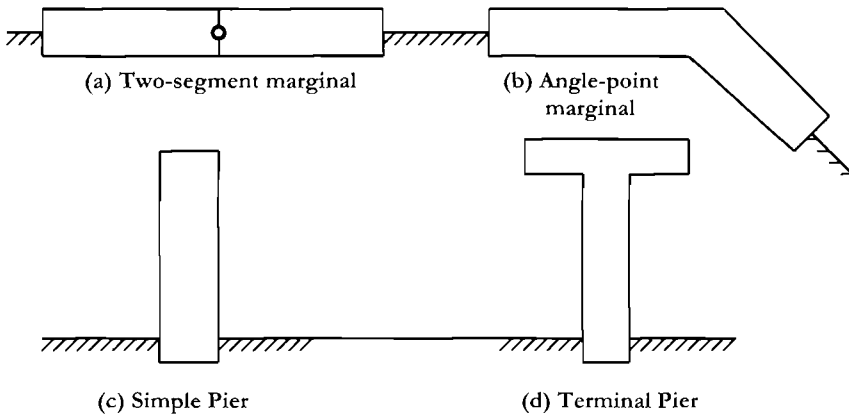**Fig. 12.1 Transverse Seismic Response of a Marginal Wharf**

Fig.12.2 Types of Wharves and Piers (plan view)

12.2 STRUCTURAL DETAILS

Piles for marginal wharves may be constructed of reinforced concrete, prestressed concrete (solid or hollow section), steel H-sections, hollow steel tubes, concrete-filled steel tubes or timber piles. However, for new construction, solid prestressed concrete or hollow or concrete-filled steel-shell piles will be most common, because of their serviceability under the rigours of pile driving, and corrosive attack from marine environments. Existing wharves and piers dating from the 1960's and earlier will often be supported on timber piles. With modern construction, piles in seismic regions will generally be driven or placed vertically, rather than raked at an angle to the vertical. Although raked piles result in a stiffer wharf or pier, they attract high seismic axial forces, which can be unpredictable in magnitude. These high axial forces induce severe bending and shear forces in the deck. The result can be pile failure (compression or pull-out), or deck failure.

Decks will normally be cast-in-situ reinforced or prestressed concrete, and because of the dimensions of the wharf or pier, the deck will essentially behave as a rigid diaphragm in the deck plane. Connection between the deck and piles will depend on the type of pile being used, but generally the connection will be moment-resisting, to improve structural efficiency and to increase the lateral stiffness. With prestressed or reinforced concrete piles, it is common to provide ducts for reinforcing dowels at the top of the pile. When the pile has been driven to the specified resistance, the section of pile extending above the specified pile-top elevation is removed, by cutting or by explosives. Dowel bars are then grouted into the pre-formed ducts in the top of the pile and anchored in the deck, when the deck concrete is placed, to provide the moment-resisting connection. Alternatively, with prestressed piles, the prestressing strand may be exposed for adequate length to develop the strand in the deck. This approach, though favoured in research documents, is not favoured in practice because of the difficulty in avoiding damage to the

strand when cutting the pile to the final elevation.

With modern marginal container wharves the wharf width will normally be dictated by details of the container cranes used to service the ships. Typically modern container cranes have a rail gauge of about 30m (100ft), and a weight of between 1500 and 2000 tonnes. In order to efficiently support the crane leg vertical reactions, and reduce deck flexural and shear forces, the seaward and landward rows of piles (e.g. rows **A** and **F**, in Fig. 12.1) will be located under the crane rails, and the distance between piles along these rows will typically be less than for piles on intermediate rows (rows **B** to **E**, in Fig. 12.1). On these crane-support lines the typical spacing of piles will be 3m (10ft) or less. For this reason it is more common with new container wharves to use comparatively close-spaced smaller diameter piles than fewer numbers of larger diameter piles. In the seismic areas of the US West Coast, 610mm (24 in) diameter octagonal prestressed piles are most common.

12.3   THE DESIGN PROCESS

12.3.1   Factors Influencing Design

Seismic design philosophy for wharves will normally be based on inelastic response of some or all of the piles, with a capacity-design process adopted to ensure that the deck, and the shear keys, if any, between deck segments, remain essentially elastic. A number of additional factors need to be considered at the start of the design process:

- Under longitudinal response, a high eccentricity will exist between the centre of mass of the deck, and the centres of stiffness or resistance. Thus torsional response will be inevitable, with significant transverse displacement resulting from longitudinal excitation. Displacement of corner piles of segments will be greater than for piles near the centre of a segment.
- The piles will be subjected to simultaneous excitation in the longitudinal and transverse direction. Since the ductile elements are the piles, it is thus essential to consider the increase in displacement resulting from combined orthogonal excitation. This is discussed further in Section 12.3.2.
- Interaction between adjacent wharf segments as a consequence of the resistance of the shear keys complicates the structural response.
- With a displacement-based design approach, design will be based on equating the displacement demand and displacement capacity of the critical piles. These piles will typically be the corner piles of the landward row (**F**, in Fig.12.1). Note that displacement demand on the seaward row (**A**, in Fig.12.1) may be a little larger than at the landward row, but displacement capacity will be much greater, and these piles will not be critical. If the wharf consists of more than one segment, linked by shear keys, it will normally be the corner pile at the end of an end segment that will govern design, as the torsional response of inner segments has been found from time-history analysis to be reduced by the restraint of the adjacent segments[P38].

- Structural response of the critical piles will involve the formation of pile plastic hinges at the pile/deck interface, and at some depth in the dyke. The latter plastic hinge is termed the "in-ground" plastic hinge. Since drift limits have little relevance for wharf structures, the displacement limits will be dictated by strain limits in the plastic hinges, and possibly by **P-Δ** effects. The strain limits depend on the performance criteria for the level of earthquake considered, and are generally different for the pile/deck and the in-ground hinge. The reason for the difference is that damage to a pile at the in-ground hinge location is difficult to inspect and repair after an earthquake, and hence the design criterion for the in-ground hinge will be to avoid damage requiring repair.
- Characterization of the soil properties of the dyke supporting the piles will inevitably be subject to some uncertainty. It is important that this uncertainty be considered in the design. Generally this will be effected by consideration of upper-bound and lower-bound properties for the soil strength and stiffness. Design should be based on whichever bound provides the higher displacement demand/capacity ratio. A further complication is that for piles embedded through a sloping dyke, the soil stiffness and strength in the upper layers may depend on the direction of inertia force; there will be greater resistance to landward response than to seaward response. However, the critical piles (Row **F** in Fig.12.1) will generally be on level ground, and response of the wharf will typically be dominated by close-spaced piles on this row. In this case, the uncertainty associated with soil properties for upslope and downslope response becomes comparatively unimportant.
- Vertical seismic response is not generally a significant issue for design of the wharves. Inelastic time-history analyses have shown that lateral displacement demands of marginal wharves are insensitive to vertical excitation. Also, the displacement capacities are not affected significantly by the levels of axial load variation expected from vertical response accelerations. An exception is the response of container cranes. Displacements and force levels in cranes have been found from time-history analyses to be significantly influenced by vertical accelerations[P39].

12.3.2 Biaxial Excitation of Marginal Wharves

With direct displacement-based design, the effective displacement at the centre of mass of the structure is required in order to facilitate a **SDOF** design approach. However, as mentioned in the previous section, design must consider both the torsional response under longitudinal excitation, and the effects of simultaneous longitudinal and transverse excitation. It is convenient to carry out the design process on the transverse response (i.e. perpendicular to the shore) since response in this direction will normally be uniform, unless soil conditions vary significantly along the length of the wharf. Thus it is necessary to be able to estimate the relationship between centre-of-mass transverse
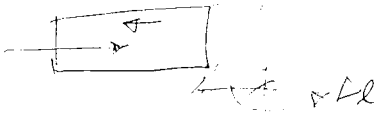
displacement Δ_t under pure transverse excitation, and displacement Δ_{cr} of the critical corner piles of the critical segment under combined longitudinal and transverse excitation.

Under pure longitudinal seismic excitation, and conservatively ignoring the effects of torsional mass inertia (see Section 6.4), the transverse displacement Δ_{tl} at the end of a single-segment wharf on uniform soil can be shown to be

$$\Delta_{tl} = (6e/L)\Delta_{ll} \tag{12.1}$$

where Δ_{ll} is the longitudinal displacement at the centre of mass, and e and L are the effective stiffness eccentricity at design response, and the segment length respectively.

It is common practice with seismic codes to consider response to biaxial excitation, where significant, on the basis of an equivalent static approach where the displacements result from excitation of 100% of the design spectrum in one direction and $X\%$ of the design spectrum in the other direction. Typically $X=30$ is adopted. Equation (12.1) indicates that transverse displacements will develop under both transverse and longitudinal excitation. For a marginal wharf the combination (100% longitudinal + $X\%$ transverse) can be shown to be more critical for the vectorial displacement of the corner pile than (100% transverse + $X\%$ longitudinal). It can easily be verified that under these conditions, and again ignoring torsional mass inertia, noting that centre-of-mass displacements under pure longitudinal and transverse excitation at full design spectral excitation will be equal, the relationship between Δ_t and Δ_{cr} is given by

$$\Delta_t = \frac{\Delta_{cr}}{\sqrt{1+\left(\dfrac{X}{100}+6\dfrac{e}{L}\right)^2}} \tag{12.2}$$

Equation (12.2) is plotted for values of X between 20 and 50, and different segment length/width aspect ratios L/B in Fig.12.3, based on the assumption that the eccentricity is $e = 0.4B$. As shown later in Fig.12.17, and in Design Example 12.1, this is a typical eccentricity ratio at design displacement response. Time-history analyses indicate that $X=40$ is adequately conservative for initial design. For an inner segment of a multi-segment wharf, a flat ratio of $\Delta_t = 0.85\Delta_{cr}$ may be conservatively assumed.

Recent on-going research has indicated, however, that critical conditions occur when the excitation components (100%, $X\%$) are rotated by 30 – 45 degrees from the longitudinal axis. Under these conditions, corner displacements can be as much as 15% higher than implied by Eq.(12.2).

12.3.3 Sequence of Design Operations

With the information given in the previous section, it is now possible to outline the steps of the displacement-based design process:
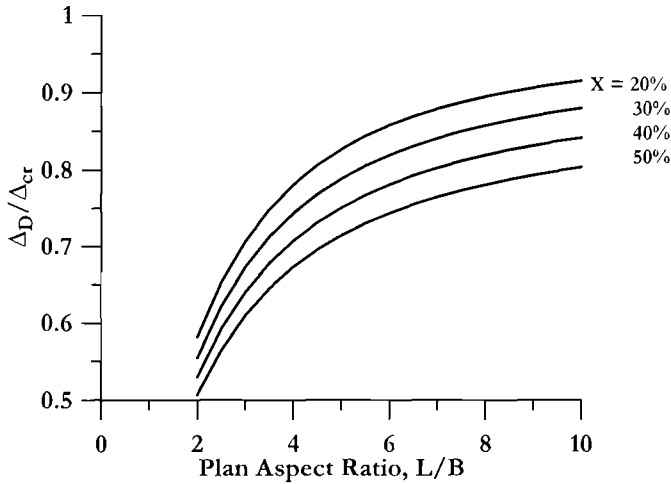
Fig.12.3   Ratio of Design Displacement for Simple Transverse DDBD to Corner Pile Critical Displacement, for 100% Longitudinal and X% Transverse Excitation

Step 1: Determine the critical pile. This will be a corner pile of an end segment (if there is more than one segment)

Step 2: Determine the expected free heights of the piles on rows **A** to **F** (assuming six rows of piles – the modification for different numbers is obvious).

Step 3: Carry out force-displacement pushover analyses for a pile of each row in accordance with procedures discussed in Section 12.5. This will be carried out for both upper and lower bound estimates of soil properties.

Step 4: Determine the limit displacement Δ_{cr} corresponding to the strain performance limits for the earthquake level being considered in the design process. This is discussed in Section 12.4.

Step 5: Using the information provided by Eqs.(12.1) and (12.2) the centre-of-mass design displacement for pure transverse response is calculated. This is the design displacement to be used in the direct displacement based design process.

Step 6: Determine the expected displacement ductility demand at the centre of mass. The system displacement ductility demand will be a little less than for the landward (**F**) pile row, since other piles contribute to the strength, but with reduced ductility demand. If Δ_y is the yield displacement of the bi-linear approximation to the **F**-row force-displacement response (see Section 12.5) then the system ductility can be approximated, for a first estimate, as:

$$\mu_{sys} = \frac{\Delta_t}{1.2\Delta_y} \tag{12.3}$$

√ **Step 7:** Determine the equivalent viscous damping. Definitive data are not yet available on equivalent viscous damping of prestressed piles, though it is expected that **POLA** tests planned at the University of California, San Diego in 2007 will provide useful data. The pile-top hinge can be expected to have characteristics similar to the "Thin" Takeda rule of Eq.(3.17), while the in-ground hinge will initially have nonlinear elastic characteristics. Soil damping will add to the global damping, as discussed in Section 10.3.5(c) in relation to pile/columns. Until definitive data are available it is recommended that Eq.(3.17a) is the most appropriate. This is reproduced here as Eq.(12.4):

$$\xi_e = 0.05 + 0.444\left(\frac{\mu_{sys} - 1}{\mu_{sys}\pi}\right) \tag{12.4}$$

√ **Step 8:** With Δ_I and ξ_e known, determine the damping reduction factor R_ξ, from Eq.(2.8), and hence the effective period T_e from the displacement spectra set, as illustrated, for example, in Fig.3.1(d)

√ **Step 9:** With respect to the typical example of Fig.12.4 (which represents the response of a 6m length of typical wharf in American standard units), and Eq.(3.1), determine the effective stiffness:

$$k_{ss} = 4\pi^2 \cdot \frac{m_e}{T_e^2} \tag{12.5}$$

In Eq.(12.5) m_e is the effective mass corresponding to the length of wharf chosen for analysis. This may be a characteristic module length of (say) 6m (20ft). The effective mass will include the entire deck mass for the module length adopted plus a contribution of the mass of each pile within the module. This should be taken as $1/3^{rd}$ of the pile mass between deck and effective depth of fixity for displacements, which may be taken as 5-pile diameters below the dyke top surface. The calculated stiffness k_{ss} will hence also correspond to the module length adopted.

√ **Step 10:** Determine the required lateral strength F_{ss} of the segment module from Eq.(12.6):

$$F_{ss} = k_{ss} \cdot \Delta_I \tag{12.6}$$

√ **Step 11:** Strengths of the piles at different rows corresponding to the design displacement Δ_I are then read from the pile force-displacement responses to determine how many piles are required for a strength of F_{ss}. Clearly there are a large number of possible combinations of pile numbers and spacing that will satisfy the required strength F_{ss}. However, there will be a number of functional constraints that will limit the choice.

For example, there will often be a requirement for a maximum pile spacing of 3 m (10ft) under crane rails, and gravity load design may dictate a maximum pile spacing, longitudinally and transversely of about 6-8 m (20-25 ft) in other locations. Referring

again to Fig.12.1, variables considered are likely to be the longitudinal spacing on **F** and **E** rows, and perhaps the transverse spacing between **F** and **E** rows, which will influence the clear height of the **E** row piles, and hence their lateral strength.
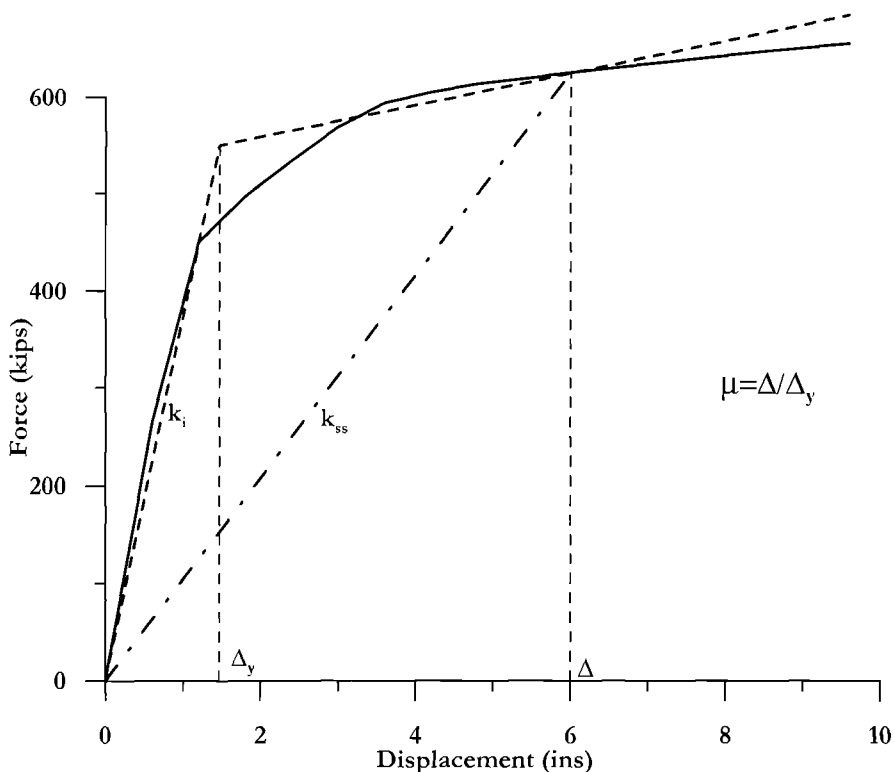

Fig.12.4 Typical Effective Stiffness and Ductility for Direct Displacement-Based Design, for a 6m (20ft) Length of Wharf. (1 in = 25.4mm, 1 kip =4.45kN)

To aid in design, approximate relationships between pile shear force and clear height between dyke and deck soffit are shown in Fig. 12.5. Note that analyses indicate that increasing the clear height between dyke and deck at the landside piles will generally result in improved (i.e. reduced) demand/capacity (**D/C**) ratios for displacement. This option should be considered when **D/C** ratios exceed, or are very close to 1.0 for rational combinations of pile spacing and numbers.

Step 12: With this preliminary design, assemble the full composite force-displacement response for the segment, corresponding to pure transverse displacement, and form a bilinear approximation to it. From this determine a revised estimate of the system ductility. If this differs significantly from the estimate given by Eq.(12.3), it may be necessary to revise the damping, the effective period, stiffness and the design lateral force level, utilizing steps 7 to 10 above.

Step 13: The above procedure, from Steps 4 to 12 should be carried out for both upper-bound and lower-bound soil conditions. It will not be obvious which condition will govern the design until both solutions are compared. However, upper-bound soil conditions will always govern the shear demand on the piles, and hence pile shear capacity will be checked for this case.

Note that the design approach above has not specifically considered wharf/crane interaction. Where it is expected that crane positioning will significantly increase the wharf displacements, then the value of the design transverse displacement found from Eq.(12.2) should be reduced accordingly. Wharf/crane interaction is considered in more detail in Section 12.6.2(d).

Clear Height (ft) , Force Ratio	
2.0	1.000
10.6	0.521
22.0	0.269
33.4	0.148
44.9	0.087
56.3	0.055
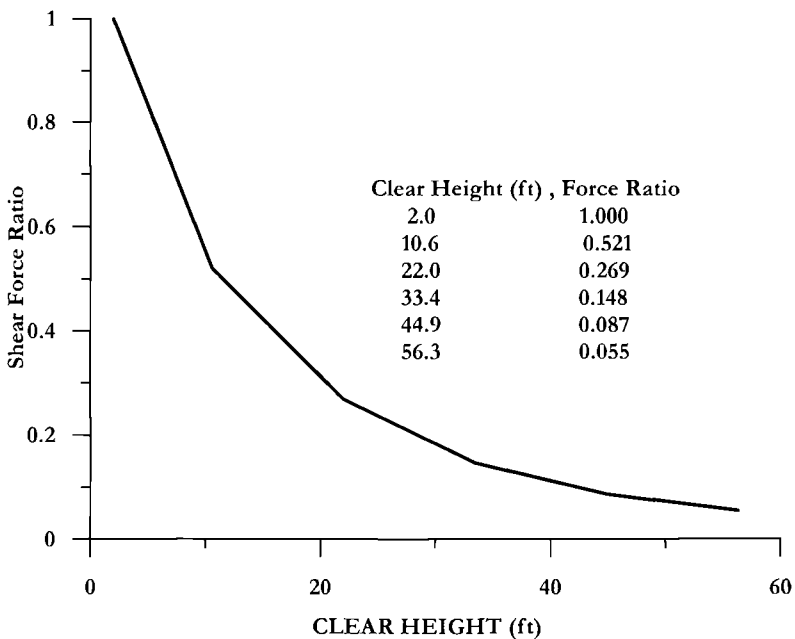
Fig.12.5 Approximate Relationship between Clear Height of a 610mm Prestressed Pile and Shear Force at a Lateral Displacement of 150mm (1ft = 305mm)

12.4   PORT OF LOS ANGELES PERFORMANCE CRITERIA.

In Section 12.3.1 it was mentioned that drift limits, which often govern design for building structures have little relevance for wharf structures, and that performance limit strains will apply when displacement-based designs are pursued. **POLA** (Port of Los Angeles) has developed a performance-based seismic design code[P40], where the structural requirements are essentially dictated by four components:

- Definition of earthquake levels to be considered.
- Definition of where inelastic action may occur (i.e. only in piles)

- Definition of performance limit strains for different pile types and different earthquake levels
- Definition of how capacity protection for elastically responding members and actions is to be applied.

This is an early example of a pure performance-based code, and as a consequence is described in some detail here. Although direct displacement-based design (**DDBD**) is defined as a preferred design approach, the designer is free to use different and more conventional methods of design, provided it can be established that the performance criteria have been satisfied.

12.4.1 POLA Earthquake Levels and Performance Criteria

In common with many seismic codes, POLA specifies that two levels of seismic intensity must be considered. These are the "Operating Level Earthquake (**OLE**)" and the "Contingency Level Earthquake (**CLE**), corresponding to a 50% and 10% probability of occurrence in a 50 year time frame respectively. These, then, correspond to Level 1 and Level 2 earthquakes in Section 2.2.2(b) In terms of average return period the **OLE** and **CLE** correspond to 72 years and 475 years respectively. The following performance criteria apply:

(a) OLE: Forces and deformations, including permanent embankment deformations shall not result in significant structural damage. Repairs shall not interrupt wharf operations. All damage shall be located where visually observable and accessible for repairs.

(b) CLE: Forces and deformations, including permanent embankment deformation may result in controlled inelastic structural behaviour and limited permanent deformation. All damage shall be repairable, and shall be located where visually observable and accessible for repairs. Collapse of the wharf must be prevented, and life safety must be maintained. There may be a temporary loss of operations, restorable within an acceptable period of time.

The strain limits for piles in the following sections are taken from the **POLA** seismic design code. Piles that satisfy these strain limits are deemed to satisfy the performance requirements for the **OLE** and **CLE**, defined in Section 12.4.1. With conventional force-based design, a check is made at the end of the design process to ensure that the strains are not exceeded. With **DDBD**, the design, using the procedure outlined in Section 12.3.3, aims to achieve the strain limits at the most critical pile for the specified earthquake level.

12.4.2 Performance Criteria for Prestressed Concrete Piles

(a) Operating Level Earthquake (OLE): The Serviceability Limit State for the **OLE** is defined by the following material strains:

(i) For solid round or octagonal prestressed concrete piles:
At the pile head (reinforced concrete capacity)
Extreme concrete fibre compression strain: $\varepsilon_c = 0.005$
Extreme tensile strain in dowels: $\varepsilon_s = 0.010$

In-ground hinge (prestressed concrete capacity)
Extreme concrete fibre compression strain: $\varepsilon_c = 0.005$
Incremental prestressing strain in strands: $\varepsilon_s = 0.005$

(ii) For round hollow concrete piles, both pile head and in-ground location:

Extreme concrete fibre compression strain: $\varepsilon_c = 0.004$

The tensile strain in the dowels at the pile head and the incremental prestressing strain in strands in-ground have the same limits as for solid piles. If the interior of the hollow pile is filled with concrete, all strain limits are the same as for solid piles.

(b) Contingency Level Earthquake (CLE): The Damage Control Limit State for the **CLE** is defined by the following material strains:

(i) For solid round or octagonal prestressed concrete piles:
At the pile head (reinforced concrete capacity)
Extreme concrete fibre compression strain:

$$\varepsilon_c = 0.004 + (1.4\, \rho_s\, f_{yh}\, \varepsilon_{smc}) / f'_{cc} \qquad \text{but} \quad 0.005 \le \varepsilon_c \le 0.020$$

Extreme tensile strain in dowels: $\varepsilon_s = 0.050$ but $< 0.6\varepsilon_{smd}$

In-ground hinge (prestressed concrete capacity)
Extreme concrete fibre compression strain:

$$\varepsilon_c = 0.004 + (1.4\, \rho_s\, f_{yh}\, \varepsilon_{smc}) / f'_{cc} \qquad \text{but} \quad 0.005 \le \varepsilon_c \le 0.008$$

Total prestressing strain in strands: $\varepsilon_S = 0.015$

where
ρ_s = effective volume ratio of confining steel (see Section 4.2.2)
f_{yh} = yield stress of confining steel
ε_{smc} = strain at ultimate stress of confining reinforcement
ε_{smd} = strain at ultimate stress of dowel reinforcement
f'_{cc} = strength of confined concrete (Eq.(4.10))

(ii) For round hollow concrete piles, both pile head and in-ground location:
At the pile head (reinforced concrete capacity)
Extreme concrete fibre compression strain $\varepsilon_c = 0.004$
Extreme tensile strain in dowels: $\varepsilon_s = 0.025$

In-ground (prestressed concrete capacity)
Extreme concrete fibre compression strain $\varepsilon_c = 0.006$
Total prestressing strain in strands: $\varepsilon_S = 0.015$

If the interior of the hollow pile is filled with concrete, all strain values are the same as for solid piles.

12.4.3 Performance Criteria for Seismic Design of Steel Pipe Piles

(a) Operating Level Earthquake (OLE):

At the pile head hinge location:
Concrete in-filled steel pipe pile:
Extreme concrete fibre compression strain $\qquad$ $\varepsilon_c = 0.008$
Extreme tensile strain in dowels $\qquad$ $\varepsilon_s = 0.010$

In-ground hinge location:
Hollow or concrete in-filled steel pipe pile
Extreme fibre strain in compression $\qquad$ $\varepsilon_s = 0.008$
Extreme fibre strain in tension $\qquad$ $\varepsilon_s = 0.010$

(b) Contingency Level Earthquake (CLE):

At the pile head hinge location
Concrete in-filled steel pipe pile:
Extreme concrete fibre compression strain $\qquad$ $\varepsilon_c = 0.025$
Extreme tensile strain in dowels: $\qquad$ $\varepsilon_s = 0.050$ but $< 0.6\varepsilon_{smd}$

In-ground hinge location:
Hollow steel pipe pile extreme tension or compression fibre strain:
$$\varepsilon_s = 0.025$$
Concrete in-filled steel pipe pile extreme fibre tension or compression strain:
$$\varepsilon_s = 0.035$$

The **POLA** limit strains apply only to prestressed concrete and steel shell (steel pipe) piles, and it is assumed that the connection in all cases will be moment-resisting and provided by dowels. Other pile types and connection details are possible. For example, large-diameter steel shell piles may be economical for wharves that service other than container vessels, such as marine oil or **LPG** terminals. If the wharf is not subjected to the heavy crane and container loading of container wharves, larger diameter seismic piles at wider spacing may be economical. With large-diameter piles, it will not generally be feasible to provide a moment-resisting connection to the wharf deck, as this would involve excessive and uneconomical depth to the deck. Consequently, the piles will just act as vertical cantilevers, with only the in-ground hinge providing seismic resistance.

Note that exposing the prestressing strand at the top of the pile and embedding it in the deck concrete to provide a moment-resisting connection is not permitted by **POLA**, because of difficulty in assuring the correct location of the strand, and also because of

large cracks at the deck/pile interface under moderate seismic response, potentially leading to corrosion problems, as well as potential for damage to strand when cutting the pile to the final elevation, noted previously.

12.5   LATERAL FORCE-DISPLACEMENT RESPONSE OF PRESTRESSED PILES

In order to illustrate the complete design process for direct displacement-based design of marginal wharves, the case of a wharf supported by 610 mm diameter prestressed piles is used as an example. Information provided in this section is adapted from material prepared for the **POLA** Resource Document[P41], which provides guidance for the application of the seismic code[P40].

12.5.1   Prestressed Pile Details

Lateral resistance in most standard **POLA** designs consists of 610 mm (24 in.) diameter octagonal piles, prestressed with 16-15.2 mm (0.6 in.) diameter prestressing strands. Connection to the deck is normally by 8-32 mm (8#10) dowels, though long piles with little contribution to the seismic resistance (e.g. Rows **A, B** and **C** in Fig.12.1) will often be connected to the deck by 4-32 mm (4#10)dowels. For piles relied on for seismic resistance, transverse reinforcement will typically be 12.7 mm (W20) spirals of A82 smooth round steel, at a pitch of 63.5 mm (3.0 in). Details of the section are shown in Fig. 12.6.
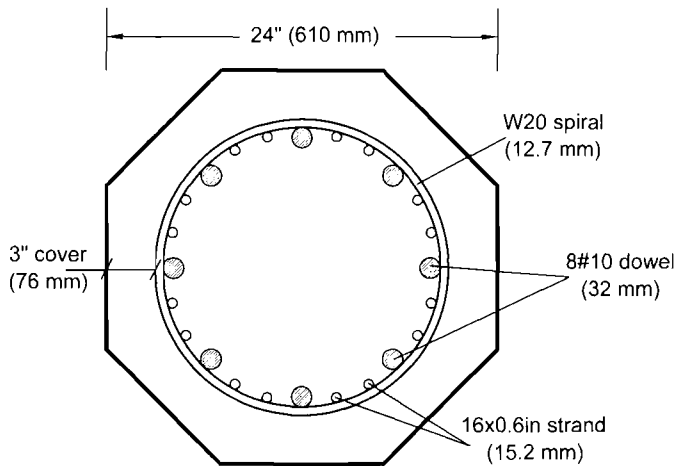
Fig. 12.6   Typical POLA 610 mm Octagonal Prestressed Pile Details

Specified material properties, and design strengths for seismic analysis are generally as follows:

Concrete compressive strength: f'_c =45 MPa (6500 psi) f'_{ce} =1.3f'_c = 58.3 MPa (8450psi)
Dowel tensile yield strength: f_y = 414MPa (60 ksi) f_{ye} =1.1f_y = 455 MPa (66 ksi)
Prestressing ultimate strength: f_{pu} =1860 MPa (270 ksi) f_{pue}=1.05f_{pu}=1955 MPa (283.5 ksi)
Spiral reinforcement: f_y = 483 MPa (70 ksi) f_{ye} = 1.0f_y = 483 MPa (70 ksi)

Cover to the spirals is normally specified as 76 mm (3.0 in). The increase in expected material strengths above specified levels is in accordance with recommendations of Section 4.2.6.

Details of typical prestressing are as follows:

Strand area: = 138.6 mm^2 (0.215 in^2)
Initial stress after losses: = 1062 MPa (154 ksi)
Ultimate tensile stress: f_{pue} = 1955 MPa (283.5 ksi)
Yield stress (0.02% proof strain):   = 1490 MPa (216 ksi)
Modulus of elasticity: = 200 GPa   (29000 ksi)
Ultimate strain: = 0.06

12.5.2 Moment-Curvature Characteristics of Pile/Deck Connection

Results of moment-curvature analysis of the pile/deck connection for different levels of axial force are shown in Fig.12.7.
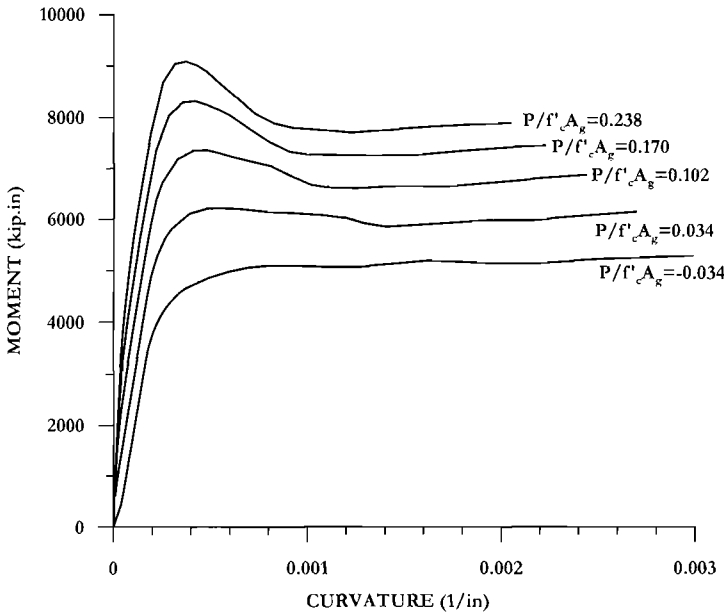
Fig. 12.7 Moment-Curvature Response of 610mm Pile/Deck Connection with 8-32mm (#10) Dowels. (1 kip.in = 113 Nm, 1 in. = 25.4mm)

The analyses were based on procedures outlined in Section 4.2, using an ultimate compression strain of 0.02. The validity of these equations had been established in many tests on columns in the past, but also on a full-scale model of a pile/deck connection[S9]. Results comparing the actual and predicted force-displacement response of the test unit are shown in Fig.12.8. It will be seen that the theoretical prediction, indicated in Fig.12.8 by the dashed line, gives a close, but slightly conservative envelope of the experimental response. Additional testing on pile/deck connections has recently been carried out at the University of California, San Diego[K5].

For structural analysis of the wharf, it will normally be appropriate to represent the force-displacement behaviour of individual piles by a bilinear approximation. This requires a similar bilinear approximation for the moment-curvature response. A typical example is shown in Fig.12.9. The actual moment-curvature response (in this case for an axial force of 1335kN (300 kips)) indicates strength degradation due to spalling of cover concrete. This is much more significant for piles than for building or bridge columns, where the cover is typically a much smaller fraction of the section diameter or width. In the typical example of Fig.12.9, the strength at the maximum curvature has regained some of the loss, as a result of strain-hardening of the dowel reinforcement, but the final strength is less than the peak flexural strength before cover spalling initiates. In such cases it would be unwise to use the peak strength as the design strength, and the value recommended is the lower of the initial peak, and the final strength.

The critical design data can be extracted in dimensionless form from the curves of Fig. 12.7. These data include the design moment, the effective elastic stiffness, and the curvatures corresponding to the yield, **OLE** and **CLE** limit states. Design results are summarized in Fig. 12.10, and discussed in the following sections:

*(a) **Design Moment:*** In Fig.12.10(a), dimensionless peak moment, and design moment (based on the elasto-plastic approximation to the moment-curvature response shown in Fig. 12.9) are plotted against dimensionless axial force. Axial load P and moment M are reduced to dimensionless forms by the usual equations:

$$P* = \frac{P}{f'_c A_g}; \qquad\qquad M* = \frac{M}{f'_c D^3} \qquad\qquad (12.7)$$

where A_g and D are the gross cross-section area ($\pi D^2/4$) and diameter respectively, and the concrete compression strength f'_c used is the specified (rather than expected) strength – in this case 6.5 ksi (44.8 MPa). With this dimensionless formulation, the information in the graph can be used for any consistent system of units – SI or American Standard, for example, and the graphs can also be expected to provide reasonable estimates of moment capacity for pile/deck connections with different pile diameters, provided the concrete compression strength, reinforcement yield strength and ratio of the dowel connection are similar to those used to generate these curves ($f'_c = 6.5$ ksi (44.8 MPa), $f_{ye} = 455$ MPa (66 ksi); $\rho_l = A_{st}/A_g = 0.0305$), and the ratio of cover to pile diameter
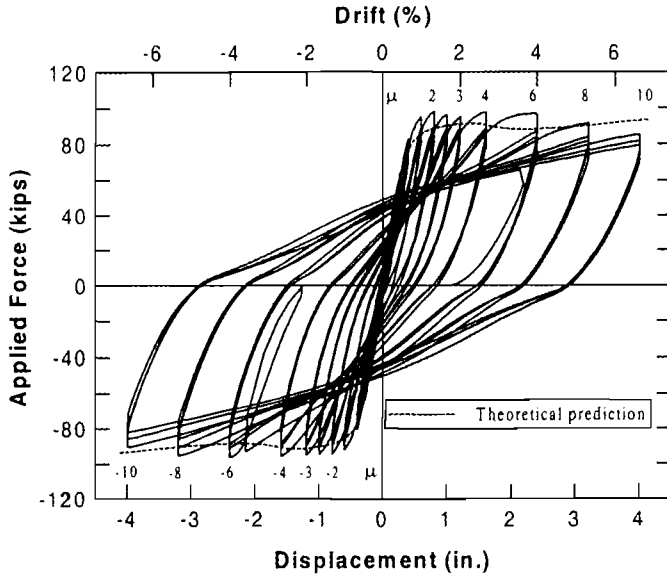
Fig.12.8   Force-Displacement Response of a Pile/Deck Connection
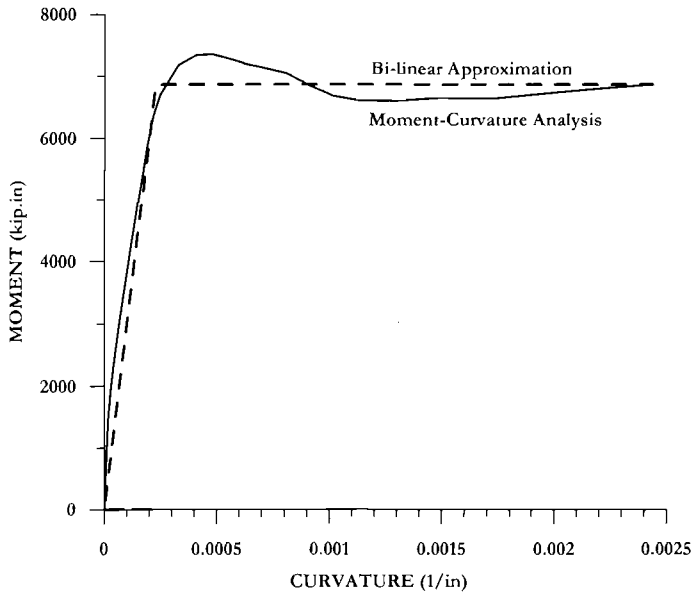**(1 kip = 4.45kN, 1 in. = 25.4 mm)**

Fig.12.9   Bilinear Approximation to Pile/Deck Moment-Curvature Response
(1 kip.in = 113 Nm, 1 in. = 25.4 mm)

is also similar to that for the piles illustrated in Fig. 12.6. It will be noted that for low
levels of dimensionless axial force, the peak and design moment are the same, but that for
higher levels, the peak moment exceeds the design moment by as much as 15%, due to
the increasing influence of cover spalling.

(a) Moment Capacity

(b) Yield and OLE Curvatures

(c) CLE Curvature

(d) Elastic Stiffness Ratio
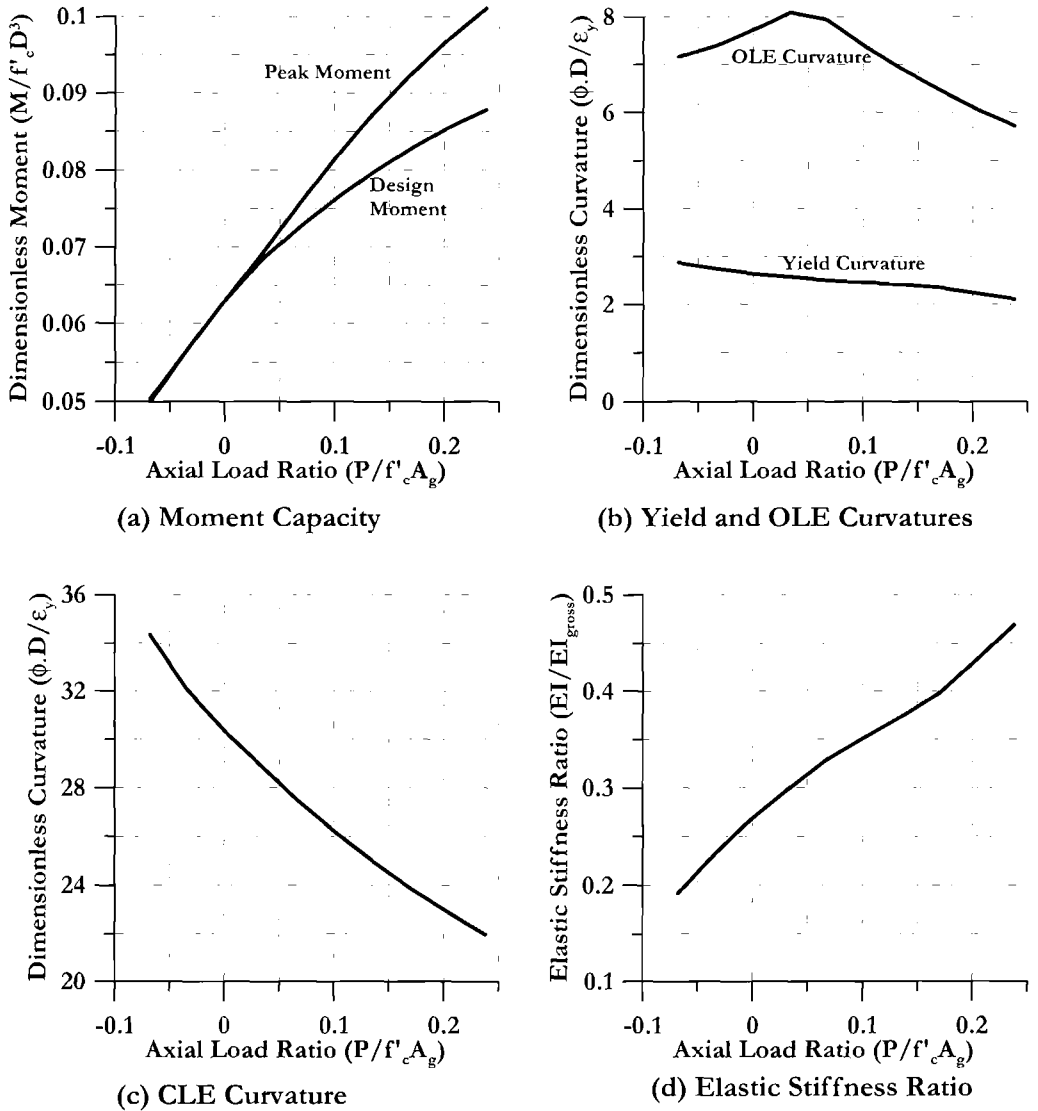
Fig.12.10   Dimensionless Strength and Ductility Parameters for 610 mm (24 in)
Pile/Deck Connection with 8-32 mm (#10) Reinforcement Dowels.

The design moment of Fig.12.10 can be represented by the dimensionless Eq.(12.8) below, with a maximum error of about 1.5%:

$$M* = 0.0621 + 0.033P* - 0.23P*^2 \tag{12.8}$$

where $M*$ and $P*$ are given by Eq. (12.7).

(b) Yield Curvature: Figure 12.10(b) plots the variation of dimensionless curvature $\phi*$ against dimensionless axial load for yield and OLE curvature. The curvatures have been made dimensionless using Eq. (12.9):

$$\phi* = \phi D / \varepsilon_y \tag{12.9}$$

where $\varepsilon_y = f_y / E_s$ is the yield strain of the dowel reinforcement.

As has been found for other section types (see Section 4.4), the dimensionless yield curvature is rather insensitive to axial load ratio, and hence the data in Fig. 12.10(b) can be expected to apply to other section diameters, and dowel properties, with only small errors. The data for yield curvature in Fig.12.10(b) can be approximated with good accuracy (errors less than 1%) by Eq. (12.10):

$$\phi_y^* = 2.68 - 2.21P* \tag{12.10}$$

(c) OLE Curvature: The design curvature corresponding to the **OLE** limit state is also plotted in dimensionless form in Fig. 12.10(b). For ease of comparison with the yield curvature, it has been put into dimensionless form using Eq.(12.9). However, it should be recognized that the **OLE** curvature is not dependent on the yield strain of the dowel reinforcement, and hence should be converted back to "real" data using $\varepsilon_y = 0.002237$; the value applying to the **POLA** piles. It will be seen that the OLE curvature is comparatively insensitive to axial load ratio $P*$. At low values of $P*$, the curvature is limited by the **OLE** tension strain limit, while for higher values of $P*$, the compression strain limit governs. The data for **OLE** curvatures in Fig. 12.10(b) can be approximated with reasonable accuracy (within 4%) by the following equation:

$$\phi_{OLE}^* = 7.68 + 5.68P* - 63.6P*^2 \tag{12.11}$$

(d) CLE Curvature: Figure 12.10(c) plots the variation of dimensionless **CLE** curvature against $P*$. Again it has been made dimensionless using Eq. (12.9), for comparison with the yield strain values, and again the specific value of $\varepsilon_y = 0.002237$ must be used to obtain valid "real" data. **CLE** curvature is strongly dependent on the axial load ratio, since the compression strain limit governs in all cases. Comparing the

CLE and yield curvatures indicates that curvature ductility capacity reduces from about μ_ϕ=12 to about μ_ϕ=10 as P^* increases from -0.05 to 0.2.   The data in Fig. 12.10(c) can be represented with good accuracy by the equation:

$$\phi_{CLE}^* = 30.4 - 45.9P^* + 46.3P^{*2} \tag{12.12}$$

(e) Elastic Stiffness (EI$_{eff}$): Finally, the effective elastic stiffness, made dimensionless by dividing by the gross section stiffness EI_{gross} is plotted against axial load ratio P^* in Fig.12.10(d). The effective stiffness is that corresponding to the initial stiffness of the bi-linear approximation to the moment curvature curve, as shown in Fig. 12.9. This is found from the line from the origin through the point corresponding to first yield of dowel reinforcement (or an extreme fibre compression strain of 0.002, if this occurs first), since this is the best representation of elastic stiffness at high elastic force levels[P4]. It will be seen that the elastic stiffness is strongly dependent on P^*, increasing by more than a factor of 2 as P^* increases from -0.05 to 0.2.   The data in Fig. 12.10(d) are represented with good accuracy by the equation:

$$EI^* = \frac{EI_{eff}}{EI_{gross}} = 0.268 + 0.852P^* \tag{12.13}$$

12.5.3 Moment-Curvature Characteristics of Prestressed Pile In-Ground Hinge

Plastic hinging normally occurs first at the pile/deck connection, as described in the previous section, and is followed by a second hinge, forming some distance below the dyke surface, which is termed the "in-ground" hinge. At this location, the reinforcing steel tension capacity contributing to the flexural strength is provided solely by prestressing, the details of which are given in Section 12.5.1.

As shown in the moment-curvature curves of Fig. 12.11, which are plotted for a range of axial force ratios, the decrease in moment capacity resulting from spalling is more pronounced than for the pile/deck connection. This is because the prestress force acts primarily in the same way as an increased axial load on the section. The curves of Fig.12.11 have been continued out to the curvature corresponding to an extreme fibre compression strain of 0.02. However, as noted in Section 12.4.2, **POLA** limit strains for the in-ground hinge are much lower than for the pile/deck hinge, where damage can be inspected after an earthquake. The condition corresponding to the **CLE** strain limits of Section 12.4.2 is represented in Fig.12.11 by the large dots, occurring soon after spalling.

It will be noted that the **CLE** compression strain limit for the in-ground hinge (<0.008), though less than the pile/deck connection, is large in comparison with normal estimates of extreme-fibre crushing strain. This is because the cover concrete at the in-ground hinge location is confined to some extent by the passive pressure of the soil, which has been found in experiments to delay the onset of cover concrete spalling[B6]. It

is also probable that the soil confinement will inhibit the steep falling branch of the moment-curvature curves after peak moment is achieved, since this strength reduction is a result of cover concrete spalling. This has yet to be confirmed experimentally.
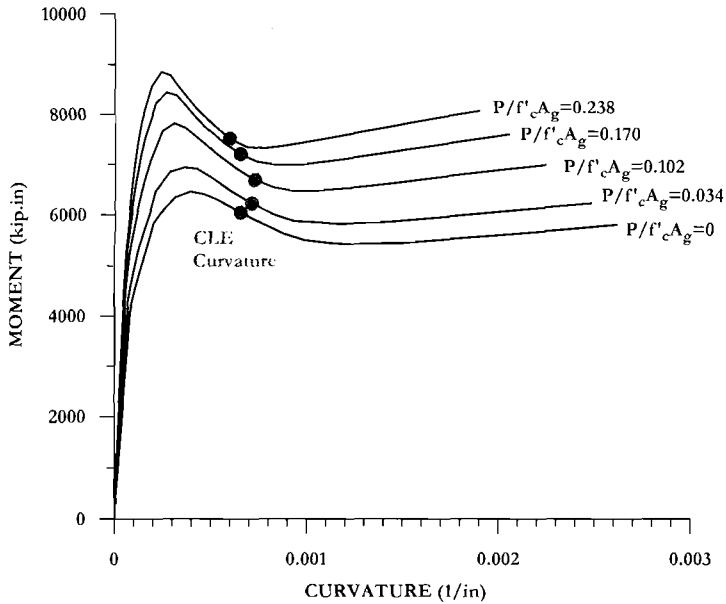

Fig.12.11 Moment-Curvature Response for 610 mm (24 in) Prestressed Piles (prestress = 16×15.2 mm (0.6 in) strands. 1 kip.in =113 kNm; 1 in =25.4 mm)

As with the pile/deck connection, it is possible to extract critical design information from the prestressed section moment-curvature analyses, and present it in dimensionless graphs and equations. The graphical formulation of these data is presented in Fig.12.12, using the same parameters to make the results dimensionless as was used in the previous section for the pile/deck connection.

(a) Flexural Strength: Figure 12.12(a) shows the variation of dimensionless design and peak moment with axial load ratio P^*. Both design and peak moment are strongly influenced by the level of axial load. Since the peak moment will need to be considered when maximum feasible shear demand on the pile is estimated, dimensionless equations for both design and peak moment are given below:

Design moment: $M_D^* = 0.0645 + 0.147P^* - 0.173P^{*2}$ (12.14a)

Peak moment: $M_P^* = 0.0718 + 0.176P^* - 0.271P^{*2}$ (12.14b)

Agreement between the equations and the graphs is within 0.5% for all values of P*.

(a) Moment Capacity

(b) Yield and OLE Curvatures

(c) CLE and Ultimate Curvature

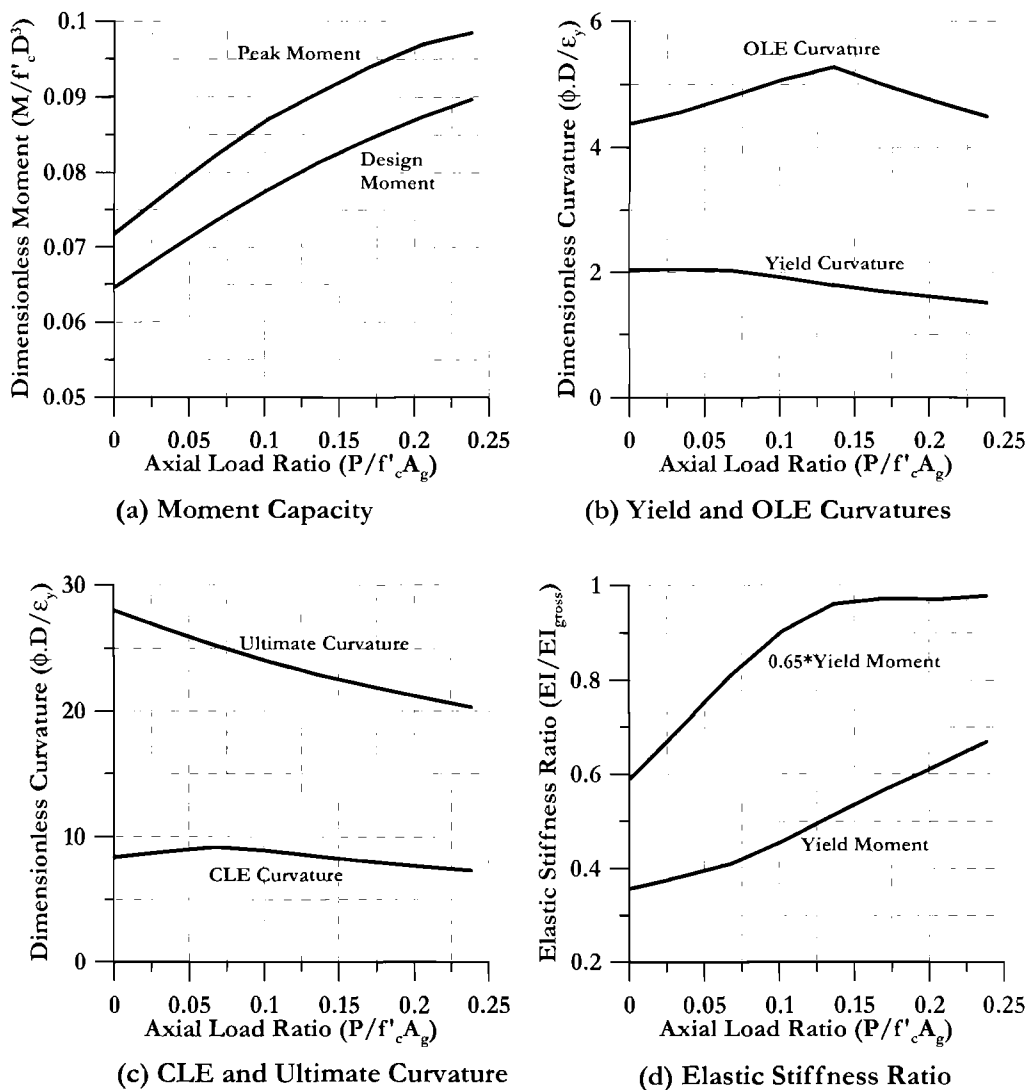(d) Elastic Stiffness Ratio

Fig. 12.12   Dimensionless Strength and Ductility Parameters for 610 mm (24 in.)
Prestressed Pile (16×15.2 mm (0.6 in) Prestressing Strands)

(b) Design Curvature Limits: Figures 12.12(b) and 12.12(c) plot the design curvature limits against P^*. To facilitate comparison with the pile/deck curvature limits, they have been made dimensionless using Eq. 12.9. However, it will be appreciated that use of the dowel yield strain is strictly inappropriate, and the values need to be multiplied by ε_y =0.002237 to obtain "real" curvatures.

Values are plotted for yield, **OLE** and **CLE** curvatures, and also for "ultimate"

curvature, corresponding to an extreme fibre compression strain of 0.02. Although this strain exceeds the **CLE** limit strain, it may be of interest if the true limit to deformation capacity, corresponding to the onset of strength degradation, is required.

The limit curvatures can be represented with adequate accuracy by the following equations:

Yield curvature: $\qquad \phi_y^* = 2.04 - 0.158P* - 9.27P*^2$ $\qquad\qquad$ (12.15)

OLE curvature: $\qquad \phi_{OLE}^* = 4.38 + 12.1P* - 51.0P*^2$ $\qquad\qquad$ (12.16)

CLE curvature: $\qquad \phi_{CLE}^* = 8.37 + 14.0P* - 86.2P*^2$ $\qquad\qquad$ (12.17)

Ultimate curvature: $\phi_{ult}^* = 28.0 - 44.6P* + 51.0P*^2$ $\qquad\qquad$ (12.18)

(c) Elastic Stiffness: (EI$_{eff}$): Two values for elastic stiffness ratio are plotted in Fig. 12.12(d). One is applicable for response at the yield moment, and the other applies to a peak moment in the prestressed pile of 65% of the nominal moment capacity. The latter value will be appropriate for those portions of the pile subjected to only moderate moments, or when deflection capacity at the pile/deck first yield condition is investigated. Equations describing the variation in relative stiffness with *P** are listed below:

At yield: $\qquad EI_y^* = \dfrac{EI_y}{EI_{gross}} = 0.357 + 0.705P*^2$ $\qquad\qquad$ (12.19a)

At 0.65*M$_D$: $\quad EI_{0.65M_D}^* = \dfrac{EI_{0.65M_D}}{EI_{gross}} = 0.588 + 4.35P* - 11.95P*^2$ $\qquad$ (12.19b)

From these equations, a trilinear approximation to the prestressed pile moment curvature relationship can be developed, as is shown in Fig. 12.13, and compared with the bilinear approximation. The trilinear approximation will provide a more accurate representation of the variation of elastic stiffness along the length of the pile, and will hence result in more accurate estimation of the pile force-displacement response.

12.5.4 Inelastic Static Analysis of a Fixed Head Pile

(a) Modelling Aspects: The wharf force-displacement response may be found by assembling the response of the individual pile rows. This is illustrated in a simplified form in Fig.12.14 where the wharf is considered to be supported by piles on six lines, **A** to **F**. **T** and **IG** represent the positions of the pile-top and in-ground plastic hinges respectively, though the position of **IG** will not be known at the start of the analysis. Prior analyses[P42] have shown that for 610mm (24 in) diameter prestressed piles, the

relative stiffness of deck and pile is such that the pile top may be considered to be fully restrained against rotation. This simplifies analysis considerably.
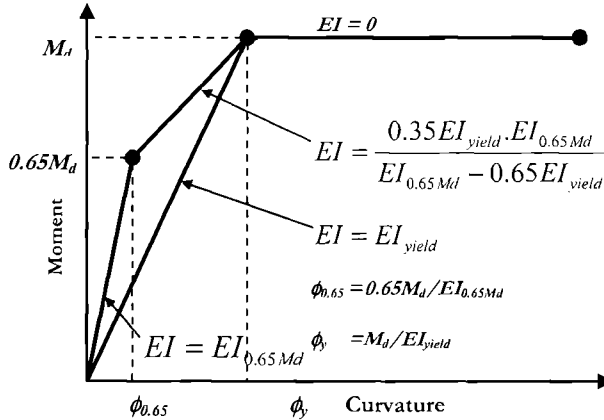

Fig.12.13   Bi-linear and Tri-linear Approximations to Prestressed Section Moment-Curvature Characteristic.

(i) Pile member properties: Modelling for a single pile is illustrated in Fig.12.14(b).   The pile is represented by a series of inelastic pile members whose end nodes are connected to lateral soil springs. The properties of both soil springs and pile members will vary with height. At the top of the pile, the pile member stiffness and strength should model that of the appropriate connection detail, using data presented in Sections 12.5.2 and 12.5.3. Section strength and stiffness will gradually change from the reinforced concrete characteristics at the top of the pile to fully prestressed characteristics. A strand development length of approximately $50d_{ps}$ is necessary to develop the ultimate capacity of prestressing strand of   diameter d_{ps} in confined conditions, such as exist in piles represented by Fig.12.6. For d_{ps}=15.2 mm (0.6in), this implies a development length of 760 mm (30in). Note that if the dowel length is significantly longer than the strand development length, then a section of the pile where the dowel and prestressing are both fully developed could occur. In this region the strength and stiffness of the pile could exceed the values predicted in Sections 12.5.2 and 12.5.3 for either connection or prestressed sections. This will not normally pose problems for analysis, since the region of increased strength and stiffness will normally be between the deck and in-ground plastic hinges where moment demand is low, and the contribution of local curvature to overall displacement will be insignificant. An exception occurs on the landside piles (Row **F**, Fig.12.14(a)) where the distance between the deck hinge and the in-ground hinge may be as low as 2.5m (100 in). If the dowels are inserted longer than this, then the moment capacity of the in-ground hinge may have contributions from both dowels and prestressing strand, and exceed expected capacity. Although this may initially be considered "safe" since lateral strength will be enhanced, it also means that the shear demand on the critical piles will be increased, and could possibly exceed shear capacity.
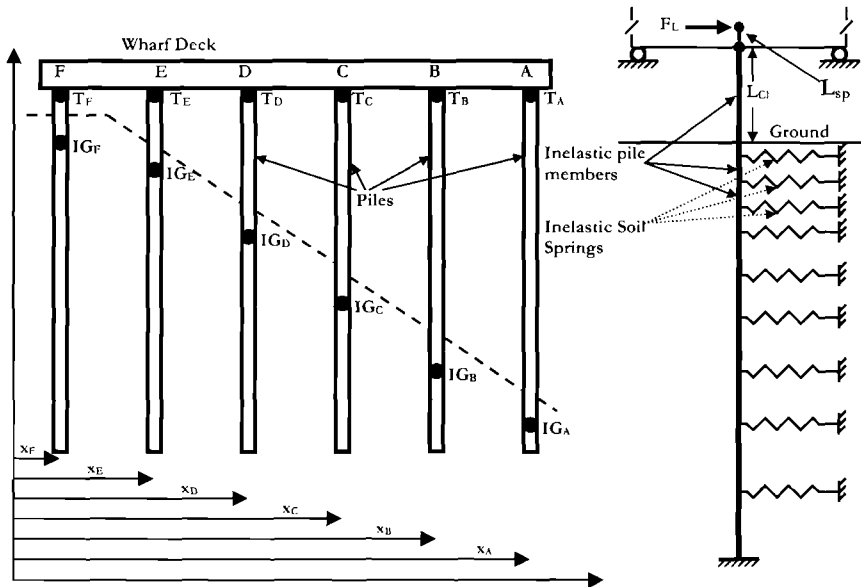
Fig.12.14   Model for Pushover Analysis of a Single Pile

Recent experiments[K5] indicate that the pile stiffness increases rapidly with distance from the deck connection. As a consequence it is recommended that the top 400 mm (16in) of pile be given the properties of the dowelled connection, and the lower regions of the pile be given the prestressed properties.

(ii) Special member at top of pile to model strain penetration: Although the deck may be modelled as infinitely rigid for resisting pile-top rotation, it is important to recognize that the strain in the dowels does not drop to zero immediately at the pile-deck interface, but gradually reduces over a finite length due to bond stress. This provides additional rotation which is not modelled if the rigid support is located at the physical top of the pile. For correct modelling, it is necessary to add an additional member at the top of the pile, penetrating a length L_{SP} into the deck, as shown in Fig.12.14. This member should be given the elastic stiffness of the dowel connection detail, and an artificially high yield moment to ensure that the analytical plastic hinge forms at the bottom of the deck, not at the top of the strain-penetration member. The length of the strain-penetration member is related to the dowel-bar diameter d_{dl} and yield stress f_{ye} in accordance with Eq.(4.30), reproduced here as Eq.(12.20):

$$L_{sp} = 0.022 f_{ye} d_{bl} \text{ mm } (f_{ye} \text{ in MPa, } d_{bl} \text{ in mm}) \qquad (12.20a)$$

$$L_{sp} = 0.15 f_{ye} d_{db} \text{ ins } (f_{ye} \text{ in ksi, } d_{bl} \text{ in ins.}) \qquad (12.20b)$$

(iii) Soil springs: Soil Springs will normally be modelled with bilinear inelastic force-displacement characteristics for pushover analyses. The initial stiffness k_{si} of the springs will be related to the lateral subgrade coefficient K_H by the expression

$$k_{si} = K_H DL_i \quad \text{kN/m (kips/in)} \tag{12.21}$$

where D is the pile diameter, L_i is the tributary height of pile from midway to the spring below to midway to the spring above the spring considered, and K_H is the value of lateral subgrade coefficient at the depth H of the spring below ground surface. K_H has the dimensions (FL^{-3}).

Maximum in-ground pile moments will normally occur at depths between 1.5 m (60 in) and 3.0 m (120 in) (the value depends on the soil stiffness and strength, and the clear height L_c between deck soffit and dyke) below the dyke surface, for 610 mm (24 in.) diameter prestressed piles. To ensure adequate precision in modelling the pile moment profile, it is thus important that the soil springs be closely spaced in the upper region of the pile. For 610 mm (24 in.) diameter prestressed piles it is recommended that the first spring be located 150 mm (6 in.) below the dike surface, then springs be spaced at no more than 300 mm (12 in.) centres to a depth of about 4 m (160 in.). Below this the spacing can be increased.

(b) Analysis: A lateral pushover analysis of the single pile shown in Fig.12.14 is carried out by either gradually increasing the lateral force F_L at the top of the strain-penetration element, which is considered free to translate but fixed against rotation, and analyzing the structure at predetermined incremental force levels, tracking stiffness changes at each force increment, and modifying the stiffness matrix accordingly, or by carrying out a similar incremental procedure where the displacement at the top node is increased incrementally. The latter is generally preferable, as the maximum resisting force is not known at the start of the analysis, whereas the range of displacement interest will generally be known.   Under force-based pushover, the analysis will become unstable when the specified lateral force exceeds the lateral strength of the pile, and the full force-displacement response may not be determined. This problem can be solved by placing an elastic horizontal spring at the top of the pile, in line with the applied force F_L and with a stiffness (say) of 50% of the pile elastic lateral stiffness. The actual stiffness value of this spring is not very important. The spring provides stability to the force-based analysis, and in this case, it will be the shear force in the top pile element, not the applied force that is plotted against the pile-top displacement. Ideally, force-increments in the initial stages of the analysis should be comparatively large, reducing as the analysis proceeds, while for displacement-controlled pushover, the initial displacement steps should be small, increasing as the structure enters the nonlinear range. The choice between force-based or displacement-based pushover will depend on the computer code being used. In either case, the required output is the force-displacement response at the top of the strain-penetration element, and the displacements at which the pile-top and in-ground hinges form. A typical example for an **F**-line pile (see Fig.12.14) is shown in Fig12.15(a).
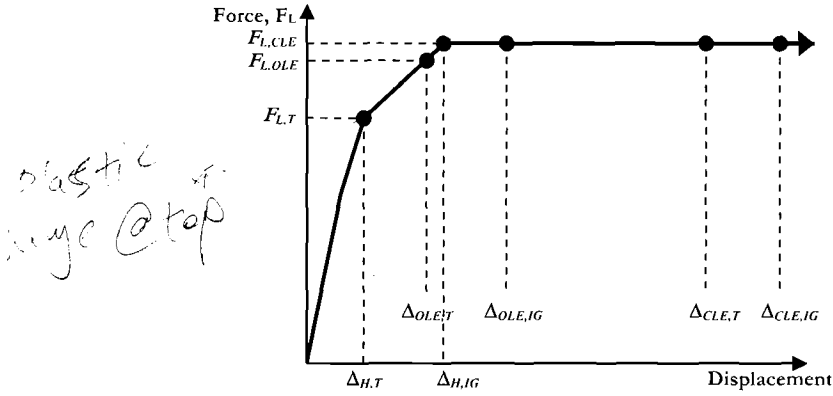
(a) Force-Displacement Response
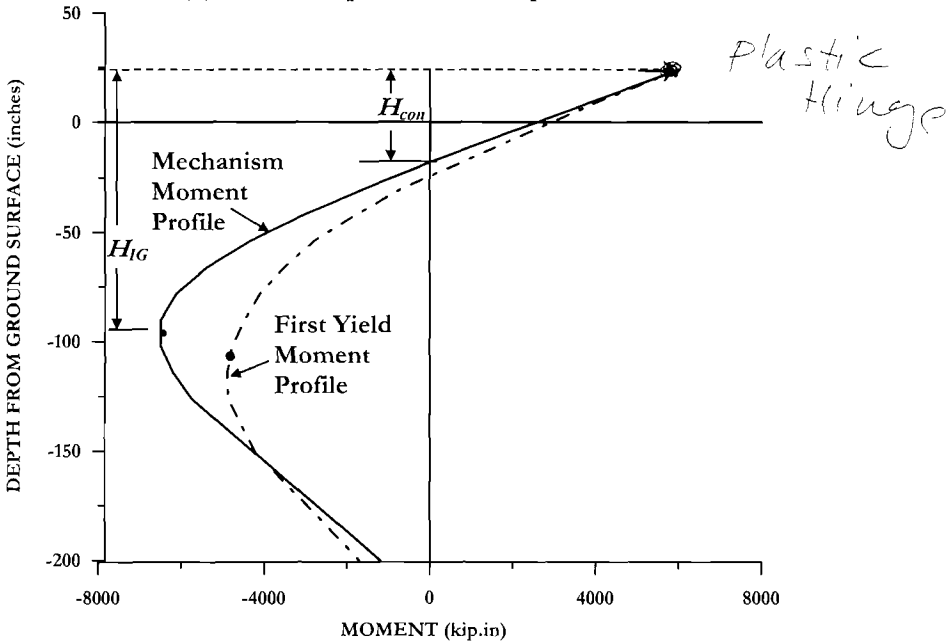
(b) Moment Profiles down Pile at First Yield and Full Mechanism

**Fig.12.15 Typical Results of 610mm (24 in) Prestressed Pile Pushover Analysis
(1 kip.in =113Nm, 1 in =25.4mm)**

The force-displacement response will be essentially linear until the first hinge forms, normally at the pile top, at a displacement of $\Delta_{H,T}$, and a corresponding force $F_{L,T}$. Slight nonlinearity may occur before this as a result of the top soil springs yielding, and the tri-linear representation of the prestressed section moment-curvature response, suggested in Fig. 12.13. At $\Delta_{H,T}$ there is an abrupt change in the slope of the force-

displacement response, with a second essentially linear segment until the in-ground hinge reaches its moment capacity at a displacement of $\Delta_{H,IG}$. Again, there may be slight nonlinearity to this segment. For displacements larger than $\Delta_{H,IG}$, the force-displacement response will be essentially flat, given the assumed elasto-plastic moment-curvature relationships of Section 12.5.2.

Also shown in Fig. 12.15(a) are the **OLE** and **CLE** limit displacements corresponding to development of the corresponding strain limits at the top, and in-ground hinges ($\Delta_{OLE,T}$, $\Delta_{OLE,IG}$, $\Delta_{CLE,T}$, and $\Delta_{CLE,IG}$). The relative magnitudes, and also the order in which the limit displacements occur may differ significantly from those shown in Fig.12.15(a). Although the displacements $\Delta_{H,T}$ and $\Delta_{H,IG}$ at which the hinges form can be determined directly from the pushover analysis, the limit displacements need further consideration.

*(i) Displacement at the **OLE** Limit State:* The displacement at the **OLE** limit state is the lesser of the displacements corresponding to the pile-top and in-ground **OLE** limit curvatures. Normally the pile top will govern. For the pile top, the **OLE** limit displacement $\Delta_{OLE,T}$ is given by:

$$\Delta_{OLE,T} = \Delta_{H,T} + \Delta_{P,OLE,T} \tag{12.22}$$

where $\Delta_{P,OLE,T}$ is the plastic displacement corresponding to the limit plastic rotation $\theta_{P,OLE,T}$ at the pile top, given by:

$$\theta_{P,OLE,T} = (\phi_{OLE,T} - \phi_{y,T}).L_{PT} \tag{12.23}$$

where $\phi_{OLE,T}$ and $\phi_{y,T}$ are the **OLE** and yield curvatures for the top connection detail (Fig.12.10b; Eqs.(12.10), (12.11)) and L_{PT} is the plastic hinge length at the top of the pile, given by Eq.(4.31), reproduced here as Eq.(12.24):

$$L_{PT} = kH_{con} + L_{sp} \geq 2L_{sp} \tag{12.24}$$

where k is defined by Eq.(4.31b). In Eq.(12.24) H_{con} is the distance from the deck soffit to the point of contraflexure in the pile (see Fig.12.15(a)), and L_{sp} is the strain-penetration length, given by Eq.(12.20). Note that a plastic hinge length of $2L_{sp}$ is the minimum value to be used in design, and this will normally govern at the pile top.

Normally, the plastic rotation at a potential plastic hinge can be directly extracted from the pushover analysis, and hence it will be straightforward to determine the displacement corresponding to $\theta_{P,OLE,T}$.

The displacement corresponding to the in-ground hinge **OLE** limit is given by:

$$\Delta_{OLE,IG} = \Delta_{H,IG} + \Delta_{P,OLE,IG} \tag{12.25}$$

where $\Delta_{P,OLE,IG}$ is the plastic displacement corresponding to the limit plastic rotation $\theta_{P,OLE,IG}$ at the in-ground hinge, given by:

$$\Delta_{P,OLE,IG} = \theta_{P,OLE,IG}.H_{IG} = (\phi_{OLE,IG} - \phi_{y,IG}).L_{P,IG}.H_{IG} \tag{12.26}$$

where $\phi_{OLE,IG}$ and $\phi_{y,IG}$ are the **OLE** and yield curvatures for the in-ground hinge, given in Fig.12.12(b) and Eqs.(12.15) and (12.16), and $L_{P,IG}$ is the plastic hinge length for the in-ground hinge.

Because of the gradual curvature of the moment profile in the vicinity of the in-ground hinge (see Fig.12.14(b), e.g.) the plastic hinge length spreads both up and down from the critical section, and is quite long. Exact determination of the plastic hinge length is not feasible, since it is influenced by the confinement provided by the surrounding soil, as well as by the curvature of the moment profile. Note that even if spalling of the cover concrete initiates, it would appear impossible for the cover to completely separate from the pile, and some integrity of the cover will remain. A reasonable approximation for the plastic hinge length is the length of pile over which the moment exceeds 90% of the peak moment. For typical soil stiffnesses, and 610mm prestressed piles, this corresponds to a length exceeding twice the pile diameter, D, and hence the in-ground plastic hinge length may be conservatively taken as $L_{P,IG} = 2D$

(ii) Displacement at the CLE limit state: The displacement at the **CLE** limit state is the lesser of the displacements corresponding to the pile-top and in-ground **CLE** curvatures, defined in Sections 12.5.2 and 12.5.3. The procedure is identical to that for the **OLE** limit state, substituting the **CLE** curvatures and rotations for the **OLE** values in Eqs.(12.22) to (12.26).

(iii) Ultimate displacement capacity based on ultimate in-ground hinge curvature: Figure 12.12(c) and Eq.(12.18) define "ultimate" curvatures, $\phi_{0.02}$ for the in-ground hinge of 610 mm (24 in.) diameter prestressed piles. These exceed the curvatures corresponding to the **CLE** limit, but provide a conservative estimate of the maximum dependable curvature capacity of the pile considered. By similarity to the in-ground **CLE** limit displacement calculated in the previous section, the ultimate displacement $\Delta_{ULT,IG}$ is given by:

$$\Delta_{ULT,IG} = \Delta_{H,IG} + (\phi_{0.02} - \phi_{y,IG})L_{P,IG}.H_{IG} \tag{12.27}$$

where the plastic hinge length is $L_{P,IG} = 2D$.

Note that the strength of the pile-top plastic hinge may have seriously degraded by this displacement, so a reduced lateral strength of the pile may be appropriate if ultimate displacement capacity is considered. However, it should also be recalled that the **CLE**

curvature for the top hinge does not correspond to a true "ultimate" or collapse condition, since the displacement capacity is expected to exceed the **CLE** limit by 50%, on average, before significant strength degradation commences.

12.6   DESIGN VERIFICATION

12.6.1   Eccentricity

After the initial design has been carried out using the procedure of Section 12.3.1, the first step of design validation will be to check the assumed value of the transverse eccentricity, and recalculate the required strength, if necessary.

Typical force-displacement plots for **A**-Line to **F** Line piles for a wharf such as that shown in Fig.12.14 are shown in Fig.12.16(a). The **OLE** and **CLE** limits for the critical **F**-Line piles are also indicated. Since the **OLE** and **CLE** displacement limits for the other piles will be greater than those for the **F**-Line piles, they are of little interest, and hence have not been shown in Fig.12.16(a). Note that the **A** and **B** line piles contribute little to the overall lateral strength of the wharf, and that their response is effectively linear-elastic up to the maximum displacement considered in the analyses, of 244mm (9.6in).

It may be useful to consider the composite lateral force-displacement response of a module of wharf consisting of a 6 m (20ft) length, and full width, since piles have generally been spaced at 6 m (20ft) centres in the longitudinal direction for the internal rows, and at some simple divisor of 6 m (20ft) on the crane-support lines (in this case, **A** and **F**). Other module lengths may be appropriate for specific designs. Figure 12.16(b) plots such a composite response based on the **F**-Line piles being at a spacing of 2 m (6ft-8in), and the **A**-Line piles being at a spacing of 3 m (10ft), using the individual pile force-displacement responses of Fig.12.16(a). The **OLE** and **CLE** limits, corresponding to the critical **F**-Line piles, are also shown. The response of an entire wharf segment in the transverse direction is determined by multiplying the force ordinates of the characteristic module by the number of modules in the segment length.

For seismic response in the transverse direction, the centre of stiffness and centre of mass of a wharf segment between movement joints will normally coincide, unless the segment has non-rectangular geometry, or the soil properties vary along the length of the segment. For seismic response in the longitudinal direction, however, the centre of stiffness will have considerable eccentricity from the centre of mass, and will generally be close to the landside row (Line **F**, in Fig. 12.14). Referring to the nomenclature of Fig.12.14, the distance of the centre of stiffness from the F-Line piles can be expressed as:

$$\overline{x} - x_F = \frac{\sum\limits_{A}^{F} k_i n_i (x_i - x_F)}{\sum\limits_{A}^{F} k_i n_i} = \frac{\sum\limits_{A}^{F} F_{Li} n_i (x_i - x_F)}{\sum\limits_{A}^{F} F_{Li} n_i} \qquad (12.28)$$

where k_i and F_{Li} are the stiffness, and lateral strength at a given displacement for the piles on row i, and n_i is the number of piles in row i in the characteristic module length considered (e.g. 6m (20ft)).
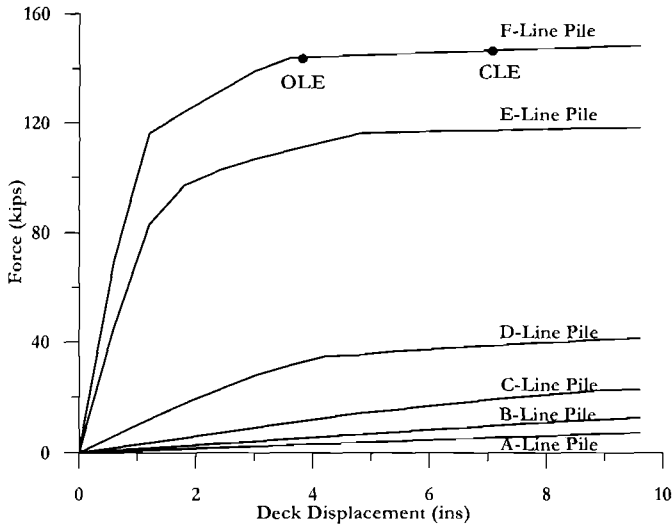
(a) Individual Pile Lateral Force-Displacement Responses
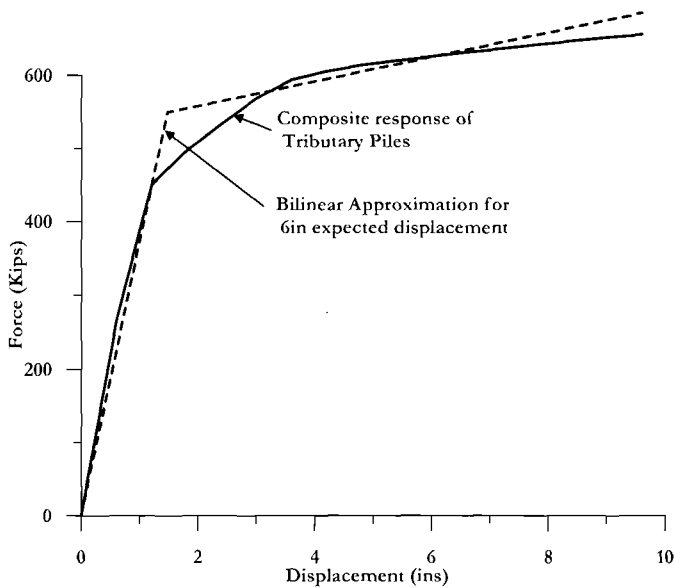
(b) Characteristic Force-Displacement Response for 20ft of Wharf

Fig.12.16   Composite Force-Displacement Response of a 6m (20ft) Length of Wharf (1 kip = 113 kN)

It will be seen from the above formulation that the position of the effective centre of stiffness is not a constant, but varies as the displacement varies, since the F- and E-Line piles will enter the nonlinear range of response earlier than the other piles, and hence their secant stiffness will decrease relative to the other piles. Figure 12.17 plots the eccentricity of the centre of stiffness from the centre of mass as a function of displacement, calculated from the data in Fig.12.16(a). In generating Fig.12.17 it was assumed that the piles on Row F were at 2m (6.67ft) centres, on Row A were at 3m (10ft) centres, and on Rows B to E were at 6m (20ft) centres. The eccentricity is expressed by ratio to the width B= 30.5m (100ft) between crane rails, which were located above Rows A and F, making the assumption that the pile rows are spaced uniformly at 6m (20ft) centres in the transverse direction. Note that in this case, the centre of mass will be approximately midway between the C- and D-Line piles. The eccentricity between the centre of mass and centre of stiffness will reduce from about 13.4m (44ft) to about 12.6m (38ft) as the displacement increases to 244mm (9.6in).
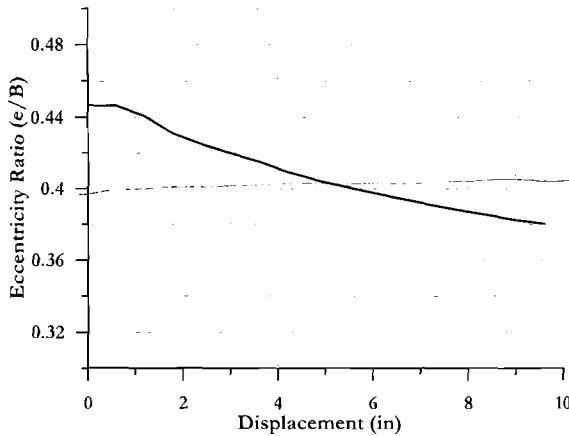
Fig. 12.17 Eccentricity between Centre of Mass and Centre of Stiffness for Data of Fig.12.16 at Different Lateral Displacements (1 in = 25.4mm)

12.6.2 Inelastic Time History Analysis

When complexities in the structural configuration of the wharf lead to uncertainty of structural response, or where special importance is placed in the verification of seismic response, the only option will be to carry out inelastic time-history response of the wharf. Since the value of the wharf will be high, this will generally be economically feasible. General issues relating to inelastic time-history analysis are covered in some detail in Section 4.9.2, with information of special relevance to wharves in Section 4.9.2(i).

(a) Substructure modelling: A typical wharf segment between movement joints will have several hundred piles. To model each of these as individual structural members is

time-consuming and unnecessary. An accurate representation of the structural characteristics of a wharf segment may be obtained by using four "SuperPiles" whose composite characteristics of stiffness and strength model the stiffness of all piles in the segment, as suggested in Fig.12.18. This representation relies on the observation that the flexural stiffness of the deck is high compared with the piles, as noted earlier in Section 12.5.4(a), and may be considered rigid, both in-plane and out-of-plane.
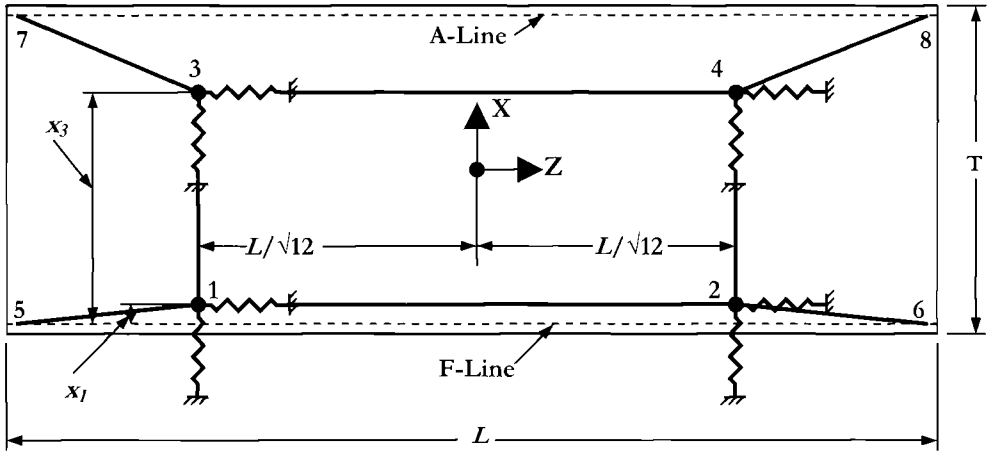

Fig.12.18 Locations of SuperPiles for a Wharf Segment (Plan View)

Note that representing the lateral strength and stiffness characteristics of the piles by horizontal springs, as shown in Fig. 12.18, enables the 3-D wharf structure to be modelled by 2-D inelastic time-history analysis. This assumes that wharf response to vertical seismic excitation is not of concern. Although this will generally be the case for "bare-wharf" studies, a full 3-D modelling and excitation will be needed when wharf-crane interaction is considered.

Figure 12.18 shows SuperPiles located at nodes **1** to **4**, connected to each other by rigid members, and also connected to nodes **5** to **8** located at the corner piles. These links are necessary to obtain the critical displacements, which will occur at corners of the segment, from the computer analyses. Additional nodes (not shown) at the midpoints of the ends of the segment will be required when adjacent segments are connected by shear keys.

Referring again to the model of Fig.12.14, the lateral resistance of the SuperPiles at nodes **1** and **2** at a given displacement Δ each represent the combined resistance of all piles on lines **D**, **E** and **F** for half the segment length. That is,

$$F_{\Delta 1} = F_{\Delta 2} = 0.5N \sum_{L-D}^{F} n_i F_{\Delta Li}, \quad \text{similarly:} \quad F_{\Delta 3} = F_{\Delta 4} = 0.5N \sum_{L=A}^{C} n_i F_{\Delta Li} \quad (12.29)$$

where, again, n_i is the number of piles on line i in the characteristic module length (e.g. 6m), and N is the number of characteristic modules in the segment length, L. The effective (secant) stiffness of the SuperPiles at the specified displacement Δ is given by:

$$k_1 = k_2 = F_{\Delta 1} / \Delta, \qquad k_3 = k_4 = F_{\Delta 3} / \Delta \tag{12.30}$$

Equations (12.29) and (12.30) can be calculated for different displacements to generate the composite force-displacement response in similar fashion to that used to generate the characteristic response of the 6m module in Fig.12.16.

The distance of Nodes **1** and **3** from the **F**-Line are given by:

$$x_1 = \frac{\sum_{L=D}^{F} n_i F_{Li} x_i}{\sum_{L=D}^{F} n_i F_{Li}} \quad \text{and} \quad x_3 = \frac{\sum_{L=A}^{C} n_i F_{Li} x_i}{\sum_{L=A}^{C} n_i F_{Li}} \tag{12.31}$$

To provide the best possible representation of the inelastic response, Eq.(12.31) should be evaluated at an initial elastic displacement, since the movement of the centre of stiffness will automatically follow onset of inelastic action. In order to ensure the correct torsional stiffness under longitudinal response, the SuperPiles must be located longitudinally at the centre of gyration of the wharf segment; that is, at a distance of $L/\sqrt{12}$ from the segment centroid.

(b) Hysteretic Rules: Hysteretic rules for the SuperPiles should be appropriate for the pile material. Thus, for concrete piles, the Modified Takeda, or some equivalent hysteresis rule should be adopted. However, it should be noted that Modified Takeda rules do not model the gapping that develops in the soil near the pile top as a result of inelastic soil response, and more sophisticated modelling options could be considered. The information provided in Sections 10.3.5(c) and 12.3.2 should be reviewed. For steel pipe piles, a bilinear elasto-plastic rule may be adequate. Reference should be made to Section 4.9.2 for general advice on time-history analysis.

(c) Movement Joints: Two issues must be considered: the modelling of the shear key itself, and the modelling of potential impact between corners of the adjacent segments. Using an elastic modal analysis, the connection between the segments is typically represented by a pin, allowing free relative rotation between the adjacent segments, but no relative transverse or longitudinal displacement. For inelastic time-history analysis, a more realistic representation of the connection, as shown in Fig.12.19(b) should be provided. For this connection, three separate elements are required. The shear key is represented by a spring, connecting nodes on adjacent segments, with high stiffness in the wharf-transverse direction, and zero stiffness in the wharf-longitudinal direction.

This allows the necessary freedom in the longitudinal direction, and modelling as an individual element enables the spring shear force to be determined from the analysis, which may not be possible if a pinned connection between the segments is used.
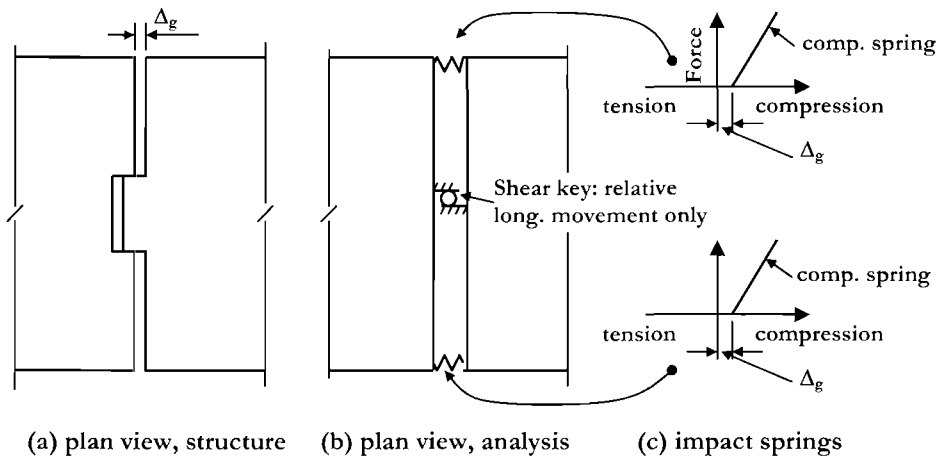

(a) plan view, structure   (b) plan view, analysis   (c) impact springs

Fig.12.19   Modelling Movement Joints between Segments

The other two elements are springs, acting in the longitudinal direction, connecting adjacent corners of adjacent segments (Fig.12.19(b)). These springs should have a finite gap in the gap-closing direction, before contact is made, to represent the movement joint opening. Note that this gap will be temperature-dependent, and it may be necessary to run the analyses with upper and lower bounds for the gap dimension. When the compression gap is closed, the spring should have a high stiffness, as shown in Fig. 12.19(c). In the tension direction the stiffness should be zero, or the gap should be set sufficiently large so that contact could not occur.

The choice of the stiffness of the shear-key and contact springs is important. It has been found that if the stiffness is set too high, numerical instability may occur, affecting the accuracy not only of the spring forces, but of the entire analysis. As a rough guide, the deformation of the springs should be realistic- in the range 0.5 · 2.5mm (0.02 – 0.10 in.) under the expected spring forces. Preliminary analyses should be carried out where the spring stiffnesses are varied by an order of magnitude to ensure that analysis results are stable.

(d) Modelling Wharf/Crane Interaction: Analyses have shown[P39] that the wharf displacements under seismic excitation are essentially insensitive to the presence and location of single or multiply cranes of the A-frame type commonly operating in ports. Consequently, the influence of A frame cranes can generally be ignored in wharf design. This observation only applies for wharves with similar cross-sections to those considered in Section 12.5. New generation low-profile cranes, however, have been found to interact

more significantly with wharves, increasing the wharf displacement response in some cases.

Although wharf/crane interaction generally has a comparatively small influence on wharf response, the influence on crane response is very significance, and must be considered in crane design. Aspects relating to this problem are outside the scope of this book.

12.7 CAPACITY DESIGN AND EQUILIBRIUM ISSUES

12.7.1 General Capacity Design Requirements

General capacity design principles have been considered in some detail in Section 4.5. The design philosophy for wharves will be that inelastic action is to be confined to plastic hinges in the piles. Shear failure of the piles must be avoided, since inelastic shear action is inherently non-ductile, and any inelastic action in the deck, whether flexural or shear related, will be proscribed. To ensure that these requirements are met, the dependable flexural strength of the deck, and the dependable shear strength of deck and piles must exceed the maximum feasible actions at these locations corresponding to the flexural overstrength at the pile plastic hinges. This requires three stages of consideration: (1) determination of the maximum flexural strength of the plastic hinges, (2) determination of the shear force in the piles, and the shears and moments in the deck corresponding to the overstrength in the piles and (3) determination of the dependable strength of the actions to be protected from inelastic response.

(a) Overstrength Flexural Capacity of Pile Plastic Hinges: Pile flexural strength may exceed the design strength M_D due to two main reasons. First, as noted in relation to Fig.12.7 and 12.11, cover spalling is expected to result in a significant loss of moment capacity. The design moment capacity thus uses a conservative estimate of the moment-curvature response. Second, the dowel reinforcement may have a yield strength that considerably exceeds the value assumed in design.

The design process outlined in this chapter, however, and recommended throughout this text, has been based on minimising the conservatism in the estimation of pile flexural strength. Thus the design flexural strength of the pile-top hinge is based on a concrete compression strength of $1.3f'_c$, and a dowel yield strength of $1.1f_y$ where f'_c and f_y are the minimum strengths specified for construction (see Section 12.5.1). Further, the design charts and equations presented in Sections 12.5.2 and 12.5.3 include the effects of strain-hardening of the dowel reinforcement, of post-yield stiffness of the prestressing, and of increased concrete strength due to confinement by the spiral reinforcement.

Reinforcing steel used for dowels in North America will normally be grade 60 (specified yield strength = 414MPa = 60 ksi) and will comply with A706 requirements, which limit the yield strength to a maximum of 30% above the specified yield. This is still a significant increase over the 10% enhancement adopted for flexural design. Analyses indicate that increasing the dowel yield strength from 455MPa (66ksi) to (517MPa (75ksi)

will increase the flexural strength of the top plastic hinge by 10% or less, with the strength enhancement decreasing as the axial load increases. The flexural strength of the in-ground hinge will increase by about 5% if the upper limit of prestressing ultimate tensile strength is considered. Combining these with the ratio of peak flexural strength to design moment apparent in Figs. 12.10(a) and 12.12(a) the maximum flexural strength enhancement can be expressed as follows:

pile-top plastic hinge: $M^o / M_{des} = 1.1 + 0.81 P*$ for P>0   (12.32a)

                              $= 1.1$ for P<0   (12.32b)

in-ground plastic hinge: $M^o / M_{des} = 1.18$ for all P.   (12.33)

Equations (12.32) and (12.33) indicate that the increase in design shear force resulting from flexural strength enhancement will be about 15%, with the actual value depending on the axial load level in the piles. Note that enhancement resulting from the concrete compression strength has not been considered in the above, since it will tend to increase the shear strength more than the shear demand, particularly at the **OLE** limit state, and for consistency, the same value must be used for both flexural strength and shear strength estimates.

Note further that Eq.(12.33) will be non-conservative if the dowels for the pile-deck connection extend down into, and past the in-ground hinge location, since the dowels will then contribute to the in-ground hinge flexural strength. It is important to avoid this condition during construction.

Although tempcore steel, which is commonly used in Europe for reinforcement has much lower strain-hardening strength increase than occurs with US steel, the enhancement due to uncertain steel properties is likely to be similar, since it relates entirely to uncertainty of yield strength, which has a similar variability to that in the USA.

(b) Equilibrium Consideration: The importance of maintaining equilibrium in all structural calculations, whether at design strength or overstrength levels has been emphasised in Section 4.6. Equilibrium must be satisfied for all forces acting simultaneously on the structure. This means that seismic axial forces in the piles must be in equilibrium with the seismic shears in the deck. These shears must be in equilibrium with the deck moments which in turn are in equilibrium with the pile moments, which depend on the pile axial force levels. It will be seen that a degree of iteration may be needed to ensure total equilibrium in analysis. The principles involved are very similar to those presented in Section 4.6 with reference to Fig.4.21, but are elaborated in some detail here as our experience is that many designers and students are less careful with equilibrium issues than they should be.

Referring again to Fig.12.1(a), moments and shears on a characteristic section (say 6m (20ft) longitudinally) between **F**-Line and **D**-Line are presented in Fig.12.20(a). It is assumed that there are three **F**-Line piles in the characteristic length, while the **E**-Line

and **D**-Line piles are spaced at 6m (20ft.) longitudinally. Deck moments and pile moments must be in equilibrium at the intersection of the pile and deck centerlines. If M_F, M_E and M_D are the pile moments at the deck soffit at the limit state under consideration, then the pile moments extrapolated to the deck centreline are:

$$M'_F = M_F + V_{S,F}.h_d / 2 \tag{12.34a}$$

$$M'_E = M_E + V_{S,E}.h_d / 2 \tag{12.34b}$$

$$M'_D = M_D + V_{S,D}.h_d / 2 \tag{12.34c}$$

where h_d is the depth of the deck.

Since there are three piles on the **F**-Line in the characteristic length, the moment extrapolated to the deck centerline is $3 \cdot M'_F$. This is the deck moment above the **F**-Line piles. At the **E**- and **D**-Lines, the pile moments will be distributed approximately equally to the deck moments on either side of the pile centrelines. The deck moments are thus $\pm 0.5 M'_E$ and $\pm 0.5 M'_D$. The seismic shear force induced in the deck in span L_{FE} between the **F**-Line and **E**-Line piles is thus:

$$V_{S,FE} = \frac{3M'_F + 0.5M'_E}{L_{FE}} \tag{12.35}$$

This shear will be critical adjacent to Pile **E**, since the effective deck width resisting $V_{S,FE}$ will be small, and based on a single pile. At the **F**-Line, the same seismic shear force will be divided between three deck zones, one adjacent to each of the three piles. By analogy to bridge footings and cap beams[P4], the effective width of deck, b_{eff} resisting the shear adjacent to a pile should not be taken larger than

$$b_{eff} = D + d_d \le L_{trans} \tag{12.36}$$

where D is the pile diameter, d_d is the effective depth of the deck, and L_{trans} is the spacing of the piles transverse to the direction considered.

For flexural resistance of the deck, the effective width may be taken as:

$$b_{eff} = D + 2d_d \le L_{trans} \tag{12.37}$$

Assuming one pile per characteristic length of deck, shear forces in the deck between pile rows **E** and **D** will be given by:

$$V_{S,ED} = \frac{0.5(M'_E + M'_D)}{L_{ED}} \tag{12.38}$$

where the symbols are defined in Fig. 12.20(a).

(a) Transverse Section (Characteristic Length)
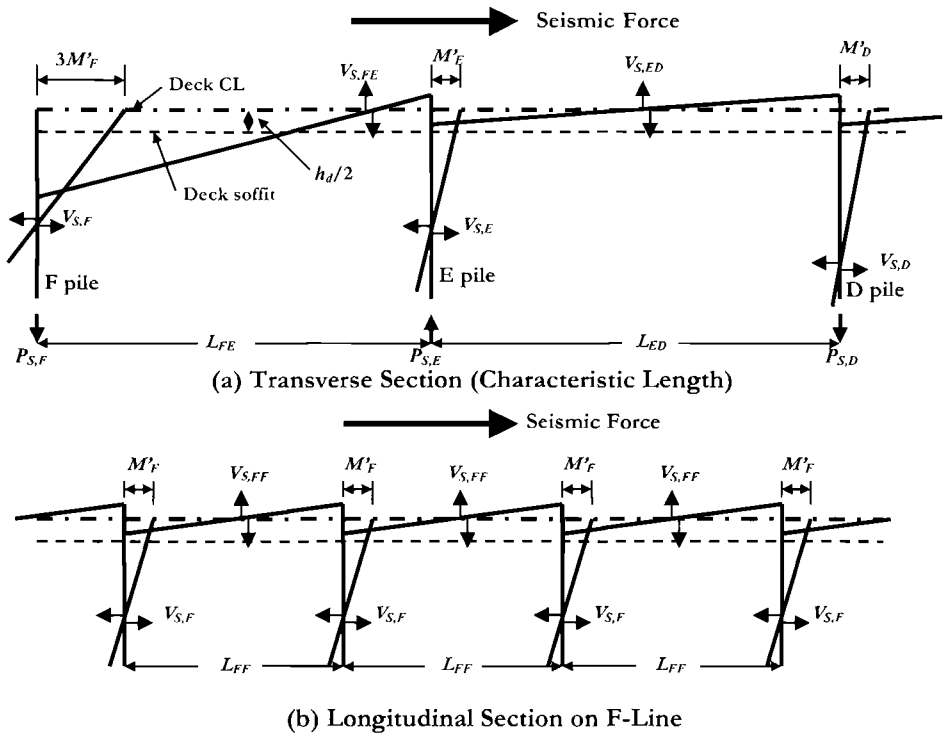
(b) Longitudinal Section on F-Line

Fig.12.20 Equilibrium of Forces and Moments on Wharf Section

The seismic axial forces in the piles must be in equilibrium with the deck shear forces. Thus the seismic tension force $P_{S,F}$ developed in a typical F-Line pile will be:

$$P_{S,F} = V_{S,FE} / 3 \qquad (12.39)$$

since the deck shear, $V_{S,FE}$ (given by Eq.(12.35)) is resisted by three piles on line F. The piles on line E will have increased compression resulting from the seismic shears. Equilibrium requires that:

$$P_{S,E} = V_{S,FE} - V_{S,ED} \qquad (12.40)$$

Of course, if the direction of seismic force is reversed, the piles at row F will be subjected to seismic compression, and those on row E will be subjected to seismic tension. Gravity loads must be added to these axial forces to obtain the total axial forces acting on the piles.

For compatibility, the moments in the piles must be those corresponding to the pile axial forces calculated above. Thus, if overstrength is considered, the deck shears and the pile axial forces will increase in proportion.

Equilibrium of forces and moments under longitudinal seismic force is represented in Figure 12.20(b), which shows moments and shears in the deck and piles along the **F**-Line. The characteristic deck shear force will be given by:

$$V_{S,FF} = 2 \times 0.5 M'_F / L_{FF} \tag{12.41}$$

where L_{FF} is the spacing of piles along the **F**-Line, and M'_F is given by Eq.12.34(a)).

The axial forces in the piles will not change significantly from the gravity values, since the shears in the deck on either side of the pile will be equal and opposite. An exception occurs for the end piles in the row, which will have seismic forces equal to $\pm 1.5 V_{S,FF}$ with the sign depending on the direction of the seismic force.

(c) Dependable Strength of Capacity Protected Actions: Normal flexural and shear strength equations may be used to determine the dependable strength of pile shear force, and deck moment and shear capacity. Reference should be made to Section 4.7.3 for shear strength equations for piles, since conventional codified equations may produce unrealistic, and not necessarily conservative answers.

12.7.2 Shear Key Forces

Modal analysis relies on the assumption that inelastic and elastic displacements are sufficiently close for the latter to be used as adequate approximations to the former. As discussed in Section 4.9.2(f) this assumption is of doubtful validity. Even if it were the case, the same approximation does not hold for force levels. It is appreciated that the force levels in piles can be determined from the displacements using inelastic force-displacement relationships, as developed in Section 12.5.4, but this does not apply to forces in members that remain elastic, such as shear keys. These cannot be determined in any reliable fashion from the elastic analysis results when other members, such as the piles, respond inelastically.

Consequently, the most reliable way to estimate shear key forces will be from inelastic dynamic analysis, where the shear key is modelled as described in Section 12.6.2. However, for regular structures with rectangular segments, inelastic dynamic analyses of two-segment and three-segment marginal wharves have indicated that the following expression provides an adequate representation of the maximum shear force developed in shear keys between external and internal segments:

$$V_{sk} = 1.35 \left(\frac{V_\Delta .e}{L} \right) \tag{12.42}$$

where V_Δ is the total lateral resistance of the outer segment under uniform transverse displacement, Δ, corresponding to the design excitation, e is the eccentricity between effective centres of stiffness and mass, and L is the length of the outer segment. This expressions has been shown to give a good estimation of response for uniform soil conditions, and is thus suitable for initial design, though higher values were found appropriate when different up-slope and down-slope strengths and stiffnesses were included in the time-history analyses[P38].

12.8   DESIGN EXAMPLE 12.1: Initial Design of a Two-Segment Marginal Wharf

The two-segment marginal wharf described in Fig.12.21 is to be located in a near-fault area with moderate seismicity. The segments have lengths of 180m (590ft) and 240m (787ft), with an overall width of 33.5m (110ft) and a distance between the outer pile lines of 30.5m (100ft) corresponding to the container crane gauge. The segments are connected by a shear key restraining transverse displacement only. A dyke slope of H:V = 1.63:1 is required for slope stability. Only **CLE** response will be considered.

Crane support requires a maximum spacing of piles on the outer rows (**A** and **F**) of 3m (9.8ft), and a maximum spacing of 7.5m (24.5ft) elsewhere for gravity load support of the deck dead plus live load. An initial design is based on six rows of piles evenly spaced at 6.1m (20ft) centres in the transverse direction, with piles at 2m (6.56ft) on the landward **F** line, at 3m (9.8ft) on the seaward **A** line, and at 6m (19.6ft) on the intermediate lines, as shown in Fig.12.21(b). The deck has a thickness of 0.9m (35.4 in) under the crane rails and up to row **E**, and is 0.6m (23.6in) elsewhere. All piles are to be 610mm (24in) diameter octagonal prestressed piles. Connection to the deck at rows **F**, **E**, and **D** is by 8D32 (#10) bars as shown in Fig. 12.6. On the other lines, contribution to seismic resistance is expected to be minor, and hence the number of dowels in the connection is reduced to 4D32 bars. This reduces the shear stress on the connection, and together with the expected elastic response of the piles allows simplified confinement details to be used for the connection. Details for the initial preliminary design are shown in Fig.12.21(b).

The elastic design displacement spectrum is shown in Fig.12.22(a), and is linear to a displacement plateau of 0.6m (23.6in) starting at a period of 3.0 sec. Because of the near-fault location, the displacement-reduction equation of Eq.(2.11) for damping levels higher than 5% is to be used in the design.

A characteristic module length of 6m (19.6ft) is used for the design which is based on the steps defined in Section 12.3.3. Prior to carrying out these steps, the effective weight and eccentricity of the 6m wharf module must be calculated. The deck is divided into three sections, separated by the dashed vertical lines visible in Fig.12.21(b). The weight of a 6m length of deck, including a seismic live-load of 0.48kPa (10lb/sq.ft), and distance of centre of mass of each section from the **F**-line pile are listed in Columns (2) and (3) respectively of Table 12.1 Also included in these columns are the tributary weight of each pile ($1/3^{rd}$ of pile weight to an effective depth of 5-pile diameters below grade) and distance from the **F** line. The result is a module weight of 3627kN (815kips) at a distance from the **F** line of

$$\bar{x}_m = 56850/3627 = 15.67 \text{ m (51.4ft)}$$

Lateral pushover analysis of the individual piles is not described here, as it is straight-forward, but lengthy. Results for the initial design, for average soil conditions, are shown in Fig.12.22(b). The critical **F**-line piles have an equivalent bilinear strength of 500kN (112kips), and a limit displacement, corresponding to **CLE** strain limits of 175mm (6.9in).
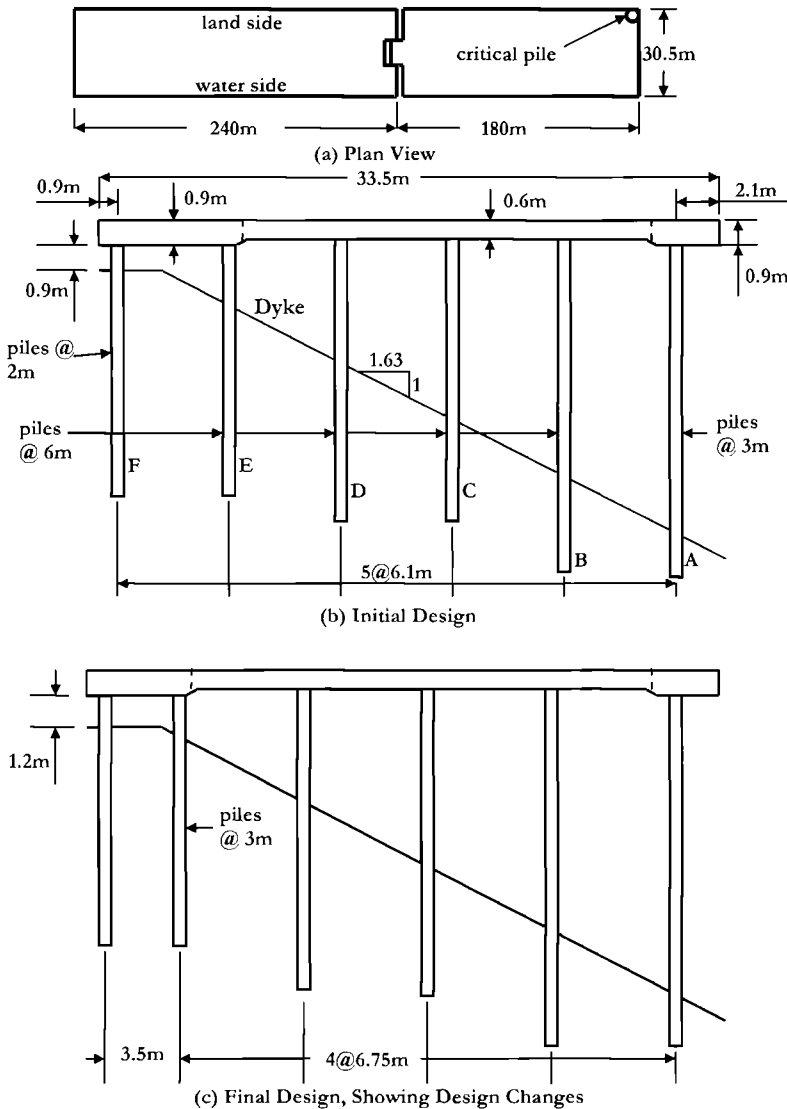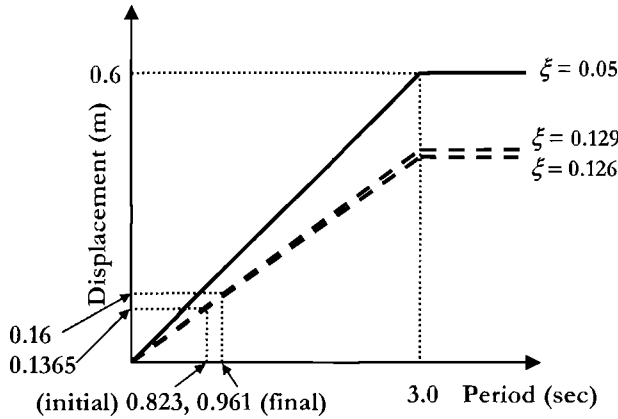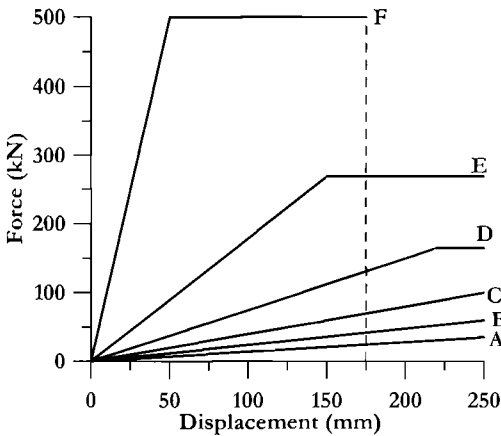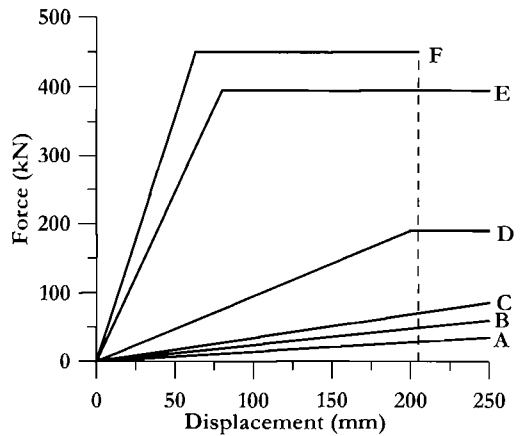

(a) Plan View

(b) Initial Design

(c) Final Design, Showing Design Changes

Fig.12.21   Structure for Design Example 12.1

(a) Design Displacement Spectrum

(b) Initial Design

(c) Final design

Fig.12.22   Data for Design Example 12.1

At the displacement of 175mm corresponding to the **F**-line **CLE** limit strain, only the piles on Rows **F** and **E** reach their strength, with the other piles still at less than yield displacement. Table 12.1 includes, in Columns (5) and (6), the pile strengths corresponding to a displacement of 175mm, and the moment of this strength about the **F**-line pile. The total strength is 2095 kN (471 kips), and the strength/stiffness eccentricity, measured from the **F**-line piles is

$$\bar{x}_s = 7454/2095 = 3.56m \ (11.7\text{ft})$$

The effective eccentricity relative to the centre of mass is thus

$$e = \bar{x}_m - \bar{x}_s = 15.67 - 3.56 = 12.11m \ (39.7\text{ft})$$

With B = 30.5m, this corresponds to an eccentricity ratio of e/B = 0.397B – very similar to the value of 0.4B used to generate Fig.12.3, which can thus be used to determine the ratio of centre-of-mass design displacement to critical pile displacement.

Table 12.1 Mass and Strength Eccentricity for Initial Design, DE 12.1 (6m module)

Segment/Pile (1)	Weight (kN) (2)	x from F (m) (3)	W.x (kN.m) (4)	Force @ 175mm (kN) (5)	For.x (kN.m) (6)
Seg.1	960	2.8	2688		
Seg.2	1969	17.75	34950		
Seg.3	467	30.8	14380		
Pile F	27	0	0	3×500	0
Pile E	14	6.1	85	269	1641
Pile D	23	12.2	281	165	2013
Pile C	32	18.3	586	70	1281
Pile B	40	24.4	976	42	1025
Pile A	95	30.5	2898	2×24.5	1495
Sum:	3627		56846	2095	7454

The information provided above essentially covers Steps 1 to 4 of the design process of Section 12.3.3. We continue with the subsequent steps:

Step 5: Design centre-of-mass (C_M) displacement: We assume a ratio of simultaneous transverse to longitudinal excitation of X=40%. The critical segment is the shorter 180m segment for which the aspect ratio is L/B = 5.9. Hence from Fig.12.3,

$$\Delta_D = 0.78 \times \Delta_{cr} = 0.78 \times 175 = 136.5mm$$

Step 6: Displacement ductility demand: From Fig.12.22(b) the yield displacement of the **F**-line pile is 50mm. We assume the conservative relationship of Eq.12.3:

$$\mu_{sys} = 136.5/(1.2 \times 50) = 2.275$$

Step 7: Equivalent viscous damping: From Eq.(12.4):

$$\xi_e = 0.05 + 0.444\left(\frac{\mu_{sys}-1}{\mu_{sys}\pi}\right) = 0.05 + 0.444\left(\frac{1.275}{2.275\pi}\right) = 0.129$$

Step 8: Effective period: The reduction factor for damping, is governed by the near-field relationship given by Eq.(2.11):

$$R_\xi = \left(\frac{0.07}{0.02 + \xi_e}\right)^{0.25} = \left(\frac{0.07}{0.149}\right)^{0.25} = 0.828$$

The damped corner displacement is thus 0.6×0.828=0.497m. By proportion, the

effective period is thus:

$$T_e = 3.0 \times 0.1365 / 0.497 = 0.823 \sec$$

Step 9: Effective stiffness: From Eq.(12.5), with $m_e = 3627/g$:

$$k_{ss} = 4\pi^2 \cdot \frac{m_e}{T_e^2} = 4\pi^2 \cdot \frac{3627}{9.805 \times 0.823^2} = 21,600 kN / m$$

Step 10: Module lateral strength requirement: From Eq.(12.6):

$$F_{ss} = k_{ss} \cdot \Delta_t = 21,600 \times 0.1365 = 2945 kN \quad (662 \text{ kips})$$

This is the required strength of the 6m module of wharf selected for design, at a lateral displacement of 175mm. By comparison, we see from Table 12.1 that the strength provided, as initially designed, is only 2095kN, which is 29% lower than required. We note that even if we reduced the spacing of piles on the **E**-line to 2m, the strength would only increase to 2633kN, which is still more than 10% below the required strength.

Redesign: Some major changes are required to provide the required strength. The following changes, illustrated in Fig.12.21(c) are considered: (1): The **E**-line row is moved closer to the **F**-line row, and the spacing of piles on the **E**-line is reduced to 3m (9.6ft). With a spacing of 3.5m (11.5ft) between **E** and **F** this requires the spacing between the other rows to be increased to 6.75m (22.1ft) which is less than the maximum of 7.5m permitted for Dead and Live load. Moving the **E**-line closer to the **F**-line reduces the clear height between deck soffit and dyke, increasing the seismic resistance of the **E**-line piles; (2) Moving the **E**-line closer to the **F**-line enables the deck thickness to be reduced closer to the landward edge, reducing the deck mass a little. (3): The clearance between the top of the dyke and the deck soffit at the **F**-line is increased from 0.9m to 1.2m. The elevation profile of the sloping portion of the dyke remains unaltered. Although this reduces the lateral shear that can be resisted by the **F**-line piles, it increases the limit-state displacements by a larger amount. Re-analysis indicates that the **F**-line strength reduces from 500kN to 450kN, while the **CLE** limit-state displacement increases from 175mm to 205mm. The yield displacement increases from 50mm to 63mm.

The redesign requires re-analysis of the force-displacement response of all except the **A**-line piles, since the clear height (dyke to soffit) has changed. The resulting force-displacement plots are included in Fig.12.22(c). Calculations for effective mass of the 6m module, and the centres of mass and effective strength/stiffness at a displacement of 205mm (8.1in) are listed in Table 12.2. From the data in Table 12.2, the mass and strength/stiffness eccentricities are calculated as 15.90m and 3.51m respectively from the **F**-line. The eccentricity between mass and strength/stiffness is thus $e = 12.39\text{m} (40.6\text{ft})$ = 0.406$\boldsymbol{B}$. Figure 12.3 is still directly applicable, and the ratio between centre-of-mass and corner displacement is unchanged from the initial design.

The strength provided with the redesign is 2514kN, which is still substantially less than the 2945kN required by the initial design. However, the increased design

displacement will result in a reduced required strength. The calculations are summarized below.

Table 12.2 Mass and Strength Eccentricity for Final Design, DE 12.1 (6m. module)

Segment/Pile (1)	Weight (kN) (2)	x from F (m) (3)	W.x (kN.m) (4)	Force @ 205mm (kN) (5)	For.x (kN.m) (6)
Seg.1	649	1.6	1038		
Seg.2	2179	16.55	36060		
Seg.3	467	30.8	14380		
Pile F	3×9.7	0	0	3×450	0
Pile E	2×10.5	3.5	73.5	2×395	2765
Pile D	21	10.25	215	190	1948
Pile C	30	17	510	86	1462
Pile B	40	23.75	950	49	1160
Pile A	2×47.5	30.5	2900	2×24.5	1490
Sum:	3531		56130	2514	8825

Step 5: C_M design displacement: $\Delta_t = 0.78 \times 205 = 160$mm (6.3in)

Step 6: System displacement ductility: $\mu_{sys} = 160/(1.2 \times 63) = 2.12$

Step 7: Equivalent viscous damping: $\xi_e = 0.126$

Step 8: Damping reduction factor: $R_\xi = 0.832$

Step 9: Effective period: $T_e = 0.961$ sec

Step 10: Effective stiffness: $k_{ss} = 15,400$kN/m

Step 11: Required module strength: $F_{ss} = 15,400 \times 0.16 = 2464$kN (554 kips)

This is 3% less than the provided strength of 2514kN, and the design is satisfactory. Note that it would be difficult, and rather pointless to refine the design to exactly match the required and provided strength.

Shear key design force: The shorter segment governs the shear key force. The total lateral resistance of the segment, which includes 30-6m modules, will be $V_\Delta - 30 \times 2514 = 75,400$kN. From Eq.(12.42) the shear key force is thus estimated as:

$$V_{sk} = 1.35 \left(\frac{V_\Delta.e}{L} \right) = 1.35 \frac{75400 \times 12.39}{180} = 7000kN \ (1575 \text{ kips})$$

The design of this structure was comparatively straightforward, and as a consequence design verification by inelastic time-history analysis is probably not warranted. It would, however, be a relatively simple task to model the wharf by two segments each with four superPiles, following the representation of Fig.12.18, with the two segments linked by the

three-node connection represented in Fig.12.19.

Although capacity design is not included in this example, the procedure is straightforward, since there is no dynamic amplification to be considered, and only strength enhancement due to material strengths possibly exceeding the specified values need to be considered.

12.9 ASPECTS OF PIER RESPONSE

Piers and terminal piers (see Fig.12.2) are likely to have piles whose clear height between grade and deck soffit increases with distance from the shore. However, it is unlikely that the height increase will be uniform with distance from the shore. Eccentricity between centres of mass and of strength/stiffness will clearly be of critical importance for such structures, even more so than for marginal wharves.

The approximate approaches developed in previous sections of this chapter should not be extrapolated to piers because of the extreme aspect ratios involved. At this stage, design will need to be by trial and error. An initial structure will be conceived, and checked using the assessment procedures outlined in Chapter 12. Successive improvements should quickly stabilize the design. It is recommended that inelastic time-history analyses be used to verify the design in all cases.

13

DISPLACEMENT-BASED SEISMIC ASSESSMENT

13.1 INTRODUCTION: CURRENT APPROACHES

There are a number of philosophical issues that must be addressed before embarking on the seismic assessment of an existing structure. The first of these is the selection of the appropriate limit state to which the structure will be assessed. Serviceability will rarely be the issue here, and though the damage-control limit state is the most common for new structures, collapse-prevention is more commonly the key limit state for existing structures.

The second issue is the acceptance criterion: what constitutes a satisfactory answer from an assessment. With new design, there is still, generally, a "pass/fail" mentality applied: if the strength is lower than the code-specified level by 5%, or the assessed drift exceeds the code limit by 5%, the design is deemed unsatisfactory. In the past the same mentality has been applied to assessment of existing structures, though the acceptance criteria are often relaxed from those defined for new structures for reasons that are often of doubtful validity. A typical reason provided in support of a reduction in acceptance criteria is that a particular structure may have been constructed (say) 50 years ago, and its expected design life is (say) 100 years. Hence the probability of the structure collapsing in its remaining design life is less than for a new structure of identical characteristics. This ignores the fact that the hazard (a measure of local seismicity) is the same for all structures, regardless of their capacity, while vulnerability (a measure of structural capacity) is clearly much worse for the older structure. The risk, which is a convolution of hazard and vulnerability, and which can be expressed as (say) a probability of failure in a given year, and which perhaps is the most relevant issue for the general public, is much higher for the older structure.

It is therefore clear that assessments of existing buildings should not be of the "pass/fail" type to artificial criteria, but should include as much probabilistic information as possible, so that an informed decision can be made about the need to strengthen.

The issue of the level to which any strengthening should be made also requires similar careful consideration. Our viewpoint is that this should be to the standard required of new structures. However, since retrofitting is not covered in this text, this issue will not be discussed further.

On first consideration it might appear that seismic assessment of existing structures is more straightforward than design of new structures. This would indeed be the case if all material properties and structural dimensions were exactly known at all locations, and the seismic characteristics for assessment were equally defined with exactitude. In fact this will rarely be the case, and considerable uncertainty will often exist as to actual material properties even if mill certificates have been recorded for reinforcement or structural steel, and 28-day compression strengths for concrete are similarly available. In extreme circumstances, with reinforced concrete or masonry structures, even the amount, distribution, and termination of flexural and shear reinforcement may be uncertain.

Some potential problems are illustrated with respect to a reinforced concrete structural member in Fig.13.1. A critical element of a displacement-based assessment methodology will be to determine the displacement capacity of the member, expressed in Fig.13.1 in terms of displacement ductility.
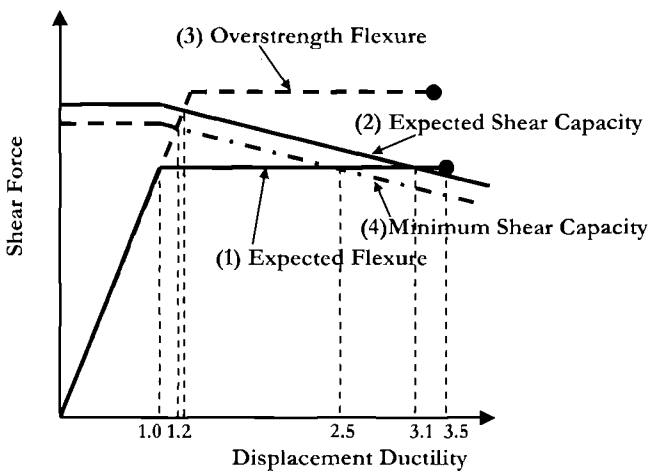
Fig.13.1 Determination of Ductility Capacity of a R.C.Member

The expected flexural response, based on a low estimate of probable material strengths is shown by line (1) and has a corresponding displacement ductility capacity of 3.5, based on moment-curvature analyses following principles outlined in Chapter 4. The shear strength of the member depends on the ductility demand, in accordance with information provided in Section 4.7.3. The shear strength envelope based on probable material strengths is shown by line (2) and intersects line (1) at a displacement ductility of 3.1. This, then, is the expected ductility capacity.

However, because of the uncertainty of material strengths, we investigate the consequences of the overstrength flexural capacity. This results in force-displacement response represented by line (3), which intersects the expected shear capacity envelope at a displacement ductility of 1.2. We further look at a worst-case scenario, where the

minimum shear capacity (line (4)) is compared with the maximum flexural overstrength, resulting in a slightly lower displacement ductility of about 1.15. Note that in these comparisons the displacement ductility is always related to the yield displacement of the expected flexural performance, and is thus not strictly a measure of ductility of the overstrength section.

From this example we see that it is possible to have very large variation in the estimated displacement capacity (in this case a displacement ductility capacity of 1.15 to 3.1) for comparatively small variations in material strengths.

The discussion above indicates that it is generally not possible to establish an absolute value for risk of an existing structure, as a consequence of uncertainties in both structural characteristics, and in seismicity characteristics – that is, in both capacity and demand. The most promising approach of the future for seismic assessment is clearly a reliability approach based on probability theory. An excellent description of the state of the science in this field is available in [P30]. Although this is clearly the way of the future for seismic assessment, it is our view that in the short term, deterministic approaches will still be needed. Since these are compatible with the design approach advocated in this text, we will limit our discussion to such approaches, and refer the interested reader to [P30] for a more comprehensive treatment of the probabilistic aspects.

13.1.1 Standard Force-Based Assessment.

Traditional seismic assessment has tended to be based on simple comparison of estimated base shear capacity, and base shear demand specified by code. In Fig.13.2(a), the required code base shear strength, V_{code} is found in the usual manner, reducing the elastic base shear force, $V_{el,code}$ corresponding to the elastic stiffness of the structure, by a code-specified force-reduction or behaviour factor. The actual assessed base shear strength V_A is then estimated. Comparison of V_A with V_{code} indicates whether the structure is satisfactory. This is a classic capacity/demand ratio (**C/D**) approach, based on strength. For values of **C/D** > 1 the structure "passes". For **C/D** < 1 the structure "fails". Problems with this rather simplistic approach include the following:

- No assessment is made of the actual displacement or ductility capacity
- No capacity design check is included to determine undesirable failure modes
- No estimate is made of the risk associated with V_A/V_{code} <1

A simple strength-based assessment, without consideration of displacement capacity or risk levels cannot be considered a satisfactory approach.

13.1.2 Equivalent Elastic Strength Assessment

An improved approach, relying on a mixed strength/displacement assessment compares the equivalent elastic strength with the code elastic strength. The characteristic force displacement response is determined, resulting in an expected strength V_A and displacement capacity $\mu\Delta_y$, as shown in Fig.13.2(a). The equivalent elastic strength V_{el} is determined from a displacement-equivalence rule – normally the equal displacement

approximation, (i.e. $V_{el} = \mu V_A$) and is then compared with the code elastic base shear requirement for the same elastic stiffness.

Note that the assessment could also have been done directly based on displacements, comparing the assessed displacement capacity $\mu \Delta_y$ with the code displacement demand Δ_{code} for the same elastic period. It is thus reasonable to describe this approach as displacement-based, yielding a capacity/demand ratio $\mathbf{C/D} = \Delta_A/\Delta_{code} = \mu \Delta_y/\Delta_{code}$. If information is available on the relationship between seismic intensity ratio, expressed as a displacement demand ratio, and probability of exceedence, p, as suggested in Fig.13.2(c), then an estimate of the risk associated with a value of $\Delta_A/\Delta_{code} < 1$ can be made.

This is a very much improved assessment approach, and is the basis of several recent assessment documents[X10,X11]. It will be noted that though it still retains elements of a force-based approach, many of the deficiencies apparent in force-based design need not apply. In particular, since the structural details should be known at the start of the assessment, estimates of elastic stiffness can be quite accurately made, based on moment-curvature analyses of critical sections, whereas in design the strength, and hence stiffness are not known at the start of the process (see Section 4.4). There are, however, still problems and deficiencies in this approach:

- The necessity to assume a displacement-equivalence rule, such as the equal-displacement approximation, reduces the accuracy of the method.
- Capacity design considerations, though not conceptually difficult to include, are rarely considered adequately in the assessment.

For a multi-degree-of-freedom (**MDOF**) structure, a non-linear static (pushover) analysis will normally be the most appropriate method for determining the displacement capacity. As discussed in Section 4.9.3, an adaptive displacement-based pushover is likely to give the most accurate results for displacement capacity. Although research is continuing towards inclusion of higher-mode response in pushover analyses, we do not consider the results at this time to be sufficiently accurate to consider multi-modal pushover analysis as a reliable or conservative way of including higher-mode effects. Different approaches, such as the simplified representations of capacity design effects included in the structural chapters of this book are likely to be more reliable.

When brittle failure modes, such as brittle shear failure of building or bridge columns, are predicted, assessed displacement capacity is generally based on elastic stiffness. That is, the displacement capacity is assessed to be less than the yield displacement. It is, however, important to recognize that displacements due to inelastic shear response, which are often ignored in analysis, can significantly increase the displacements which can be sustained by the column prior to shear failure[M6]. A method for estimating inelastic shear deformation was presented in Section 4.8.1.

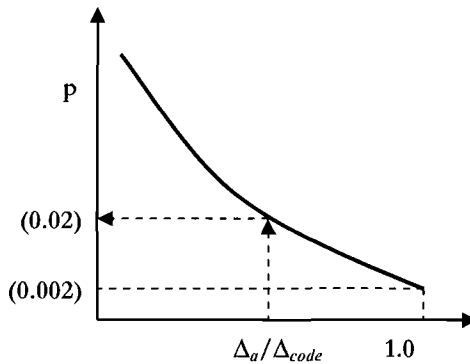### 13.1.3 Incremental Non-linear Time History Analysis

Clearly at this time the most accurate method of determining the seismic response of an existing structure is by carrying out non-linear time-history analyses. In the case of
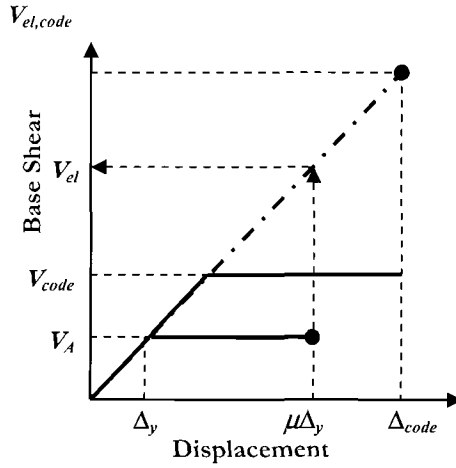
(a) Equivalent Strength Approach
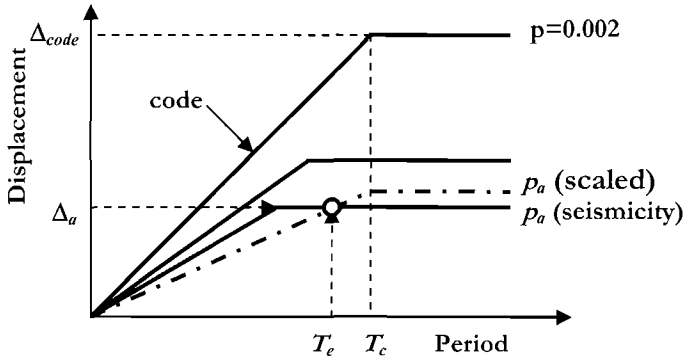
(b) Displacement Spectra

(c) Displacement Ratio vs probability of Exceedence

Fig.13.2   Aspects of Seismic Assessment of Structures

design verification of a newly designed structure the procedure is relative straightforward, and has been outlined in some detail in Section 4.9.2. An appropriate structural model is developed, a suite of spectrum-compatible accelerograms is chosen, the average structural response to the accelerograms is determined, and the critical response parameters compared with capacity. In other words, this is again, typically, a pass/fail check. Higher-mode effects are directly included in the analyses, so capacity design checks are straightforward.

With assessment of a potentially substandard structure, a simple check under the design or assessment intensity may be insufficient, as the increased risk associated with substandard response will generally need to be quantified. This requires that the level of seismic intensity associated with exceeding a specified limit state needs to be determined, so that the risk, or annual probability of exceedence of the established intensity can be found from a relationship such as that shown in Fig.13.2(c). Note, however, that the relationship between displacement ratio and hazard implied in Fig.13.2(c) is simplistic. The relationship available from seismologists will link seismic intensity to hazard, and the relationship between seismic hazard and displacement ratio will generally be nonlinear.

Because of this problem, the accepted current state-of-the-art for assessment consists of multiple structural analyses at different levels of intensity. The selected suite of records are incrementally scaled to successively larger intensities, and the response is observed at each intensity to determine at what level of intensity the limit state is achieved.

Clearly this can be a time-consuming effort, unless automated post-processing searches for exceedence of limit-state displacements or strengths. It also typically makes an assumption that may not be valid, and that is that the assessment spectral shape also applies at lower levels of seismic intensity. Material presented in Chapter 2 indicates that this is unlikely to be the case when seismic hazard for high probabilities of exceedence (i.e. low return periods) is associated primarily with smaller earthquakes than applicable for lower probabilities of exceedence. This would imply that simple amplitude scaling of the accelerograms may not be appropriate.

This is illustrated in Fig.13.2(b) in a displacement-based environment. Three displacement spectra, each corresponding to the equivalent viscous damping ratio applicable to the assessed structure are shown by solid lines. They each refer to different seismic intensities, and because the spectra with higher probabilities of exceedence are dominated by earthquakes of smaller magnitude, the corner periods differ. Also shown is a dashed displacement spectrum scaled from the code level. The assessed displacement capacity is Δ_a, and the effective period is T_e. It will be seen in Fig.13.2(b) that the point Δ_a, T_e is on the plateau of the lowest of the three seismic intensity displacement spectra. If the spectrum corresponding to the full code intensity is scaled so that the assessment data point falls on the scaled spectrum, the initial slope of the displacement/period relationship is lower than for the low intensity spectrum derived from seismicity studies. Thus the scaled spectrum will imply a higher hazard than the seismicity-derived spectrum, since the slope of the spectrum has an approximate inverse relationship with probability of exceedence.

13.2 DISPLACEMENT-BASED ASSESSMENT OF SDOF STRUCTURES

13.2.1 Alternative Assessment Procedures

On initial consideration it might appear that there are two equally valid displacement-based procedures, both fully complying with the principles of **DDBD** that could be used in seismic assessment of existing structures. In both approaches an initial stage is the development of the force-displacement response based on available structural details. This defines the displacement capacity Δ_{Cap}.

The first method is illustrated in Fig.13.3. The assessment force-displacement response is shown as the solid line in Fig.13.3(a) up to the displacement capacity, and is extrapolated as a dashed line to higher displacements. An iterative approach is used to determine the displacement demand Δ_{Dem} corresponding to the code assessment displacement spectrum, illustrated in Fg.13.3(b).

(a) Assessed Force-Displacement Response   (b) Displacement Demand Check
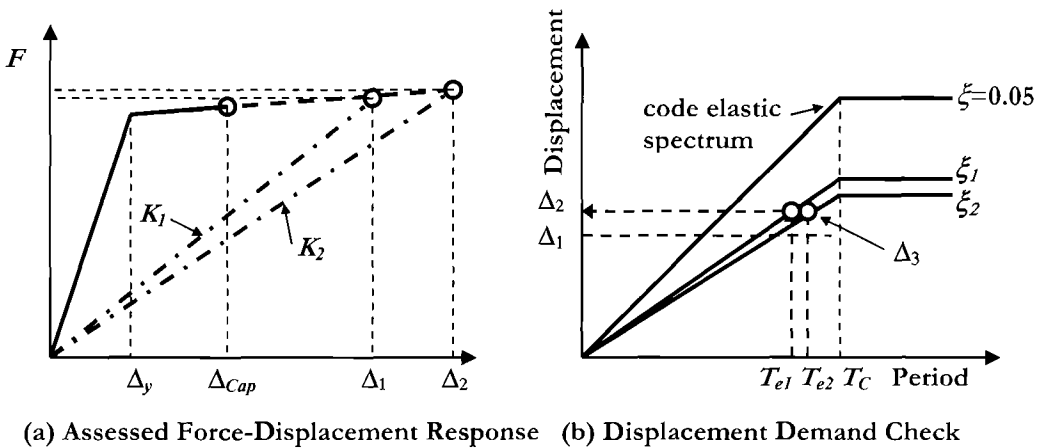
Fig.13.3 Assessment Based on Required Displacement to Satisfy Code Reference Displacement Spectrum.

The steps are as follows:
1. Determine the effective mass m_e. For a **SDOF** structure, this is the total mass
2. Guess the displacement demand for code compliance. The actual value is not critical since it will be revised in the iterations. Referring to Fig.13.3, we make an initial estimate that $\Delta_{Dem} = \Delta_1$.
3. Calculate the effective stiffness $K_e = K_1$ (See Fig.13.3(a)), including **P-Δ** effects.
4. Calculate the effective period from the **SDOF** Eqn: $T_{e1} = 2\pi\sqrt{(m_e/K_e)}$
5. Determine the yield displacement Δ_y. Refer to information provided in Chapter 3, or in the relevant structural type chapter.
6. Determine displacement ductility: $\mu = \Delta_{Dem}/\Delta_y$.

7. Calculate the effective damping ξ_e from Eq. 3.17
8. Calculate the spectral reduction factor R_ξ corresponding to ξ from Eq.(2.8) (e.g.). The reduced displacement spectrum is identified by ξ_1 for the first iteration in Fig.13.3.
9. Check the displacement demand Δ_2 corresponding to the value of T_e calculated in step 4. This is the new estimate for the Δ_{Dem}.
10. Steps 3 to 8 are cycled until displacement stabilizes. In Fig.13.3 the revised displacement Δ_2 found in the first cycle is shown, together with revised stiffnesses and periods and spectrum for the second cycle of iteration. In the figure, the displacement estimate, Δ_3 at the end of the second cycle is sufficiently close to the second estimate, and the final estimate for the displacement demand is determined.
11. Compare Δ_{Cap} and Δ_{Dem}.

This will certainly be adequate for a pass/fail assessment, but cannot strictly be used to determine risk for structures that do not pass the criterion that $\Delta_{Cap} \geq \Delta_{Dem}$. The reason for this is that the damping values corresponding to Δ_{Cap} and Δ_{Dem} differ, since the ductilities for the two displacements are not the same. Hence the damped demand spectrum is only correct if the capacity exactly equals the demand. If this is not the case, it will be difficult to relate the different spectra for capacity and demand to determine risk.

The second approach is more direct, and it would appear more consistent. It is illustrated in Fig.13.4, and determines the equivalent elastic spectral displacement corresponding to the assessed displacement capacity and associated damping. An elastic displacement spectrum is matched to the equivalent spectral displacement, enabling a direct estimate of risk to be made, provided information relating spectral intensity to risk is available (e.g. Fig. 13.2(c)).

(a) Assessed Force-Displacement Response   (b) Displacement Cap/Dem Check
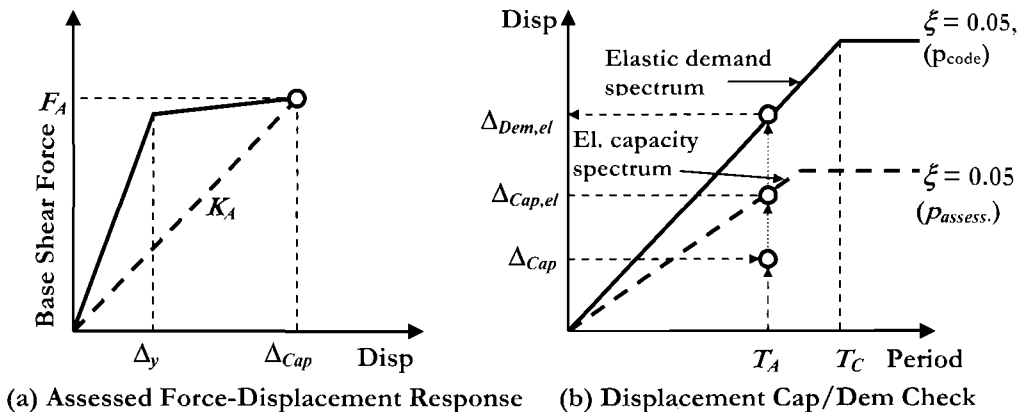
Fig.13.4 Consistent Displacement-Based Assessment Procedure

The steps in the assessment procedure are as follows:

1. Calculate effective mass m_e.
2. From the previously calculated force-displacement response, determine the effective assessment stiffness $K_A = F/\Delta_{Cap}$, including **P-Δ** effects (see Section 13.2.2), corresponding to the displacement capacity (see Fig.13.4(a)). Note that the displacement capacity will depend on what performance level is assessed.
3. Calculate the effective period from the **SDOF** equation: $T_A = 2\pi\sqrt{(m_e/K_A)}$. The point corresponding to the effective period and displacement capacity is identified by the lower open circle in Fig.13.4(b).
4. Determine the displacement ductility capacity: $\mu = \Delta_{Cap}/\Delta_y$.
5. Determine the effective damping ξ_A corresponding to μ from Eq.3.17.
6. Calculate the spectral reduction factor R_ξ corresponding to ξ_A from Eq.(2.8) (e.g.).
7. Calculate the equivalent elastic spectral displacement capacity: $\Delta_{Cap,el} = \Delta_{Cap}/R_\xi$. This is plotted as the central hollow circle in Fig.13.4(b). If a suite of elastic displacement spectra for different annual probabilities of exceedence is available, the appropriate spectrum can be matched to $\Delta_{Cap,el}$ and the risk determined directly (see dashed spectrum in Fig.13.4(b)). If not, the equivalent elastic "code" displacement demand $\Delta_{Dem,el}$ can be read off the code elastic spectrum at the effective period T_A as indicated in Fig.13.4(b). The capacity demand displacement ratio $\Delta_{Cap,el}/\Delta_{Dem,el}$ can then be used to determine the risk from a plot such as that shown in Fig.13.2(c).

Note that at present it is more likely that information will be available relating **PGA** to annual probability of exceedence, p. However, if the assumption is made that spectral shape is independent of intensity (but see discussion in Section 13.1.2), then the displacement ratio calculated above will also be the **PGA** ratio corresponding to capacity and demand, and the **PGA**/p relationship can be directly used.

13.2.2 Incorporation of P-Δ Effects in Displacement-Based Assessment

As indicated in step 2 of the alternative assessment procedures in the previous section, **P-Δ** effects may need to be considered. In accordance with the recommendations of Section 3.6.3, the required base shear capacity for new design is enhanced in accordance with Eq.(3.48) when the stability index, given by Eq.(3.45) exceeds 0.1. In assessment, we **reduce** the calculated base shear capacity by the same amount when the calculated stability index exceeds 0.1. Thus, the calculated reduction in the effective base shear capacity is taken as

$$\Delta V = C \cdot \frac{P\Delta_{cap}}{H} \tag{13.1}$$

and the effective stiffness to be used in the assessment is

$$K_A = \left(F_A - C \cdot \frac{P\Delta_{cap}}{H} \right) / \Delta_{cap} \tag{13.2}$$

where, in accordance with Section 3.6.3, C is taken as 0.5 for concrete structures, and 1.0 for steel structures.

13.2.3 Assessment Example 13.1: Simple Bridge Column under Transverse Response

The simple cantilever bridge pier depicted in Fig. 13.5(a), built in the 1970's, is to be assessed for conformity to current seismic design standards, and the annual risk that response exceeds a strain-based damage control limit state is to be assessed. The single-column pier has a height of $H = 12$m (39.4 ft) and a diameter of 2.0m (78.7 in) and is supported by a spread footing founded on strong rock. For this example we assume that the foundation is rigid, and of adequate strength to develop plastic hinging in the column.
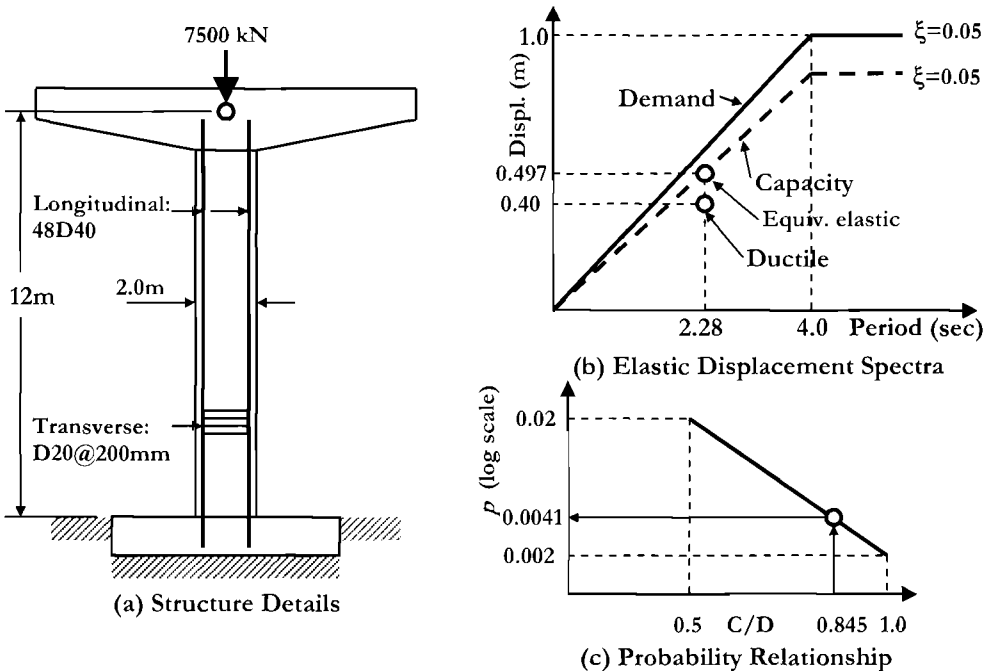
Fig.13.5   Data for Assessment Example 13.1

Design material strengths were f'_c =30MPa (4.35 ksi), and $f_y = f_{yh}$ = 420MPa (60.9 ksi). No current strength evaluation has been carried out, so we assume the conservative strengths recommended in Section 4.2.6 apply; that is, f'_{cA} = 1.3×30=39MPa (56.6 ksi), f_{yA} = 1.1×420 = 462MPa (67.0 ksi), and f_{yhA} = 1.0×420 MPa.

The pier is reinforced with 48 deformed longitudinal bars of 40mm (1.575 in) dia., and transverse hoops of 20mm (0.787 in) dia., closed by lap welding, spaced at 200mm (7.87 in) along the column axis. Cover to the longitudinal reinforcement is 50mm (1.97 in).

Superstructure weight supported by the pier is 7500kN (1670 kips), including the cap-beam weight. Column weight can be based on an assumed unit weight of 23.5kN/m³ (150 lb/cu.ft)

The structure is to be checked for conformity with the code elastic displacement spectrum of Fig.13.5(b), which has a peak response displacement of 1.0m at a period of 4.0 sec. The site is close to an active fault, and forward directivity characteristics have to be expected (see Section 2.2.3). No information is available on the possible changes of spectral shape with return period, but a tentative linear relationship between the logarithm of annual probability of exceedence, p, and **PGA** has been established. This can be interpreted as a linear relationship between $\log(p)$ and the capacity/demand displacement ratio, **C/D**, as discussed in Section 13.2.1, and shown in Fig.13.5(c).

Solution: The moment-curvature and force-displacement response of the column have been calculated using the program ***Cumbia*** available in the **CD** provided with this text. The data file for this example is used as the default input file for ***Cumbia***. Plots of moment-curvature and force-displacement response, including bilinear approximations are provided in Fig.13.6. Key data are summarized below.

Force-Displacement Response:

Axial Force at base hinge P = 7500+11×23.5× $(\pi/4)\times2^2$ = 8310 kN (1870 kips)

Transverse reinforcement ratio: ρ_v =4$(\pi/4)20^2/(1920\times200)$=0.00327

Damage control limit strain (from ***Cumbia***, or Section 4.2.5) = 0.00927

Bilinear Yield curvature: (from Cumbia): ϕ_y = 0.002572/m (64.8×10⁻⁶/in)

(note: from Eq.(4.57a), ϕ_y = 0.00260/m) (66.0×10⁻⁶/in)

Bilinear yield moment: (from Cumbia) M_N = 27570 kNm (244,000 kipin)

Damage control curvature:	ϕ_{dc} = 0.0178/m	(452×10⁻⁶/in)
Damage control moment:	M_{dc} = 28885 kNm	(256,000 kipin)
Bilinear yield displacement:	Δ_y = 0.133 m	(5.24 in)
Bilinear yield force:	F_N = 2314 kN	(520 kips)
Damage control displacement:	Δ_{dc} = 0.402 m (15.8 in) (includes shear def.)	
Damage control force:	F_{dc} = 2408 kN	(541 kips)

The **P-Δ** moment at the base of the column will result from the superstructure load acting through the full assessed displacement capacity of 0.402m, and the column weight acting at approximately half the assessment displacement. Thus

$M_{P-\Delta}$ = 7500×0.402+810×0.201 = 3178kNm

From Eq.(3.45) the stability index is thus

$$\theta_\Delta = \frac{M_{P-\Delta}}{M_{dc}} = \frac{3178}{28885} = 0.11$$

This is marginally above the reference value of 0.1, below which $P-\Delta$ effects can be ignored. For completeness, however, we will include the effect.
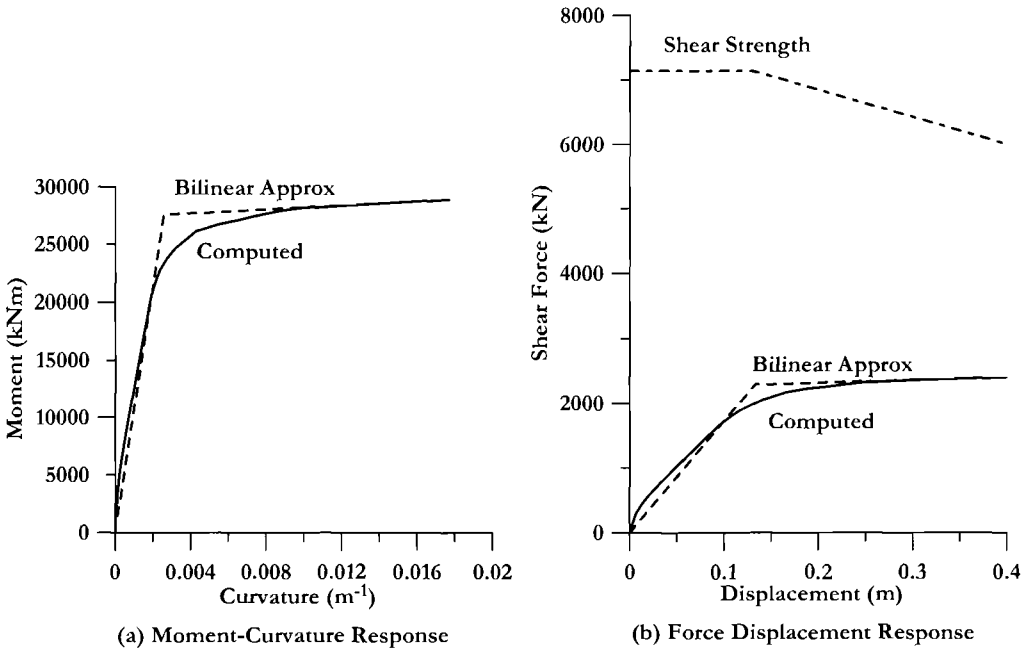

(a) Moment-Curvature Response   (b) Force Displacement Response

Fig.13.6   Assessed Structural Response for Example 13.1, using *Cumbia*.

Note that ***Cumbia*** automatically calculates the shear strength envelope, corresponding to both assessment, and design, in accordance with the recommendations of Section 4.7.3. The assessment envelope for biaxial ductility demand (i.e. ductility is expected in both longitudinal and transverse directions) is included in Fig.13.6(b). It is seen that the shear strength is significantly higher than the flexural strength, and there is thus no danger of shear failure. If the shear and flexural envelopes were close together, it would have been appropriate to carry out a second moment-curvature analysis, using upper-bound values for material properties to investigate the possibility of shear failure occurring at some level of flexural ductility (see Section 4.7.3).

We now proceed through the steps of the direct assessment procedure outlined with reference to Fig.13.4:

Step 1: Effective mass. We allocate 1/3 of the column mass to the seismic weight. Thus
   $m_e = (7500+810/3)/g = 7770/g$ kN (1750/g kips).
Step 2: Effective assessment stiffness: The lateral force corresponding to the damage-control moment capacity is $F = 28885/12 = 2407$ kN (541 kips). Including **P-Δ** effects:
   $K_A = (F-0.5M_{P-\Delta}/H)/\Delta_{dc} = (2407-0.5\times3178/12)/0.402 = 5660$ kN/m
Step 3: Effective Period:
   $T_A = 2\pi\surd(m_e/K_A) = 2\pi\surd(7770/(9.805\times5660)) = 2.35$ sec
Step 4: Displacement ductility capacity:
   $\mu = \Delta_{dc}/\Delta_y = 0.402/0.133 = 3.02$
Step 5: Effective damping: From Eq.(3.17a)
   $\xi_A = 0.05+0.444(\mu - 1)/\mu\pi = 0.05+(0.444)\times2.02/(3.02\pi) = 0.144$
Step 6: Spectral reduction factor. For near-field forward-directivity conditions, we adopt the tentative recommendations of Section 2.2.3, given in Eq.(2.11):
   $R_\xi = (0.07/(0.02+\xi_A))^{0.25} = (0.07/0.164)^{0.25} = 0.808$
Step 7: The equivalent elastic spectral displacement is thus
   $\Delta_{Cap,el} = \Delta_{dc}/R_\xi = 0.402/0.808 = 0.497$ m (19.6 in)

The actual, and equivalent elastic, displacement capacities are plotted in Fig. 13.5(b). We compare the equivalent elastic displacement with the demand elastic displacement for the same period ($T_A = 2.35$ sec):
   $\Delta_{Dem,el} = 1.0\times(2.35/4) = 0.588$.

The displacement Capacity/Demand ratio is thus
   C/D $= 0.497/0.588 = 0.845$.

It is thus apparent that the displacement capacity almost satisfies the demand. With the information presented in Fig.13.5(c) we can determine the annual probability of exceedence. Since the **C/D** ratio is linearly related to $\log(p)$ we can express the relationship as

$$p = 10^{-(0.699+2C/D)}$$

Substituting **C/D** $= 0.845$ we find

$$p = 10^{-(0.699+2\times0.845)} = 0.0041$$

This level of risk, though 100% higher than the code level, might be considered acceptable.

13.3 DISPLACEMENT-BASED ASSESSMENT OF MDOF STRUCTURES

The major difficulty associated with both force-based and displacement-based seismic assessment of existing structures is the determination of which element of the structure will first reach the specified performance limit, and what the corresponding displacement profile throughout the structure will be. In the design of a new structure, characteristic displacement profiles can generally be used, as has been established in the various

chapters of this text related to specific structural forms. Although these characteristic profiles may sometimes be appropriate for assessment, this will not always be the case, as can be seen from examination of Fig.13.7.
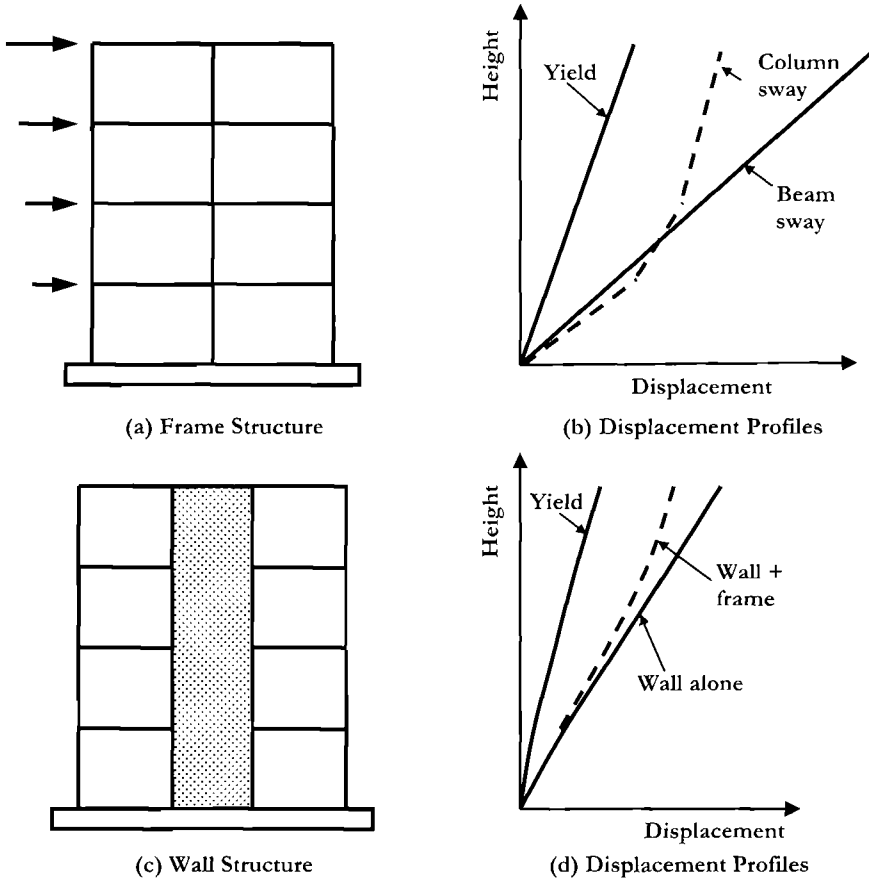

| (a) Frame Structure | (b) Displacement Profiles |

| (c) Wall Structure | (d) Displacement Profiles |

Fig.13.7   Different Displacement profiles for Seismic Assessment of Buildings

If the frame building represented by Fig.13.7(a) has been recently designed and constructed, then capacity-design principles may have been adopted in the design, ensuring that column flexural strength exceeds beam flexural strength, allowing the beam-sway mechanism advocated in Chapter 5 to develop under seismic attack. In this case, the suggested profiles defined by Eq.(5.2) may be adopted, making allowance for drift amplification in accordance with Eq.(5.28), where appropriate. However, it will often be the case with older buildings that the relative strengths of beams and columns are such that column-sway mechanisms could develop, as suggested by the dashed displacement profile of Fig.13.7(b). Definition of the displacement profile for a column-sway profile is more difficult, as it depends on the structural displacement ductility capacity, changing

from an almost linear profile at yield to a nearly bilinear profile with high drift in the storey or storeys subjected to sway. The profile for a column-sway mechanism is best determined by an adaptive displacement-based pushover analysis, though simplified approaches will be discussed shortly.

With structural wall buildings the displacement profile is generally better defined, unless flexural hinging is expected at heights above the base. However, the profile may be influenced by frame action for dual systems, as indicated in Fig.13.7(d), even where the beams and columns of the frames are intended to have a gravity-load support function only. The strength and stiffness of the gravity-load system should always be included in the assessment, even when walls are connected to columns only by apparently flexible slabs.

Some more specific comments are included in the following sections. For a more detailed coverage, reference should be made to specialized documents, such as [X10, X11, P33]. In particular, [X11 and P33] include recommendations for displacement-based assessment of buildings.

13.3.1 Frame Buildings

The recommendations made below are based on, and modified from [P33], and relate to reinforced concrete frame buildings. The general steps for steel frames are similar, with suitable modifications for different material properties.

Step 1: Assess the moment-curvature response of potentially critical members to determine flexural strength and limit-state curvatures. This may be carried out using the program **Cumbia** on the attached CD. Note that this will automatically determine the shear strength of the members for comparison with flexural strength. However, it should be noted that shears resulting from gravity-load effects are not directly considered in the program, and must be added to the seismic shear when shear integrity of beams is assessed. This step will determine whether shear reduces the limit-state curvature. For columns, the shear should be amplified for higher-mode effects in accordance with Eq.(5.65).

An issue in step 1 will be the limit-state curvature when the spacing of transverse reinforcement does not satisfy the maximum spacing limits of Section 4.2.5(c), reproduced below as Eq.(13.1):

$$s_{max} = \left(3 + 6\left(\frac{f_u}{f_y} - 1\right)\right)d_{bl} \le 6d_{bl} \tag{13.3}$$

where f_u and f_y are the ultimate and yield strength of the longitudinal rebar, of diameter d_{bl}. Although wider spacing of the transverse reinforcement will not affect the serviceability curvature, it will reduce the curvature at the more critical damage-control, limit state. Generalizing tentative displacement ductility recommendations from [P33] leads to the following displacement-based damage-control curvatures, which are summarized in Fig.13.8.
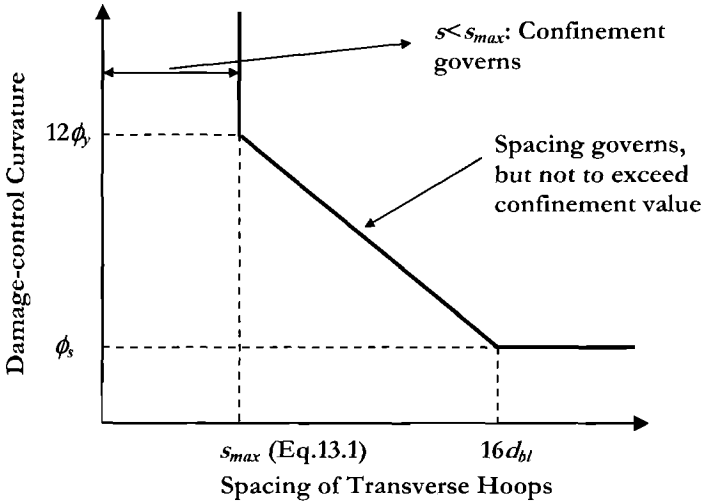
Fig.13.8   Influence of Hoop Spacing on Damage-Control Curvature

- For $s < s_{max}$, the damage-control curvature corresponds to the volumetric ratio of transverse reinforcement, in accordance with Section 4.2.5.
- For $s_{max} \leq s \leq 16d_{bl}$ the damage-control curvature should be taken as the lesser of the value corresponding to the volumetric ratio of transverse reinforcement and

$$\phi_{ls} = \phi_s + \left(\frac{16d_{bl} - s}{16d_{bl} - s_{max}} \right) \cdot \left(12\phi_y - \phi_s \right) \tag{13.4}$$

where ϕ_s is the serviceability limit-state curvature.

Alternative estimates of damage-control curvature based directly on onset of buckling of reinforcement are available (Berry and Eberhardt[B10], Moyer and Kowalsky[M8]), the former of which is included in the analyses carried out in *Cumbia* (attached **CD**) . It is not clear that these methods fully represent the propensity for inelastic buckling, which is related to reinforcement tension strain developed in the opposite direction of displacement response (see [P1]). However, as will be shown in Ex.13.2, the Berry-Eberhardt model produces results rather close to those of Eq.(13.4).

Step 2: Determine the plastic rotation capacity of plastic hinges, based on information provided in Section 4.2.8. The plastic rotation capacity is thus

$$\theta_p = \left(\phi_{ls} - \phi_y \right) L_P \tag{13.5}$$

where L_P is the plastic hinge length given by Eq.(4.28).

Step 3: Determine whether a beam-sway or column-sway inelastic mechanism is to be expected. As discussed above, this is best defined by an adaptive non-linear static (pushover) analysis. However, an approximate indication may be obtained be calculating a *sway potential index* S_i[P33] relating to the relative strengths of beams and columns at the centroids of all beam/column joints at a given floor for a given frame:

$$S_i = \frac{\sum_j \left(M_{bl} + M_{br}\right)}{\sum_j \left(M_{ca} + M_{cb}\right)} \tag{13.6}$$

where M_{bl}, M_{br} are the beam expected flexural strengths at the left and right of the joint, respectively, extrapolated to the joint centroid, including the contribution of slab reinforcement to strength, and M_{ca}, M_{cb} are the expected column flexural strengths above and below the joint, also extrapolated to the joint centroid. The beam and column moments are summed over the j joints in the frame at the floor level considered.

If $S_i < 0.85$, and the storey heights above and below the floor level considered are similar, then a column-sway mechanism is unlikely to form, and it may be assumed that the displacement profile is a beam-sway profile, defined by Eq.(5.2). If $S_i > 1.0$, then it is probable that a column-sway mechanism will develop. For $0.85 < S_i < 1.0$ either a column-sway or a beam-sway mechanism could develop, depending primarily on the actual relative material strengths of the beams and columns, which will generally not be known with any accuracy. In such cases, it would be advisable to carry out pushover analyses using a range of material strengths to determine the most likely mechanism. Alternatively, the conservative assumption must be made that a column-sway mechanism will develop.

It will be noted that the column moment capacities depend on the axial force in the columns, which in turn depends on the lateral forces, which are unknown at the start of the assessment process. This implies that some iteration will be needed to determine the actual moment capacities in Eq.(13.6). However, it is normally only the outer columns that will be significantly affected, and it should also be noted that unless the gravity axial force level is unusually high, the reduction in column moment capacity of the outer column subjected to axial tension will be almost exactly balanced by the increase in moment capacity of the opposite outer column, which is subjected to axial compression. This implies that for most situations, the sway index may be determined using column moments calculated for gravity axial loads without consideration of seismic axial forces.

Step 4: Having determined the sway mechanism, the limit-state deflected shape can be defined. Figure 13.9 shows three possibilities. In Fig.13.9(a), a beam-sway mechanism applies. The yield displacement profile may be assumed to be linear, defined by the yield drift of Eq.(5.7). It is assumed that the plastic rotation capacity of the beams at level 1 are critical for the example of Fig.13.9(a), and hence the plastic displacement at level 1 is $\Delta_{P,c} = \theta_{P1}.H_{01}$, where θ_{P1} is the plastic rotation calculated for level 1, and H_{01} is the storey

height from the ground floor to level **1**. The full displacement profile can now be calculated from the characteristic shape defined by Eq.(5.2).

(a) Beam Sway, $S_i < 0.85$, all levels

(b) Beam Sway Displacement Profiles

(c) Column Sway, $S_i > 1$, Levels 1 or 2
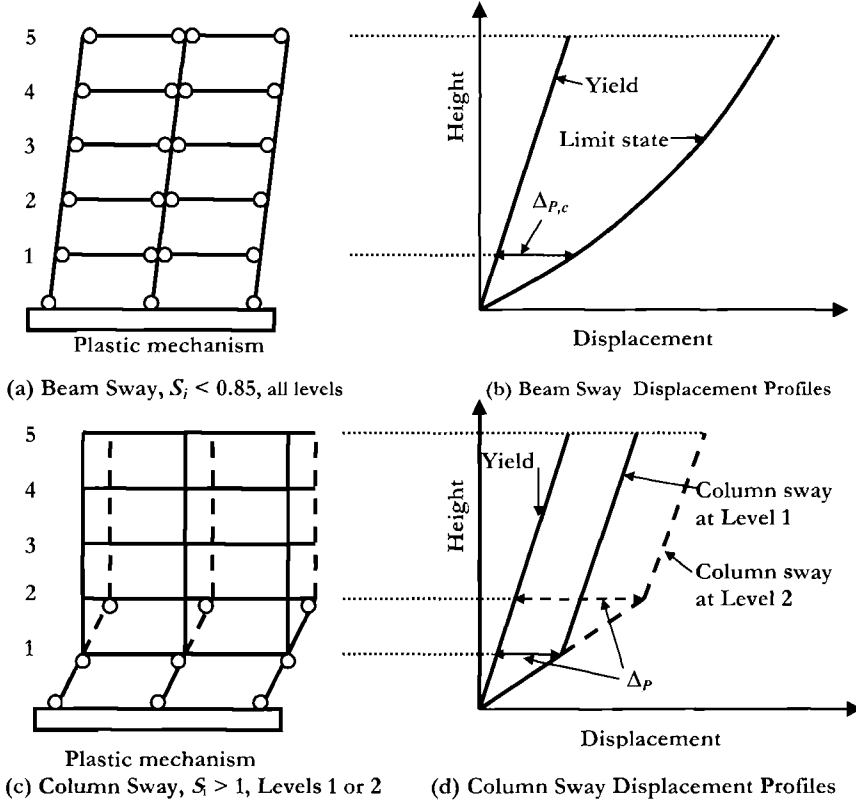
(d) Column Sway Displacement Profiles

Fig.13.9 Determining Limit-State Displacement Profile from Mechanism and Critical Drift

Figure 13.9(d) shows two possible column-sway mechanisms. In one case a column sway mechanism forms involving the column-base hinges and the columns below level **1**. In the other case, the upper hinges form below level **2**. In this case the sway index at level **2** would be higher than the index at level **1**.

Again the yield displacement profile can be approximated from Eq.(5.7). The plastic displacement at level **1** for the first column-sway mechanism will be found from the lower of the plastic rotation capacities of the column-base or level **1** hinges: $\Delta_P = \theta_P H_{01}$. This plastic displacement will be added to the yield displacements at all levels to obtain the limit-state displacement profile. For the second column sway mechanism, with column hinges below level **2**, the plastic displacement at and above level **2** will be $\Delta_P = \theta_P H_{02}$ where θ_P is the lower of the plastic rotation capacities of the column at the base or at level **3**, and H_{02} is the height from the ground floor to level **2**.

Step 5: Determine the base-shear capacity. If a beam-sway mode of inelastic deformation has been predicted, the base overturning moment ***OTM*** can be determined from Fig.5.10 as the sum of the column-base moment capacities and the moment provided by the axial forces resulting from beam seismic shears. For a structure with regular bays, as illustrated in Fig.5.10, this results in the following ***OTM:***

$$OTM = \sum_{j=1}^{m} M_{Cj} + \sum_{i=1}^{n} V_{Bi} L \tag{13.7}$$

where M_{Cj} are the column base moments (m columns), V_{Bi} are the beam seismic shears at the n levels of beams and L is the distance between the outer columns of the frame. The beam seismic shears are given by

$$V_{Bi} = \left(M_{Bi,l} + M_{Bi,r} \right) / L_{Bi} \tag{13.8}$$

where $M_{Bi,l}$ and $M_{Bi,r}$ are the beam moment capacities extrapolated to the left and right column centrelines respectively, and L_{Bi} is the bay length between column centrelines.

The effective height H_e is then found from the displaced shape and mass distribution, using Eq.(5.5), and the base shear determined from:

$$V_{Base} = OTM / H_e \tag{13.9}$$

If a column-sway inelastic mechanism is predicted, then the base shear can be determined directly from the column shears in the storey within which sway occurs. With the common case of a column sway mechanism based on flexural capacity in the bottom storey, the base shear is given by

$$V_{Base} = \sum_{j=1}^{m} \left(M_{Cj,b} + M_{Cj,t} \right) / H_{01} \tag{13.10}$$

where $M_{Cj,b}$ and $M_{Cj,t}$ are the column moment capacities at the column base, and at the level 1 beam centreline, extrapolated from the column top capacity. Note that beam and column moment capacities at the joint centroids have been used in Eqs.(13.8) and (13.10) rather than column-face or beam-face moments since these will already have been determined in assessing the sway potential index (Eq.(13.6)).

Step 6: With the limit-state displacement profile defined, the equivalent **SDOF** displacement (Eq.(5.3)), mass (Eq.(5.4)), effective height (Eq.(5.5)) if not already calculated in Step 5, displacement ductility (Eq.(5.6)), and equivalent viscous damping (Eq.(5.9)) can be calculated. From here the assessment procedure follows the approach

defined above for **SDOF** systems by the steps following Fig.13.4, and illustrated by Example 13.1.

It will be noted that there has been no discussion of the influence of the beam/column joint shear strength on the inelastic mechanism type or base shear capacity. Joint shear strength depends on axial force on the joint, amount, if any, of horizontal joint reinforcement, excess tension capacity of column longitudinal reinforcement capacity enabling it to act as vertical joint reinforcement, detailing and anchorage of the beam flexural reinforcement, and ductility demand on adjacent members, amongst other aspects. Clearly this is a very complex issue, which is at present still imperfectly understood. Since an adequate treatment here would require considerable length, and since the purpose of this chapter is to provide the framework for displacement-based assessment, rather than a complete treatment of the subject (which would require another book), joint shear will not be considered further herein. Reference should be made to recent assessment documents (e.g.[X10,X11,P33]) for guidance. However, it should be noted that joint shear failure essentially places a hinge at the beam/column centroid, for additional inelastic deformation. As such it can contribute to column-sway potential, and hence must be treated in a conservative manner in assessment.

It is emphasised that the above approach is only approximate, and a better definition of vulnerability can be expected when the displacement response is based on an adaptive pushover analysis. However, even the most sophisticated pushover methodologies are unlikely to have the capability of determining the onset of beam/column joint shear strength damage and deterioration, and the consequent influence on global response.

13.3.2   Assessment Example 2: Assessment of a Reinforced Concrete Frame

The six-storey reinforced concrete frame of Fig.13.10(a) is to be assessed for compliance with the same seismicity used in Example 13.1, except that the near-fault condition does not apply. The displacement spectrum is again shown in Fig.13.10(b). The ground floor has a storey height of 4.5m (14.8ft) to the top of the Level 1 beams, with upper storey heights all 3.5m (11.5ft). Storey masses, including seismic live load are estimated as 60 tonnes/level, including the roof. The building was designed in the 1970's, and detailing is reasonable, though spacing of transverse reinforcement exceeds current guidelines. Columns are 400×400mm (15.7×15.7 in) in section, have 8D20 (0.79in) longitudinal reinforcement for the full height, with 40mm (1.6in) cover. Transverse reinforcement is D12 (0.47in) (3-legs: see column section, Fig.13.10(a)) at 200mm (7.87in) centres throughout. Beams have a 500x300mm (19.7×11.8in) section with an integral 200mm (7.87in) slab, and have equal top and bottom reinforcement of 4D24 (0.95in dia). It is estimated that a total of 800mm^2 (1.24in^2) of slab reinforcement will contribute to the beam negative moment capacity at the outer columns, and 1600mm^2 (2.48in^2) will contribute at the inner column/

Design material strengths were f'_c = 25MPa (3.63ksi) and f_y = 400MPa (58ksi). No insitu testing has been carried out, and a quick initial estimate of seismic risk is required.
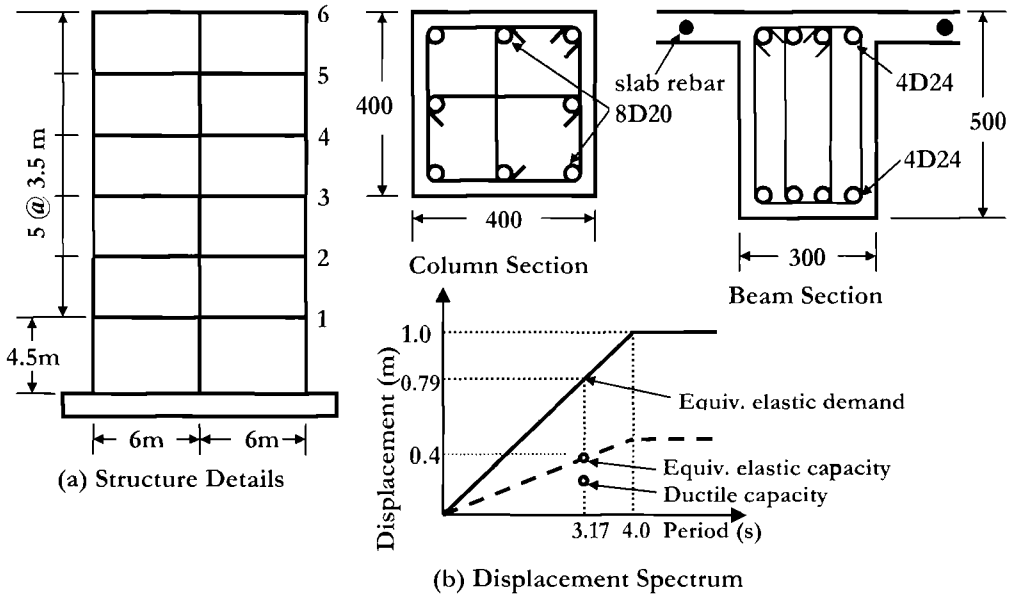
Fig.13.10   Assessment Example 2

Solution: The simple hand analysis described in the previous section is chosen, in the interests of simplicity and speed. We follow the steps essentially in order:

Step 1: Initial rough checks on relative column and beam flexural strengths indicate a strong probability of a soft-storey column-sway mechanism developing in the first storey columns. The program *Cumbia* (provided on the **CD**) is used to determine the column moment-curvature and shear response, based on expected material strengths of $1.3f'_c = 32.5$MPa (4.7ksi) and $1.1f_y = 440$MPa (63.8ksi). Axial loads due to gravity on the columns are listed in Tables 13.1 and 13.2, (Columns (2)) for outer and inner columns respectively, and the calculated moment-curvature response for a selection of storeys is shown in Fig.13.11. Note that a significant reduction in moment-capacity follows spalling. Consequently the conservative bilinear estimates of moment-curvature characteristics shown in Fig.13.11 by the dashed lines are adopted.

A summary of the results from *Cumbia* is included in Tables 13.1 and 13.2, including moment capacity at the beam face, M_{CN}, and extrapolated to the beam centrelines assuming development of column moment-capacity of opposite sign at top and bottom of the clear column height, M_{CCL} (Col(4)) (see the examples of Fig.13.12). The yield and serviceability curvatures computed by *Cumbia* are listed in Cols (5) and (6) respectively.

The spacing of transverse reinforcement is 200mm. From Eq.(13.3), with $f_u = 1.5f_y$:

$$s_{max} = \left(3 + 6\left(\frac{f_u}{f_y} - 1\right)\right)d_{bl} = (3 + 6(1.5 - 1))20 = 120 \text{ mm } (4.7\text{in})$$

The actual spacing of 200mm implies reduced confinement and anti-buckling efficiency. The damage-control limit-state curvature is thus the lesser of the calculated value, based on the volumetric ratio of confinement (see Section 4.2.8) and the value given by Eq.(13.4), which simplifies to:

$$\phi_{ls} = \phi_s + \left(\frac{16 \times 20 - 200}{16 \times 20 - 120}\right) \cdot \left(12\phi_y - \phi_s\right) = \phi_s + 0.6\left(12\phi_y - \phi_s\right)$$

Tables 13.1 and 13.2 include the damage-control curvature based on volumetric confinement ratio (Cols(7)), and Eq.(13.4) (Cols(8)). It is seen that the latter governs in all cases. The tables also include the buckling curvature ϕ_b predicted by *Cumbia* using the Berry-Eberhardt[B10] buckling model, in Cols(9). Comparison of Cols(8) and (9) indicates quite close agreement. It is decided to adopt the more conservative of the two curvatures (shown in bold in Tables 13.1 and 13.2) for assessment purposes.
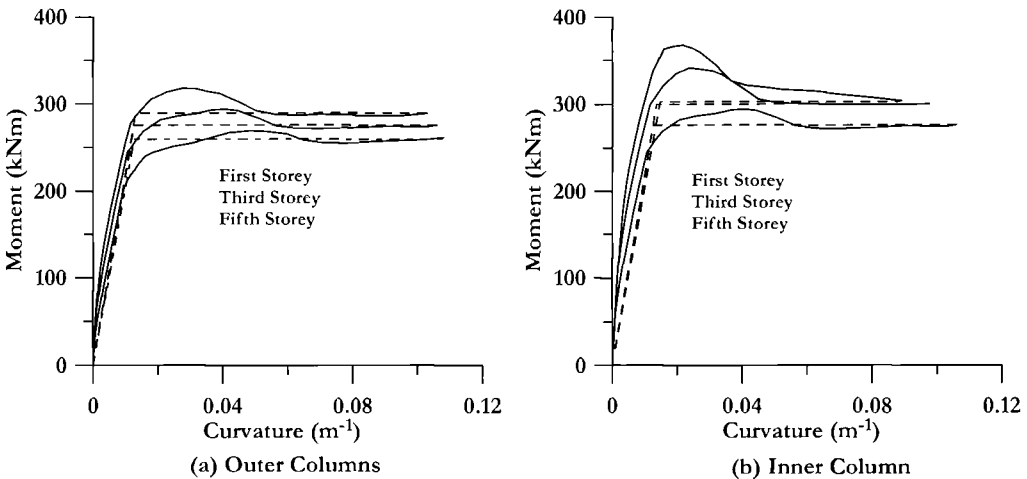
Fig.13.11   Moment-Curvature Response of Selected Columns of Example 13.2, Including Conservative Bilinear Approximations

Cumbia is also used to determine the beam flexural strengths. These are calculated at an extreme fibre compression strain of 0.004, and are listed in Table 13.3.

Table 13.1 Outer Column Moment-Curvature Data for Example 13.2

Storey (1)	P (kN) (2)	M_{CN} (kNm) (3)	M_{CCL} (kNm) (4)	ϕ_y (m^{-1}) (5)	ϕ_s (m^{-1}) (6)	ϕ_{vol} (m^{-1}) (7)	$\phi_{(Eq.13.2)}$ (m^{-1}) (8)	ϕ_b (m^{-1}) (9)
6th	147	251	293	0.0125	0.0465	0.188	**0.1086**	0.124
5th	294	267	312	0.0127	0.0420	0.171	**0.1082**	0.119
4th	441	271	316	0.0127	0.0392	0.159	**0.1071**	0.115
3rd	588	279	326	0.0127	0.0368	0.154	**0.1062**	0.111
2nd	735	284	331	0.0129	0.0342	0.149	**0.1066**	0.107
1st	882	290	326	0.0131	0.0317	0.144	0.107	**0.103**

Table 13.2 Inner Column Moment-Curvature Data for Example 13.2

Storey (1)	P (kN) (2)	M_{CN} (kNm) (3)	M_{CCL} (kNm) (4)	ϕ_y (m^{-1}) (5)	ϕ_s (m^{-1}) (6)	ϕ_{vol} (m^{-1}) (7)	$\phi_{(Eq.13.2)}$ (m^{-1}) (8)	ϕ_b (m^{-1}) (9)
6th	294	267	312	0.0127	0.0420	0.171	**0.1082**	0.119
5th	588	279	326	0.0127	0.0368	0.154	**0.1062**	0.111
4th	882	290	338	0.0131	0.0317	0.144	0.1070	**0.103**
3rd	1176	293	342	0.0137	0.0274	0.135	0.1096	**0.0976**
2nd	1470	293	342	0.0143	0.0241	0.120	0.1126	**0.0927**
1st	1764	293	330	0.0148	0.0218	0.105	0.1153	**0.0886**

Table 13.3 Beam Moment Capacities (kNm) for Example 13.2 (1 kNm=8.85kip.in)

Beam	Column Face	Column C.Line
Outer Col, +ve Mom	469	509
Inner Col, -ve Mom	-648	-688
Inner Col, +ve Mom	469	505
Outer Col, -ve Mom	-530	-566

The difference in negative moment capacity adjacent to inner and outer columns is a result of the large slab contribution to beam moment capacity at the inner column. Table 13.3 also includes the beam moment capacities extrapolated to the column centrelines, assuming development of moment capacities of opposite sign at opposite ends on the beam (see Fig.13.12).

Step 3: We defer calculating the plastic rotation capacities of potential plastic hinges, as required in Step 2, until it is determined whether a beam-sway or column-sway mechanism forms. Considering the beam-column joints of Level 1, the Sway Potential Index, computed in accordance with Eq.(13.6) is

(a) Outer Column
1st and 2nd Storeys

(b) Typical Beam
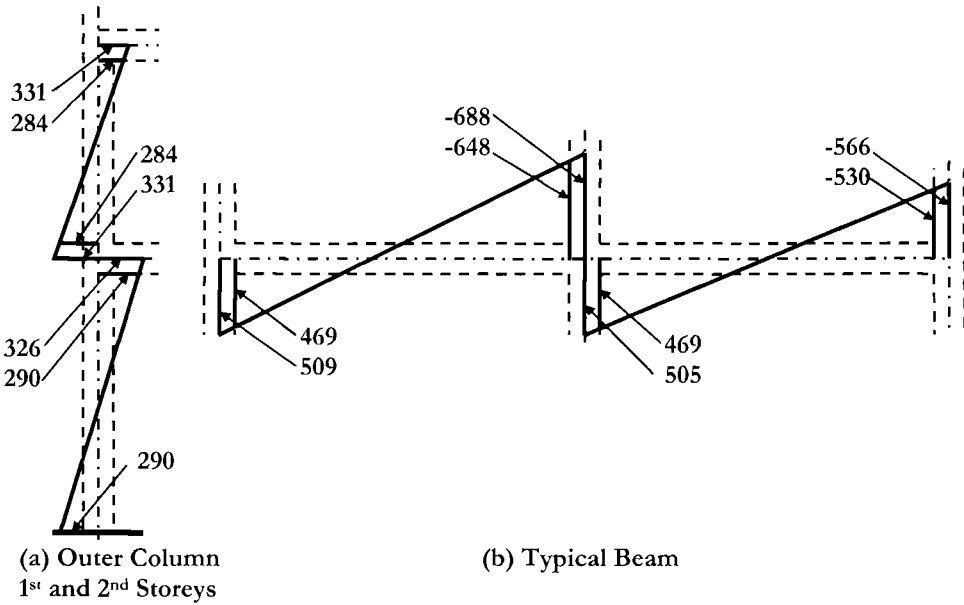
**Fig.13.12   Extrapolating Beam and Column Moments to joint Centrelines,
Example 13.2 (Moments in kNm; (1kNm =8.85 kip.in))**

$$S_i = \frac{\sum_j \left(M_{bl} + M_{br}\right)}{\sum_j \left(M_{ca} + M_{cb}\right)} = \frac{509 + 688 + 505 + 566}{(326 + 331) \times 2 + 330 + 342} = 1.14$$

Since $S_i > 1$, and plastic hinges must form at the column bases, a column-sway mechanism is predicted. Note that because the storey height of the first storey, at 4.5m is significantly greater than the upper storey heights, it is unlikely that a sway mechanism will develop involving an upper storey. The reduced height means that column moments will be lower in the upper storeys, even if the column shear force is equal to that in the first storey. As a consequence it is not necessary to quantify the Sway Potential Index at higher floors.

Step 2: Plastic rotation capacity of column plastic hinges: The analyses by *Cumbia* indicate that there is a large margin of column shear strength above the shear force corresponding to development of moment capacity at top and bottom of the first storey columns. Plastic displacement capacity is thus governed by flexure, and the limit-state curvatures in Tables 13.1 and 13.2 apply. In accordance with Eq.(4.30) the strain penetration length is

$L_{SP} = 0.022 f_{ye} d_{bl} = 0.022 \times 440 \times 20 = 194$ mm (7.6 in).

The plastic hinge length is given by Eq.(4.31), with $k = 0.08$ as

$L_P = 0.08L_C + L_{SP} \geq 2L_{SP} = 0.08\times (4/2)+194 \geq 2\times194 = 388$ mm (15.3 in)

The inner column has the lower limit-state curvature, and hence it governs the design. From Eq.(13.3) and Table 13.2 the plastic rotation capacity is

$$\theta_p = \left(\phi_{ls} - \phi_y\right)L_p = (0.0886 - 0.0148)\times0.388 = 0.0286$$

Step 4: The deflected shape corresponding to the assessment limit state can now be determined. Table 13.4 summarizes the calculations, where the yield drift is found from Eq.(5.7a) as

$$\theta_y = 0.5\varepsilon_y \frac{L_b}{h_b} = 0.5\times0.0022\times\frac{6.0}{0.5} = 0.0132$$

We assume a linear displacement profile at yield, and the floor yield displacements are thus found as $0.0132H_i$. These are listed in Table 13.4.

The plastic displacement corresponds to the first profile shown in Fig.13.9(d), with all plastic displacement, of $\Delta_P = \theta_P H_C = 0.0286\times4.0 = 0.1145$m (4.5in) concentrating in the first storey. The final displacement profile, being the sum of the yield and plastic displacements, is listed as Δ_{Ai} in Table 13.4.

Table 13.4 Data for SDOF Model for Example 13.2 (1m =39.4 in)

Floor (i)	Height H_i (m)	Δ_{yi} (m)	Δ_{Pi} (m)	Δ_{Ai} (m)	Δ_{Ai}^2 (m²)	$\Delta_A H_i$
6	21.0	0.2772	0.1145	0.3917	0.1534	8.2257
5	17.5	0.2310	0.1145	0.3455	0.1194	6.0463
4	14.0	0.1848	0.1145	0.2993	0.0896	4.1902
3	11.5	0.1518	0.1145	0.2663	0.0709	3.0625
2	8.0	0.1056	0.1145	0.2201	0.0484	1.7608
1	4.5	0.0594	0.1145	0.1739	0.0303	0.7827
0	0.0	0	0	0	0	0
Sum				1.6968	0.5120	24.0681

Step 5: Base Shear Capacity. Since a first storey column-sway mechanism develops, the base shear is given by Eq.(13.8). Using the flexural strength data from Tables 13.1 and 13.2, the base shear capacity is

$$V_{Base} = \sum_{j=1}^{m}\left(M_{Cj,b} + M_{Cj,t}\right)/ H_{01} = (2\times290 + 2\times326 + 293 + 330)/4.25 = 436.5kN \text{ (98kips)}$$

We defer **P-Δ** consideration until the effective height has been calculated.

Step 6: SDOF parameters. From the data in Table 13.4, noting all masses are equal:

Displacement: from Eq.(5.3): $\Delta_A = \Sigma\Delta_{Ai}^2/\Sigma\Delta_{Ai} = 0.512/1.697 = 0.302$m (11.9in)

Effective Mass (Eq.(5.4)): $m_e = \Sigma m_i\Delta_i/\Delta_A = 60\times1.697/0.302 = 337.2$ tonnes

Effective Height (Eq.(5.5)): $H_e = \Sigma\Delta_i H_i/\Sigma\Delta_i = 24.07/1.697 = 14.2$m (46.6ft)

Yield Displacement: $\Delta_y = \theta_y H_e = 0.0132 \times 14.2 = 0.1874$m (7.4in)

Structure Ductility (Eq.(5.6)): $\mu = \Delta_A / \Delta_y = 0.302/0.1874 = 1.61$

Equivalent Viscous damping: Since all the ductility occurs in column hinges, we adopt Eq.(4.17a) rather than Eq.(5.9a): $\xi = 0.05 + 0.444(\mu-1)/\pi\mu = 0.104$

Displacement Reduction Factor for Damping (Eq.(2.8): $R_\xi = 0.752$

Equivalent Elastic Displacement: $\Delta_{Cap,el} = \Delta_A / R_\xi = 0.302/0.752 = 0.402$m

Stability Index: (Eq.3.45) $OTM = V_{Base}H_e = 436.5 \times 14.2 = 6198$ kNm

P-Δ moment: $M_{P-\Delta} = 60 \times 6 \times 9.8 \times 0.302 = 1065$ kNm

$\theta_\Delta = 1065/6198 = 0.172$ (*P-Δ* must be considered)

Effective Stiffness: $K_e = (V_{Base} - 0.5 M_{P-\Delta}/H_e)/\Delta_A = (436.5 - 0.5 \times 1065/14.2)/0.302 = $
$= 1321$kN/m

Effective Period: $T_e = 2\pi\sqrt{(m_e/K_e)} = 2\pi\sqrt{(337.2/1321)} = 3.17$ sec.

From the displacement spectrum of Fig.13.10(b) the elastic displacement demand for a period of 3.17sec is

$\Delta_{Dem,el} = 1.0 \times (3.17/4) = 0.793$m (31.2 in)

and the displacement Capacity/Demand ratio is thus

C/D $= 0.402/0.793 = 0.507$

Using the relationship between **C/D** ratio, and probability of exceedence, *p* derived in Ex.13.1, we find

$$p = 10^{-(0.699+2\times0.507)} = 0.019$$

It will have been noted that the drift in the first storey of the structure is high: $0.0132 + 0.0286 = 0.0418$. This exceeds typical code drift limits by a factor of about 2. If the assessment was limited to the code drift limit, the probability of exceedence would be much higher. It is clear that this structure has an unacceptably high risk of structural and non structural damage, and remedial action would be needed, despite the reasonable detailing of the transverse reinforcement.

13.3.3 Structural Wall Buildings

Results of nonlinear time-history analyses of cantilever structural walls presented in Section 6.6 indicate that dynamic amplification of bending moments above the base, and of shear force over the full wall height can be very substantial. Although designing for these amplified forces is highly desirable for new structures, some relaxation is essential when assessing existing structures. This is particular important when considering the distribution of bending moment up the wall height, since existing buildings are unlikely to have been designed for full capacity design effects.

Limited non-linear time-history analyses have indicated that development of plastic hinging at levels above the base may not result in excessive curvature ductility demands when occurring solely as a result of higher-mode effects. This is because the displacement demand associated with higher-mode response is generally small. Consequently, when assessing the flexural ductility capacity, it seems reasonable to base this on expected first

mode behaviour. The sequence of assessment operations thus proceeds along the following steps, which are presented with reference to Fig.13.13.

(a) Structure   (b) Moment Profiles   (c) Displacement Profiles
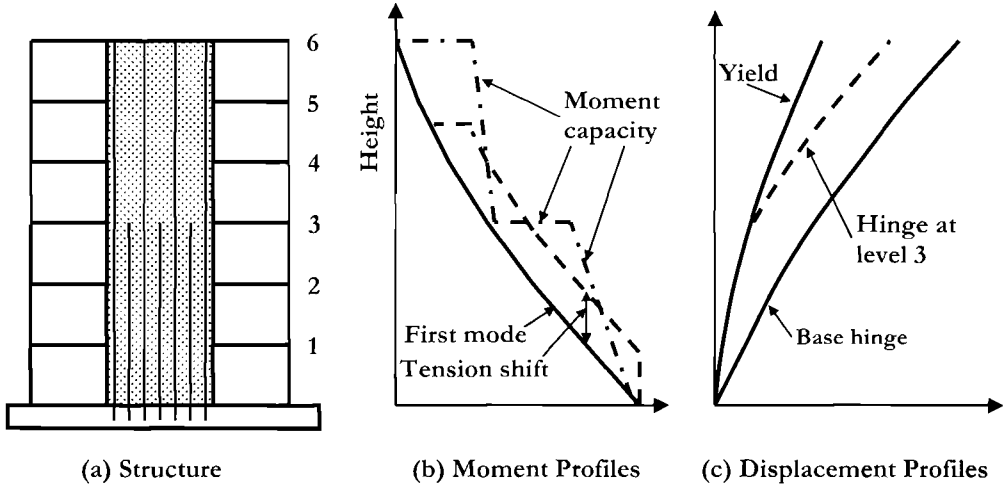
Fig.13.13   Displacement Response of a Wall Structure

Step 1: Determine the axial loads at different levels of the wall or walls, and carry out moment-curvature analyses at each level to determine moment capacities and curvature limits. In the example of Fig.13.13(a) it is seen that the wall flexural reinforcement is reduced at level 3 to approximately half the value applying at the base. Between the base and level 3 the moment capacity, shown by the dash/dot line in Fig.13.13(b) gradually reduces as a consequence of the reducing axial load on the wall. There is a step change at level 3 as a consequence of the termination of reinforcing steel, and above this level the capacity again reduces gradually due to the axial load reduction.

Step 2: Assuming a typical first-mode distribution of lateral force (an inverted triangular vector is satisfactory), determine the lateral forces corresponding to the wall-base flexural strength, and hence determine the distribution of first-mode bending moments up the wall height. This distribution of bending moment is shown by the solid line in Fig.13.13.

Step 3: Determine the extent of the wall over which the shear stress is such that diagonal cracking is to be expected. This can conservatively be assessed as the region over which the shear force exceeds V_C, the capacity of the concrete shear-resisting mechanisms, defined by Eq.(4.72) (see also Section 4.7.5). Over this region, tension shift effects resulting from diagonal cracking will increase the apparent moment above the distribution corresponding to the lateral force vector. This influence can be reasonably represented by shifting the moment profile over the affected region up by a distance equal to half the wall length. In Fig.13.13(b), inclined shear cracking is expected from the

wall base to midway between levels 4 and 5. The shifted assessment moment profile is shown in Fig.13.13(b) by the dashed line.

Step 4: Compare the capacity and demand moment envelopes, which, of course are equal at the wall base. If the capacity exceeds demands at all elevations above the base (ignoring the small discrepancy immediately above the base due to the tension shift), then the inelastic first mode response may be based on a base hinge. The corresponding displacement profile is shown in Fig.13.13(c) by the solid line. However, if the capacity is less than the demand envelope including tension shift, as is the case at level 3 in Fig.13.13(b), then plastic hinging is expected at this location, rather than at the column base. The corresponding displacement profile is shown by the dashed line in Fig.13.13(c).

Step 5: Calculate the plastic hinge length (Eq.(6.7)). The plastic rotation capacity is given by Eq.(6.9b), where the plastic curvature ϕ_P is found from the moment-curvature analyses of Step 1.

Step 6: The assessment displacement profile is found by addition of the plastic displacement profile to the yield displacement profile. For regular structures, the latter can be found from Eq.(6.5). The plastic displacement profile will depend on whether a plastic hinge is predicted at the base or at some level higher than the base. Taking the general case of a plastic hinge forming at height H_P above the base ($H_P = 0$ for a wall-base hinge), the assessment displacement profile, Δ_{Ai} can be defined by:

$$H_i < H_P: \qquad \Delta_{Ai} = \Delta_{yi} = \frac{\varepsilon_y}{l_w} H_i^2 \left(1 - \frac{H_i}{3H_n}\right) \tag{13.11a}$$

$$H_i \geq H_P: \qquad \Delta_{Ai} = \frac{\varepsilon_y}{l_w} H_i^2 \left(1 - \frac{H_i}{3H_n}\right) + \theta_P(H_i - H_P) \tag{13.11b}$$

where the symbols are as defined in Chapter 6.

Step 7: Determine the equivalent **SDOF** displacement (Eq.(3.26)), the effective height (Eq.(3.35)), the yield displacement at the effective height (Eq.(6.5)) with $H_i = H_e$), and the displacement ductility capacity (Eq.(3.36)).

Step 8: Check to see if the displacement capacity is reduced by potential for shear failure. Note that the shear demand increases as the displacement ductility increases as a consequence of higher-mode effects (see Section 6.6.2), while the shear capacity in the plastic hinge region reduces as a consequence of reduced contribution of the concrete shear-resisting mechanisms (see Section 4.7). The shear demand can conservatively be expressed by Eq.(6.49), while the assessment shear strength defined in Section 4.7 should be used. It may be necessary to check the shear capacity at a number of heights, particularly if reinforcement details vary up the wall height. This is illustrated for a single location up the wall height in Fig.13.14.
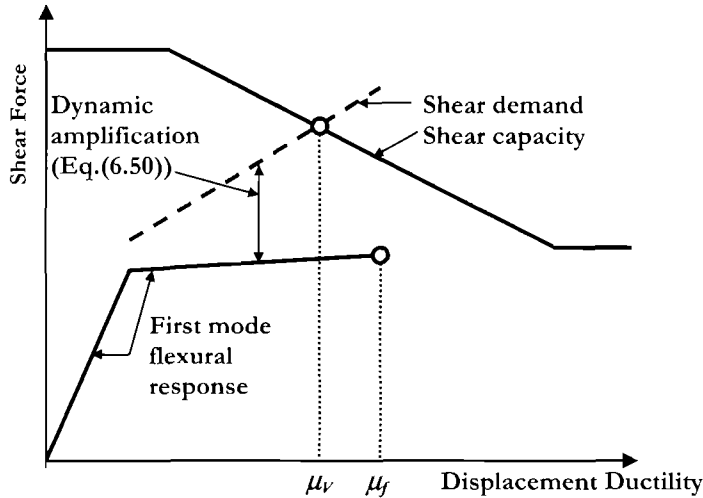
Fig.13.14   Determining Ductility Capacity of a Wall, including Dynamic Amplification

In Fig.13.14 the calculated first-mode force-displacement response is shown in terms of base shear vs. ductility. The maximum flexural displacement ductility capacity is μ_f. In this case $\mu_f \approx 3$. The shear strength at the base hinge is computed in accordance with Section 4.7.5, and the envelope is shown as a function of displacement ductility in Fig.13.14 by the upper solid line. Since the first-mode response and the shear capacity do not intersect, it might be concluded that shear does not influence the displacement capacity. However, when the shear force from the first mode is amplified for higher-mode effects in accordance with Eq.(6.50) (see the dashed line in Fig.13.14) it is seen that the shear demand intersects the capacity envelope at a displacement ductility of $\mu_V < \mu_f$. This reduced ductility capacity should be used in the assessment procedure.

It was pointed out in Section 4.7.5 that it may be conservative to reduce the shear capacity with ductility and compare with the amplified shear demand since it is unlikely that the peak shear demand will correspond to peak displacement ductility demand. It is tentatively suggested that the shear capacity be based on a reduced ductility demand, corresponding to 60% of the computed displacement ductility, while the full ductility demand be used to compute the dynamic amplification.

Note that at heights above the base, the shear capacity will not be reduced for ductility demand, unless plastic hinging occurs above the base.

Step 9: With the displacement capacity defined from Steps 7 and 8, the equivalent viscous damping can be computed (from Eq.(3.17)), and the effective mass from Eq.(3.33). The rest of the assessment procedure follows the **SDOF** approach outlined in the steps following Fig.13.4.

13.3.4 Other Structures

The modification of the assessment procedures outlined in the previous two sections to dual wall/frame buildings, bridges, and other structures is straightforward, and need not be developed further in this text. Regular buildings will be assessed independently in the orthogonal principle directions. Where torsional eccentricity is present, the displacement capacity at the centre of mass should include considerations of twist as covered in Sections 3.8 and 6.4.

14

DRAFT DISPLACEMENT-BASED CODE FOR SEISMIC DESIGN OF BUILDINGS

The draft code for building structures provided in the following pages is designed to provide guidance as to how direct displacement-based design methodology can be codified. It is not intended to be a complete document covering all aspects of building seismic design, but a framework, establishing how the key elements of **DDBD** can be codified. More detail, and a number of topics treated in the book but left out of the draft code because of space limitations, would need to be incorporated. Some of these topics are identified in the code.

This chapter is presented in a traditional "Code + Commentary" format, on a split two-column page. The commentary is by and large terse, generally providing only reference to the appropriate equation or section of the book in which the code material and further discussion is to be found. However, in a number of cases, where the treatment requires interpretation above that already provided in the book, the commentary is more detailed. In the interests of brevity, the symbols used in the code have not been defined. These, however, are the same as those used in the book, and are defined in the Symbols list.

As noted, the draft code refers to building structures. It should be clear, following the logic of this draft code, how a similar document could be written for other structures, such as bridges, or wharves, using the detailed information in the relevant chapter to augment the basic approach outlined in Chapter 3.

CODE

1. DESIGN SEISMICITY

1.1 Building structures shall be designed such that performance criteria defined in Clause 2 are met for levels of seismic intensity specified for the seismic zone designated for the building.

1.2 For buildings in Zone A (moderate to high seismicity) performance criteria for Level 1 and 2 intensity shall be met.

1.3 For buildings in Zone B (low seismicity) performance criteria for Level 3 intensity shall be met.

1.3 The defined probability of exceedence for a given intensity level depends on the building occupancy usage and damage consequences, as defined in Table 1.

Table 1: Probability of Exceedence for Different Structural Categories

Intensity	Normal structures	Hospitals, Police HQ's, CD HQ's etc	Structures containing hazardous materials
Level 1	50% in 50 years	20% in 50 years	20% in 50 years
Level 2	10% in 50 years	4% in 50 years	2% in 50 years
Level 3	2% in 50 years	1% in 50 years	1% in 50 years

1.4 Design intensity for a specified level shall be expressed in terms of an elastic displacement spectrum corresponding to an elastic damping ratio of $\xi - 0.05$, characterized by a corner period T_C and displacement $\Delta_{C,0.05}$ as shown in Fig.1.1. Values of T_C and $\Delta_{C,0.05}$ shall be based on local seismicity and the specified probability of exceedence.

COMMENTARY

C1 Two zones are specified. Zone A is representative of reasonably high seismicity, where serviceability (Level 1 EQ) and damage control (Level 2 EQ) considerations govern the design.

In Zone B earthquakes are rare. However, at very long return periods, significant seismic intensity may occur. For these structures it is inappropriate to design for serviceability or damage criteria, and the single requirement is that the building must not collapse, and there should be no loss of life under the Level 3 earthquake.

Table 1 lists tentative suggestions for seismic risk for the three categories of earthquake, and different occupancy levels. It is anticipated that these would be revised in an actual code.

Note that the approach taken is to define the acceptable risk for different categories of structure as a variable within an intensity level, but to have uniform performance criteria for all structures under a specified intensity level. This appears to us to have a more sound probabilistic background than variable performance criteria for a given probability of exceedence.

C1.4 It is anticipated that values of the corner period and elastic displacement would be specified geographically, in much the same way that existing codes specify local variation of PGA. The implication here is that the displacement spectrum is linear with period up to the corner period. This is, however, not a necessary assumption, and could be modified on the basis of locally assessed seismicity.

CODE
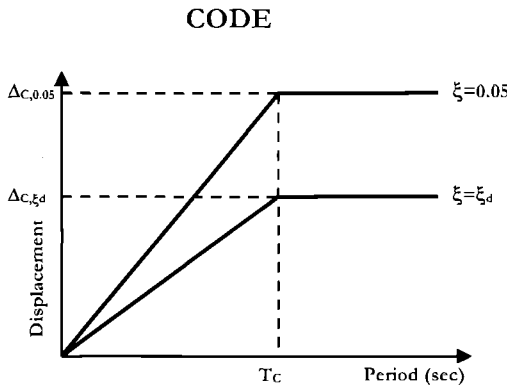
Fig.1.1 Design Displacement Spectra

1.5 The basic elastic displacement spectra defined for the building site shall be modified for the calculated building equivalent viscous damping, defined in Clause 7.6 by multiplying the displacement ordinates in accordance with Eq.(1.1)

$$\Delta_{C,\xi} = R_\xi \Delta_{C,0.05} \qquad (1.1)$$

where unless forward directivity effects are defined for the building site,

$$R_\xi = (0.07/(0.02+\xi))^{0.5} \qquad (1.2)$$

For near-field sites where forward directivity is possible,

$$R_\xi = (0.07/(0.02+\xi))^{0.25} \qquad (1.3)$$

2. PERFORMANCE CRITERIA

2.1 Structural performance under the specified design intensities shall be defined by strain and drift limits as follows:

2.1.1 Material strains associated with flexural action shall not exceed the values listed in Table 2 for different intensity levels. For concrete compression the Level 2 limit strain is defined by

$$\varepsilon_{c,dc} = 0.004 + 1.4 \frac{\rho_v f_{yh} \varepsilon_{su}}{f'_{cc}} \qquad (2.1)$$

2.1.2 Interstorey drift angles shall not exceed the limits listed in Table 3 for different intensity levels.

COMMENTARY

C1.4: The design displacement elastic spectra shown in Fig.1 increases linearly with period up to a corner period, typically in the range of 2 to 5 seconds, with a plateau of constant displacement for larger displacements. As characterization of displacement spectra, based on continuing research, improves it is probable that non-linear spectra will be defined. This does not affect the basic design methodology in any way.

C1.5 There is continuing debate over the correct formulation for the reduction of spectral displacements with equivalent viscous damping values different from $\xi = 0.05$. The values suggested here appear the best currently available options. For a discussion, refer to Section 2.2.3 of this text.

C2. The design displacement for the building may be defined by material strain limits, or by drift limits, which primarily affect non-structural components of the building. The lower of the drifts from Table 3, or the drifts corresponding to the material strain limits of Table 2 will constrain the design.

The strain and drift limits have been selected such that under Level 1 (serviceability) intensity only insignificant damage can be expected, and any necessary repairs can be carried out without affecting normal operations. Under Level 2 (damage-control) intensity, damage should be economically repairable. Under Level 3 (near-collapse) intensity the building should not collapse, though repair may not be economically repairable.

Refer to Section 4.2.5 for discussion of Eq.(2.1)

<div style="columns:2">

CODE

Table 2: Strain Limits for Different Design Intensity Levels

Material	Level 1	Level 2	Level 3
Concrete comp. strain	0.004	Eq.(2.1) <0.02	1.5Eq.(2.1)
Rebar tension strain	0.015	$0.06\varepsilon_{su}$ <0.05	$0.09\varepsilon_{su}$ <0.08
Structural steel strain	0.010	0.025	0.04
Masonry comp. strain	0.003	Eq.(2.1) <0.01	1.5Eq.(2.1)
Timber tension strain	$0.75\varepsilon_y$	$0.75\varepsilon_y$	$0.75\varepsilon_y$

Table 3: Drift Limits for Different Design Intensity Levels

Drift Limit	Level 1	Level 2	Level 3
Structures without URM, or URM infill*	0.010	0.025	No limit
Structures with URM or URM infill*	0.005	0.025	No limit

*URM= unreinforced masonry

3. Design Material Strengths

3.1 Design Material strengths for Plastic hinge regions:

- Concrete compression: $f'_{ce} = 1.3f'_c$
- Masonry compression: $f'_{me} = 1.2f'_m$
- Steel reinforcement: $f_{ye} = 1.1f_y$
- Structural steel: $f_{ye} = 1.1f_y$

3.2 Design Material strengths for Capacity-protected members or regions of members:

- Characteristic material strengths, without amplification shall be used.

4. Material strength-reduction factors:

4.1 Determination of flexural strength of plastic hinges:

- No material strength-reduction factors are applied

COMMENTARY

Table 2: Strain limits for structural steel are set lower than for concrete rebar, because of the potential for larger residual displacements with structural steel, and the susceptibility for local inelastic buckling of steel flanges of both beams and columns.

Timber strains are required to remain well within fracture strain values, since tensile failure of timber is brittle. This does not mean, however, that timber structures must respond to earthquakes within the elastic range. The appropriate design philosophy is to design timber structures with ductile connections using a capacity design approach to avoid timber failure. Refer to Chapter 9 of this text

Table 3: The drift limits for the Level 1 earthquake are intended to ensure that properly designed buildings will not suffer significant non-structural damage. Since masonry infill, and unreinforced masonry exhibit damage at drift limits significantly different from other infill materials, lower serviceability drift limits are specified.

No drift limits are specified for Level 3 intensity, for which the performance criteria only require no collapse. However, high drifts will imply significant P-Δ effects which must be included in the design. (Refer to Section 3.6 of this text)

C3. Refer to Section 4.2.6

C4. Refer to Section 4.2.6 and Section 4.7

</div>

<div style="display: flex; justify-content: space-between;">
<div>

CODE

4.2 Determination of strength of capacity-protected actions:

- Normal material strength-reduction factors are applied

5. General Structural Considerations

Consideration of the following aspects shall be included in the seismic design:

- Selection of locations of intended plastic hinges to ensure a satisfactory mechanism of inelastic deformation.
- Increase of displacements resulting from torsional eccentricity.
- Reduction in lateral resistance, and hence increase in displacements as a consequence of P-Δ effects
- Appropriate combination of gravity and seismic effects.
- Protection in accordance with capacity design principles of members and actions required to remain within the elastic range of response.

6. Design Displacement Profile

The design displacement profile for building structures shall be determined from the most critical of drift or material limit strain criteria, in accordance with the following requirements:

6.1 Frame Buildings: The design displacement profile shall be determined from the calculated drift of the critical storey Δ_c, and the inelastic first mode shape δ_i in accordance with Eq.(1)

$$\Delta_i = \omega_\theta \delta_i \cdot \left(\frac{\Delta_c}{\delta_c} \right) \qquad (6.1)$$

6.1.1 Inelastic First Mode Shape: The inelastic first mode shape to be used in Eq.(6.1) may determined by structural analysis, or by direct use of Eq.(6.2):

for n $\leq$ 4: $\delta_i = H_i / H_n$ $\qquad$ (6.2a)

for n > 4: $\delta_i = \frac{4}{3} \cdot \left(\frac{H_i}{H_n} \right) \cdot \left(1 - \frac{H_i}{4H_n} \right)$ (6.2b)

</div>
<div>

COMMENTARY

C5. In the interests of brevity, the important aspects signalled in Clause 5, though covered in the book in some detail, have not all been codified herein. The following sections of the book relate:

Location of plastic hinges: Sections 5.2.3 and 6.1.1.

Torsional response: Sections 3.8 and 6.4

P-Δ effects: Section 3.6

Combination of gravity and seismic effects: Section 3.7

Capacity Design protection (principles): Section 3.9, but see also detailed considerations in Sections 4.7, 5.8, 6.6 and 7.3

C6: Direct displacement–based seismic design relies on determining the correct displacement profile corresponding to the specified intensity level, and from this, the characteristics of the equivalent SDOF model corresponding to the inelastic first mode response.

C6.1: Frame buildings: Refer to book Section 3.5.1, and Chapter 5

C.6.1.1: Refer to book, Section 5.2.1

</div>
</div>

CODE	COMMENTARY

6.1.2 Higher Mode Drift Amplification: The design displacement profile of Eq.(6.1) shall include allowance for higher mode amplification of drift by reducing the design floor displacements by incorporation of the drift reduction factor ω_θ, given by Eq.(6.3):

$$\omega_\theta = 1.15 - 0.0034 H_n \leq 1.0 \qquad (6.3)$$

6.2 Cantilever Wall Buildings: The design displacement profile shall be defined by rational structural analysis, or by whichever of Eqs.(6.4) and (6.5) produces the lower displacements:

$$\Delta_i = \Delta_{yi} + \Delta_{pi} = \frac{\varepsilon_y}{l_w} H_i^2 \left(1 - \frac{H_i}{3H_n}\right) + \left(\phi_m - \frac{2\varepsilon_y}{l_w}\right) L_p H_i$$

$$(6.4)$$

$$\Delta_i = \Delta_{yi} + \left(\theta_c - \theta_{yn}\right) H_i = \frac{\varepsilon_y}{l_w} H_i^2 \left(1 - \frac{H_i}{3H_n}\right) + \left(\theta_c - \frac{\varepsilon_y H_n}{l_w}\right) H_i$$
$$(6.5)$$

6.3 Dual Wall/Frame Buildings: The design displacement profile shall be defined by rational analysis, or by whichever of Eqs.(6.6) and (6.7) produces the lower displacements:

$$\Delta_{Di} = \Delta_{yi} + \left(\phi_{ls} - \phi_{yW}\right) L_P H_i \qquad (6.6)$$

$$\Delta_{Di} = \Delta_{yi} + \left(\theta_C - \phi_{yW} H_{CF}/2\right) H_i \qquad (6.7)$$

6.3.1 Yield Displacement Profile: In Eqs.(6.6) and (6.7) the yield displacement profile is defined by

for $H_i \leq H_{CF}$:
$$\Delta_{iy} = \phi_{yW} \left(\frac{H_i^2}{2} - \frac{H_i^3}{6H_{CF}}\right) \qquad (6.8)$$

for $H_i > H_{CF}$:
$$\Delta_{iy} = \phi_{yW} \left(\frac{H_{CF} H_i}{2} - \frac{H_{CF}^2}{6}\right) \qquad (6.9)$$

C6.1.2: For frame buildings of about 10 storeys or more, interstorey drifts can be significantly influenced by higher mode amplification. The analytical support for Eq.(6.3) is provided in book Section 5.4
Note that building frames will normally be governed by code drift limitations, rather than material strain limits. Consequently the normal design approach will be to design for drifts, and subsequently check strain limits.

C.6.2: Refer to book Sections 3.5.2(b), and 6.2.1.

C.6.3: Dual wall/frame buildings are considered in book Chapter 7. Refer to Section 7.2.3 for background on displacement profiles.

C.6.3.1: Refer to book Section 7.2.3

CODE

In Eqs.(6.8) and (6.9) H_{CF} is the height of the wall contraflexure point under the lateral seismic forces. The yield curvature $\phi_{y,w}$ is defined by Eq.(6.10):

$$\phi_{y,w} = 2\varepsilon_y / l_w \qquad (6.10)$$

7. EQUIVALENT SDOF STRUCTURE:
The structural parameters of the equivalent **SDOF** structure to be used for determining the required base shear are defined by Eqs.(7.1) to (7.4).

7.1 Characteristic Displacement: The characteristic displacement to be used for design shall be found from Eq.(7.1):

$$\Delta_d = \sum_{i=1}^{n}\left(m_i\Delta_i^2\right) / \sum_{i=1}^{n}\left(m_i\Delta_i\right) \qquad (7.1)$$

7.2 Effective Height: The effective height is defined by

$$H_e = \sum_{i=1}^{n}\left(m_i\Delta_iH_i\right) / \sum_{i=1}^{n}\left(m_i\Delta_i\right) \qquad (7.2)$$

7.3 Effective Mass: The effective mass of the equivalent **SDOF** structure is defined by

$$m_e = \sum_{i=1}^{n}\left(m_i\Delta_i\right) / \Delta_d \qquad (7.3)$$

7.4 Displacement Ductility Demand: The design displacement ductility demand of the equivalent SDOF structure shall be found from Eq.(7.4)

$$\mu = \Delta_d / \Delta_y \qquad (7.4)$$

7.5 Yield Displacement: The yield displacement to be used in Eq.(7.4) shall be found from rational structural analysis, or from the equations in Clauses **7.5.1** or **7.5.2**:

7.5.1 Yield displacement of building frames:

$$\Delta_y = \theta_yH_e \qquad (7.5)$$

COMMENTARY

Refer to book Section 7.2.2.

C7: The essence of the **DDBD** procedure is identification of the fundamental characteristics of the equivalent **SDOF** systems (sometimes termed the *Substitute Structure*). These characteristics are based on the displacement profile, mass distribution, and geometry, and can be determined before the strength distribution is known. These characteristics are used to determine the required base shear force.

C7.1: Refer to book, Section 3.5.1

C7.2: Refer to book, Section 3.5.4

C.7.3: Refer to book, Section 3.5.3

C7.4: Refer to book, Section 3.5.4

C.7.5: Refer to book Section 3.5.4

C7.5.1: Refer to book, Section 4.4.6

CODE

In Eq.(7.5) the yield drift of frames may be taken as:

(a) reinforced concrete frames:

$$\theta_y = 0.5\varepsilon_y \frac{L_b}{h_b} \qquad (7.6a)$$

(b) structural steel frames:

$$\theta_y = 0.65\varepsilon_y \frac{L_b}{h_b} \qquad (7.6b)$$

7.5.2 Yield displacement of Cantilever Walls:

$$\Delta_y = \frac{\varepsilon_y}{l_w} H_e^2 \left(1 - \frac{H_e}{3H_n}\right) \qquad (7.7)$$

7.5.3 Yield Displacement of Dual Wall/Frame Buildings: The yield displacement of dual wall frame buildings may be found substituting $H_i = H_e$ in Eq.(6.8) if $H_e < H_{CF}$ and in Eq.(6.9) if $H_e > H_{CF}$.

7.6 Equivalent Viscous Damping: The equivalent viscous damping to be used to characterize the design displacement spectrum for the **SDOF** structure, in accordance with Eqs.(1.2) and (1.3) shall be determined from results of comprehensive inelastic dynamic analyses of structures with similar structural materials and structural forms as the building under consideration. In lieu of current analyses the appropriate equation from the following list may be used:

Concrete Wall Building, Bridges:

$$\xi_{eq} = 0.05 + 0.444 \left(\frac{\mu - 1}{\mu\pi}\right) \qquad (7.8a)$$

Concrete Frame Building:

$$\xi_{eq} = 0.05 + 0.565 \left(\frac{\mu - 1}{\mu\pi}\right) \qquad (7.8b)$$

Steel Frame Building:

$$\xi_{eq} = 0.05 + 0.577 \left(\frac{\mu - 1}{\mu\pi}\right) \qquad (7.8c)$$

COMMENTARY

C7.5.2: Refer to book, Section 3.5.2(b).

C7.5.3: Refer to book, Section 7.2.3

C7.6: Refer to book Section 3.4.3. The damping to be used is equivalent to the sum of elastic and hysteretic damping of the structure, and is calibrated by inelastic time-history analyses using realistic estimates of elastic damping, and hysteretic response. It is important the simplistic rules, such as the elastic-perfectly-plastic rule, with elastic damping of $\xi_e = 0.05$ not be used.

Refer to book, Section 3.4.3(c).

CODE

Hybrid Prestressed Frame (β=0.35):

$$\xi_{eq} = 0.05 + 0.186 \left(\frac{\mu - 1}{\mu \pi} \right) \qquad (7.8d)$$

Friction Slider:

$$\xi_{eq} = 0.05 + 0.670 \left(\frac{\mu - 1}{\mu \pi} \right) \qquad (7.8e)$$

Bilinear Isolation System (r=0.2):

$$\xi_{eq} = 0.05 + 0.519 \left(\frac{\mu - 1}{\mu \pi} \right) \qquad (7.8f)$$

7.7 Effective Response Period: The effective period of the SDOF structure is

$$T_e = \frac{\Delta_d}{\Delta_{C,\xi}} \cdot T_C \qquad (7.9)$$

7.8 Effective Stiffness: The effective stiffness of the SDOF structure is

$$K_e = 4\pi^2 m_e / T_e^2 \qquad (7.10)$$

8 DESIGN BASE SHEAR FORCE

The design base shear force is determined from the design displacement and effective stiffness of the **SDOF** structure in accordance with Eq.(8.1):

$$V_{Base} = K_e \Delta_d \qquad (8.1)$$

8.1 Lateral Force Vector Derived from Base Shear Force: The base shear force shall be distributed to the locations of floor mass of the building in accordance with the relationship:
Floors 1 to n-1:

$$F_i = k V_{Base} (m_i \Delta_i) / \sum_{i=1}^{n} (m_i \Delta_i) \qquad (8.2a)$$

Roof (Floor n):

$$F_n = (1 - k)V_{Base} + k V_{Base} (m_n \Delta_n) / \sum_{i=1}^{n} (m_i \Delta_i) \qquad (8.2b)$$

For frame buildings, the value of k to be used in Eq.(8.2) is $k = 0.9$. For all other building structure, $k = 1.0$.

COMMENTARY

Refer to book Section 3.4.3(d) for definition of β.

Note: The equation for the bilinear system has a rather steep post-yield stiffness ratio (r), and is appropriate for a specific seismic isolation system only. Bilinear systems with other post-yield stiffness need individual calibration, since the equivalent viscous damping is sensitive to this parameter.

C7.7: This equation assumes a linear displacement spectrum, as shown in Fig.(1.1). If a non-linear displacement spectrum is specified, then the period needs to be found by interpolation.

C7.8: Refer to book, Section 3.1. Eq.(7.10) is found from simple inversion of the equation for the period of a SDOF oscillator.

C8: Refer to book, Section 3.1 and Fig.3.1.

C8.1: The base shear force is distributed to the floor masses in proportion to floor mass and floor displacement. For frame buildings, particularly those of about 10 storeys or higher, 10% of the base shear must be additionally applied at roof level to reduce higher-mode drifts.

CODE

8.2 Structural Analysis to Determine Required Moment Capacity at Plastic Hinges:

8.2.1 The structure shall be analysed under the design lateral force vector to determine the required moment capacity of potential plastic hinge locations

8.2.2 The structural analysis shall be based on effective stiffness of structural members at expected displacement response, or alternatively may be determined from a rational equilibrium analysis. Lateral forces should not be distributed to members based on elastic section properties.

9. CAPACITY DESIGN REQUIREMENTS

The intended distribution and location of plastic hinges must be ensured by application of an appropriate capacity design hierarchy of strength with design moments and shears amplified to account for possible increased material strength in plastic hinge locations, and higher mode dynamic amplification. Amplified moments and shears may be determined in accordance with the *Effective Modal Superposition* method of Section 8.1, or the *Approximate* method of Section 8.2

9.1 Effective Modal Superposition to Determine Capacity Design Force Levels:

Capacity design moments and shears may be determined by combining modal moments or shears by SSRS or CQC combination rules, from a modal analysis based on effective member stiffnesses at maximum displacement response. The first mode response $S_{I,Di}$ may be taken as the design moments or shears resulting from the structural analysis defined in Section 7.2, amplified for possible enhancement of material strengths. For the SSRS combination rule, the enhanced action, $S_{CD,i}$ is found from Eq.(9.1):

$$S_{CD,i} = \sqrt{(\phi^o S_{1D,i})^2 + S_{2,i}^2 + S_{3,i}^2 + .. + S_{n,i}^2} \qquad (9.1)$$

The value of the overstrength factor ϕ^o may be determined from moment-curvature analysis of

COMMENTARY

C8.2: DDBD is intended to provide direct information on the required flexural strength of plastic hinges. Two methods of structural analysis are suggested. The first involves a conventional structural analysis, though the member stiffness adopted in the analysis should be reduced from the elastic values by dividing by the expected member displacement, or rotational ductility. As noted in book Section 5.5.1, care is needed in modelling the stiffness of first-storey columns.
The second method is based on equilibrium requirements, rather than stiffness properties. This procedure is outlined in book Section 5.5.2. In the case of frame buildings, the equilibrium method requires rational decisions to be made about the vertical distribution of beam seismic shear up the buildings.

C9.1: There are a number of modal analysis procedures outlined in different chapters of the book that have been developed to determine capacity design forces. All are based on the assumption of a modal superposition combining the inelastic first mode forces with the elastic higher mode forces, and all give similar results. Although not fully checked on all structural types, it is believed that the *Effective Modal Superposition* approach, which is based on a structural model similar to the first option described in Clause C8.2 above provides the most consistent results.

CODE

the plastic hinges. Alternatively a conservative value of $\phi^0 = 1.25$ may be assumed.

9.2 Approximate Methods for Determining Capacity Design Force Levels:
As an alternative to the consistent approach of Section 9.1, the following conservative equations may be used for different structural types and actions.

9.2.1 General Provisions:
The dependable strength of capacity-protected elements shall be determined from

$$S_{CP} = \phi^0 \omega S_E \qquad (9.2)$$

9.2.2 Frame Buildings:

(a) Column Moments
(i)One way frames:
The dynamic amplification factor ω_f for flexure is height and ductility dependent as shown in Fig.9.1, where from level 1 to the ¾ point of structure height:

$$\omega_{f,c} = 1.15 + 0.13\left(\mu / \phi^0 - 1\right) \qquad (9.3)$$

and at the top and bottom of the frame

$$\omega_f = 1.00 \qquad (9.4)$$
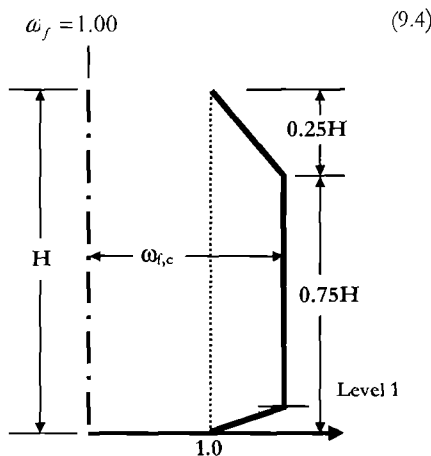
Fig.9.1 Dynamic Amplification of Column Moments

COMMENTARY

C9.2: The equations in this section are based on analyses on extensive inelastic time-history analyses, and are adequately conservative for design purposes.

C9.2.1: The basic capacity design equation (9.1) relates the required dependable strength of the capacity-protected action (generally flexural strength or shear strength) to the value calculated from the design lateral force distribution, including an overstrength factor ϕ^0 and a dynamic amplification factor ω. The overstrength factor will normally be found from moment-curvature analysis in accordance with book Section 4.5, or may conservatively be taken as 1.25, when design flexural strength follows the recommendations of book Section 4.2.6

C9.2.2(a): Refer to book Section 5.8.4(c).

<table>
<tr><td>CODE</td><td>COMMENTARY</td></tr>
</table>

CODE

(ii) **Two-way frames:** For two-way frames the design moment corresponding to lateral forces shall be based on biaxial response, with the displacement ductility factor μ in Eqs.(9.3) and (9.4) being replaced by $\mu/\sqrt{2}$.

(b) **Column shears** : Overstrength and dynamic amplification factors for shear in columns shall be combined as in Eq.(9.5) which relates the required dependable shear strength to the shear determined from the lateral force distribution:

$$\phi_S V_N \geq \phi^o V_E + 0.1\mu V_{E,base} \leq \frac{M_t^o + M_b^o}{H_c} \qquad (9.5)$$

9.2.3 Structural Walls:

(a) **Wall Moments.** The design moments for cantilever walls shall conform to the bilinear envelope of Fig.9.2, where the wall-base moment is amplified for overstrength effects, and the moment capacity at midheight is defined by

$$M_{0.5H}^0 = C_{1,T}.\phi^0 M_B \qquad (9.6)$$

where

$$C_{1,T} = 0.4 + 0.075 T_i \left(\frac{\mu}{\phi^0} - 1 \right) \geq 0.4 \qquad (9.7)$$
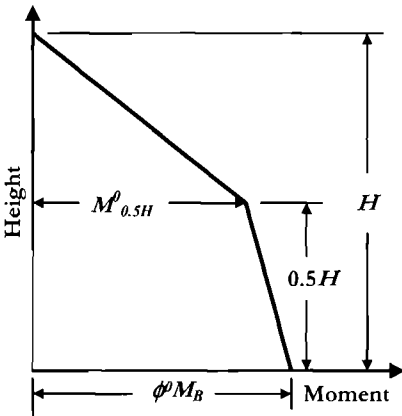
Fig.9.2 Capacity Moments for Walls

COMMENTARY

Refer to book, Section 5.8.5(c).

Refer to book, Section 6.6.2(a).

C9.2.3: The period T_i in Eq.(9.7) is the initial elastic period, including effects of cracking. Note that this period can be related with adequate accuracy to the effective period used in the **DDBD** process by $T_i = T_e/\sqrt{\mu}$. For comparatively short walls, it will normally be appropriate to carry the flexural reinforcement up the full height of the wall without terminating any bars.

<div style="display:flex">
<div>

CODE

In determining the required level of wall flexural reinforcement, allowance shall be made for variation of axial force with height, and for tension-shift effects.

(b) Wall Shear Forces: The provided shear strength of a cantilever wall shall conform to the linear envelope of Fig.9.3. The wall-base dynamic amplification factor for shear shall be taken as

$$\omega_v = 1 + \frac{\mu}{\phi^0} C_{2,T} \qquad (9.8)$$

where

$$C_{2,T} = 0.067 + 0.4(T_i - 0.5) \leq 1.15 \qquad (9.9)$$

The design moment capacity at the wall top shall be not less than

$$V_n^0 = (0.9 - 0.3T_i)V_B^0 \geq 0.3V_B^0 \qquad (9.10)$$
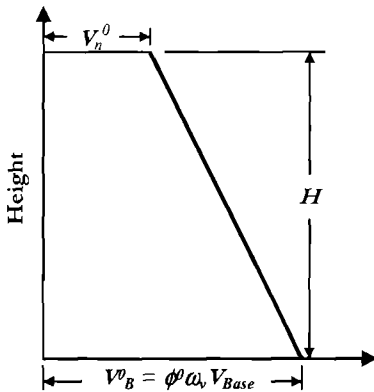
Fig.9.3 Wall Design Shear Forces

9.2.4 Dual Wall-Frame Buildings

When the proportion of base shear allocated to the frames of dual structural systems falls in the range $0.2 \leq \beta_F \leq 0.6$ the following provisions apply. When $\beta_F \leq 0.2$, the walls should be designed as cantilever walls to Cl.9.2.3, and when $\beta_F \geq 0.6$ the

</div>
<div>

COMMENTARY

Refer to book Section 6.6.2(b)

Refer to book Section 7.3.2.

C.9.2.4: When $\beta_F < 0.2$, the **frames** may still be designed to the provisions of this section, and when $\beta_F > 0.6$ the **walls** may be designed to these provisions.

</div>
</div>

CODE

frames should be designed in accordance with
Cl.9.2.2.

(a) Column Moments: Columns shall have
dependable flexural strength not less than

$$M_{C,D} = 1.3\phi^0 M_{CE} \qquad (9.11)$$

(b) Column Shear Force: Columns shall have
dependable shear strength not less than

$$V_{C,D} = 1.3\phi^0 M_{CE} \qquad (9.12)$$

(c) Wall Moments: Wall moments shall be
designed to the bilinear envelope defined in
Cl.9.2.3(a).

(d) Wall Shear Forces: The provided shear
strength of a wall of a dual structural system shall
conform to the envelope of Fig.9.3, where

$$\omega_v = 1 + \frac{\mu_{sys}}{\phi^0} C_{3,T} \qquad (8.13)$$

where

$$C_{3,T} = 0.4 + 0.2(T_i - 0.5) \le 1.15 \qquad (8.14)$$

The shear force at the wall top may be taken as

$$V_n^0 = 0.4 V_B^0 \qquad (8.15)$$

COMMENTARY

C.9.2.4(a): Influence of higher modes on
column moments is less apparent in frames of
dual systems. Also it should be noted that the
consequences of column plastic hinging are
minimal, since the wall stiffness and strength will
control the deformation, avoiding the potential
for a soft-story mechanism to form.

C.9.2.4(d): The form of the wall shear force
envelope is the same as for simple cantilever
walls, but the system ductility, rather than the
wall ductility is used, and the period-dependent
coefficient, $C_{3,T}$ results in lower amplification
than in simple cantilever walls.

REFERENCES

A1:   Aschheim, M. and Black, E.F. "Yield Point Spectra for Seismic Design and Rehabilitation", *Earthquake Spectra*, Vol. 16(2), 2000, pp 317-336

A2:   AISC, *Manual of Steel Construction: Load and Resistance Factor Design, 3rd Edition*, American Institute of Steel Construction Inc., Chicago, USA, 2001

A3:   Ang, B.G., Priestley, M.J.N. and Paulay, T. "Seismic Shear Strength of Circular Reinforced Concrete Columns". *ACI Journal*, Vol. 86(1), 1988, pp 45-59

A4:   Alvarez, J.C., *Displacement Based Design of Continuous Concrete Bridges under Transverse Seismic Excitation*, MSc Thesis, Rose School, IUSS, Pavia, 2004, 99 pp

A5:   Abrams, D., "New American Practices for Seismic Rehabilitation of Masonry Buildings", *Proceedings, U.S.-Italian Workshop on Seismic Evaluation and Retrofit*, New York City, Technical Report NCEER-97-0003, NCEE, Buffalo, 1997, pp 143-156

A6:   Anthoine, A., Magonette G. and Magenes, G., "Shear-compression testing and analysis of brick masonry walls", *Proceedings, 10th European Conference on Earthquake Engineering*, Vienna, Austria, 1995, Vol. 3, pp 1657-1662

A7:   Ayers, J.P., *Evaluation of parameters for limit states design of masonry walls*, MS Thesis, North Carolina State University, Raleigh, USA, 2000, 100 pp

A8:   Akkar, S. and Bommer, J.J., "Prediction of elastic displacement response spectra in Europe and the Middle East", *Earthquake Engineering and Structural Dynamics*, Vol. 36, 2007 (in press)

A9:   Aschheim, A.M. and Moehle, J.P., *Shear strength and deformability of RC bridge columns subjected to inelastic cyclic displacements*, Report UCB/EERC 92/04, University of California, Berkeley, 1992, 100 pp

B1:   Browning, J.P., "Proportioning of Earthquake-Resistant RC Building Structures", *ASCE Journal of Structural Engineering*, Vol. 127(2), pp 145-151

B2:   Bernal, D., "Amplification Factors for Inelastic Dynamic P-Δ Effects in Earthquake Analyses", *Earthquake Engineering and Structural Dynamics*, Vol. 15, 1981, pp 635-651

B3:   Blakeley, R.W.G., and Park, R., "Prestressed Concrete Sections with Cyclic Flexure", *ASCE Journal of Structural Engineering*, V.99, 1973, pp 1717-1742

B4:   Beyer, K., *Seismic design of torsionally eccentric buildings with RC U-shaped walls*, PhD thesis, Rose School, IUSS, Pavia, 2007 (in preparation)

B5:   Budek, A.M., Lee, C.O. and Priestley, M.J.N., *Seismic Design of Circular Bridge Columns with Unstressed Strand for Transverse Reinforcement*, Report SSRP 2001/06, University of California, San Diego, 2001

B6:   Budek, A., Benzoni, G. and Priestley, M.J.N., "In-ground plastic hinges in Column/Pile Shaft Design", *Proceedings, 3rd Annual Caltrans Seismic Research Workshop*, Caltrans, Sacramento, 1994

B7:   Boore, D.N. and Bommer, J.J., "Processing of Strong-Motion Accelerograms: Needs, Options and Consequences", *Soil Dynamics and Earthquake Engineering*, Vol. 25, 2005, pp 93-115

B8:   Bommer, J.J. and Mendis, R., "Scaling of Spectral Displacement Ordinates with Damping Ratios", *Earthquake Engineering and Structural Dynamics,* Vol. 34, 2005, pp 145-165

B9:   Buchanan, A.H. and Fairweather, R.H., "Seismic Design of Glulam Structures", *Bulletin NZNSEE,* Vol. 26(4), 1993, pp 415-436

B10:   Berry, M.P. and Eberhard, M.O., "Practical Performance Model for Bar Buckling", *ASCE Journal of Structural Engineering,* Vol. 131(7), 2005, pp 1060-1070

B11:   Beyer, K., *Design and Analysis of Walls coupled by Floor Diaphragms*, MSc thesis, Rose School, IUSS, Pavia, 2005, 100 pp

B12:   Bruneau, M., Wuang, C.M. and Whittaker, A., *Ductile Design of Steel Structures*, McGraw Hill, 1998, 485 pp

C1:   Carr, A., *RUAUMOKO: the Maori God of Volcanoes and Earthquakes*, Civil Engineering Department, University of Canterbury, Christchurch, New Zealand. 1996, 152 pp

C2:   Chopra, A.K. and Goel, R.K., "Direct Displacement-Based Design: Use of Inelastic vs. Elastic Design Spectra", *Earthquake Spectra*, Vol. 17(1), 2001, pp 47-65

C3:   Clough, R.W., "A Replacement for the SRSS Method of Seismic Analysis", *Earthquake Engineering and Structural Analysis,* Vol.9, 1988, pp 187-194

C4:   Cheok, G.S. and Lew, H.S., "Performance of Precast Concrete Beam-to-column Connections Subject to Cyclic Loading", *PCI Journal,* Vol. 36(3), 1991, pp 56-67

C5:   Crowley, H. and Pinho, R., "Period-height relationship for existing European reinforced concrete buildings," *Journal of Earthquake Engineering,* Vol. 8(SP1), 2004, pp. 93-120

C6:   Castillo, R., *Seismic Design of Asymmetric Ductile Systems*, PhD Thesis, University of Canterbury, Christchurch, New Zealand, 2004

C7:   Chai, Y.H., "Flexural Strength and Ductility of Extended Pile-Shafts 1: Analytical Model", *ASCE Journal of Structural Engineering*, Vol. 128(5), 2002, pp 586-594

C8:   Collins, M.P. and Mitchell, D., *Prestressed Concrete Structures*, Response Publications, Toronto, 1997, 766 pp

C9:   Ceccotti, A. (Editor), "Structural Behaviour of Timber Constructions in Seismic Zones", *Proceedings, CEG DG III*, Florence, Italy, 1989

C10:   Cormack, L.G., "The design and construction of the major bridges on the Mangaweka rail deviation", *Trans. of the Institution of Professional Engineers*, Vol. 15, New Zealand, 1988, pp 16-23

C11: Christopoulos, C. and Filiatrault, A., *Principles of Passive Supplemental Damping and Seismic Isolation*, IUSS Press, Pavia, 2007, 480 pp

C12: Crisafulli, F.J., *Seismic Behaviour of Reinforced Concrete Structures with Masonry Infills*, PhD Thesis, University of Canterbury, Christchurch, New Zealand, 1997,

C13: Clough, R. and Penzien, J., *Dynamics of Structures*, Computers and Structures, Inc., 2004, 700 pp

C14: Calvi, G.M., Ceresa, P., Casarotti, C., Bolognini, D. and Auricchio, F., "Effects of axial force variation on the seismic response of bridges isolated with friction pendulum systems", *Journal of Earthquake Engineering*, Vol. 8(SP 1), 2004, pp 187-224

C15: Camarillo, H.R. *Evaluation of Shear Strength Methodologies for Reinforced Concrete Columns*, M.S. Thesis University of Washington, 2003, 137pp

C16: Calvi, G. M. (Editor), *Displacement-based Seismic Design of Reinforced Concrete Buildings*, *fib* Bulletin 25, *fib*, Lausanne, 2003, 192 pp

C17: Ciampoli, M. and Pinto, P.E., "Effects of soil-structure interaction on inelastic seismic response of bridge piers", *ASCE Journal of Structural Engineering*, Vol. 121(5), 1995, pp. 806-814

D1: Dwairi, H.M, Kowalsky, M.J. and Nau, J.M., "Equivalent Viscous Damping in Support of Direct Displacement-Based Design", *Journal of Earthquake Engineering*, (in Press, March 2007)

D2: Dilger, W., "Veränderlichkeit der Biege und Schubsteifigkeit bei Stahlbetontragwerken und ihr Einflug auf Schittkraftverteilung und Traglast bei Statisch Unbestimmter Lagerung", *Deutscher Ausschuss für Stahlbeton*, Heft 179, 1966, pp 1-101 (in German)

D3: Dwairi, H. and Kowalsky, M.J., "Implementation of Inelastic Displacement Patterns in Direct Displacement-Based Design of Continuous Bridge Structures", *Earthquake Spectra*, Vol. 22(3), 2006, pp 631-662

D4: Dyke, S.J. and Spencer, B.F., Jr., "Seismic response control using multiple MR dampers", *Proceedings, 2nd International Workshop on Structural Control*, Hong Kong, 1996, pp 163–173

D5: Dodd, L.L., *The Dynamic Behaviour of Reinforced Concrete Bridge Piers Subjected to New Zealand Seismicity*, Report No. 92-04, Dept. of Civil Eng., University of Canterbury, Christchurch, New Zealand, 1992,

D6: Doherty, K.T., Griffith, M.C., Lam, N. and Wilson, J., "Displacement-Based Seismic Analysis for Out-of-Plane Bending of Unreinforced Masonry Walls", *Earthquake Engineering and Structural Dynamics*, Vol. 31, 2002, pp 833-850

D7: Drysdale, R.G., Hamid, A.A. and Baker, L., *Masonry Structures: Behaviour and Design*, 2nd Edition, The Masonry Society, Boulder, Colorado, 1999

E1: Earth Mechanics, Inc., *Port-Wide Ground Motion and Palos Verdes Fault Study*, Report Prepared for Port of Los Angeles, California, 2006

E2: Eibl, J. and Keintzel, F., "Seismic Shear Forces in RC Cantilever Shear Walls", *Proceedings, 9th World Conference on Earthquake Engineering*, Tokyo/Kyoto, Japan, 1988, Paper 9-1-1

F1: Freeman, S.A., "Development and Use of the Capacity Spectrum Method", *Proceedings, 6th US National Conference on Earthquake Engineering*, Seattle, 1998, paper No. 269

F2: Fajfar, P. "A Nonlinear Analysis Method for Performance-based Seismic Design" *Earthquake Spectra*, Vol. 16(3), 2000, pp 573-592

F3: Fenwick, R.C. and Megget, L.M., "Elongation and load deflection characteristics of reinforced concrete members containing plastic hinges", *Bulletin NZNSEE*, Vol. 26(1), 1993, pp 28-41

F4: Fajfar, P. and Krawinkler, H. (Editors), "Seismic Design Methodologies for the Next Generation of Codes", *Proceedings, Workshop on Seismic Design Methodologies for the Next Generation of Codes*, Bled, Slovenia, 1997, 436 pp

F5: Folz, B. and Filiatraut, A., "Seismic Analysis of Woodframe Structures II: Model Implementation and Verification", *ASCE Journal of Structural Engineering*, Vol. 130(8), pp 1361-1370

F6: Faccioli, E., Paolucci, R., and Rey, J., "Displacement Spectra for Long Periods", *Earthquake Spectra*, Vol. 20(2), 2004, pp 347-376

F7: Folz, B. and Filiatraut, A., "Seismic Analysis of Woodframe Structures I: Model Formulation", *ASCE Journal of Structural Engineering*, Vol. 130(8), pp 1353-1360

F8: Fenwick, R., Bull, D.K., MacPherson, C. and Lindsay, R., "The Influence of Diaphragms on Strength of Beams", *NZSEE Technical Conference*, Napier, 2006

F9: Filiatrault, A. and Foltz, B., "Performance-Based Seismic Design of Wood Framed Buildings", *ASCE Journal of Structural Engineering*, Vol. 128, 2002, pp 39-47

F10: Filiatrault, A., Christovasilis, I., Wanitkorkul, A. and Folz, B., "Displacement-Based Seismic Design of Light-Frame Wood Buildings", *Proceedings, World Conference on Timber Engineering*, Portland, 2006,

G1: Gulkan, P. and Sozen, M., "Inelastic Response of Reinforced Concrete Structures to Earthquake Motions", *ACI Journal*, Vol. 71(12), 1974, pp 604-610

G2: Grant, D.N., Blandon, C.A. and Priestley, M.J.N., *Modelling Inelastic Response in Direct Displacement-Based Design*, Report 2005/03, IUSS Press, Pavia, 2005, 104 pp

G3: Goel, R.K. and Chopra, A.K., "Role of Higher-Mode Pushover Analyses in Seismic Analysis of Buildings," *Earthquake Spectra*, Vol. 21(4), 2005, pp 1027-1041

G4: Graves, R.W. and Somerville, P.G., "Broadband Simulations for Scenario Earthquakes on the Puente Hills Fault", *Proceedings, 8th US National Conference on Earthquake Engineering*, San Francisco, 2006, paper No. 1052

G5: Griffith, M.C., Magenes, G., Melis, G. and Picchi, L., "Evaluation of Out-of-Plane Stability of Unreinforced Masonry Walls Subjected to Seismic Excitations", *Journal of Earthquake Engineering*, Vol. 7(SP1), 2003, pp 141-169

G6: Gasparini, D.A. and Vanmarcke, E.H., *SIMQKE: a program for artificial motion generation: User's manual and Documentation*, Civil Engineering Department, MIT, 1976, 32 pp

H1: Hewes, J, Priestley, M.J.N. and Seible, F, "Seismic Response of Bridge Piers with Unbonded Prestressing", *Proceedings, 5th Caltrans Seismic Design Workshop*, Sacramento, 1999

H2:   Hendry, A.W., *Structural Masonry*, 2nd Edition, Palgrave Macmillan, London, 1998

H3:   Haroun, M.A., Pardoen, G.C., and Haggaag, H.A., "Assessment of Cross-Ties Performance in Bridge Pier Walls of Modern Designs", *Proceedings, 3rd Annual Caltrans Seismic Research Workshop*, Sacramento, 1994,

H4:   Holombo J., Priestley, M.J.N. and Seible, F., *Longitudinal Seismic Response of Precast Spliced-Girder Bridges*, Report SSRP 98-05, University of California, San Diego, 1998, 298 pp

H5:   Housner, G.W., "The Behaviour of Inverted Pendulum Structures During Earthquakes", *Bulletin of the Seismological Society of America*, Vol. 53(2), 1963, pp 403-417

H6:   Hanson, R. D. and Soong, T.T., *Seismic design with supplemental energy dissipation devices*, Earthquake Engineering Research Institute, Monograph MNO-8, Oakland, USA, 2001, 149 pp

H7:   Holden, T., Restrepo, J.I., and Mander, J.B., "Seismic Performance of Precast Reinforced and Prestressed Concrete Walls", *ASCE Journal of Structural Engineering*, Vol. 129(3), 2003, pp 286-296

I1:   Iwan, W. D. and Gates, N. C., "The effective period and damping of a class of hysteretic structures", *Earthquake Engineering and Structural Dynamics*, Vol. 7, 1979, pp 199–211

I2:   Infanti, S., Papanikolas, P., Benzoni, G. and Castellano, M.G., "Rion-Antirion bridge: design and full scale testing of the seismic protection devices", *Proceedings, 13th World Conference on Earthquake Engineering*, Vancouver, Canada, 2004, paper No. 2174

J1:   Jacobsen, L. S., "Damping in composite structures", *Proceedings, 2nd World Conference on Earthquake Engineering*, Vol. 2, Tokyo and Kyoto, Japan, 1960, pp. 1029–1044

J2:   Judi, H.J., Fenwick R.C. and Davidson, B.J., "Direct displacement based design – a definition of damping", *Proceedings, NZSEE Technical Conference*, Auckland, New Zealand, 2001, paper no. 4.09

K1:   Kappos, A.J., "Feasibility of Using Advanced Analytical Tools in the Seismic Design of RC Structures", Proceedings, *G.Penelis International Symposium on Concrete and Masonry Structures*, Thessaloniki, Greece, 2000, pp 47-60

K2:   Kowalsky, M.J., Priestley, M.J.N. and MacRae, G.A., "Displacement-Based Design of RC Bridge Columns", *Proceedings, 2nd International Workshop on Seismic Design of Bridges*, Queenstown, New Zealand, 1994, pp 138-163

K4:   Kowalsky, M.J. and Priestley, M.J.N., "An improved analytical model for shear strength of circular RC columns in seismic regions", *ACI Journal*, Vol. 97(3), 2000, pp. 388-396.

K5:   Krier, C.J., *Seismic Testing of Full-Scale Precast Prestressed Pile to Deck Connections*, MS Thesis, Dept. of Structural Engineering, University of California, San Diego, 2006

K6:   Kawashima, K. and Calvi, G.M. (Editors), *Structural solutions for bridge seismic design and retrofit – a state of the art, fib* Bulletin, *fib*, Lausanne, 2007 (in press)

K7:   Khatib, I.F., Mahin, S.A, and Pister, K.S., *Seismic behavior of concentrically braced steel frames*, Report UCB/EERC-88/01, University of California, Berkeley, 1988, 222 pp

K8:   Kramer, S.L., *Geotechnical Earthquake Engineering*, Prentice-Hall, New Jersey, 1996, 653 pp

L1:   Lin, Y.Y. and Chang, K.C. "Study on Damping Reduction Factor for Buildings under Earthquake Ground Motions", *ASCE Journal of Structural Engineering*, Vol. 129(2), 2003, pp 206-214

M1:   Moehle, J.P., "Displacement-based Design of RC Structures subjected to Earthquakes*". Earthquake Spectra*, Vol. 3(4), pp 403-428

M2:   Mahin, S.A., and Boroschek, R.L., "Influence of Geometric Nonlinearities on the Seismic Response of Bridge Structures", *Proceedings, 3ʳᵈ NSF Workshop on Bridge Engineering Research in Progress*, La Jolla, 1992, pp 317-320

M3:   MacRae, G.M., Priestley, M.J.N. and Tao, J., *P-Δ Design in Seismic Regions*, Report SSRP-93-05, University of California, San Diego, 1993, 114 pp

M4:   Mander, J.B., Priestley, M.J.N. and Park, R. "Theoretical Stress-Strain Model for Confined Concrete", *ASCE Journal of Structural Engineering*, Vol.114(8), 1988, pp 1804-1826

M5:   Montejo, L.A. *ESPECTRO – Code for the Analysis of Strong Motion Data*, http://www.geocities.com/lumontv/eng.html, 2006

M6:   Miranda, P.A., Calvi, G.M., Pinho, R. and Priestley, M.J.N., *Displacement-Based Assessment of RC Columns with Limited Shear Resistance*, ROSE Research Report No. 2005/04, IUSS Press, Pavia, 2005, 153 pp

M7:   Mander, J.B., Priestley, M.J.N. and Park, R., "Observed Stress-Strain Behaviour of Confined Concrete", *ASCE Journal of Structural Engineering*, Vol. 114(8), 1988, pp 1827-1849

M8:   Moyer, M.J. and Kowalsky, M.J., "Influence of tension strain on buckling of reinforcement in RC bridge columns", *ACI Journal*, Vol. 100(1), 2003, pp 75-85

M9:   Magenes, G., Calvi, G.M. and Kingsley, G.R., "Seismic Testing of a Full-Scale, Two-Story Masonry Building: Test Procedure and Measured Experimental Response", in *Experimental and Numerical Investigation on a brick Masonry Building Prototype - Numerical Prediction of the Experiment*, G.N.D.T. Report 3.0, University of Pavia, Italy, 1995, pp 1.1-1.41

M10:   MacRae, G.A., Kimura, Y. and Roeder, C. "Effect of column stiffness on Braced Frame Seismic Behavior", *ASCE Journal of Structural Engineering*, Vol. 130(3), 2004, pp 381-391

M11:   Magenes, G. and Calvi, G.M., "In-Plane Seismic Response of Brick Masonry Walls". *Earthquake Engineering and Structural Dynamics*, Vol. 26, 1997, pp 1091-1112

M12:   Magenes, G., "A method for pushover analysis in seismic assessment of masonry buildings", *Proceedings, 12ᵗʰ World Conference on Earthquake Engineering*, Auckland, New Zealand, 2000, paper No. 1866

M13:   Magenes, G., "Masonry Building Design in Seismic Areas: Recent Experiences and Prospects from a European Standpoint", *Proceedings, 1ˢᵗ European Conference on Earthquake Engineering and Seismology*, Geneva, Switzerland, 2006, keynote 9

M14: Montejo, L.A. and Kowlasky, M.J., *CUMBIA – Set of Codes for the Analysis of Reinforced Concrete Members*, Report No. IS-07-01, Constructed Facilities Laboratory, North Carolina State University, Raleigh, NC, 2007, 41 pp

M15: Medhekar, M.S. and Kennedy, D.J.L., "Displacement-based seismic design of buildings – application", *Engineering Structures*, Vol. 22, 2000, pp 210-221

M16: Moghaddam, H. and Hajirasouliha, I., "An investigation on the accuracy of pushover analysis for estimating the seismic deformation of braced steel frames", *Journal of Constructional Steel Research*, Vol. 62, 2006, pp 343-351

N1: Nakaki, S.D., Stanton, J.F. and Sritharan, S., "An Overview of the PRESSS Five-Story Precast Test Building", *PCI Journal*, Vol. 44(2), 1999, pp 26-39

N2: Newmark, N.M. and Hall, W.J., *Earthquake Spectra and Design*, EERI Monograph, Oakland, USA, 1982, 103 pp

N3: Naeim, F. and Kelly, J.M., *Design of Seismic Isolated Structures*, Wiley, New York, 1999, 290 pp

N4: Newmark, N.M. and Rosenblueth, E., *Fundamentals of Earthquake Engineering*, Prentice-Hall, Englewood Cliffs, USA, 1971, 640 pp

O1: Otani, S., *SAKE: A Computer Program for Inelastic Response of RC Frames to Earthquakes*, Report UILU-Eng-74-2029, University of Illinois at Urbana-Champaign, 1974, 145 pp

O2: California Office of Emergency Services (OES), *Vision 2000: Performance Based Seismic Engineering of Buildings*, Structural Engineers Association of California, Sacramento, USA, 1995,

O3: Otani, S. "Development of Performance-based Design Methodology in Japan", *Proceedings, Workshop on Seismic Design Methodologies for the Next Generation of Codes*, Bled, Slovenia, 1997, pp 59-68

O4: Otani, S. "Hysteretic Models of Reinforced Concrete for Earthquake Response Analysis", *Journal of Faculty of Engineering*, University of Tokyo, Vol. 36(2), 1981, pp 407-441

P1: Paulay, T. and Priestley, M.J.N., *Seismic Design of Reinforced Concrete and Masonry Buildings*, Wiley, New York, 1992, 744 pp

P2: Priestley, M.J.N. and Amaris, A.D., *Dynamic Amplification of Seismic Moments and Shear Forces in Cantilever Walls*, ROSE Research Report 2002/01, IUSS Press, Pavia, 2002, 95 pp

P3: Priestley, M.J.N., *Myths and Fallacies in Earthquake Engineering, Revisited. The 9th Mallet Milne Lecture*, IUSS Press, Pavia, 2003, 121 pp

P4: Priestley, M.J.N., Seible, F. and Calvi, G.M., *Seismic Design and Retrofit of Bridges*, Wiley, New York, 1996, 686 pp

P5: Panagiotou, M., and Restrepo, J.I. *Computational Model for the UCSD 7-Storey Structural Wall Building Slice*, SSRP Report 07-09, Department of Structural Engineering, University of California San Diego, 2007

P6: Priestley, M.J.N. and Park, R. "Strength and Ductility of RC Bridge Columns under Seismic Loading", *ACI Journal*, Vol. 84(1), 1987, pp 285-336

P7:   Panagiatakos, T.B. and Fardis, M.N., "Deformation-controlled Earthquake Resistant Design of RC Buildings", *Journal of Earthquake Engineering*, Vol. 3(4), pp 498-518

P8:   Priestley, M.J.N., "Myths and Fallacies in Earthquake Engineering – Conflicts between Design and Reality", *Bulletin NZSEE*, Vol. 26(3), 1993, pp 329-341

P9:   Priestley, M.J.N., "Performance Based Seismic Design", *Keynote Address, 12th World Conference on Earthquake Engineering*, Auckland, 2000, paper No. 2831

P10:   Priestley, M.J.N., "Displacement-based seismic assessment of reinforced concrete buildings", *Journal of Earthquake Engineering*, Vol. 1, No. 1, 1997, pp 157-192

P11:   Priestley, M.J.N. and Kowalsky, M.J., "Direct Displacement-Based Seismic Design of Concrete Buildings", *Bulletin, NZSEE*, Vol. 33(4), 2000, pp 421-444

P12:   Paulay, T., "A Behaviour-based Design Approach to Earthquake-induced Torsion in Ductile Buildings", *Proceedings, Workshop on Seismic Design Methodologies for the Next Generation of Codes*, Bled, Slovenia, 1997, pp 59-68

P13:   Paulay, T., "Some Design Principles Relevant to Torsional Phenomena in Ductile Buildings", *Journal of Earthquake Engineering*, Vol. 5(3), 2001, pp 273-308

P14:   Pampanin, S., Christopoulos, C. and Priestley, M.J.N., *Residual Deformations in the Performance-based Seismic Assessment of Frame Structures*, ROSE Research Report No. 2002/02, IUSS Press, Pavia, 2002, 203 pp

P15:   Pinto, P.E. (Editor), *Seismic Design of RC Structures for controlled inelastic response*, CEB Bulletin No. 236, Comité Euro-International du Béton, Lausanne, Switzerland, 1997, 204 pp

P16:   Priestley, M.J.N. and Grant, D.N., "Viscous Damping in Seismic Design and Analysis", *Journal of Earthquake Engineering*, Vol. 9(SP2), 2005, pp 229-255

P17:   Pettinga, J.D. and Priestley, M.J.N., *Dynamic Behaviour of Reinforced Concrete Frames Designed with Direct Displacement-Based Design*, ROSE Research Report No. 2005/02, IUSS Press, Pavia, 2005, 154 pp

P18:   Priestley, M.J.N. and MacRae, G.A., "Seismic Tests of Precast Beam-to-Column Joint Subassemblages with Unbonded Tendons", *PCI Journal*, Vol. 41(1), 1996, pp 64-82

P19:   Priestley, M.J.N., Sritharan.S., Conley, J.R. and Pampanin, S., "Preliminary Results and Conclusions from the PRESSS Five-story Precast Concrete Test Building", *PCI Journal*, Vol.44(6), 1999, pp 42-67

P20:   Priestley, M.J.N. and Tao, J.T., "Seismic Response of Precast Prestressed Concrete frames with Partially Debonded Tendons", *PCI Journal*, Vol. 38(1), 1993, pp 58-69

P21:   Priestley, M.J.N. and Kowalsky, M.J., "Aspects of Drift and Ductility Capacity of Rectangular Cantilever Structural Walls", *Bulletin NZNSEE*, Vol. 31(2), 1998, pp 73-85

P22:   Priestley, M.J.N., "Brief Comments on Elastic Flexibility of Reinforced Concrete Frames, and Significance to Seismic Design", *Bulletin NZSEE*, Vol. 31(4), 1998, pp 246-259

P23:   Priestley, M.J.N., "Seismic behaviour of Unreinforced Masonry Walls", *Bulletin NZNSEE*, Vol. 18(2), pp 191-205

P24: Paret, T.F., Sasaki, K.K., Elibeck, D.K. and Freeman, S.A., "Approximate inelastic procedures to identify failure mechanism from higher mode effects", *Proceedings, 11th World Conference on Earthquake Engineering*, Acapulco, Mexico, 1996, Paper No. 966

P25: Pinho, R. and Antoniou, S., "A displacement-based adaptive pushover algorithm for assessment of vertically irregular frames," *Proceedings, 4th European Workshop on the Seismic Behaviour of Irregular and Complex Structures*, Thessaloniki, Greece, 2005.

P26: Paulay, T., "Some Design Principles Relevant to Torsional Phenomena in Ductile Buildings", *Journal of Earthquake Engineering*, Vol. 5(3), 2001, pp 273-308

P27: Paulay, T., "The Displacement Capacity of Reinforced Concrete Coupled Walls", *Engineering Structures*, Vol. 24, 2002, pp 1165-1175

P28: Paulay, T., "Diagonally Reinforced Coupling Beams of Shear Walls", *ACI Special Publication SP-42*, 1972, pp 579-98

P29: Paulay, T., "A Displacement-Focused Seismic Design of Mixed Building Systems", *Earthquake Spectra*, V. 18(4), 2002, pp 689-718

P30: Pinto, P.E., Giannini, R. and Franchin, P., *Seismic Reliability Analysis of Structures*, IUSS Press, Pavia, 2004, 370pp

P31: Park, R. and Paulay, T., *Reinforced Concrete Structures, Wiley*, 1976, 800 pp

P32: Priestley, M.J.N. and Calvi, G.M., "Direct Displacement-Based Seismic Design of Bridges", *Proceedings, ACI Special Seminar on Seismic Design of Bridges*, San Diego, 2003

P33: Priestley, M.J.N., "Displacement-Based Seismic Assessment of Existing Reinforced Concrete buildings", *Proceedings, Pacific Conference on Earthquake Engineering*, Waireke 1995, pp 225-244

P34: Palermo, A., Pampanin, S., Fragiacomo, M., Buchanan, A.H. and Deam, B.L., "Innovative Seismic Solutions for Multi-Storey LVL Timber Buildings", *Proceedings, World Conference on Timber Engineering*, Portland, 2006

P35: Pecker, A. and Teyssandier, J.P., "Seismic design for the foundation of the Rion-Antirion Bridge", *Proceedings, Institution of Civil Engineers, Geotechnical Engineering*, Telford, London, 1998, vol. 131(1), pp 4-11

P36: Palermo, A., Pampanin S. and Calvi G.M., "Concept and development of hybrid solutions for seismic resistant bridge systems", *Journal of Earthquake Engineering*, Vol. 9(6), 2005, pp 899-921

P37: Popov, E.P. and Engelhardt, M.D., "Seismic Eccentrically Braced Frames", *Journal of Consructional Steel Research*, Vol. 10, 1988, pp 321-354

P38: Priestley, M.J.N., *POLA Berth 400. Dynamic Analyses of Linked Wharf Segments*, Report 99/01, Seqad Consulting Engineers, Solana Beach, 1999

P39: Priestley, M.J.N., *Report to POLA on Crane/Wharf Interaction, Berth 100*, Report, Priestley Structural Engineering, Christchurch, 2005

P40: POLA, *Code for Seismic Design, Upgrading and Repair of Container Wharves*, Port of Los Angeles, San Pedro, 2004

P41: POLA, *Resource Document in Support of POLA seismic Design Code for Container Wharves* Port of Los Angeles, San Pedro, CA, 2007 (in press)

P42: Priestley M.J.N., *Pier 400: Strength and Ductility of Wharf Piles*, Report No. 00/01, Seqad Consulting Engineers, Solana Beach, 2000

P43: Priestley, M.J.N., Calvi, G.M., Petrini L. and Maggi, C., "Effects of damping modelling on results of time history analysis", *Proceedings, 1st US Italy Workshop on Seismic Design of Bridges*, Pavia, Italy, 2007

P44: Pettinga, J.D. and Priestley, M.J.N., *Accounting for P-Delta Effects in Structures when using Direct Displacement-Based Design*, ROSE Research Report 2007/02, IUSS Press, Pavia, Italy, 2007, 85 pp

R1:   Ranzo, G. and Priestley, M.J.N., *Seismic Performance of Circular Hollow Columns Subjected to High Shear*, Report SSRP 2001/01 University of Calif. San Diego, 2001, 215 pp

R2:   Rodriguez, M.E., Restrepo, J.I. and Carr, A.J., "Earthquake Induced Floor Accelerations in Buildings", *Earthquake Engineering and Structural Dynamics*, Vol.31, 2002, pp 693-718

R3:   Robinson, W.H., "Lead-Rubber Hysteretic Bearings Suitable for Protecting Structures During Earthquakes", *Earthquake Engineering and Structural Dynamics*, Vol. 10, 1982, pp 593-604

S1:   Structural Engineers Association of California, *Recommended Lateral Force Requirements and Commentary, 7th Edition*, SEAOC, Sacramento, CA, USA, 1999

S2:   Shibata, A. and Sozen, M., "Substitute Structure Method for Seismic Design in Reinforced Concrete", *ASCE Journal of Structural Engineering*, Vol. 102(1), 1976, pp 1-18

S3:   Sullivan, T.J., Priestley, M.J.N. and Calvi, G.M., *Seismic Design of Frame-Wall Structures*, ROSE Research Report No. 2006/02, IUSS Press, Pavia, 2006, 333 pp

S4:   Suarez, V. and Kowalsky, M.J., "Direct Displacement-Based Seismic Design of Drilled Shaft Bents with Soil-Structure Interaction", *Journal of Earthquake Engineering*, 2007 (in press)

S5:   Somerville, P.G., Graves, R.W., Day, S.M., and Olsen, K.B., "Ground Motion Environment of the Los Angeles Region", *Proceedings of the 2006 Annual Meeting of the Los Angeles Structural Design Council*, USC, Los Angeles, 2006

S6:   Somerville, P.G., Smith, N.F., Graves, R.G. and Abrahamson, N.A., "Modification of Empirical Strong Ground Motion Attenuation Relations to include Amplitude and Duration Effects of Rupture Directivity", *Seismological Research Letters*, Vol. 68, 1997, pp 199-222

S7:   Shearer, P.M., *Introduction to Seismology*, Cambridge University Press, 1999, 260 pp

S8:   Skinner, R.G., Robinson, W.H. and McVerry, G.H., *An Introduction to Seismic Isolation*, Wiley, New York, 1993, 376 pp

S9:   Sritharan, S. and Priestley, M.J.N., *Seismic Testing of a Full-Scale Pile-Deck Connection Utilizing Headed Reinforcement*, Report TR98/14, University of California, San Diego, 1998, 34 pp

S10: Suarez, L.E. and Montejo, L.A., "Generation of artificial earthquakes via the wavelet transform", *International Journal of Solids and Structures*, Vol. 42, 2005, pp 5905-5919

S11: SeismoSoft, *SeismoStruct - A computer program for static and dynamic nonlinear analysis of framed structures*, available from URL: http://www.seismosoft.com, 2007

T1: Tomaževič, M., *Earthquake-resistant design of masonry buildings*, Series on Innovation in Structures and Construction, Vol. 1, Imperial College Press, London, 1999

W1: Wong, P.K.C., Priestley, M.J.N. and Park, R., "Seismic Performance of Frames with Vertically Distributed Longitudinal Reinforcement in Beams", *ACI Journal*, Vol. 87(4), 1990, pp 488-498

X1: NZS 1170.5: 2004, *Structural Design Actions – Part 5 – Earthquake Actions*, New Zealand, 2004, 74 pp (text), 80 pp (commentary)

X2: Applied Technology Council, *ATC-32: Improved Seismic Design Criteria for California Bridges: Provisional Recommendations* and *Resource Document*, Redwood City, CA, 1996, 256 and 365 pp

X3: Comité Européen de Normalisation, *Eurocode 8, Design of Structures for Earthquake Resistance - Part 1: General Rules, Seismic Actions and Rules for Buildings*, prEN 1998-1, CEN, Brussels, Belgium, 1998

X4: International Code Council, *International Building Code*, Thomson Delmar Learning, 2006, pp. 663

X5: International Conference of Building Officials (ICBO), *1997 Uniform Building Code*, Vol. 2, 1997, Whittier, CA, 574 pp

X6: NZS 3101: 1992, *Concrete Structures Standard - Part 1 (Code) and Part 2 (Commentary)*, Standards New Zealand, 1992

X7: American Concrete Institute, *ACI 318-05 Building Code Requirements for Structural Concrete and Commentary*, Farmington Hills, MI, 2005, 430 pp

X8: Federal Emergency Management Agency, *NEHRP Commentary on the Guidelines for the Seismic Rehabilitation of Buildings: FEMA 274*, Washington, 1997, 492 pp

X9: Comité Européen de Normalisation, *Eurocode 8, Design of Structures for Earthquake Resistance - Part 1: General Rules, Seismic Actions and Rules for Buildings*, EN 1998-1, CEN, Brussels, Belgium, 2004, 222 pp

X10: Federal Emergency Management Agency, *Prestandard and commentary for the seismic rehabilitation of buildings*, FEMA 356, Washington, D.C., 2005

X11: NZSEE, *Assessment and Improvement of the Structural performance of earthquake risk buildings: draft for general release*, NZSEE, Wellington, New Zealand, 2006, 122 pp

X12: PIANC, *Seismic Design Guidelines for Port Structures*, International Navigation Association, Balkema, Lise, 2001, 474 pp

X13: AASHTO HB-17, *Standard Specifications for Highway Bridges*, 17th Edition, American Association of State and Highway Transportation Officials, USA, 2002, 1028 pp

X14: OPCM 3519/2006, *Criteri per l'individuazione delle zone sismiche e per la formazione e l'aggiornamento degli elenchi delle medesime zone*, G.U. No. 108, Rome, Italy, 2006 (in Italian)

X15: Xu, Y.L., Qu, W.L. and Ko J.M., "Seismic response control of frame structures using Magnetorheological/ Electrorheological dampers", *Earthquake Engineering and Structural Dynamics*, Vol. 29, 2000, pp 557-575

X16:   Comité Européen de Normalisation, *Eurocode 8, Design of Structures for Earthquake Resistance - Part 3: Strengthening and repair of buildings*, EN 1998-3, CEN, Brussels, Belgium, 2005

X17:   OPCM 3274/2003 and 3431/2005, *Primi elementi in materia di criteri generali per la classificazione sismica del territorio nazionale e di normative tecniche per le costruzioni in zona sismica*, G.U. No. 105 and G.U. No. 107, Rome, Italy, 2003 and 2005 (in Italian)

Z1:   Zonta, D., Piazza, M., Zanon, P. and Giuliani, G. "An Application of Direct Displacement Based Design to Glulam Timber Portal-Frame Structures", *Proceedings, 1ˢᵗ European Conference on Earthquake Engineering and Seismology*, Geneva, Switzerland, 2006, paper 932

Z2:   Zayas, V., Low, S.S. and Mahin, S.A., "A Simple Pendulum Technique for Achieving Seismic Isolation", *Earthquake Spectra*, Vol. 6(2), 1990, pp 317-333

SYMBOLS LIST

A_e	effective shear area of cracked section
A_h	area without full cycle of stabilized force-displacement response
A_b; A_h	spiral or hoop bar cross-sectional area
A_g	gross section area
A_r	wall aspect ratio, measured at roof level
A_S	area of tension reinforcement in concrete section
A_s	effective shear area of uncracked section
A_{sh}	area of transverse reinforcement in section perpendicular to direction considered
A_{st}	total area of reinforcing steel in concrete or masonry section
A_w	shear reinforcement in masonry wall
a	depth of flexural compression zone; acceleration
$a_{(t)}$	period-dependent acceleration from response spectrum
B	width of building plan
B_F	width of footing
b	section width
b_w	width of web of flanged beam
C	constant
C_M	centre of mass
C_R	centre of rigidity in torsional response calculations
C_S	coefficient applied to peak response displacement for different soils
C_V	centre of shear strength in torsional response calculations
C_T	basic seismic coefficient
c	distance from extreme compression fibre to neutral axis
D	diameter of circular section
D'	diameter of confined core, to centreline of hoop or spiral
d	effective depth of section to centroid of tension reinforcement
d_{bl}	reinforcing bar diameter
E	modulus of elasticity
E	force induced by seismic action
E^0	overstrength force induced by seismic action
E_c	concrete modulus of elasticity

703

E_m masonry modulus of elasticity
E_s steel modulus of elasticity
E_{sec} secant modulus of elasticity of confined concrete at peak strength
e eccentricity between centre-of-mass and centre of effective stiffness
e_R rigidity eccentricity in torsional response calculations
e_V strength eccentricity in torsional response calculations
F force
F_D damping force
F_{el} seismic force corresponding to elastic spectrum
F_m maximum force
F_P axial force in member from prestressing
F_R seismic force reduced from elastic spectrum by force-reduction factor
F_y yield force
f'_c specified (28 day) concrete compression strength
f'_{cc} compression strength of confined concrete
f'_{ce} expected compression strength for DDBD
f'_{co} maximum feasible concrete compression strength
f'_{mc} masonry compression strength
f_{pu} specified prestressing steel ultimate strength
f_{pue} expected prestressing steel ultimate strength
f_t tension strength
f'_y specified minimum or characteristic yield strength of steel
f'_{ye} expected yield strength of steel for DDBD
f_{yh} yield strength of hoop or spiral transverse reinforcement
f_{yo} maximum feasible steel strength
f_u steel ultimate stress
G shear modulus; gravity load
G_L shear modulus of lead, in lead-rubber bearing
G_m masonry shear modulus
g acceleration due to gravity, 9.805m/s
H height
H_c column height
H_{CF} height of wall contraflexure in coupled wall or dual wall/frame building
H_{CP} height from contraflexure point to deck soffit in bridge design
H_e effective height of SDOF approximation to multi-storey building
H_F height of footing
H_{IG} height from in-ground plastic hinge to superstructure
H_i height of mass i in building design
H_o height to contraflexure in masonry wall
H_n height of building to roof level
H_S storey height

h	section depth
h_b	beam section depth
h_c	column section depth
h_D	height of isolating or damping device
h_{CB}	height of coupling beam in coupled wall design
h_{SS}	depth of bridge superstructure
I	importance factor in force-based design; section moment of inertia
I	multiplier applied to design seismic intensity level
I_b	moment of inertia of beam section
I_c	moment of inertia of column section
I_{cr}	moment of inertia of cracked concrete section
I_{gross}	moment of inertia of un-cracked concrete section
I_{SS}	moment of inertia of bridge superstructure
J_R	rotational stiffness
$J_{R,\mu}$	rotational stiffness for ductile response
$J_{R,eff}$	effective rotational stiffness at design response displacement
K	structure stiffness
K_A	assessed structure stiffness at limit state
K_e	structure effective stiffness for DDBD
K_i	initial (elastic) stiffness
K_{LR}	lateral stiffness of lead-rubber bearing
K_p	lateral stiffness of friction-pendulum isolator
K_R	lateral stiffness of rubber bearing
K_s	structure secant stiffness
K_z	axial stiffness of bearing
K_θ	foundation elastic rotational stiffness
k	element stiffness
k	constant dependent on steel properties for strain penetration (Eq.(4.31a))
k	bulk modulus of rubber
k_i	initial (elastic) stiffness, including effects of cracking
k_s	shear stiffness
k_t	instantaneous tangent stiffness
k_V	vertical subgrade modulus for foundation flexibility calculations
L	length
L_b	beam length
L_C	distance from critical section to contraflexure point
L_D	length of damper coupling adjacent walls
L_{CB}	length of coupling beam in coupled wall design
L_P	plastic hinge length
L_{SP}	strain penetration length
L_{SS}	bridge superstructure span length

l_w	wall length
M	moment
M^*	dimensionless moment (Eq.(12.7))
M_B	beam moment
M_{CD}	design moment of column of two-way frame in diagonal direction
M_{cr}	cracking moment of concrete or masonry section
M_D	design base moment; also dead-load moment
M_{des}	design moment
M_E	base moment resulting from elastic acceleration response spectrum
M_G	moment caused by gravity load
M_L	live load moment
M_{MMS}	moment from modified modal superposition approach (Section 6.6.1)
M_N	nominal moment capacity
M_p; M_P	section plastic moment capacity
M_T	torsional moment
M_W	earthquake moment magnitude
M_u	ultimate moment
N	axial force on section (also P)
N_{sd}	normal force acting on bearing
m	mass
m_e	effective mass participating in the fundamental mode
n	number of storeys in multi-storey building
OTM	overturning moment
P	axial force on section (also N)
P^*	axial load ratio
$p_{b,u}$	ultimate soil bearing strength (also p_u)
PGA	peak ground acceleration
R	force-reduction factor applied to elastic spectrum in force-based design
R	reaction force
R_c	radius of curvature of friction-pendulum isolator
R_D	reaction force resulting from design-level actions
R^o	reaction force resulting from overstrength-level actions
R_ξ	reduction factor applied to displacement spectrum for damping ξ
R_μ	force-reduction factor related to ductility
RS	relative superstructure/pier stiffness ratio in bridge response
R_t	force restraining uplift in rocking wall design
r	ratio of post-yield to initial stiffness in bilinear approximation
r	distance to fault plane in km.
S	strength; shape factor
$S_{A(T)}$	period-dependent response acceleration coefficient from response spectrum
S_D	design strength

SE	strain energy
S_E	strength from design vector of lateral forces
S_{out}	out-of-plane amplification factor related to structure response period
S_R	required dependable strength
s	spacing along member axis of transverse reinforcement
T	period
T	seismic tension force in column of frame
T_B	period at end of maximum spectral response acceleration plateau
T_C	corner period in displacement response spectrum
T_e	effective period for DDBD
T_{eD}	effective period in diagonal direction
T_{eP}	effective period in principal direction
T_i	initial total tension force in prestressed section
T_{out}	period of out-of-plane response of wall
t	width of wall section; distance between adjacent plates in elastomeric bearing design
V	shear force; shear strength
V_{Base}	base shear force
V_{Bi}	seismic shear force in beam of frame at level i
V_C	shear strength from concrete shear-resisting mechanisms
V_C	column shear force
V_{CB}	shear force in coupling beam
V_{CD}	design shear force in column of two-way frame in diagonal direction
V_{cap}	total shear strength of section
V_{des}	design (dependable) shear strength of member
V_E	shear force in member corresponding to design lateral force vector
V_F	shear force carried by frame is dual wall-frame building
V_{MMS}	shear force from modified modal superposition approach (Section 6.6.1)
V_y	yield shear force
V_W	shear force carried by wall
V_u	ultimate shear force
v	velocity
Δ_w	wall displacement
V_I	inertia force
V_i	storey shear at level i
V_N	nominal shear strength
V^0	overstrength shear force
V_P	shear strength from axial force mechanisms
V_p	shear strength of link member in EBF
V_S	shear strength from transverse reinforcement mechanisms
V_{sk}	shear force in shear key between wharf segments

V_Δ	shear force at displacement Δ
W	weight
W_F	footing weight
W_S	superstructure weight transferred to pier in bridge design
W_s	weight transferred to wall from slab at one level
W_W	weight, including self-weight, supported at base of wall
w_m	masonry unit weight
Z	site zone seismic intensity factor
Z_p	section plastic modulus
α	mass-proportional coefficient for Rayleigh damping
α	exponent in damping displacement-reduction equation (Eq.(2.8))
α	factor for aspect ratio in shear strength determination (Eq.(4.72a)
α	unloading stiffness factor in modified Takeda hysteresis rule
α	wall length ratio in torsion design
α	angle of reinforcement to member axis in diagonally reinforced beam
α	exponent to velocity in viscous damper design (Eq.(11.36))
β	force-ratio in flag-shaped hysteresis rule (see Fig.3.9(f))
β	stiffness-proportional coefficient in Rayleigh damping
β	factor for longitudinal reinforcement ratio in shear strength calculations
β	reloading factor in modified Takeda hysteresis rule
β_{CB}	proportion of structure OTM carried by coupling beams in coupled walls
β_D	proportion of structure OTM carried by dampers in coupled walls
β_F	proportion of total building shear force carried by frame in dual wall-frame building
γ	factor for curvature ductility in shear strength calculations (Fig.4.22)
γ	link yield rotation in EBF analysis
γ	allowable shear strain in bearing design
Δ	displacement
Δ_a	assessed displacement capacity
Δ_B	bearing displacement
Δ_C	design displacement at critical mass (Eq.(3.27))
Δ_{cap}	displacement capacity
Δ_{CM}	displacement at centre of mass
Δ_{code}	displacement capacity required to satisfy code requirements, in assessment
Δ_{cr}	cracking displacement; critical displacement
Δ_d, Δ_D	design displacement
Δ_{dem}	displacement demand
Δ_{el}	elastic displacement
Δ_f	displacement resulting from foundation flexibility

$\Delta_{f,N}$	flexural deformation at nominal strength
Δ_i	displacement at mass i
Δ_{ls}; Δ_{LS}	limit-state displacement
Δ_{max}	maximum displacement
Δ_n	Displacement at roof level in building design
$\Delta_{(T)}$	period-dependent displacement
Δ_P	variation in axial force
Δ_p	plastic displacement
Δ_{PG}	peak ground displacement in earthquake
Δ_s	structural component of displacement
Δ_s	shear deformation
ΔT	isolator temperature increase under simulated seismic response
Δ_y	Yield displacement
Δ_u	ultimate displacement
$\Delta_{u,w}$	ultimate displacement for out-of-plane masonry wall response
Δ_w	wall displacement
δ_c	value of dimensionless inelastic mode shape at critical mass (Eq.(3.27))
$\delta_{el,i}$	dimensionless elastic mode shape at mass i
δ_i	dimensionless inelastic mode shape at mass i
δ_{max}	peak response displacement in response spectrum
ε	strain
ε_c	concrete strain
$\varepsilon_{c,s}$	spalling (serviceability limit) strain for concrete or masonry
ε_{cm}	ultimate compression strain of unreinforced masonry
ε_{cu}	ultimate concrete strain (damage control limit state) defined by Eq.(4.21)
ε_{sh}	steel strain at onset of strain-hardening
ε_{smc}	strain at peak stress of confining reinforcement in wharf design
ε_{smd}	strain at peak stress of dowel reinforcement in wharf design
ε_{su}	steel strain at ultimate strength
ε_y	yield strain of steel
$\Phi_{c(e)}$	concrete stress-strain relationship
$\Phi_{s(e)}$	steel stress-strain relationship
ϕ	curvature; strength or displacement reduction factor; friction angle
ϕ_{cr}	curvature at cracking of concrete or masonry section
ϕ_{dc}	damage-control limit-state curvature
ϕ_D; ϕ^*	dimensionless curvature
ϕ_{Dy}	dimensionless yield curvature
ϕ_Δ	displacement reduction factor

ϕ_f	flexural strength reduction factor
ϕ_{ls}	limit-state curvature
ϕ^o	overstrength factor relating maximum feasible flexural strength to design strength
ϕ_p	plastic curvature
ϕ_S	strength reduction factor related to action S
ϕ_s	shear strength reduction factor
ϕ_s	serviceability limit-state curvature
ϕ_y	yield curvature of bilinear approximation to moment-curvature curve
ϕ'_y	curvature at first yield of reinforcing steel, or compression strain of 0.002
ϕ_u	ultimate curvature
κ	constant used in effective damping equations
λ	wall strength ratio in torsion analysis (p330)
μ	ductility factor; friction factor
μ_b	beam displacement (or rotational) ductility factor
μ_D	displacement ductility in diagonal direction
μ^o	displacement ductility factor for overstrength response
$\mu_d; \mu_f$	friction factor
μ_P	displacement ductility in principal direction
μ_{sys}	structure displacement ductility factor
μ_Δ	displacement ductility factor
μ_ϕ	curvature ductility factor
μ_{mc}	friction factor in unreinforced masonry design
θ	rotation; drift angle (displacement/height); angle
θ_{CB}	coupling beam rotation
θ_y	yield drift of frame
θ_Δ	stability index in **P-Δ** design
θ_N	nominal torsional rotation
θ_y	yield drift
ξ	viscous damping ratio
ξ^*	modified damping ratio for tangent-stiffness modelling in Rayleigh damping
ξ_{CB}	equivalent viscous damping of ductile coupling beam
ξ_e	equivalent viscous damping ratio for DDBD
ξ_{el}	viscous damping ratio in elastic range of material response
ξ_{eq}	equivalent viscous damping ratio
ξ_{out}	equivalent viscous damping associated with out-of-plane masonry wall response
ξ_f	foundation damping ratio
ξ_{hyst}	hysteretic component of equivalent viscous damping ratio for DDBD

ξ_P equivalent viscous damping for a pile/column (Section 10.3.5(c))

ρ_a area ratio of transverse reinforcement in section

ρ_l longitudinal reinforcement ratio in concrete or masonry section

ρ_v volumetric ratio of transverse reinforcement

ω dynamic amplification factor for higher-mode effects; circular frequency

ω_f dynamic amplification factor for flexure.

ω_s dynamic amplification factor for shear

ω_θ higher-mode drift reduction factor for DDBD of frames

ω_V shear dynamic amplification factor

ζ angle between compression strut and member axis in shear design

ABBREVIATIONS USED IN TEXT

BI	bilinear hysteresis rule
CBF	concentrically braced frame
CD	capacity design
CLE	contingency level earthquake (POLA)
D/C	demand/capacity ratio
DDBD	direct displacement-based design
EBF	eccentrically braced frame
EMS	effective modal superposition
EP	elasto-plastic
EPP	elastic/perfectly-plastic
EVD	equivalent viscous damping
ETHA	elastic time-history analysis
FPS	friction-pendulum system
FS	flag-shaped hysteresis rule
GPS	global position system
HDRB	high-damping rubber bearing
I/D	isolator/damper device
ITHA	inelastic time-history analysis
LPG	liquid petroleum gas
MCE	maximum considered earthquake
MDOF	multi degree of freedom
MMS	modified modal superposition
NEHRP	national earthquake hazard reduction program
OLE	operating level earthquake (POLA)
PGA	peak ground acceleration
PGD	peak ground displacement
POLA	port of Los Angeles
PTFE	polytetrafluoroethylene
RO	Ramberg-Osgood hysteresis rule
SDOF	single degree of freedom
SRSS	square root sum of the squares
TF	"fat" Takeda hysteresis rule
TH	time-history

TR   torsionally restrained
TT   "thin" Takeda hysteresis rule
TU   torsionally unrestrained

INDEX

$$R_A + \frac{3}{5}w\ell - \frac{6}{5}w\ell$$

$$\to R_A = \frac{3}{5}w\ell$$

$$\frac{3}{5}w\ell \qquad \frac{3}{5}w\ell$$

$$\frac{3}{25}w\ell^2$$

$$M_A + \left(\frac{3}{5}w\ell\right)\ell - \left(\frac{6}{5}w\ell\right)\frac{3}{5}\ell$$

$$M_A = \frac{18}{25}w\ell^2 - \frac{3}{5}w\ell^2$$

$$\frac{3}{5}w\ell$$

$$\frac{2}{5}w\ell$$

$$V_\eta\, w\ell$$

$$M_A = \frac{3}{25}w\ell^2$$

max deflection $\frac{dy}{dx} = 0$ (slope)

$$\frac{dy}{dx} = \frac{1}{EI}\left(-\frac{9}{25}w\ell^2 \dots + wx^2 + \frac{3}{10}w\ell^2 \dots w\ell^3\right)$$

$$\frac{dy}{dx} = \frac{1}{EI}\left(-\frac{8}{25}w\ell^2 x - \frac{1}{3}wx^3 + \frac{3}{5}w\ell x^2 \dots w\ell^2 \right)$$

$$= \frac{1}{EI}\left(\dots w\ell \dots + \frac{3}{5}w\ell \dots wx^3\right)$$

STRUCTURAL ANALYSIS CD

The accompanying CD-ROM, found inside the back cover, features two stand-alone finite element programs capable of running inelastic time history analysis (**Ruaumoko 2D** and **SeismoStruct**), one program that can be used to carry out monotonic moment-curvature analysis and force-displacement response of reinforced concrete members (**Cumbia**), and a number of design verification examples from chapters 5, 6, 10 and 11.

All three software packages are accompanied with detailed user manuals, and may be freely used for non-commercial applications. Instructions on how to obtain technical support, in those cases where this is available, can also be found in the aforementioned user manuals and/or help systems. It is also noted that the program Ruaumoko 2D is provided in its Educational version, thus featuring a limitation in the size of the models that may be created.

For the design verification examples, in addition to the corresponding input and output program files, brief documents describing the adopted modeling assumptions as well as the attained results can also be found. These complement the information already provided at the end of the chapters to which the examples refer.

The contents of this CD-ROM, as described above, are organized in the following folders:

- Design Verification Examples
  - Design Example 5.4
  - Design Example 10.6
  - Design Example 11.7
  - Design Example 11.8
- Structural Analysis Software
  - Cumbia
  - Ruaumoko 2D – Educational Version
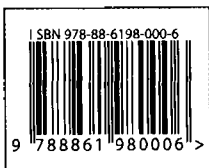 - SeismoStruct v4.0
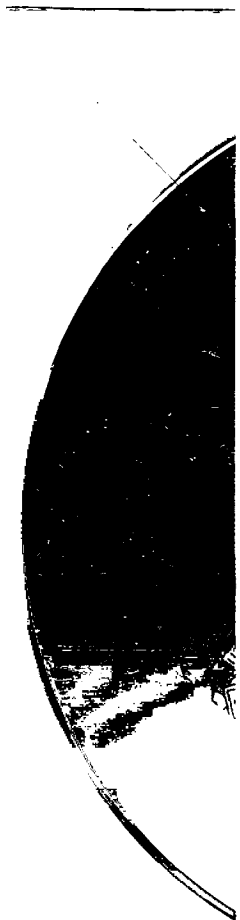
M.J.N. PRIESTLEY

Nigel Priestley is Professor Emeritus of the University of California San Diego, and co-Director of the Centre of Research and Graduate Studies in Earthquake Engineering and Engineering Seismology (ROSE School), Istituto Universitario di Studi Superiori (IUSS), Pavia, Italy. He has published more than 450 papers, mainly on earthquake engineering, and received numerous awards for his research. He holds honorary doctorates from ETH, Zurich, and Cujo, Argentina. He is co-author of two previous seismic design books "Seismic Design of Concrete and Masonry Buildings" and "Seismic Design and Retrofit of Bridges", that are considered standard texts on the subjects.

G.M. CALVI

Michele Calvi is Professor of the University of Pavia and Director of the Centre of Research and Graduate Studies in Earthquake Engineering and Engineering Seismology (ROSE School), Istituto Universitario di Studi Superiori (IUSS) of Pavia. He has published more than 200 papers and is co-author of the book "Seismic Design and Retrofit of Bridges", that is considered a standard text on the subject. He has been involved in important construction projects worldwide, such as the Rion Bridge in Greece and the upgrading of the Bolu Viaduct in Turkey, and is coordinating several international research projects.

M.J. KOWALSKY

Mervyn Kowalsky is Associate Professor of Structural Engineering in the Department of Civil, Construction, and Environmental Engineering at North Carolina State University and a member of the faculty of the ROSE School. His research, which has largely focused on the seismic behaviour of structures, has been supported by the National Science Foundation, the North Carolina and Alaska Departments of Transportation, and several industrial organizations. He is a registered Professional Engineer in North Carolina and an active member of several national and international committees on Performance-Based Seismic Design.

95,00
euro